

---

# **WIND TUNNELS AND EXPERIMENTAL FLUID DYNAMICS RESEARCH**

---

Edited by **Jorge Colman Lerner**  
and **Ulfilas Boldes**

**INTECHWEB.ORG**

## **Wind Tunnels and Experimental Fluid Dynamics Research**

Edited by Jorge Colman Lerner and Ulfilas Boldes

### **Published by InTech**

Janeza Trdine 9, 51000 Rijeka, Croatia

### **Copyright © 2011 InTech**

All chapters are Open Access articles distributed under the Creative Commons Non Commercial Share Alike Attribution 3.0 license, which permits to copy, distribute, transmit, and adapt the work in any medium, so long as the original work is properly cited. After this work has been published by InTech, authors have the right to republish it, in whole or part, in any publication of which they are the author, and to make other personal use of the work. Any republication, referencing or personal use of the work must explicitly identify the original source.

Statements and opinions expressed in the chapters are these of the individual contributors and not necessarily those of the editors or publisher. No responsibility is accepted for the accuracy of information contained in the published articles. The publisher assumes no responsibility for any damage or injury to persons or property arising out of the use of any materials, instructions, methods or ideas contained in the book.

**Publishing Process Manager** Davor Vidic

**Technical Editor** Teodora Smiljanic

**Cover Designer** Jan Hyrat

**Image Copyright** WIANGYA, 2010. Used under license from Shutterstock.com

First published July, 2011

Printed in Croatia

A free online edition of this book is available at [www.intechopen.com](http://www.intechopen.com)

Additional hard copies can be obtained from [orders@intechweb.org](mailto:orders@intechweb.org)

Wind Tunnels and Experimental Fluid Dynamics Research, Edited by Jorge Colman Lerner and Ulfilas Boldes

p. cm.

978-953-307-623-2

**INTECH** OPEN ACCESS  
PUBLISHER

**INTECH** open

**free** online editions of InTech  
Books and Journals can be found at  
**[www.intechopen.com](http://www.intechopen.com)**



---

# Contents

---

**Preface XI**

**Part 1 Wind Tunnel Facilities and Experiments  
in Incompressible Flow 1**

- Chapter 1 **Optimal Processing of Wind Tunnel Measurements  
in View of Stochastic Structural Design of Large  
Flexible Structures 3**  
Nicolas Blaise and Vincent Denoël
- Chapter 2 **Wire Robot Suspension Systems for Wind Tunnels 29**  
Tobias Bruckmann, Christian Sturm and Wildan Lalo
- Chapter 3 **Wind Tunnels for the Study of Particle Transport 51**  
Keld Rømer Rasmussen, Jonathan Peter Merrison and Per Nørnberg
- Chapter 4 **Wind Tunnel Flutter Testing of Composite T-Tail Model  
of a Transport Aircraft with Fuselage Flexibility 75**  
Raja Samikkannu and A. R. Upadhy
- Chapter 5 **Wind Tunnel: A Tool to Test the Flight  
Response to Semiochemicals 89**  
Yooichi Kainoh
- Chapter 6 **Flow Visualization in Wind Tunnels 99**  
Muzafferuddin Mahmood
- Chapter 7 **Components of a Wind Tunnel Balance:  
Design and Calibration 115**  
Miguel A. González, José Miguel Ezquerro,  
Victoria Lapuerta, Ana Laverón and Jacobo Rodríguez
- Chapter 8 **Wind Tunnel ‘Concept of Proof’ Investigations  
in the Development of Novel Fluid Mechanical  
Methodologies and Devices 135**  
N. Findanis and N.A. Ahmed

- Chapter 9 **Air Speed Measurement Standards Using Wind Tunnels 173**  
Sejong Chun
- Chapter 10 **Low Speed Turbulent Boundary Layer Wind Tunnels 197**  
U. Boldes, J. Colman, J. Marañón Di Leo and J.S. Delnero
- Chapter 11 **Wind Tunnels in Engineering Education 235**  
Josué Njock Libii
- Chapter 12 **The Importance of Turbulence in Assessment of Wind Tunnel Flow Quality 261**  
Mojtaba Dehghan Manshadi
- Part 2 Building Dynamics, Flow Control and Fluid Mechanics 279**
- Chapter 13 **The Use of Wind Tunnel Measurements in Building Design 281**  
Dat Duthinh and Emil Simiu
- Chapter 14 **Tall Buildings Under Multidirectional Winds: Response Prediction and Reduction 301**  
Aly Mousaad Aly, Alberto Zasso and Ferruccio Resta
- Chapter 15 **Wind Tunnel Tests on the Horn-Shaped Membrane Roof 325**  
Yuki Nagai, Akira Okada,  
Naoya Miyasato and Masao Saitoh
- Chapter 16 **Sport Aerodynamics: On the Relevance of Aerodynamic Force Modelling Versus Wind Tunnel Testing 349**  
Caroline Barelle
- Chapter 17 **Active and Passive Control of Flow Past a Cavity 369**  
Seiichiro Izawa
- Chapter 18 **Aerodynamic Parameters on a Multisided Cylinder for Fatigue Design 395**  
Byungik Chang
- Chapter 19 **A New Methodology to Preliminary Design Structural Components of Re-Entry and Hypersonic Vehicles 409**  
Michele Ferraiuolo and Oronzio Manca

**Part 3 Aerodynamic Field Measurements  
and Real Full Scale Analysis 427**

- Chapter 20 **A Computer-assisted Wind Load Evaluation System  
for the Design of Cladding of Buildings: A Case Study  
of Spatial Structures 429**

Yasushi Uematsu

- Chapter 21 **Monitoring of Soil Surface under Wind and  
Water Erosion by Photogrammetry 447**

Shigeoki Moritani, Tahei Yamamoto, Henintsoa Andry,  
Mitsuhiro Inoue, Taku Nishimura, Haruyuki Fujimaki,  
Reiji Kimura and Hiroataka Saito

- Chapter 22 **Public Square Design with Snow and Wind  
Simulations Using Wind Tunnel 463**

Tsuyoshi Setoguchi

**Part 4 Turbulent Structure Analysis 479**

- Chapter 23 **The Study of Details Effects in Cycling Aerodynamics:  
Comparison Between Two Different  
Experimental Approaches 481**

Giuseppe Gibertini, Gabriele Campanardi,  
Donato Grassi and Luca Guercilena

- Chapter 24 **Relationships between Large-Scale Coherent Motions  
and Bursting Events in a Turbulent Boundary Layer 493**

Yasuhiko Sakai, Kouji Nagata and Hiroki Suzuki

- Chapter 25 **Wavelet Analysis to Detect Multi-Scale  
Coherent Eddy Structures and Intermittency  
in Turbulent Boundary Layer 509**

Jiang Nan

**Part 5 Wind Tunnels in Compressible Flow 535**

- Chapter 26 **Evaluation of Local Effects of Transitional Knudsen  
Number on Shock Wave Boundary Layer Interactions 537**

R. Votta, G. Ranuzzi, M. Di Clemente, A. Schettino and M. Marini

- Chapter 27 **Investigation on Oblique Shock Wave Control by Surface  
Arc Discharge in a Mach 2.2 Supersonic Wind Tunnel 553**

Yinghong Li and Jian Wang

- Chapter 28 **Investigations of Supersonic Flow  
around a Long Axisymmetric Body 569**

M.R. Heidari, M. Farahani, M.R. Soltani and M. Taeibi-Rahni

- Chapter 29 **SCIROCCO Plasma Wind Tunnel: Synergy between Numerical and Experimental Activities for Tests on Aerospace Structures 585**  
Rosario Borrelli and Adolfo Martucci
- Chapter 30 **Study of Turbulent Supersonic Flow Based on the Optical and Acoustic Measurements 607**  
Viktor Banakh, Dmitri Marakasov,  
Ruvim Tsvyk and Valeri Zapryagaev
- Chapter 31 **Guidance of a Supersonic Projectile by Plasma-Actuation Concept 629**  
Patrick Gnemmi and Christian Rey
- Chapter 32 **Wind Tunnel Experiments for Supersonic Optical-electrical Seeker's Dome Design 661**  
Qun Wei, Hongguang Jia, Ming Xuan and Zhenhai Jiang
- Chapter 33 **Design, Execution and Rebuilding of a Plasma Wind Tunnel Test Compared with an Advanced Infrared Measurement Technique 685**  
Marco Di Clemente, Giuseppe Rufolo,  
Francesco Battista and Adolfo Martucci







---

# Preface

---

The most important fact related with fluid motion is to understand the fluid patterns, and the flow structure - vortices, recirculation zones, high mix regions, poor mix regions, calm regions, to name a few. Moreover, most of the flows have turbulent characteristics and turbulence remains one of the unsolved problems in physics. No one knows how to obtain stochastic solutions to the well-posed set of partial differential equations that govern turbulent flows.

Averaging those non linear equations to obtain statistical quantities always leads to more unknowns than equations, and ad-hoc modeling is then necessary to solve the problem. So, except for a few rare cases, first-principle analytical solutions to the turbulence phenomena are not possible.

During the last years, the trend for describing unsteady turbulent flow problems by means of numerical simulation methodologies, based on basic building blocks like elemental eddies and vortices, has increased. The objective is to achieve more realistic representations of key aspects of the dynamic pattern of the oncoming turbulent structures. These computational models are very dependent upon the quality and amount of experimental data obtained in real flow processes or at least in representative wind tunnel experiments.

Typically, flows exhibit time dependent distinctive flow structures which can be described by an acceptable amount of pattern related simple relations.

The experimentally detected flow patterns of these structures can facilitate the identification of their geometrical and dynamic behavior. Different pattern recognition procedures based on visualizations techniques, PIV velocimetry, conditional sampling, POD and diverse detection algorithms are used to recognize and describe the main flow patterns and their evolution.

It is known that a direct correlation between the instantaneous aerodynamic behavior of wings and bodies interacting with oncoming particular vortex structures cannot be determined with commonly used statistics methods disregarding pattern related aspects of the impinging flow structures. Unsteady aerodynamics should focus on the diverse changing flow-pattern aspects of a flow. During real flow experiences within a given time record, numerous turbulent structures may go by.

In particular aerodynamic problems, the most representative turbulent structures immersed in the oncoming wind must be previously identified in order to reproduce them in wind tunnel experiments. A main objective in unsteady boundary layer wind tunnel aerodynamics is the realistic reproduction of the dynamic response of a body to approaching individual turbulent structures immersed in the oncoming wind. It is a complex problem associated with various space and time scales involved in the flow. For a wing in some cases, a particular vortex structure embedded in the approaching wind producing intense turbulent velocity fluctuations may only enhance instantaneous Reynolds stresses without significant changes in the lift forces.

In the range of high velocity flow, i.e. for Mach number equal or greater than 0.5, the complex phenomena associated with compressible subsonic and transonic flows often requires experimentation. The same holds true for supersonic and hypersonic flows, including the interaction between shocks and compressible boundary layer and boundary layer transition, to mention only a part of the huge compressible phenomena. Researchers developed very good CFD codes in this area of knowledge, but the necessity to perform experiments to validate the numerical results, particularly those related with compression waves, shock waves, isentropic waves, compressible boundary layers, laminar-turbulent transition, hypersonic phenomena remains high and the main tool is the compressible flow wind tunnel, either, transonic, supersonic or hypersonic.

In general, the experimentally detected flow patterns can facilitate the identification of geometrical and dynamic relations. Different pattern recognition procedures based on visualizations techniques, PIV velocimetry, conditional sampling, POD and diverse detection algorithms are used to recognize and describe the main flow patterns and its evolution.

Due to all of the reasons exposed, performing experiments becomes necessary in studying fluid flows. Such experiments can be "in situ", that is, in real situations of the flow and in laboratories, using wind tunnels and any other scientific instrument associated with it, like constant temperature anemometers, PIV equipment pressure systems, balances, etc. At those occasions when performing "in-situ" experiments is not possible, researchers must employ the wind tunnels. But in any case, the experimental part of the work is always essential.

The Editors of this book wish to present the lecturers and researchers worldwide with a set of chapters dealing with realistic and representative experiments in fluids and practical criteria applied by the researchers in one of the essential fluid dynamic and aerodynamic tool - the wind tunnel.

**Dr. Jorge Colman Lerner and Dr. Ulfilas Boldes**

Boundary Layer & Environmental Fluid Dynamics Laboratory, Engineering Faculty,  
National University of La Plata,  
Argentina





# **Part 1**

## **Wind Tunnel Facilities and Experiments in Incompressible Flow**





# Optimal Processing of Wind Tunnel Measurements in View of Stochastic Structural Design of Large Flexible Structures

Nicolas Blaise and Vincent Denoël

*University of Liège, Structural Engineering Division  
Belgium*

## 1. Introduction

Wind loads are decisive for a wide range of structures and must therefore be modeled adequately in a structural design. Some codes and standards provide a general set of design guidelines only for structures with limited dimensions and under the assumption of a dynamic response in the fundamental mode (Eurocode, 1991). As a matter of fact, very large and flexible structures as, bridges and stadiums, do not fall within the context of application of such simplified procedures. One reason is that large flexible structures may evince a serious sensitivity to the random gust loading, although being stiff enough to limit strong aeroelastic phenomena, but flexible enough to allow for a significant dynamic response.

The buffeting analysis of civil structures, i.e. subjected to random pressures due to the fluctuations of the oncoming flow and to the weak interaction of that flow with the windward part of the structure, is typically tackled as a stochastic dynamic analysis. In this view, the usual analysis is performed with a probabilistic description of the wind velocities in the atmospheric boundary layer (local statistical properties as well as spatial coherence), as well as aerodynamic admittances. Based on site-specific and structure-specific data, they allow the determination of the probabilistic description of the loading, namely power spectral densities of (and coherence between) forces resulting from the wind loading at various spots of the structure. A traditional stochastic analysis follows (Clough & Penzien, 1993; Preumont, 1994), for which structural engineers are used to cope with. The well-known decomposition into mean, background and resonant contributions of the wind-induced responses (Davenport, 1961; Holmes, 2007) offers an affordable access to stochastic analysis in the everyday practice. As a ultimate outcome of the structural, extreme values of some structural responses, such as displacements, internal forces or stresses, have to be estimated. They are actually expressed with peak factors, for which there exist various analytical expressions, depending on the properties of the considered random process (Floris & Iseppi, 1998; Rice, 1945).

The wind tunnel testing of large flexible structures is much more realistic than the aforementioned codified procedure since it allows a precise estimation of the time-space distribution of the pressures and the modeling of a number of phenomena as the aerodynamic instabilities and aerodynamic admittance, that are difficult to estimate. Design codes therefore recommend wind tunnel measurements for large structures, with a need to model carefully the wind flow surrounding the construction site. Wind tunnels have been being developed since the 1960's with early contributions from Scanlan, Scruton among others, although the

principles of the similitude and dimensional analysis were awaiting to be applied to wind flows for more than fifteen years (Langhaar, 1951). In the context of random fluctuating pressures, wind tunnels are of course well equipped because they just require the dynamic acquisition of pressures at various locations of the structure under investigation. Even a turbulent flow may be generated with a series of well-known methods in case of fluctuating oncoming flow. Then, a statistical processing (Papoulis, 1965) of the measured pressures should provide the same probabilistic quantities as those that are necessary for the stochastic analysis. Nevertheless, outputs of wind tunnel testing are basically deterministic non repeatable measurements. Starting from this raw data, the structural design can follow different ways depending on the level at which the statistical processing is performed.

In the context of a structural analysis, two extreme data processing may be distinguished.

The first option is a deep analysis and understanding of the pressure field as measured in the wind tunnel, and before any consideration of the dynamic properties of the structure under investigation. Naturally, maps of averages of local pressures as well as their standard deviations or higher statistical moments are the basic output of that kind. Besides, data mining procedures as Karhunen-Loeve decomposition (Loeve, 1977) or the proper orthogonal decomposition (Jolliffe, 2005) offer an interesting way to better understand the air flow around structures. They are also a smart way to compress the data and extract the main information embedded in the acquired signals. In particular, the proper orthogonal decomposition has been widely applied to wind tunnel measurements (Baker, 2000; Best & Holmes, 1983; Bienkiewicz et al., 1993; 1995; Carassale, 2005; Holmes et al., 1997; Solari et al., 2007); more advanced methods such as the normalized proper orthogonal decomposition (Ruan et al., 2006) have also proved to be efficient in understanding wind tunnel measurements. Obviously statistical data such as power spectral densities of wind pressures are also a valuable outcome of the post-processing. Indeed, together with their spatial coherence, the loading information is recast into a format that matches design procedures offered by design standards.

The second possibility is to postpone the statistical treatment after the structural analysis. A deterministic structural analysis is then performed, based on the single acquired pressure histories. In this case, the structure is analyzed with usual tools as the Newmark integration scheme (Clough & Penzien, 1993). The statistical treatment is then limited to the estimation of mean, standard deviation and extreme values of displacements, strains and stresses, more generally of the structural response. It is thus left to the structural engineer, as a part of the structural design.

As a caricature, in these extreme solutions, the statistical processing is therefore left either to wind-tunnel engineers when it concerns the acquired data itself, either to structural engineers when it comes to estimating structural design quantities. In any case, we may deplore -and this is also probability a matter of sharing responsibilities and expertise a limited interaction between both parties.

Furthermore, one may disclose evidences that both the traditional deterministic and stochastic methods discussed as extreme situations before are not robust against the type of structure, loading and details of the measurement procedure. Indeed, the deterministic approach may suffer from inadequate sampling frequencies and consequences thereof, or from additional noise that may hardly be dealt with (Blaise, 2010). On the other hand, a stochastic description of the pressure field itself may result in a poor estimation of the coherence field, whenever crossed statistics between all pressure taps are considered, or from an excessive

data compression, resulting in the inability of representing properly global and local structural responses at the same time.

A wind tunnel is a convenient tool that may be run successfully only if all protagonists agree on what to measure, how to measure and more importantly what to do with the measured signals. In this chapter, we discuss and demonstrate the need to break up the border between them. It is obvious that the optimum situation should lie somewhere between both extremes described before. As a simple example, just the shape of a structure would be sufficient for a wind-tunnel engineer to measure the surrounding air flow as well as wall pressures. The trouble is that if the sampling rate considered for the wind-tunnel testing is not chosen in accordance with the natural frequencies of the structure (a detail typically pertaining to the structural engineer), the subsequent structural design may yield unrealistic results.

According to the philosophy in which design standards have been developed, it appears that the most promising analysis technique, among deterministic or stochastic, is the stochastic one. This assertion is supported by the idea that a deterministic analysis remains a single shot (a sample of a Monte Carlo simulation), while the stochastic approach provides a rational unique probabilistic description. Keeping in mind the objective of finding an optimum level to fit a probabilistic model to wind-tunnel data, and under the constraints that the fitting should be simple and reliable, and also the assumption that it is possible to find a solution involving the joint expertise of wind-tunnel and structural teams, we demonstrate the optimality of the fitting of a probabilistic model to the modal forces. In this document, the benefits of the proposed method are also illustrated and the reasons for which it provides a superior modeling are clearly pointed out.

Some advantages of the stochastic approach over a deterministic one have already been identified, such as the flexibility in pre-processing the measured pressures in order to smoothen their probabilistic description (Blaise et al., 2011). The main point developed in this document consists in investigating and comparing other probabilistic pre-processing methods.

## 2. Post-processing of measured wind pressures

Pressures recorded on a wind-tunnel model represent the time-space distribution of the loads to be considered for a structural design. Owing to the complexity of the air flow around bluff bodies, as encountered in civil engineering applications, a substantial amount of pressure taps have to be used in order to provide an accurate representation of the wind flow. Furthermore, as a result of some frequency scaling that has to be satisfied, typical sampling frequencies expressed in wind-tunnel time scale are such that the true scale 10-min observation window, as required by many standards translates into a massive amount of data. This huge amount of data has to be analyzed in a statistical manner in order to extract the most significant information, to make it therefore understandable, and if possible to suggest the probabilistic properties of the families to which the recorded signals belong.

Indeed, it is commonly agreed that statistics include both the descriptive statistics, precisely aiming at summarizing the recorded data by means of some numerical descriptors, and the inferential statistics consisting in drawing inferences about the population to which the recorded data presumably belong (Casella, 2001). In this latter case, descriptors of the population, referred to as *probabilistic models* in the following are naturally expected to be more representative of the global phenomenology. In other words, two successive wind-tunnel

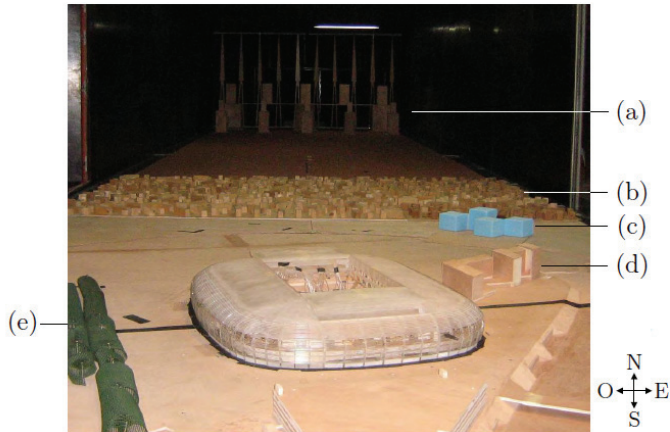


Fig. 1. Model of the stadium in the wind tunnel. (a) View of the exit of the turbine, (b) Block to create the wind velocity profile, (c) and (d) Surrounding buildings, (e) Surrounding woods - also published in: (Blaise et al., 2011)

measurements could provide different descriptive statistics (means, standard deviations, extreme values, etc.), although they belong to the same probabilistic model.

A rudimentary structural design from wind-tunnel recorded pressures may be conducted with only descriptive statistics. This section presents typical steps of such a post-processing. There is no doubt that more global statistics, as those resulting from inferential statistics, related to a population rather than a single sample in the statistical sense, would provide a more robust information about the pressure field over a structure. This more robust information is of marginal importance for means and standard deviations of pressures (which are expected to be reproducible from test to test), but is definitely crucial for extreme values which are most likely much more scattered, from test to test. This idea is developed in Section 3 where we suggest to fit probabilistic models on various quantities measured in the wind-tunnel.

This document is meant to be a treatise on these probabilistic models, rather than the presentation of a particular case study. For convenience, the following sections are however illustrated with the wind-tunnel testing and structural analysis of a stadium roof. This roof features a retractable part resting on two main longitudinal beams, which owned it to be tested for various roof configurations and wind directions. Further details of this particular structural system are given in (Blaise et al., 2011). The simulated wind targets properties of the atmospheric boundary layer, as prescribed in the Eurocodes (Eurocode, 1991) and its French national appendix. Notably, the targeted wind loads correspond to the Service Limit State ones and a IIIa category terrain is appropriate to represent the surrounding of the stadium. The mean velocity recorded at the top of the stadium  $v_m = 28.3 \text{ m/s}$  accurately corresponds to the target value and thus to an expected reference velocity pressure  $q_{mean} = 491.7 \text{ Pa}$ . Figure 1 shows the 1/200 scaled model in the wind tunnel. The velocity and time scales are 1/2.98 and 1/67 respectively. The model is assumed to be infinitely rigid. The surrounding buildings and trees are also modeled to simulate a realistic environment.

The instrumentation of the scaled model required approximately three hundred and fifty synchronous pressure sensors, sampled at 200 Hz, which corresponds to 2.94 Hz in full scale

(or a time step equal to 0.342 seconds). Each measurement lasts about 105 minutes full scale, i.e. approximately ten times as much as the typical conventional requirements, which allows for some statistical treatment.

## 2.1 First rank properties

In a first rank context, pressures  $\mathbf{q}_{tot}(t)$  recorded at different locations in space are regarded as random variables (and therefore independently from their frequency content). They are conveniently separated as

$$\mathbf{q}_{tot} = \boldsymbol{\mu}_q + \mathbf{q} \quad (1)$$

where  $\boldsymbol{\mu}_q$  and  $\mathbf{q}(t)$  respectively denote the mean pressures and (zero-mean) fluctuating parts of the pressure. A suitable dimensionless information is obtained by scaling these pressures by the reference velocity pressure, yielding thus the time-dependent pressure coefficients  $\mathbf{c}_p^{(q,tot)}(t)$  that are straightforwardly decomposed as

$$\mathbf{c}_p^{(q,tot)} = \frac{\boldsymbol{\mu}_q}{q_{mean}} + \frac{\mathbf{q}}{q_{mean}} = \mathbf{c}_p^{(q,mean)} + \mathbf{c}_p^{(q)}. \quad (2)$$

where  $\mathbf{c}_p^{(q,mean)}(t)$  and  $\mathbf{c}_p^{(q)}(t)$  represent the mean and fluctuating part of the total pressure coefficients, respectively. Because it offers a basic understanding of the wind flow around the structure, the analysis of the maps of the mean and the standard deviations of the pressure coefficients is of necessary interest for the wind tunnel engineers as well as the designing engineers. They are illustrated for the considered application in Fig. 2-(a,b), for a wind coming East, as depicted in Fig. 5. It appears that the roof is mainly in depression (with reference to the atmospheric pressure) and that the wind loads are not symmetrically distributed with respect to the axis of the incoming flow, which is explained by the unevenness of the surrounding, see Fig. 1. These figures also illustrate the local increase of mean pressures in zones with sharp edges. For instance, as a consequence of the high longitudinal main beam and an extra acroterium necessary for the moving parts to slide apart, the South-West zone exhibits very close areas with positive and negative pressures; they just result from the air flow trapped against the windward face of the vertical wall and the vortex shedding in the leeward area. Large standard deviations in this area show the substantial intensity of this shedding, and indicate the need for a proper local design of the roof in that area, for that roof configuration and wind direction.

Another interesting information consists in assessing the correlation level of the wind pressures over the whole structure. This is somehow related to the turbulence scale of the oncoming flow (Dyrbye & Hansen, 1997), as well as the signature of the flow created by the structure itself. As an illustration, Figure 2-(c) shows the correlation coefficient of a sensor localized in the center of the stadium (in blue) with all other sensors. Uneventfully, sensors close to the center show important correlation coefficients.

Higher order statistics are other interesting statistical descriptors of the recorded pressures. They are typically interesting when it comes to estimate extreme values, i.e. those related to small occurrence probabilities. For instance, the analysis of the skewness coefficient map indicates the zones of the model where the wind flow is typically non-Gaussian and requires a dedicated attention in the determination of extreme forces (Beirlant et al., 2004; Gupta & van Gelder, 2007). Alternatively, the importance of the extreme wind pressures may be

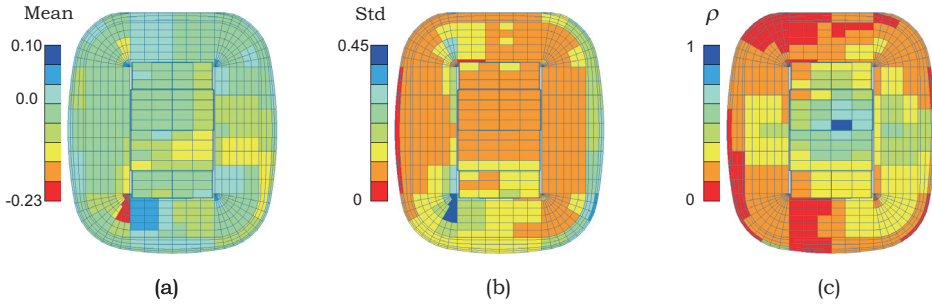


Fig. 2. Maps of (a) the mean pressure coefficients; (b) the standard deviations of pressure coefficients; (c) absolute values of the correlation coefficients of the pressure coefficients with respect to the central sensor.

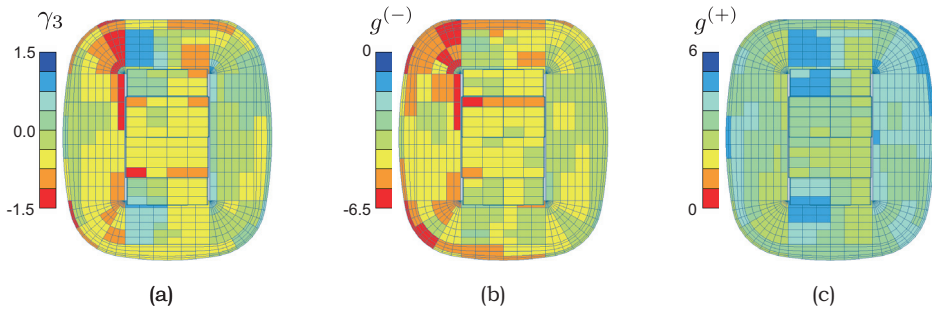


Fig. 3. Maps of (a) the skewness coefficients of the pressure coefficients; (b) the negative peak factors (c); the positive peak factors of the pressure coefficients.

appreciated by means of positive and negative peak factors, defined as

$$g^{(+)} = \frac{q_{max} - \mu_q}{\sigma_q}; \quad g^{(-)} = \frac{\mu_q - q_{min}}{\sigma_q}, \quad (3)$$

which may in some cases drastically drift from the well-know range  $g \in [3.5;4]$  as usually adopted for Gaussian processes. As an illustration, Figure 3-(a) depicts a skewness coefficient ranging from -1.5 to 1.5, which indicates a significant departure from symmetrically distributed variables in several parts of the structure. Also, Figure 3-(b,c) discloses peak factors as large a  $6 \sim 6.5$ , as well as an interesting similarity with the skewness coefficient map. In this case, positive skewness coefficients are associated to positive peak factors larger than the negative ones and vice versa, see for instance Westbound regions, which indicates that extreme pressures are in essence governed by the first three statistical moments. This observation is not universal, but may have decisive consequence, especially because positive skewness coefficients are globally associated to positive mean pressures and reversely.

For conciseness in the following illustrations, eight pressures taps as labeled in Fig. 5-(a) are mainly used. Histograms are another possible way to illustrate the statistical distribution of pressure coefficients. Figure 4-a shows the distribution of the total pressure coefficients in the alongwind direction, with maximum depression on the windward face (sensor 6, see Fig. 5-a) and minimum depression on the leeward face (sensor 4). These histograms indicate a slight

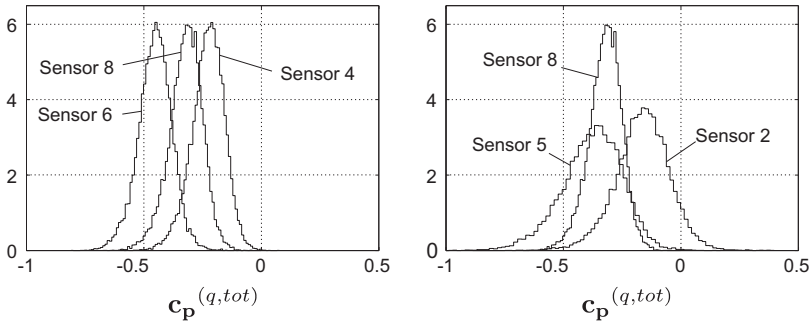


Fig. 4. Histograms of pressure coefficients at sensors 6, 8, 4 in the alongwind direction and sensors 5, 8, 2 in the across-wind direction.

tendency for negative skewing and larger flattening than normal. Similarly, the transverse evolution of the distribution is reported in Fig. 4-b, which shows that pressure coefficients are more spread on the sides than in the central part of the roof. A monotonic increase of the mean depression is however observable; it results from the uneven surrounding.

## 2.2 Second rank properties

Second rank properties describe the possible correlation in the measured pressures at two different instants delayed by a given time lag. As a particular case the auto- and cross-covariance functions translate this correlation for zero-mean weakly stationary processes. An alternative descriptor is the power spectral density (psd) describing the dispatching of the variance or covariance in the frequency domain. Among various parametric and non-parametric estimates, the latter ones are usually preferred in a descriptive stage whilst parametric estimates are the adequate tools to provide appropriate probabilistic models. These are thus discussed in Section 3.

The power spectral density of the fluctuating part of the measured pressures  $\mathbf{S}^{(q)}(\omega)$  indicates the order of magnitude of the frequency content related to turbulence, or a characteristic time scale of shortest eddies. Indeed, in case where no aeroelastic phenomena are expected to take place, the overall profile of this function decreases with frequency, which is attributable to the turbulence. Besides the decrease rate in the high-frequency range allows the identification of the admittance function.

The psd matrix of the measured pressures  $\mathbf{S}^{(q)}(\omega)$  gathers the auto- and cross-psd in the diagonal and out-of-diagonal elements, respectively. The cross-psd  $S_{ij}^{(q)}$  indicates the covariance between pressures measured at different locations, referred to as per  $i$  and  $j$ . The dimensionless coherence function  $\Gamma^{(q)}(\omega)$ , defined as

$$\Gamma_{ij}^{(q)} = \frac{S_{ij}^{(q)}}{\sqrt{S_i^{(q)} S_j^{(q)}}} \quad (4)$$

by scaling the cross-psd by the geometric mean of corresponding auto-psd's, provides a more intuitive information. Notice however that the correlation coefficient  $\rho_{ij}^{(q)}$  is not recovered by integration in the frequency space of  $\Gamma_{ij}^{(q)}$ .

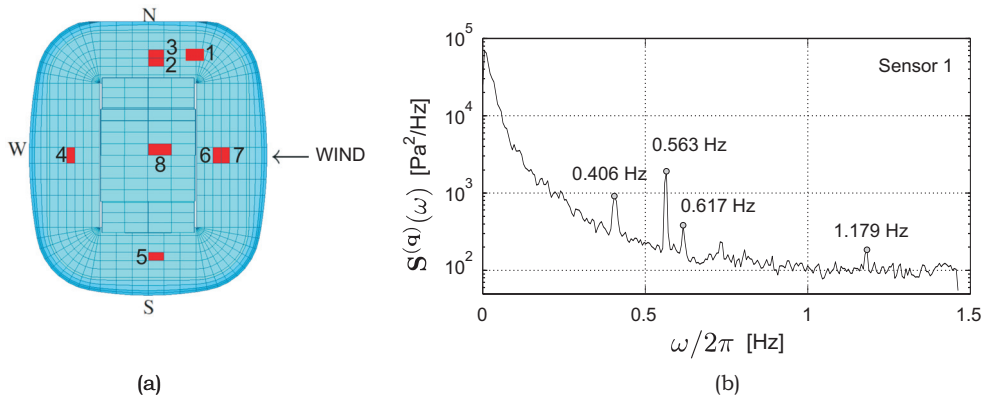


Fig. 5. (a) Localization of some interesting sensors, (b) psd of the measured pressure at sensor 1. Windowing with 512 points out of 18432 in total is used with an overlap of 50%. Noise harmonics may be observed.

Figure 5 shows an example of psd obtained with Welch's periodogram method with Hamming windowing and 50% overlapping, a common choice of non-parametric descriptor. The psd shown in Fig. 5 corresponds to sensor 1. It appears that the recorded pressure, as well as many others actually, is significantly noised by harmonic components. These spurious harmonics may result from aliased rotation speed of flans, a/c power insufficiently filtered, flexibility of the scale model, flexibility of the turning table. In any case, these are undesired (because not realistic) and should be filtered out before the structural design stage. Another possible imperfection in the recorded data appears as a constant psd beyond a certain frequency. This issue is possibly related to some measurement noise, or some insufficiently design pneumatic admittance in the acquisition system. This case was not seriously observed in the considered data set. In the structural design stage, this imperfection may provide an excessive overestimation of the loads in the resonance frequency range.

Figure 6 shows the real and imaginary parts of the coherence functions pairing sensor 7 to sensors 6, 8 and 4, located in the alongwind direction. Although standards usually neglect the imaginary part of the coherence and model the real part as a decreasing exponential (Dyrbye & Hansen, 1997), we may observe that this model (adopted from free field turbulence) is far from reality. The global decrease rather seems to show first a short plateau, then a rapid decrease, followed by a somewhat significant noise. The imaginary part is of the same order of magnitude as the real part. Also Fig. 6 indicates, for both the real and imaginary parts, more coherence between sensors 7 and 6, than 7 and 8, or even than 7 and 4.

Of paramount importance is the fact that the non-parametric estimate of the auto- and cross-psd provides an erratic result, despite the periodogram averaging. Actually an infinite set of pressures are in principle necessary to obtain a smooth non-parametric estimation of the psd. This goes naturally beyond the physical limitations of any testing. As a matter of fact, the processing of a single recorded signal, as long as it may physically be, provides an erratic non-parametric estimate; and the new beginning of another experiment under the "same" conditions would yield a different psd estimate. The discrepancy between both is as large as the signals are short. Furthermore, experience shows that the reproducibility of coherence functions is even worse.



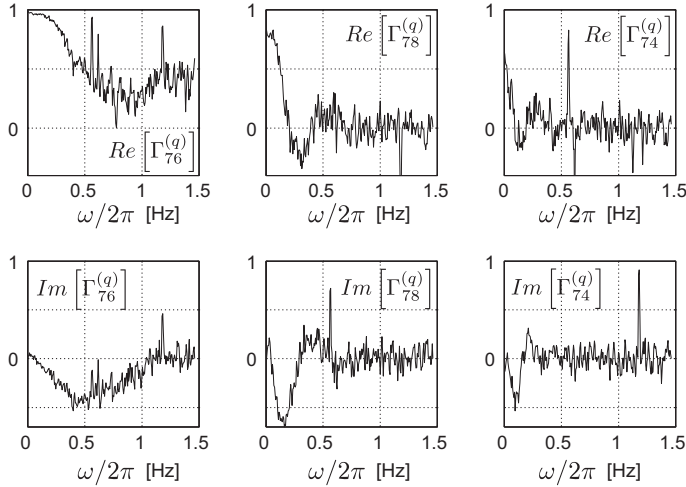


Fig. 6. Real and imaginary parts of the coherence functions of pressures measures at sensor (7,6), (7,8), (7,4). Coherence does not decrease exponentially; it also diminishes with increasing distance between sensors.

### 2.3 Principal component analysis

The principal component analysis is a mathematical procedure that consists in transforming a set of correlated data sets, such as the recorded wind pressures, to uncorrelated principal components. This transformation is made through an orthogonal transformation, which make this procedure to be also appointed proper orthogonal decomposition (Jolliffe, 2005). The transformation is such that the first principal component has a variance as large as possible, and similarly for the subsequent components but under the constraint that they be uncorrelated with the previously established ones. As a result, the computation and storage of the first few principal components may be seen as an interesting data compression means, for all that one is interested in a global representation of the total variance in a data set. Besides, the principal component analysis enables a better understanding of the air flow around the structure, as it just require the analysis of some loading components.

In a first rank context, wind pressures on a large structure may be regarded as correlated variables (without any time or frequency distribution thus), as illustrated in Fig. 2. The principal component analysis of these pressures consists therefore in diagonalizing the (zero lag) covariance matrix  $\mathbf{C}^{(q)}$  as in

$$(\mathbf{C}^{(q)} - \mathbf{C}^{(c)}\mathbf{I})\Theta = 0 \quad (5)$$

and is therefore called *covariance proper transformation (CPT)*, where  $\mathbf{C}^{(c)}$  is the new (diagonal) covariance matrix of principal components, organized with decreasing variances, and  $\Theta$  is the orthogonal transformation matrix gathering in successive columns the principal components of the loading or, more simply, the loading components. As only some principal components are conserved in the post-processing, these matrices are smaller than  $\mathbf{C}^{(q)}$  and satisfy naturally

$$\mathbf{C}^{(q)} = \Theta\mathbf{C}^{(c)}\Theta^T. \quad (6)$$

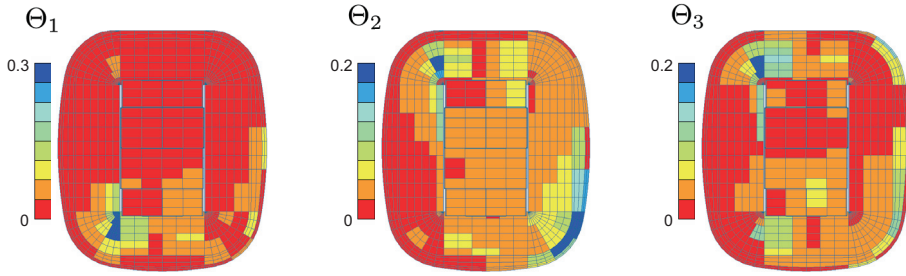


Fig. 7. First three loading components  $\Theta_1$ ,  $\Theta_2$ ,  $\Theta_3$  (in absolute value) extracted from the (zero lag) covariance matrix  $\mathbf{C}^{(q)}$ .

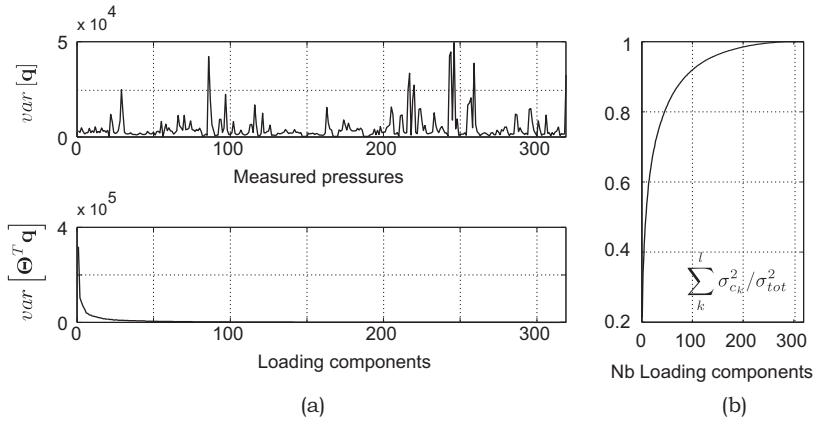


Fig. 8. (a) Variances of the measures pressures  $\mathbf{q}$  as a function of the pressure tap number, and variances of the generalized pressures  $\Theta^T \mathbf{q}$  as a function of the loading component number; (b) Cumulative summation of the variances of principal coordinates  $\mathbf{c}(t)$

Accordingly the set of recorded pressures  $\mathbf{q}(t)$  is decomposed as

$$\mathbf{q} = \Theta \mathbf{c} \quad (7)$$

where  $\mathbf{c}(t)$  represents the covariance principal coordinates, whose covariance matrix is  $\mathbf{C}^{(c)}$ . As an illustration, Fig. 7 represents the first three loading components extracted from the covariance matrix  $\mathbf{C}^{(q)}$ . As expected, the first component outlines pressures in the South-West zone, where the variance of pressures are large. The following modes may also be understood as significant pressures in a very limited portion of the roof surface, and negligible pressures elsewhere. This goes against a naive presumption that fundamental modes represent properly the global loading, which is actually the most interesting one for the determination of the background structural response. A possible solution is offered by the normalized covariance proper transform (Ruan et al., 2006), which consists in giving, in the orthonormalization process, the same importance to all sensors, regardless of their relative variance. The total variance  $\sigma_{tot}^2$  obtained as the summation of the variance of the pressures at each sensor, is non uniformly distributed between sensors, see Fig. 8-b. Conversely, as a consequence of the algorithm for the extraction of successive principal components, the

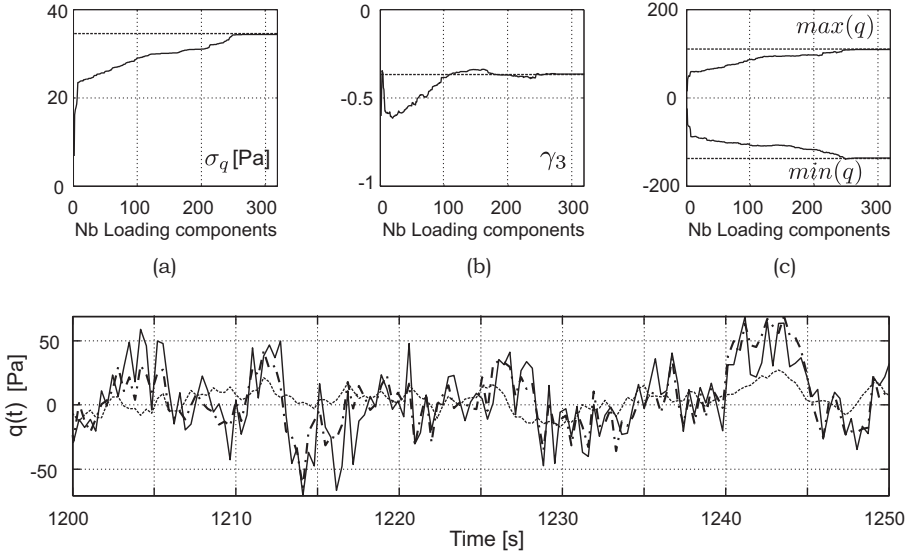


Fig. 9. Evolution of the (a) standard deviation of the measured pressure at sensor 8, (b) the skewness coefficient (c) the extreme values as a function of the number of loading components and (d) reconstruction of the time signal with 5 (dot) and 100 (dash-dot) components.

variance of the generalized pressures obtained by projection into the component basis, expressed as  $\Theta^T \mathbf{q}$ , are successively decreasing. Alternatively, the variance of the principal components  $c(t)$  are ordered with increasing values. Their cumulative distribution, see Fig. 8-a, is therefore monotonic, with negative curvature. This example shows that a substantial number of components (around 100) has to be kept in order to reproduce 90% of the total variance.

Figure 9 shows the reconstruction of the pressure history at the central pressure tap, for increasing numbers of loading components included in the reconstruction. Figure 9-a shows that more than 200 modes are necessary to provide an accurate variance. Figure 9-a shows a monotonic convergence of the reconstructed standard deviation, which is a well-known fact (Carassale et al., 2007). Nothing guarantees however the convergence of the skewness coefficient, which may be eventually problematic for an accurate description of extreme values (whenever skewness is significant). Figure 9-c indicates that extreme values related to the considered sensor are mainly governed by the variance, and not that much by the fluctuation skewness.

A second possible application of principal component analysis, in a second rank context, consists in diagonalizing the psd matrix  $\mathbf{S}^{(q)}(\omega)$ , making therefore uncorrelated the different harmonics. It thus writes

$$(\mathbf{S}^{(q)} - \mathbf{S}^{(y)} \mathbf{I}) \mathbf{\Psi} = 0 \quad (8)$$

and is called *spectral proper transformation (SPT)*, where  $\mathbf{S}^{(y)}(\omega)$  is the psd matrix of the principal coordinates (which is diagonal for every  $\omega$ ) and  $\mathbf{\Psi}(\omega)$  is the orthogonal matrix of

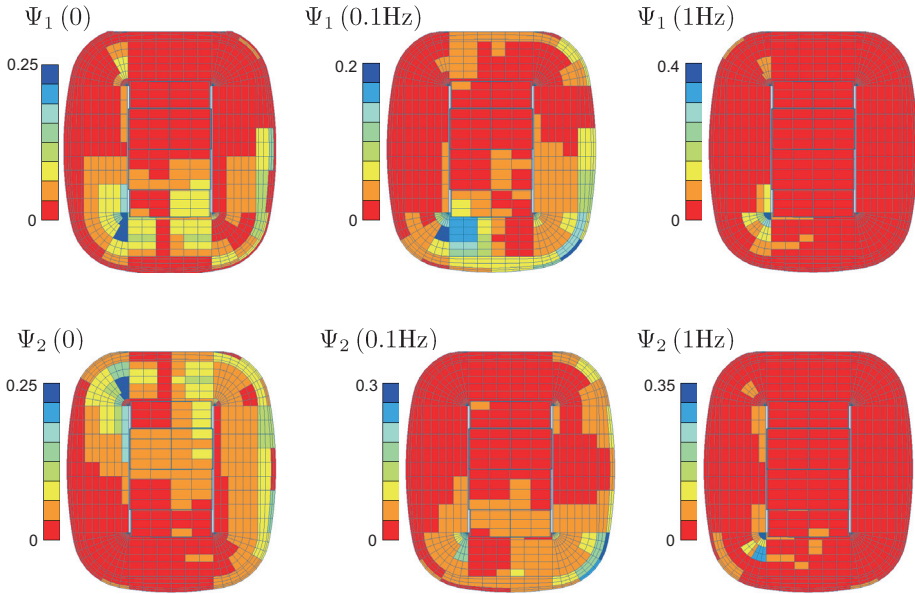


Fig. 10. First two loading components  $\Psi_1$ ,  $\Psi_2$  (in absolute value) extracted from the psd matrix  $\mathbf{S}^{(q)}$ .

principal components, as a function of the frequency  $\omega$ . Similarly to what is done for CPT, one expects that some components only will be sufficient in the reconstruction of the global data set. Some principal coordinates and components are therefore conserved,  $\mathbf{S}^{(y)}$  and  $\Psi(\omega)$  are both smaller in size than  $\mathbf{S}^{(q)}$  ( $\omega$ ) and they satisfy

$$\mathbf{S}^{(q)} = \Psi \mathbf{S}^{(y)} \Psi^T. \quad (9)$$

In the Fourier domain, the measured pressures  $\mathbf{Q}(\omega)$  may therefore be seen as the result of a particular filtering of uncorrelated components  $\mathbf{Y}(\omega)$ , the *spectral principal coordinates*, as

$$\mathbf{Q} = \Psi \mathbf{Y}. \quad (10)$$

It is clear that  $\mathbf{S}^{(y)}$  is the psd matrix of  $\mathbf{Y}(\omega)$ .

The striking similarity with (7) would indicate the duality of both presented methods, but SPT is however superior to CPT (in terms of energy representation of the initial set) because SPT allows frequency-dependent components whereas CPT considers components constant in time.

As an illustration, Figure 10 provides the absolute value of the first two spectral principal components  $\Psi_1(\omega)$  and  $\Psi_2(\omega)$  for three different frequencies,  $n = 0$  Hz,  $n = 0.1$  Hz and  $n = 1$  Hz. These components are complex pressure distributions and are represented here in absolute value. As expected, the decomposition for low frequencies is that of the psd matrix with full coherence, while the decomposition at high frequency tends to unilateral psd's, and orders the components with decreasing local variances.

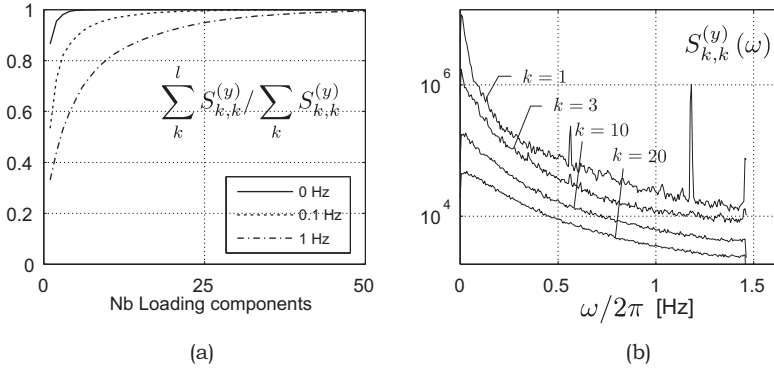


Fig. 11. (a) Cumulative summation of the psd of principal coordinates (normalized) and (b) psd of some principal coordinates (spectral proper components 1, 3, 10 and 20).

Similarly to 8-a, the rapid monotonic convergence of the variance of principal coordinates may be observed with a cumulative summation. Such an illustration is represented, in a dimensionless manner, in Fig. 11-a for three different frequencies. The power spectral densities of the principal coordinates are also reported in Fig. 11-b, for some components only. They naturally show a global profile similar to the psd of measured pressures, namely, a global decreasing function affected by some measurement noise.

#### 2.4 Connexion with a finite element structural model

In parallel to wind tunnel simulations, there exists almost always a structural model, usually a finite element model, that interprets the recorded loading and determines the structural response. As discussed in more details next, the structural design requires the solution of the equation of motion

$$\mathbf{M}\ddot{\mathbf{x}} + \mathbf{C}\dot{\mathbf{x}} + \mathbf{K}\mathbf{x} = \mathbf{p} \quad (11)$$

where  $\mathbf{M}$ ,  $\mathbf{C}$  and  $\mathbf{K}$  are respectively the mass, damping and stiffness matrices (from a finite element model), and  $\mathbf{x}(t)$ ,  $\dot{\mathbf{x}}(t)$  and  $\ddot{\mathbf{x}}(t)$  are respectively the displacements, velocities and accelerations of the nodes of this model. The external loads  $\mathbf{p}(t)$  result from the wind loading and, in some instances, other particular loadings as the self-weight. The wind related part of the loading is expressed as

$$\mathbf{p} = \mathbf{A}\mathbf{q} \quad (12)$$

where matrix  $\mathbf{A}$  allows the transformation of wind-tunnel pressures  $\mathbf{q}(t)$  acquired at given pressure taps to nodal force of the finite element model. The elements of the transformation matrix  $\mathbf{A}$  are established in accordance with the positioning of the pressures taps, respect to the nodes and elements of the structural model. Harmony between wind-tunnel and structural teams should facilitate the establishment of that matrix.

More generally, as the finite element model is usually known prior to the wind-tunnel testing, information extracted from that model should be used for an optimal planning of the wind tunnel measurements. For example the range of natural frequencies of relevant structural modes should be announced for an optimum choice of the sampling rate to be used for wind tunnel simulations.

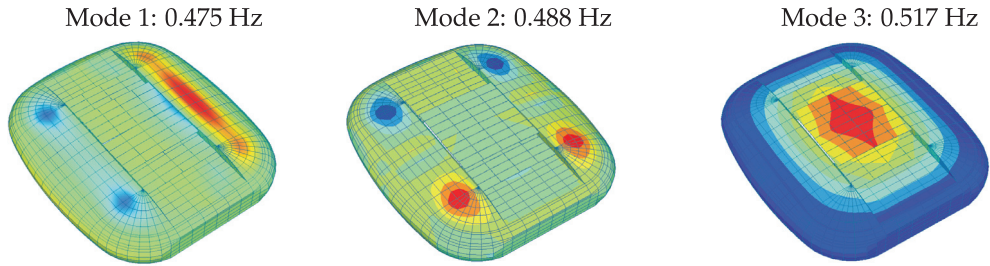


Fig. 12. Modal vertical displacements and associated frequencies.

Conveying the same spirit, at the post-processing stage, it is also optimum to scrutinize the recorded data by keeping in mind that they have to be used as external loads applied on a finite element model. Although principal component decomposition have proved to be most efficient in extracting the most pertinent information from huge sets of data, it is most likely that some other methods including the structural characteristic could offer a more adequate post-processing (but limited to that particular structure).

In particular, in case of flexible structures, it is known that the normal modes of vibration  $\phi_j$  consist an optimum basis  $\Phi$  for the representation of the structural response to a broadband loading (Gérardin & Rixen, 2002). They are obtained by solving the eigenvalue problem:

$$(\mathbf{K} - \omega_j^2 \mathbf{M})\phi_j = 0 \quad (13)$$

where  $\omega_j$  represents the  $j^{\text{th}}$  natural circular frequency. The first three mode shapes of the considered structure are illustrated in Fig. 12. In a structural design, the lowest modes usually offers global deformations, i.e. large wavelengths, as opposed, in this case, to the deep localization of loading components.

The transposition of the equation of motion (11) into the modal space yields

$$\mathbf{M}^* \ddot{\eta} + \mathbf{C}^* \dot{\eta} + \mathbf{K}^* \eta = \mathbf{p}^* = \Phi^T \mathbf{p} \quad (14)$$

where  $\mathbf{M}^* = \Phi^T \mathbf{M} \Phi$ ,  $\mathbf{C}^* = \Phi^T \mathbf{C} \Phi$  and  $\mathbf{K}^* = \Phi^T \mathbf{K} \Phi$  are respectively the generalized mass, damping and stiffness matrices, and  $\eta(t)$ ,  $\dot{\eta}(t)$  and  $\ddot{\eta}(t)$  are the modal displacements, velocities and accelerations. The optimality of the modal basis is attributable to the fact that it usually requires a small to moderate amount of mode shapes to provide a reliable estimation of the structural response. In the analysis of large scale structures with a number of degrees-of-freedom larger than or similar to  $10^4$ , the size of the modal matrices is much smaller than the original structural matrices.

In the following, we proof the simple idea that the generalized forces  $\mathbf{p}^*(t)$ , obtained from the recorded pressures  $\mathbf{q}(t)$ , the transformation matrix  $\mathbf{A}$  and the structural mode shapes  $\Phi$  as

$$\mathbf{p}^* = \Phi^T \mathbf{A} \mathbf{q}, \quad (15)$$

provide a competitive representation of the loading.

### 3. Structural design

The objective of a structural design is to assess the safety against failure. This includes several checkings against local/global resistance, stability, comfort, fatigue, etc. In the following only

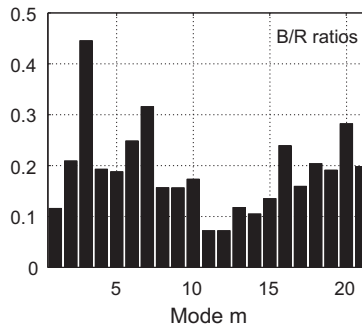


Fig. 13. The background-to-resonant ratios indicate that the considered roof structure responds essentially in a resonant regime.

the determination of extreme internal forces in structural members is discussed. The goal of the design consists therefore in determining the probability density functions of the maximum internal forces, given the total observation period during which high buffeting winds are assumed to blow.

The time scale related to the buffeting loading is usually one or several orders of magnitude above the typical structural time scales (the natural periods). As a consequence, the structural response is usually estimated as the sum of a background and a resonant contributions (Gu et al., 2002). The nodal basis is known to be optimum for the estimation of the background contribution, while the resonant one is optimally estimated in the modal basis (Chen & Kareem, 2004). However, for the sake of simplicity, we completely develop the main argument in the modal basis, although we believe this could be adapted to a hybrid nodal/modal analysis. For the considered application the background-to-resonant ratios, i.e. the ratios of variances in each contribution, are given for the first 21 modes of the roof structure. This ratio ranges from 0.1 to 0.4 but may be higher for other structures such as cable-stayed bridges or low-rise buildings.

Two different methods of analysis, deterministic or stochastic, are discussed successively in the following sections, along with their applicability to structures tested in a wind-tunnel.

### 3.1 Deterministic structural design

In a deterministic context, the equation of motion (14), recalled here for clarity

$$\mathbf{M}^* \ddot{\boldsymbol{\eta}} + \mathbf{C}^* \dot{\boldsymbol{\eta}} + \mathbf{K}^* \boldsymbol{\eta} = \mathbf{p}^* = \boldsymbol{\Phi}^T \mathbf{A} \mathbf{q} \quad (16)$$

is solved for modal coordinates  $\boldsymbol{\eta}(t)$ ; nodal displacements are then obtained by  $\mathbf{x}(t) = \boldsymbol{\Phi} \boldsymbol{\eta}(t)$  and internal forces  $\mathbf{f}(t)$  are finally obtained by

$$\mathbf{f} = \mathbf{E} \mathbf{x} \quad (17)$$

where, in a finite element context, matrix  $\mathbf{E}$  is built from adequate elements of the stiffness matrix  $\mathbf{K}$ . As an ultimate step, extreme values, i.e. probability density functions of the maximum internal forces during the observation period, are established.

According to the discussion in Section 2, there are several ways to process (or not) the recorded pressures. Each of them provides one or several ways to analyse the structure. The objective

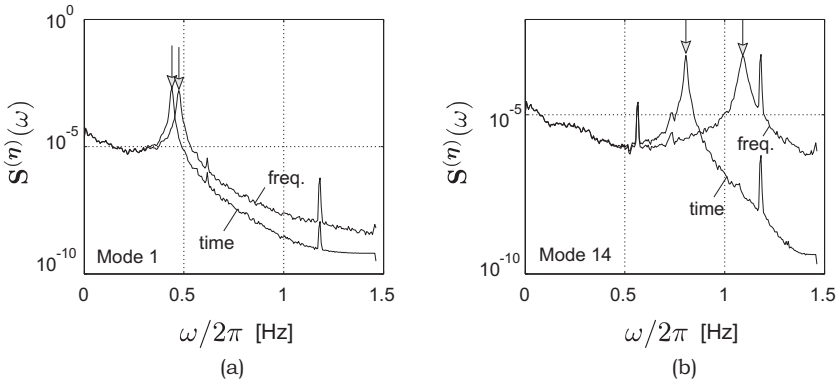


Fig. 14. Power spectral density of generalized coordinates in modes 1 and 14. Solid lines refer to a frequency domain analysis, while dashed lines indicate a distorted response provided by a step-by-step algorithm (Newmark,  $\alpha = 1/4$ ;  $\delta = 1/2$ )

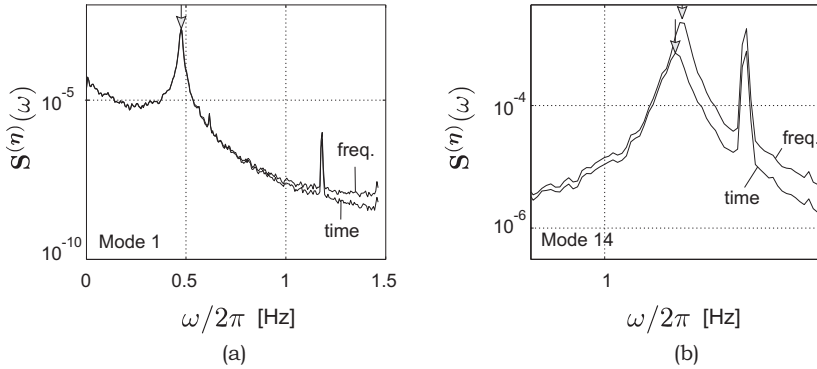


Fig. 15. Power spectral density of generalized coordinates in modes 1 and 14. Solid lines refer to a frequency domain analysis, while dashed lines indicate a distorted response provided by a step-by-step algorithm (Newmark,  $\alpha = 1/12$ ;  $\delta = 1/2$  for mode 1 and  $\alpha = 1/9$ ;  $\delta = 1/2$  for mode 14)

here is not to provide an exhaustive description of them, but well a brief overview of their applicability in the problem at hand, along with some illustrations.

As a first option, the raw data  $\mathbf{q}(t)$  is used without any other processing than the computation of generalized forces (15). The equation of motion is solved either in the time domain with (16), or in the frequency domain with

$$\boldsymbol{\eta} = \mathbf{H}^* \mathbf{P}^* \quad (18)$$

where the Fourier transform of the modal coordinates  $\boldsymbol{\eta}(\omega)$  is obtained by multiplication of the transfer function  $\mathbf{H}^*(\omega)$  and the Fourier transform of generalized forces  $\mathbf{P}^*(\omega)$ . The time evolution of the modal coordinates  $\boldsymbol{\eta}(t)$  is recovered by inverse Fourier transform and, in both cases, internal forces are then obtained from (17). A statistical treatment of the time evolution of selected internal forces provides the design values.



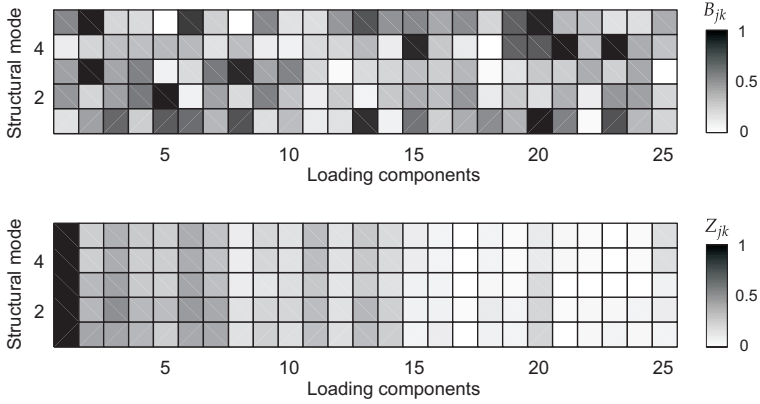


Fig. 16. (a) Normalized (line-by-line) elements of the cross-modal participation covariance matrix  $\mathbf{B}$  and (b) normalized variances of the matrix of partial principal coordinates  $\mathbf{Z}(t)$ .

Although time domain step-by-step calculations are commonly used in practice, they may not be the preferred choice in this context. Indeed they may suffer from the low sampling of wind-tunnel data, itself resulting from the need to acquire synchronously data from a large amount of pressure taps and to measure during a long time. The time step used for the numerical analysis may thus be a significant portion of the natural period, which is known to provide period elongation and excessive numerical damping (Clough & Penzien, 1993). This is illustrated in Fig. 14 where the psd of the modal coordinates in the 1<sup>st</sup> and 14<sup>th</sup> mode are compared to the results obtained with a Fourier transform (notice also that noise frequencies are still present in the response). A possible countermeasure is to adapt the parameters of the Newmark algorithm, in order to limit these undesired phenomena (Gmür, 2008). Optimum choices provide the results in Fig. 15 which show that the problem is solved for mode 1, but just reduced for mode 14. Other possible solutions would include a resampling of the acquired data, or even a generation of synthetic data compatible with the power spectral density of the acquired data. There are some important issues related to these two other methods and make their implementation rather vain in practice.

In a second option, the measured pressures are decomposed with a covariance proper transformation (7), and the structural response is analyzed in the modal basis. This combination, called *double modal transformation* (Carassale et al., 2001), consists in solving

$$\mathbf{M}^* \ddot{\boldsymbol{\eta}} + \mathbf{C}^* \dot{\boldsymbol{\eta}} + \mathbf{K}^* \boldsymbol{\eta} = \mathbf{B} \mathbf{c} \quad (19)$$

where  $\mathbf{B} = \boldsymbol{\Phi}^T \mathbf{A} \boldsymbol{\Theta}$  is the (covariance) cross-modal participation covariance matrix. By introducing the matrix of partial principal coordinates  $\mathbf{Z}(t)$  whose  $(j, k)$  element is the time domain response in the  $j^{\text{th}}$  structural mode under the  $k^{\text{th}}$  loading component, the modal responses simply write

$$\boldsymbol{\eta}_j = \sum_k B_{jk} Z_{jk} \quad (20)$$

in which the summation is performed on an a priori chosen (but limited) number of loading components. Notice that a frequency domain solution of (20) via Fourier transform is also possible. As an illustration, Fig. 16 represents  $B_{jk}$  and  $\sigma_{Z_{jk}}^2$  for 5 structural modes and 25 loading components. For clarity, values are normalized line-by-line, to a unit maximum for

each mode. While the cross-modal participations exhibit a rather scattered pattern (depending on the affinity of structural mode shapes and loading components, similarly to earthquake engineering applications), the partial principal coordinates show a similar decrease for all modes. This typical decrease is related to that of the variance of the components themselves, see Fig. 8, and because all components possess a somewhat similar frequency distribution.

As a third option, consideration of a spectral proper transformation in combination with a modal basis analysis, provides the perfect framework for a double modal transformation in the frequency domain. In this case, the recorded pressures are decomposed as (10) and the equation of motion 18 writes

$$\boldsymbol{\eta} = \mathbf{H}^* \mathbf{P}^* = \mathbf{H}^* \mathbf{D} \mathbf{Y} \quad (21)$$

where  $\mathbf{D}(\omega) = \boldsymbol{\Phi}^T \mathbf{A} \boldsymbol{\Psi}(\omega)$  is the (spectral and frequency dependent) cross-modal participation matrix. By introducing the partial principal coordinates in the frequency domain  $\mathbf{T}(\omega)$  whose  $(i, j)$  element in the frequency response of the  $j^{\text{th}}$  structural mode under the  $k^{\text{th}}$  loading component  $T_{jk}(\omega) = H_j^*(\omega) Y_k(\omega)$ , the modal response writes

$$\eta_j = \sum_k D_{jk} T_{jk}. \quad (22)$$

This deterministic method is not illustrated in this document. Actually its implementation is rather heavy as the spectral principal components  $\mathbf{Y}(\omega)$  are not a direct outcome of the analysis. Spectral proper transformation is better suits a probabilistic approach, as shown next.

### 3.2 Stochastic structural design

In a stochastic approach, the psd matrix of modal coordinates  $\mathbf{S}^{(\boldsymbol{\eta})}(\omega)$  is obtained by pre- and post-multiplication of the psd matrix of generalized forces by the transfer matrix, as

$$\mathbf{S}^{(\boldsymbol{\eta})} = \mathbf{H}^* \mathbf{S}^{(\mathbf{P}^*)} \overline{\mathbf{H}}^{*T}, \quad (23)$$

where the overbar and superscript  $T$  denote respectively matrix conjugation and transposition. In wind engineering, this stochastic formulation of the governing equation was introduced in the works of Liepmann (Liepmann, 1952) and Davenport (Davenport, 1961). Their seminal ideas, suggesting the application of statistical concepts to buffeting analysis, were extended from single-DOF systems to multi-DOF systems, with consideration of aerodynamic instabilities (Jain et al., 1996), mode correlation (Denoel, 2009; Gu & Zhou, 2009), aerodynamic admittance (Scanlan & Jones, 1999), and ended up in the accurate and adequate format available nowadays.

The main scope of this document is driven by the convenient aspect of this analysis method, especially because the analysis provides a repeatable response and an accurate probabilistic description of extreme values. On the contrary, application of Monte Carlo simulation techniques to solve the same problem, with an approach becoming deterministic then, provides a unique estimate of the response, as what would be obtained from wind-tunnel measurement.

To the light of the former descriptive .vs. inferential discussion of the measured pressures, it seems evident that classical descriptive statistics are particularly well suited to a deterministic approach with (16) or (18), while the inferential statistics and presumably more robust probabilistic models better suit the concepts of a stochastic approach, with (23).

A basic way to perform a stochastic analysis from wind-tunnel measurements is to establish the psd matrix of the recorded pressures  $\mathbf{S}^{(q)}$  through a non-parametric estimator as Welch's periodogram method. From (15), the psd matrix of generalized forces is given by

$$\mathbf{S}^{(p^*)} = \phi^T \mathbf{A} \mathbf{S}^{(q)} \mathbf{A}^T \phi. \quad (24)$$

Substitution into (23) provides, after integration along frequencies, the covariance matrix of modal coordinates, followed then by the psd matrix of nodal displacement, and of some interesting internal forces by

$$\mathbf{S}^{(f)} = \mathbf{E} \phi \mathbf{S}^{(j)} \phi^T \mathbf{E}^T. \quad (25)$$

This quantity contains the necessary information for the establishment of extreme value statistics of internal forces, in a Gaussian context.

The other stochastic analysis relies on the elegant combination of a structural modal basis and the spectral proper transformation where  $\mathbf{S}^{(q)}$  is expressed by (9). The rest of the design procedure remains unchanged with (24) and (23), or equivalently

$$\mathbf{S}^{(\eta)} = \mathbf{H}^* \mathbf{D} \mathbf{S}^{(y)} \overline{\mathbf{D}}^T \overline{\mathbf{H}}^{*T}. \quad (26)$$

Notice that the application of the covariance proper transformation would yield

$$\mathbf{S}^{(\eta)} = \mathbf{H}^* \mathbf{B} \mathbf{S}^{(c)} \mathbf{B}^T \overline{\mathbf{H}}^{*T} \quad (27)$$

where  $\mathbf{S}^{(c)}(\omega)$  stands for the psd matrix of the covariance principal components. The implementation of this formulation is however not economical because  $\mathbf{S}^{(c)}(\omega)$  is a full matrix, whereas  $\mathbf{S}^{(y)}(\omega)$  is diagonal. The spectral proper transformation is then faster and more efficient, since the frequency dependence of the loading components is accounted for. The application of CPT in a stochastic approach is therefore not pursued next.

We are thus left with just two formulations, (23) and (26). From the previous talk, we know that the smoothing and reproducibility potential of a stochastic approach is increased if we consider the statistical properties of the population, rather than a non-parametric (descriptive) estimate of some psd matrices. Similarly to what is suggested in (Kho et al., 2002), we assert the inferential statistics of the recorded pressures, seen as random processes, are accurately represented by a low-order parametric estimation. In this perspective, we analyze the optimum way of fitting a probabilistic model to the recorded pressure field or any of its by-products. It is indeed possible to do this fitting at different levels of the stochastic analysis. The first and most natural way consists in estimating in a parametric way the psd matrix of the acquired pressures. This idea appears to be applicable only for small scale structures for which the coherence field remains simple. As illustrated in Fig. (6), actual coherence functions of local pressures is far from the usually assumed real-valued exponentially decaying functions. This make the determination of sufficiently flexible analytical expression and their fitting rather cumbersome.

A second option consists in fitting the probabilistic model directly to the generalized forces. In other words, the time evolution of generalized forces is obtained deterministically; then the psd matrix of the generalized forces is represented with a simple probabilistic model. This concept is appealing for many reasons:

- the size of the matrices that need to be handled correspond to the (usually small) number of mode shapes that are necessary to accurately represent the structural response;

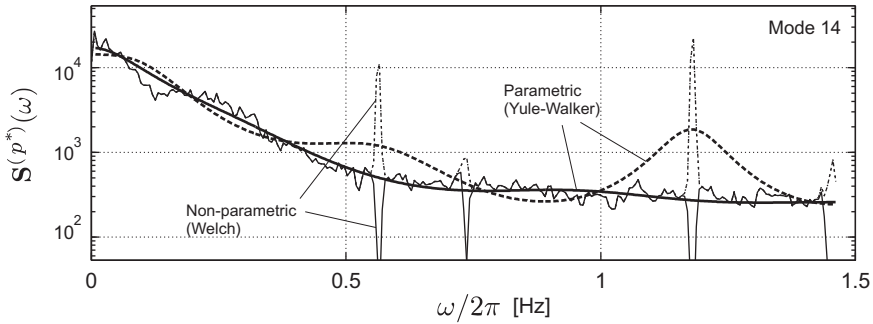


Fig. 17. Fitting of a probabilistic model (a parametric psd estimate) to the generalized force in mode 14. Various options show that the parametric estimate, after bandstop filtering provides an interesting methodology, offering smoothness and robustness against spurious harmonics.

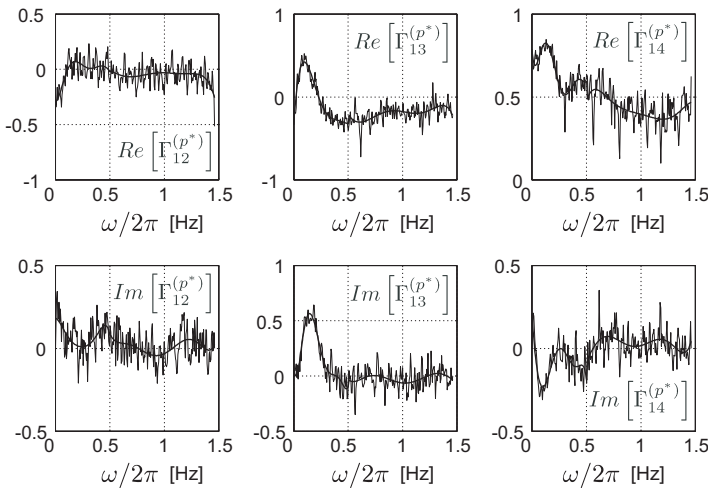


Fig. 18. Coherence functions between some generalized forces.

- the need to model properly the coherence between generalized forces is limited to structures evincing both a significant resonant response and clustered natural frequencies (Denoel, 2009);
- the possible spurious harmonics and many other deficiencies may be filtered out in the fitting process; this is discussed next.

Another possibility consists in fitting a probabilistic model to the spectral proper components and coordinates. Although the psd matrix of the proper coordinates  $\mathbf{S}^{(y)}$  may be fitted easily (because there is no coherence), the development of a smooth proper component model remains challenging. This would actually require the case-by-case study of each structure and makes the practical implementation of this idea inoperative.

The fitting of a Yule-Walker model to generalized forces is illustrated in Fig. 17 for mode 14, which is particularly affected by the spurious harmonics. The solid and dotted lines represent the non-parametric power spectral density estimates of the raw signal and of the bandstop filtered signal around the troublesome frequencies, respectively. The spurious peaks are basically transformed to spurious valleys as the cutoff and order of the bandpass filter have been roughly selected. Thick lines represent the parametric model, a 6th-order Yule-Walker model, obtained from the raw and filtered signals, respectively. One may observe that the successive application of a bandstop filtering and parametric estimation provides a smooth acceptable power spectral density. A similar procedure is adopted for coherence functions of generalized forces. The real and imaginary parts of the coherence functions between modes (1,2), (1,3) and (1,4) are represented in Fig. 18. The proposed parametric estimator give a much smoother representation of these functions.

In summary, it appears that the fitting of a probabilistic model to the generalized forces provides a simple, accurate and manageable way of performing a structural analysis from wind-tunnel measurement, with a very limited sensitivity to the variability of the acquired signals.

#### 4. Comparison

In this section, the most promising solutions introduced before are compared in terms of their faculty to accurately provide the standard deviations of two internal forces. The considered forces are a bar of the truss composing one of the two main beams of the roof (A) and a peripheral purlin of the roof (B). These two structural members have been selected because of their significant dissemblance. The one (A) is large and it affected by forces applied on the whole roof, whereas the other (B) is smaller and concerned with wind pressures acting in a short area around the element. As seen next, many mode shapes with high frequencies are necessary to model properly the response of member B.

First, we compare in Fig. 19 the power spectral densities of the two internal forces obtained either with a parametric estimate of the psd matrix of generalized forces (Yule-Walker), or a non-parametric estimate of the psd matrix of generalized forces (Welch). As discussed earlier, the first choice proves to be superior since: (i) it provides a smooth result that will therefore ensure a reliable estimate of extremes values, and (ii) spurious harmonics have been totally pruned, with an automatic procedure.

In a second comparison, the same parametric fitting of the psd matrix of generalized forces is tested against the results of a probabilistic analysis with the spectral proper transformation. In the latter case, several analyses are performed, with a different number of loading components. Figure 20 shows the psd's of internal forces obtained with 3 or 70 loading components (thin lines), as well as the same the psd's obtained with the proposed fitting. Again the erraticness of the result may be discussed. Of more importance, the results obtained with SPT show the right profile with only three loading components. The peaks in the psd's are indeed well represented, but with an inaccurate level however, since the variance of the internal forces are underestimated. This naturally results from a severe discrepancy in the representation of the total energy in the loading process, as may be seen in Fig. 11. Interestingly, the psd's obtained with 70 components virtually matches those resulting from the proposed fitting of generalized forces, with the exception of erraticness and spurious modes.

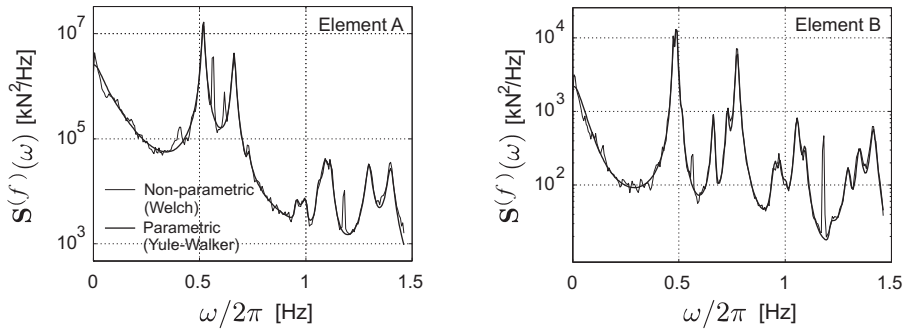


Fig. 19. Psd of two internal forces (in elements A and B) obtained with a parametric (Yule-Walker) or non-parametric (Welch) estimation of the psd matrix of generalized forces. The method promoted in this document is the smooth and robust parametric estimate.

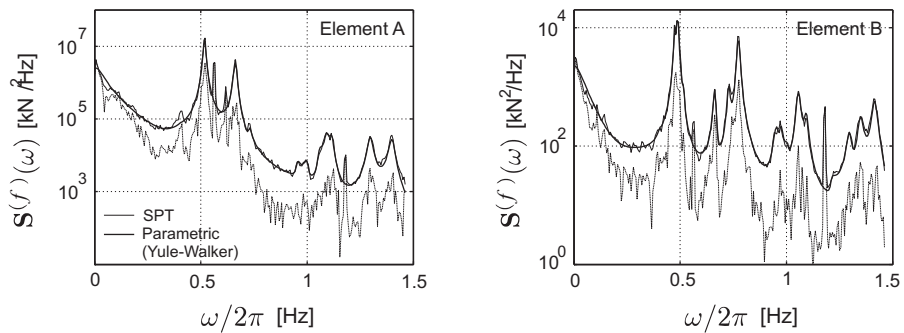


Fig. 20. Psd of two internal forces (in elements A and B) obtained with a parametric (Yule-Walker) estimation of the psd matrix of generalized forces or the use of a SPT decomposition of the pressure fields, with either 3 components (lower curves) or 70 components (upper curves).

Figure 21 shows the variances of the two internal forces, obtained with the different approaches. For both elements, the deterministic analysis in the frequency domain (1) slightly overestimates values obtained with the proposed fitting (2). One explanation is that the deterministic approach is based on the unfiltered generalized forces. The CPT approach (3), a double modal transformation in the time domain, provides excessive variances. This overestimation is due to the inaccuracy of the Newmark's algorithm, as illustrated in the previous Section. The discrepancy is naturally larger for element B (than A), as its response is composed of multiple modal responses at higher frequency, for which Newmark fails to be accurate. On the contrary, the internal force in element A essentially results from the contributions of modes 1 and 3. Lastly, the SPT approach (4) in the framework of a stochastic analysis as discussed before, produce an estimation of the variances of internal forces that is in a very good agreement with the proposed method (2), for all that fifty principal components at least as considered for the computation.

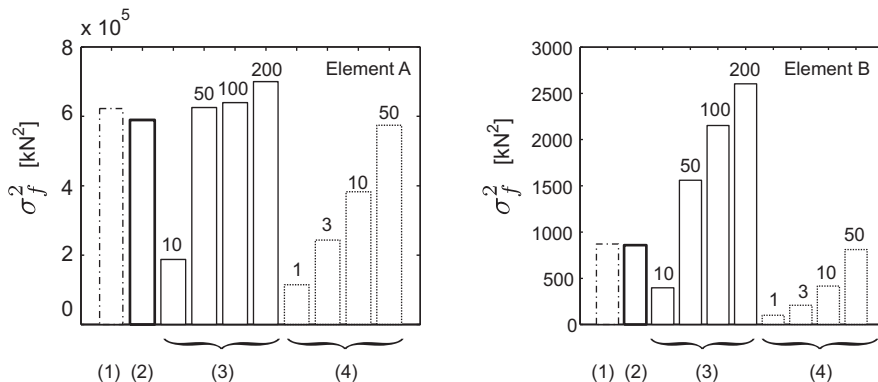


Fig. 21. Variances of two internal forces (in elements A and B) obtained with (1) a deterministic frequency domain analysis, (2) a stochastic approach with the proposed fitting, (3) a double modal transformation with CPT in the time domain (with Newmark's algorithm) and (4) a stochastic approach with SPT. Labels indicate the number of principal components used to perform the corresponding analysis.

## 5. Conclusions

Advanced post-processing of measured wind pressures of large and fully instrumented structures are compulsory to extract some valuable information from the experimental campaign. In this context, we have discussed the way to establish, in the most economical way, a global reliable probabilistic model that is useful for the structural design. The fitting of such a model to the generalized forces, and by means of a parametric psd estimate, has been demonstrated to be an interesting solution showing simplicity, accuracy and repeatability in the event of new experiments under the same conditions.

Actually non-parametric methods are rapidly dismissed because they are not able to offer the same advantages. Indeed, they still provide erratic results, and therefore inaccuracy in repeatability, even with an averaging procedure. Furthermore, it has been shown that a parametric estimate may easily solve issues related to the presence of noise in the signal.

In a structural design context, the method was benchmarked against a time domain double modal transformation (with a covariance proper transformation), as well as a stochastic analysis with a spectral proper transformation, and the conclusion is that the proposed method provides accurate results. More interestingly, these alternative techniques require the need for a substantial amount of computational effort to establish the required number of components. On the contrary, the proposed method hinges on the classical normal modes of vibration, which are usually available.

The idea of fitting a probabilistic model to other quantities than the generalized forces was studied. In particular, it was found that neither the CPT nor the SPT seem to be adapted to such a processing. This is due to the difficulty in fitting accurate components (load cases) and, for the SPT, to the frequency dependence of those components.

The present study was carried out in the context of a modal structural analysis and within the framework of a second rank stochastic analysis, which is therefore limited to Gaussian processes. Although this limitation could be justified for structures with a large resonant response, its application to stiffer structures may require consideration of non-Gaussian processes. In future developments, extension to higher order statistics should follow the same

guideline and offer the possibility to discuss the reproducibility, from test to test, of extreme values of non Gaussian processes, with advanced techniques as suggested in (Floris & Iseppi, 1998; Gurley et al., 1997). This would be performed by fitting parametric estimates to the bispectrum of generalized forces and conducting higher order stochastic analyses as described in (Denoël & Degée, 2006; Gusella & Materazzi, 1998).

## 6. Acknowledgments

The authors are grateful to CSTB (Nantes, France) and to BEG (Angleur, Belgium) for having provided a neat case study for the illustration of the proposed ideas.

## 7. References

- Baker, C. J. (2000). Aspects of the use of proper orthogonal decomposition of surface pressure fields, *Wind and Structures* 3(2): 97–115.
- Beirlant, J., Goegebeur, Y., Teugels, J., Segers, J., Waal, D. D. & Ferro, C. (2004). *Statistics of Extremes, theory and applications*, Wiley, Chichester, England.
- Best, R. J. & Holmes, J. D. (1983). Use of eigenvalues in the covariance integration method for determination of wind load effects, *Journal of Wind Engineering and Industrial Aerodynamics* 13(1-3): 359–370.
- Bienkiewicz, B., Ham, H. J. & Sun, Y. (1993). Proper orthogonal decomposition of roof pressure, *Journal of Wind Engineering and Industrial Aerodynamics* 50(1-3): 193–202.
- Bienkiewicz, B., Tamura, Y., Ham, H. J., Ueda, H. & Hibi, K. (1995). Proper orthogonal decomposition and reconstruction of multichannel roof pressure, *Journal of Wind Engineering and Industrial Aerodynamics* 54: 369–381.
- Blaise, N. (2010). *Study of a large roof structure submitted to turbulent wind*, PhD thesis.
- Blaise, N., Grillaud, G., De Ville de Goyet, V. & Denoël, V. (2011). Application of deterministic and stochastic analysis to calculate a stadium with pressure measurements in wind tunnel., *Proceedings of 8th International Conference on Structural Dynamics, Eurodyn 2011, Leuven, EASD*.
- Carassale, L. (2005). Pod-based filters for the representation of random loads on structures, *Probabilistic Engineering Mechanics* 20(3): 263–280.
- Carassale, L., Piccardo, G. & Solari, G. (2001). Double modal transformation and wind engineering applications, *Journal Of Engineering Mechanics-Asce* 127(5): 432–439.
- Carassale, L., Solari, G. & Tubino, F. (2007). Proper orthogonal decomposition in wind engineering. part 2: Theoretical aspects and some applications, *Wind and Structures* 10(2): 177–208.
- Casella, G., B. R. (2001). *Statistical Inference*, Duxbury Press, London.
- Chen, X. Z. & Kareem, A. (2004). Equivalent static wind loads on buildings: New model, *Journal of Structural Engineering-Asce* 130(10): 1425–1435.
- Clough, R. W. & Penzien, J. (1993). *Dynamics of structures*, 2nd edition edn, McGraw-Hill, New-York.
- Davenport, A. G. (1961). The application of statistical concepts to the wind loading of structures, *Proceedings of the Institute of Civil Engineers* 19: 449–472.
- Denoël, V. (2009). Estimation of modal correlation coefficients from background and resonant responses, *Structural Engineering And Mechanics* 32(6): 725–740.
- Denoël, V. & Degée, H. (2006). Non gaussian response of bridges subjected to turbulent wind. effect of the non linearity of aerodynamic coefficients.



- Dyrbye, C. & Hansen, S. O. (1997). *Wind loads on structures*, John Wiley & Sons.
- Eurocode (1991). Eurocode 1:: Actions on structures part 1-4: General actions: Wind actions (en 1991-1-4).
- Floris, C. & Iseppi, L. D. (1998). The peak factor for gust loading: A review and some new proposals, *Meccanica* 33(3): 319–330.
- Gérardin, M. & Rixen, D. (2002). *Mechanical vibrations: theory and application to structural dynamics*.
- Gmür, T. (2008). *Dynamique des structures. Analyse modale numérique.*, Presses polytechniques et universitaires romandes.
- Gu, M., Chen, S. R. & Chang, C. C. (2002). Background component of buffeting response of cable-stayed bridges, *Journal Of Wind Engineering And Industrial Aerodynamics* 90(12-15): 2045–2055.
- Gu, M. & Zhou, X. Y. (2009). An approximation method for resonant response with coupling modes of structures under wind action, *Journal of Wind Engineering and Industrial Aerodynamics* 97(11-12): 573–580.
- Gupta, S. & van Gelder, P. (2007). Extreme value distributions for nonlinear transformations of vector gaussian processes, *Probabilistic Engineering Mechanics* 22(2): 136–149.
- Gurley, K. R., Tognarelli, M. A. & Kareem, A. (1997). Analysis and simulation tools for wind engineering, *Probabilistic Engineering Mechanics* 12(1): 9–31.
- Gusella, V. & Materazzi, A. L. (1998). Non-gaussian response of mdof wind-exposed structures: Analysis by bicorrelation function and bispectrum, *Meccanica* 33(3): 299–307.
- Holmes, J. D. (2007). *Wind Loading on Structures*, 2nd edition edn, SponPress, London.
- Holmes, J. D., Sankaran, R., Kwok, K. C. S. & Syme, M. J. (1997). Eigenvector modes of fluctuating pressures on low-rise building models, *Journal of Wind Engineering and Industrial Aerodynamics* 71: 697–707.
- Jain, A., Jones, N. P. & Scanlan, R. H. (1996). Coupled flutter and buffeting analysis of long-span bridges, *Journal Of Structural Engineering-Asce* 122(7): 716–725.
- Jolliffe, I. (2005). *Principal Component Analysis*, Encyclopedia of Statistics in Behavioral Science, John Wiley & Sons, Ltd.
- Kho, S., Baker, C. & Hoxey, R. (2002). Pod/arma reconstruction of the surface pressure field around a low rise structure, *Journal of Wind Engineering and Industrial Aerodynamics* 90(12-15): 1831–1842.
- Langhaar, H. (1951). *Dimensional Analysis and Theory of Models*, Wiley, New York.
- Liepmann, H. W. (1952). On the application of statistical concepts to the buffeting problem, *Journal of Aeronautical Sciences* 19(12): 793–800.
- Loeve, M. (1977). *Probability theory I, 4th edidtion*, Probability theory I, 4th edidtion, Springer-Verlag.
- Papoulis, A. (1965). *Probability, Random Variables, and Stochastic Processes*, McGraw Hill, New York.
- Preumont, A. (1994). *Random Vibration and Spectral Analysis*, Kluwer Academic Publishers.
- Rice, S. O. (1945). Mathematical analysis of random noise, *Bell System Technical Journal* 24: 46–156.
- Ruan, D., He, H., Castañón, D. A. & Mehta, K. C. (2006). Normalized proper orthogonal decomposition (npod) for building pressure data compression, *Journal of Wind Engineering and Industrial Aerodynamics* 94(6): 447–461.

- Scanlan, R. H. & Jones, N. P. (1999). A form of aerodynamic admittance for use in bridge aeroelastic analysis, *Journal Of Fluids And Structures* 13(7-8): 1017–1027.
- Solari, G., Carassale, L. & Tubino, F. (2007). Proper orthogonal decomposition in wind engineering. part 1: A state-of-the-art and some prospects, *Wind And Structures* 10(2): 153–176.

# Wire Robot Suspension Systems for Wind Tunnels

Tobias Bruckmann, Christian Sturm and Wildan Lalo  
*Chair of Mechatronics, University of Duisburg-Essen  
Germany*

## 1. Introduction

In the past decade, the main focus in ship hydrodynamic simulation was the computation of the viscous flow around a ship at constant speed and parallel inflow to the ship longitudinal axis. Meanwhile, the numerical methods developed by extensive research allow to simulate the viscous flow around a maneuvering vessel. Having these methods at hand, experimental data are required for the validation of the applied simulation models. These data can be obtained e.g. by wind tunnel experiments. Here, particularly the velocity distribution around the body and forces of the flow during a predefined motion are of interest.

The motion of the ship model can be realized by a superposition of longitudinal motion simulated through the inflow in the wind tunnel and a transverse or rotational motion of the ship realized by a suspension mechanism.

Mechanisms for guiding a ship model along a predefined trajectory are known e.g. from towing tank applications. However, the design criteria for these mechanisms are totally different from a wind tunnel suspension system. In the towing tank, the weight of the studied vessel is compensated by the buoyancy force. On the other hand, the required forces to move the model along a trajectory are much higher due to the higher density and mass of the water in comparison with air. In the wind tunnel application, the mass of the model leads to gravity and inertia forces which have to be compensated by the suspension system.

This chapter describes the development of a suspension system based on wire robot technology. Wire robots use wires for the suspension of their end effectors. In this application, this is very advantageous since wires have a relatively small aerodynamical footprint and allow for high loads. The system described within this chapter is installed at the Technical University Hamburg-Harburg, where ship models must be moved on defined trajectories within the wind tunnel, as described above (Sturm & Schramm, 2010). The application requires the motion of heavyweight payloads up to 100kg with a frequency of up to 0.5Hz for the translational degrees-of-freedom and up to 2.5Hz for the rotational degrees-of-freedom.

Within this chapter, at first a short historical review of the very active wire robot research within the last years is given in section 2. Afterwards, an appropriate design of the wire robot system is discussed in section 3. Due to the adaptability of the wire robot concept, different geometries are possible. Based upon the mechatronic development process according to VDI (2004), two designs are investigated in section 3. Therefore, virtual prototypes using mathematical models and numerical simulation are developed in sections 3.1 and 3.2. Based on the simulation results, the two designs are compared in section 3.3. Using numerical

optimization approaches, the chosen design is adapted to the specific task, see section 4. In section 5, the mechatronic system design is described. Finally, conclusions and future steps are discussed.

## 2. History and state of the art

Wires are widely used to suspend models in wind tunnels (Alexeevich et al., 1977; Griffin, 1988). Usually, these wires are fixed and therefore, the model is installed at a statical pose. The idea of using a wire robot suspension system adds the capability for performing dynamic and repeatable maneuvers during the experiment.

This concept was already proposed by Lafourcade (Lafourcade, 2004; Lafourcade et al., October 3-4, 2002). The SACSO (SSUSPENSION ACTIVE POUR SOUFFLERIE) robot made at CERT-ONERA is an active wire suspension for dynamic wind tunnel applications.

Recently, results are presented by chinese researchers (Yangwen et al., 2010; Zheng, 2006; Zheng et al., 2007; 2010), e.g. covering the aspects of load precalculation. The WDPSS (WIRE-DRIVEN PARALLEL SSUSPENSION SYSTEM) (Zheng et al., 2007) was optimized for large attack angles. Note, that in these approaches, the mass of the prototypes was much less than in the application described here which defines new challenges and requirements as described above.

From a kinematical point of view, the wire robot suspension system described here belongs to the parallel kinematic machines. Generally, parallel kinematic machines have major advantages compared to serial manipulators in terms of precision, load distribution and stiffness. Contrary, classical parallel kinematic machines have a relatively small workspace compared to serial systems. In 1985, Landsberger (Landsberger & Sheridan, 1985) presented the concept of a parallel wire driven robot, also known as tendon-based parallel manipulator or parallel cable robot. These robots – in the following denoted as wire robots – share the basic concepts of classical parallel robots, but overcome some of their typical drawbacks:

- Flexible wires can be coiled on winches which allow larger strokes in the kinematical chain. Therefore, larger workspaces can be realized.
- No complicated joints are required. Instead, winches and deflection pulleys are used.
- Simple and fast actuators can be used. Ideally, winches integrating drives and sensors for the coiled wire length and the force acting onto each wire, respectively, are applied.

Wires can only transmit tension forces, thus at least  $m = n + 1$  wires are needed to tense a system having  $n$  degrees-of-freedom (Ming & Higuchi, 1994a;b). From a kinematical point of view, this leads to redundancy. Taking into consideration that the wire robot must always be a fully tensed system to be stiff, the solution space of the wire force distribution has dimension  $m - n$ . Thus, for each pose of the platform within the workspace, there exists an unlimited number of wire force distributions which balance the load acting onto the platform. Contrarily, the wire forces are limited by lower and upper bounds to prevent slackness and wire breaks, respectively. From a control point of view, the force distributions must also be continuous while following a continuous trajectory through the workspace. This makes the force computation a complicated task, especially when the computation has to be performed in realtime, i.e. when a cyclic control system offers only a predefined time slot for all computations during run time.

Wire robots are subject to extensive research. At the University of Duisburg-Essen, the projects SEGESTA (SEILGETRIEBENE STEWART-PLATTFORMEN IN THEORIE UND ANWENDUNG, supported by the Germany Research Council DFG under HI 370/18, and ARTIST

(ARBEITSRAUMSYNTHESE SEILGETRIEBENER PARALLELKINEMATIKSTRUKTUREN, supported by the Germany Research Council DFG under HI370/24-1 and SCHR1176/1-2, focused on aspects of workspace calculation, design optimization and wire force calculation as well as on the realization of the SEGESTA testbed. Due to its acceleration capabilities, this testbed was successfully applied e.g. for the evaluation of inclinometers used within automotive electronic control units (ECU) (Bruckmann, Mikelsons, Brandt, Hiller & Schramm, 2008a,b; Fang, 2005; Hiller et al., 2005; Verhoeven, 2004).

Besides the acceleration potential, the large workspace of wire robots is advantageous which was addressed e.g. in the ROBOCRANE project (Albus et al., 1992; Bostelman et al., 2000) at the National Institute of Standards and Technology (NIST), USA. The CABLEV (CABLE LEVITATION) prototype at the University of Rostock, Germany (Woernle, 2000) was realized to investigate problems of control and oscillation cancellation (Heyden, 2006; Heyden et al., 2002; Maier, 2004). At the Institut national de recherche en informatique et en automatique (INRIA), Merlet achieved advances in workspace analysis of wire robots e.g. by applying interval analysis (Merlet, 1994a; 2004). Aspects of practical application and control are investigated in his project MARIONET which is referenced in section 3.

Tadokoro developed the wire robot WARP (WIREPULLER-ARM-DRIVEN REDUNDANT PARALLEL MANIPULATOR) for highly dynamical motions (Maeda et al., 1999; Tadokoro et al., 2002) and as a rescue system after earthquakes (Tadokoro & Kobayashi, 2002; Tadokoro et al., 1999; Takemura et al., 2006). The acceleration potential was also exploited in the project FALCON (FAST LOAD CONVEYANCE) by Kawamura (Kawamura et al., 1995; 2000).

At the Fraunhofer Institute for Manufacturing Engineering and Automation (IPA) in Stuttgart (Germany), Pott focuses on the application of wire robots e.g. for handling of solar panels (Pott et al., 2009; 2010) and developed the prototypes IPANEMA and IPANEMA2. On the theoretical side, algorithms for fast workspace analysis are developed (Pott, 2008).

Several research groups investigate on the application of wire robots for the positioning of reflectors above a telescope (Su et al., 2001; Taghirad & Nahon, 2007a,b) which is challenging in terms of stiffness and kinematics.

At the Eidgenössische Technische Hochschule (ETH) in Zurich (Switzerland), the interaction of wire robots and humans is addressed. This includes e.g. a rowing simulator (Duschau-Wicke et al., 2010; von Zitzewitz et al., 2009; 2008) and haptical displays e.g. for tennis simulation. Additionally, sleep research has been investigated by using the SOMNOMAT setup.

Nowadays, the wire robot SKYCAM<sup>®</sup> by Winnercomm, Inc. (USA), is well known from sports television. The patent "Suspension system for supporting and conveying equipment, such as a camera" Brown (1987) was already applied in 1987. In Europe the system became very popular with the soccer championship UEFA EURO 2008<sup>™</sup>.

Wire robots using elastic springs instead of active drives were investigated by Ottaviano and Thomas Ottaviano & Ceccarelli (2006); Ottaviano et al. (April 18-22 2005); Thomas et al. (September 14-19, 2003). They propose passive wire robots for pose measurements of moving objects. In this case the forward kinematics problem has to be solved.

### 3. Topological design

Using the suspension system, a wide range of motions should be possible to realize arbitrary maneuvers. Two requirements have to be covered:

1. Generally, the maneuvers to be performed are not known a priori (which is contrary to robots and manipulators in many applications). Therefore, a generally large volume of the workspace is demanded to allow for a wide range of motion paths.

2. The system has to offer a wide range of motion dynamics. Again, generally the trajectories are not known which makes it hard to specify the power demands and force or torque requirements, respectively, for the drives and winches and to choose a geometry. As a design criterion, one example trajectory was chosen which is described later.

This leads to the problem of finding an adequate geometry design. Due to architectural limitations, the geometry of the supporting frame is fixed and forms a cuboid (see Fig. 1 and Tab. 1). A similar limitation holds for the moving end effector of the wire robot which is the ship model to be moved. Since a wire robot is used and a cuboid platform has to be moved within a cuboid frame on symmetrical paths, an intuitive decision in the topological design step is to use eight wires. Two different design concepts are developed and evaluated in the

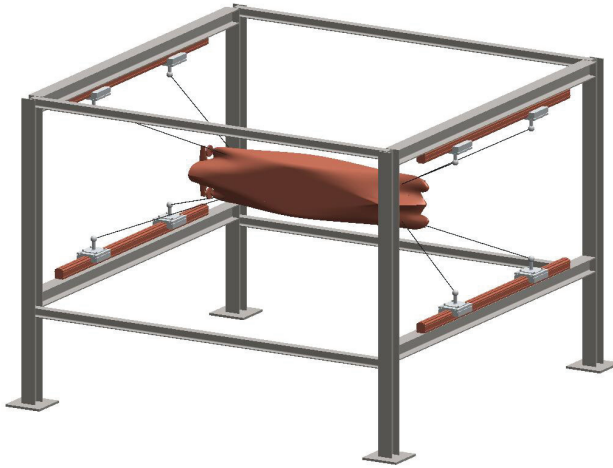


Fig. 1. Principle of application

following sections:

- The first approach uses a **rail-based system** with wires of constant length. The configuration of this mechanism is shown in Fig. 1. The wires are used as links of constant length, driven by a skid-rail system. Although each two skids share a common rail, every skid is separately operated by a DC motor via a drive belt. This equates to a linear drive. Linear drives for wire robots were introduced by Merlet (Merlet, 2008) who proposed this concept due to its enormous dynamic potential when coupled with pulley blocks. Application examples of the MARIONET robot can be found in Merlet (2010).
- The second concept – called **winch-based system** in the following – is based on classical wire robot approach using motorized winches. This principle used e.g. at the SEGESTA prototype of the University Duisburg-Essen in Duisburg, Germany (Fang, 2005), or at the IPANEMA prototypes of the Fraunhofer Institute for Manufacturing Engineering and Automation (IPA) in Stuttgart, Germany (Pott et al., 2009; 2010).

In the following, both design approaches are compared to each other using mathematical models and simulation environments. This allows to evaluate the performance of the designs at a virtual stage and eliminates the need for expensive real prototypes.

### 3.1 Kinematical and dynamical modeling of the rail-based system

#### 3.1.1 Kinematics

As a base for referencing all fixed points, an inertial frame  $\uparrow\mathbf{B}$  is introduced which may be located at an arbitrary point (see Fig. 2). Note, that it makes sense to choose a point which can be easily found on the real system, e.g. for the positioning of the deflection units or rails.

A similar approach is used for the definition of points which are attached to the end effector, i.e. which are measured with respect to the moving ship model. Therefore, a frame  $\uparrow\mathbf{P}$  is introduced.

Now the relation – or, in terms of kinematical analysis – the kinematical transformation between the coordinate systems  $\uparrow\mathbf{B}$  and  $\uparrow\mathbf{P}$  can be described: The vector  $\mathbf{r}_p$  defines the position of  $\uparrow\mathbf{P}$  with respect to the inertial frame. The orientation of the end effector with respect to the inertial system is described by "roll-pitch-yaw" angles which are very common in nautical research. The local rotation around the x-axis is given by angle  $\psi$ , around the y-axis by angle  $\theta$  and around the z-axis by angle  $\varphi$ . The end effector pose is therefore described by  $\mathbf{X} = [x \ y \ z \ \psi \ \theta \ \varphi]^T$ . To represent the rotation between  $\uparrow\mathbf{B}$  and  $\uparrow\mathbf{P}$ , the rotation matrix  $\mathbf{R}$  is introduced.

This simple kinematic foundation can already be used to calculate the inverse kinematics which allows to compute the required linear drive positions for a predefined end effector pose (Sturm et al., 2011). Note, that this description is purely kinematic – thus, elastic effects which may have a major influence in wire robots are not taken into account. As for most parallel kinematic machines, the inverse kinematics calculation is simple. Given an end effector pose  $\mathbf{X}$ , the inverse kinematics for each driving unit of this robot can be calculated by an intersection between a sphere – representing the wire – and a straight line (see Fig. 2) which represents the rail. The sphere is described by

$$(\mathbf{b}_i - \mathbf{r}_{c_i})^2 - l_i^2 = 0, \quad 1 \leq i \leq 8, \quad (1)$$

where the vector  $\mathbf{b}_i$  denotes the current position of the  $i^{\text{th}}$  skid and  $l_i$  is the constant length of the  $i^{\text{th}}$  wire. Now

$${}^B\mathbf{r}_{c_i} = {}^B\mathbf{r}_p + \mathbf{R}^P \mathbf{p}_i \quad (2)$$

describes the position of the  $i^{\text{th}}$  wire connection point  $\mathbf{p}_i$  on the end effector, referred in the inertial frame  $\uparrow\mathbf{B}$ .

The line can be described by

$$\mathbf{b}_i = \mathbf{r}_{S_i} + q_i \mathbf{n}_{R_i}, \quad 1 \leq i \leq 8 \quad (3)$$

where  $\mathbf{r}_{S_i}$  is a known point on the  $i^{\text{th}}$  fixed rail axis,  $q_i$  the actuator degree of freedom – i.e. translation along the rail – and  $\mathbf{n}_{R_i}$  a unit vector in direction of the length of the rail. In case of the proposed robot,  $\mathbf{n}_{R_i}$  is equal to  $\mathbf{e}_y$  for  $i = 1 \leq i \leq 8$ . The substitution of equation (1) into equation (3) leads to the equation

$$q_i = -\mathbf{c}_i \mathbf{n}_{R_i} \pm \sqrt{(\mathbf{c}_i \mathbf{n}_{R_i})^2 - \mathbf{c}_i^2 + l_i^2}, \quad (4)$$

where  $\mathbf{c}_i = \mathbf{r}_{S_i} - \mathbf{r}_{c_i}$ . Analytically, there exist two possible solutions for each actuator due to the quadratic equations. On the other hand, from a technical point of view, there are two skids

per rail that cannot intersect each other. Thus, it is easy to derive a unique solution. In the case of the wire robot under consideration, it is assumed that the equation

$$q_i = -\mathbf{c}_i \mathbf{n}_{Ri} + (-1)^i \sqrt{(\mathbf{c}_i \mathbf{n}_{Ri})^2 - \mathbf{c}_i^2 + l_i^2} \tag{5}$$

shall hold for the actuator  $i$ . As already mentioned, these considerations only describe the

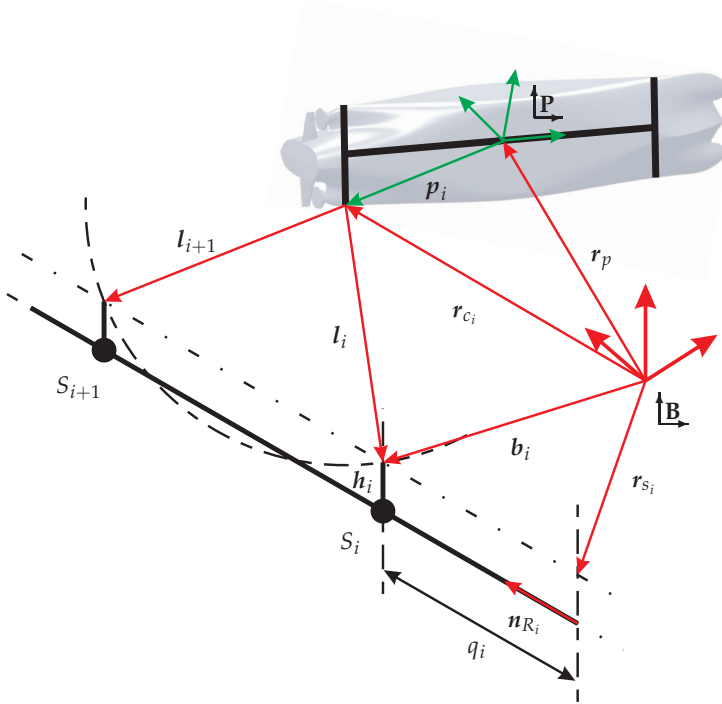


Fig. 2. Kinematic model

motion of the system without the influences of forces or torques. Therefore, also elastic effects are not covered by this model. Additionally, it is not possible to derive information regarding the required drive performance. The base for these calculations is the introduction of a dynamic model in the next section, describing the behaviour of the system under the influence of loads, forces and torques.

**3.1.2 Dynamics**

The dynamical equations of motion of the end effector can be described by

$$\underbrace{\begin{bmatrix} m_p \mathbf{E} & \mathbf{0} \\ \mathbf{0} & \mathbf{I} \end{bmatrix}}_{\mathbf{M}_p} \underbrace{\begin{bmatrix} \ddot{\mathbf{r}} \\ \dot{\boldsymbol{\omega}} \end{bmatrix}}_{\ddot{\mathbf{x}}} + \underbrace{\begin{bmatrix} \mathbf{0} \\ \boldsymbol{\omega} \times (\mathbf{I}\boldsymbol{\omega}) \end{bmatrix}}_{\mathbf{g}_c} - \underbrace{\begin{bmatrix} \mathbf{f}_E \\ \boldsymbol{\tau}_E \end{bmatrix}}_{\mathbf{g}_E} = \mathbf{A}^T \mathbf{f} \tag{6}$$

-w



with

- $\mathbf{M}_p$  mass matrix of end effector,
- $\mathbf{g}_C$  cartesian space vector of coriolis and centrifugal forces and torques,
- $\mathbf{g}_E$  vector of generalized applied forces and torques.

Here  $\mathbf{A}^T$  denotes the so-called structure matrix. This matrix describes the influence of the wire forces  $\mathbf{f}$  acting onto the end effector (Ming & Higuchi, 1994a; Verhoeven, 2004).

The structure matrix can be derived by

$$\begin{bmatrix} \mathbf{v}_1 & \dots & \mathbf{v}_m \\ \mathbf{p}_1 \times \mathbf{v}_1 & \dots & \mathbf{p}_m \times \mathbf{v}_m \end{bmatrix} \begin{bmatrix} f_1 \\ \vdots \\ f_m \end{bmatrix} = \mathbf{A}^T \mathbf{f} = -\mathbf{w}, \quad (7)$$

where  $\mathbf{l}_i = l_i \mathbf{v}_i$ , i.e.  $\mathbf{v}_i$  is the unit vector along the wires.

As already introduced in section 2, a wire robot has a redundant structure. Thus, for a body – in this case, the ship model – that moves freely in three translational and three rotational degrees of freedom at least seven wires are required. Due to symmetry and architectural considerations, in this application eight wires are applied. Accordingly, the robot is even twofold redundant.

This is also reflected by the structure matrix  $\mathbf{A}^T$  which is element of  $\mathbb{R}^{6 \times 8}$ . Accordingly, eq. 7 represents an under-determined system of linear equations. Therefore, the calculation of the wire force distribution is not straightforward and rather complicated. On the other hand, this offers a potential for optimizations. Considering that in this application fast motions of the heavy-weight end effector are desired, it is reasonable to reduce the motor power consumption and the applied load on the mechanical components.

Additionally, the unilateral properties of the wires have to be taken into account as introduced in section 2: On the one hand, wires have a limited breaking load, on the other hand, the wires need a defined minimum tension to avoid slackness.

Accordingly, the force distribution  $\mathbf{f}$  can be formulated as a constrained nonlinear optimization problem (Bruckmann, Mikelsons, Brandt, Hiller & Schramm, 2008a) with

$$\begin{aligned} \text{minimize } \|\mathbf{f}\|_2 &= \sqrt{\sum_{i=1}^m f_i^2} \\ \text{s.t. } \mathbf{f}_{\min} &\leq \mathbf{f} \leq \mathbf{f}_{\max} \quad \wedge \quad \mathbf{A}^T \mathbf{f} + \mathbf{w} = \mathbf{0}. \end{aligned} \quad (8)$$

In this paper the function *lsqlin* from the MATLAB<sup>®</sup> Optimization Toolbox<sup>®</sup> has been used to solve the problem. Note, that this implementation cannot be used for realtime control since the worst-case run-time in each control cycle cannot be guaranteed a priori. Several approaches are known to handle this problem (Borgstrom et al., 2009; Bruckmann, Mikelsons, Brandt, Hiller & Schramm, 2008a,b; Bruckmann et al., 2007b; Bruckmann, Pott, Franitza & Hiller, 2006; Bruckmann, Pott & Hiller, 2006; Ebert-Uphoff & Voglewede, 2004; Fattah & Agrawal, 2005; Oh & Agrawal, 2005; Verhoeven, 2004). In this application, a force minimizing algorithm for realtime force distribution will be implemented, using a geometric approach (Bruckmann, 2010; Bruckmann et al., 2009; Mikelsons et al., 2008).

Each wire is driven by a combination of a skid and a DC motor. The dynamics of the skid subsystems can be modeled as

$$\mathbf{M}_s \ddot{\mathbf{q}} + \mathbf{D}_s \dot{\mathbf{q}} + \mathbf{f}_y = \mathbf{f}_s \quad (9)$$

with

- $\mathbf{M}_s$  mass matrix of the skids  
 $\mathbf{D}_s$  diagonal matrix of coulomb friction between skids and rails,  
 $\mathbf{f}_y$  vector of wire force component in direction of skid movement  
 $\mathbf{f}_s$  skid driving force vector.

Motor and skid are connected by a gear belt, providing a linear drive. The elasticity of these belts – as well as the elasticity of the wires as already mentioned – are not taken into account. The dynamical equations of the DC motors can be described by

$$\mathbf{M}_m \ddot{\Theta} + \mathbf{D}_m \dot{\Theta} + \eta \mathbf{f}_s = \mathbf{u} \quad (10)$$

with

- $\mathbf{M}_m$  inertia matrix of the drive units including crown gear and motor,  
 $\mathbf{D}_m$  diagonal matrix of coulomb friction at the crown gear bearing,  
 $\eta$  radius of the crown gear,  
 $\Theta$  vector of motor shaft angles,  
 $\mathbf{u}$  electromechanical driving torque vector.

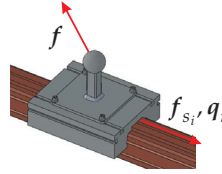


Fig. 3. Skid dynamics

### 3.2 Kinematical and dynamical modeling of the winch-based system

#### 3.2.1 Kinematics

Wire driven parallel kinematic systems that use winches instead of rails are well studied as introduced in section 2. Therefore, only a very short description of the kinematics and dynamics is given here. The end effector properties are considered to be identical for both systems. By the use of fixed eyelets as exit points for the wires, the inverse kinematics approach can be calculated by

$$l_{w_i} = \|\mathbf{b}_{w_i} - \mathbf{r}_{c_i}\|_2, \quad i = 1 \leq i \leq 8. \quad (11)$$

In this case the vector  $\mathbf{b}_{w_i}$  denotes the fixed position of the exit point of the  $i^{\text{th}}$  wire, while equation (2) is used for the transformation of the vectors  $\mathbf{p}_i$  into the inertial coordinate system. Here,  $l_{w_i}$  describes the current length of the  $i^{\text{th}}$  wire.

#### 3.2.2 Dynamics

The end effector dynamics, the structure matrix  $\mathbf{A}^T$  and the minimum force distribution are calculated in the same way as presented in section 3.1.2. The significant difference between the rail-based and the winch-based system lies in the actuator dynamics. The winch dynamics including the motor can be modeled as

$$\mathbf{J}_w \ddot{\Theta}_w + \mathbf{D}_w \dot{\Theta}_w + \mu \mathbf{f}_t = \mathbf{u}_w \quad (12)$$

with	
$J_w$	inertia matrix of the drive units including winch and motor,
$D_w$	diagonal matrix of coulomb friction at the winch bearing,
$f_t$	vector of wire forces,
$\mu$	radius of the winch,
$\Theta_w$	vector of motor shaft angles,
$u_w$	electromechanical driving torque vector.

### 3.3 Comparison of rail- and winch-based system

The concepts described in section 3 are both capable to move the ship model within the wind tunnel, but based on the different actuation principles, relevant differences in terms of

- workspace volume,
- peak forces in the wires and
- required peak motor power

are expected. Based on the introduced models, virtual prototypes within a MATLAB/Simulink<sup>®</sup> simulation environment can be derived and investigated and their suitability for the application addressed here can be evaluated.

First, preliminary design parameters have to be set. In Tab. 1, a review of the dimensions of the testbed as well as of the ship models to be moved is given. Some of the further assumptions are specific to the proposed designs:

- For the winch-based system the eyelets are considered to be attached at the corners of a cube.
- For the rail-based system, the rails are considered to be mounted at the front and back side of the cube (see Fig. 1). During the design phase, a length of  $l = 1.8\text{m}$  for each wire has been empirically determined.

	testbed	model
length [m]	5.25	3.2
width [m]	3.7	0.5
height [m]	2.4	0.5
mass [kg]	–	100

Table 1. Robot parameters

In order to compare and evaluate the two design concepts, two criteria were specified from the user's point of view as introduced in section 3:

- The achievable workspace under a predefined orientation range should be as large as possible. This allows a wide range of paths. To compute the workspace volume, the cuboid volume of the test bed has been discretized along the three translational degrees of freedom by 100 grid points in each direction. Each point in this volume has been examined to ensure the desired orientation capabilities for the end effector at each grid point. Therefore, orientations of  $\psi = \pm 30^\circ$ ,  $\theta = \pm 5^\circ$  and  $\varphi = \pm 5^\circ$  have been defined.
- Additionally, the peak power consumption of each motor is of interest (Sturm et al., 2011). Especially the required peak power per drive has a major influence on the costs of the overall system since the motors and winches must be designed to provide this mechanical

peak power. For the power consumption analysis a reference trajectory according to Fig. 4 has been defined: The end effector performs a translational ascending and descending movement with a frequency of 0.5Hz combined with an oscillating rotation of 2.5Hz around the body-fixed x-axis. This trajectory is typical for the manoeuvres to be tested in the application example.

The minimum wire force distribution was calculated according to Eq. 8. The wire force boundaries were set to  $100N \leq f_i \leq 2000N$ . In Fig. 5 and Fig. 6 the power consumptions

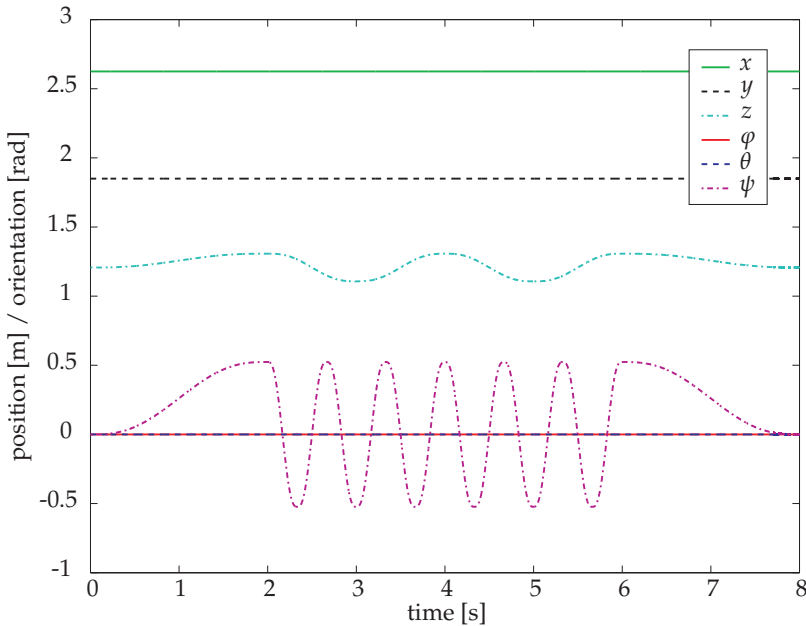


Fig. 4. Time History of the Reference Trajectory

of both the systems are shown. It is obvious that the required peak actuator power of the winch-based system is about four times higher than that of the rail-based system. This disadvantageous distribution of the required mechanical power demands for very powerful and expensive drives which should be avoided. In Fig. 7 the workspace of the winch-based system is shown. The blue colored dots define the positions of the wire deflection points. In Fig. 8 the workspace with identical properties of the rail-based system is shown. Here the four blue colored bars define the positions of the rails. Obviously, the rail-based system has a workspace which is remarkably smaller than the winch-based approach has. Nevertheless, the rail-based concept provides an acceptable volume ratio of the testbed cuboid. According to the lesser power requirements the rail-based design concept has been chosen for the realization of the wind tunnel suspension system.

### 3.4 Further optimization potential

In the last sections, the approach of using wires of constant length was chosen for realization. Thus, one of the most outstanding properties of wires – the variable length – is not exploited and a conventional parallel kinematic machine of type *PRR* (Merlet, 2006) should be

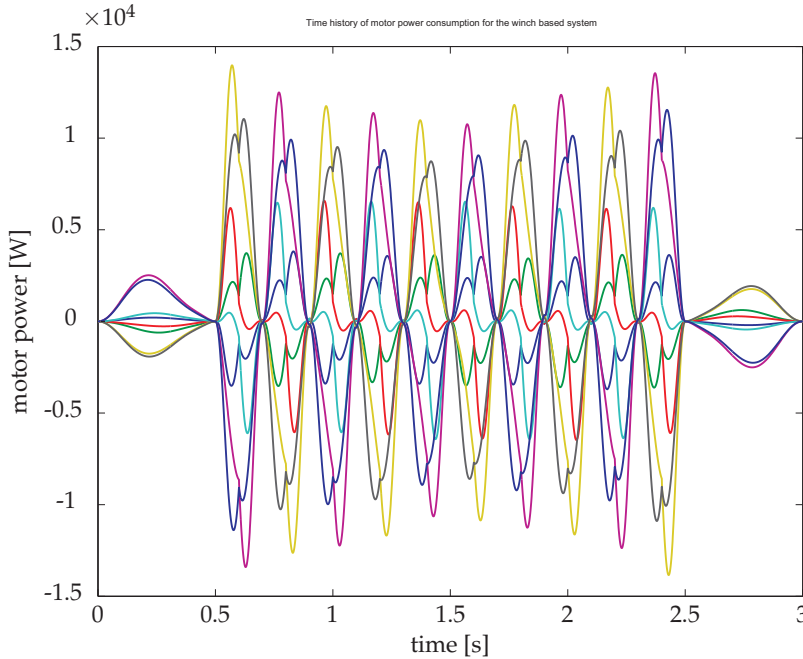


Fig. 5. Time history of the motor power consumption of the winch-based system

applicable. On the other hand, conventional parallel kinematics use very stiff and therefore massive components for legs, drives and joints to withstand both tensile and compressive forces which causes massive turbulences within the air flow. Nevertheless, applying again a redundant structure allows to control the inner tension of the system. This can be very useful as it allows to set the forces which the favorably thin links and joints have to withstand. For thin links, the Euler's second buckling mode should be avoided as the following example shows (Bruckmann, 2010; Bruckmann et al., 2010):

It is assumed that the links are realized using Rankine (Ashley & Landahl, 1985) profiles which are similar to ellipses. The ratio of the length  $L_A$  and the width  $L_B$  of the ellipse should be a compromise between a high geometrical moment of inertia  $I$  and an optimal aerodynamical shape. In this example, it is set to

$$\frac{L_A}{L_B} = 4 \quad (13)$$

The collapse load  $F_K$  for a buckling length  $s$ , a modulus of elasticity  $E$  and a geometrical moment of inertia  $I$  is defined as

$$F_K = \pi^2 \frac{EI}{ks^2}, \quad (14)$$

where Euler's second buckling mode – i.e. both ends of the link are hinged – defines  $k = 1$ . Assuming that modern fiber material can be applied to realize the links, the lightweight, but very tensile carbon fiber reinforced plastic (CFRP) is chosen. The properties of CFRP are listed in Tab. 2.

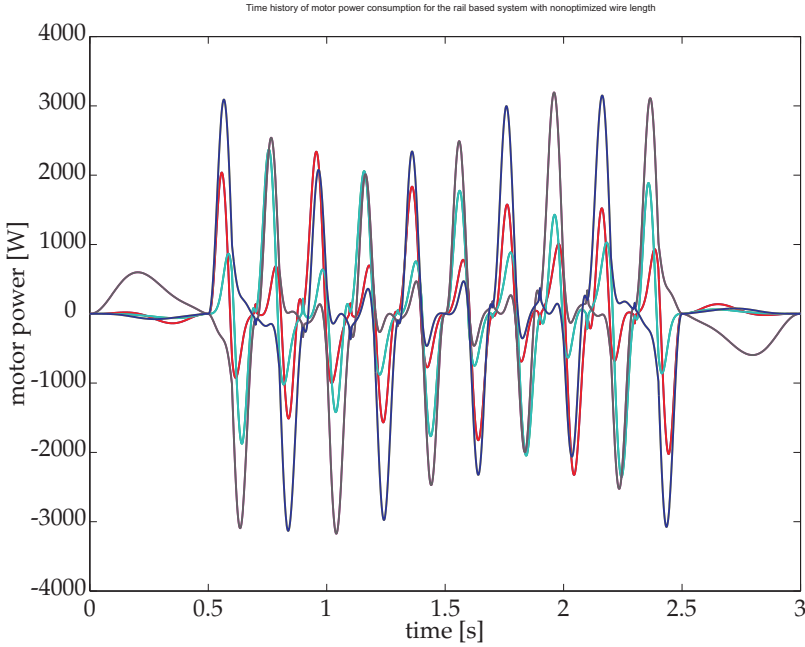


Fig. 6. Time history of the motor power consumption of the rail-based system

fiber material	carbon fiber HT
matrix	epoxy polymer
fiber volume percentage	60%
tensile strength (in direction of fibers) $R_{\parallel}^+$	2000N/mm <sup>2</sup>
modulus of elasticity $E_{\parallel}$	140000N/mm <sup>2</sup>

Table 2. Material properties of the carbon fiber reinforced plastic (CFRP)

The ellipsoid and solid link profile choosing  $L_A = 40\text{mm}$  and  $L_B = 10\text{mm}$  has a length of  $l = 2500\text{mm}$ . Thus, the smaller geometrical moment of inertia is

$$I_A = \frac{\pi}{4} L_A L_B^3 = 31415.92\text{mm}^4. \quad (15)$$

Using the buckling length  $s = l = 2500\text{ mm}$  and the CFRP proposed,

$$F_K = \pi^2 \frac{E_{\parallel} I_A}{l^2} = 6945.40\text{N} \quad (16)$$

holds. Contrarily, a collapse of the link due to pure compressive forces can be computed, using a tensile strength  $R$  and a cross section of the ellipsoid profile  $A$  as

$$F_Z = RA. \quad (17)$$

This results in

$$F_Z = R_{\parallel}^+ \frac{\pi L_A L_B}{4} = 2513274.12\text{N}. \quad (18)$$

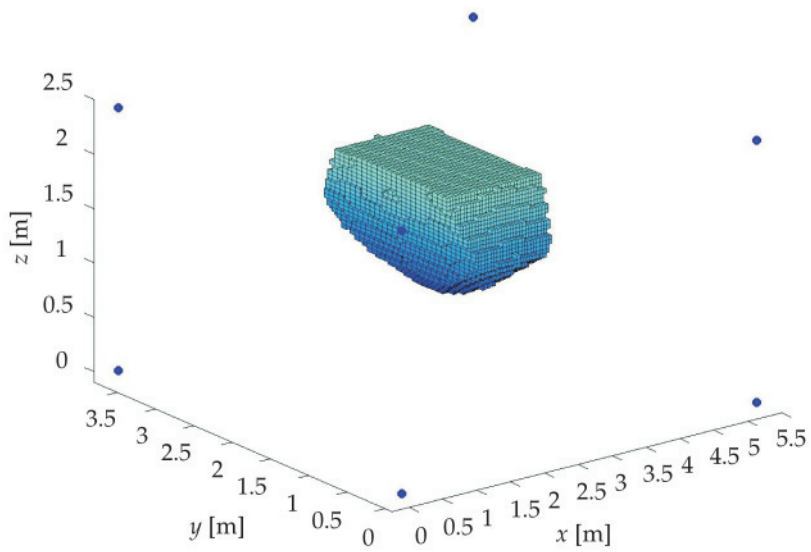


Fig. 7. Workspace of the winch-based system

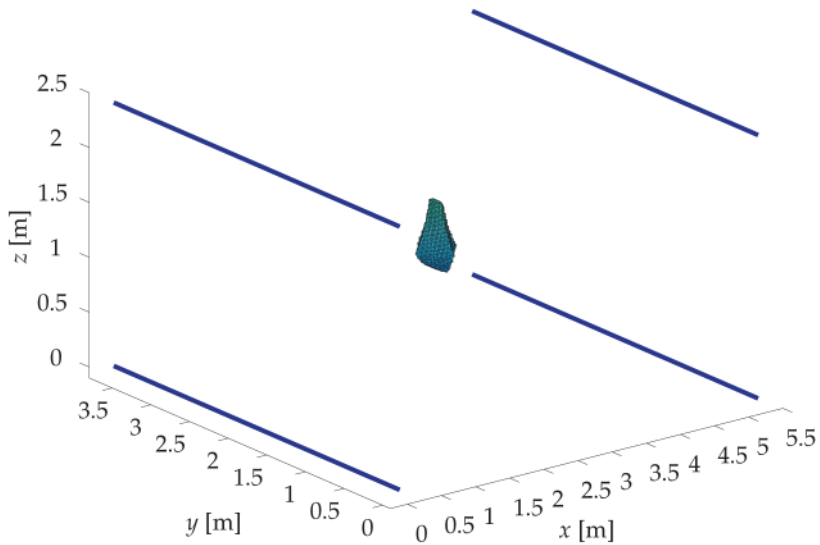


Fig. 8. Workspace of the rail-based system with  $l_i = 1.8m$

The huge ratio of  $F_Z/F_K \approx 360$  shows the potential of a tensile system. Now the application of solid links of constant length also offers the possibility to transfer small (!) and controlled

compressive forces using a force control system: While in the case of using wires of constant length the required positive tension in the lower links increases the tension in the upper links, this need vanishes for links made of solid material. Additionally, high tensions in the upper links coincide with high velocities in the respective drives. Therefore, high power peaks occur during the benchmark trajectories. At the same time some of the lower drives run at comparably low velocities while their links have advantageous angles of attack regarding the load compensation. These advantageous angles of attack could be used to support the upper links very effectively (Bruckmann et al., 2010).

These considerations are subject to current research. For the time being, they are not applied in the project described here.

#### 4. Optimization of wire lengths

For the rail-based approach, the position and the length of the rails are fixed parameters due to the limited available architectural space within the wind tunnel test facility. Nevertheless, the concept uses wires as links of constant length. This fixed length can be set during the experiment design phase, considering that the wire length has an influence onto the peak forces in the wires on a predefined trajectory.

The robot can be subject to two different optimizations which resemble the requirements during the topological design phase:

- The first criterion is a maximum available workspace with predefined orientation ranges. This is investigated in section 4.1.
- The second criterion is to minimize the maximum motor power required along a predefined trajectory in order to reduce the required actuator peak power. This is analyzed in section 4.2.

Therefore, two different optimization routines are employed and their results are discussed.

##### 4.1 Workspace criterion

Analyzing the application-specific requirements, the rotational degrees-of-freedom of the end effector are of much more interest than the translational ones. This is due to the fact that the trajectory to be performed may be located at an arbitrary domain of the workspace as long as the model stays within the parallel inflow.

Due to this aspect, the workspace has to provide possible rotations of  $\psi = \pm 30^\circ$ ,  $\theta = \pm 5^\circ$  and  $\varphi = \pm 5^\circ$  in a volume as large as possible as already introduced in section 3.3. Again, the basic discretization approach for this optimization routine is applied and at each point, the kinematical constraints (e.g. the prismatic joint limits) and force limits are checked. Accordingly, a minimum force distribution for predefined loads onto the end effector is calculated for each grid point and platform orientation in order to ensure that the wire forces are within the limits. The optimization algorithm was implemented in MATLAB<sup>®</sup>, employing a combination of an evolutionary and a gradient-based approach. Discretization approaches are also proposed in Hay & Snyman (2004; 2005).

Advanced approaches base on the continuous analysis and verification of the workspace as described in Bruckmann et al. (2007a); Gouttefarde et al. (2011; 2008; 2007). The application of those methods is subject to future work.

The task of optimizing can be formulated as follows: Let  $A = \{a_i\}$  define the set of the discretized points and  $g : A \mapsto \mathcal{R}; \mathbf{l} \mapsto n$  the function that maps a set of wire lengths onto a natural number  $n$ , where  $n$  is the number of points  $a_i \in A$  that lie in the desired workspace.



Then the optimization task is to maximize the function  $g$ . Fig. 8 shows the workspace of the proposed robot with an identical length of  $l = 1.8m$  for each wire. Fig. 9 shows the workspace after the optimization process. The results for the optimized wire length are listed in Tab. 3.

	$l_1$	$l_2$	$l_3$	$l_4$	$l_5$	$l_6$	$l_7$	$l_8$
length [m]	1.80	1.80	1.83	1.83	1.60	1.60	1.66	1.66

Table 3. Wire lengths for maximum workspace volume

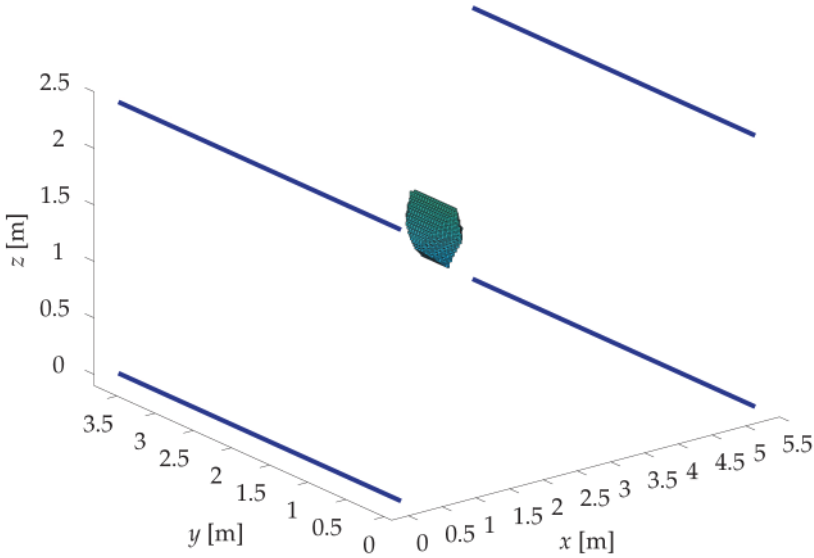


Fig. 9. Workspace using optimized wire lengths

By the comparison of the workspace calculations of both approaches it is clear that the optimization process led to an increased reachable workspace by 136% that has been therefore more than doubled.

#### 4.2 Drive power criterion

The second optimization approach attempts to minimize the peak power consumption of the drives for a given trajectory. It is clear that in upper regions of the workspace, the angles of attack of the wires become very disadvantageous which leads to high wire forces. An additional effect is that with these disadvantageous angles also that part of the reaction forces increases which is exerted onto the skids. Since this is related to the wire length, the goal is to find an optimized length that leads to a minimum peak power consumption of the motors for a given trajectory. Again this analysis was performed based on a discrete sampling of the trajectory. Advanced continuous approaches are known (Bruckmann, Mikelsons & Hiller, 2008; Merlet, 1994b) and subject to future work.

According to this goal the optimization task can be formulated as follows: Let  $b$  define a real scalar that represents maximum power per motor along a given trajectory. Let  $h : \mathbf{1} \mapsto b$  be the

function that maps a set of wire lengths onto that real number  $b$ . Then the optimization task is to minimize the function  $h$ .

Again, the reference trajectory shown in Fig. 4 has been used. The results of the wire length for an optimized power consumption are listed in Tab. 4.

	$l_1$	$l_2$	$l_3$	$l_4$	$l_5$	$l_6$	$l_7$	$l_8$
length [m]	2.00	2.00	2.00	2.00	1.83	1.70	1.81	1.70

Table 4. Wire lengths for minimum power consumption

Note the reduced peak power consumption shown in Fig. 10. By using the optimized wire lengths a peak power reduction from 3194kW (compare Fig. 6) to 3061kW could be achieved. Concluding these results, the system has to be adapted to different requirements since the

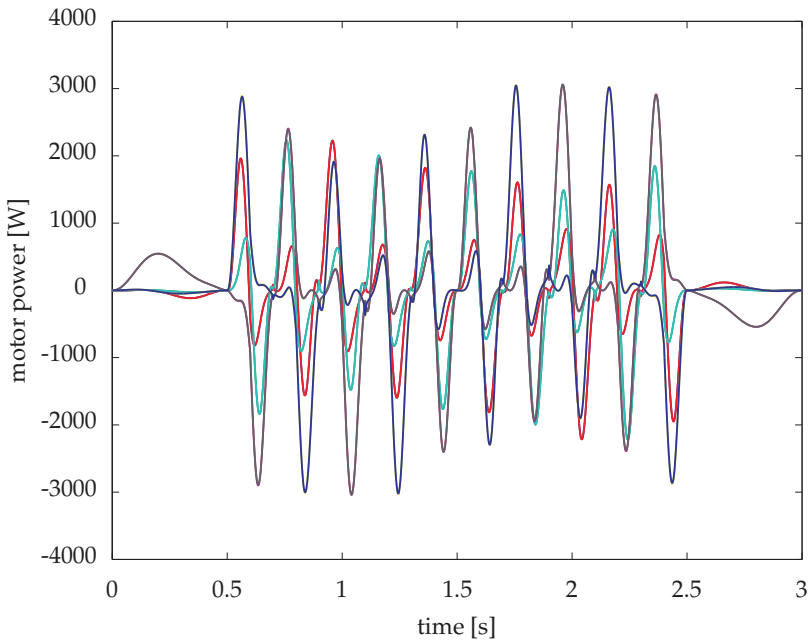


Fig. 10. Motor power consumption over time with optimized wire lengths

optimized parameters differ considerably. It depends on the specific experiment if workspace or drive power are critically, but using exchangeable wires, the adaption of the system to defined trajectories is easy and can be done quickly.

## 5. Mechatronic system design

Besides the geometrical design problem, the question of components, interfaces and control system architecture had to be solved. To guarantee a maximum flexibility, a modular controller system by dSPACE GmbH (Paderborn/Germany) was chosen for the hardware realization (Fig. 11):

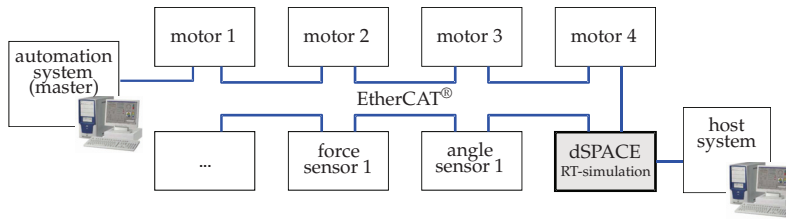


Fig. 11. EtherCAT® communication system

- **Control System:** The dSPACE DS1006 (Quadcore AMD Opteron Board, 2.8 GHz) is the CPU of the modular dSPACE hardware. This system can be programmed using MATLAB/Simulink® and is a very powerful base for data acquisition and numerically extensive computations.
- **Communication System:** A number of values has to be measured. This includes skid positions, wire forces and the state of safety systems. Due to the overall size of the wind tunnel suspension system, the distances between the different components are comparably far. As a consequence, the Ethernet-based field bus system EtherCAT® was chosen for communication. It combines robustness against electromagnetic disturbances, integrated error diagnosis and a broad bandwidth of 100MBit/s. This allows to completely process all communication (i.e. sensor values, motor commands) via one single bus system.
- **Sensors:** During testing, the skid positions and the tendon forces are monitored. All sensors have interfaces to the EtherCAT® bus.
- **Skid-Rail System:** The skids are driven by DC motors manufactured by SEW Eurodrive (Bruchsal, Germany). These motors use smart power amplifiers and can be commanded by desired torque, velocity or position. Also those power amplifiers are connected to the EtherCAT® bus which allows easy and reliable commanding and monitoring.

## 6. Conclusions

In this paper, the application of a wire robot as a wind tunnel suspension system is described. Starting with an overview of the state of the art, topological variants are described. The decision for the optimal system was based on a modeling and simulation approach which allowed to study different systems by using virtual prototypes. Additionally, the usage of solid links in a redundant structure was discussed. The chosen architecture was optimized for the application by using numerical approaches. The optimization goal was to achieve either a large workspace or a low peak motor power to limit the costs for the mechanical components and especially the motors.

Finally, a short overview of the mechatronic system design is given. Presently, the system is installed and prepared for first test runs.

## 7. References

- Albus, J., Bostelman, R. & Dagalakis, N. (1992). The NIST SPIDER, a robot crane, *Journal of research of the National Institute of Standards and Technology* 97(3): 373–385.
- Alexeevich, B. G., Vladimirovich, B. A., Pavlovich, M. S. & Sergeevich, S. K. (1977). Device for suspension of aircraft model in wind tunnel. United States Patent 4116056.
- Ashley, H. & Landahl, M. (1985). *Aerodynamics of Wings and Bodies*, Courier Dover Publications.

- Borgstrom, P. H., Jordan, B. L., Borgstrom, B. J., Stealey, M. J., Sukhatme, G. S., Batalin, M. A. & Kaiser, W. J. (2009). NIMS-PL: a cable-driven robot with self-calibration capabilities, *Trans. Rob.* 25(5): 1005–1015.
- Bostelman, R., Jacoff, A. & Proctor, F. (2000). Cable-based reconfigurable machines for large scale manufacturing, *Japan/USA Flexible Automation Conference Proceedings*, University of Michigan, Ann Arbor, MI.  
URL: [citeseer.ist.psu.edu/bostelman00cablebased.html](http://citeseer.ist.psu.edu/bostelman00cablebased.html)
- Brown, G. W. (1987). Suspension system for supporting and conveying equipment, such as a camera. United States Patent 4710819.
- Bruckmann, T. (2010). *Auslegung und Betrieb redundanter paralleler Seilroboter*, Dissertation, Universität Duisburg-Essen, Duisburg, Germany.  
URL: <http://duepublico.uni-duisburg-essen.de/servelets/DocumentServlet?id=23303>
- Bruckmann, T., Hiller, M. & Schramm, D. (2010). An active suspension system for simulation of ship maneuvers in wind tunnels, in D. Pisla, M. Ceccarelli, M. Husty & B. Corves (eds), *New Trends in Mechanism Science*, Vol. 5 of *Mechanisms and Machine Science*, Springer. ISBN: 978-90-481-9688-3.
- Bruckmann, T., Mikelsons, L., Brandt, T., Hiller, M. & Schramm, D. (2008a). Wire robots part I - kinematics, analysis & design, in A. Lazinica (ed.), *Parallel Manipulators - New Developments*, ARS Robotic Books, I-Tech Education and Publishing, Vienna, Austria, pp. 109–132. ISBN 978-3-902613-20-2.
- Bruckmann, T., Mikelsons, L., Brandt, T., Hiller, M. & Schramm, D. (2008b). Wire robots part II - dynamics, control & application, in A. Lazinica (ed.), *Parallel Manipulators - New Developments*, ARS Robotic Books, I-Tech Education and Publishing, Vienna, Austria, pp. 133–153. ISBN 978-3-902613-20-2.
- Bruckmann, T., Mikelsons, L. & Hiller, M. (2008). A design-to-task approach for wire robots, in A. Kecskeméthy (ed.), *to appear in Proceedings of Conference on Interdisciplinary Applications of Kinematics 2008*, Lima, Peru.
- Bruckmann, T., Mikelsons, L., Pott, A., Abdel-Maksoud, M., Brandt, T. & Schramm, D. (2009). A novel tensed mechanism for simulation of maneuvers in wind tunnels, *Proceedings of the ASME 2009 International Design Engineering Technical Conferences & Computers and Information in Engineering Conference*, ASME International, San Diego, CA, USA. to appear.
- Bruckmann, T., Mikelsons, L., Schramm, D. & Hiller, M. (2007a). Continuous workspace analysis for parallel cable-driven stewart-gough platforms, *Proceedings in Applied Mathematics and Mechanics* 7(1): 4010025–4010026.  
URL: <http://dx.doi.org/10.1002/pamm.200700774>
- Bruckmann, T., Mikelsons, L., Schramm, D. & Hiller, M. (2007b). A new force calculation algorithm for tendon-based parallel manipulators, *Proceedings of the 2007 IEEE/ASME International Conference on Advanced Intelligent Mechatronics (AIM2007)*, IEEE / ASME, Zurich, Switzerland, pp. 1–6.
- Bruckmann, T., Pott, A., Franitz, D. & Hiller, M. (2006). A modular controller for redundantly actuated tendon-based Stewart platforms, in M. Husty & H.-P. Schroecker (eds), *Proceedings of EuCoMeS, the first European Conference on Mechanism Science*, Innsbruck University Press, Obergurgl, Austria. ISBN 3-901249-85-0.
- Bruckmann, T., Pott, A. & Hiller, M. (2006). Calculating force distributions for redundantly actuated tendon-based Stewart platforms, in J. Lenarčič & B. Roth (eds), *Advances in Robot Kinematics - Mechanisms and Motion*, Advances in Robotics and Kinematics 2006,

- Springer Verlag, Dordrecht, The Netherlands, Ljubljana, Slowenien, pp. 403–413.  
URL: <http://dx.doi.org/10.1007/978-1-4020-4941-5>
- Duschau-Wicke, A., von Zitzewitz, J., Caprez, A., Lunenburger, L. & Riener, R. (2010). Path control: A method for patient-cooperative robot-aided gait rehabilitation, *Neural Systems and Rehabilitation Engineering, IEEE Transactions on* 18(1): 38–48.
- Ebert-Uphoff, I. & Voglewede, P. (2004). On the connections between cable-driven robots, parallel manipulators and grasping, Vol. 5, pp. 4521–4526 Vol.5.
- Fang, S. (2005). *Design, Modeling and Motion Control of Tendon-based Parallel Manipulators*, Ph. D. dissertation, Gerhard-Mercator-University, Duisburg, Germany. Fortschritt-Berichte VDI, Reihe 8, Nr. 1076, Düsseldorf.
- Fattah, A. & Agrawal, S. K. (2005). On the design of cable-suspended planar parallel robots, *ASME J. of Mechanical Design* 127(5): 1021–1028.
- Gouttefarde, M., Daney, D. & Merlet, J.-P. (2011). Interval-analysis-based determination of the wrench-feasible workspace of parallel cable-driven robots, *Robotics, IEEE Transactions on* 27(1): 1–13.
- Gouttefarde, M., Krut, S., Company, O., Pierrot, F. & Ramdani, N. (2008). On the design of fully constrained parallel cable-driven robots, in Lenarcic & P. W. eds. (eds), *Advances in Robot Kinematics (ARK)*, Springer, pp. 71–78.
- Gouttefarde, M., Merlet, J.-P. & Daney, D. (2007). Wrench-feasible workspace of parallel cable-driven mechanisms, *2007 IEEE International Conference on Robotics and Automation, ICRA 2007, 10-14 April 2007, Roma, Italy* pp. 1492–1497.
- Griffin, S. A. (1988). Wind tunnel model support and attitude control. United States Patent 4116056.
- Hay, A. & Snyman, J. (2004). Analysis and optimization of a planar tendon-driven parallel manipulator, in J. Lenarčič & C. Galetti (eds), *Advances in Robot Kinematics*, Sestri Levante, pp. 303–312.
- Hay, A. & Snyman, J. (2005). Optimization of a planar tendon-driven parallel manipulator for a maximal dextrous workspace, *Engineering Optimization*, Vol. 37 of 20, pp. 217–236.
- Heyden, T. (2006). *Bahnregelung eines seilgeführten Handhabungssystems mit kinematisch unbestimmter Lastführung*, PhD thesis, Universität Rostock. ISBN: 3-18-510008-5, Fortschritt-Berichte VDI, Reihe 8, Nr. 1100, Düsseldorf.
- Heyden, T., Maier, T. & Woernle, C. (2002). Trajectory tracking control for a cable suspension manipulator, in J. Lenarčič & M. Husty (eds), *Advances in Robot Kinematics*, Springer, Caldes de Malavalla, Spain, pp. 125–134. Caldes de Malavalla.
- Hiller, M., Fang, S., Mielczarek, S., Verhoeven, R. & Franitza, D. (2005). Design, analysis and realization of tendon-based parallel manipulators, *Mechanism and Machine Theory* 40(4): 429–445.
- Kawamura, S., Choe, W., Tanaka, S. & Pandian, S. R. (1995). Development of an ultrahigh speed robot FALCON using wire drive system, *IEEE International Conference on Robotics and Automation (ICRA)* pp. 215–220.
- Kawamura, S., Kino, H. & Won, C. (2000). High-speed manipulation by using parallel wire-driven robots, *Robotica* 18(1): 13–21.
- Lafourcade, P. (2004). *Contribution à l'étude de manipulateurs parallèles à câbles*, PhD thesis, Ecole Nationale Supérieure de l'Aéronautique et de l'Espace.
- Lafourcade, P., Llibre, M. & Reboulet, C. (October 3-4, 2002). Design of a parallel wire-driven manipulator for wind tunnels, in C. M. Gosselin & I. Ebert-Uphoff (eds), *Workshop*

- on *Fundamental Issues and Future Research Directions for Parallel Mechanisms and Manipulators*.
- Landsberger, S. & Sheridan, T. (1985). A new design for parallel link manipulator., *International Conference on Cybernetics and Society*, Tucson, Arizona, pp. 812–814.
- Maeda, K., Tadokoro, S., Takamori, T., Hattori, M., Hiller, M. & Verhoeven, R. (1999). On design of a redundant wire-driven parallel robot warp manipulator, *Proceedings of IEEE International Conference on Robotics and Automation* pp. 895–900.
- Maier, T. (2004). *Bahnsteuerung eines seilgeführten Handhabungssystems - Modellbildung, Simulation und Experiment*, PhD thesis, Universität Rostock, Brandenburg. Fortschritt-Berichte VDI, Reihe 8, Nr. 1047, Düsseldorf.
- Merlet, J.-P. (1994a). Designing a parallel manipulator for a specific workspace, *Technical Report RR-2527*.
- Merlet, J.-P. (1994b). Trajectory verification in the workspace for parallel manipulators, *The International Journal of Robotics Research* 13(4): 326–333.
- Merlet, J.-P. (2004). Solving the forward kinematics of a gough-type parallel manipulator with interval analysis, *International Journal of Robotics Research* 23(3): 221–236.  
URL: [citeseer.comp.nus.edu.sg/merlet04solving.html](http://citeseer.comp.nus.edu.sg/merlet04solving.html)
- Merlet, J.-P. (2006). *Parallel Robots (Solid Mechanics and Its Applications)*, 2 edn, Springer Netherlands.
- Merlet, J.-P. (2008). Kinematics of the wire-driven parallel robot marionet using linear actuators, *IEEE International Conference on Robotics and Automation*, IEEE, pp. 3857–3862.
- Merlet, J.-P. (2010). MARIONET, a family of modular wire-driven parallel robots, in J. Lenarcic & M. M. Stanisic (eds), *Advances in Robot Kinematics: Motion in Man and Machine*, Springer Netherlands, pp. 53–61.  
URL: <http://dx.doi.org/10.1007/978-90-481-9262-5>
- Mikelsons, L., Bruckmann, T., Hiller, M. & Schramm, D. (2008). A real-time capable force calculation algorithm for redundant tendon-based parallel manipulators, *Proceedings on IEEE International Conference on Robotics and Automation 2008*.
- Ming, A. & Higuchi, T. (1994a). Study on multiple degree of freedom positioning mechanisms using wires, part 1 - concept, design and control, *International Journal of the Japan Society for Precision Engineering* 28: 131–138.
- Ming, A. & Higuchi, T. (1994b). Study on multiple degree of freedom positioning mechanisms using wires, part 2 - development of a planar completely restrained positioning mechanism, *International Journal of the Japan Society for Precision Engineering* 28: 235–242.
- Oh, S.-R. & Agrawal, S. K. (2005). Cable suspended planar robots with redundant cables: Controllers with positive tensions, *IEEE Transactions on Robotics*. Vol. 21, No. 3, pp. 457–464.
- Ottaviano, E. & Ceccarelli, M. (2006). Numerical and experimental characterization of singularities of a six-wire parallel architecture, *Robotica* 25(3): 315–324.
- Ottaviano, E., Ceccarelli, M., Paone, A. & Carbone, G. (April 18–22 2005). A low-cost easy operation 4-cable driven parallel manipulator, *Proceedings of the 2005 IEEE International Conference on Robotics and Automation*, Barcelona, Spain, pp. 4008–4013.
- Pott, A. (2008). Forward kinematics and workspace determination of a wire robot for industrial applications, in J. Lenarčič & P. Wenger (eds), *Advances in Robot Kinematics:*

- Analysis and Design*, Springer Netherlands, pp. 451–458. ISBN 978-1-4020-8599-4 (Print) 978-1-4020-8600-7 (Online).
- Pott, A., Bruckmann, T. & Mikelsons, L. (2009). Closed-form force distribution for parallel wire robots, *Computational Kinematics 2009*.
- Pott, A., Meyer, C. & Verl, A. (2010). Large-scale assembly of solar power plants with parallel cable robots, *ISR/ROBOTIK 2010*, Munich, Germany.
- Sturm, C., Bruckmann, T., Schramm, D. & Hiller, M. (2011). Optimization of the wire length for a skid actuated wire based parallel robot, *Proceedings of the 13th World Congress on Mechanism and Machine Science (IFTOMM2011)*. to appear.
- Sturm, C. & Schramm, D. (2010). On the control of tendon based parallel manipulators, *Solid State Phenomena* 166 - 167: 395–402.
- Su, Y. X., Duan, B. Y., Nan, R. D. & Peng, B. (2001). Development of a large parallel-cable manipulator for the feed-supporting system of a next-generation large radio telescope, *Journal of Robotic Systems*, Vol. 18, pp. 633–643.  
URL: <http://dx.doi.org/10.1002/rob.8102>
- Tadokoro, S. & Kobayashi, S. (2002). A portable parallel motion platform for urban search and surveillance in disasters, *Advanced Robotics* 16(6): 537–540.
- Tadokoro, S., Murao, Y., Hiller, M., Murata, R., Kohkawa, H. & Matsushima, T. (2002). A motion base with 6-dof by parallel cable drive architecture, *Mechatronics, IEEE/ASME Transactions on* 7(2): 115–123.
- Tadokoro, S., Verhoeven, R., Hiller, M. & Takamori, T. (1999). A portable parallel manipulator for search and rescue at large-scale urban earthquakes and an identification algorithm for the installation in unstructured environments, *Intelligent Robots and Systems, 1999. IROS '99. Proceedings. 1999 IEEE/RSJ International Conference on*, Vol. 2, pp. 1222–1227 vol.2.
- Taghirad, H. & Nahon, M. (2007a). Forward kinematics of a macro–micro parallel manipulator, *Proceedings of the 2007 IEEE/ASME International Conference on Advanced Intelligent Mechatronics (AIM2007)*, Zurich, Switzerland.
- Taghirad, H. & Nahon, M. (2007b). Jacobian analysis of a macro–micro parallel manipulator, *Proceedings of the 2007 IEEE/ASME International Conference on Advanced Intelligent Mechatronics (AIM2007)*, Zurich, Switzerland.
- Takemura, F., Maeda, K. & Tadokoro, S. (2006). Attitude stability of a cable driven balloon robot, *IEEE/RSJ International Conference on Intelligent Robots and Systems, IROS, IEEE*, pp. 3504–3509.
- Thomas, F., Ottaviano, E., Ros, L. & Ceccarelli, M. (September 14–19, 2003). Coordinate-free formulation of a 3–2–1 wire-based tracking device using cayley-menger determinants, *Proceedings of the 2003 IEEE International Conference on Robotics and Automation, Taipei, Taiwan*, pp. 355–361.
- VDI (2004). Design methodology for mechatronic systems, VDI-Guideline VDI 2206.
- Verhoeven, R. (2004). *Analysis of the Workspace of Tendon-based Stewart Platforms*, PhD thesis, University of Duisburg-Essen.
- von Zitzewitz, J., Rauter, G., Steiner, R., Brunschweiler, A. & Riener, R. (2009). A versatile wire robot concept as a haptic interface for sport simulation, *Proceedings of the 2009 IEEE international conference on Robotics and Automation, ICRA'09*, IEEE Press, Piscataway, NJ, USA, pp. 269–274.  
URL: <http://portal.acm.org/citation.cfm?id=1703435.1703479>

- von Zitzewitz, J., Wolf, P., NovakoviÄ, V., Wellner, M., Rauter, G., Brunschweiler, A. & Riener, R. (2008). Real-time rowing simulator with multimodal feedback, *Sports Technology* 1(6): 257–266.  
URL: <http://dx.doi.org/10.1002/jst.65>
- Woernle, C. (2000). Dynamics and control of a cable suspension manipulator, in M. Braun (ed.), *9th German-Japanese Seminar on Nonlinear Problems in Dynamical Systems-Theory and Applications*, Universitat Duisburg.
- Yangwen, X., Qi, L., Yaqing, Z. & Bin, L. (2010). Model aerodynamic tests with a wire-driven parallel suspension system in low-speed wind tunnel, *Chinese Journal of Aeronautics* 23(4): 393 – 400.
- Zheng, Y. (2006). Feedback linearization control of a wire-driven parallel support system in wind tunnels, *Sixth International Conference on Intelligent Systems Design and Applications* 3: 9–13.
- Zheng, Y., Lin, Q. & Liu, X. (2007). Initial test of a wire-driven parallel suspension system for low speed wind tunnels, *Proceedings on 12th IFToMM World Congress*, Besanon, France.
- Zheng, Y., Lin, Q. & Liu, X. (2010). *Robot Manipulators Trends and Development*, InTech, chapter A Wire-Driven Parallel Suspension System with 8 Wires (WDPSS-8) for Low-Speed Wind Tunnels.



# Wind Tunnels for the Study of Particle Transport

Keld Rømer Rasmussen<sup>1</sup>, Jonathan Peter Merrison<sup>2</sup> and Per Nørnberg<sup>1</sup>

<sup>1</sup>*Aarhus University, Department of Geoscience,*

<sup>2</sup>*Aarhus University, Department of Physics and Astronomy  
Denmark*

## 1. Introduction

Wind tunnels for investigating the effect of wind on sand and soil movement have been constructed by many groups since Brigadier R.A. Bagnold build one of the first wind tunnels for investigating the threshold of motion of sand (Bagnold 1941). Initiated by the serious soil erosion in the American Midwest during the 1930's another wind tunnel facility was set up later in the decade at Kansas State University at the USDA-ARS Wind Erosion Research Unit for soil erosion research. A wind tunnel for studying particle motion under fluid densities as on the planet Mars was as the first of its kind build at the NASA Ames Research Centre, California in the mid 1970's under guidance of Dr. Ronald Greeley (Greeley et al. 1981). The wind tunnel laboratory at Aarhus University was started in the 1970's and have to day two sand transport wind tunnels and two low pressure wind tunnels for studying sand and dust transport under Martian conditions. This chapter will deal with descriptions of the materials used in wind tunnel experiments and research lay-outs for the wind tunnels at the Aarhus University wind tunnel laboratory.

## 2. Sand and dust size materials in wind tunnel experiments

### 2.1 Particle size classification

Over time a number of slightly different scales have been used in dividing of loose sediments or soils in particle size fractions (Krumbein and Pettijohn 1938, Pettijohn 1957, Scheffer & Schachtschabel 1998). In European context the logarithmic  $\phi$ -scale which is the same as  $2^n$  or  $\sqrt{2}^n$  are widely used and refer to sieve openings in millimetres. Here the limit between gravel and sand is set to 2mm, the limit between sand and silt to 0.063 mm and the limit between silt and clay to 0.002 mm. In USA these limits are slightly different and set up by the US Bureau of Soils. In this scale the gravel/sand limit is also 2 mm. The sand/silt limit 0.050 mm and the silt/clay limit 0.002 mm (Klute 1986, Ulery & Drees 2008).

In the field of Aeolian transport there are clear physical definitions for the descriptive terms of dust and sand. Dust grains are referred to as those which can be suspended by the atmosphere (i.e. turbulence within the flow is comparable to that of the gravitational settling velocity). Sand grains refer to particulates which can be entrained from a surface by the wind flow, but cannot be suspended. They therefore perform saltation, with repeated entrainment events and ballistic return to the surface. These definitions are physically

meaningful in a particular wind flow environment, however they vary depending on the properties of the particulates and the flow conditions and generally do not correspond to well-defined size categories. On Earth, in a typical natural environment, dust grains are typically less than  $10\mu\text{m}$  as they are on Mars.

## 2.2 Particle size concept

Particles used in wind tunnel experiments are normally single grain particles if they are of sand size. But will often aggregate during transport if they are of silt and clay size. If the particles were all spheres, no special difficulty would arise in defining and determining their size. The diameter would be a well defined parameter. However, natural particles are of irregular shape, and generally more irregular the smaller the particles are.

Measurements of the particle diameters are commonly made though the irregular shape causes difficulties. A particle could be regarded as a matchbox  $50 \times 35 \times 15$  mm or a triaxial ellipsoid and it is obvious that the 3-dimensional form is not easily described by one unique number. The term diameter varies widely in meaning with respect to the way in which it is measured. All methods of measurements end up with regarding the particles as spheres, or that the measurements made can be expressed as diameter of equivalent spheres. However, as sand, silt and clay particles from nature are not spheres the reported sizes are incorrect or inaccurate. In the laboratory we have different methods of measuring particle sizes.

*Sieves* are commonly used to separate and measure particles of loose single grain materials. But sieves do not measure size alone. Long cigar shaped particles may pass a sieve and be weighed with particles of a smaller volume but a more regular shape. Thus sieves classify particles on the basis of their smallest cross section. The holes in sieves have a certain size distribution and laboratory experiments show that the longer sieving times the bigger particles get through the sieves (pers. com. Dalsgaard, K.). They find the bigger holes.

*Sedimentation* after Stoke's law is another way of sorting particles. This is a classic statement of settling velocity of spherical particles. Under standard conditions, constant temperature, a given fluid, and a known specific gravity of the spheres  $v = Cr^2$ , where  $v$  is the velocity in cm pr. second,  $r$  is the radius of the sphere in cm, and  $C$  is a constant equal to  $(2/9)(d_1 - d_2)g/\eta$ .  $d_1$  and  $d_2$  are the densities of the sphere and the fluid, respectively,  $g$  is gravity acceleration, and  $\eta$  is the viscosity. Stokes law has been shown to hold for particles of silt size and smaller down to where Brownian movement influences the settling velocities. Sedimentation of the silt and clay size fractions for particle size determination is often done in sedimentation cylinders (Andreasen pipettes). However, if we look at particles collected in dunes of wind blown sand we can see that the equivalent diameter is a debatable expression. Figure 1, 2, 3 and 4 are from dune sand samples (Nørnberg 2002). An assumed density of  $2.65 \text{ g/cm}^3$  (quartz) is often used for natural particles, but talking about a nominal diameter as we do in Stokes law can be far away from realities, and when it comes to sedimentation in media that do not have a homogenous density like planet atmospheres this have to be taken into account.

In wind tunnel experiments glass spheres can be used to overcome problems with irregular particle shape. If we look at a single sand grain like Figure 5 it is obvious that there are a number of different answers to giving the size.

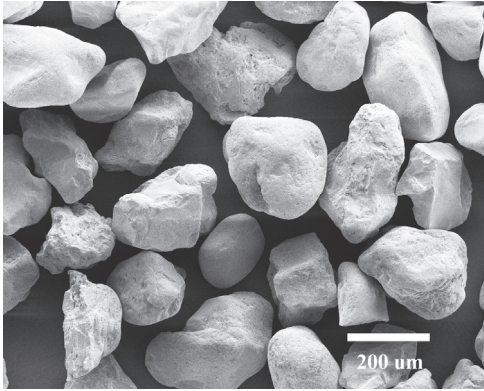


Fig. 1. Sand fraction 250-125 μm

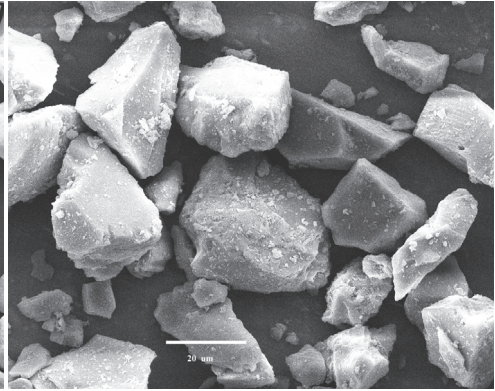


Fig. 2. Silt 63-20 μm

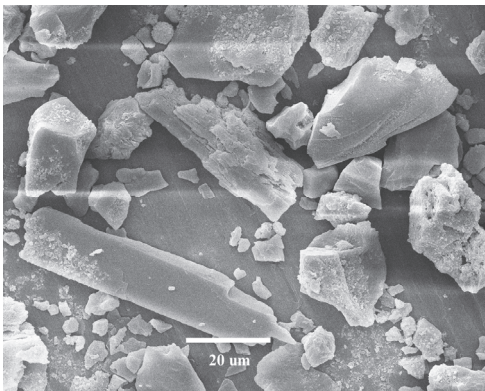


Fig. 3. Silt 20-2 μm

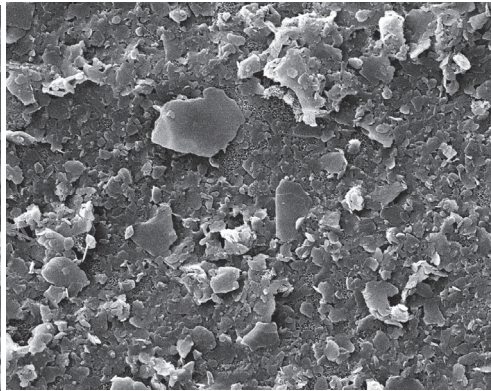


Fig. 4. Clay < 2 μm

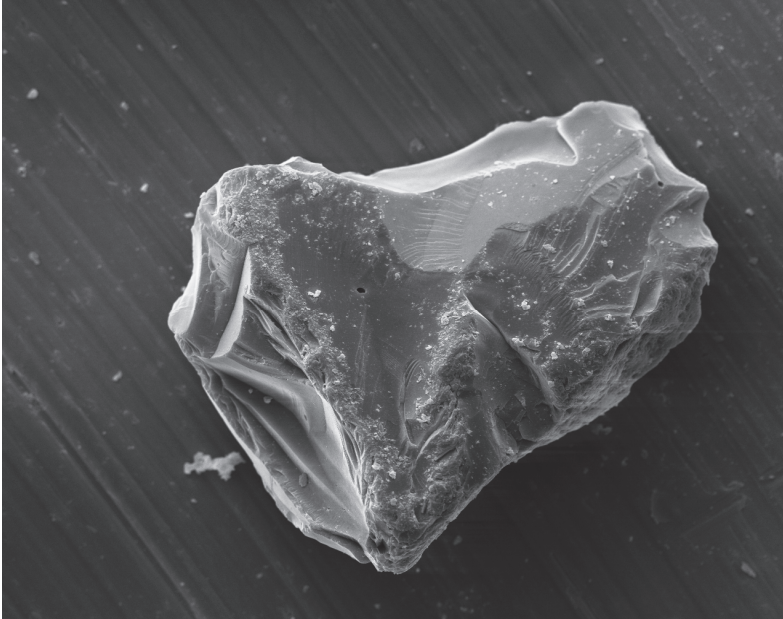


Fig. 5. A 100  $\mu\text{m}$  sand grain.

It could be 1) a sphere of the same maximum length, 2) a sphere with the same minimum length, 3) a sphere with the same weight, 4) a sphere with the same sedimentation rate, 5) a sphere passing the same sieve aperture, 6) a sphere with the same surface area, or 7) a sphere with the same volume.

This also tells us that particle size standards for e.g. sand grains are defined by the technique used for the determination. Sieves are often used to split up sand fractions and sedimentation used for silt and clay size fractionation. This is however, two very different techniques if used for particle size distribution measurements, and it is often difficult to inter calibrate the two methods. An alternative method widely used in industry production and research laboratories is the laser diffraction method. This method is based on Low Angle Laser Light Scattering (LALLS).

A laser source of coherent light like a He-Ne gas laser with a wavelength of 633 nm is the most commonly used in laser diffraction (LD) instruments. A parallel beam of light is sent through a cuvette with suspended particles, either in water or air and a Fourier Transform Lens focuses the light scattered by the particles on a ring formed multi element detector. The advantage of using this method is that the whole particle range from  $< 2 \mu\text{m}$  to  $> 3.5 \text{mm}$  can be measured by the same technique. The laser diffraction system generates a volume distribution of the sample which is directly equal to the weight distribution if the density is constant. The volume is calculated to an equivalent sphere with a certain diameter. Data determined by LD is not directly comparable with sieving or pipette methods. However, the LD method based on volume is a valid, reproducible method that is very little time consuming (Eshel et al. 2004 and Beuselinck et al. 1998).

Examples on sand size materials used in the terrestrial wind tunnels, and silt size (dust) used in experiments in the low pressure Mars wind tunnels is seen in Table 1 (all LD determinations).

Sample	>500 $\mu\text{m}$	500- 250 $\mu\text{m}$	250- 125 $\mu\text{m}$	125- 63 $\mu\text{m}$	63- 32 $\mu\text{m}$	32- 16 $\mu\text{m}$	16-8 $\mu\text{m}$	8-4 $\mu\text{m}$	4-2 $\mu\text{m}$	<2 $\mu\text{m}$
	%									
Sand (125 $\mu\text{m}$ )		1.52	80.36	15.24	0.78	2.10				
Sand (242 $\mu\text{m}$ )	0.99	74.49	22.96	1.08	0.40	0.08				
Glass balls 200-300 $\mu\text{m}$	2.77	64.53	31.16	1.42	0.08	0.04				
JSC-1		4.86	36.59	25.89	14.02	7.66	4.20	2.72	1.99	2.07
Salten Skov I < 63 $\mu\text{m}$			0.25	5.95	9.14	8.10	10.37	14.13	20.92	31.14
Clay (WB)			0.74	3.46	5.36	5.84	8.63	21.43	25.45	29.10

Table 1. Particle size data for wind tunnel materials

### 2.3 Mineralogy and chemistry of sand and dust

The sand material for experiments in the terrestrial wind tunnels is quartz sand from Miocene deposits. It contains traces of mica, but >99% of the sand is quartz. This material resembles dune sand in Denmark which has also very high quartz content.

The dust materials used in wind tunnel experiments under Mars conditions are chosen for mechanical physical properties reasons like particle size, magnetic properties, colour. These are properties which can be close to Mars dust conditions, while the chemistry is in most cases different from the chemical properties of the Martian dust. As seen in table 2 the chemical composition of JSC-1 described by Morris et al. (2001) and Moroz et al. (2009) and Salten Skov I (Nørnberg et al. 2004, Nørnberg et al. 2009) are very different, and as we have at present no quantitative chemical analyses of the dust on Mars the samples can not be compared with Mars samples. A number of other Mars analogue dust samples used World wide in experiments are described by Marlow et al. (2008). The magnetic properties of the atmospheric dust on Mars is estimated to have a saturation magnetization  $J_s$  of 2.5 Am<sup>2</sup>/kg (Morris et al. 2001), which is not far from the  $J_s$  of dust captured by Morris et al. (2001) on the Mauna Kea volcano, Hawaii which was 2.5±1.5 Am<sup>2</sup>/kg. This is significantly lower than  $J_s$  of the Salten Skov I, that is 3.9 (1) Am<sup>2</sup>/kg (Nørnberg et al. 2009).

	SiO <sub>2</sub>	TiO <sub>2</sub>	Al <sub>2</sub> O <sub>3</sub>	Fe <sub>2</sub> O <sub>3</sub>	MnO	MgO	CaO	Na <sub>2</sub> O	K <sub>2</sub> O	P <sub>2</sub> O <sub>5</sub>	Vola- tiles	Sum
	-----%----- -----											
JSC-1	37.73	3.43	21.06	15.28	0.25	3.01	5.20	1.97	0.49	0.76	10.73	99.91
SS-1 < 63 μm	16.10	0.29	3.20	61.92	1.66	0.16	0.20	0.19	0.52	0.47	14.43	99.14

Table 2. Examples on chemical composition of silt size dust material

### 3. The one bar sand transport wind tunnels

#### 3.1 The boundary layer wind tunnels

Before dealing with flow in aeolian wind tunnels it is expedient to introduce a few concepts and assumptions. Thus while the velocity field of flows in Nature is 3-dimensional (3-D) it is often simpler and described using a 2-D approximation in the wind tunnel. Thus for a wind tunnel with a rectangular test section, we may assume a 2-D flow having average horizontal velocity component  $u$  parallel to the tunnel ( $x$ -)axis and average velocity component  $w$  in the vertical ( $z$ -)direction. The corresponding fluctuating velocity components are  $u'$  and  $w'$ . The boundary layer flow in the region immediately above the bed has shear stress  $\tau$  defined as

$$\tau = -\rho \overline{u'w'} = \rho u_*^2$$

where  $u_*$  is the friction speed. The boundary layer has a logarithmic wind profile with  $u(z)$  given by

$$u(z) = \frac{u_*}{\kappa} \ln \frac{z}{z_0}$$

with  $\kappa$  being the von Karmán's constant (0.4) and  $z_0$  the aerodynamic roughness length. The friction speed at which grains can be dislodged from the bed under fluid force is the threshold friction speed ( $u_{*t}$ ) while the equilibrium velocity of a particle settling through a fluid under gravity is the terminal speed ( $u_F$ ). Both  $u_{*t}$  and  $u_F$  are functions of particle diameter (see e.g. Greeley and Iversen, 1987), and particle transport will take place if  $u_* > u_{*t}$ . Suspension will dominate for particles having  $u_F < u_*$  while bedload (saltation or creep) will be the dominant transport mode if  $u_F > u_*$  (Bagnold, 1941).

A boundary layer wind tunnel designed for testing the physics of the windborne transport of sand and dust is often referred to as an aeolian wind tunnel. Horizontal aeolian wind tunnels such as the primary wind tunnel at Aarhus University (figure 6) have been widely used to study in the laboratory processes related to sand drifting in the terrestrial as well as in planetary environments. A variety of issues have been studied such as the threshold for initiation of movement (Bagnold, 1941; Chepil, 1959; Iversen and Rasmussen, 1994), effects of grain impact and inter-particle forces (Iversen et al, 1976; Iversen et al, 1987) and the interaction between wind flow and sand transport rate (Bagnold, 1941; Williams, 1964; Owen, 1964; Rasmussen and Mikkelsen, 1991; Iversen and

Rasmussen, 1999). In nature, much sand transport (on sand dunes for example) takes place on sloping surfaces, but relatively few laboratory studies have been made in order to study the effects of slope. Therefore a second wind tunnel of variable slope was built at the Aarhus University (figure 7) and this has been used to investigate threshold and mass transport characteristics for sands of different grain sizes.

Both wind tunnels at Aarhus University are primarily made of wood. The horizontal aeolian wind tunnel (HW) is a 15 m long open circuit, suction type tunnel and the test section is 0.60 m wide and 0.90 m high. A small bell-mouth, with a screen attach to it, is placed at the inlet in order to reduce the effect from low frequency fluctuations distorting the natural turbulence characteristics of the internal boundary-layer. A sand feed mechanism follows one meter downwind of the inlet to maintain a constant transport rate downwind under the influence of a pre-designed boundary layer. Sand transported in the HW is trapped in a sand collector in the downwind end of the tunnel, just in front of the fan and motor. The working area is the section from 10-13 m downstream of the entry. The side panels of the tunnel body consists of a set of gates (windows) that can swing up thus permitting access to the interior. Another set of gates in the ceiling of the tunnel above the working section offer an alternative access to the working section. The latter set of gates is primarily used to install instruments which must be operated partly from the outside or connected to an external power supply or recording system.

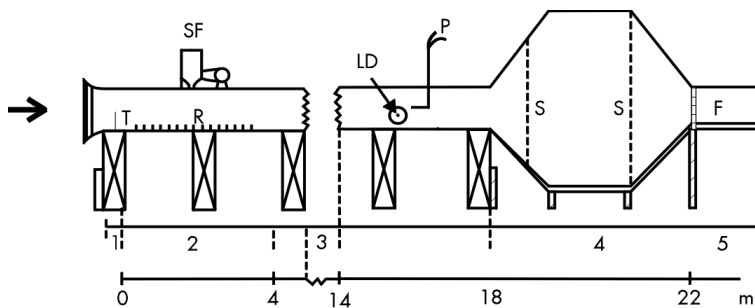


Fig. 6. The horizontal wind tunnel with main sections indicated: 1 - entry with screen (S) and bell mouth (B); 2 - boundary layer modification with turbulence spires (T), roughness array (R) and sand feed (F); 3 - working section with laser Doppler (LD) and Pitot-static tube (P); 4 - expansion box (sand collector) with screens (S); 5 - fan (F) and exhaust.

The variable slope wind tunnel (VSW) is attached to the primary wind tunnel via a tower at the sand collector. A pair of shutters can open or close either of the tunnels permitting that the sand collector and the motor-fan units are utilized for both tunnels. The cross section of the VSW is smaller than that of the HW - only 0.35 m by 0.50 m. The length of the VSW is only 6 meters which for the  $\pm 25^\circ$  variation of slope (upslope and downslope) uses the full height of the laboratory. The front of the tower is covered with gates which, when moved one by one from below to above the tunnel (or vice versa), permits the slope of the tunnel to be varied in  $5^\circ$  bins. A small bell-mount is placed at the inlet as in the primary tunnel. The side panels of the tunnel is made of glass panes which cannot be opened. Access to the interior of the tunnel is limited to gates placed almost continuously in the tunnel ceiling between the entry and the tower. The working area is from 2 m to 5.5 m downstream of the

entry. The VSW has a sand feed similar to that of the HW and sand is trapped in the common sand collector except during downslope experiments where most of the sand is trapped in a box at the bottom of the tower rather than in the sand collector.

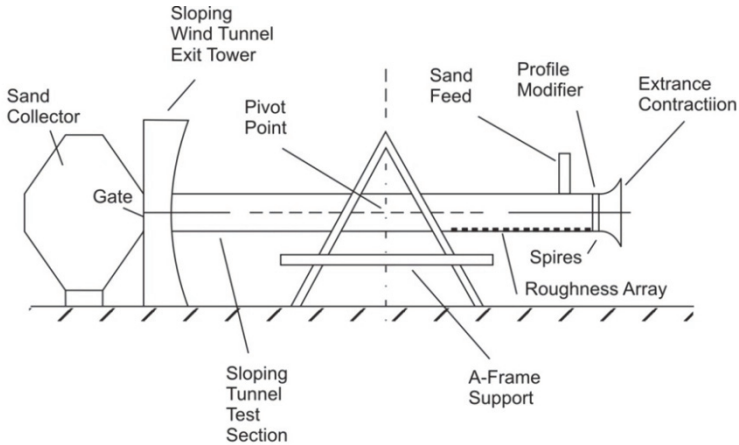


Fig. 7. Schematic diagram showing the sloping wind tunnel. The exit tower permits the slope of the tunnel to be varied in 5" increments from - 25" to +25". The tunnel is suspended in the A-frame with a pivot point at the center of symmetry. It is balanced by adjusting a counterweight with respect to its distance from the pivot point.

### 3.2 Boundary layer modification in the tunnels

When sand is introduced from the sand feed, it carries the momentum that is necessary for the chain reaction of saltating grains to create an equilibrium sand transport rate. However, both the horizontal and the sloping tunnel are too short and too shallow to allow the development of a natural boundary layer which is sufficiently deep and has turbulence characteristics equivalent to those above a sand surface in Nature. While the turbulent spectrum in a wind tunnel can never fully simulate that of the atmospheric boundary layer the average wind profile and the high frequency part of the spectrum can be artificially "designed" so that it makes a reasonable analogy to atmospheric surface layer flow. Therefore immediately downwind of the entry we aim to construct a wind flow which will be in fair equilibrium with the saltation boundary that develops downstream of the sand feed (figure 6 and 7).

Observations made in a previous, smaller wind tunnel indicated that for a high friction speed ( $u_* \approx 1$  m/s) the aerodynamic roughness  $z_0$  will increase by a factor of thousand as compared to the quiescent surface. For windblown quartz sand Rasmussen et al (1996) find that  $z_0$  typically falls in the range  $4 \times 10^{-5}$  to  $1.1 \times 10^{-3}$  m when friction speed ranges between 0.2 m/s to 0.75 m/s. No single static roughness can therefore represent this enormous range in dynamic sand roughness. It has thus been considered necessary to create, with turbulence spires and roughness blocks, a boundary layer which for some selected friction speeds matches the dynamic saltation layer roughness and required boundary layer in the test sections of the two wind tunnels. We have selected nominal values of the friction speeds  $u_* = 0.2, 0.3, 0.4, 0.6$  and  $0.7$  m/s  $u_*$  at which all experiments must be conducted, and in the



next section we shall explain how spires and roughness blocks are used to control the state of the boundary layer.

#### *Spires and roughness blocks*

A thick boundary layer which assures dynamic similitude with natural surfaces of drifting sand and which permits measurements of the velocity profile is created with triangular turbulence spires which are inserted in the flow immediately after the bell-mouth. In our test section of height  $H_0$ , the shape of the log-linear wind profile is determined at the entry by the spire geometry i.e. spire height  $H$ , base width  $b$  and spacing  $L_s$ . We have aimed for a boundary layer thickness  $\delta \approx 10$  cm at approximately 1 m downwind of the entry and the single steps in the design follows the procedure summarized by Irwin (1981). A spire design corresponding to  $u_* = 0.40$  m/s is shown in fig. 8.

On the first 2.4 m of the test section between the spires and the fully developed saltation layer we control the boundary layer by an array of cubic roughness blocks, of block size  $h$  and spacing  $D$ . Somewhat subjectively we have preferred to base the roughness arrays on 3-dimensional roughness elements (Wooding, 1973) rather than 2-dimensional elements suggested by e.g. Gartshore, 1973).

Raupach et al. (1991) have proposed that for sparse roughness arrays

$$z_0/h = \lambda \quad (1)$$

where  $\lambda$  is aspect ratio (frontal area/areal block density). They find that  $z_0/h|_{\max} \approx 0.1$ . Rather than using one block size for the entire set of nominal roughness values we use cubes with sizes of 10, 15, 20 and 25 mm placed in a cubic geometry and then control the particular roughness value by the  $\lambda$ -value. An array design corresponding to  $u_* = 0.40$  m/s is shown in figure 8. One could point out, that Irwin's method gives higher values of the exponent  $n$  in the power law profile which is fitted to the boundary layer profile than suggested for example by Counihan (1975) but this is of minor importance because of the long working section.



Fig. 8. Turbulence spires and roughness array for a nominal friction speed of 0.4 m/s.



Fig. 9. The sand feed system.

### 3.3 Sand feed

In order to avoid depletion of sand from the upstream part of the bed sand must be supplied continuously during experiments. When the airflow is above the threshold of movement saltation is initiated through the collisional chain reaction governed by the splash function (Anderson and Haff, 1991). However, when the fetch is short, such as in a wind tunnel it is imperative that an external source initially supplies momentum to the saltation cloud in order to start the saltation process almost momentarily from nil to its fully saturated value. Although the range of particle size in wind-blown sands is usually narrow it also appears that the sand feed is necessary to stimulate transport until the friction velocity is above its threshold value for almost the entire grain population (Rasmussen and Mikkelsen, 1991). Otherwise the coarser grains in the sample will slowly armour the bed and reduce or even stop saltation transport.

The sand feed used for the VSW is only 350 mm wide while for the HW it is 600 mm (figure 9). However, the cross section of the two sand feeds is the same. Sand is stored in the upper funnel from where it drops into the grooves of a rotating drum which then carries the sand to the lower funnel. The lower funnel is divided into five chambers from where the sand slides into a 10 mm steel tube and then into the wind tunnel (visible above the roughness array on Fig. 8). Depending on the wind flow (friction speed) in the tunnel the tubes stop at 0.4 m above the wind tunnel floor ( $u_* < 0.5$  m/s), at 0.2 m ( $0.5 < u_* < 0.75$  m/s) or at 0.1 m above the wind tunnel floor ( $0.75$  m/s  $< u_*$ ). Thus for the higher friction speeds it is necessary to release the particles shortly above the bed in order to prevent them from being caught by the air flow and impacting with the bed at some distance within the working section where they will create a local scouring of the bed.

The speed of rotation of the drum is controlled with a potentiometer which allows the amount of sand being released from the sand feed to match fairly well the amount of sand leaving the tunnel in the downwind end. A calibration curve for the transport capacity as function of potentiometer setting is based on many experiments with quartz sand of different grain size distributions.

### 3.4 Sediment capture

The sand arriving to the sand collector at the downwind end of the tunnel is exposed to a sudden drop in wind speed because the cross sectional area expands by a factor of almost 10 when the wind flows from the tunnel into the centre part of the sand collector. One screen (S) halfway into the expansion (figure 6) results in some divergence of the flow from its jet-like behaviour when exiting the tunnel. The screen has a 50 % porosity and 100 micron holes so it catches most airborne grains. Because of the drop in speed between the exit and the screen grains then fall to the sloping part of the floor in the first part of the sand collector. Here a 5 mm gap between the screen and the wall allows the particles to slide down to bottom of the wall. Despite the overall drop in average speed in the collector, at high speed in the tunnel some of the finer grains in the collector are occasionally picked up from the floor by forceful eddies and swept around. Eventually they are caught by the screen with 50 micron openings which is placed halfway into the downwind exit of the sand collector. After an experiment both screens must be cleaned for particles which can then be brushed up from the floor.

### 3.5 Traps

Sediment transport rate in the tunnels is estimated in two different ways. The simple way to do it is to collect the total amount of sand arriving to the sand collector during an experiment and then estimate the average flux ( $\phi_{SC}$ ) of sand by normalizing it with the duration of the experiment and the width of the tunnel. A thin boundary layer of the order of 5 cm is present along each side of the tunnel. Here the transport rate is lower than that ( $\phi_{IK}$ ) measured along the centre line of the tunnel using an isokinetic trap (Rasmussen and Mikkelsen, 1991). However, a comparison of flux values measured in the two different ways show that independent of wind speed the ratio between the two quantities is fairly constant at  $\phi_{IK} / \phi_{SC} = 1.16$ .

An isokinetic trap, i.e. a trap through which air is flowing at the same speed as that of the surrounding air, is a more precise method for measuring the transport rate. The one that has been used for many years in the Aarhus wind tunnels has six 80 mm long compartments. Each compartment is made from brass tubes with a rectangular cross section. All compartments are 8 mm wide; the lower two are 4.5 mm high, while the other four are all 9.5 mm high (Fig. 10a). Each tube is sharpened at the leading edge so that the aperture facing the flow has a well-defined cross-section. Air is sucked through each tube at approximately the same speed as that of the undisturbed air flow upwind of the trap. The apertures are positioned at 60 mm upwind of the location where the tubes go through the bottom of the tunnel, thereby reducing the obstruction to the wind, even when the lowest tube is close to, or at, the sand surface. Because the lowest tube can be placed directly at bed level, particle creep is included in the transport rate measurements. The trap is adjusted carefully during experiments so that the bottom of the lowest compartment is always kept at the same elevation as the local sand surface. The vertical position of the sample tubes can be adjusted individually. Air drawn through the tubes goes through a container where the sand grains are trapped. The air exits by a nozzle valve with which we can adjust the flow rate through each tube to an accuracy of about 10% in the range 1.3-10 m s<sup>-1</sup>. The sample containers are weighed after each experiment ( $\pm 10$  mg), and then cleaned with compressed air.

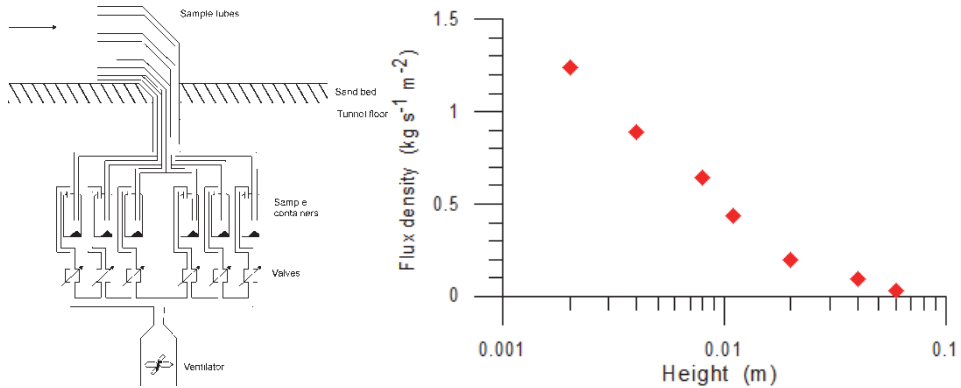


Fig. 10. **a)** Schematic view of the isokinetic trap with the suction flow control and six sample tubes; **b)** Flux-density profile measured with the isokinetic trap at a friction speed  $u_* = 0.49 \text{ m s}^{-1}$ .

### 3.6 Air and grain velocity

In an aeolian wind tunnel the purpose of measuring speed is twofold requiring that the velocity of the air as well as the velocity of the particles is recorded. The bombardment of the sensor with saltating grains requires that only rather robust sensors can be used. Yet at the same time they must be small and very sensitive so that precise measurements at precise elevations can be made within the shallow wind tunnel boundary layer. A velocity sensor is usually fixed in space and therefore it will only record the instantaneous and local velocity of saltating grains. Information about the displacement of grains during the saltation process has also been attempted and will briefly be discussed, too.

For air speed we have mostly used a pitot static tube, but occasionally a robust hot wire has been used, too. A small diameter pitot-static tube (3/16" diameter) connected to a precision barometer is used to measure detailed wind profiles. The instrument measures the pressure difference between the dynamic and static pressures at a given location. Readings are typically taken at a frequency of 2-50 Hz depending on the duration and purpose of the experiment and then converted to instantaneous wind speed. The precise manometer readings combined with the high precision of the elevation at which the orifice of the pitot-static tube can be set, allows us to record quite detailed and precise wind speed profiles (figure 11). However, the pitot-static tube is sensitive to direction of the flow and it is mostly used in simple one- or two-dimensional flows which are parallel to the centerline of the wind tunnel.

A robust, omnidirectional steel clad hot wire (Dantec 55A76) connected to a constant temperature anemometer system (Dantec 55K01/) has occasionally been used to measure wind speed in the tunnel when flow conditions are complex so that the wind vector is not parallel to the axis of the wind tunnel. For any two-dimensional flow this sensor only needs to be placed with its support parallel to the invariant flow direction then it will always measure the local or instantaneous wind vector. Besides for wind tunnel studies with complex flows this also makes it a useful sensor for field studies.

Grain speed is measured using a one-dimensional laser-Doppler instrument with a flow velocity analyser (LDA, FVA, Dantec Floware). Mostly we use optics with a 400 mm focal

length which allows measurements to be made from the outside with the beam pointing through the glass panes perpendicular to the direction of the flow. The beam height is 200  $\mu\text{m}$  so it is possible to set precisely the height of the measurements. In the direction perpendicular to the flow the crossing between the two beams is just over 4 mm so the transverse position of the beam is much less well-defined. Irregularities of the bed and the increasing number of grains makes it difficult to come quite close to the bed and the movement of the ripples continuously changes the local elevation of the bed and therefore it is difficult in practise to acquire good quality data much closer to the bed than 2-4 mm (Rasmussen & Sørensen, 2008). Two examples of grain velocity profiles recorded with the LDA-equipment are shown in fig. 11.

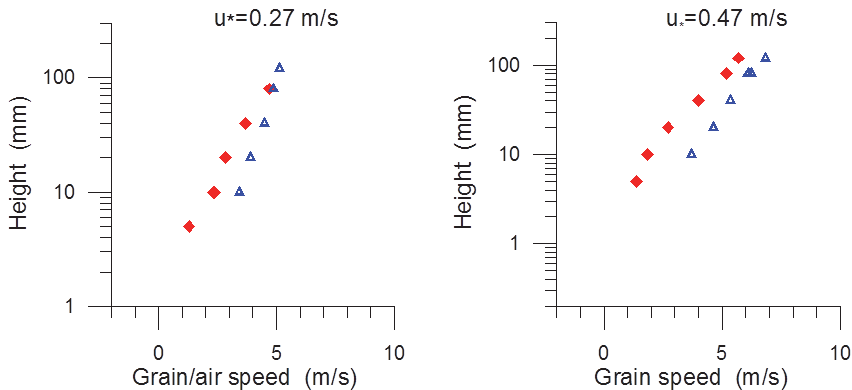


Fig. 11. Wind speed (blue triangles) measured in the horizontal wind tunnel above saltating 320  $\mu\text{m}$  quartz sand (red diamonds) at two different friction speeds ( $u^*$ ).

Finally we shall mention a few examples of techniques that have been applied to follow and measure the displacement of grains during active saltation. In the sand population approach one studies the transport characteristics of a whole population of sand grains. This may be done by dyeing samples (e.g. using Coomassie Brilliant Blue) of the grains and investigating how these are distributed by the wind along the wind-tunnel, the bottom of the wind-tunnel being covered in advance with a sand bed. The alternative individual approach to the question of the celerity of the grains consists in observation of the movement of single grains, which can be done, e.g. by labeling grains with radioactive gold. The element gold is an obvious choice for the following reasons: it has a very high neutron activation cross section and the radioactive product,  $^{198}\text{Au}$ , has a suitable half-life (2.7 days) and emits gamma-rays of a convenient energy (412 keV). However, the adhesion of gold to quartz is poor, but this problem can be solved by covering the quartz with a thin chromium layer first. Then the gold will stick so well that it is almost impossible to rub it off. So first we have coated sand grains with a layer of chromium metal, 10nm thick, by evaporation in high vacuum. Then a layer of gold metal, 250 nm thick, is evaporated onto the grains. These layers are so thin that the coating will result in an insignificant change of mass, typically 1-2% of the total mass of the grain. The position of two radioactive grain marked as described above was determined by means of a portable scintillation detector (for more information see Barndorff-Nielsen et al, 1985). During both wind tunnel experiments the bed of the

tunnel was covered with a 1.5 cm thick layer of sand. The wind speed was between 7.0 and 7.5  $\text{ms}^{-1}$  in the center of the tunnel. In each run a single radioactive grain was placed 8.0-8.5 m from the intake of the tunnel and followed during its movement. The recorded movements of two of the marked grains from the pilot experiment are shown in figure 12. Time in minutes is indicated on the abscissa, while the ordinate gives the distance travelled, in m. The experiment clearly shows that a sand grain is buried rather often while a ripple passes over it. However, the grain is not in constant motion while it is not buried. It is at rest on the surface for a period; then it is launched – either directly by the wind or by another grain that hits it – and makes a jump or a number of jumps in immediate succession. The duration of a period of motion is negligible compared to the waiting times, except for a few of the smallest grains. Grain No. 6 was, apparently, never or only a few times buried under a passing ripple for some rather long periods.

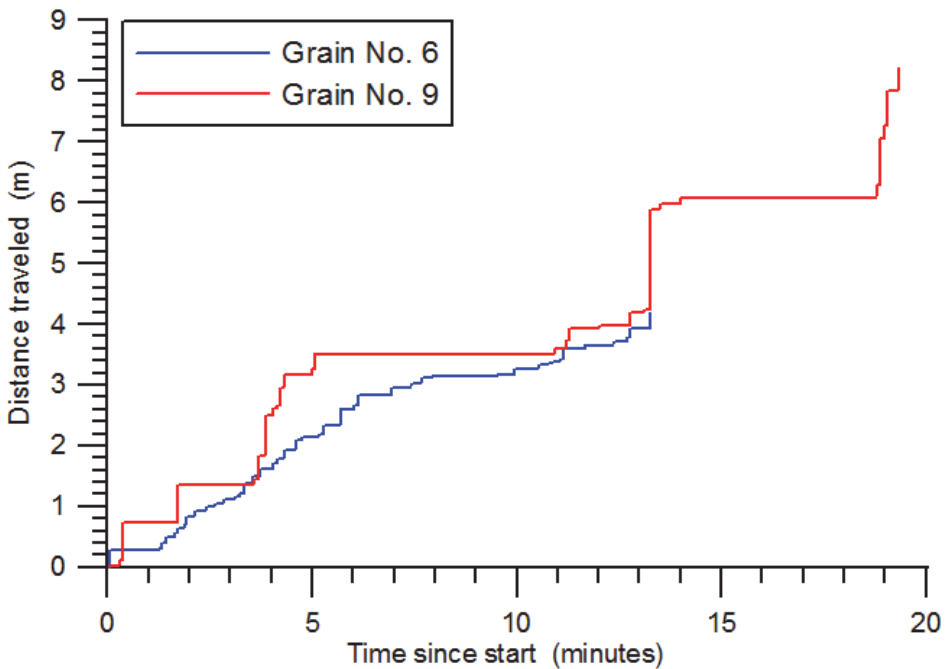


Fig. 12. Movement of two radioactively marked grains during saltation.

### 3.7 Electric field

A uniform electrical field can be created in the entire working section of the horizontal wind tunnel by suspending all the way down the working section a set of 10 parallel steel wires. The wires are made of 0.3 mm piano string and suspended at 80 mm height above the bed thereby creating one electrode with a constant distance to the bed. The inside of the (wooden) wind-tunnel bed has been painted using a conductive paint in this way forming another electrode just below the sand bed. The two electrodes can then be connected to the positive and negative terminals of a high voltage supply unit enabling us to study saltation under the influence of an electric field (Rasmussen et al. 2009).

## 4. Low pressure wind tunnels for aerosol studies

### 4.1 Planetary environmental wind tunnels

The wind tunnel laboratory at Aarhus University has developed two wind tunnels for planetary surface experiments. The smaller one has a test section 40 cm in diameter and about 50cm in length (Merrison et al. 2002, Merrison et al. 2008). The larger wind tunnel has a test section of around  $2 \times 2 \times 1$  m. In these environmental wind tunnel facilities dust suspension and aerosol studies can be performed. They are both re-circulating wind tunnels housed within low pressure (vacuum) vessels such that they can be evacuated and specific gas mixtures re-pressurized. Pressures in the range 0.01mbar and 1000mbar can be maintained. In addition a thermal control system has been constructed which consists of an insulated double walled chamber design. The cooling and fan systems are different in the two wind tunnels and we will here focus on the bigger wind tunnel (AWTSII). An exploded view of this is seen in figure 13a.

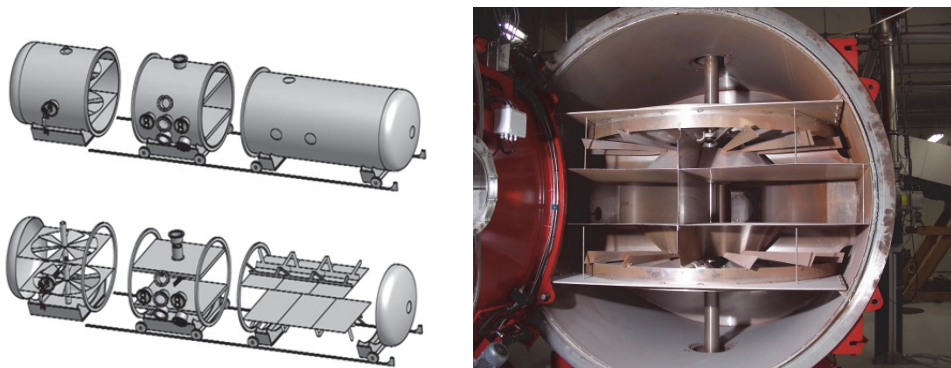


Fig. 13. a) Exploded view of the AWTSII planetary environmental wind tunnel, and b) photograph into the fan section.

The wind tunnel has large liquid nitrogen cooled sample mounting platforms. The wind circulation is achieved with the use of two 1.8m diameter fans and intricate flow steering plates (figure 13b). The wind flow is designed such that an almost rectangular test section is provided, though at the cost of a relatively complex two part flow return system. Turbulence levels, however, are maintained at around 5-15% (typical of Martian surface conditions). The wind tunnel test section has a cross section of around 1 m height and 2 m width and with a length of around 7 m. Wind speeds of around 0.5 – 20 m/s have been demonstrated at low pressure (<100mbar). The wind tunnel simulator has been designed with the goal of maintaining dust suspension (or other aerosol types), such that low turbulence and flow uniformity have been prioritized lower than allowing as little obstruction of the flow as possible to avoid deposition losses. The design therefore differs from boundary layer wind tunnels or those aimed at low turbulence (laminar flow).

### 4.2 Dust aerosol generation

A necessary process for the study of aerosols in the laboratory is the generation of suspended particulates within a simulator. In the case of solid particulates (dust) this will involve the dispersion of the fine material which will typically be in the form of aggregates.

The most effective and reliable method for aerosol generation consists of the injection of over-pressurized gas together with the required granular material such that a rapid expansion of the gas-particulate mixture causes dispersion of individual dust grains (Merrison et al. 2008). In the case of wind tunnels the high instantaneous wind speed at the injection nozzle also helps to distribute the aerosol into the wind flow. Essentially the same technique is used to generate aerosols consisting of liquids, for example water. In this case fine streams of liquid are mixed with gas (air) flow at an expansion nozzle such that the high velocity and turbulent gas flow disrupts the liquid and disperses it into individual particulates. In this way liquid particulates as small as a micrometer can be generated. With the use of controlled overpressure and quantified volumes/mass of injected gas and dust material it is possible to achieve reproducible dust aerosols i.e. controlled concentration of suspended dust within the wind tunnel simulator.

In nature the wind induced entrainment of dust occurs as a result of surface shear stress which above a certain threshold value is capable of overcoming adhesion and gravitation and lifting particulates. The low mass density of (sand sized) dust aggregates allows them to be entrained at wind speeds lower than other granular materials (shear stress). Subsequent breakup of the dust aggregates may liberate dust grains into suspension (Merrison et al. 2007). At higher wind shear solid sand grains may be entrained and perform saltation. Sand saltation is also an effective process capable of entraining dust due to collisional recoil i.e. during sand grain splash (Greeley and Iversen 1985).

A drawback with the gas-expansion technique for dust injection is that it is unlike the dust entrainment mechanism found in nature and therefore may not be directly comparable. It has been shown experimentally that wind induced dust entrainment can be used as a dust injection method within a re-circulating wind tunnel. This technique relies on accumulating a thick deposited dust layer within the wind tunnel, possibly localised to a particular section. Entrainment can then be performed by raising the wind speed temporarily above the threshold entrainment value. After achieving dust suspension the wind speed can then be reduced to the required value. This technique is effective, though it is difficult to perform in a reproducible manner i.e. to achieve a specific entrained dust concentration. For the quantitative study of aerosols, reproducibility is of primary importance making this technique unsuitable as a routine dust injection method.

The threshold wind speed at which dust becomes entrained is dependent upon several factors. Dust particulates of the order of a micrometer in size require extremely large surface wind shear to be entrained as individual grains. Dust however tends to aggregate into structures of the same scale as sand grains i.e. several hundred micrometers. Such aggregated dust structures have a low mass density (typically  $<1\text{g/cm}^3$ ) and can be removed by surface shear stress as low as  $0.01\text{ N/m}^2$  corresponding to friction velocities as low as  $0.1\text{ m/s}$  at ambient terrestrial pressure (Merrison et al. 2007). This is significantly lower than that required for sand transport.

Other methods of dust injection have been studied, for example techniques which rely on mechanical (e.g. vibrational) dispersal of dust. Unfortunately a fundamental problem with this type of dust dispersal system, also seen generally in dust feeding systems, is the tendency of dust to become compacted, adhered and cause blockage. To avoid such blockages it may be possible to keep the dust fluidized by maintaining a high gas content i.e. mixing or flowing gas through the dust, however this tends again to return to an injection system utilising pressurized gas-flow.



A physical phenomenon which has great importance to the behaviour of aerosols is the electrification of particulates as a result of contact. Contact electrification is seen widely both in nature and anthropological activities where granular materials interact, for example Aeolian transport (Stow 1969, Gilbert et al. 1991, Schmidt et al. 1999). Extensive experimental studies have revealed that the injection of dust induces a high level of particulate electrification, typically resulting in the suspension of equal amounts of positive and negative electrified dust grains (Merrison et al. 2004a). This electrification leads to the electrostatic enhancement in dust aggregate formation and may be an important factor in the transport of dust, specifically in dispersal/detachment and suspension/deposition. Following injection aggregation of dust leads to reduction of the electrification of the suspended dust. The degree of electrification of the suspended dust decreases with time and is therefore dependent upon the concentration of dust. Since the suspension time of the dust is dependent upon the wind speed, the measured electrification of dust also varies with wind speed.

### 4.3 Dust suspension

Aerosols, for example suspended dust particulates, are not stable within a re-circulating wind tunnel. Processes such as gravitational deposition (settling), adhesion and aggregation lead to loss of suspended dust and reduction of the suspended number density. Typically the suspended dust concentration falls exponentially with time after injection. The time constant for this process is dependent upon the wind speed. At high wind speeds ( $>1\text{m/s}$ ) dust deposition appears to be dominated by collision of dust particles with surfaces within the wind tunnel, leading typically to the accumulation of dust on wind facing surfaces. This gives a reduction in the suspension time with increasing wind speed. At wind speeds of around  $10\text{m/s}$  the dust suspension time within the AWTSII facility has fallen to around 30seconds.

As mentioned earlier at wind speeds above around  $7\text{m/s}$ , depending on the pressure, thick depositions of dust (dust aggregates  $>50\mu\text{m}$ ) can lead to the wind shear induced re-suspension of deposited dust. At these high wind speeds and given large amounts of dust within the wind tunnel both dust suspension and deposition can occur at the same time making dust concentration a complex function. At the lowest wind speeds (around  $1\text{m/s}$ ) gravitational settling appears to dominate the deposition rate and the dust suspension time becomes independent of wind speed. In the case of AWTSII this suspension time is around 300 seconds at around 15 mbar (i.e. Mars simulation conditions) in agreement with estimated gravitational settling time. Dust suspension as described above is relevant for dust grains of the order of a few micrometers in size and bulk mass density of up to a few thousand  $\text{kg/m}^3$ . Larger or denser dust grains will typically lead to decreased suspension times due to enhanced gravitational deposition. This will naturally lead to a mineral (compositional) dependence of dust suspension time as a result of variation in grain size, morphology, mass density and possibly cohesiveness (difficulty in dispersion). Higher gas mass density within the wind tunnel will also allow increased aerodynamic drag and therefore increased dust suspension times. However wind tunnel pressure may also affect the dust injection system, specifically the gas-expansion system will become inefficient at reduced pressure differential.

It is useful here to present a basic fluid dynamic relation relevant to the suspension of dust particulates within a (low pressure) wind tunnel. For dust particulates of the order of a few

microns Stokes relations will be valid as indicated by the low Reynolds number ( $<0.1$ ). Dust grains can typically be assumed to follow the fluid flow well (the same wind speed and turbulence). Under the action of external forces ( $F$ ) such as gravitation, electrostatic or magnetic affects, the particulates can be assumed to accelerate within a short period of time ( $\ll 1s$ ) and therefore given a uniform field achieve terminal velocity, that is to say reach a drift velocity at which the external force is balanced by the drift induced drag ( $U_T$ ) (Hall 1988, Fay & Sonwalker 1991). Values of the electric field induced drift velocity  $U_T$  have typically been calculated to be around 1cm/s for fields of order 10KV/m.

The value of this terminal velocity is given in equation 1;

$$\text{Equation 1 (field induced drift velocity); } \quad U_T = F \times \frac{S}{6\pi\mu r}$$

Here  $\mu$  is the molecular viscosity (for air  $\mu = 1.8 \times 10^{-5}$  kg/ms) and  $r$  is the dust grain radius.

At the low pressures used in most Mars simulation studies the suspended particulate size is smaller than the collision distance between gas molecules (the scattering length,  $\lambda$ ). Here an empirical relation can be used to correct for the non uniform nature of the gas, called the slip

factor;  $S = 1 + \frac{\lambda}{r} (1.257 + 0.4 \cdot \exp(-1.1 \frac{r}{\lambda}))$ . This factor is of the order of 10 in most Mars

simulation studies, though is typically negligible at ambient pressure.

The simplicity of this relation allows the accumulation of dust within a wind tunnel environment to be used to quantify (estimate) the force(s) applied to the dust particulates. This simplicity however relies on the assumption of average particulate properties such as size, mass, morphology as well as the external forces applied. It also neglects effects of the flow such as turbulence.

#### 4.4 Dust deposition

At low turbulent flows dust deposition is dominated by gravitational settlement as turbulent wind speed is small compared to the gravitational terminal velocity. In this case dust deposition within a wind tunnel will be dominated by settlement onto upward facing surfaces. At higher wind turbulence it becomes more likely that suspended grains can impact surfaces and deposition on wind facing surfaces begins to occur. This process of dust deposition is dependent upon details of the boundary layer flow around surfaces within the wind tunnel. This near surface boundary layer is conventionally divided into two regions. A region close to the surface within which the flow velocity increases linearly from zero (at the surface) and shear stress is transferred by viscous interaction. Outside this region turbulence becomes dominant as the mechanism for transferring shear stress and the flow velocity increases logarithmically. The transfer of stress through turbulence occurs through variations in the properties of macroscopically sized volumes of the fluid. Turbulence is a fundamental property of fluids and related to variations in velocity, pressure, temperature, etc. Turbulence occurs on all spatial and temporal scales above the molecular level (Monin & Yaglom 1973.) The concept of an ideal viscous region (of molecular flow) at the surface is likely to be a simplification and at odds with the inherently statistical nature of turbulence such that in reality suspended particulates can still be transported to a surface though with low probability.

At higher wind shear the boundary layer is expected to shrink (spatially) and the turbulence is expected to increase in agreement with the observed increase in surface impacts by suspended grains. It is interesting here to note that increased dust deposition (due to high turbulence) and increased dust removal (due to high surface shear stress) can occur, and in fact is expected, at the same regions within the wind tunnel.



Fig. 14. Aggregated quartz grains ( $<2\mu\text{m}$ ) deposited on an upward facing surface after wind tunnel aerosol exposure.

#### 4.5 Dust capture and sensing

Experimentally it is useful to collect suspended dust onto a surface. This could be for use in compositional or structural analysis or for the determination of concentration. It is not always sufficient to rely on gravitational or turbulent deposition of dust either because of the amount of material required or the flow conditions. Methods of enhancing dust accumulation include applying (attractive) force to the particulates. This could involve the use of electrical or magnetic fields in the case of electrified or magnetic particulates. This technique has been used to great effect to study the electrical/magnetic properties of suspended dust on Mars and in wind tunnel simulators. An alternative technique which is used industrially and in environmental sciences is the use of a pump system to extract specific volumes of gas. Suspended particulates can then be accumulated within filters or onto surfaces. Such systems have not as yet been used in wind tunnel studies, however an important application of wind tunnels is in the testing and calibration of environmental sensors and it seems likely therefore that wind tunnels will be used for this purpose in the future.

Different techniques can be used to quantify the amount of dust captured onto a surface. Microbalances can be used to determine the accumulated mass (and therefore mass density) of the suspended dust, this however requires a high degree of detector sensitivity. Alternatively optical systems could be used to quantify dust deposition. This could involve the use of imaging or the reflection/transmission of light using optoelectronic systems. Optical (also laser based) systems have been used successfully here (Merrison et al. 2006).

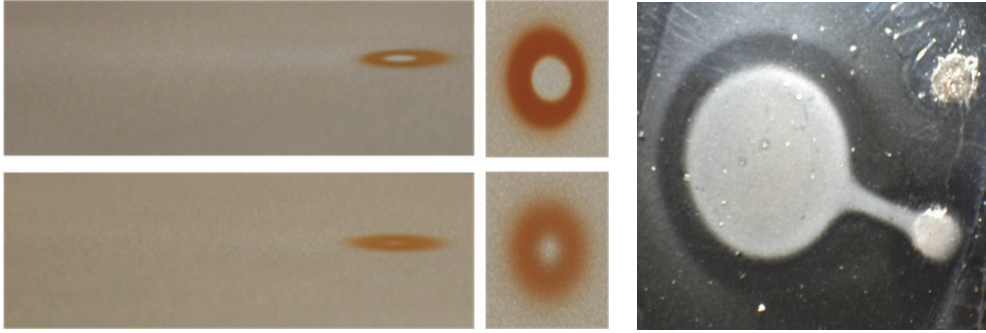


Fig. 15. Left dust capture on a NASA Phoenix camera calibration-target magnets and a model of the MSL calibration-target magnets for uni-directional wind. Right quartz dust capture on an electrostatic electrode (voltage 300V).

#### 4.6 Suspended dust sensing

The scattering of light by suspended particulates is the obvious and by far the most widespread technique for studying suspended dust aerosols. Modern techniques which are applied in meteorology include determination of the optical opacity (scattering of sun light). Such measurements tend to be simple to carry out, however detailed modelling of angular scattering intensities are required to determine suspended grain size, morphology and concentration. More advanced and direct systems for determining the spatial distribution of dust aerosols include the laser based technique LIDAR which is successful both commercially and in research for example in the study of clouds. This technique is, however, not well suited for wind tunnel operation.

Within wind tunnels other laser based techniques are used to study dust aerosols. Laser Doppler Anemometers (LDA) are primarily used for wind velocity sensing. They function by scattering light from suspended particulates and hence have the added benefit of being able to quantify the aerosol concentration (number density) typically for particulates of above around one micron. Further modifications of LDA systems enable the spatial distribution (multiple dimensions) and grain size to be quantified. In addition to such commercial sensor systems prototype (miniaturized) instruments are being developed in order to detect suspended dust and measure flow rates (Figure 16) (Merrison et al. 2004b, Merrison et al. 2006).

### 5. Modelling

Computational Fluid Dynamic modelling is in principle a useful technique for identifying and solving problems with the design of a wind tunnel by detailing the wind flow. It is however extremely time consuming (compared to typical measurement and even construction time scales) especially if three dimensional modelling is employed (Peric and Ferziger 1999). CFD models are also prone to inaccuracies resulting from insufficiently high time/space resolution (pixelisation). A combination of measurement and modelling is however a powerful combination to achieve a full understanding of the flow dynamics within a system (Kinch et al 2005).

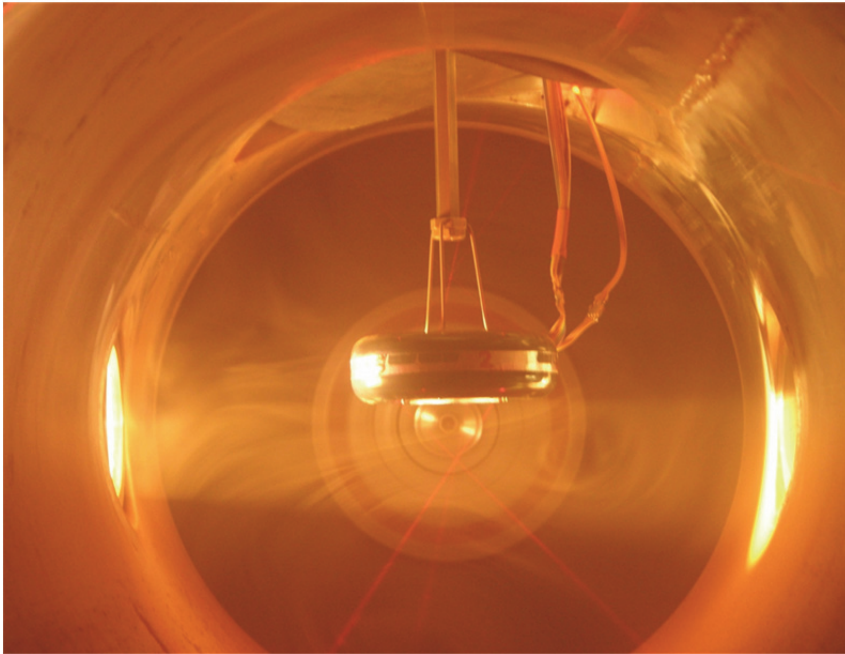


Fig. 16. Prototype laser based sensor system operating in a dust aerosol within the 40 cm  $\varnothing$  diameter environmental wind tunnel.

As explained in the preceding sections there are fundamental differences in the physics that control the movement of sand and dust. Therefore the approach to model (analytically or numerically) the transport of dust and sand follows different principles. In aeolian transport, saltation is an important link by which momentum is transmitted from the air to the bed through grain impact, but momentum transfer, impact and subsequent entrainment take place in a very shallow layer at the air-bed interface with large velocity gradients. Consequently, in addition to experimental evidence obtained from few and simplified studies of the splash (e.g. Willetts & Rice 1986, 1989, Mitha et al. 1986) theoretical reasoning and numerical modelling has played an important role (e.g. Owen 1964, Sørensen 1985, Anderson & Haff 1988, 1991, McEwan & Willetts 1991, 1993, Shao & Li 1999, Spies & McEwan 2000). After the sand grains have left the surface they are accelerated by the wind with trajectories influenced by fluid drag, gravity, particle spin and fluid shear, and electric forces. This process has been modeled by several authors (e.g. Anderson & Haff 1991, McEwan & Willetts 1991, Sørensen, 1991, Sørensen 1995, Sørensen 2005 and Kok and Renno 2009). The physics governing the splash, the grain trajectories and the momentum exchange between the fluid flow and saltating particles has been specifically formulated in the models mentioned above and is not traditionally dealt with in a CFD-context.

For aerosols where with CFD modelling it is possible to inject virtual particulates within the flow and trace their transport. It may then be possible to apply external force fields (gravitational, electrostatic or magnetic) and thereby perform a faithful reconstruction of the physical conditions within the wind tunnel. In this case an extremely detailed physical description of an observed phenomenon can be obtained and therefore the dependency

upon for example grain size, mass, electric charge, magnetisation, etc. Also physical parameters not easily varied in laboratory experiments may be modelled such as varying gravity (Kinch et al. 2005).

## 6. Acknowledgements

The authors would like to thank the Villum Kann Rasmussen Foundation, the Villum Foundation, the Danish Science Research Council and the European Space Agency (ESA) (Contract No. 21285/08/NL/GLC) for financial support to building of wind tunnels and instruments.

## 7. References

- Anderson, R.S. & Haff, P.K. (1991) Wind modification and bed response during saltation of sand in air. In O.E.Barndorff-Nielsen & B.B.Willetts(Eds) *Acta Mechanica Suppl.* 1, 21-51.
- Bagnold, R.A. (1941) *The physics of blown sand and desert dunes.* Methuen, London.
- Beuselinck, L.; Govers, G.; Poesen, J.; Degraer, G.; Froyen, L. (1998) Grain-size analysis by laser diffractometry: comparison with the sieve-pipette method. *Catena*, 32, 193-208.
- Chepil, W.S. (1959) Equilibrium of soil grains at the threshold of movement by wind, *Soil Science Society of America Proceedings*, 422-428.
- Counihan, J. (1975) Adiabatic atmospheric boundary layers: A review and analysis of the data from the period 1880-1972. *Atmospheric environment*, Vol.9, 871-905.
- Esthel, G.; Levy, G.J.; Mingelgrin,U.; Singer, M.J. (2004) Critical Evaluation of the Use of Laser Diffraction for Particle-Size Distribution Analysis. *Soil Science Society America Journal*, 68, 736-743.
- Fay, J.A. & Sonwalkar, N., (1991) "Fluid Mechanics", MIT, Boston.
- Gartshore, I.S. (1973) A relationship between roughness geometry and velocity profile for turbulent boundary layers. National Establishment of Canada, Report LTR-LA-140.
- Gilbert, J.S., Lane, S.J., Sparks, R.S.J., Koyaguchi, T. (1991) *Nature* 349, 598.
- Greeley, R. & Iversen, J.D. (1985) *Wind as a Geological Process on Earth, Mars and Venus.* Cambridge Planetary Science Series. Cambridge University Press, Cambridge.
- Greeley, R.; White, B.R.; Pollack, J.B.; Iversen, J.D.; Leach, R.N. (1981) Dust storms on Mars: Considerations and simulations. In Péwé, T., editor, *Desert Dust: Origin, Characteristics, and Effect on Man*, *Geological Society of America Special Paper*, 186, pp.101-21.
- Hall, D. J. (1988) *Fluid Mechanics*. 187, 451-466.
- Irwin, H.P.A.H. (1981) The design of spires for wind simulation. *J. Wind Eng. Industrial Aerodynamic*, 7, 361-366.
- Iversen, J.D. & Rasmussen, K.R. (1999) The effect of wind speed and bed slope on sand transport. *Sedimentology* 46, 723 -731.
- Iversen, J.D. and Rasmussen, K.R. (1994) The effect of surface slope on saltation threshold. *Sedimentology*, 41, 721-728.
- Iversen, J.D., Greeley, R., Marshall, J.R. and Pollack, J. (1987) Aeolian saltation threshold: effect of density ratio. *Sedimentology* 34, 699-706.
- Iversen, J.D., Greeley, R. and Pollack, J.B. (1976) Windblown dust on Earth, Mars and Venus. *The Journal of the Atmospheric Sciences* 33, 2425-2429.

- Iversen, J.D. and White, B.R. (1982) Saltation threshold on Earth, Mars, and Venus. *Sedimentology* 29, 111-119.
- Kinch, K. M. Merrison, J.P., Gunnlaugsson, H. P., Bertelsen, P. Madsen, M. B., Nørnberg, P. (2005) Preliminary analysis of the MER magnetic properties experiment using a CFD model. *Planetary and Space Science*. 54, 28-44.
- Klute A. (1986) Methods of Soil Analysis, Part 1, Physical and Mineralogical Methods, SSSA Book Series, Madison, Wisc. USA.
- Krumbein, W.C.; Pettijohn, F.J. (1938) Manual of sedimentary petrography. Appelton-Century-Crofts, N.Y.
- Marlow, J.J.; Martins, Z.; Sephton, M.A. (2008) Mars soil analogues. *Astronomy and Geophysics*, 49, 2, 2.20-2.23.
- Merrison, J.P., Bechtold, H., Gunnlaugsson, H., Jensen, A., Kinch, K., Nornberg, P. and Rasmussen, K. (2008) An Environmental Simulation Wind Tunnel for Studying Aeolian Transport on Mars, *Planetary and Space Science*, 56, 426-437.
- Merrison, J.P., Gunnlaugsson, H.P., Nørnberg, P., Jensen, A.E., Rasmussen, K.R. (2007) Determination of the Wind Induced Detachment Threshold for Granular Material on Mars using Wind Tunnel Simulations, *Icarus*, 191, 568-580.
- Merrison, J.P., Gunnlaugsson, H.P., Kinch, K., Jacobsen, T.L., Jensen, A.E., Nørnberg, P., Wahlgreen, H. (2006) An integrated laser anemometer and dust accumulator for studying wind induced transport on Mars, *Planetary and Space Science*, 54, 1065-1072.
- Merrison, J.; Jensen, J.; Kinch, K.; Mugford, R.; Nørnberg, P., (2004a) The electrical properties of Mars analogue dust, *Planetary and Space Science*; 52: 279-290
- Merrison, J.P.; Gunnlaugsson, H.P.; Jensen, J.; Kinch, K.; Nørnberg, P.; Rasmussen, K.R. (2004b) A Miniature Laser Anemometer for Measurement of wind speed and dust suspension on Mars, *Planetary and Space Science*; 52(13): 1177-1186.
- Merrison, J.P.; Bertelsen, P.; Frandsen, C.; Gunnlaugsson, H.P.; Knudsen, J.M.; Lunt, S.; Madsen, M.B., Mossin, L.A.; Nielsen, J.; Nørnberg, P.; Rasmussen, K.R. ; Uggerhøj, E. J. (2002) Simulation of the Martian Aerosol at Low Wind Speed. *J. Geophysical Research-Planets*, 107, 5133-5141.
- Monin, A.S. & Yaglom, A.M. (1973) Statistical Fluid Mechanics: Mechanics of Turbulence Volume 1, MIT Press.
- Morris, R.V.; Golden, D.C. Ming, D.W.; Shelfer, T.D.; Jørgensen, L.C.; Bell III, J.F.; Graff, T.G.; Mertzman, S.A. (2001) Phyllosilicate-poor palagonitic dust from Mauna Kea Volcano (Hawaii): A mineralogical analogue for magnetic Martian dust? *Journal of Geophysical Research-Planets*, 106, E3, 5057-5083.
- Moroz, L.V.; Basilevsky, A.T.; Hiroi, T.; Rout, S.S.; Baither, D.; van der Bogert, C.H.; Yokovlev, O.I.; Fisenko, A.V.; Semjonova, L.F.; Rusakov, V.S.; Khramov, D.A.; Zinovieva, N.G.; Arnold, G.; Pieters, C.M. (2009) Spectral properties of simulated impact glasses produced from martian soil analogue JSC Mars-1. *Icarus*, 202, 336-353.
- Nørnberg, P.; Gunnlaugsson, H.P.; Merrison, J.P.; Vendelboe, A.L. (2009) Salten Skov I: A Martian magnetic dust analogue. *Planetary and Space Science*, 57, 628-631.

- Nørnberg, P.; Schwertnam, U.; Stanjek, H.; Andersen, T.; Gunnlaugsson, H.P. (2004) Mineralogy of a burned soil compared with four anomalously red Quaternary deposits in Denmark. *Clay Minerals*, 39, 85-98.
- Nørnberg, P. (2002) Particle comminution and aeolian addition in young dune sand soils. *Transactions, 17<sup>th</sup>. World Congress of Soil Science*, Bangkok, Thailand, Symp. No 25, Paper no 1124.
- Owen, P.R., 1964. Saltation of uniform grains in air. *Journal of Fluid Mechanics* 20, 225-242.
- Peric, M. & Ferziger, J.H. (1999) *Computational Methods for Fluid Dynamics*, Springer, 2 Ed.
- Pettijohn F.J. (1957) *Sedimentary Rocks*, Harper and Row, N.Y
- Rasmussen, K.R., Kok, J.F., Merrison, J.P. (2009) Enhancement in wind driven sand transport by electric fields, *Planetary and Space Science*, 57, 804-808.
- Rasmussen, K.R. & Sorensen, M. (2008) Vertical variation of particle speed and flux density in Aeolian saltation measurement and modeling, *J. Geophysical Research- Earth Surface* 113(F2), F02S12.
- Rasmussen, K.R., Iversen, J.D. and Rautheimo, P. (1996) Saltation and wind flow interaction in a variable slope wind tunnel. *Geomorphology*, 17, 19-28.
- Rasmussen, K.R. & Iversen, J.D. (1993) A variable slope wind tunnel for testing wind-blown sand. Proc. 7<sup>th</sup> U.S. National Conference on Wind Engineering. Vol. 2, pp. 643-552. University of California at Los Angeles.
- Rasmussen, K.R. and Mikkelsen, H.E. (1991) Wind tunnel observations of aeolian transport rates. In: O.E. Barndorff-Nielsen and B.B. Willetts (eds) *Acta Mechanica, Suppl.* 1, 135-144.
- Raupach, M.R. (1991) Saltation Layers, Vegetation Canopies and Roughness Lengths. In O.E. Barndorff-Nielsen & B.B. Willetts (Eds) *Acta Mechanica Suppl.* 1, 135-144.
- Scheffer & Schachtschabel (1998) *Lehrbuch der Bodenkunde*, Ferd. Enke Verlag, Stuttgart.
- Stow, C.D. (1969) *Weather* 24, 134.
- Schmidt, D.S., Schmidt, R.A., Dent, J.D. (1999) Electrostatic force in blowing snow. *Boundary-Layer Meteorology*, 93 (1), 29-45.
- Tanner, W.F. (1969). The particle size scale. *Journal of Sedimentary Petrology*, 39,2, 809-812.
- Ulery, A.L. & Drees R. (2008) *Methods of Soil Analysis, Part 5 - Mineralogical Methods*, SSSA Book Series, Madison Wisc. USA.
- Williams, G., (1964) Some aspects of the eolian saltation load. *Sedimentology* 3, 257-287.
- Wooding, R.A., Bradley, E.F. and Marshall, J.K. (1973) Drag due to regular arrays of roughness elements of varying geometry. *Boundary-Layer Meteorology* 5, 285-308.



# Wind Tunnel Flutter Testing of Composite T-Tail Model of a Transport Aircraft with Fuselage Flexibility

Raja Samikkannu<sup>1</sup> and A. R. Upadhya<sup>2</sup>

<sup>1</sup>Scientist,

<sup>2</sup>Director,

National Aerospace Laboratories (CSIR-NAL),

Bangalore,

India

## 1. Introduction

Aeroelasticity is the study of interaction among aerodynamic, inertial and elastic forces. Flight vehicles experience steady and unsteady aerodynamic loads; accordingly they would develop different kinds of stability and response related problems. Transonic aeroelastic problems such as buffet and flutter have been solved through experimental techniques at National Aerospace Laboratories (Upadhya et al., 1985), (Joshi et al., 1988), (Ramamurthy and Raja, 2002), (Raja et al., 2007). Figure 1 shows the aeroelastic models that were tested in 1.2 m wind tunnel. Aeroelastic flutter is a catastrophic structural failure, which needs to be avoided within the flight envelope of an aircraft for safe operation and enhanced fatigue life (FAR AC 25.629-1A). Aircraft structures made of thin walled sections and composite materials are usually lightly damped systems. When the orthogonality of elastic modes in such systems is influenced by the unsteady aerodynamic forces, the aerodynamic damping destabilizes the vibration, meaning the structural modes may draw energy from the air stream. Frequency and damping change due to aerodynamic energy may cause coupling between two or more adjacent modes to develop a flutter in the aircraft wing or tail structure. Flutter is a divergent oscillation that may result into fatal structural failure.

Low speed aircrafts need clean airflow over the tail surfaces to have better pitch control. Therefore a T-Tail configuration is preferred for such flying machines due to its geometric location. Aircrafts with T-Tail structure are in operation; for example Boeing 727, ATR-72, Q-400, CRJ700 and Embraer ERJ145 etc. Nevertheless, aeroelastic problems such as flutter and gust are of great concern for the designers because the structurally heavy vertical stabilizer needs to carry the lift producing horizontal tail, which makes T-Tail a structure of concern in the low speed aircraft (Bisplinghoff et al., 1983). The present research work addresses the T-Tail flutter of a transport aircraft within its flight envelope through a wind tunnel study. The T-Tail configuration is normally expected to develop a dynamic coupling among its horizontal and vertical stabilizers' modes and participate in the aeroelastic flutter along with the control surface modes (Rudder, Elevators). Since for the aircraft under consideration (transport), the fuselage flexibility is appeared to be very significant on the empennage

flutter, a scaled T-Tail wind tunnel model has been designed with a flexible fuselage. Unlike the conventional horizontal tail plane, the horizontal tail sits on the top of a flexible fin in T-Tail, therefore may experience rolling, yawing and spanwise in-plane motion, in addition to pitching and plunging.

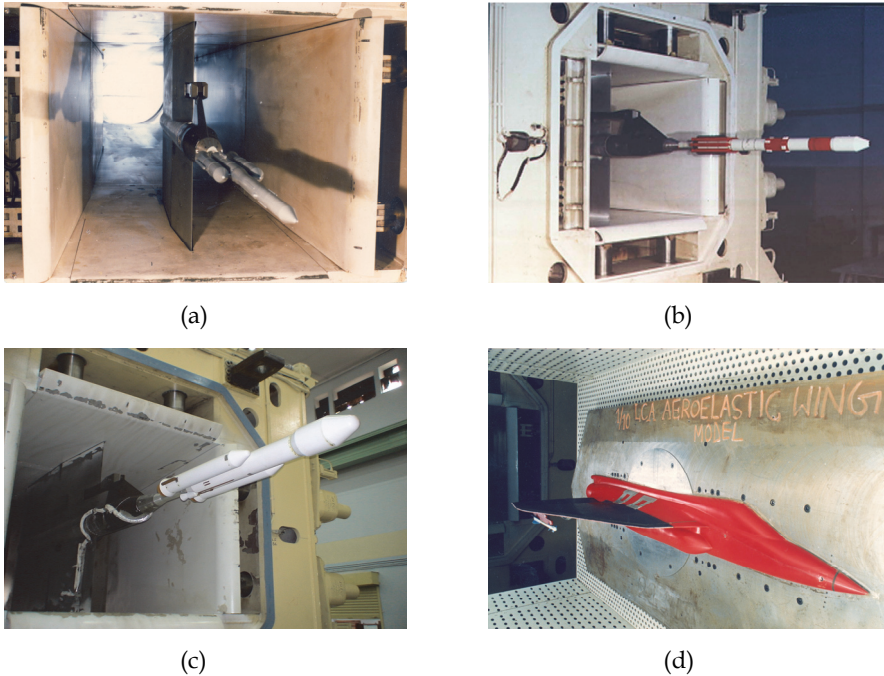


Fig. 1. Aeroelastic models in 1.2 m NAL trisonic tunnel

Thus, in-plane loads and normal loads due to in-plane motion become important while calculating T-Tail flutter, which can be easily captured through wind tunnel testing. Otherwise, an improved DLM (Doublet Lattice Method) code is required that accounts for all the aerodynamic degrees of freedom in the calculation of flutter. Further the incremental aerodynamic loads due to roll and yaw acting on the horizontal tail plane are dependent on the steady aerodynamic loads; therefore inclusion of steady loads in the flutter analysis is important (Queijo, 1968). Thus, the present experimental approach to build an aeroelastically scaled T-Tail model with a flexible fuselage to estimate empennage flutter appears to be convincing.

However, it has become a challenging design issue to introduce fuselage longitudinal bending due to a sting supported system and further the simulation of multi-modes coupling. A novel idea is then commenced into the model design scheme to incorporate the fuselage bending along with the sting bending mode. Composite materials are employed to realise the structural components of the T-Tail and fuselage structure. The model is subsequently instrumented with strain gauges and accelerometers to measure the aeroelastic responses during the wind tunnel testing. The flutter characteristics are then presented in velocity versus frequency and velocity versus damping format.

## 2. Design of scaled aeroelastic model

The aeroelastic model consists of the following components:

- Horizontal tail and elevators
- Vertical tail and rudder
- Torsion box assembly to attach the spars of the vertical tail
- Flexible fuselage
- Model supporting system

The results obtained from the wind tunnel testing are acceptable, only if the model simulates both aerodynamic and structural dynamic characteristics with respect to full scale vehicle (Bisplinghoff et al., 1983), (Megson T. H. G., 2007). This is achieved through a set of dynamic similarity laws, known as aeroelastic scale factors (Refer to table 1). A dynamically similar model only simulates frequencies and mode shapes. In contrast, an aeroelastically similar model additionally replicates the aerodynamic configuration of the vehicle. The aircraft model has been tested in 1.2 m wind tunnel. Figure 2 displays the side view of the model along with its sting mounting support system.

Geometric scale ratio	$L = L_m/L_p$
Dynamic pressure ratio	$q = q_m/q_p$
Density ratio	$\rho = \rho_m/\rho_p$
Velocity ratio	$V = V_m/V_p$
Weight ratio	$W = W_m/W_p$
Frequency ratio	$\Omega = \Omega_m/\Omega_p$
Deflection ratio	$\delta = \delta_m/\delta_p$
Flexural Stiffness ratio	$(EI)_m/(EI)_p$
Axial Stiffness ratio	$(EA)_m/(EA)_p$

Table 1. Aeroelastic scale parameters

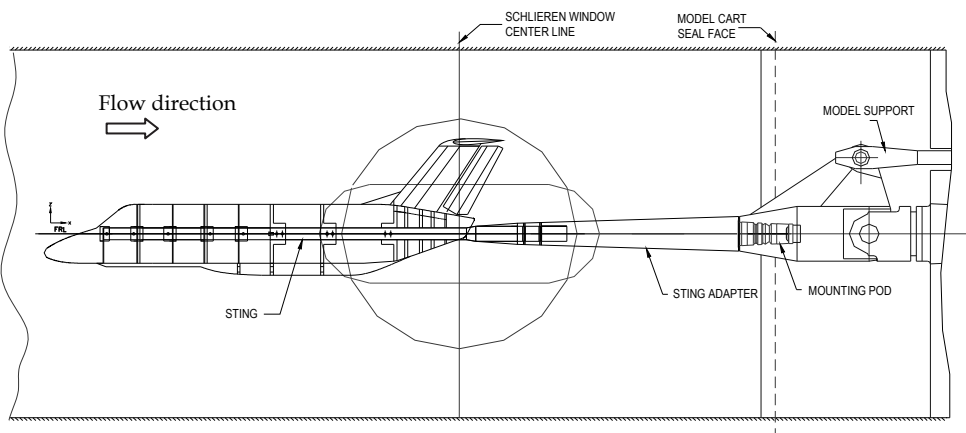


Fig. 2. Aircraft model with a sting support system

In order to accommodate the model in the test section of the wind tunnel, a 10% geometric scale is chosen for the specified test condition. Proper care is taken to minimize the blockage area (around 2%), so that there will not be any starting problem for the tunnel. Accordingly, the aeroelastic scale factors have been arrived for a fair representation of the mathematical analogue of the physical system, considering the fluid - structure interaction.

### 2.1 Model design details

Flight conditions such as flight dynamic pressure, flight altitude, air density, flight velocity and Mach number are taken as reference data for the design process. As a first step, suitable scale factors are derived, which would suit the model characteristics to the existing wind tunnel characteristics. The blow down type wind tunnel has limitation in terms of its test section, achievable dynamic pressure and run time etc. Therefore the geometric scale and dynamic pressure ratio are mostly the deciding factors to set the aeroelastic scales. The T-Tail model is designed following a replica design logic, in which a spar-rib-skin arrangement is maintained. Further, the same number of spars as in the full scale vehicle is considered at the model level. However the number of ribs is taken according to the model stiffness requirement. Figures 3, 4 present the design details of both horizontal tail plane (HTP) and vertical tail plane (VTP), respectively. HTP is constructed with two spars and VTP is made using three spars arrangement. All dimensions are given in mm. The control surfaces (elevators, rudder) are also built with spar-rib-skin construction. Fuselage is designed with metallic/composite bulkheads and stiffeners, over which a composite skin (CFRP) is provided (Refer to figure 5).

Due care is taken in the selection of appropriate materials for making the model, considering the feasibility of fabrication and availability of materials. The designed model has got nearly 70% composite components (CFRP) and the remaining is metallic. The model is required to be mounted in the specified test section of the wind tunnel, so that the T-Tail is exposed to a set and necessary flow characteristics such as Mach number, dynamic pressure etc. Therefore a sting adapter is introduced into the model supporting system (Figure 2). Thus, the designed T-Tail is pushed forward to experience the actual and set wind tunnel flow characteristics. Because of this increased exposure length of the sting, there is a need to provide sufficient torsional stiffness in order to ensure the stability and strength of the fuselage. Hence five additional CFRP disc type bulk heads have been incorporated in the front fuselage along with a CFRP tubular structure as core, which gets connected to the sting.

### 2.2 Design details of joints for sub-structural systems

To build an efficient aeroelastic T-Tail model, the joint flexibility of all the sub-structural systems must be appropriately simulated. Figure 6 (a, b, c, d) depicts the various joints, which are designed to integrate all the sub-systems. For example the control surfaces (elevator, ruder) are connected to the main surfaces with the help of torque tubes, designed to provide the required control-circuit stiffnesses.

By ensuring a proper rotational stiffness, the ruder and elevator fundamental modes are simulated.

The elevator torque tube has connected to both left and right elevators, so that they act as a single control surface. The spars of VTP are positioned in a torsion box assembly (figure 5-d), in order to reproduce the necessary flexibility as in the full scale vehicle.

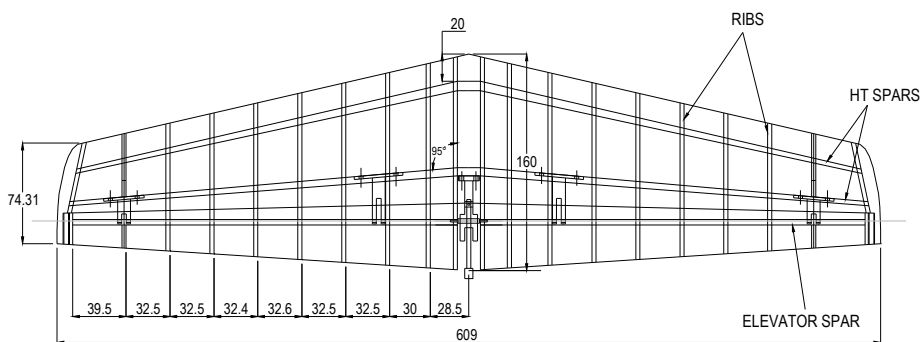


Fig. 3. Horizontal tail plane assembly

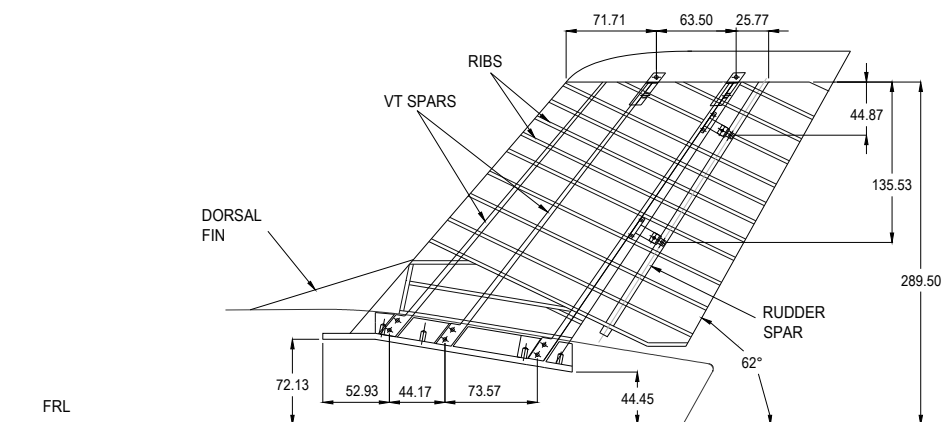


Fig. 4. Vertical tail plane assembly

### 2.3 Model fabrication and integration

After freezing the design, the production drawings are prepared using AUTOCAD 2000. The composite components are fabricated by using appropriate moulds. Skin/bulkhead/spar type of construction is adopted for fabricating the 10% fuselage. Along its length, the model fuselage consists of two circular aluminium rings, seven aluminium disc type bulkheads and five composite discs (not shown in figure 5). The skeleton is further stiffened using sets of side and top spars made of aluminium. CFRP skin of uniform thickness is fabricated in two halves using hand lay-up process and cured at room temperature. Nearly 40% resin content is achieved in the cured component.

VTP is constructed in spar-rib-skin form. It has got three aluminium spars and eighteen balsa ribs (refer to figure 4). A uniform thickness CFRP skin (top & bottom) is made to get the required aerodynamic shape. The mould is built in such a way that it could accommodate as well the rudder skin. Further, the rudder is constructed using a single aluminium spar with balsa ribs and CFRP skin. In a similar way HTP moulds (top and bottom) are fabricated first, which have got provision to include elevator skin. HTP is made

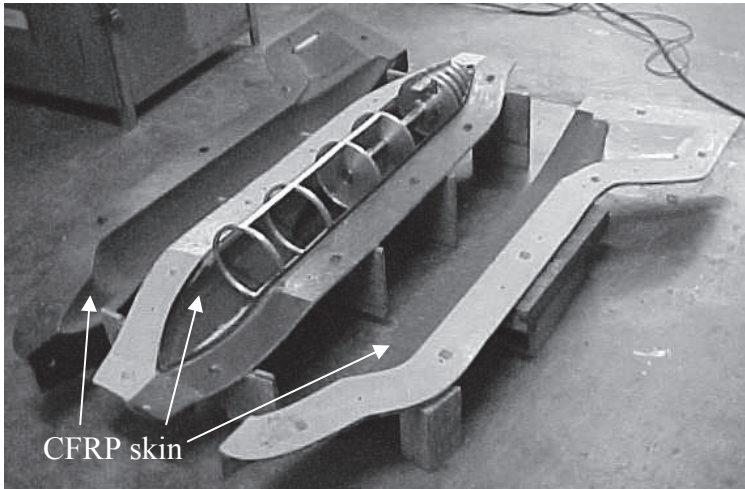


Fig. 5. Fuselage skin, bulk heads, and stiffeners with mould

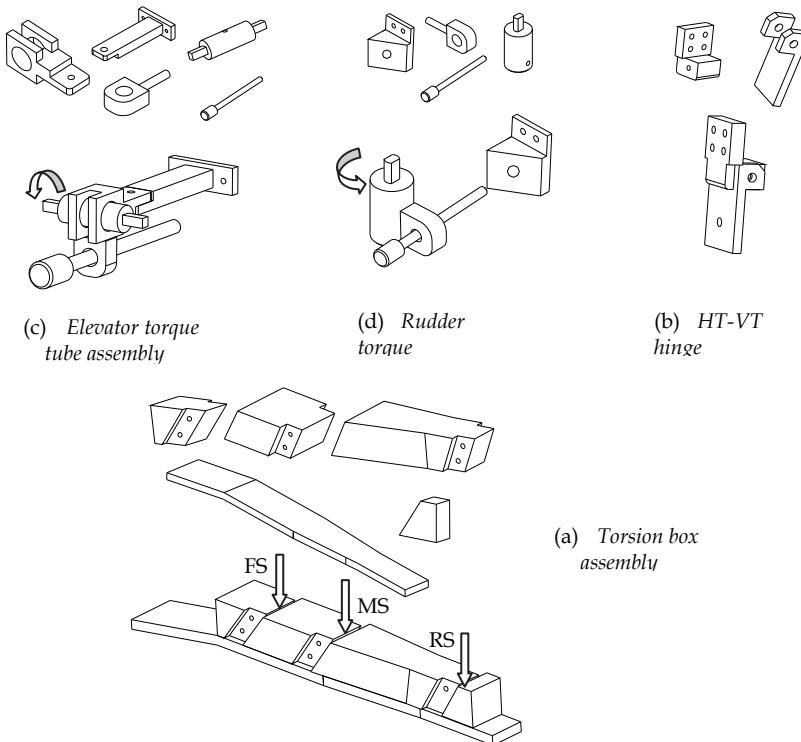


Fig. 6. Mechanical joints for structural components integration and flexibility simulation

of two aluminium spars with twenty balsa ribs (refer to figure 3). A uniform CFRP skin is provided in two parts (top & bottom) to give the required aerodynamic shape. The model supporting system essentially consists of a sting and an adapter. A sting with required strength and dimension is manufactured using EN24 material (Ultrasonic tested for flaws). Adapter is also fabricated with the same type of material, satisfying the strength adequacy requirements.

After the fabrication of major components (spar/rib/skin etc), each component is independently weighed and checked for its mass simulation. Hinges are fabricated using aluminium material for connecting the control surfaces to main surfaces. The assembled sub structural systems are weighed and checked for their required mass. The VTP spars are positioned inside the torsion boxes, which are mounted on the rear bulkheads of the fuselage. Then HTP assembly has been attached to VTP.

### 3. Vibration analysis and test correlation

A detailed free vibration analysis is performed on the designed T-Tail structure using MSC-NASTRAN (refer to figure 7). The analysis is carried out attaching the fuselage at three support points with sting, which has been fixed at one end (simulating the tunnel sting mounted condition). The fabricated model is appropriately instrumented with accelerometers and strain gauges to measure the structural responses. After the instrumentation, the model is subjected to ground tests (both static and dynamic). Ground tests are essential for two reasons, one is to check the achieved accuracy of dynamic simulation and the second is to extract the static and dynamic characteristics of the model.

The Kyowa make strain gauges and PCB type accelerometers (sensitivity: 100 mv/g) are used. The gauges are surface bonded and connected by using thin multi strand Teflon wires. Further they are numbered and terminated outside the model. Static tests are conducted by loading the structure at its  $C_p$  to monitor the strain output on the model at different locations to verify the model strength, as well as support system's ability to carry the model weight and the aerodynamic forces. The dynamic testing is subsequently performed from component level to fully assembled model. This exercise has helped to fine tune the dynamics of the integrated structure in a befitting way. However, the results are presented in a concise manner for the integrated model only (See table 2).

ModeNo.	Frequency (Hz)			Remarks
	GVT (proto)	Experiment (Model)	FEM (Model)	
1	66.04	64.11	66.40	Rudder rotation
2	102.65	100.28	102.8	Elevator rotation
3	105.17	97.67	96.67	HT anti-symmetric bending
4	149.50	149.92	151.1	VT longitudinal bending
5	170.28	174.24	162.8	VT lateral bending
6	207.72	211.90	209.8	HT symmetric bending
7	281.49	327.23	285.5	Fuselage first longitudinal bending

Table 2. Comparison of experimental and analytical results (Frequency ratio = 9.315)

A detailed modal testing is conducted using LMS SCADAS -III/ CADA-X/Modal Analysis software. The model is subjected to 50% burst random force and the responses are therefore measured by the accelerometers. The transfer function technique is adopted to extract the natural frequencies, associated mode shapes and the corresponding damping values of various modes of the model (refer to table 2 and figures 8,9).

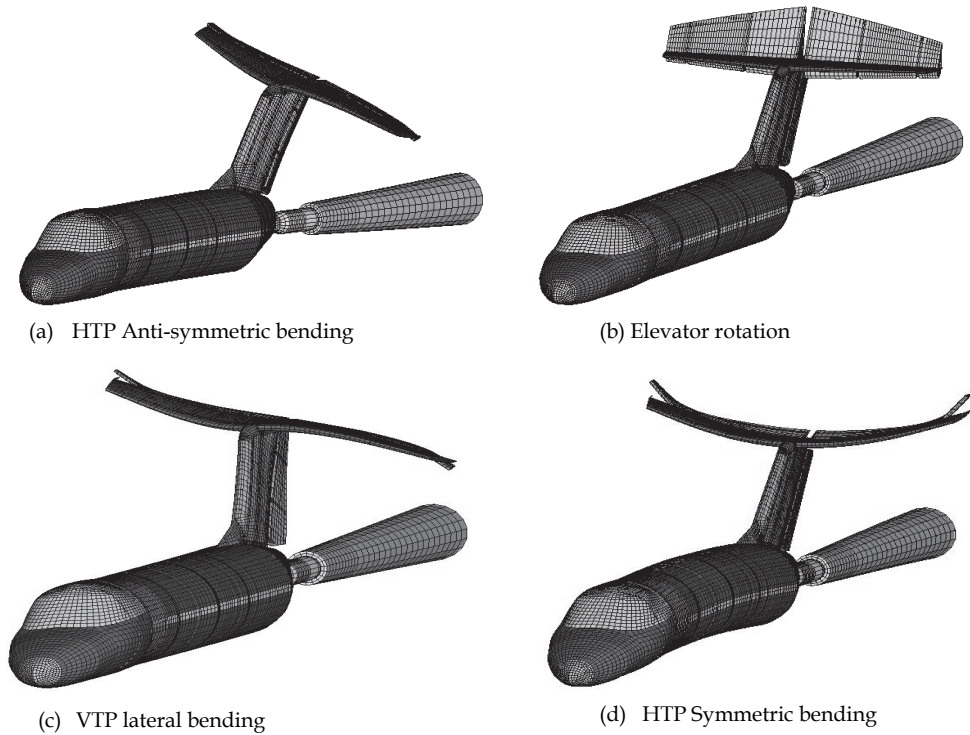


Fig. 7. FE analysis based mode shapes of the model

### 3.1 Divergence clearance

Since the model supporting system is slender body, it demands clearance from divergence instability prior to the wind tunnel testing (Sundara Murthy, 2005).

The following data are used in the static divergence calculation.

- Values of lift and moment coefficients for different angles of attack
- Centre of pressure ( $C_p$ )

for the Mach number and dynamic pressure of interest.

In order to calculate the divergence parameters, the sting and adapter assembly is loaded at  $C_p$  and as well as at its tip (equivalent static aerodynamic load  $\approx 50$  kg,  $C_L=1.0$ ). The deflections are measured at the strain gauge locations (reaction points). Using the following relations (Sundara Murthy, 2005), the divergence parameters are estimated as follows:



$$D = qS \left[ (I_R C_{M\alpha} + x C_{N\alpha}) \left( \frac{\delta_{N1} - \delta_{N2}}{l_N} \right) + C_{N\alpha} \left( \frac{\delta_{N1} + \delta_{N2}}{2} \right) \right],$$

$$D = 0.125 < 0.2.$$

$$\Delta\theta = \frac{(D \alpha_0 + C_0)}{(1 - D)},$$

$$C_0 = qS \left[ (I_R C_{M0} + x C_{N0}) \left( \frac{\delta_{N1} - \delta_{N2}}{l_N} \right) + C_{N0} \left( \frac{\delta_{N1} + \delta_{N2}}{2} \right) \right],$$

$$\Delta\theta = 0.5278^\circ < 3^\circ.$$

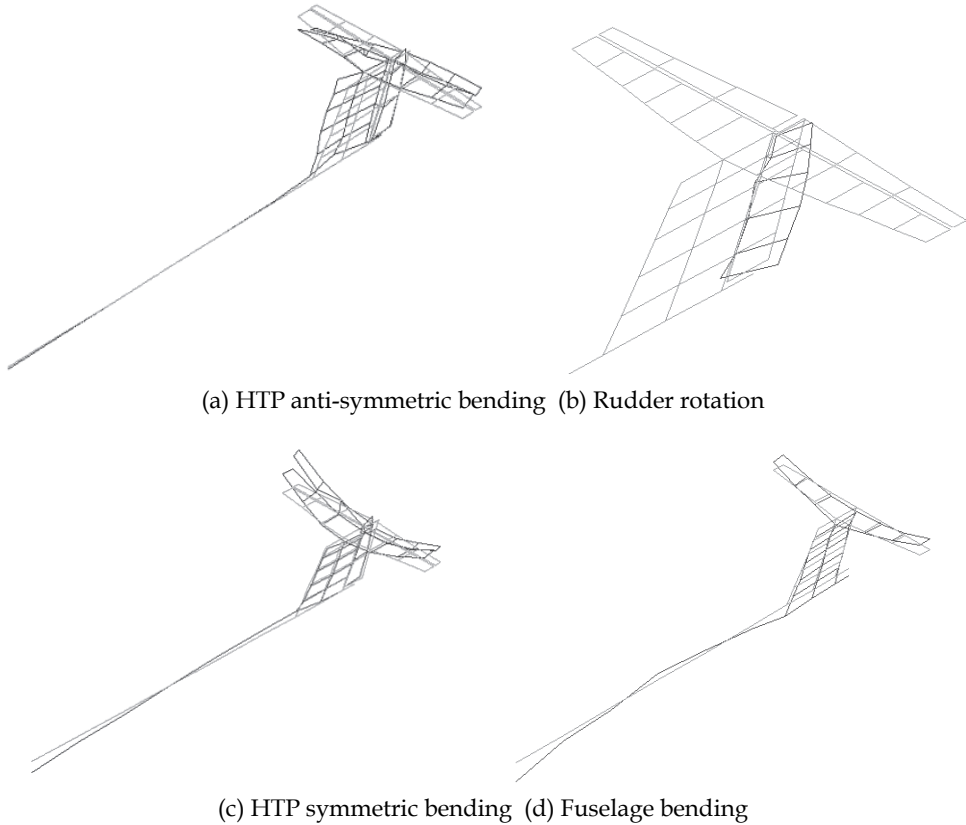


Fig. 8. Few experimental mode shapes (GVT)

It has been seen that the supporting system is free from the static divergence instability in the proposed test envelope.

#### 4. Wind tunnel testing

The wind tunnel testing is done, following the dynamic pressure variation as shown in table 3. The model needs to show flutter free condition in order to qualify the full scale T-Tail for a Mach number of 0.42.

Mach No	0.2	0.25	0.3	0.35	0.4	0.45
$q_{dynamic}$ (PSI)	1.36	2.1	2.95	3.94	5.0	6.16

Table 3. Wind tunnel test matrix

The 10% aircraft T-Tail model has been tested in 1.2 m wind tunnel (refer to figure 10). The aeroelastic scale parameters are applied to obtain a replica model through optimization process for the full scale T-Tail configuration. It has been shown through ground vibration testing that the necessary dynamic characteristics have been achieved fairly by the fabricated model (see table 2). The longitudinal fuselage mode has been simulated along with the sting bending mode. This is observed to be a quite reasonable simulation from the complexity point of view of simulating a free-free boundary effect through spring-sting arrangement. The tunnel tests are completed with 22 runs (blow downs) to cover the required dynamic pressure and Mach number range. During the wind tunnel testing, the data has been collected through 'Throughput Acquisition Monitor' of LMS® for multiple channels concurrently (refer to figure 11). The measured aeroelastic data from the accelerometers, positioned at different locations is processed with 'Operational Modal Analysis' software of LMS®. This software has got computational algorithms such as poly reference and balanced realization etc, using which the damping is estimated. The frequencies and damping values obtained from the flutter experiments are presented, following classical V-g approach in figure 12.

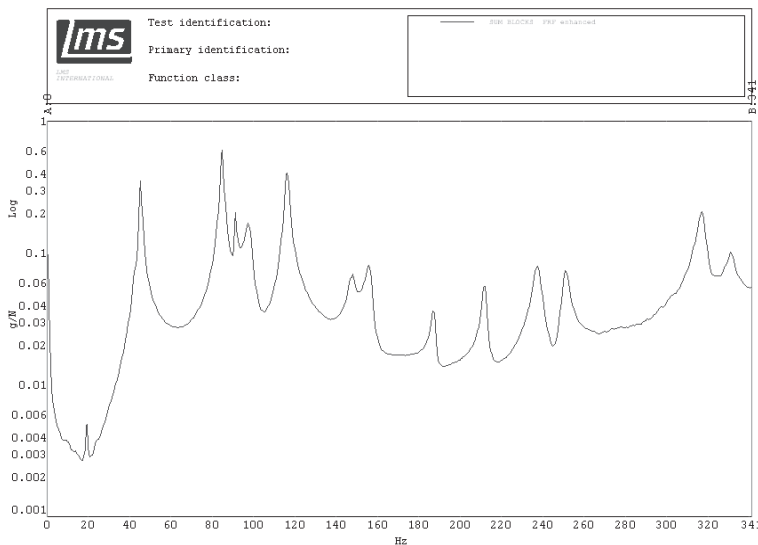


Fig. 9. Modal response during GVT

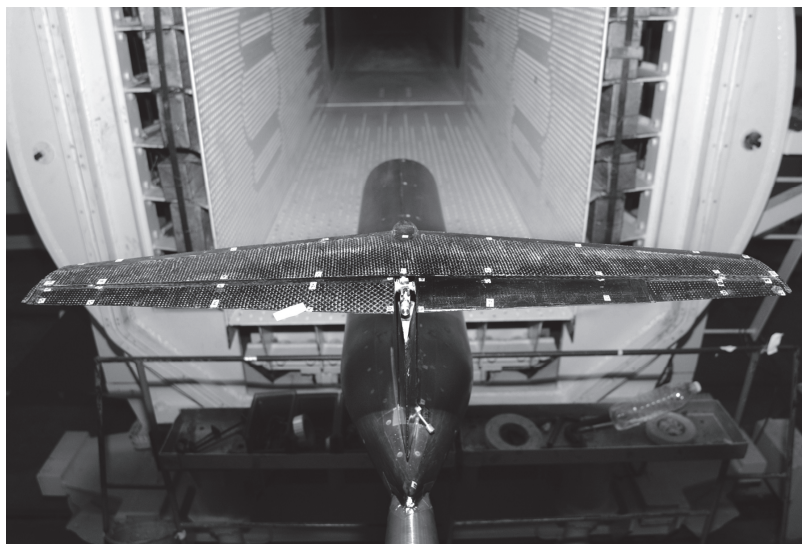


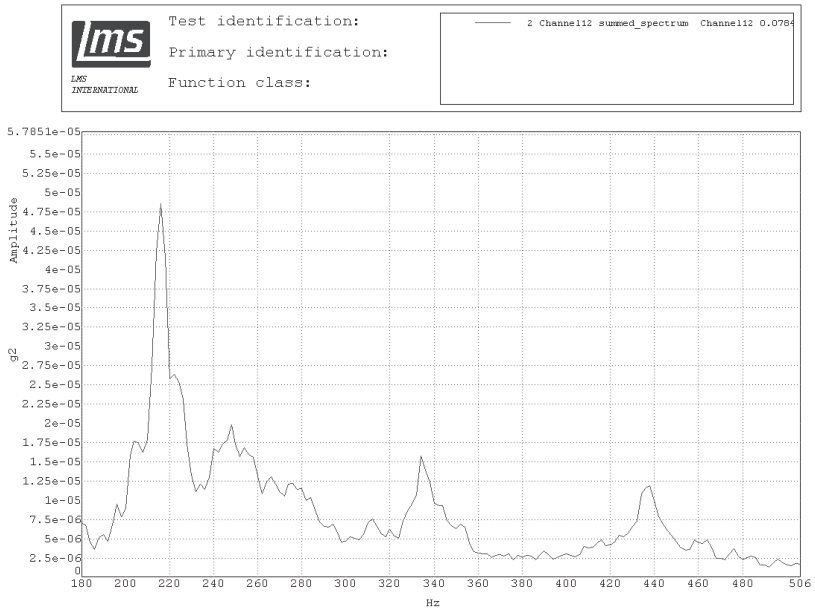
Fig. 10. Aircraft model in wind tunnel

## 5. Observations

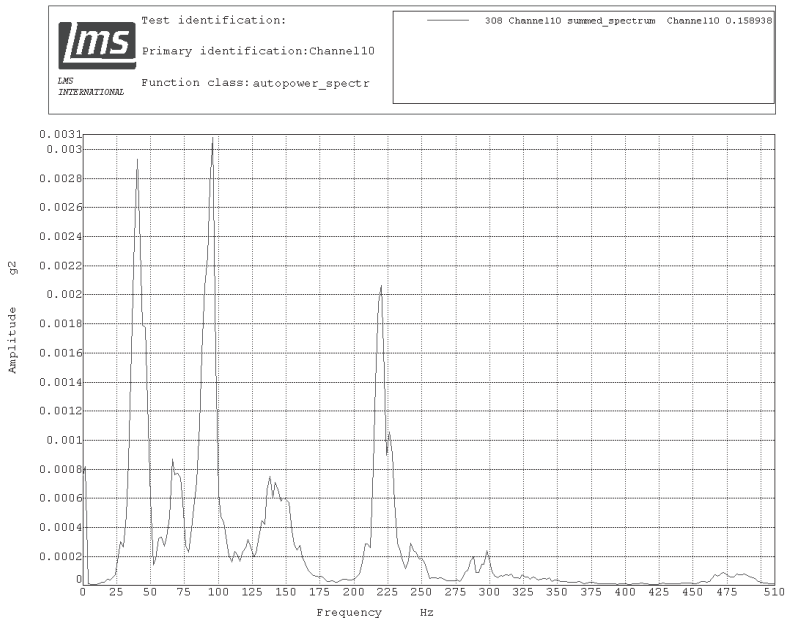
- The aircraft model is tested in the Mach range of 0.2 to 0.45
- The T-Tail has not shown any trend of flutter in the tested Mach numbers and dynamic pressures, thus qualify from flutter in the aircraft flight envelope
- Test results have shown that HTP-Symmetric bending and VTP-in-plane bending modes have nearly 2% aerodynamic damping at maximum test dynamic pressure (5 PSI) in addition to structural damping
- Fuselage longitudinal bending mode does not appear to be influenced by aerodynamic damping and the mode shows a nearly constant structural damping

## 6. Conclusion

This research work presents the details of fabrication, ground and wind tunnel testing of a scaled aeroelastic model of T-Tail with a flexible fuselage. Using composite materials and optimization procedures the required dynamics, namely frequencies and mode shapes of the T-Tail are achieved, which includes two control surface modes. After conducting a thorough ground studies, the model has been tested in 1.2 m Trisonic Wind Tunnel for the flutter clearance of T-Tail in the subsonic aerodynamic regime. The flutter characteristics are obtained as classical velocity versus damping and velocity versus frequency plots. The flutter experiments are carried out to cover a Mach range of 0.2 to 0.45. The critical modes of the T-Tail have not shown any dynamic instability nature at critical flight velocity 141.33 m/sec. Also, the total damping (Structural and Aerodynamic) of the critical modes are noticed to be around 2%. This fact has ensured that the T-Tail is qualified from flutter at maximum diving velocity.



(a)



(b)

Fig. 11. Wind tunnel test results

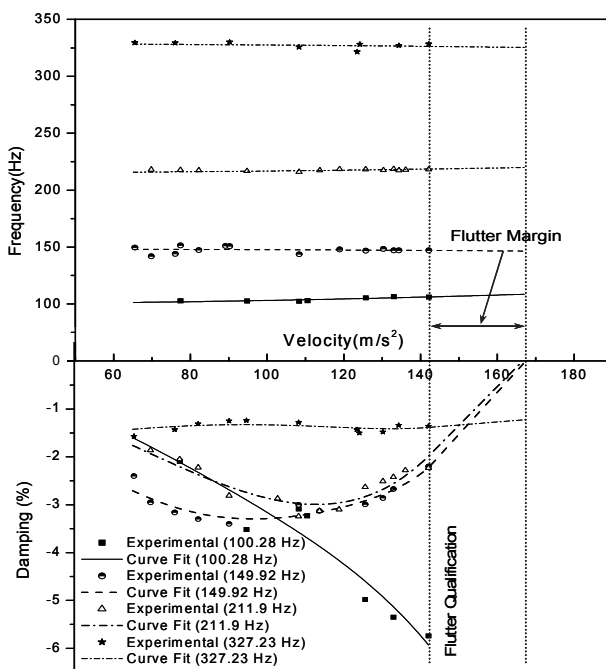


Fig. 12. Velocity vs. frequency and damping for critical modes

### 7. Acknowledgment

The authors wish to thank the contributors of this team work, namely Mrs. Shashikala Rajappa, Mr. D Sundararajan, Mr. S Janardhanam, Mrs. Annamma Samuel, Mr. Mutturaj H Medar and Mr. D Dwarakanathan, Scientists, Structural Technologies Division, National Aerospace Laboratories (NAL). Thanks are due to Mr. Ramachandra and his team, EAD, for their excellent fabrication work towards realizing the 10 percent aeroelastic model. We also would like to appreciate the Scientists of NTAf, NAL for their technical coordination and contribution. The fabrication of metallic parts from ESD, NAL has been duly acknowledged.

### 8. Nomenclature

- $L_m$  = Length of the model
- $L_p$  = Length of the full scale vehicle
- $q_m$  = Dynamic pressure in the tunnel
- $q_p$  = Flight dynamic pressure
- $V_m$  = Velocity of flow in the tunnel
- $V_p$  = Flight velocity
- $\rho_m$  = Density of air in the tunnel
- $\rho_p$  = Density of air at flight altitude
- $W_m$  = Weight of the model

- Subscripts:*
- m = model
  - p = proto
  - GVT = ground vibration testing
  - FS = Front spar
  - MS = Middle spar
  - RS = Rear spar
  - HTP = Horizontal tail plane
  - VTP = Vertical tail plane

- $W_p$  = Weight of the vehicle  
 $\Omega_m$  = Frequency of the model  
 $\Omega_p$  = Frequency of the vehicle  
 $\delta_m$  = Deflection on the model  
 $\delta_p$  = Deflection on the full scale vehicle  
 $EI$  = Bending rigidity  
 $EA$  = Axial stiffness  
 $D$  = Static divergence parameter  
 $\Delta\theta$  = Angular deflection of model-balance sting system  
 $q$  = Dynamic Pressure  
 $S$  = Reference area (Projected area of Fuselage, HTP and Elevator)  
 $C_{N\alpha}$  = Local slope of  $C_L$  vs  $\alpha$  plot at  $\alpha = 5^\circ$   
 $C_{M\alpha}$  = Local slope of  $C_M$  vs  $\alpha$  plot at  $\alpha = 5^\circ$   
 $C_{M0}$  = Intercept of the tangent to  $C_M$  vs  $\alpha$  plot  
 $C_{N0}$  = Intercept of the tangent to  $C_L$  vs  $\alpha$  plot  
 $l_N$  = Distance between front and rear attachment points  
 $l_R$  = Reference length of pitching moment coefficient  
 $x$  = Distance between  $C_p$  and centre balance attachment point  
 $\delta_{N1}$  = Deflection per unit normal force at front attachment point  
 $\delta_{N2}$  = Deflection per unit normal force at rear attachment point  
 $\alpha_0$  = Initial angle of attack of the model  
 $C_L$  = Lift coefficient  
 $C_M$  = Pitching moment coefficient  
 $\alpha$  = Angle of attack

## 9. References

- Upadhya, A. R. et al. (November 1985). Aeroelastic Testing of ASLV Models for Predicting Transonic Buffet Response- Wind Tunnel Testing and Data Analysis, *NAL PD-ST 8523*.
- Joshi A. et al. (December 1988). Aeroelastic Testing of PSLV Models, *NAL PD-ST 8833*.
- Rama Murthy, M. R. and Raja, S. (July 2002). Aeroelastic Testing on LCA Wing Model with R73E Missile, *NAL PD ST 0212*.
- Raja, S. et al. (May 2007). Transonic Buffet Response Study of gsLVM3 through Aeroelastic Model Testing : Wind Tunnel Testing and Data Analysis, *NAL PD-ST 0712*.
- Bisplinghoff, R. L., Ashley, H. & Halfman, R. L. (1983). *Aeroelasticity*, Addison - Wesley Publishing Company Inc.
- Queijo, M. J. (1968). Theory for computing span loads and stability derivatives due to sideslip, yawing, and rolling for wings in subsonic compressible flow, *NASA TN D-4929*.
- Sundara Murthy, H. (March 2005). A Method for Static Divergence Analysis of Sting - Mounted Wind Tunnel Models, *NAL PD NT 0508*.
- Megson, T. H. G. (2007). *An Introduction to Aircraft Structural Analysis*, Elsevier Pub.

# Wind Tunnel: A Tool to Test the Flight Response to Semiochemicals

Yooichi Kainoh  
*University of Tsukuba*  
Japan

## 1. Introduction

Semiochemicals mediate interactions between organisms (Law and Legnier, 1971), and the term is subdivided into two major groups, pheromones and allelochemicals, depending on whether the interactions are intraspecific or interspecific (Nordlund, 1981). Insect pheromones are the main research target for semiochemicals, because of potentials for practical use in agriculture. A wind tunnel is one olfactometer used as a bioassay method of olfactory stimuli. Wind tunnel tests have been widely used in insect pheromone research (e.g., Baker and Linn, 1984; Kainoh et al., 1984; Hiyori et al., 1986a,b), to study plant volatiles as kairomones (e.g., Kainoh et al., 1980) and to study synomones (e.g., Kainoh et al., 1999; Fukushima et al., 2001, 2002; Ichiki et al., 2008, 2011).

Sabelis and van de Baan (1983) used a Y-tube olfactometer and determined that predacious mites responded to the odors of plants infested with spider mites. This was the first demonstration of a tri-trophic interaction in which predators or parasitoids are attracted by plants infested with herbivore prey or hosts. Studies on the effects of volatile materials (Herbivore Induced Plant Volatiles, HIPVs) on the behaviors of natural enemies were conducted with olfactometers and wind tunnels as indicated by van Driesche and Bellows (1996).

## 2. Structure of wind tunnel

### 2.1 Laboratory conditions (temperature, humidity)

When a wind tunnel is set up it is necessary to consider what laboratory is suitable for the wind tunnel. If a laboratory has an exhaust fan on the wall, the downwind end of the tunnel can be connected to the fan (Fig. 1). However, air must be provided from a corridor through a louver on the door. In a closed laboratory, air must be recycled in a wind tunnel and a charcoal filter fixed at the upwind end (Fig. 2). A laboratory with a ventilation system is ideal for setting up a wind tunnel. The downwind end of the tunnel can be connected to the exhaust inlet (Fig. 3).

Temperature can be controlled by adjusting the air-conditioning system, but sometimes it is very difficult to change the temperature of a large system. We used to use an electric heater during the winter to increase the room temperature to 25°C.

For a humidifier, we fixed an electrode steam humidifier (resN200, presently CP3PRmini, PS Company Ltd., Tokyo, Japan) on the wall of the tunnel (Fig. 6) to maintain a humidity greater than 50-60% R.H., this humidifier is even used in midwinter when the outdoor temperature is below 0°C. Insects do not respond well below 50% R.H.

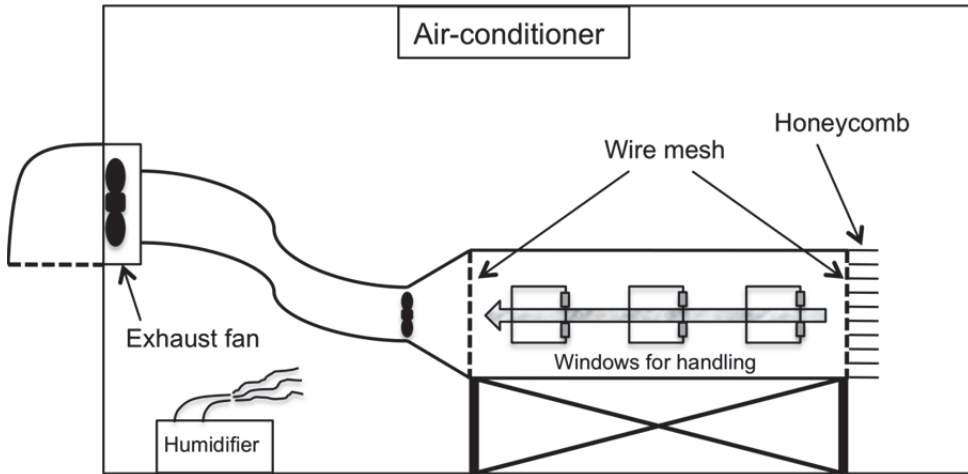


Fig. 1. Pulling-air type wind tunnel.

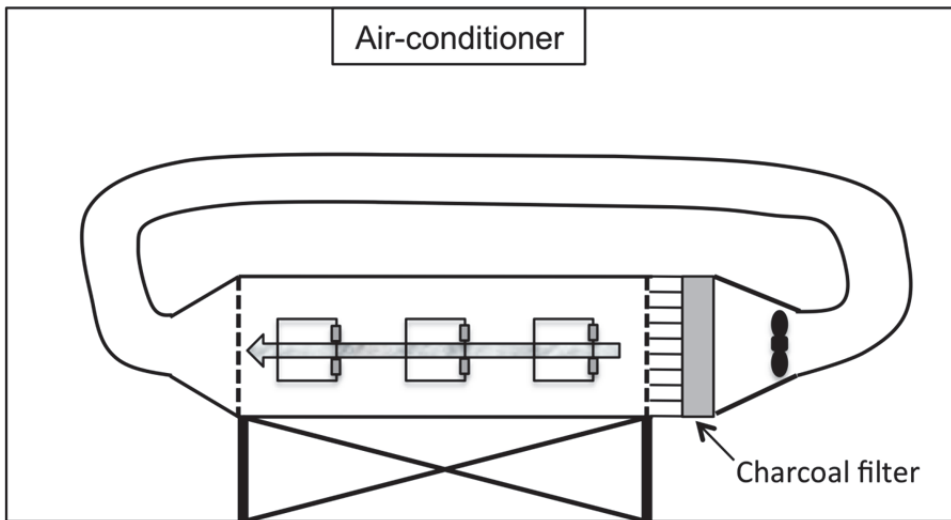


Fig. 2. Pushing-air type wind tunnel to recycle the air.



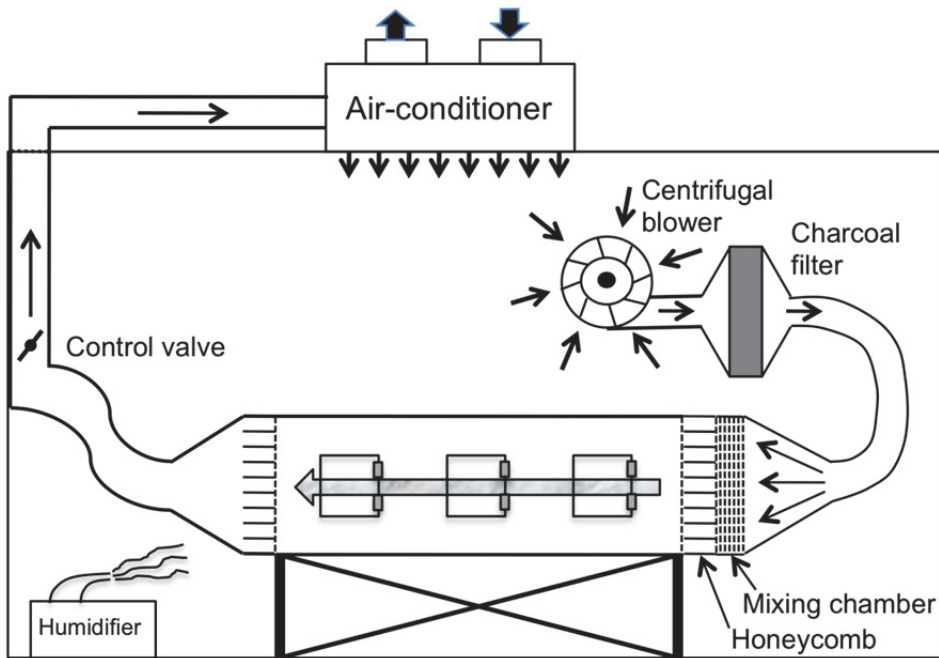


Fig. 3. Pushing- and pulling-air type wind tunnel.

## 2.2 Cylindrical or rectangular?

Two types of wind tunnels are used in entomological research: cylindrical and rectangular types. In our laboratory, we use a cylindrical tunnel for testing insect sex pheromones because the sex pheromone sample is hung from the ceiling of the tunnel, and a rectangular one to test responses of insect parasitoids to plant volatiles because the flat floor is convenient for placing potted plants. As Baker and Linn (1984) reported, there is no substantial difference between the two types of tunnels. From my point of view, an ideal air current can be produced with a cylindrical wind tunnel rather than a rectangular one because air currents are retarded at the corners of a rectangular tunnel. If insects fly into the corner of a tunnel, they may perceive lower concentrations of the odor coming from the upwind end.

## 2.3 Pulling-air and pushing-air type

One type of tunnel is the pulling-air type (Fig. 1), and another is the pushing-air type (Fig. 2, 3). As Baker and Linn (1984) pointed out, pushing-air type tunnels do not disturb the plume. Opening the window for insect handling does not disturb the air stream in the pushing-air type tunnel (Fig. 2, 3). Therefore, insects on the releasing platform can directly perceive the odor immediately after being released without any disturbance in the air stream. In our experiments, a laminar air stream of incense smoke can be observed even with the windows open. In the case of the pulling-air type wind tunnel (Fig. 1), insects on the releasing platform perceive disturbed air movement when released, but the air current gradually becomes normal after the window is closed. In addition, air should not leak from the tunnel wall and all windows must be tightly closed.

One disadvantage of a pushing-air type wind tunnel is a lack of even laminar flow inside the tunnel (Fig. 3). When an incense smoke plume is observed, the flow is laminar in the central part but not the peripheral part. Care must be taken to maintain a balance of wind pressure in both the pushing-fan side and exhaust-fan side. A stable laminar flow can not be achieved unless there is a good balance in both the inlet and outlet of the tunnel.

From my experience, especially in a pulling-air type wind tunnel, an outdoor hood should be used as the exhaust fan, so strong outdoor winds do not disturb the smooth air flow. The hood in Fig. 4 works very well and the wind speed is not disturbed on windy days.

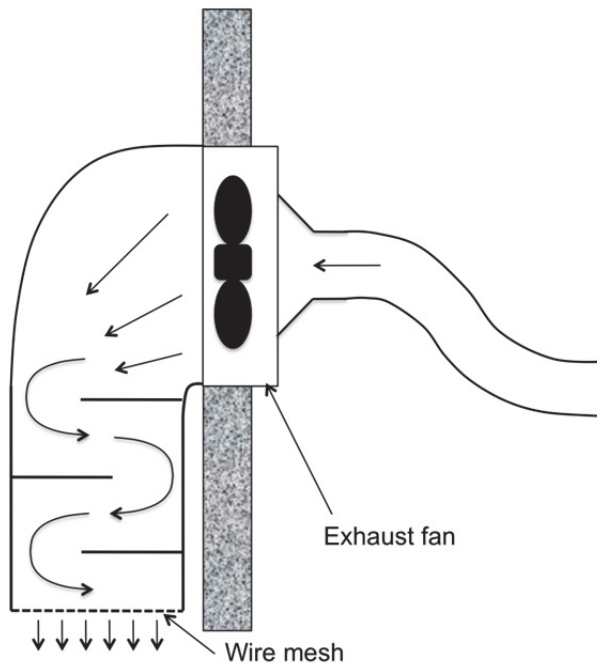


Fig. 4. Outdoor hood for exhaust fan to minimize influence of outdoor wind.

#### 2.4 Air movement (wind speed)

Wind speed is an important factor in wind tunnel experiments. Most studies in the literature use a wind speed of 25 to 30 cm/sec. Kainoh et al. (1984) performed wind tunnel experiments to test the sex pheromone of *Adoxophyes honmai* (Lepidoptera: Tortricidae) and compared the wind speed between 30 and 60 cm/sec. There was no significant difference in male moth responses in the 4-component sex pheromone system. However, the flight behavior of male moths, *A. honmai*, seemed to be more stable at a lower wind speed, so we now use 25 to 30 cm/sec.

To measure the wind speed in the tunnel, we inserted an anemometer (ISA-90; probe: P-2, SIBATA Scientific Technology Ltd., Saitama, Japan) with the probe extended to 25 cm in the upper wall of the tunnel (Fig. 5).



Fig. 5. Downwind end of the tunnel. 1: anemometer; 2: VTR camera; 3: thermometer and hygrometer; 4: platform to release insects.

### 2.5 Charcoal filter

When we first built a wind tunnel in 1996, no charcoal filter was attached to the wind tunnel (Fig. 1). Our biggest concern was the bad smell from next door, a rearing room for mice and rats. We sealed the door between the two rooms, but the smell remained. A new wind tunnel (Fig. 3) was installed with a charcoal filter (Fig. 6, left) between the centrifugal blower (Fig. 6, right) and the wind tunnel. The filter consists of 6 charcoal filter panels installed in a zigzag pattern, each panel (30×50 cm, 3 cm thick) is filled with charcoal particles. Total area of the filter panels is 9,000 cm<sup>2</sup>.



Fig. 6. Centrifugal blower (right), charcoal filter housing (left) and humidifier (center).

## 2.6 Honey comb structure (or mesh)

Turbulence in the airstream must be controlled for insect flight in a wind tunnel. A honeycomb structure fixed at the upwind end can facilitate laminar flow of the air (Figs. 1, 2, 3). If the honeycomb structure is expensive, a plastic pipe (3-5 cm in diameter) can be cut into lengths of 10 to 15 cm and tightly attach with glue to produce a structure to create laminar flow. Baker and Linn (1984) proposed a 'mixing chamber' at the tunnel opening to dampen the turbulence created by the fan blades and to balance wind velocities inside the tunnel. This mixing chamber consists of several layers of narrow-mesh cloth, screen or both. We do not use the mixing chamber in our wind tunnel but this idea is worth adopting.

We do not fix a structure at the downwind end of the tunnel to produce a laminar air flow, but Prof. K. Nakamuta (personal communication) commented that we should fix the honeycomb structure at the downwind end of the tunnel when air is pulled from the downwind end.

## 2.7 Light source

In wind tunnel tests with sex pheromones of nocturnal moths, light intensity is a significant parameter. We used *A. honmai* sex pheromones to attract male moths and varied the light intensity. In total darkness, there was no attraction of the moths, but at 0.03, 0.13, 0.77 lx attraction was 50 to 60% of the moths released. In a lighter condition at 3.5 lx the attraction was 38% and male catches were not stable (Kainoh et al., 1984). With this wind tunnel system, we tested the effect of sex pheromone disruptants on the attraction of male *A. honmai* moths and found that only the 2<sup>nd</sup> major compound (Z)-11-tetradeceny acetate has a disruptive effect on male moth flight, whereas the 1<sup>st</sup> major compound (Z)-9-tetradeceny acetate and other minor compounds have no affect (Hiyori et al., 1986a,b).

For diurnal insects, we established wind tunnel experiments for *Aphidius colemani* in our laboratory and used a light intensity of 150 lx, because female *A. colemani* did not show good orientation toward the odor source (herbivore damaged plant) under lighter conditions and flew upward to the ceiling of the tunnel at 2,000 lx (Fujinuma et al., unpublished). However, the tachinid fly *Exorista japonica* readily flew to the target plant under full light conditions (>2,000 lx) (Kainoh et al., 1999; Ichiki et al., 2008, 2011; Hanyu et al., 2009).

As a light source, we use Vitalite® (40W, 6 tubes) to maintain light conditions similar to sunlight, and the light intensity can be changed with a voltage converter from 0 to 6,000 lx. Under the Vitalite® or on a ceiling panel, a plastic light defuser was placed to scatter the light throughout the chamber.

## 2.8 Visual ground patterns

Flying nocturnal moths watch ground patterns when orientating to female sex pheromones as demonstrated by a moving-floor wind tunnel (Cardé and Hagaman, 1979). Using this type of moving-floor wind tunnel, the flight speed of the moth can be controlled and sustained flight experiments performed. Optomotor anemotaxis is the term used to explain the behavior of male moths orientating to female moths, in which they visually monitor their progress and react to this feedback (Bell et al., 1995). There are several ways to show moving patterns to insects (Baker and Linn, 1984). In our laboratory, we did not add a movable floor pattern to the wind tunnel because the system is too costly. Instead, we place green and ochre color strips (15 cm wide) to represent the soil and plants (Fig. 5). We have not yet compared the flight activity of insects with different colors or widths of the strips, but plan to evaluate these visual effects in the future.

## 2.9 Data recording

The software 'The Observer (ver. 5)' (Noldus Information Technology, Wageningen, The Netherlands) (Fig. 7) is used to record the behavior of insects in a wind tunnel (Hanyu et al., 2009). We can record each behavioral event (walking, flying, stationary or grooming) and location (release site, floor, wall, ceiling, target), and then calculate the duration, average time on the release site (latency), total time flying in the wind tunnel, total time walking on the floor, wall or ceiling and other parameters from these recordings (Fig. 8). We use a video camera (Fig. 9, Ultra Micro Color Camera, CC431+UN43H, ELMO, Japan) to record the flight of insects. The camera is placed at the downwind end, so we can record all behavioral events from the releasing site to the target. Recordings of tachinid fly (*Exorista japonica*) behavior were easily obtained, but the resolution of the camera was not high enough to see small insects, e.g., the braconid wasp *Cotesia kariyai* (Fukushima et al., 2001, 2002; Hou et al., 2005; Mandour et al., 2011) and aphid parasitoids (Takemoto et al., 2009; Fujinuma et al., 2010). To record the behavior of small insects, two cameras must be set in the tunnel, one near the releasing site and another near the target site.



Fig. 7. Laptop computer with the behavioral software 'The Observer' installed.

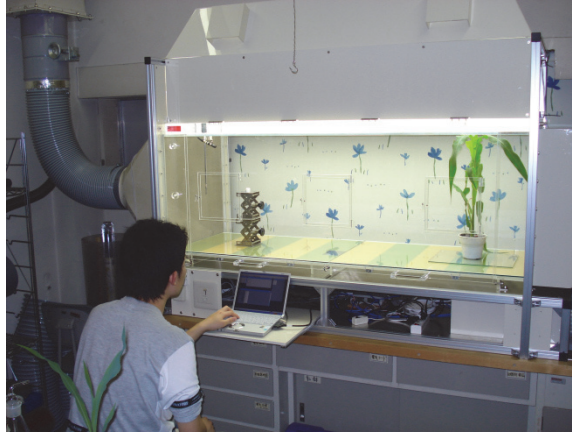


Fig. 8. An observer recording the behavior of the tachinid fly *Exorista japonica*.



Fig. 9. Microcamera fixed on the ceiling of the tunnel at the downwind end.

### 3. Conclusion

To design a wind tunnel, first choose a pushing-air or pulling-air type tunnel. A pushing-air type is usually recommended, but pulling-air type can work in some situations. A cylindrical tunnel has the ideal air flow, but a rectangular tunnel is useful for arranging potted plants on the floor. Wind speed is best regulated at 25 to 30 cm/sec with a voltage converter or a valve. A charcoal filter is recommended to clean the air before it enters the tunnel inlet. Light intensity can be changed with a voltage converter to maximize the insect flight conditions. Laminar air flow is not always necessary, but can be achieved by inserting a honeycomb structure at the inlet of the tunnel or mixing chamber of screen or mesh. Visual patterns inside the tunnel are not always critical but may sometimes affect insect flight. To record the behavioral events or state of the insect, 'The Observer' or other event recorder software is necessary. Trial-error tests are essential for initially setting up wind tunnel experiments that are optimal for the laboratory conditions and insect species.

#### 4. Acknowledgements

The author expresses his sincere thanks to Prof. Kiyoshi Nakamuta of Chiba University for giving valuable comments on the wind tunnel, and to Prof. DeMar Taylor of the University of Tsukuba for reviewing the manuscript.

#### 5. References

- Baker, T.C., and Linn, C.E., Jr. (1984) Wind tunnels in pheromone research, pp. 45-73, in H.E. Hummel and T.A. Miller (eds.). *Techniques in Pheromone Research*. Springer, New York.
- Bell, W. J., Kipp, L. R., and Collins, R. D. (1995) The role of chemo-orientation in search behavior, pp.105-152, in R. T. Cardé, and W. J. Bell (eds.). *Chemical Ecology of Insects 2*. Chapman & Hall, New York.
- Cardé, R. T. and Hagaman, T. E. (1979) Behavioral responses of the gypsy moth in a wind-tunnel to air-borne enantiomers of disparlure. *Environmental Entomology*, 8: 475-484.
- Fujinuma, M., Y. Kainoh and H. Nemoto (2010) *Borago officinalis* attracts the aphid parasitoid *Aphidius colemani* (Hymenoptera: Braconidae). *Appl. Entomol. Zool.* 45:615-620.
- Fukushima, J., Y. Kainoh, H. Honda and J. Takabayashi (2001) Learning of host-infested plant volatiles in the larval parasitoid *Cotesia kariyai*. *Entomol. Exp. Appl.* 99:341-346.
- Fukushima, J., Y. Kainoh, H. Honda and J. Takabayashi (2002) Learning of herbivore-induced and nonspecific plant volatiles by a parasitoid, *Cotesia kariyai*. *J. Chem. Ecol.* 28:579-586.
- Hanyu, K., R. T. Ichiki, S. Nakamura and Y. Kainoh (2009) Duration and location of attraction to herbivore-damaged plants in the tachinid parasitoid *Exorista japonica*. *Appl. Entomol. Zool.* 44: 371-378.
- Hiyori, T., Y. Kainoh and Y. Ninomiya (1986a) Wind tunnel tests on the disruption of pheromonal orientation of the male smaller tea tortrix moth, *Adoxophyes* sp. (Lepidoptera: Tortricidae). I. Disruptive effect of sex pheromone components. *Appl. Entomol. Zool.* 21:153-158.
- Hiyori, T., Y. Kainoh and Y. Ninomiya (1986b) Wind tunnel tests for studying the disruption of pheromonal orientation of the male smaller tea tortrix moth, *Adoxophyes* sp. (Lepidoptera: Tortricidae). II. (Z)-11-Tetradecenyl acetate as a potent disruptant and the effect of pre-exposure. *Appl. Entomol. Zool.* 21:349-350.
- Hou, M., J. Takabayashi and Y. Kainoh (2005) Effect of leaf age on flight response of a parasitic wasp *Cotesia kariyai* (Hymenoptera: Braconidae) to a plant-herbivore complex. *Appl. Entomol. Zool.* 40:113-117.
- Ichiki, R. T., Y. Kainoh, S. Kugimiya, J. Takabayashi and S. Nakamura (2008) Attraction to herbivore-induced plant volatiles by the host-foraging parasitoid fly *Exorista japonica*. *J. Chem. Ecol.* 34: 614-621.
- Ichiki, R., Y. Kainoh, Y. Yamawaki, and S. Nakamura (2011) The parasitoid fly *Exorista japonica* uses visual and olfactory cues to locate herbivore-infested plants. *Entomol. Exp. Appl.* 138:175-183.
- Law, J. H. and F. E. Regnier (1971) Pheromones. *Ann. Rev. Biochem.* 40:533-548.
- Kainoh, Y., K. Shimizu, S. Maru and Y. Tamaki (1980) Host-finding behavior of the rice bug, *Leptocoris chinensis* Dallas (Hemiptera: Coreidae) with special reference to diel patterns of aggregation and feeding on rice plant. *Appl. Entomol. Zool.* 15:225-233.

- Kainoh, Y., T. Hiyori and Y. Ninomiya (1984) Conditions for wind tunnel tests in studying pheromonal communication in the smaller tea tortrix moth, *Adoxophyes* sp. (Lepidoptera: Tortricidae). *Appl. Entomol. Zool.* 19:526-528.
- Kainoh, Y., C. Tanaka and S. Nakamura (1999) Odor from herbivore-damaged plant attracts a parasitoid fly, *Exorista japonica* Townsend (Diptera: Tachinidae). *Appl. Entomol. Zool.* 34:463-467.
- Mandour, N. S., Y. Kainoh, R. Ozawa, M. Uefune, and J. Takabayashi (2011) Effects of time after last herbivory on the attraction of corn plants infested with common armyworms to a parasitic wasp *Cotesia kariyai*. *J. Chem. Ecol.* 37:267-272.
- Nordlund, D. A. (1981) Semiochemicals: a review of the terminology, pp.13-28, in D. A. Nordlund, R. L. Jones and W. J. Lewis (eds.). *Semiochemicals - Their Role in Pest Control*. John Wiley & Sons, New York.
- Sabelis, M. W., Van de Baan, H. E. (1983) Location of distant spider mite colonies phytoseiid predators: Demonstration of specific kairomones emitted by *Tetranychus urticae* and *Panonychus ulmi*. *Ent. Exp. Appl.* 33: 303-314.
- Takemoto, H., W. Powell, J. Pickett, Y. Kainoh and J. Takabayashi (2009) Learning is involved in the response of parasitic wasps *Aphidius ervi* (Haliday) (Hymenoptera: Braconidae) to volatiles from a broad bean plant, *Vicia faba* (Fabaceae), infested by aphids *Acyrtosiphon pisum* (Harris) (Homoptera: Aphididae). *Appl. Entomol. Zool.* 44: 23-28.
- Van Driesche, R. G. and Bellows, T. S., Jr. (1996) *Biological Control*, Chapman & Hall, New York, pp.539



# Flow Visualization in Wind Tunnels

Muzafferuddin Mahmood  
*King Fahd University of Petroleum & Minerals*  
*Kingdom of Saudi Arabia*

## 1. Introduction

Flow visualization is an experimental means of examining the flow patterns around a body or over its surface. The flow is “visualized” by introducing dye, smoke or pigment into the flow in the area under investigation. The primary advantage of such a method is its ability to provide a description of the flow over a model without a complicated data reduction and analysis. Smoke- flow visualization (described by Bradshaw, 1970 and Rae and Pope 1984) involves the injection of streams of vapor into the flow. The vapor follows filament lines (lines made up of all the fluid particles passing through the injection points) in steady flow the filament lines are identical to stream lines. (Lines everywhere tangent to the velocity vector). Smoke- flow visualization thus reveals the entire flow pattern around a body.

It is difficult to exaggerate the value of flow visualization. The ability to see flow pattern on a model often gives insight into a *solution to an aerodynamic problem*. Flow visualization can be divided into two broad categories the first is surface flow visualization when the visualization media is applied to the surface such as tufts and oil flow etc. The second type is off surface such as smoke and streams.

There are basically four methods of recording the flow visualization test. The first and the best but the least permanent method is for the scientist and the engineer to observe with his eyes. Because of the depth perception one can see a three dimensional picture. The other three common methods of recording the result of flow visualization are by film, either still or movie or television camera or video and magnetic tapes. It must be realized that all three of these methods are using a two dimensional medium to often record a three dimensional phenomena. This is especially fine when using a smoke or helium bubbles to trace flow stream lines pass the model. All three of these methods can be used either black and white or color. The photography methods while recording more time for developing and printing stills, when compared to video, yield higher resolution.

## 2. Flow visualization techniques

The present chapter will deal with the visualization of flow past different types of models like flat plates, delta wings, elliptical cones and rectangular bluff bodies using

- smoke wire technique
- laser light illumination technique
- surface flow visualization techniques

The results obtained are being discussed considering the importance of different techniques.

## 2.1 Flow visualization using smoke wire technique

Flow visualization is considered an important tool to understand the nature of flow field. Its proper utilization will provide reasonable information that will help in influencing the flow characteristics. This will eventually lead to better design modification leading to development of favorable pressures.

The visualization of the flow past the building models was made possible by using the above technique originally developed by Raspet and Moore in early 1950's and subsequently improved and used by Batill and Mueller [1 ], and was further improved by Stahl and Mahmood [2 ]. The procedure involves brushing a thin wire, which then forms a large number of small droplets. Heating the wire evaporates the oil with each droplet providing a fine streak-line in the flow. Under proper illumination the smoke streaks appear bright which can be observed and photographed. This technique basically requires a fine wire of about 0.1mm in diameter of Nickel Chromium steel and suitable oil, which can vaporize quickly, and a DC current to heat the wire.. This technique was utilized, as it is very useful in studying separation especially in smooth and nominal boundary turbulent flows. The smoke-wire was placed at the upstream side of the building model to see the separating bubble from frontal edge and ground vortices at normal incidence, for both sharp and round edge model. For oblique incidences of 25° and 45° the smoke-wire was placed at a suitable position to note the separation of shear layer in the immediate vicinity of the leading edge corner where high suction pressures are developing. This technique provided a clear influence of rounding of roof edges on the separating shear layers that formed conical vortices. The influence due to change in the angle of incidence on the separation process for sharp and round edge models was found to be of interest. The smoke-wire could also be moved around the model to get useful information about the flow field.

### 2.1.1 Flow visualization in smooth flows, $\alpha = 90^\circ$

The results from smoke wire technique for an angle of incidence of 90° for smooth flows are shown in Figure 1. These indicate that for a sharp edge model the flow incident on the front surface of the model divides into two parts. Part of the flow goes up and separates from the front edge with a large bubble and a re-circulation closer to leading edge, and the rest of the flow descends down and forms a vortex near the ground. In the model with a rounded edge, the flow does not have a sharp separation but a long bubble with a height smaller than that noted for the sharp edge model emerges. The balance flow goes down forming a vortex close to the ground in a way similar to that noted in the case of the sharp edge model. The difference between smooth flow and turbulent flow is visible in the separation of flow from the frontal edge. The height of the separation bubble is comparatively smaller in turbulent flow than the smooth flow.

### 2.1.2 Flow visualization in smooth flow at $\alpha = 45^\circ, 25^\circ$

As the region near the leading edge corner is considered critical since maximum mean and peak suction pressures were recorded at hole # 50205(Texas tech University test building nomenclature), smoke wire technique was utilized to observe the flow past this region. Batill and Mueller [1] studied the transition in the flow on an airfoil using this technique. This technique was also successfully applied in studying the separation of flow past flat plates at various angles by Mahmood [2]. At incidence of  $\alpha = 45^\circ$  the smoke streaks incident on the side wall at a distance of about 15 to 20% of the length of the wall goes up and separates to

from large separation bubble (bump) on the top surface of a sharp edge model as evident in Figure 1c. The remaining flow moved down resulting in re-circulation of flow, which persisted all along the length of wall. But as the rounding is increased, the size of the bump became smaller indicating the influence of rounding at a specific location. A bump smaller in size was noted for a round model with radius of 5mm. For a model with a radius of 10 mm, the smoke streaks remain almost attached to the roof and just slide over curved roof surface with a minimum possible separation, as shown in Figure 1d. Similar changes were noted for the flow at an angle of incidence of  $25^\circ$ . For this incidence angle the sharp edge model shows more separation and the height of separation of the vortex sheets decreased with increased rounding as evident in Figure 2.

For a sharp edge model a clear separation was visible at station 1 i.e., around 15 to 20% of the distance from leading edge corner, as shown in Figure 2a. But when round edge models were placed the height of separation reduced in proportion to the magnitude of rounding, especially for  $R=10$  mm model, where the flow remained attached while moving from sidewall to the top surface, as shown in Figure 2c. This is in line with the observations made in smooth flow condition and is expected to influence the pressures that are developed on top surface of the model.

Since the influence of rounding was visible on both flows at oblique and normal incidence, its influence on the pressure characteristics was investigated and compared in both the cases.

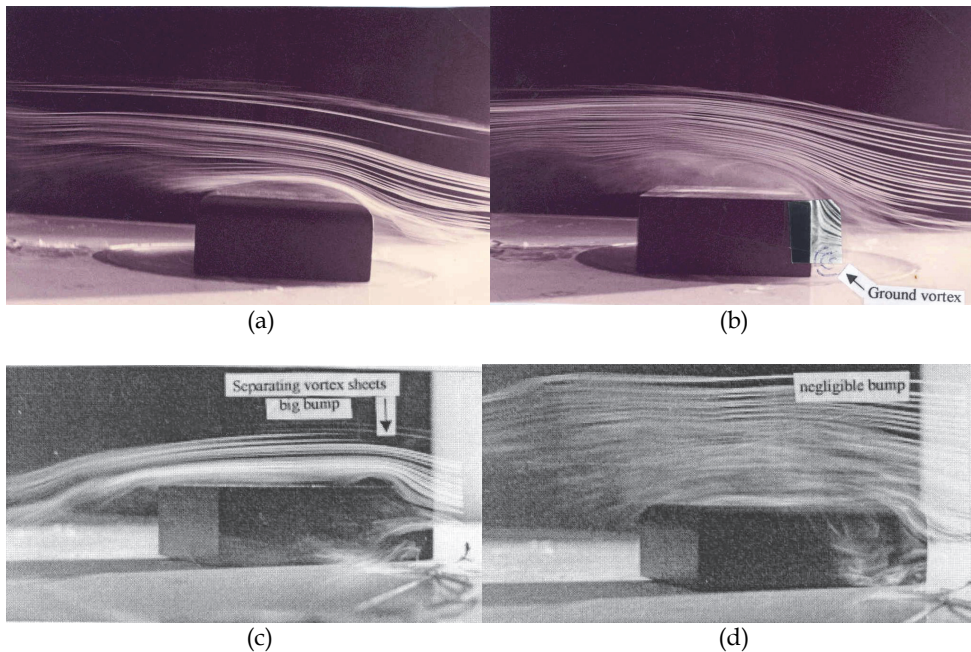
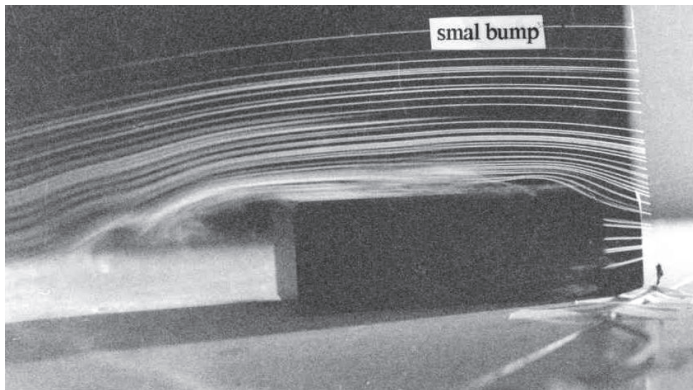


Fig. 1. Flow visualization using smoke-wire technique (smooth flow condition). View from front.

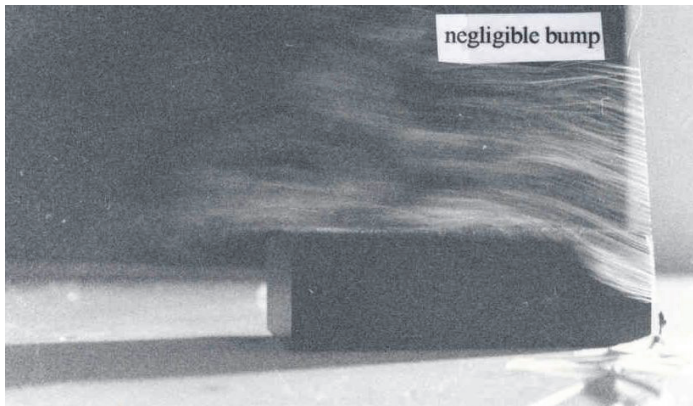
- a. Sharp edge model  $\alpha = 90^\circ$
- b. Round edge model  $R = 10$  mm,  $\alpha = 90^\circ$
- c. Sharp edge model  $\alpha = 45^\circ$
- d. Round edge model  $R = 10$  mm,  $\alpha = 45^\circ$



(a) Sharp edge model.



(b) Round edge model,  $R = 5.0$  mm.



(c) Round edge model,  $R = 10.0$  mm.

Fig. 2. Flow visualization using smoke-wire technique,  $\alpha = 25^\circ$  (smooth flow condition). View from front.

### 3. Flow visualization using laser light illumination technique

A smoke-probe was utilized to generate heavy smoke upstream side, which then passes over the model. A section of the flow was then made visible by using a laser-light sheet. This plane is generated by using a laser light source in conjunction with a lens system. This technique helped to study the flow on the top of the model. The near roof edge regions are considered important from pressure point of view, as corner vortices are said to exist there, which is a cause for severe suction. The presence of corner vortices and the changes that take place in them when edges are rounded could also be studied. Still pictures at different stations were obtained by moving the laser light plane. This technique was used for all the flow conditions. A video recording of the flow was done and when played at slow rate provided useful details of the flow over the roof and could provide further information about the flow phenomenon.

#### 3.1 Flow visualization past building model in smooth flow at $\alpha=45^\circ$

The flow was visualized at two stations on the model top surface. Figures 3a and 3b show the section of the flow near the leading edge corner at station 1 (15-20% of the distance of the leading edge), whereas Figures 3c and 3d show the section of flow at station 2, which was at about 50% of the distance. Figures 3a and 3c show that there exist concentrated vortices springing from both the leading edges at station 1 and 2, respectively in the case of sharp edge models. A similar observation was also reported by Bienkiewicz and Sun [3] on a sharp edge cubical model when surface flow visualization was carried out in a turbulent boundary layer flow. Figure 3b shows some separation and rolling at station 1 for a round edge model with edge radius  $R=5$  mm with a small vortex formation, where as at station 2 a big size vortex formed as, shown in Figure 3d. This had a diffused or burst nature, and could be observed during flow visualization. For model with a further rounded edge of  $R=10$  mm, no separation was noted at station 1 where as proceeding towards the model end to station 2, formation of a vortex was noted which can be seen in Figure 3d. This had a loose core and a burst nature. A similar vortex with a loose core is usually observed for slender sharp edge delta wings at high incidence [4].

#### 3.2 Flow visualization past elliptical cones and delta wings

As it was reported in the literature that the symmetry of vortex formation and the degree of asymmetry on elliptical cones is influenced by the thickness of the ellipses [5] and the theoretical predictions about the degree of asymmetry was also made. In order to study this phenomenon different elliptical cones whose base height to width ratio varied between 20% to 80% were taken. The model was placed in the wind tunnel using a suitable fixture. Smoke was generated upstream side of the model using a smoke probe. The laser light sheet illumination technique was then used to find flow characteristics. Fig 4 shows the vortices formation for 65% thick elliptical cone. The degree of asymmetry could be found when the plain of observation is bit normal to the axis of the cone. Similar results were reported on circular cones. Where it was possible to observe an asymmetric flow changing to almost symmetric one when a fin was fixed on the cone [6].

Experiments were conducted to study the asymmetry of vortex formation on a sharp edged delta wing of Aspect ratio  $A=0.56$  in Ref [7]. It was observed that up to certain angle of attack symmetric vortex formation takes place as can be seen from Fig.5. These vortices

looked quite concentrated sitting on the wing. When the incidence angle was increased one vortex got burst and further increase in incidence angle resulted in bursting of both the vortices. The bursting of one of the vortices can be seen in Fig.6 and no vortex asymmetry was observed for this type of configuration. A study by Terry,N et al [8] shows extensive use of laser light illumination technique in visualizing the flow past an  $80^\circ$ Delta wing

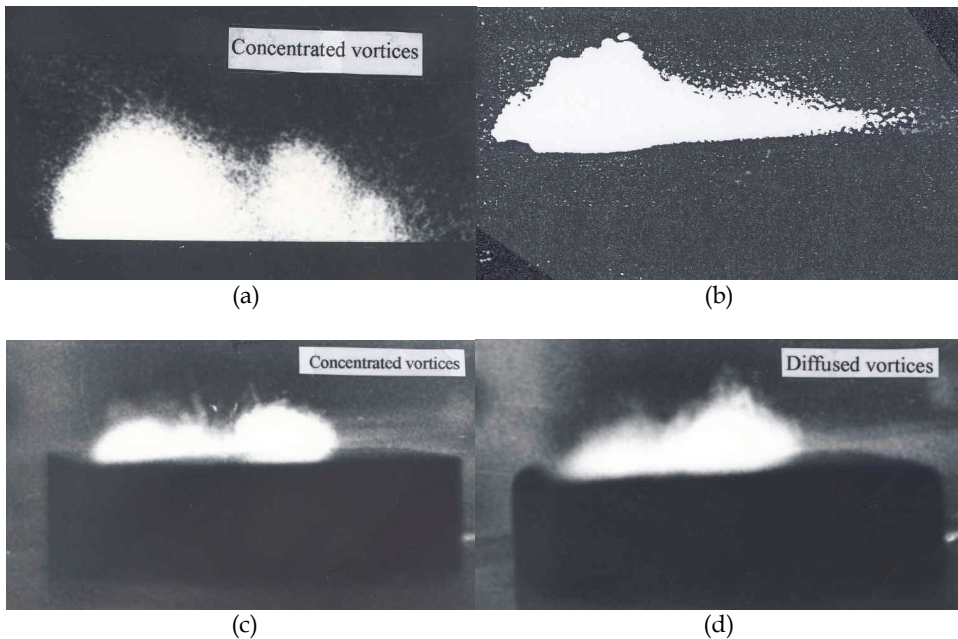
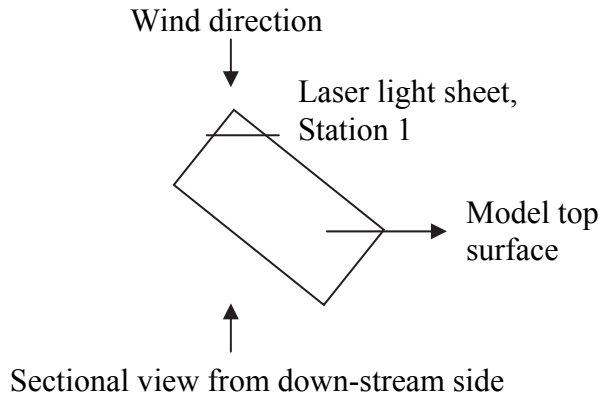


Fig. 3. Flow visualization (top surface) using laser light sheet illumination technique  $\alpha = 45^\circ$ . (a) Sharp edge model, (b) round edge model,  $R = 10.0$  mm station 1 (15% of length), (c) sharp edge model, (d) round edge model,  $R = 10.0$  mm station 2 (50% of length).



Fig. 4. Vortex formation behind elliptical cone thickness ratio=0.65, Reynolds number =132,000

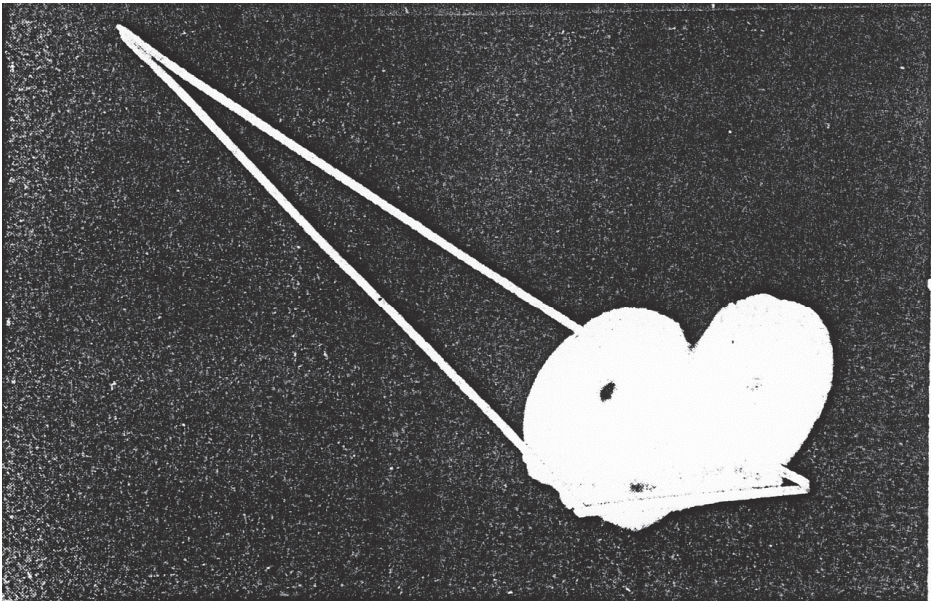


Fig. 5. Vortex formation behind Delta wing Aspect ratio=0.56, Reynolds number =132,000,  $\alpha = 30^\circ$

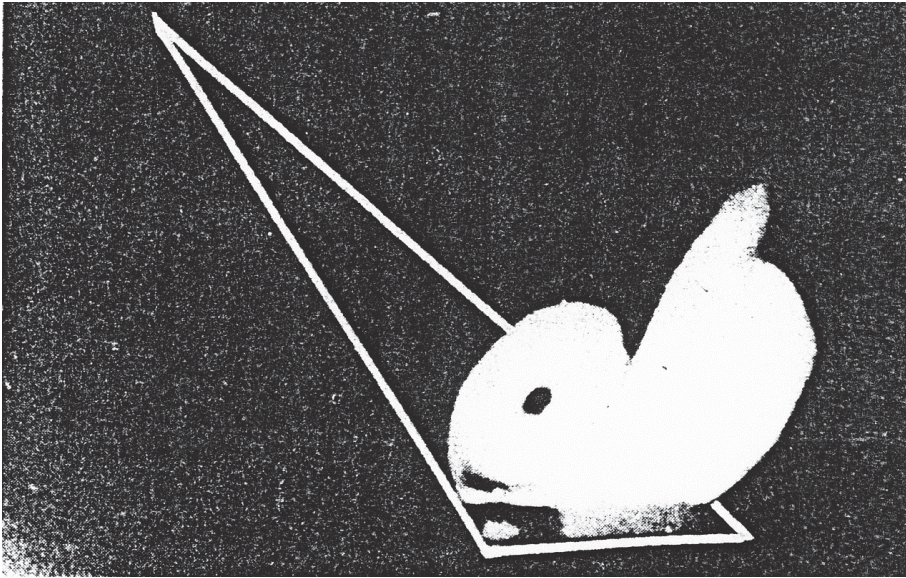


Fig. 6. Vortex formation behind Delta wing Aspect ratio=0.56, Reynolds number =132,000  $\alpha = 35^\circ$

#### 4. Surface flow visualization technique

The study of the flow near the surface of the square plate model was carried out by using the chalk powder suspended in Kerosene oil and sprayed on the model. Figure 7 shows the setup for surface flow visualization. When the flow passes the model the chalk and Kerosene mixture settles as per flow lines. The pattern of flow obtained revealed direction of surface streamlines and features like the separation of flow from the surface. The flow visualization experiments carried out by using different methods like smoke wire technique, smoke probe, surface flow etc., can be divided into two groups as one with  $\alpha \leq 28^\circ$  and another with  $\alpha \geq 32^\circ$  as the incidence angle of around  $30^\circ$  is considered critical where a sudden drop in normal force occurs.

##### 4.1 $\alpha \leq 28^\circ$

Here the investigations are limited to angles of  $\alpha = 26.5^\circ$  and  $\alpha = 28^\circ$ . The flow is essentially divided into two parts, namely the wing center flow which is accompanied by separation and the wing tip flow Fig 8. In the latter case the flow is separating from side edges which form vortex sheets which curl up over the wing into the side edge vortices. The results from various flow visualization studies are shown in Figures 12-13, Here, for the above mentioned angles  $\alpha \leq 28^\circ$ , the three dimensional separation bubble covers the central part of the plate and the flow is rotating inside the bubble, moving on the plate surface forward and outward, and frequently being drawn towards wing side edges. As a result of this induced transverse flows, considerable masses of air are involved in vortex motion along the side edges on the suction side as evident from Figs 8-9. Since the bubble is closing at a distance of about  $0.1 C$  from trailing edge, some of the flow is observed as moving forward at this junction from movie film taken using a movie camera.



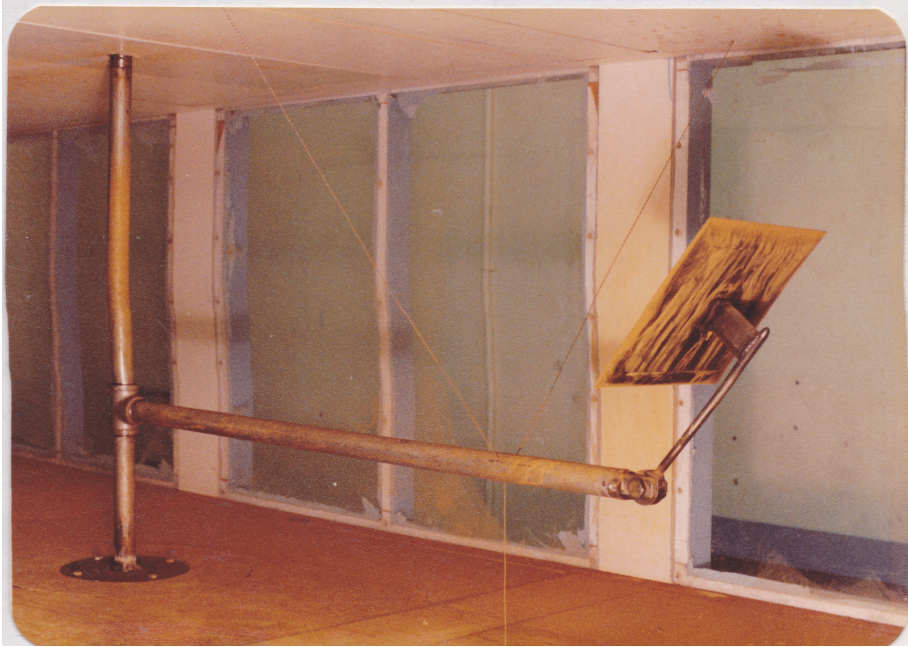


Fig. 7. Surface flow visualization setup

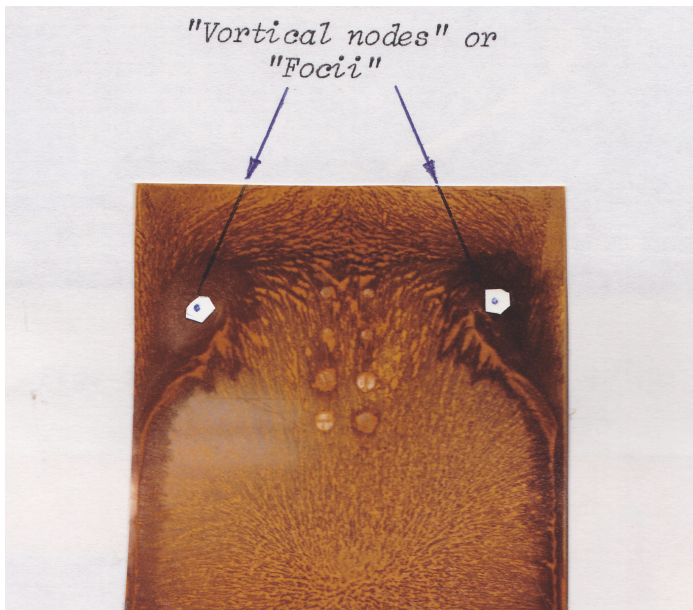


Fig. 8. Surface flow visualization on wake side of flat plate at  $\alpha = 28^\circ$

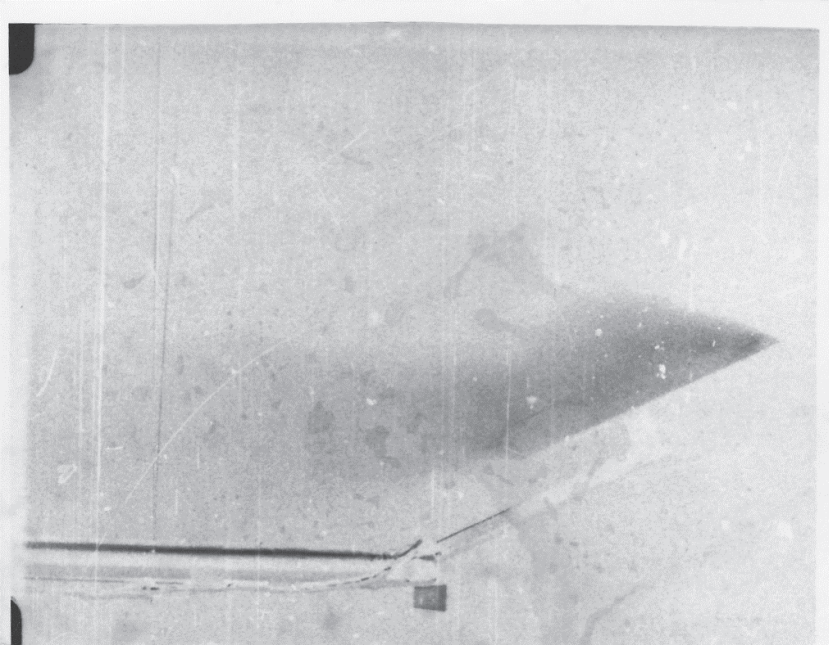


Fig. 9. Flow visualization inside of wake using smoke wire technique  $\alpha = 28^\circ$

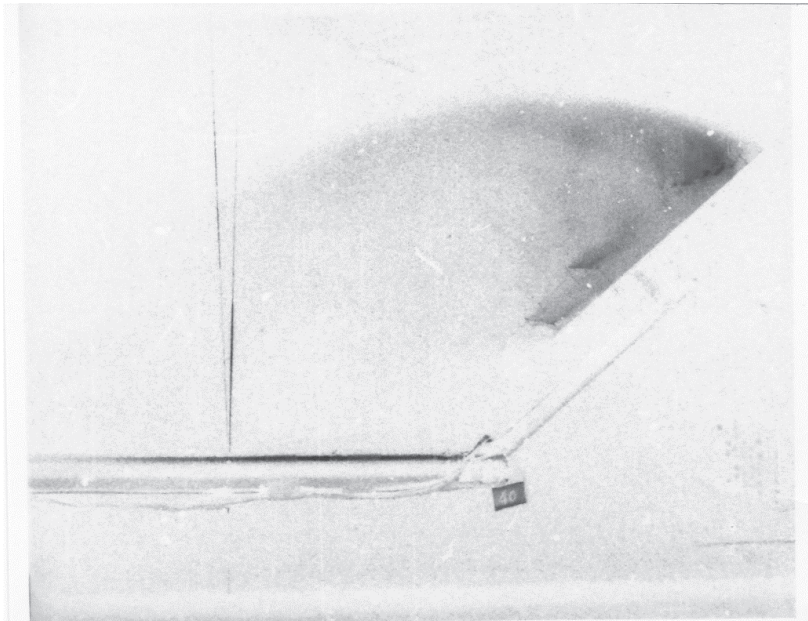


Fig. 10. Flow visualization inside of wake using smoke wire technique  $\alpha = 32^\circ$

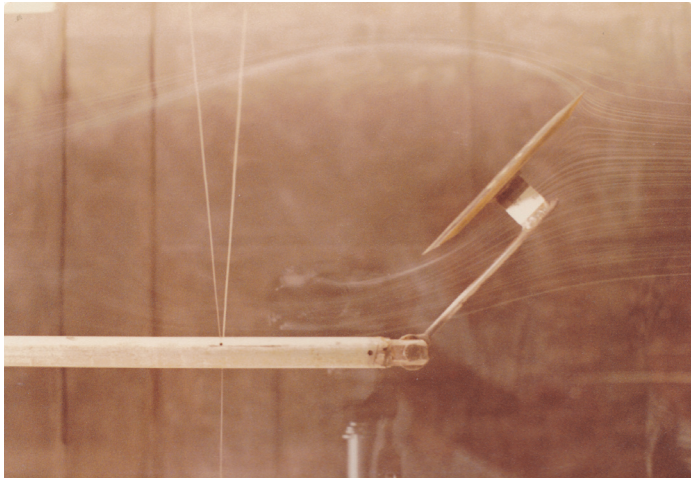


Fig. 11. Flow visualization using smoke wire technique  $\alpha = 40^\circ$

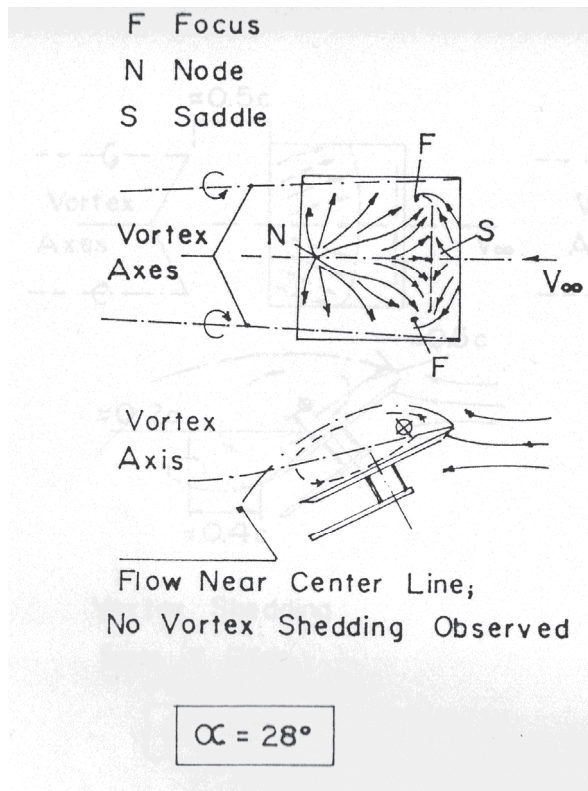


Fig. 12. Conjectured flow field on wake side of flat plate at sub critical incidence

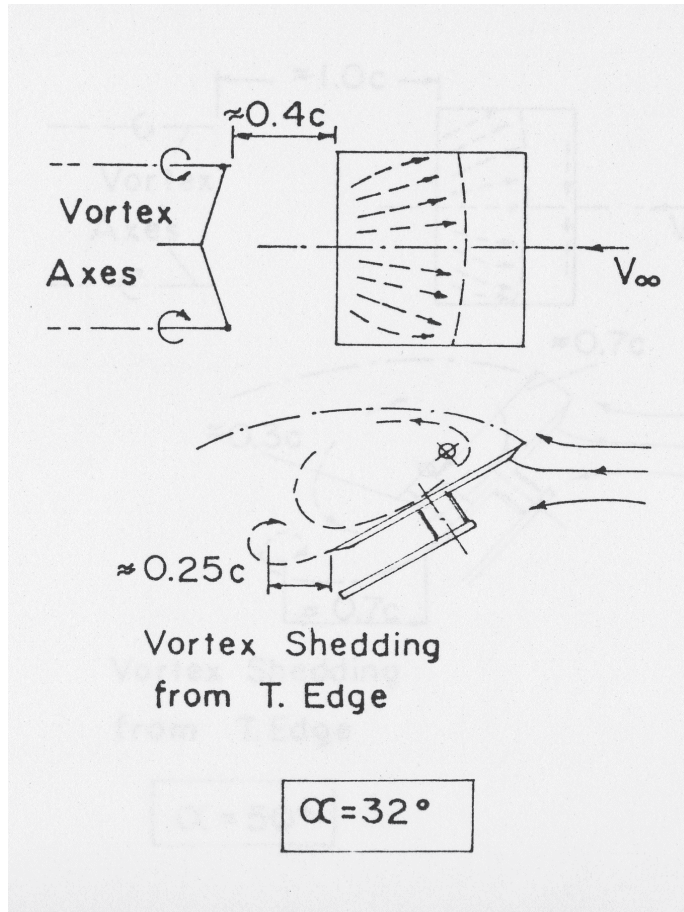


Fig. 13. Conjectured flow field on wake side of flat plate at super critical incidence

On the portion of the wing near the leading edge, on the suction side, heavy cross flows are induced which move to the side edges and bend into the stream direction. The axes of these side-edged vortices when traced reach the leading edge. The angle it makes is about half the angle of attack  $\alpha$  which the plate makes with the stream direction. The core of the three dimensional bubble is near to the leading edge at a distance of about  $0.25C$ . There was no trailing edge vortex shedding observed for these incidences. The side-edge vortices extend downstream at least six to seven times chord. The diameter of these side edges vortices increases considerably with a little change in angle from  $\alpha = 26.5^\circ$  to  $\alpha = 28^\circ$ . The side-edge vortex core axis moves straight up to trailing edge when moving upstream, where it bends a little and again moves straight up to leading edge. From the outer wake flow pictures it is observed that the flow at the center seems to be just as big bubble trying to close about  $0.1C$  to  $0.2C$  from the trailing edge which is quite different from the angle  $\alpha = 32^\circ$  where the bubble closes well away from the trailing edge. Also the wake boundary is wavy for  $\alpha = 28^\circ$  where as for  $\alpha = 32^\circ$  it is quite sharp as seen in the Figs. 9 and 10

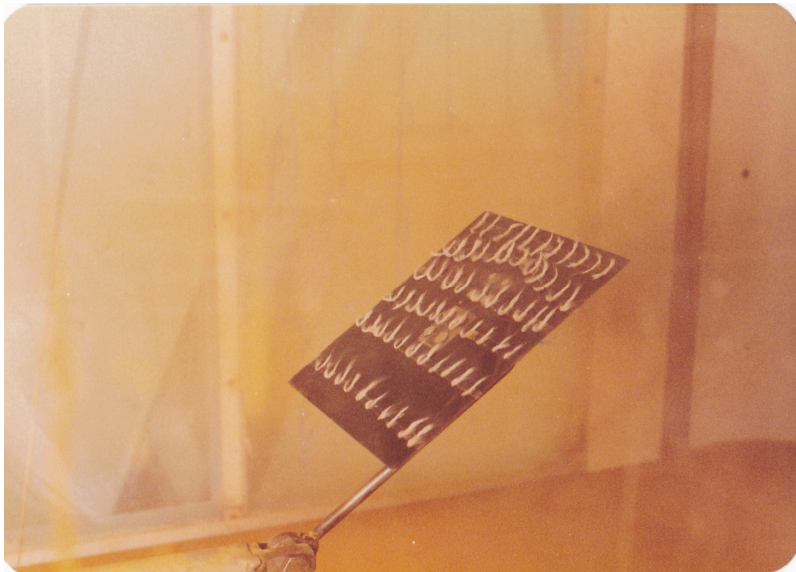


Fig. 14. Flow visualization on wake side using tuft probes.

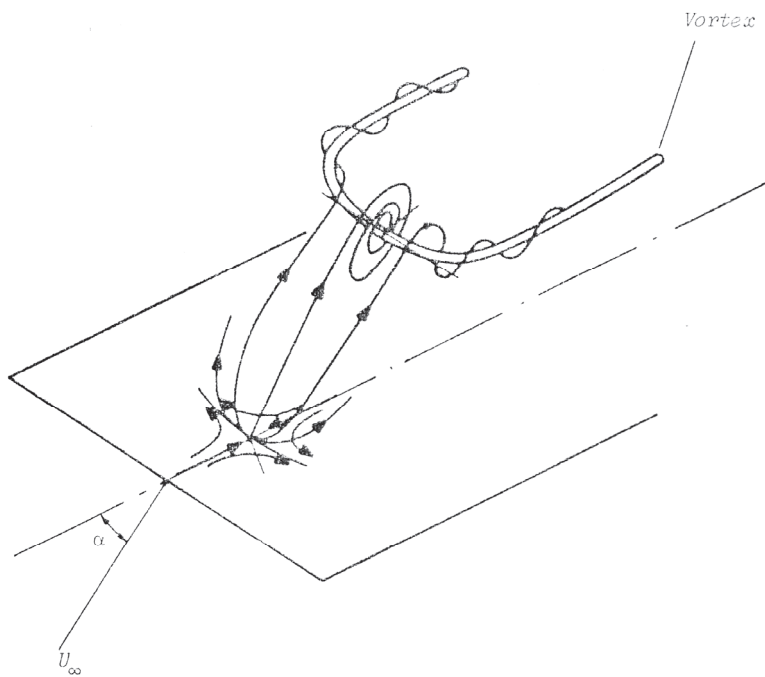


Fig. 15. Conjectured flow field on wake side of flat plate at sub critical incidence

The result of the variation flow visualization techniques have been used to construct the flow field as is shown in Figs12-13 and Fig.15 ("Flow visualization details"). This is what has been observed it is not an interpretation how the actual flow structure is. A first attempt has been made to get an idea of the flow field in the following way.

#### 4.2 $\alpha \geq 32^\circ$

For these incidences and higher up to  $\alpha = 50$ , it was observed that the wing centre flow is dominating the total span and the tip vortices are not present on the wing as shown in Fig.10, but appear further down the stream. The three dimensional bubble covers almost whole of the span with the appearance of trailing edge vortex shedding, and the flow is rotating inside this bubble. The flow near the plate surface is forward and spreading outward which is also noted from surface flow visualization pictures.

Trailing-edge vortex shedding and re-circulating flow was also observed by Calvert [9]. In the region near the leading edge on the suction side, the flow was observed as moving towards the plate centre from sides, and the flow which is moving forward is joining the main stream flow reaching from sides to form rotary motion like side edge vortices, the concentration of which is observed little downstream of the trailing edge. This distance increases gradually as the angle of incidence is increased. Also, it was found in the surface flow pictures that the two "eyes" had disappeared and with them the additional two vortices must have vanished there. For all these angles  $\alpha \geq 32^\circ$  trailing-edge vortex shedding was observed, and the frequency of vortex shedding was observed to increase as the angle of attack increases.

### 5. Conclusions

Flow visualization is considered an important tool to understand the nature of the flow field. Its proper utilization will provide reasonable information that will help in influencing flow characteristics. The above methods mentioned are not the only ways of understanding the flow but the results obtained using above methods highlight the usefulness of these flow visualization techniques.

### 6. Acknowledgements

The author is grateful for the facilities provided by King Fahd University of Petroleum and Minerals (KFUPM) and University of Sydney, Australia. The author also acknowledges the support from Dr. K Srinivas from the School of Aerospace, Mechanical & Mechatronics Engineering, University of Sydney Australia.

### 7. References

- Batill, S.M., & Mueller, T.M. (1981). Visualization of Transition in the Flow over an Aerofoil using Smoke wire technique, AIAA journal, Vol.19, pp.340-345
- Bienkiewicz, B., & Sun, Y. (1992). Local Wind loading on the Roof of a Low-rise Building, JWEIA, Vol 45, pp.11-24
- Calvert, J.R. (1967). Experiments on the flow past an inclined disk, Journal of Fluid Mechanics, vol.29, Pt.4, pp.691-703

- Fiddes, S.P., & Williams, A.L. (1989). Recent developments in the study of Separated flows past Slender bodies at incidence, Conference proceedings Roy. Aeron. Soc., London, pp 31.1-31.17.
- Mahmood, M., "Low-Speed Experiments on a Flat Square at High Angles of Attack", M.S. Thesis Dissertation, KFUPM, Dhahran, Saudi Arabia.
- Stahl, W.H., Mahmood, M. and Asghar, A., "Experimental Investigation of the Vortex flow on Delta wings at High incidences" AIAA journal, 30(4), April 1992, pp 1027-1032
- Stahl, W.H., Mahmood, M., Asghar, A., "Experimental Investigation of the Vortex flow on a very slender Sharp-edged Delta wings at High incidence", AIAA J. vol 30, No. 4, pp 1027-1032, April 1992.
- Stahl, W.H., Asghar, A., Mahmood, M., "Suppression of Vortex Asymmetry and side force on a circular cone", DLR-IB222-A12, Cologne, Germany, April 1993.
- Terry, N., Gangulee, D., "Secondary flow control on slender Sharp-edged Configurations" AIAA paper 93-3470, CP, 1993.



# Components of a Wind Tunnel Balance: Design and Calibration

Miguel A. González, José Miguel Ezquerro, Victoria Lapuerta,  
Ana Laverón, and Jacobo Rodríguez  
*Escuela Técnica Superior de Ingenieros Aeronáuticos  
Universidad Politécnica de Madrid  
Spain*

## 1. Introduction

The aim of wind tunnel tests is the simulation of the flow around bodies or their scaled models. In aeronautical applications, the measurement of aerodynamic loads in a wind tunnel, forces and momentums, is a very difficult task due to the required accuracy. The wind tunnel balances, comprised by several hardware and software components, provides directly the pursued measurements, with high accuracy and reliability. For these reasons, among others, wind tunnel balances have become a common tool in testing facilities.

This chapter starts with a general description of wind tunnel balances. The number of measuring components and the position of the balance with relation to the model and wind tunnel chamber determine the wind tunnel balances designs. The most flexible ones, in terms of usability, are the six components external balances, so these will be referenced for introducing the calibration process, which is one of the key points to achieve the required aerodynamic tests results accuracy and reliability. Because of its influence on the drag measurement accuracy, the coupling effect between lift and drag measurements is analysed very deeply as well. The analysis of the non-stationary effects are finally done taking into account the wind tunnel balance requirements and constraints, with special attention on an issue not commonly mentioned, the inertia forces generated on the balance by the model vibrations, and their influence on the aerodynamic forces to be measured. Several mentions to signal processing and acquisition are done, as this is the other key point on the measurements accuracy. However, it is easy to extrapolate these procedures to other types of balances, as the main intention is to show which are the critical points that make wind tunnel balances such a special and complex hardware.

We do not intend here to describe the design and calibration procedures of the industrial manufacturers. This is the result of a work done in the Universidad Politécnica de Madrid (UPM), and the Instituto Tecnológico y de Energías Renovables (ITER, Tenerife, Canary Island, Spain, [www.iter.es](http://www.iter.es)). Nevertheless, we do consider that is a good guide for developers of wind tunnel balances in institutions like UPM and ITER, where research and education are very important points.

## 2. Wind tunnel balance

The wind tunnels main function is to provide flow simulation on a model introduced in a fluid flow. Global forces and momentums on the model are mainly obtained by using different wind tunnel balances; although in special tests, local balances or pressure distribution measurement can be used as well. Range, accuracy and response time of the measurements are the main parameters that define such systems. The wind tunnel balances are extensively used and are an accurate method for measurements acquisition, with a wide range of measures and a fast response to loads changes. This system requires an important initial calibration effort but once the measurements are probed to be correct, the system can be used to test several low cost models with a reduced effort. Other option for aerodynamic load measurements is the pressure measurement in several model points by means of a pressure scanner or scanivalve system. This system requires a very complex and expensive test model. The measurement points are built in the model surface by making holes and connecting them with the scanivalve by means of a tube that transfer the pressure. These holes introduce also modifications in the flow around the model thus modifying the real behaviour of the model.

There are several types of wind tunnel balances. The most important are:

- External balances: They are placed outside the model, inside or outside the wind tunnel chamber test section, but they always introduce some interference in the wind flow. However the possibility to change test models with almost no effort provides a high flexibility to the wind tunnel facility. There are several degrees of complexity for these balances, depending mainly on the number of measurement channels, which can vary between 1 and 6.
- Internal balances: They are placed inside the model, thus no interferences are introduced in the wind flow by the balance components, but a mechanical support for the model is always needed to maintain it in the test chamber and change the model orientation if desired. The complexity of the test model is comparable or higher than the models for scanivalve systems, as the balance has to be installed inside. Thus this option does not provide flexibility in testing different models. These balances are normally supplied to the customer already calibrated and with the acquisition system. The number of measured components can also vary between 1 and 6. Figure 1 shows an example of internal balance.
- Rotary balances: Used for propellers, helicopter blades and other rotating models.



Fig. 1. Internal balance example. Image courtesy of STARCS.

We now focus our attention in the 6 components external balances, as they provide 3 forces and 3 momentums measurement and a high flexibility for a multi test wind tunnel. Nevertheless the results presented in this report can be applied to almost all types of balances.

### 2.1 Six components external balance

There are several wind tunnel balances manufacturers, who have solved the problems presented in section 3 and they produce internal, external and rotary balances from the range of some Newtons up to some thousands of Newtons. But expensive commercial balances are not the only option to get an accurate wind tunnel loads measurement system. Taking into account our university environment, we, together with the ITER ([www.iter.es](http://www.iter.es)), decided to manufacture our own balance for the ITER wind tunnel. The following chapters will show, as example to clearly explain the already mentioned key points, our experience, the problems we found during the calibration process and the solutions we have implemented, that will be beneficial for those who intent to build its own balance, as well as for those who want to understand the complexity of wind tunnel balance systems.

The commercial balances are used to have 6 complete coupled channels and a 6x6 decoupling matrix is provided by the vendor. This means that the forces and momentums measurements are obtained through a complex combination of the 6 channel signals by the use of a completely full decoupling matrix. The main inconvenient of this concept is that a recalibration of the balance requires a special calibration facility that is very expensive (see Figure 2).

The opposite balance design concept is a complete mechanical decoupling of the 6 loads components. Each channel output will be a unidirectional load signal (traction-compression), and the composition of the signals will be the lift, drag, lateral forces and the pitching, balance, yawing momentums. One possibility could be to use three vertical sensors to obtain the lift force (which is the dominant force in aeronautical applications), the pitching momentum and the balance momentum, two horizontal sensors in the wind flow direction to acquire the drag force and the yawing momentum and one horizontal sensor perpendicular to the flow direction to measure the lateral forces. The calibration of these balances is much easier as the matrix is almost diagonal. Nevertheless, in practice the sensors absorb lateral forces and this results in a certain coupling effect. This coupling is particularly relevant between lift and drag.

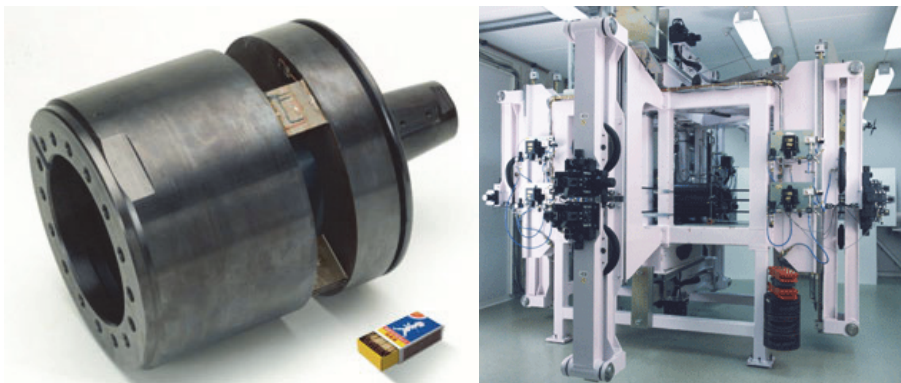


Fig. 2. External balance example on the left. Calibration facility example on the right. Images courtesy of STARCS.

Besides the model supports, a balance support is needed to fix the balance to the wind tunnel structure. These supports are placed outside the wind tunnel test chamber, so their dimensions and weight are not important, the requirement imposed on them is an elevated stiffness.

Also important is to notice that once the external balance is providing good results for aerodynamic purposes, which are very exigent, it will provide also good results for most of other test models, as per example, cars, cyclists, buildings... so the use of this type of balance provides a multi-purpose test facility.

## 2.2 Data acquisition components

The data acquisition system (DAQ) is compounded by several items that allow the conversion of physical forces into digital values that can be managed by a computer. Several components comprise the DAQ and the selection of their properties will have an important impact on the system behaviour. The main components are the following:

- a. Mechanics: The mechanics have to ensure that no friction forces are appearing thus and such not desired loads are avoided.
- b. Sensors or transducers: The sensors are devices that convert the physical load in an electrical signal. The capability of the sensors to measure the force depends on the properties of the load and the sensor itself. Several types of transducers exist (Gorlin & Slezinger, 1964):
  - Weight balanced sensors
  - Pneumatic and hydraulic sensors
  - Electromagnetic sensors
  - Spring sensors
  - Strain-gauge sensors: These are very common transducers, also called load cells, which generate the electrical signal through the mechanical deformation that causes the applied force. Usually 4 strain gauges in a Wheatstone bridge convert the deformation into electrical signals. There are many construction types but the Z shape ones have demonstrated in our own manufactured balance, that they are sensitive and accurate, with a relatively high stiffness.
- c. Electronic amplifiers: The sensor output signal is a weak signal of around a few millivolts and its power has to be increased by means of an amplifier in order to have a distinguishable signal in the analog to digital converter.
- d. Wires: The electrical signal is transferred from the sensor to the amplifier and from the amplifier to the sensor by means of wires, which are desired to be of high quality and efficient.
- e. Analog to digital converter (ADC): These devices convert a continuous analog signal (voltage or current) into a discrete time digital signal. Several parameters differentiate the ADC, the most important ones are the resolution, the sampling rate and the accuracy. As demonstrated in step 3.1, an ADC with a resolution of 16 bits ( $2^{16}$  analog-to-digital conversion levels), 8 channels and a sampling speed of some 2.500 Hz per channel, result to fit with the wind tunnel balances requirements. Nowadays the hardware available at normal prices has enough quality to proportionate low error and thus good accuracy. Also the level of integration with computers is very high and manufacturers provide their own software.
- f. Software: At the end of the data acquisition chain we encounter the software applications that post process the signal measurements in order to obtain the forces and

momentums values. Several options are available, from commercial applications to homemade applications, from calculus sheets to complex programming codes, which have to be selected in function of the wind tunnel complexity.

### 3. Wind tunnel balance calibration

At this point, the importance of the wind tunnel balance calibration for eliminating errors in the measurement acquisition is obvious. The calibration, and recalibration if needed, is absolutely indispensable to eliminate the coupling effect and to determine the DAQ behaviour. Therefore the first step is to perform a static calibration, as explained below, and after that it is desirable to perform a dynamic calibration with the help of the already existent typical test models results.

#### 3.1 Static calibration

The static calibration of the balance is not a trivial step in the chain to achieve reasonable system accuracy, although it could seem so in a first sight. As static suggest, this calibration can be done with a standalone balance, without the presence of the wind tunnel itself, and this is the standard procedure for industrial balance manufacturers. Making a calibration with the balance dismounted from the wind tunnel is much easier than calibrating it attached to its mounting supports on the tunnel. The accessibility to the balance to test every axe, in every direction and in both ways, in order to identify the behaviour of the acquisition system (mechanics, load cells, amplifier, wires, DAQ, software) is definitely easier.

Nevertheless, as shown in Figure 2, the calibration facility is very sophisticated and expensive. As this chapter treats about a self-designed and constructed balance, such calibration facility is not available, so another procedure is necessary. The gained experience shows that, in this case, instead of a standalone calibration, it is better and more accurate to do it with the balance installed in the wind tunnel. This calibration philosophy ensures that the reference axes of the balance are the same that those of the test chamber. In principle it can be though that once the balance is calibrated outside of the test chamber, it can be mounted properly by determining the local vertical and horizontal directions of the test chamber, but this may be a big mistake due to the following two reasons:

- a. The balance mounting actions could ensure a good alignment between balance axes and test chamber axes, but in any case some deviation could be expected. Although these deviations are rather small, in the case of wind tunnel testing were require very high accuracy, they could be catastrophic for the test results. To show the importance of an angular deviation, let's assume that only a 1 degree deviation has occurred between balance and test chamber vertical direction. Let's assume also that the test chamber vertical direction corresponds with the lift direction and, correspondingly, the test chamber horizontal direction corresponds with the drag direction. The drag measurement is where there is a major impact on results, for example, if a 150 N lift force is applied to the balance, around 2,6 N are incorrectly measured in the drag direction due to the misalignment. In a model of a medium speed aircraft, the drag corresponding to a 150 N lift would range from 10 to 12 N, meaning that the measured drag value has a deviation of roughly 25 %, which is an unacceptable error for aerodynamic model tests.

- b. The wind flow direction inside the test chamber has to be determined. We cannot assume that the wind direction and test chamber horizontal direction are the same, as the risk of being committing a same order error as the presented in the previous step is not acceptable.

A correct wind tunnel balance calibration must be preceded by some steps that allow the determination of fixed and reliable axes. The first action has to be the installation of the balance in its fixed final position in the test chamber. The second action has to be an accurate determination of the local wind flow direction inside the test chamber.

The flow direction determination can be done with the help of different instruments; the most common are the cobra, the wedge, the five holes and the cylindrical probes. All of these probes based their detection method on the same concept. The probes are a bundle of tubes where the leading edge of one of them is perpendicular to the flow direction while the leading edge of the others, one or two pairs, are cut at a known angle to the flow direction. The probe is placed in the test chamber, making an angle with the flow direction, then the pressure measured in the external probes (see Figure 3) are different, and through a precalibrated curve or by reorienting the probe, the angle of the flow can be determined.



Fig. 3. Vertical cut of three tubes showing the leading edges and the angle determination concept

Both attack angle and yaw angle can be determined by using one probe (with two pair of external tubes) or two probes (with one pair of external tubes) (see Figure 4). The leading edge angle to the flow direction determines the sensitivity of the probes to the changes in the flow angle, the dynamic pressure or the Reynolds number (Glenn LTP NASA and University of Cambridge web pages).

Once the flow direction is fully determined, the lift and drag forces directions are now known. The lift force perpendicular and the drag force parallel to the wind flow. The axes in which the forces (and momentums) have to be measured are properly defined.

Once checked that the flow is horizontal, the system is now ready for the calibration process. As aforementioned, we do not have specific calibration facilities. To avoid this problem, we have implemented some special calibration procedures, which are time consuming, but they give very accurate results.

As the function of the balance will be the measurements of aerodynamic forces, the calibration method should introduce loads in the proper direction and sense. Thus, the loads are introduced in the lift direction and not in weight direction, as this is the most critical direction while working with low drag aerodynamic models (for other applications the load direction will be of no issue). In order to ensure that we are loading the balance exactly in the appropriate direction, a specific system has been design.

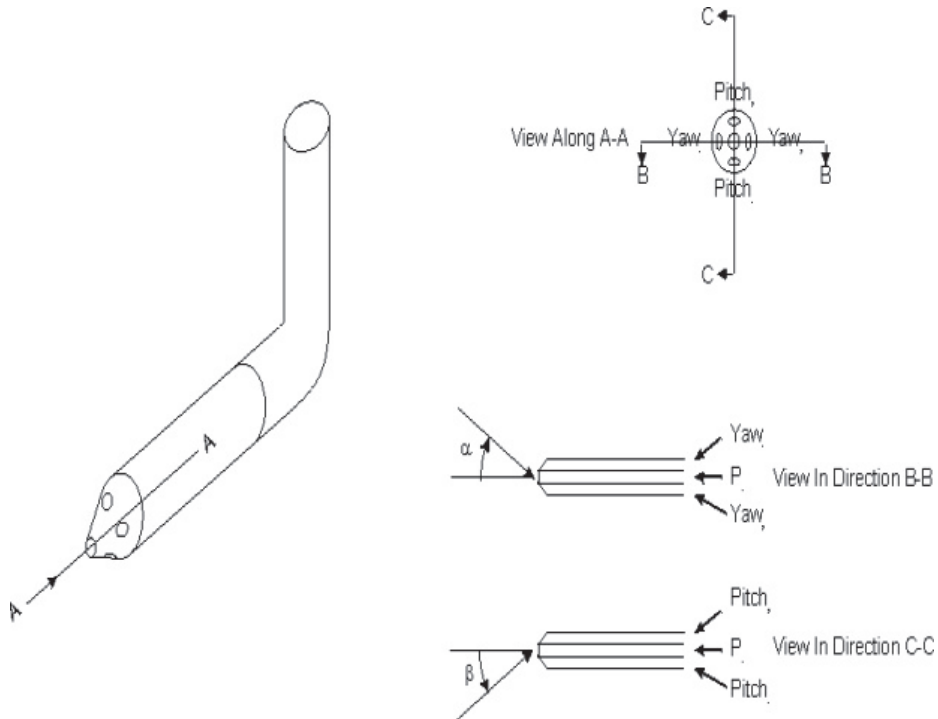


Fig. 4. A five hole truncated pyramid probe

The procedure to be shown here takes into account, that we use standard and calibrated load cells to measure the forces on each bar. Nevertheless, we apply known forces in the direction of the three axes to check not only the calibration of the load cells, but also the signal amplifier and the data acquisition system. As we expected, the manufacturer cell calibration and our calibration had a very good agreement, differences were less than 0,1%. It probes as well, that our philosophy of mechanical decoupling is a very good approach for the design of external balances.

It is important to point out that, at this moment, we were interested only in one direction each time. So small errors in the vertical or both horizontal directions (wind direction and transverse) did not introduce important errors on the true loads, because the cosines of the expected deviation angles are practically 1,0.

As abovementioned, for the current application, the only relevant coupling is between drag and lift. Taking into account that the flow in the test section is horizontal, an special device was designed to ensure that we apply a vertical load to the balance, with an error less than 0,1 mm in 600 mm. In these conditions, the coupling can be measured and corrected, and for a lift coefficient of 0,5, which is normal for cruise conditions of low speed aircrafts, the effect on drag is in the order of one drag count.

Figure 5 shows the results of the drag due to lift coupling tests, the  $x$  axis represents the loads in the vertical direction (lift) and the  $y$  axis the measured in horizontal direction (drag). It shows that the coupling effect is almost linear, being the drag 0,46% of the applied lift.

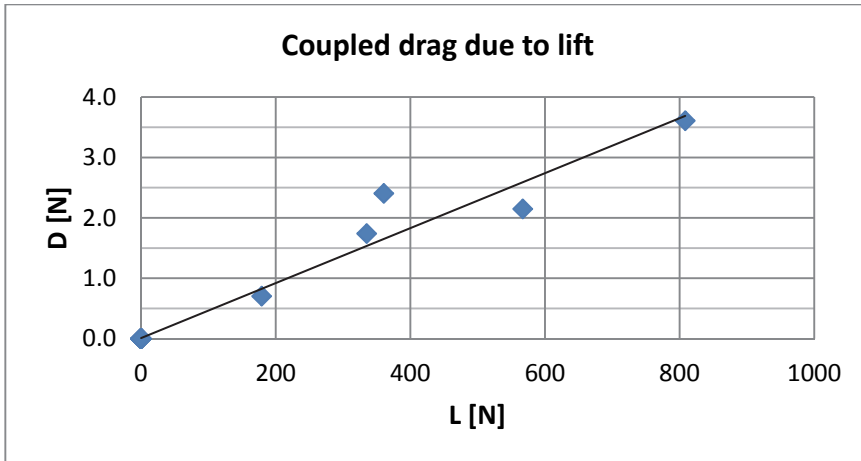


Fig. 5. Coupled drag due to lift. Horizontal axis represents the applied vertical force, and vertical axis the measured horizontal component due to coupling effect.

### 3.2 Dynamic calibration

Finally, to check all the system working in real conditions, we could use a reference model, such as a two dimensional model of the NACA 0012 wing section, to make final adjustment of the DAQ and coupling corrections. A well known standard calibration model would be another option, but the L/D ratio is well below the range we expect to make our tests. In both cases, differences in turbulence level and/or surface smoothness may produce differences of the same order than those to be checked.

Due to those reasons and the cost, in terms of time and money, it was finally decided to make a deep analysis of the measured results, to determine the DAQ requirements needed to get a high confidence level on the measured forces. The complete procedure is presented in the following paragraph.

## 4. Wind tunnel balance requirements

The better way to understand the strong requirements demanded to a wind tunnel balance is by studying the following example, where rough numbers involved in the problem are estimated.

In a 2,0x2,0 m low speed wind tunnel test section, with a testing velocity of around 50 m/s, using a model of a medium speed aircraft at cruise conditions, the lift would be roughly 150 N and the drag would range from 10 N to 12 N, for the high aerodynamic efficiency condition. For this type of model aircraft, the accuracy of the drag coefficient must be greater than 0,5 drag counts, which means that the accuracy of the balance, in the drag direction, must be higher than 0,015 N.

For the case of static loads measurements, where there is only one component, accuracy may or may not be a very tight requirement. But in the case of the wind tunnels, where we intend to measure simultaneously up to 6 components, forces and momentums, on a model under aerodynamic loads, with some non-stationary terms due to vibrations; amongst others, the following problems can be expected:



- a. The model vibrations induces inertia forces on the balance.
- b. There are aerodynamic forces on the model support system and interferences between these and the model may appear.
- c. The complete mechanical decoupling of the forces components is very difficult and expensive; therefore some coupling between lift and drag may appear.

During the setting of a new self-designed balance, all these points have been deeply treated, and the acquired experience is the base for this paragraph.

#### 4.1 Inertia loads on the balance

When testing an aerodynamic model in a wind tunnel, the forces and momentums measured come from different sources. The most important ones are the aerodynamic forces and momentums themselves, but some other undesirable loads could be expected. Although wind tunnel balances are necessarily very stiff, due to the model support and other elements, it is difficult to avoid oscillatory movements of the model, due to the aerodynamic loads. Those vibrations induce inertia forces and momentums on the balance, and might have a negative impact in the validity and/or accuracy of the measurements. Also some intrinsic data acquisition system noise has to be expected. Inertia forces and electronic noise are not desired, but measured, together with the aerodynamic loads; as those are not present in a free flight model, the study and evaluation of their impact on the pursued results is very important.

The inertia loads that appear in wind tunnel tests will depend strongly on the test facility and its components, so a specific study of each configuration should be performed. Nonetheless, the procedure, the critic analyses of the measurements and the influence range of these not desired loads are similar for all the wind tunnel tests configurations, so the results presented in these paragraphs will be of high interest for wind tunnel test engineers.

We can start making some rough calculations to show the true magnitude of the inertia loads. If we consider an amplitude in the order of 0,5 millimetres and an oscillatory frequency in the flow (drag) direction of some 5 Hz, which are very representative true values, the oscillation of the model produces accelerations in the range of 0,49 m/s<sup>2</sup>. If the mass of the model is, i.e., 50 kg, the appearing inertia forces are of the order of 24 N, which is of the same order of magnitude as the value of the drag that is to be measured. This is the reason why these inertia loads have to be carefully studied, in order to determine their magnitude, shape and relation with the aerodynamic loads.

First point to be determined is the sampling rate of the electronic signal, which is necessary for an accurate determination of the inertia terms, and thus the determination of the true aerodynamic signal. The aliasing, which is an effect that cause different sampled signals to become indistinguishable, is taken as the reference for the sample rate selection in several publications. The sampling theorem, frequently called Nyquist sampling theorem, states that a continuous signal can be properly sampled if the following expression accomplished (Smith, 1997):

$$\text{Sampling Frequency} > 2 * \text{Band Wide}$$

Following this rule, if we have a frequency signal of around 5 Hz, it can be stated that a sample rate of more than 10 Hz is enough for our purposes. As we will show, this is not enough in our case, due to several reasons, between them: the signal frequency study will not be accurate and the sample rate will impact the measurement results. The sampling rate

should be high enough to get accurate results and avoid the previous issues. Nowadays, the sampling frequency of the wind tunnel balance systems is much higher than the maximum expected frequency of the signal induced on the balance by the aerodynamic and inertia forces, thus those mentioned problems are overpassed, as well as the aliasing effect. Also with today's computer capabilities, managing an elevated quantity of data is no longer a problem. High sampling frequency produces benefits in reducing the random noise originated in the acquisition system (DAQ) as well.

While using low sampling rates, it is important to ensure that the sampled signal comprises complete cycles, so that no partial cycles are included in the signal mean and standard deviation calculation. The values obtained if, as an example, a half wave is included, could cause significant deviations with relation to the correct results. However, this effect is only recognizable using low sampling rates, and disappears if a high sampling rate is used.

In order to ensure that the noise of the measured signal is low enough for our purpose, the signal to noise ratio (SNR) has to be higher than 3, condition that ensures that every signal is recognizable. Although this is a soft requirement to the hardware currently available, there is always present a noise signal that is a not desired random signal. One simple and efficient method that can be applied to cancel out the noise signal is the time-averaging. This method, as presented in several publications (Lohninger, H., 2010), consist on registering and summing up the signal repeatedly, an action that applied to a stable signal eliminates the noise signal (our aerodynamic loads and inertia loads are supposed to be stable over hundreds of cycles once the system reaches a steady state). A high sample rate impacts positively in this noise reduction method.

Before starting aerodynamic tests, some mechanical tests were done to determine the main frequency of the complete system, balance plus model. Two free vibration movements were induced, in the flow direction and in yaw oscillation. In both conditions, the reactions on the balance were measured. The signal analyses showed that the main frequency for such unforced movement was, roughly, 5,2 Hz. In principle, this is the main frequency to be considered for the following analysis, and it will be shown that this main frequency is not modified by forced oscillations, due to aerodynamic loads.

The determination of the minimum sampling rate that provides accurate results has to take into account several considerations. The most important ones are, as already mentioned, the accuracy of the results and the main inertia frequency determination. The first measurements acquisitions, although the main inertia forces frequency is already known, have to be taken with a high sampling rate, at a minimum of 2 orders of magnitude above the expected vibration frequency (even 3 orders of magnitude are recommended for the complete analysis). As explained later on in this text, this will allow a proper frequency domain study, as no frequency components are lost due to a low sampling rate. The focus of attention is the accuracy of the results. The sampling rate has an important impact in the mean of the measured signal, which, at the end of the process, is the aerodynamic load we want to measure. Through the following example the influence of the sampling rate is clearly shown. Figure 6 shows the mean value of a real wind tunnel signal calculated each second for total signal duration of 20 seconds (blue line). The signal is the same for all the plots and the only difference is the sampling rate, from 2.500 Hz, near 3 orders of magnitude above the mechanical main frequency, to 10 Hz, double of the main frequency. The linear regression of those average values is also plotted in all the figures. The last plot is the representation of the whole average signal mean value, for the complete 20 seconds, versus the sampling rate.

As shown in Figure 6, for low sampling rates, 10 Hz and 20 Hz, which have the same order of magnitude than the Nyquist sampling rate for this signal, the accuracy and reliability of the mean value is poor. The linear regression and the mean value have important deviations. However, a sampling rate of 100 Hz gives good results although this frequency, as shown in the plot of the averaged force mean value, is at the limit. For higher sampling rates as 500 Hz and 2500 Hz the accuracy of the force mean is very good.

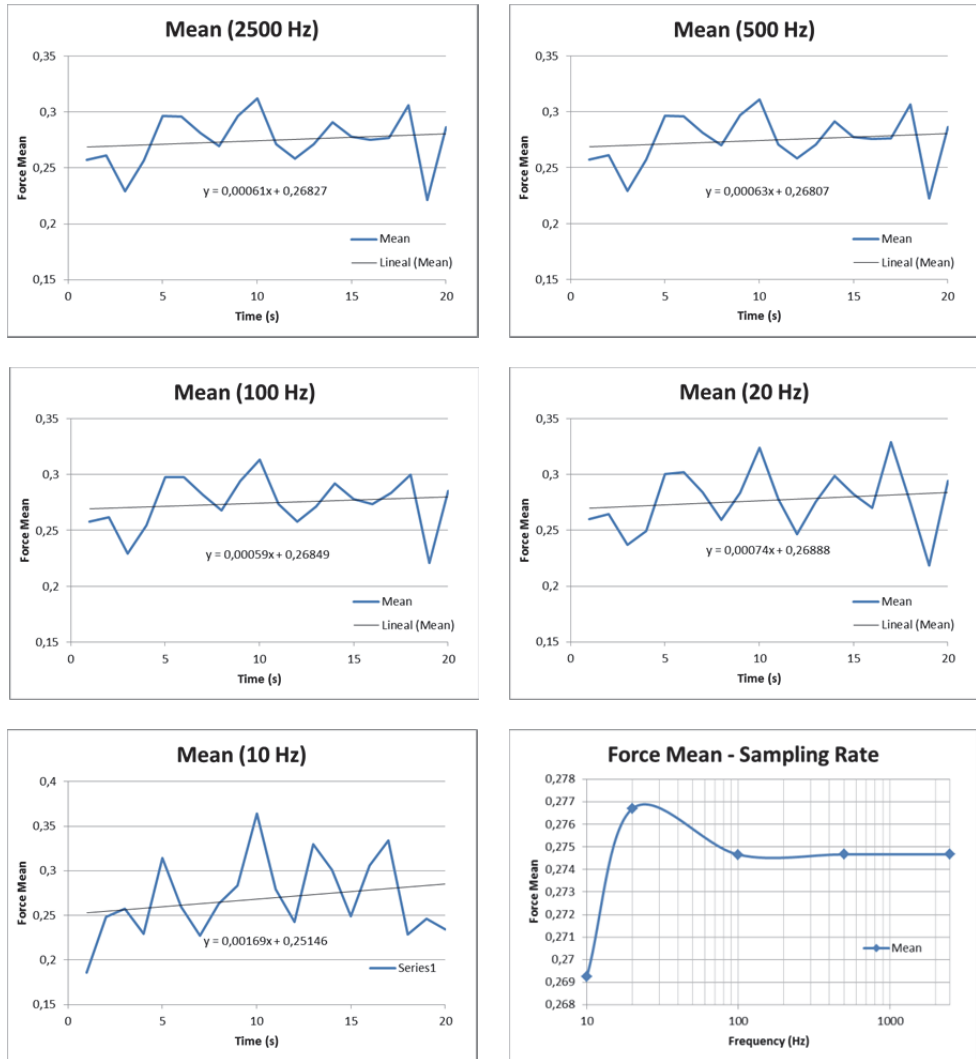


Fig. 6. Plots of a signal force mean calculated each second. Five plots for different signal sampling rates: 2.500, 500, 100, 20 and 10 Hz. Plot of the whole averaged force mean value versus sampling frequency.

Then, it can be stated that the minimum sampling rate to get accurate results has to be at least 2 orders of magnitude above the Nyquist sampling rate. Even if the sampling rate used were very high, it is always recommended to perform this study, to understand the complete phenomena that occurs.

Once the appropriate measurements are acquired, the signal properties can be studied. It is interesting to know the frequency components of a signal (in example the inertia forces frequency) but their identification by its representation in the time domain usually is a difficult task. A deeper study of the measured signals through the Fourier transform provides the frequency components of the signal. One fast approach to this Fourier transform study is to perform a discrete Fourier transform, which is identical to samples of the Fourier transform at equally spaced frequencies, by using the fast Fourier transform method (FFT) (Oppenheim & Schaffer, 1989). In the frequency domain, it is easy to identify each of the different signal sources. With the aim to clearly show the influence of each measurement source, real measurements will be presented below. Those were taken at the ITER wind tunnel, that is provided with an own manufactured balance, which is an accurate wind tunnel 6 mechanically decoupled components balance.

ITER Low Speed Wind Tunnel (ITER-LSWT) has a 2,0x2,0 m test section, 3,0 m long. In the current configuration, which includes devices to reduce turbulence, the maximum allowable speed is 50 m/s, with a turbulence level below 0,5%. The model used for the tests is a section of a wing, still under design, to be used in a solar powered aircraft, with 667 mm chord and 1.990 mm span.

It is important to look at the signals frequency spectrum from a critical point of view. It is not enough to identify the main frequency but the amplitude spectrum of the frequencies, and their importance in comparison with the constant signal (~0 Hz frequency signal) that represents the aerodynamic force acting on the model. This is clearly shown in Figure 7, where the signal is plotted in both: time and frequency spectrum.

The main frequency of the inertia forces signal is slightly higher than 5,0 Hz, the same than for the mechanical free vibration, and its amplitude value in comparison with the complete signal amplitude is near 75%.

Most of the balances obtain the forces and momentums values from a combination of several load cells measures. Then, it can be thought that the study of the resultant load could be enough to determine the inertial behaviour of the system, but this is not true. It is important to study the frequency behaviour of each measurement channel signal, before studying the combination of the measurement channels. Figure 8 shows the resultant signal of the two cells that measure the drag component in the ITER-LSWT balance. In this case, although there is a pick of frequency for the same value than the single analysis, it should be stated that the main inertia movement is occurring at around 10 Hz.

It is clearly shown that in the combined signal, although a small peak appears at 5,0 Hz, the main vibration frequency is 10 Hz. However, Figures 9 and 10 show the 2 measured signals whose combination result in the previous drag force signal.

This happens because of several coincidences: the model is symmetric, both load cells are placed equidistant along the symmetric model and the inertial vibration axis induced on the model by the aerodynamic flux is perpendicular to the load cells plane. Thus, when both channel signals are summed up, the inertia components are cancelled. This is a very good example to emphasize the necessity to study signal channels independently, prior to forces and momentums calculation, although the extreme case, with other model or in a different wind tunnel facilities configuration this behaviour could not happen.

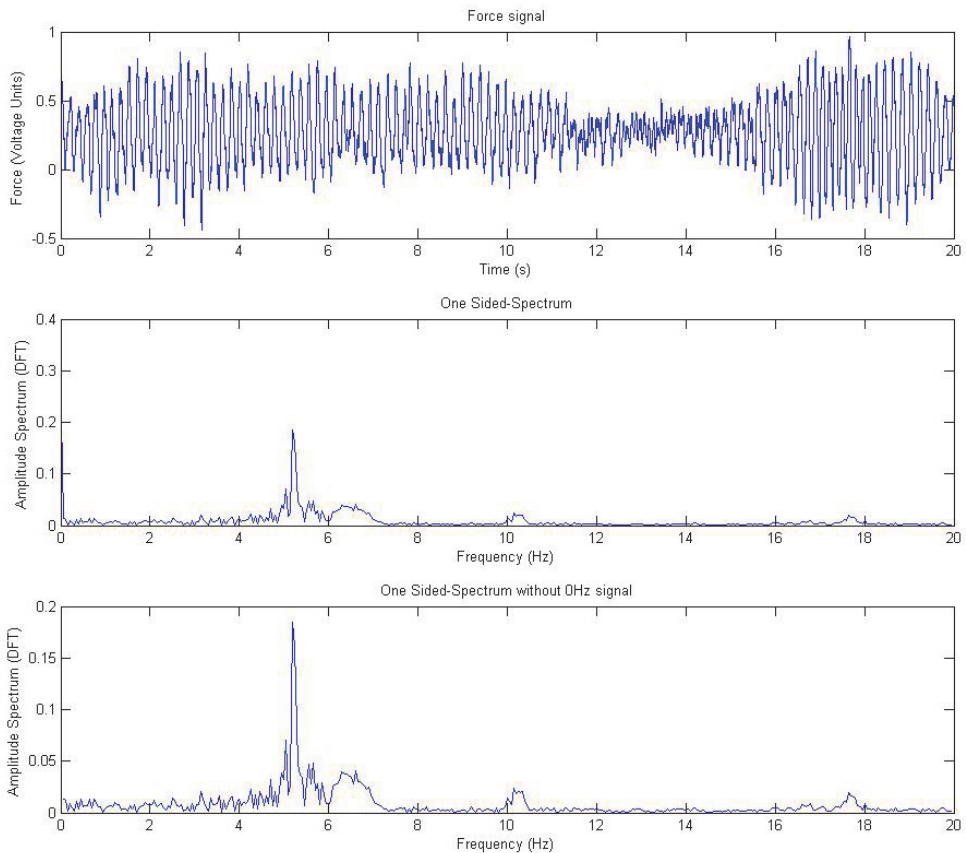


Fig. 7. Representation of a measured signal, in voltage, at 2.500 Hz sampling rate of an aerodynamic model in the ITER-LSWT, at a wind speed of 20 m/s and at angle of attack of  $8^\circ$ . Time domain signal plot during 20 sec. Frequency domain signal plots with different amplitude scales, with and without the 0 Hz component of the signal.

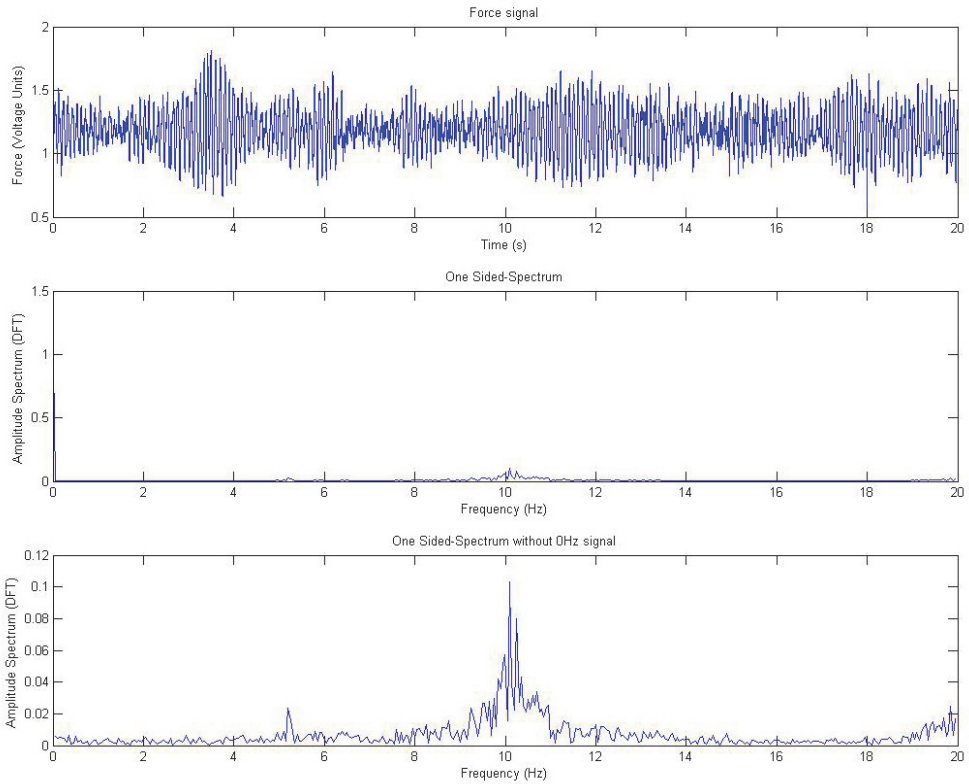


Fig. 8. Representation of a resultant force signal, combination of two drag cells, at a 2.500 Hz sampling rate of an aerodynamic model introduce in the ITER-LSWT, at a wind speed of 40 m/s and at angle of attach of  $8^\circ$ . Time domain signal plot during 20 sec. Frequency domain signal plots with and without the 0 Hz component of the signal.

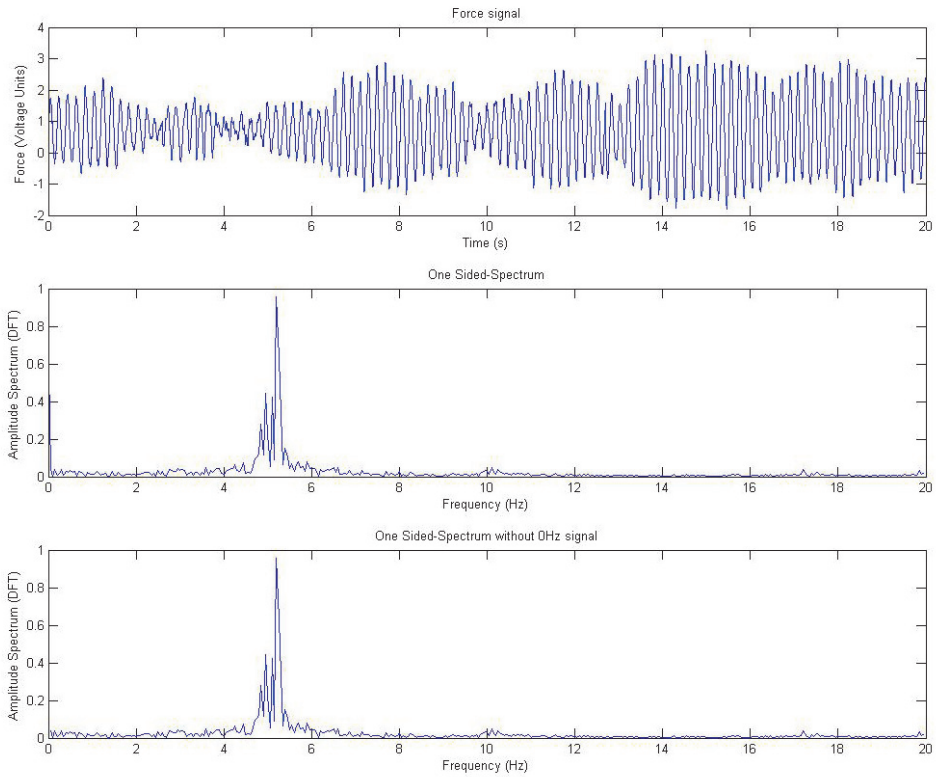


Fig. 9. Representation of channel 1 signal at a 2,500 Hz sampling rate of an aerodynamic model introduced in the ITER-LSWT, at a wind speed of 40 m/s and at an angle of attack of  $8^\circ$ . Time domain signal plot during 20 sec. Frequency domain signal plots with and without the 0 Hz component of the signal.

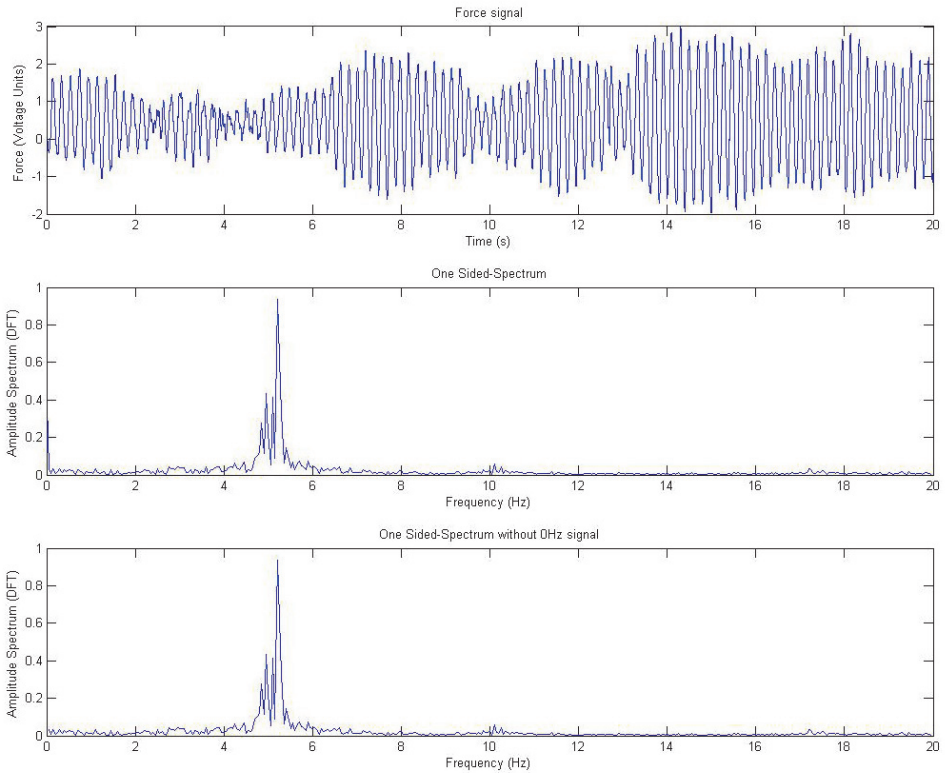


Fig. 10. Representation of channel 2 signal at a 2500 Hz sampling rate of an aerodynamic model introduced in the ITER-LSWT, at a wind speed of 40 m/s and at an angle of attack of  $8^\circ$ . Time domain signal plot during 20 sec. Frequency domain signal plots with and without the 0 Hz component of the signal.



Due to the particular characteristics of aerodynamics models, the influence in the drag measurements is much more important than in the other forces and momentums, such as the lift measurements, so it is highly recommended to focus the attention in those channels related to the drag force measures.

#### 4.2 Model support interferences

The external balances are used as fix element of the wind tunnels, however the test models are interchangeable items. The model support system is the mechanical link between the balance and model. There are several types and sizes of supports, but all of them may interfere with the aerodynamic measurements. Two origins of interferences can be highlighted:

- a. Aerodynamic forces on the model support system.
- b. Aerodynamic interference between the model support system and the model itself.

The occurrence and impact of each of the interferences depend on the shape, size and disposition with relation to the model, but in almost all cases, mainly in aeronautical purposes, the model support system is another source of problems for an accurate drag measurement.

A direct model fixation to the balance might be the best option in order to avoid interferences, but this solution will work in few and very specific cases, such as, half wings or half model aircraft. In all other cases of interest, as wings, nacelles, complete aircrafts... tests, the presence of a more or less complex support cannot be avoided; as the model has to be placed more or less in middle of the test chamber, and the aerodynamic forces have to be transmitted to the balance. Moreover, it is very common that for aeronautical tests, as a minimum, the angle of attack of the model should be variable, which introduce more complexity to the support and, therefore, more interferences.

Excluding a few cases, a support system is unavoidable. Its influence quantification and the methods to subtract the interferences are key points to gain measurement accuracy. If a very stiff support is used, its drag and interferences on the model may be very important, once more in the order of the values to be measured for cruise conditions. On the other hand, the size of the support fairings will be smaller if we just faire the supports, but in this case the supports drag becomes very important too.

There are several methods to subtract the contribution of the support to the balance forces and momentums measurements. Three methods with a complete different concept are presented here:

- Experimental method: By taking series of measurements before placing the model, it is possible to determine the support aerodynamic contribution. However, by means of this method, the possible aerodynamic interferences between support and model are not contemplated. In case the supports wake does not impact on the model, and vice versa, the mutual influence would be negligible, but in other case, the support-model interference might be studied with more detail. This is a very common method, as other none desired loads are eliminated as well, from the model and support weight.
- Theoretical method: Theoretical calculations of aerodynamic forces and momentums over the supports can be subtracted to the wind tunnel measurements. The supports

fairing geometry should be known and common, with an extensive and contrasted bibliography, so that the aerodynamic forces and momentums theoretic calculus will be reliable enough. The support fairings airfoil should be a symmetric one, and its angle of attack should be  $0^\circ$  in order to generate only drag force and one momentum component. Also, the possible interferences between support and model and vice versa have to be assessed.

- Hybrid method: It is a mix of both previous methods, providing an easier experimental part and a more reliable theoretical part (Horsten & Veldhuis, 2009).

Once support forces and momentums has been measured or computed, it is convenient to obtain the aerodynamic forces and momentums coefficients, made non-dimensional using the same characteristic surface and dimensions than for the model, in order to be able to substrate those coefficients to the measured ones. It is also convenient to test the supports for the same Reynolds number (Re) range than the model to be tested, then it should be possible to obtain a fitted curve for each coefficient, normally depending upon  $\text{Log}(\text{Re})$ .

### 4.3 Coupling effects

The balance that has been used in the ITER-LSWT facilities was designed with the philosophy of mechanical decoupling of forces. So that, the measurement of loads on six traction-compression bars allows obtaining all forces and momentums components. From the theoretical point of view, this design method supposes that there is no coupling in the three forces components, because bars cannot support any transverse load. Nevertheless, it is not absolutely true, and some coupling effects among measured loads must be expected. There are several sources that could contribute to the coupling effect. The most relevant are:

- a. Deformations of the balance forces transmission rods.
- b. Deformation of the model supports.
- c. Inaccurate assembly of balance components.

These errors can be eliminated by means of a correct calibration, as presented in step 4, but it is important to know their magnitude in order to stress the importance of this calibration.

This coupling effect is very critical in the relation between lift and drag. In a high quality balance such coupling is only about 1%, which could seem to be negligible, but, in the case of aeronautical applications, this is the order of the ratio between lift and drag, so that such coupling must be accurately measured during the calibration process. If we consider the example introduced at the beginning of this section, a lift force of around 150 N, may produce a force of 1,5 N in the drag direction, that is in the same order of magnitude than the drag forces appearing due to aerodynamic loads.

## 5. Conclusions

The first tests done with our self-designed and manufactured balance has been on a two dimensional profile. Such profile will be used in a solar powered aircraft, with critical design conditions for  $\text{Re}=500.000$  and lift coefficient,  $c_l=0,8$  and with constant cambered upper surface, in order to facilitate the installation of the solar cells. Profile aerodynamic characteristics were computed using several codes previous to its manufacturing and

testing, because a minimum aerodynamic efficiency of 80 is required in the abovementioned design conditions. Experimental results have shown a complete agreement with the expected ones, including lift curve slope and aerodynamic efficiency, proving that both, balance capabilities and calibration procedures, are good enough for our requirements: a maximum error of one drag count for critical design conditions. Of course, many balances achieve errors even one order of magnitude less, but their cost is several orders of magnitude higher.

From the technical point of view, we have learned many things, but we want to emphasize only three important aspects:

- Mechanical decoupling is a very efficient design philosophy to reduce sources of errors and to facilitate balance calibration.
- Self-designed and manufactured wind tunnel external balances should be calibrated mounted in the definitive place.
- Detailed measurement and analysis of the measured signal is highly recommended to fix DAQ performances, and can efficiently replace the dynamic calibration.

## 6. Acknowledgment

The whole activities have taken about ten years, with the participation of many professionals and students. First of all, authors wish to acknowledge to ITER and its managing director, Manuel Cendagorta, the support given in balance manufacturing, setting and tests. In particular, we must mention to Esther Friend, because of her personal compromise and enthusiast help; the support given by Guillermo Galván, Jesús Fernández, Jesús Rodríguez, Juan Enrique Martín, and many others.

Many thanks as well to Lidia Esteban and Alvaro Lozano, students of the UPM, which have collaborate in different times of the project. The latest, but not the less important, students involved in the project have been Artur Jarzabek and Christopher Field, from the Imperial College; thanks in deed for your help in final tests performance and proof reading.

## 7. References

- Gorlin, S.M. & Slezinger, I.I. (1966). *Wind Tunnels and Their Instrumentation*, Israel Program for Scientific Translations, No 1680, Israel, Jerusalem
- Horsten, B.J.C. & Veldhuis, L.L.M. (2009). *A New Hybrid Method to Correct for Wind Tunnel Wall- and Support Interference On-line*, World Academy of Science, Engineering and Technology 58
- Lohninger, H. (2010). *Fundamentals of Statistics*, Ihr Epina eBook-Team, Retrieved from <[http://www.statistics4u.com/fundstat\\_eng/](http://www.statistics4u.com/fundstat_eng/)>
- Oppenheim, Alan V. & Schaffer, Ronald W. (1989). *Discrete-Time signal Processing*, Prentice-Hall Inc., ISBN 0-13-216776-9, USA, New Jersey
- Smith, Steven W. (1997). *The Scientist and Engineer's Guide to Digital Signal Processing*, California Technical Publishing, Retrieved from <<http://www.dspguide.com/>>
- Unknown author (2010). *Pressure Probes*, Department of Engineering, University of Cambridge, Retrieved from <http://www-diva.eng.cam.ac.uk/whittle/pressure.html>

Various authors (2010). *Beginner's Guide to Wind Tunnels*, Glenn Learning Technologies Project ; NASA, Retrieved from  
<[http://www.grc.nasa.gov/WWW/k-12/ airplane/bgt.html](http://www.grc.nasa.gov/WWW/k-12/airplane/bgt.html) >

# Wind Tunnel ‘Concept of Proof’ Investigations in the Development of Novel Fluid Mechanical Methodologies and Devices

N. Findanis and N.A. Ahmed  
*Aerospace Engineering, University of New South Wales, Sydney,  
Australia*

## 1. Introduction

It may be argued that the first successful flight by the Wright brothers in 1903 would not have happened had the Wright brothers not built wind tunnels and obtained aerodynamic data in a form that could be incorporated directly in the design of an actual aircraft. The wind tunnels they built at the time were of a very crude nature, but they nevertheless demonstrated conclusively their value in the aerodynamic design loop. Immediately after the historic flight, with World War I looming, a spurt in wind tunnel construction started and they were mainly built in government-funded aeronautical laboratories of Europe in countries such as Great Britain, France and Germany to achieve technical leadership in aviation between 1903 and 1914.

Although, primarily designed for aerodynamic studies, the wind tunnels of today are used in a multitude of fluid mechanical investigations including aerodynamic studies. It is considered to be an essential experimental tool in fluids/aerodynamic laboratories to complement research and teaching activities around the world.

Today there are wind tunnels that are designed to cater for flow field investigations ranging from very low speeds to hypersonic speeds. The purpose of this chapter, however, is not to describe the design of these wind tunnels but to highlight the significance of wind tunnel investigations in the ‘concept of proof’ investigations in the development of novel fluid mechanical methodologies and devices. The materials presented here are, therefore, entirely based on the many successful and innovative works that have been carried out by N.A.Ahmed and his research teams at the aerodynamics laboratory of the University of New South Wales that spans well over a decade and supported by substantial funding from the Australian Research Council and from industry.

The chapter will start with a description of the development of novel measurement methodologies for highly three-dimensional flow fields that can be created and investigated employing a wind tunnel. In this connection the development of new methodologies for application of multi-hole pressure probes developed by the aerodynamic research group at the University of New South Wales for application in highly complex flows in wakes and in cases where reversal of flows occurs will be detailed. This will be followed by a description of the group’s works where the wind tunnel investigations have featured prominently to help advance the cause of active flow control for aerodynamic efficiency of wings for aircraft

and other fluid mechanical applications. The chapter will also demonstrate that various features and important findings from wind tunnel investigations have helped enhance the accumulation of new and significant knowledge, and validated the 'concepts of proof', that can, and also have lead to the development of practical devices such as wind driven rotating devices which are currently manufactured and marketed commercially for ventilation to ensure high inlet air quality and comfort in buildings.

## **2. Concept of proof studies**

### **2.1 Development of new flow measurement techniques and methodologies**

#### **2.1.1 Background information**

Investigation of fluid flows requires the development of appropriate measurement methodologies and techniques for use in wind tunnels. Wind tunnel works conducted at UNSW have resulted in the development of a mean and fluctuating pressure measurement system using plastic tubing [1], a new multi-hole pressure technique [2],[3] for pressure and velocity measurement in highly three-dimensional flows including reverse flows.

In this section, extension of the usage of multi-hole pressure measurement technique mentioned earlier to the development and validation of a novel shear stress measurement technique will be described in greater detail.

Measurement techniques for shear stress in three dimensional turbulent boundary layer flows have relied mainly on a combination of physical experimentation and subsequent empirical relationships or theoretical approaches supplemented by experimental correlation [4], [5]. The five-hole pressure measurement technique was first used in 1915. Since then, despite many attempts, it has not been possible to use this technique for flows greater than  $\pm 30^\circ$  angles of yaw and pitch, thereby precluding its use in many complex flow fields of practical significance. The new technique developed at UNSW showed that it can be used in flows of angularity as high as  $\pm 85^\circ$  angles of yaw and pitch by overcoming the singularity problem associated with previous existing techniques.

The initial work by Lien and Ahmed [6] involved the development of a novel skin friction measurement technique in two dimensional flow using multi hole pressure probe. This has been followed by the experimental study using wind tunnels is to further extend its application to measurements of skin friction in three-dimensional turbulent boundary layer [7] by measuring the shear stress angle more accurately.

It should be mentioned that the major difficulty associated with the measurement of shear stress angle is that its magnitude is small. The case is further complicated for three dimensional boundary layer where the presence of the pressure gradient normal to the free stream flow direction due to curvature forces the fluid particle in the boundary layer tend to accelerate in the normal direction. Due to their lower velocity, the fluid particles must travel on trajectories of smaller radius of curvature than the free stream flow in order to balance to pressure field imposed on them by the flow above. Due to the extra dimension caused by the skewing of the flow, the measurement of shear stress angle becomes important.

Skewing of the flow in three dimensional boundary layer flows which refers to the boundary layer velocity vectors not parallel to the main flow velocity which can be described in a streamline coordinate system is shown in Fig. 1. This skewing is caused by streamline divergence or convergence which the boundary layer velocity vectors are collateral with the main flow velocity vector at a point while the secondary flows are not parallel to the main flow velocity vector.

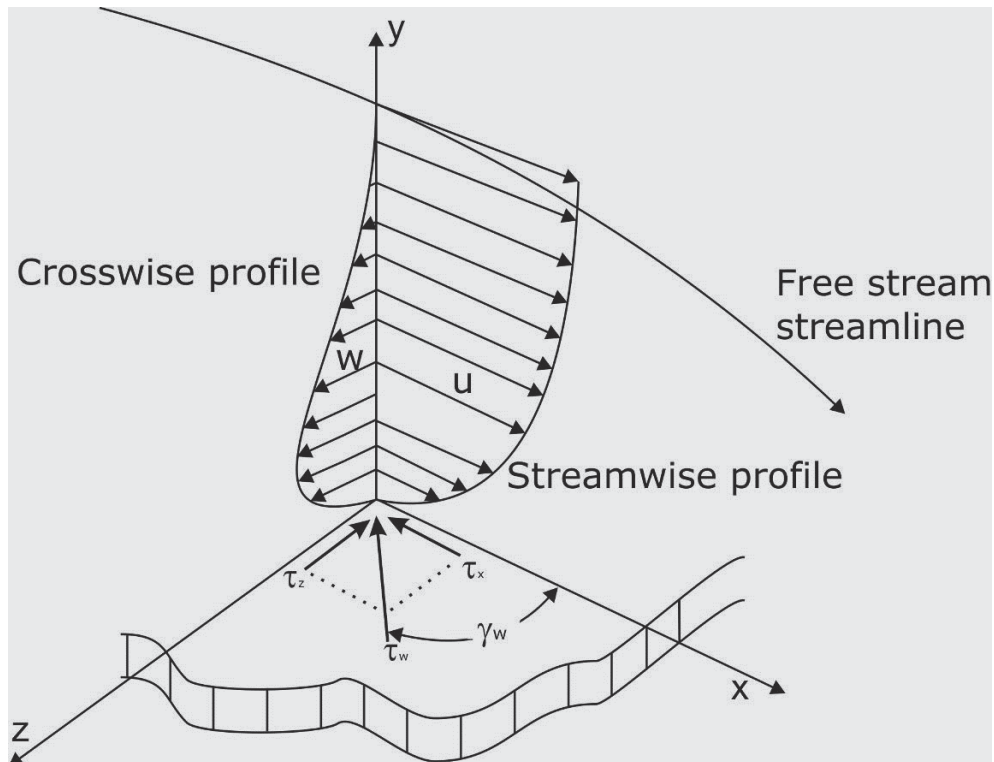


Fig. 1. Schematic of velocity profiles in three dimensional turbulent boundary layer

Several flow measurements in three dimensional flow field have been carried out using pressure probes. The measured flow parameters are usually the total, static pressure as well as the flow angle at the measurement location and these have been carried out by Pitot tubes and yaw sensing tubes or combination of them as two- or three-hole pressure probes in a nulling mode where the probe is rotated until zero pressure difference is obtained across the two side slanted tubes at each profile point. For example, Johnston [8], Elsenaar and Boelsma [9], and Chandrasekhara et al [10] use three-hole pressure probe soldered side by side and cut off at the tip with a apex angle in three dimensional flows. The use of pressure probes in a non nulling mode can also be used to determine the direction of the flow within the boundary layer where the pressure difference is pre calibrated in a known flow [11].

One major difficulty of insertion of a pressure probe into a pressure driven flow field is that it introduces error in the measurement of flow parameters as some extra flow interactions of the stream lines and the probe are induced. However studies by Vagt [11] also points out that such effects are not severe in shear driven three dimensional boundary layers or where the surface curvature is weak. The sensitivity of pressure probes technique depends largely on the probe geometry as well as the accuracy of the manometer. It was demonstrated that pressure probes are capable of measuring flow angles in turbulent boundary layer accurately within  $\pm 0.1^\circ$  with suitable choice of probe geometry and the assist of highly sensitive pressure transducer or micromanometer [11],[12]. These studies lead to a

conclusion that with careful selection of pressure probes, they can be used in accurate determination of flow quantities such as flow angles and velocity profiles even in three dimensional turbulent boundary layer.

Hence, the present study is an effort to extend the use of multi hole pressure probe for measurements of skin friction and shear stress angles in three-dimensional turbulent boundary layer.

### 2.1.2 Experiment

A test rig, Fig. 2, was constructed at the aerodynamics laboratory of the University of New South Wales. The experiments were conducted in a 76mm diameter open return, 0.2% turbulence intensity open test section wind tunnel of the Aerodynamics Laboratory of the University of New South Wales.

Uniform and parallel freestream flow is produced by an open jet wind tunnel and passes through the entry duct. The top and bottom walls are kept far apart to ensure the boundary layer on both walls will not interfere with each other. The flow is forced to turn sideways due to the effect of pressure gradient introduced by the back wall. A detailed description of the test apparatus is given in Fig. 2a.

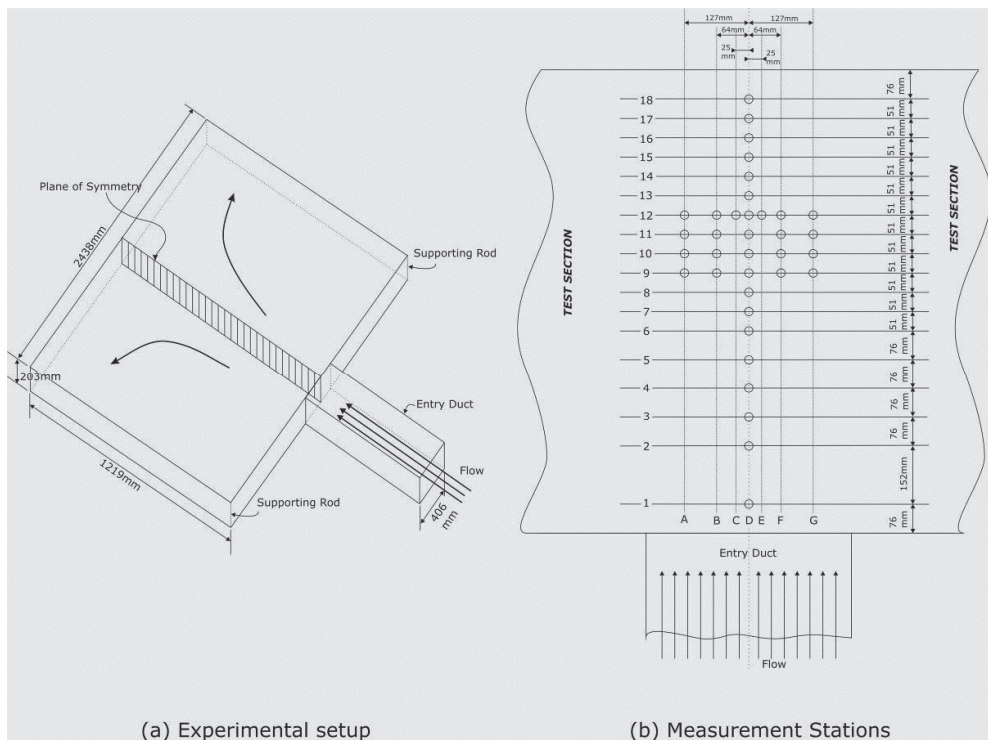


Fig. 2. (a) Experimental setup; (b) measurement stations



The reference speed of 31 m/s was held constant for all tests which is derived from the Pitot-static probe reading located at the entry of the duct. The air used in the test section was nominally at room temperature and atmospheric pressure.

The measurement stations are shown in Fig. 2b. The velocity profiles at each measurement station are determined by traversing a five hole pressure probe of 2.3mm diameter at different heights across the boundary layer. The upstream profiles are also measured at the plane of symmetry represented by Row D to ensure uniform two-dimensional condition is valid for the main entry flow.

A traversing gear, allows movement in both horizontal (X) and vertical (Y) direction with an accuracy of  $\pm 0.01\text{mm}$  was used in the investigation. A bank of Honeywell transducers and a FCO510 micro-manometer from Furness Controls, Ltd, was used to obtain the pressure data from the five-hole pressure probe and the freestream velocity from the Pitot-static probe, respectively. The manometer and the pressure transducers provide measurements ranging from  $\pm 2000$  Pa with accuracy up to 0.1 Pa. Through a set of calibration curves similar to these mentioned in Pisasale and Ahmed [13] the value of  $(P_t - P_s)$  as well as the yaw and pitch angles were found and the velocity of the flow is determined.

The experimental program was accomplished in two phases. The first phase defines the mean flow field where mean velocity profile, yaw angle and pitch angle were measured at different measuring locations. The second phase is to derive the shear stress components, including the shear stress angle from the pressure readings of each holes.

## 2.1.3 Results and discussions

### 2.1.3.1 Shear stress angle

For skewed boundary layer, the shear stress angle near the wall can be determined from its velocity profile, which is the ratio of  $w$  and  $u$ . The two velocity components ( $u$  and  $w$ ) from the five pressure probe technique at a point can be expressed as follows:

$$\begin{aligned} u &= \cos \alpha \cos \beta \\ w &= \sin \alpha \end{aligned} \quad (1)$$

Hence:

$$\begin{aligned} \gamma_w &= \tan^{-1} \left( \frac{w}{u} \right)_{near\ wall} \\ &= \tan^{-1} (\tan \alpha \cos \beta) \end{aligned} \quad (2)$$

The yaw angle measured at the plane of symmetry is presented at Fig. 3. Since the flow along the plane of symmetry will not turn before the separation zone, the shear stress angles are expected to be around zero values at this plane. The results showed that the measured shear stress angles using five hole pressure probe are closed to zero values at the plane of symmetry.

The measured shear stress angle using the multi hole pressure probe method also showed better agreement with the angles derived from the velocity profiles than those measured by Johnston for this plane.

### 2.1.3.2 Skin friction measurements

After the examination of shear stress at each measurement station, the skin friction values obtained from multi hole pressure probe technique by Lien and Ahmed [7] were compared again with calculated values using momentum integral equations in its three dimensional form.

The various momentum integrals along measurement plane D are presented in Fig. 4 which the measured skin friction using multi hole pressure probe is plotted in Fig. 5. The skin friction values measured by five hole pressure probe were found to be in good agreement with Johnston's experimental data and momentum integral technique.

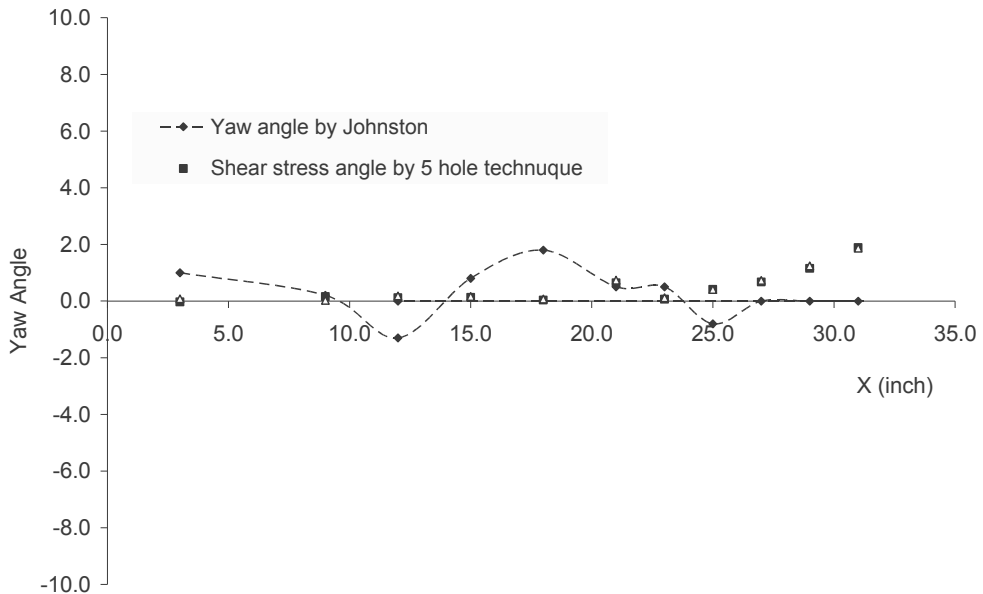


Fig. 3. Measured shear stress angle along the plane of symmetry

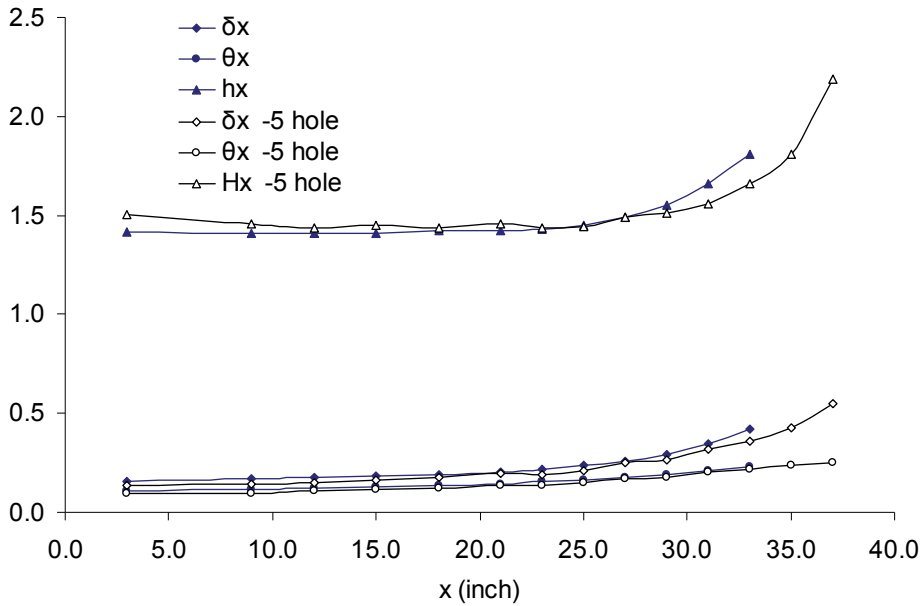


Fig. 4. Various momentum integral parameters along the plane of symmetry

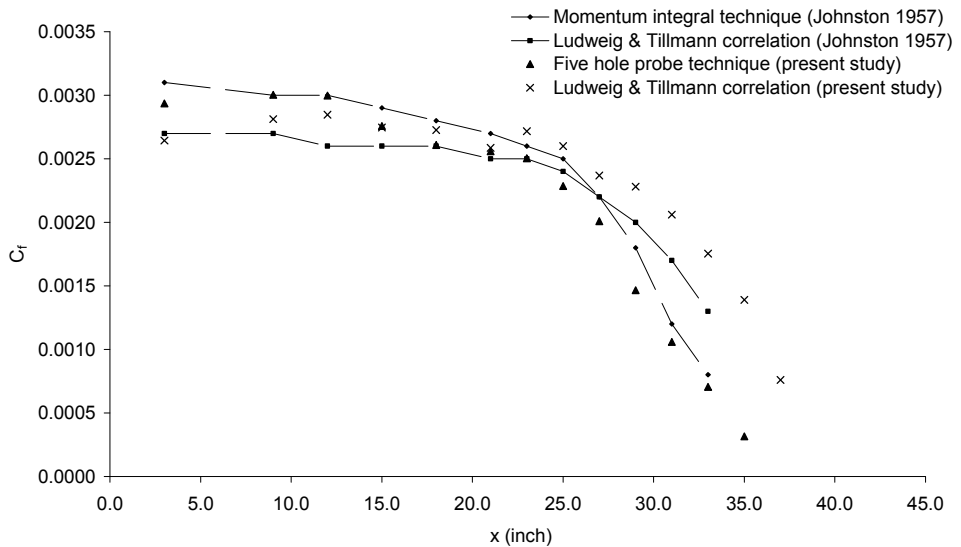


Fig. 5. Skin friction along the plane of symmetry

### 2.1.4 Conclusions

A method of determining local skin friction developed by Lien and Ahmed (2006) using multi-hole pressure probe has been presented in this study. The method is based on wall similarity law and the utilization of the logarithmic law of the wall.

Wind tunnel tests were conducted to obtain skin friction values in three dimensional turbulent flows. It is worth noting that using the present method, the skin friction is deduced from  $\Delta P$ , that is the method essentially determines a vector quantity from scalar information. The ability of non-nulling multi-hole pressure probe, however to determine  $\alpha$  and  $\beta$  values means that the directional aspect of the skin friction may be easily determined. The present study suggests that the skin friction value as well as shear stress angle can be determined from multi-hole pressure probe reading when the probe is placed within the wall region. This is very promising and points to the possibility of extending the technique to more complex three dimensional flows as well where non-zero values of  $\alpha$  and  $\beta$  occur.

Since the multi hole pressure probe method is based on similarity principle where the probe diameter is used as a characteristic parameter, it is expected that the method would be equally effective with a different probe geometry provided it is small enough to be submerged in the boundary layer and that its calibration coefficient can be accurately determined.

## 2.2 Investigation of synthetic jet for active flow control

### 2.2.1 Background information

Substantial experimental work with synthetic jets in various flow regimes and in different types of flow i.e. laminar and turbulent flows, has been performed over recent years moreover there has been an escalation as they continue to draw the attention of researchers in fluids. Some applications of the synthetic jet include flow separation control and turbulence, control of thrust vectoring, augmentation of heat transfer and mixing, and microfluidics. Specifically synthetic jets are proving to be a beneficial device in terms of active flow control in applied aerodynamics. This has been demonstrated with the use of synthetic jet in subsonic crossflows in which typically the synthetic jet emanates from the surface of a bluff or streamlined body reducing the overall drag and wake region as evidenced in the works of Glezer and Amitay [13]. Interestingly, synthetic jets improve the flow by imparting a net momentum transfer to the flow without a net mass addition thereby delaying flow separation and reattachment this altered flow also generates a separation bubble above the surface of the body. The flow structure of synthetic jets consists of a time-periodic formation of vortex pairs that eventually progress into transition to turbulence and the monotonic decrease in their stream wise velocity that ultimately leads to their dissolution.

Although several studies have been conducted on synthetic jet in a crossflow such as the flow over a circular cylinder [13], [14], [15], there is a noticeable lack of studies on true three-dimensional bodies with synthetic jet [16]. The flow over the cylinder can be described with two independent variables and as such is termed axis symmetric. It is a degenerate three-dimensional flow that exhibits certain three-dimensional effects and as such it is not really a two-dimensional flow and not fully three-dimensional either. A common phenomenon to all three-dimensional flows is the three-dimensional relieving effect that is present in flow over a sphere but not that of a cylinder. A greater understanding of the synthetic jet in three-dimensional flows is essential to enable successful inception in various engineering applications especially in the aerospace industry.

Synthetic jets may be applied either in a distributed manner or from localised sources also oscillatory streaming motions can be induced in the fluid acoustically through the transmission of sound or 'acoustic streaming' [16], [17]. A case in hand of acoustic excitation is the work of Kim and Durbin [18] of a uniform acoustic field applied symmetrically from a distance to the airflow interacting with the sphere in the Reynolds number range of  $500 < Re < 60,000$ . The results indicated that when the acoustic excitation was near to the natural instability of the flow a decrease in the wake size occurred as a consequence of the separation point being delayed and pushed further downstream towards the wake region. This created a rapidly thickening but broader and shorter recirculation zone from the inwardly directed shear layer. This also produced a lower base pressure behind the sphere and possibly in the near wake region with a higher velocity in the recirculation zone as a result of a reduced size of the separation bubble. Since the forcing was being applied away from the body, an increase in the turbulence level with a consequent increase in the base pressure over the body was produced which then resulted in higher drag.

Additionally experimental investigations carried out by Jeon et al. [16] on a sphere with a uniform acoustic field emanating from a slot located at an angle of  $76^\circ$  from the fore stagnation point but equally distributed circumferentially around the sphere, showed that for forcing frequencies equal to or greater than the critical frequency,  $St = 2.85$  or 190Hz, there was a reduction in drag of nearly 50%. This forcing frequency corresponded to the boundary-layer instability frequency that was the high shear-layer instability frequency. . The boundary layer instability frequency falls in between the low wake instability frequency (vortex shedding) and the high shear layer instability frequency which at this Reynolds number are  $St = 0.18$  and  $St = 10$  respectively. The works of Kim and Durbin [18] as described above showed that the reverse flow region became stronger and that the total drag was increased with acoustic forcing. Jeong et al. [16] has suggested that the mechanism for reducing drag at the critical frequency could be due to the corresponding high frequency boundary-layer instability.

Further to this, synthetic jet can be applied in a distributed manner. The work by Glezer and Amitay [15] with a synthetic jet placed locally on one side of a cylinder showed a reduction in surface pressure both upstream and downstream of the forcing location and induction of a local separation bubble above the location of the synthetic jet and the "virtual aeroshaping" [19] of the body that was responsible for the substantial reduction in drag values. It is not well established as to when or under what conditions these bubbles will form particularly in three-dimensional flows with the synthetic jet impinging on the cross-flow and forming a recirculation zone.

The present study was therefore conducted to contribute to the need for three-dimensional experimental work in an effort to gain a further understanding of the three-dimensional effects encountered when applying a synthetic jet on a three-dimensional body in a crossflow. A parallel purpose of this present study is to investigate the validity of using a five hole probe to measure the total and static pressures at a point and then indirectly calculate the velocities in a highly three-dimensional wake. Since the flow over the sphere is a true three-dimensional flow it also being a simple and symmetrical three-dimensional bluff body this became a suitable choice with which to perform our experiments. The present study presents a rather straightforward and effective way to examine the three-dimensional behavior of the bluff body in terms of boundary layer growth, skin friction, separation of flow and pressure drag changes in three-dimensions under the influence of a localized synthetic jet. Designing the experiment in this fashion provides the distinct

advantage of being able describe the influence of the synthetic jet at a particular angular location relative to the free stream.

It is interesting to note that the maximum Reynolds number at which Kim and Durbin [18] and Jeong et al. [16] conducted their experiments form approximately the two limits of the plateau like region on the CD curve for a sphere [20] where the drag practically remains unchanged with changes in the Reynolds number. It appears that the effect of a localised synthetic jet on the flow over a sphere at a Reynolds number that lies within those limits would be a suitable choice and the present study was, therefore, conducted at a Reynolds number of  $5 \times 10^4$ .

### 2.2.2 Experiment

The experimental work was conducted using an 18" x 18" open circuit, closed test section, NPL type wind tunnel at UNSW aerodynamics laboratory [21], [22]. The wind tunnel was operated at an air speed of  $10 \text{ms}^{-1}$ . The bluff body used for the experiments was an aluminium sphere of 80mm diameter and supported horizontally by a rod attached to one side of the sphere. Using the method of Rae and Pope [23], the blockage ratio was calculated to be 2.8%. Additional velocity profiles obtained using hot-wire anemometry on the centreline plane of the sphere showed little or no difference from the free stream velocity profile confirming that tunnel blockage was negligible. The sphere was designed with a synthetic jet orifice (labelled SJ in Fig. 6) of 1 mm diameter and oriented at a  $45^\circ$  tangent to the normal of the sphere surface and seven pressure ports or tapping points (numbered 1, 2, 3, 4, 5, 6, 7) on the centreline axis of the sphere (Fig. 6). The sphere was rotated to each predetermined angular position after which the wake survey measurements were taken. The synthetic jet actuator was composed of a modified compressor and a 12V power supply. The compressor piston was fitted with a one-way valve that was modified to cause suction and blowing as it reciprocated instead of constant compression of the air. The compressor line was connected to the synthetic jet orifice on the sphere using silicon tubing. The sphere support was fitted against a fixed protractor to measure the angle of rotation.

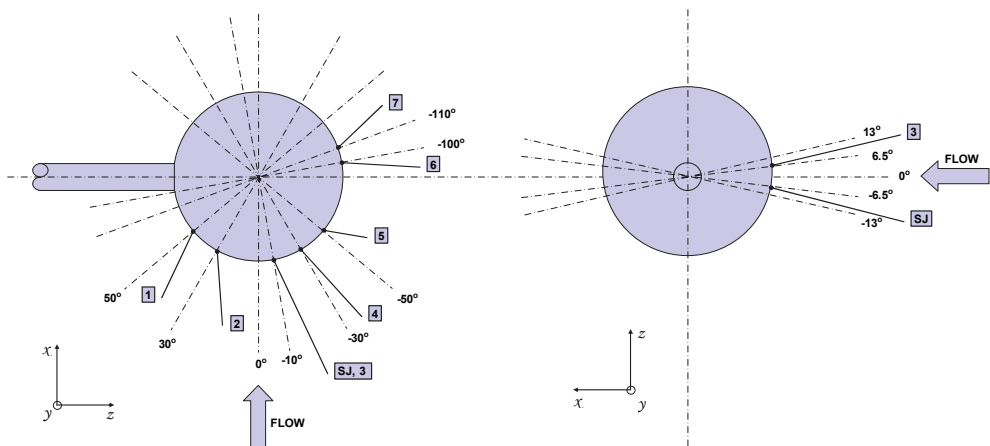


Fig. 6. Schematic diagrams of sphere: Plan view (left), Elevation view (right)

The velocity of the synthetic jet was measured using a Dantec Streamline CTA Anemometer system with a 55P14 probe. The probe was calibrated using the Dantec Flow Calibration System. The voltage supplied to the motor was through a DC power supply unit to generate the desired frequency with a range of 10Hz up to 75Hz. The frequency obtained from hot-wire measurement was cross-checked against the rotational speed of the motor using a laser tachometer. Since the hot-wire measurement was indifferent to flow direction and the two extremes, that is blowing and suction, were 180 degrees out of phase, the peaks are both positive for suction and blowing. The maximum velocity measured was about  $35 \text{ ms}^{-1}$ , and its rms value was  $15 \text{ ms}^{-1}$ . The actuation frequency was  $f = 60 \text{ Hz}$  that corresponded to a Strouhal number of  $St = 0.53$ . This value was chosen to avoid correlation with the low wake instability frequency (vortex shedding frequency) and the high instability frequency (separating shear layer instability frequency) which are at  $St = 0.19$  and  $St = 6$  respectively at the present Reynolds number. Rather than examining the effect of the synthetic jet as targeted towards flow instabilities this paper focuses on the mechanism of momentum transfer as a means to control the flow over the sphere and thereby improve aerodynamic performance through a reduction in drag. Work on a two-dimensional body [17] has shown an improvement in the delay of separation for a Strouhal number of 2.5 for a circular cylinder. Whether similar improvement of the flow over three-dimensional flow can be obtained with the application of the localised synthetic jet was, therefore, a major motivation of this project.

## 2.2.3 Results and discussions

### 2.2.3.1 Qualitative: Flow visualization

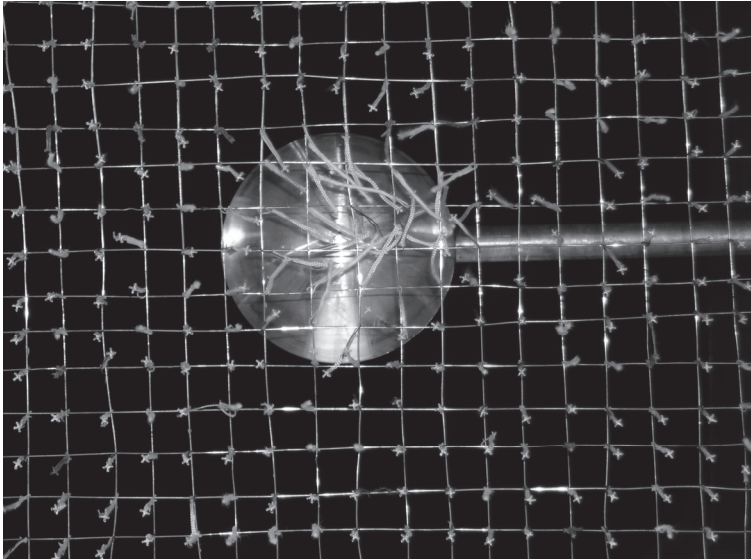
The flow visualisation using the tufts was intended to provide some qualitative clarity regarding the improvement in flow due to the activation of the synthetic jet. The synthetic jet was orientated at an angle of  $80^\circ$  which is approximately the location of separation for a standard sphere Schlichting [20]. Figs. 7a to 7d are flow visualisation results observed at wind speed of  $10 \text{ ms}^{-1}$ . Figs. 7a and 7b show that the flow is reversing as evidenced by the tufts tending to curl back onto the screen and flutter back towards the sphere. In Figs 7c and 7d, also at an airspeed of  $10 \text{ m/s}$ , a different picture emerges and the tufts can be seen pointing back in the streamwise flow direction. This shows a significant straightening of the flow field in the wake of the sphere.

Fig. 8c shows the flow pattern of the tufts at  $10 \text{ ms}^{-1}$  with the synthetic jet activated at  $50 \text{ mm}$  from the sphere. This flow pattern is similar to a wake flow pattern of  $20 \text{ ms}^{-1}$  at  $40 \text{ mm}$  from the sphere surface as shown in Figs. 8a and Fig. 8b which has the tufts at  $80 \text{ mm}$  from the sphere surface without the synthetic jet activated. These figures suggest that the wake of the sphere has been shortened by approximately  $30 \text{ mm}$  when synthetic jet is activated.

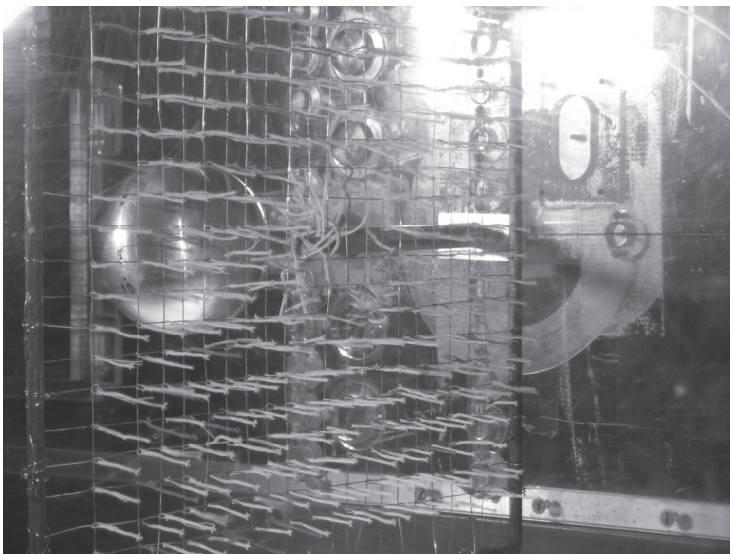
### 2.2.3.2 Quantitative: Wake flow field measurement

The wake flow field was defined in terms of velocity information obtained using pressure measurements from the five-hole probe and then plotted as 3-dimensional velocity vectors in Figs. 9(a) to 9(d) using the Matlab software program.

The difference in velocity field when the synthetic jet is activated can be seen by the increase in vector magnitude and a straightening of the vectors. The decrease in wake region also provides evidence of the effectiveness of the synthetic jet. These 3-dimensional vector plots correspond to the results of the flow visualisation where we see in both types of results a shortening of the wake region by approximately  $30 \text{ mm}$ .

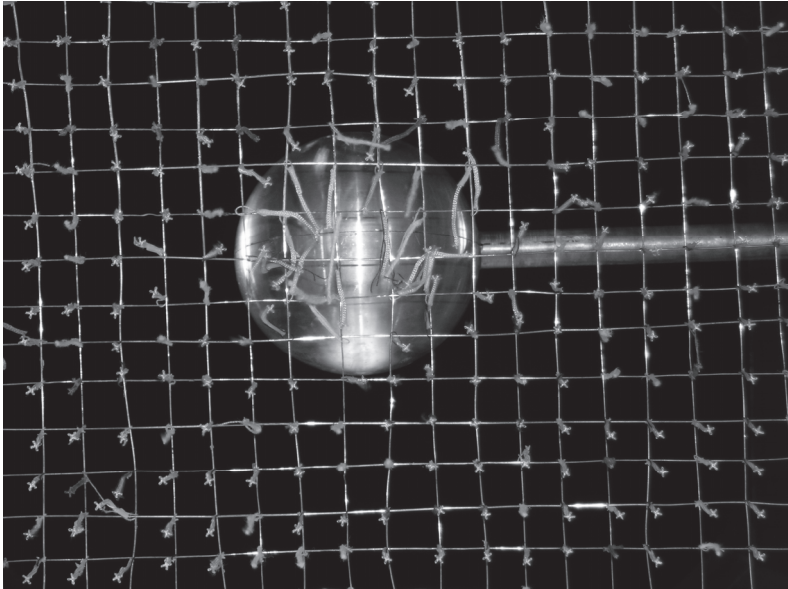


(a)

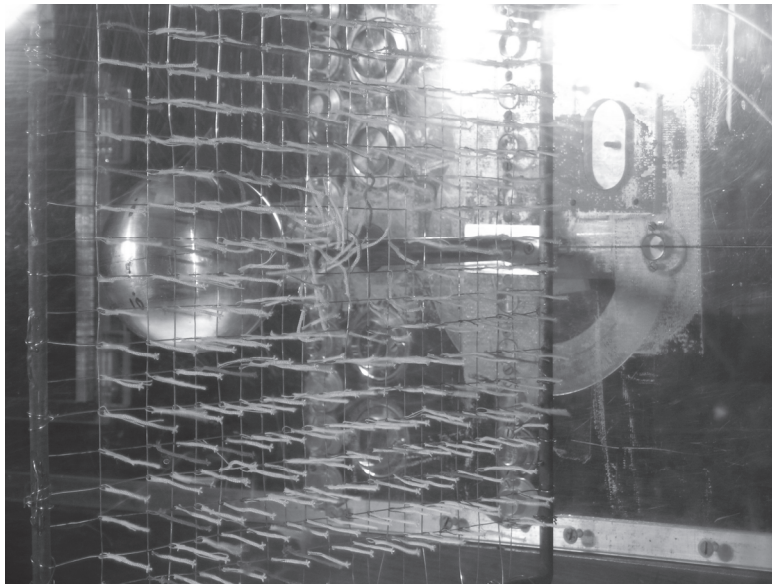


(b)



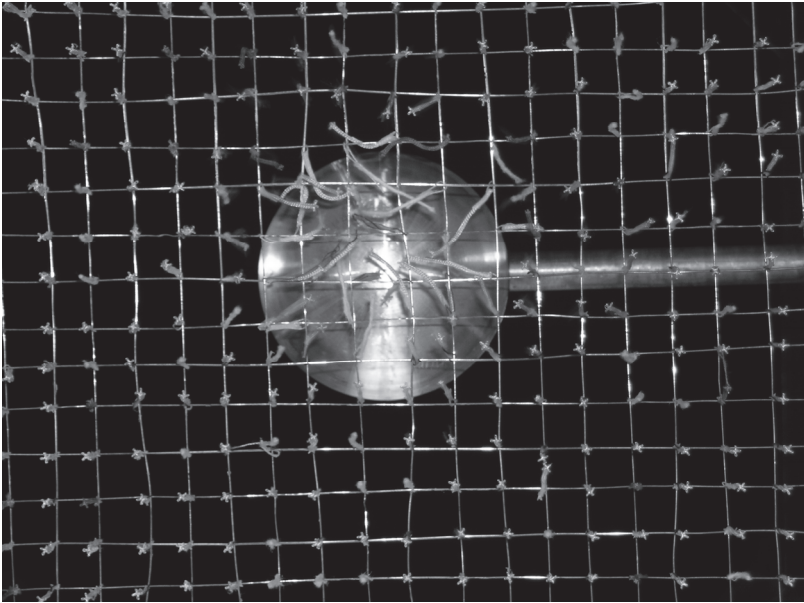


(c)

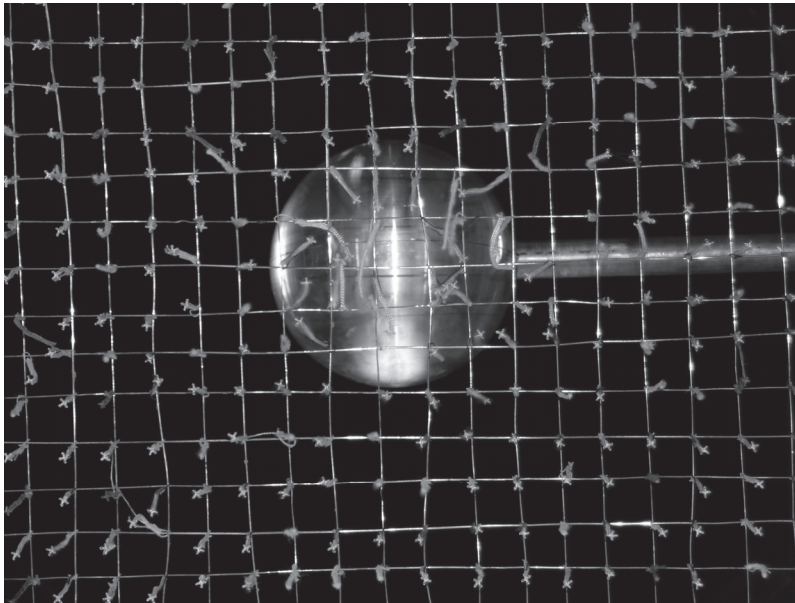


(d)

Fig. 7. (a) 10m/s without synthetic jet. Tuft screen 40mm off-set.; (b) side view of (a) ; (c) 10m/s with synthetic jet. Tuft screen 40mm offset. (d) side view of (c)

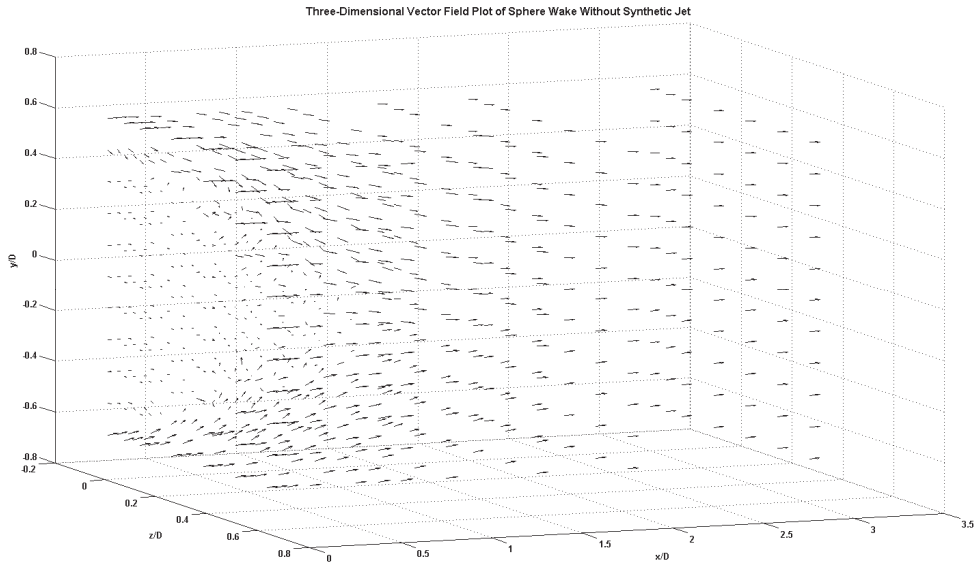


(a)

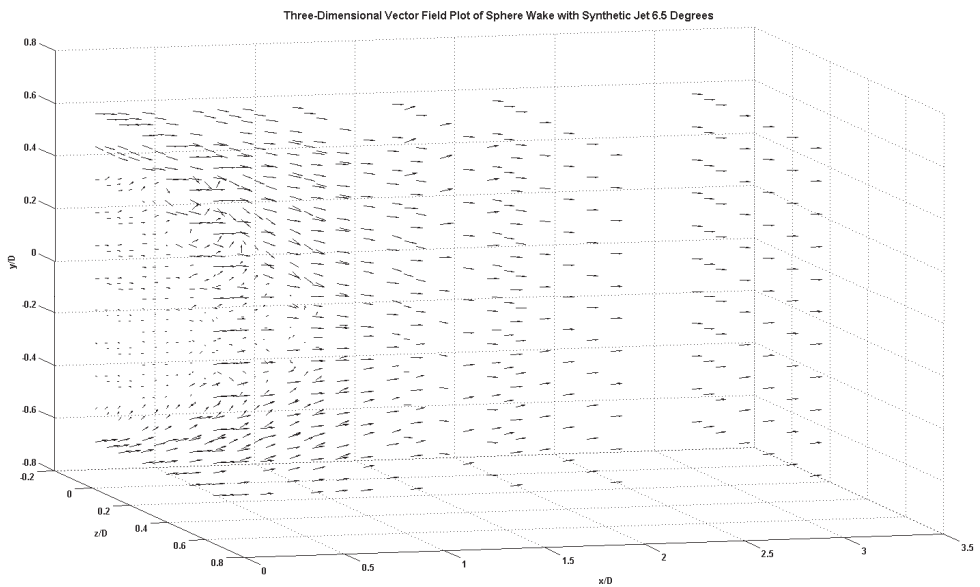


(b)

Fig. 8. (a) 20m/s with synthetic jet. Tuft screen at 40mm offset; (b) 10 m/s without synthetic jet. Tuft screen at 80mm offset ; (c). 10 m/s without synthetic jet. Tuft screen at 50mm offset.



(a)



(b)

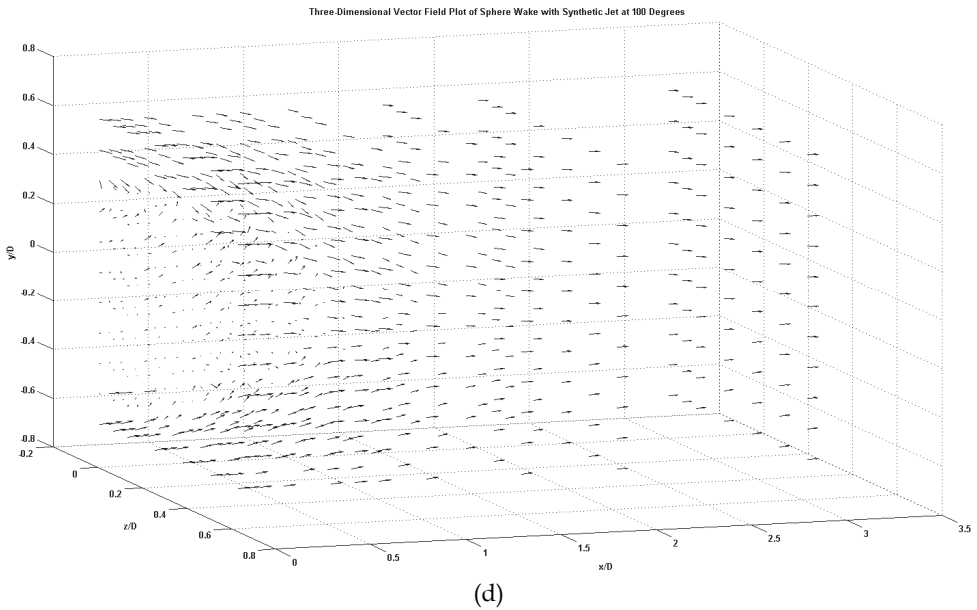
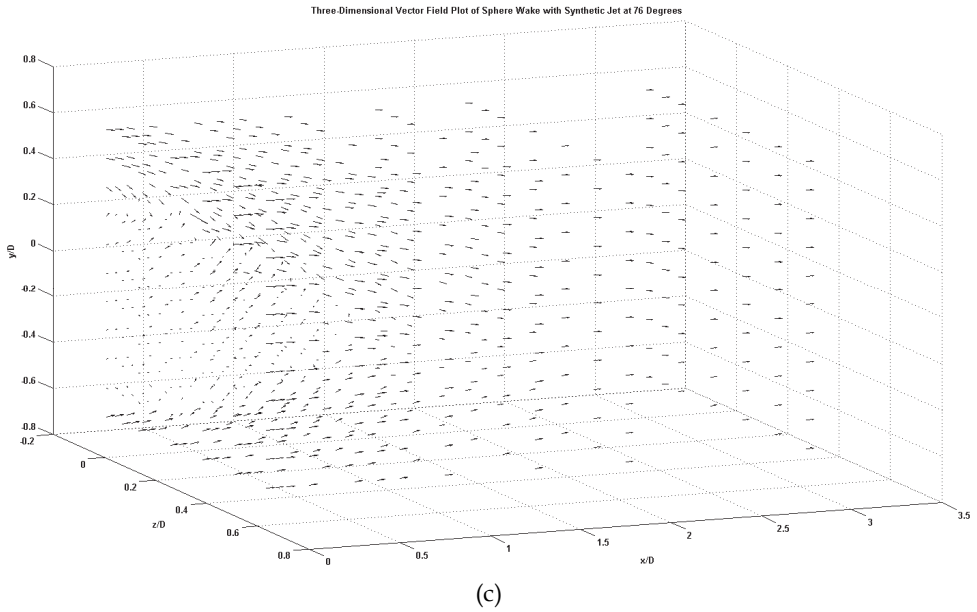


Fig. 9. (a). 3-D Vector Field Plot of Sphere Wake Without Synthetic Jet ; (b). 3-D Vector Field Plot of Sphere Wake with Synthetic Jet at 6.5 Deg; (c). 3D Vector Field Plot of Sphere Wake with Synthetic Jet at 76 Deg; (d). Three-Dimensional Vector Field Plot of Sphere Wake with Synthetic Jet at 100 Degrees

The underlying motivation is to understand the behaviour of fluid flow with a change in the flow velocity as the Reynolds Number varies with the influence of the localised synthetic jet. In the present work we show that global changes occur to the wake of sphere at the much lower angle of incidence of the synthetic jet location of  $6.5^\circ$  above the stagnation point and a higher momentum coefficient of  $2.8 \times 10^{-3}$ . Furthermore the works of Glezer and Amitay [17] show that for an angle of incidence of  $60^\circ$  that the velocity profile is reduced, that is the velocity defect is reduced, and thus this shows that the drag has been reduced. This also occurs at the lower angle of  $6.5^\circ$  for the sphere although with a lesser effect at this angle as would be expected since at this angle the effects of the synthetic jet have been much reduced since the vortices emanating from the synthetic jet orifice have a greater distance to travel inside the boundary-layer and thus the effects of skin friction would also dissipate the energy of the added effects of the synthetic jet. Whereas when we place the synthetic jet at an angle of  $76^\circ$  the added energy of the synthetic jet can affect the shear layers of the flow and thus have a straightening effect on the flow over the sphere. Thus the velocity defect in the wake region is much reduced and thus the drag which is due to pressure drag is reduced also. Since the majority of the drag for the sphere is due to the pressure drag the synthetic jet at  $76^\circ$  produces a greater reduction on drag than when the synthetic jet is at  $6.5^\circ$  which produces a reduction in skin friction drag as well some reduction although a lot less in form or pressure drag than when the synthetic jet is angled at  $76^\circ$ .

## 2.2.4 Conclusions

This flow study has shown a localised synthetic jet is an effective tool for aero-shaping typical 3-dimensional bluff bodies. The change in the coefficient of pressure is effectible over the surface of the sphere by placing the synthetic jet at a location upstream or downstream of the separation point as was the case with the cylinder experiments conducted by Glezer and Amitay[7]. The synthetic jet influence decreases as the distance from the centre of the sphere increases.

The wake region of the sphere was decreased through the use of the synthetic jet at both angular locations. The synthetic jet has the effect of tripping the flow and preventing recirculation or reversal of flow in the wake of the sphere. The wake region was seen to decrease by approximately 30mm at an airspeed of 10m/s. The 3-dimensional velocity field with the synthetic jet operating indicates an increase in the streamwise component. Indicating that the possible flow reversal has been eliminated and vorticity has been lessened.

The localised synthetic jet with a cross flow Reynolds number of  $5.1 \times 10^4$  produces a different effect on the flow field according to its location on the sphere body. When the synthetic jet is located at an angle of  $6.5^\circ$  from the stagnation point we find similarities with that of the cylinder with a reduction in the wake size of the sphere and a corresponding reduction in the drag on the sphere. Changes in the flow occur upstream and downstream of the actuation point giving rise to global effects on the flow that become reduced the further away the point is from the synthetic jet.

When the synthetic jet is placed at an angle of incidence of  $76^\circ$  the effects of localisation of the synthetic jet are amplified since the flow has almost reached the separation point. The wake region is affected more so than with the case when the synthetic jet is angled at  $6.5^\circ$ . This would suggest that less aero-shaping is occurring on the sphere surface and more energy is placed into wake modification. Although even in the wake there is more of a localised affect in the plane of the synthetic jet actuation.

The synthetic jet is capable of improving the aerodynamic performance of 3-dimensional bluff bodies through the aero-shaping mechanism. The location of the jet closer to the stagnation point of the sphere affects the flow field globally more so than when it was located closer to the separation point since its affect was more so limited to the upper hemisphere. The synthetic jet in the wake of the sphere also improves the aerodynamic performance since the momentum of the synthetic jet is mostly transferred to the wake of sphere and does not interact with the boundary layer.

## **2.3 Investigation of air jet vortex generator for active flow control**

### **2.3.1 Background information**

The maximum normal force coefficient ( $C_n$ ) that can be generated by a single element airfoil may be limited by flow separation, which can occur at higher angles of attack. This phenomenon can often result in a sharp drop in lift coefficient ( $C_l$ ), along with an associated rise in the pressure drag coefficient ( $C_{dp}$ ), thus; reducing the magnitude of flow separation is an attractive proposition with respect to improving the performance of an airfoil.

Flow separation appears to be a complex phenomenon that occurs due to a combination of fluid viscosity and adverse pressure gradients [24]. Adverse pressure gradients may reduce the relative motion between the various fluid particles within the boundary layer. If this relative motion is reduced to a sufficient degree, the boundary layer may separate from the surface [25].

Furnishing the boundary layer with additional momentum may allow greater penetration against adverse pressure gradients with a concomitant reduction in the magnitude of flow separation. Generating a series of longitudinal vortices over the airfoil surface appears to be one mechanism for achieving this aim [26]. This series of vortices may act in a manner such that high momentum fluid in the ambient flow field is brought down to the near wall region furnishing the boundary layer with additional momentum [27].

Longitudinal vortices can be generated by issuing small jets of air from the surface of the airfoil. The first practical application of the technique is usually attributed to Wallis [28]. Since this study, much research has been carried out on Air Jet Vortex Generators (AJVG's), where reductions in flow separation have been demonstrated under laboratory conditions on two dimensional wings undergoing cyclical [29] and non-cyclical [30] changes in angle of attack. In addition, AJVGs have successfully increased the power output of full-sized wind turbines [31]. Reducing the energy consumption required to achieve a given reduction in flow separation will further extend the utility of AJVGs as a technique for enhancing the performance of airfoils. The desirability of parameters such as the pitch and skew of the jet axis [32], as well as the orientation [33] and preference [34] for rectangular orifices appears to be relatively well established.

The key to further reductions in energy requirements may lie with studies focussing on the detailed dynamics of fluid jet behaviour. Experiments with jets issuing into quiescent bodies of fluid demonstrated the enhanced penetration of jet fluid that was either started impulsively [35], or issued in a non-steady manner with respect to time [36].

Studies conducted with fluid jets issuing into cross flows are particularly relevant to separation control applications about airfoils. Adding a non-steady characteristic to the jet injection scheme appears to allow the jet fluid to penetrate much further into a cross flow compared to a fluid jet issuing in a steady manner [37][38][39]. The exponential injection scheme of Eroglu & Breidenthal [40] however, appears to hold the most promise in terms of a practical application as a separation control device for airfoils as the velocity profile varies with space, not time.

The main features of the exponential jet are an injection width that increases by a given factor of "e" (2.71828), and a fluid injection velocity profile that also increases by the same given factor of "e". The vortices generated with the device appeared to penetrate much further into the cross flow whilst also having a reduced mixing rate with the ambient fluid. A possible explanation for this behaviour suggests that the exponential parameters places high momentum jet fluid into the vortices, preventing premature weakening of this structure due to entrainment of low momentum cross flow fluid [41].

This behaviour may have interesting applications for controlling flow separation about airfoils. If the premature weakening of a vortex can be prevented, and that same vortex can effectively reduce the magnitude of flow separation, it may be possible to reduce the energy requirements associated with reducing the magnitude of flow separation.

### 2.3.2 Experiment

The exponential nozzle features an injection width and injection velocity profile that both increase by a given factor of "e". An injection width and injection velocity profile that increased once by a factor of "e" was chosen for the present experiment. The initial injection width ( $D_0$ ) chosen was 1.5mm, with the total injection length along the nozzle ( $X_e$ ) set at 4mm. The width of the exponential nozzle thus increased from 1.5mm to approximately 4.08mm ( $1.5 \times e$ ) over a distance of 4mm.

The exponential nozzle was discretised into four closely spaced, individual rectangular orifices (Fig. 10). The skew and pitch angles were set at 60 degrees and 30 degrees respectively, as this combination of angles produced good results in prior studies under condition of cyclical [29] and non-cyclical changes in angle of attack [30].

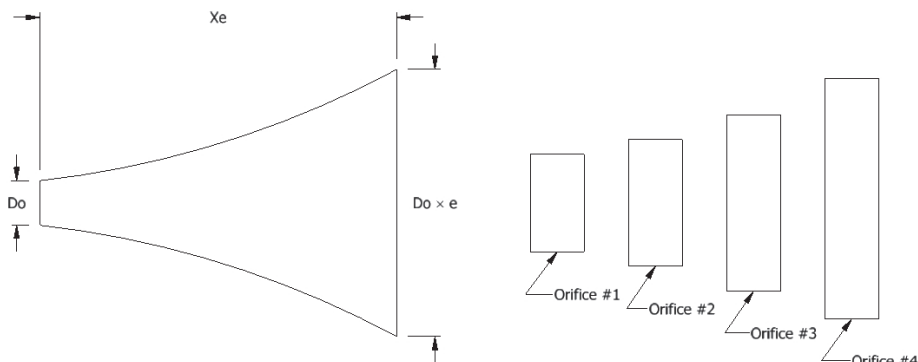


Fig. 10. Exponential nozzle & discretised equivalent

A NACA 63-421 airfoil was equipped with an array of 24 nozzles spaced at 30mm intervals positioned at the 12.5% chord wise location. The nozzles were configured to produce a co-rotating series of vortices, and are similar in layout to previous studies [31][42]. The array of nozzles was designed as a homogenous structure along with the leading edge section of the airfoil and the plenum chambers supplying air to the jets (Fig. 11).

Each of the four individual rectangular orifices making up each exponential AJVG were connected to a common plenum chamber, thus; plenum chamber one was connected to, and

supplied air to all 24 rectangular orifices labelled as #1 (Fig 10). This arrangement was mirrored for the other three orifices, and is shown in greater detail in Fig.11.

To promote an even pressure distribution along the AJVG array, perforated brass tubes were inserted into each plenum chamber. The brass tubes were fed from both ends with pressurised air, thus minimising any static pressure variations along their length. The pressurised air was metered through conical entrance orifice plate [43][44][45] assemblies to allow measurement of the mass flow rate entering each of the four plenum chambers (Fig. 12).

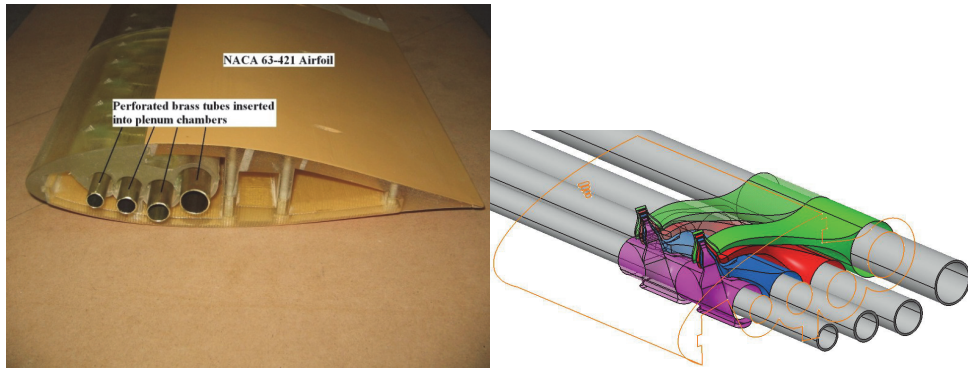


Fig. 11. Nozzle array detail

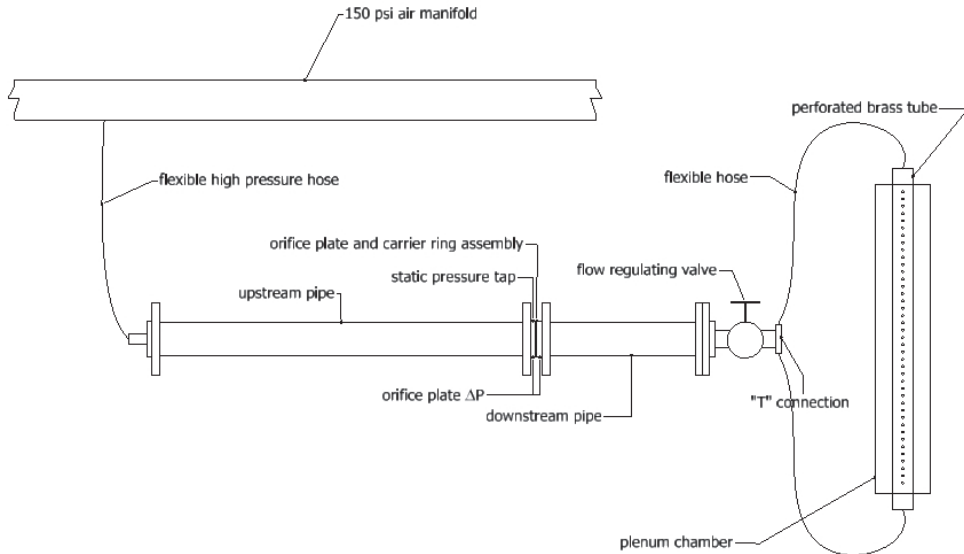


Fig. 12. Air supply schematic



The airfoil consisted of a central section equipped with jets spanning 740mm. End plates were attached to the central section to promote two dimensional flow over the airfoil. End pieces of the same NACA 63-421 section were used to make up the full distance to the wind tunnel test section walls. The end pieces were not equipped with jets. The central part of the airfoil was constructed from Fullcure 720® polymer on an Objet Eden 260® rapid prototyping machine

Testing was conducted in the 900mm x 1200mm test section of the large, closed circuit, subsonic wind tunnel located in the aerodynamics laboratory of the University of New South Wales. Testing was conducted at a velocity of 40m/s, which resulted in a Reynolds number of approximately  $6.4 \times 10^5$  based on the airfoil chord length of 250mm. The Reynolds number was the maximum achievable whilst keeping tunnel heating issues and errors due to blockage effects manageable. The airfoil was mounted vertically to minimise the blockage ratio, with testing conducted under conditions of free transition. The airfoil was equipped with three rows of static pressure taps, with 48 taps in each row. One row was located in the middle of the central span, with auxiliary rows 90mm either side of centre. The static pressure taps were connected to a multi-tube water manometer, where the pressures taken from the centre row of taps were integrated to establish  $C_n$  and the tangential force coefficient ( $C_t$ ).

The air jet injection velocities were measured using a Dantec® hotwire system. Velocity readings were taken from each of the four individual orifices making up the AJVG located nearest the centre-line of the airfoil, as well as the AJVG located on the extreme left hand side of the central airfoil section. Readings were taken at the start and finish of each test run, with all four sets of figures compensated for temperature, and averaged to establish the final velocity figures.

### 2.3.3 Results and discussions

#### 2.3.3.1 Exponential jet

The behaviour of the vortice generated by the exponential jet is affected by the relationship between the base velocity chosen for the exponential velocity injection profile ( $V_0$ ), and the velocity of the cross flow ( $V_\infty$ ). Relating these two parameters to the ratio of  $X_e$  and  $D_o$  appeared to maximise the penetration and lifespan of the vortice [40] (Eqn. 1). For the particular orifice geometry chosen ( $D_0 = 1.5\text{mm}$ ,  $X_e = 4\text{mm}$ ), the ideal ratio between  $V_\infty$  and  $V_0$  is 2.67, which gives a  $V_0$  of 15m/s for the wind tunnel velocity of 40m/s. This set of parameters is referred to as the "design condition" forthwith.

$$V_\infty = \frac{X_e}{D_o} V_0 \quad (\text{Eqn.1})$$

Two main groups of velocity profiles were thus formulated in order to test the exponential jet. The first group featured an injection velocity that increased once by a factor of "e". As with the injection width of the jet, the exponential velocity profiles were discretised into a stepwise increase in velocity (Table 1). The second group of velocity profiles had the same injection velocity across the four orifices

The mass flow rate ( $\dot{m}$ ) entering each plenum along with the measured jet velocities ( $v_{\text{jet}}$ ), dynamic pressure and wing area ( $\frac{1}{2} \rho v^2 A$ ) were combined to establish the momentum coefficient ( $C_\mu$ ), which provides an indication of the energy being consumed by the AJVG array (Eqn.2).

$$C_{\mu} = \frac{2\dot{m}v_{jet}}{\rho v^2 A} \tag{Eqn.2}$$

$V_0$ (m/s)	Orifice #1 (m/s)	Orifice #2 (m/s)	Orifice #3 (m/s)	Orifice #4 (m/s)
15	17.13	21.99	28.24	36.26
21.6	24.67	31.67	40.67	52.22
27.5	31.41	40.33	51.78	66.49
32.3	36.89	47.36	60.82	78.09
38	43.39	55.72	71.55	91.87
43.1	49.22	63.2	81.15	104.2
53.8	61.44	78.89	101.29	130.07
64.6	73.77	94.72	121.63	156.18

Table 1. Discretised exponential velocity profiles

$C_l$  is plotted as a function of angle of attack (AOA) in Fig 13. All the velocity profiles tested produced measurable gains in lift coefficient when compared to the baseline configuration with the jet array switched off. The lift curves appear to have a significant plateau region prior to the stall angle of attack, which itself appears to be affected by the operation of the jet array. The presented data has not yet been corrected for wall interference or streamline curvature, which may provide a possible explanation for this behaviour.

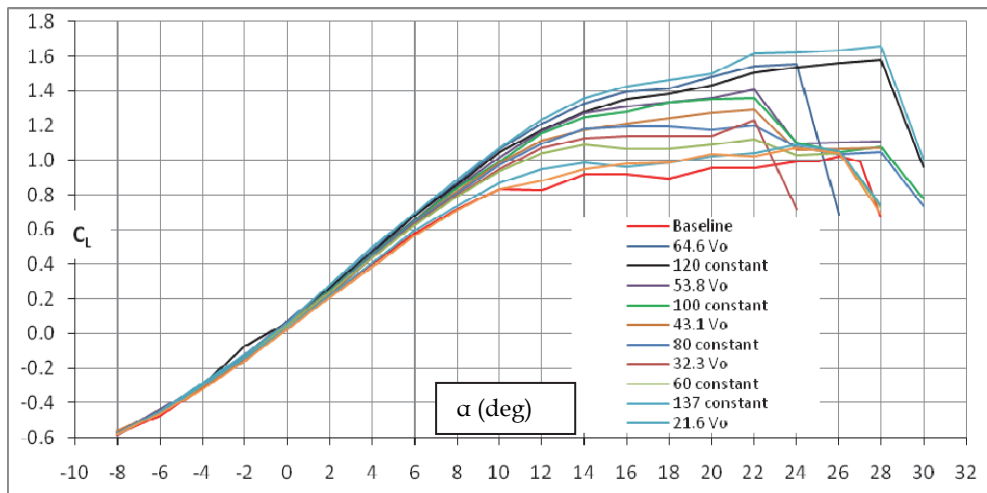


Fig. 13. Lift coefficient vs. Angle of Attack

The average, incremental increase in  $C_l$  over the baseline configuration (AJVG array off) was calculated for AOA's between 0-22 degrees. This range was selected as all the velocity profiles tested were able to produce positive incremental gains in  $C_l$  over this range of incidence angles. The total  $C_{\mu}$  was measured at each AOA tested, with the corresponding figures for the 0-22 degrees incidence range averaged to give a final figure for comparison (Fig. 14). For average incremental increases in  $C_l$  between 0.023 - 0.18, the exponential velocity profiles ( $V_0$ ) appeared to have a lower overall  $C_{\mu}$  requirement. Above this range of lift coefficients, the constant velocity profiles provided gains in  $C_l$  for less  $C_{\mu}$ .

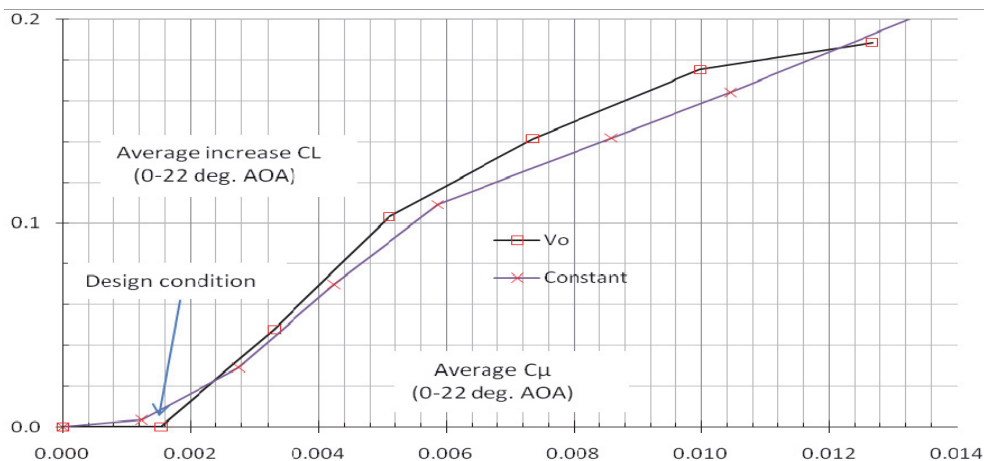


Fig. 14. Incremental increase in  $C_l$  vs.  $C_{\mu}$  (0-22degrees AOA)

The greatest increase in energy efficiency appears to occur for the incremental  $C_l$  increase of 0.16, where the exponential jet has a  $C_{\mu}$  about 12% less than that associated with using a constant injection velocity profile.

Interestingly, the exponential jet appears to provide the greatest advantages for a range of  $C_{\mu}$  that are somewhat beyond that associated with the design condition of the jet. The original study featured an exponential jet where the injection width and injection velocity profile both increased by a factor of "e" three times over a total injection length ( $X_e$ ) of 90mm. The jet was mounted on a flat plate (minimal pressure gradient) and used water as the working fluid [40]. This is in stark contrast to the present study, and may provide some possible explanations into the behaviour observed in Fig 14.

### 2.3.3.2 Multiple orifice AJVGs

Earlier studies conducted on AJVG's consisting of a series of closely space orifices appeared to indicate that the additional energy expended did not justify the incremental gains produced [9]. To gain a greater understanding of the phenomenon, two velocity profiles were tested at a fixed AOA (14 degrees).

The air jets issuing from the individual orifices were switched off in sequence, and the resulting change in lift coefficient calculated (Table 2).

43.1 Vo	$C_L$	$\Delta C_L$	$C_\mu$	$\Delta C_\mu$	$\Delta C_L / \Delta C_\mu$
All on	1.217	0	0.012882	0	0
#1 off	1.209	0.008	0.012599	0.000283	28.268
#1,2 off	1.197	0.012	0.011621	0.000978	12.260
#1,2,3 off	1.190	0.007	0.008851	0.002769	2.527
All off	0.936	0.254	0	0.008851	28.697
All on	1.182	0	0.012882	0	0
#4 off	1.075	0.107	0.004031	0.008851	12.089
#3,4 off	1.004	0.071	0.001261	0.002769	25.641
#2,3,4 off	0.977	0.027	0.000282	0.000979	27.579
All off	0.931	0.046	0	0.000283	162.544
80 constant	$C_L$	$\Delta C_L$	$C_\mu$	$\Delta C_\mu$	$\Delta C_L / \Delta C_\mu$
All on	1.201	0	0.010992	0	0
#1 off	1.168	0.033	0.009602	0.00139	23.741
#1,2 off	1.160	0.008	0.007727	0.001875	4.267
#1,2,3 off	1.143	0.017	0.005009	0.002718	6.254
All off	0.925	0.218	0	0.005009	43.522
All on	1.176	0	0.010992	0	0
#4 off	1.118	0.058	0.005983	0.00509	11.395
#3,4 off	1.069	0.049	0.003265	0.002718	18.028
#2,3,4 off	1.054	0.015	0.00139	0.001875	8.0
All off	0.919	0.135	0	0.00139	97.122

Table 2. Incremental changes in lift coefficient

The 43.1  $V_0$  and 80 constant velocity profiles were chosen as they both exhibited similar behaviour in terms of  $C_l$  vs. AOA compared with the baseline configuration (Fig. 13). In both instances, measurable changes in lift coefficient were detected whenever the air supply to a plenum chamber was turned off.

$C_\mu$  is often added to  $C_d$  to get a better picture of the overall “penalty” associated with supplying air to an AJVG array. Fig. 15 plots the ratio of  $C_l$  and the sum of  $C_{dp}$  and  $C_\mu$ . Beyond an AOA of 12.5 degrees, it appears that  $C_l / (C_{dp} + C_\mu)$  with the jets operating is superior to  $C_l / C_{dp}$  of the airfoil alone when the jets are switched off.

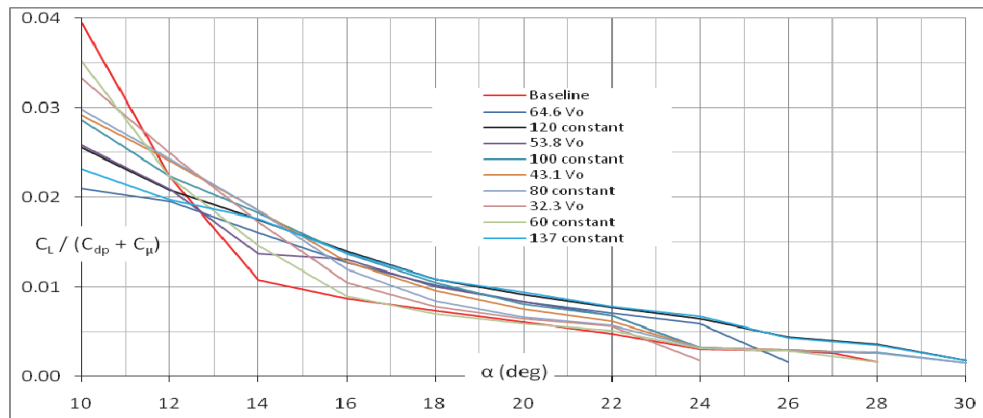


Fig. 15.  $C_1$  vs.  $(C_{dp} + C_{\mu})$

Taken together, the results of Fig. 14, Fig. 15 and Table 2 appear to suggest that an AJVG consisting of multiple, closely spaced orifices produces worthwhile performance gains. These performance gains may be enhanced further by using an injection width and injection velocity profile that both increase by some given factor of “e”.

### 2.3.4 Conclusions

An AJVG consisting of a geometrically related series of orifices was tested experimentally to determine the ability of the device to reduce the magnitude of flow separation about a NACA 63-421 airfoil. The incremental gains in  $C_1$  were measured along with the  $C_{\mu}$  consumed by the AJVG array. For a given, average incremental increase in  $C_1$  between 0.023 - 0.18, injection velocity profiles featuring an exponential characteristic provided performance gains for less  $C_{\mu}$  compared with a constant injection velocity profiles. The greatest increase in energy efficiency appeared for the incremental  $C_1$  increase of 0.16, where a reduction in  $C_{\mu}$  of about 12% was measured.

### 2.4 Investigation of wind driven ventilator for performance enhancement

Greater environmental awareness in affluent and developing countries has lead people to increasingly question the nature of progress of modern day society under pinned by technological development which in the process has also given rise to unnatural contingencies of energy utilization that have the potential to destroy the very environment which sustains life. People are, therefore, looking towards alternative energy systems that can alter the present energy use patterns that have lead to this dilemma.

One such energy system that is finding widespread use in different parts of the world is the use of natural wind as an energy source. Products such as rotating ventilators are finding use in domestic, commercial or industrial building or transport vehicles to provide optimum or at least some satisfactory environment [46], [47] in which to live or work. A rotating ventilator which is simple in structure, light in weight, cheap to install and costs nothing to operate is, therefore, proving to be an environmental friendly air extraction device. A picture of a rotating ventilator in use on the roof top of a commercial building is shown in Fig. 16.



Fig. 16. Rotating ventilators in use on the roof top of building at the University of New South Wales

Generally speaking, a rotating ventilator is operated by the action of centrifugal force by creating a pressure difference, which helps expel the air out from inside a confined space. The device uses atmospheric air to rotate the ventilator head and consequently create the suction required. This suction is used to evacuate the contaminated air from the confined space. Many of these ventilators have evolved through trial and error and the flow physics associated with these ventilators is barely understood. Apart from some recent works carried out at the University of New South Wales [48], [49], [50], very little aerodynamic investigation has been carried out on the performance or operation of wind driven ventilating device. Consequently, there is a real need to improve the performance of existing roof top ventilator under various weather conditions, particularly in rain. To achieve this, a better knowledge of the aerodynamics of the flow field around the ventilator is essential. The motivation for this work is, therefore, to obtain some preliminary information of the flow to lay down the foundation of a more effective investigative wake traverse technique [51] to define performance characteristics. Although the total lift or the total drag on a ventilator can be obtained using pressure transducer or a force balance, an accurate determination of the profile and induced drag components of the total drag, however, is not easy. Recent innovative developments of techniques [2], [3], [52], [53] at the University of New South Wales for measurement in highly complex flow appear to offer the prospect of developing an effective three dimensional wake traverse technique for use in such

situations. These considerations, therefore, prompted the formulation of the present project. Qualitative investigation of the internal flow and how it exhausts into open atmosphere is, therefore, the main objective of this study. Two differently designed rotating ventilators were used for this purpose. Some hot-wire results were also obtained to determine the mass flow extraction rate of these two ventilators.

## 2.4.1 Experiment

### 2.4.1.1 Description of wind tunnel test facility

The wind tunnel, Fig.17, used for the test is of the open circuit type. The wind speed is variable from 0 to 30m/s, air being drawn at the rounded intake by an eight bladed axial flow fan with nine down stream flow straighteners. The fan is driven by a 17.5kw variable speed DC motor. After leaving the fan, the air stream passes through a conical angle diffuser with concentric cone flow stabilizers, one flow stabilizing screen, three flow smoothing screens and a 6:1 contraction, before discharging at the 760mm diameter open test section.

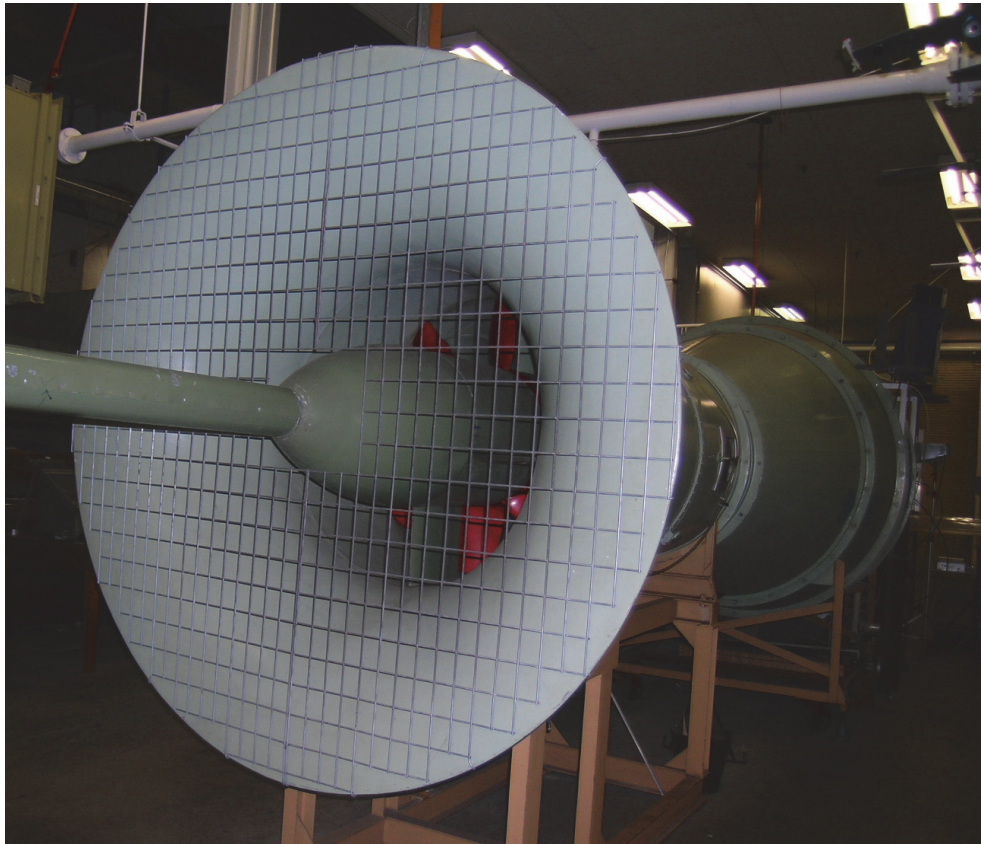
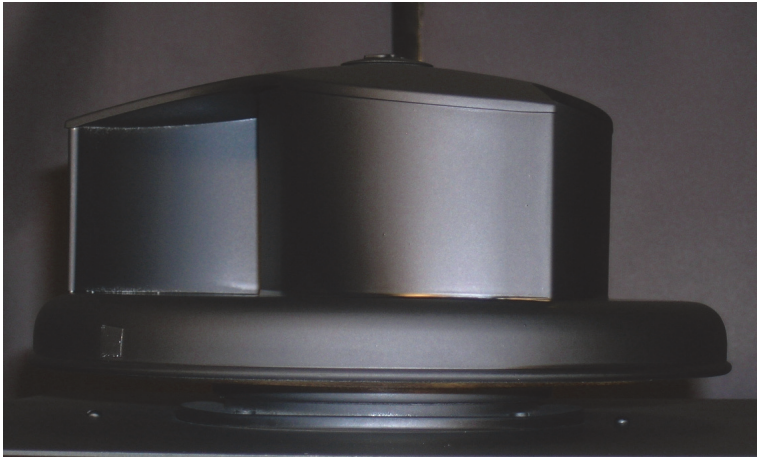


Fig. 17. Open jet wind tunnel at the University of New South Wales.

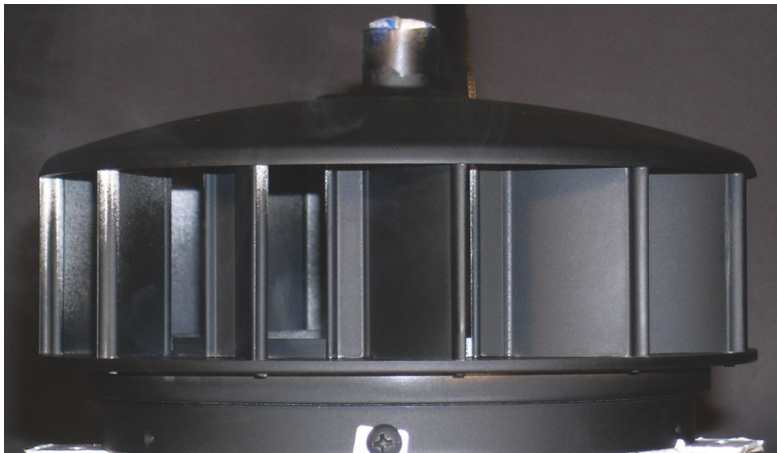
#### 2.4.1.2 Description of test models

Two ventilators were used in this study. For the sake of convenience, they will be referred to as ventilator A and ventilator B (Figs 18a and 18b) in this chapter.

Ventilator A, Fig. 18(a), has a Savonius style 3 blade structure to drive the ventilator and an eight blade centrifugal fan to extract air. There is no air flow between the driving blades and the centrifugal fan. The overall ventilator diameter is 200mm, excluding the fan weather cover and the height is 120mm. The air inlet diameter is 100mm.



(a)



(b)

Fig. 18. (a). Ventilator A; (b). Ventilator B.

Ventilator B, Fig. 18(b), has a 12 blade centrifugal fan, which is designed to both turn the ventilator and extract air. The overall ventilator diameter is 200mm and the height is 100mm. The air inlet diameter is 140mm.



### 2.4.1.3 Description of set up for flow visualization and flow measurement

The arrangement of the test set up is shown in Fig. 19. The wind tunnel velocity was measured using a Pitot-static Tube, mounted at the front of the open test section and a Furness Controls FC0510 micro manometer. The inlet pipe velocity was measured by using a Dantec fibre film hotwire anemometer type 54N60 located at the  $\frac{3}{4}$  radius position inside a 145mm diameter tube. The tube had a mitred corner with seven flow correcting vanes. Total tube length was 1620mm excluding a tapered entry cone. Rotation was measured using a CDT-2000 digital tachometer using its non contact mode. Smoke was generated by a Dick Smith M6000 fog machine, located at the entry cone. The models were painted matte black, and a black back ground was used to provide contrast with the light coloured smoke. Digital photographs were taken using a Nikon Coolpix 5400 camera.

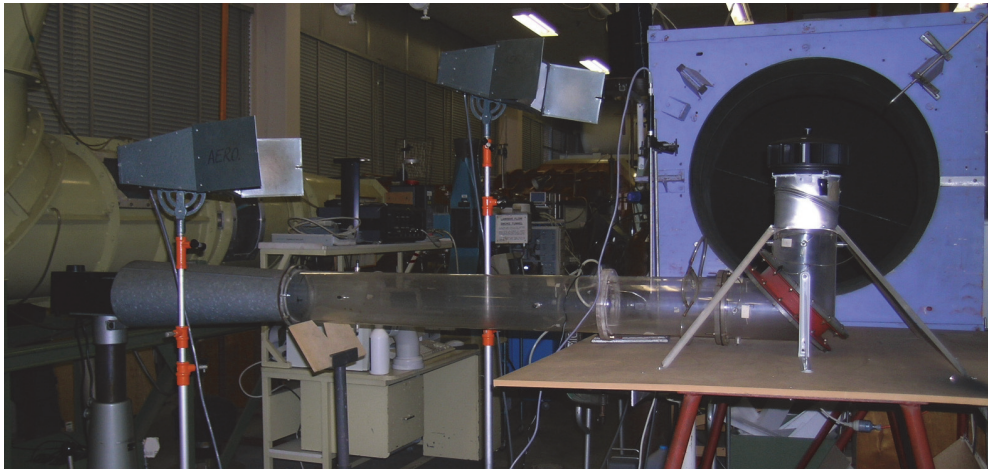


Fig. 19. Test set up

## 2.4.2 Results and discussions

### 2.4.2.1 Qualitative: Flow visualization

The results for exhaust flow visualisation are presented in Figs 20 and 21 and inlet flow visualization in Fig. 22.

It can be seen in Fig. 20 (a), when the wind tunnel velocity is 1m/s, ventilator A did not rotate, the smoke exhausts from the rear half of the ventilator, and is drawn upwards and forward mixing with the air in the turbulent area behind the driving blades.

At a higher wind tunnel velocity of 9.5m/s ventilator A rotates at 389 rpm. The exhaust is shown to emit from the sides, front and rear of the centrifugal fan. Some of the exhaust continues to be drawn up into the turbulent area behind the driving blades, Fig.20 (b).

In Fig.20 (c), the wind tunnel velocity is now 16.5m/s and the resultant ventilator rotation is 1619 rpm for ventilator A. The exhaust continues from the sides, front and rear of the centrifugal turbine and to be drawn up into the turbulent area behind the driving blades.

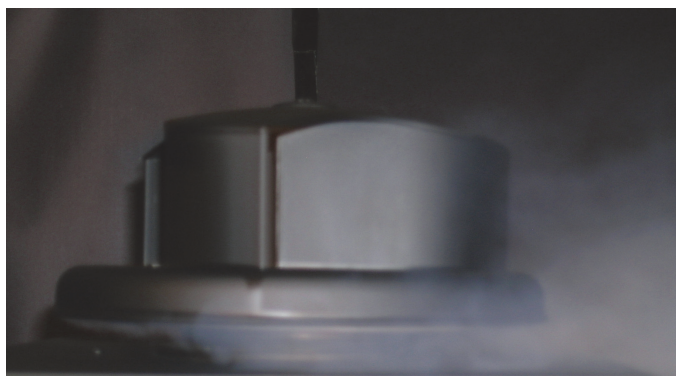
When the wind tunnel velocity is 1m/s and ventilator B does not rotate, the smoke exhausts from the rear half of the ventilator, and is drawn upward. More smoke is exhausted from the camera side of the ventilator. Free stream air is drawn through the ventilator and mixes with the smoke, Fig.21 (a).



(a)



(b)



(c)

Fig. 20. Exhaust Flow visualisation using ventilator A at (a) 1m/s and 0 rpm; (b) 9.5m/s and 389 rpm and (c) 16.5m/s, 1619 rpm



(a)



(b)



(c)

Fig. 21. Exhaust Flow visualisation using ventilator B at (a) 1m/s and 0 rpm; (b) 9.5m/s and 389 rpm and (c) 16.5m/s, 1619 rpm



Fig. 22. Smoke flow visualisation at the intake.

When the wind tunnel velocity is 9.5m/s the resultant ventilator rotation is 364 rpm for ventilator B. The smoke is exhausted from the front, back and sides. The majority of smoke is exhausted from the rear and camera side of the ventilator. Some exhaust from the front is drawn above the ventilator, Fig 21 (b).

At the higher wind tunnel velocity of 16.5m/s the ventilator rotation is 674 rpm for ventilator B. Again the smoke is exhausted from the front, back and sides and the majority of smoke is exhausted from the rear and camera side of the ventilator. Some exhaust from the front is drawn above the ventilator. Due to the higher suction, more air has mixed with the smoke before being drawn into the ventilator, making the smoke less dense, Fig. 21(c) The smoke mixed evenly inside the pipe (figure 7), making any visual interpretation of flow highly subjective. Injecting smoke into the intake tube changed the intake velocity. To confirm flow rates it was decided to use an alternative method to determine flow inside the pipe.

#### 2.4.2.2 Qualitative flow measurement

The ventilator rotation was measured using the tachometer and the intake velocity was measured with the hot wire anemometry system for different wind tunnel speeds.

As expected from rotation comparison, Fig.23 shows a linear relationship between ventilator rotation and wind tunnel speed. A linear relationship is demonstrated between wind tunnel velocity and intake velocity as is evident from Fig.24. It is estimated that the experimental repeatability of measurements is within  $\pm 1\%$  of the measured value.

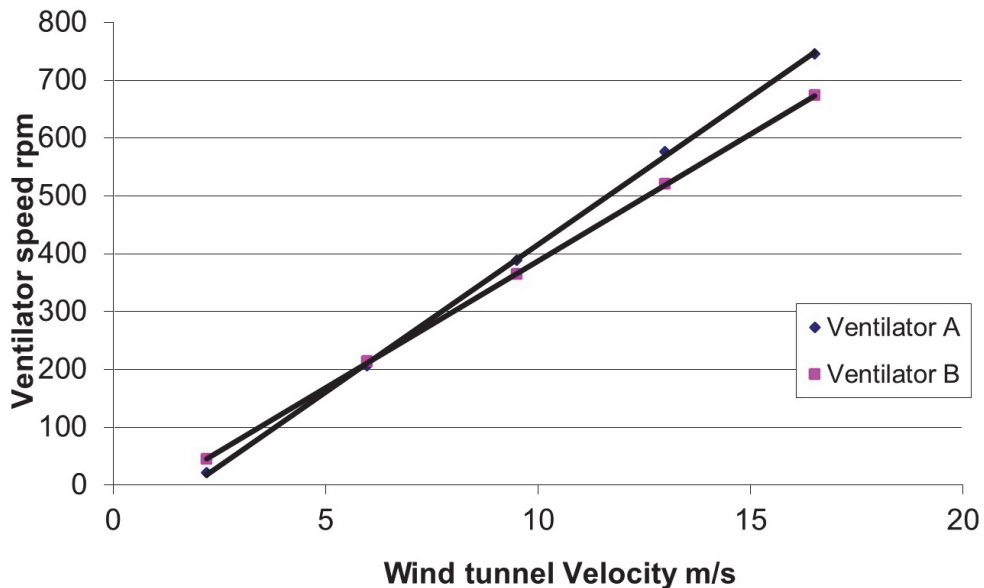


Fig. 23. Comparison of rotation speed

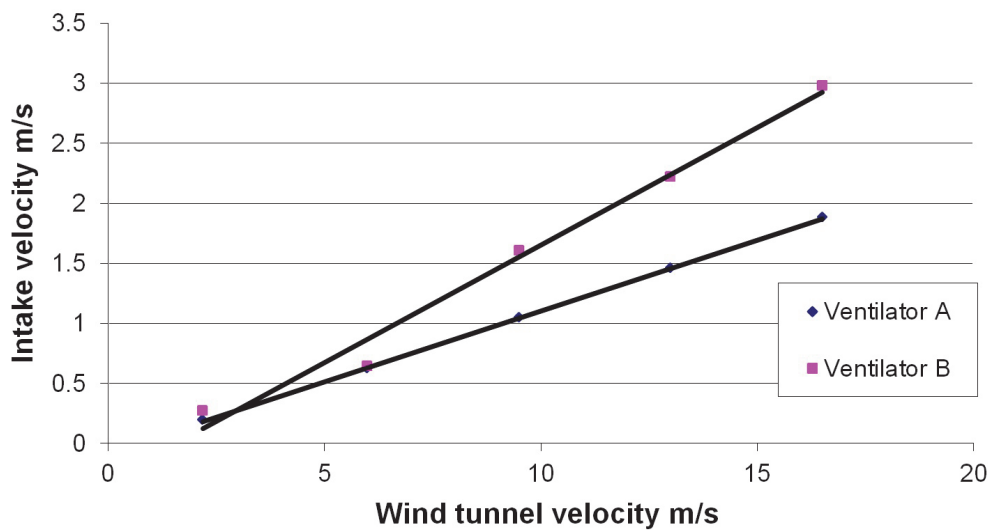


Fig. 24. Comparison of Intake velocity

### 2.4.3 Conclusions

The complex nature of the exhaust flow is demonstrated through the use of flow visualization using smoke. In both ventilators smoke is visible at the front of the ventilator if rotating, indicating both are likely to stop water from entering during wet conditions. In terms of intake velocity flow rate, ventilator B appears better. This might be due to several factors of its design including intake diameter, blade shape, number of blades and blade area and the absence of a weather cowling. In terms of rotating speed ventilator B started at a lower wind tunnel velocity and ventilator A obtained a higher rotation speed. Again this may be due to a number of factors including blade number, shape, and torque loading.

### 3. Final concluding remarks

In this chapter, the significance of modern day usage of wind tunnels to provide 'concept of proof' validations to new and innovative ideas based primarily on the works of the authors at the University of New South Wales, have been provided. The development of a novel three-dimensional skin friction methodology has the potential to contribute to more advanced and informative investigation of fluid flow field, the studies and validation of the viability of synthetic jet or air jet vortex generator as new but powerful active flow control technologies or the studies on rotating roof ventilators have the potential to produce cost-efficient high performance products. A case in point is the subsequent works on rotating wind driven ventilators mentioned in this chapter that were conducted under the Australian Research Council Industry Collaboration Linkage Grants resulting in a more efficient blade design which has been incorporated in the 'Hurricane' ventilator with nearly 15% increase in air extraction capability at low speed and enhanced safety and performance in rain and operation. The works also lead to the basis for the concept of a hybrid ventilator [54] to overcome the dependence of conventional roof top ventilators on the availability of wind. This resulted in the 2008 AIRAH Excellence award winning hybrid ventilator, the 'ECPOWER' in the HVAC-Achiever category as a distinguished Australian product, invention or innovation in heating, ventilation and air conditioning. Both the 'Hurricane' and 'ECOPOWER' are currently marketed worldwide by CSR Edmonds Pty Ltd, Australia. Stories about the outcomes of both projects have featured in ARC reports to parliament [55].

Today wind tunnels are used quite extensively to solve aeronautical as well as non-aeronautical problems in fields as diverse as transportation, architecture or environmental concerns. With rapid advances in instrumentation and computer technologies and greater use of automated systems in experimental studies, wind tunnel is a formidable device at the disposal of engineers and scientists to advance the cause of human progress and civilization opening up possibilities of new frontier technologies and products with zero or reduced carbon footprints.

### 4. Acknowledgements

The authors would like to thank Terry Flynn, the technical officer in charge of the UNSW aerodynamics laboratory, Dr. J. Lien and Simon Shun of the UNSW for their significant assistance and contribution that has made the writing of this chapter possible.

Acknowledgement is also made of the Australian Research Council and Allan Ramsay, Managing Director and Derek Munn of CSR Edmonds Products Pty Ltd, Australia for their financial support in carrying out many of the works mentioned in this chapter.

## 5. References

- [1] A. Gatto, K.P.Byrne, N.A.Ahmed and R.D.Archer, 'Pressure Measurements over a Cylinder in Crossflow using Plastic Tubing', *Experiments in Fluids*, vol 30, Issue 1, pp 43-46, 2001
- [2] A.Pissasale and N.A.Ahmed, 'Theoretical calibration of a five hole probe for highly three dimensional flow', *International Journal of Measurement Science and Technology*, vol 13, July, 2002, pp1100-1107
- [3] A.Pissasale and N.A.Ahmed, "A novel method of extending the calibration range of five hole probe for highly three dimensional flows", *Journal of Flow Measurement and Instrumentation*, vol. 13, issues 1-2, March-April, 2002, pp 23-3018.
- [4] T. Cebecci, and A. M. O. Smith, "Analysis of Turbulent Boundary Layers," Academic Press. (1974).
- [5] A. T. Degani, F. T. Smith and J. D. A. Walker, 1993 The structure of a three-dimensional turbulent boundary layer *Journal of Fluid Mechanics* , 250: 43-68
- [6] S.J. Lien and N. A. Ahmed, Application of multi-hole pressure probes in skin friction determination. 25th AIAA Aerodynamic Measurement Technology and Ground Testing Conference, San Francisco: Paper Number: AIAA-2006-3659 (2006)
- [7] J.Lien and N.A.Ahmed, 'An examination of suitability of multi hole pressure probe technique for skin friction measurement in turbulent flow', *Journal title: Flow Measurement and Instrumentation*, Article accepted for publication: 30-JAN-2011
- [8] J. P. Johnston, "Measurements in three-dimensional turbulent boundary layer induced by a swept, forward -facing step," *J. Fluid Mech*, vol. 42, part 4, 833-844 (1970)
- [9] Elsenaar A and Boelsma S H 1974 Measurements of the Reynolds stress tensor in a three-dimensional turbulent boundary layer under infinite swept-wing conditions National Aerospace Laboratory NRL TR 74095 U
- [10] N. V. Chandrasekhara Swamy, B. H. Lakshmana Gowda, V. R. Lakshminatfi, "Measurements in 3-dimensional turbulent boundary layer on a yawed flat plate induced by leading edge vortex" *Lecture notes in Physics*, Springer Berlin, 217-221 (1978)
- [11] J.D. Vagt, 'Experimental techniques in three-dimensional turbulent boundary layers' *Proceedings of the Symposium*, Berlin, West Germany, 1982 (A83-47011 22-34). Berlin, Springer-Verlag, 19-43 (1982)
- [12] S. H. Chue (1975) Pressure Probes for Fluid Measurement, *Prog. Aerospace Sci.*, Vol. 16, No. 2, pp. 147-223
- [13] M.Amitay, D.R.Smith, D.E. Parekh, A.Gleizer, 'Aerodynamic flow control over an unconventional airfoil using synthetic jet actuators', *AIAA* .,vol. 39, No. 3, 2001, pp 361-70
- [14] M.Amitay, V.Kibens, D.E. Parekh, A.Gleizer, 'Flow reattachment dynamics over a thick airfoil controlled by synthetic jet actuators', *37th AIAA Aero. Sci. Meet.*, Reno, Nevada, 1999, pp 99-1001.

- [15] C.Y. Lee and D.B. Goldstein, 'Two-dimensional synthetic jet simulation', *AIAA Fluids Meeting*, 2000-0406, Denver, Colorado, 2000.
- [16] S. Jeon, J. Choi, W. Jeon, H. Choi, J. Park, 'Active control of flow over a sphere for drag reduction at a subcritical Reynolds number', *J. of Fluid Mech.*, vol. 517, 2004, pp 113-129.
- [17] M. Amitay and A. Gleizer, 'Synthetic Jets', *Ann. Rev. of Fluid Mech.*, vol 34, 2002, pp503-529.
- [18] H.J. Kim and P.A. Durbin, 'Observations of the frequencies in a sphere wake and of drag increase by acoustic excitation', *Physics of Fluids*, vol.31, 1988, pp 3260-3265.
- [19] R. Mittal and P. Rampungoon, 'On the Virtual Aeroshaping Effect of Synthetic Jets', *Physics of Fluids*. Vol.14, No. 4, 2002, pp1533-1536.
- [20] H. Schlichting, '*Boundary-Layer Theory*', 6th Edn., 1968, McGraw Hill.
- [21] N.A. Ahmed, and R.D. Archer, 'Post-Stall Behaviour of A Wing under Externally Imposed Sound', *AIAA Journal of Aircraft*, vol 38, no.5, pp961-963, September-October, 2000
- [22] N.A. Ahmed and D.J. Wagner, "Vortex shedding and transition frequencies associated with flow around a circular cylinder", *AIAA Journal*, vol. 41, no.3, March, 2003, pp 542-544
- [23] H.R. William, Jr and Pope, A., 'Low Speed Wind Tunnel Testing', 2<sup>nd</sup> ed., 1984, John Wiley and Sons
- [24] P.K. Chang, 'Separation of Flow', 1970, pp.1, Pergamon Press.
- [25] J.D. Anderson, J.D., 'Fundamentals of Aerodynamics', 3<sup>rd</sup> ed., 2001, pp. 715-717, McGraw Hill.
- [26] R.A. Wallis, 'A Preliminary Note on a Modified Type of Air Jet for Boundary Layer Control', 1960, pp. 2, A.R.C. /CP 513.
- [27] E.L. Houghton and P.W. Carpenter, P.W., 'Aerodynamics for Engineering Students', 5<sup>th</sup> ed., 2003, pp. 513-514, Elsevier Butterworth-Heinemann.
- [28] R.A. Wallis, 'The use of Air Jets for Boundary Layer Control', *Aerodynamic Research Laboratories Australia*, Aero Note 110, 1952.
- [29] C. Singh, D.J. Peake, A. Kokkalis, V. Khodagolian, F.N. Coton and R.A.M. Galbraith, 'Control of Rotorcraft Retreating Blade Stall Using Air-Jet Vortex Generators', *Journal of Aircraft*, vol. 43 No. 4, 2006, pp. 1169-1176.
- [30] A. Krzysiak, 'Control of Flow Separation Using Self-Supplying Air-Jet Vortex Generators', *AIAA Journal*, vol. 46, No. 9, 2008, pp. 2229-2234.
- [31] A.G. Oliver, 'Air Jet Vortex Generators for Wind turbines', PhD. dissertation, 1997, City University, London.
- [32] G.V. Selby, J.C. Lin and E.G. Howard, 'Control of low-speed turbulent separated flow using jet vortex generators', *Experiments in Fluids*, vol. 12, No. 6, 1992 pp. 394-400.
- [33] A. Bridges and D.R. Smith, 'Influence of Orifice Orientation on a Synthetic Jet-Boundary Layer Interaction', *AIAA Journal*, vol. 41, No. 12, 2003 pp. 2394-2402.
- [34] X. Zhang, 'An inclined rectangular jet in a turbulent boundary layer-vortex flow', *Experiments in Fluids*, vol. 28, 2000, pp. 344-354.
- [35] H. Johari, Q. Zhang, M.J. Rose and S.M. Bourque, 'Impulsively Started Turbulent Jets', *AIAA Journal*, vol. 35, No. 4, 1997, pp. 657-662.



- [36] Q. Zhang and H. Johari, 'Effects of Acceleration on Turbulent Jets', *Physics of Fluids*, vol 8, No. 8, 1996, pp. 2185-2195.
- [37] H. Johari, M. Pacheco-Tougas and J.C. Hermanson, J, 'Penetration and Mixing of Fully Modulated Turbulent Jets in Crossflow", *AIAA Journal*, vol. 37, No. 7, 1999, pp 842-850.
- [38] H. Johari and G. S. Rixon, 'Effects of Pulsing on a Vortex Generator Jet', *AIAA Journal*, vol. 41, No. 12, 2003 pp 2309-2315.
- [39] A. Eroglu and R.E. Breidenthal, 'Structure, Penetration, and Mixing of Pulsed Jets in Crossflow', *AIAA Journal*, vol. 39, No. 3, 2001, pp 417-423.
- [40] A. Eroglu and R.E. Breidenthal , 'Exponentially Accelerating Jet in Crossflow', *AIAA Journal*, vol. 36, No. 6, 1998, pp 1002-1009.
- [41] R. Breidenthal, (1986), 'The Turbulent Exponential Jet', *Physics of Fluids*, vol. 29, No. 8, 1986, pp. 2346-2347.
- [42] T. Vronsky, 'High Performance Cost Effective Large Wind Turbine Blades Using Air jet Vortex Generators', 2000, ETSU W/41/00541/REP.
- [43] ISO 5167-1:2003(E), 'Measurement of fluid flow by means of pressure differential devices inserted in circular cross-section conduits running full - Part 1: General principles and requirements'.
- [44] ISO 5167-2:2003(E), 'Measurement of fluid flow by means of pressure differential devices inserted in circular cross-section conduits running full - Part 2: Orifice plates'.
- [45] ISO/TR 15377:2007(E), 'Measurement of fluid flow by means of pressure differential devices - Guidelines for the specification of orifice plates, nozzles and Venturi tubes beyond the scope of ISO5167'.
- [46] 'Heating Piping and Air Conditioning' Volume 47, Issue 13, December 1975, Page 59-61.
- [47] T.E. Kreichelt and G.R. Kern, 'Natural ventilation in hot process buildings in the steel industry', *Journal of Iron and Steel Engineering*, December, 1976, Page 39-46.
- [48] N.A. Ahmed and J. Back , 'Destructive wind tunnel tests', UNSW Unisearch Report no. 23214-10, Australia, 1996.
- [49] N.A. Ahmed and J. Back, 'Wind tunnel tests on two ventilators', UNSW Unisearch Report no. 29295-01, Australia, 1997.
- [50] D.H.Rashid and N.A.Ahmed, 'Study of aerodynamic forces on a rotating wind driven ventilator', *Wind Engineering*, vol. 27, no.1, 2003, pp 63-72
- [51] N.A. Ahmed, 'Implementation of a Momentum Integral Technique for Total Drag Determination', *International Journal of Mechanical Engineering Education*, vol.30, no.4, 2002, pp 62-72
- [52] A.J. Pissasale and N.A.Ahmed, 'Examining the effect of flow reversal on seven-hole probe measurements', *AIAA Journal*, vol 41, no 12, 2003, pp 2460-2467
- [53] A.J. Pissasale and N.A.Ahmed, 'Development of a functional relationship between port pressures and flow properties for the calibration and application of multi-hole probes to highly three-dimensional flows', *Experiments in Fluids*, March, vol 36, no.3, March, 2004, pp 422-436

- [54] S.Shun and N.A.Ahmed, 'Utilizing wind and solar energy as power sources for a hybrid building ventilation device', *Renewable Energy*, Volume 33, Issue 6, June 2008, Pages 1392-1397
- [55] Annual Report, 2008-2009, *Australian Res Council*, ISSN 1444-982X, p92, (2009)

# Air Speed Measurement Standards Using Wind Tunnels

Sejong Chun

*Korea Research Institute of Standards and Science  
Korea*

## 1. Introduction

Accurate air speed measurement is essential to understand flow phenomena and practical engineering problems, such as wind turbines, air ventilation systems, air filter testers, and fan testers, etc. Standard wind tunnels can provide good testing environments for calibrating and testing industrial anemometers, which are widely used for measuring air speeds in applications to various on-site air speed measurements. Air speed standards can be established by adopting a wind tunnel. In this case, some knowledges are required, regarding measurement accuracy and uncertainty assessment.

To certify an industrial anemometer, a calibration certificate is issued by an accredited laboratory, which is recognized by an accreditation organization in a country, according to the ISO/IEC 17025 guide (ISO, 2005). The national metrology institutes in every country advise the accreditation organization in recognizing the accredited laboratory by providing technical supports with the national measurement standards. Traceability is established from the national standards to the industrial standards, by transferring national measurement standards from the national metrology institutes to the accredited laboratories.

If an industrial anemometer is exported to a foreign country, an international calibration certification must be issued to provide the measurement accuracy requested by a customer in the foreign country. Mutual recognition arrangement realizes the international certification procedures by harmonizing the calibration and measurement capability (CMC) of industrial countries. International key comparisons are performed to fulfill the purpose of the mutual recognition arrangement. The international key comparisons are managed by the CIPM. In case of air speed metrology, three international key comparisons have been conducted by either world-wide or regional levels, up to date.

In this book chapter, a brief explanation, regarding the air speed metrology, is introduced. At first, some basics of statistical methods to calibrate an industrial anemometer are explained. After that, an air speed metrology is briefly introduced by considering the traceability chain from the national measurement standards to the industrial or working standards, based on the literature. Finally, some information, regarding the mutual recognition arrangement and the international key comparisons, will be mentioned. From this approach, it is expected that some basic knowledge of the air speed metrology can be useful in understanding how to measure the industrial anemometers with good measurement accuracy and uncertainty.

## 2. Basics of statistics for calibration of an anemometer

### 2.1 Basics of uncertainty measurement

When an anemometer is calibrated, people consider statistics because the measurement data for anemometer calibration generates statistical distributions. To determine a calibration coefficient of the anemometer, statistical moments such as a mean and a standard deviation are considered (Dougherty, 1990). Because the mean is an unbiased estimator, it is believed that the mean value approaches to the true value by measuring the data with infinite times. In this case, the standard uncertainty to determine the mean value becomes zero, according to the following equation.

$$\sigma_{\bar{x}} = \frac{\sigma_x}{\sqrt{n}} \quad (1)$$

Here,  $\bar{x}$  is the mean value of  $\{x_i, i = 1, 2, \dots, n\}$ ,  $n$  is the number of measurement,  $\sigma_x$  is the standard deviation of  $x_i$ , and  $\sigma_{\bar{x}}$  is the standard deviation of  $\bar{x}$ .  $\sigma_{\bar{x}}$  is referred to as the standard uncertainty, or more exactly, type A uncertainty (BIPM et al., 1993). The type A uncertainty is related with direct measurement when the device under test, or the *DUT* is calibrated. On the contrary, the uncertainty component, which is not directly related to the measurement, is referred to be type B uncertainty. The type B uncertainty includes all the other information except measurement, such as the standard uncertainty of an apparatus written in a calibration certificate, or a nominal value defined in a table, etc.

When determining the type A uncertainty, they can assume that the measuring quantity has the Gaussian distribution as a probability density function, by applying the central limit theorem (Dougherty, 1990). To assume the Gaussian distribution, the number of samples should be at least more than 50. However, in some cases, it is possible to assume the Gaussian distribution with the number of data more than 30. In case that the number of data is less than 10, the Student-*t* distribution is assumed. The difference between the Gaussian and the Student-*t* distribution is the value of coverage factor,  $k$  with the same confidence intervals of, e.g., 95 %.  $k$  is a necessary quantity when an expanded uncertainty is estimated based on a combined uncertainty, which combines the type A and the type B uncertainties (BIPM et al., 1993).

When determining the type B uncertainty, a rectangular, a triangular, and a trapezoidal distribution are usually assumed according to data types. In most cases, the rectangular distribution is preferred to represent the type B uncertainty, when a value is referred from tables, or calibration certificates, etc. Some of values of  $k$  for different probability distributions are summarized in Table 1.

Distribution	Coverage factor $k$
U-shaped	$\sqrt{2}$
Rectangular	$\sqrt{3}$
Triangular	$\sqrt{6}$
Gaussian	1.96
Student - <i>t</i>	12.71 $\nu = 1$
	4.30 $\nu = 2$
	2.57 $\nu = 5$
	2.23 $\nu = 10$
	2.09 $\nu = 20$
	2.04 $\nu = 30$

Table 1. Coverage factor  $k$  with confidence level of 95 %

Measurement uncertainty is a combination of estimated uncertainties of each component, recognized as an uncertainty factor to a measuring quantity. The combined uncertainty is calculated according to the following formula (Kirkup & Frenkel, 2006).

$$u = \sqrt{u_A^2 + u_B^2} \quad (2)$$

Here,  $u_A$  denotes the type A uncertainty,  $u_B$  denotes the type B uncertainty, and  $u$  is the combined uncertainty. The Equation (2) combines  $u_A$  and  $u_B$  by a vector sum, because the two types of uncertainties are assumed to be independent and uncorrelated with each other. However, there are some cases where the uncertainty factors are not independent and uncorrelated. In these cases, correlation coefficients among the uncertainty factors must be calculated (Kirkup & Frenkel, 2006). To calculate the expanded uncertainty, the coverage factor  $k$  is multiplied to the combined uncertainty, as follows.

$$U = ku \quad (3)$$

Because the confidence interval with 95 % is widely accepted,  $k$  can be looked up in a statistical table (Dougherty, 1990). The effective degree of freedom,  $\nu_{eff}$  gives how to determine  $k$ , when the Student- $t$  distribution is considered. The formula to calculate  $\nu_{eff}$  is as follows (Kirkup & Frenkel, 2006; BIPM, 1993).

$$\nu_{eff} = \frac{u^4}{\frac{u_A^4}{\nu_A} + \frac{u_B^4}{\nu_B}} \quad (4)$$

The Equation (4) is also referred to as the Welch-Satterthwaite formula.  $\nu_{eff}$  is used to obtain  $k$  by inverse calculation of the given probability distribution<sup>1</sup>.

## 2.2 Repeatability and reproducibility

Repeatability describes the data distribution when a bunch of data is acquainted at a time. The repeatability can be defined as a ratio between the mean and the standard deviation.

$$F' = \frac{\sigma_x}{\bar{x}} \quad (5)$$

Here,  $F'$  represents the relative deviation of  $\bar{x}$ . When several measurements are required to obtain a set of mean values, i.e.,  $\{\bar{x}_j, j = 1, 2, \dots, m\}$ , another mean value can be defined.

$$\bar{\bar{x}} = \frac{1}{m} \sum_{j=1}^m \bar{x}_j = \frac{1}{m} \frac{1}{n} \sum_{j=1}^m (\sum_{i=1}^n x_{i,j}) = \frac{1}{m} \frac{1}{n} \sum_{j=1}^m \sum_{i=1}^n x_{i,j} \quad (6)$$

Here,  $\bar{\bar{x}}$  is the mean value of  $\bar{x}_j$ ,  $m$  is the number of measurements,  $n$  is the number of samples, and  $x_{i,j}$  indicates the  $i$ -th sample of the  $j$ -th measurement. This reminds of the definition of ensemble averages in random data processing (Bendat & Piersol, 2000). According to the ergodic theory, the time average of a signal converges to an ensemble average, if the measurement time of the signal is infinitely long. In this case, the time average of the infinitely-measured signal should be as close as to the true value of the signal. If the ensemble average  $\bar{\bar{x}}$  has the same value as the time average of the signal,  $\bar{\bar{x}}$  should be equal to the true value of the measuring quantity, also. Because the  $j$ -th measurement

<sup>1</sup> In Microsoft Excel, the function, named *tinv*(0.05,  $\nu_{eff}$ ) can calculate  $k$  for the Student- $t$  distribution.

contains the time series data with  $n$  samples, each mean value for the  $j$ -th measurement, i.e.,  $\bar{x}_j$ , represents the short time-averaged value for the  $j$ -th data. Reproducibility indicates the relative variation of  $\bar{x}$  as in the following equation.

$$F'' = \frac{\sigma_{\bar{x}}}{\bar{x}} \quad (7)$$

Here,  $\sigma_{\bar{x}}$  is the standard deviation of  $\bar{x}$ , or the type A uncertainty of  $x$ . To summarize, the repeatability is obtained with a set of samples, while the reproducibility is obtained from a set of measurements. In evaluating the measurement uncertainty, the reproducibility rather than the repeatability should be considered, because the reproducibility includes the notion of repeatability and is directly related with the type A uncertainty.

### 2.3 Calibration of an instrument

Calibration coefficient is the coefficient which is obtained by comparing the readings of the device under test (*DUT*) with those of the reference device (*REF*). The measurement accuracy of the *DUT* is determined by an average value of the relative deviations between the *DUT* and the *REF*.

$$F' = \frac{\bar{x}_{DUT} - \bar{x}_{REF}}{\bar{x}_{REF}} \quad (8)$$

Here,  $\bar{x}_{DUT}$  is the mean value of the *DUT*, and  $\bar{x}_{REF}$  is the mean value of the *REF*.  $F'$  is used again in Eqn. (8), because the relative deviations resemble the repeatability of the measuring quantity,  $x$ . However, to evaluate the difference with true values, ensemble averages should be used as noted in the following equation.

$$F'' = \frac{\bar{\bar{x}}_{DUT} - \bar{\bar{x}}_{REF}}{\bar{\bar{x}}_{REF}} \quad (9)$$

Here,  $\bar{\bar{x}}_{DUT}$  is the ensemble average of the *DUT*, and  $\bar{\bar{x}}_{REF}$  is the ensemble average of the *REF*. Because Eqn. (9) resembles the definition of the reproducibility, it is thought that  $F''$  can represent the measurement accuracy of the *DUT*.

The calibration coefficient,  $\alpha$  can be either a simple ratio between  $\bar{\bar{x}}_{DUT}$  and  $\bar{\bar{x}}_{REF}$  or a set of coefficients by a curve fitting formula of the calibration data.

$$\alpha = \frac{\bar{\bar{x}}_{DUT}}{\bar{\bar{x}}_{REF}} \quad (10)$$

$\alpha$  can be validated, when  $\alpha$  is constant within a certain values in the entire calibration range. If  $\alpha$  is a variable within certain bounds,  $\bar{\bar{x}}_{DUT}$  and  $\bar{\bar{x}}_{REF}$  can be replaced with their differences,  $\Delta\bar{\bar{x}}_{DUT}$  and  $\Delta\bar{\bar{x}}_{REF}$ , to denote the calibration coefficient at specified ranges.

$$\alpha = \frac{\Delta\bar{\bar{x}}_{DUT}}{\Delta\bar{\bar{x}}_{REF}} \quad (11)$$

In the case of a set of coefficients by curve fitting,  $\bar{\bar{x}}_{DUT}$  can be compensated by the curve fitting coefficients, or  $\{\alpha_i, i = 0, 1, 2, \dots, n\}$ , with  $n$ -th order polynomials.

$$\bar{\bar{x}}_{DUT} = \sum_{i=0}^n \alpha_i \bar{\bar{x}}_{REF}^i \quad (12)$$

Although the determination of  $\alpha_i$  seems to be straightforward, uncertainty evaluation of  $\bar{\bar{x}}_{DUT}$  with respect to  $\alpha_i$  is rather a bit difficult (Hibbert, 2006). In a linear and a quadratic

calibration curve, the uncertainty can be evaluated analytically. However, when the fitting curve has third or fourth order polynomials, then the derivation of uncertainty formula becomes difficult.

### 3. Traceability of measurement standards

#### 3.1 Metrology in general

Metrology presents a seemingly calm surface, covering depths of knowledge that are familiar only to a few people, but which most of people make use of (Howarth & Redgrave, 2008). It makes people confident that the world economy is sharing a common perception of quantity measurement, which can be represented as meter, kilogram, liter, watt, mole, etc. The history of defining basic units for metrology is rather a bit long, considering the rapid developments of scientific knowledge in recent years (Howarth & Redgrave, 2008). In 1799, the French National Archives in Paris established two artifacts, which realized the length and the weight standards<sup>2</sup>. In 1946, the MKSA system, which stands for Meter, Kilogram, Second, and Ampere, was established to define the length, the weight, the time, and the electric current standards. In 1954, Kelvin and Candela were included to the MKSA system to define the thermodynamic temperature and the luminous intensity standards, respectively. In 1971, Mole, which was the unit for amount of substance, was enclosed into the MKSA system. Since then, the MKSA system was extended and renamed as the SI unit system (Howarth & Redgrave, 2008)<sup>3</sup>.

As scientific knowledge is being accumulated, the definition of units within the SI system has been changed. The method to re-define the basic units has been suggested by long-term researches, regarding physical constants, and the re-definition of units has been reviewed and discussed by the 'Conférence Générale des Poids et Mesures', or the CGPM<sup>4</sup>. The present definitions of the basic units are given as follows (Howarth & Redgrave, 2008).

1. Length: the length of the path travelled by light in a vacuum during a time interval of  $1/299,792,458$  of a second, denoted with meter [m]
2. Weight: the mass of the international prototype of the kilogram, denoted with kilogram [kg]
3. Time: the duration of 9,192,631,770 periods of the radiation corresponding to the transition between the two hyperfine levels of the ground state of the caesium-133 atom, denoted with second [s]
4. Electric current: the electric current which, if maintained in two straight parallel conductors of infinite length, of negligible circular cross-section, and placed 1 meter apart in vacuum, would produce between these conductors a force equal to  $2 \times 10^{-7}$  newton [N] per meter of length, denoted with ampere [A]
5. Thermodynamic temperature: the fraction  $1/273.16$  of the thermodynamic temperature of the triple of water, denoted with Kelvin [K]
6. Luminous intensity: the luminous intensity in a given direction of a source that emits monochromatic radiation of frequency  $540 \times 10^{12}$  hertz [Hz] and has a radiant intensity in that direction of  $1/683$  watts per steradian, denoted with candela [Cd]

---

<sup>2</sup> The 'Bureau International des Poids et Mesures', or BIPM, which is located in Paris, holds the length and the weight standards since 1799. (<http://www.bipm.org/>)

<sup>3</sup> The SI unit system stands for the 'Système international d'unités'.

<sup>4</sup> CGPM refers to the General Conference on Weights and Measures. (<http://www.bipm.org/en/home/>)

7. Amount of a substance: the amount of substance of a system that contains as many elementary entities as there are atoms in 0.012 kg of carbon-12. When the mole is used, the elementary entities must be specified and the elementary entities may be atoms, molecules, ions, electrons, other particles, or specified groups of such particles, denoted with mole [M].

Several definitions of the basic units were substituted with newer ones by advent of new technologies. In the case of the length standard, the He-Ne lasers, invented in 1960's, substituted the artefact, which had been made in 1799. In the case of the electric current standard, the Josephson semiconductor played a vital role to enhance its measurement accuracy. In the case of the time keeping, an atomic fountain technology is suggested as the primary standard. In addition, in the case of the weight standard, a watt balance is being suggested to re-define the weight, instead of the artefact, which has been the primary standard since 1799. It is noteworthy that physical constants from modern physics such as the Planck constant are considered as candidates for re-defining the basic units. It is because of the belief that the physical constants are well-defined, so that the realizations derived from these physical constants would not be changeable as large as the standards established by the artefacts. However, such a notion has not been fulfilled yet, because the current technology cannot provide measurement accuracy smaller than that of the current primary standards (Gläser et al., 2010).

Redundancy means that two independent measurement principles are compared with each other to validate their measurement accuracies and uncertainties. In the case of re-defining the weight standard with the watt balance based on the Planck constant, some metrologists consider to check the watt balance with other measuring principles, such as a silicone sphere based on the Avogadro constant. By means of redundancy, it will be convinced whether the developing measurement technique would be satisfactory to replace the current primary standard or not (Gläser et al., 2010).

A traceability chain indicates an unbroken chain of comparisons, all having stated uncertainties from primary standards to industrial standards (Howarth & Redgrave, 2008). The traceability chain has been devised to maintain the quality of measurement by relating measurement results of industrial standards to references at the higher levels, ending at primary standards. The primary standards are established by the national metrology institute, or the NMI in a country. The purpose of the NMI is to establish the national measurement standards and to realize the definition of units within the framework of the SI unit system<sup>5</sup>. Either the NMI or the national government can appoint a designated institute, or a DI, to hold some part of the national measurement standards (Howarth & Redgrave, 2008). Accredited laboratories can transfer measurement uncertainty from the primary standards to industrial standards by holding transfer standards. The accredited laboratories are licensed from the national government, according to the accreditation scheme to provide industry with an appropriate calibration service. The national measurement standard established by the NMI can be transferred to the industrial standards via the accredited laboratories. Therefore, the traceability chain, established by the NMI and the accredited laboratories, can increase the reliability of economic activities, which is supported by certifying the quality of industrial instruments with suitable scientific data.

---

<sup>5</sup> The units can be divided into the basic units (m, kg, s, A, K, Cd, M) and their derived units (N, Pa, W, V, m/s, ...).



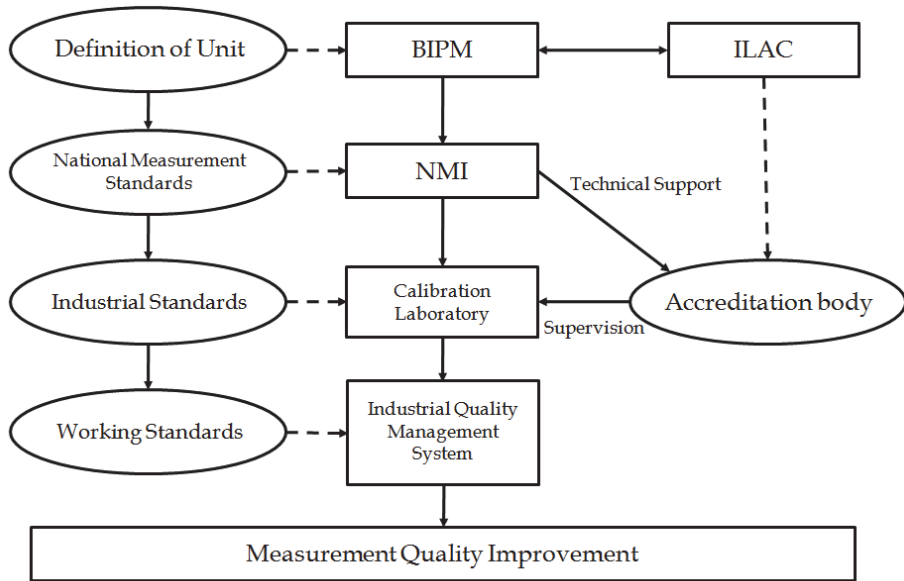


Fig. 1. Traceability of measurement standards (excerpted from Howarth & Redgrave, 2008)

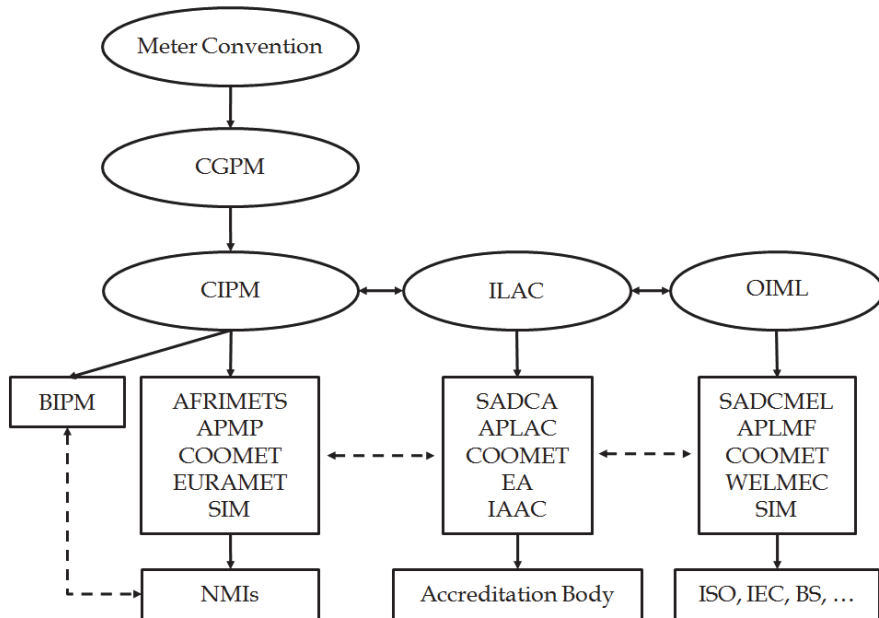


Fig. 2. Meter convention organization and its related organizations (excerpted from Howarth & Redgrave, 2008)

For the national measurement standards in a country to be recognized internationally, the country should participate in the Meter Convention and agree to the Mutual Recognition Arrangement prepared by the Comité Internationale des Poids et Mesures (CIPM), or the CIPM MRA (Howarth & Redgrave, 2008). The CIPM MRA was signed in 1999, slightly revised on some technical points in 2003, consisting of two parts (Howarth & Redgrave, 2008). The first part of the CIPM MRA relates to the establishment of the degree of equivalence of the national measurement standards in a country. The second part of the CIPM MRA concerns the mutual recognition of calibration and measurement certificates issued by participating institutes. These approaches can be supported by International Key Comparisons, or KCs, to check the degree of equivalence of the national standards, which is established by the participating NMIs. If the degree of equivalence of a participating NMI is located within a certain threshold level in comparison with the Key Comparison Reference Value, or the KCRV, then the calibration certificates, issued by the participating NMI, are recognized by other participating NMIs. In this case, a logo, engraved with the CIPM MRA, can be attached on the calibration certificates. Therefore, the CIPM MRA can enhance the international trades by removing technical barriers, regarding both import and export of measurement equipments<sup>6</sup>.

The impact of the CIPM MRA can be understood with a simple example. When an instrument produced in a country A is exported to a country B, the measurement quality of the instrument must be certified by an accredited laboratory in the country B. This is a requirement from a customer, residing in the country B. In other cases, the instrument can be calibrated in another accredited laboratory, which is internationally recognized and located in a country C. Without the CIPM MRA, the instrument must be sent to the country B or the country C to issue a calibration certificate for the instrument. After that, the instrument should be sent to the customer in the country B. However, with the CIPM MRA, the instrument can be also sent to the other accredited laboratory in the country A. In this case, the instrument can be returned to the manufacturer of the instrument soon, because the accredited laboratory is located within the country A. Then, the instrument can be exported directly to the country B with an acceptable calibration certificate. With the calibration certificate issued by the accredited laboratory in the country A, the overall cost for the calibration service would become lower than the case of calibrating the instrument in the country B or the country C. In addition, the delivery time for the instrument would be saved, which leads to providing lower price for the instrument when the manufacturer exports the item to the country B. Therefore, the CIPM MRA provides benefits to both the manufacturer and the customer in the country A and the country B<sup>7</sup>.

Because the international KC is a prerequisite to fulfill the spirit of CIPM MRA, it is necessary to learn some notions of the international KC. There are three levels of the international KCs, namely, a CC-KC, a RMO-KC, and a bilateral comparison. At first, the CC-KC is the world-wide KC, which is supervised by the Technical Committees, or the TC, in a specified field of the Consultative Committees, or the CC, belonged to the BIPM. Secondly, the RMO-KC is the regional KC, which is hosted by the Regional Metrology

---

<sup>6</sup> Some documents regarding the CIPM MRA can be found at <http://www.bipm.org/en/cipm-mra/>.

<sup>7</sup> Similar examples can be found in KRISS CIPM MRA homepage ([http://www.kriss.re.kr/eng/mra/03\\_1.html](http://www.kriss.re.kr/eng/mra/03_1.html)).

Organizations, or the RMOs<sup>8</sup>. As in the CC-KC, the RMO-KC is supervised by the TC members, belonged to the RMO. Finally, the bilateral comparison is the international comparison to check the two independent national measurement standards, established at two participating NMIs. Any of these KCs should be reported to the RMOs or the BIPM to enroll their results to the BIPM database, or the KCDB<sup>9</sup>.

To organize an international KC, a pilot laboratory, which leads the whole process of the international KC, must prepare a test protocol that describes how the KC is to be performed. The pilot laboratory provides an artifact or a transfer standard, and circulates the artifact to the participating NMIs according to the test schedule. The purpose of the artifact is to provide a guideline for estimating the degree of equivalence among the national measurement standards established in the participating NMIs. As a circulation scheme of the artifact, the round robin test is usually preferred; however, other circulation schemes can be adopted, depending on the type of the KCs. After collecting all the calibration data of the transfer standards with reference to the national measurement standards of the participating NMIs, the pilot laboratory estimates the Key Comparison Reference Value, or the KCRV. The degree of equivalence is then calculated by comparing the calibration data given by the participating NMIs with the KCRV. In some cases, the degree of equivalence is normalized within the range of (0 ~ 1). This is because sometimes the normalized degree of equivalence is easier to be understood. When more than three NMIs participate in the international KC, bilateral comparisons are also performed because KCRVs for every two participating NMIs can be estimated. After summarizing the results for the international KC, the pilot laboratory submits a draft report to the RMO office. After suitable revisions are made according to the suggestions of the technical committee members of the RMO, the draft report is approved as the final KC report, and published in both the BIPM homepage and the *Metrologia* technical supplement (Terao et al., 2007; Terao et al., 2010).

In view of traceability, the relationship between the CC-KC and the RMO-KC should be linked via the KCRV, because the RMO-KC is smaller in scale than the CC-KC. To establish linkage between the CC-KC and the RMO-KC, link laboratories, which have participated in the CC-KC, participate also in the RMO-KC to bridge between the two KC results. In this case, the same artifact, once used in the CC-KC, should be employed in the subsequent RMO-KC. If there are any changes in the characteristics of the artifact due to long-term stability, correction factors to the KCRV should be calculated. Toward this end, a weighted average of the degree of equivalence among the link laboratories can be considered to modify the KCRV in the RMO-KC, as an alternative method (Terao et al., 2007; Terao et al., 2010).

### 3.2 Air speed metrology

Air speed is a derived physical quantity, which is based on the mass measurement, according to the classification by the BIPM (Howarth & Redgrave, 2008). The Consultative Committee for Mass and related quantities, or the CCM, manages the physical quantities

---

<sup>8</sup> In the RMOs, there are the APMP (Asia - Pacific region), the COOMET (East European - Siberian region), the EURAMET (European region), the SIM (North and South American region), and the AFRIMETS (African region).

<sup>9</sup> The KCDB has a homepage at <http://kcdb.bipm.org/>

such as mass, force, torque, pressure, density, viscosity, flow rate and flow velocity<sup>10</sup>. A sub-committee under the CCM, named as the Technical Committee for Fluid Flow, or the TCFF, is in charge of the air speed metrology. The air speed metrology is classified into K3 category, therefore, the traceability for the air speed metrology is managed within the scope of the CCM.FF.K3. Hence, the CC-KC, regarding the air speed metrology, is termed as the CCM.FF.K3-KC. The first round of CCM.FF.K3-KC was held in 2005, and an ultrasonic anemometer was used as a transfer standard in the first round CC-KC (Terao et al., 2007). The reason, why the ultrasonic anemometer was used, was because the ultrasonic anemometer showed good measurement accuracy comparable with that of laser Doppler anemometers, which were established as primary standards in the participating NMIs. In the CC-KC, each participating NMI calibrated the ultrasonic anemometer (the *DUT*) with the laser Doppler anemometer (the *REF*) in a wind tunnel (Terao et al., 2007). The role of the wind tunnel was to provide a testing environment to check both the repeatability and the reproducibility of the *DUT* and to provide calibration data for estimating the *KCRV* that was a crucial part of the KC.

### 3.2.1 Wind tunnels

Wind tunnels can be divided into three categories according to the range of air speed. In the low air speed of (0.1 – 1.5) m/s, a wind tunnel, which has a test section with large cross-sectional area, is adopted to generate a low-speed environment for calibration of anemometers<sup>11</sup>. Sometimes, the low-speed wind tunnel has a sonic nozzle bank at the downstream side of a diffuser (Pereira & Jabardo, 1998). This is because the sonic nozzle bank can control the flow rate in the test section of the wind tunnel with high precision. In addition, the sonic nozzle bank can be used as a primary standard for estimating the mean air speed in the test section. In this case, an anemometer, or the *DUT* is installed within the test section of the wind tunnel, while the sonic nozzle bank, or the *REF* controls the air speed in the test section. Other than the low-speed wind tunnel, a moving rail system can be employed for calibrating the anemometers (Spazzini et al., 2009; Piccato et al., 2010)<sup>12</sup>. In the moving rail system, an anemometer is installed on top of a carriage and is moving along a rail under the carriage, as shown in Fig. 3. A laser interferometer can measure the distance between the location of the interferometer to the carriage due to a retro-reflector attached on the side of the carriage. In combination with a timer board, the reference speed of the carriage can be measured by the laser interferometer, or the *REF*. On the other hand, the anemometer, or the *DUT*, installed on the carriage, indicates a value corresponding to the moving velocity of the carriage. Note that the movement of the anemometer in the moving rail system can be viewed as the air speed toward the anemometer, installed in the test section of the low-speed wind tunnel, according to the Galilean transformation (Pope, 2000).

In the medium air speed of (1.5 – 40) m/s, several types of wind tunnels can be applied. At first, an open suction type wind tunnel can have a large test section with high contraction ratio (Barlow et al., 1999). This type of wind tunnel has a large inlet area to take quiescent air

---

<sup>10</sup> There are several Consultative Committees in the CIPM. For example, CCL (length), CCTF (time and frequency), CCM (mass), CCAUV (acoustics and vibrations), CCEM (electro magnetics), CCPR (photometry and radiometry), CCQM (quantity of substance), CCRI (radioactive irradiation), CCT (temperature), and CCU (units) are existent.

<sup>11</sup> This type of wind tunnel was introduced by the National Metrology Institute of Japan, or NMIJ.

<sup>12</sup> There are two towing carriage systems to calibrate anemometers at low air speeds in NMIJ. (<http://www.nmij.jp/english/org/lab/3/>)

to the test section. Air filters can be installed at the front of the inlet section to prevent dust from entering the test section and to provide a certain amount of pressure drop for generating uniform flows at the inlet. A honeycomb-shaped panel and several sheets of screens are installed in the settling chamber of the wind tunnel. A contraction section makes the air flows more uniform and stable. Downstream of the test section, a diffuser is placed to give less adverse pressure gradient by increasing the cross-sectional area along the main flow direction. When the open suction type wind tunnel is used for calibration purposes, air in front of the inlet section should be as quiescent as possible. Toward this end, a baffle can be installed at the side of the inlet section to prevent flow disturbances at the inlet of the wind tunnel<sup>13</sup>. When the fluctuations of air flows at the inlet of the wind tunnel are concerned, the closed-type wind tunnel can be considered (Barlow et al., 1999; Tropea et al., 2007). In the closed-type wind tunnel, air is circulated within a square duct, so that the flow quantities as well as fluid pressure, thermodynamic temperature or humidity can be stabilized more than the open suction type wind tunnel. An axial fan generates air flows, and the air flows go through mechanical parts such as the honeycomb, the screen, the contraction, the diffuser, and the test section. However, because the overall size increases due to the circulating ducts, the test section size could be smaller than that of the open suction type wind tunnel, if the installation site for constructing a wind tunnel is limited in size. In addition, the open suction type or the closed-type wind tunnels utilize a square duct as a test section, so that some problems due to the growth of a boundary layer flow at the wall of the test section can be concerned for calibration purposes.

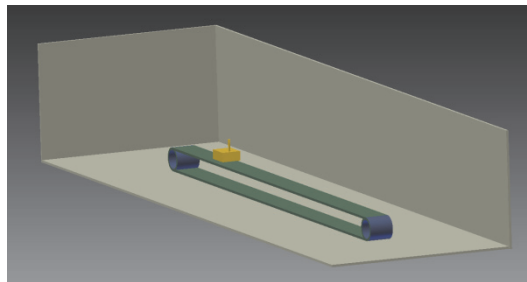


Fig. 3. Schematic diagram of low-speed facility with a towing carriage

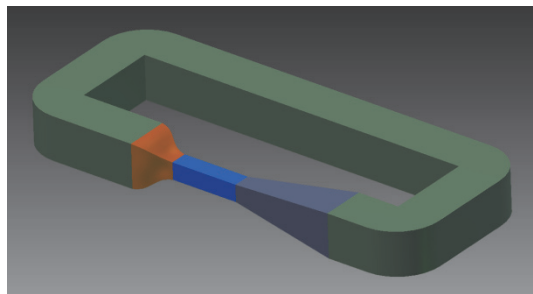


Fig. 4. Schematic diagram of a closed type wind tunnel

<sup>13</sup> The idea of installing a baffle at the side of the inlet section was given by G. E. Mattingly, when he visited at the Korea Research Institute of Standards and Science, or KRISS in 2006.

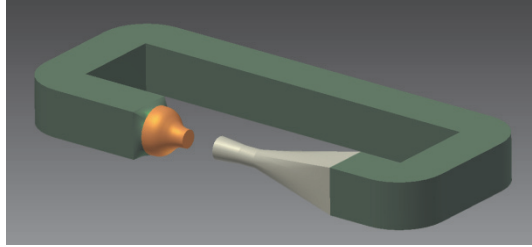


Fig. 5. Schematic diagram of a Göttingen type wind tunnel

The Göttingen type wind tunnel adapts a nozzle with a circular cross-section to generate stable air flows in the test section (Jian, 2009). Because the nozzle produces a potential core in the center of the air flows, the quality of air flows should be better than that of the square duct flows. Nonetheless, the size of the test section is limited, because of the rather a bit smaller size of the nozzle.

In the high air speed of (40 - 70) m/s, closed-type wind tunnels are mostly utilized, because of the ability generating stabilized air flows, compared with other types of wind tunnels. In the high air speed measurement, it should be careful about the thermodynamic temperature increase during anemometer calibrations due to the amount of heat, generated by friction of blades of an axial fan, transferred toward the test section (Barlow et al., 1999; Dixon, 2010). The application area of the high-speed wind tunnels can be automobile industry, aeronautics, and geographical fluid dynamics, including calibration of anemometers for meteorological purposes. Some examples of wind tunnel testing are given in the literature (Tropea et al., 2007).

### 3.2.2 Anemometers

Anemometers can be divided into several types in view of the measurement quality. The most accurate anemometer would be the Laser Doppler Anemometer, or the LDA<sup>14</sup>. The LDA can be used as the national measurement standard in air speed metrology, because the measurement accuracy of the LDA can be achieved as low as 0.07 % (Kurihara et al., 2002; Yeh & Hall, 2008; Jian, 2009; Yang et al., 2002). The LDA formula is as follows.

$$V = \frac{\lambda f_D}{2 \sin(\frac{\theta}{2})} \quad (13)$$

Here,  $V$  is the air speed [m/s],  $\lambda$  is the wavelength of a laser beam [nm],  $f_D$  is the Doppler frequency of a seeding particle [Hz], and  $\theta$  is the laser beam crossing angle [rad].  $\lambda$  can be obtained from a table, regarding lasers (Arecchi & Schulz-Dubois, 1972),  $f_D$  can be measured with a high-speed digitizer, and  $\theta$  can be measured by traversing the LDA probe carefully (ITTC, 2008; Jian, 2009; Kurihara et al., 2002; Yang et al., 2002; Yeh & Hall, 2007; Yeh & Hall, 2008).

When the LDA was invented in 1960's, it was believed that it was not necessary to calibrate the LDA (Yeh & Cummins, 1964). However, soon after its invention, it was found that the LDA was not a calibration-free instrument, because the fringe spacing, which was the most important part of the LDA, was not uniform within the measurement volume of the LDA. The characteristics of Gaussian beam optics, governing the working principles of the LDA, make the fringe spacing divergent or convergent along the laser beam axis (Miles, 1996). The

<sup>14</sup> Sometimes, the LDA can be named as the Laser Doppler Velocimeter, or the LDV.

fringe distortion is because of the locations of two laser beam waists relative to the crossing point of the two laser beams. Therefore, an endeavor to align the laser beam waists is necessary to attain an ideal fringe divergence for the LDA (Yang et al., 2002).

The ultrasonic anemometer can be used as a transfer standard because of high accuracy and good reproducibility (Terao et al., 2007; Terao et al., 2010). There are two kinds of measuring techniques to determine air speeds with the ultrasonic anemometers; One is the sing around and the other is the Doppler techniques. The sing around technique needs a pair of ultrasonic sensors to construct ultrasonic paths for measuring both the air speed and the speed of sound.

$$c + V = \frac{L_1}{t_1} \quad (14)$$

$$c - V = \frac{L_2}{t_2} \quad (15)$$

Here,  $c$  is the speed of sound [m/s],  $L_i$  ( $i = 1, 2$ ) is the path length between a pair of ultrasonic sensors (one is in the upstream direction and the other is in the downstream direction), and  $t_i$  ( $i = 1, 2$ ) is the transit time of ultrasonic waves from the transmitter to the receiver of the ultrasonic sensors. From Eqns. (14) and (15), the air speed and the speed of sound can be solved as follows.

$$c = \frac{1}{2} \left( \frac{L_1}{t_1} + \frac{L_2}{t_2} \right) \quad (16)$$

$$V = \frac{1}{2} \left( \frac{L_1}{t_1} - \frac{L_2}{t_2} \right) \quad (17)$$

Pitot tube can be also used as another transfer standard of air speed measurement, because the measured velocity by the Pitot tube is reliable (Blom et al., 2008). The working principle of the Pitot tube is the Bernoulli equation for air speed and differential pressure between the total and the static pressure holes. The equation for the Pitot tube is as follows (ISO, 2008a; Tavoularis, 2005).

$$V = (1 - \varepsilon) \sqrt{\frac{2\Delta P}{\rho}} \quad (18)$$

Here,  $(1-\varepsilon)$  is a compressibility correction factor,  $\rho$  is the air density [ $\text{kg}/\text{m}^3$ ] and  $\Delta P$  is the differential pressure indicated by the Pitot tube [Pa]. The air compressibility can be expressed as follows (ISO, 2008a).

$$1 - \varepsilon = \left[ 1 - \frac{1}{2\gamma} \frac{\Delta p}{\rho} + \frac{\gamma-1}{6\gamma^2} \left( \frac{\Delta p}{\rho} \right)^2 \right]^{1/2} \quad (19)$$

Here,  $\gamma$  is the ratio of specific heat capacities ( $c_v$  and  $c_p$ ). The air density can be expressed as follows (Picard et al., 2008).

$$\rho = \frac{PM_a}{ZRT} \left[ 1 - x_v \left( 1 - \frac{M_v}{M_a} \right) \right] \quad (20)$$

Here,  $P$  is the atmospheric pressure [Pa],  $M_a$  is the molar mass of dry air [g/mol],  $M_v$  is the molar mass of water [g/mol],  $x_v$  is the mole fraction of water vapour,  $Z$  is the compressibility factor,  $R$  is the molar gas constant [J/mol·K], and  $T$  is the thermodynamic temperature [K]. If simplified by calculations, Eqn. (20) becomes as follows.

$$\rho = [3.483\,740 + 1.4446 \cdot (x_{CO_2} - 0.0004)] \cdot \frac{P}{ZT} (1 - 0.3780x_v) \quad (21)$$

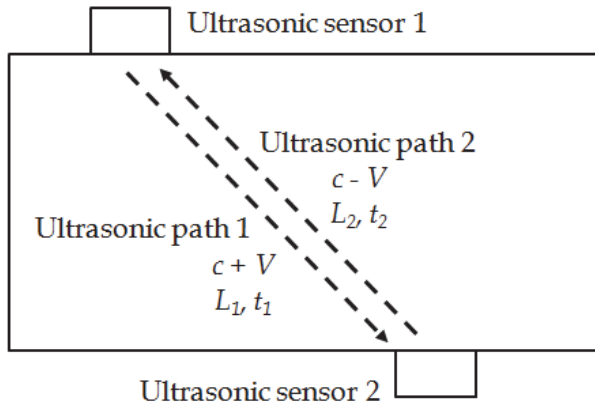


Fig. 6. Schematic diagram of sing around type ultrasonic anemometry

Here,  $x_{CO_2}$  is the mole fraction of  $CO_2$  in the air.

In industrial applications, thermal anemometers and rotational anemometers are commonly used. The equations of the thermal anemometers are as follows (Bruun, 1995).

$$E^2 = A + B\sqrt{V} \quad (22)$$

or

$$\sqrt{V} = \sum_{i=0}^4 A_i E^i \quad (23)$$

Here,  $E$  is the electric voltage [V].  $A$ ,  $B$ , and  $A_i$  are calibration coefficients. In the case of the rotational anemometers, the equation is given like this.

$$V = r\omega \quad (24)$$

Here,  $r$  is the radius of a rotational vane [mm], and  $\omega$  is the rotational frequency [rad/s].

In view of air speed metrology, the thermal and rotational anemometers have accuracy of about  $\pm 1\%$ . Their application area includes fluid machinery, environmental monitoring, and wind engineering, etc. These anemometers are to be calibrated to maintain the measurement traceability in the air speed measurement. The Pitot tubes and the ultrasonic anemometers have accuracy of about  $\pm 0.5\%$ , and these can be employed as industrial standards for air speed measurement. In many accredited institutes, the Pitot tubes and the ultrasonic anemometers are adopted as reference anemometers for calibration service. The LDA has measurement accuracy of less than  $\pm 0.2\%$ . Therefore, the LDA can be used as a national measurement standard. However, some accredited institutes have the LDA as an industrial standard. In this case, the measurement accuracy of the LDA systems, which are located in different institutes, can be estimated by performing bilateral or multilateral key comparisons. Alternatively, many NMIs establish a means of calibrating the LDA, particularly calibrating the fringe divergence within the measurement volume of the LDA, by rigid rotation. A rotating wheel or a spinning wire are good examples of the LDA calibrator (ITTC, 2008; Jian, 2009; Kurihara et al., 2002; Yang et al., 2002; Yeh & Hall, 2007; Yeh & Hall, 2008). Because the rigid rotation has measurement accuracy of less than  $\pm 0.1\%$ , these devices can be considered as the primary standard for air speed metrology.



Anemometer	Uncertainty factors
LDA	beam crossing angle, Doppler frequency, fringe divergence, wavelength
Ultrasonic	sensor distance, sound speed, time measurement, ...
Pitot tube	air density, differential pressure, expansibility, sensor alignment, ...
Thermal	curve fitting uncertainty, temperature, voltage, ...
Rotational	sensor alignment, radial location of rotating parts, rotating speed, ...

Table 2. Uncertainty factors for various types of anemometers.

### 3.2.3 Calibration of anemometers

When the anemometers are calibrated with a reference anemometer, calibration coefficient  $\alpha$  can be determined by calculating the ratio between the two anemometers.

$$\alpha = \frac{V_{REF}}{V_{DUT}} \quad (25)$$

Here,  $V_{DUT}$  is the air speed from the calibrated anemometer (*DUT*) [m/s], and  $V_{REF}$  is the air speed from the reference anemometer (*REF*) [m/s]. In view of traceability,  $\alpha$  can be obtained successively and transferred to other types of anemometers with lower measurement accuracies. Therefore,  $\alpha$  can be represented as follows.

$$\alpha = \frac{V_{REF}}{V_{DUT1}} \frac{V_{DUT1}}{V_{DUT2}} \frac{V_{DUT2}}{V_{DUT3}} \dots \frac{V_{DUT_{n-1}}}{V_{DUTn}} = \alpha_1 \alpha_2 \alpha_3 \dots \alpha_n \quad (26)$$

Here,  $\{\alpha_i, i = 1, 2, \dots, n\}$  means the calibration coefficients by subsequent comparison between two anemometers, according to the traceability chain. For example,  $\alpha_1$  can be a calibration coefficient between the spinning wire and the LDA,  $\alpha_2$  can be another calibration coefficient between the LDA and the ultrasonic anemometer, and so on. In these successive measurements, the uncertainty can be estimated as a vector sum among the calibrated apparatuses.

$$U = k \sqrt{u_{REF}^2 + u_{DUT1}^2 + u_{DUT2}^2 + \dots + u_{DUTn}^2} \quad (27)$$

Here,  $u_{REF}$  is the standard uncertainty of the *REF*, and  $\{u_{DUTi}, i = 1, 2, \dots, n\}$  is the standard uncertainties of the *DUT*. The coverage factor,  $k$  is then calculated by estimating the effective degree of freedom  $\nu_{eff}$  as explained previously.

$$\nu_{eff} = \frac{(U/k)^4}{\frac{u_{REF}^4}{\nu_{REF}} + \frac{u_{DUT1}^4}{\nu_{DUT1}} + \frac{u_{DUT2}^4}{\nu_{DUT2}} + \dots + \frac{u_{DUTn}^4}{\nu_{DUTn}}} \quad (28)$$

Here,  $\nu_{REF}$  is the effective degree of freedom of the *REF*, and  $\{\nu_{DUTi}, i = 1, 2, \dots, n\}$  is the effective degrees of freedom of the *DUT*.

### 3.2.4 Uncertainty estimation of anemometers

There are three kinds of methods to estimate the uncertainty of anemometers. The first method is to use first-order partial differentiation of an equation to the specific type of the anemometer (Thomas & Finney, 1988). If the anemometer equation is written as follows,

$$y = f(x_1, x_2, \dots, x_n) \quad (29)$$

then the uncertainty can be estimated based on the first-order partial differentiations of  $y$ .

$$u(y) = \left[ \left( \frac{\partial f}{\partial x_1} \right)^2 u(x_1)^2 + \left( \frac{\partial f}{\partial x_2} \right)^2 u(x_2)^2 + \dots + \left( \frac{\partial f}{\partial x_n} \right)^2 u(x_n)^2 \right]^{1/2} \quad (30)$$

Here,  $\partial f / \partial x_i$  can be denoted as  $c_i$ , a sensitivity coefficient (BIPM, 1993). As an example, the uncertainty of the LDA can be estimated by partial differentiation of Eqn. (13).

$$u(V) = \left[ \left( \frac{\partial V}{\partial \lambda} \right)^2 u(\lambda)^2 + \left( \frac{\partial V}{\partial f_D} \right)^2 u(f_D)^2 + \dots + \left( \frac{\partial V}{\partial \theta} \right)^2 u(\theta)^2 \right]^{1/2} \quad (31)$$

$$\frac{\partial V}{\partial \lambda} = \frac{f_D}{2 \sin\left(\frac{\theta}{2}\right)} \quad (32)$$

$$\frac{\partial V}{\partial f_D} = \frac{\lambda}{2 \sin\left(\frac{\theta}{2}\right)} \quad (33)$$

$$\frac{\partial V}{\partial \theta} = -\frac{1}{4} \frac{\lambda f_D \cos\left(\frac{\theta}{2}\right)}{\left(\sin\left(\frac{\theta}{2}\right)\right)^2} \quad (34)$$

The second method is to differentiate the anemometer equation, as seen in the first method. However, in this case, an equation with multiplication is more appropriate, because all the calculation is done by relative ratios of each independent variable.

$$y = x_1^a x_2^b \dots x_{i-1}^p x_i^q x_{i+1}^r \dots x_n^z \quad (35)$$

The first-order partial differentiation of  $i$ -th independent variable can be written as follows.

$$\frac{\partial y}{\partial x_i} = q x_1^a x_2^b \dots x_{i-1}^p x_i^{q-1} x_{i+1}^r \dots x_n^z \quad (36)$$

If the Eqn. (36) is divided by the Eqn. (35), then the ratio of  $\frac{\partial y}{\partial x_i}$  to  $y$  is calculated as follows.

$$\frac{\frac{\partial y}{\partial x_i}}{y} = \frac{q}{x_i} \quad (37)$$

Therefore, the ratio of uncertainty of  $y$  can be represented as follows.

$$\frac{u(y)}{y} = \left[ \left( \frac{\partial y}{\partial x_1} \right)^2 \left( \frac{u(x_1)}{y} \right)^2 + \left( \frac{\partial y}{\partial x_2} \right)^2 \left( \frac{u(x_2)}{y} \right)^2 + \dots + \left( \frac{\partial y}{\partial x_n} \right)^2 \left( \frac{u(x_n)}{y} \right)^2 \right]^{1/2} \quad (38)$$

Further simplified,

$$\frac{u(y)}{y} = \left[ \left( \frac{a}{x_1} \right)^2 u(x_1)^2 + \left( \frac{b}{x_2} \right)^2 u(x_2)^2 + \dots + \left( \frac{z}{x_n} \right)^2 u(x_n)^2 \right]^{1/2} \quad (39)$$

In case of the rotational anemometers, the uncertainty can be estimated referring to Eqn. (24).

$$\frac{u(V)}{V} = \left[ \left( \frac{1}{r} \right)^2 u(r)^2 + \left( \frac{1}{\omega} \right)^2 u(\omega)^2 \right]^{1/2} \quad (40)$$

The third method is to use a simplified version of Monte-Carlo simulation (ISO, 2008b; Landau & Binder, 2005). An input variable is composed of a large number of data more than 1,000,000, according to the Gaussian random process. The input variables to the anemometer equation should be independent and uncorrelated, to ensure a rigorous simulation for uncertainty estimation<sup>15</sup>. The mean and the standard deviation of each input variable are used to scale a Gaussian random signal. After that, the output variable, or the measuring quantity, is estimated by calculating the equation with the input variables. An example to estimate the measurement uncertainty of the Pitot tube is given as follows.

(Example) Estimate the standard (or Type A) uncertainty of the Pitot tube by using a Monte-Carlo simulation. The mean values and the standard deviations of each input variable are listed as follows. The number of simulation is 1,000,000.

- $\Delta P$  : mean value = 5 Pa, standard deviation = 0.05 Pa (or 1 %)
- $\rho$  : mean value = 1.18 kg/m<sup>3</sup>, standard deviation = 0.012 kg/m<sup>3</sup> (or 1 %)
- $\varepsilon$  : mean value = 0.00002, standard deviation =  $2 \times 10^{-7}$  (or 1 %)

(Solution) The uncertainty estimation can be performed by programming with MATLAB<sup>16</sup>. To generate three Gaussian random signals with 1,000,000 samples, the command can be written as follows.

```
[s1, s2, s3] = RandStream.create('mlfg6331_64', 'NumStreams', 3);
r1=randn(s1, 1000000, 1);
r2=randn(s2, 1000000, 1);
r3=randn(s3, 1000000, 1);
```

To confirm the uncorrelated signals, correlation coefficients can be calculated in matrix form.

```
A = corrcoef([r1, r2, r3]);
```

To give the above-mentioned mean values and standard deviations, following commands can be written.

```
% For differential pressure
del_P_avg = 5;
del_P_std = 0.05;
del_P = del_P_avg + del_P_std * r1;
% For air density
rho_avg = 1.18;
rho_std = 0.012;
rho = rho_avg + rho_std * r2;
% For expansibility coefficient
epsilon_avg = 0.00002;
epsilon_std = 2E-7;
epsilon = epsilon_avg + epsilon_std * r3;
```

<sup>15</sup> In the case of correlated input variables, there should be another assumptions to generate random signals, which can give cross-correlation coefficients among the input variables. However, the book chapter only focuses on the case of the uncorrelated input variables.

<sup>16</sup> In this example, MATLAB (R2010b) was used to generate Gaussian random signals.

To calculate the Pitot tube velocity, the following commands can be added.

```
% For Pitot tube velocity
V=(1-epsilon).*(2*del_P./rho).^0.5;
V_avg=mean(V);
V_std=std(V);
V_ratio=V_std/V_avg*100;
```

The rests are to look at the calculated results for uncertainty estimations.

```
sprintf('V: mean=%12.4e, std=%12.4e, ratio=%12.4e %%', V_avg, V_std, V_ratio)
figure('Name','Pitot tube velocity','NumberTitle','off')
subplot1 = subplot(4,1,1); box(subplot1,'on'); hold(subplot1,'all');
plot(del_P); ylabel('ΔP [Pa]');
subplot2 = subplot(4,1,2); box(subplot2,'on'); hold(subplot2,'all');
plot(rho); ylabel('ρ [kg/m³]');
subplot3 = subplot(4,1,3); box(subplot3,'on'); hold(subplot3,'all');
plot(epsilon); ylabel('ε');
subplot4 = subplot(4,1,4); box(subplot4,'on'); hold(subplot4,'all');
plot(V); ylabel('V [m/s]'); xlabel('number of realization');
```

Here are some results for estimating the standard deviation of  $V$ .

```
A =      1.0000  0.0008 -0.0004
      0.0008  1.0000  0.0012
      -0.0004  0.0012  1.0000
V [m/s]: mean = 2.9111e+000, std = 2.0741e-002, ratio = 7.1248e-001 %
```

Therefore, the mean and the standard deviation of  $V$  are 2.91 m/s and 0.021 m/s, respectively. The standard (or Type A) uncertainty of  $V$  would be  $\frac{0.021}{\sqrt{1,000,000}} = 2.1 \times 10^{-5}$  [m/s]<sup>17</sup>. From the matrix  $A$ , it is noticed that cross-correlation coefficients among  $r_1$ ,  $r_2$ , and  $r_3$ , are small enough to assume the uncorrelated random signals among  $\Delta P$ ,  $\rho$ , and  $\epsilon$ .

### 3.2.5 Uncertainty estimation of a calibration curve

When a curve fitting formula is considered to give a customer an estimate of air speed correction, uncertainty that is based on least square methods should be included (Hibbert, 2006). In many cases, in graphing the calibration data, the reference quantity ( $REF$ ) is located in the horizontal axis, while the tested quantity ( $DUT$ ) is drawn in the vertical axis. Assuming the homoscedacity, there is no variance in the  $REF$ , or the horizontal axis (Hibbert, 2006). However, when estimating the measurement uncertainty, variances of the  $DUT$  by  $m$  measurements (reproducibility) premises the variance of the  $REF$ . Therefore, in this case, the variance of the  $REF$  can be estimated by calculating the residual standard deviation (Hibbert, 2006). In case of a linear regression, the calibration curve can be defined as follows.

$$\bar{y} = \hat{a} + \hat{b}\bar{x} \quad (41)$$

<sup>17</sup> This standard uncertainty considers only the type A uncertainty, which is determined by measurements. The type B uncertainty, which can be obtained from tables, calibration certificates, etc., should be included to complete the uncertainty estimation.

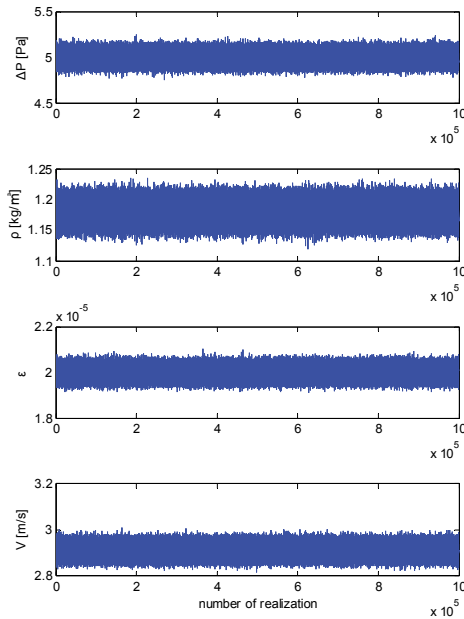


Fig. 7. An example of a simplified Monte Carlo simulation

Here,  $\hat{a}$  and  $\hat{b}$  are calibration coefficients.  $\bar{x}$  and  $\bar{y}$  are mean values of  $n$ -realizations, i.e.,  $\{x_i, y_i, i = 1, 2, \dots, n\}$ . Then, the residual standard deviation,  $s_y$  can be calculated as follows (Hibbert, 2006).

$$s_y = \sqrt{\frac{\sum_i (y_i - (\hat{a}x_i + \hat{b}))^2}{n-2}} \quad (42)$$

Then, the standard uncertainty can be derived from the following equation (Hibbert, 2006).

$$s_{\hat{x}_0} = \frac{s_y}{b} \sqrt{\frac{1}{m} + \frac{1}{n} + \frac{(y_0 - \bar{y})^2}{b^2 \sum_i (x_i - \bar{x})^2}} \quad (43)$$

Here,  $y_0$  is the mean value of  $m$  responses, at a single point of  $y_i$ , and  $\hat{x}_0$  is the estimate of  $x_0$  by using Eqn. (41). ( $m$  means the reproducibility, and  $n$  means the number of calibration points.)

## 4. International comparisons

### 4.1 CC-KC

The international Key Comparison aims to compare the national measurement standards among participating NMIs and to harmonize the measurement traceability for establishing the MRA. The meaning of the Key Comparisons is like this; when a person holds a key to a box, then other people should also have the same keys to open the box. This means that the measurement uncertainty among the participating NMIs should be located within an acceptable level so that the national measurement standards are recognized to be equal.

The first round of the CC-KC, which was an world-wide level, was performed from April to December in 2005, and its final report was published in October 2007 (Terao et al., 2007). Four NMIs, including NMIJ (Japan), NMI-VSL (Netherlands), NIST (USA), and PTB (Germany), participated in the CC-KC. NMIJ was the pilot laboratory for the CC-KC. A three-dimensional ultrasonic anemometer was used as a transfer standard to be calibrated in a wind tunnel or a specially-designed circular duct using the LDA. The calibration results were summarized with air speeds of 2 m/s and 20 m/s as a calibration coefficient,  $x_i$ , which has the same meaning as  $\alpha$  in Eqn. (25). Repeatability was checked by measuring the air speed for 60 s to report the averaged air speed at 2 m/s and 20 m/s. Reproducibility was also checked by several sets of air speed data.

To obtain the KCRV, which can be established as a standard value to compare the national measurement standards among the participating NMIs, a weighted average was used and a chi-squared test was performed to validate the weighted average. According to the Cox method, the weighted average was acceptable as the KCRV if the chi-squared test was passed (Cox, 2002). When the chi-squared test was failed, another method such as the simplified Monte Carlo simulation with  $10^6$  random samples should be tried (ISO, 2008b; Terao et al., 2007).

To harmonize the national measurement standards of the participating NMIs, the degree of equivalence,  $d_i$  was defined as follows (Terao et al., 2007).

$$d_i = x_i - x_{REF} \quad (44)$$

Here,  $x_i$  is the calibration coefficient of  $i$ -th participating NMI, and  $x_{REF}$  is the KCRV. Another definition of the degree of equivalence was introduced to compare the two national measurement standards between two participating NMIs.

$$d_{i,j} = x_i - x_j \quad (45)$$

The standard uncertainties of  $d_i$  and  $d_{i,j}$  can be determined by vector sums between  $x_i$  and  $x_{REF}$ , or between  $x_i$  and  $x_j$ , as follows (Terao et al., 2007).

$$u(d_i) = \sqrt{u(x_i)^2 + u(x_{REF})^2} \quad (46)$$

$$u(d_{i,j}) = \sqrt{u(x_i)^2 + u(x_j)^2} \quad (47)$$

The number of equivalence, or the normalized degree of equivalence can be derived as follows (Terao et al., 2010).

$$En_i = \frac{|d_i|}{ku(d_i)} \quad (48)$$

$$En_{i,j} = \frac{|d_{i,j}|}{ku(d_{i,j})} \quad (49)$$

Here,  $En_i$  is the number of equivalence for  $d_i$ ,  $En_{i,j}$  is the number of equivalence for  $d_{i,j}$ , and  $k$  is the coverage factor. The role of the number of equivalence is to provide a guideline whether the national measurement standard of each participating NMI has an equivalence in comparison with the KCRV or other national measurement standards from other NMIs. If the value is less than 1, then it can be said that the national measurement standard has equivalence with those of other NMIs.

#### 4.2 RMO-KC

An RMO-KC, named as the APMP.M.FF.K3-KC, was performed from February to December in 2009 to give a supporting evidence for fulfilling the spirit of MRA (Terao et al., 2010). In the APMP-KC, five air speeds of (2, 5, 10, 16, 20) m/s were tested, and two of the air speeds, i.e., 2 m/s and 20 m/s, were selected to link the results to those of the CC-KC. The participating laboratories in the APMP-KC were NMIJ (Japan), CMS/ITRI (Chinese Taipei), KRISS (Korea), NIST (USA), NMC A\*STAR (Singapore), and VNIIM (Russia). NMIJ was the pilot laboratory. In addition, there were two link laboratories (NMIJ and NIST) to link the KC results to those of the CC-KC. For this purpose, the three-dimensional ultrasonic anemometer, which had been adopted in the CC-KC, was also chosen in the APMP-KC. To link between the APMP-KC and the CC-KC results, a weighted sum was calculated using the calibration data from the two link laboratories as in the following equations (Terao et al., 2010).

$$D = \sum_i w_i D_i \quad (50)$$

$$D_i = x_{i,CCM} - x_{i,APMP} \quad (51)$$

$$w_i = \frac{\frac{1}{u_i^2}}{\frac{1}{u_{NMIJ}^2} + \frac{1}{u_{NIST}^2}} \quad (52)$$

Here,  $D_i$  is the difference between the CC-KC and the APMP-KC results.  $x_{i,CCM}$  is the CC-KC results of the link laboratories, and  $x_{i,APMP}$  is those of the APMP-KC.  $w_i$  is a weighting coefficient, which can be calculated from the standard uncertainties of the link laboratories. In particular,  $u_{NMIJ}$  is the standard uncertainty of the NMIJ and  $u_{NIST}$  is the standard uncertainty, given by the NIST, respectively.

Through these calculations, the APMP-KC results could be linked to those of the CC-KC by modifying the APMP-KC results as follows (Terao et al., 2010).

$$x'_i = x_{i,APMP} + D \quad (53)$$

Here,  $x_{i,APMP}$  is the APMP-KC result of  $i$ -th participating NMI and  $x'_i$  is its modified value. With  $x'_i$ , the normalized degree of equivalence, or the number of equivalence,  $En_i$  could be estimated to harmonize the national measurement standards among the participating NMIs. In 2008, another RMO-KC, named as Euromet.M.FF-K3 KC, was reported. The participating laboratories were NMi-VSL (Netherlands), CETIAT (France), DTI (Denmark), SFOMA (Swiss), PTB (Germany), TUMET (Turkey), University of Tartu (Estonia), LEI (Lithuania), INTA (Spain), and MGC-CNR (Italy). NMi-VSL was the pilot laboratory. The Euromet-KC was rather a bit an independent Key Comparison, because the transfer standards used in the KC were different from those used in the CC-KC or the APMP-KC (Blom et al., 2008). A Pitot tube with an amplifier and a thermal anemometer were chosen in the Euromet-KC as two transfer standards. Several air speeds between 0.2 m/s and 4.5 m/s were tested, which was prone to low air speed range, compared with the air speed ranges in the CC-KC. There was no linkage between the Euramet-KC and the CC-KC, due to the different measurement ranges of air speeds. The KCRV was calculated from a weighted average as follows.

$$KCRV = \frac{\sum_i \frac{x_i}{u(x_i)^2}}{\sum_i \frac{1}{u(x_i)^2}} \quad (54)$$

$$u_{KCRV} = \frac{1}{\sqrt{\sum_i \frac{1}{u(x_i)^2}}} \quad (55)$$

The chi-square test was performed to validate the KCRV, and the chi-square test was passed in the Euramet-KC. With the calibration coefficient  $x_i$ , the degree of equivalence or the number of equivalence could be estimated to harmonize the national measurement standards among the participating NMIs.

## 5. Conclusion

To enhance international trades with low technical barriers, some common perceptions of measurement standards are necessary. In the early stages of measurement standards, definition of basic units was the most important issue. With technological advancements, the re-definitions of the basic units based on the physical constants have been suggested to increase the measurability of the international standards. Traceability chain was probably the second issue to establish an industrial infrastructure with reliable measurement standards. Mutual recognition arrangement could be the third issue to enhance the economic activity by lowering technical barriers, such as calibration certificates. This was supported by the traceability chain and the international key comparisons in view of metrologists.

In air speed measurement, various types of anemometers, including the rigid body rotation, the LDA, the ultrasonic anemometer, the Pitot tube, the thermal and the rotational anemometers, consisted the hierarchy of the traceability chain. Wind tunnels, such as the open suction, the close, and the Göttingen type wind tunnels, were used to generate a stable test environment for anemometer calibrations. Uncertainty estimation of anemometers was performed in three ways; first-order partial differentiation, a modified partial-differentiation with a multiplicative equation form, and a simplified Monte Carlo simulation.

Finally, some aspects of the international key comparisons, regarding the air speed measurement, was surveyed. In the key comparisons, the key comparison reference value was deduced from a weighted average, and validated using the chi-square test. In some cases, a Monte Carlo simulation was applied to obtain a suitable reference value for the key comparison. To link between two different key comparison results, link to the key comparison reference value was discussed. Throughout the analysis on the key comparisons, the degree of equivalence among the participating national metrology institutes was validated and the analysis was used as a supporting evidence to fulfill the embodiment of the mutual recognition arrangement.

## 6. Acknowledgement

The author is grateful to Mr. Kwang-Bock Lee and Dr. Yong-Moon Choi for their helpful advices, regarding general directions and criticism in preparation for the book chapter. This work was partially supported by Korea Institute of Energy Technology Evaluation and Planning (KETEP), which belonged to the Ministry of Knowledge Economy in Korea (grant funded with No. 2010T100100 356).



## 7. References

- Arecchi, F. T. & Schulz-Dubois, E. O. (1972). *Laser Handbook*, North-Holland, ISBN 0-720-40213-1, Amsterdam, Netherlands
- Barlow, J. B.; Rae, Jr., W. H. & Pope, A. (1999). *Low-Speed Wind Tunnel Testing*, John Wiley & Sons, ISBN 0-471-55774-9, New York, USA
- Beckwith, T. G.; Marangoni, R. D. & Lienhard, J. H. (1993). *Mechanical Measurements*, Addison-Wesley, ISBN 0-201-56947-7, New York, USA
- Bendat, J. S. & Piersol, A. G. (2000). *Random Data: Analysis & Measurement Procedures*, John Wiley & Sons, ISBN 0-471-31733-0, New York, USA
- BIPM; IEC IFCC; ISO; IUPAC; IUPAP & OIML (1993). *Guide to the Expression of Uncertainty in Measurement*, International Organization for Standardization, ISBN 92-67-10188-9, Geneva, Swiss
- Cox, M. G. (2002). The Evaluation of Key Comparison Data, *Metrologia*, Vol.39, pp.589-595, ISSN 0026-1394
- Blom, G.; Care, I.; Frederiksen, J.; Baumann, H; Mickan, B.; Cifti, V.; Jakobson, E.; Pedisius A.; Sanchez, J. & Spazzini, P. (2008). *Euromet.M.FF-K3 Euromet Key Comparison for Airspeed Measurements*, EUROMET Project No. 514
- Bruun, H. H. (1995). *Hot-Wire Anemometry: Principles and Signal Analysis*, Oxford University Press, ISBN 978-0-19-856342-6, Oxford, U.K.
- Dixon, S. L. & Hall, C. A. (2010). *Fluid Mechanics and Thermodynamics of Turbomachinery*, Butterworth-Heinemann, ISBN 1-856-17793-9, New York, USA
- Dougherty, E. R. (1990). *Probability and Statistics for the Engineering, Computing and Physical Sciences*, Prentice-Hall, ISBN 0-13-715913-7, New Jersey, USA
- Gläser, M.; Borys, M.; Ratschko, D. & Schwartz, R. (2010). Redefinition of the kilogram and the impact on its future dissemination. *Metrologia*, Vol.47, pp.419-428, ISSN 0026-1394
- Hibbert, D. B. (2006). The Uncertainty of a Result from a Linear Calibration. *The Analyst*, Vol.131, pp.1273-1278, ISSN 0003-2654
- Howarth, P. & Redgrave, F. (2008). *Metrology – In Short*, EURAMET, ISBN 978-87-988154-5-7, Albertslund, Denmark
- ISO (2005). *General requirements for the competence of testing and calibration laboratories*, International Organization for Standardization, ISO /IEC17025:2005, Geneva, Swiss
- ISO (2008a). *Measurement of Fluid Flow in Closed Conduits – Velocity Area Method Using Pitot Static Tubes*, International Organization for Standardization, ISO 3966:2008, Geneva, Swiss
- ISO (2008b). *Propagation of distributions using a Monte Carlo method*, International Organization for Standardization, ISO/IEC Guide 98-3:2008/Suppl 1:2008, Geneva, Swiss
- ITTC (2008). *Uncertainty Analysis: Laser Doppler Velocimetry Calibration*, *ITTC Recommended Procedures and Guidelines*, International Towing Tank Conference, 7.5-01-03-02
- Jian, W. (2009). Realization of a Primary Air Velocity Standard Using Laser Doppler Anemometer and Precision Wind Tunnel, *XIX IMEKO World Congress, Fundamental and Applied Metrology*, September 6-11, 2009, Lisbon, Portugal
- Kirkup, L. & Frenkel, B. (2006). *An Introduction to Uncertainty in Measurement Using the Gum*, Cambridge University Press, ISBN 0-521-60579-2, New York, USA

- Kurihara, N.; Terao, Y. & Takamoto, M. (2002). LDV Calibrator for the Air Speed Standard between 1.3 to 40 m/s, Paper No. 61, *5<sup>th</sup> International Symposium on Fluid Flow Measurement*, April, 2002, Arlington, Virginia, USA
- Landau, D. P. & Binder, K. (2005). *A Guide to Monte Carlo Simulations in Statistical Physics*, ISBN 978-0-52-184238-9, New York, USA
- Miles, P. C. (1996) Geometry of the Fringe Field Formed in the Intersection of Two Gaussian Beams, *Applied Optics*, Vol.35, No.30, pp.5887-5895, ISSN 0003-6935
- Pereira, M. T. & Jabardo, P. J. S. (1998). A Wind Tunnel to Calibrate Probes at Low Velocities, *Proceedings of FLOMEKO'98 9<sup>th</sup> International Conference on Flow Measurement*, pp. 65-70, ISBN 91-630-6991-1, Lund, Sweden, June 15-17, 1998
- Pope, S. B. (2000). *Turbulent Flows*, Cambridge University Press, ISBN 0-521-59886-9, Cambridge, U.K.
- Piccato, A.; Malvano, R. & Spazzini, P. G. (2010). Metrological features of the rotating low-speed anemometer calibration facility at INRIM, *Metrologia*, Vol.47, pp.47-57, ISSN 0026-1394
- Spazzini, P. G.; Piccato, A. & Malvano, R. (2009). Metrological features of the linear low-speed anemometer calibration facility at INRIM, *Metrologia*, Vol.46, pp.109-118, ISSN 0026-1394
- Tavoularis, S. (2005). *Measurement in Fluid Mechanics*, Cambridge University Press, ISBN 978-0-52-181518-5, New York, USA
- Terao, Y.; van der Beek, M.; Yeh, T. T. & Müller, H. (2007). Final Report on the CIPM Air Speed Key Comparison (CCM.FF-K3). *Metrologia*, Vol.44, Tech. Suppl., 07009, ISSN 0026-1394
- Terao, Y.; Choi, Y. M.; Gutkin, M.; Jian, W.; Shinder, I. & Yang, C.-T. (2010). Final Report on the APMP Air Speed Key Comparison (APMP.M.FF-K3). *Metrologia*, Vol.47, Tech. Suppl., 07012, ISSN 0026-1394
- Thomas, G. B. & Finney, R. L. (1988). *Calculus and Analytic Geometry*, ISBN 0-201-17069-8, Addison-Wesley, New York, USA
- Tropea, C.; Yarin, A. L. & Foss, J. F. (2007). *Handbook of Experimental Fluid Mechanics*, Springer, ISBN 978-354-025141-5, Heidelberg, Germany
- Yang, C. -T.; Wu, M. -C. & Chuang, H. -S. (2002). Adjustment and Evaluation of an LDA Probe for Accurate Flow Measurement, *Optics and Lasers in Engineering*, Vol.38, pp.291-304, ISSN 0143-8166
- Yeh, T. T. & Hall, J. M. (2007). An Uncertainty Analysis of the NIST Airspeed Standards, ASME Paper FEDSM2007-37560, *5<sup>th</sup> Joint ASME/JSME Fluids Engineering Conference*, July 30 - August 2, 2007, San Diego, California, USA
- Yeh, T. T. & Hall, J. M. (2008). Uncertainty of NIST Airspeed Calibrations, *Technical document of Fluid Flow Group*, NIST, Gaithersburg, Maryland, USA
- Yeh, Y. & Cummins, H. Z. (1964). Localized Fluid Flow Measurements with a He-Ne Laser Spectrometer, *Applied Physics Letters*, Vol.4, pp.176-178, ISSN 0003-6951

# Low Speed Turbulent Boundary Layer Wind Tunnels

Boldes, U., Colman, J., Marañón Di Leo, J. and Delnero, J.S.  
*Boundary Layer & Environmental Fluid Dynamics Laboratory*  
*Aeronautical Department, Engineering Faculty*  
*National University of La Plata,*  
*Argentina*

## 1. Introduction

Turbulence is the last great unsolved problem of classical physics. Or so, it goes for a quote, frequently attributed to one of the great modern physicists Albert Einstein, Richard Feynman, Werner Heisenberg, or Arnold Sommerfeld. A humorous fable, also attributed to several of the great ones, goes as follows - As he lay dying, the modern physicist asked God two questions: Why relativity (or quantum mechanics, depending on who is departing), and why turbulence? "I really think", said the famed physicist, "He may have an answer to the first question."

Due to often unnoticeably perturbations, a particular flow starting from given initial and boundary conditions can often progress reaching quite different flow patterns.

It is a fact that most fluid flows are turbulent, and at the same time fluids occur, and in many cases represent the dominant physics, on all macroscopic scales throughout the known universe, from the interior of biological cells, to circulatory and respiratory systems of living creatures, to countless technological devices (all sizes of planes, wind farms, a wide range of structures, buildings, buildings arrays, etc) and household appliances of modern society, to geophysical and astrophysical phenomena including planetary interiors, oceans and atmospheres. And, despite the widespread occurrence of fluid flow, and the ubiquity of turbulence, the "problem of turbulence" remains to this day a challenge to physicists, engineers and fluid dynamics researchers in general.

No one knows how to obtain stochastic solutions to the well-posed set of partial differential equations that govern turbulent flows. Averaging those non linear equations to obtain statistical quantities always leads to more unknowns than equations, and ad-hoc modeling is then necessary to close the problem. So, except for a rare few limiting cases, first-principle analytical solutions to the turbulence conundrum are not possible.

The problem of turbulence has been studied by many of the greatest physicists and engineers of the 19th, 20th and early 21th Centuries, and yet we do not understand in complete detail how or why turbulence occurs, nor can we predict turbulent behavior with any degree of reliability, even in very simple (from an engineering perspective) flow situations. Thus, the study of turbulence is motivated both by its inherent intellectual challenge and by the practical utility of a thorough understanding of its nature.

Our particular concern is related with the low atmospheric turbulent boundary layer, that is, the part of the surface layer between ground level and a 400m height (this last value depends, more or less, upon the criteria of researchers). Inside this range of height most of human activities are undertaken, specially, those associated with fluid flow over airplanes during takeoff and landings, wind farmers, small and medium size unmanned aerial vehicles, buildings and group of buildings, diverse structures - all immersed in a turbulent boundary layer flow. But, in such "random type flow", we could find turbulence structures, which retain their shape and/or vorticity during a time period, named "coherent structures". These coherent structures are responsible for a great part of the momentum and energy exchanges within the boundary layer. Moreover, many of the problems associated with turbulent low Reynolds number aerodynamics are unsteady.

During the last years, the trend for describing unsteady turbulent flow problems by means of numerical simulation methodologies, based on basic building blocks like elemental eddies and vortices, has increased. The objective is to achieve more realistic representations of key aspects of the dynamic pattern of the oncoming turbulent structures. These computational models are very dependent upon the quality and amount of experimental data obtained in real flow processes or at least in representative wind tunnel experiments. It is known that a direct correlation between the instantaneous aerodynamic behavior of wings and bodies interacting with oncoming particular vortex structures cannot be determined with commonly used statistics methods. Unsteady aerodynamics is a flow-pattern dependent phenomenon. During real flow experiences within a given time record, numerous turbulent structures may go by.

One interesting finding about turbulence was that along with the path to turbulence, very diverse flows run through similar foreseeable phases exhibiting particular predictable pattern characteristics. Turbulent flow patterns often reveal a remarkably self-similar organization. It seems reasonable to hypothesize a correlation between a limited number of particular flow structures and the diffusion transport and mixing behavior of the flow. This picture leads to the known low dimensional approaches. A major issue is how to detect recognize and extract the flow patterns of the turbulent structures governing the flow.

In particular aerodynamic problems, the most representative turbulent structures immersed in the oncoming wind must be previously identified in order to reproduce them in wind tunnel experiments. A main objective in unsteady boundary layer wind tunnel aerodynamics is the realistic reproduction of the dynamic response of a body to oncoming individual turbulent structures immersed in the approaching wind. It is a complex problem, associated with the various space and time scales of the turbulent flow structures. It is known that flying through turbulence changes the aerodynamic forces increasing overall drag and fuel consumption. Nevertheless it is worth to mention that in some cases, a wing submitted to a particular vortex structure embedded in the approaching wind producing intense turbulent velocity fluctuations may only experience an instantaneous Reynolds stresses enhancement without significant changes in the lift forces. The receptivity of two-dimensional laminar boundary layers on the curved surface of an airfoil passing through usual atmospheric turbulent free-stream vortices should be considered. It is important to point out that the boundary-layer receptivity to external perturbations characterizes the laminar-turbulent transition problem and therefore the local generation of vortex structures. At first, the dynamic and geometric characteristics of the usually invisible flow pattern of the relevant turbulent structures associated with a particular aerodynamic problem in real flow experiments should be identified. In boundary layer wind tunnel experiments

adequate inflow turbulence generating mechanisms should be developed in order to obtain an acceptable reproduction. Moreover, despite many years researching turbulent structures, no general detection procedures have been found.

Considering the arguments previously exposed, the study of fluid flows in general and turbulent ones in specific, is necessary to have experimental equipment and computational capability. In the case of turbulent flows and turbulent boundary layer type flows, the necessity of wind tunnels are of upmost importance, together with the possibility to take "in situ" measurements, in order to check the data obtained using the wind tunnel and to also feed the researchers with good "in situ" data in order to reproduce, as closely as possible, the real situation in the wind tunnel. Our concern is on low speed wind tunnels, which are capable to simulating as close as possible, the windy conditions of the lower atmospheric turbulent boundary layer, in particular, coherent structures which are dominant regarding the transport phenomena "modulation", known as *boundary layer wind tunnels*. It could be of closed circuit or open circuit types.

If we wish to carry out a good job, it will be necessary to perform experiments as close to real conditions as possible (in many cases a lot of experiments), which could be complemented with computational techniques (CFD), but the first ones are almost impossible to avoid. Precisely, CFD is validated with experimental data which could be from wind tunnel experiments reproducing previously known real scenario previously known from "in situ" visualizations and measurements.

In that way, some researchers are interested in the overall flow conditions of wings (and also airfoils) others may focus on small aerial vehicles while others may study the aerodynamics of wing components like flaps, spoilers, etc.

The oncoming turbulent structures immersed in the wind may exhibit very different scales. These scales are usually related to characteristic dimension of the wings and/or airfoils, for example, the chord.

Such turbulent free flow, shape the turbulent boundary layer over the body which researchers wish to manage, with the aim to achieve one (or more) of the following goals: Enhance of the local and/or global lift coefficient, enhance of the maximum lift coefficient, promote or delay the transition, delay the stall, drag reduction or aerodynamic efficiency enhancement. This part of fluid dynamics is known as *flow control* and is one of the most important branches of current fluid dynamics research in the world.

We could use *passive* or *active* devices to attain flow control.

In many cases of interest, for example, wind turbine rotor blades, the Reynolds number based upon the mean free stream velocity and the blade mean chord is of the order or less than  $10^6$ . The aerodynamics for such Reynolds numbers (or lesser) is called *low Reynolds number aerodynamics*. Following the example cited above, the rotor blade will work under a turbulent free stream flow, at least, on windy days. The "associated" aerodynamic branch is known as *low Reynolds number aerodynamics in turbulent flow*.

To summarize, the aim and concern of this chapter is to introduce the reader in the fascinating field of the low speed turbulent boundary layer wind tunnels, turbulent boundary layer flows, coherent structures, flow control passive and active devices, action upon airfoils and wings, and wind engineering phenomena in general.

Study of turbulent flows, are of the most importance in several technological applications: aeronautical, naval, mechanical and structural engineering; internal and external flows; transport phenomena; combustion processes; etc.

The particular characteristics of a turbulent flow structure are directly associated with the aerodynamics forces which promotes upon bodies immersed in the flow, because the flow pattern changes affect lift and drag forces. Typically, lost of momentum due eddies production and viscous dissipation, are usually founded in aeronautical, naval, internal and external flows applications.

If we pretend to improve or optimize an engineering problem which evolves turbulence, it'll necessary to understand and control, at least, the particular group of turbulent structures that govern such phenomena of interest.

Fluid could flow with predictable instantaneous physical magnitudes, as velocities, density, pressure, temperature, etc. If the initial and boundary conditions remain unaltered in time, the non-turbulent flow properties will be associated with those initial and boundary conditions, becoming also time independent or time predictable (periodic oscillations).

In contrast, the instantaneous turbulent velocities will not depend upon initial and boundary conditions. Generally speaking, those velocities are random type. If we perform a lot of experimental velocities measurements, the flow will remain random, that's, the random nature of the instantaneous turbulent flow velocities are independent of how much measurements we could perform. Precisely, random behavior is the main characteristic of turbulent flow.

If we visualize a turbulent flow we'll observe continuous changes in the flow pattern, as a disordered and confused flow. If the turbulent flow will develop without any imposed restrictions, we called it "full developed turbulent flow". What we intend as imposed restrictions? Well, could be gravitational, buoyancy, centrifugal, viscous, electric, magnetic forces, etc.

For example, if we analyze the flow inside a channel, we couldn't considerer developed flow such eddies which scales are similar to the channel scale, because the flow is hard influenced by the forces which govern the flow inside the channel. In other example, eddies of the propeller wake will not be fully developed flow. With these arguments we conclude that almost none turbulent flow could be considered as fully developed, at least, in scales directly associated with high energy.

Small scale low energy turbulent structures could be assumed as fully developed, if viscous forces are of less importance in the flow.

Despite the global random characteristics of turbulent flows, an experimental deep analysis allows us to detect turbulent structures which preserve its form and/or vorticity for a time period. Those structures exhibit an ordered behavior in contrast with the surrounding flow. Those are known as "coherent structures". Moreover, such coherent structures flows immersed in the global random flow. They are responsible and/or play an important contribution to the transport phenomena in the flow.

Researchers, since '60 to the present found that an important part of the turbulent kinetic energy were associated with those coherent structures.

The modern approach to turbulent study is focused on the identification of the various turbulent structures, in particular, those coherent ones.

The understanding of a turbulent flow field implies, by one side, a global analysis and, by other side, an adequate resolution. Global analysis will help us to recognize the large scale structures and, the adequate resolution, the small scale ones. Therefore the need to perform flow experiments, under controlled situations and, also, "in-situ" experiments. The experiments under controlled situations are carried out with proper wind tunnels, named "boundary layer wind tunnels" or "turbulent boundary layer wind tunnels".

If we are planning to solve turbulent flows by only computational methods, we'll must validate the results with the help of experimental data. For that reason it is essential to build appropriate wind tunnels, together with their associate experimental equipments. For appropriate we mean a wind tunnel capable to "reproduce" as close as possible, the wind characteristics of the low atmospheric boundary layer and/or any other turbulent type boundary layer.

Different methodologies are employed to process the huge acquired data in order to extract flow structures from measured time series, the classical statistics, quadrant analysis, Wavelets transforms, Proper Orthogonal Decomposition (POD), etc. Also there are various visualization flow techniques, because it's of most importance to "see" how the flow is, that's, the global flow pattern, with the aim to try to identify eddies, its spatial distribution and orientation its time dependent geometry its scales. The usual initial approach is to find position and track the larger vortices.

The resulting data will be very useful and necessary to characterize the turbulent flow pattern and, also, try to identify distinct geometric and dynamic features of the main coherent structures in the flow.

## 2. Coherent structures

Almost all the fluid dynamics researchers are coincident in their opinion about that coherent structures are responsible of the fluid behavior prediction failures employing classical turbulence theories. One of those examples is the use of only mean velocities gradients to describe the turbulent wake of porous bodies, no predicting the secondary maximum.

With the aim of detecting, identifying and examining coherent flow structures, a variety of detection techniques are commonly used in diverse flows (e.g. Bonnet et al., 1998).

On the other hand despite decades of investigation on coherent structures and their characterization no general detection methodology has been established.

Turbulent organized structures have decisive influence upon transport phenomena due their capacity to establish the way to be follow by important fluid mass volumes (See, for example, McWilliams & Weiss (1994) and Babiano et al (1994)).

A coherent structure could be imagine as a random space region which, for certain amount of time, exhibit some organization degree in, at least, one of their flow properties, that's velocity, vorticity, pressure, density, temperature, etc.

On speaking about "organization" we mean that what happens in one instant in one space point is connected with the behavior of the flow in other time interval and/or another space points. So, a coherent structure moves exhibiting some organization degree. We could imagine the situation like a part of the fluid with random behavior, is transported by the flow, preserving its cohesion. This part of the flow could rotate (which imply a vortical coherent structure) and also could deform, stretch, longing, heating or cooling.

Vortical structures, like eddies, are usually founded in many fluid flows. Sometimes are easily visible, great and well defined scale; sometimes are hard to identify due their small scale and/or their unclear boundaries and, in some occasions, we are unable to distinguish they at a plain sight. Moreover, at the present there wasn't, in the fluid dynamics researchers world, an unified, clear and complete definition of what's a vortex, where it begins and ends.

For example, definitions based on such flow zones where there are vorticity is not precise, because they are unable to distinguish between a zone with non-rotating flow but with high

shear with those zone where fluid rotates. Also, until the present, researchers had not found a clear boundary between vortex structures and the surrounding turbulent flow.

Conceptually, we could say that *coherent structures* are:

- a. A space zone where vorticity is concentrated as a way that promotes the fluid to follow trajectories which rolls around it.
- b. Following the structure movement, it could change its shape (for example, from cylindrical to elliptical), splitting in small structures or merging with neighbor structures becoming bigger vortices or disintegrating.
- c. This coherent structures, appears in the flow in an unpredictable way.

Robinson (1991), for example, made the following definition of a coherent structure: “a coherent movement is defined as a tridimensional flow region, upon which at least one fundamental flow magnitude (velocity component; density; temperature; etc) exhibits a significant correlation between itself and/or with other magnitude in a spatial/temporal range bigger than the flow micro-scales”.

Hussain (1986), by other side, provides a more restrictive definition: “Coherent structure is a connected mass flow, in turbulent flow, which vorticity is instantaneously correlated in all mass flow spatial extension”.

The apparently flow random behavior is due, mainly, to the random size and intensities of the different organized structures which belong to the fluid flow. Coherent structures are, in general, easier to detect in free flows than wall type flows.

Researchers challenge is, precisely, the identification of such coherent structures present in a whole random flow, when such structure belong to a complex velocity, temperature or pressure signal.

### 3. Low atmospheric turbulent boundary layer (general remarks)

In windy conditions, shear stresses are very important from the surface terrain to 300m to 400m height, becoming the typical *boundary layer flow*, mainly turbulent. The part of the layer, in direct contact with the surface, is called the *viscous sublayer*. This layer is characterized by very strong vertical wind shear (change of direction with height). The depth of the viscous sublayer is a few millimeters.

Close to the ground lies a region in which the *friction velocity* is essentially constant and equal to the value at the surface. This region is known as the *surface layer* or *constant-stress layer*. It is above the viscous sublayer and has a typical depth of 20-300 m/400m. In fact, the viscous sublayer is part of the surface layer and some researchers don't distinguish between them, calling both with the general specification of *surface layer*.

Very close to the earth's surface the wind velocity is reduced to zero by the drag of surface elements. This takes place in the *roughness layer*, the depth of which is comparable to the size of the surface roughness elements (grass, houses, group of houses, buildings, woods, etc). The flow above the roughness layer contains small-scale, time-dependent motions, or eddies. Velocities, temperatures, and other state variables may be expressed formally as the sum of the mean variables and eddy variables (velocities, momentum, entropy, etc). That's the classical approach to turbulence study, mentioned above by us.

If we take account that many of the human activities take place inside such layer, it's natural to understand why fluid dynamics researchers try to understand and carefully study the flow characteristics of such region. Woods's induced turbulence; suburban areas; cities; etc, are immersed in such boundary layer turbulent flow. Theoretical and/or computational



study, only, will not drive them self to obtain good explanation of how the flow is, how are coherent structures in such layer and, subsequently, which are the associated aerodynamic forces.

For that reason we need to perform experiments, which will be “in situ” and wind tunnel ones. Moreover, such wind tunnels must be capable to reproduce, as close as possible, the flow conditions in the surface layer. Such wind tunnels type, are known as *turbulent boundary layer wind tunnels*.

Due the complexity of the flow in the surface layer, early researchers like Monin and Obukhov (1954), developed a *similarity theory* with the objective to organize and group the acquired experimental data. The theory aim was the identification of the most important physical parameters and, then, to define dimensionless groups with it. After that, experimental data were used to find functional relations between such dimensionless groups. Once he functional relations are known, they were used as part of a parameterization scheme.

Under this context, the relevant parameters for the surface layer were: momentum flux, buoyancy flux and the dimensionless height above the earth surface. Precisely, this last parameter is the turbulent length scale; due that eddies scales are determined by their distance from the earth surface.

One of the parameters is the Monin-Obukhov length  $L$  (see Monin et al, 1954) and, together with the friction velocity  $u^* = (\tau_w/\rho)^{1/2}$ , was possible to establish a simple relation between mean time turbulent velocities and the dimensionless height  $z/L$ , being for example, one of them:

$$[k z u^* \sqrt{-u'w'}](\partial V / \partial z) = \Phi_M(z / L)$$

This function  $\Phi_M(z/L)$  relates the friction velocity  $u^*$ , the vertical gradient  $\partial V / \partial z$  and the shear as a function of  $z/L$ . Note:  $\tau_w$  and  $\rho$  are the shear over the terrain and air density, respectively.

Also, it's possible to relate the vertical mean velocities profile with the dimensionless  $z/z_0$ , being  $z$  the height and  $z_0$  the “roughness medium height” which will be different if we are dealing with a plane grass field, the sea and/or ocean, suburban areas and urban ones. Such relations are known as *logarithmic mean velocities profile* and *mean velocities power law*:

$u(z) = (u^*/k) \ln (z/z_0)$  (logarithmic, valid for very short vegetation and neutral atmosphere)

$u(z)/U_m = (z/z_0)^\alpha$  (potential law, useful for roughness terrain and small roughness terrain and sea)

In both equations  $u$  is mean velocity along x-axis (parallel to the floor). In the last equation, the exponent  $\alpha$  will vary according the terrain roughness, decreasing proportionally to roughness values.

Monin-Obukhov length,  $L$ , is a *stability parameter* which serve as “indication parameter”, that's for example when  $z/L \ll 1$  is valid the logarithmic law (mentioned above).

At this stage the authors doesn't wish to show and/or develop the whole *surface layer theory* and the *similarity one*, just only to point out the essential concepts of them, with the purpose to show up the spirit of the design, building and operation of *turbulent boundary layer wind tunnels* and, subsequently, to display some of the fluid dynamic experiments carried out with their help.

## 4. Turbulent boundary layer wind tunnels at the boundary layer & environmental fluid dynamics laboratory

### 4.1 Closed circuit wind tunnel

Since 1984 is operating, at the Aeronautical Department, Engineering Faculty, National University of La Plata, Argentina, the first turbulent boundary layer wind tunnel, closed circuit one. The test section dimensions are 7.5m length and  $1.4 \times 1\text{m}^2$  traverse section. The tunnel has a direct current 50HP motor with their corresponding electronic speed control and 6 blades. The maximum velocity, at the test section, is 20m/s. The wind tunnel is equipped, at the begin of the test section, with a honeycomb in order to achieve a flow with directional preference along x-axis (test section) and, after that, a vertical array of aluminum profiles, parallel to the tunnel floor, distributed with a given variable vertical distance between them. Each profile is capable to manually rotate along its longitudinal axis. These arrays serves as turbulence generators which allow to obtain different power law exponents and also the logarithmic law and, also, different turbulence intensities with their corresponding vertical evolution. Roughness elements (parallelepipeds) are distributed over the tunnel floor to achieve the roughness turbulence for different conditions according the real ones in urban, suburban and field scenarios.

Figures 1 and 2 shows the turbulent generators profiles, in vertical array after honeycomb, together with the turbulence generators triangles (after profiles), and details of the test section, included the roughness elements. At the test section we could see the portable Dantec Flowmaster anemometer arm. We use such anemometer to continuously verify the mean velocity stream at the test section. The instantaneous velocities measurements are made with the Dantec Streamline 6 channels hot-wire constant temperature anemometer.



Fig. 1. Triangular mixing spikes

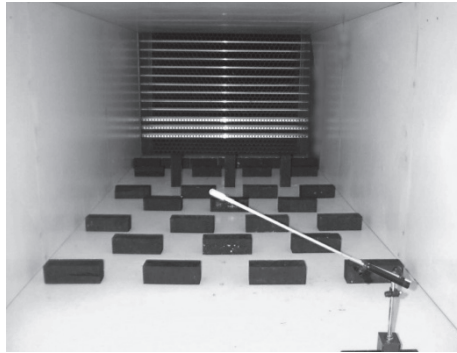


Fig. 2. Roughness elements

Figures 3 and 4 show us, respectively, the external view of the test section, with the 6 channels anemometer and data acquisition PC and a wing model between two double panels, inside the test section.

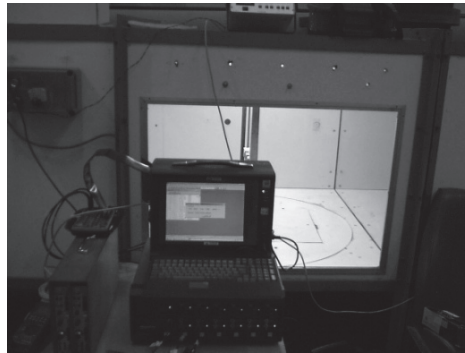


Fig. 3. Test section and Measuring equipment



Fig. 4. Test section

Figures 5 and 6 corresponding to typical power law mean velocities distribution vs. height and autocorrelation, respectively.

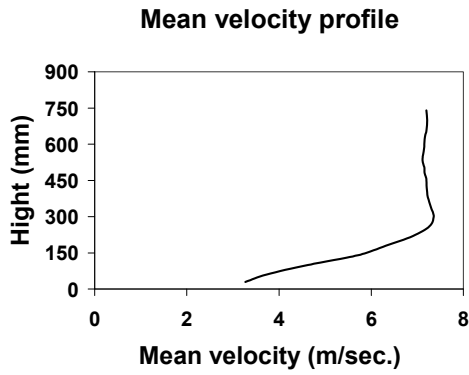


Fig. 5. Mean velocity profile

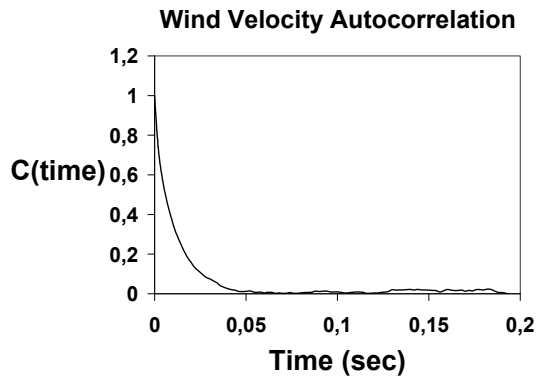


Fig. 6. Wind velocity autocorrelation

Figures 7 and 8 corresponds to typical turbulence intensity distribution vs. height and shear stress distribution vs. height

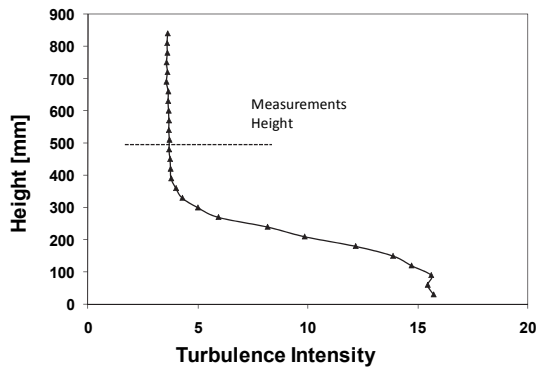


Fig. 7. Turbulence Intensity distribution

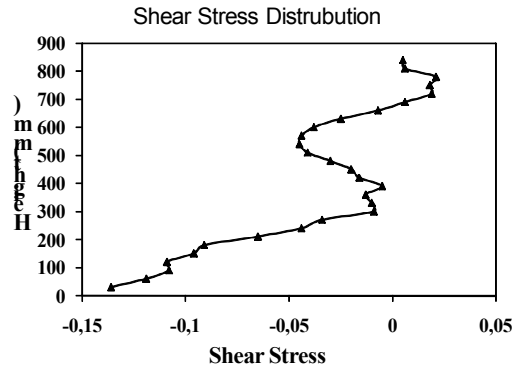


Fig. 8. Shear Stress distribution

#### 4.2 Open circuit wind tunnel

During 2005 began the design and building of a bigger turbulent boundary layer wind tunnel, open circuit one. The aim was to have a wind tunnel capable to improve, regarding the previous closed circuit one, the experimental simulation of wind conditions at the surface layer. Also, the aim to build this new tunnel as open circuit model was to have the possibility to simulate *dispersion plumes* and any other flow condition related with atmospheric pollution.

Such wind tunnel is 24m length, which include the entrance nozzle (2m length), the long test section (17m) with constant cross area of  $2.6 \times 1.8 \text{ m}^2$  and the 5m length diffuser at which end are 9 alternating current motors (15 HP each), totalizing 135HP electric power. These motors, together, have a precise velocity control, varying frequency type. The motors suction the air from the nozzle, to obtain a uniform flow, after passing the huge honeycomb. Then, the flow is "perturbed" by vertical (equal horizontally spaced) obstacles (triangular shape) to "transform" it in turbulent one, as close as possible to the wind characteristics at the surface layer. After those obstacles, the turbulent flow passes through multiple roughness elements at the floor, before to reach the test area. In this area there is a rotating disc in order to simulate, on the models, different wind directions. The rotating disc has an electric control capable to promote, manually, a very slow rotation motion to the disc.

The maximum velocity at the test section is 30 m/s. For certain details see Figures 9 to 12:

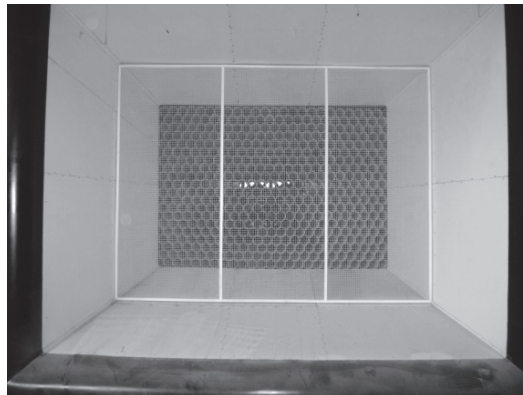


Fig. 9. Wind tunnel nozzle front view

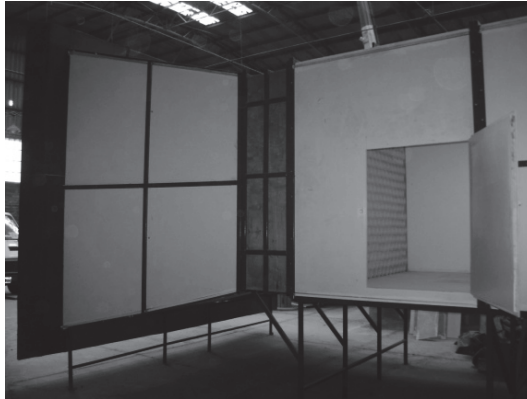


Fig. 10. Nozzle and honeycomb lateral view

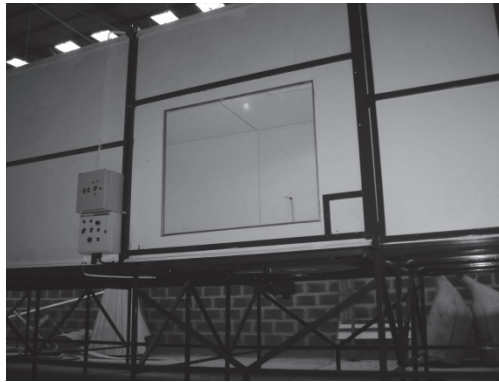


Fig. 11. Lateral external view of test section

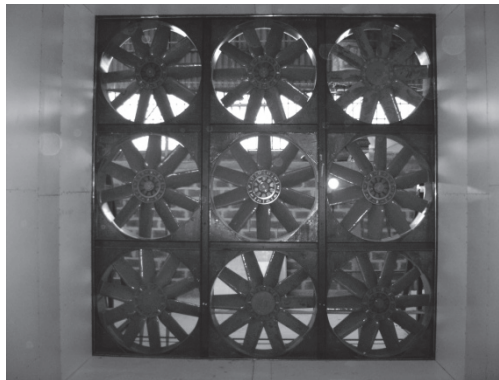


Fig. 12. Motors view from inside the diffuser

In order to give clarity to the photos, the vertical development turbulence generators (usually located after honeycomb) and the roughness elements were removed.

At the time of the elaboration of this Chapter, authors haven't begun with experiments about turbulent flow characterization in this open circuit wind tunnel. Such step is necessary prior to plan any experimental work regarding, for example, flow control over wings. We planned to begin with the flow characterization in this tunnel on May 2011.

## 5. Brief considerations about flow control

Generally speaking we could say that *flow control* implies a beneficial change in the flow behavior over a body, by different passive or active devices, in comparison with such flow behavior without such devices.

The proposed tasks are various: promote the delay or early boundary layer transition; reduce or enhance the turbulence; induce or prevent separation; enhance the lift; reduce the drag; reduce the flow-induced noise.

By *passive* flow control we means the use of devices, for example over wings, without any movement, that's, the device acts on the flow by a passive way as an "obstacle" immersed in the flow.

By other hand, there are devices capable to move by some mechanism, acting upon the flow. Such devices could have some "feedback" being a more sophisticated *active mechanism*.

The authors, with the collaboration of other researchers at the Laboratory, were performed various experimental works evolving, either passive and/or active flow control devices. In the next sections we'll describe some of them.

In the following works, the experiments were carried out at the Boundary Layer and Environmental Fluid Dynamics Laboratory (LaCLyFA) closed circuit wind tunnel, at the Faculty of Engineering, National University of La Plata, Argentina. In each work there will be indicated the corresponding Reynolds number but, in all cases, corresponds to *low Reynolds number aerodynamics*.

### 5.1 The wake asymmetry of an airfoil with a Gurney flap, and their connection with the observed lift increase. Boldes, U.; Delnero, J. S.; Marañon Di Leo, J.; Colman, J. and Camocardi, M.E.

**Abstract** – *The present research analyzes the asymmetry in the rolling up shear layers downstream the blunt trailing edge of airfoils with Gurney flaps as a lift enhancing mechanism. Experimental investigations relating the asymmetry of the vortex flow in the near wake region, able to distort the flow increasing the downwash of an airfoil, have been performed. We examine the lift behaviour and near wake region characteristics of the low Reynolds number airfoil HQ17 without and with Gurney mini-flaps of different lengths. The flow immediately downstream the trailing edge down to 2 mini-flap lengths is explored in order to identify signs of asymmetry of the initial counter rotating vortex structures. Experimental evidence is presented showing that for typical lifting conditions the shear layer rollup process within the near wake is different for the upper and lower vortices: the shear layer separating from the pressure side of the airfoil begins its rollup immediately behind the trailing edge creating a stronger vortex while the shear layer from the suction side begins its rollup more downstream creating a weaker vortex. Aspects of a mechanism connecting the different evolution and pattern of these initial vortex structures with the lift increase due to these flaps are presented.*

**Experimental procedures and results discussion** - In what follows, the airfoil is considered with the suction and pressure surfaces located above and below respectively. The basic tested model was an untwisted wing with a rectangular platform with a chord length of 45cm and a span of 80cm. Each model with the different Gurney flaps was horizontally placed in the test section (1.4

$\times 1 \text{ m}^2$ ). The wing was examined within the range of  $-12$  degrees and  $+24$  degrees of angle of attack. Airfoils with miniflaps with similar dimensions have been studied by numerical simulations [Schatz et al, 2004]. The lift and drag of a low Reynolds number airfoil HQ17 without and with Gurney flaps of four different lengths: 1%, 1.5%, 2% and 2.5% of the wing chord have been measured. Simultaneously the near wake vortex region was explored in order to recognize the initial location of the region in which the detached shear layers start to rollup, and the strength and features of the generated vortices.

Lift and drag data were acquired by an aerodynamic two components balance, built by the authors according to [Tusche, 1984], based on strain-gages type cells, arranged as a double Wheatstone bridge. Horizontal and vertical loads were measured simultaneously [Delnero et al, 2005].

Velocities were acquired by means of a six channel Dantec Streamline constant temperature anemometer, using an X-wire Dantec sensor probe 55R51 at an acquisition frequency of 2000 Hz per channel. The data was processed by a Vishay series 2310 signal conditioners and amplifiers. Due to the minimal frontal area of the wing sections ( $0.8 \times 0.10 \text{ m}^2$ ), no blockage correction was applied to the results. Temperature was continuously measured in order to adjust the air density. Turbulent velocities were acquired, at the free stream (upstream of the model), in order to characterize the upcoming flow. Also, measurements were made downstream of the trailing edge along a grid with two horizontal points placed at distances of 2% and 4% of the airfoils chord and 13 vertical intervals of 2mm (see, for details, Figure 14).

By analogy with the flow behind usual blunt bodies the width of the blunt trailing edge, which coincides with the length of the mini-flap  $H$ , was taken as a significant scale of the motion in the near wake region. The leading edge of the miniflap is attached to the trailing edge of the airfoil.

Figure 13 shows the schema of a Gurney mini-flap configuration and the anemometer sensor location. Figure 14 shows the grid measurement schema.

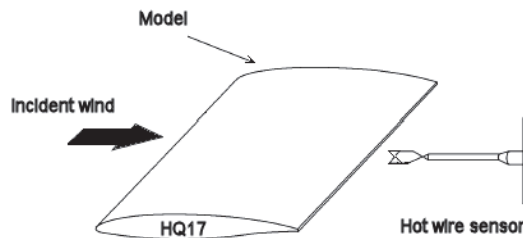


Fig. 13. Experimental setup

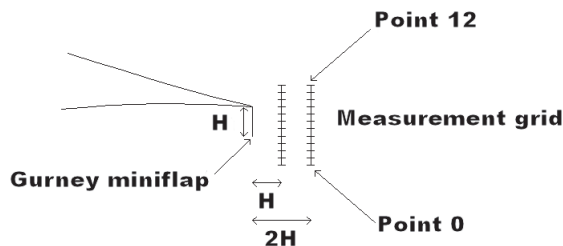


Fig. 14. Measurement grid details



Figures 15 and 16 shows the  $C_L$  and  $C_D$  obtained values, plotted as a function of the angle of attack, for the plain wing and for the different miniflaps sizes. We could say that all the miniflaps increase the lift and drag coefficients, in comparison with the clean airfoil. From the drag point of view, for all the Gurney sizes, a little bit less drag is exhibit by the smaller one (1%c).

In order to obtain more accurate information about the scale of the turbulent structures which appear intermittently in the flow downstream the trailing edge, a wavelet analysis was performed. This procedure retains information in time domain as well as in the frequency domain. The wavelet analysis of the velocity data allows the identification of aspects of turbulent structures which can be connected to transport events. The continuous wavelet transform used in this paper, is known to be appropriate for analyzing turbulent flow data [Farge, 1992], [Farge, 1990].

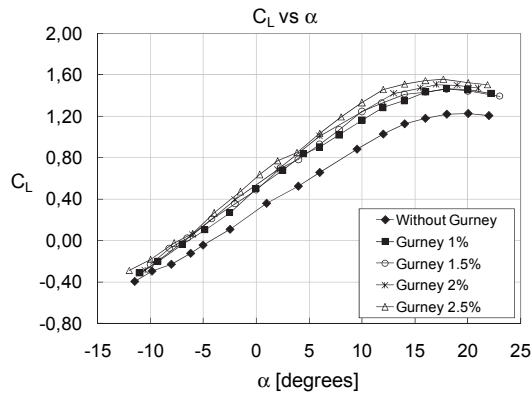


Fig. 15.  $C_L$  vs angle of attack

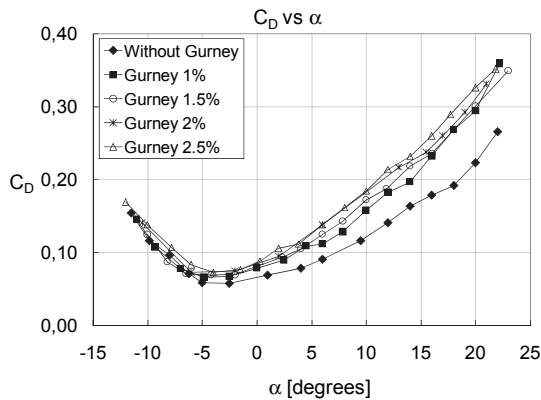


Fig. 16.  $C_D$  vs angle of attack

Our aim was to compare time scales, intensities and frequencies of the turbulent structures in the wavelet map behind the Gurney flap. Some wavelet interpretation criteria used by Mahrt (1991), estimating the time extent and frequency of a particular detected structure directly from its wavelet graph scale. The velocity-time records were explored in order to detect features related to the second derivative of a Gaussian  $g_2$  (usually called the "Mexican hat" wavelet). Assuming frozen flow theory, one can deduce the Turbulent Spatial Scale for the velocity component, looking for the maximum in the wavelet map.

The measured lift values are consistent with those described by Schatz et al (2004) in their computational experiments. It is also interesting to point out that these authors subscribe to our perception in considering the influence of features of the wake flow on the wing aerodynamics when they mentioned that particular characteristics of the wake had direct influence upon the increase of the section drag coefficient.

From the top and the trailing edge of a mini-flap two shear layers emerge which roll up into a pattern of alternating counter rotating vortices establishing *absolute wake instability* [Huerre et al, 1985]. The Karman vortex street in the wake of a cylinder exhibits this type of instability.

When an absolutely unstable scenario exists, arbitrary disturbances injected in the flow stay at or propagates upstream and/or downstream of its point of introduction. Therefore it is to be expected that the vortex structures generated behind the airfoil are able to influence upstream and downstream conditions.

Absolute instabilities can be found in laminar and turbulent flows. They are characterized by a clear peak in the spectrum of the fluctuations in the wake and its surroundings. The near wake regions where the rollup of the shear layers evolve into the initial vortical structures behind the tested airfoils display a significant peak in the spectra of the velocity fluctuations indicating a clearly identifiable absolute instability shown in Figures 17 and 18.

However we were not interested in finding the exact location of the regions where the vortices develop. In our experiments we explored the flow immediately behind the trailing edge in regions exhibiting a dominant spectral peak, with the aim to find evidences of an enduring asymmetry able to deviate the flow in the near wake region, enhancing the downwash. By exploring the near wake region searching for regions with the highest spectral peaks we found the following differences in the behavior of the shear layers separating from the suction and pressure surfaces of the airfoils.

For typical lifting conditions the shear layer rollup process within the near wake was always different for the upper and lower vortices: the shear layer separating from the pressure side of the airfoil began its rollup immediately behind the trailing edge of the mini-flap creating a stronger vortex, while the shear layer from the suction side initiated its rollup more downstream generating a weaker vortex. These results are summarized in Tables 1 and 2.

The larger intensity of the vortex generated by the rolling up of the shear layer separating from the pressure side of the airfoil found for all the flap sizes is illustrated by the spectra shown in Figures 17 and 18. Also, closer examination of the wavelet graphs displayed in Figs 19 and 20 shows that the highest strength of the vortex from the suction side is more diffused involving a larger region of the wake than the more energetic vortex generated by the shear layer separating from the pressure side of the airfoil, which exhibits its highest intensity concentrated in a smaller region.

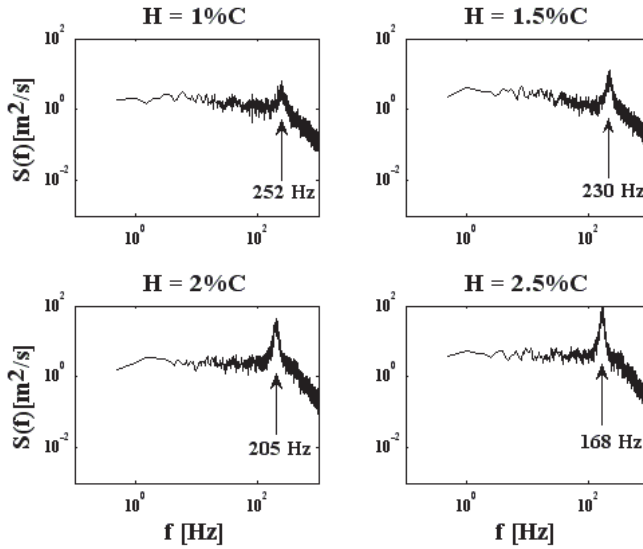


Fig. 17. Power Density Spectra Distribution for different Gurney flap sizes related to the airfoil chord (C) at point 2 of the grid and 2H downstream into the wake (v component)

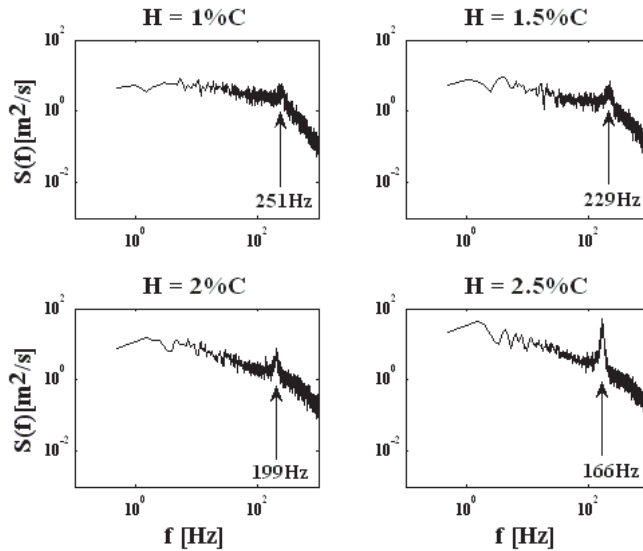


Fig. 18. Power Density Spectra Distribution for different Gurney flap sizes of the airfoil chord (C) at points 7, 8, 9, and 10 of the grid, corresponding to the trailing edge of the profile, and at 2H downstream into the wake (v component)

1% - 1H		
Point	Frequency [Hz]	$S(f)v [m^2/s]$
2	251	5,7
7	251	4,46
1,50% - 1H		
Point	Frequency [Hz]	$S(f)v [m^2/s]$
2	215	7,32
8	229	6,15
2% - 1H		
Point	Frequency [Hz]	$S(f)v [m^2/s]$
2	199	28,5
9	203	4,14
2.5% - 1H		
Point	Frequency [Hz]	$S(f)v [m^2/s]$
2	167	146
10	169	45,3

Table 1. Power Density Spectra Peaks and peak Frequency for Gurney flaps of different sizes, at the downstream distances H.

1% - 2H		
Point	Frequency [Hz]	$S(f)v [m^2/s]$
2	252	7,36
7	251	5,96
1,50% - 2H		
Point	Frequency [Hz]	$S(f)v [m^2/s]$
2	230	13,6
8	229	6,39
2% - 2H		
Point	Frequency [Hz]	$S(f)v [m^2/s]$
2	205	53,4
9	199	8,5
2.5% - 2H		
Point	Frequency [Hz]	$S(f)v [m^2/s]$
2	168	117
10	166	55,7

Table 2. Power Density Spectra Peaks and peak Frequency for Gurney flaps of different sizes, at the downstream distances 2H. (Points 7, 8, 9 and 10 are located at the trailing edge level of the airfoil for each Gurney flap size and Point 2 always corresponds to the level indicating the trailing edge of the Gurney flap). It can be seen that the spectral peak  $S(f)$  of the flow behind the trailing edge of the mini-flap is always larger than the corresponding peak behind the leading edge of the mini-flap

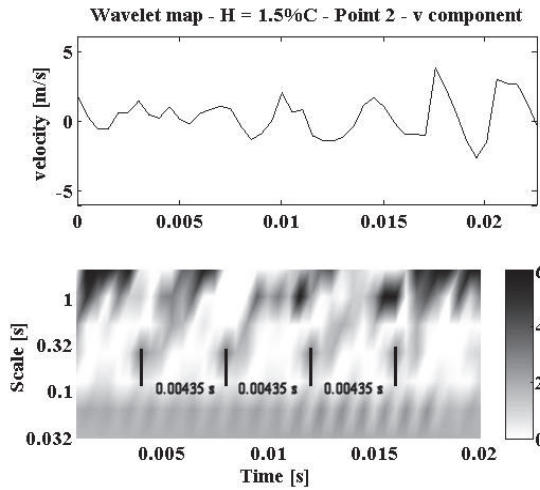


Fig. 19. Wavelet map for the Gurney flap of 1.5% of the airfoil chord (H) at point 2 of the grid and 2H downstream into the wake (v component). It shows the scale of the structures, period of 0.00435 s.

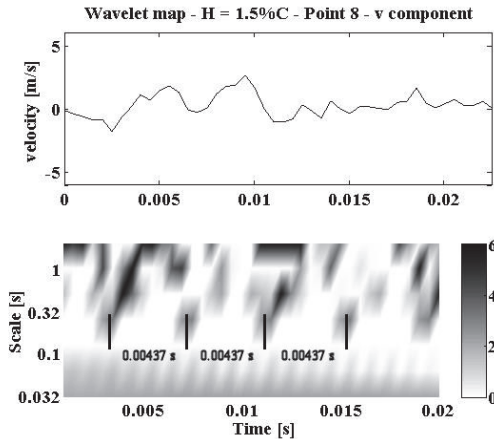


Fig. 20. Wavelet map for the Gurney flap of 1.5% of the airfoil chord (H) at point 8 of the grid and 2H downstream into the wake, (v component). It shows the scale of the structures, period of 0.00437 s.

It seems reasonable to infer that the increased strength of the lower vortex and its proximity to the downwind surface of the mini-flap deflects the location of the free rear stagnation point.

Due to the asymmetry of the initial vortices the mean location of this stagnation point is slightly shifted downstream and downward in comparison with the mean position of the stagnation point behind a blunt body with a classic Karman vortex street.

**Conclusions** - How can we explain the asymmetric behavior of the initial vortices? Existing research shows that the shear layer separating from the pressure side of the airfoil is influenced by the intermittent shedding of the vortex structures originated along the upstream surface of the mini-flap. Such structures have been recently visualized [Trolin, 2006].

These authors carried out detailed time-resolved PIV visualizations of the flow around an airfoil with Gurney flap. They reported the presence of a new mode, not described in previous experimental or numerical works, in addition to the known Karman type vortex shedding mode. They showed that this mode was originated by the intermittent shedding of fluid from the upstream side of the gurney flap which interacts with the Karman type vortex wake. They suggested that this interaction could be part of a mechanism responsible for a significant portion of the overall lift increment. Such observations are qualitatively consistent with a simple interpretation of a mini-flap acting as a small barrier behaving as a passive perturbation device.

The intermittent shedding of vortex structures from the upwind region of the mini-flap into the wake reported [Trolin, 2006], can be interpreted as a perturbation mechanism acting on the shear layer emerging from the pressure side of the airfoil at its separation point from the trailing edge. The shear layer detaching from the suction side is submitted to a very different perturbation. Therefore it is to be expected that the corresponding vortex structures generated by the rollup of the shear layers will also be different introducing asymmetry in the vortex pattern of the near wake region.

It is known that turbulent shear flows are very sensitive to small changes in initial or boundary conditions and to different types of perturbations applied during transition [Oster et al, 1982]. Such perturbations could generate particular perturbation dependent shear layer organized structures that dominate the downwind evolution of the layer [Ho et al, 1985].

The mentioned shedding of the vortex structures generated in the gap upstream of the mini-flap into the wake region where the shear layer is generated, fulfill the conditions of a specific perturbation acting on the region where the shear layer is generated and therefore able to influence the shape and evolution of vortex structures. The studies of Kiya et al (1986; 1999a and 1999) describe interesting aspects of the response of a shear layer perturbed by vortices which also corroborate the asymmetric behavior detected in our experiments.

## **5.2 Experimental study of a NACA 4412 airfoil with movable Gurney flap** **Camocardi, M.; Marañón Di Leo, J.; Delnero, J. S. & J. Colman**

**Abstract** - A NACA 4412 airfoil was tested, in a boundary layer wind tunnel, with the aim to study the effect of a Gurney flap, as an active and passive flow control device submitted to a turbulent flow field. The main objective was the experimental determination of flow pattern characteristics downstream the airfoil in the near wake. The untwisted wing model used for the experiments had 80cm wingspan and 50cm chord, with airfoil NACA 4412. Three different movable Gurney flap mechanisms were tested, as active devices. The flap, in all cases, was located on the lower surface at a distance, from the trailing edge, of 8%*c* (*c* airfoil chord). The Reynolds number, based upon the wing chord and the mean free stream velocity was 326,000 and 489,000. The turbulence intensity was 1.8%. The models were located in the wing tunnel between two panels, in order to assure a close approximation to two-dimensional flow over the model. One was a movable up-down flap geared by an electromagnetic mechanism; from the analysis of the obtained results one could appreciate an increment of  $C_l$  when the excitation frequency increases, in comparison with the clean airfoil. Also is observed that the  $C_l$  values of the model with the Gurney flap fixed are something greater than the

corresponding values for the movable Gurney condition. Regarding the  $C_d$  behavior, it diminishes when the frequency increases, but its minimum value is something greater than the case for the clean airfoil. The others were rotating flaps, geared by an electro-mechanical system, one rotate to a  $90^\circ$  (vertical) position, and the other rotate to a  $30^\circ$  position. In these cases the wake pattern and pressure values near the trailing edge were measured. The results obtained, for these mechanism, show us that the oscillating flap change the wake flow pattern, alleviating the near wake turbulence and enhancing the vortex pair near the trailing edge at the flap level and below that level, magnifying the effect described first by Liebeck (1978). That effect is more evident as the oscillating frequency grows. Additionally, the wake alleviation probably affects also the far wake. All of these facts suggest us to continue with the experiments, trying to measure the pressure distribution around the airfoil in all the cases, obtaining the lift and drag characteristics.

**Experimental procedures and results discussion** - The models were located in the wing tunnel between two panels, in order to assure a close approximation to two-dimensional flow over the model.

Figure 21 shows a diagram of how were positioned each wing model inside the wind tunnel test section.

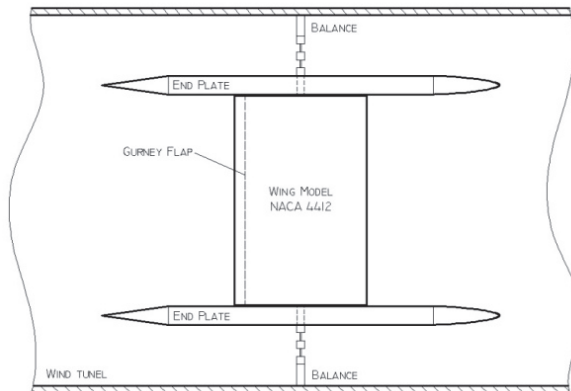


Fig. 21. Diagram of wing model inside the wind tunnel test section

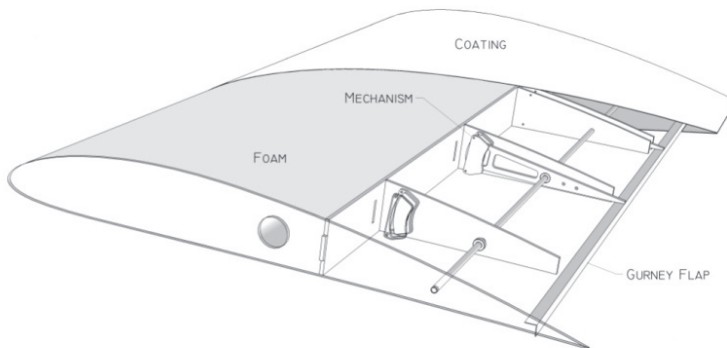


Fig. 22. Tested wing model, with vertical oscillating Gurney flap.

The untwisted three wing model dimensions tested were 50cm chord ( $c$ ) and 80cm wingspan, with a NACA 4412 airfoil. The Reynolds number, based upon the wing chord and the mean free stream velocity were 326.000 and 489000, based upon the mean free stream velocity (at 1.5m ahead the model at its height) and the model chord, corresponding to values of it of 10m/s and 15m/s respectively, depending on the test. The turbulence intensity was 1.8% (minimum turbulence intensity of the wind tunnel). The closest possible distance from the trailing edge, for the Gurney flap position, was determined by the implemented mechanism inside the model [Wassen et al, 2007].

The first model with the aim to study the section lift and drag coefficients behavior, when a Gurney flap located on the lower surface near the trailing edge, used as passive and active flow control device. As an active device an up-down Gurney flap was designed, geared by an electromagnetic system. Such mechanism is an electro-magnetic one excited by an electrical frequency and variable amplitude signal. By this way the Gurney flap, fixed to the seesaws (see Figure 22), was capable to make an oscillatory movement from the lower surface (0mm displacement) to the maximum amplitude (5mm). The Gurney flap was a movable plate of 5mm height (1% $c$ ), corresponding to its maximum vertical displacement, and 1mm width with a wingspan length, located on the model lower surface, at 8% $c$  from the trailing edge.

The second and third models, with the Gurney flap capable to rotate along the wingspan, were tested with the objective to measure the wake at different positions behind the trailing edge, for different rotation frequencies of the Gurney. These rotating flaps, were geared by an electro-mechanical system (see Figure 23), one rotate to a 90° (vertical) position, and the other rotate to a 30° position. In these cases the wake pattern and pressure values near the trailing edge were measured.

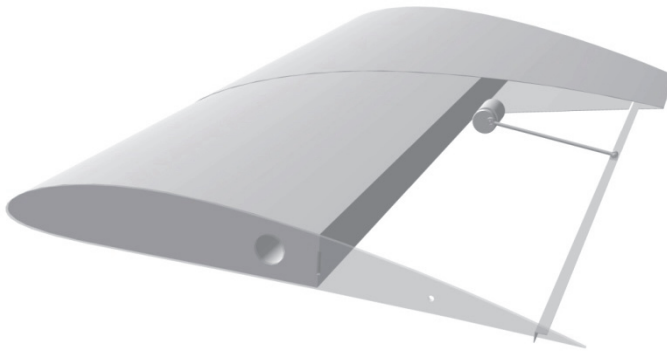


Fig. 23. Tested wing model, with rotational oscillation Gurney flap.

These models had a 10mm movable plate (2% $c$ ), capable to rotate along its longitudinal axe. The rotation movement, with a variable frequency, was produced by an 8 pole brushless electric motor of 28mm diameter, located inside the model, actuated by a tiny frequency control, with a crankcase which transmits the rotation movement to a small brace located on the Gurney plate, closed to the longitudinal hinge of it. So, the rotation movement of the electric motor was converted in an oscillatory movement of the small Gurney plate.

The aerodynamic loads were measured by a system of two components aerodynamic balance with strain gages, with the wing model mounted built in – built in, with a built in



mechanism to change the angle of attack. The strain gages were arranged as two complete Wheatstone bridges. The signals output were processed by a signal conditioner and a data acquisition computer. With the acquired and processed data the section coefficients were calculated and then elaborated the characteristic polar curves.

Instantaneous velocities were measured by means of a constant temperature hot wire anemometer Dantec Streamline, with X-wire sensor probes. Pressure measurements were made by mean of a Pressure System (NetScanner, equipped with piezoelectric sensors). The connection between the pressure taps and the Pressure System was by tubes of 1.8mm inside diameter, each of the same length. Such pressure taps were located upstream of the perturbation zone (flap position) with the aim to obtain instantaneous pressure data not perturbed, directly, by the flap position itself. The flaps frequencies were measured with a laser tachometer.

Three different experiments were carried out, one with each Gurney flap system configuration.

**Case 1:** This was the case of the Gurney flap with up-down movement system. In this case the characteristic polars were obtained for a Reynolds number of 326.000, based upon the model chord and the free stream mean velocity. The experiments were divided in two steps. The first evolve tests with the clean model and with the model with the Gurney flap as passive flow control device. The second with the Gurney flap with movable capabilities, as described above. In this second step we planned to investigate the influence of the excitation frequency upon characteristic polars, for three frequency values: 5, 10 and 15Hz. It's necessary to point out that many technical difficulties were founded along the test, due probably to the fact that those were our first experiences with movable Gurney flaps.

**Case 2:** This was the case of the rotating Gurney flap (to  $90^\circ$  position). The experiments were carried out as follows. Once mounted the wing model inside the test section, at zero angle of attack, the velocities field were measured at different positions behind the trailing edge, using an X-wire anemometer probe. We carried on, at a give Gurney rotating frequency, velocities determinations at various y-positions for each x-position, being "y" the vertical axis and "x" the horizontal axis. We repeated such measurements for other frequencies. The x-positions were two: at 2%c and 75%c from the trailing edge (see Figure 24). In each position, the vertical points were 30 separated each 0.4%c. The acquisition frequency was 600 Hz, filtered at 300 Hz. Were taken 8192 samples in each position. The Gurney's rotating frequencies were three: 26 Hz; 35 Hz and 41 Hz. Each frequency was measured by a laser tachometer.

The whole experiments evolve five steps: The first was with the wing model without Gurney; then with a fixed Gurney, at 90 degrees respect the wing chord; and the third to five with the Gurney moving at each frequency (as described above).

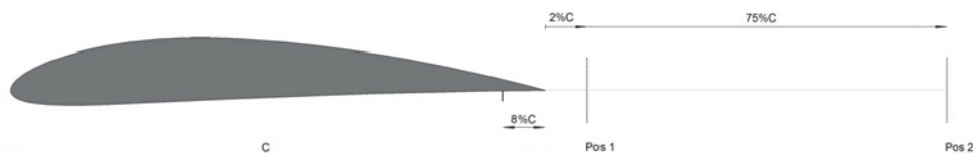


Fig. 24. Wake measurements sketch for the rotating Gurney flap at  $90^\circ$ .

**Case 3:** This was the case of the oscillating Gurney flap, around its axe, up to  $30^\circ$ . The experiments were focused on the instantaneous velocity measurements in the near wake, in three “x” positions, 1H, 2H and 5H (Positions 1, 2 and 3 respectively, being H the flap height) and, at each “x” position, the data were measured in 20 vertical points, which upper limit was  $1.5\%c$  and lower limit  $2\%c$ , separated each  $0.04\%c$ . Turbulence intensity was  $1.8\%$ . The essays were performed for two Reynolds numbers, 326000 and 489000, based upon the mean free stream velocity (at 1.5m ahead the model at its height) and the model chord, corresponding to values of it of 10m/s and 15m/s respectively.

Experiments were carried out in three steps, for each Reynolds number: 1<sup>st</sup> step with the clean model; 2<sup>nd</sup> step with the flap deployed but fixed (as a passive flow control device); 3<sup>rd</sup> step with the flap oscillating at three frequencies each time (22Hz, 38Hz and 44Hz). In all steps, for four values of the angle of attack:  $-3^\circ$ ,  $0^\circ$ ,  $5^\circ$  and  $11^\circ$  (this last near stall angle). We measured instantaneous velocities in the points cited above. The acquisition frequency was 4000 Hz, filtered at 1000Hz, taken 8192 samples per channel in each measuring point. The wing model had two pressure taps at the same “x” position ( $0.88c$ ), one on the upper surface and the other on the lower surface. The connection between the pressure taps and the Pressure System was the same that in Case 2.

Figure 25 shows a schema of the wake measuring positions, along “x” axis and the corresponding vertical points, indicating only the 0 and -10 points:

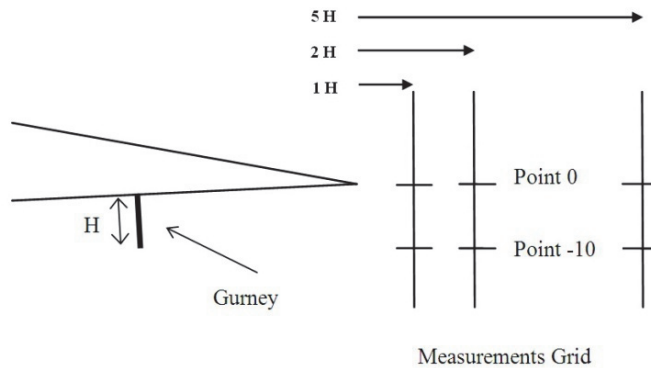


Fig. 25. Wake measurements sketch for the rotating Gurney flap up to  $30^\circ$ .

According previous works [Bacchi et al (2006), Wassen et al (2007)], we assume that a Gurney flap modify the circulation around the airfoil and, hence, its aerodynamics behavior. In this work we study such behavior on a NACA 4412 airfoil without and with a Gurney flap and, acting it as a passive and active flow control mechanism.

- a. **Case 1.** Using the Gurney flap as a passive device we found the following. Watching the  $C_l$  vs. angle of attack (Figure 26) is noticeable an increment of 6% of the  $C_l$  for the model with the fixed Gurney flap in comparison with the clean wing. Also the stall angle diminishes from  $14^\circ$  to  $12^\circ$  and the zero lift angle of attack increase, in absolute terms, from  $-3.5^\circ$  to  $-5^\circ$ . Comparing the  $C_d$  vs. angle of attack curves (Figure 27), a section drag increment is observed along the curve being more important in the range of high angles of attack. Also there was a 30% increment of the  $C_{d_0}$  in comparison with the clean airfoil. The  $C_l$  vs. angle of attack slope, don't show significant changes in comparison with the clean airfoil. All of these conclusions have a good agreement with other authors for different airfoils.

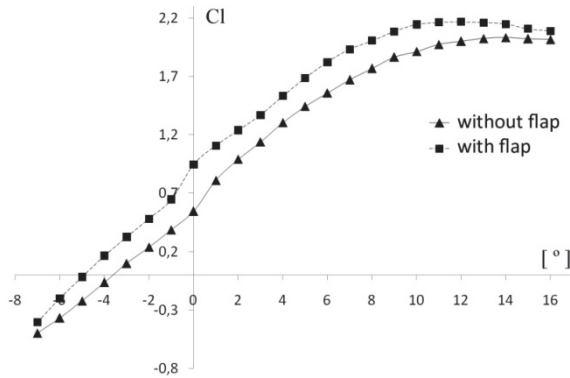


Fig. 26. Polar curve  $C_l$  vs angle of attack

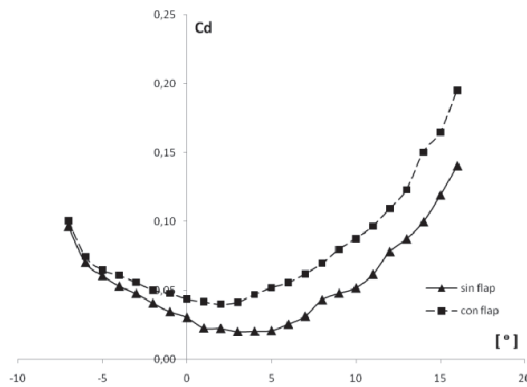


Fig. 27. Polar curve of  $C_d$  vs. angle of attack

For the Gurney flap with vertical movement (oscillation), working as an active device, we found the following. The aerodynamic loads were measured, in a first instance, for two angles of attack,  $0^\circ$  and  $8^\circ$ , with the movable flap at 5, 10 and 15Hz frequencies, with the motivation to obtain preliminary results about the device behavior. Table 1 shows the section coefficients for those two angles of attack and the different excitation frequencies.

Frequency	$\alpha$	$C_l$	$C_d$
5 Hz	$0^\circ$	0,499	0,084
	$8^\circ$	1,423	0,173
10 Hz	$0^\circ$	0,523	0,049
	$8^\circ$	1,435	0,160
15 Hz	$0^\circ$	0,524	0,033
	$8^\circ$	1,479	0,150

Table 3. Aerodynamic coefficients, for  $0^\circ$  and  $8^\circ$  at 5, 10 and 15 Hz.

In a second instance the curves  $C_l$  vs.  $\alpha$  were determined measuring loads for a range of angles of attack from  $-6^\circ$  to the stall at approximate  $17^\circ$ , for the excitation frequencies of 5 and 10Hz (see Figure 28).

From the analysis of such curves one could appreciate an increment of  $C_l$  when the excitation frequency increases, in comparison with the clean airfoil. Such behavior is consistent with the values of Table 1 and Figure 28. Also is observed that the  $C_l$  values of the model with the Gurney flap fixed are something greater than the corresponding values for the movable Gurney condition. Regarding the  $C_d$  behavior, from Table 3, it diminishes when the frequency increases, but its minimum value is something greater than the case for the clean wing.

**Case 2.** For the case of the rotating Gurney flap ( $90^\circ$ ) the experiments show us the following: Regarding the clean wing, there were found minor velocity variations at the wake, for the two  $x$ - positions (upstream mean velocity of 10 m/s). The wing with the fixed Gurney exhibit Power Density Spectrum peaks around 100 Hz, for both  $x$ -positions.

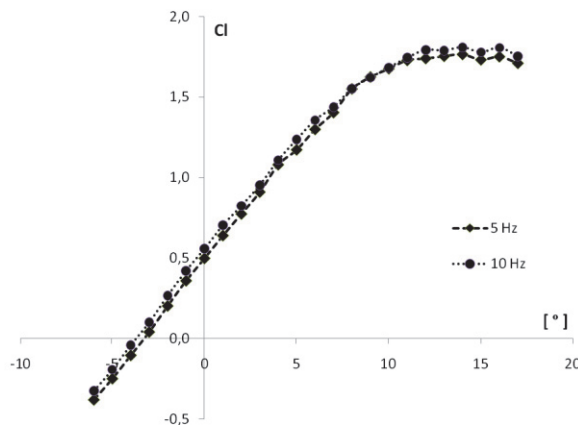


Fig. 28.  $C_l$  vs. angle of attack, for excitation frequencies of 5 and 10 Hz.

But the wing with the movable Gurney, showed such peaks, for both  $x$ -positions, at frequency values closed to the own rotating flap frequencies (see Tables 4 and 5). So, we detected a very good agreement between the rotating frequencies and the Power Density Spectrum peaks for both  $x$ -positions at the wake.

Frequency 1	26 Hz
Frequency 2	35 Hz
Frequency 3	41 Hz

Table 4. Gurney flap frequency oscillations.

The example shown in Tables 4 and 5 corresponds to the second measurement position in the wake ( $x$ -position of  $75\%c$  from the trailing edge), for a  $y$ -position of 2 mm below the trailing edge. In general, all the values are similar for both  $x$ -positions. Outside the wake the flow behavior is as expected.

	Frequency 1	Frequency 2	Frequency 3
Position 1	25	35	40
Position 2	25	30	39

Table 5. Power Density Spectrum peak frequencies.

In Figures 29 and 30 we show the mean v-component velocity distributions for the two measured positions (Position 1 and Position 2) and for the different Gurney flap frequency movement. MFF1P1 means: movable flap at Frequency 1 at Position 1, and then so on. Gurney 90° means a fix flap at 90° from the chord.

In such Figures we could appreciate the difference between the curves for the fixed Gurney and the corresponding for the moving one, for the three frequencies. At the level of the moving flap, between points 0 and -4, the difference between velocities are very small. It seems that the vertical velocities were almost independent of the frequency in those points.

**Case 3.** Below we show up some of the rotating Gurney flap (up to 30°) experimental results. We displayed part of the huge instantaneous velocity and static pressure measurements, with the aim to explore qualitatively and quantitatively the particular fluid dynamic pattern, promoted by the flap oscillations, in the near wake region and their relation with the corresponding pressure distribution around the airfoil, as a consequence of the active flow control of such device upon the airfoil’s aerodynamic characteristics. We observed the almost perfect matching between the flap oscillating frequencies and the special wake structure, with a peak at the same frequency than the oscillating one and other peaks which are other structures, not harmonics because they aren’t multiples of the first (fundamental). In order to support such assumptions, we also showed the corresponding velocities spectra at some selected vertical points (Figure 32) and the horizontal and vertical velocities components on each “x” position (1H, 2H and 5H) for all the vertical points (mean free stream of 10m/s and 0° angle of attack):

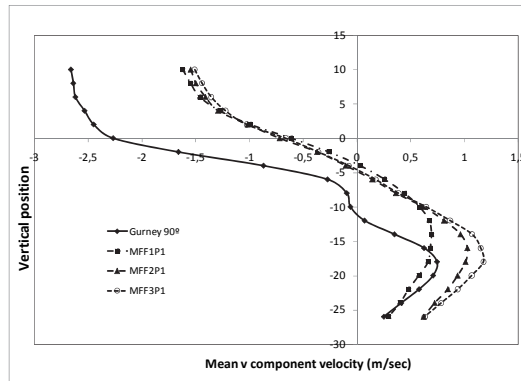


Fig. 29. Mean v-component velocity distributions along different y-positions for 2% c x-position

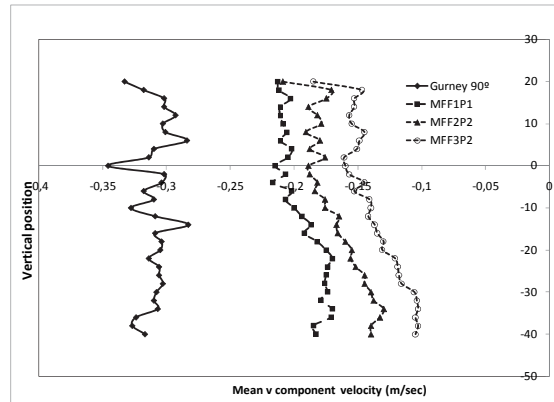


Fig. 30. Mean v-component velocity distribution along different y-positions for 75% c x-position

Figure 31 shows a Power Density Spectra, corresponding to the fixed Gurney, measured at 2% c x-position (Position 1). Figure 32 shows the power density spectra evolution of the downstream vertical velocities, at the 2H "x" position in a vertical point located at the same horizontal level of the flap's trailing edge (point -10), for the clean airfoil (PS), the flap deployed fixed (GF) and for the flap oscillating at 22; 38 and 44 Hz. In all cases, the free stream upstream velocity was 10 m/s.

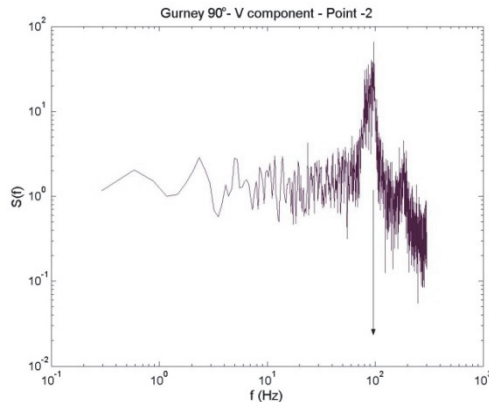


Fig. 31. Power Density Spectra for Position 1 at the trailing edge of the Gurney flap.

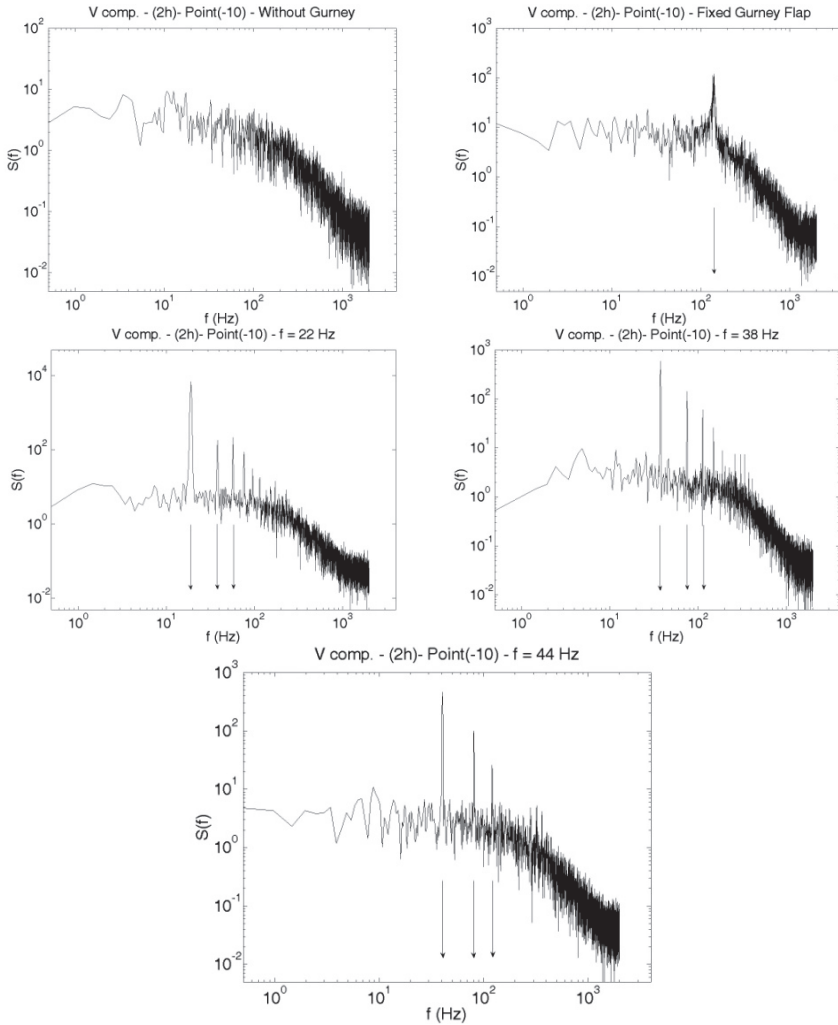


Fig. 32. V component velocities spectra, for the clean airfoil, fixed Gurney and moving one (three frequencies), 2H x-position and vertical point -10.

The spectra peaks were as follows: For 22 Hz (oscillating frequency), first peak at 22 Hz and successively (approximate) 39 Hz, 58 Hz, 74 Hz, 92 Hz and 110 Hz; for 38 Hz (oscillating frequency), the peaks were at 30 Hz, 78 Hz, 110 Hz, 124 Hz, 190 Hz; for 44 Hz (oscillating frequency), the peaks were 44 Hz, 82 Hz, 108 Hz. For the fixed GF condition, the peak was at 142 Hz. One could see how the oscillation of the flap made important changes on the wake characteristics.

One could see how the oscillation of the flap made important changes on the wake characteristics. The periodic (coherent) vortex street, generated by the oscillating flap, had enough strength to overlap and diminish the intensity of the turbulent structures typical of the airfoil with the fixed flap. This behavior is more significantly as the oscillating

frequency grows. In that way, the important changes in the wake, promoted by the oscillating flap, will affect directly the general circulation around the airfoil. Thus, our main concern is to measure the near wake with some detail.

Figure 33 shows the instantaneous velocities at the point -10. The curves exhibit peaks, of course, in accordance with those power density spectra (Figure 32). We could see how the turbulent intervals between peaks, are reduced as the oscillating frequency grows. This is due, probably, to the fact that once we overcome some frequency step, the characteristics of the periodic structures, shed by the oscillating flap, become almost independent of the frequency and, so, the near wake structure will be similar for frequencies above such step.

Figures 34, 35 and 36 shows the horizontal and vertical velocities, for a free stream of 10m/s and  $0^\circ$  angle of attack, for all vertical points in each "x" position (1H, 2H and 5H), for the clean airfoil, the fixed deployed flap and the oscillating condition for the three frequencies.

Regarding the Figure 34, we could conclude that the U-component has small variations between the different conditions (clean airfoil; fixed flap; etc), being always positive above and below the trailing edge, but with a reduction of its magnitude from the trailing edge level to the end of flap level. The vertical velocities exhibit important differences, above the trailing edge, between the clean airfoil and the fixed flap case. Respect the oscillating flap, there are small differences between the vertical velocities for the three frequencies but, if we look close the vertical velocities at the flap level and lower, their values are greater than the corresponding to clean airfoil or even the fixed flap case. Qualitatively, the situation is similar for the 2H "x" position (Figure 35). Analyzing both Figures, it's clear that we have an anticlockwise vortex behind the flap. This is consistent with the results founded by other authors [Liebeck (1978), Neuhart et al (1988), Storms et al (1993), Bloy et al (1995), Myose et al (1998), van Dam et al (1999), Gay et al (2003), Boldes et al (2008) and Tang et al (2007)].

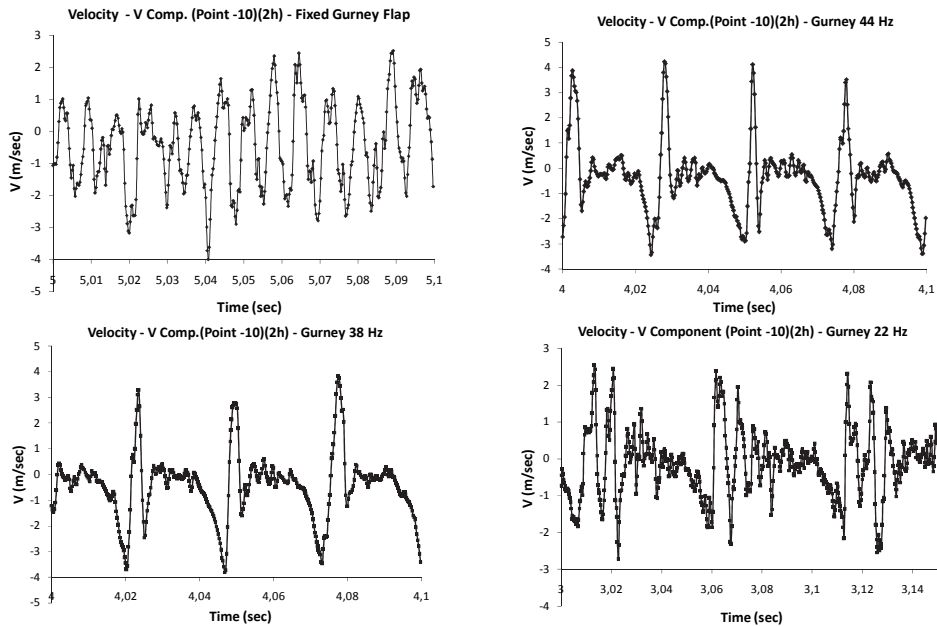


Fig. 33. Instantaneous vertical velocities curves at -10 points for the wing with GF fixed and wing for the three mini-flap frequencies oscillation



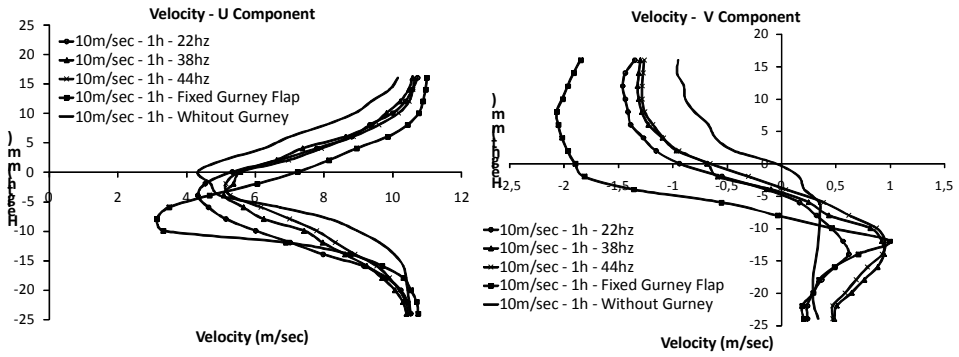


Fig. 34. U-component and V-component velocities for the fixed and movable mini-flap for different frequencies at 1H x-position

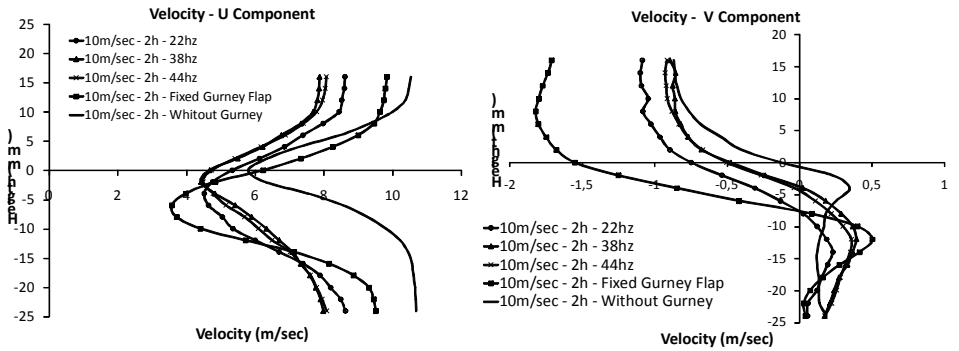


Fig. 35. U-component and V-component velocities for the fixed and movable mini-flap for different frequencies at 2H x-position

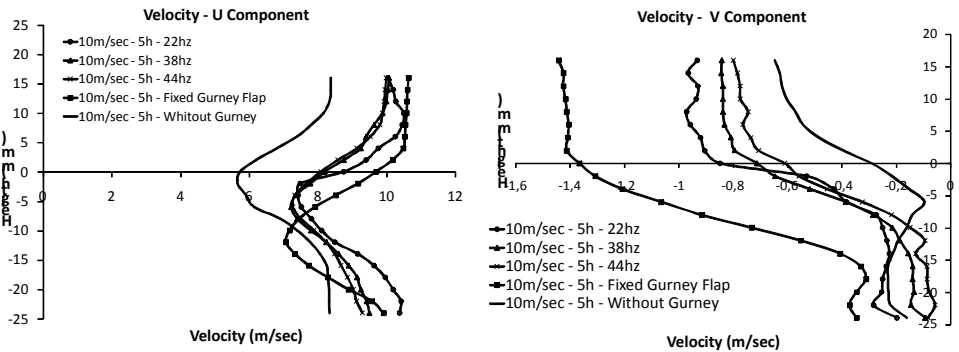


Fig. 36. U-component and V-component velocities for the fixed and movable mini-flap for different frequencies at 5H x-position

Following some of the ideas exposed by [Tang et al (2007)], we selected two upstream points, one on the upper surface and the other on the lower surface (see Experimental procedure), to analyze the pressure time history. Our pressure taps were located at the “x” position 0.88c being the flap location at 0.96c. Such pressure taps were designated, Up (for upper surface) and Low (for lower surface). The main difference, regarding the procedure followed by Tang et al [20], was our election of the pressure taps location, upstream the perturbation device (flap) location. Figures 37a and 37b show the  $C_p$  time history for  $5^\circ$  angle of attack (AOA) and 22Hz and 38Hz oscillating frequencies, respectively. Figures 37c and 37d are for those two frequencies but for  $11^\circ$  of angle of attack.

Figure 37a shows some irregularities in the pressure fluctuations, than Figure 37b. It seems that as frequency grow, the pressure fluctuations become similar in amplitude, both in the upper and lower surfaces. The difference between those times histories could be associated with the changes in the near wake as the frequency grows (see Figure 33). Although velocities spectra showed in Figure 12 corresponds to  $0^\circ$  of angle of attack, we could made a comparison between such results and the pressure time histories for  $5^\circ$  angle of attack, bearing in mind the similar qualitative behavior of the airfoil for  $0^\circ$  and  $5^\circ$  angles of attack. Moreover, such times history behavior is also associated with the pair of vortex structures in the near wake (described above, regarding Figures 34 and 35).

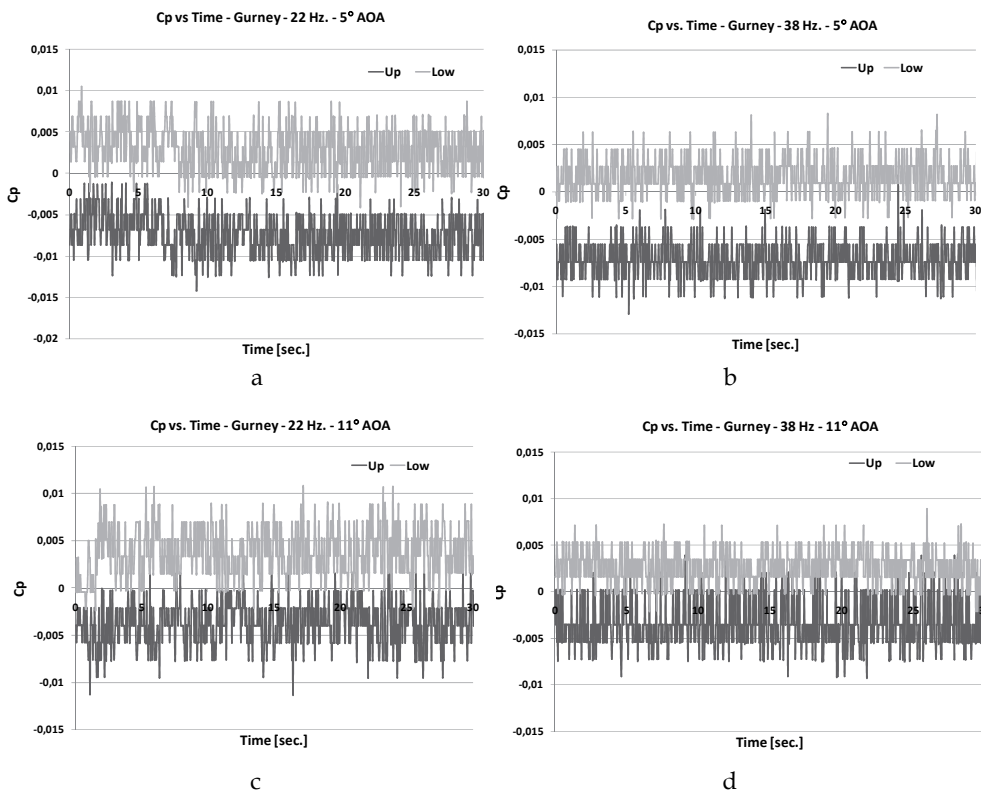


Fig. 37.  $C_p$  vs. time

If we observe carefully, for the same angle of attack and far away from the stall, as frequency grow, the upper  $C_p$  becomes more negative whereas the lower  $C_p$  becomes a bit less positive as the frequency grow. From an overall point of view we could conclude that as frequency grows the lift will enhance. Figures 17c and 17d show us the situation for  $11^\circ$  of angle of attack, exhibiting an overall increase of the pressure fluctuations, in comparison with the case for  $5^\circ$  of angle of attack, but with they seems to diminish the difference between the upper and lower  $C_p$ 's. So, that could imply a small lift lowering, in comparison with the  $5^\circ$  angle of attack. Such behavior, on the upper surface, could be a result of the interaction of the external turbulent flow and the boundary layer near to stall and, in the lower surface, the interaction of the external flow and the fluctuations induced by the oscillating flap.

Finally, looking to achieve an overall understanding of the whole phenomena, we prepared the Table 6 in order to compare the upper and lower  $C_p$ 's, for the airfoil with the fixed mini-flap and the airfoil with the oscillating flap, for the three frequencies.

Device		Position		
		Cp Up	Cp Low	
Deployed Gurney Flap		$0^\circ$	-0,1673516	0,2247924
		$5^\circ$	-0,413925	0,2588836
		$11^\circ$	-0,2374264	0,2957263
Movable Gurney Flap	22 Hz.	$0^\circ$	-0,1477534	0,1360552
		$5^\circ$	-0,3680741	0,142911
		$11^\circ$	-0,1969174	0,1875045
	38 Hz.	$0^\circ$	-0,0647598	0,1507643
		$5^\circ$	-0,3591227	0,0808359
		$11^\circ$	-0,1732171	0,1346238
	44 Hz.	$0^\circ$	-0,0308086	0,1724985
		$5^\circ$	-0,3501714	0,0187608
		$11^\circ$	-0,2016496	0,1066335

Table 6. Upper and lower  $C_p$ 's for the airfoil with the fixed mini-flap and with the oscillating one

**Conclusions:** Three NACA 4412 airfoil model were studied, in a boundary layer wind tunnel, to investigate the aerodynamic effect upon them by a Gurney flap, as passive and active flow control device. Owing this flap was located at a distance of  $8\%c$ , from the trailing edge, our work is reasonable compared with other works performed with the Gurney located exactly at the trailing edge [Wassen et al, 2007].

The fixed Gurney flap increase the maximum section lift coefficient, in comparison with the clean airfoil, but increasing something the section drag coefficient. These results had good agreement with Liebeck's work [1978], who concluded that increasing the flap height until  $2\%c$  the drag increases. The motivation to employ Gurney flap as an active flow control device, is to found the frequency that produce the more convenient vortex shedding from the point of view of reinforcing the airfoil circulation. If the device is fixed, in some instances the vortex shedding is favorable to enhance the lift but in other instances is unfavorable. But moving the flap, we could find the more adequate frequency in the sense to be favorable to increase the circulation and, hence, the airfoil's lift.

In the first model for excitation frequencies up to 15Hz, the section lift coefficient grows meanwhile the section drag decreases. According other works [Liebeck (1978), Neuhart et al (1988)], the vortex wake close to the trailing edge, had clockwise and counterclockwise vortices. If the movable (vertical) Gurney flap oscillates outside and inside the wing, with a frequency that allows moving down the rear stagnation point of the airfoil, the lift will grow. So, according the flap frequency, it will promote an increase or decrease of the lift. Such changes are reflected in the  $C_l$  and  $C_d$  table shown. The main disadvantage of these experiments is to build a reliable mechanism capable to produce frequencies similar to that corresponding to the shedding vortex frequencies from a fixed Gurney flap, and also the calibration of such mechanism.

We worked at the same time in a different approach to get a movable Gurney flap, capable to reach higher frequencies, using a rotating plate of the same height of the Gurney flap used in the other system. Finally we reach a reliable mechanism, as was described above, which works at higher frequencies than the other one.

Regarding the rotating system (mini-flap to  $90^\circ$ ), we observed a very good agreement between the Gurney rotation frequencies and the peak frequencies detected in the wake, for both x-positions (Position-1 and Position-2, at  $2\%c$  and  $75\%c$  behind the trailing edge). The instantaneous velocities at the wake were measured by hot-wire constant temperature anemometer. Another noticeable fact is the difference in the vertical velocities components, between the fixed and the movable (rotating) Gurney, at both x-positions at the trailing edge height. Such vertical velocities are of less magnitude for the movable Gurney case than for the fixed one. Vertical velocities are directly connected with the drag and, so, we could presume that the drag of the wing, with the rotating Gurney, will be less than the corresponding to the fixed Gurney.

In the third case, rotating Gurney flap, up to  $30^\circ$ , the periodic vortex street had enough strength to overlap and diminish the intensity of the turbulent structures typical of the airfoil with the fixed flap. This behavior is more significantly as the oscillating frequency grows. The important changes in the wake, produced by the rotating flap, will affect the general circulation around the airfoil. The differences between the vertical and longitudinal velocities, for the three frequencies, showed to us the existence of the anticlockwise vortex behind the flap.

In the case of the pressure, the  $C_p$  differences between the lower and upper surfaces, for three reference angles of attack ( $0^\circ$ ,  $5^\circ$  and  $11^\circ$ ), are greater for the fixed flap than the oscillating one. Also we observed that the corresponding  $C_p$  differences between the lower and upper surfaces diminish as the oscillating frequency grows, but in all cases the values are lesser than the fixed flap case.

In any case, this situation will be confirmed not until we perform in future experiments, loads measurements and also pressure distribution around the airfoil. We also will perform the measurements for more x-positions in the wake than in the present work.

Bearing in mind this is our first work with active flow control devices, in particular, the mini-flaps Gurney type, we found that a mini-flap capable to move up and down at different frequencies, seems to enhance the lift regarding the clean airfoil and the case with such mini-flap fixed. Nevertheless those are primary assessments which should be object of future and more elaborated experiments. For other side, in order to test the mini-flap with a different kind of movement, we build a model with such mini-flap capable to make an

oscillating motion around its axe (along wingspan). Such device could oscillate with  $30^\circ$  of amplitude but with higher frequencies than the former model. In this case we performed more measurements in the near wake region. The first obtained results showed us that this mini-flap produce a wake alleviation, that is, both in the near wake and probably in the far wake, but their effect upon lift enhancement was, in some way, opposite to the up-down movement mini-flap. This was an effect not predictable for us, at a first sight.

Finally, due the different results obtained from the models with mini-flaps of the same size but with different kind of motions, we are planning to go deep in our experiments looking to obtain, in all cases, the aerodynamic forces, the pressure distribution around the airfoil and more detailed near and far wake measurements. We hope to reach a better understanding of the process evolved and, then, to contribute to the practical implementation in wings and/or rotor blades of such type of active devices.

## 6. Acknowledgements

Authors wish to express, in particular, their recognition for the kindly and valuable assistance gave by Dra. Ana Scarabino - researcher at the Boundary Layer & Environmental Fluid Dynamics Laboratory - related with wavelets data process and their fluid dynamics interpretation. Also wish to recognize the constant support to our work by the other Laboratory members.

## 7. References

- Babiano, A., Boetta, G., Provenzale, A., and Vulpiani, A. (1994). Chaotic advection in point vortex models and 2D turbulence, *Phys. Fluids*, 6, 2465-2474.
- Bacchi F., Marañón Di Leo J., Delnero J.S., Colman J., Martinez M., Camocardi M. & Boldes U. (2006). Determinación experimental del efecto de miniflaps Gurney sobre un perfil HQ - 17. IX Reunión sobre Recientes Avances en Física de Fluidos y sus Aplicaciones. Mendoza, Argentina.
- Bendat J. S. and Piersol, A. G. (1986). *Random Data: Analysis and Measurement Procedures*, 2<sup>nd</sup> ed. John Wiley & Sons, New York.
- Bloy, A. W., and Durrant, M. T. (1995). "Aerodynamic Characteristics of an Aerofoil with Small Trailing Edge Flaps. *Journal of Wind Engineering*, Vol. 19, No. 3, pp. 167-172.
- Boldes, U.; Delnero, J.; Marañón Di Leo, J.; Colman, J.; Camocardi, M. & François, D. (2008). "Influencia en la sustentación, de los vórtices de la estela de un perfil con miniflap tipo Gurney". *Actas 1er Congreso Nacional de Ingeniería Aeronáutica*. La Plata.
- Bonnet, J.P., Delville, J., Glauser, M.N., Antonia, R.A., Bisset, D.K., Cole, D.R., Fiedler, H.E., Carem, J.H, Hilberg, D., Jeong, J., Kevlahan, N.K.-R., Ukeiley, L.S., Vincendeau, E. (1998). Collaborative testing of eddy structure identification methods in free turbulent shear flows. *Experiments in Fluids* 25, 197-225.
- Bruun, H. H. (1995). *Hot wire anemometry*, Oxford University Press, 507 p.
- Castro, I. P. (1989). *An Introduction to the Digital Analysis of Stationary Signals*. Adam Hilger, Bristol

- Couder Y and Basdevant C. (1986). Experimental and numerical study of vortex couples in two-dimensional flows. *Journal of Fluid Mechanics* 173, pp. 225 - 251.
- Daubechies I. (1992). *Ten Lectures on Wavelets*, Society for Industrial and Applied Mathematics.
- Delnero, J.S. et al. (2005). Experimental determination of the influence of turbulent scale on the lift and drag coefficients of low Reynolds number airfoils, *Latin American Applied Research*. Vol 35 No.4 - pp. 183 - 188.
- Dunyak J., Gilliam X., Peterson R., Smith D. (1998). Coherent gust detection by wavelet transform, *J. of Wind Engineering and Industrial Aerodynamics* 77 & 78, pp 467-478.
- Farge, M. (1990). Transformee en ondelettes continue et application a la turbulence, *Journ. Annu.Soc. Math., France*, 17-62.
- Farge, M. (1992). Wavelet Transforms and their applications to Turbulence, *Annual Rev. Fluid Mechanics*, 24, 395-457.
- Finnigan J. (2000). Turbulence in plant canopies, *Ann. Rev. of Fluid Mechanics* 32: 519-571
- Fouillet Y. (1992). Contribution a le etude par experimentation numerique des ecoulements cisailles libres. Effets de compressibilite. These. Universite de Grenoble.
- Gai, S. L., and Palfrey, R. (2003). "Influence of Trailing-Edge Flow Control on Airfoil Performance," *Journal of Aircraft*, Vol. 40, No. 2, pp. 332-337.
- Hinze, J.O. (1975). *Turbulence*. 2nd edition, McGraw-Hill.
- Ho, C.M. et al. (1985). Perturbed free shear layers, *Annual Review of Fluid Mechanics*, Vol. 16, pp. 365-424.
- Huerre, P. et al. (1985). Absolute and convective instabilities in free shear layers, *Journal of Fluid Mechanics*, Vol. 159, pp. 151-168.
- Hussain A. K. M. F. (1986). Coherent structures and Turbulence *Journal of Fluid Mech.* 173, pp303-356.
- Jenkins J. M. and Watts D. G. (1968). *Spectral Analysis and its Applications*, Holden Day, San Francisco.
- Jeong, G., & Hussain F. (1995). On the identification of a vortex. *Journal of Fluid Mechanics* 285, pp: 69-94.
- Jimenez, J. & Pinelli, A. (1999). The autonomous cycle of near wall turbulence, *J. Fluid Mech.* 389, 335 - 359.
- Jimenez, J. & Simens, M. P. (2001). Low-dimensional dynamics in a turbulent wall, *J. Fluid Mech.* 435, 81, 91.
- Kaimal J. C and Finnigan J. J. (1994). *Atmospheric Boundary Layer Flows*. Oxford University Press.
- Kline, S.J., Reynolds, W.C., Schraub, F.A., and Runstadler, P.W. (1967). The structure of turbulent boundary layers. *Journal of Fluid Mechanics*, Vol. 30, pp. 741-773.
- Kiya, M. et al. (1986). Vortex pairs and rings interacting with shear-layer vortices, *Journal of Fluid Mechanics*, Vol. 172, pp. 1-15.
- Kiya, M. et al. (1999a). Turbulent elliptic wakes, *Journal of Fluids and Structures*, Vol. 13, pp. 1041-1067.

- Kiya, M. et al. (1999). Separation Control by Vortex projectiles, *AIAA-1999-3400 - AIAA Fluid Dynamics Conference, 30th, Norfolk, VA.*
- Liebeck R.H. (1978). Design of subsonic airfoils for high lift. *Journal of Aircraft*, Vol. 15, No. 9.
- Lomas C. G. (1986). *Fundamentals of Hot Wire Anemometry*. Cambridge University Press.
- Mahrt, L. (1991). Eddy asymmetry in the sheared heated boundary layer. *J. Atmos. Sci.*, 48, 472-492.
- McWilliams, J.C., and Weiss, J.B., (1994). Anisotropic Geophysical Vortices, *CHAOS*, 4, 305-311.
- Monin, A. S., and Obukhov, A. M. (1954). 'Basic laws of turbulent mixing in the surface layer of the atmosphere', *Tr. Akad. Nauk SSSR Geofiz. Inst.* 24, 163-187. English translation by John Miller, 1959.
- Myose, R., Papadakis, M., and Heron, I. (1998). "Gurney Flap Experiments on Airfoils, Wings, and Reflection Plane Model," *Journal of Aircraft*, Vol. 35, No. 2, pp. 206-211.
- Neuhart H. & Pendergraft O.C. (1988). A water tunnel study of gurney flaps. NASA-TM-4071.
- Oster, D. et al. (1982). The forced mixing layer between parallel streams, *Journal of Fluid Mechanics*, Vol. 123, pp. 91-130.
- Panofsky H. A. and Dutton, J. A. (1984). *Atmospheric Turbulence. Models and Methods for Engineering Applications*, John Wiley & Sons, New York, 397 pp.
- Raupach M. R., Finnigan, J.J. and Brunet Y (1996): Coherent eddies and turbulence in vegetation canopies: the mixing layer analogy, *Boundary-Layer Meteorology* 78: 351-382
- Robinson, S.K. (1991): Coherent motions in the turbulent boundary layer. *Annual Reviews of Fluid Mechanics*, Vol. 23, pp. 601-639.
- Schatz, M; Guenther, B; Thiele, F. (2004). Computational Modelling of the Unsteady Wake behind Gurney-Flaps, *2<sup>nd</sup> AIAA Flow Control Conference, AIAA-2417, Portland, Oregon, USA.*
- Schwartz M. and Shaw L. (1975). *Signal Processing*, McGraw Hill, 396 pp.
- Soldati, A. & Monti, R. (2001). *Turbulence Modulation and Control*. Springer-Verlag, Wien.
- Storms B.L. & Jang C.S. (1993). Lift enhancement of an airfoil using a Gurney Flap and Vortex Generators. *AIAA* 1993-0647.
- Tang, D. & Dowel, E.H. (2007). Aerodynamic loading for an airfoil with an oscillating Gurney flap. *Journal of Aircraft*, Vol. 44, Nr. 4, pp. 1245-57.
- Tennekes H. and Lumley, J. L. (1972). *A First Course in Turbulence*, MIT Press, Cambridge, Massachusetts.
- Troolin, D.R. et al. (2006). Time resolved PIV analysis of flow over a NACA 0015 airfoil with Gurney flap, *Experiments in Fluids* Vol. 41, pp. 241-254.
- Tusche, S. (Interne Bericht) (1984). *Beschreibung des Konstruktiven Aufbaus und Kalibrierung von 6-Komponenten-DMS Windkanalwaagen*, DLR, Goettingen.
- van Dam, C. P., Yen, D. T., and Vijgen, P. M. H. W. (1999). "Gurney Flap Experiments on Airfoil and Wings," *Journal of Aircraft*, Vol. 36, No. 2, pp. 484-486.

Wassen E., Guenther B. & Thiele F. (2007). Numerical and Experimental Investigation of Mini-Flap Positions on an Airfoil. Technical University Berlin, 10119 Berlin, Germany. Delnero J.S., Marañón Di Leo J., Boldes U., Colman J., Bacchi F. & Martinez M.A.M. Departamento de Aeronáutica, Universidad Nacional de La Plata, (1900) La Plata, Argentina.



# Wind Tunnels in Engineering Education

Josué Njock Libii  
Indiana University-Purdue University Fort Wayne  
USA

## 1. Introduction

The subject of fluid mechanics is filled with abstract concepts, mathematical methods, and results. Historically, it has been a challenging subject for students, undergraduate and graduate. In most institutions, the introductory course in fluid mechanics is accompanied by a laboratory course. While institutional philosophy and orientation vary around the world, the goal of that laboratory is to strengthen students' understanding of fluid mechanics using a variety of laboratory exercises (Feisel & Rosa, 2005).

The literature has identified six basic functions of experimental work. Indeed, the report of the Laboratory Development Committee of the Commission on Engineering Education identified six key functions and objectives of the instructional laboratory (Ernest, 1983):

- a. Familiarization
- b. Model identification
- c. Validation of assumptions
- d. Prediction of the performance of complex systems
- e. Testing for compliance with specifications
- f. And exploration for new fundamental information.

The report states that "The role of the undergraduate instructional laboratory is to teach student engineers to perform these six functions. Hence the primary goal of undergraduate laboratories is to inculcate into the student the theory and practice of experimentation. This includes instrumentation and measurement theory." (Ernst, 1983).

The wind tunnel is one such instrument. This chapter focuses on the measurement theory on which the wind tunnel is based and presents examples of its use in the undergraduate fluid mechanics laboratory at Indiana University-Purdue University Fort Wayne, Fort Wayne, Indiana, USA.

The remainder of the chapter is organized in the following manner:

1. *Basic concepts* discuss definitions, classifications, and various uses of wind tunnels.
2. *Fundamental Equations* present the equations that are used as foundations for the theory and application of wind tunnels.
3. *Applications of wind tunnels in teaching fluid mechanics* present nine different examples that are used in our laboratory to teach various aspects of fluid mechanics and its uses in design, testing, model verification, and research.
4. *References* list all cited works in alphabetical order.

## 2. Basic concepts

### 2.1 Definition of a wind tunnel

A wind tunnel is a specially designed and protected space into which air is drawn, or blown, by mechanical means in order to achieve a specified speed and predetermined flow pattern at a given instant. The flow so achieved can be observed from outside the wind tunnel through transparent windows that enclose the test section and flow characteristics are measurable using specialized instruments. An object, such as a model, or some full-scale engineering structure, typically a vehicle, or part of it, can be immersed into the established flow, thereby disturbing it. The objectives of the immersion include being able to simulate, visualize, observe, and/or measure how the flow around the immersed object affects the immersed object.

### 2.2 Classifications of wind tunnels

Wind tunnels can be classified using four different criteria. Four such criteria are presented.

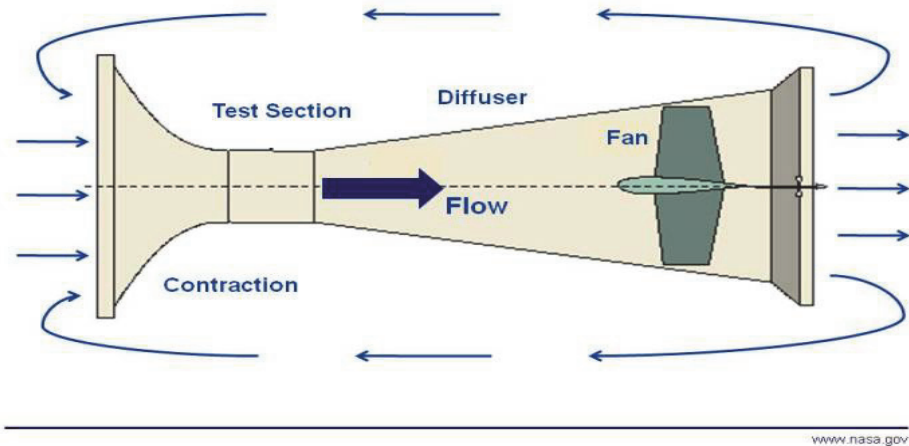
#### 2.2.1 Type 1 classification – The criterion for classification is the path followed by the drawn air: Open- vs. closed-circuit wind tunnels

Open-circuit (open-return) wind tunnel. If the air is drawn directly from the surroundings into the wind tunnel and rejected back into the surroundings, the wind tunnel is said to have an open-air circuit. A diagram of such a wind tunnel is shown in Figure 1.

National Aeronautics and Space Administration



## Open Return Wind Tunnel



www.nasa.gov

Fig. 1. Diagram of an open-circuit, also known as open-return, wind tunnel (from NASA)

An open-circuit wind tunnel is also called an open-return wind tunnel.

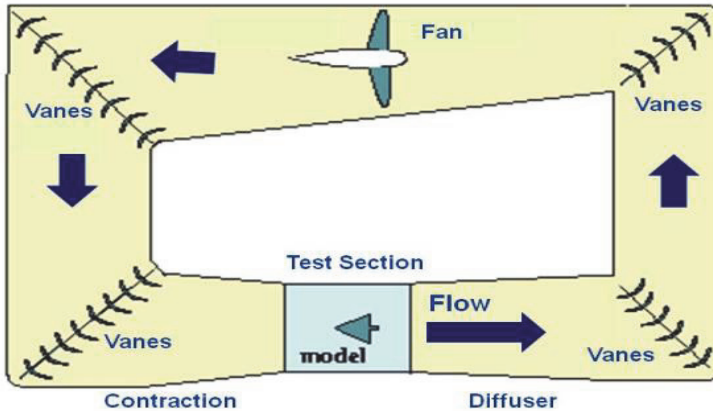
Closed-circuit, or closed-return, wind tunnel. If the same air is being circulated in such a way that the wind tunnel does neither draw new air from the surrounding, nor return it into

the surroundings, the wind tunnel is said to have a closed-air circuit. It is conventional to call that a closed-circuit (closed-return ) wind tunnel. Figure 2 illustrates this configuration.

National Aeronautics and Space Administration



## Closed Return Wind Tunnel



www.nasa.gov

Fig. 2. Top view of a closed-circuit, also known as closed-return, wind tunnel ( NASA)

### 2.2.2 Type 2 classification

The criterion for classification is the maximum speed achieved by the wind tunnel: subsonic vs. supersonic wind tunnels. It is traditional to use the ratio of the speed of the fluid, or of any other object, and the speed of sound. That ratio is called the Mach number, named after Ernst Mach, the 19<sup>th</sup> century physicist. The classification is summarized in Table 1. Schematic designs of subsonic and supersonic wind tunnels are compared in Figure 3.

**Subsonic wind tunnels.** If the maximum speed achieved by the wind tunnel is less than the speed of sound in air, it is called a subsonic wind tunnel. The speed of sound in air at room temperature is approximately 343 m/s, or 1235 km/hr, or 767 mile/hr. The Mach number,  $M < 1$ .

**Supersonic wind tunnels.** If the maximum speed achieved by the wind tunnel is equal to or greater than the speed of sound in air, it is called a supersonic wind tunnel.

Range of the Mach number , M	Name of flow , or conditions
$M < 1$	Subsonic
$M = 1$ , or near 1	Transonic
$1 < M < 3$	Supersonic
$3 < M < 5$	High supersonic
$M > 5$	Hypersonic
$M \gg 5$	High Hypersonic

Table 1. Classification of flows based upon their Mach numbers.



# Wind Tunnel Design

Glenn  
Research  
Center

Increase in Area :

For subsonic flow ( $M < 1$ )  
velocity decreases & pressure increases  
For supersonic flow ( $M > 1$ )  
velocity increases & pressure decreases

$M$  = Mach  
 $V$  = velocity  
 $p$  = pressure  
 $A$  = area

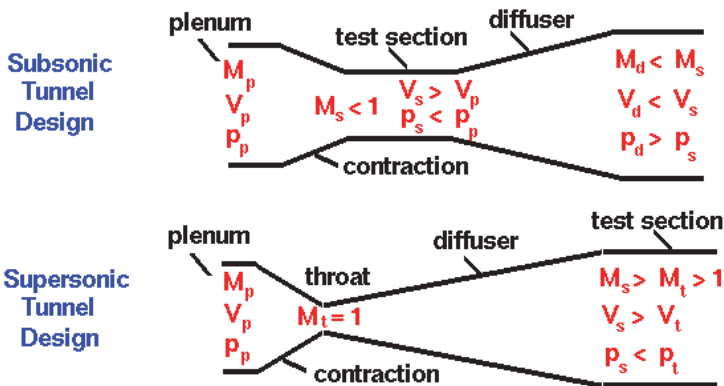


Fig. 3. Schematic designs of subsonic and supersonic wind tunnels (NASA).

### 2.2.3 Type 3 classification

The criterion for classification is the purpose for which the wind tunnel is designed: research or education. If the wind tunnel is for research it is called a research wind tunnel. If however, it is designed to be used for education, then, it is called an educational wind tunnel.

### 2.2.4 Type 4 classification

The criterion for classification is the nature of the flow: laminar vs. turbulent flow. Boundary-layer wind tunnels are used to simulate turbulent flow near and around engineering and manmade structures.

## 2.3 Uses of wind tunnels

There are many uses of wind tunnels. They vary from ordinary to special: these include uses for Subsonic, supersonic and hypersonic studies of flight; for propulsion and icing research; for the testing of models and full-scale structures, etc. Some common uses are presented below. Wind tunnels are used for the following:

### 2.3.1 To determine aerodynamic loads

Wind tunnels are used to determine aerodynamic loads on the immersed structure. The loads could be static forces and moments or dynamic forces and moments. Examples are

forces and moments on airplane wings, airfoils, and tall buildings. A close-up view of a model of an F-5 fighter plane mounted in the test section of a wind tunnel is shown in Figure 4.

### 2.3.2 To study how to improve energy consumption by automobiles

They can also be used on automobiles to measure drag forces with a view to reducing the power required to move the vehicle on roads and highways.

### 2.3.3 To study flow patterns

To understand and visualize flow patterns near, and around, engineering structures. For example, how the wind affects flow around tall structures such as sky scrapers, factory chimneys, bridges, fences, groups of buildings, etc. How exhaust gases ejected by factories, laboratories, and hospitals get dispersed in their environments.

### 2.3.4 Other uses include

To teach applied fluid mechanics, demonstrate how mathematical models compare to experimental results, demonstrate flow patterns, and learn and practice the use of instruments in measuring flow characteristics such as velocity, pressures, and torques.

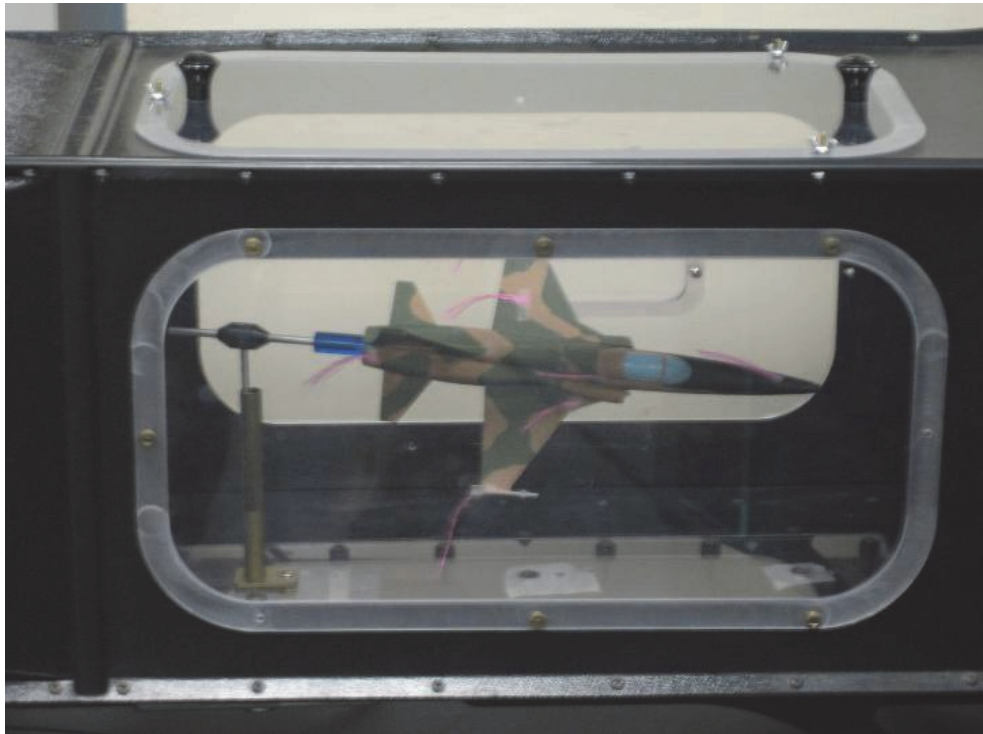


Fig. 4. Close-up of a tufted model of an F-5 fighter plane in the test section of a wind tunnel (NASA)

### 3. Fundamental equation for flow measurement

Velocity from pressure measurements. One very important use of wind tunnels is to visualize flow patterns and measure the pressure at a selected point in the flow field and compute the corresponding speed of air. The major equation used for this purpose is Eq.(1). It relates the speed of the fluid at a point to both the mass density of the fluid and the pressures at the same point in the flow field. For steady flow of an incompressible fluid for which viscosity can be neglected, the fundamental equation has the form

$$V = \sqrt{\frac{2(p_0 - p)}{\rho}} \quad (1)$$

Where  $V$  is the speed of the fluid,  $P_0$  is the total, also called the stagnation, pressure at that point of measurement, and  $p$  is the static pressure at the same point. This equation comes from the application of Bernoulli's equation for the steady flow of an incompressible and inviscid fluid along a streamline. Bernoulli's equation is typically obtained by integrating Euler's equations along a streamline. It will be recalled that Euler's equations are a special case of the Navier-Stokes equations, when the viscosity of the fluid has been neglected. The Navier-Stokes' equations, in turn, are obtained from Newton's second law when it is applied to a fluid for which the shear deformation follows Newton's law of viscosity. Accordingly, in order to establish the theoretical validity of this equation for use in educational wind tunnels, it is important to review some basic results from the theory of viscous and inviscid flows. For the interested reader, these are available in all introductory textbooks of fluid mechanics (e.g. Pritchard, 2011). For this reason, the rest of this chapter will emphasize applications of the results of fluid mechanics theory as they pertain to the use of wind tunnels for instructional purposes.

### 4. Applications of wind tunnels in teaching fluid mechanics

This section discusses nine different laboratory exercises in which the wind tunnel is used to measure fluid flow parameters. They are: 1) measurement of air speed; 2) verification of the existence of the boundary layer over a flat plate; 3) determination and characterization of the boundary layer over a flat plate; 4) searching for evidence of turbulence in boundary layer flow; 5) measurement of pressure distributions around a circular cylinder in cross flow; 6) determination of the viscous wake behind a circular cylinder in cross flow; 7) determination of lift and drag forces around airfoils; 8) reduction of drag by the introduction of turbulence in the boundary layer; and 9) determination of the Richardson's annular effect in flow through a duct.

#### 4.1 Measurement of air speed using an open-circuit wind tunnel

##### 4.1.1 Purpose

The purpose of this experiment is to learn how to use the wind tunnel to measure the difference between the stagnation (total) pressure and the static pressure at a specific point of a flow field and use that difference to compute the wind speed at that point using Bernoulli's equation.

##### 4.1.2 Key equation

The key equation is

$$V = \sqrt{\frac{2(p_0 - p)}{\rho}} \quad (1)$$

#### 4.1.3 Experimental procedure

The experimental procedure consists of four steps:

1. Read the temperature and the pressure inside the lab, or inside the wind tunnel, or both.
2. Use these values to compute the mass density of air inside the lab using the ideal gas law. Or use these values to look up the mass density of air on a Table.
3. Use the wind tunnel to measure the pressure difference,  $p_0 - p$ , at the point of interest.
4. Use Eq. (1) to compute the speed of the air at that point.

A sketch of the open-circuit wind tunnel used in our lab is shown below. It is a subsonic wind tunnel that is equipped with static- and dynamic-pressure taps, a pressure-sensing electronic device (See Figure 5).

In this setup, the stagnation pressure is measured by the pressure probe, while the static pressure is measured using a wall tap. This is illustrated graphically in Figure 6(a).

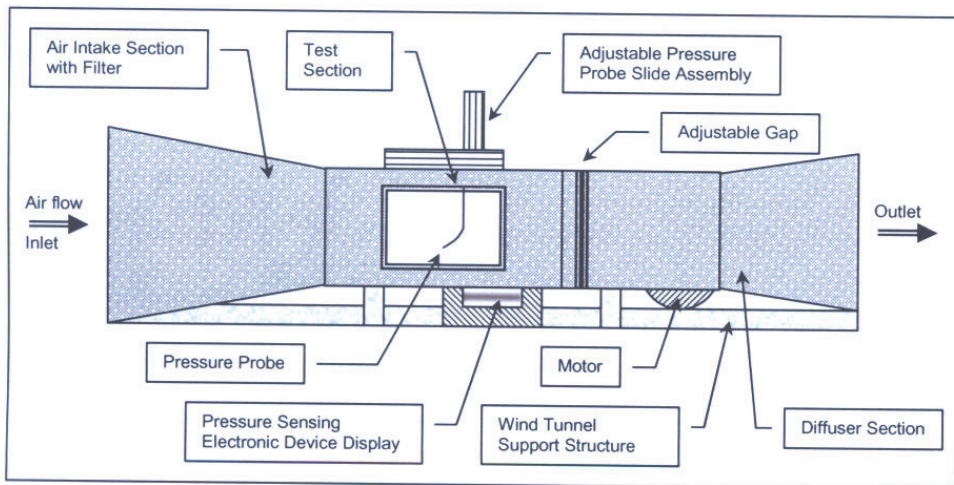


Fig. 5. Sketch of the wind tunnel used (Courtesy of Joseph Thomas, 2006)

Students often wonder whether or not the use of a wall tap is correct; that is, if it can be justified using analysis. And the answer is that it is and it can. The use of a wall tap is allowable because the flow is presumed, and is in fact, essentially parallel. An illustration of parallel flow is shown in Figure 7.

Under parallel-flow conditions, Eq.(2), which is Euler's equation, written along a coordinate axis that is normal to the local streamline, indicates that the curvature of the local streamlines is extremely large, which causes the pressure gradient in the direction perpendicular to the streamlines to be zero, making the pressure constant in the direction

normal to the streamline. Therefore, the value of the static pressure measured by the wall tap is the same as that which would have been measured at the tip of the stagnation probe.

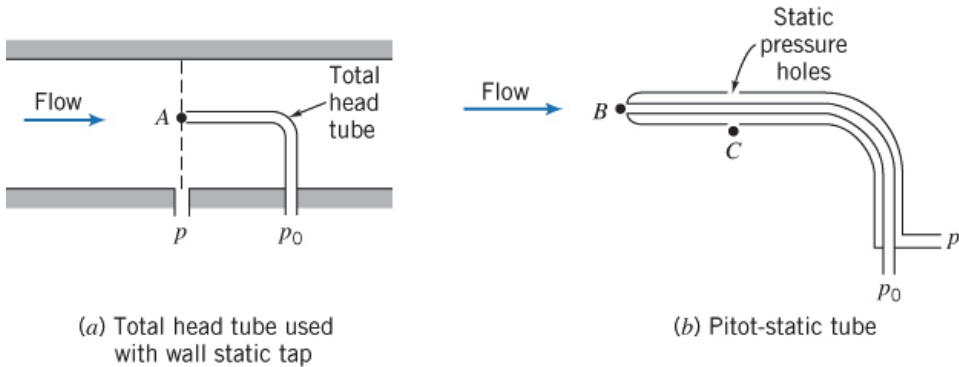


Fig. 6. Two different ways to measure the total and static pressures inside the test section (Pritchard, 2011).

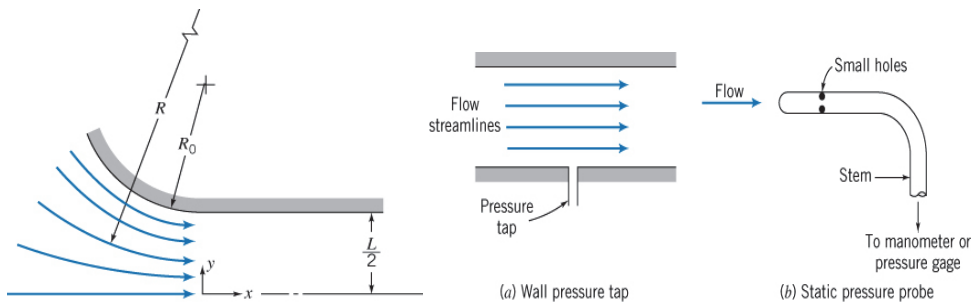


Fig. 7. Illustration showing that the radius of curvature becomes very large inside the test section (Pritchard, 2011).

$$\rho \left( \frac{V^2}{R} \right) = \frac{\partial p}{\partial n} \Rightarrow \frac{1}{\rho} \frac{\partial p}{\partial n} = \frac{V^2}{R} ; \tag{2}$$

$$\text{Parallel - flow} \Rightarrow R \rightarrow \infty, \frac{\partial p}{\partial n} \rightarrow 0$$

#### 4.1.4 Experimental results

The speed in the test section can be changed by increasing, or decreasing, the air gap between the diffuser section and the intake section of the wind tunnel (Fig. 5). When the air gap is completely closed, the speed in the test section is at its maximum value; when it is as large as possible, the speed in the test section is at its minimum. By starting with the gap completely closed, opening it by very small increments, and measuring the speed of air at each step, one gets a calibration curve that relates the speed in the test section to the size of the air gap. A sample curve obtained after executing this procedure in our wind tunnel is shown below (Njock Libii, 2006).



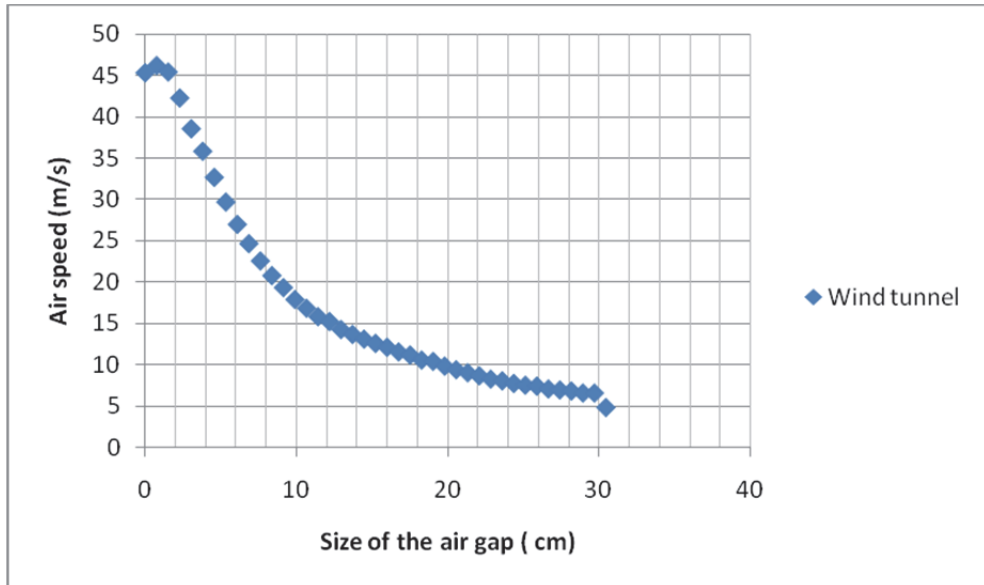


Fig. 8. Variation of wind speed in the test section with the size of the air gap.

## 4.2 Experimental verification of the existence of the boundary layer over a flat plate

### 4.2.1 Purpose

The purpose of this experiment is to learn how to use the wind tunnel to measure the difference between the stagnation (total) pressure and the static pressure at a series of points located on a vertical line selected in the flow field and use those differences to compute the wind speeds at each such point using Bernoulli's equation. The plotting of the resulting velocity profile and its examination will be used to determine whether or not the existence of the boundary layer can be detected.

Many viscous flows past solid bodies can be analyzed by dividing the flow region into two subregions: one that is adjacent to the body and the other that covers the rest of the flow field. The influence of viscosity is concentrated, and only important, in the first subregion, that which is adjacent to the body. The effects of viscosity can be neglected in the second subregion, that is, outside of the region adjacent to the body. The first region has been called the boundary layer historically. This phrase is a translation of the German phrase used by Prandtl, who introduced this concept. A big problem in fluid mechanics is locating the line that demarcates the boundary between the two subregions. Locating this line is also called determination of the boundary layer, or simply the boundary-layer problem.

The symbol used for the local thickness of this boundary layer is  $\delta$ . It denotes the distance between a point on the solid body and the point beyond which the effect of viscosity can be considered to be negligible.

### 4.2.2 Key equations

Thickness of the laminar boundary layer over a flat plate: Exact solution due to Blasius. For a semi-infinite flat plate, the exact solution for a laminar boundary layer was first derived by

Blasius (Pritchard, 2011). In conformity with his work, the continuity equation and the Navier-Stokes equation with the corresponding boundary conditions are ordinarily written as shown below:

$$\begin{aligned}\frac{\partial u}{\partial x} + \frac{\partial v}{\partial y} &= 0 \\ u \frac{\partial u}{\partial x} + v \frac{\partial u}{\partial y} &= \nu \frac{\partial^2 u}{\partial y^2} \\ u(y=0) &= 0; v(y=0) = 0 \\ u(y=\infty) &= U; \frac{\partial u}{\partial y}(y=\infty) = 0\end{aligned}\quad (3)$$

Where  $u$  is the component of velocity along the plate and  $v$  is the component of velocity perpendicular the plate. The origin of the coordinate system is at the leading edge of the plate, with the  $x$  direction along the plate and the  $y$  direction perpendicular to it. The magnitude of free-stream velocity, far from the plate is  $U$ .

Using similarity transformations, one introduces a change of variables as shown below. Let

$$\begin{aligned}\eta &\propto \frac{y}{\delta} \Rightarrow \frac{u}{U} = g(\eta); \\ \delta &\propto \sqrt{\frac{\nu x}{U}} \Rightarrow \eta = y \sqrt{\frac{U}{\nu x}} \\ u &= \frac{\partial \psi}{\partial y}; v = -\frac{\partial \psi}{\partial x}; f(\eta) = \frac{\psi}{\sqrt{\nu x U}}\end{aligned}\quad (4)$$

Applying this change of variables allows the second-order partial differential equation given above to become a nonlinear, third-order, ordinary differential equation, with the associated boundary conditions shown below:

$$\begin{aligned}2 \frac{d^3 f}{d\eta^3} + f \frac{d^2 f}{d\eta^2} \\ f(\eta=0) &= 0; \frac{df}{d\eta}(\eta=0) = 0 \\ \frac{df}{d\eta}(\eta \rightarrow \infty) &= 1.\end{aligned}\quad (5)$$

The solution to this equation is obtained numerically. From that numerical solution, it is seen that, at  $\eta = 5.0$ ,  $u/U = 0.992$ . If the boundary layer thickness is defined as the value of  $y$  for which  $u/U = 0.99$ , one gets

$$\delta \cong \frac{5.0x}{\sqrt{\text{Re}_x}}; \text{with } \text{Re}_x = \frac{Ux}{\nu}\quad (6)$$

Using boundary-layer theory, a sketch of the velocity profile along a vertical line in the test section of the wind tunnel is expected to look as shown below. In this application of the

wind tunnel, one wishes to compare this profile to that obtained experimentally in the test section of the wind tunnel (See Figure 9).

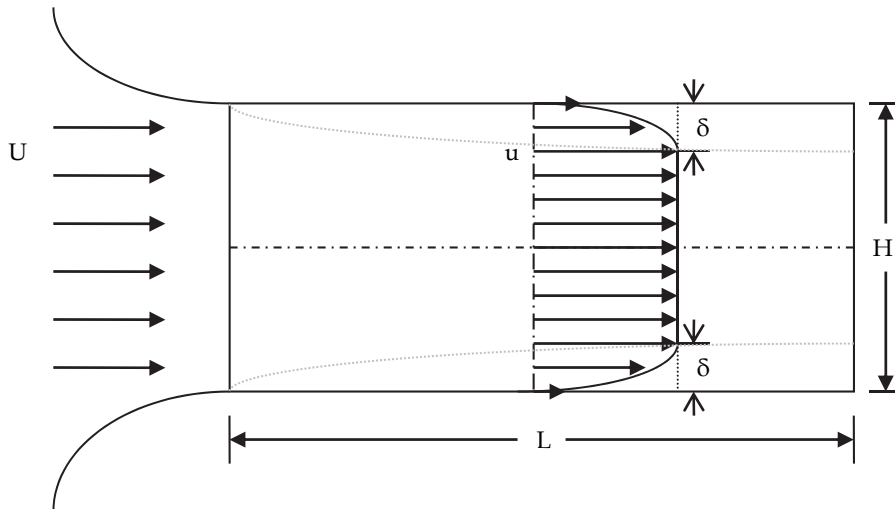


Fig. 9. Graphical Representation of Boundary Layer Theory in Wind Tunnel Test Section

#### 4.2.3 Experimental procedure

The experimental procedure consists of the following steps:

1. Choose a vertical plane in the test section.
2. Choose a vertical line within that vertical plane.
3. Select a series of points along that vertical line where the velocity of the air will be determined.
4. Read the temperature and the pressure inside the lab, or inside the wind tunnel, or both.
5. Use these values to compute the mass density of air inside the lab using the ideal gas law. Or Use these values to look up the mass density of air on a Table.
6. Select a wind speed and set the wind tunnel to generate that wind speed inside the test section.
7. Use the wind tunnel at that set speed to measure the pressure difference,  $p_0 - p$ , at each point that was identified along the preselected vertical line. This process is known as traversing a cross section of the flow space.
8. Use Eq. (1) to compute the speed of the air at each such point.

#### 4.2.4 Experimental results

A sample curve obtained after executing this procedure in our wind tunnel is shown below (Njock Libii, 2010). The wind speed was set at 46 m/s, approximately. By comparing Fig. (9) and Fig. (10), it can be concluded that experimental data clearly show the existence of the boundary layer. Note. Because the tip of the probe had a finite thickness (of 5 mm), students could not get infinitely close to the wall in measuring the speed of air in the wind tunnel (Njock Libii, 2010).

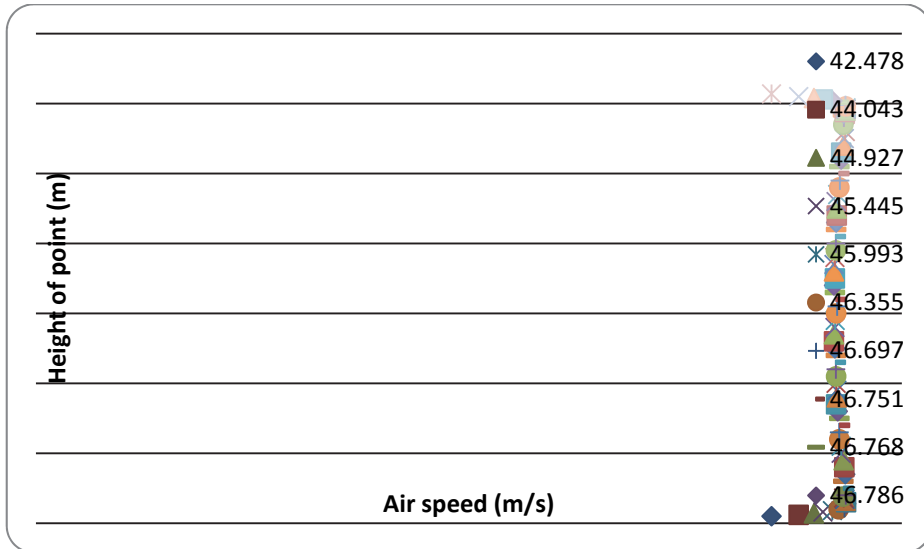


Fig. 10. Experimental velocity profile of the flow in the test section for a speed of 46 m/s

### 4.3 Determination and characterization of the boundary layer along a flat plate

#### 4.3.1 Purpose

The purpose of this experiment is to learn how to use experimental data collected in a wind tunnel to determine the thickness of the boundary layer and to characterize the type of boundary layer that is represented by such data.

#### 4.3.2 Key equations

The boundary layer over a flat plate can be laminar, turbulent, or transitional, meaning that it is somewhere between laminar and turbulent. Whether boundary layer is laminar or turbulent depends upon the magnitude of the Reynolds of the flow. Such a Reynolds number is defined as shown in Eq.(7),

$$Re_x = \frac{Ux}{\nu} \quad (7)$$

Where  $U$  is the freestream velocity,  $\nu$  is the kinematic viscosity, and  $x$  is the distance from the leading edge of the plate to some point of interest. By convention, a boundary player becomes turbulent when the Reynolds number of the flow exceeds  $5 \times 10^5$ .

For flow inside the test section, where, instead of inserting a plate, it is the bottom surface of the test section that takes the role of the flat plate, the location of the leading edge of the plate must be estimated. In the case of the data reported here, it was estimated in the following way: the leading edge was defined as the line where the curved section that constitutes the intake of the tunnel becomes horizontal, and hence, tangential to the inlet to the test section. In the wind tunnel used for these tests, that line was at a distance of  $0.356 \text{ m} < x < 0.457 \text{ m}$  from the plane that passes through the geometric center (centroid) of the test section. The free stream speed was  $U = 46 \text{ m/s}$ ; and using a kinematic viscosity of  $15.68 \times 10^{-6} \text{ m}^2/\text{s}$

$10^{-6} \text{ m}^2/\text{s}$ , corresponding to a room temperature of ( $20^{\circ} \text{ C}$ ) on the day of the experiment, the Reynolds number was found to be

$$1.05 \times 10^6 < \text{Re}_x = \frac{Ux}{\nu} < 1.40 \times 10^6 \quad (8)$$

From these results,  $5 \times 10^5 < 1.05 \times 10^6 < \text{Re}_x = \frac{Ux}{\nu} < 1.40 \times 10^6$ , and the boundary layer is turbulent. Therefore, the boundary layer thickness given by the Blasius solution is not applicable. Instead, one can use the momentum- integral equation to estimate the thickness of the boundary layer. That equation is given by

$$\frac{\tau_w}{\rho} = \frac{d}{dx} (U^2 \theta) + \delta^* U \frac{dU}{dx} \quad (9)$$

Where  $\tau_w$  is the shear stress at the wall,  $\theta$  is the momentum thickness, and  $\delta^*$  is the displacement thickness. These are defined as follows:

The displacement thickness:  $\delta^*$

$$\delta^* = \int_0^{\infty} \left(1 - \frac{u}{U}\right) dy = \int_0^{\delta} \left(1 - \frac{u}{U}\right) dy \quad (10)$$

The momentum thickness:  $\theta$

$$\theta = \int_0^{\infty} \frac{u}{U} \left(1 - \frac{u}{U}\right) dy = \int_0^{\delta} \frac{u}{U} \left(1 - \frac{u}{U}\right) dy \quad (11)$$

And the boundary-layer thickness is  $\delta$ .

Since the expression for the flow inside the boundary layer is not known, one uses the power-law formula for pipe flow but adjusted to boundary layer flows. It is

$$\frac{u}{U} = \left(\frac{y}{\delta}\right)^{1/n} = \eta^{1/n} \quad (12)$$

Where  $n$  is unknown. Using different values of  $n$  allows one to construct a Table such as the one shown below (Njock Libii, 2010).

$\frac{u}{U} = \eta^{1/n}$	$\frac{\theta}{\delta}$	$\frac{\delta^*}{\delta}$	$H = \frac{\delta^*}{\theta}$	$a \equiv \frac{\delta}{x} (\text{Re}_x)^{1/5}$	$b = C_f (\text{Re}_x)^{1/5}$
$\eta^{1/6}$	0.107143	0.142857	1.333333	0.337345906	0.057830727
$\eta^{1/7}$	0.097222	0.125	1.285714	0.381143751	0.059289028
$\eta^{1/8}$	0.088889	0.111111	1.250000	0.423532215	0.060235693
$\eta^{1/9}$	0.0818181	0.100000	1.222222	0.464755563	0.060840728
$\eta^{1/10}$	0.0757575	0.9090909	1.200000	0.504990077	0.061210918

Table 2. Turbulent boundary layer over a flat plate at zero incidence: results

For the case of  $n = 7$ , one has

$$\frac{u}{U} = \left(\frac{y}{\delta}\right)^{1/7} = \eta^{1/7} \quad (13)$$

The boundary layer thickness is then given by

$$\delta \cong \frac{0.382x}{(\text{Re}_x)^{1/5}}; \text{with } \text{Re}_x = \frac{Ux}{\nu} \quad (14)$$

In the case tested here, where  $U = 46 \text{ m/s}$ ,  $0.356 \text{ m} < x < 0.457 \text{ m}$ , and for which  $1.05 \times 10^6 < \text{Re}_x = \frac{Ux}{\nu} < 1.40 \times 10^6$ , the thickness of the boundary layer is found to be

$$8.5\text{mm} < \delta < 10.4\text{mm} \quad (15)$$

### 4.3.3 Experimental procedure

Using the data shown in Fig. 10, the boundary layer thickness can be estimated by extracting the  $y$  coordinate of the point where the velocity profile begins to turn toward (or, away from) the wall.

### 4.3.4 Experimental results

Using the data shown in Fig. 10, the boundary layer thickness was estimated by extracting the  $y$  coordinate of the point where the velocity profile begins to turn toward (or, away from) the wall. That value is  $y = 0.01087 \text{ m} = 10.87 \text{ mm}$ . This value is close to the upper bound obtained from theory, Eq.(14), by the power law formula with  $n=7$ . Using  $n=8$ , instead of  $n=7$ , however, the theoretical range of thicknesses becomes  $9.4\text{mm} < \delta < 11.53\text{mm}$ . A comparison Table is shown on Table 3.

n	Thickness from analysis	Thickness from experiment
7	$8.5\text{mm} < \delta < 10.4\text{mm}$	10.87 mm
8	$9.4\text{mm} < \delta < 11.53\text{mm}$	10.87 mm

Table 3. Tabulated comparisons of the thicknesses of turbulent boundary layers

## 4.4 The existence of turbulence in the flow stream

### 4.4.1 Purpose

The purpose of this experiment is to learn how to use experimental data collected in a wind tunnel to determine the fluctuations in the air pressure inside the test section.

### 4.4.2 Key equations

Flow in the test section is presumed to be steady. However, because of the rotation of the fan blades and the vibration in the housing that supports the wind tunnel, fluctuations are introduced in the air stream. Some of these are detectable using pressure measurements.

$$\text{Fluctuation} \equiv \left(\frac{P_{\max} - P_{\min}}{P_{\max}}\right) \times 100 \quad (15a)$$

#### 4.4.3 Experimental procedure

At each point where pressures were measured, each measured pressure fluctuated rapidly between minimum and maximum values. These could be displayed by the pressure sensors. Although it was not done for the data presented, it was also possible, if one wished, to measure the instantaneous fluctuations that occurred.

#### 4.4.4 Experimental results

Figure 11 displays the averaged fluctuations, that is the differences between the maximum and minimum values of pressures at each tested point during the experiment, Eq. (15a). The average fluctuation was around 3 %.

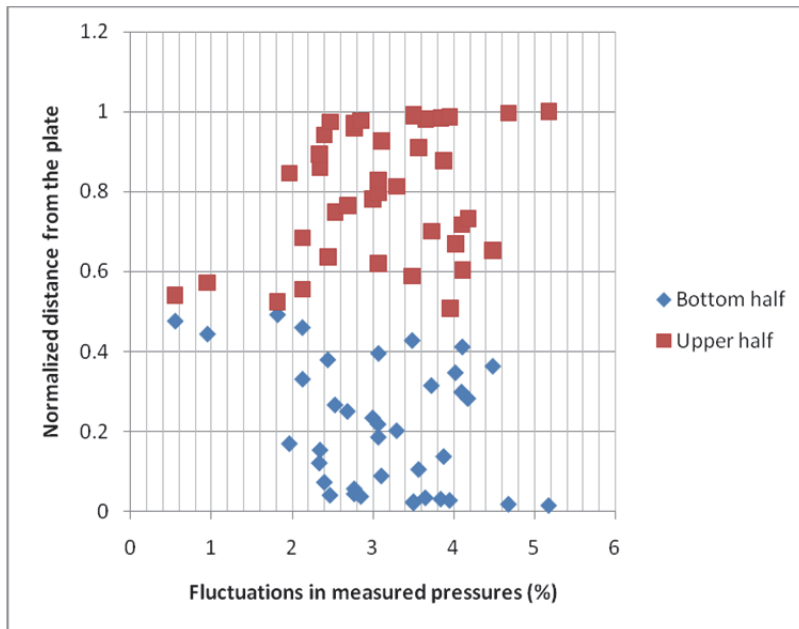


Fig. 11. Pressure fluctuations inside the test section at an air speed of 46 m/s.

### 4.5 Measuring pressure distributions around a circular cylinder in cross flow

#### 4.5.1 Purpose

The purpose of this laboratory exercise is to measure the pressure distribution on a right circular cylinder and compare the result to those predicted by inviscid-flow theory and to experimental results found in the literature.

#### 4.5.2 Key equations

For steady, frictionless, and incompressible flow from left to right over a stationary circular cylinder of radius "a" the velocity is given by

$$\vec{V} = v \left[ \left( 1 - \frac{a^2}{r^2} \right) \cos \theta \right] \vec{e}_r - v \left[ \left( 1 + \frac{a^2}{r^2} \right) \sin \theta \right] \vec{e}_\theta \quad (16)$$

Using Bernoulli's equation, the pressure distribution on the surface of the cylinder is found to be

$$\frac{P_c - P_\infty}{\rho} = \frac{v^2}{2} (1 - 4 \sin^2 \theta) \quad (17)$$

from which the pressure coefficient,  $C_p$ , can be deduced. Thus,

$$C_p = \frac{P_c - P_\infty}{\frac{1}{2} \rho v^2} = 1 - 4 \sin^2 \theta \quad (18)$$

Unfortunately, an expression of  $C_p$  vs.  $\theta$  similar to the one in equation (18) cannot be obtained analytically for the steady flow of an incompressible viscous fluid. However, one can obtain experimental data by measuring the pressure on the surface of the cylinder as a function of the position,  $\theta$ . Such data can be plotted and compared with the graph of equation (18). Generating such a plot is the purpose of this lab.

Such plots are available in the literature and in almost all textbooks of fluid mechanics.

#### 4.5.3 Experimental procedure

A wind tunnel is used so that students can collect their own data and generate these curves themselves. This can be done, say, by following the procedure shown below:

1. Install the cylinder inside the wind tunnel and connect it to the pressure tap.
2. Set the speed in the tunnel to the desired value
3. Measure the pressure on the surface of the cylinder for angles of rotation from  $0^\circ$  to  $360^\circ$ , in  $10^\circ$  increments. Perform the rotations in both the clockwise and counterclockwise directions. Record the measurements at each station.

#### 4.5.4 Experimental results

A wind tunnel has been used; students collected their own data and generated curves similar to those shown below by themselves. Sample results are shown in reference cited below. This conceptual approach was implemented in our laboratory and the collected data verified what is reported in the literature (Njock Libii, 2010).

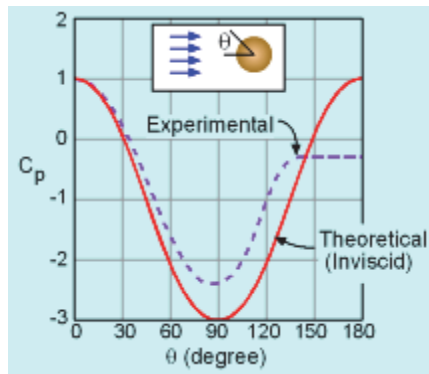


Fig. 12. Comparison of  $C_p$  for: inviscid and viscous flows (Pritchard, 2011).



## 4.6 Experimental determination of the viscous wake behind a circular cylinder

### 4.6.1 Purpose

The purpose of this laboratory exercise is to use the pressure probe to measure the pressure behind a right circular cylinder and use the results to estimate the width of the viscous wake behind the circular cylinder. Then, compare the results to those predicted by inviscid-flow theory.

### 4.6.2 Key equations

When flow is inviscid, there is no flow separation and, therefore, no viscous wake. The introduction of viscosity allows for flow separation to occur and for the generation of a viscous wake. By sensing the pressure across the wake, students can compare their measured values to those that are expected to occur outside the wake. This allows for the estimation of the width of the wake behind the cylinder.

### 4.6.3 Experimental procedure

1. Install the cylinder inside the wind tunnel and connect it to the pressure tap.
2. Set the speed in the tunnel to the desired value.
3. Choose a distance that is two diameters away and upstream from the leading edge of the cylinder.
4. Measure the pressure at that section. This pressure will be used as a reference pressure.
5. Identify and mark ten preselected sections behind the cylinder. Use the following distances:  $d$ ,  $2d$ ,  $3d$ ,  $4d$ ,  $5d$ ,  $6d$ ,  $7d$ ,  $8d$ ,  $9d$ , and  $10d$ , where  $d$  is the diameter of the cylinder and each distance is measured from the leading edge of the cylinder.
6. Measure the pressure behind the surface of the cylinder at each predetermined section.
7. At each distance, traverse the corresponding vertical cross section of the wake until the pressure registered becomes approximately equal to that which was measured in step 4. Note the points at which this occurred. Measure their vertical distances from the horizontal axis of symmetry of the cylinder.

### 4.6.4 Experimental results

Plot the points from your experiment that represent the boundary curve that separates the wake from the external flow. This curve estimates the width and length of the viscous wake behind the cylinder. Curves will resemble Fig. 13.

## 4.7 Experimental determination of lift and drag forces on an airfoil

### 4.7.1 Purpose

Students measure the lift and drag of several different airfoils using a force balance and a subsonic wind tunnel, and they compare the results to published data and theoretical expectations.

### 4.7.2 Key equations

The lift coefficient,  $C_L$ , is given by

$$C_L = \frac{F_L}{\frac{1}{2}\rho V^2 A} \quad (19)$$

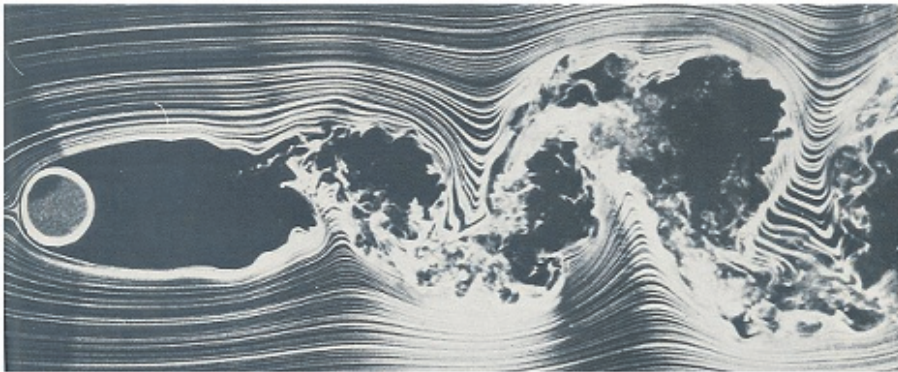
Where  $F_L$  is the lift force,  $V$  is the average speed, and  $A$  is the reference area. The drag coefficient,  $C_D$ , is given by

$$C_D = \frac{F_D}{\frac{1}{2}\rho V^2 A} \quad (20)$$

Where  $F_D$  is the drag force,  $V$  is the average speed, and  $A$  is the reference area.

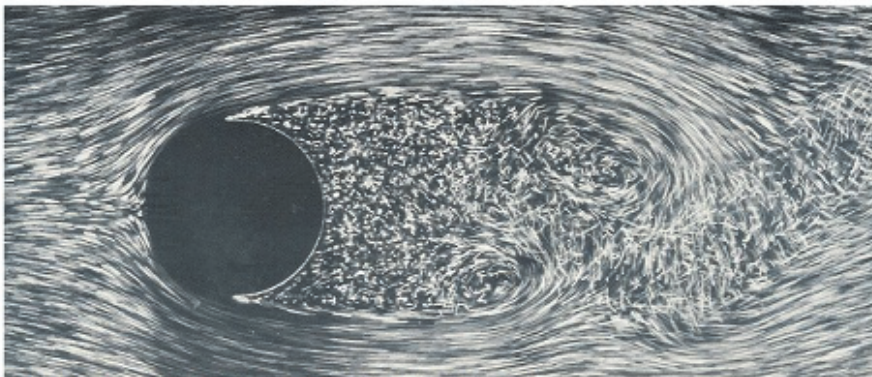
#### 4.7.3 Experimental procedure

With the appropriate equipment one can measure lift and drag on an airfoil in a wind tunnel. Many universities have these setups and corresponding experiments. A particularly nicely presented one is that for a course on Aerospace Engineering Laboratory at Rutgers University (Rutgers, 2011). In that experiment, students measure the lift and drag of several different airfoils using a force balance and subsonic wind tunnel, and they compare the results to published data and theoretical analysis.



(a) Visualizing turbulent cylinder wake at  $Re = 10000$

[Courtesy: Thomas Corke and Hassan Nagib; from *An Album of Fluid Motion* by van Dyke (1982)]



(b) a closer look at  $Re = 2000$  - patterns are identical as in (a)

[Courtesy: ONERA pic. Werle & Gallon (1972) from *An Album of Fluid Motion* by van Dyke (1982)]

Fig. 13. Experimentally-determined wakes behind a circular cylinder in viscous flow

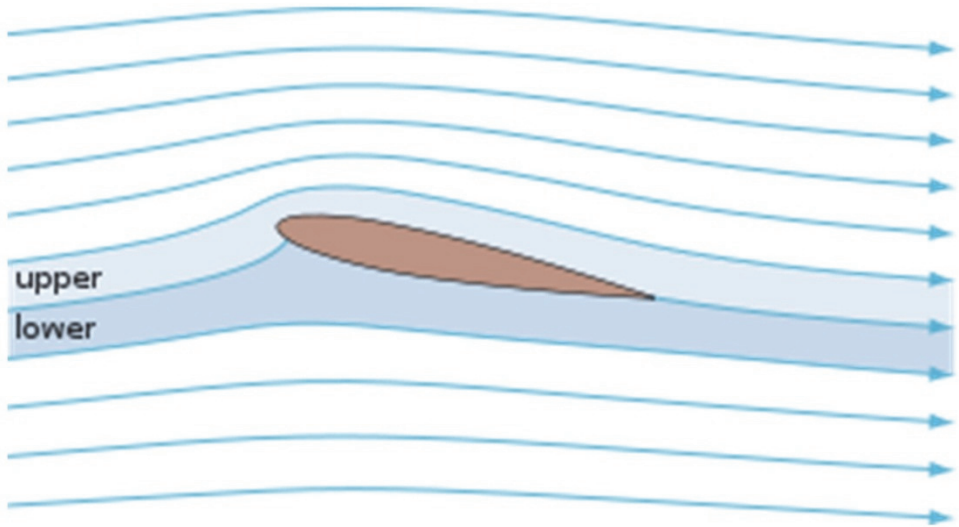


Fig. 14. Streamlines around a NACA 0012 airfoil at a moderate angle of attack.

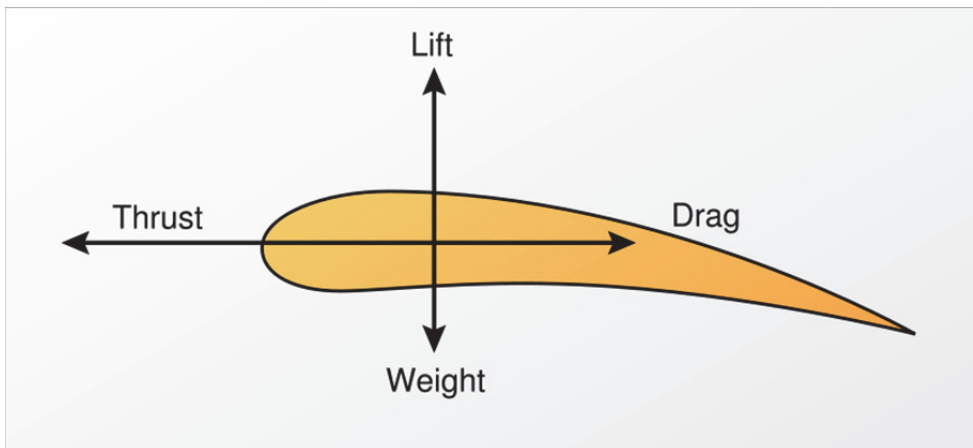


Fig. 15. Schematic representation of lift, drag, thrust, and weight on an airfoil.

#### 4.7.4 Experimental results

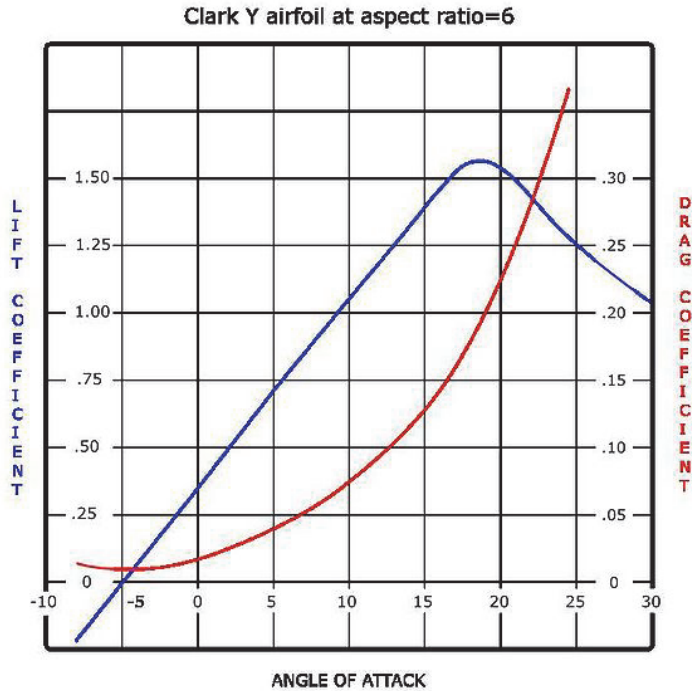


Fig. 16. Sample variation of lift and drag on an airfoil with the angle of attack.

### 4.8 Reduction of drag by inducing turbulence in the boundary layer

#### 4.8.1 Purpose

The purpose of this laboratory exercise is to measure and compare drag forces exerted on smooth and rough spheres of the same size and use collected data to verify the claim that roughness on the surface of a sphere reduces the drag force on it.

#### 4.8.2 Key equations

The drag coefficient is defined as the ratio obtained by dividing the drag force by the inertial force of the fluid stream, Eq.(20). From this equation, the drag force on a sphere of diameter  $d$  is

$$F_D = \frac{(\pi \rho v^2 d^2)}{8} C_D \quad (21)$$

From Eq.(21), if a rough sphere and a smooth sphere of equal diameters are in the same fluid, the differences in their drag forces would be borne by the drag coefficient,  $C_D$ .

If a sphere is suspended in the test section of the wind tunnel in such a way as to create a simple pendulum that makes an angle  $\theta$  with the vertical, and for which the sphere is the

bob, then, neglecting the lift force, the drag force is related to the deflection of the pendulum by

$$F_D = mg \tan \theta \quad (22)$$

Using Eq. (22), the drag force per unit weight becomes

$$\frac{F_D}{mg} = \tan \theta \quad (23)$$

If one uses a rough sphere and a smooth sphere of equal weights, then, the effect of the roughness on the drag force would be borne by the deflection angle.

#### 4.8.3 Experimental procedure

1. Create equal numbers of smooth and rough spheres
2. Make sure that for each smooth sphere, there is a rough sphere of the same size and weight
3. Place each sphere by itself in the fluid stream of the wind tunnel
4. Select a wind speed for the test
5. Measure the drag force on that sphere
6. Repeat this process for each sphere in the whole set
7. Select a set of wind speeds to be used for the test
8. Repeat steps 3 through 6 for each wind speed selected
9. Use collected data to compare the drag forces in each pair
10. Determine whether or not your data allow you to verify the claim that adding roughness to the surface of a sphere reduces the drag force on it.

#### 4.8.4 Experimental results

This conceptual approach was implemented in our laboratory and the collected data verified that roughness on the surface of a sphere reduces the drag force on it. A sample plot of results is shown in Figure 17. The procedures followed to create this experiment are detailed in a paper by the author (Njock Libii, 2006), while the complete set of data and discussion are presented in another paper (Njock Libii, 2007).

### 4.9 Demonstration of the Richardson's annular effect

#### 4.9.1 Purpose

The purpose of this exercise is to use data obtained from wind tunnel tests to demonstrate the overshoot that occurs near the wall in the velocity profile of a flow in a duct when the flow is subjected to oscillations in the axial pressure gradient.

#### 4.9.2 Key equations

Although Richardson's annular effect is ordinarily beyond the scope of the first course in fluid mechanics, it represents a very practical use of experimental data that are obtainable from the study of boundary-layer flows in a duct.

Consider unsteady flow in a duct that is very long and in which one assumes that fully developed flow has been achieved. Let the duct be a pipe of circular cross section. One

assumes that the flow is entirely in the axial direction, and its velocity is only a function of two variables, the radial position,  $r$ , and the time,  $t$ . If one further assumes that the pipe is horizontal with internal radius  $r_0$  and that the pressure gradient in the axial direction is  $-\rho K \cos(\omega t)$ , then, the solution of the thus-simplified Navier-Stokes equations for the velocity is given by the real part of

$$u = \frac{K}{i\omega} e^{i\omega t} \left[ 1 - \frac{J_0\left(r\sqrt{\frac{i\omega}{\nu}}\right)}{J_0\left(r_0\sqrt{\frac{i\omega}{\nu}}\right)} \right] \tag{24}$$

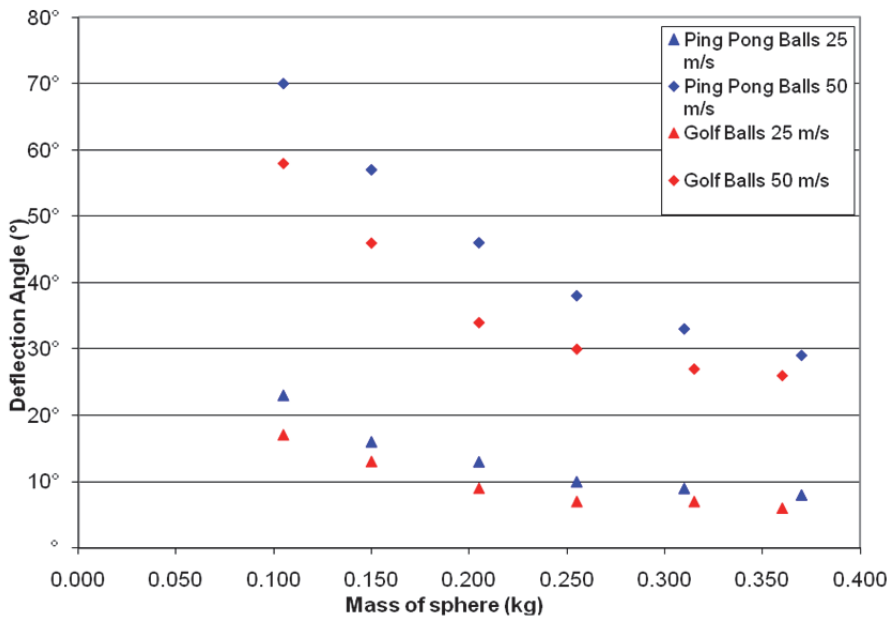


Fig. 17. Deflection angle of the pendulum in the test section vs. mass of the sphere.

Where  $J_0$  denotes the Bessel function of the first kind and zero order,  $K$  is a constant,  $\rho$  is the mass density of the fluid and  $\omega$  is the circular frequency of the oscillation. One introduces non-dimensional quantities such that

$$r^* \equiv \frac{r}{r_0}; \omega^* \equiv \frac{\omega r_0^2}{\nu}; u^* \equiv \frac{u}{u_{max}} \tag{25}$$

Where  $u_{max}$  is the maximum centerline velocity for a steady Poiseuille flow in the same pipe that has a constant pressure gradient equal to  $-\rho K$ . It is known that oscillating flows of this type may become turbulent when  $\omega^*$  exceeds 2000. For large values of  $\omega^*$  a region of large velocity is established near the wall of the pipe and the mean square velocity is given by

$$\frac{\overline{u^2}}{K^2 / 2\omega^2} = 1 - \frac{2}{\sqrt{r^*}} e^{-B} \cos(B) + \frac{e^{-2B}}{r^*} \quad (26)$$

where

$$B = (1 - r^*) \sqrt{\frac{\omega^*}{2}} \quad (27)$$

When this equation is plotted as  $B$  vs.  $\frac{\overline{u^2}}{K^2 / 2\omega^2}$ , one observes that the velocity displays an overshoot near the wall, indicating that the maximum velocity occurs near the wall and not at the center of the pipe, as is the case for Poiseuille flow in a circular pipe. Such a plot is shown in Figure 18.

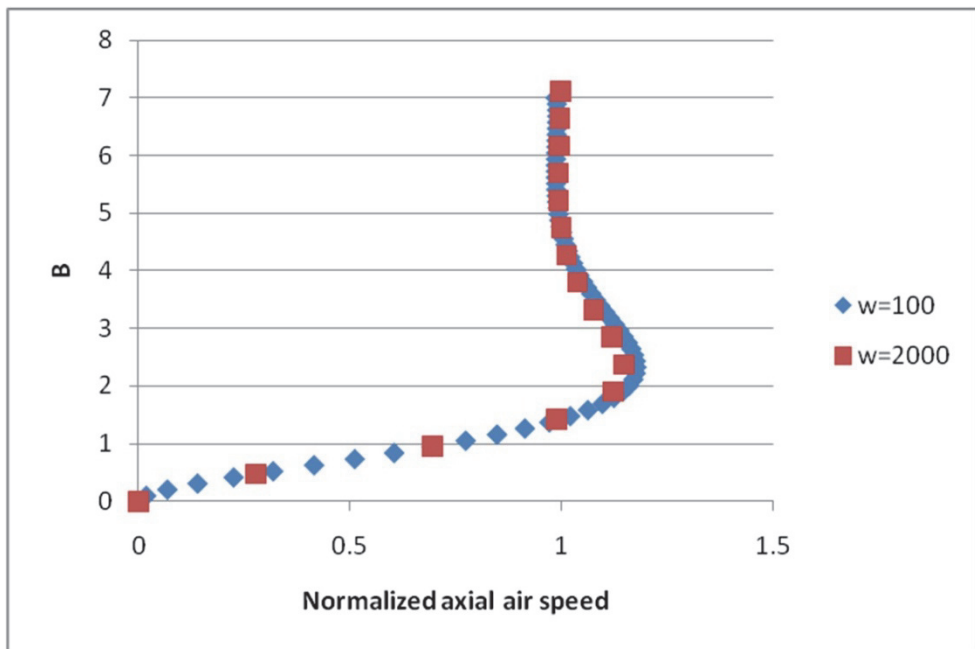


Fig. 18. Overshoot of velocity near the wall, known as Richardson's annular effect

A similar phenomenon was observed in the velocity profile of flow in the wind tunnel that was shown in Figure 10.

#### 4.9.3 Experimental procedure

One needs a close-up view of the plot of collected data near the maximum values achieved by the velocity. This can be achieved by zooming in on the velocity profile of the flow in the test section and by focusing of the velocity near the wall in Figure 10.

#### 4.9.4 Experimental results

The graph in Figure 10 has been enlarged near the maximum values achieved by the velocity. The result is shown in Figure 19. The overshoot of the velocity near the wall, which is Richardson's annular effect, becomes plain and evident in that Figure.

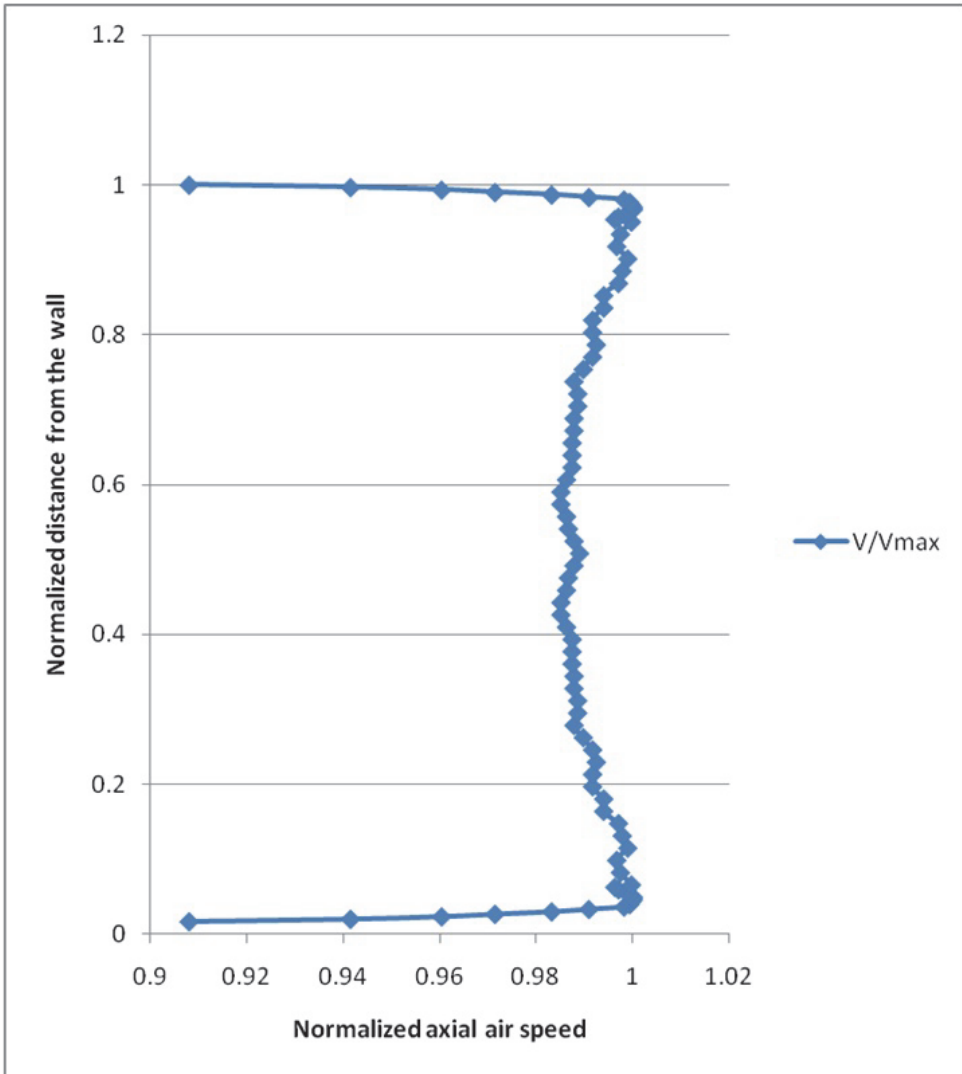


Fig. 19. Demonstration of Richardson's annular effect in the test section  $\alpha \equiv (\omega / 2\nu)^{1/2}$ .

A pulsating laminar flow of a viscous incompressible liquid in a rectangular duct of cross-sectional dimensions  $a$  and  $h$  was solved numerically (Yakhot et al., 1998,1999). Yakhot et al. performed calculations for low and high frequency regimes ( $1 \leq \alpha h \leq 20$ ) in a rectangular



duct with different aspect ratios ( $a/h = 1$  and  $10$ ). Their results clearly demonstrate the existence of Richardson's annular effect, Figure 20. The results in that Figure are very similar to those that were obtained from the wind tunnel and are shown in Figure 19.

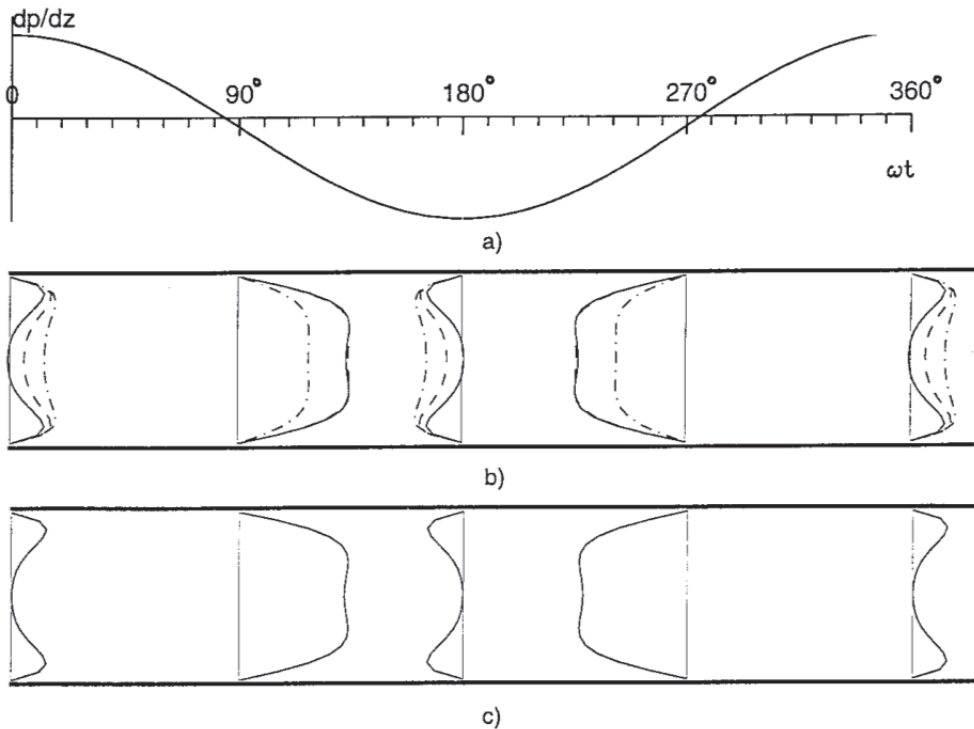


Fig. 20. Velocity profiles in pulsating flow at different instants of one period. (a) Pressure gradient variation with time. (b) Duct flow,  $\alpha h = 8$ : solid line,  $x/a = 0.5$ ; dashed,  $x/a = 0.25$ ; dot-dashed,  $x/a = 0.1$ . (c) Flow between two parallel plates (Yakhot et al., 1999).

## 5. References

- Ernst, E. (1983). *The Undergraduate Engineering Laboratory*, Proceedings of an Engineering Foundation Conference, Edward W. Ernst, Editor, ISBN: 0939204215, New England College, Henniker, New Hampshire, July 1983
- Feisel, L., Rosa, A. (2005) The role of the engineering laboratory, *Journal of Engineering Education*, Vol. (January 2005), pp. (121-130), ISBN 0-309-08291-9.
- Njock Libii, J. (2006) Design of an experiment to test the effect of dimples on the magnitude of the drag force on a golf ball. *World Transactions on Engineering and Technology Education (WTE&TE)*, Vol.5, No. 3, (December 2006), pp. (477-480), ISSN 1446-2257
- Njock Libii, J. (2007) Dimples and drag: Experimental demonstration of the aerodynamics of golf balls. *American Journal of Physics*, Vol. 75, No. 8, (August 2007), pp. (764 -767), ISSN 0002-9505.

- Njock Libii, J. (2010) Laboratory exercises to study viscous boundary layers in the test section of an open-circuit wind tunnel, *World Transactions on Engineering and Technology Education(WTE&TE)*, Vol. 8, No. 1, (March 2010), pp. (91-97), ISSN 1446-2257.
- Njock Libii, J. (2010) Using wind tunnel tests to study pressure distributions around a bluff body: the case of a circular cylinder, *World Transactions on Engineering and Technology Education(WTE&TE)*, Vol. 8, No. 3, (December 2010), pp.( 361-367), ISSN 1446-2257
- Njock Libii, J. & Russell R. Tobias, R. (2006). Lifting Bodies, In: *USA in Space (Third Edition)*, Russell R. Tobias and David G. Fisher, pp. (744-748), Salem Press, ISBN: 1-58765-259-5, Pasadena, California
- Pritchard, P. (2011). *Fox and McDonald's Introduction to Fluid Mechanics* (Eighth edition ), John Wiley & Sons, ISBN-13 9780470547557, ISBN-10 0470547553, New York, NY.
- Rutgers, <http://coewww.rutgers.edu/classes/mae/mae433/lab3.pdf>, n.d.
- Sonntag, R., Borgnakke, C., & Van Wylen, G. (1998). *Fundamentals of Thermodynamics* (Fifth Edition), John Wiley & Sons, Inc., ISBN 0-471-18361-X, New York, 1998.
- Yakhot, A., M. Arad, M., & Ben-Dor, G. (1998). Richardson's Annular Effect in Oscillating Laminar Duct Flows. *Journal of Fluids Engineering*, Vol. 120, 1, (March 1998) pp. (209-301), ISSN 0098-2202
- Yakhot, A., M. Arad, M., & Ben-Dor, G. (1999). Numerical investigation of a laminar pulsating flow in a rectangular duct. *International Journal For Numerical Methods In Fluids*, Vol. 29, (1999) , pp. (935-950), ISSN 0271-2091

# The Importance of Turbulence in Assessment of Wind Tunnel Flow Quality

Mojtaba Dehghan Manshadi

*Department of Mechanical Engineering, Isfahan University of Technology,  
Iran*

## 1. Introduction

The objective of obtaining a spatially standardized steady stream of air across and along the test section of a wind tunnel has been considered by several researchers. When a wind tunnel is manufactured or montage or move to another position, the study about variation of pressure, Mach number, density and temperature distribution, the variation of pitch and yaw components of flow angularity, boundary layer treatment near the walls, noise and acoustics and the behaviors of vortexes in the entire parts of it must be identify. Flow Field Survey by rake or hot-wire in different stations, pressure and velocity contours, boundary layer total pressure survey are another activities that must applied for flow quality. White explains that the most important measure of performance in a wind tunnel is its turbulence; the level of unsteady velocity fluctuations about the flow's average velocity [1]. Designer of wind tunnels strive to grade up the flow quality of wind tunnels by using the best design rules and some manipulators to improve the role of wind tunnel in industrial designs. One area that has of high importance is the reduction of the turbulence intensity across the test section that more discussion about it will be considered in this study.

## 2. The definition of turbulence

Today, one of most complicated area under discussion in physics, mathematics, fluid mechanics, and also different industries i.e. aerospace engineering, wind turbines, buildings, combustion, biology, climate behaviors, oceanography is turbulence. Turbulence is highly versatile motion that it is impossible to predict it in any way. There are various definitions for turbulence that they are similar concepts. Turbulence has been defined by Bradshaw as:

"A three-dimensional time-dependent motion in which vortex stretching causes velocity fluctuations to spread to all wavelengths between a minimum determined by viscous forces and a maximum determined by the boundary conditions of the flow. It is the usual state of fluid motion except at low Reynolds numbers." [2].

Jean Leary presents the following state for turbulence[3]:

"Turbulence is due to the formation of point or line vortices on which some component of the velocity becomes infinite" and Hintz define according to the below sentences: "Turbulent Fluid motion is an irregular condition of flow in which the various quantities show a random variation with time and space coordinates, so that statistically distinct

average values can be observed [3]". At the result, from abovementioned definitions for turbulence, one may conclude that Turbulence has its origins in the inherent instabilities of laminar flow. Turbulence dies out because of viscous damping unless some mechanism carries on pumping energy into the velocity fluctuations. The most important mechanism for generating and maintaining turbulence is shear in the mean flow. Another important mechanism consists of different forms of stirring. In geophysical flows and in combustion, turbulence can be generated by buoyancy forces associated with variations in the mass density of the fluid [4]. In other word, shear stress, secondary flows, vortex shedding, noise and unwanted fluctuations are the most sources for turbulence. Turbulent flow is chaotic and the flow velocity is very insightful to perturbations and fluctuates wildly in time and in space, and also contains swirling flow structures (eddies) with characteristic length, velocity and time scales which are spread over very wide ranges [4].

### 3. Undesirable effects of turbulence in experimental measurements

The unwanted effects of turbulence on the results of wind tunnel are studied by author in [3]. These studies show that if the turbulence intensity in the test section is large enough, they may trigger unfavorable transition and the measurements i.e. drag, lift and velocity profiles may be incorrect. In the other word, the flow shift from laminar to turbulent flow on the model surface significantly upstream of its actual location in an environment where the free stream turbulence level is more than real value. Further, it has long been documented that free stream turbulence can alter the effective Reynolds number in turbulent flow somewhere, the almost of significant parameters are the function of Reynolds number. Small variations of the free stream turbulence can change the behavior of boundary layer, skin friction and shape factor. However, the influence of free stream turbulence scale has not been determined completely. Wind tunnels with identical levels of turbulence can produce different test results due to differences in their turbulence spectra [5]. An acceptable value for turbulence level of wind tunnel is a provision and preliminary condition for dynamic similarity between the flow around the aircraft in flight and the flow around the model in the wind tunnel. Turbulence also can excite the local Mach number, pressure, density and other coupled parameters in the test section. The flow angularity distorted in high turbulence level. Briefly, the turbulence can produce menace errors in measurements. For example, Eiffel in 1911 and Fopple in 1912 reported the drag coefficient of similar sphere equal to 0.18 and 0.44 respectively, in different subsonic wind tunnel. Wieelsberger by using screens show that this dissimilarity in the drag coefficient of the sphere is due to different turbulence level of wind tunnels. As the result, the turbulence can lead to more errors in aerodynamic measurements in wind tunnels.

Some possible sources of errors or discrepancy in empirical data, related to the effects of free-stream turbulence on the flow about bluff bodies, have been examined by Bell [6]. Figure 1 shows, first of all, a so-called "standard" drag curve which illustrates the major features of the drag sustained by a circular cylinder in a very-low-turbulence flow. The drag coefficient lies approximately in the range 1.0-1.2 until the critical region is reached at a Reynolds number of about  $2 \times 10^5$ . Here, natural instabilities cause the previously-laminar flow in the boundary layer to become turbulent through a linear disturbance amplification process known as the Tollmien-Schlichting (T-S) instability

mechanism. The higher kinetic energy associated with the turbulent boundary layer permits greater penetration into the adverse pressure gradient on the rear half of the cylinder so that, compared to the laminar case, separation is delayed, the wake width is substantially reduced and base pressure recovery is improved. The net result is drastic relatively low intensity turbulence in the free-stream can trigger the T-S instability waves, leading to an early onset of the critical regime. The Bruun and Davies (1975) data in Fig. 1, for a turbulence intensity of 3.8%, illustrate this well-known and expected phenomenon. Bell believe that The influence of turbulence, and the parameters of importance, vary with the phenomenon considered. Properties averaged over the entire turbulent spectrum appear not to be wholly satisfactory for correlating the various effects; most often it seems that the intensity over a particular bandwidth is of primary importance. Free-stream turbulence increases entrainment into the shear layers at the surface of a body, or in its wake, affecting the energy distribution and altering the locations of transition, separation and reattachment. There is an enhanced diffusion of organized vorticity, presumably affecting eddy-shedding phenomena and base pressures. Distortion of the vorticity field, with resultant changes in intensity, occur in the flow about an object. All of these factors influence the fluid-dynamic forces on a bluff body in a way which has not yet been fully or satisfactorily explained. This study shows that more information is required for an improved understanding of the forces on a body immersed in a turbulent flow [6].

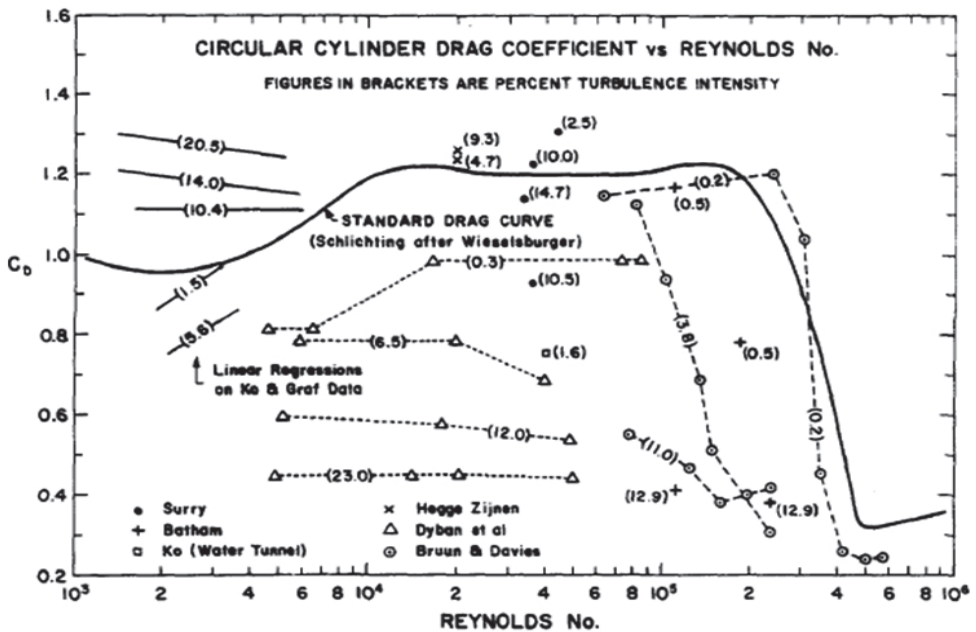


Fig. 1. Circular Cylinder drag coefficient vs Reynolds number as obtained by several investigations at various values of turbulence intensity [6]

#### 4. Measurements of turbulence

A chief research tool for the majority of turbulent air/gas flow studies is Hot-Wire Anemometry (HWA) that is used to measure the flow parameters such as turbulent intensity, mean velocity and root mean squares. There are two categories for hot wire anemometry, i.e., single and X-probes. Single wire probes, where the wire is oriented normal to the mean flow direction, are used to measure the velocity component in the mean flow direction. Where, crossed wire probes or X-probes, consisting of two wires arranged in an X-configuration, are used to measure both stream-wise and cross-flow velocity components simultaneously. A normal wire is usually calibrated by recording its output voltage as a function of the velocity. The sensitivity is then given by the slope of the velocity-voltage relationship and curve-fitting is commonly used to reduce the error in differentiating the discrete data. Polynomials as well as curves based on the King's law have been used by various researchers [7-10].

In a 2-D crossed wire probe the sensitivity may be found by a method similar to that used in calibrating a normal wire. To determine the sensitivity to the cross-flow velocity, 'static' or 'dynamic' methods may be used [10]. In a static calibration scheme, two ways are possible: the  $V_c$ -analysis method [8] and the  $(\tilde{V}, \theta)$  direct analysis [8, 9]. Manshadi et-al introduce a new genetic algorithm based method for direct calibration of 2-D hot-wire probe [10]. This new method is an alternative for the previous QR method that is commonly used for calibration of the X-probe hot wires. Proposed genetic algorithm method in [10] resulted in a much smaller error in velocity estimation while preserving the number of sentences in its calibration equation format. In addition, it preserves the magnitude of its error even when the number of sentences in the calibration equation is decreased while the error in the QR method increases substantially for the same situation [10]. Figure 2 show that the calculated velocities from the GA method are closer to the reference velocities while preserving the number of terms of the calibration equation.

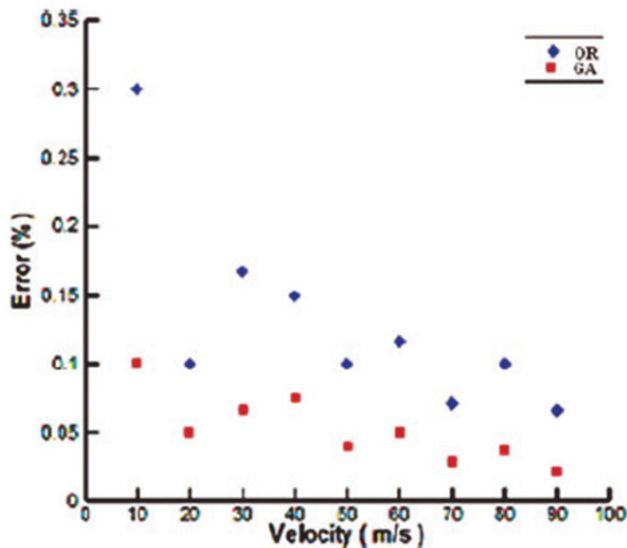


Fig. 2. Comparison of the error generated by the QR and the GA method [10].

In Fig.3 and Fig.4, the longitudinal and lateral components of the turbulent intensity,  $T_u$  and  $T_v$ , on the center line of the test section are shown against the velocity for the two aforementioned methods. The results show that considerable differences exist between the two calibration schemes. Note that the values of the longitudinal turbulence intensity for the center of the test section of the present wind tunnel are reported by the manufacturing company and it varies between 0.33 and 0.37 for the free stream velocities of  $V_\infty$  equal to 30 and 90 m/s, respectively. These two data points are shown in Fig. 3 and as seen the predicted GA method values are much closer to those reported by the company than those obtained by the QR method [10]. The reader can study the detail of above methods in [10].

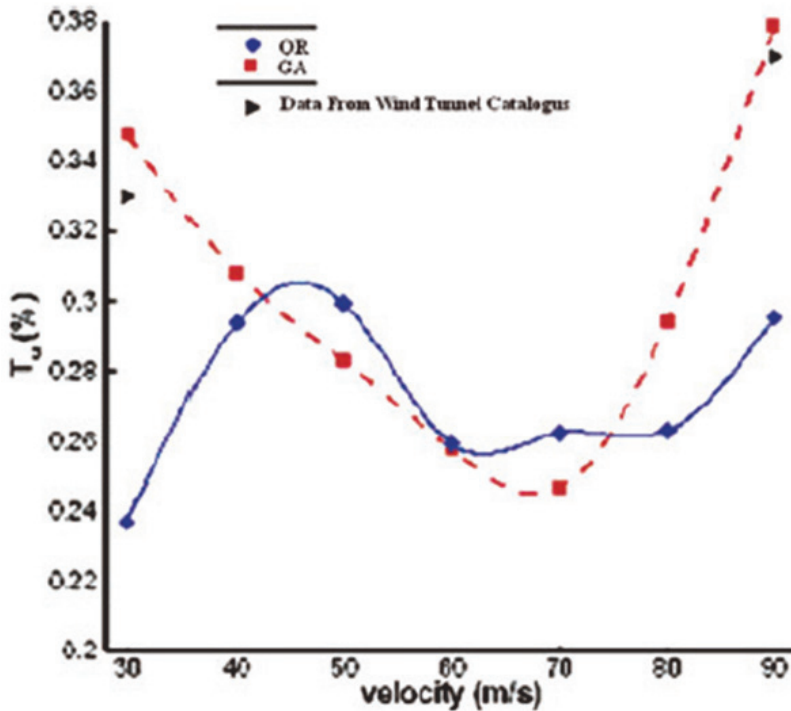


Fig. 3. Variation of  $T_u$  obtained from the two calibrations method [10]

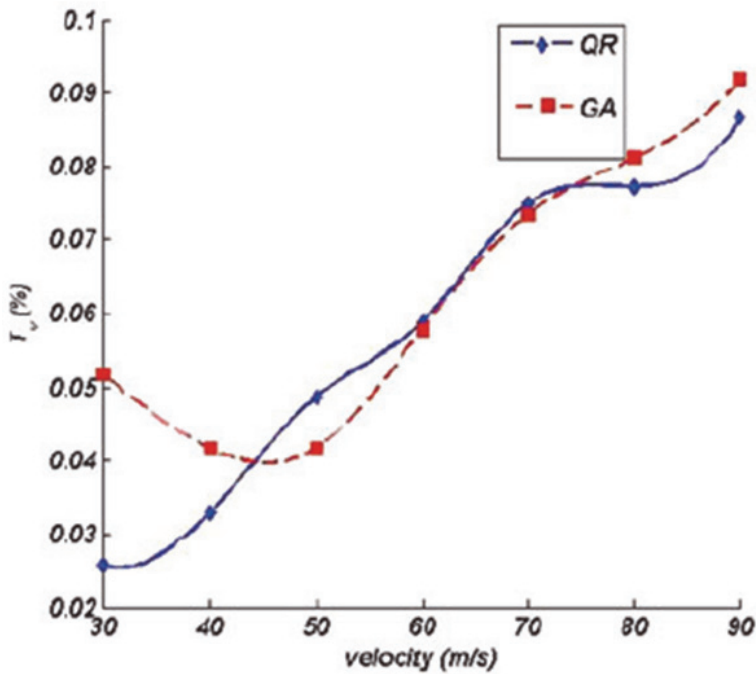


Fig. 4. Variation of  $T_v$  obtained from the two calibrations method [10]

One can find the detail of more principal of turbulence measurement by hot-wire in ref [8]. LDA, PIV and Turbulent Sphere are other devices for turbulence measurements. The measurement of turbulent sphere only can describe the feature of turbulence in wind tunnel. Further, LDA and PIV have the frequency response less than hot wire. Hot wire can responded up to 100 KHz.

## 5. The important parameters for turbulence measurement

All raw values of hot-wires were converted to the corresponding flow velocities using a suitable transfer function e.g., forth order polynomial. In X-probe hot wires, multi-sensor probes are decomposed into velocity components in the probe coordinate system. Then the effective velocities will determined and translate to the wire-coordinate system. As a result, the velocities component in the probe coordinate system, U and V will determine [7].

Subsequently, one may obtain the time averaged velocity,  $U_{mean}$  and  $V_{mean}$ , of the flow at a particular point by taking the average of the instantaneous velocity U and V. By taking the difference of the time averaged velocity and the instantaneous velocity, the instantaneous fluctuating velocity u and v is obtained. Furthermore, the root mean square (rms) velocity at a given location has been determined as below:

$$u_{rms} = \sqrt{\frac{\sum_{i=1}^n (u_i - \bar{u})^2}{(n-1)}}$$



$$v_{rms} = \sqrt{\frac{\sum_{i=1}^n (v_i - \bar{v})^2}{(n-1)}}$$

where n is the sample size.

Finally, the relative turbulence intensity, indicating the fraction of the total energy of the flow which resides in the turbulent regime, can be estimated. The value of relative turbulence intensity ( $T_u$  and  $T_v$ ) and the total turbulence intensity (TI) has been obtained as bellows:

$$T_u = \frac{u_{rms}}{\bar{u}} \times 100$$

$$T_v = \frac{v_{rms}}{\bar{v}} \times 100$$

$$TI = 100 \times \frac{((u_{rms}^2 + v_{rms}^2) / 2)^{1/2}}{(U_{mean}^2 + V_{mean}^2)^{1/2}}$$

Two simultaneous velocity time series provide cross-moments basis for Reynolds shear stresses and higher order cross moments i.e., lateral transport quantities. These moments has been defined by:

$$\overline{u'v'} = \frac{1}{N} \sum_1^N (U_i - \bar{U})(V_i - \bar{V})$$

$$\overline{u^2v} = \frac{1}{N} \sum_1^N (U_i - \bar{U})^2 (V_i - \bar{V})$$

$$\overline{v^2u} = \frac{1}{N} \sum_1^N (V_i - \bar{V})^2 (U_i - \bar{U})$$

Other parameters that are used for statistical analysis are skewness and flatness. The Skewness is a measure of the lack of statistical symmetry in the flow, while the Kurtosis is a measure of the amplitude distribution (flatness factor). These parameters are defined according to:

$$S_u = 1/N \sum_1^N \frac{(U(n) - \bar{U})^3}{\sigma_u^3}$$

$$S_v = 1/N \sum_1^N \frac{(V(n) - \bar{V})^3}{\sigma_v^3}$$

$$Ku = 1/N \sum_1^N \frac{(U(n) - \bar{U})^4}{\sigma_u^4}$$

$$Kv = 1 / N \sum_1^N \frac{(V(n) - \bar{V})^4}{\sigma_v^4}$$

## 6. The source of turbulence in wind tunnels

The source of turbulence of wind tunnel may briefly divide in two parts; i.e., turbulence due to eddies (vortex shedding, boundary layer, shear stress, secondary flows) and noise (mechanical, vibration and aerodynamic) that There is a correlation between them. Manshadi et-al in [11] studied the effects of turbulence on the sound generation and velocity fluctuations due to pressure waves in a large subsonic wind tunnel. The results of this research determine that while the share due to the monopole is dominant, the share due to the dipole and quadrupole remains less important. Furthermore, it is found that sound waves have a modest impact on the measured longitudinal turbulence and is essentially generated by eddies [11].

On the assumptions that first these sound waves are of plane type and contribute only to the u component and second that the turbulence and sound are statistically independent, Uberoi [12] has shown that the spatial correlation coefficient at two different points 1 and 2 for large separation of the points is defined by:

$$\rho_{12} = \langle u_1 u_2 \rangle / [\langle u_1^2 \rangle \langle u_2^2 \rangle]^{1/2} \cong \frac{u_p'^2}{u_p'^2 + u_e'^2}$$

where  $u_p'$  and  $u_e'$  represent the velocity due to the sound and eddy turbulence, respectively, and  $\langle \rangle$  denote a time mean value. Since the measured u component is made up  $u_p'$  and  $u_e'$ , one may conclude:

$$u'^2 = u_p'^2 + u_e'^2$$

A comparison of above equations reveals that:

$$u_e' = (1 - \rho_{12})^{1/2} u'$$

The above equation states that one may determine the velocities due to the sound and eddy turbulence by calculating the correlation coefficient.

In a wind tunnel, pressure waves may be generated aerodynamically along the tunnel circuit which may be considered as plane sound waves. These pressure waves may enter the test section either from the downstream direction or through the nozzle and thus altering the test condition. Consequently, the lowest velocity fluctuation level in the wind tunnel is determined by the abovementioned pressure fluctuations [11]. i.e.:

$$\tilde{u}_p = \frac{\tilde{p}}{\rho a_0}$$

manshadi et-al in [11] investigated the effect of monopole, dipole, and quadrupole for different turbulence intensity, Fig.5. The turbulence intensity was decreased after trip installation at diffuser and contraction rather than clean condition. The less turbulence

intensity was obtained for trip in the diffuser. Figure 5 show that the shares for the clean condition for monopole, dipole and quadrupole are equal to 56%, 26% and 18% and for  $X/L=0.115$  condition are 64%, 21% and 15% correspondingly. In addition, the shares for the case when the trip is installed in the diffuser are equal to 79%, 13% and 8% respectively. A comparison between the results of the clean condition to those for the diffuser and  $X/L=0.115$  condition indicate that while the shares due to the dipole and quadrupole decreases, the share due to the monopole increases considerably. Recalling that the aerodynamic sources of sound for the dipole and quadrupole are generated in the boundary layer, one may state that trip strip control to some extent the unsteady behavior of the fluctuating gradients. In the next, the effect of trip installation on the turbulence reduction in the subsonic wind tunnel will be discussed.

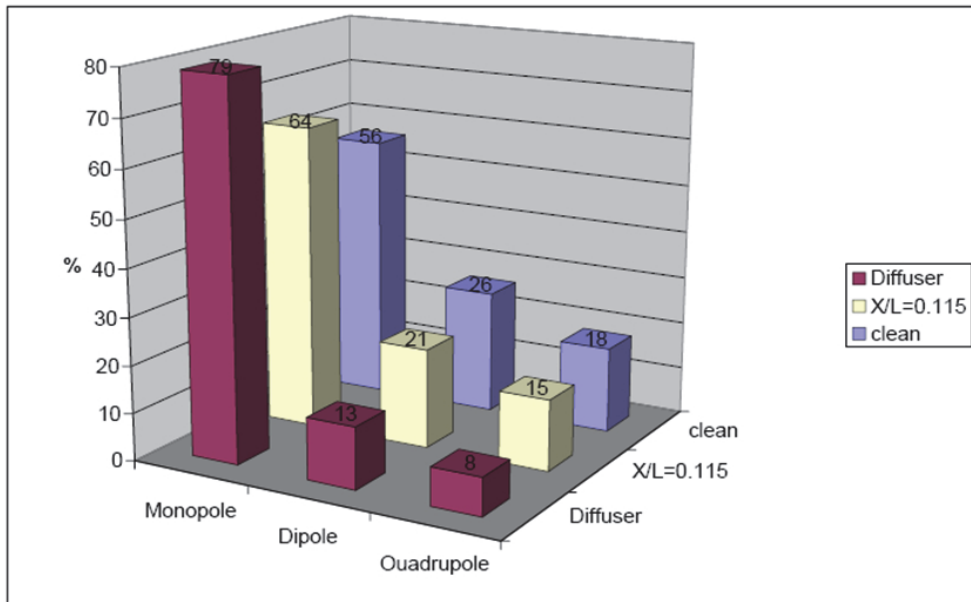


Fig. 5. Distinguished parts of each aerodynamic sound source for different conditions [11].

As abovementioned, there is a correlation between turbulence and sound. The spatial correlation for velocities equal to 60 and 70 m/s was measured at  $X/L=0.79$  for clean and trip conditions at a subsonic wind tunnel. The results are summarized in table 1. It is evident that while the value of the correlation coefficient for the clean condition at velocities 60 and 70 m/s is 0.22 and 0.24, respectively, it is decreased to 0.16 and 0.168 for the trip condition.

Further, the table provides a comparison of  $u_p'$  as well as  $\frac{u_e'}{u}$  values using sound level meter and spatial correlation measurement. It is evident that for the clean condition at the velocities of 60 and 70 m/s, sound waves have a modest impact on the measured longitudinal turbulence and over 80% of the turbulence is generated by the eddies. Furthermore, for strips at  $X/L=0.79$  and at aforementioned velocities, the share on the

measured longitudinal turbulence due to eddies is amplified. Consequently, one may conclude that trip strip reduces the turbulence in the test section [11].

Condition	Velocity (m/s)	Correlation coefficient	$u_p'$ (SLM)	$u_p'$ (Correlation)	Error (%) ( $u_p'$ )	$u_e'/u_i'$ (SLM)	$u_e'/u_i'$ (Correlation)
Clean	60	0.22	0.057	0.066	12.3	0.81	0.9
	70	0.24	0.072	0.081	12.25	0.89	0.95
X/L=0.79	60	0.16	0.035	0.030	15.7	0.88	0.98
	70	0.168	0.058	0.042	27.4	0.83	0.97

Table 1. Results for spatial correlation approach [11].

## 7. The methods of turbulence reduction

Aforementioned before, turbulence can have dramatic effects on the flow measurement in the wind tunnels, therefore, designers and researchers try to reduce it. Various methods such as employment of honeycombs [13,14], anti turbulence screens [15-17], and appropriate contraction ratio [18] are possible means to reduce the turbulence level in wind tunnels. In an attempt to improve the test section flow quality, sudden expansion downstream of the corner turning vanes was incorporated into the wind tunnel [19]. Further, Significant flow quality improvements were also achieved by vertical flow treatment in the diffuser and downstream of the fan. Wigeland et al used a 45 degree honeycomb flow manipulator, mounted parallel to the corner turning vanes, to improve the flow quality in the wind tunnel with little or no settling chamber length [20]. Flow quality in wind tunnels is improved through subsequent installation of acoustic baffles and dense honeycomb [19]. If one decides to remove the unwanted turbulence, he must smooth the walls, ignore sudden changes in geometry and manage the vortex stretching and separation in the entire loop of wind tunnel.

## 8. Turbulence reduction by using anti-turbulence screens and honeycomb

Significant devices for turbulence reduction in wind tunnels are screens. Screens are employed to even the velocity variation of flow out of the settling section. They can remove fine vortex structures and honeycombs can remove large vortex structures. They also break large vortices into smaller eddies that decay rapidly at short distances. The author in his PhD thesis shows that by utility of screens could reduce the turbulence to acceptable value [21]. Figure 6 shows variations of the turbulence intensity for one and four screens. This result exhibits that by the addition of three anti-turbulence screens located in a suitable place in the settling chamber, the tunnel turbulence was reduced for all operating speeds. Of course, the behavior of the two curves is similar and both of them exhibit humps around tunnel speeds of 20, 50 and 80 m/s. The error bar for uncertainty analysis is added for minimum and maximum velocities in Figure 6. The details of screens and their ability for turbulence reduction are reported in [15-17, 21].

Honeycomb and screens for a wind tunnel is very much dependent on the test type to which the tunnel is intended. Honeycomb may be considered as an effective mean for reducing swirl, turbulent length scales, and mean flow gradients. Further, it reduces the lateral turbulence components which are inhibited by the cells. Nevertheless, honeycombs also shed turbulence, the strength of which is proportional to the shear layer thickness in the cells. Therefore, honeycomb is supposed to break the large eddies into small ones, thus a deep honeycomb performs better than a shallow one but the pressure loss across it is larger [7]. Furthermore, the choice of appropriate screens is also difficult. Theoretically, the screens which are used for turbulence reduction should have porosity greater than 0.57 [14, 22]. Screens with smaller porosity suffer from a flow instability that appears in the test section. Whether screens or honeycombs, the obtained reduction in the free stream turbulence level is accompanied with a power loss due to manipulator pressure drop and hence reducing the maximum attainable velocity in the test section of the wind tunnel [7].

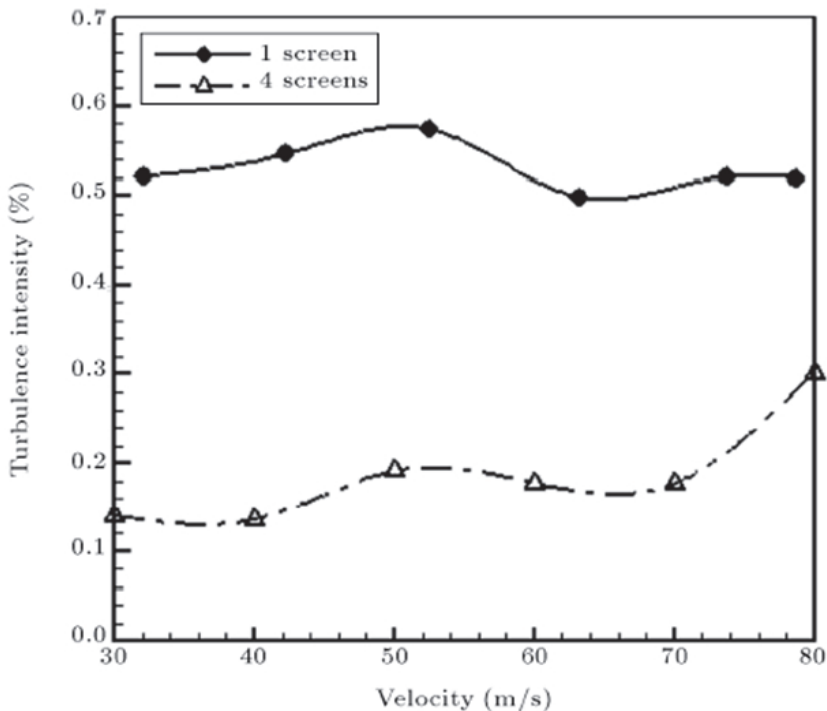


Fig. 6. Variations of turbulence intensity Vs. velocity with one screen and four screens [21]

The normal probability of outputs of hot wire at two different case, 1 and 4 screens, are shown in Figs. 7,8. The normal probability plots indicate that for cases with screens the hot wire data may be modeled by normal distribution. However, in cases where high turbulence intensity is present, 1 screen, the data moves away from normal distribution. Consequently, in cases where the turbulence intensity has been brought back towards low levels through any means, i.e. Figure 8, one may model the data again by normal distribution [21].

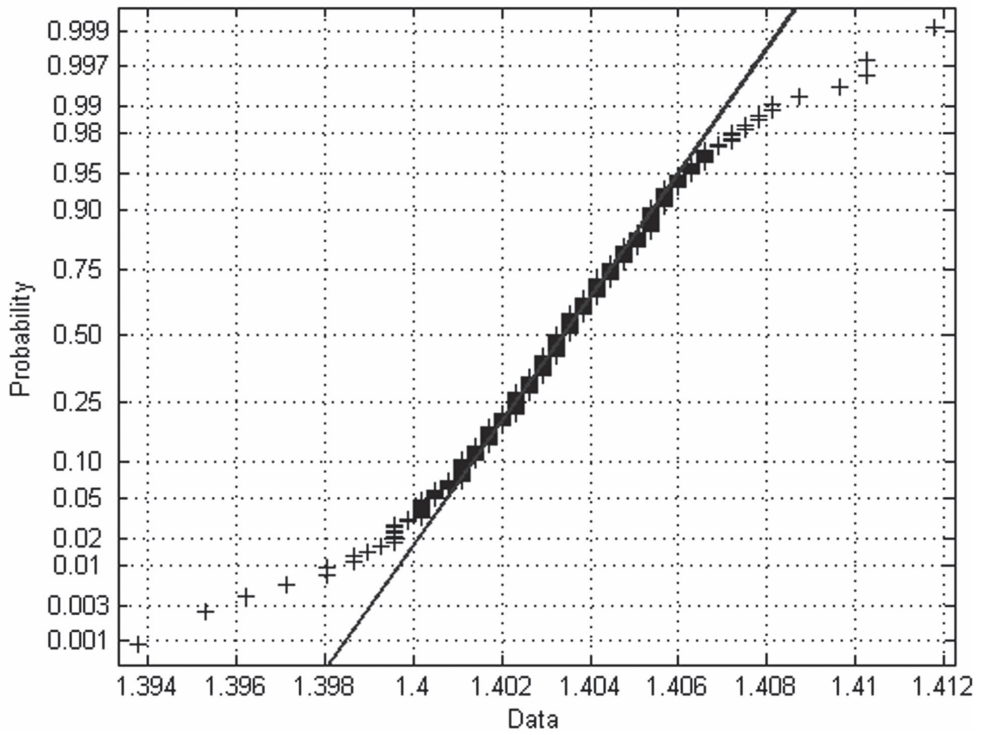


Fig. 7. Normal probability plot for one screen,  $V_1 = 80$  m/s [21].

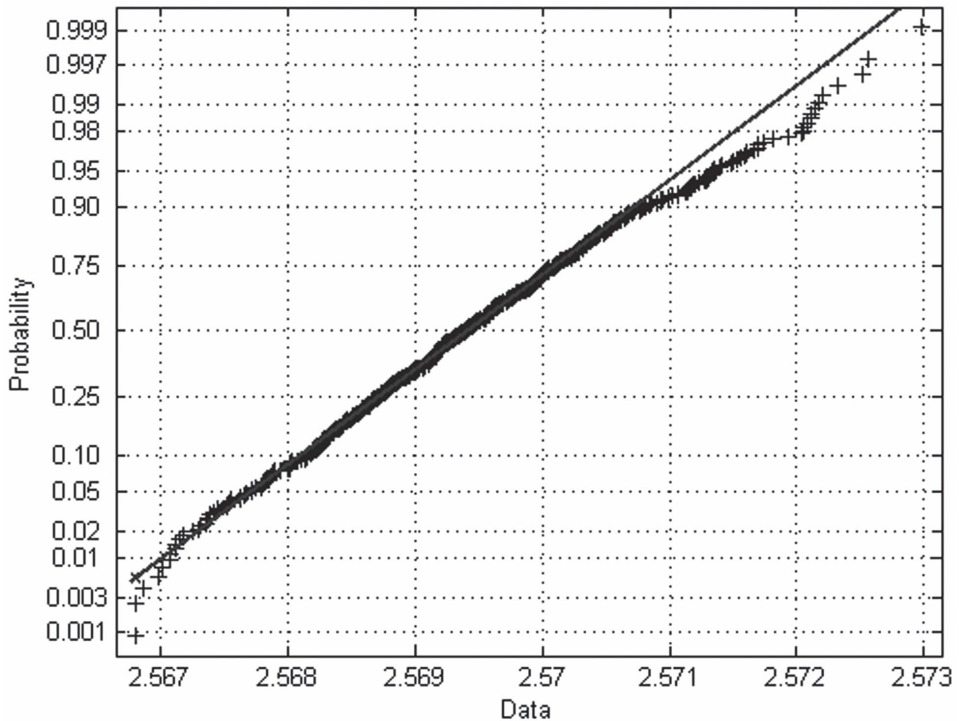


Fig. 8. Normal probability plot for four screens,  $V_1 = 80$  m/s [21].

## 9. Turbulence reduction by using trip strip in contraction

The contraction of the wind tunnel accelerates and aligns the flow into the test section. The size and shape of the contraction dictates the final turbulence intensity levels in the test section and hence the flow quality. Further, the length of the contraction should be kept as long as possible to minimize the boundary layer growth and reduce the effect of Gortler vortices. The flow leaving the contraction should be uniform and steady. For a finite-length inlet contraction, there exist a maximum and a minimum value for the wall static pressure distribution along the wall close to the entrance and exit, respectively. Thus, one may consider these two regions as regions of adverse pressure gradients with possible flow separation. If separation occurs, then the flow uniformity and steadiness will be degraded which may lead to an increase in turbulence intensity in the test section. In summary, contractions in the wind tunnels may produce several different unsteady secondary flows which are undesirable and can have dramatic effects on the behavior of the downstream boundary layers and turbulence intensity in test section [7, 23].

The boundary layer flow over a surface with a region of concave curvature is susceptible to centrifugal instabilities in the form of Gortler vortices [23]. Researches [24] showed that the laminar boundary layer was distorted by an array of large-scale longitudinal vortices spawned by the Gortler instability in the inlet of the contraction that can cause adverse pressure gradient. The onset of Gortler vortices can be predicted using a dimensionless

number called Gortler number. It is the ratio of centrifugal effects to the viscous effects in the boundary layer and is defined as  $GO = \frac{U\theta}{\nu} \left(\frac{\theta}{R}\right)^{0.5}$  that  $\theta$  refers to the momentum

thickness. Gortler instability occurs when the Gortler Number exceeds, about 0.3 [3].

Figure 9 shows the measured static pressure distributions in the contraction region of the tunnel at various test section velocities [23]. This plot indicates that the distributions are nearly smooth and the pressure gradient is almost favorable along the contraction wall except for the inlet and exit regions. Further, for a few velocities there exits a sharp pressure drop, reduction in  $C_p$  at distance of  $X = 70$  to  $90\text{cm}$  as seen from Fig. 10. It seems that this pressure drop at low velocities,  $V_\infty = 20$  and  $30\text{m/s}$ , is due to the special behaviors of the flow. However, as the free stream velocity increases, this adverse pressure gradient weakens and eventually for velocities higher than  $40\text{ms}^{-1}$  the adverse pressure in the inlet of the contraction diminishes. When flow arrives in the test section, which can be considered as a flat surface, the velocity profile becomes uniform and the streamline velocity near the wall decreases. Consequently, adverse pressure gradient increases. Pressure distribution and the locations of the adverse pressure gradient for the clean conditions show that at higher velocities probability of separation at the inlet of contraction decreases [23].

In figure 10, the above results are obtained for trip condition. The trip is glued at a location of  $x/L = 0.115$ ,  $30\text{cm}$  from the inlet of contraction. The results confirm significant impact of the tripped boundary layer on the control of the adverse pressure gradient. The trip strip installed at  $x/L = 0.115$  had favorable effects on the pressure distribution and reduced the turbulence intensity in the test section for all range of velocity examined in this investigation. In other word, trip strip if installed at a suitable location, may move the adverse pressure gradient to the inlet of the contraction.

This will allow the flow to become uniform in the test section as it passes along the wall [23].

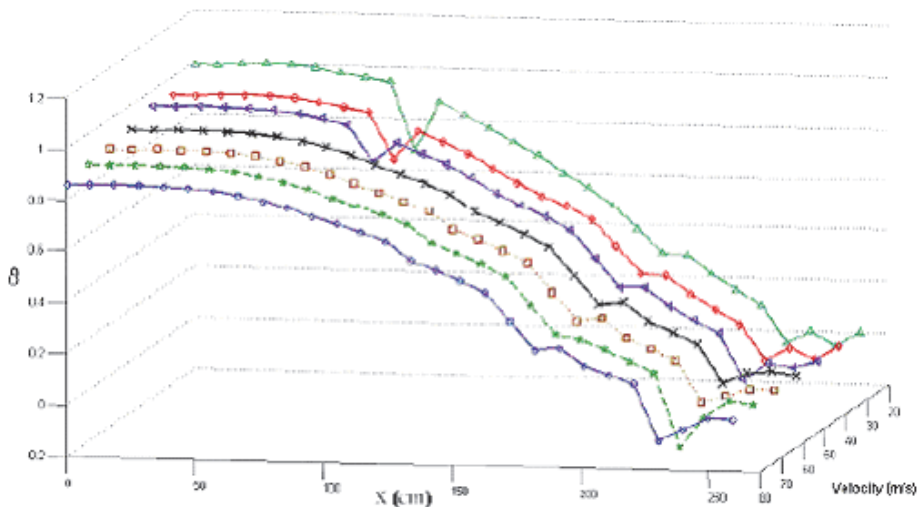


Fig. 9.  $C_p$  distribution along the contraction for the clean case [23]



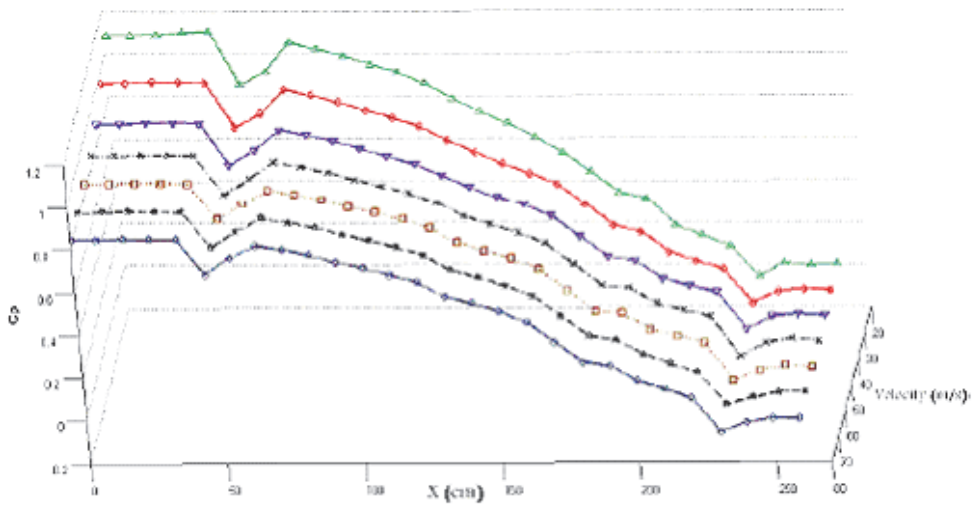


Fig. 10.  $C_p$  distribution along the contraction for the Trip case,  $X/L=0.115$  [23]

The studies of Takagi et al [25] showed that a row of Gortler vortices develops and eventually breaks down to turbulence in the concave region of the contraction. The resultant turbulent boundary layer was laminarized in the convex region due to acceleration of the mean flow. The details of the laminarization and subsequent re-transition of the boundary layer along the contraction and flow physics in such a process has been studied by [3]. After re-transition process in the outlet of the contraction, the boundary layer encounters an adverse pressure gradient. This unfavorable pressure gradient at the exit of the contraction may be due to the inflection-type instability, changed from a curved to flat surface along the wall [25].

Author in his PhD thesis made a series of experimental investigations on turbulence intensity reduction in the test section of four different contraction tunnels [3]. While the addition of suitable trip strips on different positions of the contraction section of the tunnel is examined, the tripping of the boundary layer at its early development stage in the contraction region is also exploited. Thin wire strips were placed on the contraction walls and the turbulence intensity in the test section was measured by using hot wire.

Figure 2 summarizes the results related to the author's investigations. It is evident that for  $X/L=0.79$  and  $0.115$ , which are placed in convex and concave portion of the contraction, respectively, the TI has relatively the highest reduction [3, 7]. Here,  $L$  is the length of the contraction and  $X$  is from the beginning of the contraction.

The results by author in [3, 7] indicate that the installation of the trip strips has significant effects on the TI in the test section of all four wind tunnels. The magnitude of reductions in the free stream turbulence is affected by the positions of the trip strips. For one of wind tunnels, the minimum TI is obtained when a trip strip with a diameter of  $0.91\text{mm}$  is installed at  $X/L=0.79$  or in the wide portion of the contraction, at  $X/L=0.115$ , Fig. 2. Further, it is shown that the installation of the trip strip in a suitable location not only reduces but also smoothes the turbulence level. However, the zones between concave and convex region of the contraction, that is at  $X/L=0.192$  and  $0.615$ , are not proper locations for trip strips. In general, one may conclude that the TI in the test section of the right wind tunnels may be reduced to some degrees by simply introducing trip strip with the right dimensions at the proper positions [3, 7].

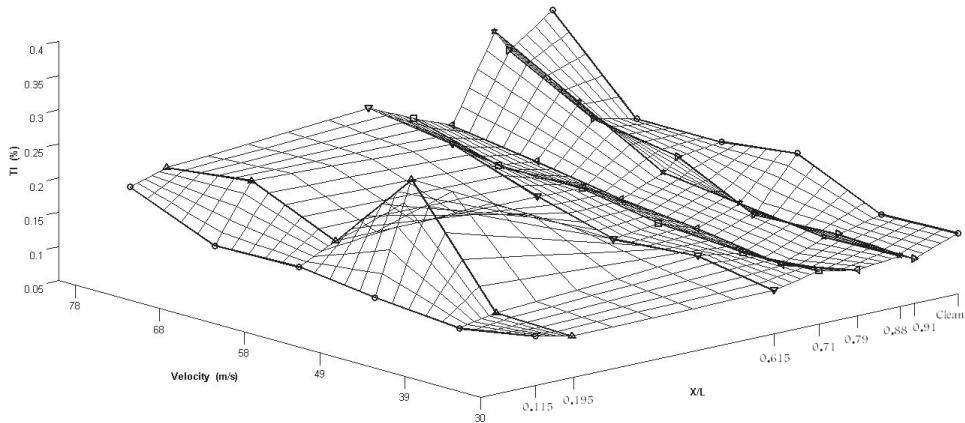


Fig. 11. Variation of TI with velocity at diameter of trip equal to 0.91mm for all various  $X/L$  at center point, WT1 [7]

## 10. Conclusion

In this chapter, the role of turbulence in obtaining a spatially uniform steady stream of air across and along the test section of wind tunnels considered. The study shows that the turbulence has a major character in flow quality of wind tunnel and can excite uncorrected results in experimental investigations of wind tunnels. Noise and eddy are the sources of turbulence that must try to reduce them. Screens, honeycomb, high contraction ratio and installation of trip strip at suitable portion of the contraction for handling of gortler vortices and inflection type instabilities are useful for turbulence reduction. Hot wire anemometry is a useful device for turbulence measurement that can operate at frequency up to 100 kHz.

## 11. References

- [1] White, F. M., "Viscous Fluid Flow", 2nd ed., McGraw-Hill, New York, 1992
- [2] Bradshaw P., "The Understanding and Prediction of Turbulent Flow", Engineering Foundation Conference on Turbulent Heat Transfer, San Diego, 1996.
- [3] Dehghan Manshadi M., "A New Approach for Turbulence Reduction in a Subsonic Wind Tunnel ", Sharif University of Technology, PhD Thesis, Tehran, Iran, 2009.
- [4] Burden T., "The First Few Lectures in a First Courses on Turbulence", Lecture Notes, 2008.
- [5] Hugh L. D., Ira H. A., "Reduction of Turbulence in Wind Tunnels", NACA Technical note, No. 1755, 1948.
- [6] Bell W. H., "turbulence vs drag-some future consideration", Ocean Engng, Vol. 10, No. 1, pp. 47-63, 1983.

- [7] Ghorbanian K., Soltani M. R., Manshadi M. D., "Experimental Investigation on Turbulence Intensity Reduction in Subsonic Wind Tunnels", *Aerospace science and Technology*, Volume 15, Issue 2, March 2011, Pages 137-147.
- [8] Bruun, H. H. *Hot-wire Anemometry*, Oxford science publications, 1995.
- [9] Perry, A. E., *Hot-Wire Anemometry*, Oxford, Clarendon, 1982.
- [10] Manshadi M. D., Keshavarz B., Soltani M. R., and Ghorbanian K., "An Innovative Genetic Algorithm Approach for Direct Calibration of X-Probe Hot-wires", *Experimental Technique*, doi:10.1111/j.1747-1567.2011.00705.x, 2011.
- [11] Manshadi M. D., Ghorbanian K., Soltani M. R., "Experimental Investigation on Interaction between Turbulence and Sound in a Subsonic Wind Tunnel", *ACTA Mechanica Sinica*, 26(4):531-539, 2010.
- [12] Uberoi, M. S., "Effect of wind-tunnel contraction on free stream turbulence", *J. Aeronaut. Sci.*, 1956, 23, 754-764.
- [13] Mikhailova N. P., Repik E.U., Sosedko Y.P., "Optimal Control of Free Stream TI by Means of Honeycombs", *Fluid Dynamics*, Vol. 29, No.3, 1994.
- [14] Scheiman J., Brooks J. D., "Comparison of Experimental and Theoretical Turbulence Reduction from Screens, honeycomb, and Honeycomb-Screen Combinations", NASA Langley Research Center, 1981.
- [15] Mehta R. D., "Turbulent Boundary Layer Perturbed by a Screen", *AIAA Journal*, Vol. 23, No.9, 1985.
- [16] Schubauer G. B., Spangenberg, "Effect of Screens in Wide Angle Diffusers", National Advisory Committee for Aeronautics, Report 949, 1947.
- [17] Laws, E. M., Livesey, J.L., "Flow through Screens," *Ann. Rev. Fluid Mech.*, 10, 247-266, 1978.
- [18] Derbunovich G. I., Zemskaya A. S., Repik E. U. and Sosedko P., "Effect of Flow Contraction on the Level of Turbulence", Translated from *Izvestiya Akademii Nauk SSSR*, No. 2, pp. 146-152, March-April, 1987.
- [19] Owen F. K., Stainback P.C., Harvey W.D., "Evaluation of Flow Quality in Two NASA Transonic Wind Tunnels", *Journal of aircraft*, VOL. 18, NO. 6, JUNE 1981.
- [20] Wigeland R. A., Tanaticat J., Nagib H. M., "Evaluation of a New Concept for Reducing Freestream Turbulence in Wind Tunnels", 11th Aerodynamic Testing Conference, Paper No. 80-0432, 1980.
- [21] Soltani M. R., Ghorbanian K. and Manshadi M. D., "Application of Screens and Trips in Enhancement of Flow Characteristics in Subsonic Wind Tunnels", *International Journal of Scientia Iranica*, 17 (1), 2010.
- [22] Barlow J.B., and Rae, W.H, Pope A., "Low-Speed Wind Tunnel Testing", Third Edition, John Wiley and Sons, 1999.
- [23] Ghorbanian K., Soltani M. R., Manshadi M. D. and Mirzaei M., "Control of Separation in the Concave Portion of Contraction to Improve the Flow Quality", the *Aeronautical journal*, Volume 113, Number 1141, pp 177-182, March 2009.
- [24] Nishizawa A., Takagi S., Tokugawa N., Sobagaki T., "Rebirth of Turbulence in Laminarized Boundary Layers along the Wind Tunnel Contraction ", 39th AIAA Aerospace Sciences Meeting and exhibit,, AIAA 2001-0277, 2001.

- [25] Takagi S., Tokugawa N., Shiomi J. and Kohama Y., "Laminar Turbulent Transition along the Contraction Nozzle in Subsonic flow", 37th AIAA Aerospace Sciences Meeting and exhibit, Reno NV, 1999.

## **Part 2**

# **Building Dynamics, Flow Control and Fluid Mechanics**



# The Use of Wind Tunnel Measurements in Building Design

Dat Duthinh and Emil Simiu

*National Institute of Standards and Technology, Gaithersburg, Maryland,  
United States of America*

## 1. Introduction

The ASCE 7-10 Standard contains provisions on the use of the wind tunnel, but those provisions are incomplete. For this reason estimates of structural response to wind can vary significantly depending upon the laboratory that provides them. This has been the case, for example, for New York City's World Trade Center's twin towers, for which such differences have exceeded 40 % (NCSTAR 1-2, Appendix D, 2004). While the emphasis here is on the testing of buildings in wind tunnels, it is therefore necessary to review the inter-related elements involved in the estimation of the response of buildings to wind, namely, micrometeorology, aerodynamics, similitude, wind climatology, statistics, and structural reliability. The chapter also discusses the validation of wind tunnel measurements, and their application to low-rise and tall buildings, and concludes with a description of a time-domain method for designing structural members known as Database-Assisted Design. For additional materials on wind tunnel testing the reader is referred to, e.g., ASCE (1999), Reinhold (1982), and Simiu (2011).

## 2. Micrometeorology

Estimates of aerodynamic pressures and forces depend upon the features of the atmospheric flow being adequately simulated in the wind tunnel. This section briefly reviews the description of atmospheric flows affecting buildings and other structures in strong winds. The description includes the characterization of mean wind profiles (Sect. 2.1) and of atmospheric turbulence (Sects. 2.2-2.5).

### 2.1 The atmospheric boundary layer and the mean wind profile

Before the 1960's aerodynamic tests of buildings were typically conducted in wind tunnels with uniform flow. Later measurements were made in boundary-layer wind tunnels, thanks to the influence of Jensen (1954), who rediscovered Flachsbart's observation, made in 1932 (Flachsbart, 1932), that wind pressures in shear flows can differ markedly from measurements in uniform flow. In this section we discuss the effects of the wind tunnel flow features on the aerodynamic effects of interest.

The mean wind profile in horizontally homogeneous terrain can be described by the power law, characterized by its exponent  $\alpha$  that depends on terrain roughness (Hellman, 1916, Davenport, 1965):

$$\frac{U(z_1)}{U(z_2)} = \left(\frac{z_1}{z_2}\right)^\alpha \quad (1)$$

where  $U(z_1)$  and  $U(z_2)$  are the wind speeds at elevations  $z_1$  and  $z_2$ . An alternative description of the mean wind profile in horizontally homogeneous terrain is the logarithmic law, characterized by the surface roughness length  $z_0$ :

$$U(z) = \frac{1}{k} u_* \ln \frac{z}{z_0} \quad (2)$$



Fig. 1. Meteorological wind tunnel, Wind Engineering Laboratory, Colorado State University. Model and turntable are in the foreground, and spires are in the background (courtesy of Professor Bogusz Bienkiewicz; photo by Gregory E. Stace).



where  $k \approx 0.4$ ,  $u_*$  is the flow shear velocity, and  $U(z)$  is the wind speed at elevation  $z$ . For strong winds the applicability of the logarithmic law up to elevations of about 400 m has been established theoretically by Csanady (1967) (for additional references and details see also Simiu, 1973, Simiu & Scanlan, 1996) and by measurements in the atmosphere by Powell et al. (2003). These results supersede the earlier belief (Davenport, 1965) that the logarithmic law is valid for any wind speed up to about 50 m elevation. Typical values of  $z_0$  range from 2 m to 0.005 m depending on the exposure category (Table C26.7-1, ASCE 7-10).

Over a rough floor, a tunnel length of 20 m to 30 m is required to develop a boundary layer of 0.5 m to 1 m (Marshall, 1984). To increase the depth of the boundary layer, wind tunnels make use of passive devices such as grids, barriers, fences and spires (Fig. 1). In general, similitude in the turbulence of air flows in the natural and the experimental settings is not achieved, even for long wind tunnels, and especially for short ( $\approx 5$  m) ones. Cermak (1982) discusses the flow features downwind of a floor covered with different kinds of roughness elements.

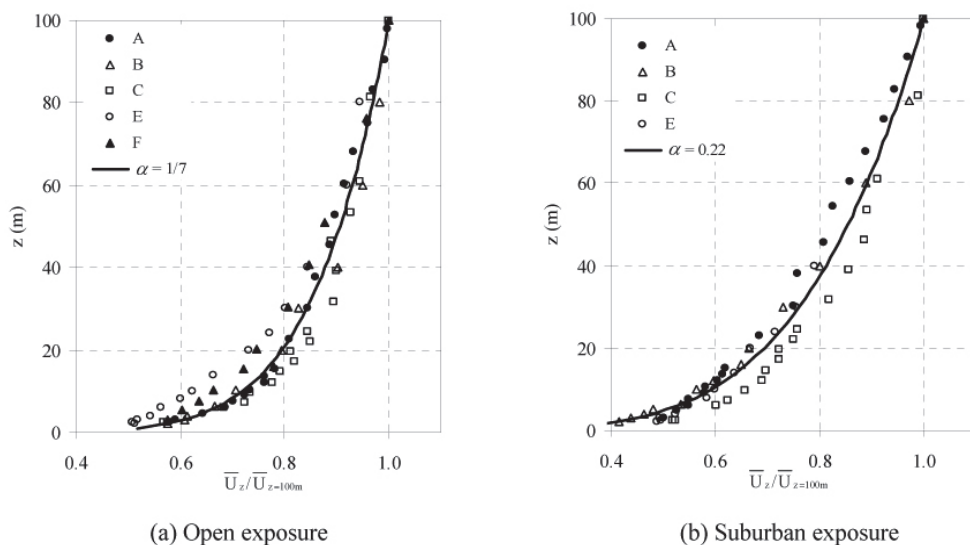


Fig. 2. Wind speed profiles in simulations by wind tunnels participating in the Fritz et al. (2008) comparison (Bienkiewicz et al., 2009). Open exposure refers to flat open country, grasslands, and water surfaces, with scattered obstructions less than 9 m high. Suburban exposure refers to wooded areas or other terrains with numerous, closely spaced single family dwellings.

The various experimental set-ups used by various laboratories to simulate atmospheric flows can result in fairly widely varying properties of the respective flows. Laboratories that participated in an international comparison of wind tunnel estimates of wind effects on low-rise buildings (Fritz et al., 2008) achieved mean wind profiles with power law exponents  $\alpha$  that varied between 0.139 and 0.191 (typical target value  $1/7 = 0.143$ ) and between 0.165 and 0.234 (target value 0.22) for open and suburban exposures, respectively (Bienkiewicz et al., 2009), see Fig. 2. These differences contributed to the significant discrepancies among the respective values of the wind effects of interest.

## 2.2 The turbulence intensity

The turbulence intensity  $I(z)$  at elevation  $z$  corresponding to the longitudinal flow fluctuations (i.e., the fluctuations  $u(z)$  in the mean speed direction) is defined as the ratio between the fluctuations' root mean square and the mean wind speed  $U(z)$ :

$$I(z) = \frac{\sqrt{u^2(z)}}{U(z)} \quad (3)$$

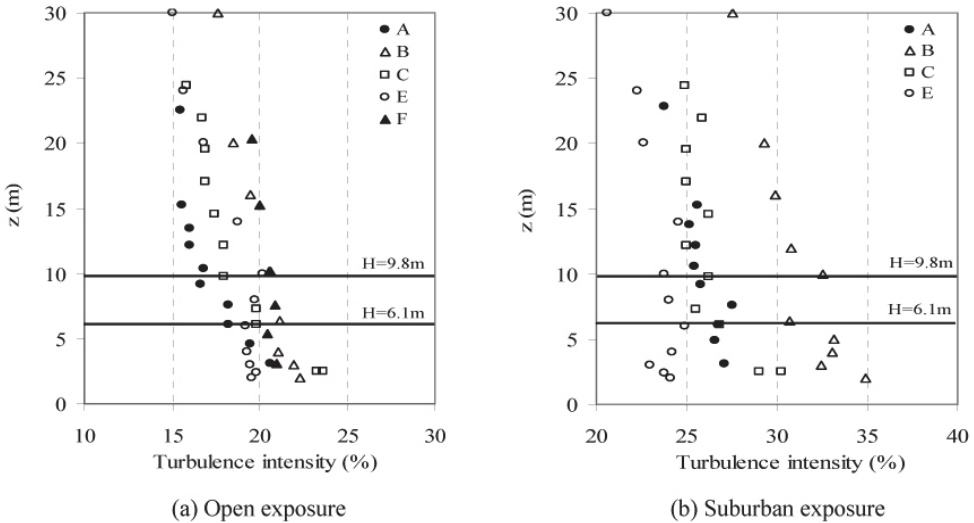


Fig. 3. Turbulence intensities in simulations by wind tunnels participating in the Fritz et al. (2008) comparison (Bienkiewicz et al., 2009).

Similar definitions hold for flow fluctuations in the lateral and vertical directions. Longitudinal turbulence intensities achieved in flows simulated by six laboratories (Fritz et al., 2008) exhibited strong variations, especially for suburban exposure (Fig. 3). For structures with equivalent height of 10 m,  $I(z)$  ranges from 0.30 to 0.15 depending on the exposure (ASCE 7-10 Sect. 26.9.4).

## 2.3 The integral turbulence length

The integral turbulence lengths of the longitudinal flow velocity fluctuations at a point are measures of the average spatial dimensions of those fluctuations. Similar definitions hold for the lateral and vertical flow fluctuations (see, e.g., Simiu & Scanlan (1996) for details). The larger the turbulence scale, the larger is the building dimension affected by the corresponding turbulent fluctuations. For example, a sufficiently large longitudinal integral turbulence scale of the longitudinal turbulent fluctuations means that, if the flow is normal to the windward face of a structure, those fluctuations can affect both its windward and leeward faces. A large lateral scale of the longitudinal turbulent fluctuations means that those fluctuations impinge almost simultaneously over a relatively large area normal to the mean wind speed, resulting in correspondingly large longitudinal fluctuating wind loads.

## 2.4 The spectral density (or spectrum)

The spectral density (or spectrum) of the longitudinal velocity fluctuations provides a measure of the strength of the fluctuations' frequency components. It is a plot representing the contributions of components with various frequencies to the variance of the fluctuations. Similar definitions hold for lateral and vertical fluctuations. Note that the turbulence intensity and the integral turbulence length are related to the spectral density. In practice the spectra of the turbulent fluctuations cannot be reproduced in civil engineering wind tunnels owing partly to the violation of the Reynolds number by several orders of magnitude, a fact that prevents the simulation of high-frequency velocity fluctuations, and partly to the difficulty of achieving large integral turbulence scales in the laboratory.

The Reynolds number is a measure of the ratio of inertial to viscous forces and is defined as:

$$R_e = \frac{\rho UL}{\mu} = \frac{UL}{\nu} \quad (4)$$

where  $U$  is the velocity,  $L$  a typical surface dimension,  $\rho$  the density,  $\mu$  the viscosity and  $\nu$  the kinematic viscosity of the fluid ( $\nu = \mu/\rho$ ). Tennekes & Lumley (1964) suggest a Reynolds number of the order of  $10^5$  to ensure the existence of an inertial subrange in the turbulent flow generated in the wind tunnel. Turbulent velocity fluctuations can be represented by eddies of various wavelengths, and the inertial subrange is the portion of the spectrum in which eddy motion may be determined by the rate of energy transfer from larger eddies to smaller ones independently of viscosity (Kolmogorov's second hypothesis).

The *cross-spectral density* of longitudinal velocity fluctuations at two points is an approximate measure of the degree of coherence between the respective fluctuations. Similar definitions apply to lateral and vertical fluctuations. For *small structures*, (e.g., typical homes) for which the turbulence length scales of interest are sufficiently large in relation to the structure's dimensions, the bulk of the fluctuating longitudinal wind speed components may be assumed to be almost perfectly coherent over lengths comparable to the dimensions of the structures' exterior faces. This observation allows the use in the wind tunnel of flows from which the low-frequency fluctuations present in the atmosphere are eliminated and are replaced by an increment in the mean wind speed (Simiu et al., Fu et al., in press).

In addition to inducing resonant fluctuations in flexible structures, *high-frequency turbulent fluctuations* have an important aerodynamic effect insofar as they transport across separation layers particles with high momentum from zones outside the separation bubbles, thereby promoting flow reattachment and affecting suction in separation zones (Simiu & Miyata, 2006). Because, as was mentioned earlier, in commercial wind tunnels, the Reynolds number is orders of magnitude smaller than at full scale, the viscous stresses within the small (high-frequency) eddies of the laboratory flow are higher. The wind tunnel counterparts of full-scale high-frequency fluctuations are therefore partly suppressed by those stresses. This can affect significantly the extent to which laboratory and full-scale suction are similar, especially in flow separation regions where the suction are strong. Indeed, measurements have shown that, in zones of strong suction, absolute values of pressure coefficients are far lower in the wind tunnel than at full scale (Fig. 4).

## 2.5 Wind speeds as functions of averaging times

The *relation between wind speeds averaged over different time intervals* (e.g., the ratio between wind speeds averaged over 3 s and wind speeds averaged over 10 min) varies as a function of the time intervals owing to the presence of turbulence in the wind flow.

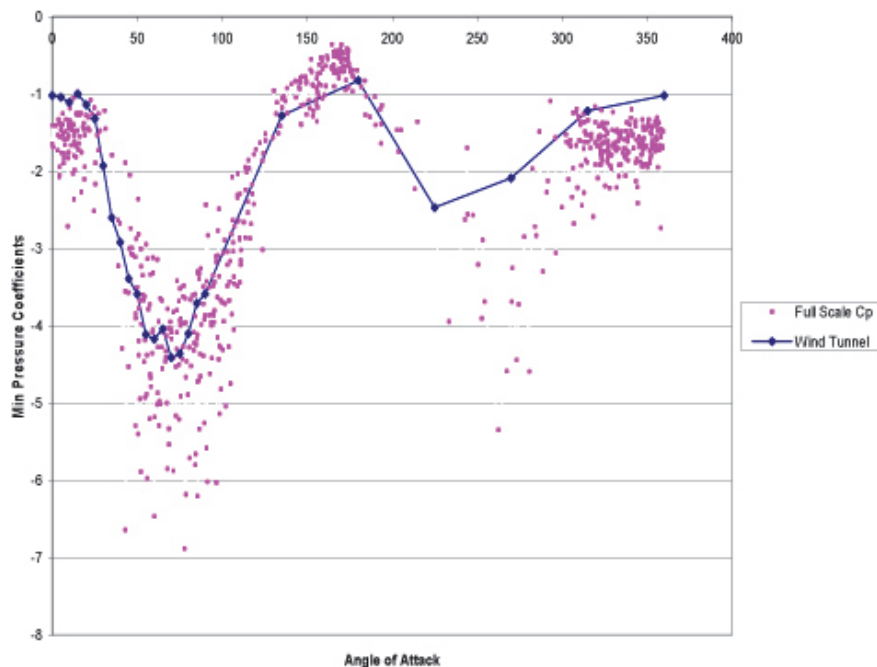


Fig. 4. Pressure coefficients measured at building corner, eave level, Texas Tech University Experimental Building (Long et al., 2006).

The flow characteristics discussed in Sections 2.1 through 2.5 depend to a significant extent upon whether the storm to which the structure is subjected is of the large-scale extratropical (synoptic) type, or a hurricane, a thunderstorm, a chinook wind, and so forth. In current commercial practice the type of flow being simulated is the atmospheric boundary layer typical of synoptic storms (straight line winds), and it is assumed that simulations in this type of flow are adequate even if the structure is subjected to other types of storm.

In wind engineering practice it is important to remember that the parameters of any given model of the wind flow are characterized by uncertainties in the sense that they can vary from storm to storm. Such variability should be accounted for in any uncertainty analysis of the wind effect estimates.

### 3. Aerodynamics and similitude

Although computational fluid dynamics has made tremendous progress in the last decade thanks to high speed computing, its use has not reached routine level in the structural design of buildings, and its predictions need to be verified by experiments. Wind tunnel testing remains the primary tool for determining wind pressures on buildings. Aerodynamic measurements can be performed simultaneously at large numbers of ports by using current pressure measurement capabilities. The quantities of interest are primarily pressure coefficients for mean pressures and for peak pressures (see, e.g., Fig. 4). This state of affairs is changing, owing in part to approximate methods that replace low-frequency fluctuations by increments in the mean speed, as discussed in Sect. 2.4.

Proper length scaling in boundary-layer wind tunnel requires:

$$\left(\frac{L_x}{D}\right)_m = \left(\frac{L_x}{D}\right)_p \quad (5)$$

where  $D$  is a characteristic length of the structure being tested, and subscripts  $m$  and  $p$  refer to the model and the prototype respectively.  $L_x$  is the longitudinal integral turbulence scale, or length of the fluctuating longitudinal component of the wind speed. It is difficult to produce large values of  $L_{xm}$  in wind tunnels, and this can be a limiting factor for the size of models testable in the laboratory.

As explained in the preceding section, it is in current practice desirable to ensure similitude between prototype and model for the variations with height of mean speed and turbulence effects, measured by turbulence intensities, integral scales, and spectral characteristics. The following numbers are important in aerodynamics and scaling.

### 3.1 Reynolds number

Since flow separation occurs at sharp corners regardless of the value of the Reynolds number, this phenomenon is assumed to be modeled correctly in a wind tunnel. Violation of Reynolds number scaling, however, does affect the flow reattachment in long, bluff bodies, and this affects the aerodynamic pressures. For curved bodies, the boundary layers at high Reynolds number tend to be turbulent, and it is possible to generate approximately the same behavior by roughening the surface of scaled models.

### 3.2 Froude number

The Froude number is the ratio of inertial to gravity forces:

$$F_r = \frac{U^2}{Lg} \quad (6)$$

where  $g$  is the acceleration of gravity. Take for example a model scaled at  $L_m/L_p = 1/400$ . Froude scaling requires  $U_m/U_p = 1/\sqrt{400} = 1/20$ . The Reynolds number for the model is:

$$R_{em} = \frac{U_m L_m}{\nu_m} = \frac{(U_p/20)(L_p/400)}{\nu_p} = \frac{R_{ep}}{8000} \quad (7)$$

Thus it is seen that Froude scaling and Reynolds scaling are incompatible if the laboratory uses the same gravity constant and the same fluid (air) as the atmosphere.

### 3.3 Rossby number

The atmospheric boundary layer depth  $\delta$  is proportional to the Rossby number  $R_o$ :

$$\delta = cR_o \quad (8)$$

where  $c \approx \frac{0.25 h}{2.5 \ln(h/z_0)}$ ,  $R_o = \frac{U(h)}{hf_c}$ ,  $U(h)$  is the mean wind speed at a height  $h$ ,  $z_0$  is the roughness length and  $f_c$  is the Coriolis parameter. As the wind speed increases, so does the boundary layer depth. For wind speeds of interest to the structural engineer, the boundary layer is several kilometers deep. Most buildings are situated entirely in the lower one-tenth of the boundary layer, where the longitudinal velocity spectrum  $S(z, n)$  in the inertial subrange can be expressed as:

$$\frac{nS(z,n)}{u_*^2} = 0.26f^{-2/3} \quad (9)$$

where  $n$  is the frequency of turbulent eddies,  $z$  the height,  $u_*$  the shear velocity of the flow, and  $f = nz/U(z)$  the Monin (or similitude) coordinate.

In a long wind tunnel, a boundary layer of the order of 1 m develops over a rough floor, and the above equation only applies to the bottom 0.1 m. A 200 m tall building modeled to the scale of 1/400 would only see its bottom 40 m exposed to the spectrum described by the equation above.

### 3.4 Strouhal number

Vortex shedding is a regular phenomenon characterized by the Strouhal number:

$$S = \frac{N_s D}{U} \quad (10)$$

where  $N_s$  is the frequency of full cycles of vortex shedding, and  $D$  is a characteristic dimension of the body normal to the mean flow velocity  $U$ .

### 3.5 Scaling effects of turbulent flow around bluff bodies

Davenport et al. (1977) compare wind pressure measurements for three models at scales of 1/500, 1/250 and 1/100. The prototype is a low-rise building 30.5 m x 24.4 m x 5.9 m with a gable roof of slope 4.7 degrees. The ratios between corresponding measurements, in terms of peak, mean and root-mean-square, differ significantly from unity in some instances and do not follow any discernable pattern. For example, the ratio of the peak pressure of the 1/100 model to the 1/500 model measured at a roof corner is 1.34, and the ratio of the peak pressure of the 1/250 model to the 1/500 model at the center of the long side is 0.63.

One reason for these discrepancies is the difficulty in determining the characteristic length (integral scale) of turbulence at full scale (measurements can vary by a factor of five, even ten), and in scaling this length to that of the model. In the investigation mentioned above (Davenport et al., 1977), the integral scale of turbulence in the wind tunnel was estimated to be 1/500 of its nominal value in atmospheric flow. Another possible reason for the discrepancies is that the change in actual elevation of the corresponding measurement points of the various models causes changes in turbulence intensities.

In the testing of rigid trussed frameworks, the effect of high-frequency turbulence components may be assumed to be insignificant, since no flow reattachment can be expected to occur on typical truss members, even in the presence of high-frequency turbulence fluctuations. Low-frequency turbulence components may be assumed approximately to be perfectly coherent over the width of vertical frameworks or the depth of horizontal frameworks. The tacit acceptance of these assumptions explains why, even after the advent of boundary-layer wind tunnels, aerodynamic testing of trussed frameworks has been performed in smooth flow (Whitbread, 1980), i.e., flow with constant velocity and no significant turbulence fluctuations. For bluff bodies with small dimensions (e.g., residential homes, or tributary areas of individual portal frames in industrial buildings) this extreme simplification of the testing may not be appropriate because high-frequency flow fluctuations can strongly influence test results.

### 3.6 Blockage

A structural model placed in the air flow provides partial blockage to the flow and causes it to accelerate. Correction factors have been worked out for a limited number of

measurements and geometries. In general, for a blockage ratio of 2 %, the corrections are of the order of 5 % and proportional to the blocking ratio (Melbourne, 1982).

#### 4. Wind climatology

The wind tunnel method typically uses directional wind speed data whenever such data are available. In some cases, directional wind speed observations are available for each of a number of equally spaced directions, but for some of the directions the number of observations is too small to allow meaningful estimates of the respective extremes. In those cases a conservative assumption is required to construct appropriate sets of data for the directions with insufficient observations by using data available for other directions. For an example of such an assumption, see Grigoriu (2009).

#### 5. Statistics of peak effects

In this section, we are concerned with the estimation of peak effects of a one-dimensional stochastic process *induced by a given wind speed*. Such peak effects may pertain to accelerations at the top of the structure, inter-story drifts, internal forces, and sums of demand-to-capacity ratios used in interaction equations (e.g., the sum of (a) the ratio of the axial force divided by axial force capacity and (b) the ratio of the bending moment divided by the moment capacity). The estimation can take advantage of the fact that most wind effects of interest are sums of many comparable randomly distributed contributions, rendering those effects Gaussian. For this case simple, well-known techniques are available for estimating the mean values of the peaks. If the wind effects of interest are not Gaussian (this may be the case, e.g., for wind effects in low-rise buildings), techniques for estimating statistics of their peaks are also available, see e.g., Sadek & Simiu (2002) or [www.nist.gov/wind](http://www.nist.gov/wind), item III.

Two cases are of interest. The first case involves stochastic processes specified by their time histories (i.e., in the *time domain*). For example, such a stochastic process may consist of the internal force induced in a member by the sway responses in directions  $x$  and  $y$ . The peak internal force of interest is then simply the peak of the sum of the internal forces associated with the two sway responses. A similar simple summation yields the requisite peaks of processes consisting of sums of any number of stochastic processes.

The second case involves stochastic processes specified by their spectral densities (i.e., in the *frequency domain*). Such specification was -- and still is -- routinely used in wind engineering dynamic analyses on account of the difficulty, up to the 1980s, of dealing computationally with the solution of dynamic problems in the time domain. Obtaining the peak of a sum of several stochastic processes is no longer possible by summing up those processes, because in the frequency domain as used in typical wind engineering applications the phase information inherent in the respective time histories is lost. Therefore the estimation of peaks requires the use of sums of weighted component processes (e.g., axial forces and bending moments), with weights specified by engineering judgment. As many as dozens of such weighted combinations are prescribed to structural designers by wind engineering laboratories, in an attempt to make sure that relevant peaks are not missed. This is time-consuming from the point of view of the designer, as well as less accurate than the much simpler, more transparent, and more effective time-domain approach. Additional

drawbacks are the difficulty of accounting for wind directionality effects in a transparent and physically meaningful way (see Simiu, 2011).

If wind directionality is not taken into account explicitly (i.e., other than through the use of a blanket reduction factor, as is done in ASCE 7, 2006), then the *mean recurrence intervals* (MRI) of a peak wind effect is simply assumed to be the MRI of the wind speed inducing it. Estimation methods for extreme wind speeds with specified MRIs, regardless of their direction, are discussed, e.g., in Simiu (2011). If directionality is explicitly accounted for in the calculations, the peak wind effects with specified MRI are obtained as follows. Assume the directional wind speed data consist of  $m$  sets (e.g.,  $m$  storm events) of  $n$  directional wind speeds each (corresponding to, e.g.,  $n = 16$ , or  $n = 36$  directions). For each of the  $m$  sets, calculate the peak response induced by each of the  $n$  directional wind speeds, and retain only the largest of these  $n$  responses. This yields a set of  $m$  largest peak responses. The  $m$  peak responses are then rank-ordered. If the rate of arrival of the events associated with the  $m$  sets is  $r$ /year, then the estimated MRI of *a*) the largest of the  $m$  peak responses is  $(m+1)/r$  years; *b*) the  $p$  largest is  $(m+1)/(pr)$  years. This estimate is non-parametric.

In hurricane-prone regions, directional wind speeds in any specified number of storms are typically obtained by Monte Carlo simulation using physical and probabilistic storm models (e.g., Batts et al. 1980; Vickery & Twisdale, 1995; Vickery et al., 2009). If the size of an existing database of hurricane wind speeds needs to be augmented (as may be necessary for the only public hurricane wind speeds database that covers the entire Gulf and Atlantic coasts of the United States, and contains 999 simulated storms for each station, listed on [www.nist.gov/wind](http://www.nist.gov/wind)), this augmentation can be achieved by using software developed by Grigoriu (2009). For straight line (synoptic) and thunderstorm wind speed data, large sets of simulated data and associated errors in their estimation can also be obtained using the methods developed by Grigoriu (2009).

## 6. Structural reliability

The purpose of structural reliability is to develop design criteria assuring that the probability of inadequate strength and serviceability performance is acceptably small. The traditional approach to design, Allowable Stress Design (ASD), is no longer in use but is relevant for the understanding of the Strength Design (SD) approach, currently specified in ASCE 7-10 (2010). In its simplest form allowable stress design (ASD) achieves this purpose by requiring, for each member, that the stress induced by the sum of the basic design loads not exceed the allowable stress, typically defined as the nominal yield stress divided by a safety factor. The basic design loads and the safety factor are based on experience gained in past practice. For example, the basic design wind load is typically specified as the wind load with a nominal 50-yr MRI. If for A36 steel (nominal yield stress 36 ksi or 249 MPa), the allowable stress for non-compact sections is 22 ksi (152 MPa), then the safety factor is  $36/22 = 1.64$ . ASD's probabilistic content consists of the specification of the MRI of the basic design wind load and of the definition of the nominal yield stress as a specified percentage point of its probability distribution.

Strength design (SD) requires in its simplest form that, for each member, the stress induced by the sum of the basic design loads, each multiplied by a load factor that depends upon the type of load, not exceed the yield stress multiplied by a resistance factor smaller than unity. Consider, for example, the case where wind is the only significant load acting on an A36 steel member with non-compact cross section. The wind load factor specified by ASCE 7 is 1.6, and if the resistance factor is 0.9, SD design requires that the basic wind load induce in the member



a stress of at most  $36 \times 0.9/1.6 = 20.25$  ksi (139.6 MPa), rather than 22 ksi (151.7 MPa) as required by ASD. In this example SD is more conservative than ASD. This is in part due to the specification by ASCE 7 of a wind load factor equal to 1.6, even though the original intent of the standard was to specify a wind load factor equal to 1.5 (see ASCE 7-05 Commentary Sect. C6.5.4). Had the latter value of the wind load factor been specified, the SD would have required that a stress of  $36 \times 0.9/1.5 = 21.6$  ksi (148.9 MPa) not be exceeded under the basic wind load, i.e., a stress substantially equal to the 22 ksi (151.7 MPa) stress required in ASD.

To see why the difference between ASD and SD can be significant, consider the case of a member subjected to dead load and wind load. The uncertainties inherent in the wind load being larger than those inherent in the dead load, it is appropriate that the safety margin with respect to the loading (i.e., the load factor) be larger for the wind than for the dead load. This is reflected in ASCE 7-05, Section 2.3, which specifies for the dead load factor a value smaller than 1.5 or 1.6. In contrast, for ASD, the dead loads and the wind loads are both affected by a factor equal to unity. (Reference to ASCE 7-05 is warranted in this section for two reasons. First, ASCE 7-05 is still being widely used. Secondly, ASCE 7-10 provisions on SD are based on the rationale inherent in the ASCE 7-05 SD provisions, in terms of substance if not of format.)

The probabilistic content is richer for SD than for ASD inasmuch as the various load factors account for estimated probability distributions of the total uncertainties, which include uncertainties in the wind speed and in the wind effect.

*Uncertainties in the wind speed.* The design value may well be smaller than the actual value affecting the structure during its life, since the wind speed is a random variable characterized by a probability distribution. In addition, that distribution may be affected by modeling errors (e.g., it could be a Type I Extreme Value distribution, a Type III Extreme Value distribution, a penultimate distribution, a mixed distribution of synoptic and thunderstorm wind speeds, and so forth). Finally, the assumed distribution and/or its estimated parameters are affected by sampling errors due to the relatively small size of the observed data sample, by observation errors, and, in the case of hurricanes, by physical modeling errors of climatological parameters used in Monte Carlo simulations of the wind speeds, e.g., the radius of maximum wind speeds, the pressure defect at the center of the eye of the storm, and so forth.

*Uncertainties in the wind effect.* Uncertainties in aerodynamic pressure or force coefficients are due to measurement errors and/or to errors in the simulation of the flows that induce those pressures. For rigid structures the responses induced by aerodynamic pressures are proportional to the square of the wind speeds. For flexible structures the responses are proportional to the wind speeds raised to powers larger than two. The contribution to errors in the estimation of the wind response of estimation errors in the wind speeds is therefore greater for flexible than for rigid structures. Another contribution is due to the effect of errors in the estimation of natural frequencies of vibration, modal shapes, and damping ratios.

The wind load factor specified in ASCE 7 was estimated by accounting in an approximate manner for the uncertainties in the wind speeds and wind effects affecting *rigid* structures in *non-hurricane* wind climates. The resulting estimate was approximately 1.6 (or 1.5, depending upon the version of ASCE 7 being considered). To simplify codification, the ASCE 7 conventional methods assume, for non-hurricane regions, that the MRI of the wind effect that induces yield stresses is the MRI of the wind speed defined by the basic wind speed times the square root of the wind load factor. Calculations based on simplifying assumptions described

in the ASCE 7 Commentary show that this MRI is nominally about 500 years for a wind load factor of 1.5 and about 720 years for a wind load factor of 1.6. SD calculations can then be based on wind effects on rigid structures induced by 500-yr (or 720-yr) wind speeds. Note that in ASCE 7 the effective value of the wind load factor for hurricane-prone regions is larger than 1.6. This is achieved by maintaining the nominal 1.6 value of the load factor, while increasing the MRI of the basic speeds (see ASCE 7-05 Commentary C6.5.4).

It is assumed in current wind engineering practice that this approximate approach is applicable not only to rigid structures, but to flexible structures as well. To see why this assumption can be unwarranted, we consider the following first-order second-moment calculation (Ellingwood et al., 1980) for typical rigid structures. The approximate value of wind effect of interest may be written in the form

$$W_r = cC_pGE_zv^2 \quad (11)$$

where  $c$ ,  $C_p$ ,  $G$ ,  $E_z$ , and  $v$  denote a proportionality factor, pressure coefficient, peak (gust response) factor, terrain exposure factor, and wind speed, respectively, and the subscript  $r$  denotes "rigid". The approximate value of the coefficient of variation of  $W_r$  is then

$$V_{W_r} = (V_{C_p}^2 + V_G^2 + V_{E_z}^2 + 2V_v^2)^{1/2} \quad (12)$$

where  $V$  followed by a subscript denotes coefficient of variation. For tall, flexible buildings the wind effect is proportional to the velocity raised to a power larger than 2; assuming for simplicity

$$W_f = cC_pGE_zv^3 \quad (13)$$

where the index  $f$  denotes "flexible", the approximate value of the coefficient of variation of  $W_f$  is

$$V_{W_f} = (V_{C_p}^2 + V_G^2 + V_{E_z}^2 + 3V_v^2)^{1/2} \quad (14)$$

Assume  $V_{C_p} = 0.10$  for both rigid and tall buildings;  $V_G = 0.10$  for rigid buildings and  $V_G = 0.14$  for tall buildings, since the uncertainty in the dynamic parameters adds to the uncertainty in the ratio between peak and mean response;  $V_{E_z} = 0.12$  for rigid buildings and  $V_{E_z} = 0.10$  for tall buildings, since the uncertainties in the features of the wind flow are likely to be smaller if ad-hoc testing is performed; and  $V_v = 0.18$ , including aleatory variability, observation errors, and sampling errors.

Given these assumptions we have:  $V_{W_r} = 0.315$  and  $V_{W_f} = 0.37$ . The difference between the respective estimates is about 17.4 %. Since the wind load factor is, very approximately, an increasing linear function of the coefficient of variation of the wind effect, it follows that the load factor should indeed be larger for tall buildings than for rigid buildings. Estimates based on coefficients of variation are crude, and far more accurate estimates can be obtained by numerical simulations based on a detailed model of the dynamic response that accounts for the effect of wind directionality<sup>1</sup> (Gabbai et al., 2008; Simiu et al, 2008). Note that the

---

<sup>1</sup> Estimates of wind load factors based on the along-wind and across-wind response due to wind normal to a building face do not reflect correctly the margins of safety applicable to a building subjected, as it is in reality, to winds blowing from any direction. Note also that the notion of along-wind and across-

value of the load factor depends upon the characteristics of the building and upon the structural member being considered. Current calculations assume that one wind load factor is appropriate for all buildings and all their structural members. A far more differentiated approach is needed, however. The development of highly efficient software now allows the use of such an approach.

As was noted earlier, the ASD and SD approaches are applied to individual members and do not consider the reliability of the building as a whole. A step forward was achieved by applying methods that allow the estimation of the MRI of incipient structural collapse, a limit state beyond which it may be assumed that the structure's strength reserves have largely been exhausted for practical purposes. Modern finite element methods and sets of directional wind tunnel pressure data obtained simultaneously at large numbers of taps have been applied recently to obtain such estimates for rigid buildings (Jang et al., 2002; Duthinh et al., 2008).

## 7. Validation of wind tunnel testing

Dalgliesh (1975), Dalgliesh (1982) and Dalgliesh et al. (1983) compared measurements of wind pressure at full-scale and on a 1/200 aeroelastic wind tunnel model of the Commerce Court West Tower in Toronto. The 57-story steel frame (36.5 m x 69.7 m x 239 m) was the tallest building in Canada when it was completed in 1973. Agreement between model and full-scale measurements of mean pressures is satisfactory, but there are significant differences between the two sets of measurements of fluctuating pressures caused by vortex shedding. The model, with mass lumped at seven levels, agreed reasonably well with full scale measurements at the low and high end of the acceleration spectrum, but underestimated the response in the intermediate frequency range.

Richardson & Surry (1991) compare full scale and wind tunnel measurements for low-rise, gable roof buildings and conclude that flow separation on the windward roof is not modeled correctly, causing significant errors in roof pressures derived from the model. Tieleman (1992) confirms that wind tunnel measurements are inadequate for roof corners, but acceptable for wall pressures. Tieleman (1993) suggests the use of small spires upstream of the model to improve the turbulence characteristics of the flow and the fidelity of wind pressures at roof corners.

Comparison of measurements by six wind tunnels showed significant discrepancies for low-rise buildings (Fritz et al. 2008). For example, the largest estimate of the bending moment at the knee of portal frames with 6 m and 9.75 m eave height is more than twice the smallest. Comparison between ASCE 7 Standard and calculations of wind loads based on wind tunnel tests at the University of Western Ontario shows differences exceeding in some cases 50 %, attributable in part to errors inherent in wind tunnel testing of low-rise buildings (Surry et al. 2003, Ho et al., 2005, St. Pierre et al., 2005, Coffman et al., 2010).

For taller buildings, results between various laboratories appear more consistent, although discrepancies exceeding 40 % have been reported (NCSTAR 1-2, Appendix D, 2004).

---

wind response, assumed in the past to apply only to the case of wind normal to a building face, in fact also applies to the case of winds skewed with respect to a building face.

## 8. Wind tunnel testing of low-rise buildings

Low-rise buildings typically have natural frequencies much greater than their response frequencies to fluctuating wind forces, and thus their aeroelastic behavior can be neglected, i.e., they can be considered rigid. Current procedures in the US for the wind design of rigid buildings (in practice buildings with fundamental natural frequencies greater than 1 Hz - ASCE 7 Section 26.9) rely on ASCE 7 Standards that are based on wind tunnel measurements on a fairly modest number of geometries (about ten) that do not encompass all the building configurations covered by the provisions. In addition, the reduction of aerodynamic data to a few tables and curves amenable to hand calculations can lead to significant errors (Ho et al., 2005, St. Pierre et al., 2005, Coffman et al., 2010). Here we present an alternative method, called the Database-Assisted Design (DAD) method, allowed by ASCE 7-10 Standards (2010), that is more accurate and relies on modern computer technology.

### 8.1 Database-assisted Design (DAD) method for low-rise buildings

DAD takes the wind and structural engineers from wind tunnel pressure data to the sizing of structural members to resist wind forces, through the following steps:

Step 1. Interpolation of pressure data to the building being designed: Wind tunnel models are equipped with hundreds of pressure taps installed in a grid pattern on the walls and roof. These taps are scanned nearly simultaneously at high frequencies to provide time histories of wind pressure. The measured pressures are multiplied by tributary areas centered at the taps and defined by lines that bisect the grid defined by the taps, and in this way, forces and moments on the main wind resisting frames can be calculated. The peak responses corresponding to a unit wind speed for a particular wind direction, called Directional Influence Coefficients (DIF), have proven to be convenient and useful for structural design. Since the building is rigid, its linear response is not affected by dynamic effects, and the peak wind response is the product of the DIF and the square of the wind speed.

Most of the time, the building to be designed does not match the geometry of any model in the database, and thus interpolation is necessary. This works best when there are two models in the database of similar geometry but slightly different dimensions that bracket the building. First the coordinates of the pressure taps on the models are scaled to the dimensions of the building. DIFs are calculated from one model, or from several by interpolation, with more weight given to the models that more closely match the dimensions of the building. Main (2005) shows the interpolation agrees well with data obtained directly for the building of interest, although interpolation between roofs of different slopes needs further research.

Step 2. Influence coefficients required to calculate internal forces can be obtained from standard structural analysis software, based on a preliminary building design. Likewise statistics of peak values can be obtained from standard software, provided for example in the DAD software package [www.nist.gov/wind](http://www.nist.gov/wind), which also includes an interpolation scheme and methods to calculate demand-to-capacity indices (DCI) for structural members, inter-story drifts and peak accelerations with their respective mean recurrence intervals (MRI).

DAD accounts for wind directionality by explicitly using wind tunnel measurements for different wind directions (currently up to 36) and calculating statistics on the peaks of these effects. This is a clear improvement on the current practice of applying a

directionality factor of 0.85 to wind effects calculated with no consideration of wind directionality. DAD is an expansion of the method of simultaneous pressure integration leading to wind loading pioneered by the University of Western Ontario. DAD provides wind loading as well as wind effects on buildings, and checks building performance for strength and serviceability.

## 9. Wind tunnel testing of tall buildings

### 9.1 The High-Frequency Force Balance (HFFB) method

In this method, which is relatively inexpensive and fast, the building model is rigid and a high frequency balance at its base measures shear forces, bending and torsional moments. The method works best for buildings with linear mode shapes along the principal axes, although correction factors that assume a wind pressure distribution have been derived for other buildings. The bending moment measured at the base of a building of height  $H$  due to wind forces per unit height in the  $x$  direction  $w_x(z, t)$  is:

$$M_x(t) = \int_0^H w_x(z, t)z dz \quad (15)$$

where  $z$  is the vertical coordinate. If the first fundamental mode shape is linear,  $\varphi_{x1} = z/H$ , then the generalized force

$$Q_{x1}(t) = \int_0^H w_x(z, t)\varphi_{x1} dz \quad (16)$$

is proportional to the measured moment. The same conclusion obtains for moment and generalized force in the  $y$  direction, but not for the generalized aerodynamic torsional moment (since the fundamental torsional mode shape is not uniform,  $\varphi_{T1} \neq 1$ ).

### 9.2 Aeroelastic method

In this method, the model reproduces the mass distribution and stiffness of the building, and thus renders faithfully its modal shapes and dynamics. This kind of model is rarely used because of the cost and time involved in its fabrication. A more affordable and simpler type of model is the so-called "stick" model that is similar to the HFFB model, but in addition approximates the aeroelastic response of the building by accounting for its flexibility and damping characteristics. Aeroelastic modeling is deemed unnecessary if the across-wind response is insignificant (roughly speaking and for a rectangular building, when the height is less than seven times the width).

Fortunately, aeroelastic effects on tall buildings tend to be small for the following reasons:

1. The frequency range of vortex-induced forces is rather broad, and only a small fraction produces lock-in oscillations.
2. Three-dimensional flow in buildings with small or no taper impedes the formation of vortices near the building top, where they have the greatest effect.
3. Non-uniform wind profiles reduce the coherence of the vorticity in the vertical direction. This effect can be enhanced by a strong taper in the building, or varying the cross section to provide discontinuities in the vertical dimension. Introducing slits, chamfering corners can also impede vortex formation.

### 9.3 Database-assisted design of tall buildings

DAD can be used for tall as well as low-rise buildings. Unlike current design methods that rely on spatially averaged wind pressures, the Database-Assisted Design (DAD) is a time-domain method that uses directional pressure time histories recorded by a sufficiently large number of pressure taps in wind tunnel tests. In addition, the method accounts for directional wind data recorded at weather stations and supplemented by Monte Carlo simulations. The wind engineer relates the pressures on the prototype building to the wind tunnel pressures by calculating the ratio of the wind speed measured at the weather station to the reference wind speed at the top of the building model, accounting for the building's exposure. With this information and the use of standard software to calculate influence coefficients, the structural engineer can obtain the demand-to-capacity index (DCI) of various members, as well as other quantities of interest, such as the inter-story drift and the top floor acceleration, corresponding to a given mean return interval (MRI). The DCI calculations are based on current American building practice embodied in ASCE 7, AISC (American Institute of Steel Construction) and ACI (American Concrete Institute international).

The DAD method takes advantage of modern computer technology in providing designers direct access to wind tunnel as well as weather station and simulation data. Increases in computer memory and speed make possible the simultaneous scanning of hundreds of pressure taps via calibrated plastic tubes. Furthermore, DAD accounts for wind directionality and any building modal shape in an explicit and transparent manner. As a time domain approach, it also allows superposition of wind effects. The main disadvantage of the method is its cost and duration, since the wind tunnel tests require multiple pressure taps as opposed to the simpler HFFB. In some instances, architectural details may make it impractical to install pressure taps.

## 10. Wind effects estimation

To assure transparency and accountability in the estimation of wind effects, *wind engineering laboratories should provide:*

1. Records of the requisite wind climatological data. These consist of relevant measured and/or synthetic directional wind speeds obtained from legitimate sources, e.g., meteorological stations or reliable hurricane wind speed databases, augmented if necessary by methods such as those developed by Grigoriu (2009).
2. Information, typically based on wind tunnel tests, on the ratio between directional wind speeds at the reference site (e.g., 3-s peak gusts or 1-min speeds at 10 m above ground over terrain with open exposure) and the corresponding nominal mean hourly wind speeds at the top of the building being considered. This information is required because wind tunnel data are referenced with respect to those mean speeds. In addition, the wind tunnel laboratory needs to provide estimates of veering angles. Veering in atmospheric flows, which can be aerodynamically significant for tall buildings, is an effect of the Coriolis acceleration, which is not reproduced in the wind tunnel.
3. Wind tunnel measurement records of primary wind effects on structures.
  - For *rigid structures* the measurement records of interest typically consist of time histories of simultaneously measured pressures at large numbers of taps on the structure's exterior surface.
  - For *dynamically active structures* with no significant aeroelastic effects under winds that may be expected to occur during their lifetime, the measurement records consist, for

each of the wind directions for which wind speed data are considered, either of time histories of simultaneously measured pressures at large numbers of taps on the structure's exterior surface, or of time histories of strains measured on a high-frequency force balance at the base of rigid building models.

- For *structures that exhibit aeroelastic effects*, we refer the reader to Zhou & Kareem (2003) and Diana et al. (2009).

Once the structural designer has these data, he/she can use them as input to available procedures that produce the requisite design information. This information is far more comprehensive and differentiated than what wind engineering laboratories currently provide and includes, for any given set of the building's structural member sizes, demand-to-capacity ratios (which typically account for axial force and bending moment in interaction formulas), and inter-story drift, corresponding to the respective specified MRIs. The calculations involve structural analyses to obtain the requisite sets of influence coefficients. In addition, for flexible structures, analyses are needed to estimate natural frequencies of vibration and the corresponding modal shapes. For details, see Main (2006), Simiu & Miyata (2006), Simiu et al. (2008), and Spence (2009). Initial member sizes are based on preliminary calculations. Final member sizes are obtained by repeating the calculations if necessary. Research is ongoing on an iterative optimization process for obtaining member sizes consistent with strength and serviceability constraints (Spence & Giofrè, 2008).

The innovation that makes possible the clear separation between tasks incumbent on the wind engineering laboratory on the one hand and the structural designer on the other is the estimation of wind effects by using time domain instead of frequency domain methods. Frequency domain methods, in which differential equations are converted into algebraic equations at the cost of losing phase information, were introduced by Liepmann (1952) for aeronautical engineering applications and were adapted to structural engineering applications by Davenport (1961). As was noted earlier, their use was justified by the fact that, for computational reasons, modal equations of motion could not in practice be solved in the time domain. This constraint no longer exists. Nevertheless the use of frequency domain methods persists in spite of their significant drawbacks.

## 11. Conclusion

A fundamental difficulty in achieving reproducible wind tunnel measurements of wind effects, especially on low-rise buildings, is the simulation of atmospheric flows. In particular, the correct simulation of suction in separation bubbles requires the reproduction of high-frequency atmospheric turbulence, which is prevented in large part by the action of viscous dissipation at model scales typically used in commercial wind tunnels. Low-frequency fluctuating components, which are the major contributors to the flow's turbulence intensities and integral turbulence scales, may be expected to affect aerodynamic response insignificantly provided (i) that the characteristic dimensions of the structure of interest are sufficiently small, as is the case for, e.g., residential homes, and (ii) that the mean speeds in the simulated flow are commensurate with the peak speeds in the atmospheric flow. For structures with dimensions for which testing proves that this proposition holds, valid aerodynamic simulations can be obtained in flows that simulate only mean speeds and high-frequency flow fluctuations, provided that the mean velocity profile is correctly modeled (Huang et al., 2009). Using rapid scanning equipment, fast computers with vast storage,

modern wind tunnels can provide simultaneous measurements of numerous pressure taps, thus allowing the development of time domain methods of calculating the response of buildings to wind.

## 12. References

- ASCE Manual of Practice No. 67 (1999). Wind Tunnel Studies of Buildings and Structures, American Society of Civil Engineers, Reston, VA.
- ASCE Standards ASCE/SEI 7-05 (2006), 7-10 (2010). Minimum Design Loads for Buildings and Other Structures, American Society for Civil Engineers, Reston, Va
- Batts, M.E., Russell, L.R. & Simiu, E. (1980). Hurricane Wind Speeds in the United States, *J. Struct. Div. ASCE*, 100, 2001-2015
- Bienkiewicz, B., Endo, M. & Main, J.A. (2009). Comparative Inter-Laboratory Study of Wind Loading on Low-rise Industrial Buildings, *ASCE/SEI Structural Congress*, Austin, Tx
- Cermak, J.E. (1982). Physical Modeling of the Atmospheric Boundary Layer in Long Boundary-Layer Wind Tunnels, *Wind Tunnel Modeling for Civil Engineering Applications*, T.A. Reinhold ed., Cambridge Univ. Press, Cambridge, 97-125
- Coffman, B. F., Main, J. A., Duthinh, D. & Simiu, E. (2010). Wind Effects on Low-Rise Metal Buildings: Database-assisted Design versus ASCE 7-05 Standard Estimates, *J. Struct. Eng.*, 136, 744-748
- Csanady, G.T. (1967). On the Resistance Law of a Turbulent Ekman Layer, *J. Atmospheric Science*, 24, 467-471
- Dalglish, W.A. (1975). Comparison of Model/Full Size Scale Wind Pressures on a High-Rise Building, *J. Industrial Aerodynamics*, 1, 55-66
- Dalglish, W.A. (1982). Comparison of Model and Full Scale Tests of the Commerce Court Building in Toronto, *Wind Tunnel Modeling for Civil Engineering Applications*, T.A. Reinhold ed., Cambridge Univ. Press, Cambridge, 575-589
- Dalglish, W.A., Cooper K.R. & Templin, J.T. (1983). Comparison of Model and Full-Scale Accelerations of a High-Rise Building, *J. of Wind Engineering and Industrial Aerodynamics*, 13, 217-228, also Div. Building Research 1172, NRCC 23112
- Davenport, A.G. (1961). The Application of Statistical Concepts to the Wind Loading of Structures, *Proc. Institution of Civil Engrs.* 19, 449-472
- Davenport, A.G. (1965). The Relationship of Wind Structure to Wind Loading, *Proc. Symp. Wind Effects on Buildings and Structures*, Nat. Phys. Lab., Teddington, UK, 1, 53-102
- Davenport, A.G., Surry, D., Stathopoulos, T. (1977). Wind Loads on Low-rise Buildings, *Final Rep. on Phases I and II*, BLWT-SS8-1977, Univ. Western Ontario, London, Ontario, Canada
- Diana, G., Giappino, S., Resta, F., Tomasini, G. & Zasso, A. (2009). Motion Effects on the Aerodynamic Forces for an Oscillating Tower through Wind Tunnel Tests, *Proceedings, European-African Conference on Wind Engineering*, Florence, Italy, C. Borri et al., eds., July 19-23
- Duthinh, D., Main, J.A., Wright, A.P., & Simiu, E. (2008). Low-Rise Steel Structures under Directional Winds: Mean Recurrence Interval of Failure, *J. Struct. Eng.*, 134, 1383
- Ellingwood, B., Galambos, T.V., MacGregor, J.G., & Cornell, A.C. (1980). Development of a Probability Based Load Criterion for American National Standard A 58, *National Bureau of Standards*, Washington, D.C.



- Flachsbart, O. (1932). Winddruck auf geschlossene und offene Gebäude, *Ergebnisse der Aerodynamischen Versuchsanstalt zu Göttingen*, IV Lieferung, Prandtl, L. & Betz, A. eds., Verlag von R. Oldenbourg, Munich & Berlin
- Fritz, W.P., Bienkiewicz, B., Cui, B., Flamand, O., Ho, T.C.E., Kikitsu, H., Letchford, C.W., & Simiu, E. (2008). International Comparison of Wind Tunnel Estimates of Wind Effects on Low-Rise Buildings: Test-related Uncertainties, *J. Struct. Eng.*, 134, 1887-1890
- Fu, T.-C., Aly, A.M., Chowdhury, A.G., Bitsuamlak, G., Yeo, D. & Simiu, E. (in press). A Proposed Technique for Determining Aerodynamic Pressures on Residential Homes, *Wind and Structures*
- Gabbai, R.D., Fritz, W.P., Wright, A. P., & Simiu, E. (2008). Assessment of ASCE-7 Standard Wind Load Factors for Tall Building Response Estimates, *J. Struct. Eng.* 134, 842-845
- Grigoriu, M. (2009). Algorithms for Generating Large Sets of Synthetic Directional Wind Speed Data for Hurricane, Thunderstorm and Synoptic Winds, *NIST Tech. Note 1626*, National Institute of Standards and Technology, Gaithersburg, MD
- Hellman, G. (1916). Über die Bewegung der Luft in den untersten Schichten der Atmosphäre, *Meteorol. Z.*, 34, 273
- Ho, T. C. E., Surry, D., Morrish, D. & Kopp, G. A. (2005). The UWO Contribution to the NIST Aerodynamic Database for Wind Loads on Low Buildings: Part I. Archiving Format and Basic Aerodynamic Data, *J. Wind Eng. Ind. Aerodyn.*, 93, 1-30
- Huang, P., Chowdhury, G.A., Bitsuamlak, G., & Liu, R. (2009). Development of Devices and Methods for Simulation of Hurricane Winds in a Full-scale Testing Facility, *Wind and Structures*, 12
- Jang, S., Lu, L.-W., Sadek, F. & Simiu, E. (2002). Database-assisted Design Wind Load Capacity Estimates for Low-rise Steel Frames, *J. Struct. Eng.*, 128, 1594-1603
- Jensen, M. (1954). Shelter Effect Investigations, Danish Technical Press, Copenhagen
- Liepmann, H.W. (1952). On the Application of Statistical Concepts to the Buffeting Problem, *J. Aeronaut. Sciences* 19, 793-800, 822
- Long, F., Smith, D.A., Zhu, H., & Gilliam, K. (2006). Uncertainties Associated with the Full Scale to Wind Tunnel Pressure Extrapolation, *Rep. to NIST by Univ. of Texas, Lubbock, Tx, NIST/TTU Coop. 70NANB3H5003*
- Main, J. A. (2005). Interpolation Issues in the Estimation of Peak Internal Forces using Pressure Databases, *Proceedings of the 6th Pacific-Asia Conference on Wind Engineering* (C. K. Choi, ed.), Seoul, Korea
- Main, J.A., (2006). Database-Assisted Design for Wind: Concepts, Software, and Examples for Rigid and Flexible Buildings, *Building Science Series 180*, Chapter 3
- Marshall, R.D. (1984). Wind Tunnels Applied to Wind Engineering in Japan, *J. Struct. Eng.* 110, 1203-1221
- Melbourne, W.H. (1982). Wind Tunnel Blockage Effects and Correlations, *Wind Tunnel Modeling for Civil Engineering Applications*, T.A. Reinhold ed., Cambridge Univ. Press, Cambridge, 197-216
- NCSTAR 1-2, Appendix D (2004). Report on Estimation of Wind Effects on the World Trade Center Towers, <http://wtc.nist.gov/NCSTAR1/NCSTAR1-2index.htm>
- Powell, M.D., Vickery, P.J. & Reinhold, T.A. (2003). Reduced Drag Coefficient for High Wind Speeds in Tropical Cyclones, *Nature*, 422, 279-283

- Reinhold, T.R., ed. (1982). *Wind Tunnel Modeling for Civil Engineering Application*, Proceedings of the International Workshop on Wind Tunnel Criteria and Techniques in Civil Engineering Applications, Gaithersburg, Maryland, USA.
- Richardson, G.M. & Surry, D. (1991). Comparisons of Wind-Tunnel and Full-Scale Surface Pressure Measurements on Low-Rise Pitched Roof Buildings, *J. Wind Eng. Ind. Aerodyn.* 38, 249-256
- Sadek, F. & Simiu, E. (2002). Peak Non-Gaussian Wind Effects for Database-Assisted Low Rise Building Design, *J. Eng. Mech.*, 128, 530-539
- Spence, S.M.J., Giofrè M. (2008). A Database-Assisted Design approach for Lateral Drift Optimization of Tall Buildings, *14th IFIP WG 7.5 Working Conference on Reliability and Optimization of Structural Systems (IFIP 08-WG 7.5)*, Mexico City, Mexico, August 6-9
- Spence S.M.J. (2009). High-Rise Database-Assisted Design 1.1 (HR\_DAD\_1.1): Concepts, Software, and Examples, *NIST Building Science Series 181*
- Simiu, E. (1973). Logarithmic Profiles and Design Wind Speeds, *J. Eng. Mech. Div. ASCE* 99, 1073-1083
- Simiu, E. & Scanlan, R.H. (1996). *Wind Effects on Structures: Fundamentals and Applications to Design*, 3<sup>rd</sup> Ed., Wiley, New York
- Simiu, E. & Miyata, T. (2006). *Design of Buildings and Bridges for Wind*, Wiley, Hoboken, N.J.
- Simiu, E., Gabbai, R.D., & Fritz, W.P. (2008). Wind-induced Tall Building Response: a Time-Domain Approach, *Wind and Structures*, 11, 427-440
- Simiu, E. (2011). *Designing Buildings for Wind*, Wiley, Hoboken, NJ
- Simiu, E., Bitsuamlak, G., Chowdhury, A.G., Teclé, E., Li, J. & Yeo, D. (in press). Testing of Residential Structures under Wind Loads, *ASCE Nat. Haz. Rev.*, doi:10.1061/(ASCE)NH.1527-6996.0000034
- St. Pierre, L. M., Kopp, G. A., Surry, D. & Ho, T. C. E. (2005). The UWO Contribution to the NIST Aerodynamic Database for Wind Loads on Low Buildings: Part II. Comparison of Data with Wind Load Provisions, *J. Wind Eng. Ind. Aerodyn.*, 93, 31-59
- Surry, D., Ho, T. C. E. & Kopp, G. A. (2003). Measuring Pressures Is Easy, Isn't It? *Proceedings of the International Conference on Wind Engineering*, Texas Tech University, Lubbock, Tx, 2, 2618-2623
- Tennekes, H. & Lumley, J.L. (1972). *A first course in Turbulence*, MIT Press, Cambridge, MA
- Tieleman, W.H. (1992). Problems Associated with Flow Modeling Procedures for Low-Rise Structures, *J. Wind Eng. Ind. Aerodyn.*, 41-44, 923-934
- Tieleman, W.H. (1993). Pressures on Surface-Mounted Prisms: The Effects of Incident Turbulence, *J. Wind Eng. Ind. Aerodyn.*, 49, 289-300
- Vickery, P.J. & Twisdale, L.A. (1995). Prediction of Hurricane Wind Speeds in the United States, *J. Struct. Eng.*, 121, 1691-1699
- Vickery, P.J., Wadhwa, D., Twisdale, L.A. Jr., & Lavelle, I. (2009). U.S. Hurricane Wind Risk and Uncertainty, *J. Struct. Eng.*, 13, 310-330
- Whitbread, R.E. (1980). The Influence of Shielding on the Wind Force Experienced by Arrays of Lattice Frames, *Proc. 5<sup>th</sup> Int. Conf. on Wind Engineering*, Fort Collins, Co. July 1979, J.E. Cermak ed., Pergamon Press, Elmsford, NY, *Wind Engineering*, 1, 405-420
- Zhou, Y. & Kareem, A. (2003). Aeroelastic Balance, *J. Eng. Mech.*, 129 283-292

# Tall Buildings Under Multidirectional Winds: Response Prediction and Reduction

Aly Mousaad Aly<sup>1</sup>, Alberto Zasso<sup>2</sup> and Ferruccio Resta<sup>2</sup>

<sup>1</sup>*Department of Mechanical Engineering, Faculty of Engineering, Alexandria University,*

<sup>2</sup>*Department of Mechanical Engineering, Politecnico di Milano,*

<sup>1</sup>*Egypt*

<sup>2</sup>*Italy*

## 1. Introduction

Civil engineering structures are an integral part of our modern society. Traditionally, these structures are designed to resist static loads. However, they may be subjected to dynamic loads like earthquakes, winds, waves, and traffic. Such loads can cause severe and/or sustained vibratory motion, which can be detrimental to the structure and human occupants. Because of this, safer and more efficient designs are sought out to balance safety issues with the reality of limited resources. Wind-induced vibrations in buildings are of increasing importance as the use of high-strength, lightweight materials, longer floor spans, and more flexible framing systems result in structures that are more prone to vibrations. In tall buildings, wind-induced vibrations may cause annoyance to the occupants (especially in the upper floors), impaired function of instruments, or structural damage.

Traditionally, wind-induced response of tall buildings in the along-wind direction is evaluated using some codes and formulas (ASCE 7-05 2006; Eurocode 1 2004; Simiu 2009; Chen 2010). However, these standards provide little guidance for the critical cross-wind and torsional responses. This is due to the fact that the cross-wind and torsional responses result mainly from the aerodynamic pressure fluctuations in the separated shear layers and the wake flow fields, which made it difficult to have an acceptable direct analytical relation to the oncoming velocity fluctuations (Zhou, *et al.* 2003; Kwon, *et al.* 2008). In addition, these methods may have some limitations, especially for accounting of surrounding tall buildings. Moreover, responses are restricted to some few modes and the process of evaluating such response depends on much assumption. On the other hand, wind tunnel pressure measurements and finite element modeling (FEM) of the structures are an effective alternative for determining these responses. Wind tunnel tests have been industry wide accepted reliable tools for estimating wind loads on tall buildings. For tall buildings, there are two types of testing: (1) high frequency base balance (HFBB) and (2) high frequency pressure integration (HFPI). Inherent in the HFBB approach is the fact that only the global wind loads at the base of the test model are known. The test results from the HFBB measurements can be analyzed using frequency-domain or time-domain techniques to get the building responses. The frequency domain approach has been dominant over time

domain approach for its lesser requirement of computational power though it involves more approximations compared to the time-domain approach. Nevertheless, with the current technology where computational power is no longer a problem, the time domain method is becoming a popular analysis technique. The time domain method allows determination of wind responses directly from the equation of motion using the measured time history thereby avoiding all the simplifying assumptions used in the frequency domain technique (Simiu, et al. 2008). However, even if the more accurate time domain approach is used for the analysis of the response, the three-dimensional (3D) mode shapes found in complex tall buildings complicate the use of the HFBB test results for predicting the response (Wu, et al. 2008; Huang, et al. 2010). In general, mode shape correction factors for the HFBB technique are necessary for the assessment of wind-induced responses of a tall building. This is to account for the significant uncertainties in the prediction of generalized forces due to the non-ideal mode shapes as well as presumed wind loading distributions (Tse, et al. 2009; Lam and Li 2009). HFPI with the time domain approach can be more accurate provided that enough coverage of pressure taps on the model's outer surface is performed.

HFPI technique is based on simultaneous pressure measurements at several locations on a building's outer surface. Pressure data can be used for the design of the claddings as well as the estimation of the overall design loads. The HFPI technique cancels out any inertial effects that may be included in the overall loads measured by the base balance if the HFBB technique was used. Time histories of wind forces at several levels of tall building models can be obtained in the wind tunnel with a multi-channel pressure scanning system. This enables the building responses to be computed directly in the time domain for buildings with simple or complex mode shapes. Finite element models (FEM) can be used for describing the dynamic behavior of the structures. HFPI with FEM have the advantages of considering complex shapes of structures with non-uniform mass distribution and can easily account for any required number of mode shapes to be considered in the response analysis.

Preliminary analysis of tall buildings in their preliminary design stages can help the designer to make decision like modifying the design or adding passive, active, or semi active control techniques. Structural control *has recently been the subject of much discussion among structural designers*. Structural control can potentially provide safer and more efficient structures. The concept of employing structural control to minimize structural vibrations was proposed in the 1970s (Yao 1972). The purpose of structural control is to absorb and to reflect the energy introduced by dynamic loads. The reduction of structural vibrations can be achieved by adding a mechanical system that is installed in a structure. The control of structural vibrations can also be done by various means such as modifying rigidities, masses, damping, or shape, and by providing passive or active counter forces (Housner, et al. 1997; Zhou, et al. 2008). Passive, active and semi-active (Aly and Christenson 2008a; Aly, et al. 2010) types of control strategies have been proposed.

McNamara (1977) studied the tuned mass damper (TMD) as an energy-absorbing system to reduce wind-induced structural response of buildings in the elastic range of behavior. Active control techniques are studied intensively for the control of the response of tall buildings under wind loads (Facioni, et al. 1995; Gu and Peng 2002; Lu, et al. 2003; Soong 1990; Wu and Pan 2002). The most commonly used active control device for tall buildings is the active tuned mass damper (ATMD). TMDs and ATMDs are shown to be effective in the

response reduction of tall buildings under wind loads (Aly, *et al.* 2008b; Aly 2009; Li, *et al.* 2009; Mohtat, *et al.* 2010; Park, *et al.* 2009; Homma, *et al.* 2009).

The aim of this study is to present practical procedure for the response prediction and reduction in a very slender high-rise building under multidirectional wind loads. The procedure is schematically presented in Fig. 1. Wind loads were obtained from an HFPI experiment conducted in a wind tunnel. The tower responses in the two lateral directions combined with the torsional responses (effect of higher modes on the responses is studied) are evaluated. Two important voids associated with procedures to aid in the design are considered: the first is on the distributions of the wind loads; the second is on the effects of the higher modes. Consideration of these two problems needs wind tunnel pressure measurements on the surface of the building and FEM. The building is modeled using the finite element techniques and a 3D lumped mass model. The uncontrolled responses obtained using the two techniques of modeling are compared. Active control of the structure using LQR and fuzzy logic controllers under wind that is attacking from different directions is proposed. In this study, the lateral responses of the building in the two directions are controlled at the same time, while the effects of the uncontrolled torsional responses of the structure are simultaneously considered.

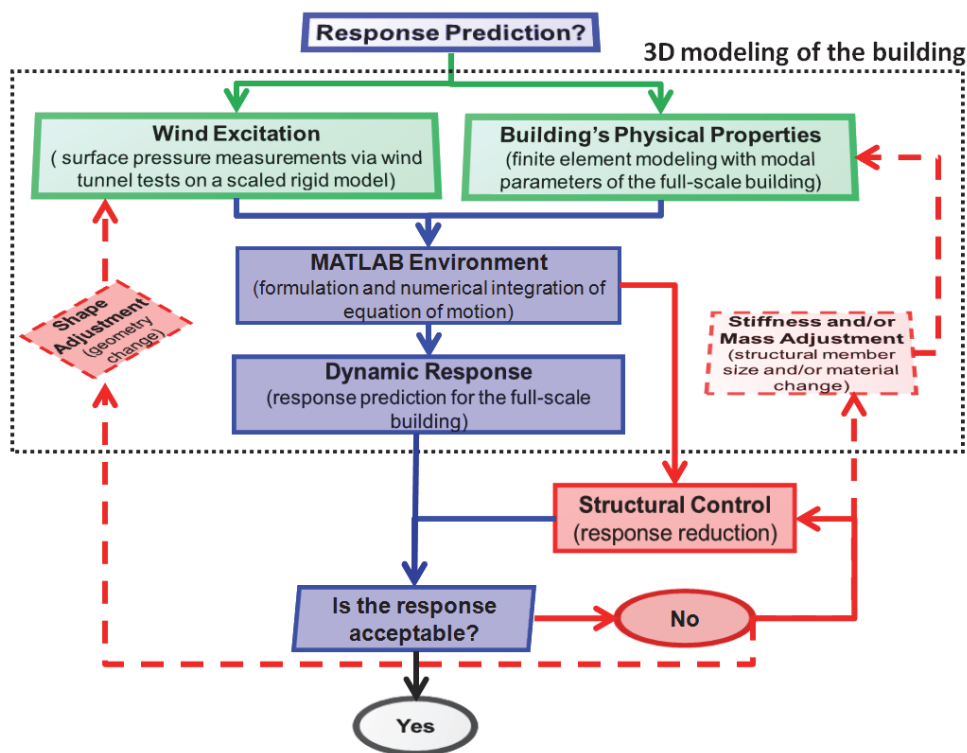


Fig. 1. Schematic Representation of the Proposed Procedure for Response Prediction and Reduction in Tall Buildings under Wind Loads

## 2. 3D modeling of tall buildings

A 48-storied steel tower proposed in Aly, *et al.* (2008b) is used in this research. The FEM of the tower, along with the coordinate system, is shown in Fig. 2. The full-scale building has a height of about 209 m and a rectangular cross section of  $B/D \approx 3$  (B: chord length, D: thickness). The aspect ratio in the y-direction is about 11, which makes it very sensitive to strong winds. Modal parameters of the FEM for the first six modes are given in Table 1.

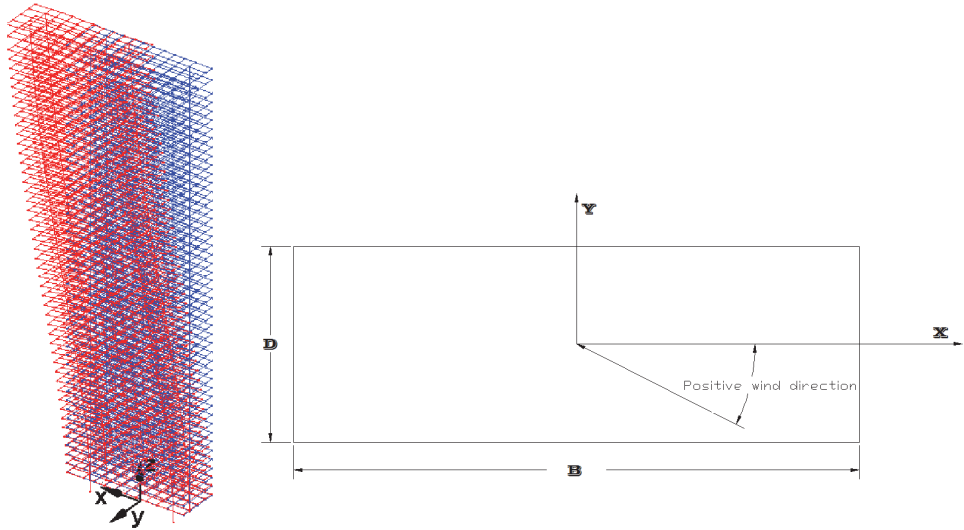


Fig. 2. Finite Element Model with the Coordinate System and Wind Direction ( $B = 57.6$  m and  $D = 19$  m).

Mode Number *	Generalized Mass $\times 10^7$ (kg.m <sup>2</sup> )	Generalized Stiffness $\times 10^9$ (N.m)	Frequency (Hz)	Modal Damping
1	1.2953	0.0147	0.1694	0.0102
2	0.9937	0.0178	0.2132	0.0112
3	0.4945	0.0222	0.3370	0.0150
4	0.8724	0.1115	0.5689	0.0234
5	0.8273	0.2153	0.8120	0.0326
6	0.3544	0.1600	1.0695	0.0426

\* Modes 1 and 4 are lateral displacements in x-direction; modes 2 and 5 are lateral disp. in y-direction while modes 3 and 6 are torsion

Table 1. Modal Parameters of the FEM Model

## 2.1 Equations of motion in modal form

Equations of motion governing the behavior of the structure under wind loads are

$$\mathbf{M}\ddot{\mathbf{X}} + \mathbf{C}\dot{\mathbf{X}} + \mathbf{K}\mathbf{X} = \mathbf{F}(t) \quad (1)$$

where  $\mathbf{X} = [\mathbf{x} \ \mathbf{y}]^T$  is a  $2n \times 1$  vector and  $n$  is the number of nodes while  $\mathbf{x}$  and  $\mathbf{y}$  are vectors of nodal displacements in  $x$  and  $y$  directions respectively.  $\mathbf{F}(t) = [\mathbf{F}_x(t) \ \mathbf{F}_y(t)]^T$ , in which  $\mathbf{F}_x(t)$  and  $\mathbf{F}_y(t)$  are  $n \times 1$  vectors of external forces acting in  $x$  and  $y$  directions respectively. Using the first  $N$  modes obtained by FEM with the next transformation

$$\mathbf{X} = \Phi \mathbf{Q} \quad (2)$$

where  $\Phi$  is  $2n \times N$  matrix of eigenvectors and  $\mathbf{Q}$  is  $N \times 1$  vector of generalized displacements, i.e.

$$\Phi = \begin{bmatrix} \phi_1(x_1) & \phi_2(x_1) & \dots & \phi_N(x_1) \\ \phi_1(x_2) & \phi_2(x_2) & \dots & \phi_N(x_2) \\ \vdots & \vdots & \ddots & \vdots \\ \phi_1(x_n) & \phi_2(x_n) & \dots & \phi_N(x_n) \\ \phi_1(y_1) & \phi_2(y_1) & \dots & \phi_N(y_1) \\ \phi_1(y_2) & \phi_2(y_2) & \dots & \phi_N(y_2) \\ \vdots & \vdots & \ddots & \vdots \\ \phi_1(y_n) & \phi_2(y_n) & \dots & \phi_N(y_n) \end{bmatrix}, \quad \mathbf{Q} = \begin{Bmatrix} q_1 \\ q_2 \\ \vdots \\ q_N \end{Bmatrix}. \quad (3)$$

Substituting by Eq. (2) into Eq. (1) and premultiplying by  $\Phi^T$ , one obtains

$$\Phi^T \mathbf{M} \Phi \ddot{\mathbf{Q}} + \Phi^T \mathbf{C} \Phi \dot{\mathbf{Q}} + \Phi^T \mathbf{K} \Phi \mathbf{Q} = \Phi^T \mathbf{F}(t). \quad (4)$$

By assuming the damping matrix,  $\mathbf{C}$ , to be proportional damping, Eq. (4) results into six uncoupled equations

$$\left. \begin{aligned} m_{11}\ddot{q}_1 + c_{11}\dot{q}_1 + k_{11}q_1 &= \sum_{i=1}^n \phi_1(x_i) F_{x,i}(t) + \sum_{i=1}^n \phi_1(y_i) F_{y,i}(t) = GF_1 \\ m_{22}\ddot{q}_2 + c_{22}\dot{q}_2 + k_{22}q_2 &= \sum_{i=1}^n \phi_2(x_i) F_{x,i}(t) + \sum_{i=1}^n \phi_2(y_i) F_{y,i}(t) = GF_2 \\ &\vdots \\ m_{NN}\ddot{q}_N + c_{NN}\dot{q}_N + k_{NN}q_N &= \sum_{i=1}^n \phi_N(x_i) F_{x,i}(t) + \sum_{i=1}^n \phi_N(y_i) F_{y,i}(t) = GF_N \end{aligned} \right\} \quad (5)$$

where  $m_{ii}$ ,  $c_{ii}$ ,  $k_{ii}$ , and  $GF_i$  are generalized mass, generalized damping, generalized stiffness, and generalized force of the  $i^{\text{th}}$  mode respectively. Using the measurements obtained by the pressure transducers, pressure coefficients (matrix  $\mathbf{C}_p$ ) are evaluated at each tap location as a function of time. These values are used with the full-scale model (prototype) to give the pressure distribution on the surface. The pressure values on the surface of the prototype can be calculated as

$$\mathbf{P}(space, time) = \frac{1}{2} \rho U^2 \mathbf{C}_p(space, time) \quad (6)$$

where  $\mathbf{P}(space, time)$  is a matrix containing the pressure values on the surface of the full scale model as a function of space ( $x$ ,  $y$ , and  $z$ ) and time;  $\rho$  is the air density which is assumed to be  $1.25 \text{ kg/m}^3$  (according to Eurocode 1 2004), and  $U$  is the prototype mean wind speed. The wind load at any node of the outer surface is the integration of the pressure over the surface area in the vicinity of the node as

$$\mathbf{F}(nodes, time) = \int \mathbf{P}(space, time) dA. \quad (7)$$

This means that once the time history of the pressures on the outer surfaces is calculated, the external forces acting on the nodes of the surface can be computed. The excitation forces acting on the internal nodes are of course equal to zero. The  $q_i(t)$  are then solved from each of Eq. (5). SIMULINK is used for the numerical solution of these equations (MATLAB 2008).

## 2.2 3D lumped mass model

For control purposes, a 3D lumped mass model is derived from the original FEM. In this model, the total mass of the building was assumed to be lumped at the positions of the floors, and it was assumed for the floors to perform a general 3D movement (each floor has two translations in the  $x$  and  $y$  directions in addition to the torsional rotation). The building alone (without the control devices) is modeled dynamically using a total of 144 degree-of-freedom. In general, the equations of motion for an  $n$ -story building moving in both the two transverse directions and in torsion are written as

$$\mathbf{M}_s \ddot{\mathbf{x}} + \mathbf{C}_s \dot{\mathbf{x}} + \mathbf{K}_s \mathbf{x} = -\mathbf{F} + \mathbf{\Lambda} \mathbf{f} \quad (8)$$

where  $\mathbf{x} = [\mathbf{X} \ \mathbf{Y} \ \mathbf{\Theta}]^T$ . The terms  $\mathbf{X} = [x_1 \ x_2 \ \dots \ x_n]$  and  $\mathbf{Y} = [y_1 \ y_2 \ \dots \ y_n]$  are row vectors of the displacements of the centre of mass of each floor in the  $x$  and  $y$  directions respectively, and  $\mathbf{\Theta} = [\theta_1 \ \theta_2 \ \dots \ \theta_n]$  is the vector of the rotations of each floor about the vertical axis ( $z$ -axis) while  $n$  is the number of stories. The mass matrix,  $\mathbf{M}_s$ , and the stiffness matrix,  $\mathbf{K}_s$ , have the following form

$$\mathbf{M}_s = \begin{bmatrix} \mathbf{M} & \mathbf{0} & \mathbf{0} \\ \mathbf{0} & \mathbf{M} & \mathbf{0} \\ \mathbf{0} & \mathbf{0} & \mathbf{I} \end{bmatrix}, \quad \mathbf{K}_s = \begin{bmatrix} \mathbf{K}_x & \mathbf{0} & \mathbf{0} \\ \mathbf{0} & \mathbf{K}_y & \mathbf{0} \\ \mathbf{0} & \mathbf{0} & \mathbf{K}_\theta \end{bmatrix} \quad (9)$$

where  $\mathbf{M} = \text{diag}([m_1 \ m_2 \ \dots \ m_n])$  is a diagonal matrix of lumped masses,  $\mathbf{I} = \text{diag}([I_1 \ I_2 \ \dots \ I_n])$  in which  $I_i$  is the moment of inertia of the  $i^{\text{th}}$  floor,  $\mathbf{K}_x$ ,  $\mathbf{K}_y$  and  $\mathbf{K}_\theta$  are the stiffness matrices in the transverse directions ( $x$  and  $y$ ) and the torsional direction, respectively. The stiffness matrix of the spatial model (3D lumped mass model) is obtained by assuming the stiffness between floors as a combination of cantilever and shear rigidities. MATLAB codes (MATLAB 2008; Attaway 2009) were written and used to derive the best stiffness matrix that gives the closest mode shapes to those of the FEM and the same first six natural frequencies. In Eq. (8), the disturbance  $\mathbf{F} = [\mathbf{F}_x \ \mathbf{F}_y \ \mathbf{T}]^T$  is a vector of excitation in which  $\mathbf{F}_x$  and  $\mathbf{F}_y$  are two vectors of the horizontal loads acting in the  $x$  and  $y$  directions respectively, and  $\mathbf{T}$  is a vector of the external torsional wind loads. Also,  $\mathbf{f}$  is the vector of control forces, where its coefficient matrix  $\mathbf{\Lambda}$  is the matrix determined by the location of control devices.



Wind loading vectors ( $F_x$ ,  $F_y$ , and  $T$ ) lumped at the position of floors are obtained from wind tunnel pressure tests conducted at the wind tunnel of Politecnico di Milano (Diana et al., 1998) on a scaled 1:100 rigid model of the tower (Fig. 3 and Fig. 4). Such large-scale allows for the advantage of testing the model at high Reynolds number with minimum blockage due to the huge dimensions of the test section. Pressure taps were distributed on the outer surface of the test model. To allow for sufficient pressure measurements (see Simiu, *et al.* 2008), 400 taps were mapped on the outer surface of the model. Pressure taps were distributed to cover the entire outer surface with more intense at the upper part of the test model [see Fig. 5(a)]. Pressure data were integrated on the outer surface of the building [see Fig. 5(b)] to obtain the corresponding time history of the two directional wind loads at each floor in addition to torsion. For the estimation of the wind loads at each floor, the tributary area for each floor was gridded into smaller areas and the time history of the wind loads at each area was found by using the  $C_p$  records of the closest pressure tap (see Fig. 6). Codes were written in MATLAB to estimate the time histories of the wind forces acting at the center of each smaller area. After that, the floor forces in the two directions were obtained from the summation of the forces in each lateral direction. The torsion at each floor was the resultant of the summation of the force moments about the floor center. The surrounding buildings within a radius of 500 m from the centre of the tower were also scaled 1:100 to be presented on the turning test table according to the type of the test configuration used. The wind profile represents a typical urban terrain as shown in Fig. 3 (Zasso, *et al.* 2005). The reference mean wind speed ( $U_{ref}$ ) was measured at a height of 1 m. Prototype reference mean wind speed is assumed to be 30 m/s. The target for the wind profiles is the Eurocode 1 (2004). The turbulence intensities in the longitudinal, lateral, and vertical directions are referred to by  $I_u$ ,  $I_v$ , and  $I_w$  respectively. Two different test configurations with the same wind profile are considered (see Fig. 4). In the first configuration, the building is subjected to the wind load without the existence of other tall buildings, and is referred to as Config. # 1. In the second configuration, the rigid model of the building was tested with the existence of all the surrounding buildings. This configuration is referred to as Config. # 2. Further details about the wind tunnel experiment are given in Aly (2009).

Due to the fact that the building's mass is symmetrical, and the study is based on the assumption that the structure is responding in the linear region, lateral and torsional behavior of the building may be studied alone, then the response time histories may be combined simultaneously. In this study, the plane motion of the structure in the x-direction is controlled using both the TMDs and ATMDs. However, due to the fact that the controlling the response in the x-direction will not affect the response of the building in the y-direction, another TMD and ATMD are designed to control the lateral in-plane response in the y-direction. Following that, the uncontrolled torsional response is added simultaneously to the two lateral responses to give the overall response in the two lateral directions.

The state reduction approach derived by Davison (1966) and summarized later in Wu et al. (1998) is used in this study (also see Lu et al., 2003). In this approach, the 48 degree-of-freedom (DOF) in-plane system is reduced to 15 DOF, where the first 30 modes are retained (Aly, *et al.* 2008c). Note that a condition for this approach was that the response in terms of displacements and accelerations of the 15 DOF and 48 DOF are very much the same (see section 4). This model is referred to as Reduced Order System (ROS). The addition of the TMD increases the DOF to 16. The system with the TMD is referred to as ROS-TMD. In a similar task, ROS-ATMD refers to ROS utilizing ATMD.

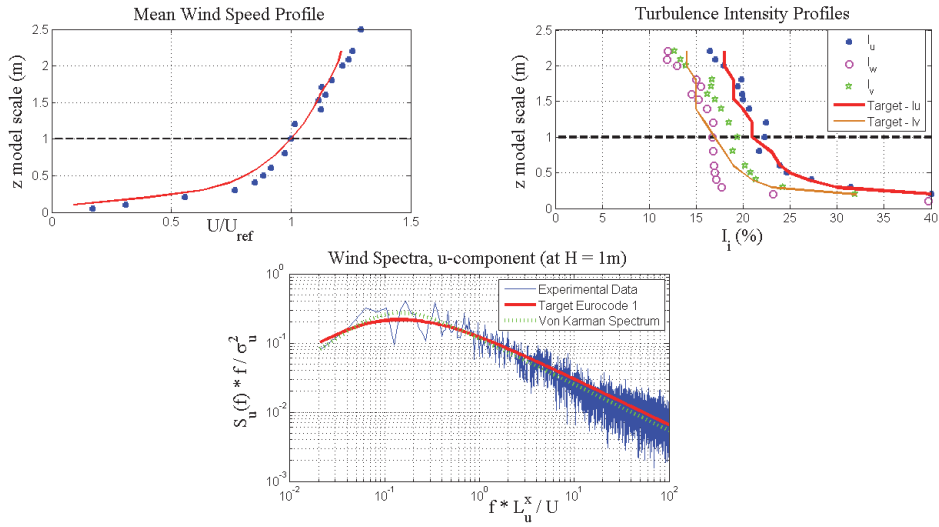


Fig. 3. Mean Wind Speed Profile, Turbulence Intensity Profiles, and Wind Spectra (L is the Integral Scale)

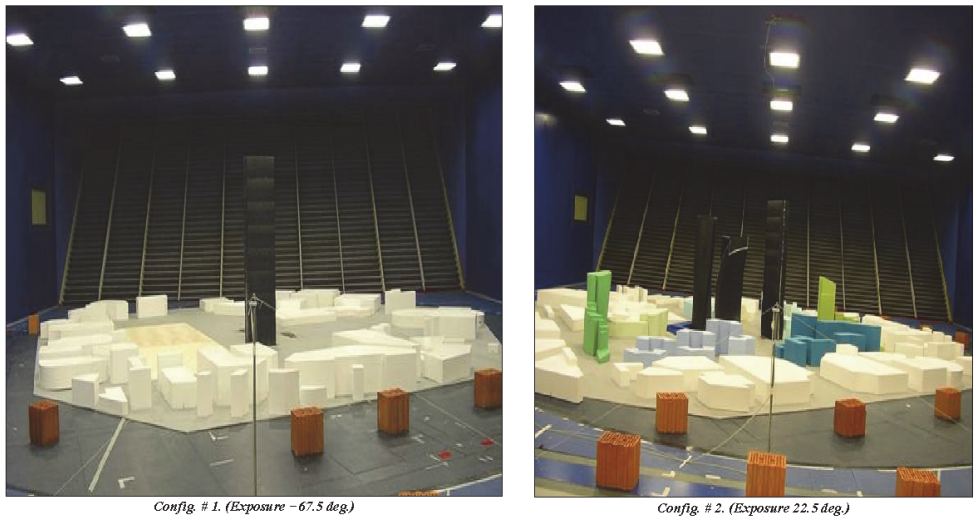


Fig. 4. Two Different Configurations were used

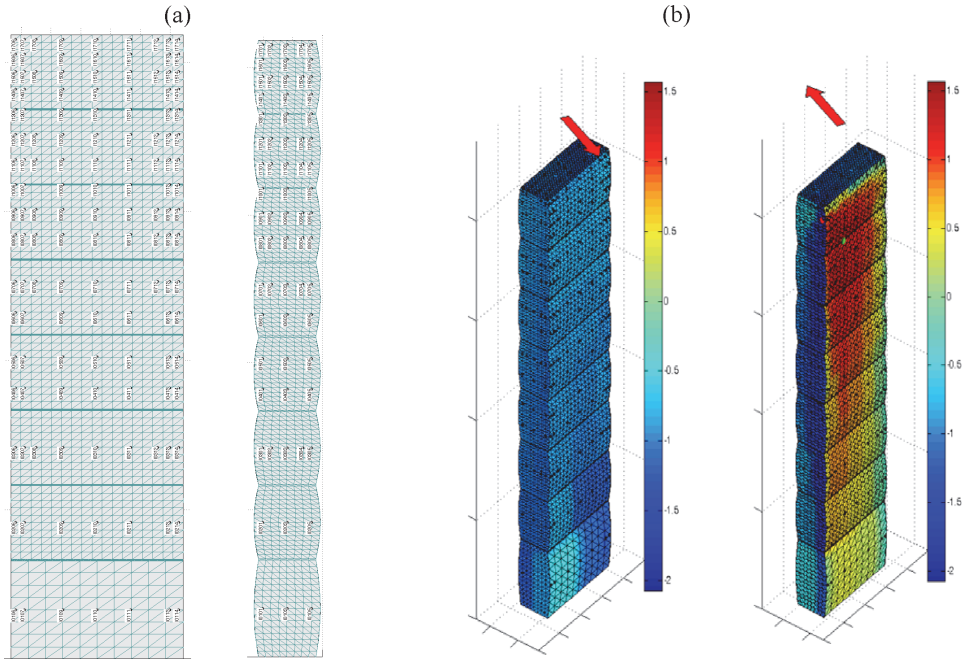


Fig. 5. Pressures on the Outer Surfaces of a Scaled 1:100 Model were Obtained from a Wind Tunnel Test: (a) Pressure Tap Distribution (Elevation and Side View), (b) Mean Surface Pressure Coefficient Distribution (for 292.5 deg)

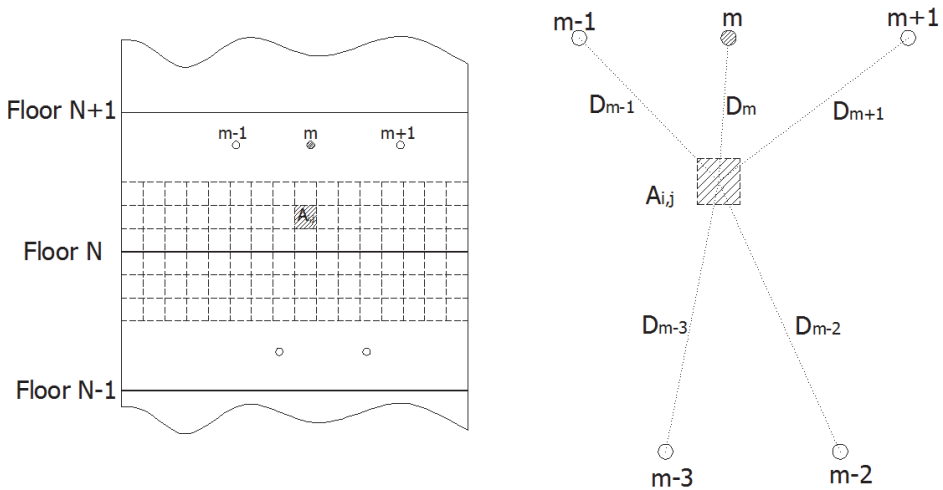


Fig. 6. Wind Load Estimation from Pressure Data: The Tributary Area of Floor N was Divided into Smaller Areas; Pressure Forces Acting on each Smaller Area,  $A_{i,j}$ , were Calculated Based on Pressure Data at the Nearest Pressure Tap, m

The state equation of the ROS that corresponds to the full order system (FOS) in Eq. (8) can be expressed as

$$\dot{\mathbf{z}} = \mathbf{A}\mathbf{z} + \mathbf{B}f + \mathbf{E}\mathbf{w} \quad (10)$$

in which  $\mathbf{z} = [\bar{\mathbf{X}}'; \dot{\bar{\mathbf{X}}}']$  is the 32-dimensional state vector,  $\bar{\mathbf{X}}$  is a vector of the in-plane displacements of floors 3, 6, 9, 12, 16, 19, 22, 26, 29, 32, 35, 38, 41, 44 and 48 in addition to the displacement of the inertial mass of the damper.  $\mathbf{A}$  is a (32×32) system matrix,  $\mathbf{B}$  is a 32 location vector, and  $\mathbf{E}$  is a 32 excitation vector. In this reduced system, the wind loads acting on each of the 15 floors are computed from the wind loads  $\mathbf{F}$  acting on each of the 48 floors by lumping wind forces on adjacent floors at the locations that correspond to the 15 DOF model.

The controlled output vector,  $\mathbf{y}_c$  and the measured output,  $\mathbf{y}_m$ , of the ROS described by Eq. (10) can be expressed as

$$\begin{aligned} \mathbf{y}_c &= \mathbf{C}_c\mathbf{z} + \mathbf{D}_c f + \mathbf{F}_c\mathbf{w}_x \\ \mathbf{y}_m &= \mathbf{C}_m\mathbf{z} + \mathbf{D}_m f + \mathbf{F}_m\mathbf{w}_x + \nu \end{aligned} \quad (11)$$

where  $\mathbf{C}_c$ ,  $\mathbf{D}_c$ ,  $\mathbf{F}_c$ ,  $\mathbf{C}_m$ ,  $\mathbf{D}_m$  and  $\mathbf{F}_m$  are matrices with appropriate dimensions and  $\nu$  is the measurement noise vector. The model used for controller design was further reduced as follows:

$$\left. \begin{aligned} \dot{\mathbf{z}}_r &= \mathbf{A}_r\mathbf{z}_r + \mathbf{B}_r f + \mathbf{E}_r\mathbf{w}_x \\ \mathbf{y}_{cr} &= \mathbf{C}_{cr}\mathbf{z}_r + \mathbf{D}_{cr} f + \mathbf{F}_{cr}\mathbf{w}_x \\ \mathbf{y}_{mr} &= \mathbf{C}_{mr}\mathbf{z}_r + \mathbf{D}_{mr} f + \mathbf{F}_{mr}\mathbf{w}_x + \nu_r \end{aligned} \right\} \quad (12)$$

where  $\mathbf{z}_r$  is a 6-dimensional state vector of the reduced order system;  $\mathbf{y}_{cr}$  is a controlled output vector identical of  $\mathbf{y}_c$  defined by Eq. (11);  $\mathbf{y}_{mr}$  is the measured output vector;  $\nu_r$  is the measurement noise and  $\mathbf{C}_{cr}$ ,  $\mathbf{D}_{cr}$ ,  $\mathbf{F}_{cr}$ ,  $\mathbf{C}_{mr}$ ,  $\mathbf{D}_{mr}$  and  $\mathbf{F}_{mr}$  are appropriate matrices.

### 3. Controllers and limitations

In this study, both TMDs and ATMDs are used for the reduction of the lateral responses of the building. However, in order to make the design of such control systems more realistic and applicable, the following restrictions and assumption were applied:

- The mass of the TMD in the x-direction is 100 ton, while the mass of the TMD in the y-direction is 150 ton. Such restrictions are applied to avoid excessive weight on the roof (the overall mass on the roof is about 0.625% of the overall building's mass).
- The TMDs are tuned to the first vibrational mode in each corresponding lateral direction. The damping factor is taken to be 20% of the critical. This amount of damping is selected higher than the optimal value for the sake of restricting the stroke of the ATMDs.
- The maximum stroke of the actuators is restricted to 1.5 m.
- The maximum control force of the actuator in the y-direction is restricted to 100 kN, and that in the x-direction is restricted to 25 kN.
- The computational delay and the sampling rate of the digital controller are 0.001 s.
- Three acceleration measurements are available for each lateral direction.

Note that the tower required a TMD with heavier mass and ATMD with higher control force in one lateral direction than the other, which was basically attributed to geometry.

A Linear-quadratic regulator (LQR) design with output weighting is selected to give the desired control force using the MATLAB function (*lqry.m*). The state-feedback law  $f = -\mathbf{G}z_r$  minimizes the cost function

$$J(f) = \int_0^{\infty} (\mathbf{y}'_{mr} \mathbf{Q} \mathbf{y}_{mr} + f' \mathbf{R} f) dt \quad (13)$$

where  $\mathbf{G}$  is the feedback gain matrix,  $z_r$  is a 6-dimensional state vector of the reduced order system,  $y_{mr}$  is the measured output vector, the symbol ( $'$ ) denotes transpose,  $\mathbf{Q}$  and  $\mathbf{R}$  are weighting matrices. Parametric studies were performed with various weighting matrices  $\mathbf{Q}$ , corresponding to various regulated output vectors. The results of these parametric studies indicated that an effective controller could be designed by selecting a vector of regulated responses to include the velocities of each floor.

For comparison reasons, fuzzy logic controllers are used in this study to command the actuators of the ATMDs (see Nguyen et al. 2003). From a design point of view, fuzzy logic controllers do not require the complexity of a traditional control system. The measured accelerations can be used directly as input to the fuzzy controller. The main advantages of using a fuzzy control algorithm are summarized in Battaini, *et al.* (1998) and Samali, *et al.* (2004). According to Samali, *et al.* (2004), uncertainties of input data are treated in a much easier way by fuzzy control theory than by classical control theory. Since fuzzy controllers are based on linguistic synthesis, they possess inherent robustness. Fuzzy controllers can be easily implemented in a fuzzy chip with immediate reaction time and autonomous power supply. Furthermore, the design of fuzzy controller does not require state reduction or concerning about observers. Only two acceleration measurements were used (floor 30 and roof).

The input variables to the fuzzy controller were selected as accelerations of floors 30 and 48, and the output as the control force. The membership functions for the inputs were defined and selected as seven triangles with overlaps as shown in Fig. 7. For the output, they were defined and selected as nine triangles with overlaps as shown in Fig. 8. The fuzzy variables used to define the fuzzy space are ZR (zero), PVS (positive very small), PS (positive small), PM (positive medium), PL (positive large), PVL (positive very large), NVS (negative very small), NS (negative small), NM (negative medium), NL (negative large), and NVL (negative very large). The rule-base for computing the desired current is presented in Table 2 (Samali, et al. 2004).

Acceleration of 48th floor	Acceleration of 30th floor						
	NL	NM	NS	ZR	PS	PM	PL
NL	PVL	PVL	PL	PVS	ZR	ZR	ZR
NM	PL	PL	PM	PVS	ZR	ZR	ZR
NS	ZR	NVS	PM	PS	PVS	ZR	ZR
ZR	ZR	ZR	NVS	ZR	PVS	ZR	ZR
PS	ZR	ZR	NVS	NS	NM	PVS	ZR
PM	ZR	ZR	ZR	NVS	NM	NL	NL
PL	ZR	ZR	ZR	NVS	NL	NVL	NVL

Table 2. Control Rule Base (Samali, *et al.* 2004)

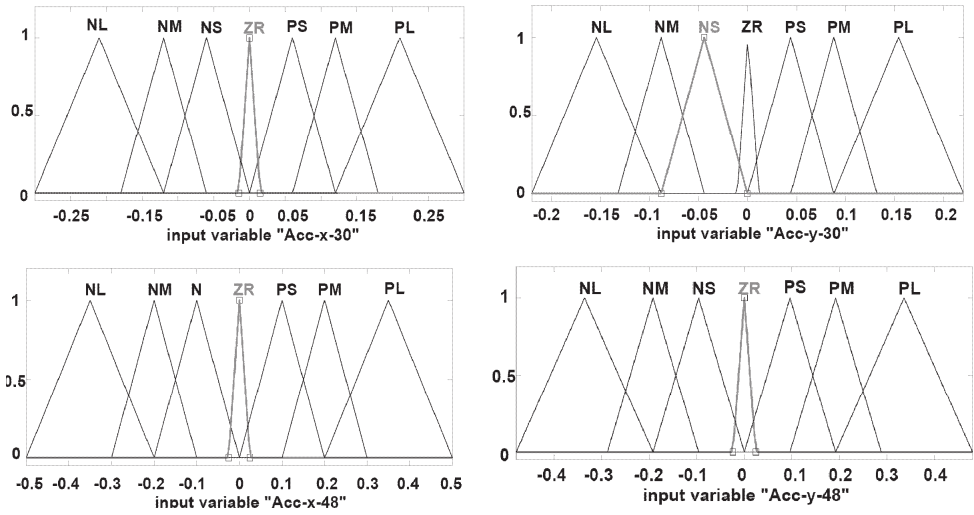


Fig. 7. Membership Functions for the Input Measured Accelerations in the x-direction (Acc-x-30, Acc-x-48) and the y-direction (Acc-y-30, Acc-y-48)

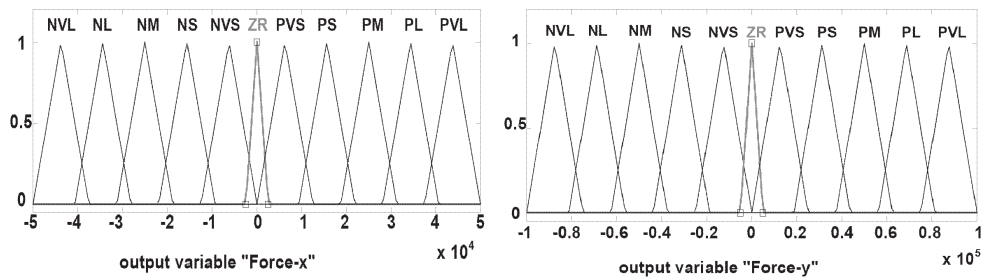


Fig. 8. Membership Functions for the Output Control Force in the x-direction (Force-x) and the y-direction (Force-y)

#### 4. Results and discussion

Table 3 gives the response of the top corner of the building in the y-direction for an incident angle of  $0^\circ$  under different consideration of mode shapes. It is shown that the displacement response of this building is dominated by the first lateral mode in the y-direction (modes 1:2 in the table). Nevertheless, this underestimates the displacement response by 3 % to 4.4 % and the acceleration response by about 12 % to 17 %. Note that the aspect ratio of this building in the y-direction is about 11. This means that for very slender buildings, solo consideration of the first lateral mode may lead to significant error in the estimation of the response, especially for the acceleration response. Table 4 lists the response of the top corner of the tower in the x-direction for an incident angle of  $90^\circ$  under different consideration of mode shapes. It is shown that the displacement and acceleration response are dominated by the first lateral mode in the x-direction (modes 1 in the table). Note that the aspect ratio of this building in the x-direction is about 3.6. This means that for buildings with low aspect ratio, solo consideration of the first lateral mode may be sufficient for the estimation of the response. Fig. 9 shows the power spectra of the acceleration response of the top corner of the building in the two lateral directions. The figure shows that the third mode (torsion) contributes significantly to the acceleration in the y-direction. In general, results given by Table 3, Table 4, and Fig. 9 show that the responses of tall buildings under winds are dominated by the first few modes (for this specific building, the first two lateral modes and the first torsional mode can be sufficient).

Mode	RMS-disp. (m)	Max-disp. (m)	RMS-accel. (m/s <sup>2</sup> )	Max-accel. (m/s <sup>2</sup> )
1	0.000 (-100 %)	0.001 (-99.8 %)	0.000 (100 %)	0.001 (-99.9 %)
1:2	0.129 (-4.4 %)	0.587 (-2.8 %)	0.199 (-17.1 %)	0.855 (-11.8 %)
1:3	0.136 (0.7 %)	0.613 (1.5 %)	0.238 (-0.8 %)	0.980 (1.1 %)
1:4	0.136 (0.7 %)	0.613 (1.5 %)	0.238 (-0.8 %)	0.980 (1.1 %)
1:5	0.135 (0 %)	0.606 (0.3 %)	0.239 (-0.4 %)	0.966 (-0.3 %)
1:6	0.135 (0 %)	0.604 (0 %)	0.240 (0 %)	0.969 (0 %)

Table 3. Response of the Top Corner of the Tower in the y-direction for an Incident Angle of  $0^\circ$

Mode	RMS-disp. (m)	Max-disp. (m)	RMS-accel. (m/s <sup>2</sup> )	Max-accel. (m/s <sup>2</sup> )
1	0.188 (1.1 %)	0.646 (-0.5 %)	0.203 (-0.5 %)	0.654 (-3.5 %)
1:2	0.188 (1.1 %)	0.646 (-0.5 %)	0.203 (-0.5 %)	0.654 (-3.5 %)
1:3	0.187 (0.5 %)	0.648 (-0.2 %)	0.204 (0 %)	0.653 (-3.7 %)
1:4	0.186 (0 %)	0.649 (0 %)	0.204 (0 %)	0.676 (-0.3 %)
1:5	0.186 (0 %)	0.649 (0 %)	0.204 (0 %)	0.676 (-0.3 %)
1:6	0.186 (0 %)	0.649 (0 %)	0.204 (0 %)	0.678 (0 %)

Table 4. Response of the Top Corner of the Tower in the x-direction for an Incident Angle of  $90^\circ$

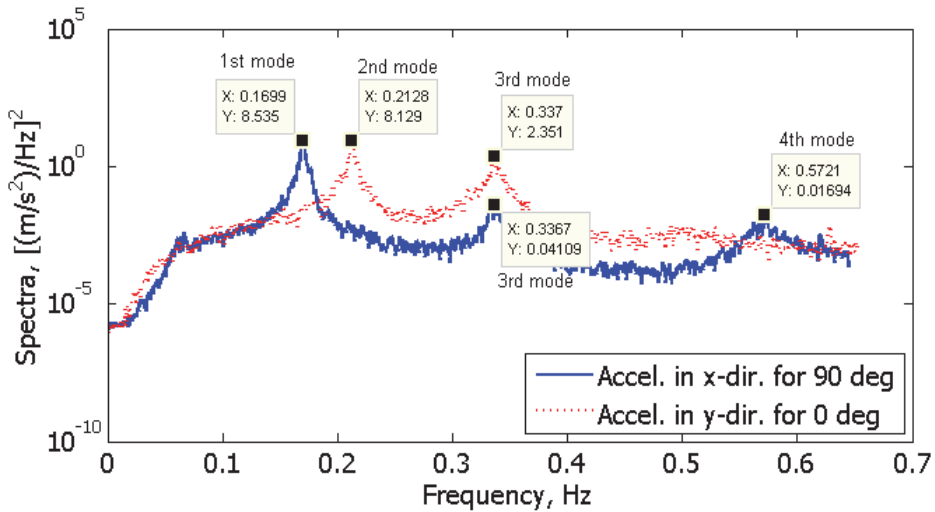


Fig. 9. Power Spectra of the Acceleration Response of the Top Corner of the Building in the Two Lateral Directions

Fig. 10 gives displacement and acceleration responses of a point at the top corner of the building for the FEM, the 3D full order system (3D-FOS), and the 3D reduced order system (3D-ROS). The figure shows that the response in terms of displacements and accelerations for the three types of modeling are very much the same. This means that FE modeling, 3D lumped mass modeling, and 3D reduced order modeling of tall buildings under wind loads can give an accurate assessment of the response provided that the first dominant modes are retained. The figure shows also that the cross-wind response is higher than the along-wind response. This reveals the importance of the procedure proposed in this study as many design codes and formula may provide accurate estimate of the along-wind response but less guidance for the estimation of the critical cross-wind and torsional response. The results show that the building is very much vulnerable to wind loads. This may be due to its low weight along with low dominant frequencies.

The building required a TMD with heavier mass and ATMD with higher control force in one lateral direction than the other. This may be attributed to geometry. Figures 11-14 show the controlled and uncontrolled responses of the tower under wind loads for two test configurations at different incident angles. Two examples of control are considered, TMDs and ATMDs with LQR and fuzzy logic controllers. For each example, the controlled responses in the x and y directions are plotted with the uncontrolled responses. The controlled and uncontrolled responses of the tower are evaluated by simulations (MATLAB 2008). Four evaluation criteria are used to examine the performance of the proposed controllers. Evaluation criteria include: rms-displacements, maximum displacements, rms-accelerations, and maximum accelerations of the top corner of the tower in the two lateral directions. The figures are superimposed by ellipses indicating the position of the most unfavourable responses (uncontrolled, with TMDs, with ATMDs [LQR], and with ATMDs [fuzzy]) over the two configurations in both x and y directions. The percentage of reduction in the highest response achieved by TMDs and ATMDs over the worst uncontrolled response is indicated in the figures.



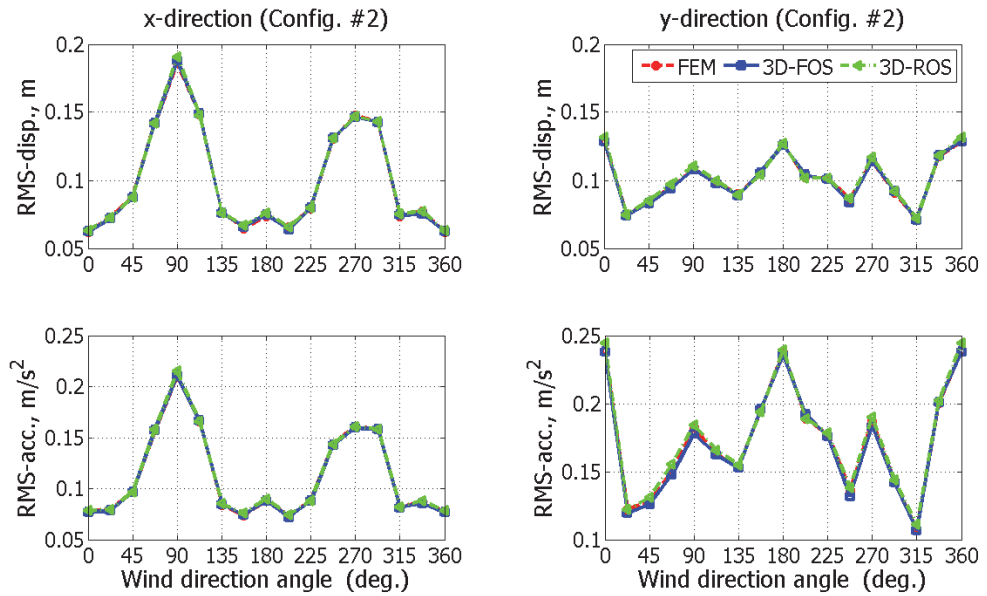


Fig. 10. Displacement and Acceleration Responses of a Point at the Top Corner for FEM, 3D Full Order System (3D-FOS), and 3D Reduced Order System (3D-ROS)

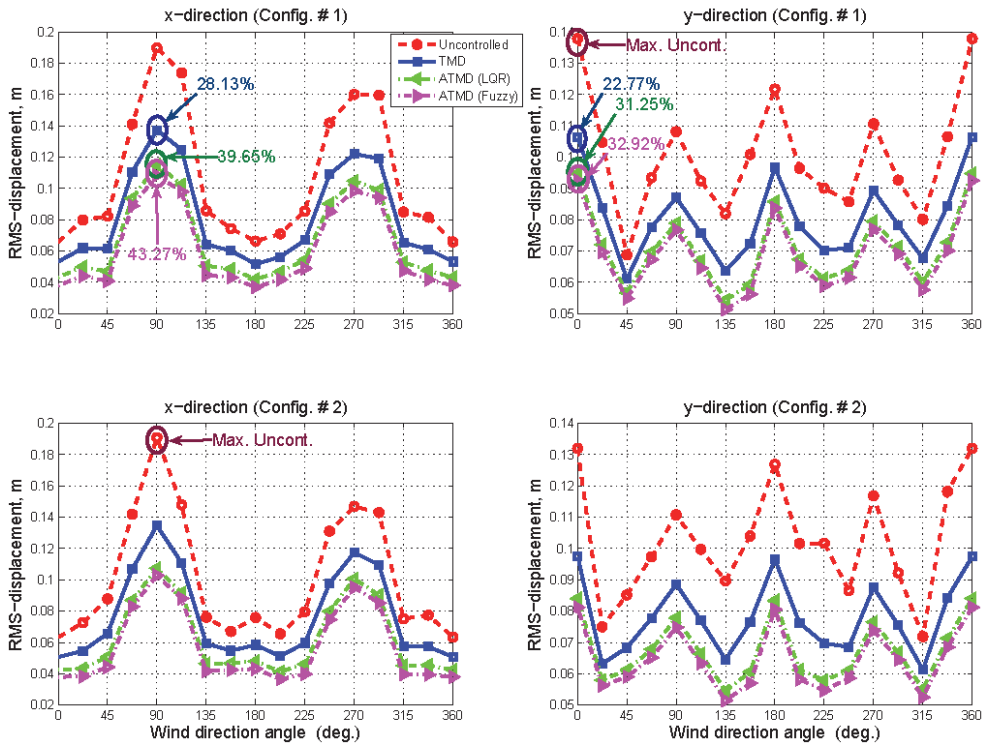


Fig. 11. RMS-Displacements of the Top Corner of the Tower

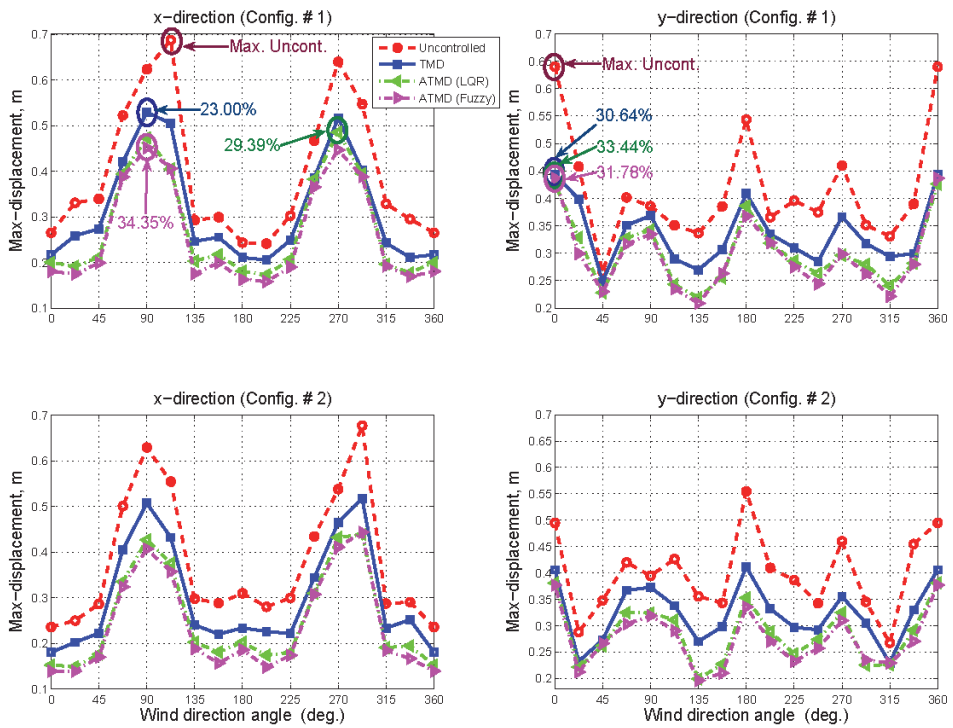


Fig. 12. Maximum Displacements of the Top Corner of the Tower

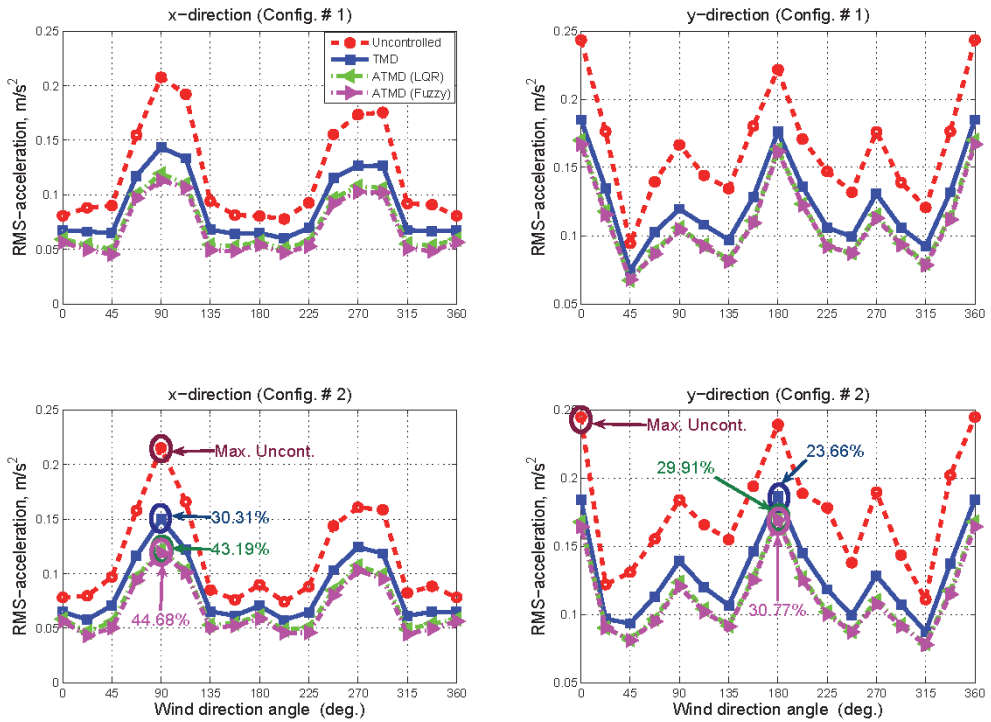


Fig. 13. RMS-accelerations of the Top Corner of the Tower

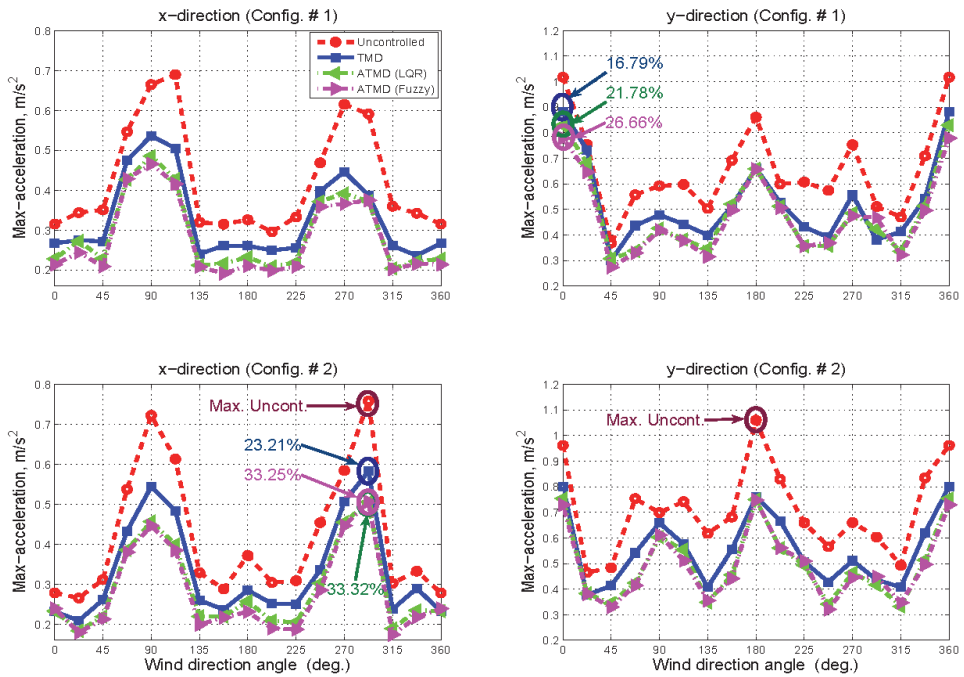


Fig. 14. Maximum Accelerations of the Top Corner of the Tower

Figures 11 and 12 give controlled and uncontrolled rms-displacements and max-displacements of the top corner of the tower in both the x and y directions. It is shown that TMDs have a great effect on the reduction of the displacement response of the building. Reductions achieved by TMDs in the displacements responses range from 22-30 % over the worst uncontrolled response. Generally, TMDs are able to give good reduction in the rms-displacements in both the x and y directions for all wind incident angles. Reductions achieved by ATMDs in the displacement responses range from 29-43 % over the worst uncontrolled response. ATMDs with fuzzy logic controllers are able to enhance the reduction in the displacement responses over LQR most of the time (by about 1% to 5%). They also have a general similar trend over all of the wind attack angles.

Figures 13 and 14 give controlled and uncontrolled rms-accelerations and maximum accelerations of the top corner of the tower in both the x and y directions. It is shown that the TMDs have a significant effect on the reduction of the acceleration response of the building. Reductions achieved by TMDs in the acceleration responses range from 16-30 % over the worst uncontrolled response.

Generally, TMDs are able to give good reduction in the rms-displacements in both the x and y directions for all of the wind incident angles. However, the performance is limited in reducing the along-wind maximum acceleration of the tower in the y-direction under Config. # 2, when the wind attack angle is  $90^\circ$ . This may be due to the interference effects of two high-rise buildings in the oncoming wind (see Fig. 4). Results also show that ATMDs are able to enhance the reduction in the responses. Reductions achieved by ATMDs in the acceleration responses range from 21-43 % over the worst uncontrolled response. ATMDs with fuzzy logic controllers are able to enhance the reduction in the acceleration responses like LQR, and in general, they have a similar trend over all of the wind incident angles.

As a general comment on Figures 11-14, one can see that the performance of the controllers is much better in the x-direction. In addition, the capability of the controllers to reduce the responses (especially maximum accelerations at angles  $0^\circ$  and  $180^\circ$ ) in the y-direction is limited. This may be due to the effect of vortex shedding on the across-wind responses. Moreover, the structure is slender in x-direction (see Fig. 2). The structure is also stiffer in the y-direction (see Table 1 for natural frequencies). However, the procedure presented in this study permits the response of tall buildings to be assessed and controlled in the preliminary design stages which can help decision makers, involved in the design process, to choose among innovative design solutions like structural control, considering several damping techniques, modifying geometry, or even changing materials (e.g., from steel to concrete).

## 5. Conclusions

This chapter presents practical procedure for the response prediction and reduction in high-rise buildings under wind loads. To show the applicability of the procedure, aerodynamic loads acting on a quasi-rectangular high-rise building based on an experimental approach (surface pressure measurement) are used with a mathematical model of the structure for the response prediction and reduction. The building represents a case study of an engineered design of a very slender tower that is instructive. The conclusions can be summarized as follows:

1. The methodology based on HFPI and FEM proposed for the estimation of the response of high-rise buildings under wind loads has the advantage of combining lateral along-

- wind, lateral cross-wind, and torsional responses altogether. The technique allows for the consideration of any number of modes.
2. Results show that the responses of tall buildings under winds are dominated by the first few modes. Consequently, FEM, 3D lumped mass modeling, and reduced order 3D modeling of tall buildings under wind loads give an accurate assessment of the response provided that the first dominant modes are retained.
  3. Results show that the response of tall buildings in the cross-wind direction (lateral response combined simultaneously with torsion) can be higher than the response in the along-wind direction. This reveals the importance of the procedure proposed in this study as many design codes and formula may provide accurate estimate of the along-wind response but less guidance for the estimation of the critical cross-wind and torsional response.
  4. The building represents an engineered steel design of a structure that is very much vulnerable to wind loads. This may be due to its low weight as well as high flexibility related to the low dominant frequencies and the high aspect ratio.
  5. The building demands TMD with heavier mass and ATMD with higher control force in one lateral direction than the other. This may be attributed to geometry.
  6. For the purpose of the use of active control, LQR and fuzzy logic controllers are shown to be effective in enhancing the response reduction over the TMD. ATMDs with fuzzy logic controllers show similar trend like LQR controllers under multidirectional wind loads. In addition, from a design point of view, fuzzy logic controllers do not require the complexity of traditional control systems.
  7. The procedure presented in this chapter permits the response of tall buildings to be assessed and controlled in the preliminary design stages. This can help decision makers, involved in the design process, to choose among innovative design solutions like structural control, considering several damping techniques, modifying geometry, or even changing materials.

## 6. Acknowledgements

The authors would like to express appreciation to the work team at the Wind Tunnel of Politecnico di Milano, Milan, Italy. The first author wishes to thank Ms Corey Ginsberg, Florida International University, for her helpful comments.

## 7. References

- Aly, A.M. (2009). On the dynamics of buildings under winds and earthquakes: Response Prediction and Reduction. Ph.D. Dissertation, Department of Mechanical Engineering, Politecnico di Milano, Milan.
- Aly, A.M. and Christenson, R.E. (2008a), "On the evaluation of the efficacy of a smart damper: a new equivalent energy-based probabilistic approach", *Smart Mater. Struct.*, 17 045008 (11pp). DOI: 10.1088/0964-1726/17/4/045008
- Aly, A.M., Resta, F. and Zasso, A. (2008b), "Active Control in a High-Rise Building under Multidirectional Wind Loads", *SEI 2008 Structures Congress*, Vancouver, Canada. DOI: 10.1061/41016(314)285

- Aly, A.M., Zasso, A. and Resta, F. (2011), "On the dynamics of a very slender building under winds: response reduction using MR dampers with lever mechanism", *Struct. Des. Tall Spec. Build.*, 20(5), 541-553. DOI: 10.1002/tal.646
- ASCE 7-05 (2006) Minimum design loads for buildings and other structures. American Society of Civil Engineers, 424 pages. ISBN: 0784408092
- Attaway S. (2009). *Matlab: A Practical Introduction to Programming and Problem Solving*. Butterworth-Heinemann: Amsterdam.
- Battaini, M., Casciati, F. and Faravelli, L. (1998), "Control algorithm and sensor location," *Proc., 2nd World Conf. on Structural Control*, Kyoto, Japan, 1391-1398.
- Chen, S.X. (2010), "A More Precise Computation of Along Wind Dynamic Response Analysis for Tall Buildings Built in Urban Areas", *Engineering*, 2, 290-298. DOI: 10.4236/eng.2010.24038
- Davison, E.J. (1966) "A method for simplifying linear dynamic systems", *IEEE Transactions on Automatic Control*, AC-11(1), 93-101.
- Diana, G., De Ponte, S., Falco, M. and Zasso, A. (1998), "New large wind tunnel for civil environmental and aeronautical applications", *J. Wind Eng. Ind. Aerodyn.*, (74-76), 553-565. DOI: 10.1016/S0167-6105(98)00050-6
- Eurocode 1. (2004). *Actions on structures - Part 1-4: General actions - Wind actions*. prEN 1991-1-4, *European Standard*.
- Facioni, R.J., Kwok, K.C.S. and Samali, B. (1995), "Wind tunnel investigation of active vibration control of tall buildings", *J. Wind Eng. Ind. Aerodyn.*, (54-55), 397-412. DOI: 10.1016/0167-6105(94)00056-J
- Gu, M. and Peng, F. (2002), "An experimental study of active control of wind-induced vibration of super-tall buildings," *J. Wind Eng. Ind. Aerodyn.*, 90, 1919-1931. DOI: 10.1016/S0167-6105(02)00298-2
- Homma, S., Maeda, J., Hanada, N. (2009), "The damping efficiency of vortex-induced vibration by tuned-mass damper of a tower-supported steel stack", *Wind Struct., An Int. Journal*, 12(4), 333-347.
- Housner, G.W., Bergman, L.A., Caughey, T.K., Chassiakos, A.G., Claus, R.O., Masri, S.F., Skelton, R.E., Soong, T.T., Spencer, B.F., J., Yao, T.P. (1997), "Structural control: Past, present, and future", *J. of Eng. Mech.-ASCE*, 123(9), 897-971. DOI: 10.1061/(ASCE)0733-9399(1997)123:9(897)
- Huang, M.F., Tse, K.T., Chan, C.M., Kwok, K.C.S., Hitchcock, P.A., Lou, W.J., Li, G. (2010), "An integrated design technique of advanced linear-mode-shape method and serviceability drift optimization for tall buildings with lateral-torsional modes", *Eng. Struct.*, 32(8), 2146-2156. DOI: 10.1016/j.engstruct.2010.03.017
- Kwon, D., Kijewski-Correa, T., Kareem, A. (2008). "e-Analysis of High-Rise Buildings Subjected to Wind Loads", *J. Struct. Eng.-ASCE*, 134(7), 1139-1153. DOI: 10.1061/(ASCE)0733-9445(2008)134:7(1139)
- Lam, K.M. and Li, A. (2009), "Mode shape correction for wind-induced dynamic responses of tall buildings using time-domain computation and wind tunnel tests", *J. Sound Vibr.*, 322(Issues 4-5), 740-755. DOI: 10.1016/j.jsv.2008.11.049
- Li, C., Han, B., Zhang, J., Qu, Y. and Li, J. (2009), "Active Multiple Tuned Mass Dampers for Reduction of Undesirable Oscillations of Structures under Wind Loads", *Int. J. Struct. Stab. Dyn.*, 9(1), 127-149.



DOI: 10.1142/S0219455409002928

- Lu, L.T., Chiang, W.L., Tang, J.P., Liu, M.Y. and Chen, C.W. (2003), "Active control for a benchmark building under wind excitations", *J. Wind Eng. Ind. Aerodyn.*, 91(4), 469-493. DOI: 10.1016/S0167-6105(02)00431-2MATLAB, User Guide. The MathWorks, Inc, 2008.
- McNamara, R.J. (1977) "Tuned Mass Dampers for Buildings", *J. of Struct. Division, ASCE*, 103(9), 1785-1798.
- Mohtat, A., Yousefi-Koma, A. and Dehghan-Niri, E. (2010), "Active vibration control of seismically excited structures by ATMDs: Stability and performance robustness perspective", *Int. J. Struct. Stab. Dyn.*, 10(3), 501-527. DOI: 10.1142/S0219455410003592
- Nguyen, H.T., Nadipuram, R.P., Walker, C.L. and Walker, E.A. (2003), A first course in fuzzy and neural control, Chaoman & Hall/CRC, Boca Raton, FL.
- Park, S.J., Lee, J., Jung, H.J., Jang, D.D. and Kim, S.D. (2009), "Numerical and experimental investigation of control performance of active mass damper system to high-rise building in use", *Wind Struct., An Int. Journal*, 12(4), 313-332.
- Samali, B., Al-Dawod, M., Kwok, K.C. and Naghdy, F. (2004), "Active control of cross wind response of 76-story tall building using a fuzzy controller", *J. of Eng. Mech.-ASCE*, 130, p. 492-498.  
DOI: 10.1061/(ASCE)0733-9399(2004)130:4(492)
- Simiu, E. (2009), "Wind loading codification in the Americas: Fundamentals for a renewal", *Proceedings of 11<sup>th</sup> Americas Conference on Wind Engineering*, San Juan, PR, USA, June 22-26.
- Simiu, E., Gabbai, R.D. and Fritz, W.P. (2008), "Wind-induced tall building response: a time-domain approach", *Wind Struct., An Int. Journal*, 11(6), 427-440.
- Soong, T.T. (1990). *Active Structural Control. Theory and Practice*. Longman.
- Tse, K.T., Hitchcock, P.A. and Kwok, K.C.S. (2009), "Mode shape linearization for HFBB analysis of wind-excited complex tall buildings", *Eng. Struct.*, 31(3), 675-685. DOI: 10.1016/j.engstruct.2008.11.012
- Wu, J. R., Li, Q.S. and Tuan, A.Y. (2008), "Wind-induced lateral-torsional coupled responses of tall buildings", *Wind Struct., An Int. Journal*, 11(2), 153-178.
- Wu, J.C. and Pan, B.C. (2002), "Wind tunnel verification of actively controlled high-rise building in along-wind motion", *J. Wind Eng. Ind. Aerodyn.*, 90(12-15), 1933-1950. DOI: 10.1016/S0167-6105(02)00299-4
- Wu, J.C., Yang, J.N., Schmitendorf, W. (1998), "Reduced-order  $H_{\infty}$  and LQR control for wind-excited tall buildings," *J. Eng. Struct.*, 20(3), 222-236.
- Yao, J.T.P. (1972), "Concept of Structural Control", *J. of Struct. Division, ASCE*, 98(7), 1567-1574.
- Zasso, A., Giappino, S., Muggiasca, S. and Rosa, L. (2005), "Optimization of the boundary layer characteristics simulated at Politecnico di Milano Boundary Layer Wind Tunnel in a wide scale ratio ranger", *The Sixth Asia-Pacific Conf. on Wind Eng.*, Seoul, Korea.
- Zhou, Y., Kijewski, T., Kareem, A. (2003), "Aerodynamic Loads on Tall Buildings: Interactive Database", *J. Struct. Eng.-ASCE*, 129(3), 394-404. DOI: 10.1061/(ASCE)0733-9445(2003)129:3(394)

Zhou, Y, Wang, D.Y. and Deng, X.S. (2008), "Optimum study on wind-induced vibration control of high-rise buildings with viscous dampers", *Wind Struct., An Int. Journal*, 11(6), 497-512.

# Wind Tunnel Tests on the Horn-Shaped Membrane Roof

Yuki Nagai, Akira Okada, Naoya Miyasato and Masao Saitoh  
*College of Science and Technology, Nihon University  
 Japan*

## 1. Introduction

Membrane structure is tensile surface structure consisted by textile. The materials used for architectural membranes generally consist of a woven fabric coated with a polymeric resin (Seidel & David, 2009). For example, PVC coated polyester fabrics and PTFE coated glass fabrics are commonly used. Membrane structures provide widespan enclosures of great spatial interest and variety require minimal supporting elements of "hard" structure and provide very good overall levels of natural daylight. Membrane structures create various forms. In the architecture and civil engineering area, membrane forms and systems are divided into two categories, namely "pneumatic membrane" and "tensile membrane" shown in figure 1 (Saitoh, 2003). The pneumatic membrane such as "BC Place (1983)"

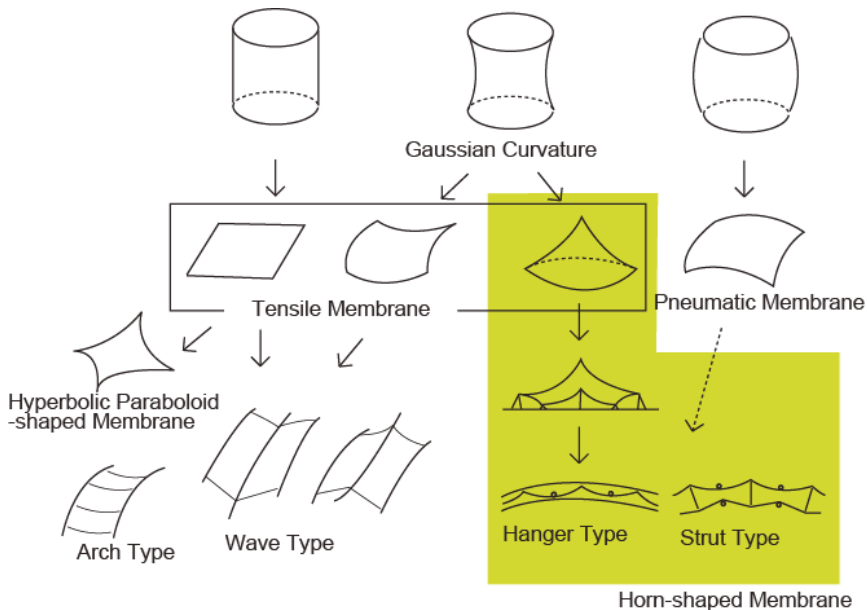


Fig. 1. Structural Systems and forms of Membrane structures

(Janberg, 2011a) and "Tokyo Dome (1988)" (Shinkenchiku-Sha Co. Ltd., 1988) is supported by internal pressure. On the other hand, the tensile membrane keeps stable by form and tensile force of itself. For example, "high point surfaces", which are called "horn-shaped membrane" in this paper, are pulled to one or more high points from inside or outside.

A Wind load is the most dominant load for light-weight structures such as the membrane structures. Therefore, verification against wind load is important for membrane structures. The engineer usually use the wind tunnel test and CFD simulation to evaluate the wind load for membrane structures. In recent years, the CFD simulation becomes major with the development of computers. But the wind tunnel test for membrane is sometimes useful to evaluate the wind pressure, because the membrane structure has complex form.

From this points of view, this paper describes about wind tunnel tests of a membrane roof focusing on the horn-shaped membrane roof.

The horn-shaped membrane roof divides into 'stand-alone type' and 'multi-bay type' as shown in figure 2. The stand-alone type is consisted by one unit horn-shaped membrane, and it is often used as temporally space without wall. On the other hand, the multi-bay type consists several horn units, and it is used as roofs of parking spaces, stands without wall, and as roofs of gymnasium hall with wall. These horn shaped membrane structures are supported by cables, struts, and so on.

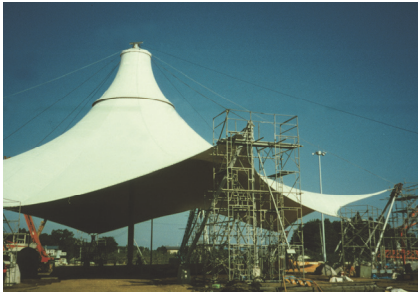
In general, there are three types of wind-tunnel test on the membrane roof, namely "Local Pressures Test", "Area and Overall Wind Loads Tests" and "Aeroelastic Tests" as shown in figure 3 (Cermak & Isyumov, 1998).

According to American Society of Civil Engineers (ASCE), "local pressure tests" use scaled static models instrumented with pressure taps (see figure 3(a)). These tests provide information on the mean and fluctuating local pressures on cladding and roof components. "Area and overall wind loads tests" are tests of wind load on specific tributary areas, using scaled static models and spatial or time averaging of the simultaneously acting local pressures (see figure 3(b)). These tests provide information on mean and fluctuating wind load on particular tributary area due to external or internal pressures, or both. "Local pressure tests" and "area and overall wind loads tests" measure wind pressures and wind forces acting on buildings around buildings. These wind tunnel tests need to consider the model scale depending on wind scale and time scale.

On the other hand, "aeroelastic tests" use dynamically scaled models of buildings and structures (see figure 3(c)). These tests provide information on the wind-induced response of buildings and structures due to all wind-induced force, including those which are experienced by objects that move relative to the wind. In addition, these tests measure the overall mean and dynamic loads and response of buildings and structures, including displacements, rotations and accelerations. These tests have to consider stiffness scale in addition to model scale. This paper focuses on the local pressures tests. The wind local pressure around membrane roof was measured by scaled static models, and then wind pressure coefficients were calculated by dynamic pressure.

In these tests, it is important to model the wind in the wind tunnel in order to obtain wind-effect data representative of full-scale conditions. In general, natural wind around buildings is duplicated using turbulent boundary layer flow which simulates a velocity scale, an aerodynamic roughness length of terrain, a gradient wind height of boundary-layer, and a scale of turbulence. The methods of modeling wind and similarly model are shown in guidelines and building standards of each country.

This paper reports results under a uniform flow in the chapter 4 and 5, because of comparing effects for the model scale, the velocity and etc. as simply as possible. And then, chapter 6 presents the result under a turbulent boundary layer flow.



Tsukuba Expo., Japan(1985)



Rest Dome, Japan(1989)

(a) Stand-alone Type



Lord's Cricket Ground, UK (1987)



Hyper Dome E, Japan (1990)



Kashiwa no Mori, Japan (2008)

(b) Multi-bay Type

Fig. 2. Examples of the horn-shaped membrane roof (Saitoh & Kuroki, 1989; Janberg, 2011b; Shinkenchiku-Sha Co. Ltd., 1992; Shinkenchiku-Sha Co. Ltd., 2007)

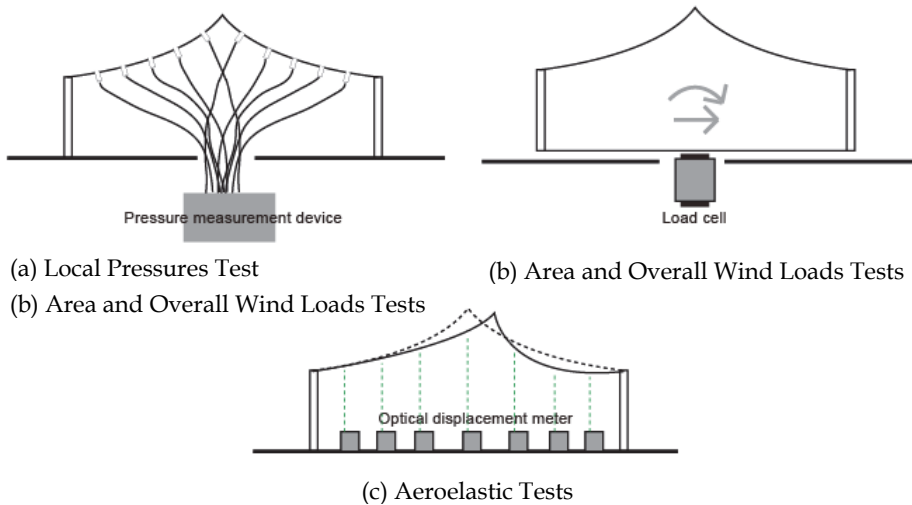


Fig. 3. Three types of the wind tunnel tests for membrane roofs

### 1.1 Past research about the wind tunnel on the horn shaped membrane structures

Wind pressure coefficients of typical building type such as box-type are defined in guidelines and standards in each country, but wind pressure coefficients of complicated shapes such as the horn-shaped membrane roof have not been sufficiently reported yet.

The basic studies, which were about the theory and the analysis method, on the horn-shaped membrane roof were reported by F. Otto, M. Saitoh et al and also shown the wind-pressure coefficients of the horn-shaped membrane roof under regulated conditions in several reports and books (Otto, 1969; Saitoh & Kuroki, 1989; Nerding, 2005). In the recent years, studies on the numerical simulation against the horn-shaped membrane roof were reported by J. Ma, C. Wang et al (Ma et al., 2007; Wang et al., 2007). Furthermore, dissertation by U. Kaiser indicated wind effects on weak prestressed membrane structure which is 30m horn shaped membrane by aeroelastic models (Kaiser, 2004).

There are many other references on this field. However, the basic data for the wind-force coefficient of the stand-alone and the multi-bay horn-shaped membrane roof has not been sufficiently reported yet.

### 1.2 The composition of this paper

This paper composes nine chapters and three main parts as shown in figure 4. This paper describes three types of test. Before these tests, chapter 2 shows a form of the horn-shaped membrane roof and example of a technique to find this shape. Chapter 3 shows definitions of symbols and calculation formulas on this paper. Chapter 4 and 5 show wind tunnel tests under the uniform flow; stand-alone model tests parameterized model scales and velocity in chapter 4, and multi-bay models parameterized the number of the horn-unit in chapter 5. These tests indicate mean wind pressures around the horn-shaped membrane structures under the uniform flow. Chapter 6 shows wind tunnel tests of the stand-alone model under the turbulent boundary layer flow. In this chapter indicate mean wind pressures and peak wind pressures and compare these results with the results under the uniform flow.

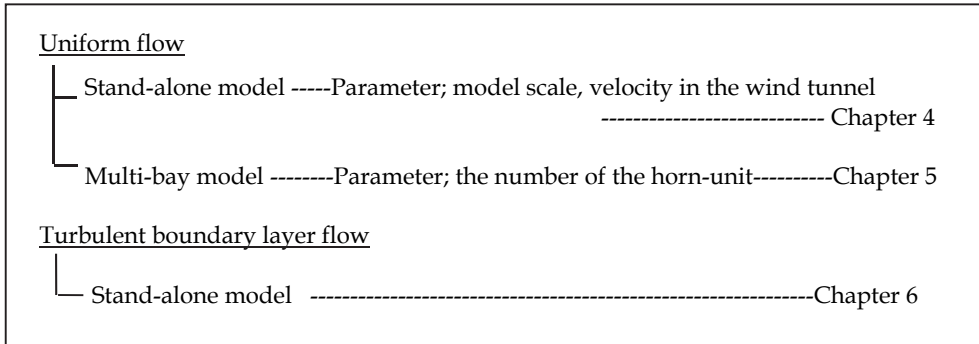


Fig. 4. The composition of this paper

### 2. Form of the horn-shaped membrane roof

The horn-shaped membrane roofs have several kind of planar shape, namely a circle, a square and a hexagon based horn-shaped membrane roof. This paper describes about the square based horn-shaped membrane roof. In general, the membrane structure needs to find appropriate forms to resist external force. ‘European Design Guide for Tensile Surface’ by TensiNet presents some methods of form-finding for the membrane structures (Forster & Mollaert, 2004). This paper used nonlinear finite element method to find the appropriate form on the square based horn-shaped membrane.

In this paper, the membrane material was defined as low stiffness material (see figure 5). On the other hand, a strut was defined as high stiffness material. A strut was transferred point B from point A in order to get the appropriate form using FEM analysis. A rise-span ratio  $H/L$

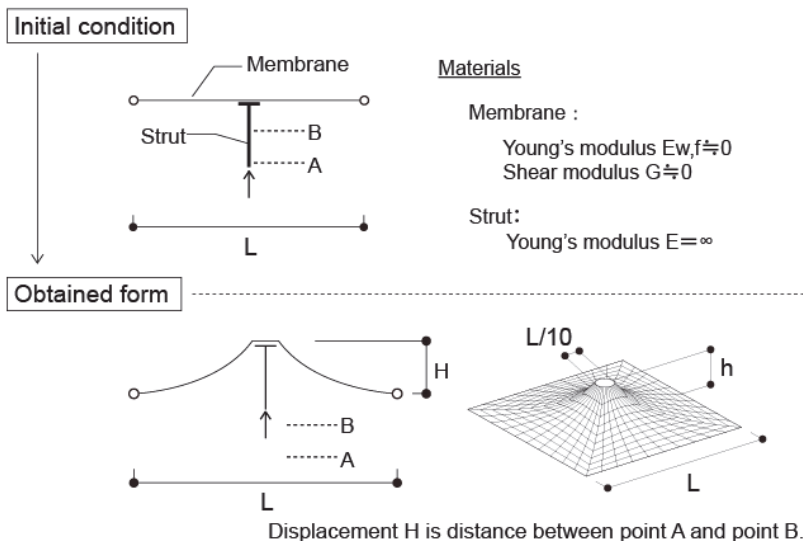


Fig. 5. Form finding method on the horn-shaped membrane structures

was defined as the ratio of a span  $L$  to a height of the horn-shaped roof  $H$ , and an appropriate form of  $H/L=0.2$  was obtained by finite element method with geometrical nonlinear in this paper. Additionally, the top of strut was  $L/10$  and there wasn't a hole on the middle of the horn-shaped roof. The final shape get three-dimensional curved surface.

### 3. Definitions of symbols and calculation formula on this paper

The wind pressure coefficient was calculated based on The Building Standard Law of Japan (The building Center of Japan, 2004), Recommendations for Load on Buildings 2004 (Architectural Institute of Japan, 2004) and ASCE Manuals (Cermak & Isyumov, 1998). Definitions of the symbols in this paper are shown in figure 6. As for the signs of wind pressure coefficient, the positive (+) means positive pressure against the roof and the negative (-) means negative pressure against the roof.

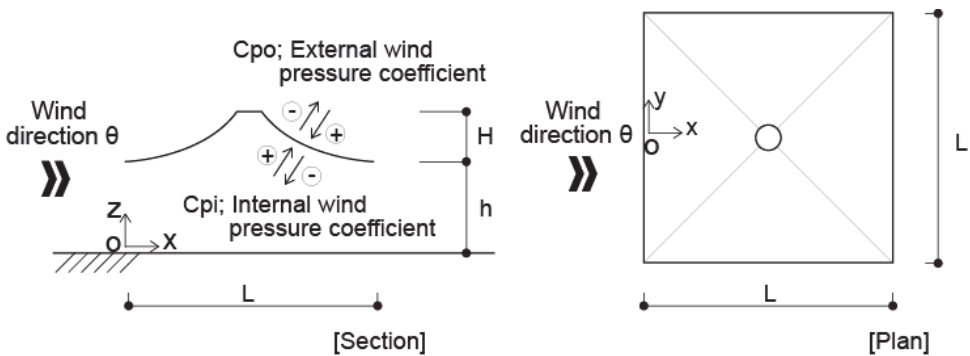


Fig. 6. The definitions of symbols in this paper

The wind pressure coefficient is obtained from follows;

$$C_{pj} = C_{poj} - C_{pij} \tag{1}$$

$$C_{pij} = \frac{P_{ij} - P_s}{q_z}, \quad C_{poj} = \frac{P_{oj} - P_s}{q_z} \tag{2}$$

$$q_z = \frac{1}{2} \rho \bar{v}_z^2 \tag{3}$$

in which  $C_{pj}$  is the wind pressure coefficient at measurement pressure tap  $j$ ,  $C_{poj}$  is the external wind pressure coefficient at measurement tap  $j$ ,  $C_{pij}$  is the internal wind pressure coefficient at measurement tap  $j$ ,  $P_{ij}$  is the internal pressure at measurement tap  $j$ ,  $P_o$  is the external pressure at measurement tap  $j$ ,  $P_s$  is the static, or the barometric, pressure at a reference location,  $\bar{q}_z$  is the mean value of dynamic pressure at the reference location  $z$ ,  $\rho$  is the density of the air, and  $\bar{v}_z$  is the mean value of wind velocity at the reference location  $z$ . In this paper, the reference location  $z$  with the uniform flow means the position of the pitot tube. On the other hand, the reference location  $z$  with the turbulent boundary layer flow was obtained from the following equations;



$$z = h + \frac{H}{2} \quad (4)$$

in which  $h$  is the eave height of the roof, and  $H$  is the rise of the horn-shaped roof. Particularly, the mean value of wind pressure coefficient  $C_{p\_mean}$  and the peak value of wind pressure coefficient  $C_{p\_peak}$  are expressed respectively as follows;

$$C_{p\_mean} = C_{po\_mean} - C_{pi\_mean} \quad (5)$$

$$\begin{cases} C_{p\_peak, \max} = C_{po\_peak, \max} - C_{pi\_peak, \min} \\ C_{p\_peak, \min} = C_{po\_peak, \min} - C_{pi\_peak, \max} \end{cases} \quad (6)$$

in which  $C_{po\_mean}$  and  $C_{pi\_mean}$  are the mean value of external and internal wind pressure coefficient,  $C_{po\_peak}$  and  $C_{pi\_peak}$  are the tip value of external and internal wind pressure coefficient.

Additionally,  $C_{pi\_mean}$ ,  $C_{po\_mean}$ ,  $C_{po\_peak}$  and  $C_{pi\_peak}$  are given by the following equations;

$$C_{pi\_peak} = \frac{P_{i\_mean}}{q_z}, \quad C_{po\_peak} = \frac{P_{o\_mean}}{q_z} \quad (7)$$

$$C_{pi\_mean} = \frac{P_{i\_mean}}{q_z}, \quad C_{po\_mean} = \frac{P_{o\_mean}}{q_z} \quad (8)$$

in which  $P_{i\_mean}$  and  $P_{o\_mean}$  are the mean value of internal and external wind pressure on the pressure measurement tap respectively, and  $P_{i\_peak}$  and  $P_{o\_peak}$  are the tip value of internal and external wind pressure on the tap. In case of the enclosed type which is constructed with side walls,  $P_i$  is neglected on these calculations.

#### 4. The wind tunnel test on the stand-alone model under the uniform flow

In this chapter, the authors focus on Reynolds number, i.e. the model scale and the wind velocity, under the uniform flow on the stand-alone model. This study aims to clarify about the relationship between Reynolds number and the wind pressure coefficients obtained from wind tunnel tests.

Generally, the Reynolds number  $Re$  is shown by the following equation and it is closely related to the aerodynamic characteristics (Cook, 1990).

$$Re = \frac{UL_B}{\nu} \quad (9)$$

in which  $U$  is characteristic wind velocity,  $L_B$  is characteristic building dimension,  $\nu$  is kinematic viscosity of the air;  $\nu=0.145 \times 10^{-4}$  [m<sup>2</sup>/sec] at 15 degrees. Several studies have reported about Reynolds number around a cylinder as shown in figure 7 and these studies indicated influence of Reynolds number on the curved surface shape. The horn-shaped membrane roof has three-dimensional curved surface. Therefore, the authors presume that the aerodynamic characteristics around the horn-shaped membrane roof show some effect depending on changes of Reynolds number. From the point of view, this chapter examine the influence of Reynolds number on the horn-shaped membrane roofs.

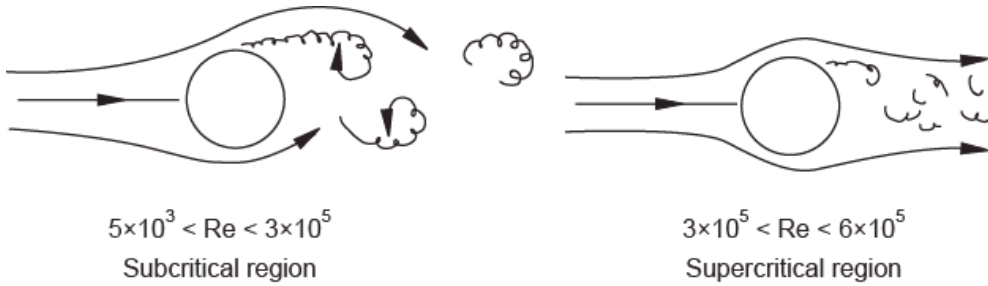


Fig. 7. Reynolds number  $Re$  around cylinder

#### 4.1 Outline of tests

These tests measured local wind pressures on the stand-alone model using the Göttingen type wind tunnel as shown in figure 8. The  $P_j - P_s$ , which  $P_j$  is the pressure at the measurement pressure tap  $j$  and  $P_s$  is the static pressure at the pitot tube, was measured directly by the laboratory pressure transducer as a differential pressure and represents the wind pressure acting at the particular pressure tap location  $j$  within the computer as shown in figure 9.

Main parameters are the model scale and the wind velocity depending on Reynolds number  $Re$ . Table 1 shows conditions on this test. This test used the uniform flow in order to clarify the influence of the parameter (i.e. the model scale and the wind velocity). The wind velocities used the value at the pitot tube. This test neglected friction by the floor.

The six types of model which is open type and enclosed type in each model scale (i.e. 20cmx20cm, 30cmx30cm, and 60cmx60cm), were prepared for this test as shown in figure 10 and figure 11. These models were made from acrylic plastic and have 21 taps on the 20cmx20cm model and 30cmx30cm model, 39 taps on the 60cmx60cm model.



Fig. 8. Göttingen type wind tunnel facility in Research Institute of Science and Technology, College of Science and Technology, Nihon University

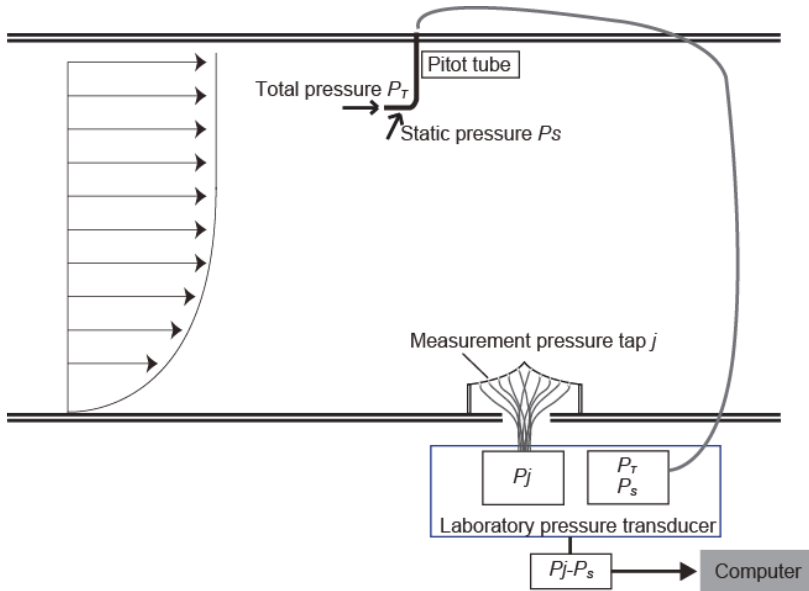


Fig. 9. The wind pressure acting at the particular pressure tap location  $j$

Wind Tunnel Facility	Göttingen type Wind Tunnel
Flow	Uniformed Flow
Sampling Speed	500Hz
Sampling Time	10sec
Wind Velocity	4m/sec, 5m/sec, 6m/sec, 7.5m/sec, 9m/sec, 10m/sec, 15m/sec
Rise-Span Ratio H/L	0.20
Model Scale	20cmx20cm, 30cmx30cm, 60cmx60cm
Wall	Open Type / Enclosed Type

Table 1. The parameter of the test

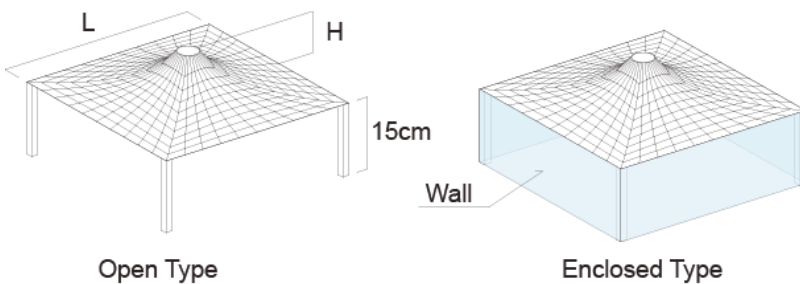


Fig. 10. Experimental models; open type and enclosed type

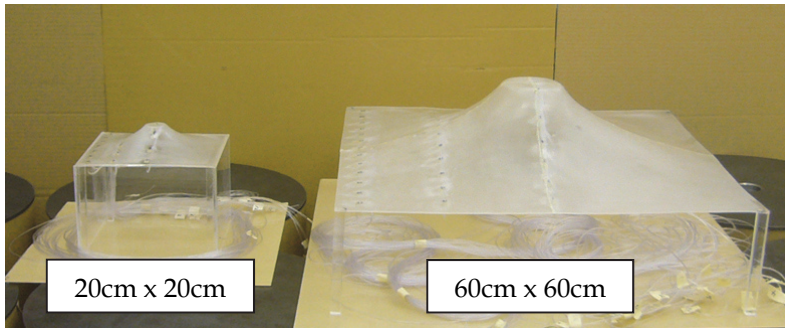


Fig. 11. The experimental model; 20cmx20cm model, and 60cmx60cm model

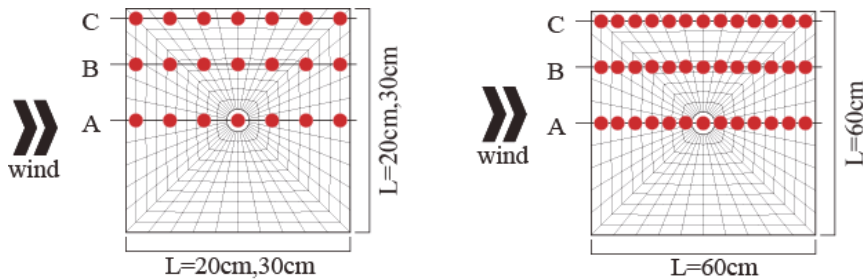


Fig. 12. Location of Pressure taps; 21 taps on the 20cmx20cm and 30cmx30cm model, and 39 taps on the 60cmx60cm model.

#### 4.2 Result of tests

The external wind pressure coefficients  $C_{po}$ , the internal wind pressure coefficients  $C_{pi}$  and the wind pressure coefficients  $C_p$  of each the scale models on the open type are shown in figure 13. The horizontal axis is  $x/L$  which is the ratio of the distance from the peak of a roof to a side of roof (see figure 6). The maximum points of the wind pressure coefficients  $C_p$  were moving to windward from leeward depending on the change of the velocity. Particularly, the velocity affected the external pressure coefficients  $C_{po}$  and the negative pressure became larger as the wind velocity is increase. On the other hand, the internal wind pressures  $C_{pi}$  on the 20x20 model and 30x30 model indicate the same tendency, but the internal wind pressure around  $x/L=0.05$  on the 60cmx60cm model was bigger than  $C_{pi}$  on the 20cmx20cm model and 30cmx30cm model.

The result of the enclosed type is shown in figure 14. In this model, the internal pressure coefficients  $C_{pi}$  was neglected. The velocity didn't effect on the wind-forced coefficient on each model, but the value around  $x/L=0.2-0.4$  changed as the model scale was large.

The wind pressure coefficients depending on Reynolds number which was calculated according to equation (9) are shown in figure 15. This chapter defined a side length  $L$  as the characteristic building dimension  $L_B$ . In the open type, when Reynolds number was  $2.06 \times 10^5$  and  $3.10 \times 10^5$ , the wind pressure coefficients showed the same tendency. On the other hand, in the enclosed type, as the Reynolds number was high, the negative pressure became smaller at  $x/L=0.2$ .

In particular, the results of figure 13 and figure 15 clarified that the wind pressure distributions changed near  $Re=1.2 \times 10^5$  on the open type. Based on these result, the distribution of the mean wind pressure coefficient, which are  $Re > 1.2 \times 10^5$  and  $Re < 1.2 \times 10^5$ , on the open type are shown in figure 16. This distribution illustrated great distinctions between  $Re > 1.2 \times 10^5$  and  $Re < 1.2 \times 10^5$  around the tip of the roof. These tests clarified that every test has to choose the appropriated model scale and velocity depending on the test conditions.

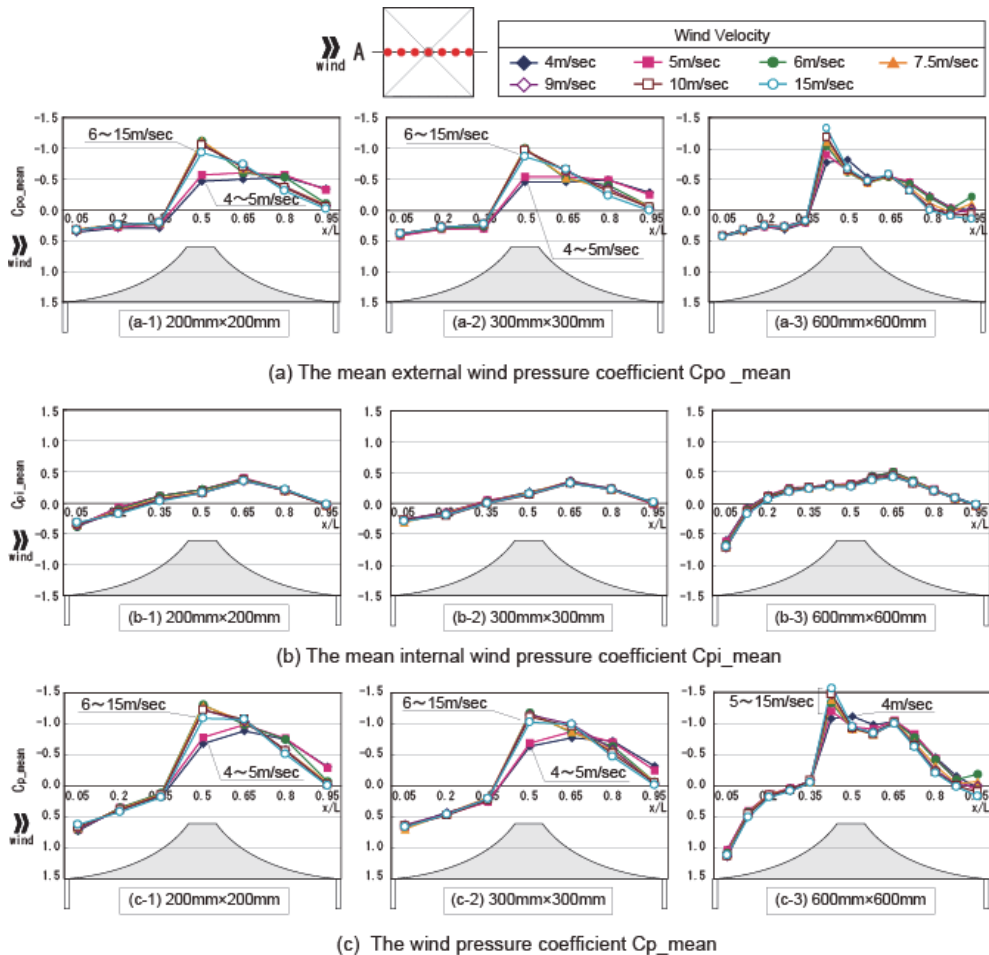


Fig. 13. The mean value of the external wind pressure coefficient  $C_{po\_mean}$  and the internal wind pressure coefficient  $C_{pi\_mean}$ ; and the wind pressure coefficient  $C_{p\_mean}$  under the uniform flow on the open type.

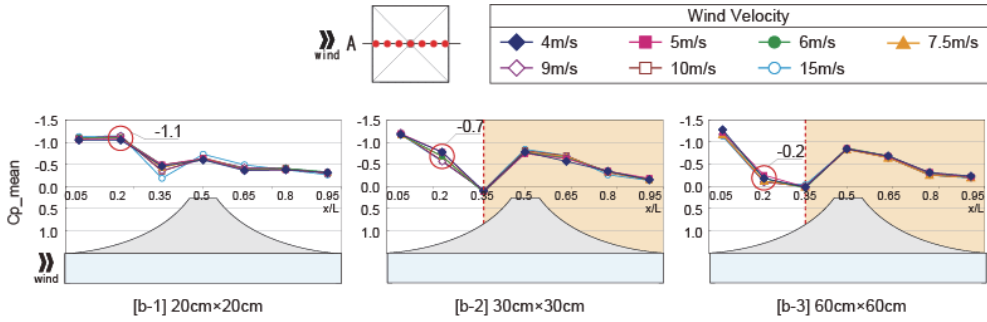


Fig. 14. The mean wind pressure coefficient  $C_p$  under the uniform flow on the enclosed type.

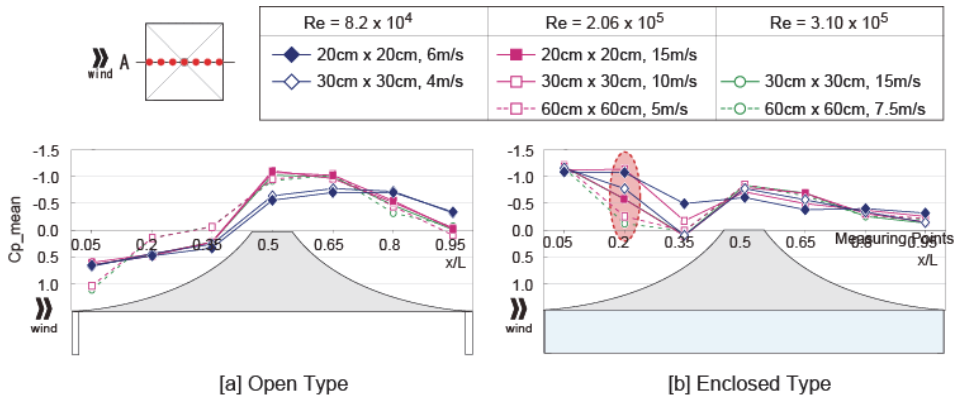


Fig. 15. Comparing the wind pressure coefficients obtained under each Reynolds number

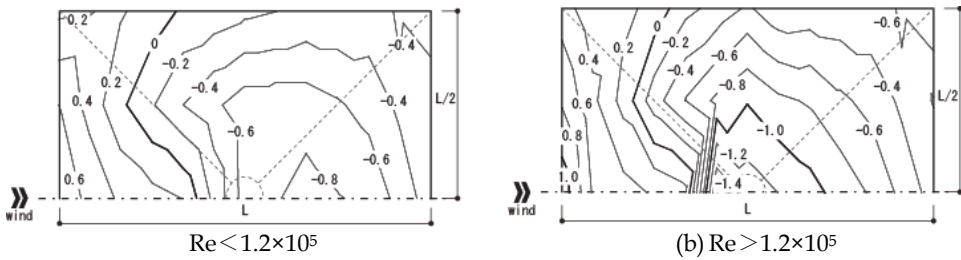


Fig. 16. Contour of the wind pressure coefficient on the open type

## 5. The wind tunnel test on the multi-bay model under the uniform flow

In most cases, the horn shaped membrane structure is used as the multi-bay type. The number of horn unit depends on the scale of the building and building uses. This chapter focuses on the number of the horn-unit. This experiment was carried out to clarify about the relationship between the number of the horn-unit and the wind pressure coefficient.

### 5.1 Outline of tests

The experiment used same facilities and the measurement method as chapter 4. A model scale of a horn unit was 20cm x 20cm and the maximum number of unit was 5 wide, 7 bays (see figure 17). The measurement was carried out adding horn units from  $n=1$  to  $n=7$  in the leeward side and the wind pressures were measured with each case (see figure 17). The pressure measurement taps were set up maximum 104 taps on the 5 wide, 7 bays model roof. These tests measured the mean wind pressure under the uniform flow as well as chapter 4. Additional conditions of this test show in table 2.

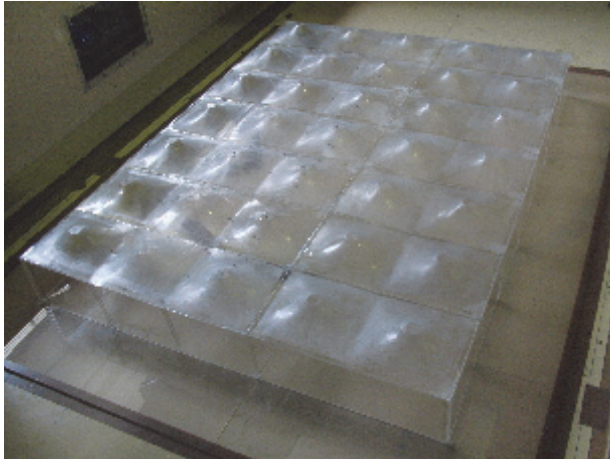


Fig. 17. The experimental model; 5 wide, 7 bay model

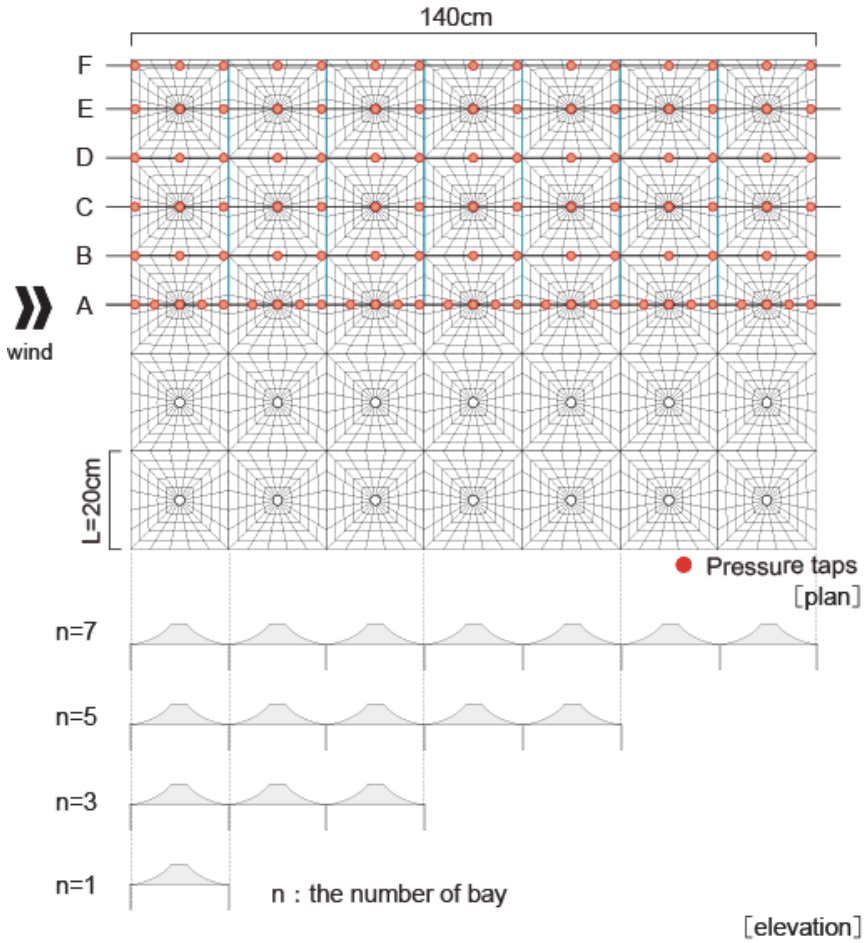


Fig. 18. Parameter and pressure measuring taps on the multi-bay model

Wind Tunnel Facility	Göttingen type Wind Tunnel
Flow	Uniform Flow
Sampling Speed	500Hz
Sampling Time	10sec
Wind Velocity	5m/sec, 10m/sec, 12.5m/sec, 14m/sec, 15m/sec
Rise-Span Ratio H/L	0.20
Model Scale	20cmx20cm(n=1), 100cmx140(n=7),
Wall	Open Type / Enclosed Type

Table 2. The parameter of the test



### 5.2 Result of tests

The mean wind pressure coefficients with the velocity 10m/s show in figure 19, because almost parameter indicated the same result.

These results clarified that the unit numbers had little influence on the distributions of the wind pressure on each model. However, the value around boundary areas indicated the different value from the value of the inside area. These results provide that the n=5 model is able to estimate the value of n=7 model. Therefore, as an example, the distribution of wind pressure coefficient on the open type (n=5) shows in figure 20. But it is necessary to consider other conditions, particularly another wind direction, because these views depend on regulated conditions.

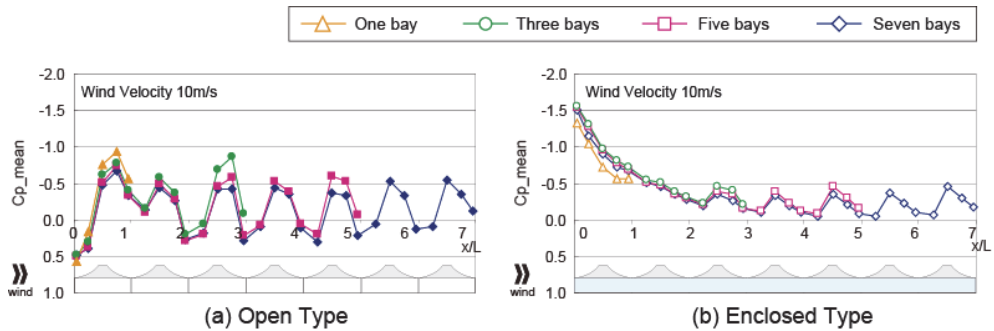


Fig. 19. The mean wind pressure coefficient under the uniformed flow with 10m/s

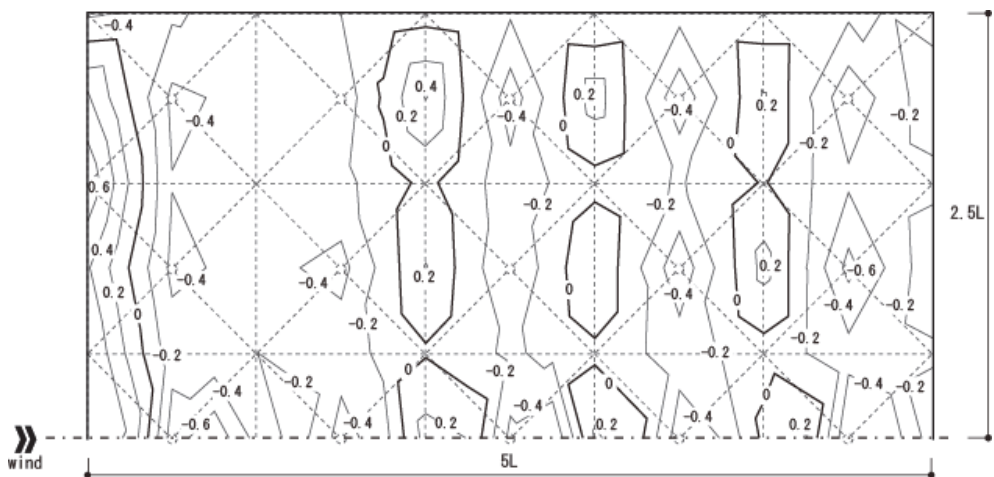


Fig. 20. Contour of wind pressure coefficient on the open type (n=5)

## 6. The wind tunnel test on the stand-alone model under the turbulent boundary layer flow

In general, structural engineers use wind pressures obtained from wind tunnel tests or simulations under the turbulent boundary layer flow when they design buildings. This chapter shows the wind tunnel test under the turbulent boundary layer flow in order to confirm the turbulent intensity around the horn shaped membrane roof. Additionally, this result is compared with the results under the uniform flow in chapter 4.

### 6.1 Outline of tests

The wind tunnel facility is same as chapter 4. The turbulent boundary layer flow was made by the blocks which are made from styrofoam (see in figure 21 and 22). Two types of flow were prepared for this test as follows;

- Turbulent intensity is 16%, wind velocity is 7.2 m/s at approx.  $z=150\text{mm}$ , using twenty seven the  $100\times 100\times 100\text{mm}$  blocks.
- Turbulent intensity is 25%, wind velocity is 5.7 m/s at approx.  $z=150\text{mm}$ , using twenty seven the  $100\times 100\times 150\text{mm}$  blocks.

The turbulent intensity was calculated as follows,

$$I(z) = \frac{\sigma_u(z)}{V(z)} \quad (10)$$

where  $\sigma_u(z)$  is root mean square value of wind speed fluctuation at height  $z$ ,  $V(z)$  is mean wind speed at height  $z$ .

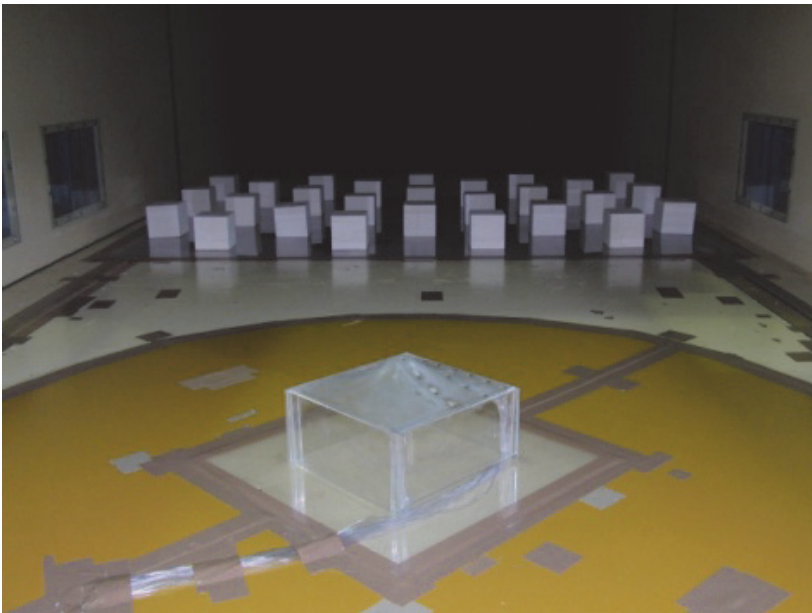


Fig. 21. Photo of the facility and the model under the turbulent flow

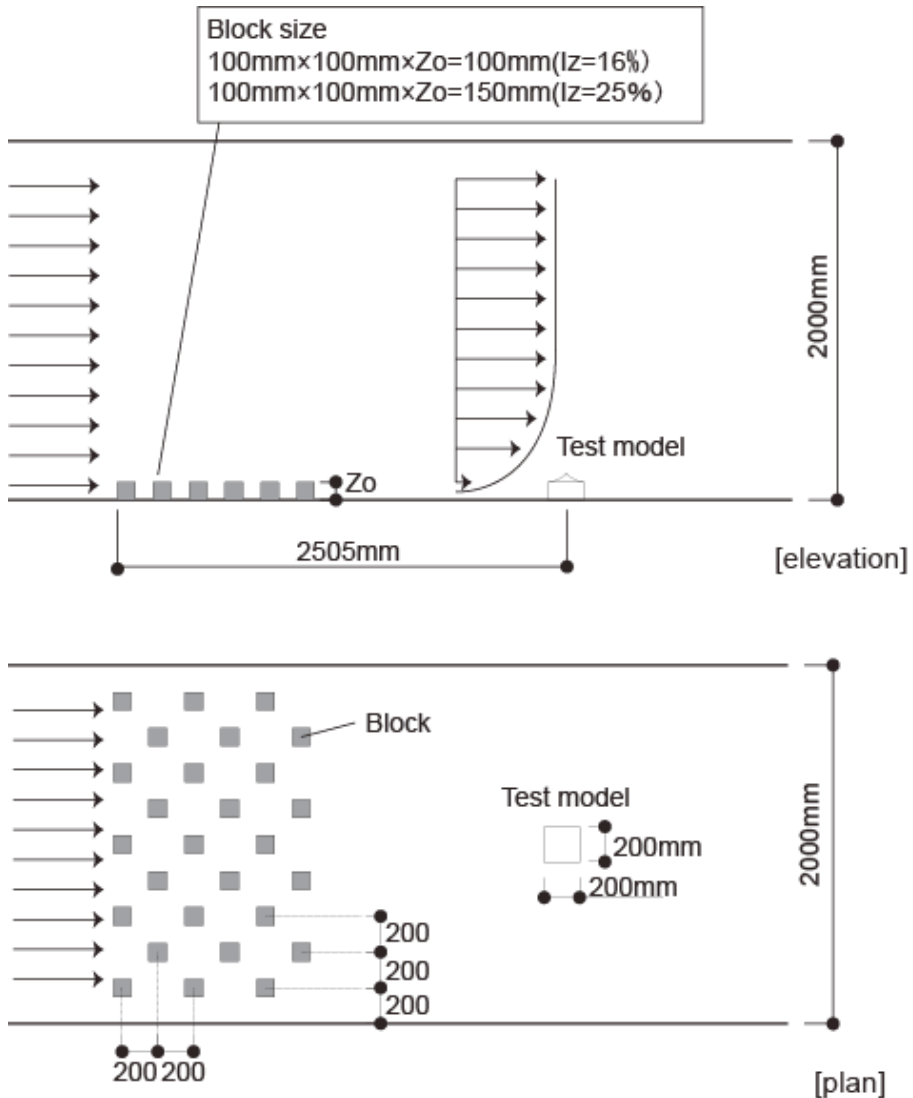


Fig. 22. Outline of wind tunnel facility and layout of turbulent blocks

The 20cm x 20cm model was used in this test as well as chapter 4 and chapter 5. It was assumed that a model scale was 1: 50, a velocity scale was 1/5 at the full scale wind speed 30m/s. In this case, time scale was 11/125. In this chapter, the velocity pressure to calculate wind pressure coefficients was obtained from the mean velocity at  $z=150\text{mm}$ . Table 3 shows the experimental conditions. The main parameters are two types of the wind directions and the wind flows and the walls. The models and measurement taps show in figure 23. This test provides the mean wind pressure coefficients and the peak wind pressure coefficients by the equation (5)-(8).

Wind-Tunnel Facility	Closed Circuit Wind Tunnel
Flow	Turbulent boundary layer flow
Sampling Speed	500Hz
Sampling Time	20sec
Turbulent intensity ( $I_z$ )	(a)15%, (b)25% ( at $z=150\text{mm}$ )
Rise-Span Ratio $H/L$	0.20
Model Scale	100cmx20cm( $n=1$ ), 100cmx140( $n=7$ ),
Wall	Open Type / Enclosed Type
Wind Direction	0deg, 45deg

Table 3. The parameter of the test

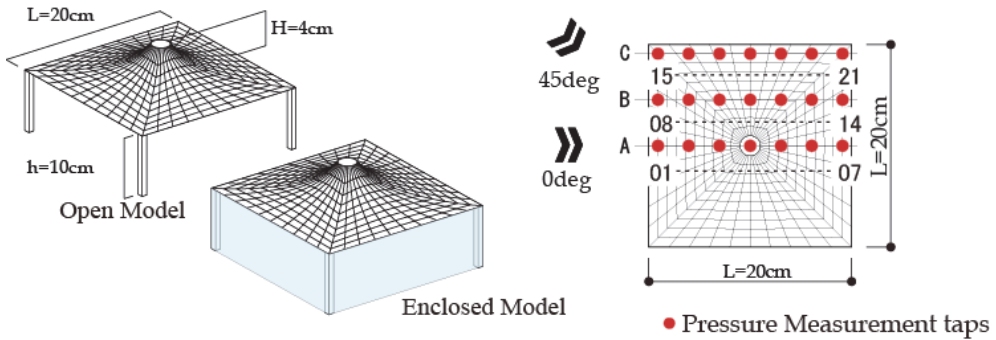


Fig. 23. Experimental models and measuring points

**6.2 Result of tests**

The distributions of the wind pressure coefficient show in figure 24 and 25. The figure 24 is the result of the open type and the figure 25 is the result of the enclosed type. These figures show half panel of roof based on symmetrical shape.

Generally, peak wind pressures around corner of roofs distinct from distributions of the internal area. However, this test showed that wind pressure coefficients around the middle of roof (i.e. the top of roof) were the maximum negative value. Furthermore, the wind direction influenced to the value of wind pressure coefficients. The peak value of wind pressure coefficients depended on the turbulent intensity, the peak wind pressure coefficients of  $I_z=25\%$  exceeded the value of  $I_z=16\%$ .

The mean wind pressure coefficient, max./min. peak wind pressure coefficient at line A is shown in figure 26 and 27. In addition to these results, the mean wind pressure coefficients with  $Re=1.0 \times 10^5$  under the uniform flow, which showed in chapter 4, are illustrated in figure 26 and 27. The mean wind pressure coefficient indicate same tendency despite the difference of the flow. However, the turbulence affected the peak wind pressure coefficient on each model.

As for the open type, the mean wind pressure coefficients under the turbulent flow indicated almost the same as the mean wind pressure coefficient under the uniform flow. On the other hand, as for the enclosed type, the mean wind pressure coefficients under  $I_z=25\%$  and it under the uniform flow illustrated the different value.

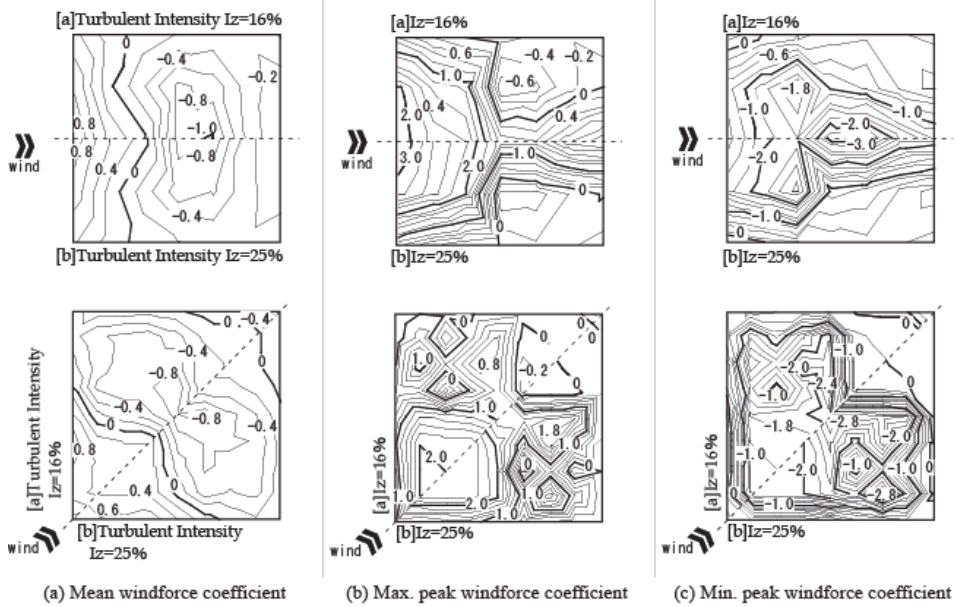


Fig. 24. Contour of the wind pressure coefficient on the open model; comparison of turbulent intensity 16% (upper part) with 25% (lower part)

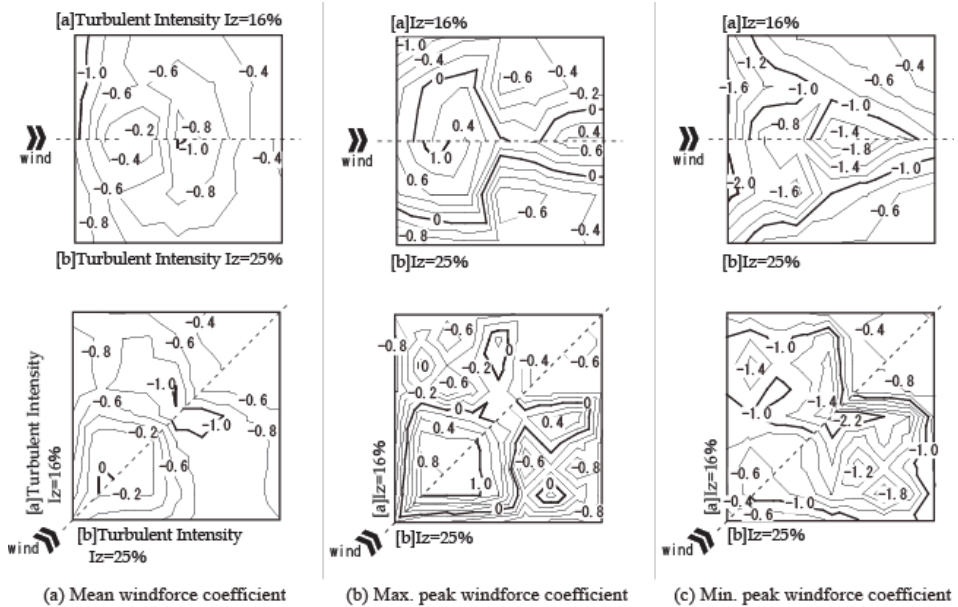


Fig. 25. Contour of the wind pressure coefficient on the enclosed model; comparison of turbulent intensity 16% (upper part) with 25% (lower part)

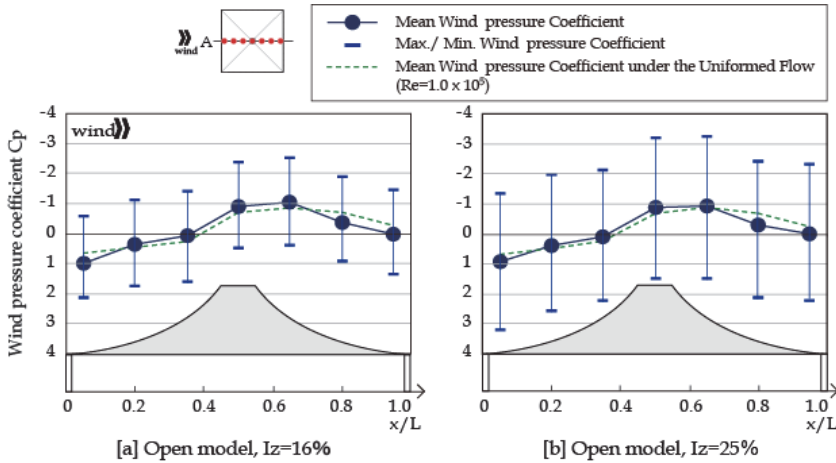


Fig. 26. Comparison of mean wind pressure coefficient with peak wind pressure coefficient on the open type

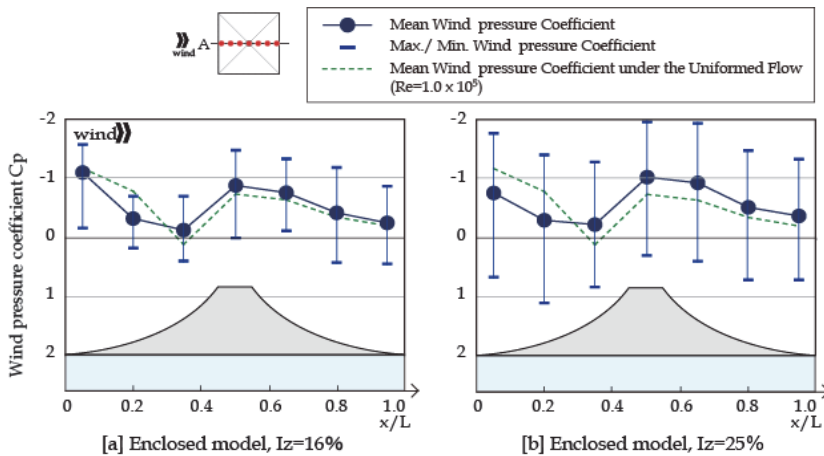


Fig. 27. Comparison of mean wind pressure coefficient with peak wind pressure coefficient on the enclosed type

Figure 28 and 29 show the comparison of mean wind pressure coefficients with peak wind force coefficients on the open type at the measuring point 01, 04, 15 and 21.

The open type and the enclosed type show the same tendency at each measuring point.

The measurement point 01 indicated that there is great distinction between the maximum peak wind pressure coefficient  $C_{p\_peak,max}$  and the minimum peak wind pressure coefficient  $C_{p\_peak,min}$  with 0, but the result of 45 degree didn't indicate distinction between the  $C_{p\_peak,max}$  and the  $C_{p\_peak,min}$ , the distinction between the  $C_{p\_peak,max}$  and the  $C_{p\_peak,min}$  at the measurement point 15 and 21 is relatively small with each degree. The measurement point 04 shows the same tendency as the measurement point 01 with 0 degree. These results clarify that the areas affected by wind degree and the areas unaffected by wind degree were available on the roof.

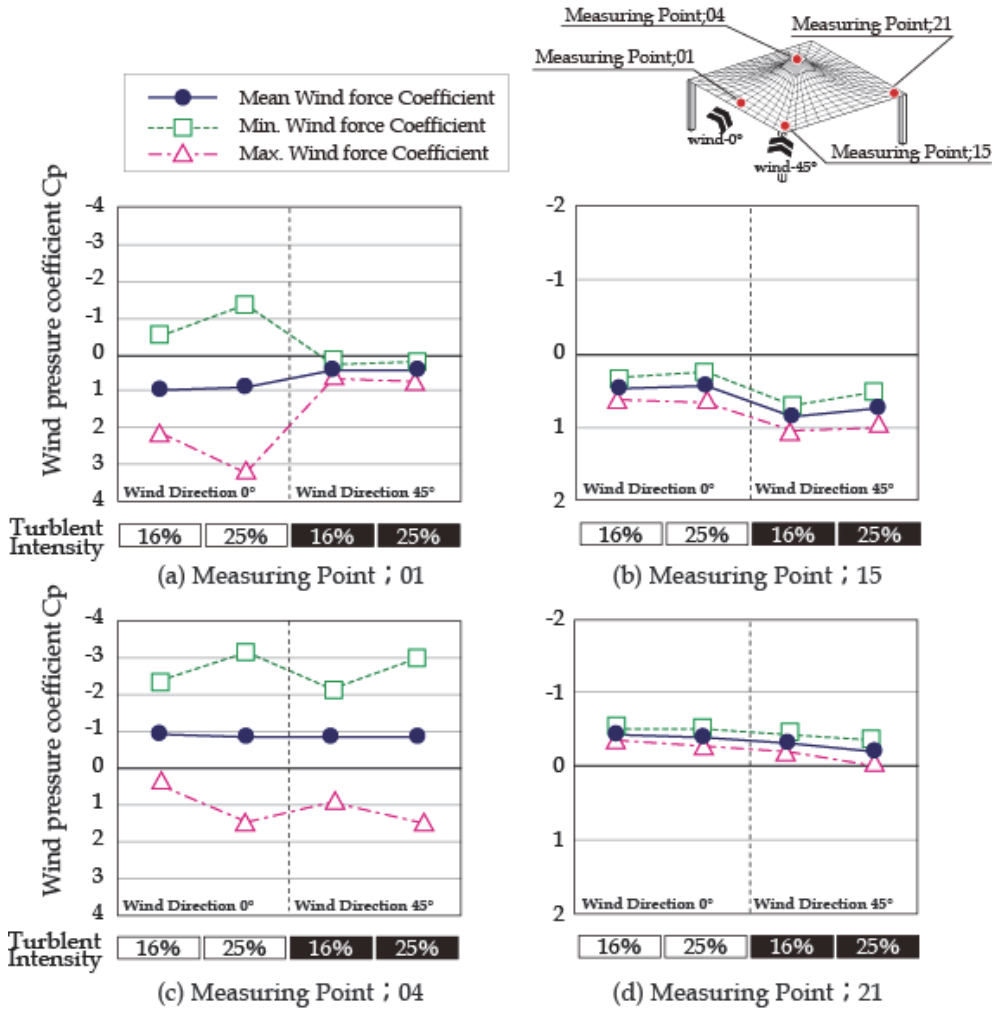


Fig. 28. Comparison of mean wind pressure coefficients with peak wind force coefficients on the open type at the measuring point 01, 04, 15 and 21

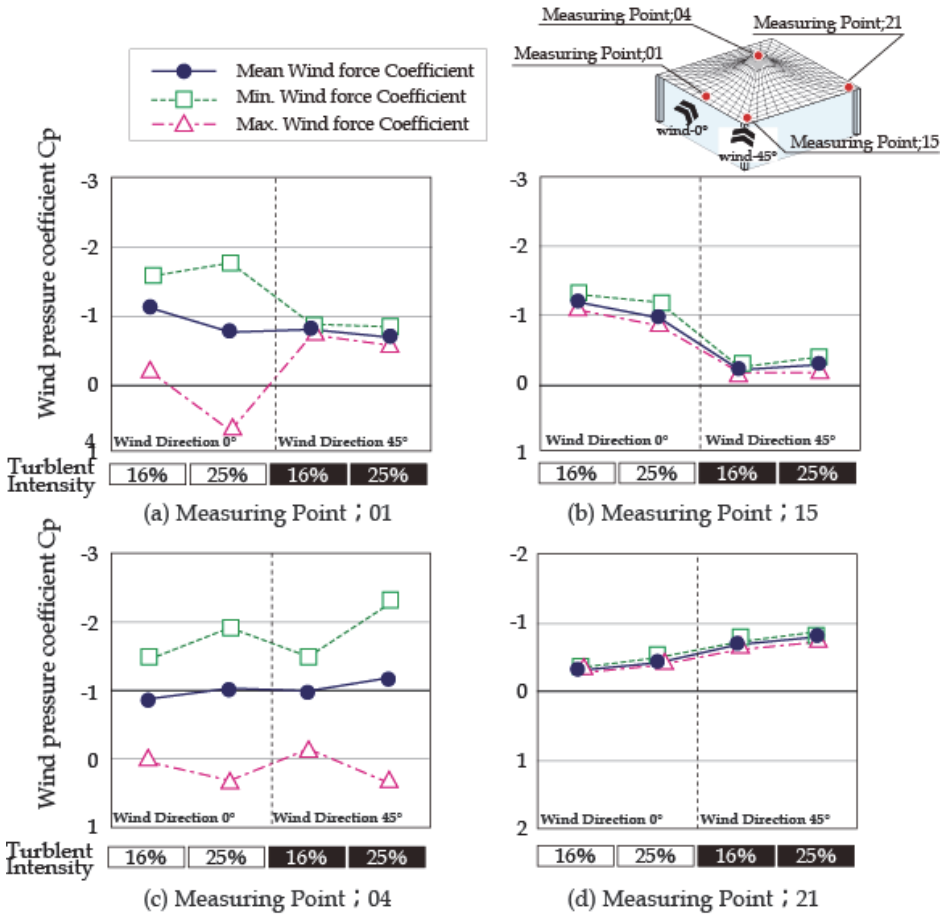


Fig. 29. Comparison of mean wind pressure coefficients with peak wind force coefficients on the enclosed type at the measuring point 01, 04, 15 and 21

**7. Conclusion**

In this paper, the characteristics of the wind pressure coefficients on the horn-shaped membrane roof were presented by the wind tunnel tests. Particularly, the followings are clarified that;

- The wind pressure coefficients of the stand-alone model depended on the model scale and the wind speed.
- The value of the turbulent intensity affected on the value of the wind pressure coefficient, particularly at the top of the roof.
- As for the multi-bay model, the increasing number of horn unit had no effect on the distributions of the wind pressure coefficients except for the boundary area.

Furthermore, the representative distributions of the wind pressure coefficient were shown on each parameter.



## 8. Acknowledgment

This work was supported by Japan Society for the Promotion of Science, Grant-in-Aid for JSPS Fellows, KAKENHI 22-7895. All of tests were carried out on "Research Institute of Science and Technology, College of Science and Technology, Nihon University". I have had the support of Takanori Fukuda, Yamashita Sekkei, Inc., Ayu Matsuda, Graduate School of Science and Technology, Nihon university for the experiments.

## 9. References

- Architectural Institute of Japan. (2004). *Recommendations for Load on Buildings (2004)*, Architectural Institute of Japan, ISBN 481890556, Japan.
- Cermak, J.E. & Isyumov, N., with American Society of Civil Engineers Task Committee. (1998). *Wind Tunnel Studies of Buildings and Structures (Asce Manual and Reports on Engineering Practice)*, American Society of Civil Engineers, ISBN 0784403198
- Cook, N.J. (1990). *Designer's Guide to Wind Loading of Building Structures Part 2: Static structures*, Laxton's, ISBN 0408008717
- Forster, B. & Mollaert, M. (2004). *European Design Guide Tensile Surface Structures*, TensiNet, , ISBN 908086871x
- Kaiser, U. (2004). *Windwirkung auf schwach vorgespannte membranstrukturen am beispiel eines 30m-membranschirmes*, Der Andere Verlag, ISBN 3899591623, Germany
- Ma, J., Zhou, D., Li, H., Zhu, Z. & Dong, S. *Numerical simulation and visualization of wind field and wind load on space structure*, *Proceedings of IASS 2007*, Beijing, 2007
- Nerdinger, W. (2005). *Frei Otto Complete Works: Lightweight Construction Natural Design*, Birkhäuser Architecture, ISBN 3764372311
- Janberg, N. (2011). BC Place stadium, In: *Nicolas Janberg's Structurae*, March 21, 2011, Available from: <http://en.structurae.de/structures/data/index.cfm?id=s0000708>
- Janberg, N. (2011). Lord's Cricket Ground Mound Stand, In: *Nicolas Janberg's Structurae*, March 21, 2011, Available from: <http://en.structurae.de/structures/data/index.cfm?id=s0000694>
- Otto, F. (1969). *Tensile Structures: Cables, Nets and Membranes v. 2*, MIT Presse, ISBN 0262150085, USA
- Saitoh, M. (2003). *Story of Space and Structure -Structural Design's Future*, Shoukokusha, ISBN 4395006396, Japan
- Saitoh, M. & Kuroki, F. *Horn Type Tension Membrane Structures*, *Proceedings of IASS 1989*, Madrid, 1989
- Seidel, M. & David, S. (2009). *Tensile Surface Structures - A Practical Guide to Cable and Membrane Construction: Materials, Design, Assembly and Erection*, Wiley VCH, ISBN 3433029229, Germany
- Shinkenchiku-Sha Co. Ltd. (1992). Hyper Dome E, In: *Shinkenchiku March,1992*, Shinkenchiku-Sha Co. Ltd. ISSN 1342-5447, Japan
- Shinkenchiku-Sha Co. Ltd. (1988). Tokyo Dome, In: *Shinkenchiku May, 1988*, Shinkenchiku-Sha Co. Ltd. ISSN 1342-5447, Japan

- Shinkenchiku-Sha Co. Ltd. (2007). BDS Kashiwanomori Auctionhouse, In: *Shinkenchiku October, 2007*, Shinkenchiku-Sha Co. Ltd. ISSN 1342-5447, Japan
- The building Center of Japan. (2004). *The Building Standard Law of Japan June 2004*, The building Center of Japan. , ISBN 4-88910-128-4, Japan
- Wang, C., Zhou, D. & Ma, J. *The interacting simulation of wind and membrane structures, Proceedings of IASS 2007*, Beijing, 2007

# Sport Aerodynamics: On the Relevance of Aerodynamic Force Modelling Versus Wind Tunnel Testing

Caroline Barelle  
*National Technical University of Athens*  
Greece

## 1. Introduction

In sports events, performance analysis is not an easy task since multiple factors, such as physiology, psychology, biomechanics, and technical progress in equipment are simultaneously involved and determine the final and ultimate outcome. Identification of individual effects are thus complicated, however from a general point of view, aerodynamics properties are recognized to play a determinant role in almost every sports in which the performance is the result of the optimal motion of the athlete (multi-jointed mechanical system) and/or is equipment (solid system) in the air. From ball games like golf, baseball, soccer, football and tennis to athletics, alpine skiing, cross-country skiing, ski jumping, cycling, motor sport and many others, the application of some basic principles of aerodynamic can make the difference between winners and losers.

If the general shape of the athlete/equipment system in terms of postural strategies and equipment customization is not optimized, it can either be made to deviate from its initial path, resulting in wrong trajectories and/or loss of speed and leading to failure in terms of performance. Coaches should thus be able to assess the aerodynamic efficiency of the motor task performed by the athlete with accuracy and in almost real time. Indeed, quick answers and relevant information can help the athlete to focus on specific aspects of his technical behaviour to improve his performance. So far for this purpose, two solutions are available i.e. dedicated wind tunnel testing or implementation of aerodynamic force models during the athlete training sessions. According to the complexity of sport performance and the necessity of almost real time answers for stakeholders, issue concerning the relevance of aerodynamic force modelling versus controlled experiments in wind tunnel must be discussed. In particular when searching to optimize athletes' performances, what are the advantages to develop and implement aerodynamic models comparing to controlled experiments in wind tunnel and for which purpose?

After a short description in section 2 of the aerodynamic principles commonly applied in sport to help optimize performance, the current chapter will document in section 3 both approaches (wind tunnel testing and aerodynamic force modelling) to assess the aerodynamics properties of a particular mechanical system: the athlete with or without his equipment. It will among others present a review of particular wind tunnel setting and modelling methods dedicated to specific sports such as cycling and skiing as well as shows

in section 4, how appropriate applications of them can lead to an increase of athletes' performances.

## 2. Aerodynamic principles applied to help optimize performance in sport

### 2.1 The performance in sport

Athletic performance is a part of a complex frame and depends on multiple factors (Weineck, 1997). For sports such those involving running, cycling, speed skating, skiing ... where the result depends on the time required to propel the athlete's body and/or his equipment on a given distance, the performance is largely conditioned by the athlete technical skills. Success then is the outcome of a simple principle i.e. the winner is the athlete best able to reduce resistances that must be overcome and best able to sustain an efficient power output to overcome those resistances.

In most of the aforementioned sports, those resistances are mainly the outcome of the combination of the contact force and the aerodynamic force acting on the athlete (Fig. 1.) The goal in order to optimise the performance consists to reduce both of them as much as possible.

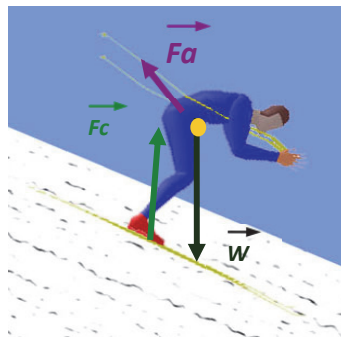


Fig. 1. Force acting on a downhill skier. With  $\vec{W}$  the weight of the skier,  $\vec{F}_c$  the ski-snow contact force and  $\vec{F}_a$  the aerodynamic force.

However, whether cycling, speed skating, skiing, given optimal physical capabilities, it has been shown that the main parameters that can be decreased to reduce the race time considerably is the aerodynamic behaviour of the athlete and/or his equipment. Indeed, in cycling, the aerodynamic resistance is shown to be the primary force impeding the forward motion of the cyclist on a flat track (Kyle et al., 1973; Di Prampero et al., 1979). At an average speed close to  $14 \text{ ms}^{-1}$ , the aerodynamic resistance represents nearly 90% of the total power developed by the cyclist (Belluè & Cid, 2001). The statement is the same in downhill skiing. The aerodynamic resistance is the parameter that has the greatest negative effect on the speed of the skier. For a skier initially running with a speed of  $25 \text{ ms}^{-1}$ , the transition from a crouched posture to a deployed posture can induce in 2 seconds (1.8% of the total run) almost a decrease of 12% of the skier speed whereas in the same condition, the ski-snow contact force only leads to a decrease of 2.2% (Barelle, 2003).

It is thus obvious that in such sports where a maximal speed of the system athlete/equipment is needed in order to reduce as much as possible the racing time, an optimisation of the system aerodynamic properties is crucial compared to the optimization of its contact properties.

## 2.2 Fundamentals of aerodynamic

Aerodynamics in sport is basically the pressure interaction between a mechanic system (athlete and/or his equipment) and the surrounding air. The system in fact moves in still or unsteady air (Fig.2).



Fig. 2. A downhill skier passing over a bump (photo: Sport.fr).

By integrating the steady and static pressure field over the system, the resulting aerodynamic force acting on this system can be obtained (Nørstrud, 2008). This force is generally divided into two components, i.e. the drag force  $\vec{D}$  and the lift force  $\vec{L}$  (Fig.3.).

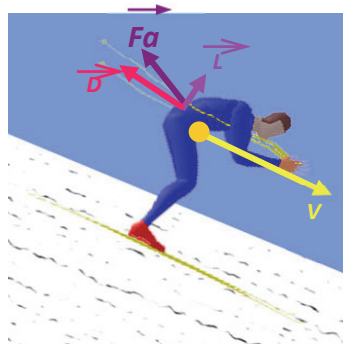


Fig. 3. Aerodynamic force applied on a skier and its two components:  $\vec{D}$  the drag (axial component) and  $\vec{L}$  the lift (normal component).  $V$  represents the speed of the skier.

The drag  $\vec{D}$  is defined as the projection of the aerodynamic force along the direction of the relative wind. This means that if the relative wind is aligned with the athlete/equipment system, the drag coincide with the aerodynamic force opposite to the system motion.  $\vec{D}$  depends on three main parameters: (i) the couple athlete/equipment frontal surface area (defined as the surface area of the couple athlete/equipment projected into the plane perpendicular to the direction of motion), (ii) the drag coefficient depending on the shape and the surface quality of the system and (iii) the athlete speed. The drag is thus expressed using the following equation (1).

$$D = \frac{1}{2} \cdot \rho \cdot A \cdot C_D \cdot V^2 \quad (1)$$

Where  $D$  denotes the drag (N),  $\rho$  is the air density ( $\text{kgm}^{-3}$ ),  $A$  is the projected frontal area of the couple athlete/equipment ( $\text{m}^2$ ),  $C_D$  is the drag coefficient and  $V$  is the air flow velocity ( $\text{ms}^{-1}$ ) equivalent to the athlete speed.

The drag is essentially proportional to the square of the velocity and its importance grows more and more as the speed increases. If speed is doubled, the drag increases by four-fold. The drag coefficient  $C_D$  is dimensionless and depends on the Reynolds number (ratio of inertial forces and forces due to the viscosity of air) and the speed of the airflow. If  $C_D$  varies for low speed values (Spring et al., 1988), in most of the sports considered in this chapter, it can be considered as constant (Di Prampero et al., 1979 ; Tavernier et al., 1994). In fact, the athletes never reach the critical speed which cause the fall in  $C_D$  due to the change from laminar to turbulent regime. So at a steady and relatively high speed, variations of drag are mainly induced by variations of the projected frontal area of the couple athlete/equipment, thus by posture variations (Watanabe & Ohtsuki, 1977; 1978). The figure 4 shows in which proportion the  $A \cdot C_D$  factor of a downhill skier varies with changes in posture.

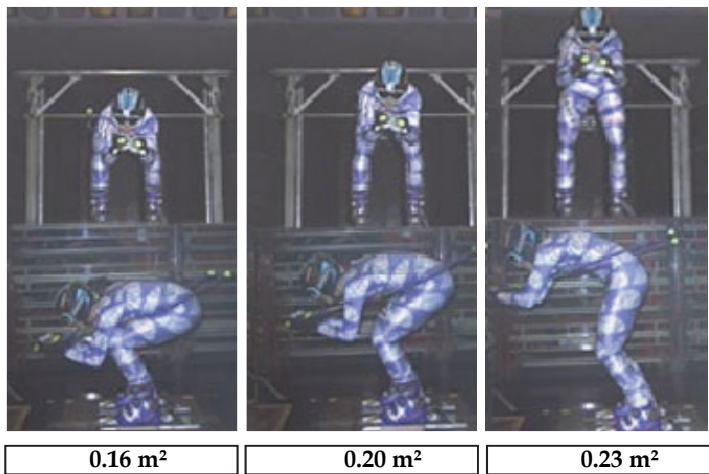


Fig. 4. Variation of the  $A \cdot C_D$  factor of a downhill skier according to posture variations (Wind tunnel of IAT, France).

The lift  $\vec{L}$  is the component of the aerodynamic force that overcomes gravity. It is acting normal to the drag component. As the drag, it depends also on three main parameters: (i) the couple athlete/equipment frontal surface area (defined as the surface area of the couple athlete/equipment projected into the plane perpendicular to the direction of motion), (ii) the lift coefficient depending on the shape and the surface quality of the system and (iii) the athlete speed. The lift is thus expressed using the following equation (2)

$$L = \frac{1}{2} \cdot \rho \cdot A \cdot C_L \cdot V^2 \quad (2)$$

Where  $L$  denotes the lift (N),  $\rho$  is the air density ( $\text{kgm}^{-3}$ ),  $A$  is the projected frontal area of the couple athlete/equipment ( $\text{m}^2$ ),  $C_L$  is the lift coefficient and  $V$  is the air flow velocity ( $\text{ms}^{-1}$ ) equivalent to the athlete speed.

Bernoulli's law explains the phenomenon of lift from pressure differences between the lower and upper surfaces of the profile of a mechanical system (Fig. 5).

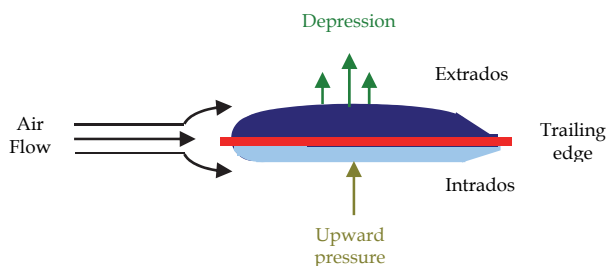


Fig. 5. The lift effect according to Bernoulli's law.

The distance travelled by the air flow is more important above the extrados than below the intrados. To avoid creating a vacuum of air at the trailing edge, the air flow following the extrados must move faster than the one following the intrados. An upward pressure is thus formed on the intrados and a depression appears on the extrados, thereby creating a phenomenon of lift. The shape of the mechanical system and its surface quality have thus, an effect on the lift intensity. However in the same manner as the drag coefficient  $C_D$ , the lift coefficient can be considered constant for the ranges of speed practiced during the aforementioned sports. Variations of the surface opposing the airflow induced by variations of the angle between the system chord line and the longitudinal axis (Fig.6.) namely the angle of incidence ( $i$ ), impact the variability of the lift (Springings & Koehler, 1990). For an angle of incidence greater than  $0^\circ$ , the lift will tend to increase while for an angle of incidence lower than  $0^\circ$ , a phenomenon of "negative lift" will appear (down force).

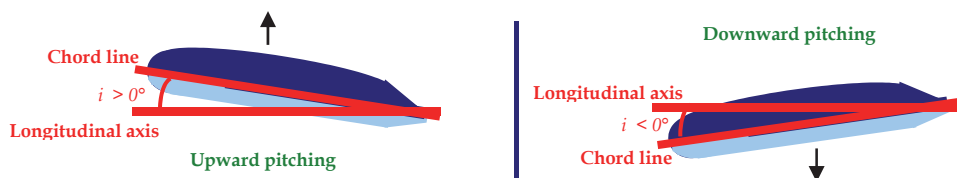


Fig. 6. Profile of an object according to its angle of incidence.  $i$  correspond to the angle of incidence.

In the aforementioned sports (running, cycling, skiing, skating), the equipment surface is rather small with respect to the athlete surface and therefore the main part of the aerodynamic force acts on the athlete who can be regarded as bluff body (non streamlined line body). The bluntness leads to the fact that the aerodynamic resistance is mainly pressure drag instead of friction drag and thus, on a general point of view, it's more important to reduce the frontal area than to reduce the wet area. Then as lift is generally not required, it's better to keep it as small as possible in order to avoid the production of induced drag. However, in particular sport like ski jumping, it is obvious that the flight length is sensitive both to lift and drag. Small changes in the lift and or drag can have important effect for the jump quality and the skier must find the right compromise between an angle of incidence that will lead to an increase of the lift but not to an increase of the drag. The athlete must thus produce an angular momentum forwards in order to obtain an advantageous angle of incidence as soon as possible after leaving the ramp (Fig.7.). If the forward angular

momentum is too low, the flight posture will induce a high drag thus a low speed and a low lift, resulting in a small jump. Too much forward angular momentum on the other hand can increase the tumbling risk.



Fig. 7. A ski jumper during the flight phase just after leaving the ramp (photo: Photo by Jed Jacobsohn/Getty Images North America).

### 2.3 Reducing the aerodynamic force to optimize the performance

Reducing the air resistance in sport events typically involved improving the geometry of the athlete/equipment system. Optimisation of the athlete postures as well as the features of his equipment is generally required since they have a pronounced impact on the intensity of the aerodynamic force.

Firstly, by proper movement of the body segments (upper limbs, trunk, lower limbs) in order to minimize the frontal surface area exposed to the air flow, the posture can become more efficient aerodynamically. For example, in time trial cycling, it is now well known that four postural parameters are of primary importance in order to reduce the drag resistance i.e. the inclination of the trunk, the gap between the two elbows, the forearms inclination with respect to the horizontal plan, the gap between both knees and the bicycle frame (McLean et al., 1994). The back must be parallel to the ground, the elbow closed up, the forearms tilted between  $5^\circ$  and  $20^\circ$  with respect to the horizontal and the knees closed up to the frame (Fig.8.). Such a posture (time trial posture) can lead to average reduction of the drag resistance of 14,95 % compared to a classical "road posture" ( $37.8 \pm 0.5$  N vs.  $44.5 \pm 0.7$  N;  $p < 0.05$ ) and that merely because of significantly lower frontal area ( $0.342 \pm 0.007$  m<sup>2</sup> vs.  $0.398 \pm 0.006$  m<sup>2</sup>;  $p < 0.05$ ) (Chabroux et al., 2008).



Fig. 8. An optimal aerodynamic posture in time trial cycling.

In downhill skiing, the principle is the same. The intensity of the aerodynamic resistance is even lower that the skier adopts a compact crouched posture for which the back is round and horizontal, the shoulders are convex and the upper limbs do not cross the outer contour of the skier and especially do not obstruct the bridge created by the legs.



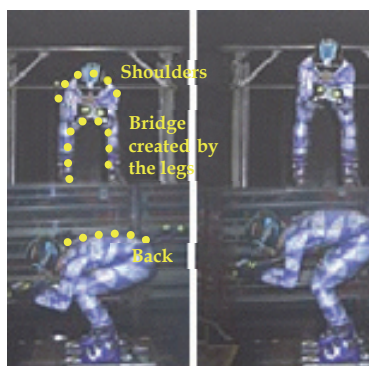


Fig. 9. An optimal aerodynamic posture in downhill skiing on the left compare to a posture a little bit more open on the right (Wind tunnel of IAT, France).

For an initial skier speed of  $25\text{ms}^{-1}$ , such a crouched posture can lead to a gain of 0,04 second after a straight run of 100 meters thus to a victory compared to a posture a little bit more open (Barelle, 2003).

Secondly suitable aerodynamic customisation of the equipment can also strongly reduce the negative effect of the aerodynamic resistance. Indeed as example, in cycling, the comparison between time trial helmet and normal road helmet shows a drag resistance improvement that can range from 2,4 % to 4 % according to the inclination of the head (Chabroux et al., 2008).



Fig. 10. Two cycling helmets, one aerodynamically optimised for time trial event (left) and the other a simple road helmet (right).

It is worth noting that an efficient optimisation of the aerodynamic properties of the athlete/equipment system must take into consideration precisely the interaction between the posture features and the equipment features. The aerodynamic quality of the equipment is totally dependent of the geometry characteristics of the athlete during the sport activity. An efficient optimization cannot be done without taking this point into consideration. In particular in time trial cycling, the interaction between the global posture of the cyclist and the helmet inclination given by the inclination of the head is significant from an aerodynamic point of view. The drag resistance connected with usual inclination of the head (Fig.11) is lower ( $37.2\pm 0.6\text{ N}$ ) than the one related to the low slope of the head ( $37.8\pm 0.5\text{ N}$ ), which is itself significantly lower than the one generated by a high slope of the head ( $38.5\pm 0.6\text{ N}$ ). In fact according to the helmet shape, the inclination of the head can have different impact on the projected frontal area of the couple helmet /athlete head thus on the aerodynamic drag.

Hence, it is also important for coaches and athletes to optimize postures in a way that it will not affect the athlete physical power to counteract the resistance. In most of the sport and

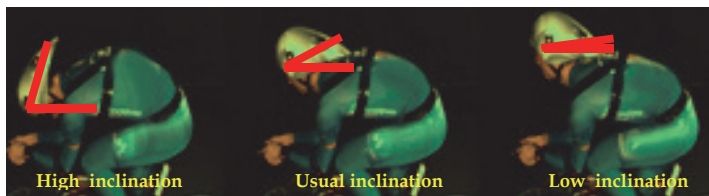


Fig. 11. Inclination of the head in time trial and corresponding inclination of the helmet (Wind tunnel of Marseille, France).

for aerodynamic purposes, athletes are asked to adopt a tightly crouched posture to reduce their frontal areas exposed to the air stream but if it is not well done, it can also have bad biomechanical and physiological consequences for the athlete performance such as a decrease of physiological qualities. Everything is a compromise. In ice skating for example, although a tightly crouched posture reduces leg power, it reduces air drag to an even greater extent and thus produces higher skating velocities.

### 3. Methods for assessing the aerodynamic force applied on an athlete with or without his equipment

To assess the aerodynamic performance of an athlete and/or his equipment, two methods are available, i.e. either to perform wind tunnel testing to single out only one specific determinant of the performance in this case aerodynamic properties of the athlete or/and his equipment, or to develop and implement aerodynamic force models that can for example be apply in a real training or competitive conditions which mystifies the role of other factors such as for instance mental factors. The real question here, concern the relevance of the inferences drawn from the results obtain with this two methods according to the fact that the performance in sport is the outcome of the efficient interaction of multiple factors at the right time. Indeed, "a fact observed in particular circumstances can only be the result of particular circumstances. Confirming the general character of such a particular observation, it is taking a risk of committing a misjudgement." (Lesieur, 1996). Both approaches are further detailed below as well as their relevance according to the performance goal pursue by the principles stakeholders i.e. athletes and coaches.

#### 3.1 Wind tunnel testing

Wind tunnel tests consist in a huge apparatus used to determine the complex interactions between a velocity-controlled stream of air and the forces exerted on the athlete and his equipment. The tunnel must be over sized compare to the athlete to be assessed in order to avoid side effects that may disturb the measurement of the aerodynamic force. The athlete with or without his equipment is fasten on a measured platform (6 components balance) in the middle of the test section. The athlete is thus stationary in the flow field and the air stream velocity around him generally corresponds to the ones observed during the sport practice (e.g.  $14\text{ms}^{-1}$  in time trial cycling,  $25\text{ms}^{-1}$  and more in alpine skiing.). The aerodynamic balance enables to measure the smallest aerodynamic force imposed on the athlete/equipment system in particular its axial (drag) and normal (lift) components (Fig.12).

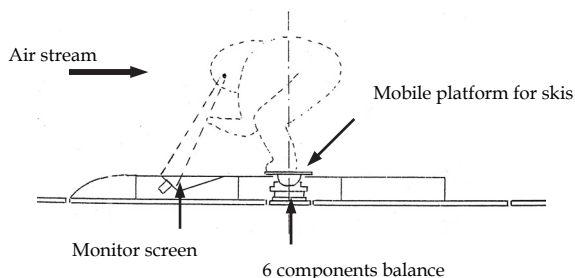


Fig. 12. Diagram of a data acquisition system for the assessment of the aerodynamic properties of a downhill skier (Wind tunnel of IAT, France).

For a better understanding, the path of the air stream around the system can be made visible by generating smoke streams (Fig.13).



Fig. 13. Smoke stream around a time trial cyclist and his equipment (Wind tunnel of Marseille, France).

A tomography gate can also be installed in the wind tunnel behind the athlete to explore the air flow wake behind him (Fig.14).

The figures below shows different wind tunnel settings that have been used for the measurement of the aerodynamic force applied on downhill skiers and time trial cyclists.

In alpine skiing, most of the time, the skier is in contact with the snow and only an accurate assessment of the drag applied on him is necessary. However in particular conditions and especially when he passes over a bump (Fig.2), it is interesting to quantify the lift applied on him. It has to be the smallest as possible since the skier as to be as soon as possible in contact with the snow to manage his trajectory. The length of the jump must be very short according to the initial and following conditions and the goal for the skier is to adopt in the air a posture that will generated the smallest lift. For both purposes i.e. measuring accurately the drag and the lift, two wind tunnel setting must be considered (Barelle, 2003; 2004).

On Fig.15, the goal is only to measure the aerodynamic drag applied on a skier adopting a crouched posture. The measuring device is the one of the Fig.12. The skier is fastening in the middle of a wind tunnel (rectangular section, 5 meters wide by 3 meters in height and 10 meters length) on a 6 components balance that enables ones to have access to multiple variables, among other the aerodynamic drag. Wind-less balance signals acquisition (during which the skier has to keep the crouched posture) are generally performed before each

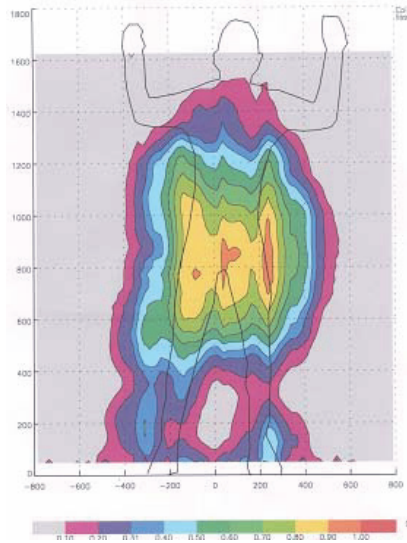


Fig. 14. Mapping of the air flow behind a cross country skier (Wind tunnel of IAT, France). The more colours are warm, the more the aerodynamic resistance is important.

aerodynamic measurement trial, in order to correct the measurements for zero drift and mass tares. After the zeros acquisition, the wind tunnel is started and when the required speed of the air flow is reached, the athlete can optimized is posture according to the strategy build with his coach. A mobile platform allowed him to adjust the posture of his legs whenever he wants according to the information he can read on the monitor screen.

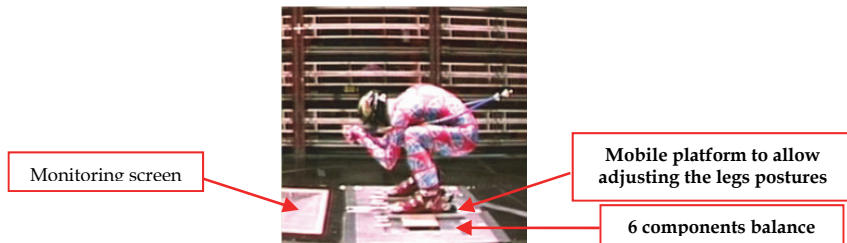


Fig. 15. Measuring device for the assessment of the drag applied on a downhill skier (Wind tunnel of IAT, France).

If the skis have not a great impact on the variability of the drag intensity, their contribution to the variability of the lift has to be taken into account. It is therefore necessary to position the skis outside the boundary layer which is near the ground. Although it is relatively thin, the velocity of the airflow in this area varies significantly and disturbs the measurement of the lift. Sections of boat masts (Fig.16) located under each skis have thus allowed to overcome this problem and allowed to remove the skis from this thin layer where the air stream can transit from a laminar to turbulent conditions.

In time trial cycling, in order to determine the drag force of the system bicycle /cyclist, a cycletrainer is fastened on a drag-measurement platform mounted in the middle of the test-

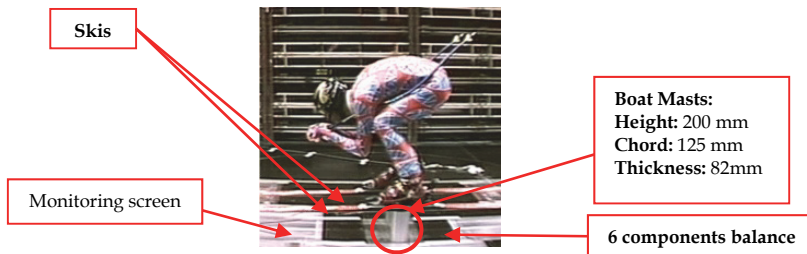


Fig. 16. Measuring device for the assessment of the lift applied on a downhill skier (Wind tunnel of IAT, France).

section of a wind tunnel which dimensions (octagonal section with inside circle of 3 meters in diameter and 6 meters length) allowed to avoid walls boundary layer effects that can interfering measurements (Fig.17). This platform is equipped with ball-bearing slides in the direction of the wind tunnel as well as a dynamometer measuring the drag force. As for assessing the aerodynamic properties of a skier, the general procedure for a cyclist is the same. A preliminary measurement without wind is performed in order to correct the measurements for zero drift and mass tares. Then a second measurement with wind but without the athlete allowed obtaining the drag force of solely the platform equipped with the cycletrainer. Finally, the drag force of the couple bicycle/cyclist can be measured while the cyclist adjusted his posture with a wind speed similar to that found in race conditions (around  $14 \text{ ms}^{-1}$ ).



Fig. 17. Measuring device for the assessment of the drag applied on a time trial cyclist.

If such a measurement tools provides accurate recording of the aerodynamic force apply on the athlete, it has the disadvantages of not being able to be used anytime it is needed. Specific and dedicated wind tunnel program has to be perform and sometimes far away from the athletes current concerns. Moreover, the usual environmental conditions of the sport practice are requirements that cannot be taken into account in a wind tunnel setting.

### 3.2 Modelling methods

For numerical models, the method consists in computing correlation between postural parameters observe during the practice as well as equipment characteristics when or if needed and the value of the aerodynamic force. It requires most of the time and previously wind tunnel data of the aerodynamic characteristics of the athlete according to various postures and if necessary within a wide range of orientations relative to the air flow (Fig.18). Indeed, the functions are generally determined with athletes or model of athletes positioned in a wind tunnel in accordance with postures observed during competition in the field.

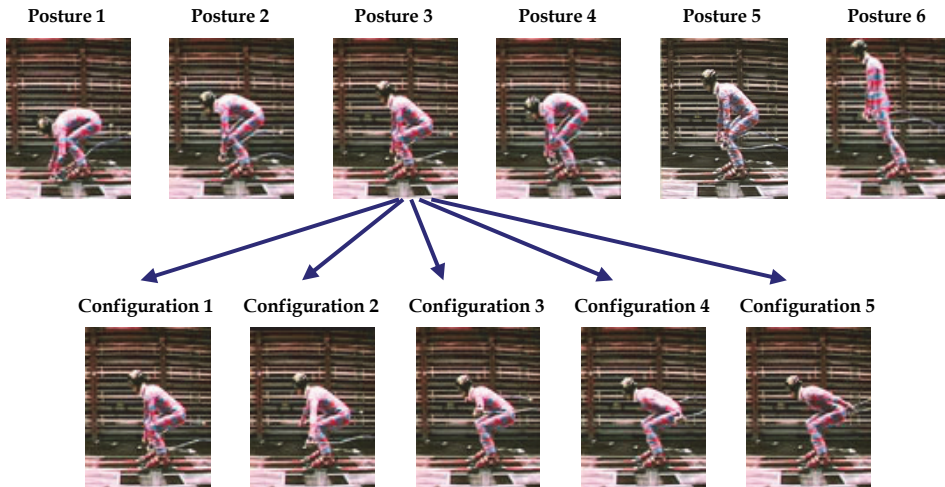


Fig. 18. 30 postures assed in wind tunnel prior the development of a model of the aerodynamic lift applied on a downhill skier when passing over a bump. These postures correspond to postures observed in real conditions (Barelle, 2003).

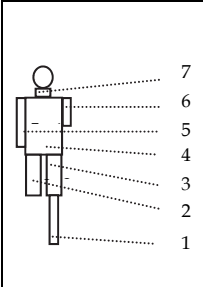
The results of such models can then serve for example as input for simulations based on the Newton laws to estimate variations in time, loss in speed performance induced by different postural strategies as well as equipment interactions. When dedicated simulators integrating such models already exist, an almost real time feedback can be provided to the stakeholder on the aerodynamic properties of the athletes' posture. This can be a cost effective solution since it needs few human and material resources and it can be performed anytime it is needed during normal training sessions.

Examples of the development approach of some models for the evaluation of the aerodynamic performance in running, skiing, cycling are presented and discussed below.

### 3.2.1 Modelling of the aerodynamic force in running

Shanebrook & Jaszczak (1976) have developed a model for the determination of the drag force on a runner. They have considered the human body as a multi-jointed mechanical system composed of various segment and showed that the drag assessment applied on an athlete could be realized by considering the athlete's body as a set of cylinders. Their model is thus composed of a series of conjugated circular cylinders, to simulate the trunk and the lower and upper limbs, as well as a sphere to simulate the head. Projected surface area was measured for each segments (head, neck, trunk, arm, forearm, tight, shank) of the body of three runners representing respectively, adult American males in the 2.5, 50 and 97.5 percentiles of the population. Then the drag coefficient of cylinders and sphere representing these segments has been measured in a wind tunnel. The results for the 50 percentiles are proposed in the table here after (Table 1).

If such a model has the merit to enable one to reach the drag coefficient of the body segments of a runner, it doesn't consider the athlete body has a whole as well as the succession of body segments orientations that can generate different projected surface area and thus variation of the air resistance throughout the global motion of the runner.



Cylinders	A (in <sup>2</sup> )	C <sub>D</sub>
1	64.5	1.2
2	67.7	1.2
3	67.7	1.2
4	312	1.1
5	78.1	1.2
6	43.2	1.2
7	11	1.2
sphère	48.3	0.43

Table 1. Models to determine the drag coefficient of the body part of a runner according to their projected surface area according to Shanebrook & Jaszczak (1976).

Moreover the adaptation of such model to different runners or to different kind of sportsmen during their practice is time consuming and not in accordance with the stakeholders (coaches, athletes) requirement of a quick assessment of the aerodynamic performance of an athlete.

### 3.2.2 Modelling of the aerodynamic force in skiing

The aerodynamic resistance in alpine skiing has been largely investigated, leading to different approaches to model the aerodynamic force. Luethi & Denoth (1987) have used experimental data obtained in a wind tunnel in their approach of the aerodynamic resistance applied on a skier. They have attempted to assess the influence of aerodynamic and anthropometric speed skier. By combining the three variables most influencing the speed of the skier i.e. his weight, is projected surface area (reflecting its morphological characteristics), and the drag coefficient C<sub>D</sub>, they established a numerical code (ACN: Anthropometric Digital Code) representing the aerodynamic characteristics of skiers. The model is written as follow (3):

$$ACN = \left( \frac{mg}{A \cdot C_D} \right)^{1/2} \tag{3}$$

Where *m* is the skier mass, *A* is the projected frontal area, C<sub>D</sub> is the drag coefficient. If the factors *mg* and C<sub>D</sub> (invariable for skiers dressed with the same race clothes) are easily accessible, this model set the problem of assessing the projected frontal area of the skier in real condition. The observer (coaches) because of its placement on the side of the track can hardly have a front view of the athlete in action and even if he had it, it would not allow him to determine directly and easily the *A*. The model of Springings et al. (1990) for the drag and lift lead to the same problem. For this purpose, Besi et al. (1996) have developed a an images processing software to determine *A* but the processing time is once again too important for field application.

Spring et al. (1988) uses the conservation of energy principle in order to model the term *A.C<sub>D</sub>* (4).

$$A \cdot C_D = \frac{m(V_D^2 - V_F^2) - 2k \cdot V \cdot mg \cdot d}{V^2 \cdot \rho \cdot d} \tag{4}$$

Where  $m$  is the skier mass,  $A$  is the projected frontal area,  $C_D$  is the drag coefficient,  $V_D$  is the initial speed of the skier,  $V_F$  is the final speed of the skier,  $V$  is the mean speed of the skier,  $k$  the snow friction coefficient and  $\rho$  the air density,  $d$  the distance travelled by the skier.

While this model takes into account as input data, field variables (speed of the skier, travelled distance), it does not incorporate the influence of postures variations. Once again the results obtained from this model can only be an approximation for use in real conditions since it cannot explain with accuracy the performance variations induced by changes in posture.

The modelling of the aerodynamic force as it is described above is not relevant and efficient for rapid application in real conditions. If in straight running, skiers can easily maintained an optimal crouched posture, in technical sections (turns, bumps, jumps), they must manage their gestures to ensure an optimal control of their trajectory, while minimizing the aerodynamic effects. To be relevant for such real conditions applications, posture variations must be taken into account in the modelling and thus whatever the considered sport.

### 3.2.3 Modelling of the aerodynamic force in cycling

As cyclists' performances depend mainly on their ability to get into the most suited posture in order to expose the smallest area to the air flow action, the knowledge of their projected frontal area can be useful in order to estimate their aerodynamic qualities. By the way, several authors have either reported values of  $A$  or developed specific equations to estimate the projected frontal area (Gross et al., 1983; Neumann, 1992; Capelli et al., 1993; De Groot et al., 1995; Padilla et al., 2000; Heil, 2001). However, this has been generally done only for riders of similar size and adopting the same posture on a standard bicycle. Such estimations have then shown large divergences and methodological differences may have widely contributed to such variability. Thus to be useful, models mustn't be developed as black boxes but by indicating accurately why they have been develop for and in which condition they can be used, by being transparent on the variables that have served to its construction and the results accuracy it can provided.

For example, Barelle et al. (2010) have developed a model estimating accurately  $A$  as a function of anthropometric properties, postural variations of the cyclist and the helmet characteristics. From experiments carried out in a wind tunnel test-section, drag force measurements, 3D motion analysis and frontal view of the cyclists were performed. Computerized planimetry measurements of  $A$  were then matched with factors related to the cyclist posture and the helmet inclination and length. A Principal Component Analysis has been performed using the set of data obtained during the experiment. It has shown that  $A$  can be fully represented by a rate of the cyclist body height, his body mass, as well as the inclination and length of his helmet. All the above mentioned factors have been thus taken into account in the modelling (5).

$$A = 0.045 \times h^{1.15} \times m_b^{0.2794} + [0.329 \times (L \times \sin \alpha_1)^2 - 0.137 \times (L \times \sin \alpha_1)] \quad (5)$$

where  $h$  is the height of the cyclist,  $m_b$  the body mass of the cyclist,  $L$  the length of the helmet, and  $\alpha_1$  the inclination of the head.

The prediction accuracy was then determined by comparisons between planimetry measurements and  $A$  values estimated using the model. Within the ranges of  $h$ ,  $m_b$ ,  $L$  and  $\alpha_1$



involved in the experiment, results have shown that the accuracy of the model is  $\pm 3\%$ . Within the objective to be easy to use, this accuracy can be considered sufficient enough to show the impact of postural and equipment changes on the value of the frontal area of cyclists. This model is explicit and it has been developed to take into consideration variation of posture i.e. inclination of the head. It can easily be applied to a variety of cyclists with different anthropometric characteristics since the height and body mass are input data. Moreover it can also considered the shape characteristic of the helmet including ( $L$ ) its interaction with the inclination of the head ( $\alpha_l$ ). Finally its conditions of use are specified since its accuracy can only be guaranteed for input data that are within the ranges of  $h$ ,  $m_b$ ,  $L$  and  $\alpha_l$  involved in the experiment. It can thus provide pertinent indications useful for both coaches and cyclists.

### **3.3 On the relevance of aerodynamic force modelling versus wind tunnel testing**

Individual and accurate optimization of the aerodynamic properties of athletes on very details modifications by means of wind tunnel measurements is essential for high performance. However, such comprehensive experiments in large scale wind tunnels lead to excessive measurement time and costs and require the disposability of athletes over unreasonably long periods. Even if accurate, wind tunnel tests have the disadvantage of not being able to be used anytime it is needed as it is required for high level sport. Moreover, the usual environmental conditions of the sport practice that can widely influence the performance are requirements that cannot be taken into account in a wind tunnel setting.

Instead, the computer modelling approach if well oriented allows studying the impact of all variables, parameters and initial conditions which determine the sport performance. In terms of aerodynamic, models implemented in the years 1980 and 1990 (Shanebrook, 1976; Watanabe & Ohtsuki, 1978; Luethi et al., 1987; Springings et al., 1990 ... ), do not report the low dispersion of athletic performance neither because of the technical means available for their implementation nor because they were not designed for this purpose.

Several authors have tried to formalize the different steps to develop useful model (Vaughan, 1984; Legay, 1997) but this process is not as linear as it seems. The first stage involves identifying the system under study. This is a situation analysis which will determine and describe the framework within which will take place all the work ahead. When the frame is set, it is about to implement procedures to collect data relating to the objective pursued. The choice of tools for collecting and processing experimental data must be consistent with the model and the desired accuracy. Wind tunnel testing can thus in this case be useful if it takes into consideration postures observed during training and racing, athlete/equipment interactions, boundary conditions. Then to build the model, dependencies between different recorded variables are considered. These relationships are then translated in the form of equations giving the model structure. According Orkisz (1990), it must be hierarchical and give the possibility to adapt to all levels of complexity, depending on the nature of the results to be obtained. Such models have an important value in the quest for performance if their results are express in term of objective benchmarks (time, speed, trajectories ...) that can extend the observation of the coaches.

They could have two exploitation level i.e. analytical or global since they enable stakeholders respectively to focus on a particular aspect of performance such as the specific influence of the aerodynamic resistance (analytical approach of the Newton's law) or on the interaction of factors determining the performance (global approach of the Newton's law)

with the aerodynamic resistance among others (Barelle, 2003). When such models are used for simulation, they allow stakeholders to go further than the simple description. Beyond the fact that they can be used anytime it is needed, they have also predictive capacities and that, at a lower cost.

#### 4. Application and valorisation: towards an optimization of downhill skiers' performances when passing over a bump

For each discipline in Alpine skiing (downhill, slalom, giant slalom ...), the difference in performance among the top world skiers is lower than one percent. Taking into account this low variability, coaches are confronted with the problem of assessing the efficiency of different postural strategies. Numerical models may provide an adequate solution. The method consists in computing a correlation between skiers' kinematics and postural parameters observed during training and each of the forces involved in the motion's equation (Barelle, 2003, Barelle et al., 2004; Barelle et al.; 2006). For postural strategies such as pre-jump or op-traken in downhill, models of the projected frontal area for the lift (6) (Barelle, 2003) and for the drag (7) (Barelle et al., 2004) are calculated based on postural parameters (length and direction of skier's segments).

$$A_L = 0.1167\sin(\gamma) + 0.0258\sin(\beta) + 0.0607 + 0.024E_T((\sin(2.\theta_3) - \cos(\theta_4)) \quad (6)$$

Where  $A_L$  is the projected frontal area,  $\gamma$  is the orientation of the trunk,  $\beta$  is the orientation of the thigh in the sagittal plan,  $\theta_3$  and  $\theta_4$  are the arms orientation respectively in the frontal and horizontal plan.

$$A_D = 0.0003(L_1 \sin(\alpha) + L_2 \sin(\beta) + L_3 \sin(\gamma)) - 0.026 + 0.041(|\sin\theta_1| + |\sin\theta_2|) \quad (7)$$

Where  $A_D$  is the projected frontal area,  $\gamma$  is the orientation of the trunk,  $\beta$  is the orientation of the thigh,  $\alpha$  is the orientation of the shank in the sagittal plan,  $\theta_1$  and  $\theta_2$  are both arms orientations in the horizontal plan.

Ground reaction and skis-snow friction are computed according to skiers' postural kinematics (skier's amplitude variation and duration of spread movements). Skiers' weight is easy to obtain. Thus the external forces exerted on the skis-skier system (Fig.1) are known, the motion's equation can be solved and simulations performed (Fig.19). These can be used to estimate variations in time and loss in speed performance induced by different postural strategies.

Such simulations find an application in the field of training as they enable to assess the impact on performance of a given strategy compared with another (Barelle, 2003; Barelle et al., 2006). Simulation results can be presented in the form of animations, using DVD technology. Such tool enables trainers to show skiers very quickly the variability of performance induced by different postural strategies (Fig.20.).

Broken down in this form, the simulation becomes a way of learning transmission. The aerodynamic drag model (7) can be used directly, if the coach chooses to particularly focus his attention on the aerodynamic effects. A first level of use is then given to the model. Then the model can have a second level of use, if the coach wants to have a general view of the skier performance since it is also designed to be an integral part of the modeling of the postural strategies implemented by skiers when passing over a bump in downhill skiing (simulator, Fig.19.).

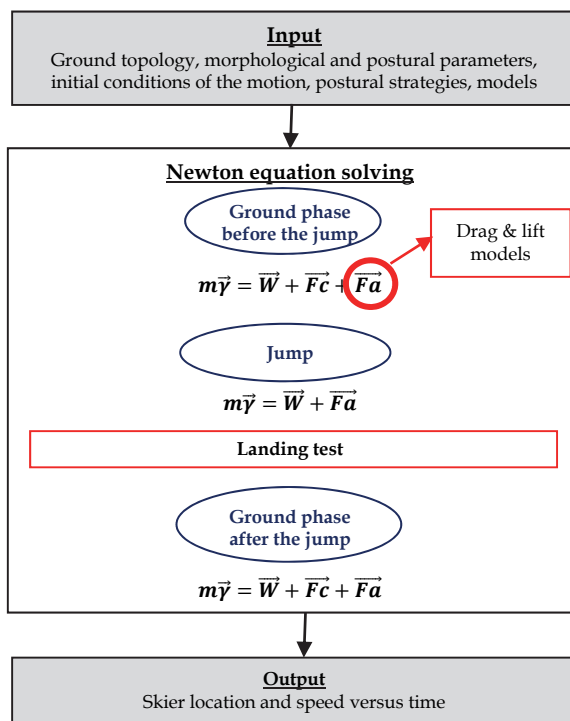


Fig. 19. Structure overview of the simulator of the trajectory of the centre of mass of a skier according to his anthropometric characteristics and his postural strategy as well as the topology of the downhill slope.

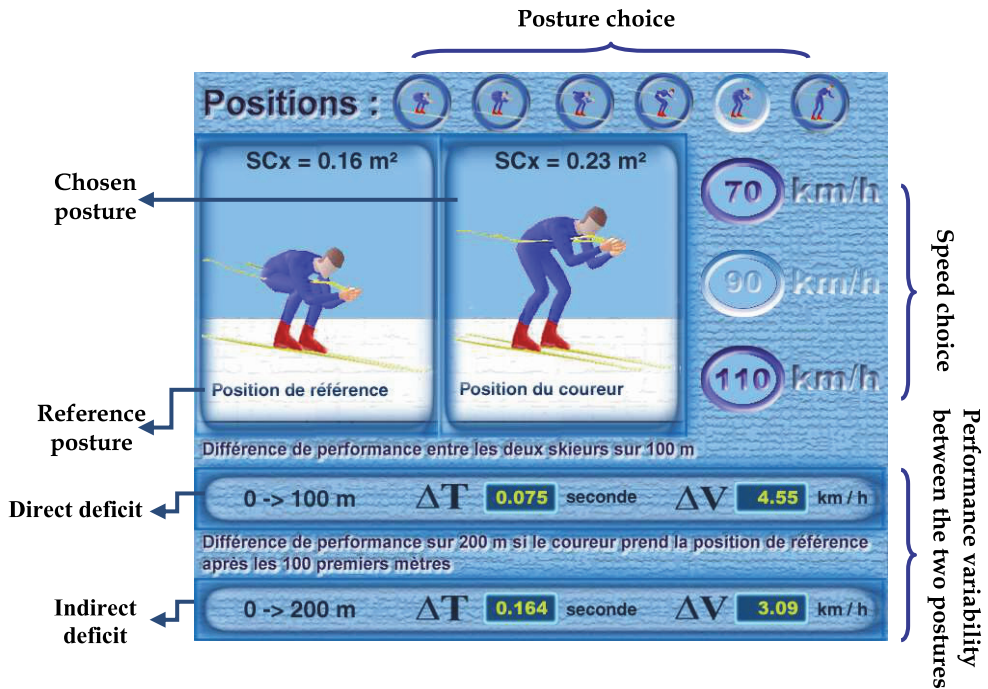


Fig. 20. Overview of DVD application built for the downhill skiers of the French Ski Federation. The choice of a posture enables ones to see the aerodynamic drag impact on performance for three input speed. The choice of a particular input speed enables to see the aerodynamic drag impact according to six different postures usually observed during races. The direct performance variability in terms of time deficit and loss of speed between the reference posture and the chosen posture is given after 100 meters of straight running (Direct deficit). Then stakeholders can visualize the indirect deficit generate 100 meters further (200m) even if the skier adopt again an aerodynamic crouched posture (like the reference one) on the last 100 meters (Indirect deficit).

## 6. Acknowledgment

Researches on downhill skiing are a compilation of several wind tunnel tests (Wind tunnel of IAT, France) conducted each years from 2000 to 2003 by the French Ski Federation in order to optimize the downhill posture of its athletes. The author wishes to thanks particularly all the coaches and skiers that have widely contribute to obtain such results.

Researches on time trial cycling were performed in 2007 (Wind tunnel of Marseille, France) and supported by a grant between Bouygues Telecom, Time Sport International and the University of Mediterranean. The author wishes to thank all members of the cycling team for their active contribution to the wind tunnel testing campaigns.

## 7. Reference

- Barelle, C. (2003) Modélisation dynamique du geste sportif à partir de paramètres posturaux. Application à l'entraînement en ski alpin. *PhD Thesis*, Claude Bernard University, Lyon, 99-102.
- Barelle, C.; Ruby, A.; Tavernier, M. (2004). Experimental Model of the Aerodynamic Drag Coefficient in Alpine Skiing. *Journal of Applied Biomechanics*, No.20, pp167-176.
- Barelle, C.; Ruby, A.; Tavernier, M. (2006). Kinematic analysis of the performance based on simulations of the postural strategies produced by the alpine skiers. *Science et Motricité*, Vol.3, No.59, pp.99-111.
- Barelle, C.; Chabroux, V.; Favier, D. (2010). Modeling of the Time Trial cyclist projected frontal area incorporating anthropometric, postural and helmet characteristics, *Sports engineering*, Vol.12, No. 4, pp.199-206.
- Belluye, N. & Cid, M. (2001). Approche biomécanique du cyclisme moderne. *Science et Sports*, No.16, pp. 71-87.
- Besi, M. Vedova, D.D., Leonardi, L.M. (1996) Sections : un programma di analisi dell'immagine applicato allo sport. *Scuola dello sport*. No.34, pp. 72-77.
- Chabroux, V.; Barelle, C.; Favier, D. (2008). Aerodynamics of time trial bicycle helmets. *The engineering of sport*, No. 7, pp.401-410.
- Capelli, C.; Rosa, G.; Butti, F.; Ferretti, G.; Veicsteinas, A.; Di Prampero, P.E (1993) Energy cost and efficiency of riding aerodynamic bicycles. *European Journal of Applied Physiology*, No.67, pp.149-165.
- De Groot, G.; Sargeant, A.; Geysel, J. (1995). Air friction and rolling resistance during cycling. *Medecine and Science in sports and exercise*, pp.1090-1095.
- Di prampero, P.E.; Cortili, G.; Mognoni, P. & Saibene, F. (1979). Equation of motion of a cyclist. *Journal of applied physiology*, No.47, pp.201-206.
- Gross, A.C; Kyle, C.R; Malewicki, D.J (1983) The aerodynamics of human-powered land vehicles. *Scientific American*, No.249, pp. 126-134.
- Heil, D.P (2001). Body mass scaling of a projected frontal area in competitive cyclists. *European Journal of Applied Physiology*, No.85, pp. 358-366.
- Kyle, C.R.; Crawford, C. & Nadeau, D. (1973). Factors affecting the speed of bicycle. *Engineering report 73-1*. California State University. Long Beach, California.
- Legay, J.M. (1997) L'expérience et le modèle : un discours sur la méthode. *Sciences en question*. INRA éditions.
- Lesieur P. (1996) L'étude de cas : son intérêt et sa formalisation dans une démarche clinique de recherche. *Colloque interface INSERM / FFP*.

- Luethi, M.S., Denoth J. (1987). The influence of aerodynamic and anthropometric factors on speed in skiing. *International journal of sport biomechanics*, No.4, pp.345-352.
- Padilla, S.; Mujika, I.; Angulo, F.; Goiriena, J.J. (2000). Scientific approach to the 1h cycling world record : a case study. *Journal of Applied Physiology*, No.89, pp.1522-1527.
- McLean, B.D.; Danaher, R.; Thompson, L.; Forges, A.; Coco, G. (1994). Aerodynamic characteristics of cycle wheels and racing cyclists. *Journal of Biomechanics*, Vol. 27, pp.675.
- Neumann, G. (1992) Cycling. Endurance in sport. Edition R.J. Shepard and P.O. Astrand, London : blackwell, pp.582-593.
- NØrstrud, H. (2008). Basic Aerodynamics. *Sport aerodynamics. CISM International centre for mechanical sciences*, Vol. 506, pp.1-8.
- Orkisz M. (1990). Traitement d'image pour l'analyse du mouvement humain. *Cinesiologie*, No.29, pp.133-140.
- Shanebrook, R.J., Jaszczak R.D. (1976) Aerodynamic drag analysis of runners. *Medecine and science in sports*, Vol. 8, No.1, pp.43-45.
- Spring, E.; Savolainen, S.; Erkkilä, J.; Hämmäläinen, T.; Pihkala, P. (1988). Drag area of a cross country skier. *International journal of sport biomechanics*. Vol.4, pp.103-113.
- Springings, E.J. & Koehler, J.A. (1990). The choice between Bernoulli's or Newton's model in predicting lift. *International Journal of sport biomechanics*, No. 6, pp.235-245.
- Tavernier, M.; Cosserat, P.; Joumard, E.; Bally, P. (1994). Influence des effets aérodynamiques et des appuis ski - neige sur la performance en ski alpin. *Science et motricité*, No.21, pp.21-26.
- Watanabe, K. & Ohtsuki, T. (1977). Postural changes and aerodynamic forces in alpine skiing. *Ergonomics*, Vol. 20, No.2, pp.121-131.
- Watanabe K. & Ohtsuki T. (1978). The effect of posture on the running speed of skiing. *Ergonomics*, Vol. 21, No.12, pp.987-998.
- Vaughan, C.L. (1984). Computer simulation of human motion in sports biomechanics. *Exercice and sport sciences reviews*, No.12, pp. 373-416.
- Weineck, J. (1997). *Manuel d'entraînement*. Vigot, collection Sport + Enseignement. 4<sup>ème</sup> édition.

# Active and Passive Control of Flow Past a Cavity

Seiichiro Izawa  
Tohoku University  
Japan

## 1. Introduction

Flow past open cavities is well known to give rise to highly coherent and self-sustained oscillations, leading to undesirable aeroacoustic resonance. Cavity flows are encountered not only in engineering applications but also our daily life, for example, the weapon bays, landing gears and wheel wells of aircrafts, in the depressions of submarine and ship hulls, in the pantograph recess of high-speed train, in the sunroof of cars or in the closed side branches of pipelines. Periodic and intense aeroacoustic vibrations deriving from the self-sustained oscillations of cavity flows can give rise to structural fatigue, optical distortion and store separation problems, especially for high-speed aircrafts. For a typical open-cavity flow, the induced acoustic level exceeds 160dB at transonic Mach numbers (MacManus & Doran, 2008) and it still reaches approximately 130dB at around 100 ~110km/h for passenger vehicles because the passenger compartment acts as a Helmholtz resonator (Gloerfelt, 2009). Cavity-like geometries are also observed in places such as urban canyons, rivers and lakes. For these environmental fields, cavity flows affect the mass transfer processes of various pollutants and chemical toxic substances that occur between the cavity and the main flow (Chang et al., 2006). In the last decade, open cavities have attracted many researchers engaged in scramjet engines with regard to mixing and flame-holding enhancement for supersonic combustion (Asai & Nishioka, 2003; Kim et al., 2004). Because of these issues across a wide range of applications, cavity flows have been of practical and academic interests for more than a half-century.

The flow-induced oscillations in an open cavity arise from a feedback loop formed as a result of successive events that take place in sequence. Figure 1 illustrates the schematic of cavity flows with an acoustic resonance. A boundary layer of thickness  $\delta$  separates at the upstream edge of the cavity of length  $L$  and depth  $D$ . The resulting separating shear layer is convectively unstable due to Kelvin-Helmholtz instability, and it soon rolls up into vortices. Every time the organized vortical structures collide the downstream corner, the expansion waves are radiated from the corner owing to the vorticity distortion at low Mach numbers (Yokoyama & Kato, 2009), while as Mach number increases, the compression waves are generated near the downstream corner, especially for supersonic flows (Nishioka et al., 2002). It should be noted that the hypersonic shear layers do not always roll up into isolated vortices, just forming wavy patterns. The strength of these induced waves is determined by the relative position of the traveling vortices and the downstream corner. Rockwell & Knisely (1978) classified the vortex-corner interactions into four possible events on the basis of flow visualizations: Complete Escape (CE), Partial Escape (PE), Partial Clipping (PC) and Complete Clipping (CP). The incident acoustic waves propagate inside the cavity towards the upstream corner and

determine the initial amplitude and phase of the instability waves in the separating shear layer through the receptivity process. In particular, when the process is coupled with an acoustic cavity resonance, intense aerodynamics tones are generated in and around the cavity. This mechanism is common to basically all cavity tones regardless of the Mach number, known as shear-layer mode or Rossiter mode (Rossiter, 1964). This type of aeroacoustic tones is referred as the cavity noise. According to Rossiter's empirical formula, the resonant frequencies are given by

$$\frac{fL}{U_\infty} = \frac{m - \alpha}{M + 1/\kappa} \quad (1)$$

where  $f$  is the frequency at a given mode number  $m = 1, 2, 3, \dots$  and  $M$  is the freestream Mach number. The empirical constants  $\alpha$  and  $\kappa$  correspond to the average convection speed of vortices traveling over the cavity normalized by freestream speed and the phase delay of vortices against the upstream traveling acoustic waves. For example,  $\alpha = 0.25$  and  $\kappa = 0.57$  are derived from the experiment under the condition that  $L/D = 4$  and the Mach number range  $M = 0.4 \sim 1.2$ . These values are intrinsically dependent on the flow conditions and the aspect ratio of the cavity,  $L/D$ . Some modified formulas have been proposed in the past (e.g., Heller et al., 1971; Asai & Nishioka, 2003). In addition to experimental studies, a number of computational studies have been performed to predict the vibration and acoustics associated with cavity flows for various Mach numbers (e.g., Grace, 2001; Gloerfelt et al., 2003; Larchevêque et al., 2007; De Roeck et al., 2009). The noise generated by circular cavities, not rectangular cavities, was also investigated by Marsden et al. (2008) and Chicheportiche & Gloerfelt (2010).

Flow patterns over the cavity can be roughly categorized into two different types, depending on the aspect ratio  $L/D$ . As the cavity is elongated, a free shear layer eventually reattaches on the floor of the cavity before reaching the downstream wall. Once the reattachment occurs, one more recirculating region with opposite rotating direction appears near the downstream side. This type of cavities is called the "closed cavity". Closed cavity flows can be regarded as

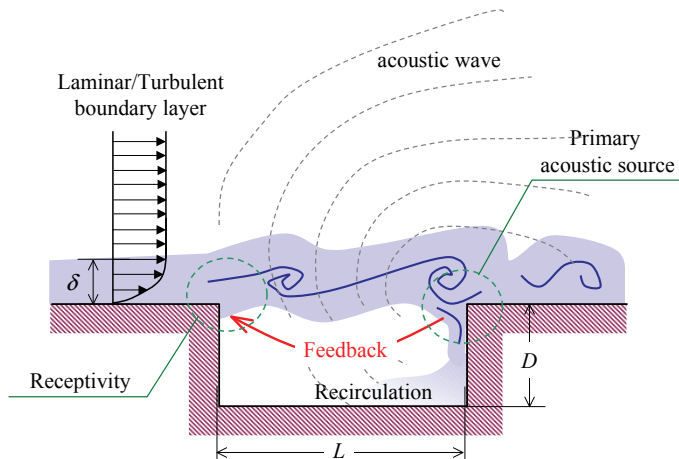


Fig. 1. Schematic of cavity flows.



the flow, which combines the backward-facing step with the forward-facing step. The cavities without reattachment are termed "open cavity". Between these two states, the cavity flows exhibit both characteristics, and are called the "transitional cavity". The open cavity flows are much more complex than the closed cavity flows, because the self-sustained oscillations only occurs in the upstream cavities. Flow visualizations have been presented to observe fluid motions inside the open cavity with different aspect ratios  $L/D$  (e.g., Faure et al., 2006).

A variety of control techniques for cavity resonance suppression have been tested over the years. These approaches can be classified into three types by the controlling locations: the leading edge, downstream edge, and the floor of the cavity. Most of the methods to control cavity flows tried to actively control the separating flow by introducing minute velocity fluctuations at the leading edge of a cavity, where the receptivity of the flow is most sensitive to the small disturbances. Raman et al. (1999) investigated the effect of miniaturized bi-stable fluidic oscillator on the cavity noise resonance, where its frequency and velocity depended on the supplied pressure. The fluidic device located at the upstream end of the cavity floor could suppress the cavity noise by 10db with mass injection rates of the order of 0.12% of the main flow, while it lost the effect near the downstream end of the cavity. Hémon et al. (2002) used piezoelectric bimorph elements as a flap-type actuator, which allows to generate a series of two-dimensional vortices forced at a different frequency from the natural resonance frequency. Kegerise et al. (2002) have tested the adaptive feedback controller together with the infinite-impulse filter response (IIR) filters to activate similar piezoelectric flaps. Rowley et al. (2003, 2005) injected the zero-net-mass airflows at the leading edge on the basis of pressure information at the wall inside the cavity. Huang & Zhang (2010) reported that the streamwise plasma actuators located on the upstream surface of the cavity was more effective than the spanwise actuators in cavity noise attenuation.

Besides the leading edge control, Micheau et al. (2005) used the vibrating surface that is an aluminum beam located along the downstream edge and attached to a shaker. They obtained significant cavity noise attenuation with an adjustable narrow-band controller using wall-mounted microphones placed at the bottom of the cavity. Yoshida et al. (2006) numerically investigated the effect of sliding floor of the cavity on the flow-induced cavity oscillations. The shear layer oscillations could be suppressed by creating stationary vortices inside the cavity, when the floor velocity was larger than 19% of the freestream velocity in the streamwise direction, or less than  $-10\%$ . Detailed reviews of active control have been provided by Williams & Rowley (2006) and Cattafesta et al. (2008).

In addition to various active control techniques, passive control approaches have also been tested, though their numbers are smaller. For instance, MacManus & Doran (2008) added a backward-facing platform at the leading edge of the cavity against transonic Mach number flows,  $M = 0.7 \sim 0.9$ . They pointed out that a large recirculation bubble sitting on top of the step face might contribute to the noise attenuation. Kuo & Chang (1998) and Kuo & Huang (2003) discussed the effect of horizontal plate above the cavity on the oscillating flow structures within the cavity below. They (2001) also investigated the influence of sloped floor or fence on the flat floor of the cavity, focusing on the recirculating flow inside the cavity.

On the other hand, our wind tunnel experiments for cavity flows were conducted at low Mach numbers. The present work reviews a series of our studies to control cavity flows actively and passively, discussing their noise suppression mechanism. As an active control device, we use an array of piezoelectric actuators, oscillating vortex generators (VG), synthetic jets and fluidic oscillators. Synthetic jets, which are generated by a combination of loudspeaker and resonator, are ejected through open slots, while the intermittent jets are provided by the fluidic

oscillators. Vortex generators attached on the upstream surface are designed to introduce the streamwise vortices of alternate rotating directions into the shear layer. These devices are attached on the upstream wall of a cavity except for VG to add the weak periodic velocity fluctuations to the shear layer. Their operating frequency is chosen as the natural frequency of the shear layer. It should be noted that our method, quite different from any others, controls only the timing of the separation at the leading edge depending on the spanwise location. Therefore, the wavy patterns of velocity fluctuations side-by-side with 180 degrees phase difference are generated in the flow. As a result, the pressure fluctuations hence the sound waves coming out will also be 180 degrees out of phase, and then, these opposite-signed sound waves will eventually cancel each other faraway from the cavity though the noise generation at the source itself is not reduced. The competitive advantage of phase control is ascribed to low energy consumption compared with other methods, which changes the frequency of the oscillation or eliminates the oscillation itself. We have also performed the passive control experiments using a small thin plate inserted inside the shear layer and a small blockage set at the bottom of the cavity. The effect of the size and location of the obstacle on the noise suppression is investigated.

This paper consists of two main sections. The first section reviews our open-loop control of flow-induced cavity noise. In the second part, we describe the passive control experiments.

## 2. Experimental setup

Experiments were conducted in the small-scale low-turbulence wind tunnel at the Institute of Fluid Science (IFS) of Tohoku University. The wind tunnel is a closed circuit type and has an octagonal nozzle with a cross section dimensions 293mm from wall to wall, and 911mm-long open type test section. The freestream turbulence level at the test section was roughly 0.1 ~ 1.5% of freestream velocity  $U_\infty$  that is 18 ~ 30 m/s.

Figure 2 shows a rectangular cavity model used in the experiment. The model was slightly tilted raising the trailing edge to prevent flow separation near the leading edge. The cavity of streamwise length  $L$  and depth  $D$  was placed 300 ~ 450mm downstream from the leading edge. Beneath the flat plate surface, a resonator is used to simulate a deep cavity environment because the peaky noise is not generated in the shallow cavity case when the flow before separation is turbulent. The natural wavy pattern of velocity fluctuation in the cavity is two-dimensional so that two end plates are attached on both spanwise ends of the plate to maintain the flow conditions. The origin of coordinate system is at the center of the upstream edge of the cavity, where  $x$ ,  $y$ ,  $z$ -axes are in the streamwise, wall-normal, and spanwise directions.

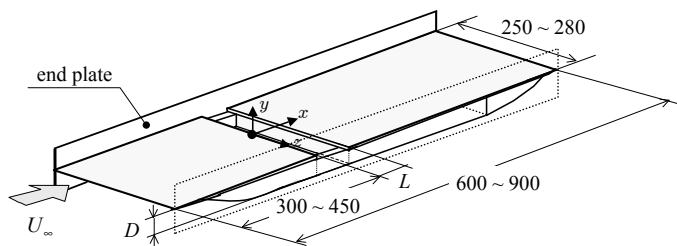


Fig. 2. Schematic of cavity model.

The velocity fields are mainly measured by a hot-wire probe on a three-dimensional traversing mechanism. The acoustic measurement are made using a 1/2-inch (1.27mm) condenser microphone from the location at 500 ~ 1,000mm above the center of the cavity, which is determined by the frequency of radiated cavity noise to ensure the far field. The signals from the hot-wire probe and microphone are digitized by a 16 bit (5kHz) A/D converter after passing an anti-alias filter, which has a 2.5kHz cut-off frequency. And then, the data are stored and processed by a computer running on a Linux operating system.

### 3. Active control

Open-loop control of cavity flows has been performed using various type actuators: an array of piezoelectric actuators, oscillating vortex generators, synthetic jets and fluidic oscillators. In the following sections, we describe the control effects of each actuator on the cavity noise attenuation.

#### 3.1 Piezoelectric actuator

Some certain materials can acquire a charge in response to mechanical strain, and vice versa, they become lengthened or shortened if they are exposed to an electric field. This characteristic is known as piezoelectricity. Lead zirconate titanate ( $\text{Pb}[\text{Zr}_x, \text{Ti}_{1-x}]\text{O}_3$ ,  $0 < x < 1$ ), called PZT, is a popular material that shows the piezoelectric effect. PZT is deformed by approximately 0.1% of the static dimension when an external electric field is applied. We use two types of PZT ceramic elements (FUJI CERAMICS CORPORATION), unimorph and bimorph, as an actuator (Yokokawa et al., 2000, 2001; Fukunishi et al., 2002). A bimorph element consists of two unimorph elements so as to produce large displacement, because electric field causes one element to extend and the other element to contract. The dimensions of one PZT ceramic element used in our experiments are 50mm long, 60mm wide and 0.3mm thick for unimorph type, and 25mm long, 30mm wide and 0.5mm thick for bimorph type. Four unimorph and eight bimorph actuator pieces are installed at the leading edge of the cavity of length  $L = 50\text{mm}$ , depth  $D = 27.5\text{mm}$  and width  $W = 250\text{mm}$  respectively, as shown in Fig. 3. Since the upstream side or lower side of these actuators are glued onto the wall, streamwise displacement can be obtained by expanding and contracting motions for unimorph type and bending motion for bimorph type. It should be noted that the maximum displacements are several micrometers for unimorph type and approximately tenfold increase in bimorph type, when  $70V_{\text{rms}}$  is applied to the actuators. Thus, a thin plastic plate of 0.2mm thick is inserted between the upstream sidewall and each bimorph actuator to prevent unfavorable noise generation caused by the actuator hitting the solid wall.

Each actuator is wired separately so as to operate them independently. The sinusoidal operating signals of voltage are generated by a frequency synthesizer (TOA FS-1301) and amplified by a high-speed voltage amplifier (NF ELECTRONIC INSTRUMENTS 4020), and then, energized the actuators through the electrodes attached on the both sides of actuators. The frequency of operating signals is chosen as the fundamental frequency of cavity flows. Several operating modes are tested in addition to single-phase mode, here the mode number  $n$  is defined as the number of neighboring actuators driven by the same signals. For instance, mode 2 means that the sign of signals becomes opposite between every two neighboring actuators, i.e., 180 degrees out-of-phase, while mode 4 in the unimorph type and mode 8 in the bimorph type are equal to the single-phase mode. Consequently, the possible modes are common divisions of total number of actuators.

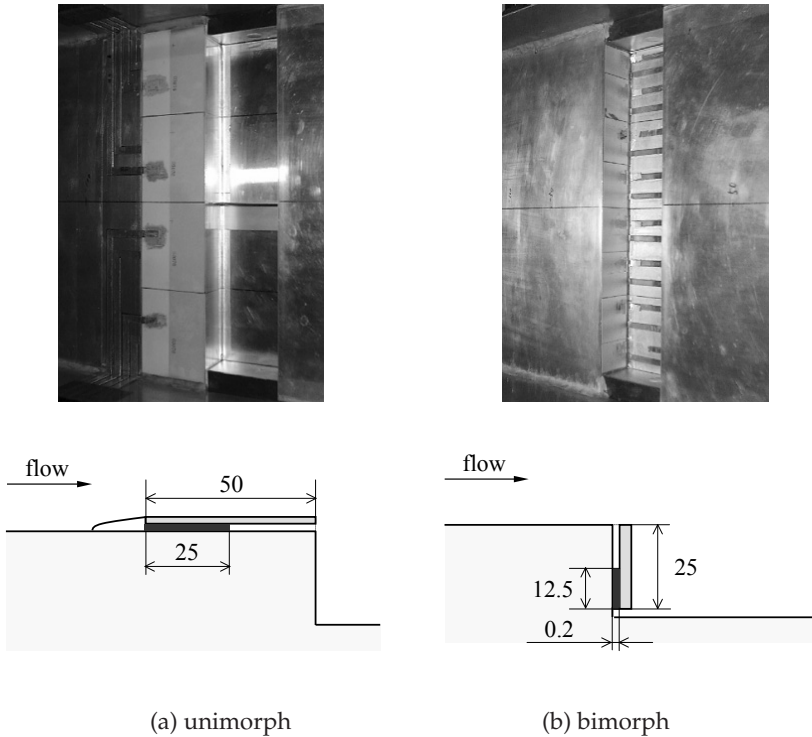


Fig. 3. Piezoelectric actuators.

type	No. of pcs.	mode
<b>unimorph</b>	4	1, 2, 4 (= single-phase)
<b>bimorph</b>	4	1, 2, 4, 8 (=single-phase)

Table 1. Operating modes of actuators.

We use these actuators to control the turbulent-separating cavity flows at  $U_\infty = 30\text{m/s}$ , where the boundary layer is tripped by a wire ( $\phi = 0.5\text{mm}$ ) together with a piece of sandpaper (No.80) attached to the surface. The thickness of turbulent boundary layer is approximately 7.5mm at the upstream edge of the cavity, 300mm away from the leading edge. Figure 4 shows the FFT spectral analyses of cavity noise and velocity fluctuation inside the shear layer. Both signals have an outstanding peak at around 520Hz. Therefore, this frequency is chosen as the control frequency of actuators. Figures 5 and 6 show the contour map of velocity fluctuations  $u'$  in  $xz$  plane at  $y = 0\text{mm}$  when the supply voltage  $V_{\text{rms}} = 70\text{V}$ . These graph are obtained by the ensemble averaging method with the conditional sampling, where the sound signal captured by the microphone is used as the reference signal. The broken lines in the figures indicate the boundaries of the actuators that have the same operating signal. Two-dimensional fluctuation patterns appear along the spanwise direction in the without control case. In particular, these stripe patterns become intense when all actuators are activated by the same operating signal, because the timings of rolling up process are in phase owing to the actuators' motions. The

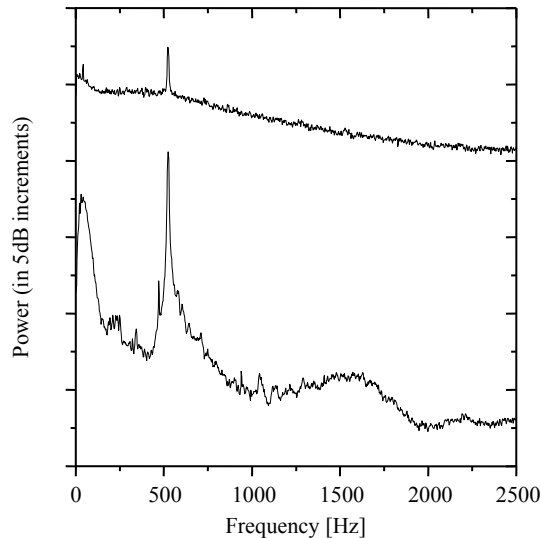


Fig. 4. Power spectra of velocity and pressure fluctuation.

distance between positive and negative stripes is approximately  $0.26L \sim 0.28L = 13 \sim 14\text{mm}$ . Supposing that the rolled-up vortices travel downstream at the half of the freestream velocity,  $15\text{m/s}$ , the frequency of cavity noise can be roughly estimated as  $536 \sim 577\text{Hz}$ . As shown in Fig. 5, more or less two-dimensional patterns are still observed and no wavy patterns with spanwise phase difference can be found, whether the unimorph-type actuators are activated or not. On the other hand, it is clearly found that the phase of velocity fluctuations is switched from positive to negative or negative to positive at the boundaries of bimorph-type actuators for each operating mode.

Figure 7 presents the noise reduction effects for different supply voltages. The data is plotted as the difference from the peak level of the fundamental frequency around  $520\text{Hz}$  without control case, as shown with a dotted line in the figure. The cavity noise increases when all actuators move at the same phase (single-phase), because the two-dimensionality is enhanced by the actuators (see, Fig. 5 (b)). On the other hand, the noise levels go down for each operating mode in both types. It is also found that the bimorph type actuators attached on the upstream sidewall are more effective than the unimorph type actuators (see, Fig. 5 (c), (d) and Fig. 6). Although the unimorph type actuators have the ability to suppress the cavity noise for laminar separating flows, they lose the control effect in the turbulent separating flows since the displacement of actuators becomes relatively smaller in the turbulent boundary layers. Even if the incoming boundary layer is laminar, same problem becomes obvious as the Reynolds number increases.

To obtain the larger displacement, it is necessary to amplify the actuator's displacement in some way. Thus, in this study, we take advantage of the natural frequency of thin aluminum plate, as shown in Fig. 8, where  $l_1$  and  $w_1$  are the length and width of beam 1,  $l_2$  and  $w_2$  the length and width of extra rectangular mass 2. Their thickness  $h$  is  $1\text{mm}$ . A piece of unimorph actuator, that is  $60\text{mm}$  long,  $15\text{mm}$  wide and  $0.3\text{mm}$  thick, is glued onto the one surface of the T-shaped plate. The actuator is activated at the natural frequency of the T-plate. The frequency can be adjusted by changing the length of the head of the T-plate. Since the

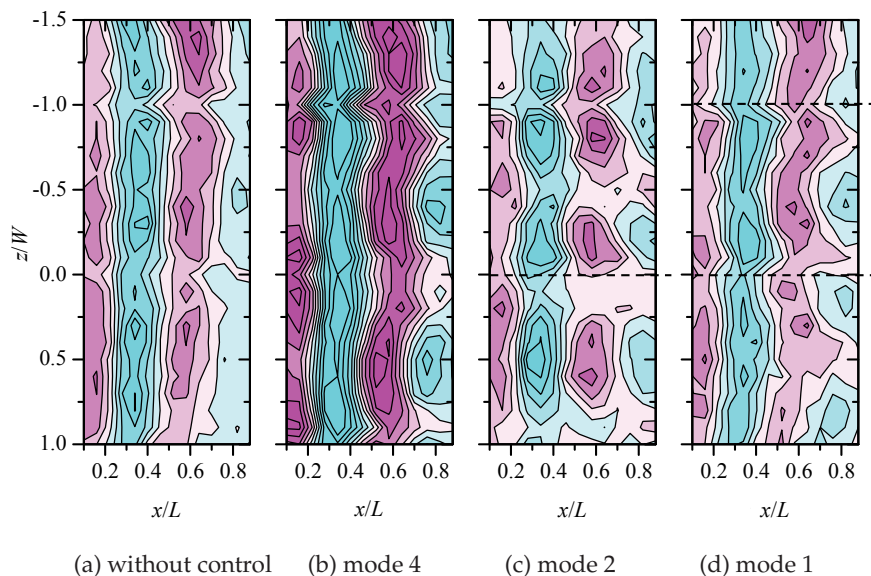


Fig. 5. Contour maps of velocity fluctuations  $u'$  in  $xz$  plane at  $y = 0\text{mm}$ ,  $U_\infty = 30\text{m/s}$  and  $V_{\text{rms}} = 70\text{V}$ . Contour interval is  $0.03U_\infty$ . (a) Without control, (b) mode 4 (single-phase), (c) mode 2, (d) mode 1. (Unimorph type)

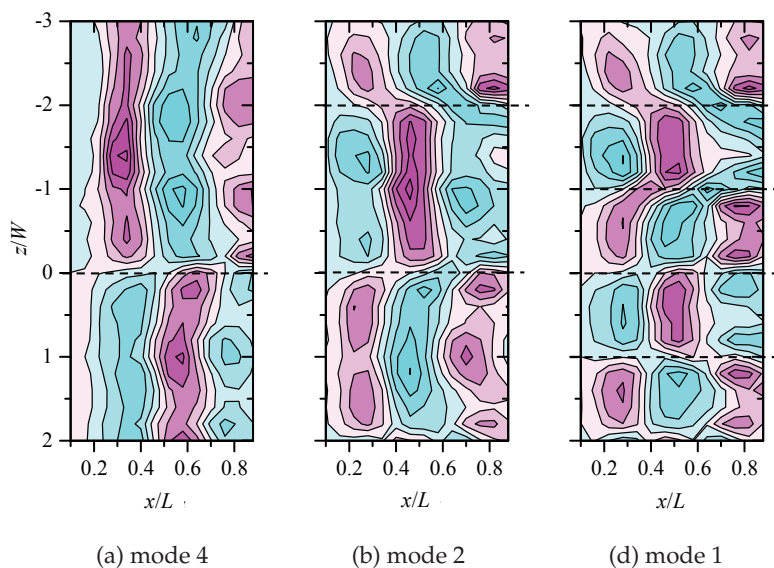
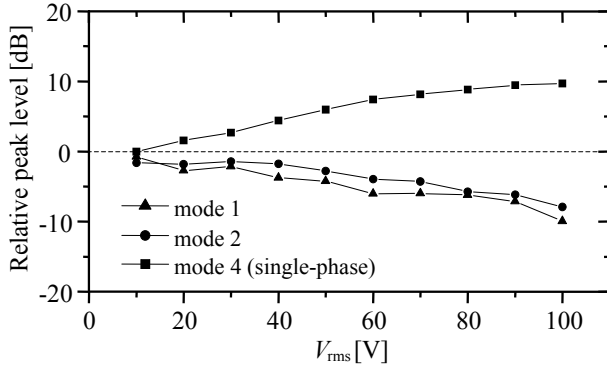
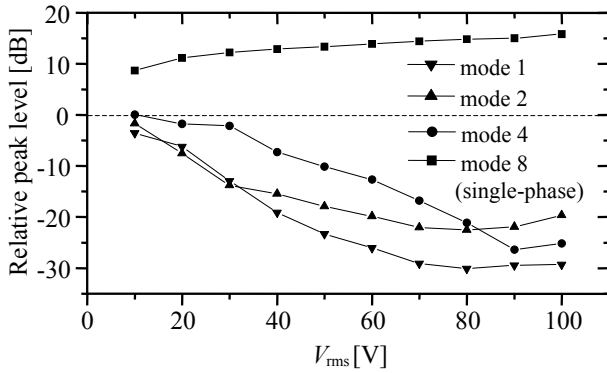


Fig. 6. Contour maps of velocity fluctuations  $u'$  in  $xz$  plane at  $y = 0\text{mm}$ ,  $U_\infty = 30\text{m/s}$  and  $V_{\text{rms}} = 70\text{V}$ . Contour interval is  $0.03U_\infty$ . (a) Mode 4, (c) mode 2, (d) mode 1. (Bimorph type)



(a) unimorph type



(b) bimorph type

Fig. 7. Peak level dependence on supply voltage.

bottom of the T-plate is screwed to the wall and fixed, the tip of the plate vibrates back and forth in response to the actuator’s expanding and contracting motion. The maximum stroke of the T-plate reaches 1mm, which is hundred times larger than that of an unimorph-type actuator. Twelve such T-plate actuators are set along the spanwise direction 1mm away from the upstream sidewall of the cavity, in a similar way as the bimorph-type actuators.

From the analogy of spring-mass system, the first natural frequency of T-shaped cantilever is written by (Narducci et al., 2007)

$$f = \frac{1}{2\pi} \sqrt{\frac{k + \Delta k}{c_1 m_1 + m_2}} \tag{2}$$

where  $c_1 = 0.24$ ,  $k + \Delta k$  is the spring constant after the extra mass  $m_2$  is added,  $c_1 m_1$  is the effective mass of the cantilever beam. The spring constant  $k + \Delta k$  is given by

$$k + \Delta k = \frac{Eh^3}{4} \frac{w_1 w_2}{l_2^3 w_1 + l_1^3 w_2 + 3l_1^2 l_2 w_2 + 3l_1 l_2^2 w_1} \tag{3}$$

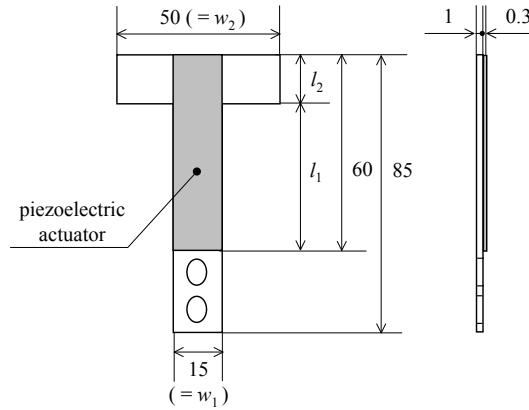
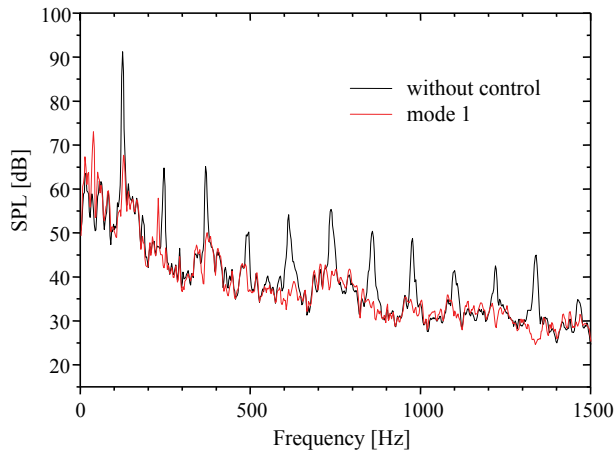


Fig. 8. T-shaped actuator.

Fig. 9. Noise suppressing effect with the T-shaped actuators at  $U_\infty = 21\text{m/s}$ .

where  $E$  is the Young modulus of the material. For instance, the first natural frequency of the aluminum plate can be estimated to be approximately  $112.4\text{Hz}$  for  $l_1 = 15\text{mm}$  and  $139.5\text{Hz}$  for  $l_2 = 8\text{mm}$ . However, the actual frequency is expected to be slightly higher than these estimated values, because the piezoelectric actuator is attached. Thus, considering that the target frequency of cavity noise under the current experimental setup is  $124.5\text{Hz}$ , we determine the length of extra mass  $l_1$  to be  $15\text{mm}$  and the operating frequency of actuators  $116\text{Hz}$ .

Figure 9 shows the noise suppression effect of T-shaped actuators when the freestream velocity is  $21\text{m/s}$  and the incoming boundary layer is turbulent. The voltage supplied to the actuators is  $50V_{\text{rms}}$ . As shown the figure, the peak level at  $124.5\text{Hz}$  decreases by  $23.5\text{dB}$ , and all the higher harmonics components disappear from the spectrum except for the second harmonics. The control effect drops to  $17.3\text{dB}$  for larger operating frequency  $124\text{Hz}$  ( $l_2 = 8\text{mm}$ ). Thus, the noise suppression effect depends on the operating frequency because the



stroke of vibrating T-shaped actuators changes. At the same time, it can be expected that the maximum control effect can be achieved when the operating frequency, the natural frequency of the oscillating device and the fundamental frequency of cavity noise exactly match.

### 3.2 Synthetic jets

Conventional synthetic-jet type of actuation is usually provided by the direct movement of compression-driver diaphragm or piezoelectric arrays inside slots beneath the surface, and so on. On the other hand, we have tested the different synthetic-jet type actuators based on the acoustic resonance as a candidate for new control device, which can generate stronger fluctuations at the upstream of the cavity. Figure 10 shows the schematic of cavity model with synthetic jet actuators. One actuator consists of a loudspeaker of diameter 2 inches and a resonance box. Both ends of the resonance box can be shifted in the streamwise direction within the range of  $0 \leq L_R \leq 580$ , where  $L_R$  is the distance between them. The loudspeaker is placed at a distance  $L_S$  from the upstream edge of the cavity and a urethane form is stuffed as an acoustic insulator behind the loudspeaker. Synthetic jet is ejected through a slot of 1mm in width on the upstream sidewall of the cavity. Same four actuators are installed side by side beneath the cavity. Freestream velocity  $U_\infty$  is 25m/s and incoming boundary layer is tripped by a wire ( $\phi = 0.8\text{mm}$ ) to be turbulent. A resonator is attached beneath the downstream plate to form a deep cavity.

First of all, the optimum condition ( $L_R, L_S$ ) is investigated by measuring the jet velocity at the slot exit for six different actuators, shown in Tab. 2. The length of actuators is determined by the wavelength of target cavity noise. First two conditions, Runs S-1 and S-2, have a symmetrical arrangement about the slot on the upstream sidewall of the cavity. The rest

Run	$L_R$	$L_S$
S-1	$\lambda$	$\lambda/2$
S-2	$\lambda/2$	$\lambda/4$
R-1	$\lambda/2$	$\lambda/2$
R-2	$\lambda/4$	$\lambda/4$
L-1	$\lambda/2$	0
L-2	$\lambda/4$	0

Table 2. Slot location and streamwise length of synthetic jet actuators.

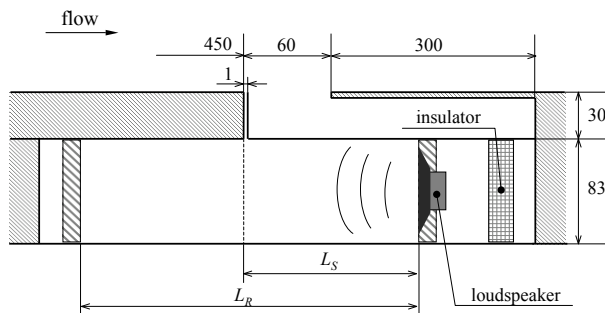


Fig. 10. Schematic of cavity model with synthetic jet actuators.

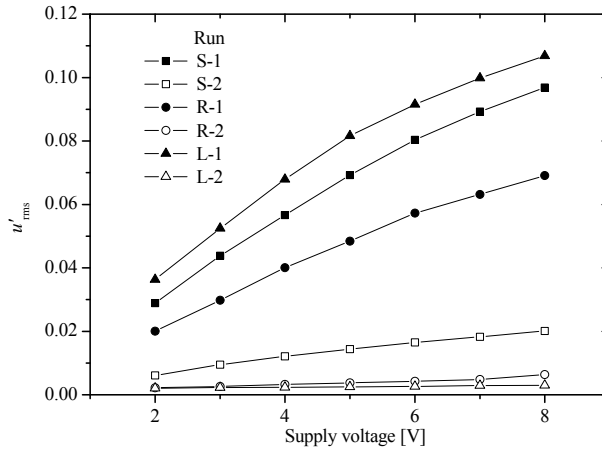


Fig. 11. Variation of the RMS of velocity fluctuation  $u'_{rms}$  at  $f = 700\text{Hz}$  for different actuator configurations.

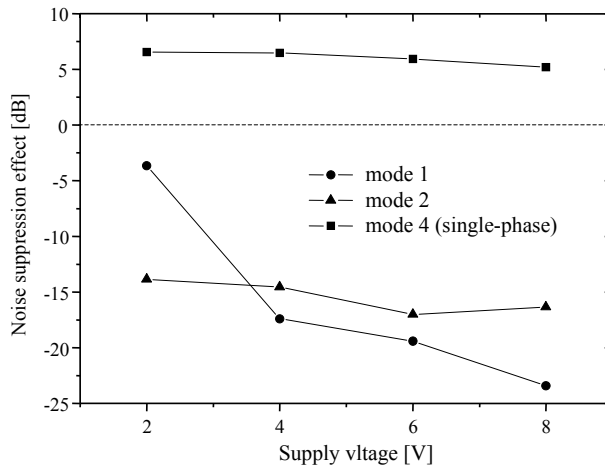


Fig. 12. Noise suppression effects of different operating modes, mode 1, 2 and 4 (single-phase), as a function of the supply voltage at  $U_\infty = 25\text{m/s}$ . Actuators of  $(L_R, L_S) = (\lambda/2, 0)$  are activated at  $780\text{Hz}$ .

four conditions can be divided into two groups, whether the actuators is located downstream (Runs R-1 and R-2) or upstream of the slot (Runs L-1 and L-2). Figure 11 plots the velocity fluctuations  $u'_{rms}$  for different supply voltages to the loudspeaker. Measurements are carried out in a light wind  $U_\infty = 2\text{m/s}$  to keep the sensitivity of hot-wire probe. It is clearly found that the ejection velocity of synthetic actuators depends on their configuration. The velocity fluctuation is proportional to supply voltage for Runs S-1, R-1 and L-2, while it is almost constant at very weak level for Runs S-2, R-2 and L-2 even if the supply voltage is increased.

This is due to the effect of acoustic resonance inside the resonance box otherwise the slot position is not proper. Considering that fluid motion occurs at the opening end not the closing end in a general acoustic-resonance tube, the velocity node equals to the pressure antinode, vice versa. In the current resonator conditions, Comparing the results of Runs R-1 and R-2 or L-1 and L-2, the strong velocity fluctuations are obtained when  $L_R$  equals to  $\lambda/2$ , not to  $\lambda/4$ . Besides, the results of Runs S-1 and S-2 or L-1 and S-2 indicate that the loudspeaker works as an opening end. In other wards, the loudspeaker creates not the fluid motion but the pressure fluctuation. Consequently, we can obtain the strong synthetic jets when the control device satisfies the following two conditions:

**Resonance condition :**  $L_R = \lambda/2 \times n$  ( $n = 0, 1, 2, \dots$ )

**Slot position :** Slots should be placed at the velocity node, i.e. the pressure antinode.

And we determine the configuration of synthetic jet actuators as  $(L_R, L_S) = (\lambda/2, 0)$ .

Figure 12 shows the noise suppression effects of different operating modes, mode 1, 2 and 4 (single-phase), as a function of the supply voltage, where the freestream velocity  $U_\infty = 25\text{m/s}$  and the incoming boundary layer is turbulent. The resonance length  $L_R$  is determined to 224mm since the target cavity noise has a distinct peak around 780, i.e.  $\lambda = 446\text{mm}$ , at 88dB that is approximately 38dB larger than the background noise. Vertical axis represents the relative peak levels of cavity noise from that without the control. The cavity noise becomes louder when the all actuators are operated at the same signal (mode 4), while the SPL of the cavity noise goes down for mode 1 and 2 especially for high supply voltage. This means that the synthetic jets are not so strong to blow the shear layer upward never hitting the downstream corner of the cavity, and the noise is suppressed by the superposition of sound sources with 180 degrees out-of-phase.

### 3.3 Fluidic oscillators

Fluidics is a popular technology that uses the flows and pressures of fluids to control the systems, with no moving parts. The advantage of fluidic-type controllers is that it can introduce much stronger velocity fluctuations than the piezoelectric actuators. Figure 13 shows the schematic of the fluidic-based control device used in this experiment (Shigeta et al., 2008). The behavior of the flow inside the fluidics can be explained as the following: when the airflow supplied by a fan comes into the diffuser section, the Coanda effect makes the flow

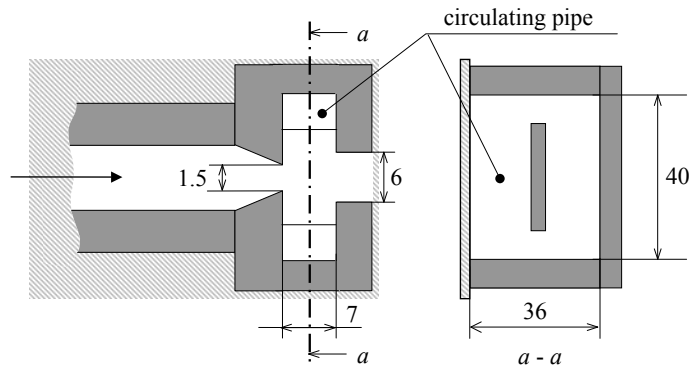


Fig. 13. Schematic of single fluidic oscillator.

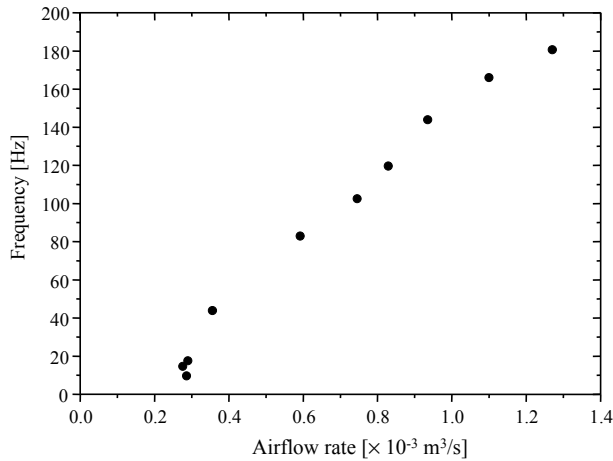


Fig. 14. Variation of oscillating frequency of single fluidic oscillator for different airflow rates.

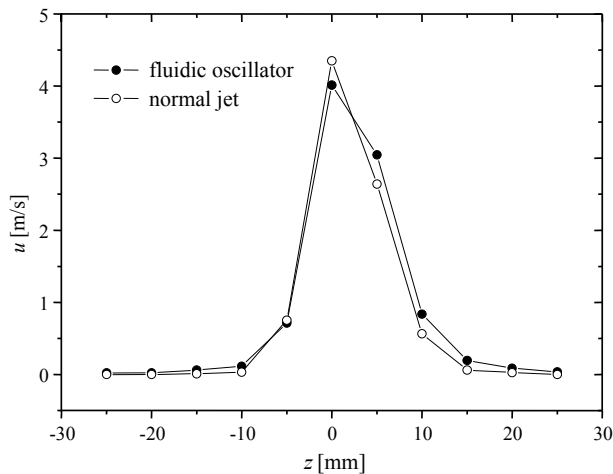


Fig. 15. Mean velocity profiles of oscillating jet and continuous jet.

to blow along one side of the walls. As a result, the difference between the static pressures on both sides arises, which generates a flow through the square pipe. The flow through the circulating pipe then pushes the jet at the other end changing the direction of the jet at the diffuser inlet. This process is successively repeated at a constant frequency. Owing to this self-oscillatory nature of fluidics, self-sustained intermittent jets of a certain frequency are generated. We installed this fluidic oscillator at the center of upstream sidewall of the cavity and 20mm below the upstream surface. Thus, the jet issues from a slot of length 20mm and width 1mm.

The relation between an oscillating frequency and an airflow rate for single fluidic oscillator shown in Fig. 13 is plotted in Fig. 14. The jet frequency increases almost linearly with the

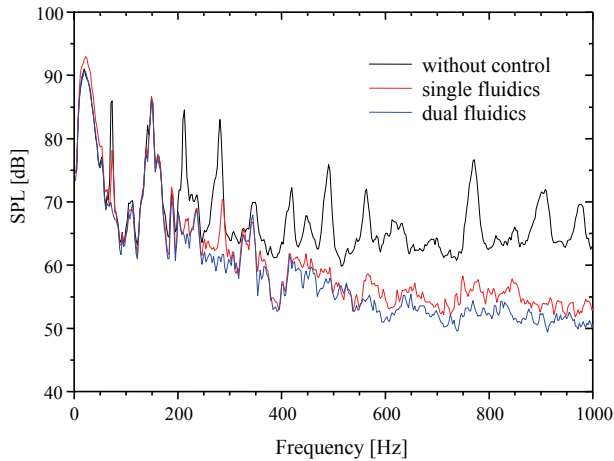


Fig. 16. Noise suppression effect at  $U_\infty = 23.3 \text{ m/s}$ .

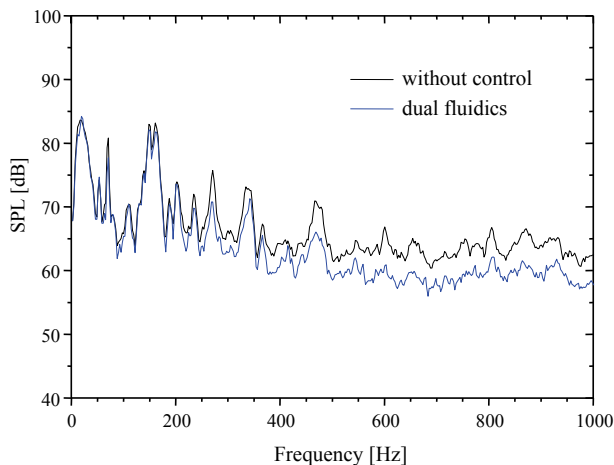


Fig. 17. Noise suppression effect at  $U_\infty = 26.1 \text{ m/s}$ .

airflow rate from the fan. This characteristic implies the feasibility of controlling the frequency by changing the airflow rate. It should be noted that if one use the multiple fluidic oscillators, it is necessary to synchronize their oscillating phases in some way. Figure 15 shows the mean velocity profiles of oscillating jet and continuous jet issuing from a simple diffuser without a recirculating pipe. The velocity is measured at the slot exit, and the airflow rate is  $0.55 \times 10^{-3} \text{ m}^3/\text{s}$ . Almost identical distributions can be found. The half width is approximately 10mm, and the maximum velocity exceeds 4m/s. However, the flow velocity is not too high as to change the trajectory of shear layer by pushing it upward.

Figure 16 represents the acoustic spectra with and without control, where the frequency of fluidic oscillators are adjusted to that of the cavity noise. The freestream velocity  $U_\infty$  is 23.3m/s and the upstream boundary layer is turbulent. The size of the cavity is 150mm long ( $= L$ ) and 90mm deep ( $= D$ ). A resonator is used to simulate a deep cavity environment because the peaky noise is not generated in the shallow cavity when the flow before separation is turbulent. From the figure, it can be found that the strong peak at 75Hz and its harmonics appearing in the spectrum before control become weaker or disappear after the control which uses the single-fluidic system. However, the peak level of the fundamental frequency is suppressed by only 9dB that corresponds to 47% noise suppression relative to the background noise level. This noise suppressing effect is considerably lower compared to the laminar separating flow case. Hence, we introduced one more fluidic oscillator to enhance the flow controlling effect. The oscillations of the two fluidic controllers are synchronized by connecting each recirculating pipe. The blue line in the figure presents the result of the dual-fluidic system. Compared with the single-fluidic case, the noise suppression effect is much improved by adding the second fluidic oscillator. The cavity noise, including higher harmonic components, disappears from the spectrum. However it drops again to a lower value for higher Reynolds numbers ( $U_\infty = 26.1\text{m/s}$ ), as shown in Fig. 17. These results indicate that more fluidic oscillators are required for controlling the flows of even higher Reynolds numbers. Besides, we also investigated the effect of the continuous jet on the cavity noise for laminar separating flows and the results were compared with the single-fluidic case. As a result, we found that the control effect of the single-fluidic system is superior to that of the continuous jet, even though their time-averaged velocity profiles are nearly equal. This means that the periodical oscillation of jet plays a dominant role in controlling the cavity flows under the current experimental conditions.

#### 4. Passive control

The key point of above active control methods is to control the cavity flows by changing only the timing of vortex rolling up using less energy. Flow receptivity enables this phase-based control. Since the velocity disturbances are added into a boundary layer at the upstream edge of the cavity before the vortex formation, these active control methods can be interpreted as a kind of vaccine against the cavity noise. On the other hand, passive controls usually work on the rolled-up vortices directly. Thus, they have the side of symptomatic treatment. In this study, passive control has also been attempted using a small thin plate and small blockage inserted into a cavity. In the following sections, we discuss the effect of the size and location of the obstacle on the noise suppression, where the obstacle is directly inserted inside the shear layer or just settled on the bottom of the cavity. These studies were started when we happened to notice that the target cavity noise vanished before activating the actuators, during the active control experiments.

##### 4.1 Static plate

First of all, we describe the effect of a thin two-dimensional plate as a static controlling device to suppress the cavity noise when it is inserted vertically into a cavity (Kuroda et al., 2003; Izawa et al., 2006 & 2007). The experiments were conducted using two different-size wind tunnels: the conventional wind tunnel at IFS in Tohoku University and the large-sale, low-noise wind tunnel of the Railway Technical Research Institute (RTRI). The latter wind tunnel has a rectangular cross-section nozzle of 3m in width and 2.5m in height, and the

turbulence levels of freestream at the test section are about 0.4% at 60m/s. Both results are compared and the effect of scale difference on the noise suppression is also discussed.

Figure 18 shows the cavity models used in each wind tunnel experiment. The geometry of the model is basically the same as that used in the active control experiments, shown in Fig. 2, but the streamwise length of the rectangular cavity  $L$  of the RTRI model is ten times as long as that of the IFS model. The model is mounted in the freestream for the IFS experiment, while it is installed so that its leading edge is smoothly connected to the lower side floor of the nozzle for the RTRI experiment. Upstream boundary layer is turned into turbulent by a combination of trip wire ( $\phi = 0.5\text{mm}$ ) and sandpaper (No. 400) for the IFS tunnel, or a trip wire ( $\phi = 1.5\text{mm}$ ) for the RTRI tunnel. The length of a resonator is adjusted to according to the frequency of the cavity noise. A flow-controlling plate with various lengths  $H_p$  in the  $y$  direction is placed inside the cavity. The plate is fixed on the floor by L-shape supports. For convenience, we designed that the streamwise plate position can be easily changed using a ball screw without turning off the wind tunnel during the RTRI experiment. It should be noted that the RTRI model is made strong enough by a combination of 16mm thick wooden fat plates and aluminum frames, since the plate surface is exposed to the strong negative pressure of the freestream. The freestream velocity  $U_\infty$  is set at 30m/s for the IFS tunnel and

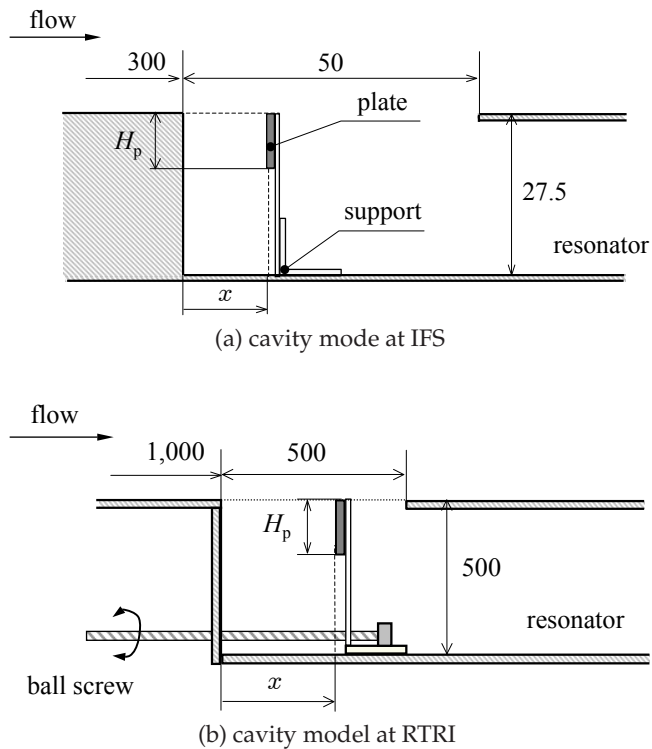


Fig. 18. Schematic of the cavity models used at (a) IFS and (b) RTRI.

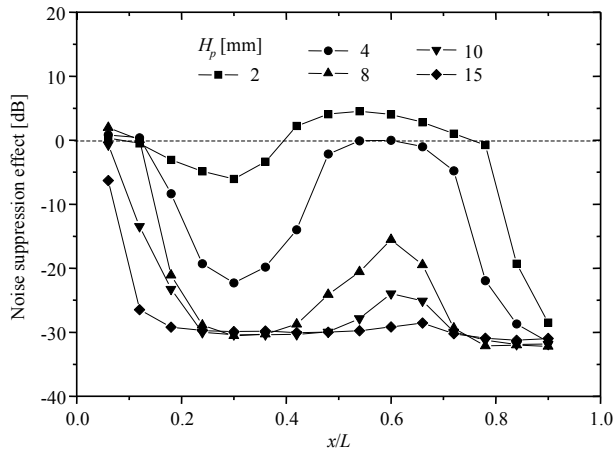


Fig. 19. Variation of peak level with different plate height  $H_p$  and streamwise locations  $x$  at IFS.

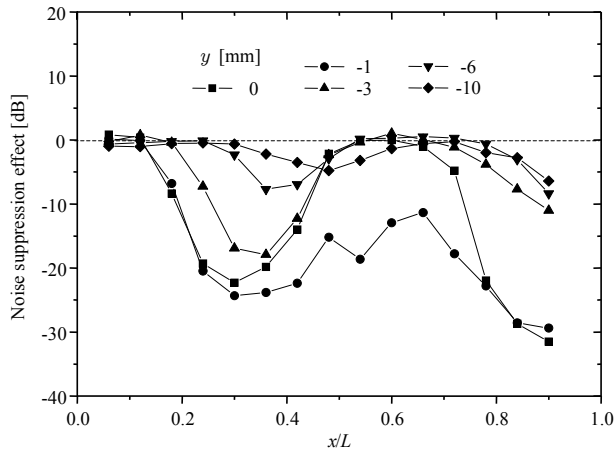
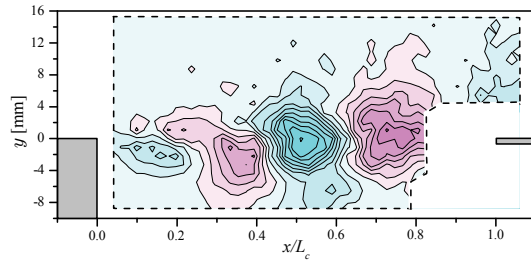


Fig. 20. Variation of peak level with different wall-normal locations  $y$  for  $H_p = 4$  mm at IFS.

60m/s for the RTRI tunnel, where the thickness of turbulent boundary layer at the upstream edge of the cavity is approximately 11mm and 104mm, respectively.

Variation of noise suppression effect for various plate height  $H_p$  and positions  $(x, y)$  for the IFS experiment is shown in Figs. 19 and 20. The frequency of the cavity noise is 480Hz and the resonator length is set at 140mm. The peak level of the cavity noise strongly depends on the plate location, not only the streamwise but also the wall-normal directions. In particular, the noise suppression effect becomes obvious at two streamwise positions, around  $x/L = 0.3$  and near the downstream edge of the cavity. Besides, the effect is gradually saturated except for the region near the upstream and downstream edges with the increase in the vertical length of





(a) without plate

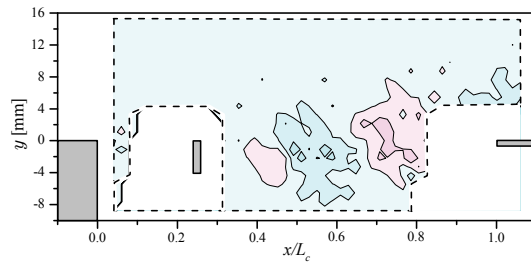
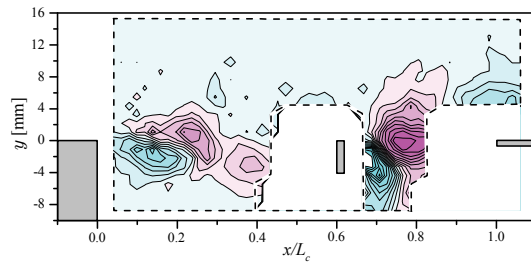
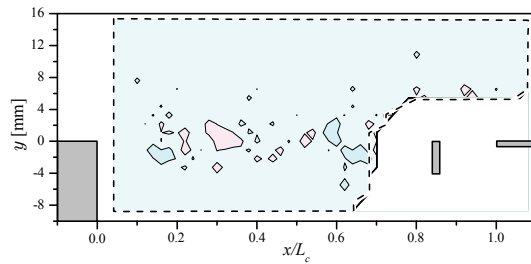
(b) plate at  $x/L = 0.24$ (c) plate at  $x/L = 0.6$ (d) plate at  $x/L = 0.84$ 

Fig. 21. Contour maps of spanwise vorticity fluctuation  $\omega'_z$  without plate (a) with plate at  $x/L = 0.24$  (b), 0.6 (c) and 0.84 (d). Contour interval is 0.66. ( $H_p = 4\text{mm}$  and  $y = 0\text{mm}$ , IFS)

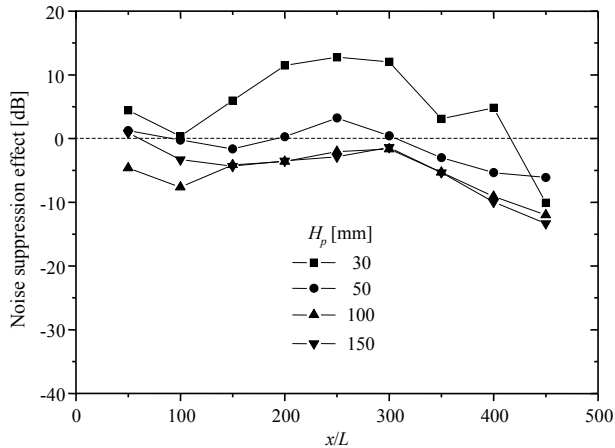


Fig. 22. Variation of peak level with different plate height  $H_p$  and streamwise locations  $x$  at RTRI.

the plate. The maximum value of noise reduction reaches approximately 30dB that is nearly equivalent to the amount amplified by the existence of the resonator. These facts imply that the resonance inside the cavity may be damaged by a large plate covering the cavity. It is also found that the noise reduction effect is lost when the plate is lower than  $y = -6\text{mm}$ , which is the outer edge of the shear layer. On the other hand, the effect suddenly drops near the downstream edge, when the plate position is changed from  $y = -1\text{mm}$  to  $-3\text{mm}$ . This implies that the noise suppression mechanism is different in the two cases.

Figure 21 shows the contour maps of the spanwise vorticity fluctuation measured by X-type hot-wire probe when the plate of  $H_p = 4\text{mm}$  is placed at various streamwise positions,  $y = 0\text{mm}$ . The strong pattern causing the intense cavity noise becomes weaker or disappears at  $x/L = 0.24$  and  $0.84$ . The upstream plate directly discourages the rolling-up process of the shear layer, while the downstream plate weakens the feedback loop by easing the pressure fluctuation generated by the periodical impingement of rolled-up vortices into the downstream corner of the cavity. Besides, considering that the vortices hit the corner at  $y = -3 \sim 2.5\text{mm}$ , the plate whose position is lower than  $y = -3\text{mm}$  has no influence on the vortices. This is the reason of the rapid decrease in the control effect of the plate at  $y = -3\text{mm}$  near the downstream edge, shown in Fig. 20. When the plate is placed at  $x/L = 0.6$ , no obvious effect is also observed because the vertical size of the plate  $H_p$  is so small compared to the thickness of the shear layer that the rolled-up vortices cannot be destroyed by the plate.

The noise suppression effect at the large wind tunnel of RTRI is plotted in Fig. 22. The frequency of the cavity noise is 89Hz and the resonator length is determined to be 800mm from the preliminary experiment. As well as the small wind tunnel experiment at IFS, after the SPL decreases at  $x/L = 0.2 \sim 0.3$ , it increases near the center of the cavity and decreases again as the plate becomes closer to the downstream edge. The maximum effect is obtained when  $H_p$  is equal to the thickness of the shear layer. However, the noise suppression effect is smaller compared to the IFS experiment, since the noise generation of the plate itself cannot be ignored in such a high-speed flows.

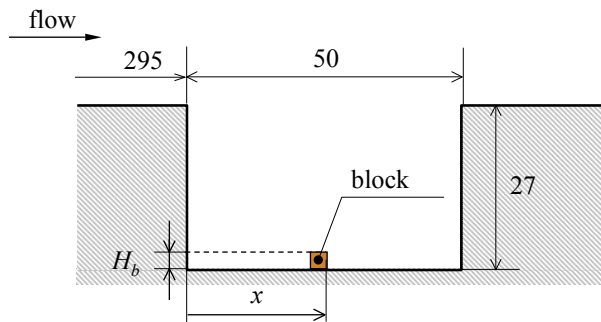


Fig. 23. Schematic of static block placed on the floor of a cavity.

#### 4.2 Small block on the floor

When a shear layer passes a cavity, it mainly keeps flowing downstream but the rest comes into the cavity and forms a recirculating flows. In this section, we discuss the feasibility of suppressing the cavity noise generation by controlling the recirculating fluid motions inside a rectangular cavity without a resonator (Izawa et al., 2010). Figure 23 shows the schematic of static block inserted on the floor of a cavity of 50mm in length and 27mm in depth. A block has a square cross section,  $H_b$  mm on a side, and its noise suppression effect is investigated by changing the size and position. The freestream velocity is constant at  $U_\infty = 18\text{m/s}$  and the target flow is laminar. At the upstream edge of the cavity, the laminar boundary thickness is approximately 2.6mm.

Figure 24 present the spectra of the cavity noise with and without a block of  $H_b = 2\text{mm}$  that is placed at the center of the cavity,  $x/L = 0.5$ . The dominant peak at 820Hz shown in the original spectrum completely disappears owing to the small block on the floor. Both sound signals are analyzed using a wavelet transform and the results are compared. Figure 25 shows the wavelet spectra of both signals. When there is no block, an intense streak is clearly observed independently in time around the fundamental frequency of the cavity noise, 820Hz. It is interesting that when the block is installed, the streak pattern becomes intermittently but still left in the spectrum, though the corresponding peak cannot be seen in the FFT spectrum shown in Fig. 24. This means that the continuous feedback loop is destroyed but it still alive on and off. Variation of effective size and position of the block is plotted in Fig. 26. The solid lines connecting two dot points in the figure represent the regions where the SPL of the cavity noise decreases to the background noise level. The optimum block position shifts toward the upstream side of the cavity, as the block size  $H_b$  increases. Besides, it is also found that the optimum position moves downstream for longer cavity,  $L/D = 2$ .

### 5. Conclusion

We have successfully suppressed the cavity noise for through both the active and passive control approaches at low Mach numbers ( $M \leq 0.18$ ). Active control is achieved with the use of piezoelectric actuators, synthetic jets and fluidic oscillators. These actuators are attached on the upstream wall of a cavity side by side, for the purpose of adding weak periodic velocity fluctuations to the shear layer. Their operating frequency is chosen to be the natural frequency of the shear layer and only the timing of the separation at the leading edge is controlled in the spanwise direction. Thanks to flow receptivity, resulting pressure fluctuations hence

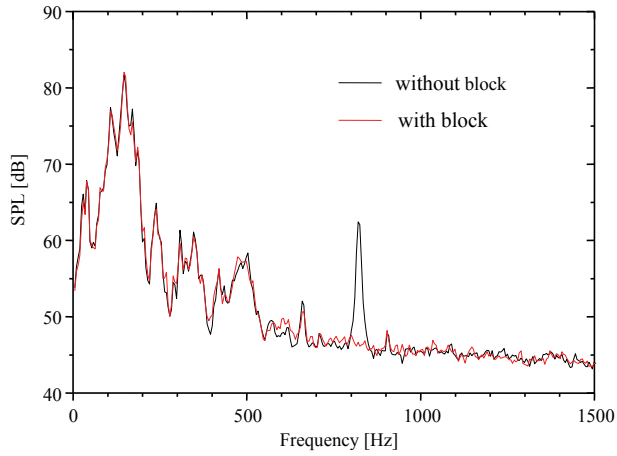


Fig. 24. SPL of cavity noise with and without a block of  $H_b = 2\text{mm}$  at  $x/L = 0.5$ .

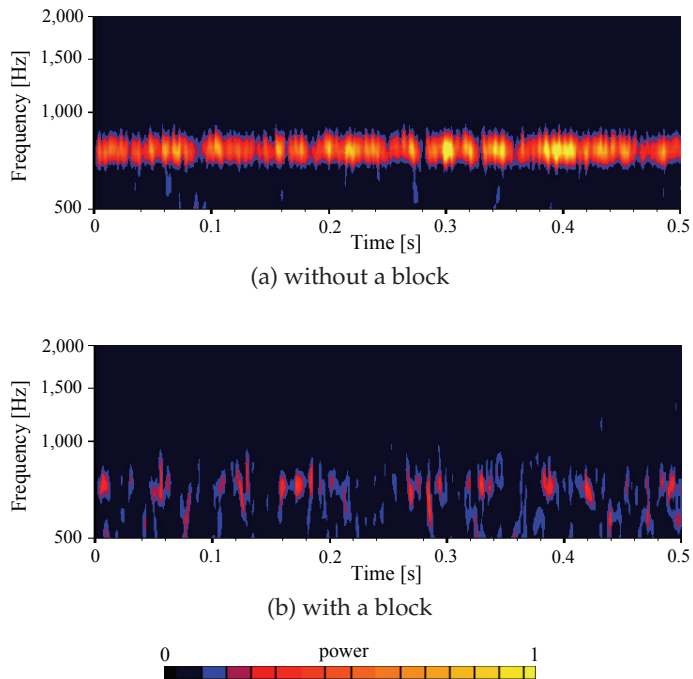


Fig. 25. Wavelet spectra (a) without and (b) with a square block of  $H_b = 2\text{mm}$  at  $x/L = 0.5$ .

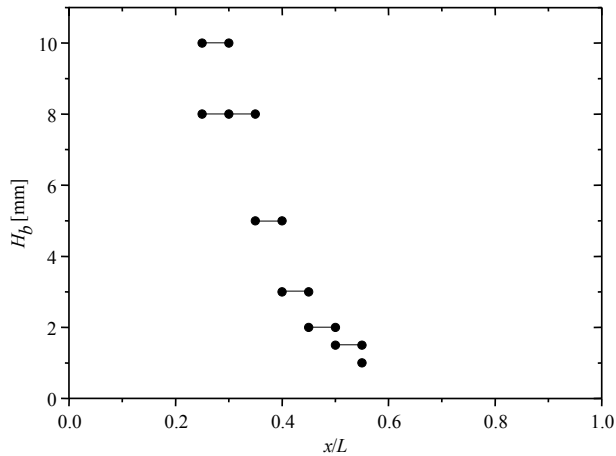


Fig. 26. Effective sizes and positions of the plate for noise suppression. Solid lines represent the positions where the cavity noise completely disappears.

the sound waves coming out become 180 degrees out of phase, and consequently, these opposite-signed sound waves cancel each other faraway from the cavity, though the noise generation itself is not reduced at the source. In addition to active control, passive control experiments are also performed using a small thin plate and small block inserted into the cavity.

The phase control method at the upstream edge of the cavity is capable of effectively suppressing the noise, while the thin plate inserted inside the shear layer also shows large noise suppression effect when it is placed near the upstream edge or the downstream edge. Besides, the cavity noise can be suppressed by a small block placed at the bottom surface, which is inserted in the middle of the cavity. However, the sound suppression efficiency has limitations depending on the scale of the flow field, because the magnitude of the velocity fluctuations introduced by the actuators becomes relatively smaller owing to the limitation in the size and power of the piezoelectric device, and the noise generated from the plate itself cannot be neglected in large-scale experiments, cutting down the noise suppression effect.

## 6. Acknowledgments

Forepart of this work was supported by the Grant-in-Aid for Scientific Research (A)#11355009, Japan Society for Promotion of Science. The support of the Railway Technical Research Institute (RTRI) is also greatly acknowledged. The series of these experiments have been performed by our former graduate students as research projects for their Ph.D. and master theses. The author wishes to thank all of them, Yuzuru Yokokawa, Masafumi Kuroda, Hiroshi Maita, Katsuo Kobayashi, Shota Maehara, Toshimasa Miura, Ryuzo Sakamoto, Hiroaki Nishida, Hiroyuki Nakashima, and my colleagues Prof. Fukunishi and Asst. Prof. Shigeta.

## 7. References

- Asai, T. & Nishioka, M. (2003). An Experimental Study on the Mechanism of Supersonic Cavity Flow Oscillations, *Journal of Japan Society of Fluid Mechanics* Vol. 22 (No. 2), 131-145 (in Japanese).
- Cattafesta III, L.N., Song, Q., Williams, D.R., Rowley, C.W. & Alvi, S.F. (2008). Active control of flow-induced cavity oscillations, *Progress in Aerospace Sciences* Vol. 44, 479-502.
- Chang, K., Constantinescu, G. & Park, S.-O. (2006). Analysis of the flow and mass transfer processes for the incompressible flow past an open cavity with a laminar and a fully turbulent incoming boundary layer, *Journal of Fluid Mechanics* Vol. 561, 113-145.
- Chicheportiche, J. & Gloerfelt, X. (2010). Direct noise computation of the flow over cylindrical cavities, *AIAA Paper* 2010-3775, 1-12.
- De Roeck, W., Rubio, G., Baelmans, M. & Desmet, W. (2009). Toward accurate hybrid prediction techniques for cavity flow noise applications, *International Journal for Numerical Methods in Fluids* Vol. 61, 1363-1387.
- Faure, T.M., Adrianos, P., Lusseyan, F. & Pastur, L. (2006). Visualization of the flow inside an open cavity at medium range Reynolds numbers, *Experiments in Fluids* Vol. 42 (No. 2), 169-184.
- Fukunishi, Y., Yokokawa, Y. & Izawa, S. (2002). ACTIVE CONTROL OF TURBULENT SEPARATING FLOW OVER A CAVITY FOR NOISE SUPPRESSION, *Proceedings of the Ninth Asian Congress of Fluid Mechanics, ACFM9*, 1-6.
- Gloerfelt, X., Bailly, C. & Juvé, D. (2003). Direct computation of the noise radiated by a subsonic cavity flow and application of integral methods, *Journal of Sound and Vibration* Vol. 266, 119-146.
- Gloerfelt, X. (2009). Noise from automotive components, *Aerodynamic noise from wall-bounded flows*, coll. VKI Lectures, March 9-13.
- Grace, S.M. (2001). AN OVERVIEW OF COMPUTATIONAL AEROACOUSTIC TECHNIQUES APPLIED TO CAVITY NOISE PREDICTION, *AIAA Paper* 2001-0510, 1-13.
- Heller, H.H., Holmes, D.G. & Covert, E.E. (1971). FLOW-INDUCED PRESSURE OSCILLATIONS IN SHALLOW CAVITIES, *Journal of Sound and Vibration* Vol.18 (No. 4), 545-553.
- Hémmon, P., Amandolése, X., Santi, F. & Wojciechowski, J. (2002). STUDY OF THE ACOUSTIC OSCILLATION OF FLOW OVER CAVITIES. PART 2. SOUND REDUCTION, *Proceedings of IMECE2002 ASME International Mechanical Engineering Conference & Exposition, IMCE2002-33376*, 1-7.
- Huang, X. & Zhang, X. (2008). Streamwise and spanwise plasma actuators for flow-induced cavity noise control, *Physics of Fluids* Vol. 20 (No. 3), 1-10.
- Izawa, S., H. Maita, Terashima, O., Xiong, A.K. & Fukunishi, Y. (2006). Sound Suppression of Laminar Separating Flow Over Cavity, *JSME International Series B* Vol.49 (No.4), 1092-1097.
- Izawa, S., Kuroda, M., Ido, A. & Fukunishi, Y. (2007). Effect of Static Control Device on Suppression of Cavity Noise, *Journal of Environmental and Engineering* Vol.2 (No.1), 194-202.
- Izawa, S., Nishida, H., Shigeta, M. & Fukunishi, Y. (2010). SUPPRESSION OF AERODYNAMIC NOISE GENERATION BY CONTROLLING THE CIRCULATING FLUID MOTION INSIDE A CAVITY, *Proceedings of the International Conference on Jet, Wakes and Separated Flows ICJWSF-2010*, 1-3.

- Kegerise, K.A., Cattafesta, L.N. & Ha, C. (2002). Adaptive Identification and Control of Flow-Induced Cavity Oscillations, *AIAA Paper* 2002-3158, 1-10.
- Kim, C.-K., John Yu, S.-T. & Zhang, Z.-C. (2004). Cavity Flow in Scramjet Engine by Space-Time Conservation and Solution Element Method, *AIAA Journal* Vol. 42 (No. 5), 912-919.
- Kuo, C.H. & Chang, C.W. (1998). Shear-layer characteristics across a cavity with a horizontal top plate, *Fluid Dynamic Research* Vol. 22, 89-104.
- Kuo, C.H. & Huang, S.H. (2001). Influence of flow path modification on oscillation of cavity shear layer, *Experiments in Fluids* Vol. 31, 162-178.
- Kuo, C.H. & Huang, S.H. (2003). Effect of surface mounting of upper plate on oscillating flow structure within cavity, *Experimental Thermal and Fluid Science* Vol. 27, 755-768.
- Kuroda, M., Izawa, S., Xiong, A.K. & Fukunishi, Y. (2003). SUPPRESSION OF AERO-ACOUSTIC NOISE OVER A CAVITY, *Proceedings of the 4th ASME/JSM E Joint Fluid Engineering Conferences*, FEDSM2003-45194, 1-6.
- Larchevêque, L., Sagaut, P. & Labbe O. (2007). Large-eddy simulation of a subsonic cavity flow including asymmetric three-dimensional effects, *Journal of Fluid Mechanics* Vol. 577, 105-126.
- MacManus, D.G. & Doran, D.S. (2008). Passive Control of Transonic Cavity, *Journal of Fluids Engineering* Vol. 130 (No. 6): 1-4.
- Marsden, O., Jondean, E., Souchotte, P., Bogey, C., Bailly, C. & Juvé, D. (2008). Investigation of flow features and acoustic radiation of a round cavity, *AIAA Paper* 2008-2851, 1-13.
- Micheau, P., Chatellier, L., Laumonier, J. & Gervais, Y. (2005). Stability analysis of active control of self-sustained pressure fluctuations due to flow over cavity, *Journal of Acoustic Society of America* Vol. 119 (No. 3), 1496-1503.
- Narducci, M., Figueras, E., Gràacia, I., Fonseca, L., Santander, J. & Cané, C. (2007). MODELING OF T-SHAPED MICROCANTILEVER RESONATORS, *Proceeding of the Symposium on Design, Test, Integration and Package of MEMS / MOEMS*, DTIP2007, 100-105.
- Nishioka, M., Asai, T., Sakaue, S. & Shirai, K. (2002). Some Thoughts on the Mechanism of supersonic Cavity Flow Oscillations. Part 1. Generation and Propagation Processes of Compression Waves, *Journal of Japan Society of Fluid Mechanics* Vol. 21 (No. 3), 280-294.
- Raman, G., Raghu, S. & Bencic, T.J. (1999). Cavity Resonance Suppression Using Miniature Fluidic Oscillators, *AIAA Paper* 99-1900, 1-22.
- Rockwell, D. & Knisely, D. (1979). The organized nature of flow impingement upon a corner, *Journal of Fluid Mechanics* Vol. 93, 413-432.
- Rossiter, J.E. (1964). Wind-Tunnel Experiments on the Flow over Rectangular Cavities at Subsonic and Transonic Speeds, *Aeronautical Research Council Reports and Memoranda* No. 3438.
- Rowley, C.W. & Williams, D.R. (2003). CONTROL OF FORCED AND SELF-SUSTAINED OSCILLATIONS IN THE FLOW PAST A CAVITY, *AIAA Paper* 2003-0008, 1-8.
- Rowley, C.W., Juttijudata, V. & Williams, D.R. (2005). Cavity Flow Control Simulations and Experiments, *AIAA Paper* 2005-02592, 1-11.
- Shigeta, M., Miura, T., Izawa, S. & Fukunishi, Y. (2008). Active Control of Cavity Noise by Fluidic Oscillators, *Theoretical and Applied Mechanics* Vol. 57, 127-134.
- Williams, D.R. & Rowley, C.W. (2006). Recent Progress in Closed-Loop Control of Cavity Tones, *AIAA Paper* 2006-0712, 1-12.

- Yokokawa, Y., Fukunishi, Y. & Kikuchi, S. (2000). SUPPRESSION OF AERO-ACOUSTIC NOISE BY SEPARATION CONTROL USING PIEZO-ACTUATORS, *AIAA Paper* 2000-1931, 1-9.
- Yokokawa, Y. & Fukunishi, Y. (2001). Reduction of Aerodynamic Noise Generation at the Cavity by Active Flow Control Using Thin Ceramic Actuator Pieces, *Theoretical and Applied Mechanics* Vol. 50, 281-287.
- Yokoyama, H. & Kato, C. (2009). Fluid-acoustic interactions in self-sustained oscillations in turbulent cavity flows. I. Fluid-dynamic oscillations, *Physics of Fluids* Vol. 21 (No. 10), 1-13.
- Yoshida, T., Watanabe, T., Ikeda, T. & Ito, S. (2006). Numerical Analysis of Control of Flow Oscillations in Open Cavity Using Moving Bottom Wall, *JSME International Journal Series B* Vol. 49 (No. 4), 1098-1104.



# Aerodynamic Parameters on a Multisided Cylinder for Fatigue Design

Byungik Chang  
*West Texas A&M University*  
USA

## 1. Introduction

Cantilevered signal, sign, and light support structures are used nationwide on major interstates, national highways, local highways, and at local intersections for traffic control purposes. Recently, there have been a number of failures of these structures that can likely be attributed to fatigue. In Iowa, USA (Dexter 2004), a high-mast light pole (HMLP), which is typically used at major interstate junctions, erected for service in 2001 along I-29 near Sioux City collapsed in November 2003 (see Figure 1 (a)). Fortunately, the light pole fell onto an open area parallel to the interstate and injured no one. Figure 1 (b) shows another high-mast lighting tower failure in Colorado, USA (Rios 2007) that occurred in February of 2007. Similar to the failure in South Dakota, fracture initiated at the weld toe in the base plate to pole wall connection, and then propagated around the pole wall until the structure collapsed. It appears that these structures may have been designed based on incomplete and/or insufficient code provisions which bring reason to reevaluate the current codes that are in place.

A luminary support structure or HMLP is generally susceptible to two primary types of wind loading induced by natural wind gusts, or buffeting and vortex shedding, both of which excite the structure dynamically and can cause fatigue damage (AASHTO 2009). Vortex shedding is a unique type of wind load that alternatively creates areas of negative pressures on either side of a structure normal to the wind direction. This causes the structure to oscillate transverse to the wind direction. When the vortex shedding frequency (i.e., the frequency of the negative pressure on one side of the structure) approaches the natural frequency of the structure, there is a tendency for the vortex shedding frequency to couple with the frequency of the structure (also referred to as “lock-in” phenomenon) causing greatly amplified displacements and stresses.

## 2. Background and objectives

While vortex shedding occurs at specific frequencies and causes amplified vibration near the natural frequencies of the structure, buffeting is a relatively “broad-band” excitation and includes frequencies of eddies that are present in the natural wind (usually up to 2 Hz) as well as those caused by wind-structure interactions. The dynamic excitation from buffeting can be significant if the mean wind speed is high, the natural frequencies of the structure are below 1 Hz, the wind turbulence intensity is high with a wind turbulence that is highly



Fig. 1. A collapsed high-mast light pole; (a) Iowa (Dexter 2004), (b) Colorado (Rios 2007)

correlated in space, the structural shape is aerodynamically odd with a relatively rough surface, and the mechanical damping is low. In practice, a structure is always subject to both vortex shedding and buffeting excitations. But unlike vortex shedding, where amplified dynamic excitation occurs within a short range of wind speeds, buffeting loads keep increasing with higher wind speeds.

For multisided slender support structures, the current American Association of State Highway and Transportation Officials (AASHTO) Specification does not provide all the aerodynamic parameters such as the static force coefficients, their slopes with angle of attack, Strouhal number, the lock-in range of wind velocities and amplitude of vortex-induced vibration as a function of Scruton number, etc, that are needed for proper evaluation of aerodynamic behavior. Thus, wind tunnel testing was required to obtain these parameters. Buffeting, self-excited and vortex shedding responses are those significant parameters in the design of a slender support structure.

A number of experimental and theoretical investigations have been made by Peil and Behrens (2002) to obtain a realistic basis for a reliable and economic design for lighting and traffic signal columns. The investigations were based on a nonlinear spectral approach which is confined to the correlated parts of the wind turbulence and the associated wind forces. Gupta and Sarkar (1996) conducted wind tunnel tests on a circular cylinder to identify vortex-induced response parameters in the time domain. Chen and Kareem (2000, 2002) worked on modeling aerodynamic phenomena, buffeting and flutter, in both time and frequency domains, and Scanlan (1984, 1993), Caracoglia and Jones (2003), Zhang and Brownjohn (2003), and Costa (2007) and Costa and Borri (2006) studied the aerodynamic indicial function for lift and admittance functions for structures. Together this collection of work provides the motivation for the model discussed herein. The effects of aerodynamic coupling between the buffeting and flutter responses have been addressed by past studies based on the theoretical expression. The aerodynamic admittance function for lift of a thin symmetrical airfoil, known as Sears function, was theoretically derived by Sears (1941), and a somewhat simpler form of the Sears function was suggested by Liepmann (1952). Jancauskas (1983) and Jancauskas and Melbourne (1986) verified the Sears' theoretical plot experimentally for an airfoil and suggested a simplified but approximate expression. An empirical function for aerodynamic admittance for drag on a square plate was developed by Vickery (1965) based on limited experimental data. In previous research, Skop and Griffin (1975) derived an empirical formula to predict the maximum displacement amplitude for a circular cylinder based on Scruton numbers. Repetto and Solari (2004) developed an analytical model based on frequency-domain methods and quasi-steady theory to determine the along-wind and across-wind fatigue estimation of urban light pole. This model considers all modes of vibration and thereby avoids overestimation of base stress and underestimation of top displacement of the slender support structure.

### 3. Wind tunnel testing

The primary objective of this study is to develop aerodynamic parameters for multisided shapes. To be able to calculate the needed data for the structure, many wind parameters, such as the static drag coefficient, the slope of aerodynamic lift coefficient, Strouhal number, the lock-in range of wind velocities producing vibrations, and variation of amplitude of vortex-induced vibration with Scruton number, are needed. From wind tunnel experiments, aerodynamic parameters were obtained for an octagonal shape structure. Even though aerodynamic coefficients are known from past test results, they need to be refined by conducting further wind tunnel tests.

The use of wind tunnels to aid in structural design and planning has been steadily increasing in recent years (Liu 1991). Kitagawa et al. (1997) conducted a wind tunnel experiment using a circular cylinder tower to study the characteristics of the across-wind response at a high wind speed. The authors found from the tests that both the vortex induced vibration at a high wind speed and the ordinary vortex induced vibration were observed under uniform flow.

Bosch and Guterres (2001) conducted wind tunnel experiments to establish the effects of wind on tapered cylinders using a total of 53 models representing a range of cross sections, taper ratios, and shapes (circular, octagonal, or hexagonal cross section), which were intended to be representative of those commonly found in highway structures. In a test of drag coefficient versus Reynolds number for the uniform circular cylinders, the results

showed a consistent trend of convergence with a range of Reynolds numbers for which the drag coefficient flattens out to a constant value. It was also found that the introduction of a taper ratio significantly altered the aerodynamic behavior of the cylinder shapes. Wind tunnel experiments by James (1976) were performed to establish the effects of wind on uniform cylinders using several models representing a range of shapes (octagonal, dodecagonal and hexdecagonal cross section), model orientations, and corner radii based on Reynolds number ( $Re$ ) between  $2.0 \times 10^5$  and  $2.0 \times 10^6$ . Lift and drag coefficients were developed for an octagonal cylinder by Simui and Scanlan (1996). In the study, the slope of the mean drag coefficient ( $C_D$ ) was found to be near zero and the slopes of the mean lift coefficient ( $C_L$ ) were calculated to be approximately  $-1.7 \pi$  for flat orientation and  $0.45 \pi$  for corner orientation.

Wind tunnel testing is routinely used to study various aerodynamic phenomena and determine aerodynamic parameters of civil engineering structures. Also, the general flow pattern around structures can be determined from wind tunnel testing, particularly in the case of unusual structural shapes. Wind tunnel testing aids in structural design and planning because required aerodynamic coefficients may not always be available in codes or standards (Liu, 1991).

### 3.1 Wind tunnel and test models

The wind tunnel that was used for this study is the Bill James Open Circuit Wind Tunnel (see Figure 2), which is located in the Wind Simulation and Testing Laboratory (WiST Lab) at Iowa State University (ISU), Ames, USA. This is a suction orientation wind tunnel with a 22:1 contraction ratio. The wind tunnel test section is of the dimensions 3ft x 2.5ft and 8ft length following the contraction exit. The test section has an acrylic viewing window next to the wind tunnel control/data station with an access door opposite the side of the station. The fan, which is located downstream of the test section, is powered by a 100hp, 3-phase, 440 volt motor. The fan is controlled either by an analog remote control knob which is located at the wind tunnel control station and connected to the variable frequency fan, or directly by using the digital control screen mounted on the actual motor control power box. The fan speed can be changed in minimal steps of 0.1 Hz or approximately 0.51 ft/s (0.16 m/s) using these controls.

For all of the tests, a wooden cylindrical model with an octagonal (8-sided) and a dodecagonal (12-sided) cross section of diameter 4 in. (flat to flat distance) and length of 20 in. were used. These dimensions were selected based on the need to maintain a wind tunnel blockage criterion of 8% or less. The actual blockage was 7.4% and, therefore, blockage effects could be neglected. The length of the model, 20 inches, was chosen to maximize the area of the model that would be exposed to the air stream while at the same time leaving enough room on both sides of the model to attach any additional fixtures that are required in order to change certain parameters.

End plates, which are made out of clear plastic, were attached to the model to minimize the three-dimensional end effects on the model and to, in turn, maintain a two-dimensional flow on the model. To test multiple modifications of the model with a different mass, pairs of commercially available C clamps were clamped to the end plates at equal distances from the centerline of the model to avoid any torsion.

### 3.2 Static tests

For the static tests, each model was fixed horizontally in the wind tunnel with zero yaw angle and the aerodynamic forces were measured at various wind speeds. The angle of

attack was varied by rotating the model about its longitudinal axis. Wind speeds were carefully chosen to provide a large range of Reynolds numbers. The load cells for this system were fixed to the test frame as shown in the figure. Thin strings were attached to the aluminum block at each end of the model to avoid vertical deflection of the model.

The wind speeds in this test were varied from 0.6 to 30.5 m/s (2 to 100 ft/s) to yield a range of Reynolds Number ( $Re$ ) from  $2.5 \times 10^4$  to  $2.3 \times 10^5$ . The drag coefficients,  $C_D$  were calculated from the mean drag force and variable mean wind speeds using the following equation.

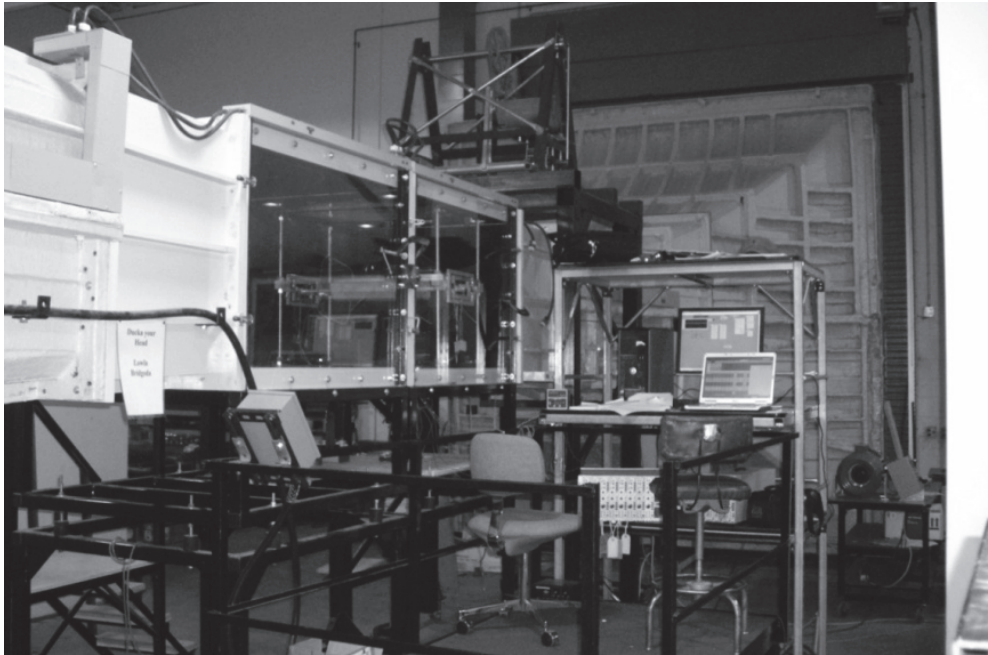


Fig. 2. Bill James Wind Tunnel at Iowa State University

$$C_D = \frac{F_D}{\frac{1}{2} \cdot \rho \cdot U^2 \cdot A} \quad (1)$$

where  $F_D$  = mean drag force;  $\rho$  = air density;  $U$  = mean wind speed; and  $A$  = projected area of model (=  $D \cdot L$ ).

To verify the force-balance system, drag coefficients for a circular cylinder was measured at several  $Re$  and compared with other references. The average difference of drag coefficient measured with respect to other reference values for  $Re$  varying between  $4.0 \times 10^4$  and  $1.0 \times 10^5$  was approximately 2.3 %.

Figure 3 presents  $C_D$  versus  $Re$  for the uniform dodecagonal shape cylinder. In this plot, it can be observed that the  $C_D$  for the cylinder with corner orientation increases until  $Re$  equals approximately  $1.5 \times 10^5$ , beyond which it tends to converge to 1.45. With flat orientation, the  $C_D$  appears to stabilize at 1.56 at approximately the same  $Re$ . The static

tests indicated that the angle of attack ( $\alpha$ ) of the wind on the cylinder influences the  $C_D$  and also showed that the flat orientation results in a slightly higher  $C_D$  than those for the corner orientation.

According to Scruton (1981), the drag coefficients for a dodecagonal shape with flat orientation are 1.3 in the subcritical region and 1.0 in the supercritical region. James (1976) also conducted several wind tunnel tests to measure drag and lift coefficients on various polygon shaped cylinders. For a dodecagonal shape with sharp corners, James found the drag coefficient as 1.3 and 1.2 for flat and corner orientation, respectively, in  $Re$  varying from  $3.0 \times 10^5$  to  $2.0 \times 10^6$ . Based on their research, drag coefficients of 1.2 and 0.79 for subcritical and supercritical region, respectively, are prescribed in the current AASHTO Specification and used for design. It is noted that the drag coefficients of 1.45 and 1.56 for both the orientations of the dodecagonal shape, as measured in the ISU Bill James Wind Tunnel for the sub-critical region, are higher than the value of 1.2 used currently for design."

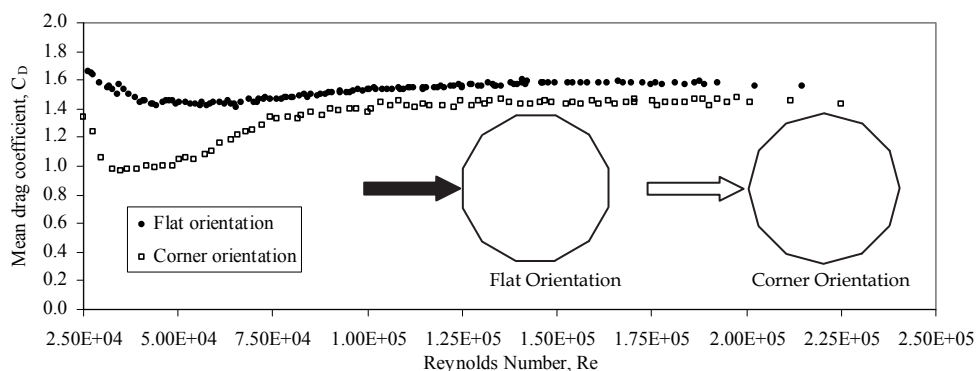


Fig. 3. Mean drag coefficients ( $C_d$ ) for a dodecagonal cylinder.

A similar force-balance system was used to obtain lift force in the static tests. The model was fixed in the vertical direction perpendicular to the air flow in the wind tunnel. The mean lift coefficients ( $C_L$ ) were calculated from the mean lift force and mean wind speed using the following equation.

$$C_L = \frac{F_L}{\frac{1}{2} \cdot \rho \cdot U^2 \cdot A} \quad (2)$$

where  $F_L$  = mean lift force.

The slopes of  $C_L$  with respect to the angle of attack,  $dC_L/d\alpha$ , were calculated to be approximately  $-0.7\pi$  and  $0.5\pi$  for flat- and corner-orientation, respectively. The  $Re$  varied from  $9.3 \times 10^4$  to  $1.6 \times 10^5$  in these tests (see Figure 4).

### 3.3 Dynamic tests

Many tests were conducted on the models to obtain all of the needed aerodynamic parameters. Results of most importance include Strouhal number ( $St$ ), lock-in range of wind

velocities for vortex shedding, and the amplitude of vortex-induced vibrations as a function of the Scruton number ( $Sc$ ).

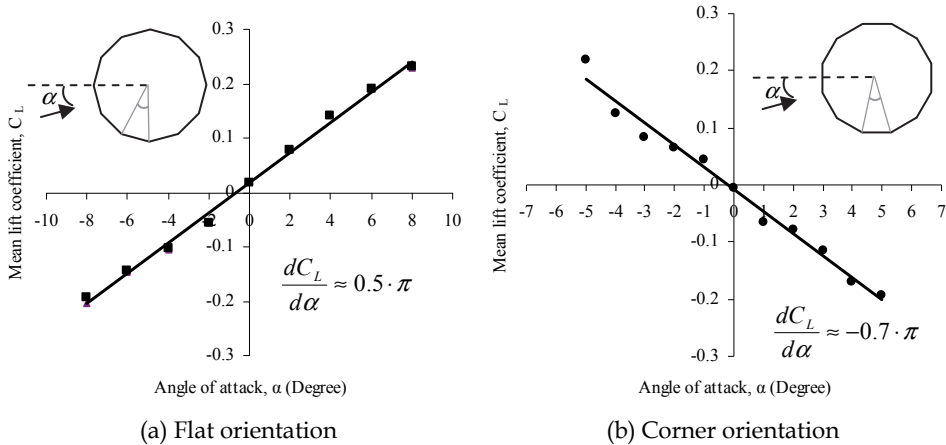


Fig. 4. Lift coefficient ( $C_L$ ) and its slope for the dodecagonal cylinder.

For the dynamic test, the vertical motion dynamic setup was designed to allow only a single-degree-of-freedom, which means that the test model was designed to only allow motion along the vertical axis perpendicular to the wind direction. Each model was suspended by a set of eight linear coil springs and chains, with four of each on each side of the model. Two cantilever type force transducers were used with one placed at the top and one at the bottom, at diagonally opposite springs.

*Spring Suspension System*

The spring suspension system was attached to a frame that was fixed to the test section floor and ceiling immediately adjacent to the side walls. A load cell frame was constructed with small structural channels and four 0.75 inch diameter threaded steel walls with two on each side of the test section which spanned vertically from the floor to the ceiling of the test section. Figure 5 shows a schematic diagram of the dynamic test suspension system.

*Lock-in range and Strouhal number*

The lock-in range and Strouhal number ( $f_s \cdot D/U \approx 0.17$  and  $0.2$  for a 8-sided and 12-sided shape respectively) were determined based on the dynamic tests. Lock-in occurs when the vortex shedding frequency matches the natural frequency of the actual system which occurs at a critical wind speed causing the response at the lock-in region to be much larger than that of the normal region. The lock-in region stays consistent over a certain range of wind speeds. Figure 6 shows the frequency spectrum of the displacement response of the elastically supported cylinder for the three different instances of (a) before lock-in, (b) at lock-in, and (c) after lock-in, all for the flat orientation, where  $f_s$  and  $f_n$  are the vortex-shedding frequency and the natural frequency, respectively, of the test model. These figures show that the model produces much higher amplified displacements when the vortex shedding frequency and the natural frequency match one another.

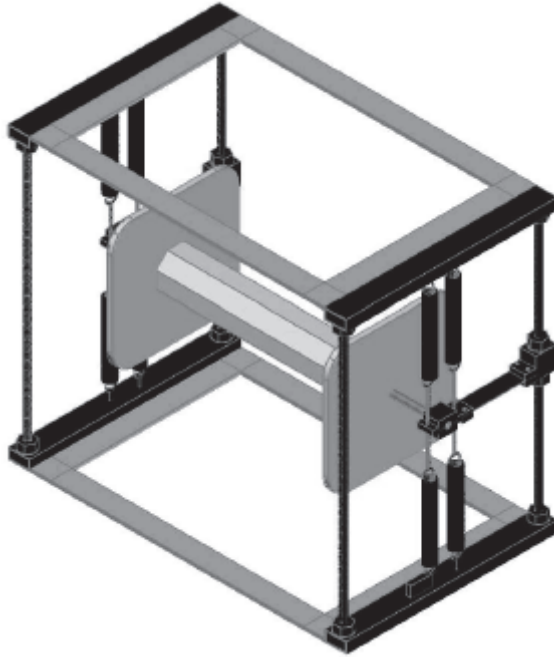


Fig. 5. Schematic diagrams of the dynamic suspension system



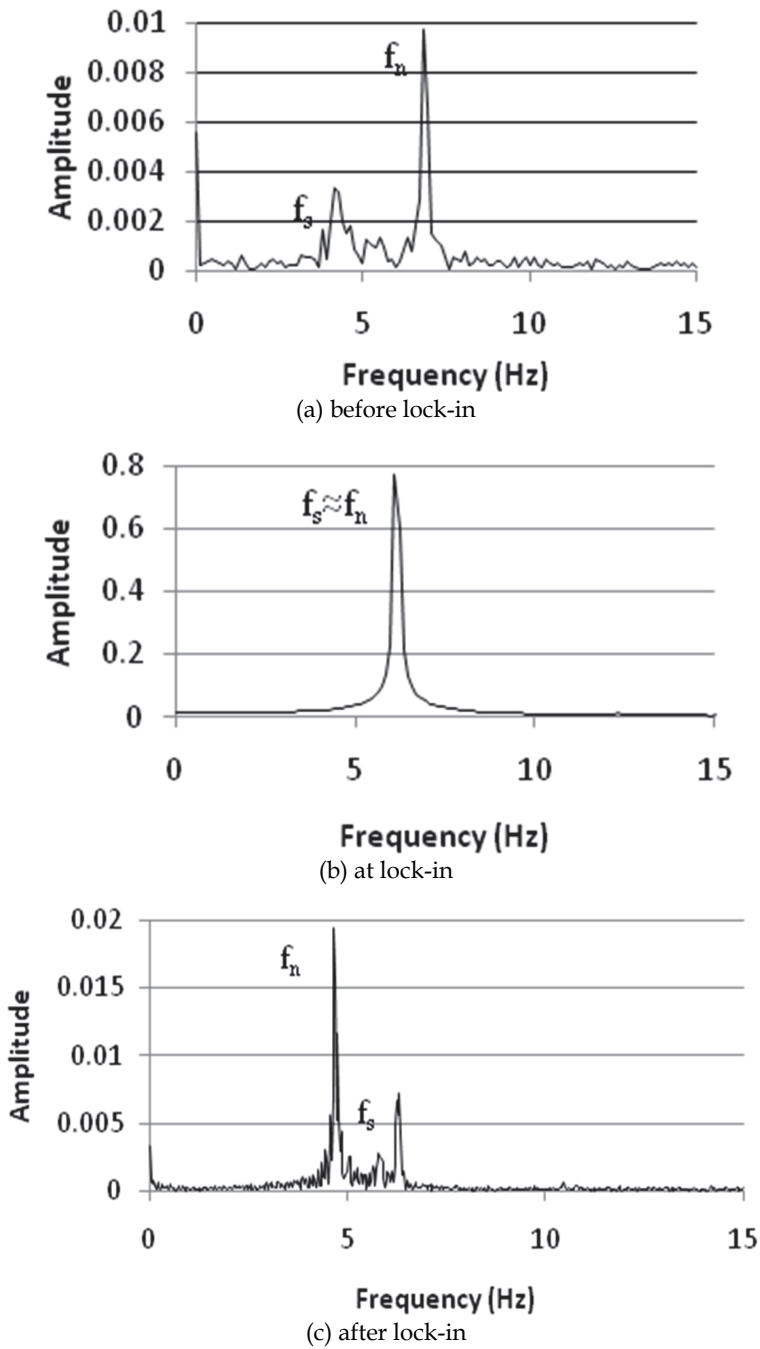


Fig. 6. Frequency spectra of displacement response of the octagonal cylinder

Scruton number

The amplitude of the model is directly related to the Scruton number ( $S_c$ ). In order to determine the amplitude versus the  $S_c$ , it was necessary to obtain several different parameters. These parameters include the inertial mass, stiffness, natural frequency, and the system damping ratio. The  $S_c$  is solved using the following:

$$S_c = \frac{m \cdot \zeta}{\rho \cdot D^2}, \tag{3}$$

where  $m$  = mass per unit length;  $\zeta$  = critical damping ratio;  $\rho$  = flow density; and  $D$  = cross-wind dimension of the cross-section.

The inertial mass, stiffness, and natural frequency for each case were determined using the added mass method, by adding masses incrementally. This was done by testing multiple specimens of the model with different masses, added by clamping pairs of commercially available C-clamps with different weights to the previously described plastic end plates. A total of five pairs of clamps and one thin steel plate were used. To avoid the introduction of torsion on the testing model, the clamps and the steel plate were added to the plastic end plates on opposite sides of the cylinder. The system damping was determined for each case experimentally by using the logarithmic decrement method.

The  $S_c$  for each case of added mass was calculated using Eq. 3 and the reduced amplitude ( $y_0/D$ , max amp./diameter of the model) was obtained from the measurement that was taken when the maximum displacement occurred. The best fit line was also plotted and is shown in Figure 7.

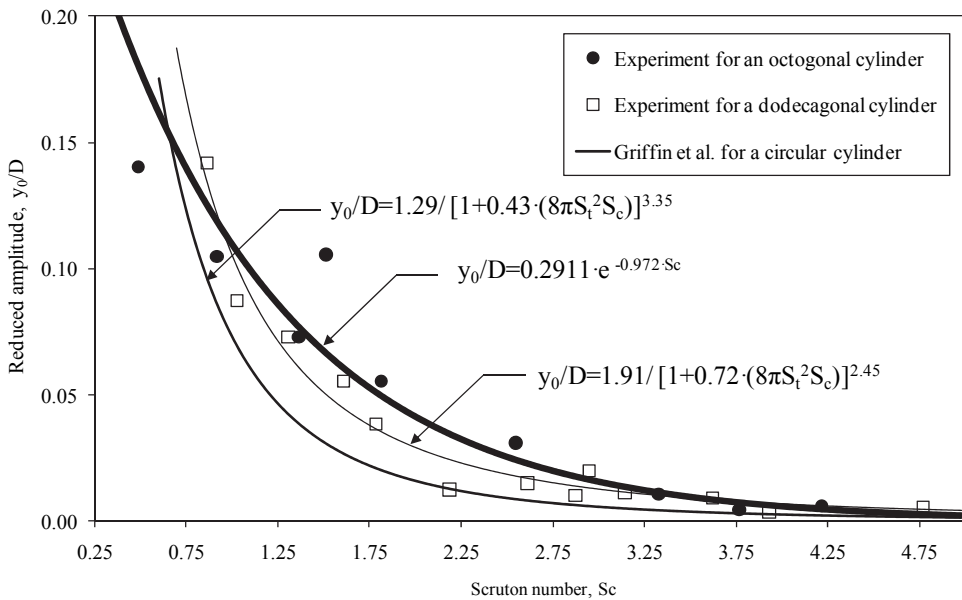


Fig. 7. Scruton number vs. maximum amplitude

### 3.4 Buffeting test

The relationship in the frequency domain between the power spectral density of turbulence in the upstream flow and the power spectral density of fluctuating wind load that it induces on a structure can be defined in terms of an aerodynamic admittance that is a function of the reduced frequency. A similar relationship in the time domain can be defined in terms of buffeting indicial functions. Generally, these relationships need to be determined experimentally since the flow around a structure in turbulent wind is too complex to be derived analytically.

These are also referred as impulse response functions (Chen and Kareem 2002) and counterparts of the indicial functions that are used to define the aeroelastic forces. Generally, these relationships need to be determined experimentally since the flow around a structure in turbulent wind is too complex to be handled analytically. For a dodecagonal cylinder, the aerodynamic admittance functions for drag and lift forces were obtained experimentally from static wind-tunnel model tests.

To accomplish this, a gust generator was fixed upstream of the model to generate a sinusoidal gust, with vertical and horizontal velocity fluctuations, at a fixed frequency. This device is made up of two thin airfoils with a gap of 203 mm (8 in.) between them. The airfoils are linked together and driven by a set of levers attached to a step motor. The gust generator system was placed at an upstream distance of 152 mm (6 in.) from the front surface of the cylinder and could oscillate with a maximum amplitude of approximately  $\pm 6$  degree to produce the wind gust. An x-hot-wire probe was used to obtain the horizontal and vertical wind velocity fluctuations and force transducers were used to simultaneously measure the aerodynamic lift or drag on the model. The hot-wire x-probe was placed along the centerline of the model between the model and the gust generator. The buffeting indicial functions for drag and lift forces were derived from the obtained aerodynamic admittance functions. The power spectral density functions for the buffeting forces in along-wind and lateral-wind directions are follows:

$$S_{F_b^x F_b^x}(n) = \left(\frac{1}{2} \cdot \rho \cdot U^2 \cdot A \cdot C_D\right)^2 \cdot \frac{4 \cdot S_{uu}(n)}{U^2} \cdot \chi_u^2(n) \quad (4)$$

$$S_{F_b^y F_b^y}(n) = \left[\frac{1}{2} \cdot \rho \cdot U^2 \cdot A \cdot \left(C_D + \frac{dC_L}{d\alpha}\right)\right]^2 \cdot \frac{4 \cdot S_{ww}(n)}{U^2} \cdot \chi_w^2(n) \quad (5)$$

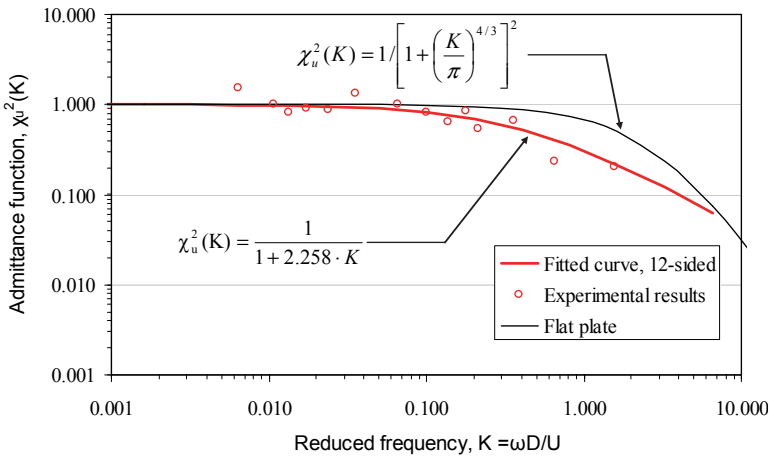
Where,  $S_{F_b^x F_b^x}(n)$  and  $S_{F_b^y F_b^y}(n)$  = power spectral density function for the along and lateral buffeting forces, respectively,  $S_{uu}(n)$  and  $S_{ww}(n)$  = power spectral density function for the along and lateral-wind velocity fluctuations respectively, and  $\chi_u^2(n)$  and  $\chi_w^2(n)$  = aerodynamic admittance function for along and lateral forces, respectively.

Figure 8 shows the aerodynamic admittance functions calculated from the buffeting wind-tunnel tests. The frequency of the gust generator and the wind speed were both chosen to obtain a range of the reduced frequency (K) from 0.005 to 1.5. Specifically, the frequency of the gust generator ranged from approximately 0.2 to 4 Hz while the wind velocity varied approximately 5 to 65 ft/s (1.5 to 19.8 m/s).

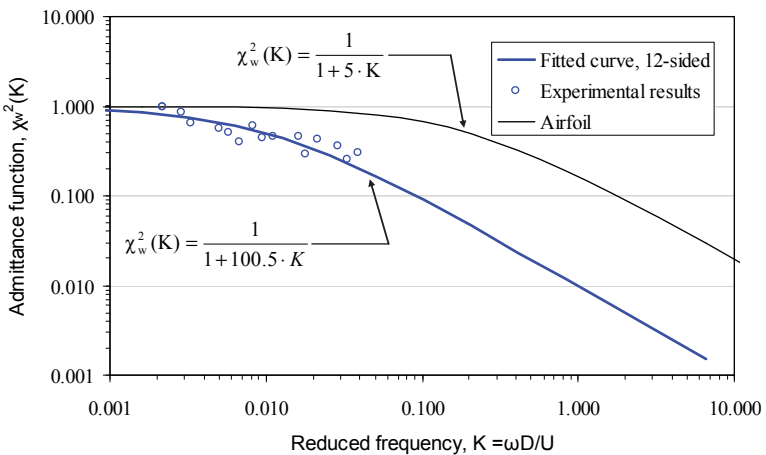
## 4. Conclusion

The objective of the work presented here was to develop a universal model for predicting buffeting, self-excited and vortex shedding induced response of a slender structure in time domain for fatigue design. To accomplish this, wind tunnel tests of the multisided cross section to extract its aerodynamic properties was used as inputs in the coupled dynamic equations of motion for predicting the wind-induced response.

The wind tunnel tests on section models of the HMLP cross section (8 and 12-sided cylinders) were conducted in the Bill James Wind Tunnel in the WiST Laboratory at Iowa State University. Finally, the dynamic models that were developed for predicting the wind-excited response was validated by comparing the simulation results, obtained with aerodynamic parameters and wind speed parameters measured in wind tunnel and field, respectively, with the data collected in the field. The study contributes to the procedure for the extraction of indicial functions that define the buffeting forces and their actual forms in addition to systematically finding other aerodynamic parameters of a 12-sided cylinder. The following conclusions can be drawn based on the current work as presented in this paper:



(a) Along-wind admittance function ( $\chi_u^2$ )



(b) Lateral-wind admittance function ( $\chi_w^2$ )

Fig. 8. Aerodynamic admittance functions for a dodecagonal cylinder

## 5. References

- American Association of State Highway and Transportation Officials (AASHTO). (2001). Standard specifications for structural support for highway signs, luminaries, and traffic signals, Washington, D.C.
- Bosch, H.R. and Guterres, R. M. (2001). Wind tunnel experimental investigation on tapered cylinders for highway support structures. *Journal of wind Engineering and Industrial Aerodynamics*, 89, 1311-1323.
- Caracoglia, L., and Jones, N. P. (2003). Time domain vs. frequency domain characterization of aeroelastic forces for bridge deck sections. *J. Wind. Eng. Ind. Aerodyn.*, 91, 371-402.
- Chen, X., and Kareem, A. (2000). Time domain flutter and buffeting response analysis of bridges. *J. Eng. Mech.*, 126(1), 7-16.
- Chen, X., and Kareem, A. (2002). Advances in modeling of aerodynamic forces on bridge decks. *J. Eng. Mech.*, 128(11), 1193-1205.
- Costa, C. (2007). Aerodynamic admittance functions and buffeting forces for bridges via indicial functions. *J. Fluids and Struct.*, 23, 413-428.
- Costa, C., and Borri, C. (2006). Application of indicial functions in bridge deck aeroelasticity. *J. Wind Eng. Ind. Aerodyn.*, 94, 859-881.
- Dexter, R. J. (2004). Investigation of Cracking of High-Mast Lighting Towers. Final Report, Iowa Department of Transportation, Ames, IA.
- Gupta, H., and Sarkar, P. P. (1996). Identification of vortex-induced response parameters in time domain. *J. Eng. Mech.*, 122(11), 1031-1037.
- Henry Liu, Wind Engineering, Prentice Hall, New Jersey, 1991
- James, W. D. (1976). Effects of Reynolds number and corner radius on two-dimensional flow around octagonal, dodecagonal and hexdecagonal cylinder, Doctoral dissertation, Iowa State University, Ames, Iowa.
- Jancauskas, E. D. (1983). The cross-wind excitation of bluff structures and the incident turbulence mechanism, Doctoral dissertation, Monash Univ., Melbourne, Australia.
- Jancauskas, E. D., and Melbourne, W. H. (1986). The aerodynamic admittance of two-dimensional rectangular section cylinders in smooth flow. *J. Wind. Eng. Ind. Aerodyn.*, 23 (1986) 395-408.
- Kitagawa, Tetsuya et al. (1997), An experimental study on vortex-induced vibration of a circular cylinder tower at a high wind speed. *Journal of wind Engineering and Industrial Aerodynamics*, 69-71, 731-744.
- Liepmann, H. W. (1952). On the application of statistical concepts to the buffeting problem. *J. Aeronau. Sci.*, 19, 793-800.
- Peil, U., and Behrens, M. (2002). Fatigue of tubular steel lighting columns under wind load. *Wind and Struct.*, 5(5), 463-478.
- Repetto, M. P., and Solari, G. (2004). Directional wind-induced fatigue of slender vertical structures. *J. Struct. Eng.*, 130(7), 1032-1040.
- Rios, C (2007). Fatigue Performance of Multi-Sided High-Mast Lighting Towers. MATER'S Thesis, The University of Texas at Austin, Austin, Texas.
- Scanlan, R. H. (1984). Role of indicial functions in buffeting analysis of bridges. *J. Struct. Eng.*, 110(7), 1433-1446.
- Scanlan, R. H. (1993). Problematics in formulation of wind-force models for bridge decks. *J. Eng. Mech.*, 119(7), 1353-1375.

- Scruton, C. (1981), An introduction to wind effects on structures, Engineering design guides 40, BSI&CEI.
- Sears, W. R. (1941). Some aspects of non-stationary airfoil theory and its practical applications. *J. Aeronau. Sc.*, 8, 104-108.
- Skop, R. A., and Griffin, O. M. (1975) On a theory for the vortex-excited oscillations of flexible cylindrical structures. *J. Sound Vib.*, 41, 263-274.
- Simiu, E., and Scanlan, R. H. (1996). *Wind Effects on Structures, Fundamentals and Applications to Design*, 3<sup>rd</sup> ed., John Wiley & Sons, New York, NY.
- Vickery, B. J. (1965). On the flow behind a coarse grid and its use as a model of atmospheric turbulence in studies related to wind loads on buildings, National Physical Laboratory Aero Report 1143.
- Zhang, X., and Brownjohn, J. M. W. (2003). Time domain formulation of self-excited forces on bridge deck for wind tunnel experiment. *J. Wind. Eng. Ind. Aerodyn.*, 91, 723-736.

# A New Methodology to Preliminary Design Structural Components of Re-Entry and Hypersonic Vehicles

Michele Ferraiuolo<sup>1</sup> and Oronzio Manca<sup>2</sup>

<sup>1</sup>CIRA-Italian Aerospace Research Centre

<sup>2</sup>Seconda Università di Napoli  
Italy

## 1. Introduction

The aim of the hot structure design process is to ensure the structural integrity of the component minimizing two fundamental parameters: mass and thickness. The former influences the total weight of the vehicle, the latter influences the vehicle efficiency (Thornton, 1996; Kelly et al, 1983; Shih et al, 1988).

In order to perform the thermo-structural sizing of the component it is necessary to evaluate the stress and temperature distribution. Usually numeric methods (finite element or finite difference codes) are adopted to estimate those distribution (Daryabeigi, 2002; Poteet et al, 2004). In a preliminary design phase where accurate results are not required, approximate analytic solutions can be used (Kunihiko, 1998).

Analytic solutions, whether exact or approximate, are always useful in engineering analysis, because they provide a better insight into the physical significance of various parameters affecting the problem. When exact analytic solutions are impossible or too difficult to obtain or the resulting analytic solutions are too complicated for computational purposes, approximate analytic solutions provide a powerful alternative approach to handle such problems. There are numerous approximate analytic methods for solving the partial differential equations governing the engineering problems. One of the most powerful method is the Integral one (Crank, 1979; Syed et al, 2010). It is simple to use and gives the opportunity to solve non linear problems such as thermal radiation/conduction ones.

In the frame of thermal structures preliminary design activities the adoption of the integral method together with appropriate assumptions give the possibility to develop analytic/numeric models that allow to solve non linear transient thermal phenomena. Those methods are very useful since they are very simple to use and allow to save a significant amount of time with respect to numeric Finite Element models in a thermal structure preliminary design phase. As a consequence, complex optimization analyses characterized by several design objectives, constraints and variables in a reasonable length of time could be conducted. The proposed approach allows to define a preliminary thermal design of the hot structure. Obviously, in a subsequent design phase structural sizing must be performed starting from the configuration resulted from the previous thermal sizing process.

The present paper describes in detail how the proposed model works. An application of the simplified model on the wing leading edge of a re-entry vehicle is presented.

## 2. Description of the method

### 2.1 Integral method

The integral method is an approximated analytical method since it is based on the assumption that the temperature distribution is described by a chosen expression (polynomial, logarithmic, etc.) (Necati, Ozisik, 1993).

The method is simple, straightforward, and easily applicable to both linear and nonlinear one-dimensional transient boundary value problems of heat conduction for certain boundary conditions. The results are approximate, but several solutions obtained with this method when compared with exact solutions have confirmed that the accuracy is generally acceptable for many engineering applications. In general when the differential equation of heat conduction is solved exactly in a given region subject to specified boundary and initial conditions, the resulting solution is satisfied at each point over the considered region; but with the integral method the solution is satisfied only on the average over the region.

The heat conduction equation is integrated over the spatial domain of the body; the result of the integration is the so called "energy integral equation". An appropriate expression for the temperature distribution is chosen; the coefficients of the temperature expression are function of the boundary conditions. Then the temperature expression is introduced in the integral equation; its solution gives the temperature variation with time. Once temperature variation with time is available,  $T(x,t)$  is known.

The use of the integral method can be divided into two sequential stages.

1. Approximation of semi-infinite body. It is valid when the thermal layer  $\delta(t)$ , that is the distance beyond which there is no heat flux, is less than the body thickness.
2.  $\delta(t) > L$ . The concept of thermal layer has no physical significance. Starting from the solution of the first stage, the heat conduction equation is integrated over the body thickness.

Several applications of the integral method have been found in literature. However none of them considers non linear boundary conditions and thermal properties.

### 2.2 Proposed model

In order to take into account the heat flux variation with time and thermal properties variation with temperature it is necessary to divide the trajectory time into a chosen number of time steps. The choice is such that the heat flux variation in a single time step must be less or equal than 1% of the maximum heat flux encountered during the flight trajectory, that is:

$$|q_w(t_{i+1}) - q_w(t_i)| < 0.01 \cdot q_{w,\max} \quad (1)$$

Where:

- $t_i$  is the  $i$ th time instant at the beginning of the  $i$ th time step
- $t_{i+1}$  is the  $i+1$ th time instant at the end of the  $i$ th time step
- $q_w$  is the aerodynamic heating
- $q_{w,\max}$  is the maximum aerodynamic heating value

The aerodynamic heat flux value is considered constant in the  $i$ th time step and equal to the algebraic mean value between the heat flux values encountered at the  $i$ th and  $i+1$ th time instants:

$$0.5 \cdot [q_w(t_i) + q_w(t_{i+1})] \quad (2)$$



$\bar{t}_i$  is the  $i$ th time step.

Thermal conductivity  $k$  and specific heat  $c_p$  values are considered constant and equal to:

$$k = k(T_i) \quad (3)$$

$$c_p = c_p(T_i) \quad (4)$$

Where  $T_i$  is the temperature evaluated at the end of the  $i$ -1th time step.

In the first stage (approximation of semi-infinite body), radiation contribution is neglected, then linear boundary conditions are applied. In the  $i$ th time step the heat conduction differential equation is integrated between  $\delta_i$  and  $\delta_{i+1}$ , that is thermal layer values respectively at  $t_i$  and  $t_{i+1}$  time instants.

$$\int_{\delta_i}^{\delta_{i+1}} \frac{\partial^2 T}{\partial x^2} dx = \frac{1}{\alpha} \int_{\delta_i}^{\delta_{i+1}} \frac{\partial T}{\partial t} dx \quad (5)$$

The boundary and initial conditions to be applied are:

$$\begin{aligned} T(x_1 = \delta_i) &= T_{in} \\ -k \cdot \frac{\partial T}{\partial x}(x = 0) &= q_w \\ \frac{\partial T}{\partial x}(x = \delta_{i+1}) &= 0 \end{aligned} \quad (6)$$

Where  $T_{in}$  is the initial temperature. A further condition may be derived by evaluating the heat conduction differential equation at  $x = \delta_{i+1}$  where  $T = T_{in} = \text{constant}$ .

$$\frac{\partial^2 T}{\partial x^2}(x = \delta_{i+1}) = 0 \quad (7)$$

Since the time parameter to be evaluated in the integral equation is the thermal layer  $\delta_{i+1}(t)$  and since the available conditions for the thermal problem are 4 (see Eq. (6) and (7)), then a polynomial expression with more than 4 parameters cannot be selected. As a consequence, the temperature profile chosen is a cubic one:

$$T(x, t) = a + b \cdot x + c \cdot x^2 + d \cdot x^3 \quad (8)$$

The parameters  $a$ ,  $b$ ,  $c$  and  $d$  are functions of  $\delta_{i+1}(t)$ . Once the conditions (6) and (7) are applied and the ordinary differential integral Eq. (5) is solved, the temperature distribution  $T(x, t)$  is known.

Figure 1 illustrates the physical significance of the "thermal layer".

The energy integral equation is:

$$-\alpha \cdot \frac{\partial T}{\partial x}(x = 0) = \frac{d}{dt}(\theta - T_i \cdot \delta_i) \quad (9)$$

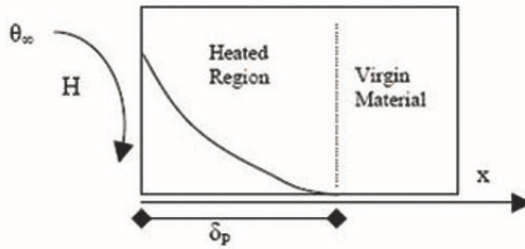


Fig. 1. Physical significance of thermal layer

Where:

$$\theta = \int_{\delta_i}^{\delta_{i+1}} T(x,t) dx \tag{10}$$

Then the temperature distribution  $T(x,t)$  is known:

$$T(x,t) = T_i + \frac{q_w}{3 \cdot k} \cdot (\delta_{i+1}(t) - \delta_i(t)) - \frac{q_w}{k} \cdot x + \frac{q_w}{k \cdot (\delta_{i+1}(t) - \delta_i(t))} \cdot x^2 - \frac{q_w}{3 \cdot k \cdot (\delta_{i+1}^2(t) - \delta_i^2(t))} \cdot x^3 \tag{11}$$

Where:

$$\delta_i = \sqrt{12 \cdot \alpha \cdot t_i} \tag{12}$$

$$\delta_{i+1} = \sqrt{12 \cdot \alpha \cdot t_{i+1}} \tag{13}$$

When  $\delta(t)$  is greater than the thickness  $L$ , the semi-infinite body approximation cannot be considered. The heat conduction differential equation is integrated over the thickness  $L$ :

$$\int_0^L \frac{\partial^2 T}{\partial x^2} dx = \int_0^L \frac{1}{\alpha} \frac{\partial T}{\partial t} dx \tag{14}$$

Giving the following energy integral equation:

$$\frac{\partial T}{\partial x}(x=L) - \frac{\partial T}{\partial x}(x=0) = \frac{1}{\alpha} \cdot \frac{d}{dt} (\theta - T_i \cdot L) \tag{15}$$

The origin of the  $x$  axis is on the external surface where aerodynamic heating is applied. At  $x=L$  adiabatic boundary conditions are considered (see figure 2).

The boundary conditions are:

$$\begin{aligned} -k \cdot \frac{\partial T}{\partial x}(x=0) &= q_w - \sigma \cdot \epsilon \cdot (T_s(t)^4 - T_e(t)^4) \\ \frac{\partial T}{\partial x}(x=L) &= 0 \end{aligned} \tag{16}$$

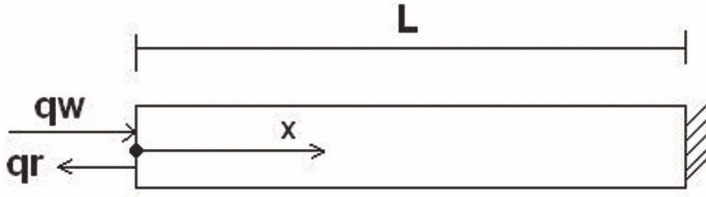


Fig. 2. Schematic representation of the thermal problem

Where  $T_e$  is the ambient temperature and  $T_s$  is the temperature at  $x=0$ .

For the same arguments explained above, the temperature distribution chosen is a quadratic one:

$$T(x,t) = a + b \cdot x + c \cdot x^2 \quad (17)$$

As mentioned before the thermal layer has now no physical significance. Then it is necessary to introduce a new time-dependent parameter. Two kind of parameters can be considered:

1.  $T_s(t)$
2.  $\bar{r} = T_s(t) + TL(t)$

Where  $TL(t)$  is the temperature at  $x=L$ .

In paragraph 2 it will be demonstrated that the second approach gives better results with respect to the first one when compared to one-dimensional finite element model results. In fact, in the second approach the solution of the energy integral equation has an information on the temperature distribution of the previous time step since the parameter  $\bar{r}$  represents the sum of the temperature values at the extreme points of the body. On the contrary in the first approach it is not possible to give any information on the previous temperature distribution.

The energy integral equation is:

$$-\alpha \cdot \frac{\partial T}{\partial x}(x=0) = \frac{d}{dt}(\theta - T_i \cdot L) \quad (18)$$

Where:

$$\theta = \int_0^L T(x,t) dx \quad (19)$$

When boundary conditions are applied, the integral equation becomes:

$$(A + B \cdot T_s(t)^3) \cdot \frac{dT_s}{dt} + C \cdot T_s(t)^4 = D \quad (20)$$

For the second case:

$$(A + B \cdot \bar{r}(t)^3) \cdot \frac{d\bar{r}}{dt} + C \cdot \bar{r}(t)^4 = D \quad (21)$$

The terms  $B \cdot T_s(t)^3$  and  $B \cdot \bar{r}(t)^3$  are neglected when:

$$\frac{4}{3} \frac{\sigma \varepsilon}{k} T_s^3 L \lll 1 \quad (22)$$

Where  $\sigma$  is the Stefan-Boltzmann constant,  $\varepsilon$  is the surface emissivity. The terms A, B, C and D are thermal properties and heat flux functions. The temperature expressions for the two cases are respectively:

$$T(x, t) = T_s(t) + \left[ \frac{\sigma \cdot \varepsilon \cdot (T_s(t)^4 - T_e^4)}{k} - \frac{q_w}{k} \right] \cdot x + \left[ \frac{q_w}{2 \cdot L \cdot K} - \frac{\sigma \cdot \varepsilon \cdot (T_s(t)^4 - T_e^4)}{2 \cdot L \cdot k} \right] \cdot x^2 \quad (23)$$

$$T(x, t) = \frac{\bar{r}}{2} - \frac{1}{4k} \left[ q_w - \sigma \varepsilon \left( \frac{\bar{r}}{2} \right)^4 \right] + \frac{1}{k} \left[ \sigma \varepsilon \left( \frac{\bar{r}}{2} \right)^4 - q_w \right] \cdot x - \frac{1}{2Lk} \left[ \sigma \varepsilon \left( \frac{\bar{r}}{2} \right)^4 - q_w \right] \cdot x^2 \quad (24)$$

Following the same approach and changing adequately the boundary conditions it is possible to take into account the heat radiation exchange with an internal structure (see figure 3).

In particular, the first expression in (16) becomes:

$$\frac{4}{3} \frac{\sigma \varepsilon}{k} T_s^3 L \lll 1 \quad (25)$$

Where  $T_M$  represents the external surface temperature of the internal structure. The temperature distribution inside the internal structure is evaluated following the same approach described for the hot structure in a radiative environment; in this case the aerodynamic heating is substituted with the heat radiation flowing from the hot structure. The final expression for the temperature distribution in the hot structure is:

$$T(x, t) = \frac{\bar{r}}{2} - \frac{L}{2k} \left[ \sigma \varepsilon_1 (r/2)^4 - \sigma \varepsilon_1 (T_r)^4 - q_w \right] - \frac{L}{4k} \left[ \sigma (\varepsilon_1 + \varepsilon_2) (r/2)^4 - \sigma \varepsilon_1 (T_r)^4 - q_w \right] + \frac{1}{k} \left[ \sigma \varepsilon_1 (r/2)^4 - \sigma \varepsilon_1 (T_r)^4 - q_w \right] x - \frac{1}{2Lk} \left[ \sigma (\varepsilon_1 + \varepsilon_2) (r/2)^4 - \sigma \varepsilon_1 (T_r)^4 - q_w \right] x^2 \quad (26)$$

Where  $\varepsilon_1$  is the external emissivity and  $\varepsilon_2$  is the internal emissivity. The model can be also applied to double-layer structures.

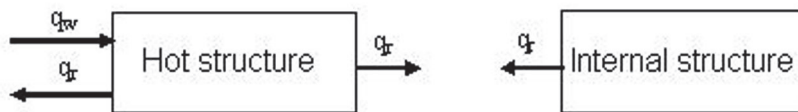


Fig. 3. Schematic representation of the thermal problem-internal radiation

### 2.3 Comparison with Finite Element results

The model described in the previous paragraph has been validated comparing the results of a one-dimensional thermal problem obtained with the proposed model with the results obtained with the Finite Element method. The Finite Element Analyses have been performed on one-dimensional conduction bars LINK32 elements that simulate the heat conduction phenomenon between two nodes (Ansys 12.0). The element is characterized by a single degree of freedom (temperature), the thermal properties and the cross sectional area. The external radiation has been simulated by means of LINK31 elements that are characterized by two nodes, a view factor, emissivity and the Stefan-Boltzmann constant. The net heat radiation between node I and node J is defined by equation (26):

$$q_r = \sigma \epsilon FA [T(I)^4 - T(J)^4] \quad (27)$$

A convergence analysis has been conducted on the mesh of the finite element model. The benchmark is characterized by the following properties:

$$\rho = 5000 \text{ kg/m}^3$$

$$L = 0.05 \text{ m}$$

Where  $\rho$  is the density and  $L$  is the slab thickness. The thermal conductivity  $k$  and the specific heat  $c_p$  variations with time are illustrated in figures 4 and 5.

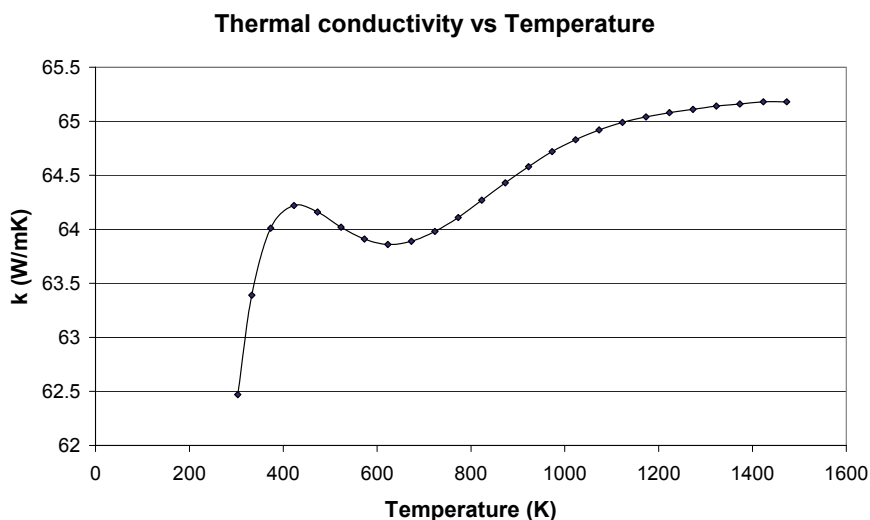


Fig. 4. UHTC Thermal conductivity vs Temperature

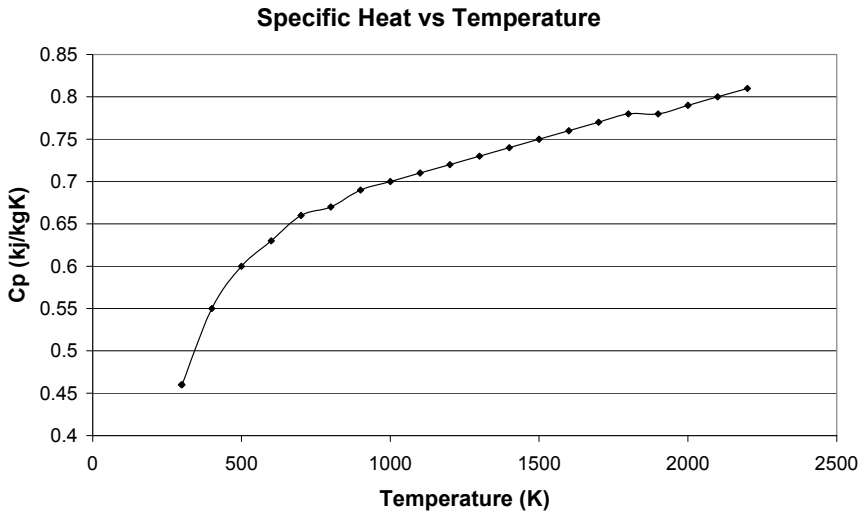


Fig. 5. UHTC Specific Heat vs Temperature

The aerodynamic heating variation with time is depicted in figure 6.

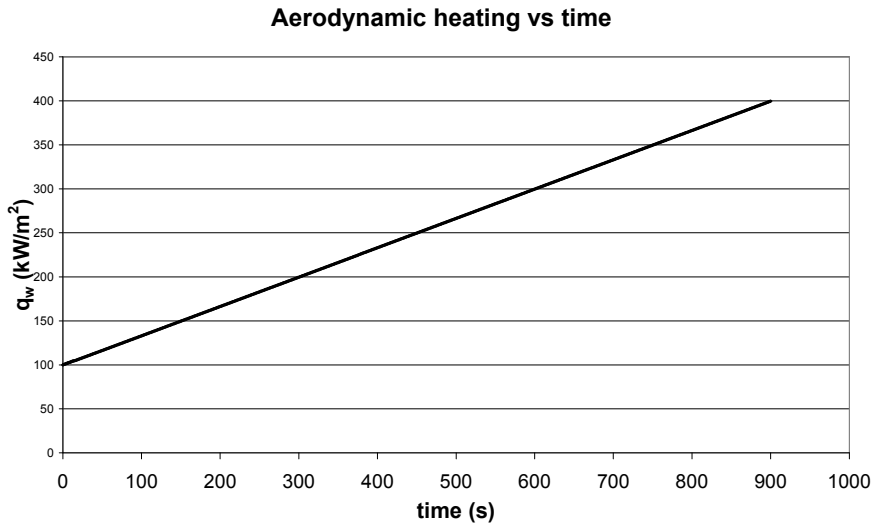


Fig. 6. Aerodynamic heating vs time

The temperature of the external environment is considered constant and equal to:

$$T_e = 300 \text{ K}$$

The initial temperature of the structure is:

$$T_i = 300 \text{ K}$$

Figure 7 shows the location of the points of the structure that will be considered for the results comparison.



Fig. 7. Position of the points considered for the validation

Figures 8 and 9 illustrate  $T_1$  and  $T_2$  variations with time. The labels “I model” and “II model” refer respectively to the results obtained considering  $r(t)$  and  $T_1(t)$  as time parameters.

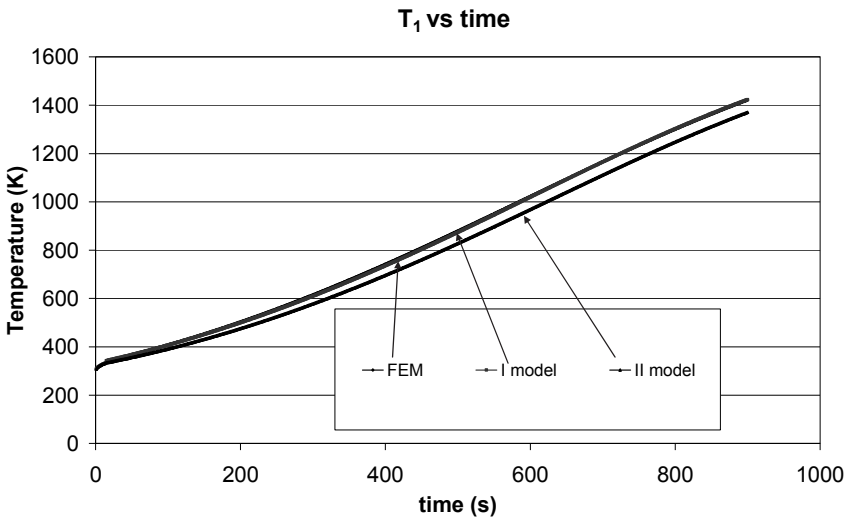
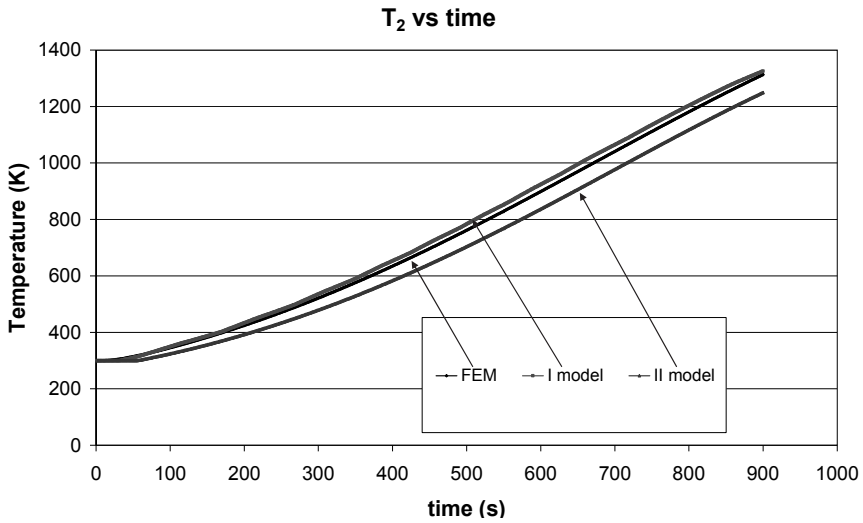
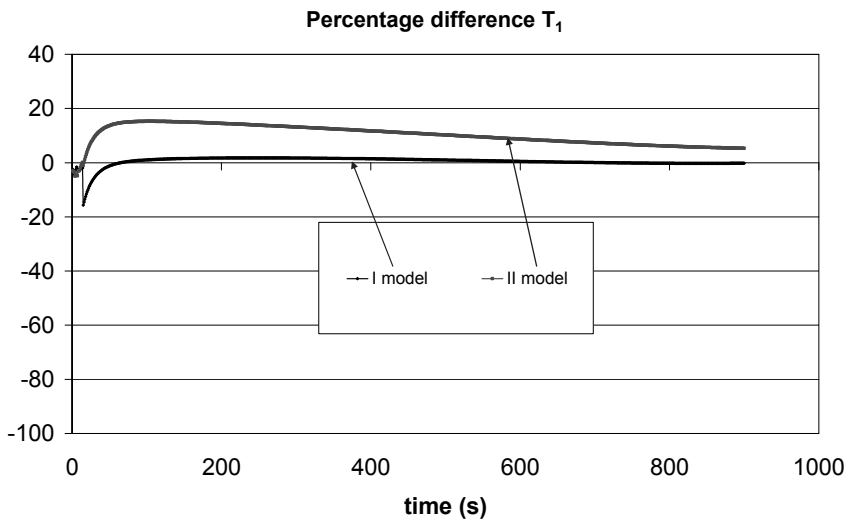


Fig. 8. Temperature  $T_1$  vs time

A good accordance between the FEM and the I model results is recorded. The maximum percentage difference is 15.7% (see also figure 9 and 10). On the contrary the second model curve is characterized by significantly greater differences with respect to the FEM results (see figure 10 and table 1); this means that the adoption of a parameter that gives precious information regarding the previous temperature distribution is fundamental in order to evaluate the temperature distribution.

Figures 9 and 10 show that the maximum percentage difference occurs after about 50 seconds; more precisely it occurs when the passage from the semi-infinite body approximation to the finite body approximation. This is due to the different temperature distributions chosen for the two solutions (third order polynomial for the semi-infinite body, second order polynomial for the finite body).

Fig. 9. Temperature  $T_2$  vs timeFig. 10. Percentage difference-Temperature  $T_1$  vs time



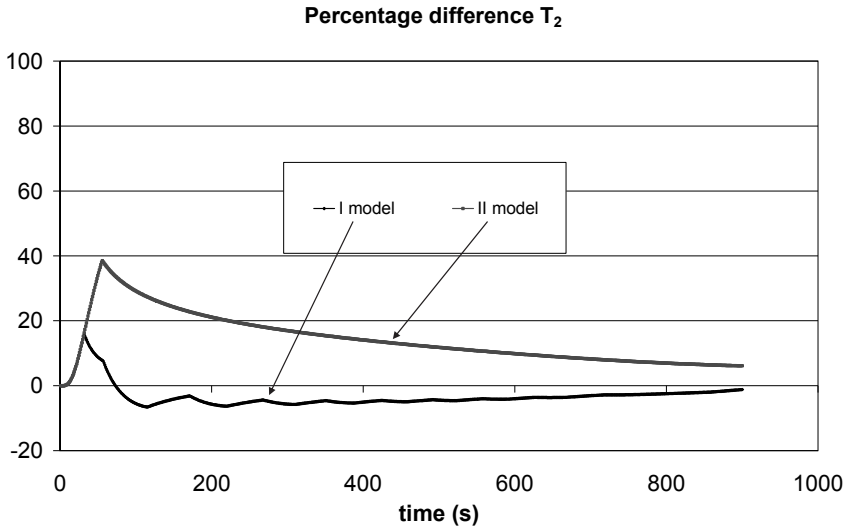


Fig. 11. Percentage difference-Temperature  $T_2$  vs time

The same remarks can be made for the temperature  $T_2$ . The percentage differences are slightly greater (see table 1).

	$T_1$	$T_2$
I model	15.7 %	16 %
II model	-18%	39%

Table 1. Maximum percentage differences for I and II model

Finally, the first model is useful in a preliminary design phase where the one-dimensional approximation can be applied. The model can be used in an optimization tool in order to find the lighter configuration of a given thermo-structure. Since it is very simple and fast, complex optimizations characterized by a relevant number of design and constraint variables can be performed. Then significant amount of computational time can be saved adopting the proposed model instead of the Finite Element method approach.

### 3. Application

The described model has been applied to preliminary design the ceramic wing leading edge of a re-entry vehicle. This activity has been performed in the frame of a project founded by the Italian Space Agency (ASI). The aim of the project is to develop advanced reusable structures able to sustain the high thermal loads encountered by re-entry and hypersonic vehicles (Ferraiuolo et al, 2008, 2009; Glass, 2008). Previously, the wing leading edge had been sized adopting a Finite Element commercial code (ANSYS) together with a first order optimization method (Ryszard, 2006; Hackman, Richardson, 2000). In the preliminary

design phase, a two-dimensional geometry has been considered since the aero-thermal loads do not vary significantly along the wing.

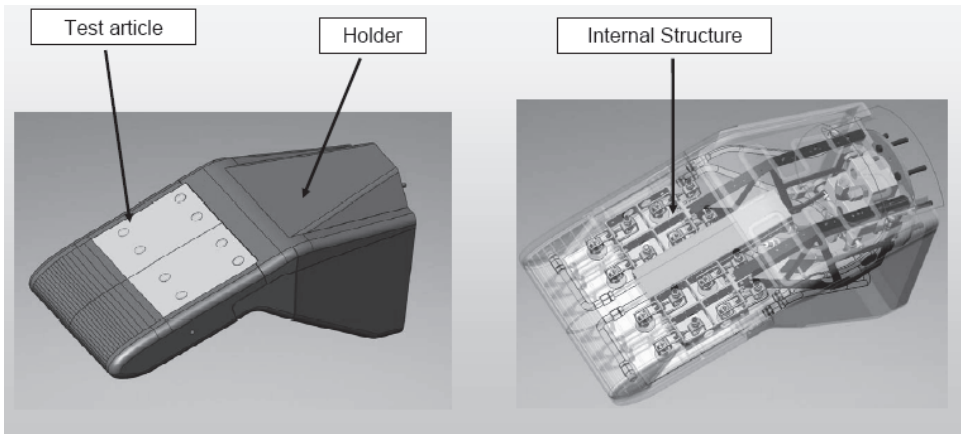


Fig. 12. Scheme of the Test Article

The components of the Test-Article are (see figure 13):

1. UHTC (Ultra High Temperature Ceramic) wing leading edge,
2. C/C panel to be joined with the UHTC WLE and the radiative shield,
3. Steel and Inconel slabs representing the internal structure of the Test Article,
4. Radiation shield used to minimize the heat transfer between the UHTC and the internal structure.

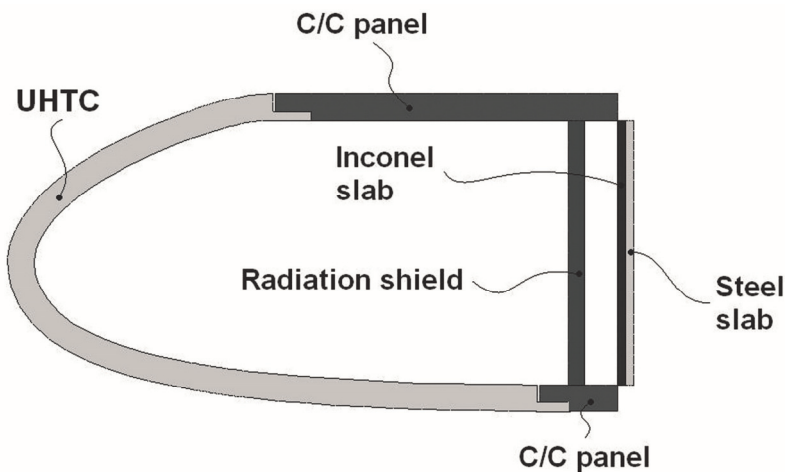


Fig. 13. 2d scheme of the internal structure of the WLE

The design variables considered for the optimization phase are:

1. UHTC WLE thickness
2. Radiation Shield Thickness

3. UHTC material (discrete variable; 3 UHTC material have been considered in the optimization phase).

The constraint variables are:

1. Limit use temperatures for the UHTC and the radiation shield,
2. Maximum temperature of the steel slab that must not exceed 430 K (this constraint has been chosen since measurement devices in the steel slab cannot operate at a greater temperature value).

The objective is to minimize the weight of the structure.

The result of the optimization is an almost constant UHTC thickness of 10 mm and a 8 mm thickness for the radiation shield. The time needed to perform that optimization was about 160 hours. Figure illustrates the 3D final configuration of the UHTC wing leading edge.

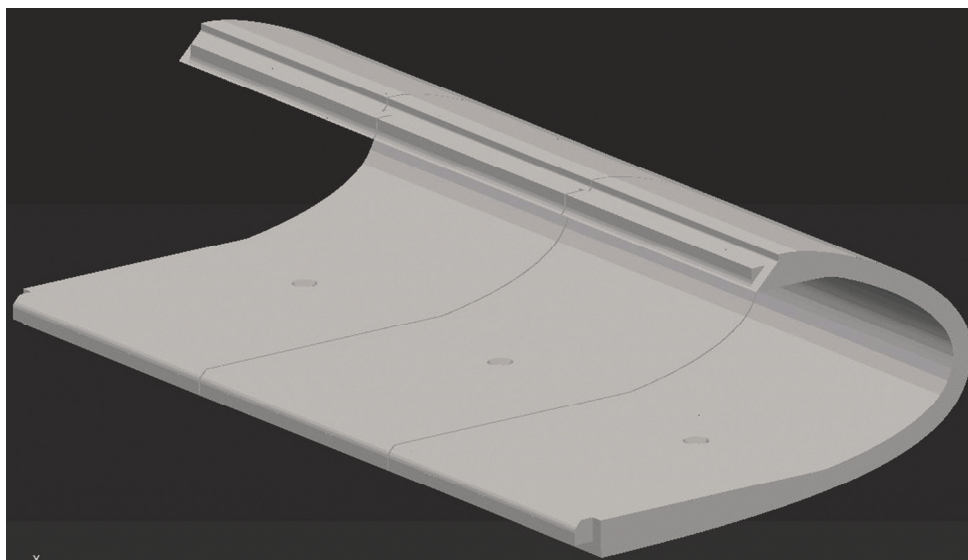


Fig. 14. 3d scheme of the WLE

### 3.1 Optimization of The WLE with the proposed model

The model described in paragraph II has been adopted to preliminary design the above described Wing Leading edge. An optimization code (MODEFRONTIER) has been used in order to perform the optimizations. The model has been implemented in Excel and then in MODEFRONTIER.

Figure 15 illustrates where the proposed model has been used. In particular, in the “\*1” rectangles the model considering the internal radiation has been adopted; in the “\*3” one the model considering only the external radiation has been adopted; the “\*4” rectangle refers to the double-layered model and the “\*2” one refers to a numeric model able to evaluate the thermal and the structural responses of multi-layered structure subjected to aerodynamic heating (Ferraiuolo et. al, 2008).

The structural sizing has been performed only in rectangles “\*2” since they include the junction between The UHTC leading edge and the C/C panel which is more critical from a structural point of view (Blosser, Mcwithey, 1983, Thomas, 2002;Milos, Squire, 1999).

Structural sizing on the remaining areas will be performed in a subsequent detailed design phase.

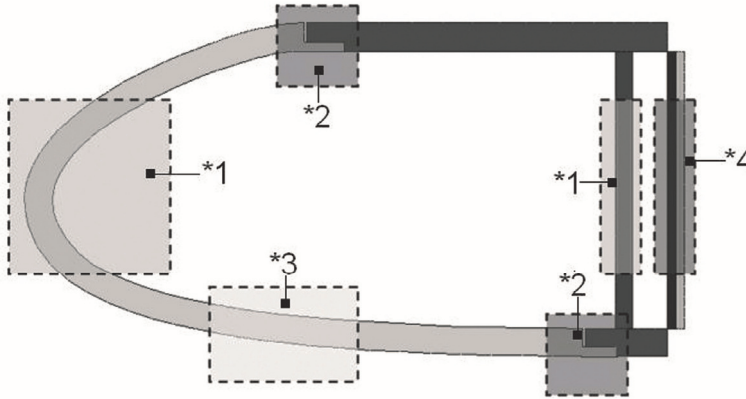


Fig. 15. Models adopted for the preliminary design

The optimization phase has been enriched considering the possibility to change the UHTC material. Then, a discrete design variable has been added in MODEFRONTIER. Figure 16 illustrates the scheme built in MODFRONTIER.

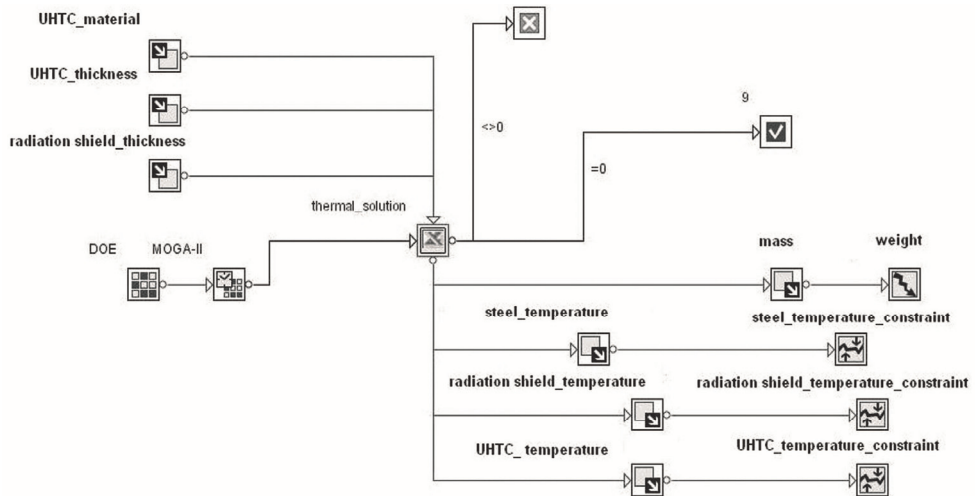


Fig. 16. Modefrontier optimization scheme

Ten points have been chosen for the optimization of the WLE (see figure 17).

A gradient based method has been chosen to perform the optimization. The time needed to perform the optimization is 20 hours, 8 times smaller than the time needed adopting finite element codes. The outputs of the optimizations are summarized in tables 2,3 and 4.

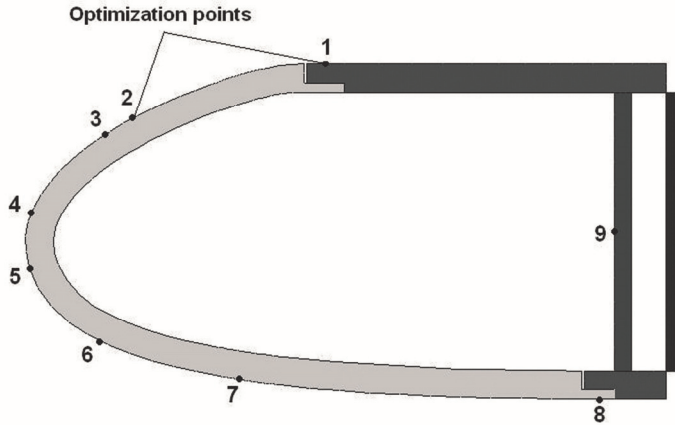


Fig. 17. Optimization points

Points	Optimized thickness (mm)	Material Number
2	9	3
3	8.5	1
4	8	1
5	8	1
6	9.5	1
7	10	1

Table 2. Optimized thicknesses and materials- points 2-7

Points	UHTC Thickness (mm)	C/C Thickness (mm)	Material number
1	4	5	3
8	4.1	5.9	1

Table 3. Optimized thicknesses and materials- points 1 and 8

Point	Optimized thickness
9	8

Table 4. Optimized thickness - point 9

Interpolating the optimized thicknesses along the wing leading edge, the following configuration is obtained (figure 18):

The final weight is 12% less than the starting configuration. All the optimized thicknesses are less than 10 mm, except for the point 7. The material 3 chosen for the upper portion of the wing leading edge, is characterized by a smaller density and Temperature limit use with respect to materials 1 and 2. The design of the connection between the UHTC WLE and the C/C panel will be performed in the detailed design phase [19].

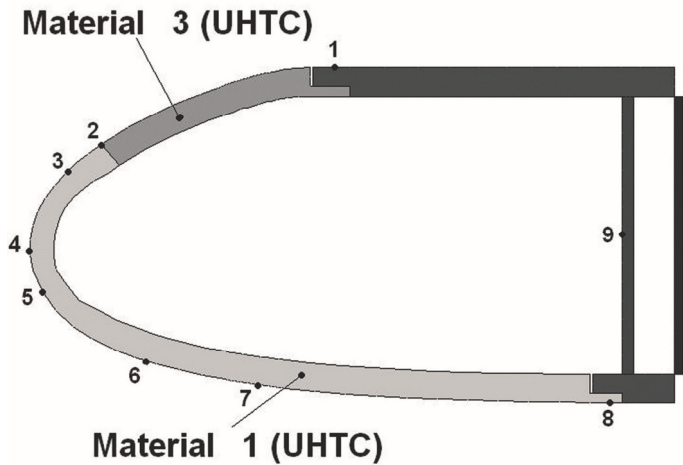


Fig. 18. Optimized configuration

Figure 19 illustrates the linearized thickness distribution for that starting and the optimized configuration. the black area highlights the weight saving amount obtained by adopting the numeric-analytic model proposed.

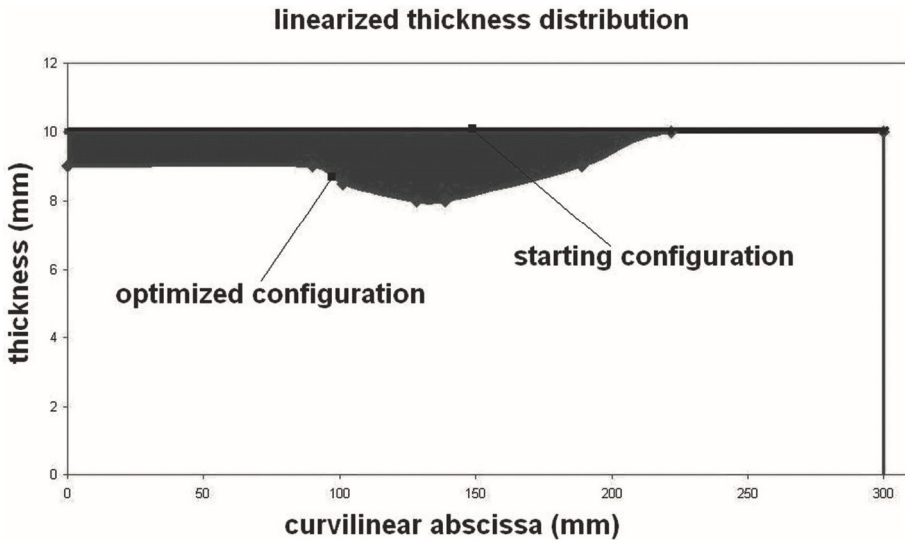


Fig. 19. Wing leading edge - linearized thickness distribution

A finite element model representing the optimized configuration has been built in order to compare the results obtained by means of the proposed model and the results obtained by means of the Finite Element Method.

Table 5 contains the temperature values evaluated at the time instant characterized by the maximum heat flux.

Points	Temperature (K) Fem model (2D)	Temperature (K) Proposed model (1D)	Percentage difference
1	766.5	786.24	-4
2	1351.1	1403.9	-4.9
3	1397.6	1483.9	-5.9
4	1496.6	1557.7	-5
5	1533.7	1582.9	-3.9
6	1633.6	1713.1	-5.9
7	1613.0	1696.1	-6.2
8	956.4	983.7	-4
9	712.2	734.1	-5

Table 5. FEM and proposed model results-Temperature

Table 6 contains the principal stress S1 values for points 1 and 8.

Points	Stress S1 (MPa) FEM model (2D)	Stress S1 (MPa) Proposed model (2D)	Percentage difference
1	202	183.8	-9
8	185	166.9	-9.8

Table 6. FEM and proposed model results – stress values

The proposed model overestimates the temperature values with respect to the Finite element model. The maximum percentage difference is always less than 10%. As a consequence the presented numeric-analytic model is applicable to two-dimensional geometries where the heat transfer contribution in a direction is negligible with respect to the other ones.

#### 4. Conclusion

A simplified numeric-analytic one-dimensional model able to simulate the thermal behavior of thermal structures has been developed. Radiation and thermal properties non linearities have been taken into account. The model is useful to minimize the computational time needed to perform the preliminary design phase of structural components of re-entry or hypersonic vehicles. The time saving is possible since the proposed model is very simple and does not foresee a spatial discretization of the geometry. Then complex optimizations characterized by several design constraints, variables and objectives can be performed in a reasonable amount of time. The results obtained with the simplified model have been compared with the results obtained by means of the finite element method giving good results (the maximum percentage difference never exceeds 20%).

The model has been applied to preliminary design the ceramic wing leading edge of a re-entry vehicle allowing to save 12% of the weight with a computational time 8 times smaller with respect to the previous optimization performed on a two-dimensional finite element model. A thermostructural finite element analysis performed on the optimized configuration has demonstrated a good accordance between the results obtained with the proposed model and those obtained with the two-dimensional Finite element method.

Finally, the proposed simplified approach is well suited for thermal protection systems and hot structures where the one-dimensional assumption is acceptable. Particular attention must be paid on curved geometries like the wing leading edge where the approach can be used only in certain areas.

## 5. References

- Thornton Earl A. *Thermal Structures for Aerospace Applications 2nd ed.*, AIAA series, 1996, pp. 103-118, Chap. 4
- Kelly H. Neale, D.R. Rummeler and R. Jackson. *Research in Structures and Materials for Future Space Transportation Systems – An Overview*, Journal of Spacecrafts and Rockets, 20, pp.89-96, 1983.
- Shih, P.K., Prunty, J., Mueller, R.N. *Thermostructural Concepts for Hypervelocity Vehicles*, AIAA Paper 88-2295, April 1988
- Daryabeigi K., *Thermal Analysis and Design Optimization of Multilayer Insulation for Re-entry Aerodynamic Heating*, Journal of Spacecraft and Rockets, Vol.39, No.4, August 2002
- Poteet C., Hasan Abu-Khajeel, Su-Yuen Hsu, *Preliminary Thermal-Mechanical Sizing of a Metallic Thermal Protection System*, Journal of Spacecraft and Rockets, Vol. 41, No. 2, March-April 2004
- Kunihiko O., *Thermal analysis of the thermal protection system for the re-entry vehicle*, Computer methods in applied mechanics and engineering, 1998
- J. Crank, *The Mathematics of Diffusion*, Oxford Science Publication, 1979
- Syed M. , A. F. M. Arif, and Mostafa H. Sharqawy. *Thermal Analysis and Optimization of Orthotropic Pin Fins: A Closed-Form Analytical Solution*, J. Heat Transfer 132, 031301 (2010) (8 pages), 2010
- Necati, OzisiK. *Heat conduction*, second edition, , John Wiley and sons, 1993
- ANSYS® and ANSYS Workbench® *Reference Documentation*, Version 12.0
- Ferraiuolo M., Riccio A., Gigliotti M., Tescione D., Gardi R., Marino G. *Thermostructural design of a Flying Winglet Experimental Structure for the EXPERT Re-entry Test*, Journal of Heat Transfer, ASME, July 2009, Vol. 131
- Ferraiuolo M., Riccio A., Tescione D., Gardi R., Marino G. *Contact Sensitivity Analysis of a coupling pin for the Nose cap of a launch reentry vehicle*, JBIS, 61, pp.14-19, 2008.
- Glass D. *CMC-based hot structures*, 1st Workshop on Science and Technology of UHTC-Based Hot Structures, CIRA, Capua, Italy October 28-29, 2008
- Ryszard K. *Sensitivity analysis and shape optimization for transient heat conduction with radiation*, International Journal of Heat and Mass Transfer 49 (2006) 2033-2043, 2006
- Hackman L. E., Richardson J. E. *Design Optimization of Aircraft Structures with Thermal Gradients*, Journal of aircraft, 2000
- Ferraiuolo M., Riccio A., Tescione D., Gigliotti M. *A fast procedure for optimizing Thermal Protection Systems for Re-entry vehicles*, JBIS Vol. 61 pp. 478-486, 2008
- Blosser M. L., Mcwithey R., "Theoretical Basis for Design of Thermal-Stress-Free Fasteners", NASA Technical Paper 2226 December 1983
- Thomas J.D. *Design and Analysis of UHTC Leading Edge Attachment*, NASA/CR 2002-211505, 2002
- Milos F., Squire T. H. *Thermostructural Analysis of X-34 Wing Leading-Edge Tile Thermal Protection System*, Journal of Spacecraft and Rockets Vol. 36, No. 2, March-April 1999



## **Part 3**

# **Aerodynamic Field Measurements and Real Full Scale Analysis**



# A Computer-assisted Wind Load Evaluation System for the Design of Cladding of Buildings: A Case Study of Spatial Structures

Yasushi Uematsu  
*Tohoku University*  
Japan

## 1. Introduction

Thin sheet metal and/or membrane are often used for roof cladding of spatial structures because of their strength and lightness (Noguchi et al., 2003). Being light and flexible, such roofing materials are vulnerable to dynamic wind actions. Since wind pressures acting on spatial structures vary spatially as well as in time, the design wind loads should be determined based on the dynamic characteristics of wind pressures. Fatigue of cladding elements, such as roofing material and its fixings, may play an important role in the wind resistant performance of cladding systems, although it is seldom considered in the design.

Roof cladding is usually designed based on the worst peak pressure coefficients irrespective of wind direction. The conventional codification provides a single peak design pressure coefficient for each roof zone considering a nominal worst-case scenario. Neither the probability distribution of the peak pressure coefficients nor the peaks other than the largest one are considered. Hence, they are not suitable for fatigue and risk-consistent designs. Building design has recently shifted to a performance-oriented one. Therefore, it is hoped to develop a new methodology that provides the peak pressure coefficients according to predetermined risk levels and the loading sequence for estimating the fatigue damage to roof cladding and its fixings. Computer simulation of wind pressure time series may be useful for this purpose.

Kumar and Stathopoulos (1998, 1999, 2001) proposed a novel simulating methodology that generates both Gaussian and non-Gaussian wind pressure fluctuations on low building roofs. Despite its simple procedure, the technique is successfully applied to fatigue analysis as well as to the evaluation of extreme pressures in a risk-consistent way. Therefore, this technology is used in this chapter and a simplification of this method is discussed. Gaussian and non-Gaussian pressure fluctuations can be simulated from the statistics of wind pressures, i.e. the mean, standard deviation, skewness, kurtosis and power spectrum. These statistical values change with location as well as with many factors related to the structure's geometry and the turbulence characteristics of approach flow. For such a complicated phenomenon, in which a number of variables involve, artificial neural networks (simply neural networks or ANN's) can be used effectively. Artificial neural networks can capture a complex, non-linear relationship via training with informative input-output example data pairs obtained from computations and/or experiments. Among a variety of artificial neural

networks developed so far, Cascade Correlation Learning Network (Fahlman and Lebiere, 1990) is applied to the present problem. It is a popular supervised learning architecture that dynamically grows layers of hidden neurons of a fixed non-linear activation (e.g. sigmoid), so that the topology (size and depth) can also be efficiently determined.

This chapter proposes a computer-assisted wind load evaluation system for the design of roof cladding of spatial structures. Focus is on spherical domes and vaulted roofs, as typical shapes of spatial structures. The composition of the system is schematically illustrated in Fig. 1. This system provides wind loads for the design of cladding and its fixings without carrying out any additional wind tunnel experiments. An aerodynamic database, artificial neural network and time-series simulation technique are employed in the system. Finally, applications of the system to risk-consistent design as well as to fatigue design are presented.

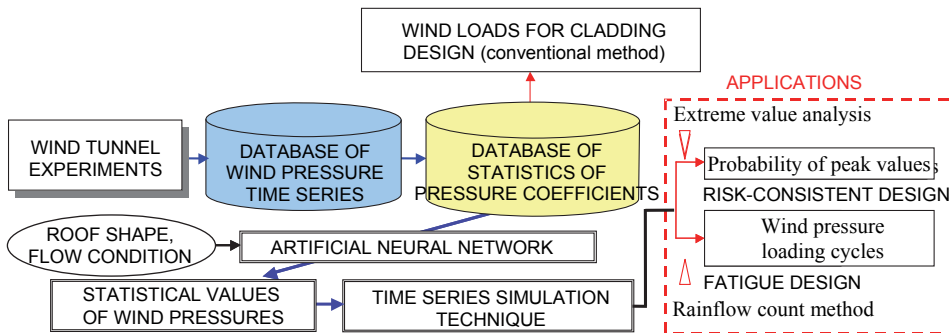


Fig. 1. Wind load evaluation system for the roof cladding of spatial structures

The wind load evaluation system proposed here is based on our previous studies (Uematsu et al., 2005, 2007, 2008). It can be applied not only to spherical domes and vaulted roofs but also to any other structures. However, such a system may be more useful for designing the cladding of spatial structures because of its sensitivity to dynamic load effects of fluctuating wind pressures. The spatial variation of statistical properties and the non-normality of pressure fluctuations on spherical domes and vaulted roofs are less significant than those on flat and gable roofs. Therefore, an ANN and a time-series simulation technique can be used more efficiently for these structures. This is the reason why we focus on the cladding of spherical domes and vaulted roofs in this chapter.

## 2. Aerodynamic database

### 2.1 Wind tunnel experiments

Two series of wind tunnel experiments were carried out; one is for spherical domes and the other is for vaulted roofs. The experimental conditions are somewhat different from each other. The outline of the experimental conditions is presented here.

#### 2.1.1 Spherical dome

The experiments were carried out in a closed-circuit-type wind tunnel with a working section 18.1 m long, 2.5 m wide and 2.0 m high. Two kinds of turbulent boundary layers simulating natural winds over typical open-country and urban terrains were generated; these flows are respectively referred to as Flows 'II' and 'IV' in this chapter. The geometric

scale of these flows ranges from 1/400 to 1/500, judging from the longitudinal integral scale of turbulence.

The geometry of the wind tunnel model is schematically illustrated in Fig. 2(a). The rise/span ratio ( $f/D$ ) is varied from 0 to 0.5, while the eaves-height/span ratio ( $h/D$ ) from 0 to 1. The span  $D$  of the wind tunnel model is 267 mm and the surface of the model is nominally smooth. Each model is equipped with 433 pressure taps of 0.5 mm diameter, as shown in Fig. 2(b). The pressure taps are connected to pressure transducers in parallel via 80 cm lengths of flexible vinyl tubing of 1 mm inside diameter. The compensation for the frequency response of this pneumatic tubing system is carried out by using a digital filter, which is designed so that the dynamic data up to approximately 500 Hz can be obtained without distortion. The signals from the transducers are sampled in parallel at a rate of 1 kHz on each channel for a period of approximately 33 seconds. All measurements are made at a wind velocity of  $U_{ref} = 10$  m/s at a reference height of  $Z_{ref} = 267$  mm. The velocity scale is assumed 1/5. The wind velocity  $U_{top}$  at the level of rooftop ranges from 5.3 to 10.2 m/s; the corresponding Reynolds number  $Re$ , defined in terms of  $D$  and  $U_{top}$ , ranges from approximately  $9.4 \times 10^4$  to  $1.8 \times 10^5$ . The turbulence intensity  $I_{u,top}$  at the level of rooftop ranges from 0.13 to 0.20 for Flow II and from 0.12 to 0.27 for Flow IV.

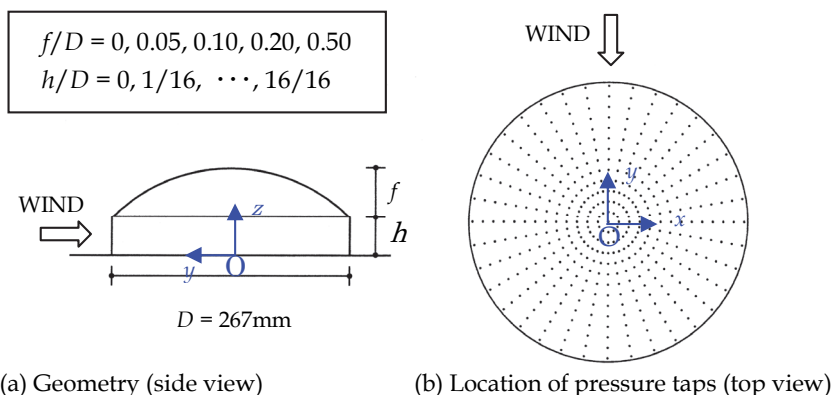


Fig. 2. Wind tunnel model and coordinate system (spherical domes)

### 2.1.2 Vaulted roof

The experiments were carried out in a closed-circuit-type wind tunnel with a working section 18.9 m long, 2.6 m wide and 2.1 to 2.4 m high. Two kinds of turbulent boundary layers similar to those used for spherical domes were generated; these flows are respectively referred to as Flows 'II'' and 'IV'' in this chapter.

The geometry of the wind tunnel model is schematically illustrated in Fig. 3(a). The rise/span ratio ( $f/D$ ) is varied from 0.1 to 0.4, while the eaves-height/span ratio ( $h/D$ ) from 1/30 to 20/30. The span  $D$  of the wind tunnel model is 150 mm and the length  $W$  is 300mm. Each model is equipped with 228 pressure taps of 0.5 mm diameter, as shown in Fig. 3(b). The turbulence intensity  $I_{w,H}$  at the mean roof height  $H$  is approximately 0.16 for Flow II' and approximately 0.19 for Flow IV'.

The experimental procedure is the same as that for spherical domes except that the wind direction is varied from 0 to 90° at a step of 5°.

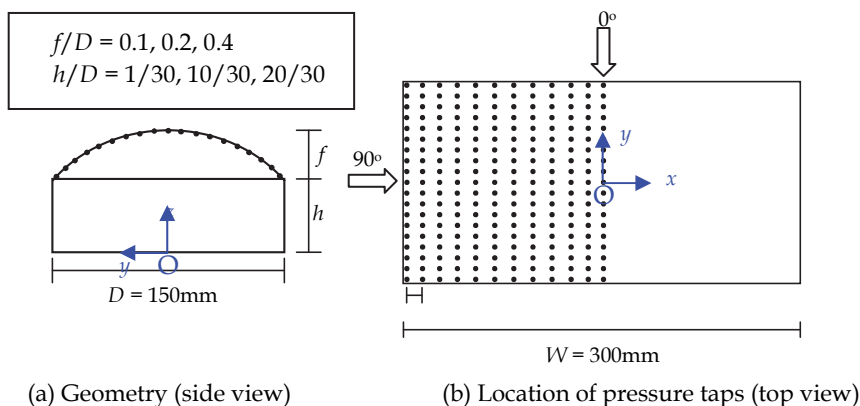


Fig. 3. Wind tunnel model and coordinate system (vaulted roofs)

## 2.2 Database of the statistics of wind pressures

The data from the simultaneous pressure measurements are stored on a computer in the form of pressure coefficient; the pressure coefficient  $C_p$  is defined in terms of the velocity pressure  $q_H$  ( $= 1/2\rho U_H^2$ , with  $\rho$  and  $U_H$  being the air density and the wind velocity at the mean roof height  $H$ , respectively). Then, the statistical values of pressure coefficients, i.e. mean  $\bar{C}_p$ , standard deviation  $C_p'$ , maximum and minimum peaks,  $C_{p\max}$  and  $C_{p\min}$ , during a full-scale period of 10 min, skewness  $S_k$ , kurtosis  $K_u$  and power spectrum  $S_p(f)$ , with  $f$  being the frequency, are computed. In the spherical dome case, the distributions of  $\bar{C}_p$ ,  $C_p'$ ,  $C_{p\max}$ ,  $C_{p\min}$ ,  $S_k$  and  $K_u$  in the circumferential direction are smoothed by using a cubic spline function. Furthermore, the values at two points that are symmetric with respect to the centreline parallel to the wind direction are replaced by the average of the two values, which makes the distribution symmetric with respect to the centreline. In the case of vaulted roofs, the distributions along the roof's periphery are smoothed by using a cubic spline function. Such a smoothing procedure may eliminate noisy errors included in the experimental data. Sample results on  $\bar{C}_p$  are shown in Figs. 4 and 5. The smoothed data for all the cases tested are stored in the database, together with the coordinates  $(x, y)$  of pressure taps, the values of geometric parameters (i.e.  $f/D$  and  $h/D$ ), and the turbulence intensity  $I_{uH}$  of approach flow at the mean roof height  $H$  and the wind direction (only for vaulted roofs). The power spectrum  $S_p(f)$  is approximated by the following equation:

$$\frac{S_p(f)}{\sigma_p^2} = a_1 \exp\left(-c_1 \frac{f\sqrt{DH}}{U_H}\right) + a_2 \exp\left(-c_2 \frac{f\sqrt{DH}}{U_H}\right) \quad (1)$$

where  $\sigma_p$  is the standard deviation of pressure fluctuation;  $a_1$  and  $a_2$  are the position constants and  $c_1$  and  $c_2$  are the shape constants. The first and second terms of the right-hand side of Eq. (1) control the position and shape of  $S_p(f)/\sigma_p^2$  at lower and higher frequencies, respectively. Similar representation was used by Kumar and Stathopoulos (1998) for pressures on low building roofs. In the above equation, however, the frequency  $f$  is reduced

by  $\sqrt{DH}$ , not by  $H$ . This is related to a three-dimensional effect of the flow around the roofs. The values of the four constants are determined based on the least squares method applied to the experimental data.

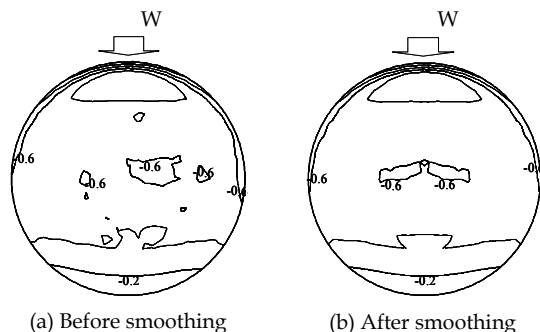


Fig. 4. Distributions of  $\bar{C}_p$  on a spherical dome ( $f/D = 0.1$ ,  $h/D = 4/16$ , Flow II)

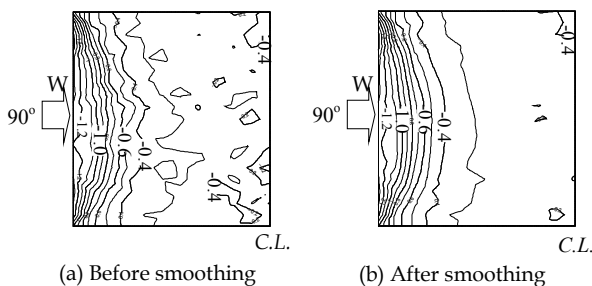


Fig. 5. Distributions of  $\bar{C}_p$  on a vaulted roof ( $f/D = 0.1$ ,  $h/D = 1/30$ , Flow IV')

In the spherical dome case, the general shape of  $S_p(f)/\sigma_p^2$  changes only slightly in the  $x$ -direction (Noguchi and Uematsu, 2004). Therefore, focus is on the variation of  $S_p(f)/\sigma_p^2$  only in the  $y$ -direction. The values of  $a_1$ ,  $a_2$ ,  $c_1$  and  $c_2$  at the pressure taps on the dome's centreline are computed for all the cases tested and stored in the database. In the wind load evaluation system, we use the values of the four constants at a point on the centreline that gives a  $y$ -axis value closest to that of the target point (evaluation point). Fig. 6 shows sample results of comparison between experiment and formula for the power spectra at two points on a spherical dome. The experimental results are plotted by the circles and the empirical formula is represented by the solid line. It is seen that the approximation by Eq. (1) is generally satisfactory.

In the vaulted roof case, the wind pressures are affected by the wind direction. Hence, the power spectra are calculated for all pressure taps and wind directions. Fig. 7 shows sample results of comparison between experiment and formula for the power spectra at two points on a vaulted roof. Again, the agreement is generally good.

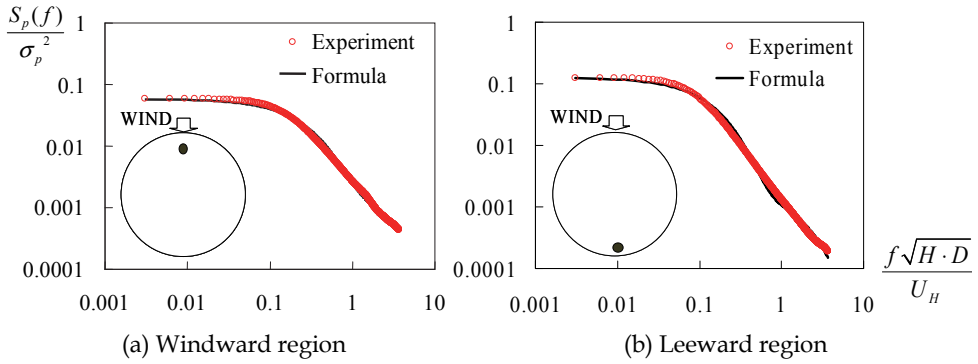


Fig. 6. Wind pressure spectra for a spherical dome ( $f/D = 0.1, h/D = 4/16$ , Flow II)

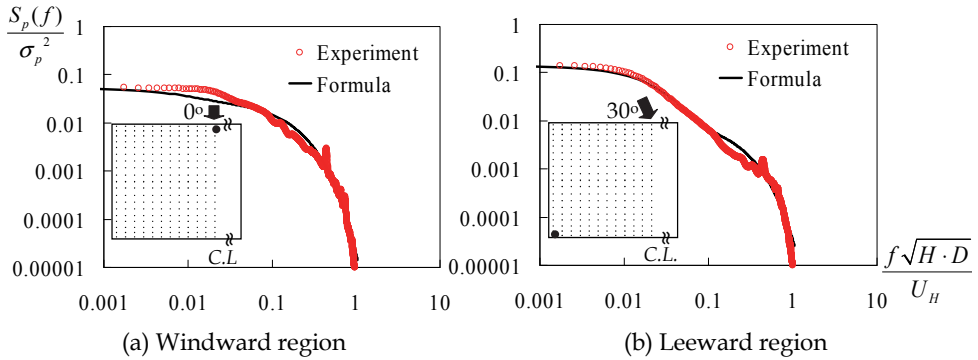


Fig. 7. Wind pressure spectra for a circular arc roof ( $f/D = 0.1, h/D = 1/30$ , Flow IV')

### 3. Artificial neural network

#### 3.1 Spherical dome

Although the wind pressures were measured simultaneously at several hundreds points in the wind tunnel experiments, spatial resolution may be still limited from the viewpoint of cladding design. Cladding or roofing cover is sensitive to the spatial variation and fluctuating character of the time-dependent wind pressures. The turbulence of approach flow also affects the wind pressures significantly. Hence, an artificial neural network based on Cascade Correlation Learning Network (CCLN, Fahlman and Lebiere, 1990) is used to improve the resolution.

Fig. 8 illustrates the network architecture, which has a layered structure with an input layer, an output layer and a hidden layer between the input and output layers. The input vector consists of five parameters, that is, two geometric parameters of the building ( $f/D$  and  $h/D$ ), the coordinates  $(x, y)$  of measuring point, and the turbulence intensity  $I_{uH}$  of the approach flow at the mean roof height  $H$ ; the coordinate system is defined as shown in Fig. 2. There is also a bias unit, permanently set to +1. Each network is constructed for each of the four parameters,  $\bar{C}_p, C_p', S_k$  and  $K_u$ .

The quickprop algorithm (Fahlman, 1988) is used to train the output weights. Training begins with no hidden units. As the first step, the direct input-output connections are



trained as well as possible over the entire training set. The network is trained until either a predetermined maximum number of iterations is reached, or no significant error reduction has occurred after a certain number of training cycles. If the error is not acceptable after the first step, a new hidden unit is added to the network to reduce this residual error. The new unit is added to the network, its input weights are frozen, and all the output weights are once again trained. This cycle repeats until the error becomes acceptably small.

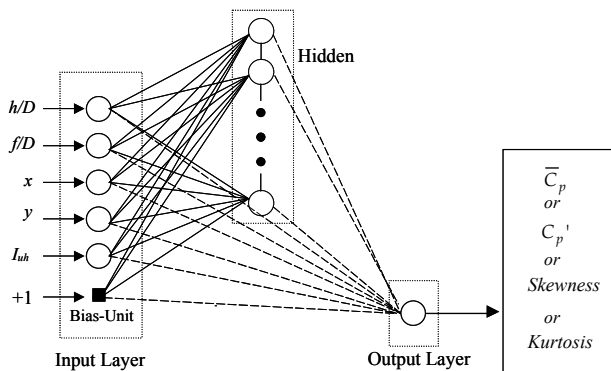


Fig. 8. CCLN for the statistics of wind pressures on spherical domes

Well-distributed representative data are required for training the network. In the above-mentioned database, pressure data at 230 locations are stored each for five  $f/D$  ratios, seventeen  $h/D$  ratios and two kinds of turbulent boundary layers (open-country and urban exposures). Note that the  $h/D$  ratio is varied from 1/16 to 1 in the flat roof case ( $f/D = 0$ ). Therefore, the number of data set is 38,640 ( $= 2 \times (16+17 \times 4) \times 230 = 168 \times 230$ ). Ten typical cases of experimental conditions are selected from these 168 cases. Forty-six locations are randomly selected from the 230 points for testing. Therefore, the number of test data is 460 ( $= 10 \times 46$ ). The other data are used for training the network. The sigmoid function represented by the following equation is used to process the net input signals and provide the output signals at hidden nodes:

$$f(s) = \frac{S_{\max} - S_{\min}}{1 + e^{-s}} + S_{\min} \tag{2}$$

where  $S_{\max}$  and  $S_{\min}$  represent the upper and lower limits of the output from the neuron. Appropriate values of  $S_{\max}$  and  $S_{\min}$  depend on the output vector. In the training phase of the network using the quickprop algorithm, three empirical terms, i.e. learning rate  $\eta$ , maximum growth factor  $\mu$ , and weight decay term  $\lambda$ , are introduced to improve the convergence of training and the stability of computation. Appropriate values of these terms are determined by trial and error, considering the behaviour of the mean square error that the network produces. The weights are initialised to random numbers between +1.0 and -1.0. The number of epochs also affects the convergence of training, which is again determined by trial and error. Table 1 summarizes the values of  $\eta$  and the numbers of

epochs for  $\bar{C}_p$ ,  $C_p'$ ,  $S_k$  and  $K_u$ , together with the values of the error index  $I_E$  in the training phase; the error index is defined by the following equation:

$$I_E = \frac{\sqrt{\frac{1}{N} \sum_{k=1}^N (T_k - O_k)^2}}{\sigma} \tag{3}$$

where  $T_k$  and  $O_k$  represent the target value and the actual output for training pattern  $k$ , respectively;  $N$  = number of training patterns; and  $\sigma$  = standard deviation of the target data. Because the values of  $S_k$  and  $K_u$  change over a wide range, these values are divided by some factors.

Statistical value	$\eta$	Number of epochs	$I_E$ (training phase)
$\bar{C}_p$	0.5	100	0.144
$C_p'$	0.5	50	0.333
$S_k$	0.02	200	0.478
$K_u$	0.2	300	0.421

Table 1. Characteristics of the neural network for spherical domes

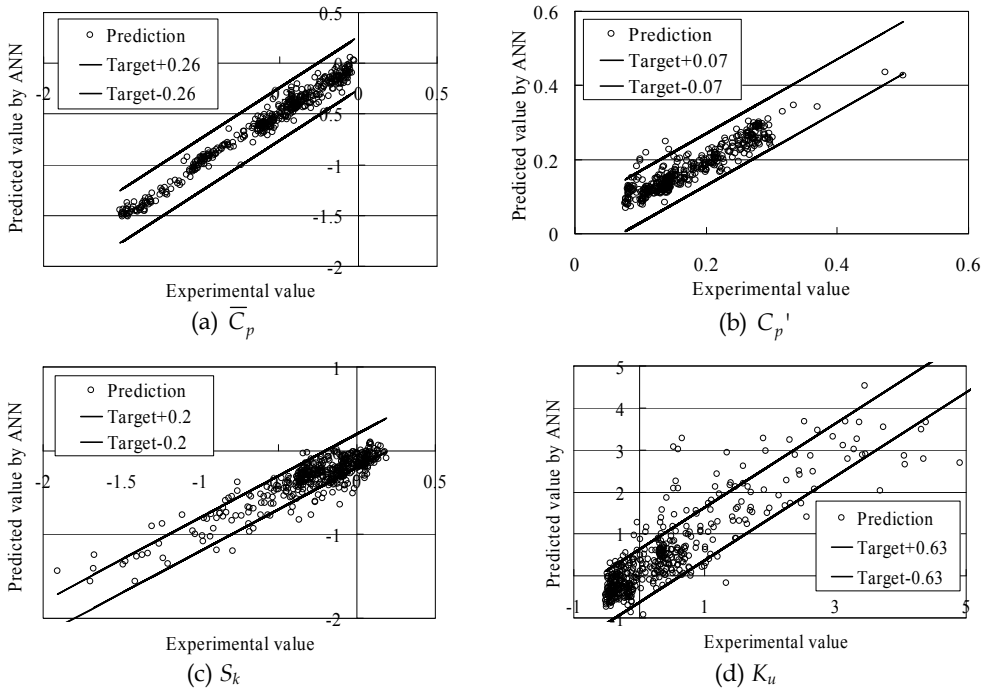


Fig. 9. Comparison between experiment and ANN prediction for  $\bar{C}_p$ ,  $C_p'$ ,  $S_k$  and  $K_u$

Fig. 9 shows comparisons between experiment and prediction by ANN for  $\bar{C}_p$ ,  $C_p'$ ,  $S_k$  and  $K_u$ , respectively; 460 data are plotted in each figure. The solid lines in the figures represent permitted limits, which are tentatively chosen as a standard deviation of the experimental values. Regarding  $\bar{C}_p$  and  $C_p'$ , the agreement is generally good. Regarding the skewness and kurtosis, on the other hand, the agreement is somewhat poorer than that for  $\bar{C}_p$  and  $C_p'$ , although the ANN captures the general trend of the experimental data. This is because the skewness and kurtosis exhibit large values in magnitude in relatively small areas. Furthermore, their variation in these areas is also remarkable. However, as will be described later, the effects of  $S_k$  and  $K_u$  on the simulated time-series of wind pressures are relatively small. This feature implies that the neural networks constructed for  $S_k$  and  $K_u$  can be used in the practical applications.

To discuss the application of the ANN to practical situations, a comparison is made between the prediction by the ANN and the experimental data for Nagoya Dome (Fig. 10). The geometry of this building is as follows: i.e. span  $D = 187.2$  m, rise  $f = 32.95$  m, eaves-height  $h = 30.7$  m ( $f/D = 0.18$ ,  $h/D = 0.16$ ). This dome is constructed in the suburb of Nagoya City, Japan. The wind tunnel experiment was carried out with a 1/500 scale model in a turbulent boundary layer with a power law exponent of  $\alpha = 0.25$  and the turbulence intensity of 0.19 at the level of rooftop. The actual situation in the circular area with a radius of 450 m around the dome was modeled exactly. The experimental data on  $\bar{C}_p$  and  $C_p'$  were provided by Takenaka Corporation that had carried out the wind tunnel experiment. Fig. 11 shows comparisons between the ANN prediction and the experimental data for  $\bar{C}_p$  and  $C_p'$ . The agreement is relatively good, particularly for  $\bar{C}_p$ . The ANN somewhat overestimates the values of  $C_p'$ . However, such a difference up to about 0.1 may be acceptable in practical applications.



Fig. 10. Nagoya Dome (provided by Takenaka Corporation)

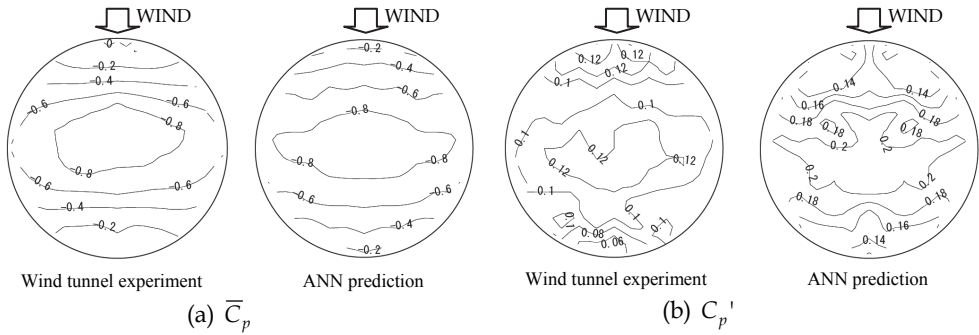


Fig. 11. Comparison between ANN and experiment for the  $\bar{C}_p$  and  $C_p'$  distributions

**3.2 Vaulted roof**

Fig. 12 shows the ANN architecture for vaulted roofs. In this case, the wind direction  $\theta$  is considered in the input vector. The network is trained in the same manner as that for spherical domes. Eighteen typical cases of experimental conditions are selected from the 342 cases. Forty-five locations are randomly selected from the 228 points for testing. The number of test data is 810 (= 18×45). The other data are used for training the network. Table 2 summarizes the characteristics of the network obtained.

Fig. 13 shows comparisons between experiment and prediction by ANN for  $\bar{C}_p$ ,  $C_p'$ ,  $S_k$  and  $K_u$ , respectively; 810 data are plotted in each figure. The behaviour of the networks for vaulted roofs is similar to that for spherical domes shown in Fig. 9. However, the ANN prediction is somewhat poorer than that for spherical domes. This may be related to a wider variation of the characteristics of wind pressures with many parameters in the vaulted roof case.

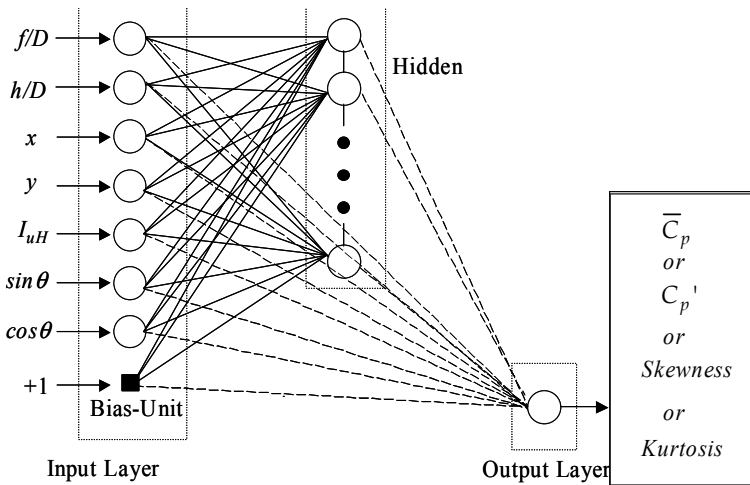


Fig. 12. CCLN for the statistics of wind pressures on vaulted roofs

Statistical value	$\eta$	Number of epochs	$I_E$ (training phase)
$\bar{C}_p$	0.2	150	0.229
$C_p'$	0.5	150	0.378
$S_k$	0.2	300	0.446
$K_u$	0.2	500	0.827

Table 2. Characteristics of the neural network for vaulted roofs

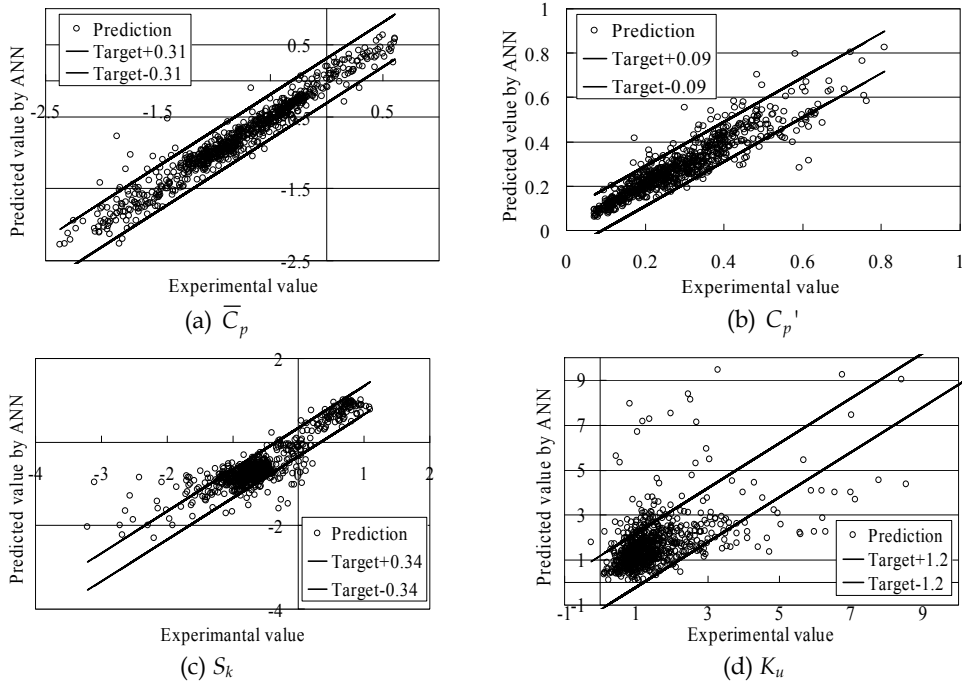


Fig. 13. Comparison between experiment and ANN prediction for  $\bar{C}_p$ ,  $C_p'$ ,  $S_k$  and  $K_u$

#### 4. Time series simulation of wind pressures

##### 4.1 Outline of the procedure

First, the application of the Kumar and Stathopoulos’s method (1999, 2001) to the present problem is discussed. The flow chart for the simulation is described in Fig. 14. The approach is based on an FFT Algorithm. The Fourier amplitude is constructed from the power spectrum  $S_p(f)$  of pressure fluctuations, which is represented by Eq. (1). The values of the four coefficients involved in the equation are obtained from the database. The spike features inducing the non-Gaussian character to the pressure fluctuations are achieved by preserving the target skewness and kurtosis given by the ANN and the database. A simple stochastic model with a single parameter  $b$  has been suggested for the simulation of phase. The

computation of  $b$  is accomplished by minimizing the sum of the squared errors in skewness and kurtosis. In practice, changing the value of  $b$  from 0 to 1 with a small increment (e.g. 0.01), the skewness  $S_k$  and kurtosis  $K_u$  of the simulated time series are computed. The sum of the squared errors (SSE) in  $S_k$  and  $K_u$  are calculated for each value of  $b$  and the value giving the least SSE is chosen as the optimum one.

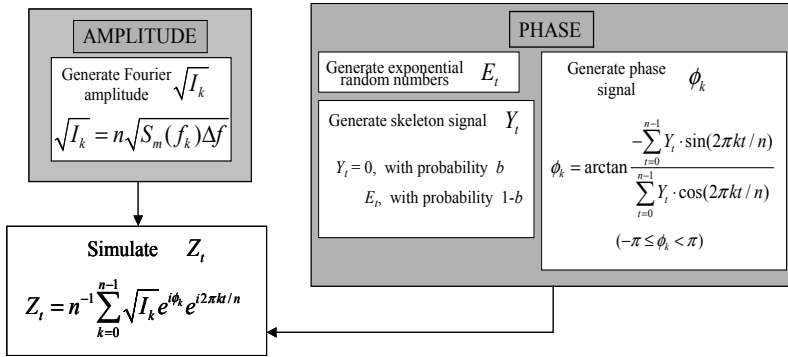


Fig. 14. Schematic of the generation of non-Gaussian wind pressure time series (Kumar and Stathopoulos, 1999, 2001)

**4.2 Toward simplification of the procedure**

The most troublesome and time-consuming procedure is the determination of the optimum value of  $b$ . Fig. 15 shows sample results on the variation of  $S_k$  and  $K_u$  with  $b$ . Note that the ordinate of the figure for kurtosis is represented by  $K_u-3$ , considering that  $K_u = 3$  for Gaussian processes. Because the skewness and kurtosis are related to each other, both  $S_k$  and  $K_u$  show similar behavior. They increase monotonically with an increase in  $b$ . When the value of  $b$  is relatively small, such as  $b < 0.6$ , for example, the variation is quite small. On the other hand, they increase significantly with increasing  $b$  for larger values of  $b$ . In practice, the optimum value of  $b$  is not so large and the values of  $S_k$  and  $K_u$  are less sensitive to  $b$ . Therefore, the variation of  $S_k$  and  $K_u$  can be approximated by a simple function of  $b$  with a small number of data points in the practical range. The cubic spline function is used here. Using such a function, the optimum value of  $b$  can be calculated easily.

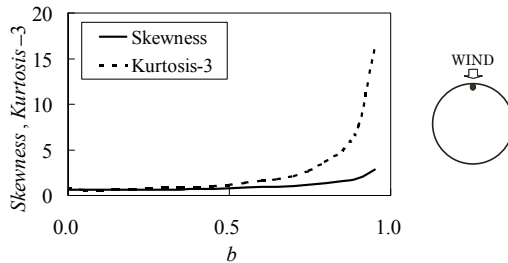


Fig. 15. Variation of  $S_k$  and  $K_u$  with  $b$  for a spherical dome ( $f/D = 0.1$ ,  $h/D = 0.25$ , Flow II)

### 4.3 Results and discussion

A comparison of the wind pressure time series between experiment and simulation is shown in Fig. 16. The spike features of pressure fluctuations are simulated well. Tables 3 and 4 summarize comparisons between experiment and simulation for the statistics of the wind pressures at two typical points on a spherical dome and a vaulted roof, respectively. Note that the averaging time for evaluating the peak pressure coefficients is 1 sec and the values in the table are all the ensemble averages of the results from six consecutive runs. A good agreement between experiment and simulation is seen for both points. Similar comparisons are made for ninety-two points shown in Fig. 17 (points on the solid lines). The results for  $C_{pmax}$  and  $C_{pmin}$  are plotted in Fig. 18. The agreement is relatively good. Approximately 95 % of the simulated results is within a range of the target value  $\pm 0.1$  for  $C_{pmax}$  and  $\pm 0.2$  for  $C_{pmin}$ . These results indicate that the method proposed here can be used for evaluating the design wind loads by combining the database of the statistics of wind pressures and the ANN.

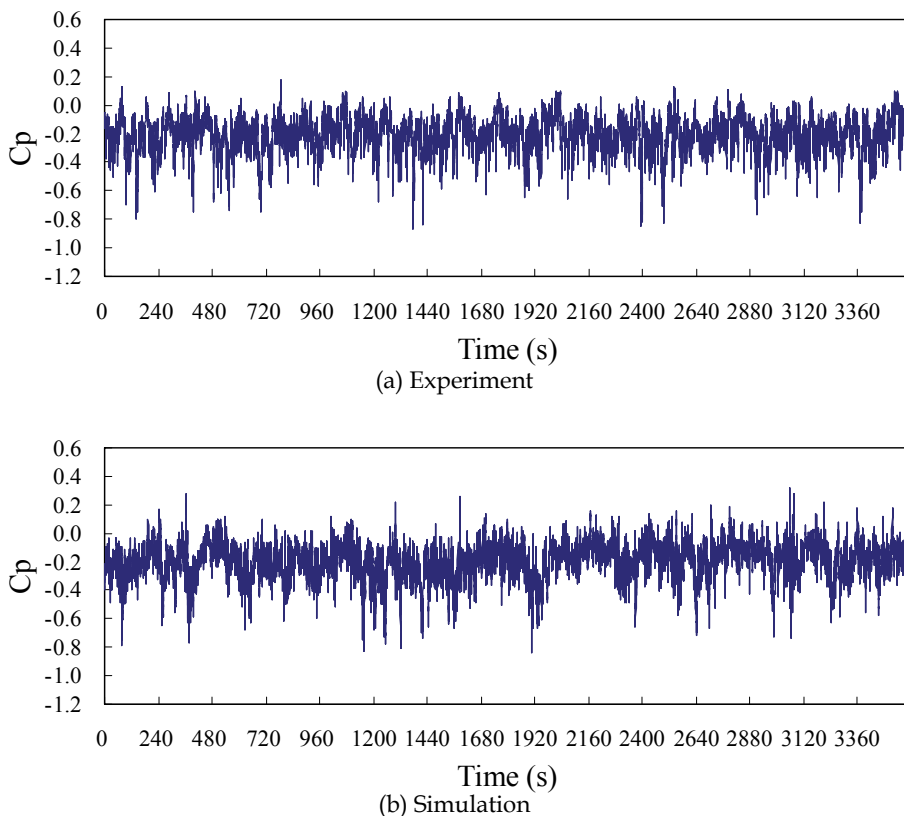


Fig. 16. Experimental and simulated time series of wind pressure coefficient at a point near the leeward edge of a spherical dome ( $f/D = 0.2$ ,  $h/D = 4/16$ , Flow II)

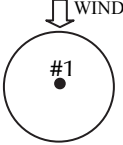
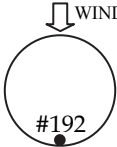
Statistics	$\bar{C}_p$	$C_{pmax}$	$C_{pmin}$	$S_k$	$K_u$	Tap location
(a) Point 1						
Experiment	0.226	-0.394	-1.872	-0.385	3.065	
Simulation	0.211	-0.395	-1.685	-0.436	3.057	
Error	0.015	0.001	-0.187	0.051	0.008	
(b) Point 192						
Experiment	0.126	0.208	-0.742	-0.647	4.225	
Simulation	0.120	0.154	-0.732	-0.661	4.212	
Error	0.006	0.054	-0.010	0.014	0.013	

Table 3. Comparison between experiment and simulation for the statistics of wind pressures on a spherical dome ( $f/D = 0.2$ ,  $h/D = 0.25$ , Flow II)

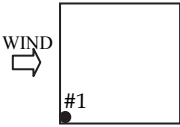
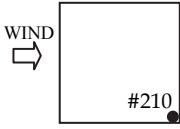
Statistics	$\bar{C}_p$	$C_{pmax}$	$C_{pmin}$	$S_k$	$K_u$	Tap location
(a) Point 1						
Experiment	0.475	-0.437	-3.188	-1.367	3.302	
Simulation	0.437	-0.386	-3.084	-1.188	2.852	
Error	0.038	-0.051	-0.104	-0.179	0.450	
(b) Point 210						
Experiment	0.206	0.115	-1.209	-0.884	2.708	
Simulation	0.190	0.066	-1.142	-0.852	2.332	
Error	0.016	0.049	-0.067	-0.032	0.376	

Table 4. Comparison between experiment and simulation for the statistics of wind pressures on a vaulted roof ( $f/D = 0.3$ ,  $h/D = 10/30$ , Flow II')

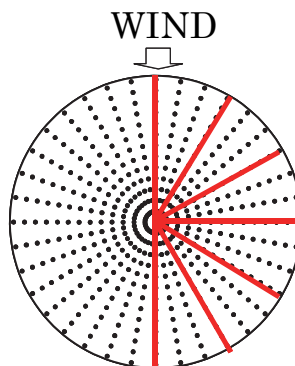


Fig. 17. Tap locations where the time series of pressure fluctuations is simulated (92 points on the solid lines)



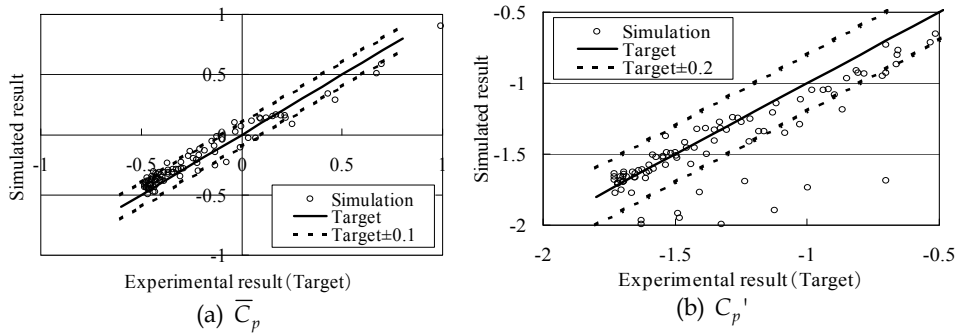


Fig. 18. Comparison between experiment and simulation for a spherical dome ( $f/D = 0.2$ ,  $h/D = 4/16$ , Flow II)

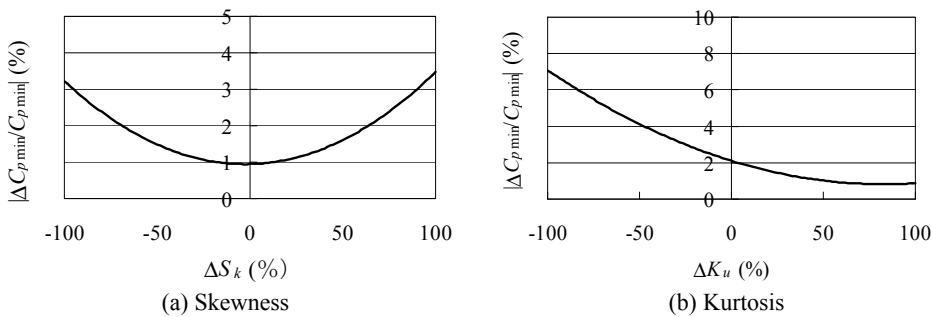


Fig. 19. Effects of  $S_k$  and  $K_u$  on the simulated value of  $C_{pmin}$  for a spherical dome ( $f/D = 0.2$ ,  $h/D = 9/16$ ,  $x/D = 0$ ,  $y/D = -1/4$ )

As mentioned above, the accuracy of the ANN prediction for  $S_k$  and  $K_u$  is not so high, compared with that for  $\bar{C}_p$  and  $C_p'$ . Then, the effects of  $S_k$  and  $K_u$  on the simulated results are investigated. The time series is simulated by changing either  $S_k$  or  $K_u$  from the optimum value. Fig. 19(a) shows the variation of the change of  $C_{pmin}$  ( $\Delta C_{pmin}$ ) with the change of  $S_k$  ( $\Delta S_k$ ) from the optimum value. A similar result for  $K_u$  is shown in Fig. 19(b). It is found that the simulated results are not sensitive to the variation of  $S_k$  and  $K_u$ . In practice, the simulated result of  $C_{pmin}$  changes some 5 percent when the values of  $S_k$  or  $K_u$  change by 50 percent.

### 5. Application of the wind load evaluation system to wind resistant design

The wind load evaluation system proposed here can provide peak pressure coefficients according to a predetermined risk level by combining the extreme value analysis. Fig. 20 shows the probability of non-exceedence for  $C_{pmin}$  at a windward edge point of a spherical dome. The thick solid line shows the result calculated from a set of 200 extremes that the evaluation system predicted. For comparative purpose, the results predicted from 33 sets of six extremes by using BLUE (Lieblein, 1974) are represented by thin solid lines. These results exhibit a considerable scatter around the 200 data curve. The result predicted from

the six experimental data is also quite different from the 200 data curve. Such a difference implies that we need a lot of data for predicting the probability of non-exceedence precisely. It takes a long time to collect so much data in a wind tunnel experiment. By comparison, the proposed wind load evaluation system can provide much data more easily. This is one of the advantages of the system over the wind tunnel experiment.

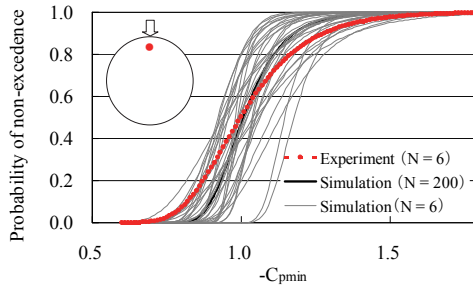


Fig. 20. Probability of non-exceedence for  $C_{pmin}$  (Spherical dome;  $f/D = 0.2, h/D = 4/16$ , Flow II)

Furthermore, by introducing a load cycle counting method, such as the rainflow count method, the system can provide the wind load cycles for fatigue design. Fig. 21 shows a sample result on the frequency distribution of wind pressure coefficient fluctuations, represented as a function of mean and amplitude of fluctuation at the center of a dome. By combining such a result with the influence coefficients, we can easily compute the stresses or strains induced in the cladding and its fixings, which are used for evaluating the fatigue damage.

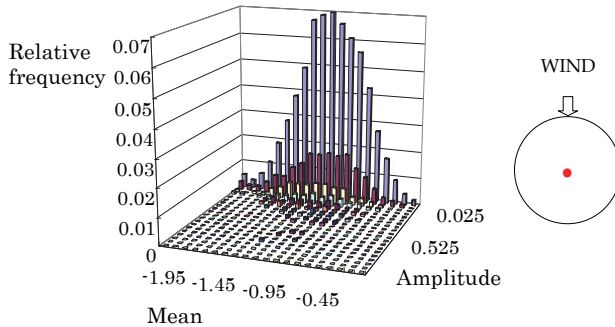


Fig. 21. Number of load cycles (Spherical dome;  $f/D = 0.2, h/D = 4/16$ , Flow II)

**6. Concluding remarks**

A computer-assisted load evaluation system for the design of roof cladding of spatial structures using an aerodynamic database, artificial neural network and time-series simulation technique has been proposed. Focus is on spherical domes and vaulted roofs as typical roof shapes used for spatial structures. The proposed methodology is capable of

providing peak pressure coefficients according to pre-determined risk levels by combining the extreme value analysis; this can generate risk consistent and more economical design wind loads for the roof cladding. Furthermore, by introducing a load cycle counting method, such as the rainflow count method, the system can provide the wind load cycles to be used for fatigue design.

This chapter describes the components of the load evaluation system proposed by the author. Although there are some problems to be investigated further, the results presented here indicate that the proposed system is promising. In this chapter the subject is limited to spherical domes and vaulted roofs. However, it is possible to apply the proposed method to the cladding of any buildings, once the database of the statistics of wind pressures has been constructed based on a wind tunnel experiment and/or CFD computations.

## 7. Acknowledgment

A part of the study is financially supported by Nohmura Foundation for Membrane Structure's Technology. The authors are much indebted to Dr. Takeshi Hongo of Kajima Technical Research Institute and Dr. Hirotochi Kikuchi of Shimizu Corporation for providing them the wind tunnel test data. Thanks are also due to Mr. Raku Tsuruishi, Ms. Miki Hamai and Chihiro Sukegawa, who were then graduate students of Tohoku University, for assistance in constructing the neural networks.

## 8. References

- Fahlman, S.E. (1988). Faster-learning variations on back-propagation: an empirical study, *Proceedings of the 1988 Connectionist Models Summer School*, Morgan Kaufmann.
- Fahlman, S.E. & Lebiere, C. (1990). The cascade-correlation learning architecture, *Advances in Neural Information Processing Systems*, Vol. II, Morgan Kaufmann, pp. 524-532.
- Kumar, K.S. & Stathopoulos, T. (1998). Fatigue analysis of roof cladding under simulated wind loading, *Journal of Wind Engineering and Industrial Aerodynamics*, Vol. 77&78, pp. 171-184.
- Kumar, K.S. & Stathopoulos, T. (1999). Synthesis of non-Gaussian wind pressure time series on low building roofs, *Engineering Structures*, Vol. 21, pp. 1086-1100.
- Kumar, K.S. and Stathopoulos, T. (2001). Generation of local wind pressure coefficients for the design of low building roofs, *Wind and Structures, An International Journal*, Vol. 4, No. 6, pp. 455-468.
- Lieblein, J. (1974). Efficient methods of extreme-value methodology, *National Bureau of Standards*, U.S. Department of Commerce, NBSIR 74-602.
- Nogchi, M.; Uematsu, Y. & Sone, T. (2003). Structural characteristics and wind resistant design of spatial structures constructed in Japan, *Eleventh International Conference on Wind Engineering*, pp. 1595-16002, Lubbock, Texas, USA, June 2-5, 2003.
- Nogchi, M. & Uematsu, Y. (2004). Model of fluctuating wind pressures on spherical domes for load estimation of cladding, *Proceedings of the 18th National Symposium on Wind Engineering*, December 1-3, 2004, Tokyo, Japan, pp. 353-358 (in Japanese).
- Uematsu, Y., Araki, Y., Tsuruishi, R. & Hongo, T. (2005). Wind load evaluation system for cladding of spherical domes using aerodynamic database, neural network and simulation, *Proceedings of the 6th Asia-Pacific Conference on Wind Engineering*, 12-14 September, 2005, Seoul, Korea (CD-ROM).

- Uematsu, Y., Tsuruishi, R., Hongo T. & Kikuchi, K. (2007). A computer-assisted wind load evaluation system for the design of cladding of spatial structures, *Proceedings of the 11th International Conference on Civil, Structural and Environmental Engineering Computing*, 18-21 September, 2007, St. Julians, Malta (CD-ROM).
- Uematsu, Y. & Tsuruishi, R. (2008). Wind load evaluation system for the design of cladding of spatial structures, *Journal of Wind Engineering and Industrial Aerodynamics*, Vol. 96, pp. 2054-2066.

# Monitoring of Soil Surface under Wind and Water Erosion by Photogrammetry

Shigeoki Moritani et al.\*

*Arid Land Research Center, Tottori University,  
Japan*

## 1. Introduction

Soil degradation resulting from accelerated water and wind-induced erosion is a serious problem in drylands, and will remain so throughout this century. The detachment and transport of soil particles degrade the fertility of agricultural land and consequently reduce its productivity (Lyles and Tartako 1986). Many of the particles involved in soil erosion processes, such as raindrops, wind velocity, soil aggregates, sediment, and siltation have characteristic dimensions on the millimeter scale (Huang 1998). The addition of organic matter increases the connection between aggregate by physical and chemical bonding. The strongly bonding aggregation induces the increase of soil porosity and permeability, which result the decrease of water erosion. The bigger aggregate also decrease the wind erosion due to their heaviness. The modeling and quantification of such processes require detailed measurements of the physical, chemical, and biological properties of soils (Soil Conservation Service 1976). However, these measurements are too slow, tedious, and expensive for routine or regular monitoring.

Several researchers have already used aerial photography to assess soil erosion. A precise form of this photography, photogrammetry, has the advantage of very efficiently and cost effectively providing detailed information about a large area. Together with aerial photography, the use of remotely sensed data forms the basis for land use mapping and change detection (Pellikka et al. 2004). In particular, for inaccessible areas, photogrammetry is far superior to traditional ground surveys. The subsequent convergence in recent years of photogrammetry and digital imaging technology has led to an increase in the use of digital elevation models (DEMs) in modern studies involving the monitoring of landscape changes (Prosser and Abernethy 1996; DeRose et al. 1998).

The areas measured experimentally in microtopographical studies of soil erosion range from 1 to approximately 20 m<sup>2</sup>. In general, the DEMs used for analysis have grid resolutions of 1 to 15 mm (Elliot et al. 1997; Darboux and Huang 2003). A variety of instruments and methods are used by soil scientists to acquire measurement coordinates, including mechanical point gauges (Elliot et al. 1997) that make contact with the soil surface,

---

\*Tahei Yamamoto, Henintsoa Andry, Mitsuhiro Inoue, Taku Nishimura, Haruyuki Fujimaki, Reiji Kimura and Hiroataka Saito  
*Arid Land Research Center, Tottori University, Japan*

optoelectronic measurement devices such as laser scanners (Huang et al. 1988; Darboux and Huang 2003), and image processing techniques (Abd-Elbasit et al. 2008). Point gauges have been widely replaced by laser scanners, because the former make contact with the soil and can thus disturb it or sink into it (Römkens et al. 1988). While laser scanners have proven their usefulness in many experiments, a photogrammetric system is more advanced, comparatively cheaper, and provides images and morphological properties simultaneously (Hodge et al. 2009; Chandler et al. 2005).

Automated digital photogrammetry allows DEMs to be generated with sufficient resolution for microtopographical analysis. Jeschke (1990) applied correlation matching to soft-copy images taken by a Zeiss SMK 40 camera to analyze soil microtopography. Recent advances in digital image processing and camera calibration techniques make it possible to use the digitized images taken by consumer-grade analog cameras to automate the generation of DEMs (Brasington and Smart 2003; Abd-Elbasit et al. 2009). Some researchers, e.g., Chandler et al. (2002) and Lascelles et al. (2002), have calibrated consumer-grade cameras and employed the images taken with them to generate DEMs automatically on digital photogrammetric workstations, which are becoming increasingly accessible to non-photogrammetrists.

Analytical photogrammetry has often been used in geomorphological studies of gully and rill formation (Elliot et al. 1997; Pyle and Richards 1997; Helming et al. 1998; DeRose et al. 1998; Pellikka et al. 2004; Rieke-Zapp and Nearing 2005). In these previous studies, the DEM resolutions were generally produced from photographs taken under a no-rainfall condition, i.e., the photographs were taken just before and after the rainfall and wind events (Rieke-Zapp and Nearing 2005). Moreover, study reporting this method to monitor sheet and wind erosions, which predominate in drylands, is relatively few. It is necessary to evaluate the reliability of the DEM produced using either a camera and rainfall simulator or camera and wind tunnel at the laboratory scale before field scale application. The purpose of this study was to generate DEMs with high spatial and temporal resolutions from soil surfaces that developed sheet and wind erosions. Digital photogrammetry was used to measure the erosion rates and to monitor the evolution of the soil surface network under laboratory simulated conditions.

## 2. Overview of the photogrammetry system

In order to study in three dimensions the soil surface evolution that results from water erosion, a new automated photogrammetry system was developed by Tottori University's Arid Land Research Center (ALRC), in collaboration with Asia Air Survey Co., Ltd. Fig. 1 shows a flow chart of this photogrammetry system (Moritani et al. 2006).

Two Nikon D2H digital cameras were focused on the center of the target object, as shown in Fig. 2. A focus length of 50 mm was used. The CCD sensor had a matrix of  $2464 \times 1632$  picture elements (pixels). The distance between two pixel centers,  $\delta_{CCD}$ , was 0.0094 mm. The memory card used was capable of storing approximately 60 7.9-MB images, allowing the analysis to be performed on uncompressed Tagged Image File Format (TIFF) images. A PC software program was used to analyze the pictures taken by the D2H cameras. The inner orientation factor was obtained from a calibration factor called the calibration field (CF), as shown in Fig. 3.

It is well known that even two cameras of the same type do not have exactly equal characteristics such as the shape of the lens and the spatial arrangement of the CCD and lens (Weng et al. 1992). This made inner orientation calibration necessary for each camera to

obtain more accurate DEM data. As shown in Fig. 5, the camera calibration was performed using a three-dimensional calibration field (CF) with 32 well-distributed control points, known with an accuracy of 0.2 mm. This CF was equipped with 20 square poles with three different lengths, and 12 points on the planar table (which was placed between the square poles by 3 horizontal lines). Pictures of the CF were taken by each camera from a fixed distance,  $H$  (camera pair to object), of approximately 3.0 m. During this photography process, the camera position was shifted parallel with the CF board to capture six multiple images of the entire area of the image plane, including every corner of the image plane, where there were large amounts of radial distortion. The least-square of the bundle adjustment among these images was then used to determine the inner orientation parameters, lens focus length, principal point offsets, and radial distortion (Hung and Mitchell 1995; Rieke-Zapp et al. 2001; Abd-Elbasit et al. 2008).

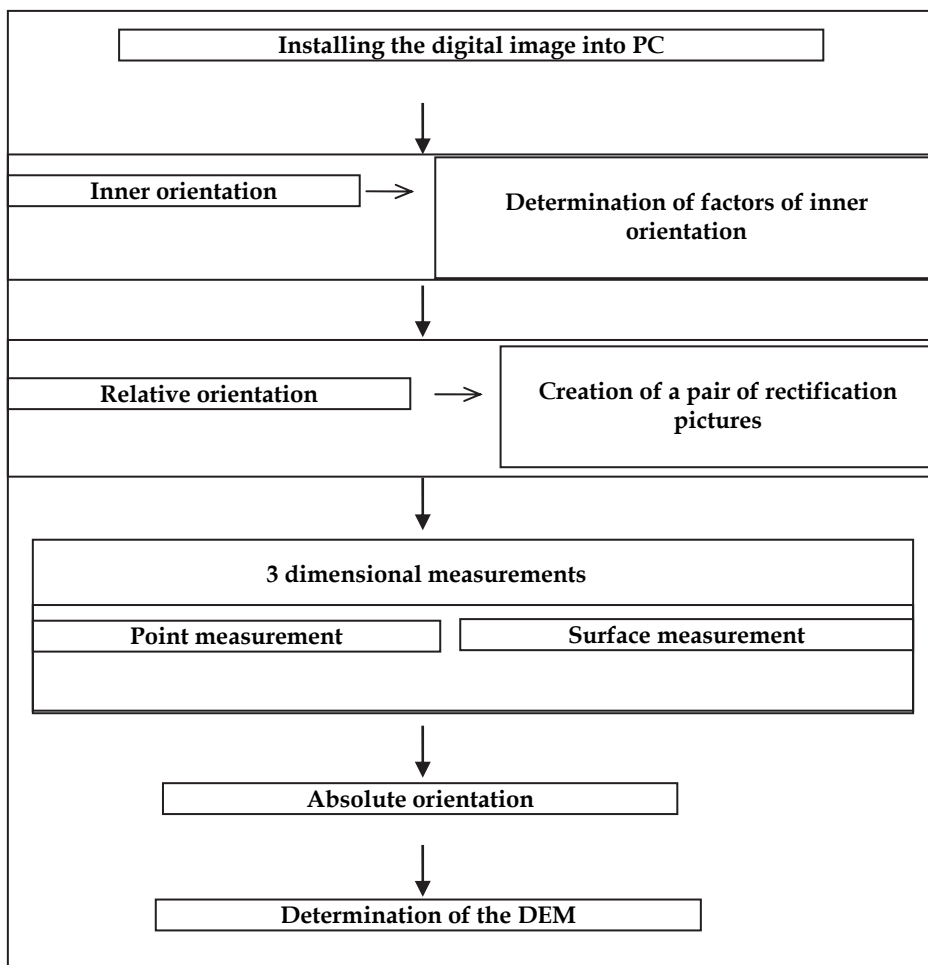


Fig. 1. Flowchart of photogrammetry measurement.

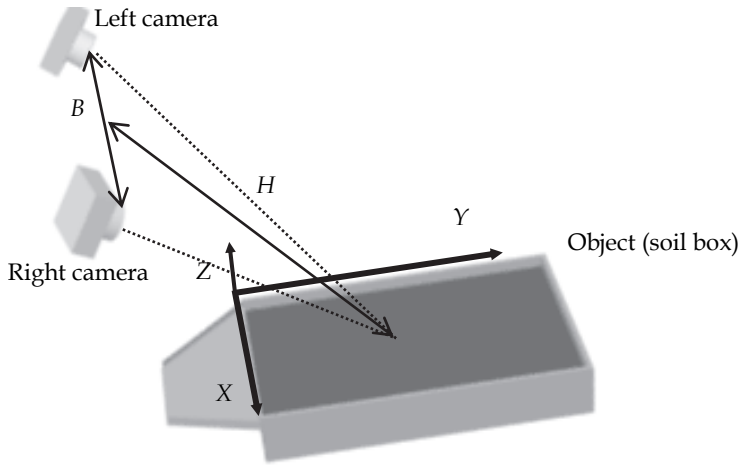


Fig. 2. The layout of two cameras and object. Each dashed line is oriented direction by pair of cameras

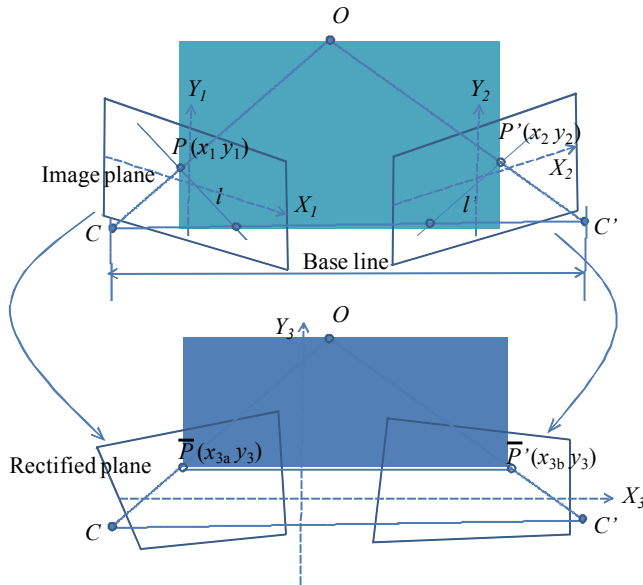


Fig. 3. Illustration of the coplanar condition and rectification. The object point  $O$  is projected onto the image planes corresponding to  $P$  and  $P'$  from different viewpoints of  $C$  and  $C'$ . The coplanar is defined by the point  $O$  and the base line.  $l$  and  $l'$  are the epipolar lines, which are the intersections of the coplanar and the two image planes (upper). The rectification involves both image planes to be at the same coordinate system  $(X_3 Y_3)$  and makes the y-axis of  $P$  and  $P'$  to be at the same position  $(\bar{P}$  and  $\bar{P}')$ .



The gradient of the pair of pictures was adjusted to minimize the parallax, and then the relative orientation was determined with the resulting points fixed on the x-axis. The result of this process is called a rectified photograph. The relative orientation yielding the rectified images was determined by a complicated equation based on a geometric consideration of the coplanar condition (Fig. 3), in which the image points  $P$  and  $P'$  always lay on the epipolar lines  $l$  and  $l'$ , respectively (Huang and Mitchell 1995; Heipke 1997). The rectification required that both image planes used the same coordinate system ( $X_3, Y_3$ ) and that the y-axes of  $P$  and  $P'$  were at the same position ( $\bar{P}$  and  $\bar{P}'$ ). This reduced the search space for  $P$  and  $P'$  from two dimensions to one, and thus increased the speed and reliability of the matching (Jeong et al. 2004).

The three-dimensional calculation consisted of two methods: (1) point measurement and (2) surface measurement. Point measurement was used for visual matching to acquire a limited number of DEMs, while surface measurement was used to automatically calculate an enormous number of dense DEMs such as for the contour line of a surface. In the point measurement, as illustrated in Fig. 4, the cursor (shown as a ☆) was first moved onto a reference pixel point selected in the left rectified picture. The corresponding cursor in the right picture automatically followed along the y-axis to a position that matched that on the left. Then, the cursor in the right picture was moved along the x-axis (epipolar line) to the same corresponding point. Three-dimensional data were calculated based on the absolute orientation from the  $x_1y_1$  and  $x_2y_2$  coordinates of the image points (Fig. 3). In the case of surface measurement, a quadrangular analytical frame was placed in each of the rectified images. These frames were aligned as closely as possible to cover and represent the same image area to reduce the matching error. Finally, approximately 16,000 pixels (shown as ○ marks) were calculated and automatically matched in a few seconds to acquire DEMs, based on a coarse-to-fine matching strategy using multi-resolution representations, with a Laplacian of Gaussian filter (Kim et al. 1997; Cruz et al. 1995).

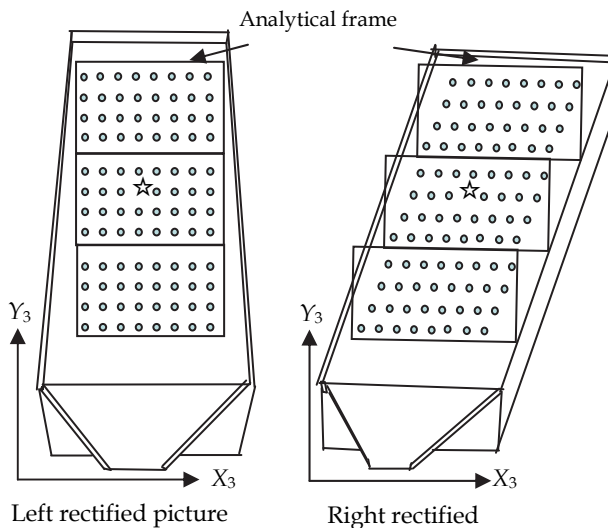


Fig. 4. Three-dimensional measurement in rectified photograph. The marks of ☆ and ○ in the figure indicate the measurement point used for point and surface measurement, respectively.

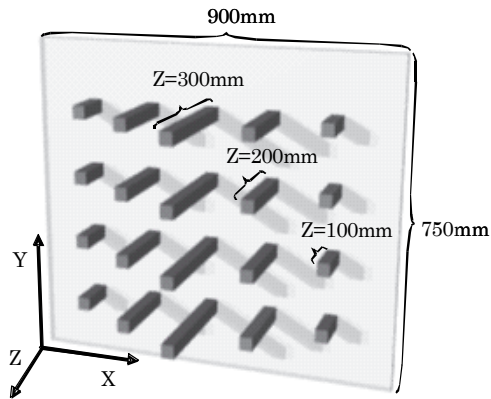


Fig. 5. Calibration field (CF)

### 3. Materials and methods

#### 3.1 Accuracy of the DEM

The accuracy of this inner orientation was examined using the known DEM values of the CF board. The positions of the two D2H cameras were oriented to the CF board to include the 32 ground control points (GCPs). The CF was photographed at five different positions, ranging from a distance  $H$  of 2.0 to 6.0 m, and with a base length  $B$  (between the cameras) of 1.0 m. The point measurement process was used for the three-dimensional measurements of the 32 points on the CF, and the precision of the system was determined by comparing the results after the inner orientation against those without calibration.

The accuracy of the photogrammetry system was also evaluated under a no-rainfall condition using a soil box with a width, length, and height of 30 cm, 50 cm, and 10 cm, respectively. Sandy soil was packed into the soil box and twenty nails were inserted into the soil surface to be used as "unknown" measurement points, with a  $\times$  mark made on the top of each nail. The measured values,  $M_p$  (mm), on the z-axis were obtained using the point gauge method similar to that described by Abd-Elbasit et al. 2009, which consist of vertical pins, with wooden supporter, stinging on the nails put on the soil surface. A micrometer caliper was used to record the elevation of the soil surface by measuring the length of each pin with accuracy in the order of  $\pm 0.01$  mm (Model 19971, Shinwa Rules Co., LTD).

Point measurement was used to determine the photogrammetric value  $A_p$  (mm) on the z-axis, with ten marks on the frame of the soil box used as the ground control points (GCPs). The object was then photographed from 11 different positions, with  $H$  values ranging from 2.4 to 4.7 m and  $B$  values ranging from 0.3 to 1.0 m. Then, the simulated depth of the soil erosion was evaluated after removing 50 mg (36 mL) of the air-dried sandy soil from the soil surface. This process was repeated 16 times until approximately 800 mL of soil was collected. The surface measurement process was used to calculate the DEM of the soil surface in each image. The average depth of the eroded soil,  $A_s$  (mm), was calculated from the average value of the DEMs on the z-axis, while the value of  $M_s$  (mm) was calculated based on the amount of collected soil (g), the bulk density ( $\text{g}/\text{cm}^3$ ), and the measured area ( $\text{cm}^2$ ).

### 3.2 Accuracy of the DEM under the rainfall application

Water erosion experiment was conducted using the rainfall simulator at ALRC. Three soil bulk densities, 0.91, 0.98, and 1.09 g/cm<sup>3</sup> were prepared, which was taken from a paddy field in Tottori prefecture, Japan. The soil was saturated from the bottom of the soil box with tap water, and then gravimetrically drained for one day to obtain a condition similar to the soil's field capacity. Simulated rain was delivered from a tower 12 m high. The rainfall distribution uniformity, which was calculated from the equation of uniformity coefficient developed by Christiansen, was set at 80%, and about 85% of the drops had a diameter of less than 2 mm (Andry et al. 2007). A rainfall intensity of 60 mm/h, developing an energy of 27.1 J m<sup>-2</sup> mm<sup>-1</sup> (Van Dijk et al. 2002; Andry et al. 2008), was applied for an hour to the soil box under a 10° slope. The runoff and splashed soil samples were collected every 5 or 10 minutes, just after taking pictures at  $H = 2.7$  and  $B = 0.8$ . The two D2H cameras were controlled with a cable release in order to simultaneously capture a pair of images and suppress the camera shake from clicking the shutter. This helped to shorten the time for the photogrammetry since the GCP points in each image were represented by the same pixels. A high optimal image quality was attained by using an aperture setting of f/5.6 and a 1/250 s exposure time, which was sufficiently rapid to follow the flow of the runoff water on the soil surface. The splashed soil was collected on a sheet that was placed under the soil box. This sheet also helped to reduce the effect of halation in the images as a result of direct sunlight on the soil surface. The surface measurement process was used to obtain the value of  $A_s$  (mm). The measurement area for the DEM was reduced to 80% of the entire soil surface, because the shade produced by the sides of the soil box, as seen in the images, was removed from the study. The value of the eroded soil depth,  $M_s$  (mm), was calculated from the amount of the soil loss obtained after oven dried at 105 °C for 48 hours, each initial soil bulk density and soil surface area.

### 3.3 Generating DEM of soil surface induced by wind erosion

The sandy soil is high tolerance against water erosion because of its high permeability. However sandy soil is easily transported by wind erosion, which lead to damage for agriculture. In the field, sand particles start to move as saltation when wind velocity is reaching the critical friction velocity. The particle of saltation crashes another particle in upward, which result in the acceleration of wind erosion. Wind tunnel is usually designed with the long length of working section such as 7 to 16 m enough to studying saltation and crash (Shao et al, 1993; Liu et al, 2007). However, this wind tunnel size costs much and also occupies large space. In this research the wind tunnel experiment was conducted inside an existence climate chamber whose width, height and length are 2, 2, and 3 m, respectively. This chamber can be used to control wind velocity at maximum of 3 m/s which is not enough for producing wind erosion. As a result, the wind tunnel was redesigning in order to produce a wind velocity of 12 m/s by narrowing the cross-section of wind path by wood boards.

The friction speed is usually determined from the altitudinal profile of wind velocity. The wind speed closed to zero at the soil surface due to increase in soil roughness which in turn increases the resistance against wind. The logarithm of height increases the wind velocity proportionally. The friction speed is defined as this gradient of proportional line (Leys and Raupach, 1991). The wind tunnel used was low height of 20 cm which was not enough to measure the profile of wind by altitude. Therefore the wind velocity at 20 cm height was representative as measured velocity. The wind velocity when sand particle started taking off was considered as critical wind velocity.

The dune sand was put inside the soil box whose width, length and height were 23, 35, and 3 cm, respectively. The soil box with sand was fit in the opening on basal plane. In front of the soil box, the inclined plane was put to prevent the eddy flow at edge of soil box. Additionally, the effect of organic matter incorporated in the dune sand was assessed on the wind erosion. The organic matter made from bark of acicular tree which consists of bark of cedar and cypress at the weight ratio of 80 to 20%. The mixing weight ratios used in this study were 0% as control, and 1.0, 5.0, 10 and 100%. Wind was applied after packing the soil in soil box. At first, wind velocity of 4 m/s was applied for 3 min on the soil box known weight. Then the soil box was weighted after wind, and the soil was again refilled with soil. And next, the wind velocity was incremented by 1 m/s and repeated same procedure until the velocity reaching 12 m/s. The eroded soil (cm/hour) was calculated from the following Eqn 1.

$$Q = \frac{W}{\delta \times A \times T} \quad (1)$$

, where  $W$  is the difference of weight of soil box (g) between before and after wind.  $\delta$ ,  $A$  and  $T$  are the bulk density ( $\text{g}/\text{cm}^3$ ), surface area of soil box ( $\text{cm}^2$ ) and time (hour) under wind.

The photogrammetry experiment to capture the wind ripple was carried out in the straight-line puff wind tunnel at ALRC (Fig.6). There were difficulties encountering when taking photograph during the wind application. The cameras were not easily to put inside the wind tunnel due to the small space. Even if cameras were put, the picture was not clear due to the camera shaking by wind energy and the interfering of the saltation as well. As a result, the experiments of photogrammetry and soil sampling were separately conducted, which was not the same with rainfall experiment that could be performed simultaneously. Moreover, to overcome these difficulties, the experiment of photogrammetry was performed only on the working section of this wind tunnel with open superior wall of 2.0 m long, 0.45 m wide, and 0.55 m high. A 2 cm depth of air-dried sandy soil was placed in the wind tunnel and subjected to wind velocity of 4.5 m/s for 45 min. The soil surface was photographed using a selected target object at a distance of 0.6 m, using a base length of 0.3 m, before and after the wind events. The DEM soil surface data were obtained using the surface measurement process. The accuracy of the photogrammetry system was evaluated using the DEM values for 20 nails on the z-axis, i.e., comprising the  $M_p$  (mm) values measured from the soil surface with a point gauge against the  $A_p$  values from the point measuring method.

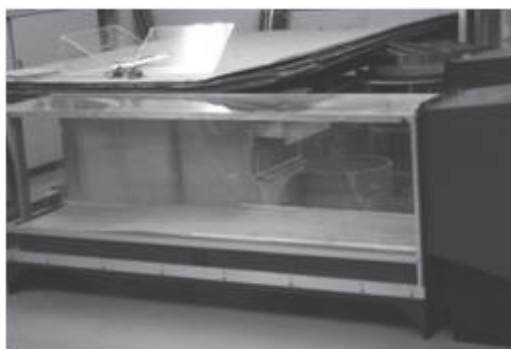


Fig. 6. Layout of wind tunnel

## 4. Results and discussions

### 4.1 The influence of inner orientation on the DEM accuracy

The accuracy of the DEM along the z-axis, which is the soil depth  $\delta_z$ , was affected by (1) the resolution of the camera,  $\delta_{CCD}$  (mm), (2) the distance between the camera and object,  $H$  (m), (3) the base distance between the pair of cameras,  $B$ , (m), and (4) the focus length  $f_c$  (mm) (Fig. 2). The relationships between these 4 factors can be expressed as shown in Eqn 2 (Moritani et al, 2006):

$$\delta_z = \frac{H}{f} \frac{H}{B} \delta_{CCD} \quad (2)$$

It was found that accuracy was also influenced by (5) the declinations in the principal coordinate points of the lenses in the longitudinal and horizontal directions and (6) the distortion of the lenses. However, factors (5) and (6) can be compensated for by calculating the inner orientation of each camera.

The precision along the z-axis was evaluated using the mean absolute error (MAE) and the mean relative error (MRE) (%), shown respectively in Eqns 3 and 4:

$$MAE = 1/N \sum_{i=1}^N |M_{(p,s)i} - A_{(p,s)i}| \quad (3)$$

$$MRE = 1/N \sum_{i=1}^N |M_{(p,s)i} - A_{(p,s)i}| / M_{(p,s)i} \times 100\% \quad (4)$$

where  $N$  is the number of samples. Here,  $\delta_z$  is proportional to  $H^2/B$  as described in the Eqn 2, which highlights the importance of the positional relation for precision, although few clear reports are available in the literature. Therefore, integrating the value of  $L$  into these positional lengths was introduced to indicate the precision, as shown in Eqn 5.

$$\delta_z = L \times \frac{\delta_{CCD}}{f} \quad (5)$$

where  $L$  is  $H^2/B$ .

Thus, the precision is proportional to the factor of  $L$ . In fact, a precision comparison under different conditions was performed based on the correlation value of the relationship between  $L$  and MAE from the equation  $MAE = a \times L$ .

In a case where the inner orientation was not accounted for, the value of  $a$  was 0.74, which represents a low precision compared to a  $\delta_z$  of 0.19 (Fig. 7). However, when the inner orientation was applied, the value of  $a$  was 0.057, indicating a higher precision compared with the  $\delta_z$  of 0.19. This is because the  $\delta_z$  value calculated from Eqn 2 indicates the variation along the z-axis when two points in the rectified pair of images were located one pixel apart in the relative vicinity of matching points. However, in a matching process such as point measurement, these two points were effectively converged into a single pixel. It was found that this photogrammetry system with the inner orientation was 4.5 times as accurate as the results of Rieke and Nearing (2005) at the same distance,  $L$ , due to the use of a lower focus length of 19 mm. Based on its performance, the application of this photogrammetry system

in a research field such as wind and/or water erosion could be helpful in reducing the necessary time and labor. However, the interference effects of rainfall and the physical properties of soil on the system have to be tested in a laboratory before any large field scale application.

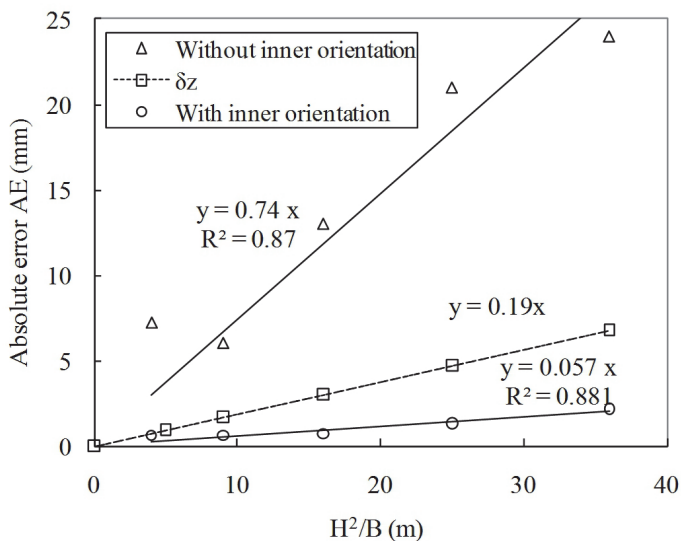


Fig. 7. Relationships between  $H^2/B$  and absolute error (AE). The formulas indicate approximate equation and coefficient of determination.

#### 4.2 Accuracy of the DEM without the application of rainfall or wind

The accuracy of the DEM was determined using point and surface measurements with inner orientation. In the point measurement, the value of  $a$  was 0.049, which was a higher precision than the value of 0.057 obtained by the same methods, as previously discussed. This better value was the result of using a closer camera-to-object distance, which produced clearer images. The maximum  $H$  was 4.7 m, compared to 7 m for the above experiment, although the same range was used for  $L$  (5 to 35 m).

In the surface measurement, the value of  $a$  was 0.030, or 63% higher than for the point measurement; this was because the matching process was conducted automatically based on multi-resolution representations (Kim et al. 1997; Cruz et al. 1995). The DEM value for the cumulative eroded depth was proportional to the measured value. When this proportionality was given as  $b$ , this value differed from 1.0 according to the increase in  $L$ , although the coefficient of determination in every case was larger than 0.97. It was also found that the equilateral was significantly correlated at a 1% level when the number of samples ranged from 13 to 18.

#### 4.3 Accuracy of the DEM under the application of rainfall

In the field water-capacity procedure, soil samples with three different bulk densities (0.91, 0.98, and 1.09 g/cm<sup>3</sup>) were subjected to a rainfall intensity of 60 mm/h. Fig. 8 shows the amount of soil erosion, as determined by the sampling and photogrammetry methods. As

the soil bulk density increases to 1.09 g/cm<sup>3</sup>, the relationship between the sampling and photogrammetry values approaches a slope of 1.0 with a high correlation coefficient. The MAE (MRE) values for densities of 1.09, 0.98, and 0.91 g/cm<sup>3</sup> were 0.59 (57.6%), 1.07 (126.4%), and 2.21 mm (392.5%), respectively. The accuracy of the DEM was improved considerably when the bulk density increased from 0.91 to 1.09 g/cm<sup>3</sup>. This could have been because of the additional compacting of the soil by the rainfall, which likely had less of a compaction effect on the soil surfaces with higher bulk densities. The influence of soil consolidation on the accuracy was also confirmed under different soil conditions, and also with laser scanners under different monitoring capabilities (Scholl et al. 2007; Moritani et al. 2007). The lower accuracy was also confirmed using dry soil subjected to rainfall even under the higher bulk density since the soil was swelled during wetting process, and on the other hand, the soil surface was easily disturbed by drops of rain, especially at the first stage of the experiment as reported in the studies of Moritani et al. (2006). This study shows that the accuracy of DEM under the rainfall could be improved when the additional parameters such as antecedent moisture and hardness condition of the soil surface were investigated.

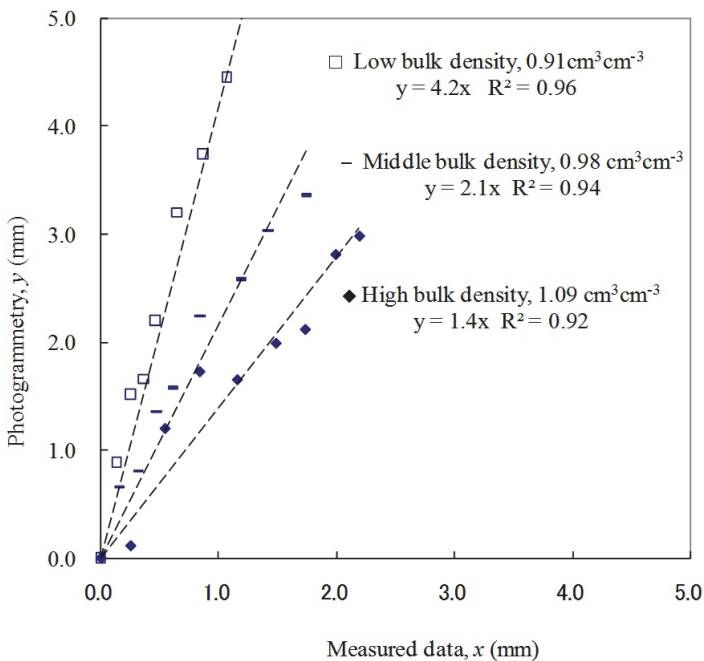


Fig. 8. Relationships between measured and photogrammetry for depth eroded by the rainfall. The formulas indicate approximate equation and coefficient of determination.

80% of the soil surface was divided into two regions, upstream and downstream, along the slope. The results show that the quantity of soil eroded in the upstream region was 0.49 mm greater than in the downstream region (Fig. 9). This observation implies that it is possible to evaluate the amount of soil eroded in a specific area, and monitor the erosion mechanisms. When  $L$  was 9.1 m, the characterizing factors for accuracy,  $b$ , MAE, and MRE, were 1.06, 0.21 mm, and 15.8%, respectively.

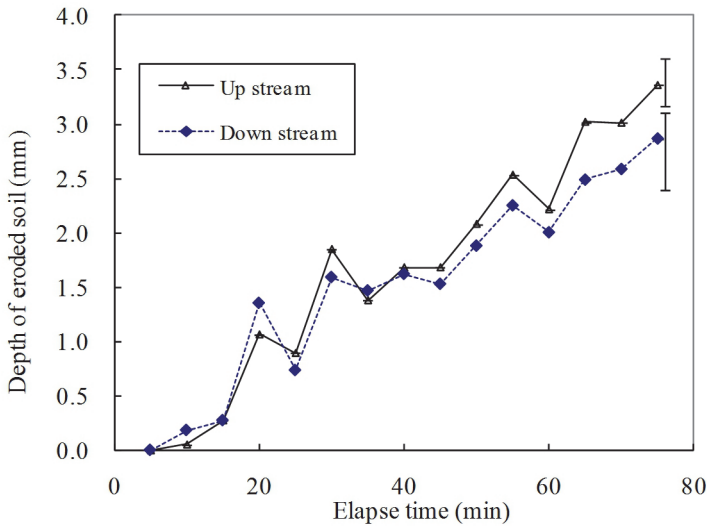


Fig. 9. Depth of eroded soil with elapsed time for up stream and down stream conditions under high bulk density.

Bar is the value of AE at the end of experiment

**4.4 Accuracy of the DEM under the application of wind**

The relationship between wind velocity and the amount of eroded soil is shown in Fig. 10. The curve in the figure was calculated from Eqn. 6 which has been modified based on the equation of Bagnold (1936).

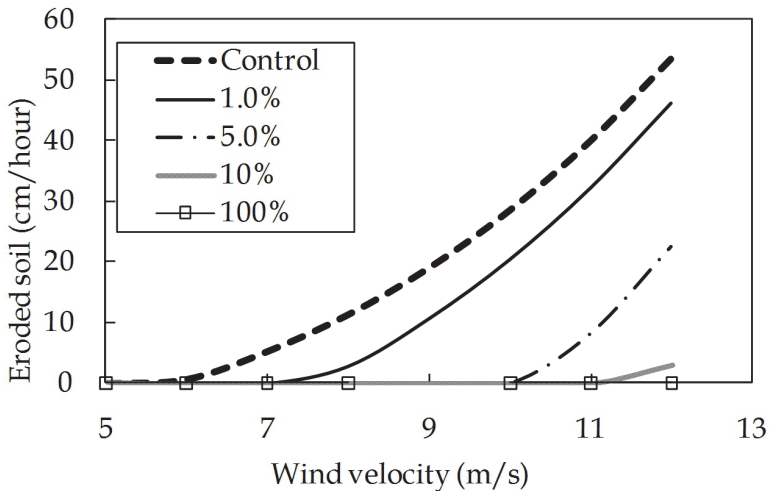


Fig. 10. Relationships between wind velocity and depth of eroded soil The percentage indicate the contents of organic matter



$$Q = b(u - u_t)(u + u_t)^2 \tag{6}$$

,where  $u$  and  $u_t$  are wind velocity and critical wind velocity at 20 cm height, respectively. RMSE shows the low value of 0.2-4.1 cm/hour, which was low error between measured and estimated value. The control soil started to be eroded with 0.01 mm/hour with low value from 5.0 m/s of wind velocity, which was assumed as critical wind velocity. The eroded soil increased sharply from 5.0 m/s with increasing wind velocity. Maximum eroded soil of 56.4 cm/hour was found at the maximum wind velocity of 12 m/s. The mixture of organic matter reduced the eroded soil. The critical wind velocity in 1.0, 5.0 and 10 % of organic matter were 7.7, 8.4 and 8.9 cm/hour. The treatment of 1, 5 and 10% mixture with organic matter decreased the eroded soil by 14.2, 68.3 and 92.2%, respectively. This result showed the organic material reduced the wind erosion significantly. The eroded soil in 100% of organic matter was 0.32 cm/hour at 12 m/s of wind velocity with over than 99% of reduction than that of control since the cohesion between particles was strongly increased as a result of organic matter application. This result shows that incorporation of the organic material with fiber shape can be use as wind erosion conservation that leads to the sustainable agriculture in the sandy soil.

Fig. 11 shows the shapes of the wind ripples. Here the MAE value for data obtained by the point gauge photogrammetry methods was 0.21 mm. This high precision was obtained because the images were taken before and after the wind events. Monitoring the soil surface under the condition of wind application involves some difficulties such as unclear soil displacement-settlement and dust interference during the photographic process. Therefore, an approach of how to use photogrammetry system method during a wind erosion simulation is needed for further consideration and study. This research focused on the accuracy of photogrammetry when used to measure soil erosion. However, a more specific investigation of soil surfaces in relation to the spatial coherence of erosion/deposition patterns should be performed.

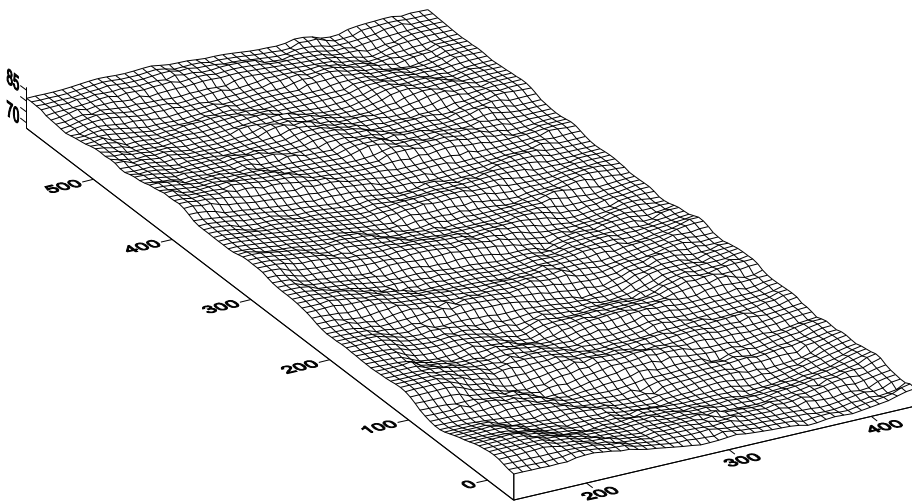


Fig. 11. Grids of the sandy soil surface after wind erosion experiment

## 5. Conclusion

The experiments of wind and water erosion were performed using wind tunnel and rainfall simulator, respectively. The amount of eroded soil was measured by applying photogrammetry and soil sampling. The amount of soil erosion was estimated by a digital photogrammetry system that used two cameras from difference of soil surface changing. It was found that the accuracy was influenced by declinations in the principal coordinate points of the lenses and the distortion of the lenses. However, these factors could be compensated for by calculating the inner orientation of each camera. The value of the cumulative eroded depth determined by photogrammetry under a no-rainfall or wind condition was significantly proportional to the measured value at the 1% level, although the accuracy under rainfall was influenced by the soil compaction as a result of the raindrop impact. Therefore, because of its high accuracy, this system could be applied when monitoring the changes in soil surface as result of water and wind erosion, or when measuring the amount of eroded soil in the case of soil with a high bulk density.

The sandy soil is high tolerance against water erosion because of its high permeability. However sandy soil moves easily by wind erosion, which lead to damage for agriculture. It was found that monitoring the sandy soil surface using photogrammetry method under wind application involves some difficulties such as unclear soil displacement-settlement and dust interference. Further study on appropriate use of photogrammetry system method during a wind erosion application is needed to consider. This research focused on the accuracy of photogrammetry when used to measure soil erosion. However, a more specific investigation of soil surfaces in relation to the spatial coherence of erosion/deposition patterns should be performed.

## 6. References

- Abd Elbasit MAM, Yasuda H, Anyoji H (2008) Development and application of digital elevation model rectification method in monitoring soil microtopography changes during rainfall. *Journal of Japan Society of Hydrology and Water Resources* 21 (2), 114-125.
- Abd Elbasit MAM, Anyoji H, Yasuda H, Yamamoto S (2009) Potential of low cost close-range photogrammetry system in soil microtopography quantification. *Hydrological Processes* 23 (10), 1408 - 1417.
- Andry H, Yamamoto T, Inoue M (2007) Effectiveness of hydrated lime and artificial zeolite amendments and sedum (*Sedum sediforme*) plant cover in controlling soil erosion from an acid soil. *Australian journal of soil research* 45, 266-279.
- Andry H, Yamamoto T, Rasiah V, Fukada M (2008) Physico-mechanical processes involved in sediment generation in a simulated acid soil. *Transactions of the Japanese Society of Irrigation, Drainage and Rural Engineering* 257, 1-9.
- Bagnold RA (1936) The movement of desert sand, *Proc. R. Soc. London Ser. A* 157, pp. 594-620.
- Brasington J, Smart RMA (2003) Close range digital photogrammetric analysis of experimental drainage basin evolution. *Earth Surface Processes and Landforms*, 28 (3), 231-247.
- Chandler JH, Ashmore P, Paolo C, Gooch M, Varkaris F (2002) Monitoring river-channel change using terrestrial oblique digital imagery and automated digital

- photogrammetry. *Annals of the Association of American Geographers* 92 (4), 631-644.
- Chandler JH, Fryer JG, Jack A (2005) Metric capabilities of low-cost digital cameras for close range surface measurement. *The Photogrammetric Record* 20 (109) 12-26.
- Cruz JM, Pajares G, Aranda J, Vindel JLF (1995) Stereo matching technique based on the perceptron criterion function. *Pattern Recognition* 16 933-944.
- Darboux F, Huang C (2003) An instantaneous-profile laser scanner to measure soil surface microtopography. *Soil Science Society of America Journal* 67 (1), 92-99.
- DeRose RC, Gomez B, Marden M, Trustrum NA (1998) Gully erosion in Mangatu Forest, New Zealand, estimated from digital elevation models. *Earth Surface Processes and Landforms* 23, 1045-1053.
- Elliot WJ, Laflen JM, Thomas AW, Kohl KD (1997) Photogrammetric and rillmeter techniques for hydraulic measurement in soil erosion studies. *Transactions of the American Society of Agricultural Engineers* 40 (1), 157-165.
- Heipke C (1997) Automation of interior relative and absolute orientation. *ISPRS Journal of Photogrammetry & Remote Sensing* 52, 1-19.
- Helming K, Römkens MJM, Prasad SN (1998) Surface roughness related processes of runoff and soil loss. A flume study. *Soil Science Society of America Journal* 62, 243-250.
- Hodge, R., Brasington J, Richards K (2009) In-situ characterization of grain-scale fluvial morphology using Terrestrial Laser Scanning. *Earth Surface Processes and Landforms*. doi:10.1002/esp.1780
- Huang CT, Mitchell OR (1995) Dynamic camera calibration. *Institute of Electrical and Electronics Engineers, International Symposium on Computer Vision in 1995*, 169-174.
- Huang C (1998) Quantification of soil surface microtopography and surface roughness. *Fractals in Soil Science* (Eds. P Baveye, J-Y Parlange, BA Stewart) CRC Press, Boca Raton 432, 153-168.
- Huang C, White I, Thwaite EG, Bendeli A (1988) A noncontact laser system for measuring soil surface topography. *Soil Science Society of America Journal* 52 (2), 350-355.
- Jeong S, Cho J, Choi B (2004) An epipolar rectification for object segmentation. *Transactions of Institute of Electronics Information and Communication Engineers* 87 (5), 1434-1437.
- Jeschke W (1990) Digital close-range photogrammetry for surface measurement. *International Archives of Photogrammetry and Remote Sensing* 28 (5), 1058-1065.
- Kim YS, Lee JJ, Ha YH (1997) Stereo matching algorithm based on modified wavelet decomposition process. *Pattern Recognition* 30 (6), 929-952.
- Lascelles B, Favis-Mortlock D, Parsons T, Boardman J (2002) Automated digital photogrammetry: a valuable tool for small-scale geomorphological research for the non-photogrammetrist. *Transactions in GIS* 6 (1), 5-15.
- Leys JF, Raupach MR (1991) Soil flux measurement using a portable wind erosion tunnel. *Australian journal of soil research* 29 533-552.
- Liu LY, Li XY, Shi PJ, Gao SY, Wang JH, Ta WQ, Song Y, Liu MX, Wang Z, Xiao BL (2007) Wind erodibility of major soils in the farming-pastoral ecotone of China. *Journal of Arid Environment* 68 611-623.
- Lyles L and Tartako J (1986) Wind erosion effect on soil texture and organic matter. *Journal of soil water conservation* 41 191-193.

- Moritani S, Yamamoto T, Henintsoa A, Muraki H (2006) Monitoring of soil erosion using digital camera under simulated rainfall. *Transactions of the Japanese Society of Irrigation, Drainage and Rural Engineering* 244, 143-149.
- Moritani S, Yamamoto T, Henintsoa A, Muraki H (2007) Monitoring Of Soil Erosion Using Digital Camera Under Simulated Rainfall. American Geophysical Union, Fall Meeting 2007, abstract #H51E-0826
- Pellikka P, Clark B, Hurskainen P, Keskinen A, Lanne M, Masalin K, Nyman-Ghezelbash P, Sirviö T (2004) Land use change monitoring applying geographic information systems in the Taita Hills, Se-Kenya. *Proceedings of the 5th AARSE conference (African Association of Remote Sensing of the Environment)*, 18-21 October, 2004, Nairobi, Kenya.
- Prosser IP, Abernathy B (1996) Predicting the topographic limits to a gully network using a digital terrain model and process thresholds. *Water Resources Research* 32 (7), 2289-2298.
- Pyle CJ, Richards KS (1997) Digital photogrammetric monitoring of river bank erosion. *Photogrammetric Record* 15 (89), 753-764.
- Rieke-Zapp DH, Wegmann H, Santel F, Nearing MA (2001) Digital photogrammetry for measuring soil surface roughness. *Proceedings of the American Society of Photogrammetry & Remote Sensing 2001 Conference, Gateway to the New Millennium*, St Louis, Missouri, p8.
- Rieke-Zapp DH, Nearing MA (2005) Digital close range photogrammetry measurement of soil erosion. *The Photogrammetric Record* 20 (109) 69-87.
- Römkens MJM, Wang JY, Darden RW (1988) A Laser Microreliefmeter. *Transactions of ASAE* 31 (2), 408-413.
- Scholl BN, Bogonko M, He Y, Beighley RE, Milberg CT (2007) Quantifying the spatial distribution of hill slope erosion using a 3-D laser scanner. American Geophysical Union, Fall Meeting 2007, abstract #H51E-0826
- Shao Y, McTainsh GH, Leys JF Raupach MR (1993) Efficiencies of sediment samples for wind erosion measurement. *Australian journal of soil research* 31 519-532.
- Soil Conservation Service (1976) *National range handbook*, U.S. Department of Agriculture, Soil Conservation Service, Washington.
- Van Dijk AIJM, Bruijnzeel LA, Rosewell CJ (2002) Rainfall intensity-kinetic energy relationships: a critical literature appraisal. *Journal of Hydrology* 261, 1-23.
- Weng J, Cohen P, Herniou M (1992) Camera calibration with distortion models and accuracy evaluation. *IEEE Transactions on Pattern Analysis and Machine Intelligence* 14 (10)

# Public Square Design with Snow and Wind Simulations Using Wind Tunnel

Tsuyoshi Setoguchi

*Faculty of Engineering, Hokkaido University  
Japan*

## 1. Introduction

### 1.1 The purpose of the research

A Snow is one of the most influence points to urban design for snow and cold region. In cities that are located in heavy snowfall and cold regions like Hokkaido, it is important to clarify how to apply urban design principles to protect areas with a harsh winter climate. Specifically, significant issues should be addressed concerning the environmental impact of snow and wind on public spaces of the urban renewal projects.

In addition, desirable urban designs providing better environments in public spaces that protect against snow and wind in winter should be developed. The need has been felt for original approaches to urban design in such cities. An urban design which reduces snow problems (e.g. snowdrifts or blowing snow) is one method promoting “symbioses” between humans, snow and cold climate in those cities.

In this paper, the author targeted the redevelopment project of the new Wakkanai Station Square, in Hokkaido Japan. The actual project was started in 2003 and produced by City of Wakkanai, as part of the Urban Revitalization Program in Japanese Local Cities. This author and Wakkanai City started the co-research project for a desirable design for Wakkanai Station Square with consideration given to the local climate in winter.

In Wakkanai City northernmost city of Japan, the Wakkanai Station and Station Square redevelopment project have been launched. For the Square desirable space design preventing from snow and strong wind is required on the public square. In this paper, the author targeted the redevelopment project of the new Wakkanai Station Square, in Hokkaido Japan.

Author focused on a Covered-Walk (CW) design for the square for protecting passengers and pedestrians against snow and wind <sup>\*1</sup>. Two types of CW design were tested in a snow simulation, a leeward side CW type and a windward side CW type. The snow simulation tests were carried out using the wind tunnel in the Hokkaido Northern Regional Building Research Institute. The results of this simulation will be reflected in the square planning and design of this project.

### 1.2 Previous studies

Many environmental assessments for urban design have been conducted in Japan incorporating wind simulation tests, but there has been little published research with both

snow and wind factors taken into account other than that by Yoshizaka et al. (1942)<sup>1</sup>) and this author. They had indicated desirable low-rise building locations and directions against snow and wind in mountainous rural area of the Tohoku region in Japan, where it snows heavily in winter.

Bosselmann (1984), 1989, 1998) produced useful studies of downtown San Francisco in the U.S. and downtown Toronto in Canada, and showed that new developments with high-rise buildings cause environmental problems due to alterations in wind and sunlight patterns in the surrounding areas. He compared the environmental impact of high-rise and medium-rise buildings in wind simulation tests using a wind tunnel. These results showed that new developments with medium-rise buildings had a reduced negative environmental impact on their surrounding areas, and proved that medium-rise buildings were one of the more desirable urban designs for the downtown area. In San Francisco, environmental impact evaluations of new developments are required by ordinance and the findings must be considered in a public hearing by the city planning committee. Wind simulation tests studying environmental impact can provide useful data and can influence the outcome of public hearings.

Tomabechi (2002)<sup>5</sup>) carried out a different kind of simulation, that of snow impact, using a wind tunnel. His approach was to show desirable building locations regarding snow and wind in Hokkaido, Japan. The results of the simulation tests were useful, but the effectiveness of those results was only applicable to building design, not to city planning or urban design. The useful snow simulation approaches using wind tunnel for urban design, it is required to expand the targeted area to the district level.

To this author's knowledge, there has been little research on the environmental influence of snow and wind for urban design using snow simulation tests utilizing a wind tunnel (Table 1).

Simulation	Building Design	Urban Design
Using Only Wind	(Many researches)	Bosselmann (1984, 1989, 1998)
Using Wind & Snow	Tomabechi (2002)	Setoguchi (2003 <sup>6</sup> ), 2004 <sup>7</sup> )

Table 1. References of Researches for Environmental Impacts with Snow or Wind Using Wind Tunnel

## 2. Wind tunnel for the snow simulation tests

### 2.1 Wakkanai city: The most serious winter climate in Japan

#### 2.1.1 Snowfall regions in Japan

In Japan, there are many cities and villages that are located in areas that experience heavy snowfall <sup>\*2</sup>. Around 51% of the land is in areas that experience heavy snowfall, and 16% of the population lives in such areas. Heavy snowfall is one of the most important issues for city planning, but enough consideration of the problem is not given by urban planners. Wakkanai City is the northernmost city in Japan, and is definitely located in an area of heavy snowfall (Fig. 1).

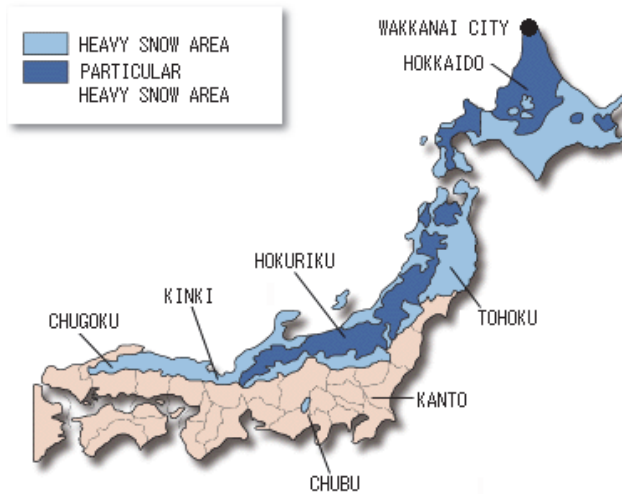


Fig. 1. Heavy snow areas in Japan (Source: Ministry of Land Infrastructure and Transport)

### 2.1.2 Local winter climate of Wakkanai city

Hokkaido is located in the northern part of Japan, which is a cold and heavy snowfall region. There are many cities and towns which experience snowstorms in winter in Hokkaido. Cities in the cape area, including Wakkanai City especially, experience strong snowstorms frequently. Table 2 shows the frequency of snowstorms for cities and towns in Hokkaido. Wakkanai City is hit by snowstorms frequently, and is second only to Rumoi City in terms of such frequent cities. On a typical day in winter its chance of experiencing a snowstorm is 35.7 times the national average, and so its citizens must cope with snowstorms almost every day. Although heavy snowfall and snowstorms are one of the most important issues concerning urban design, not enough consideration is given to this problem by planners. As Japan's northernmost city Wakkanai City is definitely located in a strong snowstorm area.

Order	Name of Municipality	City, Town or Village	Frequency of Snowstorms (per day)
1	Rebun	Town	51.7
2	Suttsu	Town	44.2
3	Matsumae	Town	42.5
4	Esashi	Town	42.5
5	Rumoi	City	42.5
6	Haboro	Town	37.9
7	Iwanai	Town	36.9
8	<b>Wakkanai</b>	<b>City</b>	<b>35.7</b>
9	Rishiri	Town	35.5
10	Enbetsu	Town	34.2

Table 2. Frequency of Snowstorms in Cities and Towns in Hokkaido (snowstorms hitting to the downtown area)



Photo 1. Wakkanai station covered with snow in winter

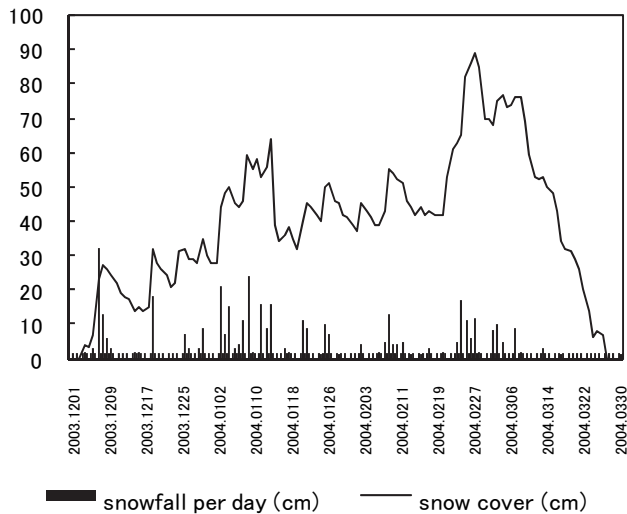


Fig. 2. Snow accumulating data of downtown Wakkanai

Figure 2 shows snow data during the winter season in downtown Wakkanai as observed by the Meteorological Agency. In that year, snow cover began from the beginning of December and it continued until the end of March of the following year. Thus, the land was covered with snow for around four months in downtown Wakkanai. The depth of the snow increased step by step from December and reached a peak of 89cm on February 28th. It means pedestrians way also covered by snow during four month winter in the downtown Wakkanai.



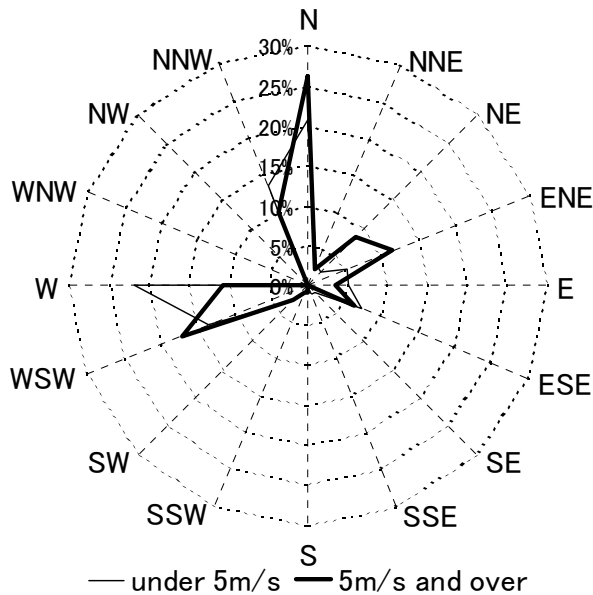


Fig. 3. Wind velocity data of downtown Wakkanai

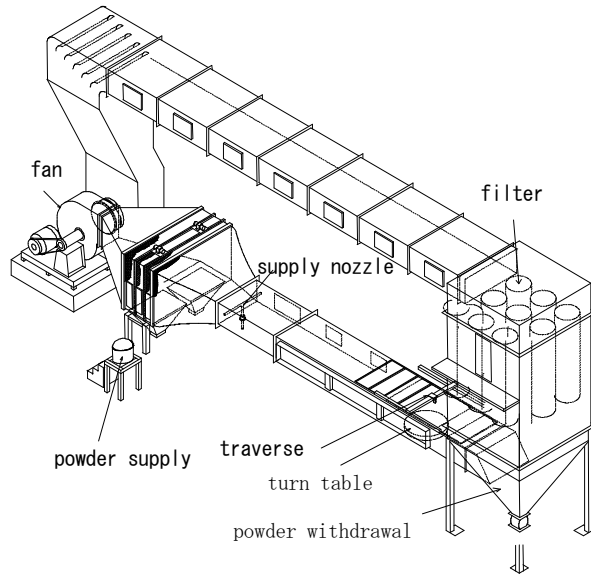
According to the climate data of the Meteorological Agency during last five years, as for the wind environment, there was strong wind with snow blow from the north (N) and west-southwest (WSW). Strong wind velocities mostly come from the north in Wakkanai City, so the strongest wind velocity from a northerly direction was adopted for the snow simulation tests (Fig. 3).

## 2.2 The wind tunnel for the snow and wind simulations

The snow simulation tests were carried out using the wind tunnel in the Hokkaido Northern Regional Building Research Institute. The wind tunnel simulation test area is seven meters long, 150cm wide and 70cm high in the tunnel cross section. (Fig. 4)

The first step in the procedure is to assess the differences between the actual weather data and that of the snow simulation tests with models, and try to modify the weather data for the simulations. Local wind conditions are quantified by testing scale models of the district in a boundary layer of the wind tunnel. The wind tunnel tests give, for each wind direction, a ratio between the wind speeds at the location where the weather data was recorded. The turbulence intensity or gustiness was recognized in the district, but these factors were also considered in changing wind velocities in the wind tunnel simulations in the several trials. Increased turbulence is assumed to be equivalent to an increase in wind speed, using a relationship that has been found for the mechanical effects of wind. The vertical distribution of the wind velocities is shown in Fig. 5.

For the snow simulation tests, the author assumed a snow blow and snowdrift area on the ground as well as a blown white soil and drifted white soil area on the ground model. And the laser device <sup>3</sup> of the wind tunnel measured the heights of the white soil drifts automatically. It was measured at intervals of 2 mm on the model of the district.



(Hokkaido Northern Regional Building Research Institute)

Fig. 4. Wind Tunnel for the snow simulations

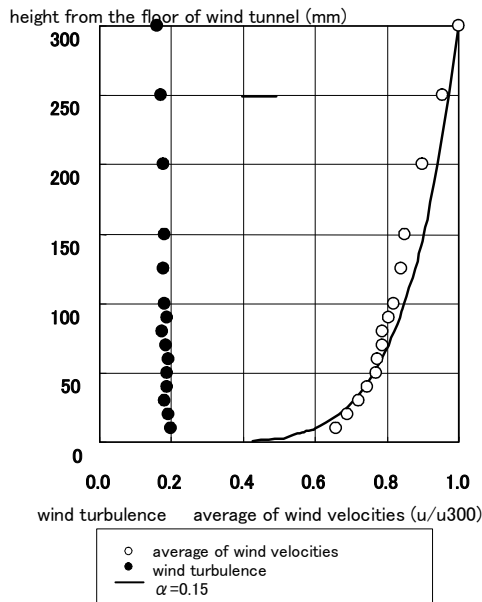
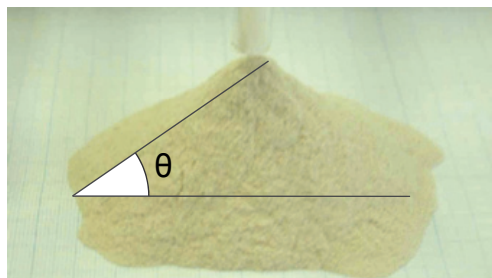


Fig. 5. Vertical distribution of wind velocities in the wind tunnel

The characteristic point between pure snow in Wakkanai and white soil are similar. Both of drifting angle and shape are similar, the angle of pure snow assumes around from 45 to 50 and the angle of white soil is 46. This is the reason author adopted white soil for the snow simulations (Fig. 6).



Drifting Angle	
Pure snow in Hokkaido	45 - 50 degree
White soil	46 degree

Fig. 6. Comparison the drifting angle between pure snow and white soil

### 2.3 Models for snow simulation experiments

For the snow simulation tests, block models of the target area, the Wakkanai station district, were made of styro-foam in the scale of 1 to 300. The size of the district is 540m (in the north-south direction) by 360m (in the east-west direction); therefore the models of the district measured 1800mm long by 1200mm wide for the snow simulation tests.

The snow models were made of white soil powder<sup>\*4</sup>. This soil tends to have a drifting pattern similar to that of snow in Hokkaido. It gives a static-free performance in wind tunnels; therefore there was no friction between the powder particles themselves. The ground model boards were painted; therefore there was no friction between the powder and the ground models. The powder for the snow models was supplied from windward side nozzles to the testing area of the tunnel by an air compressor. The CW models were made of acrylic plastic board for no friction with the snow soil powder.

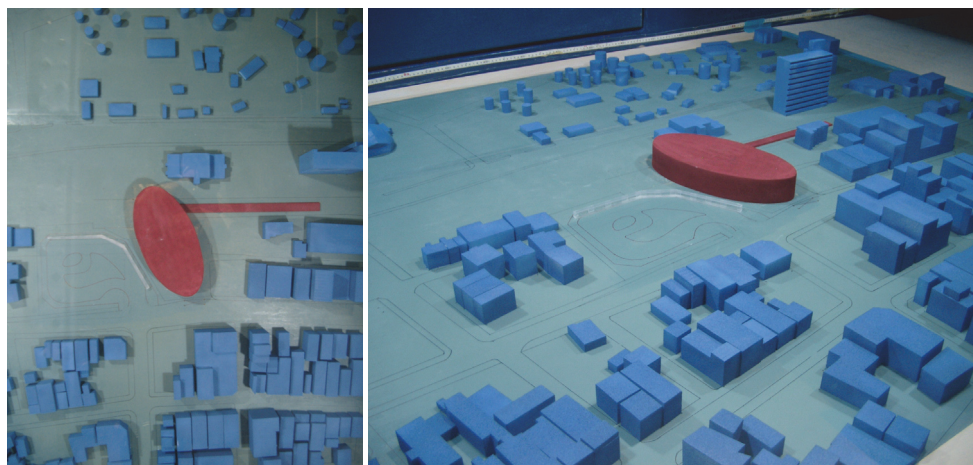


Photo 2. The targeted district models of Downtown Wakkanai

### 3. Assessment items depend on the planning issues

#### 3.1 Nine planning approaches for the Wakkanai station project

On the Wakkanai Station renewal project the nine planning approaches are addressed for the downtown revitalization program as follows.

1. Accessibility: Pedestrians and passenger are able to access easy to the station, bus terminal and the commercial facilities even in winter.
2. Barrier Free: The accessibility is also ensured for elderly and handicapped.
3. Connection: The pedestrians' connection between downtown and water front area is one of the most important network for the downtown revitalization. The urban axis along to the Wakkanai station square will be required less snow damage and snowdrift.
4. Walk-able: Walk-able environment for pedestrian may be ensured on the no snowdrift walkway in winter.
5. Comfortable: Even the outside on the station square comfortable environment should be required for pedestrians and citizens during a year.
6. Community: Making community spaces for citizen will be helpful for their communications. Some of them are inside of the building and some are outside with better comfort environment.
7. Facilities: The Wakkanai Station renewal project promote important facilities rail station and bus terminal. People have much chance to meet together.
8. Mixed Use: The Wakkanai Station renewal project include the development of commercial area and elderly apartments inside the new building. The pedestrian ways have chance that various pedestrian especially elderly people walk on the ways many times.
9. Information: The information for tourist and citizens should be provided accurately. The locations of the information board and signs are also important.

The CW design is also significant to contribute to the Wakkanai Station program for above items Accessibility, Barrier Free, Connection, Walk-able and Comfortable.

#### 3.2 Planning issues regarding the Wakkanai station square project

For planning regarding the Wakkanai Station Square <sup>5</sup>, the following three issues were addressed. They were pointed out as urban design issues before the snow simulation tests. The Wakkanai station and Station Complex Center were planed integrally and the site was as see Fig. 7. The height of the building was 13.5 meter (45mm heights on the model).

##### a) Planning for an urban axis with a desirable pedestrian mall for connecting downtown and the port area

The downtown area and the port area are divided by the JR railway line, and Wakkanai station is located between them. Since a big park is planned for the port area in next decade, an urban axis with a pedestrian mall connecting them is required in the redevelopment plan.

##### b) Planning for enough area for vehicular traffic in the Station Square

Enough area is required for vehicular traffic, such as public buses, taxis and private vehicles, in the Wakkanai Station Square even in winter.

### c) Planning for the integration of public transportation

No barrier should be required for pedestrian to transfer between JR train and public bus. Especially the cross point of the urban axis and the pedestrian route from JR train to Station Square are significant no snow drifting for the desirable pedestrian networking.

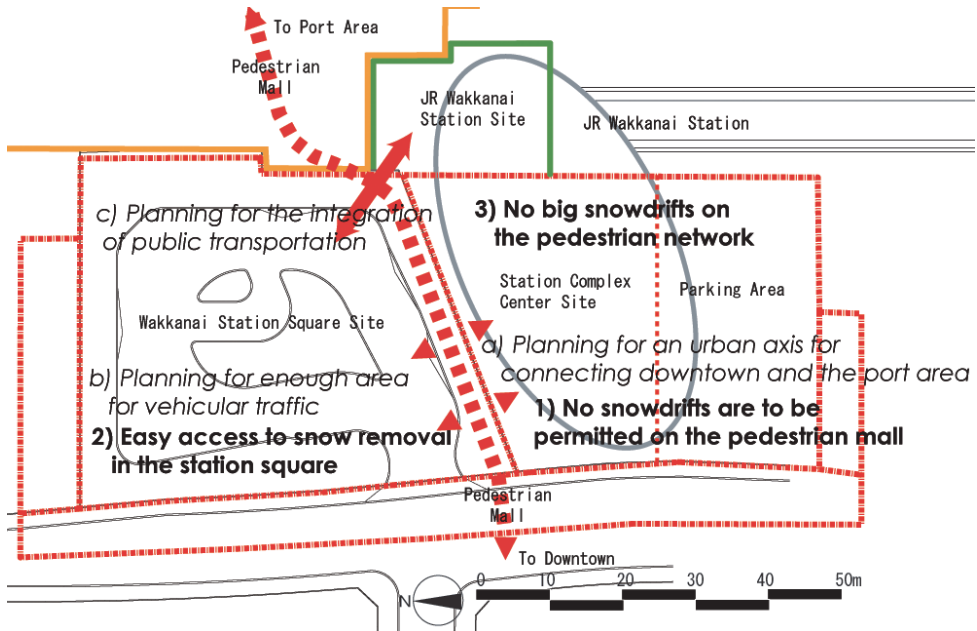


Fig. 7. Planning Issues and Assessment Items on the Wakkanai Station Square Project  
 < a) b) c) are the planning issues, 1) 2) 3) are the assessment items for the snow simulation >  
 <The gray elliptical line means the site of the location of the Station Complex Center>

### 3.3 Assessment items regarding snow simulation

For implementing those planning objectives even in winter, the following three assessment items were addressed regarding each issue. These assessment items were verified in snow simulation tests using the wind tunnel. Basically, these items were based on the concept of reducing the impingement upon pedestrian activity caused by winter snowdrifts in the new redevelopment of Wakkanai Station Square (Fig. 7).

1. No snowdrifts are to be permitted on the pedestrian way connecting downtown and the port area and CW. Various activities will be assumed on the pedestrian way and CW, such as transfer among the various forms of public transportation, flow from downtown to the port area and entrance to the station complex center. Even in winter, snowdrifts should not be an obstacle to the pedestrian network.
2. Easy access to snow removal is to be required in the station square in winter. Enormous piles of snow should not be left in the square because it would interfere with vehicular and pedestrian traffic. Snow storage space is also required in the square.
3. No big snowdrifts are to be permitted on the pedestrian network among the public transportation points in winter. People want to transfer between the JR line and a public bus or taxi without the barrier of snowdrifts.

### 3.4 Comparing the covered walk design for preventing from the snow

The JR Wakkanai railway station, a public bus station, a taxi bay and the requirements of private vehicular traffic should be integrated with the station square to allow for smooth transfer among them. At present they are separate and transfer is inconvenient. Consideration given to pedestrian access among these transportations will be required in the redevelopment plan.

Author focused on snow impacts of distinguish of the CW site plan between Leeward side and Windward side type. The both general site plan showed on Fig. 8. and Fig.9. The idea of Leeward side CW type was protecting pedestrian's activities on the station square and pedestrian's activities on the pedestrian way from snow and strong wind. Windward side CW type also had a concept protecting pedestrian's activities from snow and strong wind. Both CW type had sidewalls partially around one-third of the total length.

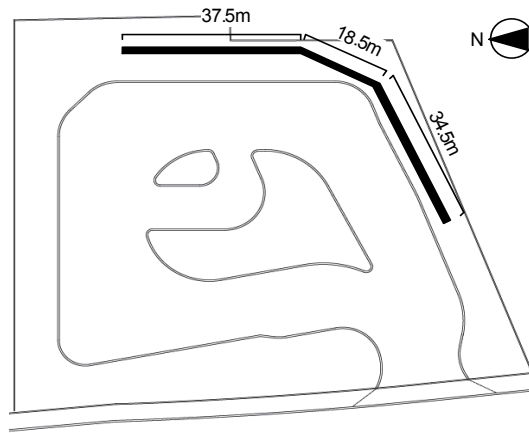


Fig. 8. Site plan of Leeward side CW type

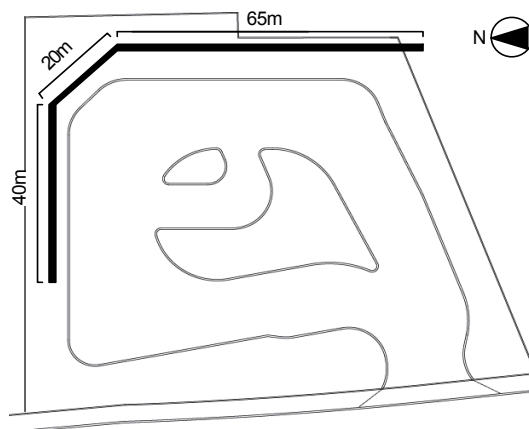


Fig. 9. Site plan of Windward side CW type

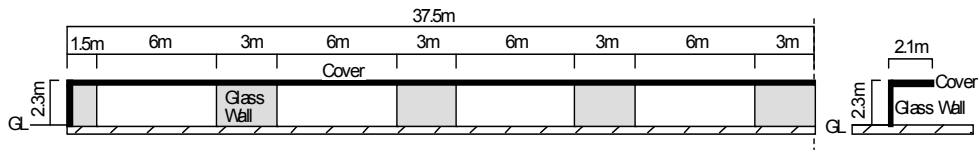


Fig. 10. Section of the Covered-Walk (part) (gray parts are glass walls)

Fig. 10 shows the section plan of the both CW type. The height of the CW should be as low as possible because of preventing from the snow storm. The length of the roof 2.1m is similar to the height for the same reason. The CW has 3m glass walls every 9m pitch, the walls may prevent pedestrian from snow storm. All of the side of CW covered the glass walls is not good design because it will cause the snowdrift inside the CW.

#### 4. Results of the snow simulation experiments

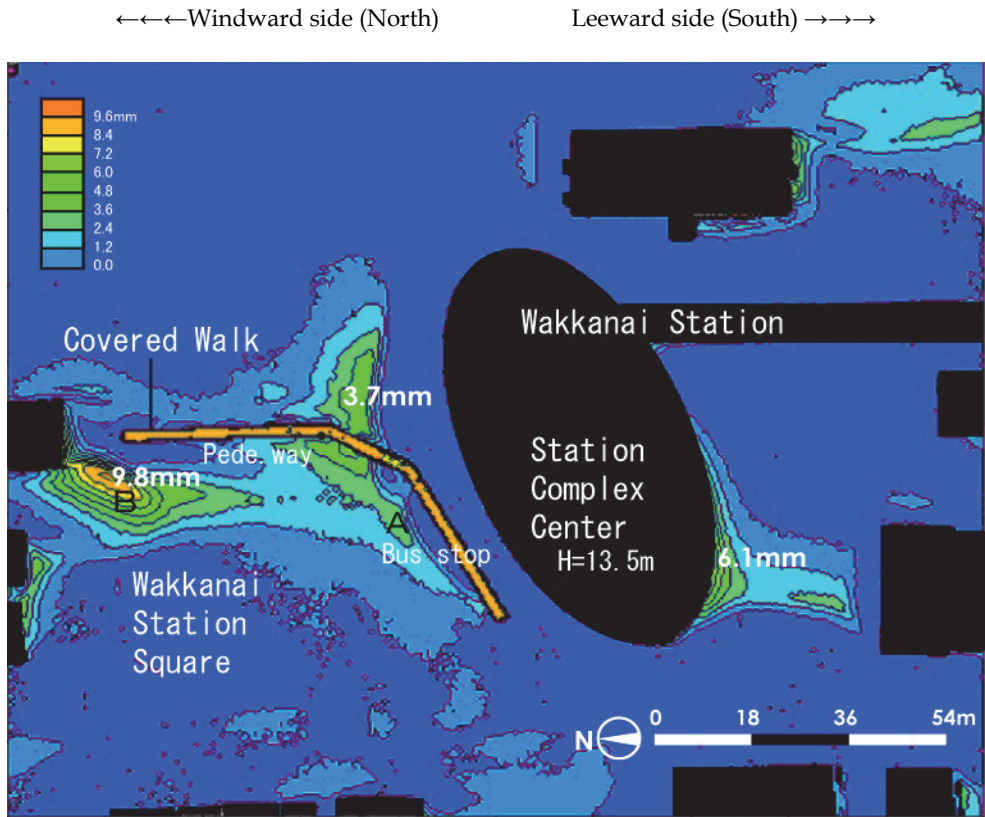
In the findings of the snow simulation tests with snow and wind, several snow problems were observed with both of the CW designs for the new Wakkanai Station Square planning.

##### 4.1 Leeward side CW type (fig. 11)

1. A big snowdrift was formed around the leeward side CW comparing to Windward side type (see point A). The snowdrifts in the station square were caused by the backlash of snow and wind from the Station Complex Center. The backlash of snow and wind flooded the CW, reducing its wind velocity, thereby causing the snowdrifts there. Snowdrifts at the bus stops negatively impact passengers.
2. A big snowdrift was formed on the windward side of the station square even though no CW is located there (see point B). It was assumed to be caused by the reduced velocity of the wind as it streamed from the narrow street to the wide station square. If a snowdrift forms along the CW in the square, it will negatively impact the vehicles there.

##### 4.2 Windward CW type (fig. 12)

1. On the windward CW type, a big snowdrift was not formed around the bus stops comparing to Leeward side type (see point C). There was no barrier backlash of snow and wind from the Station Complex Center, as wind streamed through to the center of the square. No passengers or vehicles will be inconvenienced by snowdrifts in this situation. But grass shelters will be required at the bus stops for protecting the passengers from the strong and cold winds.
2. The snowdrift on the windward side of the square was big, but it formed smaller than the Leeward side CW type (see point D). Author figured out the reason that the CW prevented wind and snow from north and northeast direction for making snowdrift on the windward side of the station square. The spread of the snowdrift would have less impact on vehicular traffic in the square. Bus stops and taxi bays should be planned to exclude this area.



(Numeric values mean the height of powder draft of the model)

Fig. 11. Snow and wind simulation test of Leeward side Covered Walk (CW) type

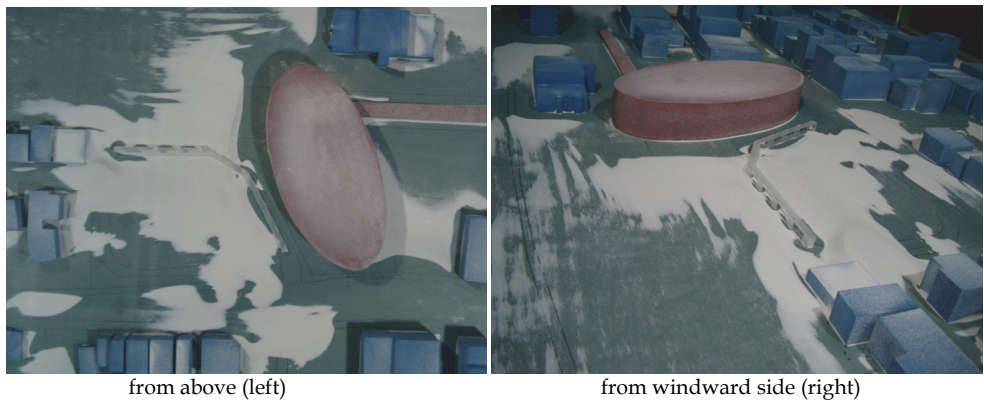
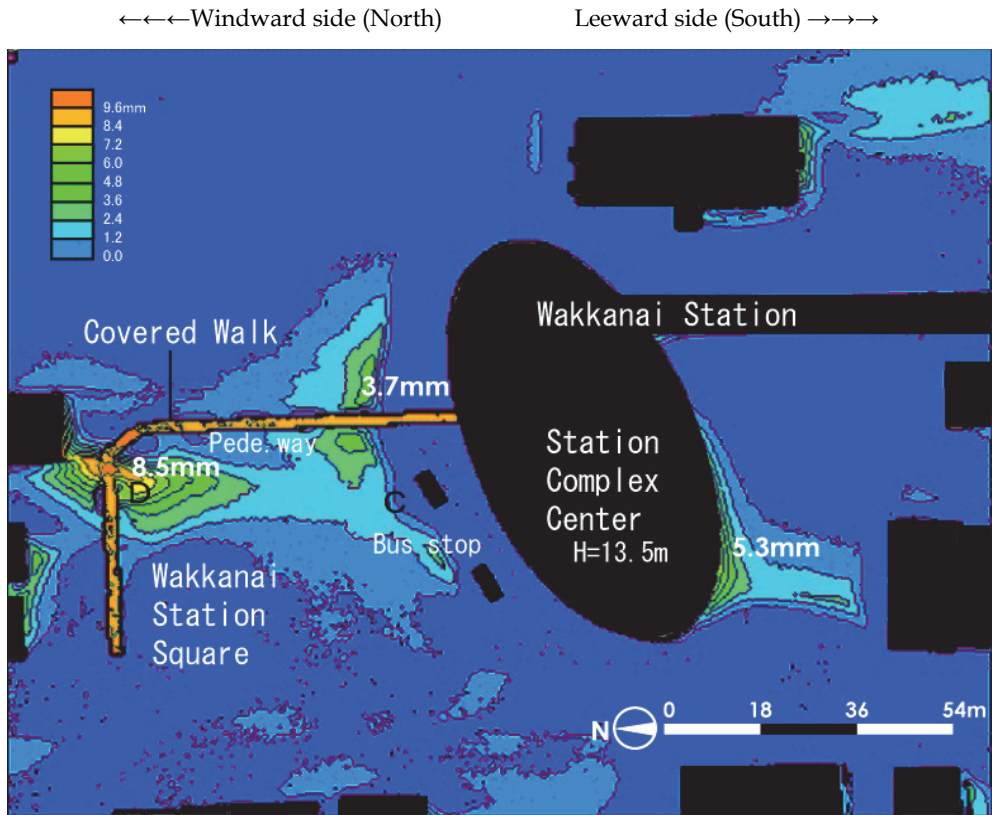


Photo 3. Snow simulation result of Leeward side Covered Walk type





(Numeric values mean the height of powder draft of the model)

Fig. 12. Snow and wind simulation test of Windward side Covered Walk (CW) type

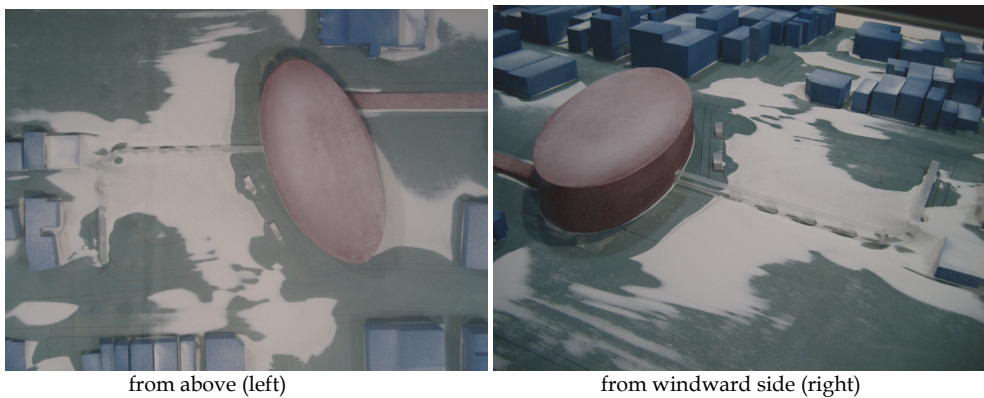


Photo 4. Snow simulation result of Windward side Covered Walk type

## 5. Conclusions

In the findings of the snow simulation tests with snow and wind, several snow problems were observed with both of the CW designs for the Wakkanai Station Square renewal planning.

On the leeward side CW type simulation, a big snowdrift was formed around the leeward side of CW (Fig. 11). On the other side, on the windward CW type, a big snowdrift was not formed around the bus stops (Fig. 12). Comparing the two types of CW design, the Windward side CW type is better suited to alleviate the impact of heavy snowfall in the new Wakkanai Station Square development because the formation of snowdrifts are less likely to occur to the passenger area that riding on the buses and pedestrian areas walking along the CW. The finding that a big snow barrier like the CW caused snowdrifts to form around it and snow inconveniences to pedestrian and bus transit during the winter season in Wakkanai was very interesting. It is assumed that the CW reduced wind speed and contributed to form the snowdrift along the CW. The CW has not to be located at right angle to the main wind direction in winter. The CW has to be designed carefully to its site plan and section plan.

It is very important to make the snow and wind simulations using wind tunnel on the process of the public square design project in these snowy and cold regions. The problems caused by snow and wind are pointed out clearly and those problems should be reflected to the public space design and urban design. The results of this simulation also should be reflected in the square planning and design of this project.

These snow simulations were tested only two site design type of CW, then more variable CW design e.g. wall design and height have to be tested on the snow simulations. Further more, the snow simulation on real atmospheric phenomena should be required because this was verifiable only through the conduction of snow simulation tests incorporating a wind tunnel.

## 6. Sustainable design approach relationship between urban design and environmental planning

On the Wakkanai Station Square design studies with snow simulations author realized the new sustainable design approaches relationship between Urban Design and Environmental Planning. Especially in these cold and snowy cities, this sustainable design approaches should be required on these urban design projects. Author developed the new urban design approach with snow simulations using wind tunnel as follow steps (Table 3).

## 7. Notes

1. The Designing CW is one of the most important items for pedestrian network on this project.
2. Heavy Snow Area: The local government that has 5,000 cm by days and more snowfall in total in last 30 years. Multiplying the height of snow stock per day by snow stock days gives the cm\*days.

Particular Heavy Snow Area: The local government that has 15,000cm\*days and more snowfall in total in last 20 years.

3. Manufactured by Keyence LK2500
4. The white soil powder has 8.5% of moisture content and the average of diameter has 20 $\mu$ m. It means very dry and small particle powder.
5. The station square is planned four bus bays, three taxi bays and four bays for private vehicles on the Wakkanai Station Square project.





Urban Design Approaches	Environmental Planning Approaches
<p><b>1) Urban design approach #1</b>            - Making planning criteria contribute to the downtown revitalization.            - Several alternative designing plans are proposed depend on these planning criteria.</p>	
<p><b>Urban Design Approaches</b> (continue)</p>	<p><b>Environmental Planning Approaches</b> (continue)</p>
	<p><b>2) Environmental planning approach #1</b>            - The experiments of the snow simulations using wind tunnel for the alternative design plans.            - Environmental evaluations to the results of the snow simulations on the alternative design plans.</p>
<p><b>3) Urban design approach #2</b>            - Development to the design guidelines depend on the results of the snow simulations. Each alternative design plan has good and considerable points in the results of the simulations. For promoting more useful to the results of the snow simulations, the design guidelines are able to reflect those ideas of the simulations.</p>	
	<p><b>4) Environmental planning approach #2</b>            - More response to the environmental conditions of snow problems, snow drifting and strong wind on the detail planning of the projects.</p>
<p><b>5) Urban design approach #3</b>            - On the designing process of the station square more detail designing points reflect from the design guidelines.</p>	

Table 3. Sustainable design approach relationship between Urban Design and Environmental Planning

## 8. References

- [1] Bosselmann, P. (1984). Sun, wind, and comfort - A Study of Open Spaces and Sidewalks in Four Downtown Area -. Environmental Simulation Laboratory University of California Berkeley, USA,
- [2] Bosselmann, P. and Arens, E. (1989). Wind, sun and temperature - predicting the thermal comfort of people in outdoor spaces. Building and Environment, Vol.24, No.4, pp315-320, USA

- [3] Bosselmann, P. (1998). Representation of Places - Reality and Realism in City Design -, Downtown Toronto Urban Form and Climate, University of California Press, USA
- [4] Pressman, N. and Zepic, X. (1986), Planning in cold climates. Institute of Urban Studies, Canada
- [5] Pressman, N. (1995), Northern cityscape - linking design to climate -. Winter Cities Association, Canada
- [6] Setoguchi, T. (2003). A Study on Efficiencies for Reducing Snow Damages on Infill Developments in Downtown Area, The proceedings of International Symposium on City Planning, 2003.9, Japan
- [7] Setoguchi, T. (2004), Efficiencies of Infill Developments against Snow Problem in Winter Cities - The Snow Simulations for Desirable Block Designs Using Wind Tunnel -, Journal of Asian Architecture and Building Engineering, 2004.11, pp335-340
- [8] Tomabechi, T. (2002). Influence of snow around the building on evacuation activities, Journal of Architecture, Planning and Environmental Engineering, No.560, 2002.10, pp167-172, Japan
- [9] Yoshizaka, T. (1942). The Model Study on the Snow Stock Environments Surrounding of Buildings, Snow and Ice, Japan

## **Part 4**

# **Turbulent Structure Analysis**



# The Study of Details Effects in Cycling Aerodynamics: Comparison Between Two Different Experimental Approaches

Giuseppe Gibertini<sup>1</sup>, Gabriele Campanardi<sup>1</sup>, Donato Grassi<sup>1</sup>  
and Luca Guercilena<sup>2</sup>

<sup>1</sup>*Politecnico di Milano - Dipartimento di Ingegneria Aerospaziale*

<sup>2</sup>*Quick Step Pro Tour*

<sup>1</sup>*Italy*

<sup>2</sup>*Belgium*

## 1. Introduction

Aerodynamics is quite important for racing cyclists and particularly in time-trial competitions. In fact, the aerodynamic resistance, i.e. the breaking action of the relative wind, increases quadratically with the speed while the rolling resistance depends linearly on the speed (Kyle, 1989). Thus, due to the rather high velocity (in the order of 50 km/h), the aerodynamic resistance acting on a time-trial racer is about the 90% of the total resistance. Aerodynamics is thus very important for the cyclists performances and many experimental studies, addressed to find the best cyclist position as well as the best articles, have been carried out in the past (Garcia-Lopez et al., 2008; Gibertini & Grassi, 2008; Grappe et al., 1997; Lukes et al., 2005). Furthermore, although they are outside of the subject of the present treatise, some interesting computational works begin to appear in literature (see for example Defraeye et al. (2010a;b)).

### 1.1 The aerodynamic resistance

Following a widely used notation, the component of the aerodynamic force opposite to the bicycle motion is called  $F_x$  and its non-dimensional coefficient is  $C_x = F_x / (\frac{1}{2} \rho V_b^2 S)$  where  $\rho$  is the air density,  $V_b$  the bicycle speed and  $S$  a reference area that has to be defined. In absence of natural wind, all the relative wind is due to the bicycle motion and thus the force  $F_x$  corresponds to the aerodynamic drag and  $C_x$  is the drag coefficient.

For the typical racing velocities the coefficient  $C_x$  slightly depends on the Reynold number  $Re = \rho V_b \sqrt{S} / \mu$  (where  $\mu$  is the air viscosity) so that the drag is essentially proportional to the air density and to the square of the velocity (Basset et al., 1999). In order to avoid the arbitrary definition of  $S$  it can be more convenient to express the aerodynamic resistance in terms of drag area  $SC_x$  instead than in terms of non-dimensional drag coefficient. On the other hand, in order to compare the position aerodynamic efficiency of different cyclists apart from their different dimensions effect, the normalized resistance (i.e. the  $C_x$ ) can be interesting and in this case the projected frontal area can be taken as reference area (Heil, 2001 and 2002). More in general, when the drag of two or more bodies (whatever they are, men or objects) is compared, the decomposition of the drag area  $SC_x$  in terms of drag coefficient  $C_x$  and reference area  $S$

can help to evaluate how much a drag difference is due to a difference in the size or to a difference in the shape efficiency.

As reported by Gibertini & Grassi (2008), the time-trial cyclist overall  $C_x$  is slightly less than 1 (typically about 0.8) denoting that the cyclist is definitively a bluff body.

### 1.2 The testing methodologies

The experimental study of cycling aerodynamics is made difficult by the fact that the cyclists are not machines and their motion is not completely deterministic. As a matter of fact, although the motion of an elite cyclist is rather controlled and repeatable, nevertheless there are many possible differences (also in nominally equal positions) that can sensibly (and sometime strongly) affect the aerodynamic efficiency. The problem becomes more serious when the focus of the study is a detail effect as the effect of a bicycle part (handlebar, fork, wheels, etc.) or the effect of a particular of the cyclist dressing (as the shoes or the suit). In fact, the effects of that single details (Alam et al., 2008; Blair & Sidelko, 2008; Chabroux et al., 2008; Kyle, 1989; 1990; Sayer & Stanley, 1994; Tew & Sayers, 1999; Underwood & Jeremy, 2010) are often smaller than the global uncertainty of the drag measurement of a test involving the athlete (Flanagan, 1996).

It could be observed that so small effects, that can be easily masked from a slightly different position, are not so important for the cyclist performance. Nevertheless two considerations can be done: the first one is that also a small drag reduction can produce a sensible effect on the resulting race time (Kyle, 1989), and the second one is that an aerodynamic effect not strictly related to the cyclist position is anyway added to the global drag, independently to the capacity of the cyclist to keep the optimal position. Furthermore the sum of different small detail effects can results in a considerable value. Thus the problem of the better methodology for the study of this kind of detail effects is an important item for the cycling aerodynamics.

Generally speaking we can consider three possible experimental approaches. The first one is the wind tunnel testing of the single isolated detail: this way allows for very accurate and repeatable measurements and requires a relatively small wind tunnel (which means relatively low costs) but, on the other hand, the working condition of the isolated detail are not, in principle, the real working conditions. In principle tests can be carried out "in-field" as it has been done both directly on the road (Martin et al., 2006) and on a track (Gibertini, Campanardi, Guercilena & Macchi, 2010; Grappe et al., 1997). Unfortunately this tests are unavoidably affected by a considerable measurement uncertainty. In the middle between these two testing approaches, a third possible way is the wind tunnel testing including the real pedaling cyclist that surely produce more accurate results respect to the in-field testing. Nevertheless also wind tunnel results are affected by problems of repeatability.

An evaluation of the relative advantage and disadvantage of these three approaches is not simple. The present paper presents a reasoned comparison between the results obtained with "manned" wind tunnel testing and a partial model test (Gibertini, Grassi, Macchi & De Bortoli, 2010) on the effect of the overshoes.

### 1.3 Shoe testing

The choice of the shoes is a typical problem of the aerodynamic optimization of a time trial cyclist. Of course this choice depends on many aspects and not only on the aerodynamic point of view, but nevertheless it is interesting to evaluate the amount of drag (and thus the amount of power) due to the shoes. An interesting point that is a valid example to compare the two cited wind tunnel testing approaches is the effect of the overshoes: this accessories



are widely used in the time trial competitions with the aim of drag reduction. In the study already mentioned here before (Gibertini, Grassi, Macchi & De Bortoli, 2010) this subject was investigated by means of wind tunnel tests with a shank and foot model. These tests showed that the overshoes produce a drag increasing instead of a reduction. This counter-trend results could not be taken as conclusive because the tests were carried out on a static partial model (reproducing just the shank and the foot) that could not include all the real effects. A recent series of tests was carried out with an elite team of six cyclists. The aim of these tests was mainly the optimization of cyclists position (see Gibertini, Campanardi, Guercilena & Macchi (2010)) but it has been a precious occasion to get some confirmation of the results obtained with the shank and foot model.

**2. The reference tests of overshoe effect on a partial model of foot and shank**

The leading idea of the partial model tests was to represent, as well as possible, the working condition of the foot with a relatively simple setup (Gibertini, Grassi, Macchi & De Bortoli, 2010). The model was essentially a beam terminating with a shank model. The foot model was hinged to the shank in the ankle position. At the other extremity the beam was hinged to the balance interface. Thus, the model allowed to set both the angle of the shank and the angle of the foot. The shoe, put on the foot model, included the pedal. The test layout is shown in Fig. 1.

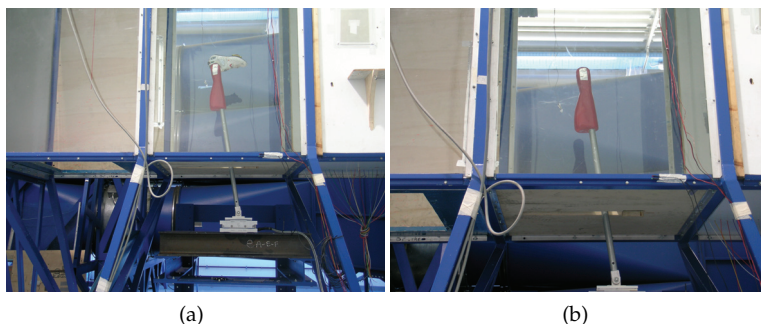


Fig. 1. The partial model test layout in the complete model configuration (a) and in foot-off tare configuration(b)

The test conditions have been defined on the base of shank and foot angles (defined as in Fig. 2a) at four pedaling phases  $\theta$  of a specific cyclist taken as reference example (the values are reported in Table 1). The shank and foot angles in the four reference positions have been deduced from the analysis of the frames of a video recorded during a previous "manned" wind tunnel test carried out in the Large Wind Tunnel of Politecnico di Milano. The obtained values have been taken as indicative as it was already clear that different cyclists have different angles of shank and foot (with differences that can be in the order of some degrees).

$\theta = 0^\circ$		$\theta = 90^\circ$		$\theta = 180^\circ$		$\theta = 270^\circ$	
$\epsilon_F$	$\epsilon_S$	$\epsilon_F$	$\epsilon_S$	$\epsilon_F$	$\epsilon_S$	$\epsilon_F$	$\epsilon_S$
$-22.9^\circ$	$49.3^\circ$	$8.6^\circ$	$80.8^\circ$	$-16.6^\circ$	$83.7^\circ$	$-40.7^\circ$	$40.7^\circ$

Table 1. Pedaling angle values assumed for the partial model test

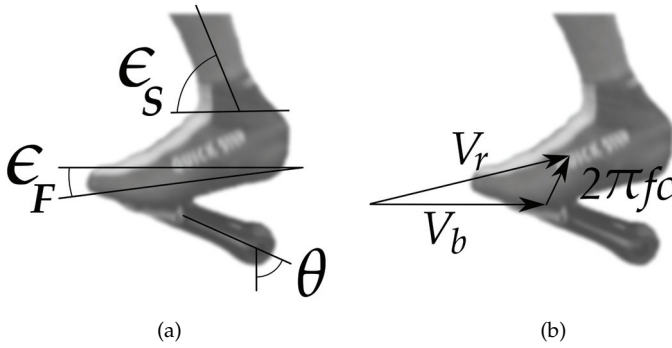


Fig. 2. Geometrical and kinematical quantities definition

These measured angles have been used to set the wind tunnel test conditions taking into account also the additional (positive or negative) incidence  $\alpha_p$  induced by the the foot vertical translation due to the pedaling (see Fig. 2b). Referring again to Fig. 2a,  $\Delta\epsilon = \epsilon_S - \epsilon_F$  while the relative velocity  $V_r$  and its incidence angle  $\alpha$  have been determined by the following Equation 1 and 2 where  $f$  is the pedaling frequency and  $c$  is the crank arm lenght.

$$V_r = \sqrt{(V_b + 2\pi f c \cos\theta)^2 + (2\pi f c \sin\theta)^2} \tag{1}$$

$$\alpha = \epsilon_F + \alpha_p ; \quad \alpha_p = \arctan\left(\frac{2\pi f c \sin\theta}{V_b + 2\pi f c \cos\theta}\right) \tag{2}$$

The test conditions for the foot model, computed by means of Equations 1 and 2, are listed in the Table 2. The sketch of Fig. 3 illustrates the meaning of these quantities

$\theta = 0^\circ$		$\theta = 90^\circ$		$\theta = 180^\circ$		$\theta = 270^\circ$	
$V_r$	$\alpha$	$V_r$	$\alpha$	$V_r$	$\alpha$	$V_r$	$\alpha$
17.0 m/s	-22.9°	15.1 m/s	16.1°	13.0 m/s	-16.6°	15.1 m/s	-48.2°

Table 2. Test conditions set for the partial model test

The aerodynamic resistance is the force component  $F_x$  opposite to the bicycle motion (Equation 3).

$$F_x = \mathbf{F} \cdot \mathbf{V}_r \cos(\alpha_p) \tag{3}$$

The average resistance was computed taking the mean value of the four resistance values measured at the four different pedaling phases of Table 1.

Of course, the main limitation of this approach is that some interference effects with the other real components are missing (first of all the crank arms). An other possible objection is that also the real foot and shank dynamics is not completely reproduced: the incidence angle and the velocity are set to taken into account the motion due to pedal rotation but the rotation of the foot itself as well as the rotation of the shank are not reproduced. On the other hand, the measurements were quite accurate and repeatable indeed.

The tests were carried out assuming a reference riding condition of 15 m/s (i.e. 54 km/h) speed and 1.8 Hz pedaling frequency. Two different shoe models (one laced and one strap fastened) and the overshoe have been tested with two different pedal models. In order to obtain the

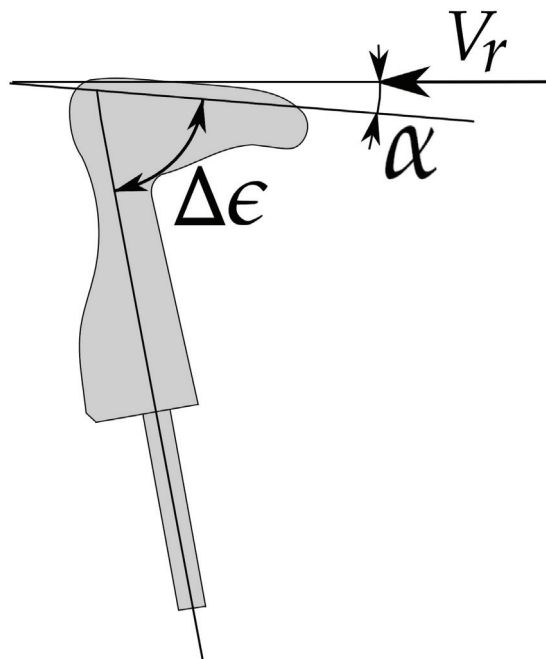


Fig. 3. The test parameters

aerodynamic loads acting on the foot only, previous aerodynamic tare tests with just the beam and the shank have been carried out as can be seen in Fig. 1b. The loads measured without the foot have been subtracted from the load measured with the complete model. One of the most curious results was the overshoe effect. In these test it resulted that the overshoe over a strap fastened shoe model produces an over drag for all the four tested phases as can be seen in Fig. 4 that shows the results obtained by Gibertini, Grassi, Macchi & De Bortoli (2010) for the strap fastened shoe model, with and without the overshoe, with a clipless single-sided pedal (33 mm high).

Taking the arithmetic mean of the four results related to the four phases, the measured drag area increase resulted to be equal to  $0.001 \text{ m}^2$  for each foot. The total amount of cyclist and bicycle drag area is in the order of  $0.2 \text{ m}^2$  (Defraeye et al., 2010a) thus the effect of the two overshoes is in the order of 1% of the total drag.

In order to verify the results of Gibertini, Grassi, Macchi & De Bortoli (2010), a new test campaign has been carried out using the same test conditions (as described here before) and using the same models (all the pictures of the partial model tests included in this chapter have been taken during this new test campaign). The new tests confirmed the results published in the cited journal paper. As in that reference work, the tests have been repeated with another pedal model obtaining essentially the same results: the drag area absolute values were slightly different as the pedals were different but the differences between different shoe models drag, as well as the difference due to the overshoe, were the same within a tolerance of  $10^{-4} \text{ m}^2$ .

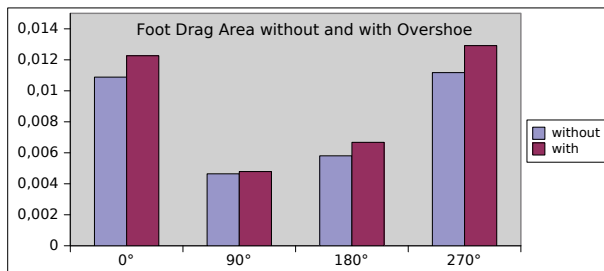


Fig. 4. Comparison between the foot drag areas without and with the overshoe at four different pedaling phases (drag areas expressed in  $m^2$ )

### 3. The manned wind tunnel tests of overshoe effect

The wind tunnel tests of the "complete system" (including the cyclist) were carried out in the large wind tunnel of Politecnico di Milano (Campanardi et al., 2003). This facility is equipped with a specific test rig for cycling aerodynamic tests. The test chamber is wide enough (Fig. 5) to get a negligible blockage effect: in fact, a typical value for the projected front area of a cyclist in time trial position is about  $0.3 m^2$  while the test section area in cycling test configuration is  $14.5 m^2$  leading to a solid blockage of about 2% that is an unusually low value (Defraeye et al., 2010a) assuring very low blockage effects (Barlow et al., 1999). Nevertheless, although it was very small indeed, blockage effect correction has been applied to the results following the procedure indicated in Barlow et al. (1999) for the case of unconventional shape.



Fig. 5. The wind tunnel test chamber

The test rig, that is in details described by Gibertini & Grassi (2008), allows to reproduce a realistic condition with the athlete pedaling and both wheels spinning (Fig. 6). The rear wheel axle is held by two vertical beams so that the wheel can spin over a small roller that, by means of a toothed belt, transmits the rotation to the front roller and finally to the front wheel; the front wheel axle is free so the cyclist has to drive the wheel as in a real condition. A brake system provides an adjustable resistance torque to the rollers producing a realistic effort and thus a realistic cyclist body attitude. A sketch of the test rig is shown in Fig. 7. The drag contribution of the support system (i.e. the aerodynamic tare) is measured in a test

run without rider and bicycle. The bicycle is equipped with a tachometer so that, during the test run, the cyclist is able to maintain the correct rotational speed of the wheels matching the wind velocity.



Fig. 6. Cyclist pedaling in the wind tunnel

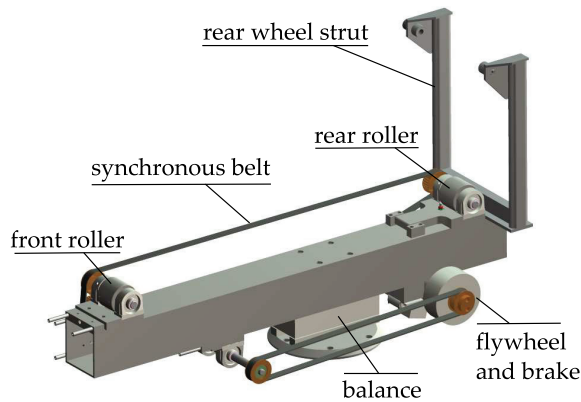


Fig. 7. The test rig for the cyclist

As mentioned before, the tests concerned a team of six cyclists with the aim of optimizing their position for time trial competitions. This gave the possibility to test the overshoe effect on a rather large base of athletes. The comparison with the reference tests of Gibertini, Grassi, Macchi & De Bortoli (2010) was made more meaningful by the fact that the most of these cyclists (four over six) adopted the same shoe model used in that study (Fig. 8a). The overshoe model was the same for all the six cyclists and was of the same kind of the one used in the partial tests (Fig. 9).

In Table 3 the anthropometric data of the six cyclists are listed, including the pedaling angles (see Fig. 2a for the definition) measured from the wind tunnel video-camera frame as showed in Fig. 10.

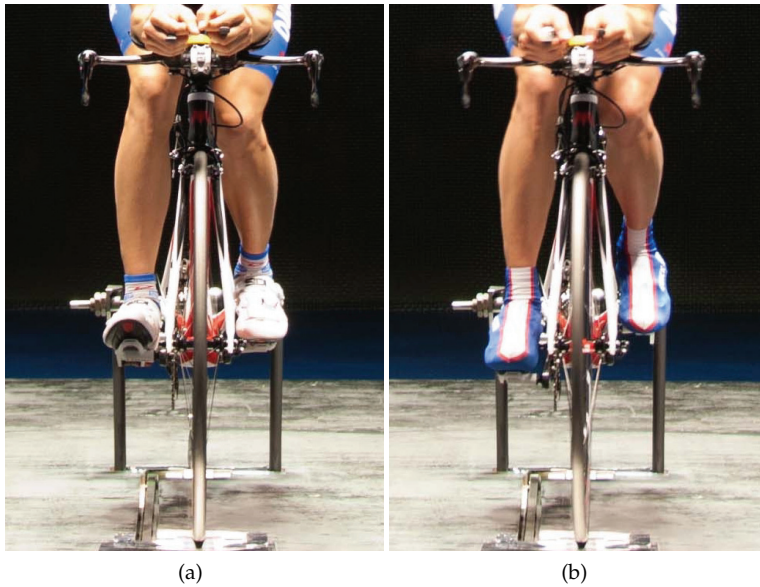


Fig. 8. Front view of cyclist legs without (a) and with (b) the overshoes



Fig. 9. The overshoe

By Equations 1 and 2 is possible to compute, for each cyclist and for each pedaling phases, the foot incidence  $\alpha$ . In Fig. 11 these incidences are plotted together and compared with the

Cyclist	Height	$\theta = 0^\circ$		$\theta = 90^\circ$		$\theta = 180^\circ$		$\theta = 270^\circ$		Shoe Size
		$\epsilon_F$	$\epsilon_S$	$\epsilon_F$	$\epsilon_S$	$\epsilon_F$	$\epsilon_S$	$\epsilon_F$	$\epsilon_S$	
AK	184 cm	-31°	39°	-2°	61°	-13°	66°	-52°	36°	43.5
TK	182 cm	-33°	48°	-6°	74°	-23°	76°	-59°	45°	43
KS	173 cm	-29°	41°	0°	66°	-21°	73°	-50°	39°	42.5*
DD	177 cm	-24°	47°	2°	72°	-21°	73°	-50°	42°	43.5
SD	182 cm	-29°	43°	-3°	67°	-24°	71°	-50°	41°	44
KD	182 cm	-29°	39°	-6°	64°	-19°	73°	-49°	38°	43*

\* different shoe models

Table 3. Cyclists anthropometric data

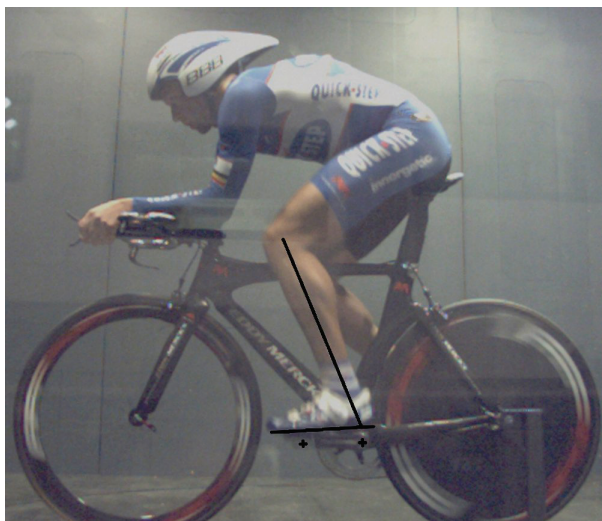


Fig. 10. Frame of the wind tunnel video-camera with drawn lines highlighting the pedaling angles

reference values used in the partial model tests.

As discussed in the introduction of the present paper, the manned tests are affected by a low degree of repeatability so that in principle, in order to obtain a result statistically meaningful, the test should be repeated several times. On the other hand the tests number are limited by reasons of wind tunnel costs and also by the fact that the cyclists tend to loose the concentration after too many repetitions (so that the result is not necessarily improving). In the present activity the cyclist position were tested twice, with any repetition test just subsequent to the first one, while the overshoes effect has been tested, for each cyclist, with an overshoes-on test just subsequent to an overshoe-off test at the same cyclist position (only for the cyclist KS the overshoe-on test preceded the other one). The single results is poorly meaningful as the chased effect is in the order of the test repeatability but the set of the all six data (one for each cyclist) gives a reasonable estimation of its order of magnitude.

Each test consisted in a 30 s acquisition at 12.5 m/s and, except for AK and TK, in a second acquisition at 13.9 m/s during the same wind tunnel run. As the two velocities are quite close each to the other so that the Reynolds number is essentially the same, for each test the

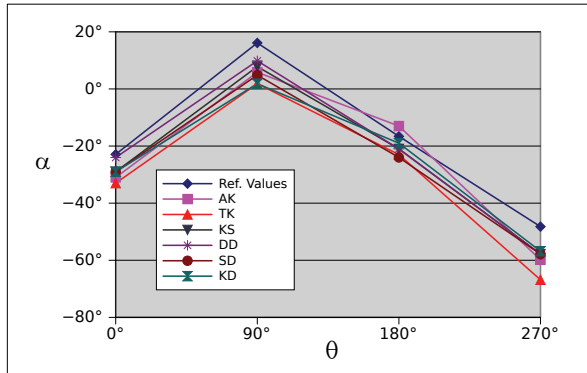


Fig. 11. Foot incidences

drag area was averaged over the two acquisitions (when applicable). The pedaling frequency was 1.5 Hz for 12.5 m/s and 1.7 Hz for 13.9 m/s. In Table 4 the measured values of  $\Delta SC_x$  (the drag area increase due to the overshoes) are presented. The parameter RP, computed for each cyclist, is the root mean square of the differences between the drag areas measured in two related tests (a position tests and its repetition). Due to the small statistical base (from 3 to 5 positions tested for each cyclist) this parameter is only indicative but nevertheless gives a rough quantification of the test repeatability. It appears clear that the measured values of  $\Delta SC_x$  are in the order of the tests uncertainty but nevertheless it is remarkable that in no one case the overshoes showed an advantage. The mean value (taking the mean of all the cyclist) resulted to be  $0.003 \text{ m}^2$  that, taking into account all the uncertainties, is quite well comparable with the value of  $0.002 \text{ m}^2$  obtained with the partial model tests. These results are summarized in Fig. 12.

Cyclist	$\Delta SC_x$ [ $\text{m}^2$ ]	RP [ $\text{m}^2$ ]
AK	0.006	0.004
TK	0.004	0.006
KS	0.004	0.003
SD	0.001	0.003
KD	0.002	0.002
DD	0.001	0.002

Table 4. The overshoe effect

### 4. Conclusions

The results of the present experimental investigation well highlight the difficulties of evaluating details effects by means of complete manned wind tunnel tests. The present investigation essentially confirmed the results obtained with the partial model: the overshoes produced an increase in the aerodynamic drag. Also the order of magnitude of the measured effect is essentially confirmed although the present manned tests are affected by a problem of repeatability that does not allow to estimate accurately such a small effect. Of course this degree of uncertainty does not allow to consider the present tests as a quantitative



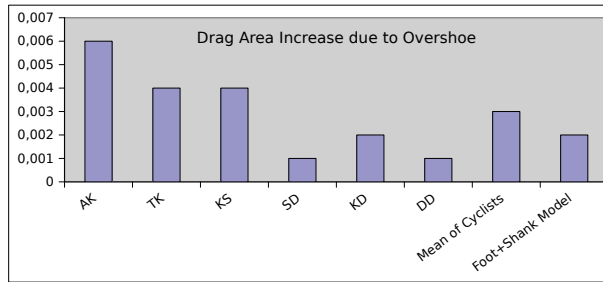


Fig. 12. The overshoe effect (drag areas expressed in  $m^2$ )

validation of the simplified test procedure but, nevertheless, the present results demonstrate that the complete manned configuration does not produce, respect to the simplified setup, any important aerodynamic effect that can drastically change the results. It can be concluded that, for the case of shoes aerodynamics, the partial test in a relatively small wind tunnel is a very reasonable way, more convenient respect to a more expensive and less accurate manned test. Of course this results is due to the fact that the adopted procedure and setup included all the main effects of the real condition and this was due to a reasoned approach but also to the fact that the foots are essentially undisturbed by the wake of the other components. This is not the case, for example, of the rear wheel that is completely immersed in the wakes of the cyclist legs and of the bicycle itself so that the drag measured by means of isolated wheel tests result to be not applicable to the real condition.

Generally speaking it is clear from the presented activity results that the question about the way for an accurate experimental definition of so small aerodynamic effects is still an open question.

## 5. References

- Alam, F., Subic, A. & Akbarzadeh, A. (2008). Aerodynamics of bicycle helmets, in M. Estivalet & P. Brisson (eds), *The Engineering of Sport 7, vol. 1*, Springer, Paris, pp. 337–344.
- Barlow, J., Rae, W. & Pope, A. (1999). *Low-speed wind tunnel testing*, Wiley and Sons, New York.
- Basset, D., Kyle, C., Passfield, L., Broker, J. & Burke, E. (1999). Comparing cycling world hour records, 1967-1996: modeling with empirical data, *Medicine & Science in Sports & Exercise* 31(11): 1665–1676.
- Blair, K. & Sidelko, S. (2008). Aerodynamic performance of cycling time trial helmets, in M. Estivalet & P. Brisson (eds), *The Engineering of Sport 7, vol. 1*, Springer, Paris, pp. 371–377.
- Campanardi, G., Gibertini, G., Pozzi, M. & Quici, M. (2003). La camera di prova aeronautica della galleria del vento del politecnico di milano (in italian), *Proceedings of XVII Congresso nazionale AIDAA*, Roma, Italy, pp. 2073–2077.
- Chabroux, V., Barelle, C. & Favier, D. (2008). Aerodynamics of time trial bicycle helmets, in M. Estivalet & P. Brisson (eds), *The Engineering of Sport 7, vol. 2*, Springer, Paris, pp. 401–410.
- Defraeye, T., Blocken, B., Koninckx, E., Hespel, P. & Carmeliet, J. (2010a). Aerodynamic study of different cyclist positions: Cfd analysis and full-scale wind-tunnel tests, *Journal of Biomechanics* 43(7): 1262–1268.

- Defraeye, T., Blocken, B., Koninckx, E., Hespel, P. & Carmeliet, J. (2010b). Computational fluid dynamics analysis of cyclist aerodynamics: Performance of different turbulence-modelling and boundary-layer modelling approaches, *Journal of Biomechanics* 43(12): 1262–1268.
- Flanagan, M. (1996). Considerations for data quality and uncertainty in testing of bicycle aerodynamics, *Cycling Science* 8(1): 7–10 and 22–23.
- Garcia-Lopez, J., Rodriguez-Marroyo, J., Juneau, C., Peleteiro, J., Cordova Martinez, A. & Villa, J. (2008). Reference values and improvement of aerodynamic drag in professional cyclists, *Journal of Sports Sciences* 26(3): 277–286.
- Gibertini, G., Campanardi, G., Guercilena, L. & Macchi, C. (2010). Cycling aerodynamics: wind tunnel testing versus track testing, in J. Goh Cho Hong (ed.), *6th World Congress of Biomechanics (WCB 2010), IFBME Proceedings 31*, Springer, pp. 10–13.
- Gibertini, G. & Grassi, D. (2008). Cycling aerodynamics, in H. Nørstrud (ed.), *Sport Aerodynamics, CISM Courses and Lectures, vol.506*, Springer, Wien, pp. 23–47.
- Gibertini, G., Grassi, D., Macchi, M. & De Bortoli, G. (2010). Cycling shoe aerodynamics, *Sports Engineering* 12(3): 155–161.
- Grappe, F., Candau, R., Belli, A. & Rouillon, J. (1997). Aerodynamic drag in field cycling with special reference to the obree's position, *Ergonomics* 40(12): 1299–1311.
- Heil, D. (2001). Body mass scaling of projected frontal area in competitive cyclists, *European Journal of Applied Physiology* 85(3-4): 358–366.
- Heil, D. (2002). Body mass scaling of frontal area in competitive cyclists not using aero-handlebars, *European Journal of Applied Physiology* 87(6): 520–528.
- Kyle, C. (1989). The aerodynamics of handlebars & helmets, *Cycling Science* 1(1): 22–25.
- Kyle, C. (1990). Windtunnel tests of bicycle wheels & helmets, *Cycling Science* 2(1): 27–30.
- Lukes, R., Chin, S. & Haake, S. (2005). The understanding and development of cycling aerodynamics, *Sports Engineering* 8(2): 59–74.
- Martin, J., Gardner, A., Barras, M. & Martin, D. (2006). Aerodynamic drag area of cyclists determined with field-based measures, *Sportscience* 10: 68–69.
- Sayer, A. & Stanley, P. (1994). Drag force on rotating racing cycle wheels, *Journal of Wind Engineering and Industrial Aerodynamics* 53(3): 431–440.
- Tew, G. & Sayers, A. (1999). Aerodynamics of yawed racing cycle wheels, *Journal of Wind Engineering and Industrial Aerodynamics* 82(1): 209–222.
- Underwood, L. & Jeremy, M. (2010). Optimal hand position for individual pursuit athletes, in A. Sabo, P. Kafka, S. Litzenberger & C. Sabo (eds), *The Engineering of Sport 8 - Engineering Emotion, Procedia Engineering*, vol.2, Elsevier, Amsterdam, pp. 2425–2429.

# Relationships between Large-Scale Coherent Motions and Bursting Events in a Turbulent Boundary Layer

Yasuhiko Sakai, Kouji Nagata and Hiroki Suzuki  
*Nagoya University*  
*Japan*

## 1. Introduction

A turbulent boundary layer (TBL) over a flat rigid surface can be seen in many industrial and environmental flows. Therefore, for the prediction and control of turbulence and design of better industrial apparatus, it is of great importance to elucidate the spatiotemporal structure of the TBL. In TBLs, it is well known that coherent motions associated with the bursting events exist near the wall. In the outer turbulent/nonturbulent (potential) interface of the TBL, large-scale coherent motions exist, which have the size of order of the boundary-layer thickness. The latter structures are called 'bulge' and 'valley' and are unsteady in space and time (Robinson 1991). Therefore, it is of importance to clarify the spatiotemporal structures of these coherent motions in order to elucidate the structure of the TBL. However, it is difficult to study the entire structure of the TBL by a single-point measurement using an I- or X-type hot-wire probe. In addition, previous studies (Ichijo & Kobashi 1982, Kobashi et al. 1984, Thomas & Bull 1983) have suggested that these coherent motions are closely associated with wall static pressure fluctuations. Therefore, the simultaneous measurement of multipoint instantaneous velocities and wall static pressure fluctuations is appropriate for clarifying the spatiotemporal structure of the TBL.

In this chapter, we will show the experimental results on the relationships between the bursting events occurring near the wall and the large-scale bulge and valley structures in the outer turbulent/nonturbulent interface of the TBL, and the spatiotemporal structures of the coherent motions in a zero-pressure-gradient TBL. With regard to the experiments, multipoint instantaneous streamwise velocities and instantaneous wall static pressures are simultaneously measured using a combination of a rake consisting of 23 I-type hot-wire probes, which covers the entire TBL, and a microphone pressure sensor. The velocity signals are analysed by the KL (Karhunen-Loève) expansion (also known as the proper orthogonal decomposition (POD) method). The flow field is reconstructed by using either lower- or higher-order modes to investigate the coherent motions in the TBL. The bursting events are detected by applying the VITA (Variable Interval Time Average) technique to the instantaneous velocity signals in the original flow. The large-scale bulge and valley structures are detected by using the newly proposed conditional sampling method, which is applied to both the original flow and the reconstructed flow by using the KL expansion. Further, to show the future research direction, the experimental data on the statistical

properties of TBL affected by the disturbances in the outer mainstream are demonstrated. The disturbances are generated using the bi-plane square grid. The effect of the disturbance on the velocity statistics is discussed.

## 2. Analytical methods

### 2.1 VITA technique

The VITA (Variable Interval Time Average) technique (Blackwelder & Kaplan 1976, Blackwelder & Haritonidis 1983, Chen & Blackwelder 1978, Osaka et al. 1986) is one of the conditional mean methods used to detect coherent motions in turbulent flows. The VITA technique is appropriate for detecting the bursting events in a TBL since the bursting events accompany the large velocity fluctuations. Following the general VITA technique (Blackwelder & Haritonidis 1983), we define the variable-interval time average of the fluctuating streamwise velocity  $\tilde{u}$  as

$$v_a(t; x, T) = \frac{1}{T} \int_{t-T/2}^{t+T/2} \tilde{u}(t')^2 dt' - \left[ \frac{1}{T} \int_{t-T/2}^{t+T/2} \tilde{u}(t') dt' \right]^2 \quad (1)$$

where  $T$  is the averaging time. Note that  $v_a$  approaches the conventional time-averaged result as  $T$  increases. The detection criterion is established by introducing a threshold value for the VITA variance signal. Thus, the detection function  $\alpha_u(t)$  is defined as (Blackwelder & Haritonidis 1983, Chen & Blackwelder 1978, Osaka et al. 1986)

$$\alpha_u(t) = \begin{cases} 1; v_a(t) \geq K u_{rms}^2 \text{ and } \frac{d}{dt} [\tilde{u}(t) - \bar{u}] > 0 \\ 0; \text{otherwise,} \end{cases} \quad (2)$$

where  $\bar{u}$  is the time-averaged mean velocity,  $u_{rms}$  is the rms (root mean square) value of velocity fluctuations, and  $K$  is the threshold value, which is constant. In general, the selection of  $K$  and  $T$  is important for detecting the bursting events using the VITA technique. In this study, we chose  $K=1$  and  $T^+ = T u_\tau^2 / \nu = 20$ , on the basis of a previous study (Osaka et al. 1986), where  $u_\tau$  is the friction velocity and  $\nu$  is the kinematic viscosity. We have carefully verified that the detected burst frequency is in a good agreement with previously published data (Blackwelder & Haritonidis 1983, Osaka et al. 1986).

### 2.2 Methods for detecting large-scale coherent motions

The large-scale coherent motions in the outer turbulent/nonturbulent interface of the TBL are detected using the following method. The first probe from the top of the rake, which is placed near the turbulent/nonturbulent interface of the TBL ( $y/\delta = 1.23$ ;  $y$  and  $\delta$  are the distance from the wall and the thickness of the boundary layer, respectively), is used to detect the large-scale coherent motions since these motions pass through this probe. The detection of the motions depends on both  $u$  and  $\partial u / \partial t$  at  $y/\delta = 1.23$ . Note that the direction of the rotation is based on the configuration shown in Figs. 1 and 2; the flow is from the left to the right along the  $x$ -direction. Therefore, the mean spanwise vorticity is in the clockwise direction.

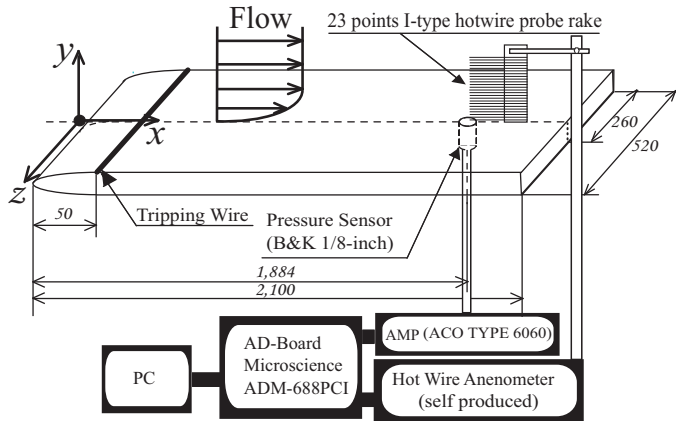


Fig. 1. Experimental setup

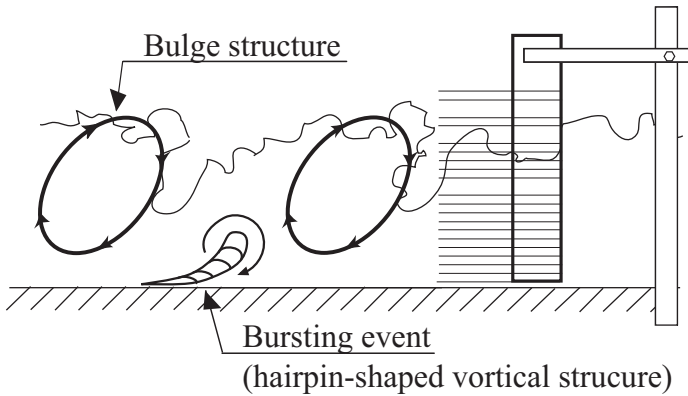


Fig. 2. Schematic of bulge structure and bursting event (not to scale)

**2.2.1 Detection of clockwise large-scale coherent motions**

The large velocity fluctuation at  $y / \delta = 1.23$  with *acceleration* is associated with the 'bulge' structure, which is the large-scale ( $\delta$ -scale) vortical structure rotating in the same direction as the mean vorticity (i.e. in the clockwise direction). Therefore, we detect the bulge structure by using the following conditions:

$$[\tilde{u}(t) - \bar{u}]^2 \geq K' u_{rms}^2 \quad \text{and} \quad \frac{d}{dt} [\tilde{u}(t) - \bar{u}] > 0 \tag{3}$$

where  $K'$  is the threshold value, which is constant. In this study, from a careful inspection of the detected signals,  $K'$  has been chosen equal to 3.

**2.2.2 Detection of anticlockwise large-scale coherent motions**

The large velocity fluctuation at  $y / \delta = 1.23$  with *deceleration* is associated with the 'valley' structure, which is the large-scale ( $\delta$ -scale) structure at the edge of the bulges (Robinson

1991) rotating in the opposite direction of the mean vorticity (i.e. in the anticlockwise direction). Therefore, we detect the valley structure by using the following conditions:

$$\left[ \tilde{u}(t) - \bar{u} \right]^2 \geq K' u_{rms}^2 \quad \text{and} \quad \frac{d}{dt} \left[ \tilde{u}(t) - \bar{u} \right] < 0 \quad (4)$$

It has been verified that the value of  $K' = 3$  is appropriate for detecting the valley structures.

### 2.3 KL expansion

The KL (Karhunen-Loève) expansion, which is also known as the proper orthogonal decomposition (POD) method and is an extension of the general Fourier series (Davenport & Root 1958, Lumley 1967, 1981), is the representation of a stochastic process as a linear combination of orthogonal functions. The basis functions of the expansion are defined such that the coefficients are uncorrelated (independent) with each other and are arranged in the descending order according to the magnitude of their eigenvalues. The sum of all the eigenvalues corresponds to the sum of the mean square values in the entire region where the KL expansion is applied. Here, the KL expansion is applied for the simultaneous measurement of the streamwise velocities at 23 points in the TBL. Therefore, there are 23 modes ( $n=1 \sim 23$ ) in the KL expansion. The lower modes are expected to extract the turbulence structures in the near-wall region (i.e., the inner region), where turbulence energy is larger, and the higher modes are expected to extract the turbulence structures from the outer region to the outside of boundary layer, where turbulence energy is smaller. In this study, the sum of the first three modes (lower modes) retains 65% of the total energy; therefore, the flow field reconstructed by using the lower modes ( $n=1 \sim 3$ ) is considered to represent the energetic coherent motions. The modes from 4 to 23, which contain the rest of the 35% energy, are regarded as the higher modes in this work.

## 3. Experiments

### 3.1 Experimental apparatus

Experiments are carried out in an Eiffel-type wind tunnel. The length, height, and span of the test section of this tunnel are 2,600, 300, and 520 mm, respectively. The TBL is developed along a smooth flat plate (Fig. 1) placed horizontally in the wind tunnel. The plate is 2,100 mm in length, 8 mm in thickness, and 520 mm in span and is made of Bakelite in order to reduce the heat loss from the hot-wire probe in near-wall measurements. The leading edge of the plate has a parabolic shape. To generate a fully developed TBL in a short distance from the leading edge, transition was promoted by using a tripping wire of 1.0 mm diameter placed 50 mm downstream from the leading edge of the plate, as shown in Fig. 1. The zero-pressure-gradient condition is achieved by adjusting the height of the test section. The coordinate system is as follows: the  $x$ -axis is along the streamwise direction starting from the leading edge, the  $y$ -axis is in the vertical direction, and the  $z$ -axis is along the spanwise direction (see Fig. 1).

### 3.2 Velocity and wall static pressure measurements

A constant-temperature hot-wire anemometer (CTA) is used for the velocity measurement. The rake consists of 23 I-type probes, which covers the entire TBL at  $x=1,884$  mm; the sensors of the rake cover a length of  $y=0.1 \sim 48.5$  mm. The wires are made of tungsten. The length of the sensor is  $l=1$  mm and its diameter is  $d=5 \mu\text{m}$ , giving an aspect ratio of

$l/d = 200$ . By comparing the data obtained from a single I-type probe with those from the rake of I-type probes, it has been confirmed that there is no interference between the probes, which are placed with 2.2 mm apart from each other.

To measure the instantaneous static pressure at the wall, the 1/8 inch microphone pressure sensor (Brüel & Kjær Type 4138) is used. The sensor is mounted flush to the wall surface at the measurement position ( $x = 1,884$  mm) through a pressure hole of  $D = 0.6$  mm diameter. The frequency response of the pressure sensor has been checked; both the phase difference  $\phi$  and the magnitude ratio  $M$  between the input signal and the output signal from the sensor exhibit flat responses up to 7 kHz. These results suggest that the frequency response limit of the pressure sensor is 7 kHz. Note that nondimensional diameter of the sensing area in this study is  $D^+ = Du_\tau/\nu = 18$ . Previous studies (Gravante et al. 1998, Schewe 1983) have shown that when  $D^+ < 19 \sim 20$ , the spatial resolution is sufficient to resolve the essential structures of the static pressure fluctuations at the wall. Therefore, in addition to the frequency response, the spatial resolution is sufficient to measure the static pressure fluctuations at the wall. In fact, we have confirmed that when  $D^+ < 18$ , the power spectra of wall static pressure fluctuations are identical.

### 3.3 Experimental conditions and data sampling method

The mean speed of the uniform flow is set at  $U_0 = 10.9$  m/s. The unit Reynolds number is  $Re = U_0/\nu = 7.38 \times 10^5 \text{ m}^{-1}$ , and the Reynolds number based on the momentum thickness at the measurement point ( $x = 1,884$  mm) is  $Re_\theta = 2,820$ . Note that the spatial resolution of the hot-wire probe in the near-wall measurement is sufficient for  $Re_\theta < 5,000$  (Robinson 1991). The  $\delta$  and  $u_\tau$  at the measurement point ( $x = 1,884$  mm) are 41 mm and 0.453 m/s, respectively. We have confirmed that there is no pressure gradient in the streamwise direction, and the mean flow is two-dimensional. The sampling frequency and sample size are 10 kHz and 229,376, respectively, and are sufficient to obtain reliable statistics: these parameters are based on the performance of the A/D converter (Microscience ADM-688PCI) and the computer (Dell Dimension 8200) used. The output voltage signals from the hot-wire anemometer and the pressure sensor are converted into 12-bit digital data by the A/D converter and recorded on the hard disc of the computer. The A/D converter and the digital output board are PCI interface boards and are synchronized through master-slave connections. The time lag between the output of the clock signal from the master unit and the input of the signal into the slave unit is only 125 ns; therefore, very fast multichannel sampling is achieved. To confirm this point, we input the same wave pattern generated by the function generator into the whole channels simultaneously, and compare the output signals. The result showed that the output signals are the same and no discernible time lag is observed. Statistical processing of the digitized data was carried out using the computer.

## 4. Results and discussion

### 4.1 Reliability of measurements

The vertical profile of streamwise mean velocity is shown in Fig. 3, where  $U^+ = U/u_\tau$  and  $y^+ = yu_\tau/\nu$ . The log-law region can be seen for  $30 < y^+ < 200$ . Figures 4 and 5 show the power spectrum of streamwise velocity fluctuations normalized by the squared rms value of

the velocity fluctuations,  $u_{rms}^2$ , and the power spectrum of the wall static pressure fluctuations normalized by the squared rms value of the wall static pressure fluctuations,  $p_{rms}^2$ , respectively. Figure 4 shows that the power spectrum of the longitudinal velocity fluctuations collapses irrespective of  $y^+$ . The spectrum also shows the -1 and -5/3 decay regions (Perry et al. 1986). On the other hand, the power spectrum of wall static pressure fluctuations (Fig. 5) has the -1, -7/3, and -5 decay regions, and the result agrees with that of previous experiments carried out by Gravante et al. (1998) and Löfdahl (1996). In addition, turbulence intensities and probability density functions (not shown) are in good agreement with those found in previous studies. Therefore, it is confirmed that the present measurements of velocity and wall static pressure fluctuations are highly accurate.

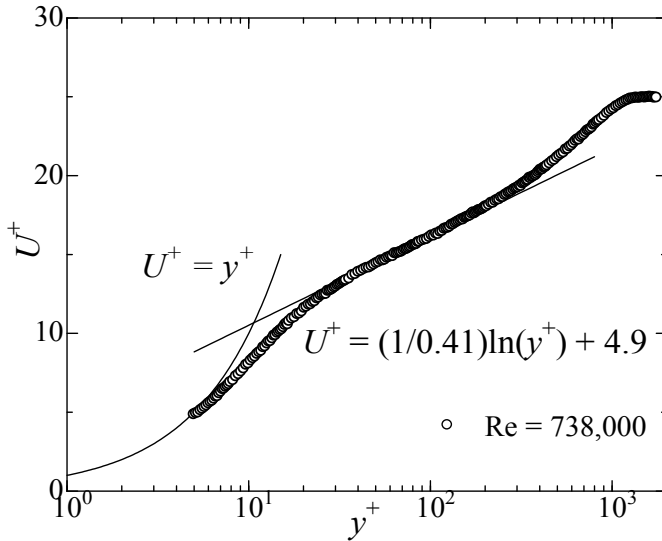


Fig. 3. Vertical profile of streamwise mean velocity

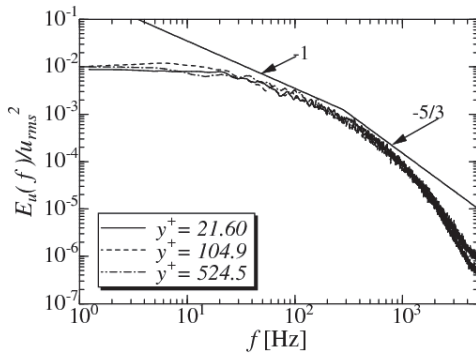


Fig. 4. Power spectrum of streamwise velocity fluctuations

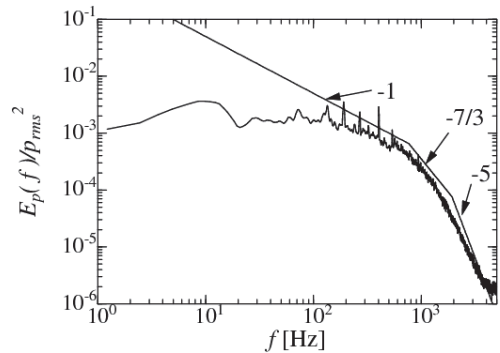


Fig. 5. Power spectrum of wall static pressure fluctuations



### 4.2 Relationships between bursting events and large-scale coherent motions

The clockwise and anticlockwise large-scale coherent motions are detected using the method proposed in the subsection 2.2, and the results are shown in Figs. 6 and 7, respectively. In Figs. 6 and 7, the upper and lower graphs show the conditionally averaged time histories of the normalized velocity,  $\langle \tilde{u}(\tau) \rangle' = (\langle \tilde{u}(\tau) \rangle - \bar{u}) / u_{rms}$ , and the conditionally averaged time histories of normalized wall static pressure,  $\langle \tilde{p}(\tau) \rangle' = (\langle \tilde{p}(\tau) \rangle - \bar{p}) / p_{rms}$ , respectively. Here,  $\langle \tilde{u}(\tau) \rangle$  and  $\langle \tilde{p}(\tau) \rangle$  are the ensemble-averaged values of conditionally sampled velocity and wall static pressure, respectively, and  $\bar{u}$  and  $\bar{p}$  are the ordinary (non-conditional) time-averaged velocity and wall static pressure, respectively. In Figs. 6 and 7,  $\tau$  is the time lag from the detection time at which the instantaneous velocity signal takes the maximum or minimum value at the detection point of  $y/\delta = 1.23$ , and is normalized by using  $U_0$  and  $\delta$ . Figure 6 shows that when the clockwise large-scale coherent motion passes, the velocity increases outside the TBL ( $y/\delta > 1$ ) and decreases inside the TBL ( $y/\delta < 1$ ). The result suggests the presence of a rotational flow whose center is located near the turbulent/nonturbulent interface: this structure corresponds to the bulge (Kobashi et al. 1984). It is also observed from Fig. 6 that the wall static pressure decreases when the clockwise large-scale coherent motion passes. It is presumed that measured decrease in the wall static pressure is associated with the low pressure in the clockwise large-scale coherent motion (Robinson 1991).

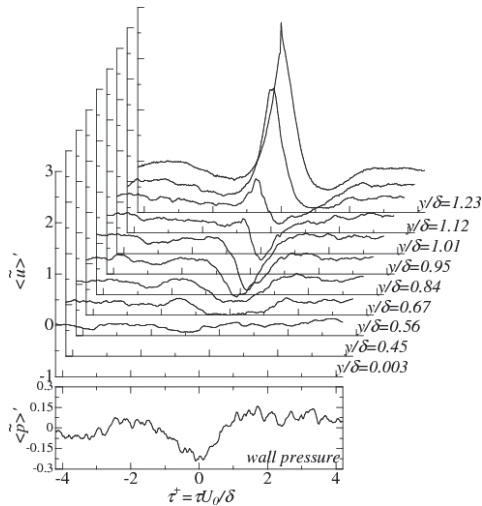


Fig. 6. Ensemble-averaged time histories of conditionally sampled velocity and wall static pressure corresponding to the bulge structure

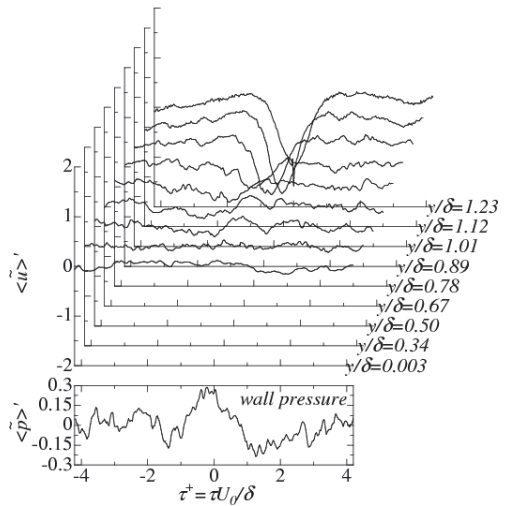


Fig. 7. Ensemble-averaged time histories of conditionally sampled velocity and wall static pressure corresponding to the valley structure

On the other hand, Fig. 7 shows that when the anticlockwise large-scale coherent motion passes, the velocity decreases outside the TBL ( $y/\delta > 1$ ) and slightly increases inside the TBL ( $y/\delta < 1$ ). The detected signals suggest the valley, which exists at the edge of the bulges. It

has been reported (Robinson 1991, Thomas & Bull 1983) that there is an inflow from the free-stream flow into the turbulent region, and the inflow has an instantaneous velocity vector that is against the mean flow. Therefore, it is expected that the decrease in the velocity in the outer region in Fig. 7 is associated with the inflow from the free-stream flow. The wall static pressure increases when the anticlockwise large-scale coherent motion passes. These results are in agreement with the model for the structure of a TBL proposed by Thomas & Bull (1983). The VITA technique is applied to the raw signals to detect the bursting events. Figure 8 shows the ensemble-averaged time histories of conditionally sampled velocity

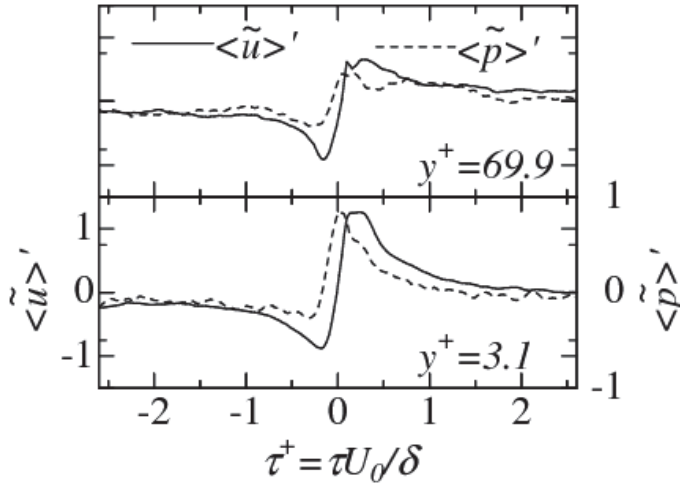


Fig. 8. Ensemble-averaged time histories of conditionally sampled velocity and wall static pressure. The detection is based on the VITA technique

$\langle \tilde{u}(\tau) \rangle' = (\langle \tilde{u}(\tau) \rangle - \bar{u}) / u_{rms}$  and of conditionally sampled wall static pressure  $\langle \tilde{p}(\tau) \rangle' = (\langle \tilde{p}(\tau) \rangle - \bar{p}) / p_{rms}$ . Here,  $\langle \tilde{u}(\tau) \rangle$  and  $\langle \tilde{p}(\tau) \rangle$  are the conditionally averaged velocity and wall static pressure by the VITA technique, respectively. The solid and broken lines in Fig. 8 denote  $\langle \tilde{u}(\tau) \rangle'$  and  $\langle \tilde{p}(\tau) \rangle'$ , respectively.  $\tau$  is the time lag from the detection time at which the instantaneous velocity  $\tilde{u}(t)$  is the same as the ordinary (non-conditional) time-averaged velocity  $\bar{u}$  at each measuring point. Figure 8 shows the cycle of events of ejection ( $\langle \tilde{u}(\tau) \rangle' < 0$ ) at  $\tau < 0$ , which is the upward motion of a low-speed fluid lump, and sweep ( $\langle \tilde{u}(\tau) \rangle' > 0$ ) at  $\tau > 0$ , which is the downward motion of a high-speed fluid lump (Osaka et al. 1986). The wall static pressure exhibits a rapid increase when the burst occurs above the measurement point (Kobashi et al. 1984). Considering the results shown in Figs. 6 and 7 together with the result in Fig. 8, it is concluded that the bulge structure, which is accompanied by the pressure decrease, cannot coexist with the bursting event, which is accompanied by the pressure increase. On the other hand, the valley structure, which is accompanied by the pressure increase, can coexist with the bursting event.

### 4.3 Flow field reconstructed by using lower modes ( $n=1 \sim 3$ )

Using the method proposed in the subsection 2.2, the clockwise and anticlockwise large-scale coherent motions are detected in the flow field reconstructed by using the lower

modes ( $n=1\sim 3$ ) of the KL expansion, and the results are shown in Figs. 9 and 10, respectively. Figures 9 and 10 show that both the clockwise large-scale coherent motion (i.e. bulge), which is accompanied by the pressure decrease, and the anticlockwise large-scale coherent motion (i.e. valley), which is accompanied by the pressure increase, exist in

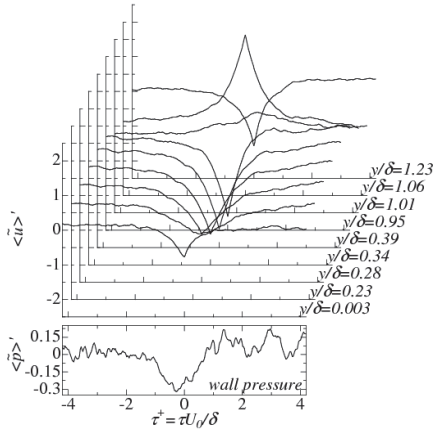


Fig. 9. Ensemble-averaged time histories of conditionally sampled velocity and wall static pressure when the velocity is reconstructed by the lower modes ( $n=1\sim 3$ ) and the detection method of the clockwise bulge structure is applied.

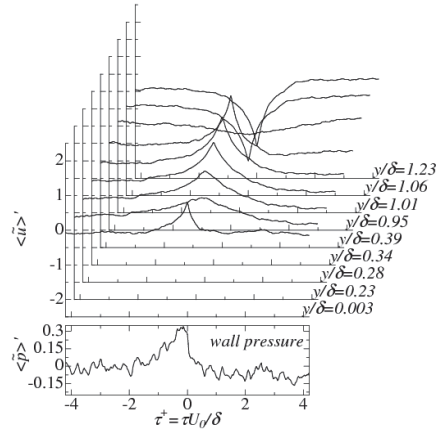


Fig. 10. Ensemble-averaged time histories of conditionally sampled velocity and wall static pressure when the velocity is reconstructed by the lower modes ( $n=1\sim 3$ ) and the detection method of the anticlockwise valley structure is applied.

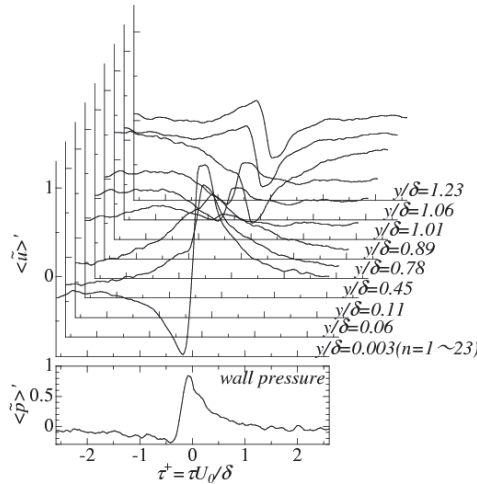


Fig. 11. Ensemble-averaged time histories of conditionally sampled velocity and wall static pressure when the velocity is reconstructed by the lower modes ( $n=1\sim 3$ ). The detection is based on the VITA technique applied to the original flow field ( $n=1\sim 23$ ) at  $y/\delta = 0.003$

the flow field reconstructed by using the lower modes. Comparing these results with those shown in Figs. 6 and 7, which are obtained by applying the method to the original flow field ( $n=1\sim 23$ ), it is found that these structures are more clearly observed in the flow field reconstructed by using the lower modes and they are observed even near the wall.

Figure 11 shows the ensemble-averaged time histories of conditionally sampled velocity and wall static pressure when the velocity is reconstructed by the lower modes ( $n=1\sim 3$ ) and the detection by the VITA technique is applied to the original flow field ( $n=1\sim 23$ ) at  $y/\delta=0.003$ . It is observed from Fig. 11 that the velocity inside the TBL (in the reconstructed flow) increases and the velocity outside the TBL (in the reconstructed flow) decreases when the bursting event occurs. These velocity patterns are similar to those during the anticlockwise large-scale coherent motion (i.e. valley). Thus, the results suggest that the bursting event and valley can coexist at the same longitudinal location in the flow reconstructed by using the lower modes ( $n=1\sim 3$ ).

#### 4.4 Flow field reconstructed by using higher modes ( $n=4\sim 23$ )

Using the method proposed in the subsection 2.2, the clockwise and anticlockwise large-scale coherent motions are detected in the flow field reconstructed by using the higher modes ( $n=4\sim 23$ ) of the KL expansion, and the results are shown in Figs. 12 and 13, respectively. Figure 12 (for the bulge) shows a velocity variation near the wall. However, the velocity hardly changes near the wall in Fig. 13 (for the valley). These results suggest that in the flow field reconstructed by using the higher modes, only the clockwise large-scale

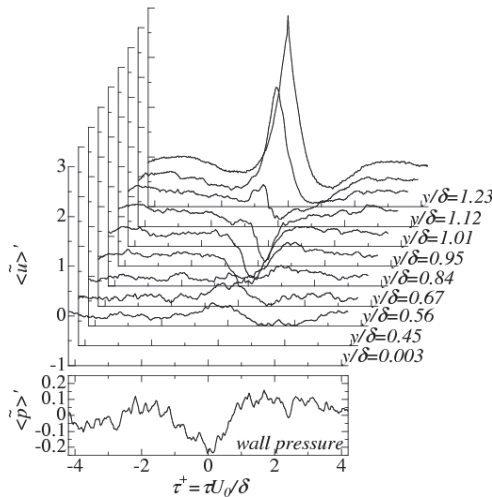


Fig. 12. Ensemble-averaged time histories of conditionally sampled velocity and wall static pressure when the velocity is reconstructed by the higher modes ( $n=4\sim 23$ ) and the detection method of the clockwise bulge structure is applied.

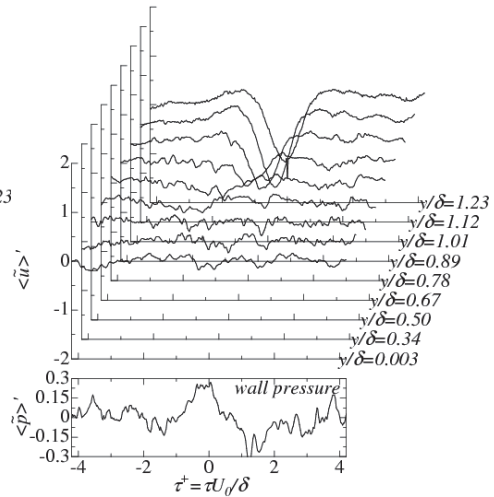


Fig. 13. Ensemble-averaged time histories of conditionally sampled velocity and wall static pressure when the velocity is reconstructed by the higher modes ( $n=4\sim 23$ ) and the detection method of the anticlockwise valley structure is applied.

coherent motion (i.e. bulge) exists near the wall and the anticlockwise large-scale coherent motion (i.e. valley) does not influence the flow field near the wall. These results also suggest that the turbulent kinetic energy in the bulge structure is larger than that in the valley structure. This result is consistent with the fact that the valley is generated by the bulge structures. Figure 14 shows the ensemble-averaged time histories of conditionally sampled velocity and wall static pressure when the velocity is reconstructed by the higher modes ( $n = 4 \sim 23$ ) and the detection by the VITA technique is applied to the original flow field ( $n = 1 \sim 23$ ) at  $y/\delta = 0.003$ . Figure 14 shows that when the bursting events are detected, the velocity in the outer region does not change in the reconstructed flow. This result suggests that in the flow field reconstructed by using the higher modes, the large-scale coherent motions are weakly associated with the bursting events.

#### 4.5 Effect of freestream turbulence on the Turbulent Boundary Layer

In the industrial flows such as those in turbomachines and heat exchangers, inflow streams often contain the turbulent eddies generated by the upstream structures. These free stream turbulence influences the large scale coherent structure and the turbulence characteristics of the TBL. In this subsection, some experimental data on the statistical properties of TBL affected by the freestream turbulence generated by the square grid are demonstrated.

The experiments are performed by using the experimental apparatus shown in the subsection 3.1. The turbulence-generating grid is installed at 100mm upstream from the leading edge of the plate. The square-mesh biplane grid M10 is used. M10 was constructed from square-sectioned aluminium rods. The mesh size  $M$  and the rod thickness  $d$  are  $3 \times 10^{-2}$ m and  $6 \times 10^{-3}$ m, respectively, and therefore, its solidity is  $\sigma = 0.36$ . The mean speed of free stream flow when the grid is installed is set at  $U_0 = 10.1$ m/s. The unit Reynolds number is  $Re = U_0/\nu = 6.84 \times 10^5 \text{m}^{-1}$  and the Reynolds number based on the momentum thickness at the measurement point ( $x=1,880$  mm) is  $Re_\theta = 3,000$ . When the grid is not installed, the flow condition is adjusted to realize  $Re_\theta = 3,000$  at the same measurement point ( $x=1,880$  mm). The instantaneous streamwise velocity is measured by the hot-wire CTA with the I-type probe. The wire is made of tungsten. The length of sensor is 1.0 mm and its diameter is  $5\mu\text{m}$ , giving an aspect ratio of  $l/d = 200$ . The output signals from the CTA are digitized and recorded on the hard disc using the data recording unit (KEYENCE WR-60). The sampling frequency and sample size are 20 kHz and  $524,288 (=2^{19})$ , respectively.

The vertical profiles of  $y^+ dU^+/dy^+$  in both cases with and without the grid are shown in Fig.15, where the result by the Direct Numerical Simulation (DNS) in the case of  $Re_\theta = 1,410$  (Spalart 1988) is also depicted for the comparison. Note that in the logarithmic region the value of  $y^+ dU^+/dy^+$  should be constant, i.e.,  $y^+ dU^+/dy^+ = 1/\kappa$ . From Fig.15, it is found that the logarithmic region for the case with the grid expands to the outer side of the TBL in comparison with the case without the grid. Figure 16 shows the vertical profiles of the velocity fluctuation rms value  $u_{rms}$  normalized by the friction velocity  $u_\tau$  i.e.,  $u_{rms}^+ = u_{rms}/u_\tau$ . It is found that  $u_{rms}^+$  in the case with the grid increases in comparison with the case without the grid. However it should be noted that in general the free-stream disturbance does not always increase  $u_{rms}^+$ , and in some cases  $u_{rms}^+$  decreases (Hancock & Bradshaw 1989, Nagata et al. 2011). The effects of free-stream disturbance on the characteristics of the TBL are still open question. The future works are expected to elucidate the relation between the free-stream disturbance and the flow dynamics of the TBL.

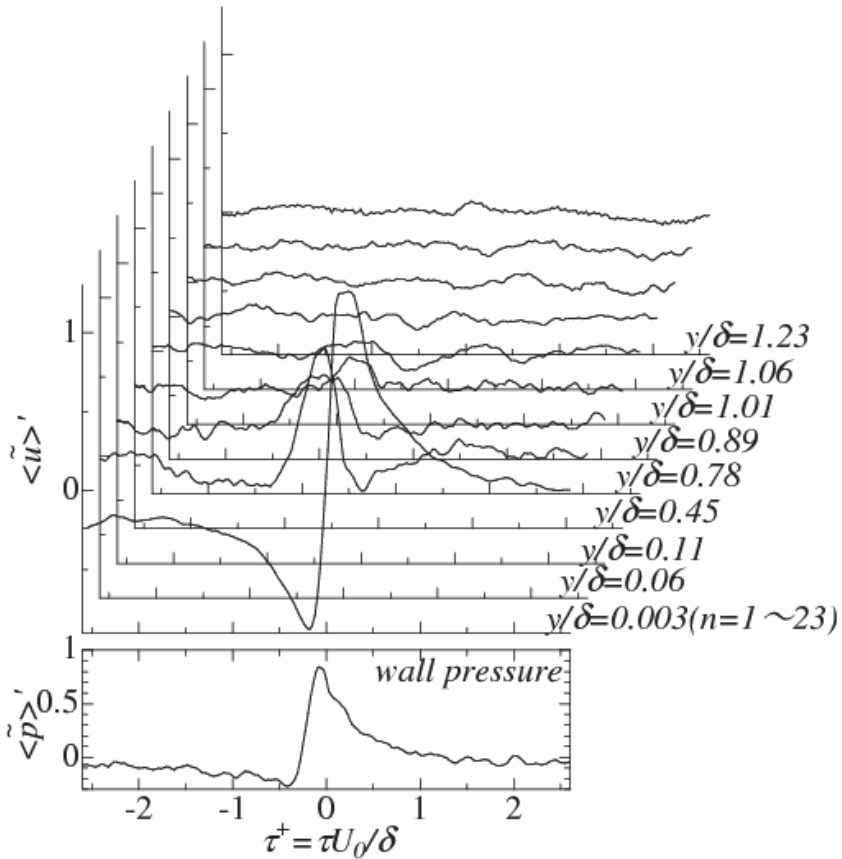


Fig. 14. Ensemble-averaged time histories of conditionally sampled velocity and wall static pressure when the velocity is reconstructed by the higher modes ( $n = 4 \sim 23$ ). The detection is based on the VITA technique applied to the original flow field ( $n = 1 \sim 23$ ) at  $y/\delta = 0.003$

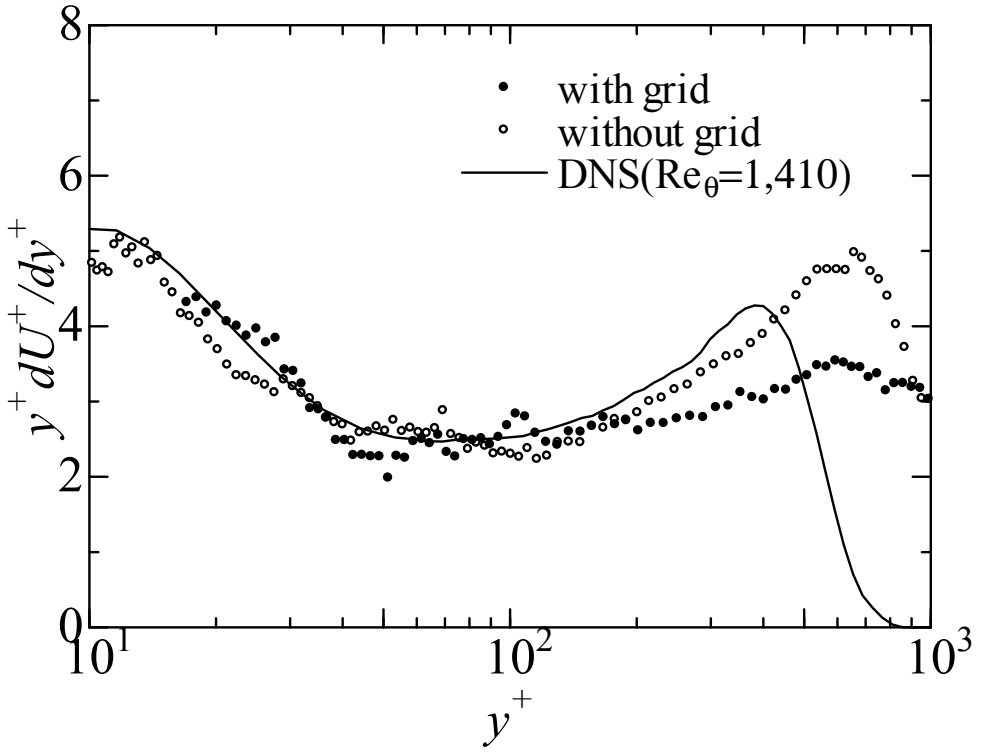


Fig. 15. The vertical profiles of  $y^+ dU^+/dy^+$

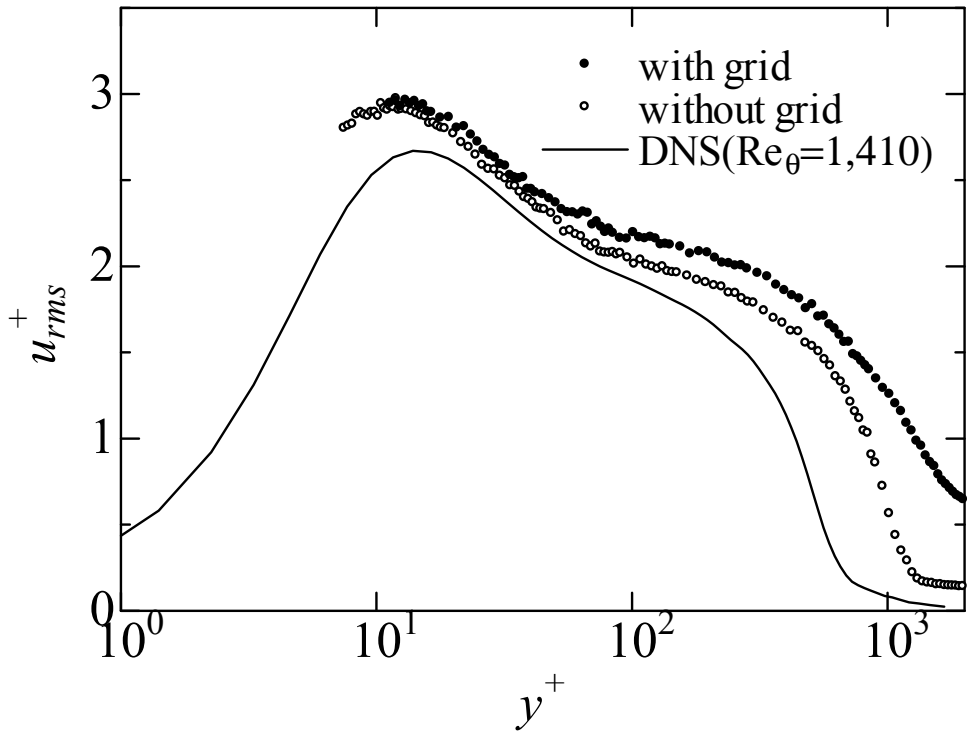


Fig. 16. The vertical profiles of  $u_{rms}^+$



## 5. Conclusions

Multipoint instantaneous streamwise velocities and instantaneous wall static pressures have been simultaneously measured by using a combination of a rake consisting of 23 I-type hot-wire probes and a microphone pressure sensor in a fully developed, zero-pressure-gradient turbulent boundary layer (TBL) in a wind tunnel. The KL (Karhunen-Loève) expansion, the VITA technique and the newly proposed method for the detection of large-scale coherent motions were applied to examine the relationships between large-scale coherent motions and the bursting events. Further, the statistical properties of the TBL affected by the freestream turbulence generated by the square grid were investigated.

The main results obtained in this chapter are summarized as follows:

1. The structure of the TBL inferred from the present experiment is in agreement with the TBL model proposed by Thomas & Bull (1983).
2. The bursting events and valley structure (both accompanied by an increase in wall static pressure) can coexist at the same longitudinal location, whereas the bursting events and bulge structure cannot coexist with each other.
3. In the flow field reconstructed by using the lower modes, both the bulge structure, which is accompanied by bursting events, and the valley structure, which is not accompanied by the bursting events, exist. On the other hand, in the flow field reconstructed by using the higher modes, the large-scale coherent structures are weakly associated with the bursting events.
4. The grid turbulence introduced into the outer mainstream has the effect to enlarge the logarithmic region to the outer side of turbulent boundary layer.

## 6. Acknowledgment

This study was partially supported by the Japanese Ministry of Education, Culture, Sports, Science and Technology through Grants-in-Aid (Nos. 22360076 and 22360077).

## 7. References

- Blackwelder, R. F. & Kaplan, R. E. (1976). On the Wall Structure of the Turbulent Boundary Layer. *Journal of Fluid Mechanics*, Vol.76, pp.89-112
- Blackwelder, R. F. & Haritonidis, J. H. (1983). Scaling of the Bursting Frequency in Turbulent Boundary Layers. *Journal of Fluid Mechanics*, Vol.132, pp.87-103
- Blair, M. F. (1983). Influence of free-stream turbulence on turbulent boundary layer heat transfer and mean profile. Part 1 - Experimental Data. *Transactions of the ASME: Journal of Heat Transfer*, Vol.15, pp.33-40
- Chen, C-H. P. & Blackwelder, R. F. (1978). Large-scale Motion in a Turbulent Boundary Layer: A Study Using Temperature Contamination. *Journal of Fluid Mechanics*, Vol.89, pp.1-31
- Gravante, S. P.; Naguib, A. M.; Wark, C. E. & Nagib, H. M. (1998). Characterization of the Pressure Fluctuations Under a Fully Developed Turbulent Boundary Layer. *AIAA Journal*, Vol. 36, No. 10, pp.1808-1816
- Davenport, W. B. Jr. & Root, W. L. (1958). *An Introduction to the Theory of Random Signals and Noise*, pp.96-101, McGraw-Hill

- Hancock, P.E. & Bradshaw, P. (1989). Turbulence Structure of a Boundary Layer Beneath a Turbulent Free Stream. *Journal of Fluid Mechanics*, Vol.205, pp.45-76
- Hoffman, J. A. (1981). Effects of free-stream turbulence on diffuser performance, *Transactions of the ASME: Journal of Fluids Engineering*, Vol.103, pp.385-390
- Ichijo, M. & Kobashi, Y. (1982). The Turbulence Structure and Wall Pressure Fluctuations of a Boundary Layer. *Nagare*, Vol.1, pp. 350-359
- Kobashi, Y.; Komoda, H. & Ichijo, M. (1984). Wall Pressure Fluctuation and the Turbulent Structure of a Boundary Layer. In: *Turbulence and Chaotic Phenomena in Fluids*, ed. Tatsumi, T., pp.461-466, Elsevier
- Löfdahl, L. (1996). Small Silicon Pressure Transducers for Space-Time Correlation Measurements in a Flat Plate Boundary Layer. *Transactions of ASME: Journal of Fluids Engineering*, Vol.118, pp.457-463
- Lumley, J. L. (1967). The Structure of Inhomogeneous Turbulent Flows. In: *Atmospheric Turbulence and Radio Wave Propagation*, eds. Yaglom, A. M. and Tararsky, V. I., pp.166-178. Nauka, Moscow
- Lumley, J. L. (1981). In: *Transition and Turbulence*, ed. Meyer, R. E., pp.215-241. Academic, New York
- McDonald, H. & Fish, R.W. (1973). Practical Calculations of Transitional Boundary Layers. *International Journal of Heat and Mass Transfer*, Vol.16, pp.1729-1744
- Nagata, K.; Sakai, Y. & Komori, S. (2011). Effects of Small-Scale Freestream Turbulence on Turbulent Boundary Layers with and without Thermal convection. *Physics of Fluids*, in press
- Osaka, H.; Mochizuki, S. & Nishi, S. (1986). On the Detection of the Bursting Events with the VITA Technique. *Transactions of the Japan Society of Mechanical Engineers, Series B* (in Japanese). Vol.52, No.481, pp.3224-3229
- Perry, A. E.; Henbest, S. & Chong, M. S. (1986). A Theoretical and Experimental Study of Wall Turbulence. *Journal of Fluid Mechanics*, Vol.165, pp.163-199
- Robinson, S. K. (1991). Coherent Motions in the Turbulent Boundary Layer. *Annual Review of Fluid Mechanics*, Vol.23, pp. 601-639
- Schewe, G. (1983). On the Structure and Resolution of Wall-pressure Fluctuations Associated with Turbulent Boundary-layer Flow. *Journal of Fluid Mechanics*, Vol.134, pp.311-328
- Spalart, P. R. (1988). Direct Simulation of a Turbulent Boundary Layer up to  $R_\theta = 1410$ . *Journal of Fluid Mechanics*, Vol.187, pp.61-98
- Thomas, A. S. W. & Bull, M. K. (1983). On the Role of Wall-pressure Fluctuations in Deterministic Motions in the Turbulent Boundary Layer. *Journal of Fluid Mechanics*, Vol.128, pp.283-322

# Wavelet Analysis to Detect Multi-scale Coherent Eddy Structures and Intermittency in Turbulent Boundary Layer

Jiang Nan<sup>1,2</sup>

<sup>1</sup>Department of Mechanics, Tianjin University

<sup>2</sup>Tianjin Key Laboratory of Modern Engineering Mechanics, China

## 1. Introduction

In the early stage of turbulence study, turbulent flow was deemed fully random and disorder motions of fluid particles. Thus physical quantity describing turbulence was considered as the composition of random fluctuations in spatial and temporal field. Reynolds (1895) divided the turbulent field into mean field and fluctuating field and then theories and methods based on statistics for turbulence research were developed. Kolmogorov<sup>[1]</sup> analyzed the relative motion of fluid particles in fully development isotropic and homogeneous turbulent flow based on random field theory and presented the concept of structure functions, which described the relative velocity of two fluid particles separated by distance of  $l$ , to investigate the statistical scaling law of turbulence:

$$\langle |\delta u(l)|^p \rangle \propto l^{\zeta(p)} \quad \eta \ll l \ll L \quad (1)$$

Where  $\delta u(l) = u(x+l) - u(x)$  is the velocity component increment along the longitudinal direction at two positions  $x$  and  $x+l$  respectively separated by a relative separation  $l$ ,  $\eta$  is the Kolmogorov dissipation scale of turbulence,  $L$  is the integral scale of turbulence,  $\langle \rangle$  denotes ensemble average and  $\zeta(p)$  is scaling exponent.

Kolmogorov (1941)<sup>[1]</sup> successfully predicted the existence of the inertial-range and the famous the linear scaling law which is equivalent to the -5/3 power spectrum:

$$\zeta(p) = \frac{p}{3} \quad (2)$$

Because of the existence of intermittence of turbulence, scaling exponents increases with order nonlinearly which is called anomalous scaling law. In 1962, Kolmogorov<sup>[2]</sup> presented Refined Similarity Hypothesis, and thought that the coarse-grained velocity fluctuation and the coarse-grained energy dissipation rate are related through dimensional relationship:

$$\langle \delta u(l) \rangle \propto (\varepsilon_1 l)^{1/3} \quad (3)$$

$$\langle \varepsilon_1^p \rangle \propto l^{\tau(p)} \quad (4)$$

Where  $\varepsilon_1$  is the coarse-grained turbulent kinetic energy dissipation rate over a ball of size of  $l$ .

So it yields the relationship between the scaling exponent  $\zeta(p)$  for the velocity structure function and the scaling exponent  $\tau_p$  for the turbulent kinetic energy dissipation rate function as:

$$\zeta(p) = \frac{p}{3} + \tau\left(\frac{p}{3}\right) \quad (5)$$

Jiang<sup>[3]</sup> has demonstrated that scaling exponents of turbulent kinetic energy dissipation rate structure function is independent of the vertical positions normal to the wall in turbulent boundary layer, so the scaling law of dissipation rate structure function is universal even in inhomogeneous and non-isotropic turbulence. However, scaling exponent,  $\zeta(p)$ , is very sensitive to the intermittent structures and is easy to change with the different type of shear flow field because the most intermittent structures change with spatial position and direction<sup>[4]-[8]</sup>. The systematic change of  $\zeta(p)$  shows the variation of physical flow field<sup>[9]</sup>. Scaling exponent,  $\zeta(p)$ , has been found to be smaller in wall turbulence than that in isotropic and homogeneous turbulence by G Ruiz Chavarria<sup>[5]</sup> and F.Toschi<sup>[6][7]</sup> both in numerical and physical investigations. The scaling laws appear to be strongly depending on the distance from the wall. The increase of intermittence near the wall is related to the increase of mean shear of velocity gradient.

After 1950s', turbulent fluctuation was extendedly studied with the development of experimental technique of fluid mechanics. Large-scale motions, which were relatively organized and intermittent, were found in jet flow, wake flow, mixing layer and turbulent boundary layer. This kind of large-scale structure was universal and repeatable on intensity, scale shape and process to a certain type of shear flow. So it was called coherent structure (or organized motion). Research on coherent structure done by Kline group (1967)<sup>[10]</sup> of Stanford University, a great breakthrough in the study of turbulent boundary layer, found the low-speed streak structure and burst in the near wall region. This result, which has been verified by Corino(1969)<sup>[11]</sup> · Kim (1971)<sup>[12]</sup> and Smith (1983)<sup>[13]</sup>, is one of a few conclusions universally accepted in this field. The discovery of coherent structures, a great breakthrough in turbulent study, which has greatly changed traditional view of turbulent essence, indicates the milestone of study on turbulence essence from disorder stage to organized stage<sup>[14]</sup>.

Coherent structures exist not only in large scales, but also in small scales<sup>[15][16]</sup>. Indeed, as indicated by Sandborn<sup>[17]</sup> in 1959, who analyzed band passed signals, the presence of low speed streaks might be indicated by "bursts in the over all frequencies". In recent years, universal and organized small-scale coherent structures have been discovered in turbulent flows. The recently experimental measurements and DNS results present that small-scale filamentary coherent structures also exist in homogeneous and isotropic turbulence<sup>[18]-[21]</sup>. G Ruiz Chavarria<sup>[5]</sup>, F.Toschi<sup>[6][7]</sup>, Ciguel Onorato<sup>[8]</sup> R. Camussi<sup>[15]</sup>, T. Miyauchi<sup>[16]</sup> discovered that small-scale coherent structures also exist in turbulent channel flow and turbulent boundary layer with strong intermittency. Using the detection criterion for multi-scale coherent eddy structure, the anomalous scaling law, as well as intermittency of turbulence,

is found to be dependent on the probability density functions of structure function characterized by increasingly wider tails [8][22].

However, in spite of all of above improvements, the dynamical mechanism and behavior of multi-scale coherent structure has been unclear. The relationship between the statistical intermittency and the dynamics for the multi-scale coherent structure still remains poorly understood. Researchers are very actively trying to explain the underlying physical mechanism of intermittency and multi-scale coherent structures in shear turbulence. Dynamical description of intermittency and multi-scale coherent structures in shear turbulence has become one of the most fascinating issues in turbulence research. The advance of research on the intermittency of multi-scale coherent structures in shear turbulence have an important impact on establishing more effective numerical simulation method and sub-grid scale model based on the decomposition of multi-scale structures. Characterizing the intermittency of multi-scale coherent structures in shear turbulence in terms of their physics and behavior still should be undertaken as a topic of considerable study. Farge [23] has recently presented a coherent vortex simulation method instead of wave number decompositions generally used. This new method is in coincidence with the physical characteristics of turbulence and provides a new access to direct numerical simulation. Charles Meneveau [24] has recently advanced some new physical concepts, such as turbulent fluctuation kinetic energy, transfer of turbulent fluctuation kinetic energy, flux of turbulent fluctuation kinetic energy and so on, which is the foundation to set up more effective turbulence model and sub-grid scale model.

In this chapter, we concentrate on some fundamental characteristics of intermittency and multi-scale coherent structures in turbulent boundary layer. We separate turbulence fluctuating velocity signals into two components based on information of wavelet transform, one component containing multi-scale coherent structure characterized by intermittency, while the other containing the remaining portion of the signal essentially characterized by the random component. The organization is as follow: in section 2, wavelet transform and its applications to turbulence research is introduced. In section 3, the experimental apparatus and technique are described. The results and discussion are given in section 4 and finally, conclusions are drawn in section 5.

## 2. Multi-scale coherent eddy structure detection by wavelet transforms

### 2.1 Wavelet transform

Wavelet transform[25] is a mathematic technique developed in last century for signals processing. It convolutes signals with an analytic function named wavelet at a definite position and a definite scale by means of dilations and translations of mother wavelet. It provides a two-dimensional unfolding of one-dimensional signals resolving both the position and the scale as independent variables. So it comprises a decomposition of signals both on position and scale space simultaneously.

Wavelet is a local oscillation or perturbation with definite scale and limited scope in certain location of physical time or space. If a function  $\psi(t) \in L^2(\mathbb{R})$  satisfies the so-called “admissibility” condition :

$$C_{\psi} = \int_{-\infty}^{+\infty} \frac{|\hat{\psi}(\omega)|^2}{|\omega|} d\omega < +\infty \quad (1)$$

Where  $\hat{\psi}(\omega)$  is the Fourier transform of  $\psi(t)$ ,  $\psi(t)$  is called a "mother wavelet".

Relative to every mother wavelet  $\psi(t)$ ,  $\psi_{ab}(t)$  is the translation (by factor  $b$ ) and dilatation (by factor  $a > 0$ ) of  $\psi(t)$ :

$$\psi_{ab}(t) = \frac{1}{\sqrt{a}} \psi\left(\frac{t-b}{a}\right) \text{ with } a, b \in R \text{ and } a > 0 \quad (2)$$

The wavelet transform  $\psi_f(a, b)$  of signal  $s(t) \in L^2(R)$  with respect to  $\psi_{ab}(t)$  is defined as their scalar product defined by:

$$\psi_s(a, b) = \int_{-\infty}^{+\infty} s(t) \overline{\psi_{ab}(t)} dt \quad (3)$$

The total energy of the signal can be decomposed by:

$$E = \int_{-\infty}^{+\infty} |s(t)|^2 dt = \int_0^{+\infty} \frac{da}{a^2} \int_{-\infty}^{+\infty} \frac{2}{C_\psi} |\psi_s(a, b)|^2 db = \int_0^{+\infty} \frac{da}{a^2} \int_{-\infty}^{+\infty} I(a, b) db \quad (4)$$

with

$$I(a, b) = \frac{2}{C_\psi} |\psi_s(a, b)|^2 \quad (5)$$

and

$$E(a) = \langle I(a, b) \rangle_b \quad (6)$$

where  $\langle \rangle_b$  denotes ensemble average over parameter  $b$ .

Equation (5) is the local wavelet spectrum function and equation (6) is the multi-scale wavelet spectrum function respectively. Based on equation (5), the kinetic energy of signal is decomposed into one-to-one local structures with definite scale  $a$  at definite location  $b$ . Wavelet spectrum function defined by (6) means the integral kinetic energy on all structures with individual length scale  $a$ .

On the concept of wavelet transformation, skew factor of multi-scale eddy structure can be defined by wavelet coefficient as:

$$Sk(a) = \frac{\langle \psi_s(a, b)^3 \rangle_b}{[E(a)]^{3/2}} \quad (7)$$

Skew factor is the enhancement of wavelet coefficient  $\psi_f(a, b)$ , which is capable of revealing the signal variation across scale parameters. So skew factor is the qualitative indicator of intermittency of multi-scale structure.

Another indicator of intermittency is the flatness factor of the wavelet coefficients:

$$FF(a) = \frac{\langle \psi_s(a, b)^4 \rangle_b}{[E(a)]^2} \quad (8)$$

Flatness factor is the enhancement of the amplitude of wavelet coefficient  $\psi_f(a, b)$  in spite of its sign, which is capable of revealing the amplitude difference of wavelet coefficient across scale parameters.

## 2.2 Wavelet and turbulence eddy

Wavelet transform provides the most suitable elementary representation of turbulent flows. "Eddies" are the fundamental element in turbulent flows. As TENNEKES & LUMLEY<sup>[27]</sup> pointed out "An eddy, however, is associated with many Fourier coefficients and the phase relations among them. Fourier transforms are used because they are convenient (spectra can be measured easily); more sophisticated transforms are needed if one wants to decompose a velocity field into eddies instead of waves." Eddy and wavelet share common features in many physical aspects, and wavelet can be regarded as the mathematical mode of an eddy structure in turbulent flows<sup>[28][29]</sup>. As a new tool, wavelet transform can be devoted to identify coherent structure in wall turbulence instead of the conditional sampling methods traditionally used. JIANG<sup>[30]</sup> has performed the wavelet decompositions of the longitudinal velocity fluctuation in a turbulent boundary layer. The energy maximum criterion is established to determine the scale that corresponds to coherent structure. The coherent structure velocity is extracted from the turbulent fluctuating velocity by wavelet inverse transform.

Figure 1 presents the time trace signal of instantaneous longitudinal velocity measured by hot-wire probe in the buffer sub-layer of turbulent boundary layer with its wavelet coefficients contour transformed by wavelet transform. From the standard (a,t) plane representation of the wavelet coefficients, it can be seen that there exist one-to-one events at different positions and different scales correspond to the signal. The large-scale eddies seem to be randomly distributed and are fairly space filling. A typical process in which a large eddy creates two or more small eddies can be seen clearly. This subdivision repeats until eddies reach the scale at which they are readily dissipated by the fluid viscosity. There is a kinetic energy flux from larger eddies to smaller ones. The smaller eddies obtain their energy at the expense of the energy loss in larger eddies. In turbulent boundary layer, the colorful spots have special physical meaning related to the coherent structures burst events which are the most important structures in wall turbulence and contribute most to the turbulence production in the near wall region. The red spots represent the accelerating events at different scales which are the high-speed fluids sweep to the probe and cause the high-speed velocity output from the hot-wire probe while the blue spots stand for the decelerating events which is the low-speed fluids eject from the near wall region to the probe and cause the low-speed velocity output from the hot-wire probe.

Figure 2(a) shows the typical shape of an "eddy" correlation function and spectral function proposed by TENNEKES & LUMLEY<sup>[27]</sup> based on turbulence interpretation. Figure 2(b) shows the typical shape of a wavelet both in correlation function and spectral space. Figure 2(c) shows the shape of an "eddy" of turbulence both in correlation function and spectral space obtained by wavelet decomposition from turbulent flow in experimental measurement. From figure 2(a), figure 2(b) and figure 2(c), it can be found that they are fit each other.

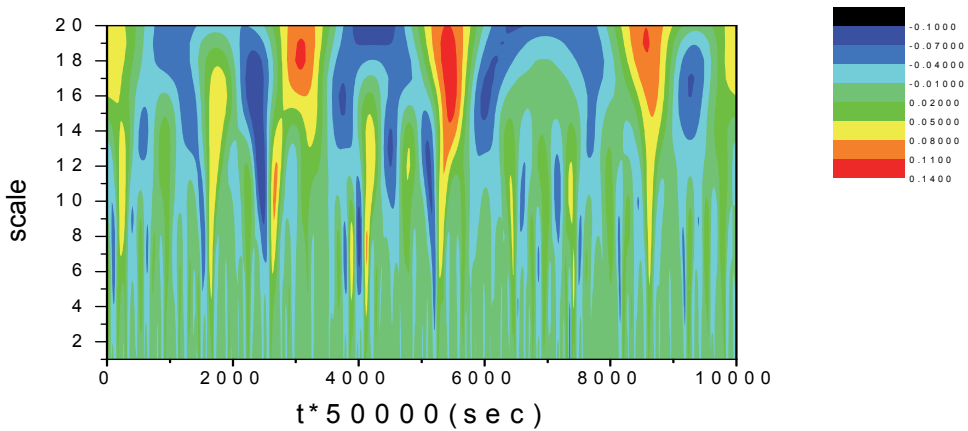
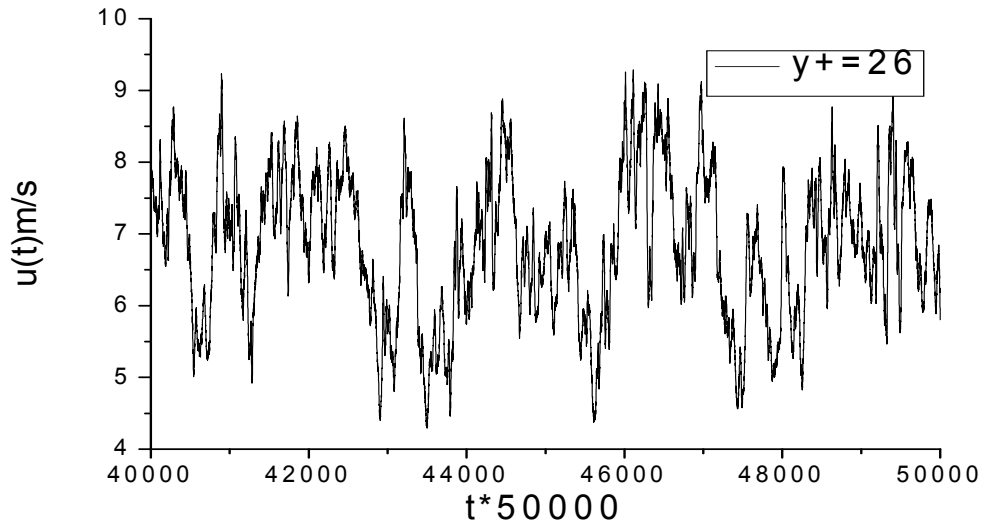


Fig. 1. Wavelet coefficients magnitude contour of the longitudinal fluctuating velocity signal



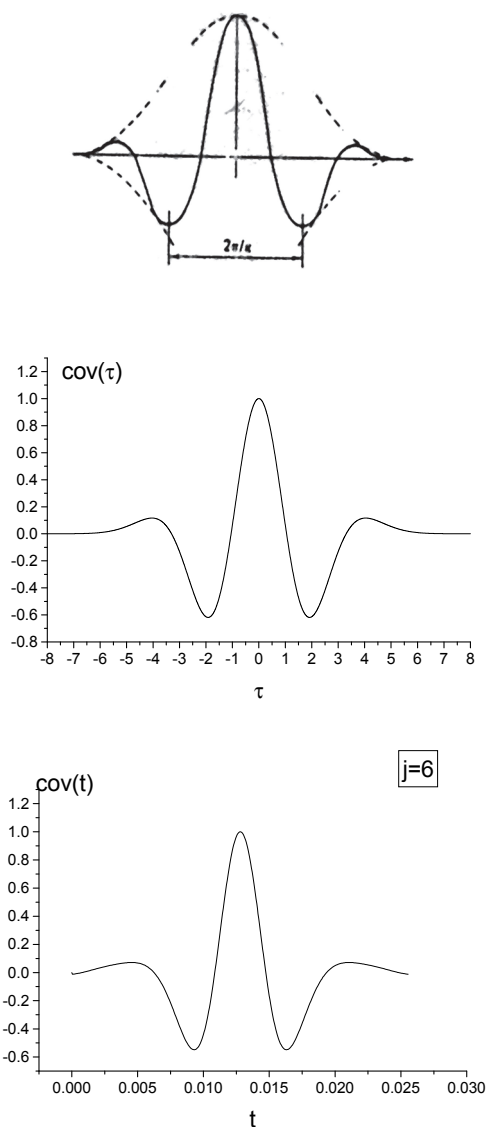


Fig. 2. An eddy typical shape defined by (a) TENNEKES & LUMLEY<sup>[27]</sup> based on turbulence interpretation (b) a wavelet function (c) wavelet transform of turbulent flow

Figure 3 is the eddy structure velocity signals for each single scale decomposed by wavelet transform. Figure 4 is the correlation functions of them. They are in agreement with the concept of a typical “eddy” structure proposed by TENNEKES & LUMLEY<sup>[27]</sup> for turbulence interpretation. The eddy wavelength for each scale can be measured between the troughs of the correlation functions as defined by TENNEKES & LUMLEY<sup>[27]</sup> in figure 2(a).

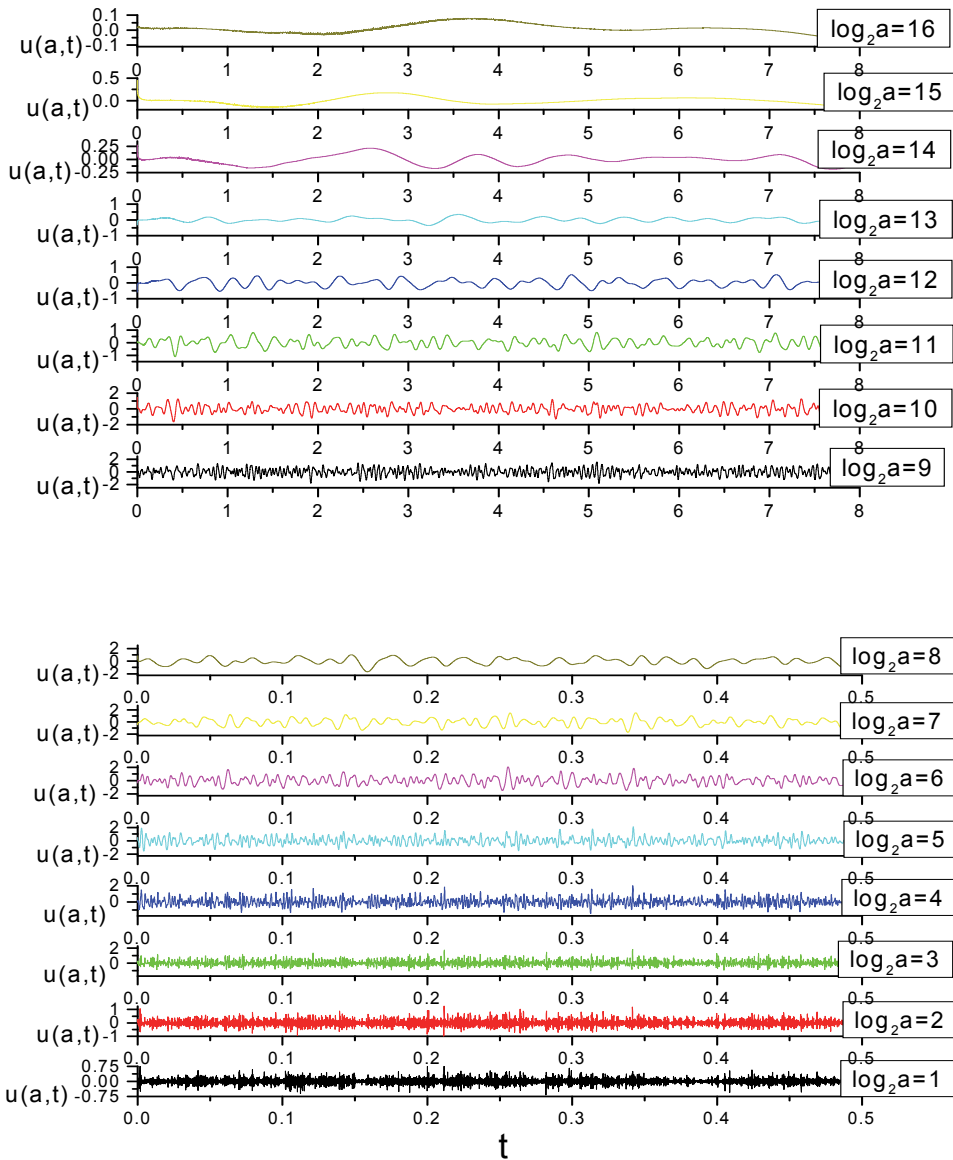


Fig. 3. Multi-scale eddy structure velocity decomposed by wavelet transformation of turbulence fluctuation

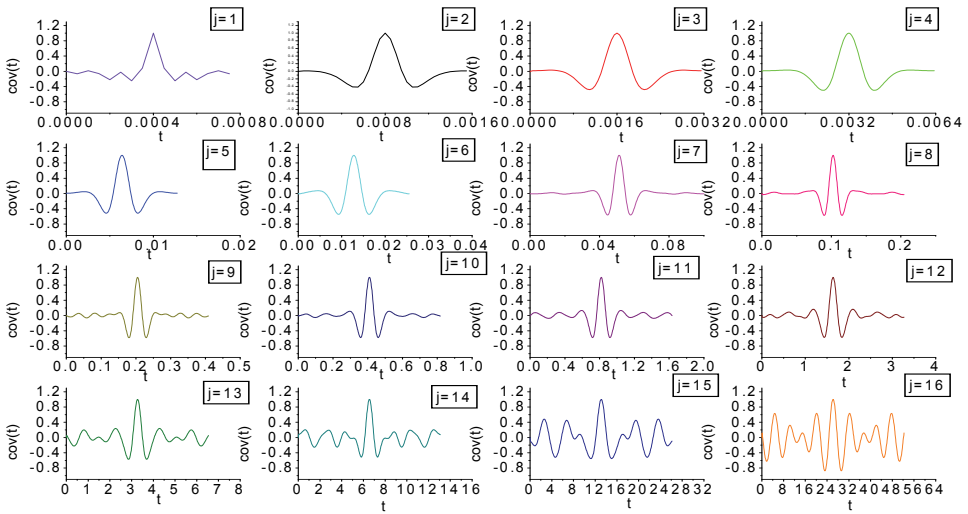
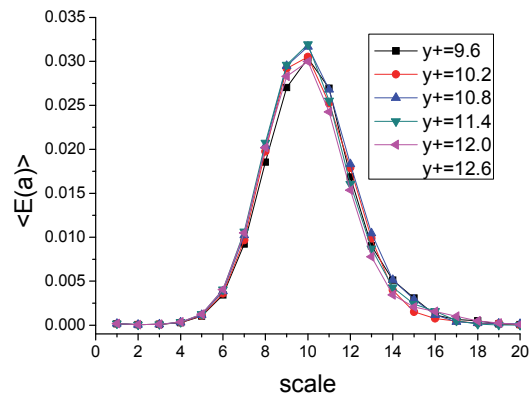
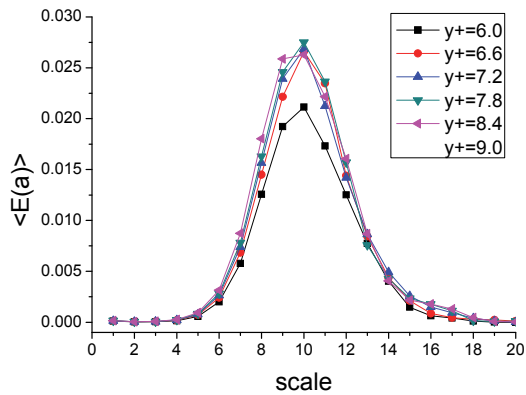
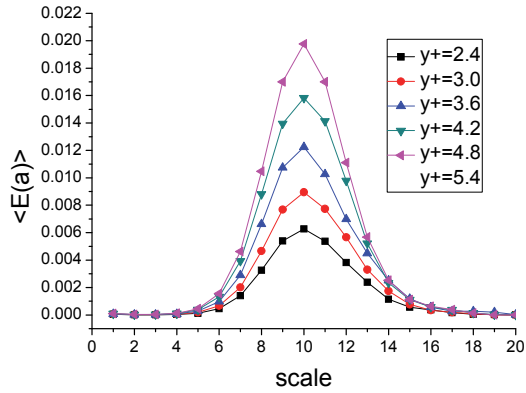


Fig. 4. Correlation functions and scale measurements of multi-scale eddy structures

In order to detect the multi-scale coherent eddy structure in turbulence, a deduce method by conditional sampling scheme using the intermittency factor of wavelet coefficients, is used to extract the phase-averaged evolution course for multi-scale coherent eddy structures in wall turbulence. The method can be simply summarized as follows: computing the flatness factor  $FF(a)$  at each wavelet scale, if  $FF(a)$  is less then 3, coherent eddy structures are not detected and turn to the next scale. If  $FF(a)$  is greater than 3 for a given scale, imposing a threshold level  $L$  on  $I(a,t)$  and excluding those wavelet coefficients whose  $I(a,t)$  is greater than  $L$ , then recalculated the flatness factor  $FF(a)$ . If  $FF(a)$  is less then 3, then turns to the next scale. If the flatness factor  $FF(a)$  is still larger than 3, the threshold level  $L$  is lowered and the process is iterated until the flatness factor  $FF(a)$  equals to (or less than) 3 for all scales<sup>[31][32]</sup>.

Figure 5 shows the energy contribution of each scale eddies versus scale  $a$  by integrating the square of the modulus of wavelet coefficients over the temporal location parameter  $t$ . It can be found from figure 5 that the energy distribution of each scale eddies are not constant and varies across scale parameter  $a$ . There is a scale that corresponds to the peak of energy contributions. This energy maximum is related to the large-scale coherent structures in the near region of turbulent boundary layer and is called burst. Coherent structures are found to be particularly important “eddies” and they are a major contribution to the production of turbulence in turbulent boundary layer. As can be seen, for buffer layer, the maximum energy scale is scale 10, while for logarithm-law layer; scale 9 is the maximum energy scale. The flatness factor  $FF(a)$  calculated by averaging the 4-th power of the modulus of wavelet coefficients over the temporal location parameter  $t$  at each scale  $a$  is shown in Figure 6. Flatness factor decreases with scale from significantly larger than 3 to about 3. In comparison to Figure 5, the flatness factor at scales less than the most energetic scale correspond to the peak of energy contributions satisfies  $FF(a) > 3$ , which indicates that lots of intermittent structures satisfying  $FF(a,t) > 3$ , namely coherent structures, exist. While in

scales larger than the most energetic scale corresponds to the peak of energy contributions, the flatness factors almost satisfy  $FF(a) < 3$ , which indicates that few coherent structures satisfying  $FF(a,t) > 3$  exist.



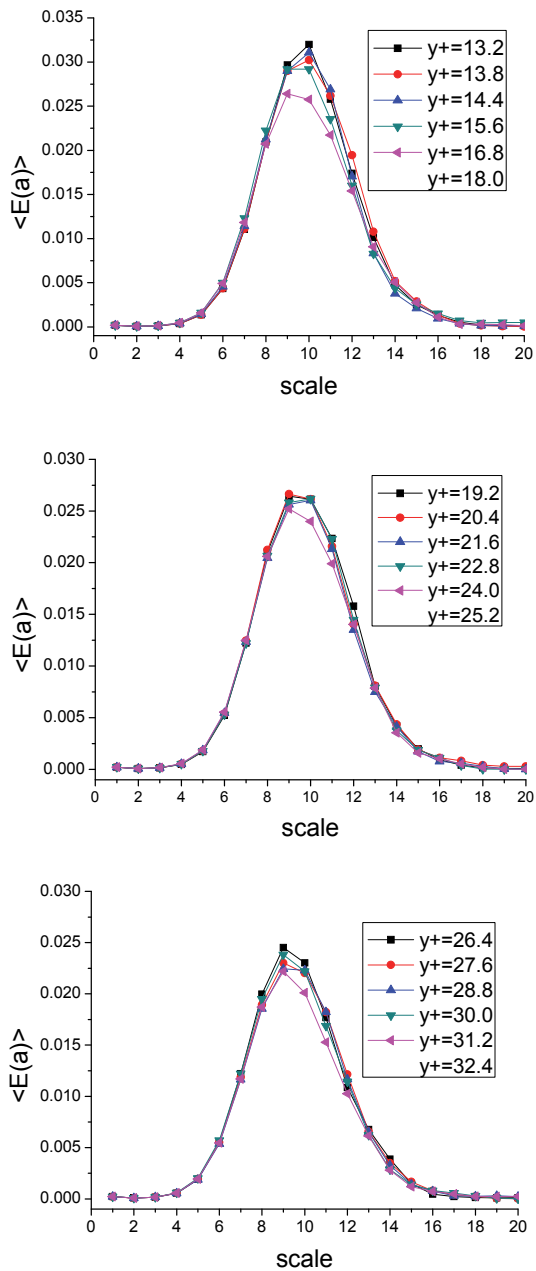


Fig. 5. Energy distribution as a function of wavelet scales at different locations in turbulent boundary layer

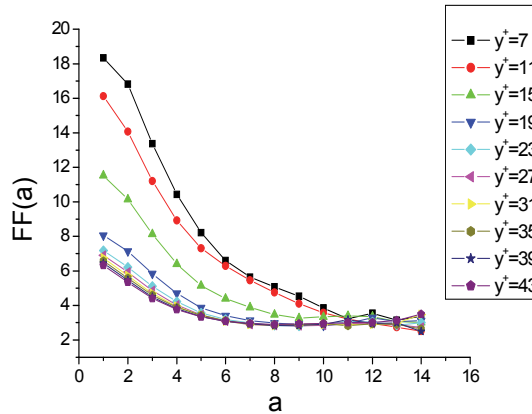


Fig. 6. Flatness as a function of wavelet scales at different locations in turbulent boundary layer

### 3. Experimental apparatus and technique

The experiment has been performed in a low turbulent level wind tunnel. The working section, length is 4500mm, with cross-section is welding rectangular of height 450mm and width 350mm, adopted controllable silicon timing system, power of 7.5Kw. Wind velocity in test section continuously varies from 1.0m/s to 50.0m/s, and primal turbulent level is less than 0.07%. The test flat plate is fixed on the horizontal center of the test section, parallel with the direction in which the wind comes. The leading edge of the plate faced to the wind direction is symmetry wedged. The length of plate is 4500mm, with width of 350mm and thickness of 5mm. A piece of sandpaper stuck on the leading edge of the plate as a trigger to trip transition from laminar flow to turbulent flow and forms fully developed turbulence downstream. When the longitudinal velocity component in 10m/s, the thickness of boundary layer is  $\delta = 160$  mm, Reynolds number  $Re_\delta = \frac{U_\infty \delta}{\nu} = 100000$ . IFA300 constant-

temperature anemometer, made by TSI Corporation in America, is used to acquire the digital velocity signal output from the hot-wire probe, controlled by computer and has the best automatic frequency to deserve the best frequent correspondence instantaneously. The probe used in the experiment is TSI-1211-T1.5 hot-wire probe with single sensor. The temperature sensitive material is tungsten filament with diameter of  $2.5\mu m$ . The time sequence of longitudinal velocity component at 100 locations, with the nearest distance from the plate surface is  $y=0.5$ mm has been finely measured by IFA300 with resolution higher than Kolmogorov dissipation scale. For each measurement position, the sampling frequency is 50K, sampling time is 21s, 1048576 samples of the anemometer output signal are digitized in each database file by the 12-bit A/D converter of model UEI-WIN30DS4. Before measurement, each probe should be calibrated solely, in order to obtain the finest frequency correspondence and the relationship between output voltage and flow velocity. TSI-1128A type hot wire velocity calibrator can provide standard jet flow field with continuous velocity between 0 and 50m/s to calibrate the probe. The diameter of jet nozzle is  $D=10$ mm. The semi logarithmic mean velocity profile normalized by wall unit is given in Fig 7, where

$u^+ = U/u_*$ ,  $y^+ = yu_* / \nu$ . The skin friction velocity estimated by regression between  $y^+ = 40$  and  $y^+ = 200$  is  $u_* = 0.3906$  m/s and the skin friction coefficient is  $c_f = 0.0039$ . Buffer layer, log-layer and bulk region can be distinguished in the single wall distance regions by their characteristic curvatures, while the linear viscous sub-layer region could not be resolved sufficiently.

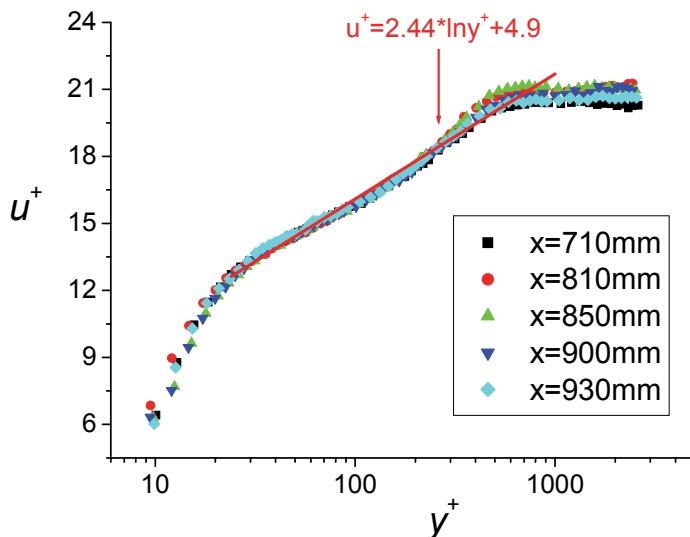


Fig. 7. Mean velocity profile of turbulent boundary layer on a smooth flat plate

#### 4. Results and discussion

Various techniques for educing coherent structure component using the information provided by wavelet phase plane have been described in the literature<sup>[31][32]</sup>. Our object is to partition a turbulence fluctuating signal into two parts using the information provided by wavelet phase plane, one containing coherent structures component and the other containing the residual random component. Two criterions should be assigned for separating the two fluctuating velocity components; one is for the intermittent scale by  $FF(a) > 3$  and the other for detecting coherent structure by  $I(a,t) > L$ . The reconstruction can be performed from the wavelet phase plane information detected by these two criterions from the most energetic scale to small scales. Once the dominant scale is determined by the most energetic criterion, the local coherent structure can be identified from the significant maxima amplitudes of wavelet coefficients. The partition then is performed from the most energetic scale to the small-scale reconstruction. Figure 8 presents some single scale coherent structure fluctuating velocity signals reconstructed from each single scale wavelet coefficients. Figure 9 presents the coherent structure velocity signal reconstructed from intermittent wavelet coefficients detected by the intermittency index.

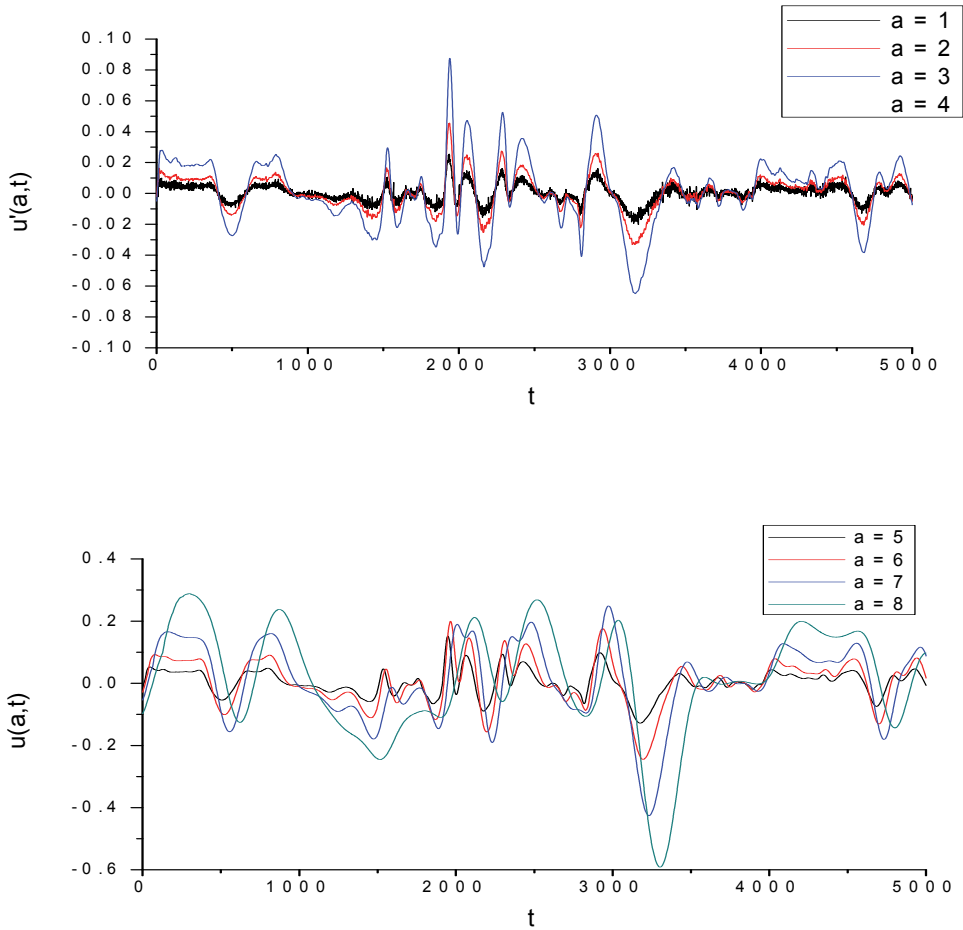


Fig. 8. Time trace of each single scale coherent structure longitudinal fluctuating velocity signal



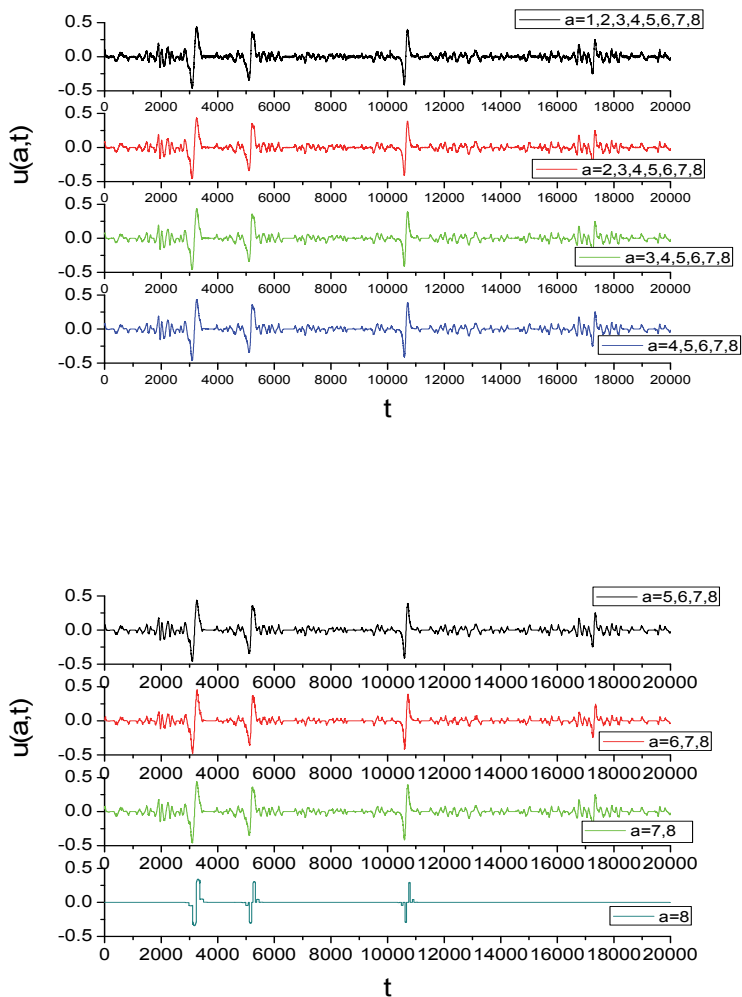
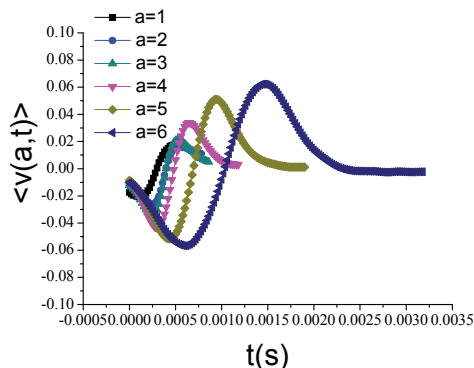
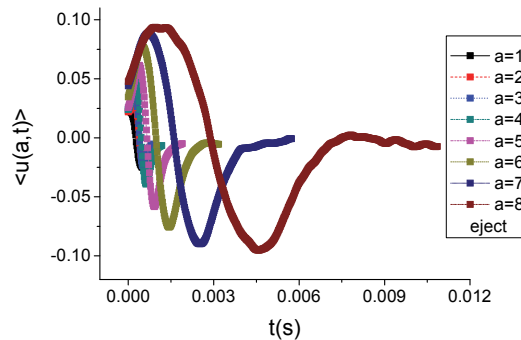


Fig. 9. Time trace of coherent structure velocity signal reconstructed from multi-scale wavelet coefficients

Figure 10 and 11 shows conditional phase-averaged waveforms of fluctuating velocity component during sweep and eject events for different scales at  $y^+=26$  in the buffer region of turbulent boundary layer. The vertical axis in figure 10 and 11 represents the phase-averaged fluctuating velocity component normalized by the local mean velocity, while abscissa axis represents the time. The shapes of different scales are quite similar though their time scales are different. They are self-organized and self-regenerated. Their development and evolution process of coherent structures on different scales share some characteristics in common. In figure 10, the downstream (earlier in time) longitudinal fluctuating velocity component of fluid particles is little faster than the upstream (late in time) one, which cause a decelerating or stretching process which means the low-speed streak flow slowly lifts up away from the wall and makes the longitudinal velocity component of the measuring point reduced. In figure 11, the downstream (earlier in time) longitudinal fluctuating velocity component is slow, while the upstream (late in time) longitudinal fluctuating velocity component accelerates, which cause a compressing process, which denotes that high-speed fluid from the outer layer sweeps downwards and makes the local longitudinal fluctuating velocity component of the measured location increased. The time of this process is very short, but the effect is very strong and their behaviors are similar. These universalities provide important clues to understand the mechanism of turbulence production and transport of heat, mass, momentum in wall turbulence.



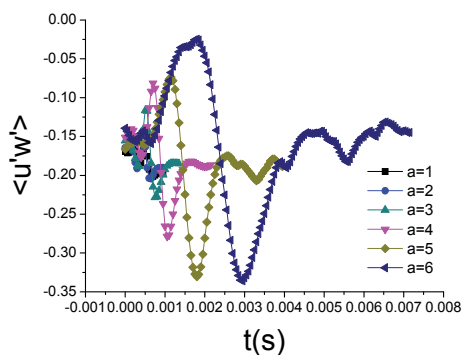
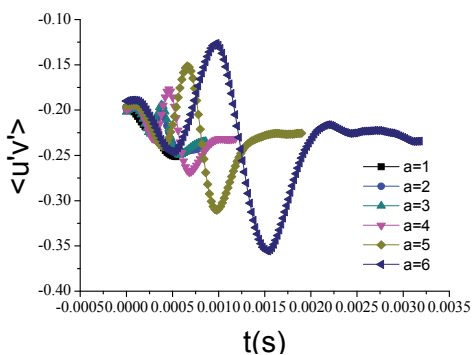
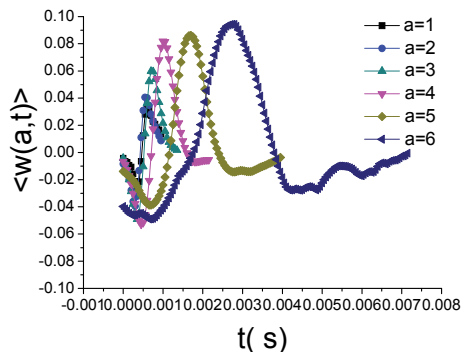
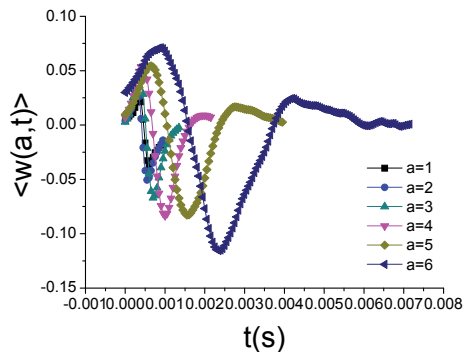
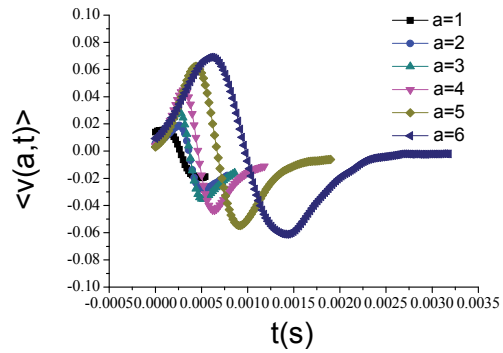
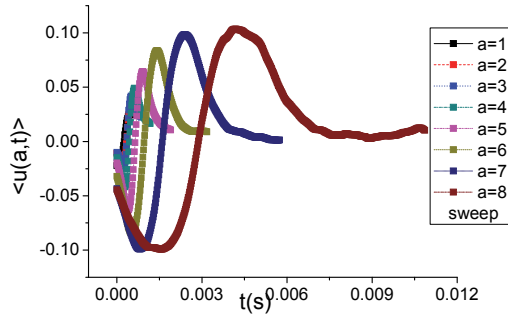


Fig. 10. Conditional phase-averaged waveform of fluctuating velocity and Reynolds stress for multi-scale coherent structures eject with different scale



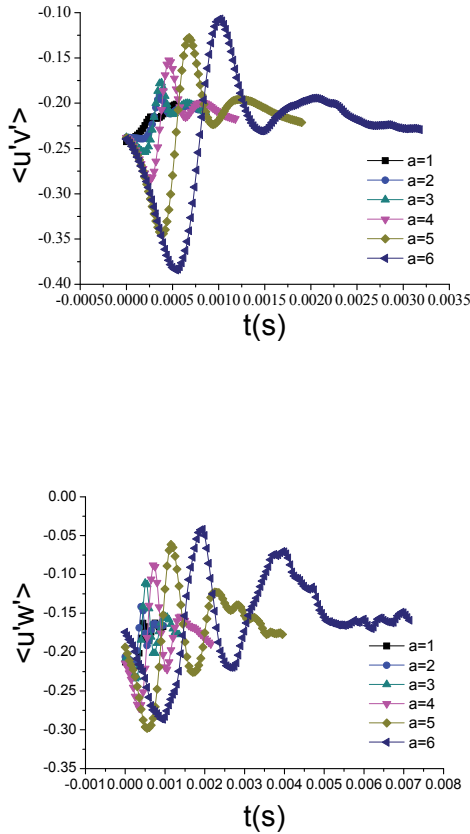


Fig. 11. Conditional phase-averaged waveform of fluctuating velocity and Reynolds stress for multi-scale coherent structures sweep with different scale

Figure 12 and 13 shows the conditional phase-averaged waveforms of the fluctuating velocity component and Reynolds stress during sweep and eject events for the most energetic scale at different locations across turbulent boundary layer. The shapes of them are similar but their amplitudes are quite different. It indicates that buffer layer is the most important and active region of turbulent boundary layer where coherent structures burst with the largest amplitude. These coherent motions contribute significantly to turbulence production and transport of heat, mass, momentum in the near wall region. The intensities of them decay versus their locations far away from the wall to the out region. Out of the turbulent boundary layer, their intensities are so small and can be neglected.

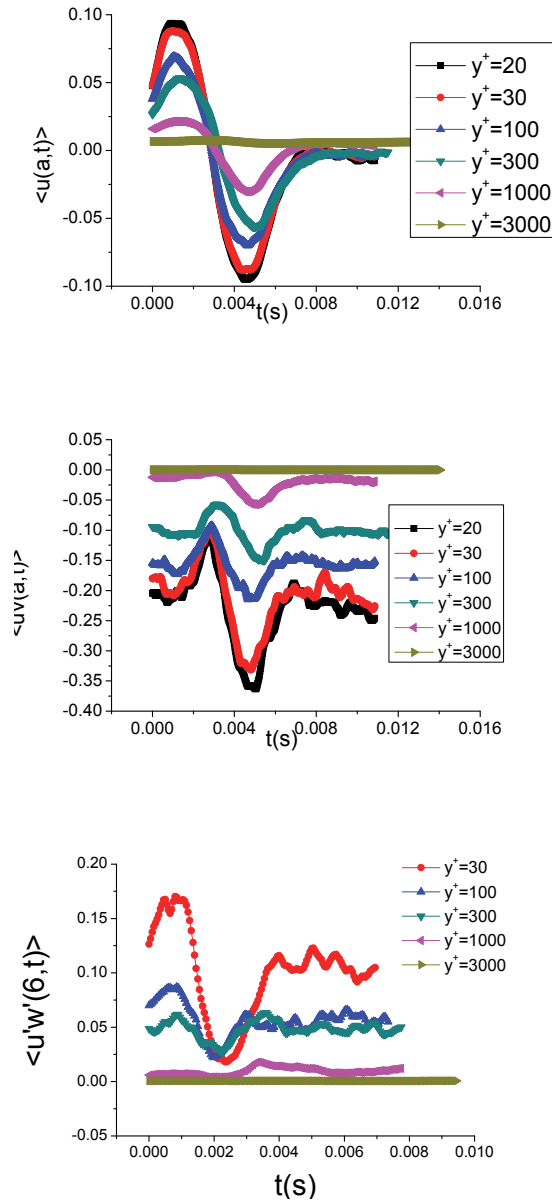


Fig. 12. Conditional phase-averaged waveform of fluctuating velocity and Reynolds stress for multi-scale coherent eddy structures eject for the most energetic scale at different locations in turbulent boundary layer

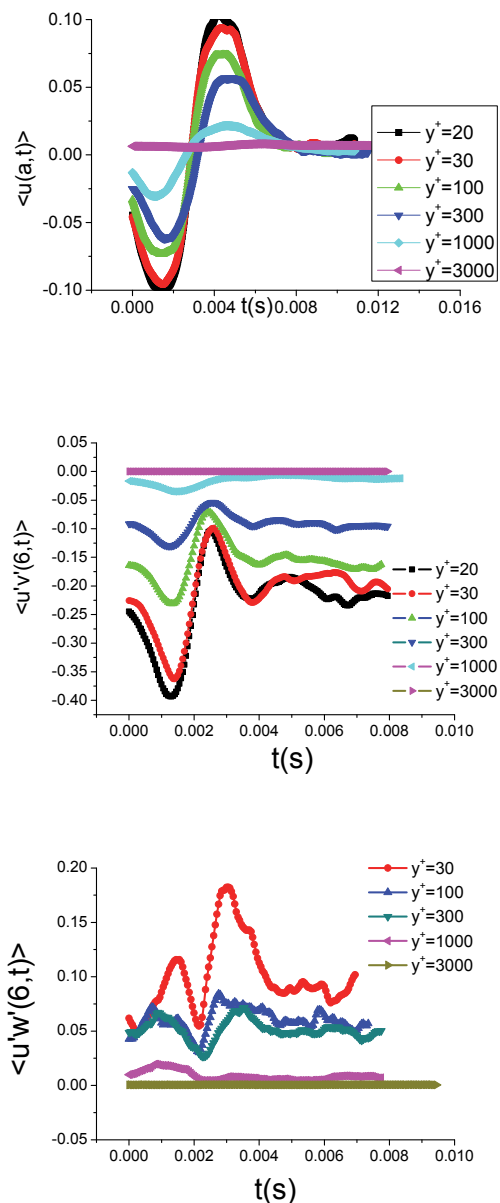


Fig. 13. Conditional phase-averaged waveform of fluctuating velocity and Reynolds stress for multi-scale coherent eddy structures sweep for the most energetic scale at different locations in turbulent boundary layer

Figure 14 shows the  $p$ -th order from the first to the sixth structure functions of wavelet coefficients for  $y^+ = 14$  calculated by the extended self-similarity scaling law (ESS)<sup>[33][34]</sup> within multi-scale coherent structures. The anomalous scaling law calculated by wavelet coefficients is shown in figure 15. Thus the anomalous scaling exponents  $\zeta(p,3)$  can be obtained by linear fit their slopes of these lines. They are substantially different with the Kolmogorov linear scaling law of  $\zeta(p,3) = p/3$ . Figure 16 shows the  $p$ -th order structure functions calculated by ESS after multi-scale coherent eddy structures have been eliminated. It is clear that the scaling exponents without multi-scale coherent eddy structures are exactly fit to the Kolmogorov linear scaling law of  $\zeta(p,3) = p/3$  in figure 17. This means that multi-scale coherent eddy structures are responsible for the intermittence and the anomalous scaling law in turbulence boundary layer. When multi-scale coherent structures are removed by the present conditional sampling technique, the scaling law returns to the linear scaling law  $\zeta(p,3) = p/3$ .

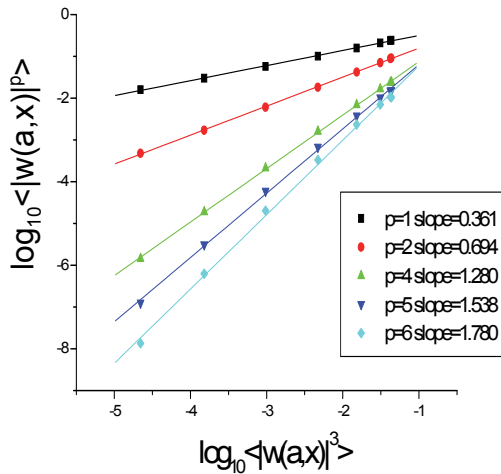


Fig. 14. The  $p$ -th order structure functions as a function of the third order structure function calculated using wavelet coefficients within coherent structures at  $y^+ = 14$



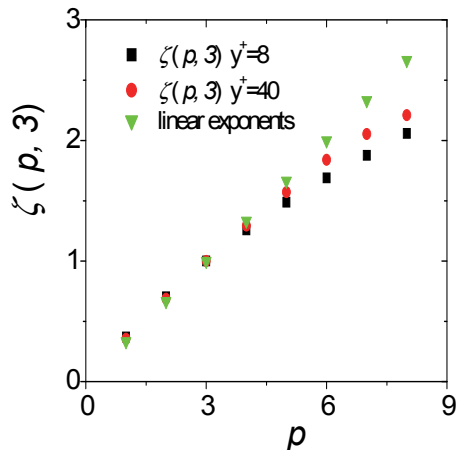


Fig. 15. Relative scaling exponents calculated by wavelet coefficients including coherent structures at  $y^+=8$  and 40.

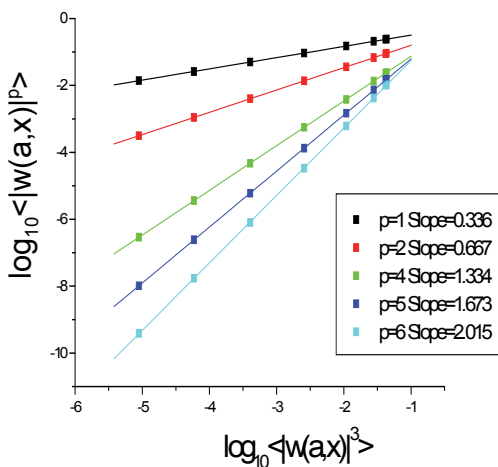


Fig. 16. The  $p$ -th order structure functions as a function of the third order structure function calculated using wavelet coefficients without coherent structures

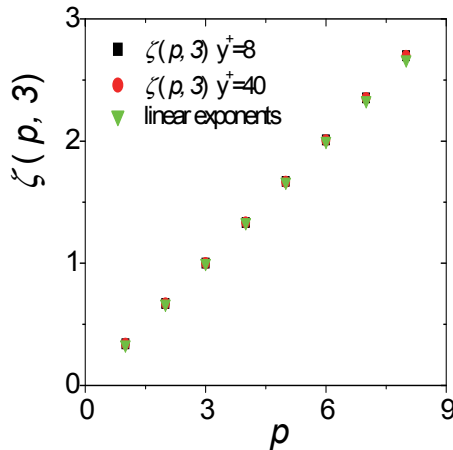


Fig. 17. Relative scaling exponents calculated without coherent structures at  $y^+=8$  and 40.

## 5. Conclusions

Turbulent flow is made up of multi-scale eddy structures, and different scale coherent eddy structures exist at different scales that are smaller than the most energetic scale corresponds to the peak of energy contributions. Coherent structures play an important role in turbulence. Coherent eddy structures are much more intensive than non-coherent eddy structures at the same scale.

The energy percentage of large-scale coherent eddy structures at buffer layer is much greater than that of other scales and that of other locations in turbulent boundary layer. Buffer layer is the most important region of turbulent boundary layer for turbulence production with the most active coherent structures.

Besides scales of coherent eddy structures are quite different, phase-averaged evolution shapes of multi-scale coherent eddy structures are similar, which implies the evolvement process of coherent eddy structures on different scales share common characteristics.

Multi-scale coherent eddy structures are responsible for the intermittence and anomalous scaling law in turbulent boundary layer. Multi-scale coherent eddy structures lead to the anomalous scaling law that deviate Kolmogorov linear scaling law. When multi-scale coherent structures are eliminated, the ESS scaling exponents calculated by wavelet coefficients are in agreement well with the Kolmogorov linear scaling law.

## 6. Acknowledgment

Supported by the National Natural Science Foundation of China (Grant No. 100832001 10872145) and science innovation fund of Tianjin University

## 7. References

Kolmogorov A N, Dissipation of energy in the locally isotropic turbulence [J]. *Dokl Akad Nauk SSSR*, 1941, 32(1): 19~21

- Kolmogorov A N, A refinement of previous hypothesis concerning the local structure of turbulence in a viscous incompressible fluid at high Reynolds number [J]. *J Fluid Mech.*, 1962, 13 (1): 82~85
- Jiang Nan, Wang Yu-chun, Shu Wei, Wang Zhen-dong, Experimental study of measurement for dissipation rate scaling exponents in heated wall turbulence[J], *Applied Mathematics and Mechanics* , 2002 , Vol 23, No 9: 1035-1044
- Jiang Nan, Wang Zhen-dong, Shu Wei, Extended self-similarity scaling law of multi-scale eddy structure in wall turbulence , *Applied Mathematics and Mechanics* , 2000 , Vol 21, No 9: 1016-1023
- G Ruiz Chavarria, S Ciliberto, C Baudet, E Leveque, Scaling properties of the streamwise component of velocity in a turbulent boundary layer [J]. *Physica D*, 2000, 141: 183-198
- F Toschi, G Amati, S Succi, R Benzi, R Piva, Intermittency and structure functions in channel flow turbulence [J]. *Phys Rev Lett*, 1999, 82(25): 5044~5047
- F Toschi, E Leveque, G Ruiz Chavarria, Shear effects in non-homogeneous turbulence [J]. *Phys Rev Lett*, 2000, 85(7): 1436~1439
- Miguel Onorato, Roberto Camussi, Gaetano Iuso, Small scale intermittency and bursting in a turbulent channel flow [J], *Physical Review E*, Vol. 61, No 2: 1447~1454
- She Z-S, Su Wei-dong, Hierarchical structures and scaling in turbulence [J] *Advances in Mechanics*, 2000, Vol.29, No.3: 289~303 (in Chinese)
- Kline S J, Reynolds W C, Schraub F H, Runstadler P W, The structure of turbulent boundary layer [J], *J Fluid Mech.*, 1967, 30: 741-774
- Corino E R, Brodkey R S, A visual investigation of the wall region in turbulent flow [J], *J Fluid Mech.*, 1969, 37: 1-30
- Kim H T , Kline S J and Reynolds W C. The Production of Turbulence Near a Smooth Wall in a Turbulent Boundary Layer [J] , *J. Fluid Mech.* , 1971 , 50 : 133~160
- Smith C R, Metzler S P, The characteristics of low speed streaks in the near wall region of a turbulent boundary layer [J], *J. Fluid Mech.* , 1983 , 129 : 27~54
- Liepmann, H. W., Narasimha, R., Turbulence management and relaminarisation, *IUTAM symposium*, 1987, Bangalore, India
- R. Camussi, G. GUJ, Orthonormal wavelet decomposition of turbulent flows: intermittency and coherent structures [J], *J. Fluid Mech.*, Vol. 348: 177~199
- Susanta K. Das, Mamoru Tanahashi, Kentaro Shoji, Toshio Miyauchi, Statistical properties of coherent fine eddies in wall-bounded turbulent flows by direct numerical simulation, *Theor. Comput. Fluid Dyn.* (2006) 20(2): 55~C7
- V.A.Sandborn, Measurements of intermittency of turbulent motion in a boundary layer[J], *J. Fluid Mech*, 1959, 6(2): 221-240
- Douady S, Couder Y. & Brachet M E, Direct observation of intermittency of intense vorticity filaments in turbulence [J]. *Phys.Rev.Lett.*1991, 67: 983-986
- Siggia E D, Numerical study of small-scale intermittency in 3-dimensional turbulence [J], *J. Fluid Mech.* 1981, 107: 375-406
- Vincent A & Meneguzzi M, The spatial structure and statistical properties of homogeneous turbulence [J]. *J. Fluid Mech.* 1991, 225: 1-20
- She Z-S, Jackson E & Orszag S A, Intermittent vortex structures in homogeneous isotropic turbulence [J]. *Nature* 1990, 344: 226-228

- Jiang, N, Chai, Y-B. Experimental investigation of multi-scale eddy structures' intermittency in turbulent flow using probability density function of wavelet coefficients, *Journal of Aerospace Power*, 20(5), 2005, p 718-724
- Marie Farge, Kai Schneider, Coherent vortex simulation (CVS), A semi-deterministic turbulence model using wavelet [J], *Flow, Turbulence and Combustion*, 2001, Vol.66: 393-426
- Charles Meneveau, Analysis of turbulence in the orthonormal wavelet representation [J], *J. Fluid Mech.*, 1991, Vol. 232: 469~520
- Farge M., Wavelet transforms and their applications to turbulence [J], *Annu. Review Fluid Mech.* · 1992 · 24 : 395-457
- Marie Farge, Nicholas Kevlahan, Valerie Perrier, Eric Goirand, Wavelet and turbulence [J], *Proceedings of the IEEE*, 1996, Vol.84, No. 4: 639~669
- Tennekes H · Lumley J.L. *A First Course in Turbulence* [M], M.I.T.Press Cambridge · Massachusetts and London · England · 1972
- Liu JH, Jiang N, Two phases of coherent structure motions in turbulent boundary layer, *Chinese Physics Letters*, 2007, Vol 24, No 9: 2617-2620
- Liu JH, JIANG N, WANG ZD, et al. Multi-scale Coherent Structures in Turbulent Boundary Layer Detected by Locally Averaged Velocity Structure Functions [J], *Applied Mathematics and Mechanics*, 2005, Vol 26(4): 456-464
- Jiang N, Wang ZD, Shu W. The maximum energy criterion for identifying burst events in wall turbulence using wavelet analysis. *Acta Mechanica Sinica*, 1997, 29(4): 406~411 (in Chinese)
- Jiang N, Liu W, et al. Phase-averaged waveforms of Reynolds stress in wall turbulence during the burst events of coherent structures. *Science in China (Series G)*, 2008, 51(7): 857–866
- Jiang N, Zhang J, Detecting multi-scale coherent eddy structure and intermittency in turbulent boundary layer by wavelet analysis, *Chinese Physics Letters*, 2005, Vol 22, No 8: 1968-1971
- Benzi R, Ciliberto S, Tripiccone R, Extended self-similarity in turbulent flow [J]. *Phys.Rev.E*, 1993, Vol.48, No.1: R29-R32
- Liu W, Jiang N. Three kinds of velocity structure function in turbulent flows. *Chinese Physics Letter*, 2004, 21(10): 1989-1992

## **Part 5**

### **Wind Tunnels in Compressible Flow**



# Evaluation of Local Effects of Transitional Knudsen Number on Shock Wave Boundary Layer Interactions

R. Votta, G. Ranuzzi, M. Di Clemente, A. Schettino and M. Marini  
*CIRA Italian Aerospace Research Centre  
Capua (CE),  
Italy*

## 1. Introduction

In the frame of the Italian aerospace research programme PRORA, two research activities are being performed in parallel, that are considered critical in the design of a re-entry vehicle: the evaluation of the Shock Wave - Boundary Layer Interaction (SWBLI) over a control surface and the analysis of rarefaction effects at high altitude. It is well known that on one side the SWBLI phenomenon strongly affects the efficiency of control surfaces during the re-entry, and on the other side the behavior of a hypersonic vehicle at high altitude is very different with respect to what happens in continuum regime, in particular for what concerns both the aerodynamic coefficients and the heat loads. Therefore, the correct evaluation of both phenomena is crucial in the design phase. The SWBLI phenomenon can be simulated in flight by means of advanced numerical codes, provided that a good accuracy of both the numerical scheme and the grid is attained; due to the high energy that typically characterizes the upper part of a re-entry path, the CFD code must be also capable to solve the Navier-Stokes equations taking into account chemical and vibrational non-equilibrium. Since a few experimental data are available for dissociated flows, in the frame of PRORA program some specific tests have been designed to validate the CIRA code H3NS; moreover, the goal of such experiments is to improve the understanding of the phenomenon, in order to be able to correlate flight and wind tunnel conditions and to extrapolate from flight and to flight the experimental data (Di Clemente et al., 2005).

However, since the stagnation pressure of a facility like the CIRA Plasma Wind Tunnel (PWT) Scirocco is very low with respect to a classic aerodynamic wind tunnel, a question arises about the possible rarefaction effects that can occur and that can influence the results of the tests; indeed the unit free-stream Knudsen number in Scirocco ranges from a value of  $5.375 \cdot 10^{-5}$  for the higher pressures, to a maximum of  $1.467 \cdot 10^{-3}$  in the lower pressure conditions ( $P_0=1$  bar); in **Fig. 1** the variation of Kn is reported as function of the reservoir pressure and enthalpy for both the nozzles D and F; these values could justify local rarefaction effects, for example over the nose, even though much of the flow domain is in continuum regime (Markelov et al., 2000).

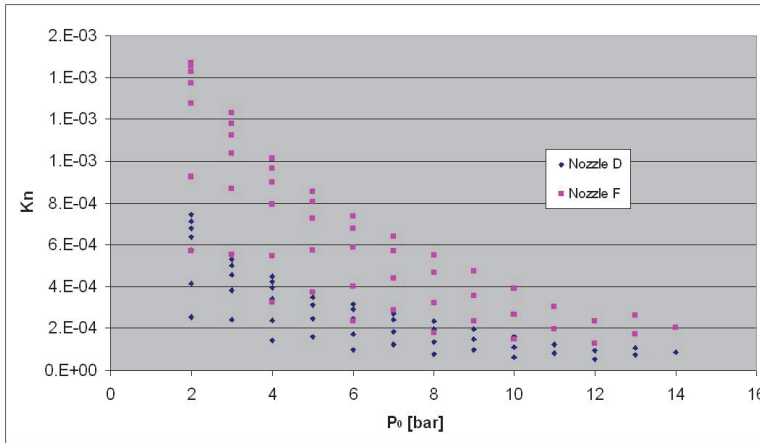


Fig. 1. Kn vs Reservoir pressure in Scirocco PWT.

Moreover, the SWBLI phenomenon itself can be affected by rarefaction effects (Markelov et al., 2000). Therefore, the same numerical tools that are typically used in flight to assess the rarefaction effects on the aerodynamic coefficients of a full vehicle have been used in wind tunnel conditions in order to verify if they occur in the experimental test. Two different tools are available at CIRA for this purpose: on one side, a DSMC code developed (Bird, 1995) for rarefied flows; on the other side, suitable slip flow conditions have been implemented in the H3NS CIRA code in order to allow the Navier-Stokes solver to deal with rarefied flows. Some details about both codes are given in the following section. In order to validate the code with the slip conditions, a classic numerical test case has been used, and the H3NS results have been compared with both numerical and experimental results (Markelov et al., 2000 and Marini, 2002). The comparisons were very satisfactory and are summarized in section 3.

Then, the same tools have been applied to rebuild the Scirocco tests, in order to check if rarefaction effects locally occur. The results are presented in section 3.

## 2. Numerical approaches

### 2.1 Navier-Stokes method

The continuum regime results have been obtained by using the CIRA Computational Fluid Dynamics (CFD) code H3NS developed at the Aerothermodynamics and Space Propulsion Laboratory by Ranuzzi et al. (2006). The code solves the full Reynolds Averaged Navier-Stokes (RANS) equations and considers the air flow in thermo-chemical non-equilibrium. Park model (1989) with five species (O, N, NO, O<sub>2</sub>, N<sub>2</sub>) and 17 chemical reactions is implemented and the energy exchange between vibrational and translational temperature is based on Landau-Teller non-equilibrium equation, with average relaxation times taken from the Millikan-White (1963) theory modified by Park (1993). The viscosity coefficient for the single specie is computed by means of Yun and Mason (1962) collision integrals, while the conductivity coefficient using Eucken's law. These coefficients for the gas mixture are calculated using semi-empirical Wilke formulas. Diffusion coefficients are obtained by Yun and Mason tabulated collision integrals (1962).



From the numerical point of view, the code is based on a finite volume approach with a cell centered formulation. The inviscid fluxes are computed by Flux Difference Splitting scheme (Borrelli, 1990) and second order approximation is obtained with an Essentially Non Oscillatory (ENO) reconstruction of interface values. Time evolution is performed by an explicit multistage Runge-Kutta algorithm coupled with an implicit evaluation of the chemistry and vibration source terms.

To take into account the effects of rarefaction, slip boundary conditions have been employed. From the large number of available formulations of this kind of conditions, the one proposed by Kogan (1969) has been chosen. These boundary conditions have been obtained by matching the solution of Boltzmann equation in the Knudsen layer to the solution of the macroscopic Navier-Stokes equations, thus yielding:

$$V_s = 1.012\lambda \left( \frac{\partial V_\tau}{\partial n} \right)_w \quad (1)$$

$$T_s - T_w = 1.73 \frac{\gamma}{\gamma-1} \frac{\sqrt{\pi}}{4} \lambda \left( \frac{\partial T}{\partial n} \right)_w \quad (2)$$

where  $V_s$  is the "slip velocity" and  $T_s$  the "slip temperature".

## 2.2 Direct Simulation Monte Carlo method

The Direct Simulation Monte Carlo (DSMC) software used in this paper is the DS2V code of Bird (1995) which is briefly described in the following.

The DSMC method (Bird, 1994) considers the gas as made up of discrete particles that are represented by millions of simulated molecules; it relies on formulas from the kinetic theory of gases. Movement and evolution of each molecule in the simulated physical space is produced by collisions with other molecules and with the body under study, in both cases exchanging momentum and energy. Excitation of rotational and vibrational degrees of freedom and chemical reactions (if any) can be also taken into account.

The computational domain, including the test body, is divided in cells; these are used only for sampling the macroscopic properties and for selecting the colliding molecules. Movement of each molecule from a cell to another one is the product of the velocity (that is the resultant of the convective and thermal velocities) and a time step.

Macroscopic thermo-fluid-dynamic quantities of the flow field (density, temperature, pressure and so on) are computed in each cell as an average over the molecules.

DS2V uses transient subcells in which a transient background grid is built on a single cell and the collision routine, based on nearest-neighbor collisions, is applied. The resolution of the transient grid depends on the number of simulated molecules and, approximately, one simulated molecule corresponds to one subcell.

DS2V provides in output, during the run, the ratio of the local mean separation between collision partners to the local mean free path ( $mcs/\lambda$ ). This parameter is indicative of the quality of a run; it should be less than unity every where in the computational domain. Bird (1994, 1995) suggests the value of 0.2 as a limit value.

The present applications rely on the fully accommodated Maxwell gas-surface interactions.

### 3. Results and discussion

#### 3.1 Hollow cylinder flare test case

In order to validate the methodologies for the prediction of local effects of rarefaction in hypersonic regime and, in particular, concerning the shock wave boundary layer interaction, a typical experimental test case has been selected: the hollow cylinder flare. The hollow cylinder has a sharp leading edge with a bevel angle of 15 deg. The compression flare is inclined of 30 deg with respect to the cylinder and is ended by a hollow cylindrical section. The model total length is 0.17 m and the reference length  $L$  is the distance between the leading edge and the beginning of the compression flare. The experiment was carried out in the R5Ch blow-down hypersonic wind tunnel of ONERA at Chalais-Meudon, France by Chantez (1998). A complete numerical Navier-Stokes investigation has been performed by Marini (2002), while a comparison between continuum and kinetic approach compared with experimental results is reported by Markelov (2000). A description of the experiment is briefly reported hereinafter.

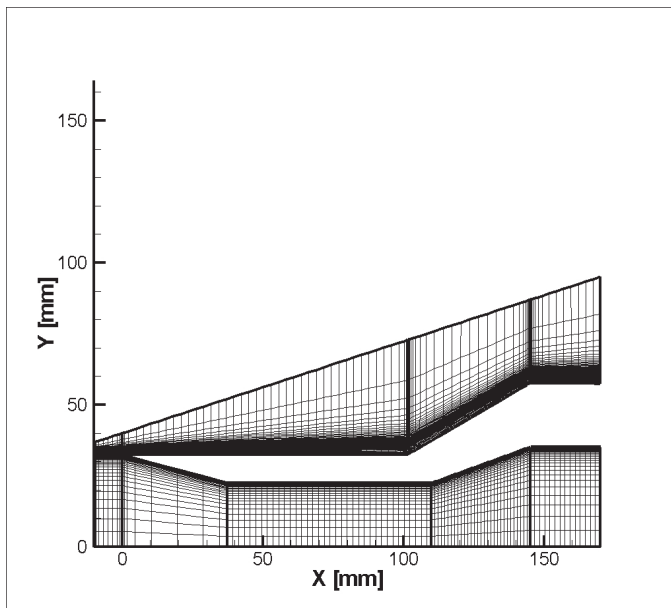


Fig. 2. Validation test case: geometry and computational grid (medium grid level)

The flow conditions for the validation test case are obtained under the nominal stagnation conditions  $p_0 = 2.5 \times 10^5$  Pa and  $T_0 = 1050$  K, which yield an upstream flow characterized by the following properties:  $M_\infty = 9.91$ ,  $Re_\infty/m = 1.86 \times 10^5$ ,  $T_\infty = 51$  K and  $p_\infty = 6.3$  Pa. The surface temperature of the model is assumed to be constant and equal to  $T_w = 293$  K, the Reynolds number based on the reference length  $L = 0.1017$  m is equal to  $Re_{\infty,L} = 188916$ , the mean free path is  $\lambda_\infty = 9.5103 \times 10^{-4}$  m and the Knudsen number:  $Kn_\infty = \lambda_\infty/L = 9.35 \times 10^{-4}$ .

It is worth to underline that much of the flow domain is in continuum regime except, obviously, the sharp leading edge and the region along the surface where local effect of rarefaction are significant.

A sketch of the geometric configuration is reported in Fig. 2 together with the computational grid. The following experimental data are available (Chantez et al., 1998): i) pressure coefficient surface distribution (accuracy of 2%); ii) Stanton number (from temperature variations at wall) surface distribution (accuracy of 7%); iii) surface oil-flow visualization (the pattern of skin friction lines over the model indicates the separation and attachment lines, respectively at  $X_{sep}/L = 0.76 \pm 0.01$  and  $X_{rea}/L = 1.34 \pm 0.015$ ); iv) flow field visualization by the Electron Beam Fluorescence (EBF) technique; and v) density profile measurements by X-rays detection at the streamwise sections  $x/L = 0.3; 0.6$  (accuracy of 15%) and  $x/L = 0.76$  (accuracy of 8%). The two-dimensional grid, used for both no slip wall boundary conditions and slip flow ones, is a structured grid composed by 14 blocks, 165888 cells and 169062 points. The grid convergence has been checked.

The location of separation has been used as a parameter to check the needed number of molecules, since it is the most sensitive property to the variation of number of molecules. Table 1 summarizes the performed simulations and shows that the third solution is the converged one.

Solution	Molecules	$X_{sep}$ [mm]
1	$8.116 \cdot 10^6$	816.64
2	$12.174 \cdot 10^6$	788.24
3	$18.258 \cdot 10^6$	787.98

Table 1. Influence of number of molecules on separation

The next Fig. 3 and Fig. 4 show the predicted Mach number contour maps and streamlines for CFD with slip boundary conditions and DSMC computations: the strong viscous interaction at the cylinder leading edge appears as well as the evident shock wave boundary layer interaction around the corner, and the subsequent recirculation bubble.

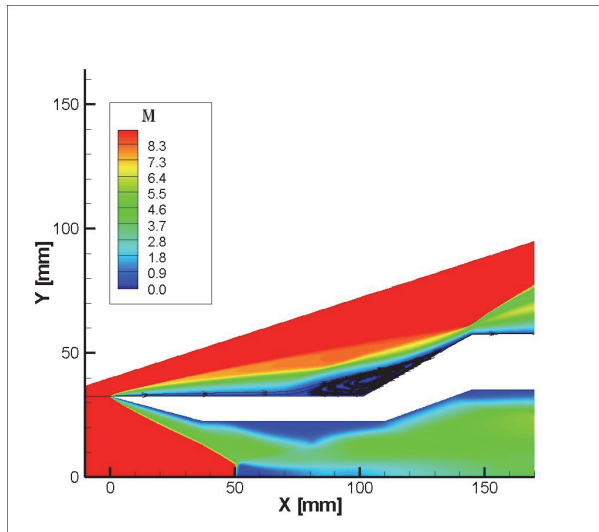


Fig. 3. CFD Slip: Mach number contours and streamlines

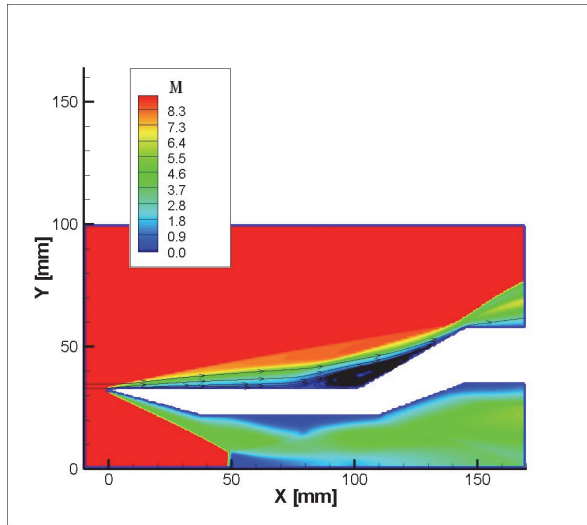


Fig. 4. DSMC: Mach number contours and streamlines

Fig. 5 displays the normalized slip velocity wall distribution ( $V_s/V_\infty$ ) predicted by DSMC and CFD with the boundary conditions of Equations 1 and 2. In the first part of the wall CFD overestimates the results predicted by DSMC, while downstream of the separation the matching between the two methodologies is rather good.

It is worth to underline that slip velocity along the wall, and in particular ahead of separation location, reaches about 10% of freestream velocity, therefore not negligible rarefaction effects are expected.

Fig. 6 exhibits the pressure coefficient distribution on the wall for the three calculations (CFD No Slip, CFD Slip and DSMC) compared to experimental results. A low initial decrease of pressure coefficient is predicted due to the strong viscous interaction, followed by a first increase of  $C_p$  at separation and, then, a strongest one (forty times higher) due to the reattachment shock wave.

DSMC simulation slightly overestimates the experimental pressure coefficient, while both continuum results (CFD No Slip and CFD Slip) show a good agreement with measured values. All computations overestimate the  $C_p$  peak at reattachment, and classic CFD is the nearest to the experimental value since at this point the conditions are close to continuum ones, being the local Knudsen number based on boundary layer thickness  $\delta$ , evaluated as:

$$Kn_\delta = \lambda/\delta \approx 5.28 \times 10^{-3}$$

The analysis of skin friction distribution (Fig. 7 and Fig. 8) shows a different prediction of the three used methodologies for the location of separation. In particular, the predicted separation length is larger as the “amount of rarefaction of the method” decreases. In fact, the value of  $X_{sep}/L$  for CFD No Slip, CFD Slip and DSMC, is respectively 0.7245, 0.7555 and 0.7748. The experimental value (0.76) is included between CFD Slip and DSMC values as a proof of the local effects of rarefaction, being the local Knudsen number:

$$Kn_\delta = \lambda/\delta \approx 2.17 \times 10^{-2}$$

Note that the reattachment point is not significantly affected by the computation methodology (Fig. 7).

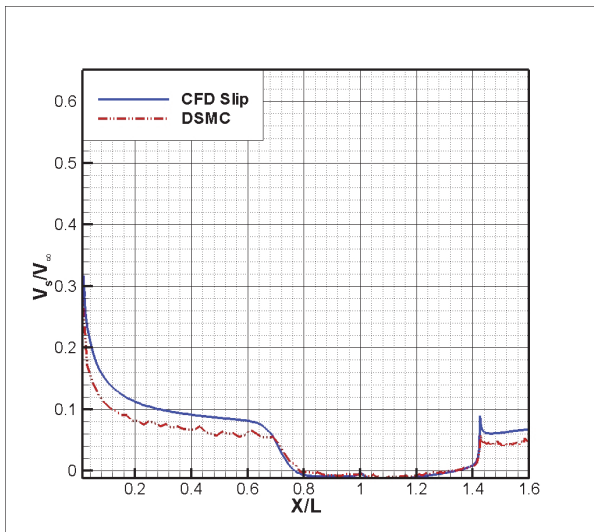


Fig. 5. Slip velocity distribution

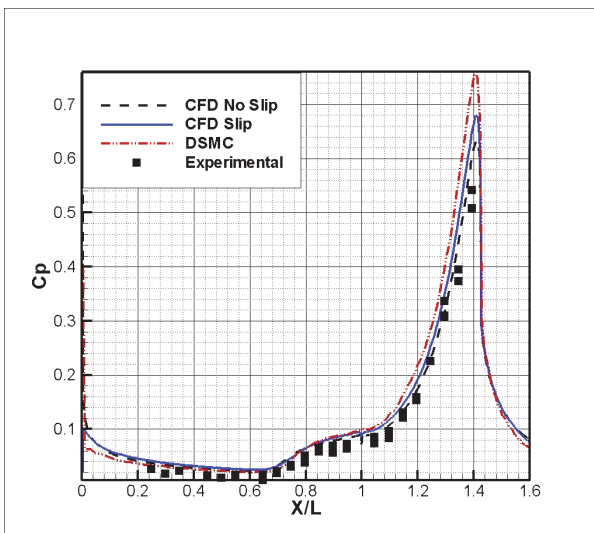


Fig. 6. Pressure coefficient distribution

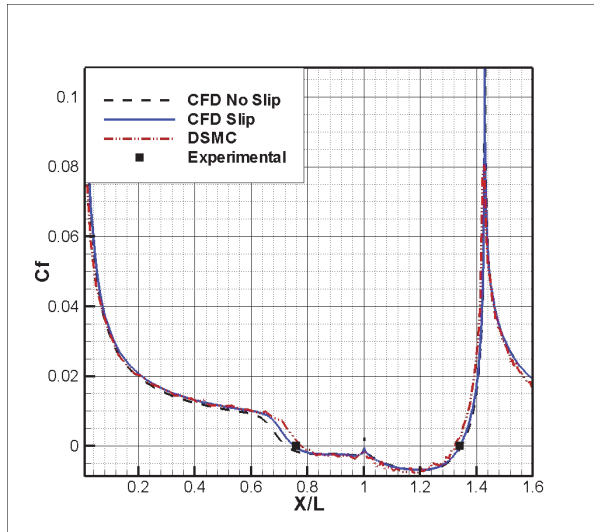


Fig. 7. Skin friction coefficient distribution

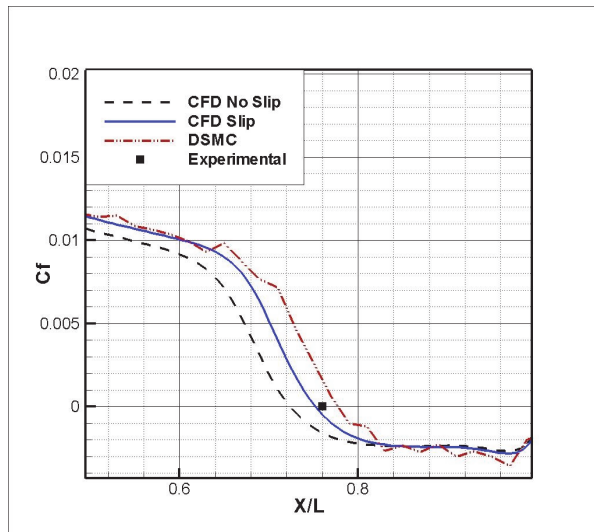


Fig. 8. Skin friction coefficient distribution (zoom)

The same considerations made in the analysis of skin-friction and pressure coefficients apply to the Stanton number distribution (see Fig. 9).

Note that on the leading edge Navier-Stokes with classic boundary conditions (CFD No Slip) overestimates the Stanton number, in fact in this region the boundary layer thickness  $\delta$  is of the same order of magnitude of the mean free path  $\lambda$ , so

$$Kn_{\delta} = \lambda/\delta \approx o(1)$$

and the rarefaction effects are maximum.

A comparison of the results obtained by means of numerical simulations with the measured normalized density profiles inside the boundary layer is reported in Fig. 10 and Fig. 11.

In the cross section  $X/L=0.3$  the correlation between numerical and experimental data in the case of Navier-Stokes with slip flow boundary conditions and DSMC is good, while it is fair for CFD with the classic boundary condition (CFD No Slip). In particular, the shock wave inclination predicted by classic CFD is higher with respect to measured one (compare also the Mach number contours of Fig. 3 and Fig. 4).

At the section  $X/L=0.76$  the three numerical methodologies are closer each other and a good agreement with experimental results has been obtained. Note that the predicted inclination of shock wave is nearly the same.

In conclusion, the analysis of the two density profiles shows that the rarefaction effects, as expected, are more significant in the region near the leading edge.

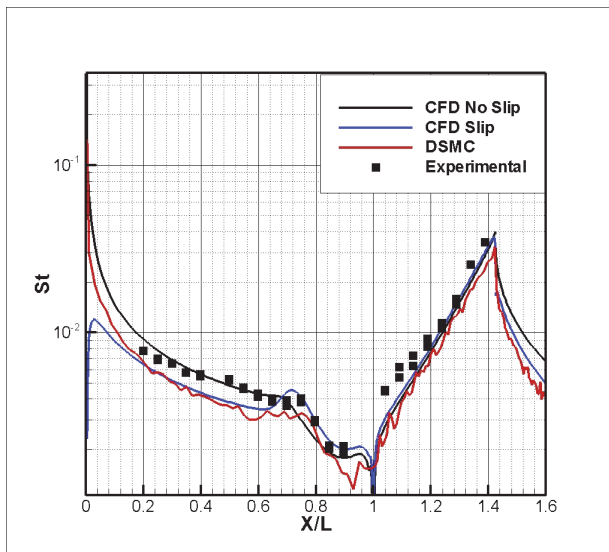


Fig. 9. Stanton number distribution

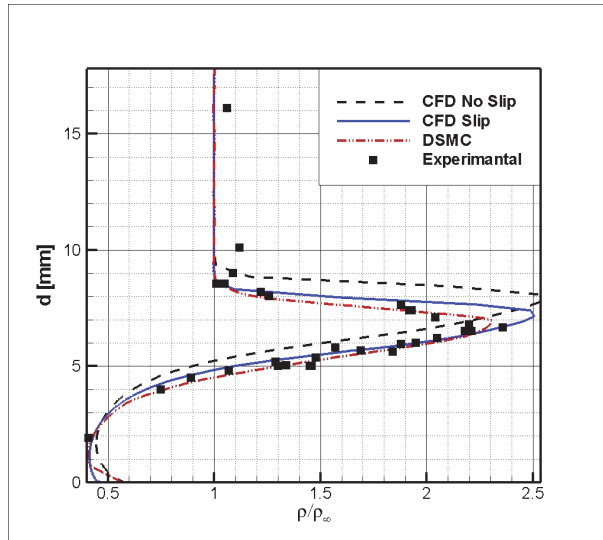


Fig. 10. Density profile:  $X/L=0.3$

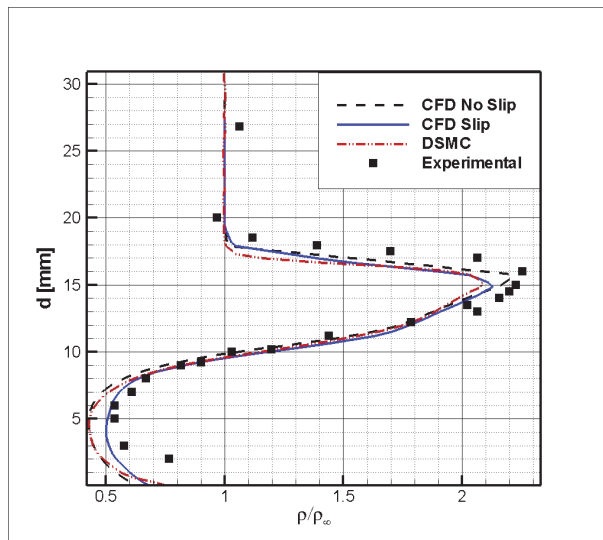


Fig. 11. Density profile:  $X/L=0.76$

Finally, the analysis of the present wind tunnel test case simulated with the three different methodologies (classis CFD, CFD with slip flow boundary conditions and DSMC) has shown that local rarefaction effects are significant for the prediction of important aspects of shock wave boundary layer interaction as the sizing of recirculation bubble. Moreover, it has been also shown that CFD with slip flow boundary conditions is, in this case, a good compromise between computational cost and accuracy.



### 3.2 Scirocco PWT test case

Within the EXPERT program funded by European Space Agency, a number of experiments to be performed in the CIRA Plasma Wind Tunnel "Scirocco", representative of the capsule flight conditions with respect to the shock wave boundary layer interaction phenomenon occurring around the 20 deg open flap, has been designed: PWT driving conditions, model configuration and attitude and model instrumentation have been defined, by means of a massive CFD activity performed by using the CIRA code H3NS, in order to duplicate on a forebody full-scale flap model both pressure and heat flux levels estimated in critical flight conditions.

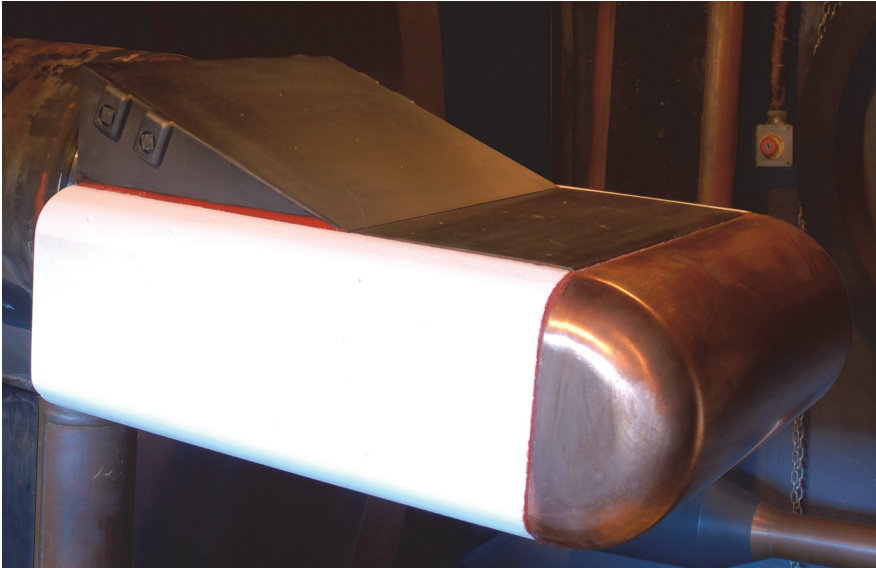


Fig. 12. Model configuration

The model reproduces the EXPERT (Di Clemente et al., 2005) capsule full-scale flap (Fig. 12) characterized by 20 deg deflection angle; it is mounted on an holder with a flat plate ahead of the flap with rounded leading and lateral edges. In order to be consistent with the EXPERT capsule, the model will be built by using as much as possible the same materials: in particular, considering the zone of our interest, the upper part is covered by a flat plate of PM1000 (or similar material) equipped with pressure taps, thermocouples and combined heat flux/pressure sensors, whereas the flap is covered by a 4mm thick plate of C-SiC with a deflection angle of 20 deg with respect to the flat plate, and it is equipped with pressure taps and thermocouples. The cylinder leading edge has a radius of 100 mm and a length of 400 mm, the flat plate is 400 mm wide and 200 mm long, the flap is 400 mm wide and 300 mm long. All the lateral edges are rounded with a radius of 50 mm in order to avoid localized over heating, whereas the flap C-SiC plate has a radius of curvature at the lateral edges equal to 4mm (i.e. its thickness). Detailed 2D and 3D computations of the flow around the model with proper thermal and catalytic modeling of the surface have been carried out in different PWT operating conditions determined to duplicate either the SWBLI phenomenon around the body flap either the associated thermo-mechanical loads acting on it during the EXPERT re-entry flight.

For the present qualitative analysis two dimensional computations carried out over the model symmetry plane are taken under consideration; in particular the conditions  $H_0=35$  MJ/kg,  $P_0=2$  bar are analyzed (this condition corresponding to the lower freestream Knudsen number:  $1.47 \cdot 10^{-3}$ ) by comparing the results obtained with a classical Navier-Stokes approach and DSMC method, in order to check possible local effects of rarefaction. Note that for this high enthalpy case it has been decided to not perform the CFD slip computation since more accurate DSMC calculations are not strongly CPU-time demanding due to the reduced number of needed particles. Specifically, this test case is characterized by the following flow properties  $M_\infty = 12.94$ ,  $Re_\infty/m = 9.03 \times 10^3$ ,  $T_\infty = 240$  K and a model attitude of 12 deg. A grid-independence study for CFD simulations has been carried out as well as a study of DSMC solution sensitivity to the number of particles (not shown).

A preliminary analysis has been carried out considering the wall at fixed temperature of 300 K, and the following **Fig. 13** and **Fig. 14** show the Mach number contours and the streamlines for the two performed computations. Figures show the strong bow shock wave ahead of the model, that is more inclined, as expected, in the case of DSMC simulation, the strong expansion on the bottom part of the model, and finally the shock wave boundary layer interaction around the corner and the subsequent recirculation bubble, that is in incipient conditions in the case of rarefied flow simulation.

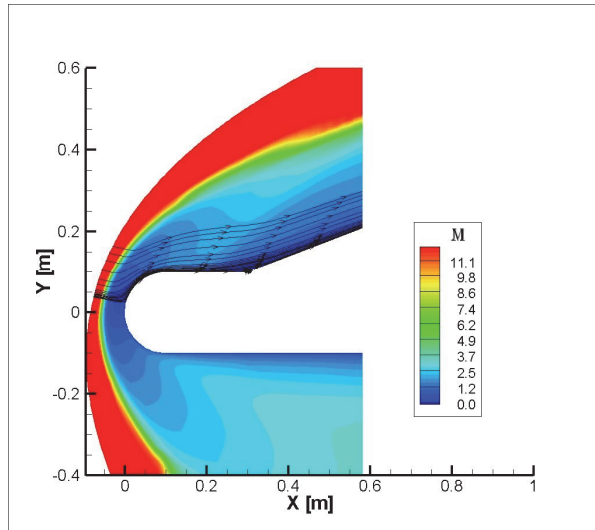


Fig. 13. CFD: Mach number contours and streamlines

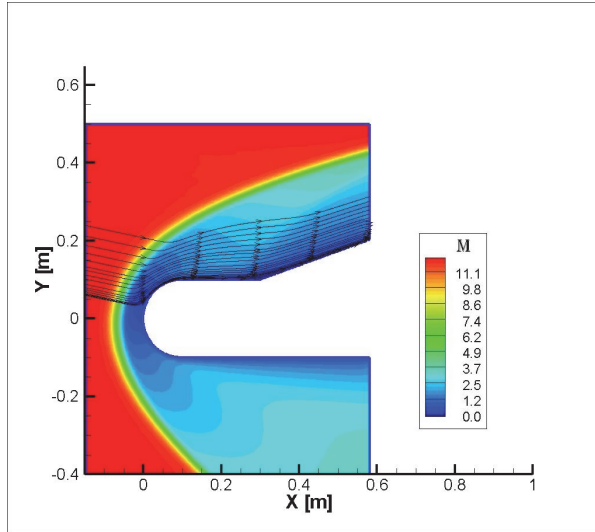


Fig. 14. DSMC: Mach number contours and streamlines

The Fig. 15 exhibits the slip velocity wall distribution predicted by DSMC calculation showing a peak value of about 1,3% of freestream velocity in correspondence of the beginning of the flat plate downstream of the model nose. It can be underlined that these low values of slip velocity were expected since, differently from the validation test case (i.e. the hollow cylinder flare), no sharp leading edge is present in this PWT model, therefore *continuum* regime flow conditions are predicted around the nose. Looking also at Fig. 15 , it can be observed that the same qualitative cuspid-like distribution has been predicted in correspondence of the corner, where a separation (or incipient separation like in this case) occurs.

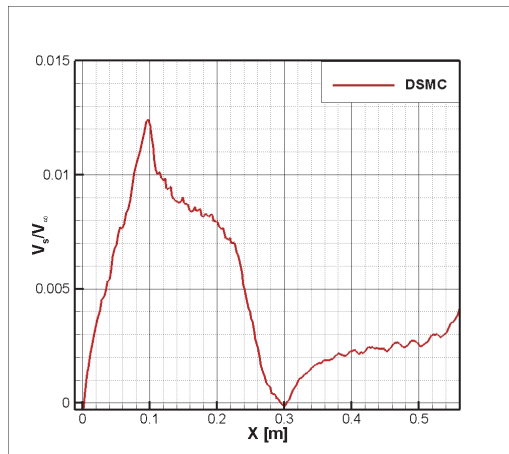


Fig. 15. Slip velocity distribution

By carefully examining **Fig. 16** and **Fig. 17**, and remembering the analysis performed for the validation test case, the same considerations apply to the present applicative case in high enthalpy conditions. In particular, a reduction of separation extent is observed with DSMC calculation (see **Fig. 13** and **Fig. 14**), as well as a slight reduction of the mechanical load acting on the flap (see **Fig. 16**).

Finally, also looking at **Fig. 15**, in correspondence of the section where the maximum of slip velocity occurs, i.e.  $X=0.1$  m, the local Knudsen number is:

$$Kn_{\delta} = \lambda/\delta \approx 4.05 \times 10^{-2}$$

and this value justifies the occurrence of local effects of rarefaction on the prediction of important aspects of shock wave boundary layer interaction as well as the extent of separation region.

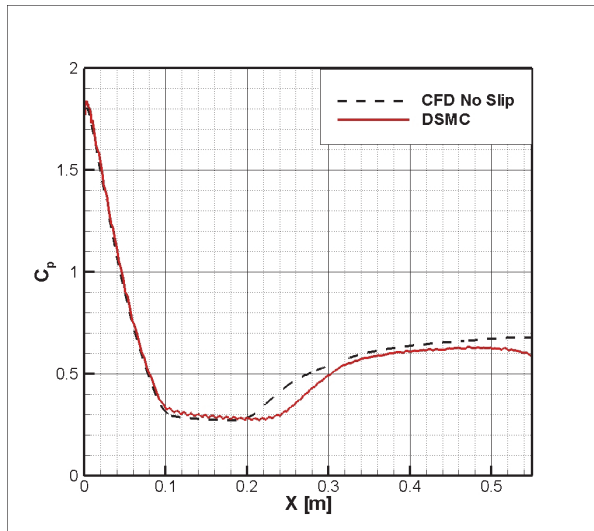


Fig. 16. Pressure coefficient distribution

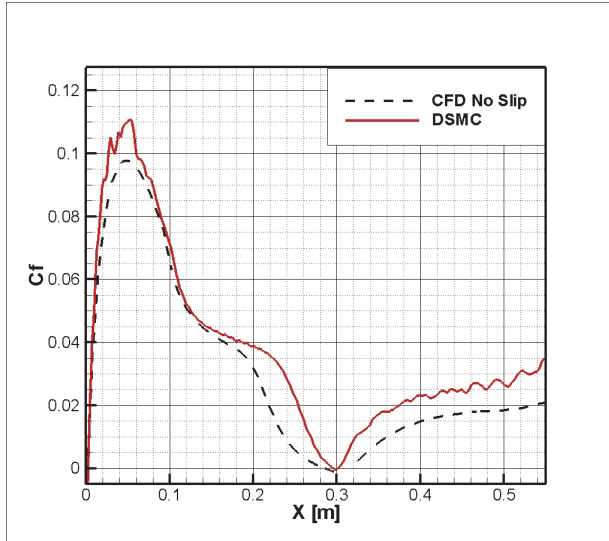


Fig. 17. Skin friction coefficient distribution

As a conclusion, it must be stressed the fact that local rarefaction effects must be taken into account when designing plasma wind tunnel tests at limit conditions of the facility envelope, in particular for very low pressures and high enthalpies as in the present case. This is particularly true when plasma test requirements are represented by the reproduction on the test model (or on parts of it) of given values of mechanical and thermal loads, as well as of shock wave boundary layer interaction characteristics (i.e. separation length, peak of pressure, peak of heat flux, etc.).

#### 4. Conclusion

Local effects of rarefaction on Shock-Wave-Boundary-Layer-Interaction have been studied by using both the *continuum* approach with the slip flow boundary conditions and the kinetic one by means of a DSMC code.

The hollow cylinder flare test case for ONERA R5Ch wind tunnel conditions was numerically rebuilt in order to validate the methodologies. The free stream Knudsen number for the selected test case implies that much of the flow is in continuum conditions, even though local effects of rarefaction have been checked. In particular, the comparison with experimental data has shown that rarefactions effects are not negligible in prediction of the separation length. The CFD code with slip flow boundary conditions has shown good predicting capabilities of the size of the recirculation bubble, and the analysis of the density profiles inside boundary layer has shown a good agreement between DSMC and CFD with slip conditions in different sections along the body. Definitely, the present wind tunnel test case, simulated with the three different methodologies (classics CFD, CFD with slip flow boundary conditions and DSMC), has shown that local rarefaction effects are significant for the prediction of important aspects of shock wave boundary layer interaction as the sizing of recirculation bubble and it has been also shown that CFD with slip flow boundary conditions is, in this case, a good compromise between computational cost and accuracy.

The same considerations apply to a CIRA Plasma Wind Tunnel test case, where significant rarefactions effects were found on the SWBLI phenomenon; therefore they must be taken into account when designing plasma wind tunnel tests at limit conditions of the facility envelope, in particular for very low pressures and high enthalpies as in the present case.

## 5. References

- Bird, G. A., *Molecular Gas Dynamics and the Direct Simulation of Gas Flows*, Clarendon, Oxford, 1994.
- Bird, G. A., "The DS2V/3V Program Suite for DSMC Calculations" *Rarefied Gas Dynamics, 24th International Symposium*, Vol. 762 edited by M. Capitelli, American Inst. Of Physics, NY, 2005, pp. 541-546, February, 1995.
- Borrelli S., Pandolfi M., "An Upwind Formulation for the Numerical Prediction of Non Equilibrium Hypersonic Flows", *12th International Conference on Numerical Methods in Fluid Dynamics*, Oxford, United Kingdom, 1990.
- Chanetz, B., Benay, R., Bousquet, J., M., Bur, R., Pot, T., Grasso, F., Moss, J., "Experimental and Numerical Study of the Laminar Separation in Hypersonic Flow", *Aerospace Science and Technology*, No. 3, pp. 205-218, 1998.
- Di Clemente M., Marini M., Schettino A., "Shock Wave Boundary Layer Interaction in EXPERT Flight Conditions and Scirocco PWT", *13th AIAA/CIRA International Space Planes and Hypersonics Systems and Technologies Conference*, Capua, Italy, 2005.
- Kogan N. M., *Rarefied Gas Dynamics*, Plenum, New York, 1969.
- Markelov, G., N., Kudryavtsev A. N., Ivanov, M., S., "Continuum and Kinetic Simulation of Laminar Separated Flow at Hypersonic Speeds", *The Journal of Spacecraft and Rockets*, Vol. 37 No. 4, July-August 2000.
- Marini, M., "H09 Viscous Interaction at a Cylinder/Flare Junction", *Third FLOWNET Workshop*, , Marseille, 2002.
- Millikan R.C., White D.R., "Systematic of Vibrational Relaxation", *The Journal of Chemical Physics*, Vol. 39 No.12, pp. 3209-3213, 1963.
- Park C., "A Review of Reaction Rates in High Temperature Air", *AIAA paper 89-1740*, June 1989.
- Park C., Lee S.H., "Validation of Multi-Temperature Nozzle Flow Code NOZNT", *AIAA Paper 93-2862*, 1993.
- Ranuzzi, G., Borreca, S., "CLAE Project. H3NS: Code Development Verification and Validation", *CIRA-CF-06-1017*, 2006.
- Yun K.S., Mason E. A., "Collision Integrals for the Transport Properties of Dissociating Air at High Temperatures", *The Physics of Fluids*, Vol. 39 No.12, pp. 3209-3213, 1962.

# Investigation on Oblique Shock Wave Control by Surface Arc Discharge in a Mach 2.2 Supersonic Wind Tunnel

Yinghong Li<sup>1</sup> and Jian Wang<sup>2</sup>

<sup>1</sup>Engineering College, Air Force Engineering University

<sup>2</sup>Army Aviation Institute

China

## 1. Introduction

A shock wave is a typical aerodynamic phenomenon in a supersonic flow, and if controlled effectively, a series of potential applications can be achieved in aerospace fields, such as reducing wave drag and sonic boom of the supersonic vehicle, optimizing shock waves of the supersonic inlet in off-design operation states, decreasing pressure loss induced by shock waves in the supersonic wind tunnel or aeroengine internal duct, controlling shock waves of the wave rider, changing shock wave symmetry to achieve flight control and inducing shock waves in the aeroengine nozzle to achieve thrust vector control.

Shock wave control can be achieved by many mechanical or gas dynamic methods, such as the ramp angle control in supersonic inlet and the holl/cavum control in self-adapted transonic wing. Because the structural configurations of these methods are somewhat complex and the flow control response is also slow, plasma flow control based on gas discharge physics and electromagnetohydrodynamics (EMHD) theory has been developed recently in the shock wave control field. Using this method, substantial thermal energy can be added in the shock wave adjacent areas, then the angle and intensity of shock wave change subsequently.

Meyer *et al* investigated whether shock wave control by plasma aerodynamic actuation is a thermal mechanism or an ionization mechanism, and the experimental results demonstrated that the thermal mechanism dominates the shock wave control process [1, 2]. Miles *et al* investigated the shock wave control by laser energy addition experimentally and numerically, and the research results showed that when the oblique shock wave passed by the thermal spot induced by laser ionization, the shock wave shape distorted and the shock wave intensity reduced [3]. Macheret *et al* proposed a new method of virtual cowl induced by plasma flow control which can optimize the shock waves of supersonic inlet when its operation Mach number is lower than the design Mach number [4]. Meanwhile, they used the combination method of e-beam ionization and magnetohydrodynamic (MHD) flow control to optimize the shock waves of supersonic inlet when operating in off-design states, and the research results demonstrated that the shock waves can reintersect in the cowl adjacent area in different off-design operation states with the MHD acceleration method and the MHD power generation method, respectively [5]. Leonov *et al* used a quasi-dc

filamentary electrical discharge, and the experimental results showed that shock wave induction, shock wave angle transformation and shock wave intensity reduction, etc could all be achieved by plasma flow control [6-8]. Other than oblique shock wave control, the bow shock wave control by plasma aerodynamic actuation was also studied by Kolesnichenko *et al* [9], Ganiev *et al* [10], and Shang *et al* [11] for the purpose of reducing peak thermal load and wave drag.

This paper used the arc discharge plasma aerodynamic actuation, and the wedge oblique shock wave control by this plasma aerodynamic actuation method was investigated in a small-scale short-duration supersonic wind tunnel. The change laws of shock wave control by plasma aerodynamic actuation were obtained in the experiments. Moreover, a magnetic field was applied to enhance the plasma actuation effects on a shock wave. Finally, a qualitative physical model was proposed to explain the mechanism of shock wave control by plasma aerodynamic actuation in a cold supersonic flow.

## 2. Experimental setup

The design Mach number of the small-scale short-duration supersonic wind tunnel is 2.2 and its steady operation time is about 30-60 s. The test section is rectangular with a width of 80mm and a height of 30 mm. The gas static pressure and static temperature in the test section are 0.5 atm and 152 K, respectively. The groove in the test section lower wall is designed for the plasma aerodynamic actuator fabrication.

The power supply consists of a high-voltage pulse circuit and a high-voltage dc circuit. The output voltage of the pulse circuit can reach 90 kV, which is used for electrical breakdown of the gas. The dc circuit is the 3 kV-4 kW power source, which is used to ignite the arc discharge.

The plasma aerodynamic actuator consists of graphite electrodes and boron-nitride (BN) ceramic dielectric material. Three pairs of graphite electrodes are designed with the cathode-anode interval of 5mm and the individual electrode is designed as a cylindrical structure which is embedded in the BN ceramic. The upper gas flow surface of electrodes and ceramic must be a plate to ensure no unintentional shock wave generation in the test section. The controlled oblique shock wave is generated by a wedge with an angle of 20°. As shown in figure 1, the plasma aerodynamic actuator is embedded in poly-methyl-methacrylate (PMMA) and then inserted into the groove of the test section lower wall. There are 10 pressure dots with a diameter of 0.5mm along the flow direction for the gas pressure measurement.

As shown in figure 2, the static magnetic field is generated by a rubidium-iron-boron magnet which consists of four pieces. Two pieces construct the N pole and the other two pieces construct the S pole. The magnetic field strength in the zone of interaction is about 0.4 T. Based on the MHD theory, the main purpose of adding magnetic field is applying a Lorentz body force to the charged particles in the arc plasma, which can influence the plasma actuation effects on shock wave.

The test systems consist of a gas pressure measurement system, a schlieren photography system and an arc discharge voltage-current measurement system. The gas pressure measurement system is used to measure and compute the oblique shock wave intensity with the data-acquisition frequency of 1 kHz and the acquisition time of 3-10 s. The schlieren photography system is used to photograph the configuration of the oblique shock wave. It uses the Optronis® high-speed CCD camera with the maximum framing rate of 200 000 Hz.



For the purpose of acquiring the pulsed arc discharge process in the flow, the framing rate in this paper is selected as 8000 Hz with an exposure time of 0.0001 s and a resolution of  $512 \times 218$  pixels. The arc discharge voltage and current are monitored by a voltage probe (P6015A, Tektronix Inc.) and a current probe with a signal amplifier (TCP312+TCPA300, Tektronix Inc.), respectively. The two signals are measured by a four-channel digital oscilloscope (TDS4104, Tektronix Inc.).

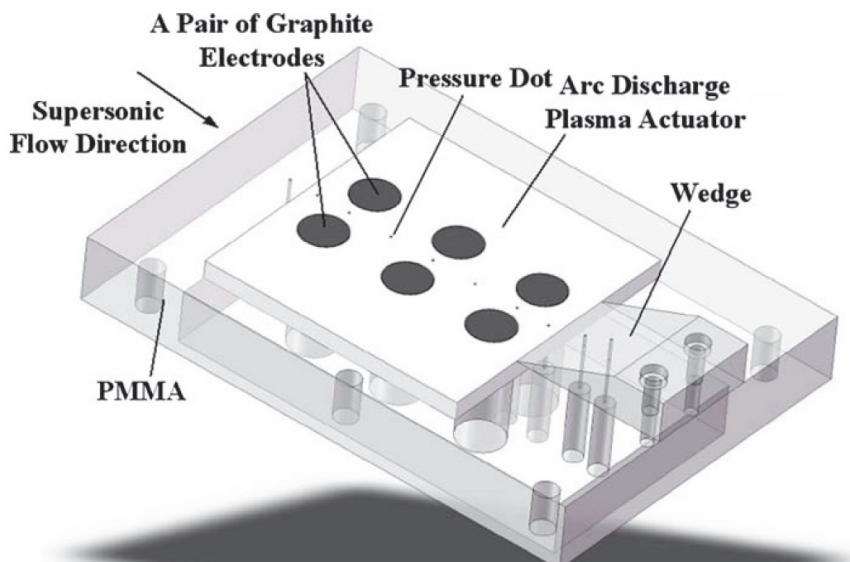


Fig. 1. Sketch of arc discharge plasma aerodynamic actuator.

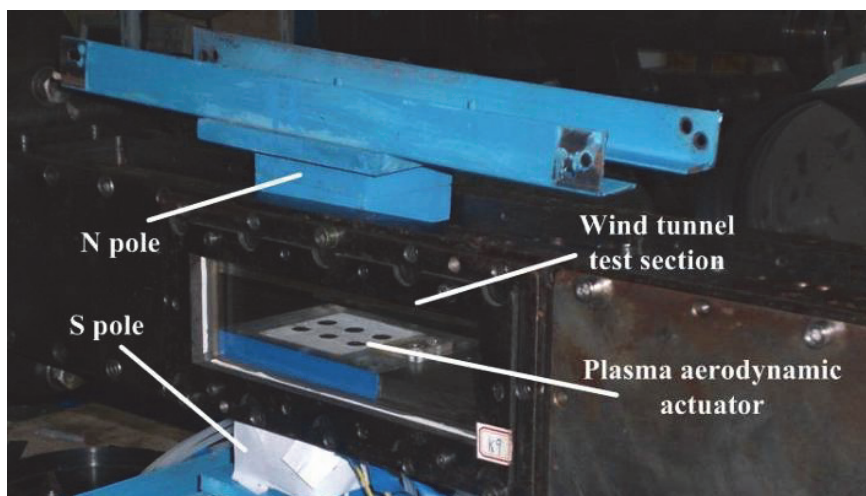


Fig. 2. Sketch of magnet fabrication on the wind tunnel test section.

### 3. Test results and discussion

#### 3.1 Electrical characteristics

Under the test conditions of Mach 2.2, the arc discharge is a pulsed periodical process with a period of 2-3 ms, and the discharge time only occupies 1/20 approximately in a period. The discharge voltage-current curves including several discharge periods are shown in figure 4(a). It can be seen that the discharge intensity is unsteady with some periods strong but some other periods weak. The discharge voltage-current-power curves in a single period are shown in figure 4(b). The discharge process in a single period can be divided into three steps. The first step is the pulse breakdown process. When the gas breakdown takes place, the discharge voltage and the current can reach as high as 13 kV and 18 A, respectively, and the discharge power reaches hundreds of kilowatts. However, this step lasts for an extremely short time of about  $1 \mu\text{s}$ , which indicates that it is a typical strong pulse breakdown process. The second step is the dc hold-up process. After the pulse breakdown process, arc discharge starts immediately. The discharge voltage decreases from 3 kV to 300-500V and the discharge current increases to 3-3.5A correspondingly. The discharge power is maintained at 1-1.5 kW. This step lasts for a long time of about  $80 \mu\text{s}$ . The third step is the discharge attenuation process. Because the supersonic flow blows the plasma channel of the arc discharge downstream strongly, the Joule heating energy provided by the power supply dissipates in the surrounding gas flow intensively. As a result, the discharge voltage increases gradually. Both the discharge current and power decrease. When the power supply cannot provide the discharge voltage, the discharge extinguishes. After some time, the next period of discharge will start again. This attenuation step lasts for about  $20 \mu\text{s}$ . The time-averaged discharge power of the above three steps within  $100 \mu\text{s}$  is about 1.3kW.

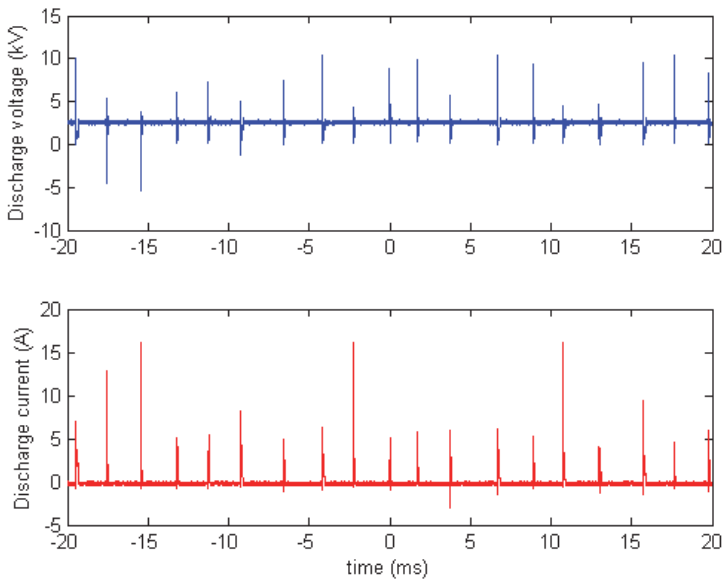
From figure 3 we can see that the arc discharge plasma is strongly bounded near the wall surface and blown downstream by the supersonic flow. The arc discharge is transformed from a large-volume discharge under static atmospheric conditions to a large-surface discharge under supersonic flow conditions.



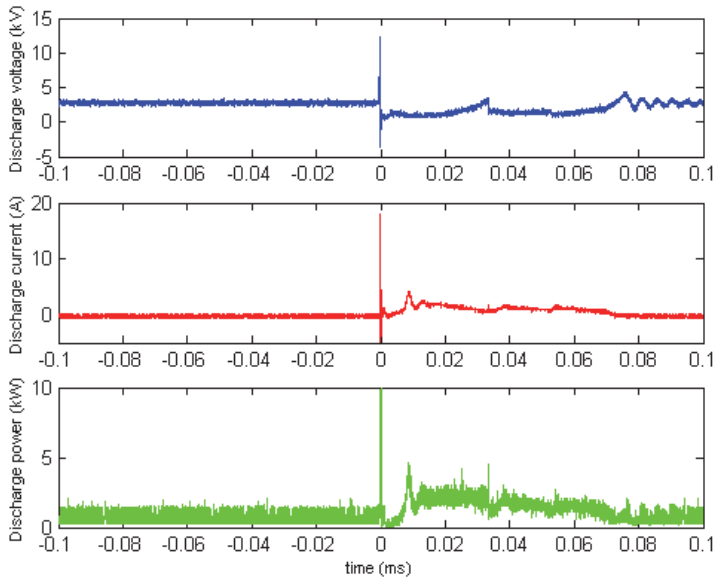
Fig. 3. Arc discharge picture in the supersonic flow.

#### 3.2 The wedge oblique shock wave control by typical plasma aerodynamic actuation

Three pairs of electrodes discharge simultaneously in the experiments. Under the conditions of an input voltage of 3 kV and an upwind-direction magnetic control, the wedge oblique shock wave control by this plasma aerodynamic actuation was investigated in detail. Because of the fabrication error and actuator surface roughness, there are some unintentional shock waves in the test section before the wedge. The wedge in the supersonic flow generates a strong oblique shock wave, which can be seen from figure 5(a). Because the boundary layer in the test section lower wall before the wedge is somewhat thick with a thickness of about 3-4 mm, the start segment of the oblique shock wave is composed of many weak compression waves, which intersect in the main flow to form the strong oblique shock wave.



(a)



(b)

Fig. 4. Electrical characteristics of arc discharge in supersonic flow. (a) Discharge voltage-current curves including several discharge periods. (b) Discharge voltage-current-power curves in a single period.

When applying plasma aerodynamic actuation, the schlieren test results showed that the structure of the wedge oblique shock wave changed distinctly. Within the discharge time, the intensity of the shock wave change was from weak to strong and then to weak again, which indicated that the shock wave control was a dynamic process, which was consistent with the unsteady characteristics of the three discharge steps discussed in section 3.1. However, within the extinction time, the shock wave recovered to the undisturbed state as before, which demonstrated that the arc discharge control on shock wave was a pulsed periodical process. The mostly strong shock wave control effect within the discharge time is shown in figure 5(b). We can see that the start segment of the wedge oblique shock wave is transformed from a narrow strong wave to a series of wide weak waves, and the start point of the shock wave shifts 4mm upstream, its angle decreases from  $35^\circ$  to  $32^\circ$  absolutely and 8.6% relatively, and its intensity weakens as well. This phenomenon is somewhat similar to the supersonic inlet design method of transforming a strong shock wave to a series of weak shock waves for the purpose of reducing flow pressure loss.

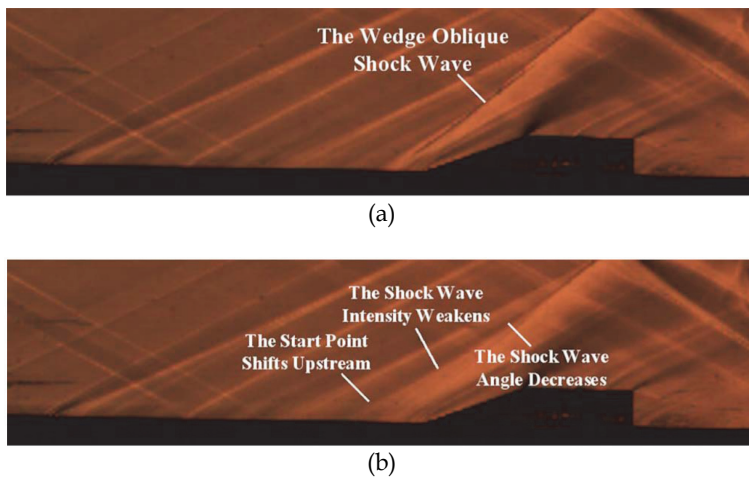


Fig. 5. Influence of plasma aerodynamic actuation on the structure of wedge oblique shock wave. (a) Schlieren picture without plasma aerodynamic actuation. (b) Schlieren picture with plasma aerodynamic actuation.

Confined by the upper limit 1 kHz of data-acquisition frequency, the pressure measurement system cannot precisely distinguish the pulsed process of shock wave control, so the pressure data in this paper are just the macro time-averaged description of plasma flow control on shock wave. The intensity of wedge oblique shock wave is defined as the pressure ratio of shock wave downstream flow (pressure dot 10) on shock wave upstream flow (pressure dot 7). Because of flow turbulence and unsteadiness in the wind tunnel test section, the pressure data have a little fluctuation with the intensity less than 1%. As seen from figure 6, when applying plasma aerodynamic actuation, the shock wave intensity greatly decreases with the time-averaged intensity from 2.40 to 2.19 absolutely and 8.8% relatively. Hence, we can conclude that the plasma aerodynamic actuation controls the wedge oblique shock wave effectively.

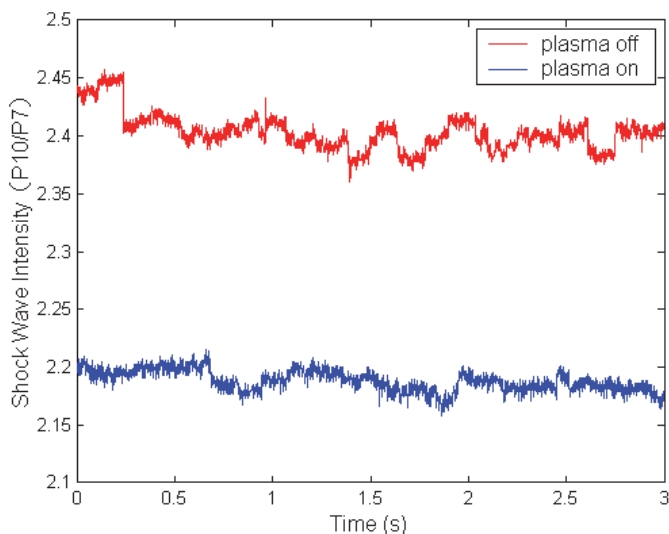


Fig. 6. Influence of plasma aerodynamic actuation on the intensity of wedge oblique shock wave.

### 3.3 Magnetic control on shock wave

The basic principle of magnetic control is applying the Lorentz body force to the arc discharge current. The mathematical expression is  $\vec{F} = \vec{j} \times \vec{B}$ , where  $\vec{j}$  refers to the discharge current density vector,  $\vec{B}$  refers to the magnetic field intensity vector and  $\vec{F}$  refers to the Lorentz body force vector. By changing the direction of the discharge current, both the upwind-direction and the downwind-direction Lorentz force can be achieved, as shown in figure 7.

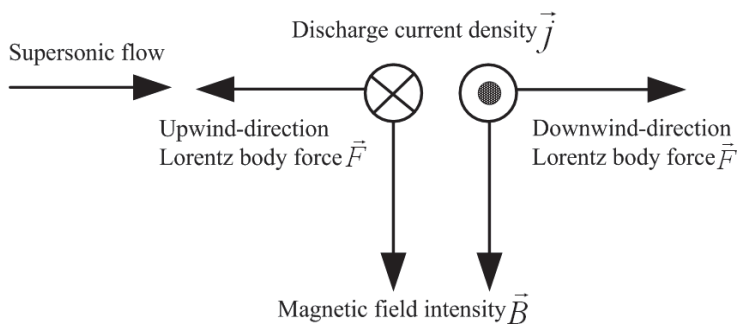


Fig. 7. Basic principle of magnetic control on gas discharge.

From the shock wave intensity measurements in figure 8, we can see that magnetic control greatly intensifies the shock wave control effects. When applying plasma aerodynamic actuation without magnetic control, the intensity of the wedge oblique shock wave

decreases only by 1.5%, but when applying the upwind-direction magnetic control, it decreases by 8.8%. Moreover, when applying the downwind-direction magnetic control, it decreases by 11.6%. The experimental results showed that the maximum shock wave intensity decrease is 20.2%. Hence we can conclude that magnetic control greatly intensifies the shock wave control effects and the downwind-direction magnetic control is better than the upwind-direction magnetic control.

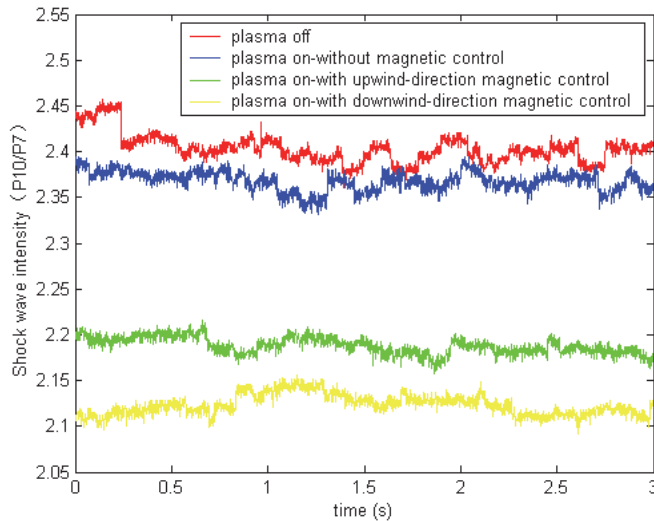


Fig. 8. Influence of magnetic control on shock wave intensity.

Then the mechanism of enhancement of plasma actuation effects on the shock wave by magnetic field is discussed. The discharge characteristics without or with magnetic field under the conditions of no flow are measured and the results demonstrate that they are very different. The voltage, current and power measurements without magnetic field are shown in figure 9. The gas breakdown voltage between the graphite electrodes is about 2 kV and when the input voltage provided by the power supply exceeds this value, arc discharge happens. At the instant of gas breakdown, voltage decreases from 2 kV to about 300 V and current increases to about 1 A. The discharge power is calculated as 300 W. Then the voltage holds at 300 V, but the current decreases gradually. After about 0.5 s, the current sustains at about 440 mA and the discharge power holds at about 130 W. Until now, the steady state of arc discharge is achieved. The above discharge characteristics demonstrate that the arc discharge without magnetic field can be separated into two phases, which correspond to the strong pulsed breakdown process and the steady discharge process, respectively.

When the magnetic field is applied, the discharge characteristics are shown in figure 10 and we can see that the arc discharge transitions from the continuous mode to the pulsed periodical mode. The discharge period is very unstable from tens of milliseconds to several seconds. In a typical discharge period, the discharge time only occupies several milliseconds, which demonstrates that the discharge extinguishes within most time of a period. At the instant of pulsed discharge, voltage decreases to about 500 V and current increases to about 1.2 A. The discharge power is calculated to be about 600 W. These discharge characteristics with magnetic field are very similar to the conditions in the flow

and show great differences under the conditions without the magnetic field. Two remarkable differences are concluded.

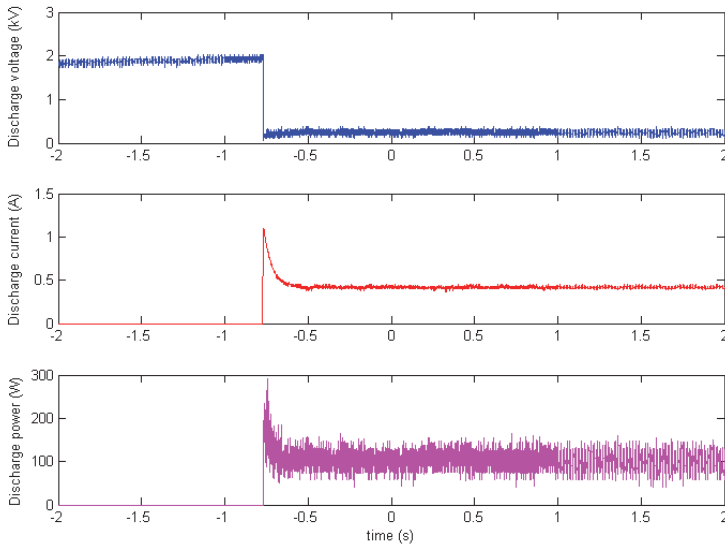


Fig. 9. Electrical characteristics of arc discharge under the conditions of no magnetic field and no flow.

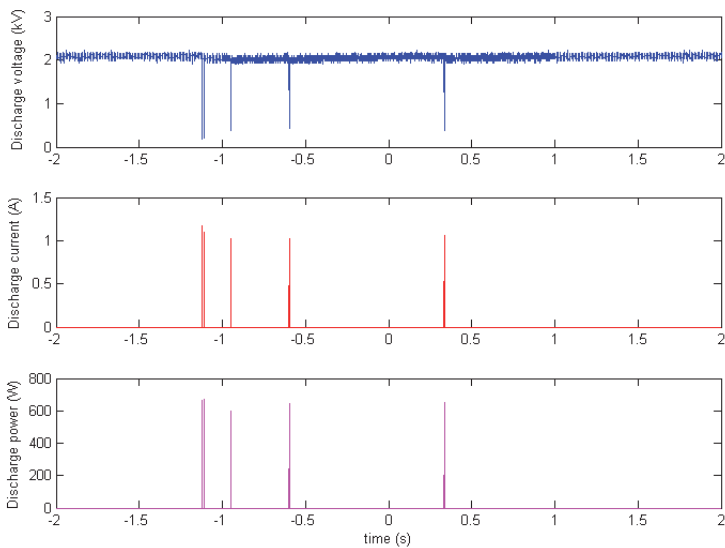


Fig. 10. Electrical characteristics of arc discharge under the conditions of magnetic field and no flow.

Firstly, the arc discharge transitions from the continuous mode to the pulsed periodical mode. When the arc discharge reaches the steady state, the Joule heating energy provided by the power supply must balance the dissipated energy, such as convection loss, conduction loss and radiation loss. Under the conditions of no magnetic field and no flow, convection loss mainly refers to the energy loss of natural convection process that the hot arc plasma transfers thermal energy to the cold surrounding air. Conduction loss mainly refers that the hot arc plasma transfers the thermal energy to the cold electrodes and the ceramic surfaces. As the Joule heating energy can balance the dissipated energy, the arc discharge can reach the steady state. However, under the condition of magnetic field, the plasma channel of the arc discharge is greatly deflected by the Lorentz body force, which is shown in figure 11. Besides the natural convection process, the arc plasma also endures intensive constrained convection process, which dissipates the Joule heating energy substantially. Therefore, the Joule heating energy provided by the power supply cannot balance the dissipated energy, so the discharge extinguishes quickly.

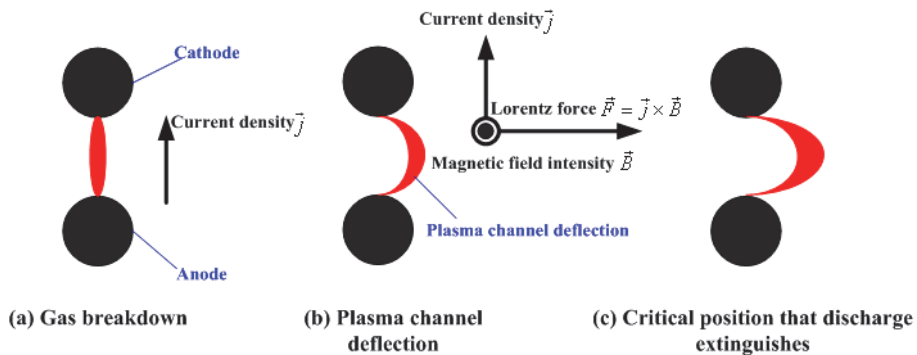


Fig. 11. Sketch of plasma channel deflection by Lorentz force under the condition of magnetic field.

Secondly, the discharge power increases. At the instant of gas breakdown, the power deposition by the arc discharge increases from 300 to 600 W under the condition of magnetic field. So we can deduce the preliminary fact that the power deposition in the flow also increases after the application of the magnetic field. Therefore, the shock wave control effect is intensified by the magnetic field as measured in the experiments. So we suppose that the observed enhancement of discharge effect in the magnetic field is due to the rise in power release but not the proposed EMHD interaction! This important conclusion is very different from the authors' initial intentions to use a magnetic field in the experiments.

### 3.4 Discussion on shock wave control mechanisms

A qualitative physical model is proposed in this section to explain the mechanism of shock wave control by surface arc discharge. The sketch of physical problem for modeling is shown in figure 12, and the phenomenon can be simplified as a 2-D problem. In order to generate an oblique shock wave, a wedge is placed at the lower wall surface in the cold supersonic flow duct. The arc discharge electrodes are mounted in front of the wedge. The surface arc discharge plasma is generated and blown downstream by the cold supersonic flow, which can be seen from figure 3. From the discharge picture in experiments, the arc



discharge plasma covers large areas in front of the wedge and we suppose that the height of arc discharge plasma is less than the height of wedge. Flow viscosity is disregarded, so the boundary layer effects can be neglected. Because we just deduce the qualitative change laws of oblique shock wave control by arc discharge, the parameters quantities are not set concretely in this physical model.

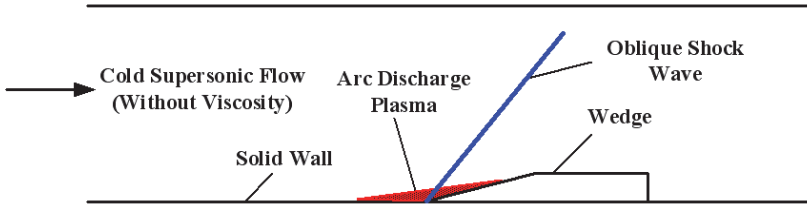


Fig. 12. Sketch of physical problem for modelling.

In the 1-D, steady and ideal gas flow, heating can accelerate the gas and decrease the gas pressure. As a result, the mass flux density of gas flow decreases, which is the mechanism of thermal choking phenomenon in the flow system. The influence of thermal choking effect on gas flow can be described as parameter

$$\varepsilon = \frac{\dot{m}_{\text{heat}}}{\dot{m}_{\text{unheat}}} = \frac{1}{\sqrt{1 + \frac{s_0}{c_p T_0}}} \quad (1)$$

where  $\varepsilon$  is the ratio of mass flux density,  $\dot{m}_{\text{heat}}$  and  $\dot{m}_{\text{unheat}}$  are the mass flux density with and without gas heating respectively,  $s_0$  is the amount of gas heating with unit mass,  $c_p$  and  $T_0$  are the specific heat coefficient with constant pressure and gas static temperature without heating respectively, and  $c_p T_0$  is the gas static enthalpy without heating. Defining nondimensional parameter  $H_e = \frac{s_0}{c_p T_0}$  and it's the energy ratio of gas heating on initial static enthalpy with unit mass. Because  $s_0 > 0$ ,  $H_e > 0$  and  $\varepsilon < 1$ , which indicates that gas heating decreases the mass flux density of 1-D flow. When  $H_e \rightarrow \infty$ ,  $\varepsilon \rightarrow 0$ , which indicates that if the amount of gas heating is extremely large, the mass flux density will decrease to zero and the gas flow will be totally choked. As arc discharge plasma can increase the gas temperature of cold supersonic flow from the level below 200 K to kilos of K rapidly, the amount of gas heating is very large, and the thermal choking phenomenon must be very remarkable in the flow duct.

Then we broaden the above 1-D analysis to the 2-D problem of shock wave control by arc discharge plasma. If the height of arc discharge plasma along the flow direction doesn't change, the flow area can be separated into two distinct regions with region *a* that corresponds to the cold supersonic flow area between arc discharge plasma and upper duct wall, and region *b* that corresponds to the high-temperature area of arc discharge plasma. The sketch is shown in figure 13. As the gas pressure of cold supersonic flow is about the high level of  $10^4$  Pa, arc discharge plasma often reaches the Local Thermal Equilibrium (LTE)

state approximately which indicates that the electron temperature equals to the ion and neutral gas temperature. Therefore, we can use one temperature to describe the thermal characteristics of arc discharge plasma.

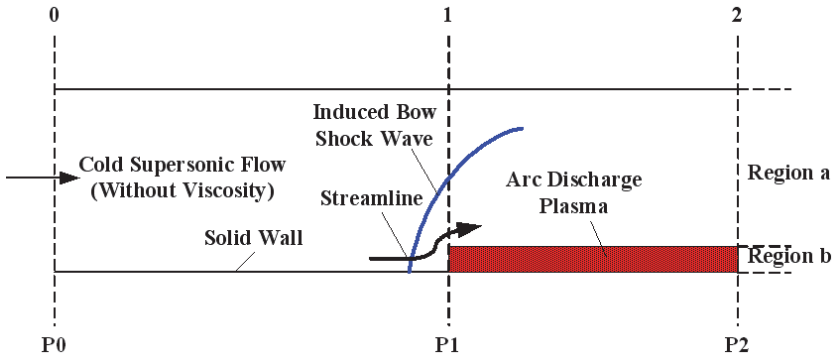


Fig. 13. Sketch of bow shock wave induction by arc discharge plasma.

When gas flows through the thermal area of arc discharge plasma, the mass flux will decrease because of thermal choking effect, then part of gas will pass to the cold gas flow area and the streamline will bend upward at section 1. When the uniform flow reaches section 1, we suppose that the mass flux of region *a* and *b* will rearrange, so the 2-D problem is reduced to 1-D again after the flow passing through section 1. The gas pressure at the cross section of region *a* and *b* reaches equilibrium. Based on the above hypothesis, the mass flux density of region *a* and *b* can be described as

$$\dot{m}_a = \sqrt{\frac{(P_0 - P_2)P_2}{RT_{a,unheat}}} \tag{2}$$

$$\dot{m}_b = \sqrt{\frac{(P_0 - P_2)P_2}{RT_{b,heat}}} \tag{3}$$

where  $\dot{m}_a$  and  $\dot{m}_b$  are the mass flux density of region *a* and *b* respectively,  $P_0$  and  $P_2$  are the gas pressure of section 0 and 2 respectively,  $T_{a,unheat}$  and  $T_{b,heat}$  are the gas temperature of region *a* and *b* respectively and  $R$  is the universal gas constant. From equation (2) and (3), the mass flux density ratio of two regions is

$$\frac{\dot{m}_a}{\dot{m}_b} = \sqrt{\frac{T_{b,heat}}{T_{a,unheat}}} \tag{4}$$

So the mass flux ratio of two regions is

$$\frac{\dot{M}_a}{\dot{M}_b} = \frac{A_a}{A_b} \sqrt{\frac{T_{b,heat}}{T_{a,unheat}}} \tag{5}$$

where  $A_a$  and  $A_b$  are the cross section area of region  $a$  and  $b$  respectively,  $\dot{M}_a$  and  $\dot{M}_b$  are the mass flux of region  $a$  and  $b$  respectively.

Supposing the height of region  $a$  and  $b$  are 30mm and 2mm, respectively, so  $A_a/A_b = 15$ . In our experiments, the Mach number and gas stagnation temperature of the cold supersonic flow are 2.2 and 300 K, respectively. From the gas stagnation-static temperature equation

$$T^* = T \left( 1 + \frac{\gamma + 1}{2} M^2 \right) \quad (6)$$

The gas static temperature is about 152 K, so  $T_{a,unheat} = 152K$ . From the measurement in reference [8], the temperature of arc discharge plasma in the above cold supersonic flow can be estimated as 3000 K, so  $T_{b,heat} = 3000K$ . Then  $\dot{M}_a/\dot{M}_b \approx 67$  is acquired, which indicates that when cold supersonic gas meets the arc discharge plasma area, only little gas passes through the thermal area and most of the gas passes to the cold area. Therefore, we can conclude that the arc discharge plasma area can be regarded as a solid obstacle approximately and the gas flow cannot pass through it. Because the height of arc discharge plasma area is set constant in figure 6, the plasma area can be regarded as a rectangular blunt obstacle, which will induce a bow shock wave in the supersonic flow. However, in real conditions, the arc discharge plasma is streamlined by flow and the height of arc discharge plasma area increases from zero to larger value gradually, so the plasma area seems as a solid wedge, which can be called 'plasma wedge'. As a result, the plasma wedge will induce an oblique shock wave instead of a bow shock wave, which is shown in figure 14.

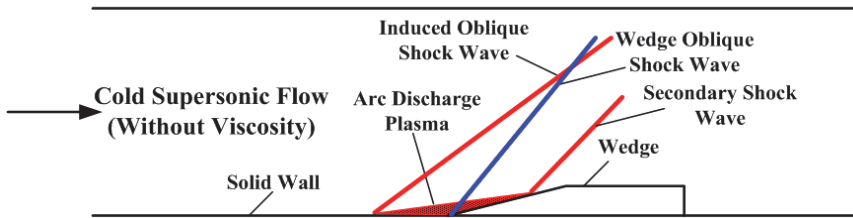


Fig. 14. Sketch of oblique shock wave control by arc discharge plasma.

Based on the above judgment of new shock wave induction by arc discharge plasma in cold supersonic flow, the wedge oblique shock wave control by arc discharge plasma is discussed as follows, which can be seen from figure 14. The wedge angle is designated as  $\theta$ . Without arc discharge, the angle and intensity of wedge oblique shock wave are designated as  $\beta$  and  $\pi_s$ , respectively. After arc discharge, the plasma wedge will induce a new oblique shock wave in front of it and the old wedge oblique shock wave will disappear. Because the height of plasma wedge is less than the height of solid wedge, there is a secondary shock wave formed at the intersection point of plasma wedge and solid wedge. The plasma wedge angle is designated as  $\theta^*$ . The angle and intensity of the induced oblique shock wave are designated as  $\beta^*$  and  $\pi_s^*$ , respectively. As  $\theta^* < \theta$  and on the condition of constant Mach number, the relationships of  $\beta^* < \beta$  and  $\pi_s^* < \pi_s$  can be concluded based on the oblique shock wave relations of  $(Ma \sim \theta \sim \beta)$ .

Therefore, based on the above thermal choking model, we can conclude that the change laws of oblique shock wave control by arc discharge plasma are (1) the start point of shock wave will shift upstream, (2) the shock wave angle will decrease and (3) the shock wave intensity will weaken. The deduced theoretical result is consistent with the experimental result which demonstrates that the thermal choking model is rational to explain the problem of shock wave control by surface arc discharge.

#### 4. Numerical simulation

Based on thermal mechanism, the arc discharge plasma is simplified as a thermal source term and added to the Navier-Stokes equations. The nonlinear partial difference equations are solved in ANSYS FLUENT® software. The flow modelling software is a widely used powerful computational fluid dynamics program based on finite volume method. It contains the broad physical modelling capabilities to model flow, turbulence, heat transfer, and reactions for industrial applications. It has excellent ability to simulate compressible flows. A user-defined function written in the C programming language is developed to define the thermal source term. The thermal source term uses the form of temperature distribution. The geometric shape of thermal source areas is supposed as rectangular and the gas temperature is uniform (3000 K). 2D coupled implicit difference method and k-epsilon two-equation turbulence models are used. The inlet flow conditions are consistent with the test conditions. As shown in figure 15, the width and height of rectangular thermal source area are 2 and 1 mm, respectively. According to the test condition of three pairs of electrodes discharging simultaneously, there are three pairs of thermal source areas with interval 2 mm.

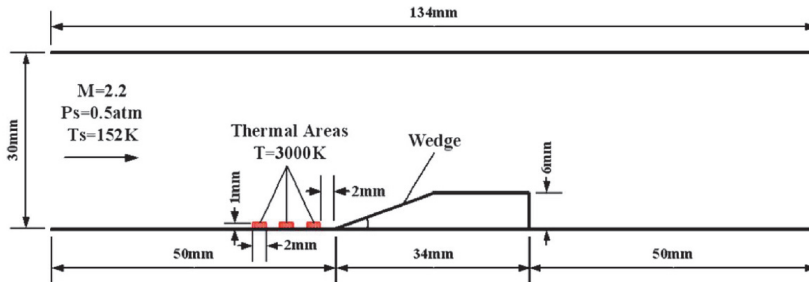


Fig. 15. Sketch of the numerical model.

As shown in figure 16(a), an oblique shock wave generates in front of the wedge, which matches the experimental results. After thermal energy addition to the supersonic flow field, we can see that the rectangular thermal source areas are blown downstream by the supersonic flow, which is shown in figure 16(b). It is consistent with the actual arc discharge picture in experiments. The geometric shape of the thermal area looks like a new wedge in front of the solid wedge and it is similar to the plasma wedge in the theoretical analysis. The influence of thermal energy addition on the wedge oblique shock wave is shown in figure 16(c). We can see that the start point of shock wave shifts upstream to the new wedge apex point and the shock wave angle decreases. The comparison curves of shock wave intensity are shown in figure 16(d), and we can see that the shock wave intensity decreases. These changes in shock wave are consistent with the experimental and theoretical results, which

demonstrate that the numerical method is reasonable. Also the thermal mechanism and thermal choking model are both validated.

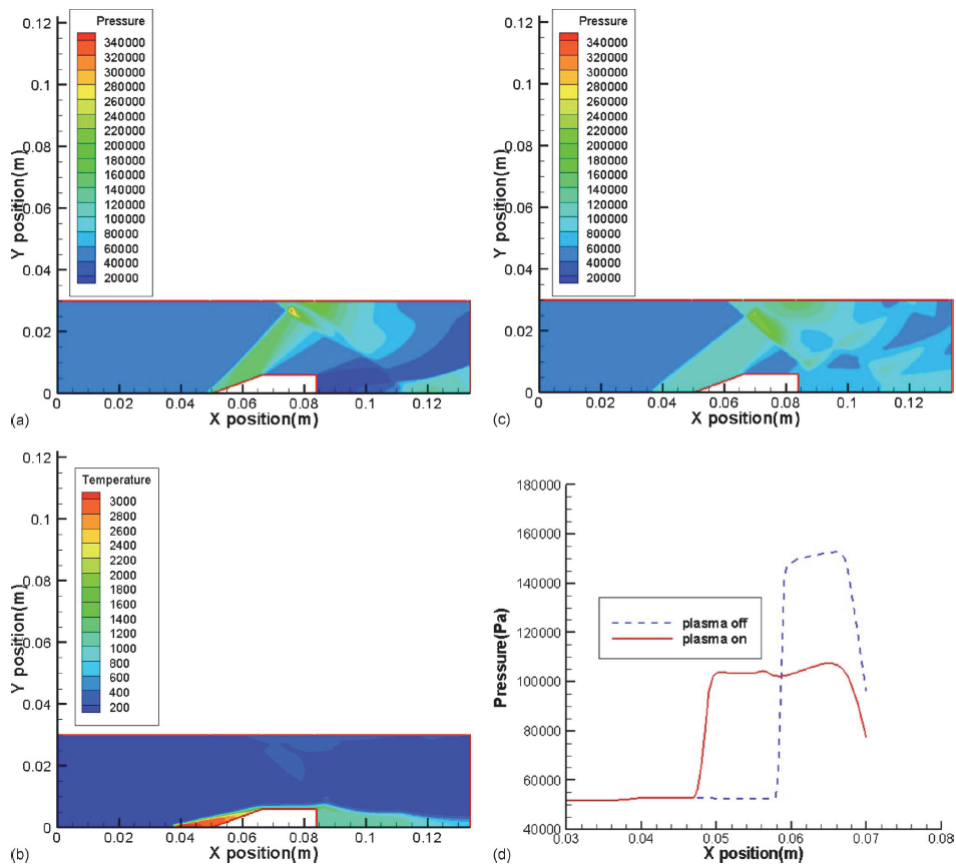


Fig. 16. Simulation results of oblique shock wave control by thermal energy addition. (a) Static pressure (Pa) contours without thermal energy addition. (b) Static temperature (K) contours with thermal energy addition. (c) Static pressure (Pa) contours with thermal energy addition. (d) Comparison curves of gas pressures along the centreline flow direction.

## 5. Conclusion

The wind tunnel experimental results demonstrate that the arc discharge plasma aerodynamic actuation controls the wedge oblique shock wave effectively, which shifts the start point of shock wave upstream, decreases the shock wave angle and weakens the shock wave intensity. Moreover, when applying magnetic control, the above shock wave control effect is greatly intensified. Under the typical plasma aerodynamic actuation conditions, the start point of the shock wave shifts 4 mm upstream, the shock wave angle decreases by 8.6% and its intensity weakens by 8.8%. Then the thermal choking model is proposed to explain

the thermal mechanism of shock wave control by plasma aerodynamic actuation. As the arc discharge adds substantial thermal energy to the cold supersonic flow field, the plasma area can be seen as a solid obstacle, which is called the 'plasma wedge'. Then the shock wave angle and the intensity change. The change laws of shock wave deduced by the thermal choking model are consistent with the experimental results, which demonstrate that the thermal choking model can effectively forecast the plasma actuation effects on a shock wave in a cold supersonic flow. Based on thermal mechanism, the arc discharge plasma was simplified as a thermal source term that added to the Navier-Stokes equations. The simulation results of the change in oblique shock wave were consistent with the test results, so the thermal mechanism indeed dominates the oblique shock wave control process.

## 6. References

- Meyer, R., Palm, P. & Plonjes, E. (2001). The Effect of a Nonequilibrium RF Discharge Plasma on a Conical Shock Wave in a  $M=2.5$  Flow, *32nd AIAA Plasmadynamics and Lasers Conference*, pp. 2-10, Anaheim, CA, USA, June 11-14, 2001
- Merriman, S., Plonjes, E. & Palm, P. (2001). Shock Wave Control by Nonequilibrium Plasmas in Cold Supersonic Gas Flows, *AIAA Journal*, Vol.39, No.8, (August 2001), pp. 1547-1552, ISSN 0001-1452
- Miles, R., Macheret, S. & Martinelli, L. (2001). Plasma Control of Shock Waves in Aerodynamics and Sonic Boom Mitigation, *32nd AIAA Plasmadynamics and Lasers Conference*, pp. 1-8, Anaheim, CA, USA, June 11-14, 2001
- Macheret, S., Shneider, M. & Miles, R. (2003). Scramjet Inlet Control by Off-body Energy Addition: a Virtual Cowl, *41st AIAA Aerospace Sciences Meeting and Exhibit*, pp. 1-15, Reno, Nevada, USA, January 6-9, 2003
- Shneider, M., Macheret, S. & Miles, R. (2003). Comparative Analysis of MHD and Plasma Methods of Scramjet Inlet Control, *41st AIAA Aerospace Sciences Meeting and Exhibit*, pp. 1-12, Reno, Nevada, USA, January 6-9, 2003
- Leonov, S., Yarantsev, D. & Soloviev, V. (2006). High-speed Inlet Customization by Surface Electric Discharge, *44th AIAA Aerospace Sciences Meeting and Exhibit*, pp. 1-9, Reno, Nevada, USA, January 9-12, 2006
- Leonov, S., Bityurin, V. & Yarantsev, D. (2005). High-speed Flow Control Due to Interaction with Electrical Discharges, *AIAA/CIRA 13th International Space Planes and Hypersonics Systems Technologies Conference*, pp. 1-12, Capua, Italy, May 16-20, 2005
- Leonov, S., Yarantsev, D. & Isaenkov, Y. (2005). Properties of Filamentary Electrical Discharge in High-enthalpy Flow, *43rd AIAA Aerospace Sciences Meeting and Exhibit*, pp. 1-14, Reno, Nevada, USA, January 10-13, 2005
- Kolesnichenko, Y., Brovkin, V. & Leonov, S. (2001). Investigation of AD-body Interaction with Microwave Discharge Region in Supersonic Flows, *39th AIAA Aerospace Sciences Meeting and Exhibit*, pp. 1-12, Reno, Nevada, USA, January 8-11, 2001
- Bletzinger, P., Ganguly, B. & VanWie, D. (2005). Plasmas in High Speed Aerodynamics, *Journal of Physics D : Applied Physics*, Vol.38, No.4, (April 2005), pp. R33-57, ISSN 0022-3727
- Ganiev, Y., Gordeev, V. & Krasilnikov, A. (2000). Aerodynamic Drag Reduction by Plasma and Hot-gas Injection, *Journal of Thermophysics and Heat Transfer*, Vol.14, No.1, (January-March 2000), pp. 10-17, ISSN 0887-8722
- Shang, J. (2002). Plasma Injection for Hypersonic Blunt-body Drag Reduction, *AIAA Journal*, Vol.40, No.6, (June 2002), pp. 1178-1186, ISSN 0001-1452

# Investigations of Supersonic Flow around a Long Axisymmetric Body

M.R. Heidari, M. Farahani, M.R. Soltani and M. Taeibi-Rahni  
*Garmsar Branch of Islamic Azad University,  
Sharif University of Technology  
Iran*

## 1. Introduction

One of the most important parameters affecting missiles' length and diameter is the required space for their apparatus, systems, etc. Increasing this space causes an increase in both the body length and the missile's fineness ratio,  $L/d$  (Fleeman, 2001). For such bodies, the problems of flow separation and boundary layer growth at various flight conditions are very important. Of course, the boundary layer growth and its separation, affect the aerodynamic characteristics, particularly the drag force and the stability criterion. Both of these have important roles in the missile performance and its mission implementations. Also, the performance of various control surfaces (especially those located close to the end of the body) varies with flow separation (Cebeci, 1986).

For some rockets and missiles, the after body cross-section changes longitudinally (particularly in space vehicles). Furthermore, due to the lack of sufficient space for arranging the systems (e.g., actuator of controlled fins, avionics, etc.), it is necessary to increase the body cross section near those systems. The lack of space may also appear when controlled fins are installed on the motor surface. Hence, in many occasions the body cross-section needs to be increased (Chin, 1965; Soltani et al., 2002).

However, the computation of the flow parameters and their variations for non-zero angles of attack, when bodies are tapered, is not an easy task, e.g., it takes a considerable amount of memory and CPU time to compute the flow over such bodies. In addition, as the angle of attack increases, the flow over a portion of the body may separate, making the flow more complicated. Moreover, experimental data for flow properties along tapered bodies to validate CFD codes are rare (Soltani et al., 2002; Perkins & Jorgensen, 1975).

The computational simulation of flow over complex geometries usually requires structured multi-block grids. On the other hand, the geometric complexity requires more blocks and also more grid points. Even though, the computer programming (using multi-block grid for such flows) is very troublesome, it is computationally very efficient and quick. On the other hand, suitable grid generation plays the first and the most important role, when using multi-block grid.

Grid generation needs to be consistent with flow solution. In some methods, the discretization error increases due to the inaccurate adoption of the grid boundaries with the real flow boundaries, which could be due to the non-orthogonality of the grid lines, especially near the walls.

There have been many research performed on the areas of generation and use of multi-block grids, grid generation techniques, data management methods in different blocks, production of grid generation softwares which optimally require less trained users, and quicker grid generation, especially for complex geometries (Amdahl, 1988; Sorenson & McCann, 1990).

The different steps to compute the flow using multi-block grid are: 1. geometric recognition and setting a suitable block structure, 2. grid generation inside each block and finding the nodes on the block boundaries, and 3. solving the flow inside each block and then in the whole domain. Also, multi-block grid generation has four steps, namely, dividing the flow domain into different blocks, determining the exact geometric characteristics of each block, grid generation in each block, and optimization of the overall grid (Boerstoel et al., 1989). The situation and the location of the boundaries between the blocks are very important and thus an inefficient structuring can lead to the divergence of the overall solution. The flow physics, such as shock waves and separated flow regions, determine the required number of blocks and how they are distributed.

In the present work, a series of wind tunnel tests on a long axisymmetric body were performed to investigate the pressure distribution, the boundary layer profile, and other flow characteristics at various angles of attack and at a constant supersonic Mach number of 1.6. Because of low maneuverability of high fineness ratio missiles, the range of angles of attack for the present study was chosen to be moderate. Then, the effects of the cross sectional area variations on the surface static pressure distribution and on the boundary layer profiles were thoroughly investigated. This was performed by installing two belts (strips) having different cut-off angles on the cylindrical portion of the model. One of these belts was installed at the beginning of the after body part ( $x/d=7.5$ ), while the other was located near the end ( $x/d=13.25$ ). By changing the belt leading edge angles, different bodies were generated and thus the effects of varying the body cross-section were studied.

In the numerical part of this work, a stationary turbulent supersonic axisymmetric flow over the same body at zero angle of attack (in the absence of body forces and heat sources) was investigated using the computer code developed in this work (MBTLNS). Adiabatic wall with negligible variations of the viscous fluxes in the streamwise direction was assumed. Also, the flow domain was blocked in streamwise direction and patched method was used in the block boundaries. In each block, the thin layer Navier-Stokes (TLNS) equations were solved, using the implicit delta form finite difference method with Beam and Warming central differencing scheme (Beam, & Warming, 1978). For turbulence modeling, the algebraic two-layer Baldwin-Lomax model was used and the shock waves were captured using shock capturing technique. In each iteration of the overall solution, the flow domain is swept from the first block at the nose to the last block at the end of the body. The computational results for zero angle of attack, Mach number of 1.6, and Reynolds number of  $8 \times 10^6$  for flow over an axisymmetric ogive-cylinder with two sets of strips with angles 5 and 15 degrees were compared with the related experimental results obtain in this work. The most important ability of the present software is that, it can solve the flow around complex geometries, using a personal computer with relatively small memory.

## 2. Experimental equipments and tests

All tests were conducted in the trisonic wind tunnel of QRC. The equipments used for this investigation include: Schlieren visualization system, A/D board, traversing mechanism, rake, vacuum pump, manometer, computer, data acquisition software, pressure transducer, and multiplexer board.



The QRC wind tunnel is an open-circuit blow down tunnel and operates continuously between Mach numbers 0.4-2.2, via engine RPM and nozzle adjustments. It has a test section of  $60 \times 60 \times 120$  cm<sup>3</sup> and is equipped with various internal strain gauge balances for force and moment measurements, pressure transducers, Schlieren visualization system, etc. (Masdari, 2003).

The model used in this study had a fineness ratio of 2.5 and a circular-arc, ogival nose tangent to a cylindrical after body with  $L/d=15$  (Fig. 1.a). It was equipped with 36 static pressure ports located both longitudinally and circumferentially. To study the effects of cross section changes, two belts with various leading edge angles were installed on the model (Fig. 1.b). Here, the first model is used when talking about the main or simple model (the one without belts), the second model for the one with (5, 5) degrees belts, and the third model for the one with (15, 12) degrees belts.

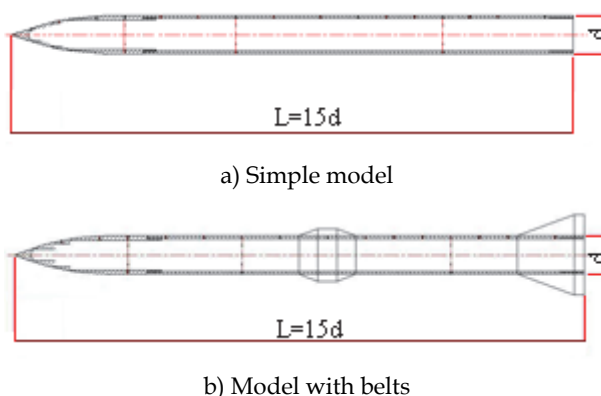


Fig. 1. Schematic of different models used.

The traversing mechanism, which was designed and built particularly for this study, is capable of moving the rake perpendicular to the body axis with small steps of about 0.003 mm in  $z$  direction. This system was installed on the  $\alpha$ -mechanism base such that, the tubes (pitot total pressure) of the rake were always parallel to the model. Note, the entire traversing mechanism was fully controlled by a computer.

Various tests were conducted to study the flow characteristics along the model. The free stream Mach number was 1.6, while the angle of attack was varied between -2 and 6 degrees. At each angle of attack and for all models, the rake at several longitudinal stations for at least 11 locations in  $z$  direction obtained the total pressure data. An accurate linear potentiometer was used to determine the distances between the body surface and the rake. Note, all experimental data shown here are ensemble averaged of several hundred data taken several times to ensure repeatability.

### 3. Governing equations and computational methodology

In the present study, a turbulent supersonic flow over a long axisymmetric body at zero angle of attack was computationally simulated. The Reynolds averaged TLNS equations were solved using Beam and Warming central differencing and Baldwin-Lomax turbulence model. This model is frequently used, because of its simplicity and its reliability. Even

though in some flow situations, it is up to about 10% less accurate compared to some other models, it can reduce the amount of computations up to about 50%.

The first step in grid generation is the correct nodal distribution along the body surface. Then is the blocking of the domain and finally comes the grid generation inside each block. Since we are not ignoring the viscosity, much finer grid is required near the surfaces. Also, finer grid is required in the block which may contain shock waves, flow separation, or other high flow gradient regions. For most blocks, where there are relatively simple geometries, algebraic grid generation is usually used.

The location of the block interfaces is very important. In this work, the blocks were structured in the streamwise direction. For blocking of the domain, one needs to first estimate different flow phenomena and the complexity of the body geometry, which may encounter. Then, the block interfaces are located. Here, we used connected and disconnected uniform patched method at the interfaces. Note, whenever connected meshes are used, the lines from one block are continued into the next block. This way, interpolation is not usually required at the interfaces. Besides the limitations this may bring along, it eliminates the errors due to non-conservative data along the interfaces.

Even when continuous grid (same grid type in each block) is used, any sudden change along the block interfaces (such as angles between the lines of the two neighboring blocks) may cause drastic discontinuity of the grid transformation metrics. On the other hand, for more accurate application of the wall boundary conditions and the flow solutions in each block, it may be required to increase the number of nodes and the grid lines, especially in the direction perpendicular to the wall. This usually leads to disconnected grid at the interfaces. Mostly, this is done by halving or doubling the grid points in the blocks neighboring the interfaces (Bohbot et al., 2000).

In each block, the boundary conditions and the information received from the neighboring blocks affect the flow solution. Thus, any error related to the transfer of information within the blocks directly affects the solution in each block and the overall solution and its convergence. Therefore, we need to use interpolation techniques at the interfaces with the least error, which is preferably conserved.

In the present work, a suitable linear interpolation technique was used for computations at points of a block extended into the neighboring block. Thus, the distribution of lines in the left and the right sides of the interfaces is quite arbitrary and without any limitations. After breaking down the flow domain into several blocks, the information set for each block is obtained. This set includes the block number, the interface numbers and types, the geometric locations of the corners of each block, and the numbers and types of the neighboring interfaces. Also, other internal information of each block, such as the number of the nodes and their arrangements, the CFL number, the artificial viscosity coefficient, etc., have to be known, before the flow solution is performed.

Even though, the solution may be converged in each block, the overall solution may well be diverged. This difficulty mainly arises from the inappropriate ordering of the solution procedure for different blocks, which needs to be simple and smooth. Also, it is very important that, different flow variables have the same weight and harmony. In this work, using a simple and suitable procedure, we start from the first block at the nose, which contains the upstream inflow information, and pass through the chain of the blocks, until we reach the last one, located at the end of the body, containing the outflow information. In each block, the solution is only performed in one time step. Note, if we were having any type of iterations in any block, it should be harmonized with the other blocks, especially the

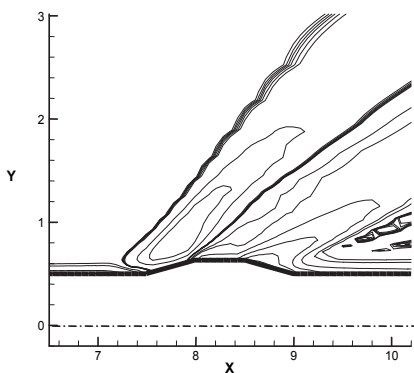
neighboring ones. This is a considerably difficult task and can lead to convergence problems of the overall solution.

Here, the solution accuracy has been compared to the single block case. As far as the convergence speed is concerned, different parameters, such as the numbering and the arrangement of the nodes, the CFL number, the initial conditions, the time step, the artificial viscosity coefficient, etc. for each block, and the position and type of block interfaces have been thoroughly investigated and evaluated.

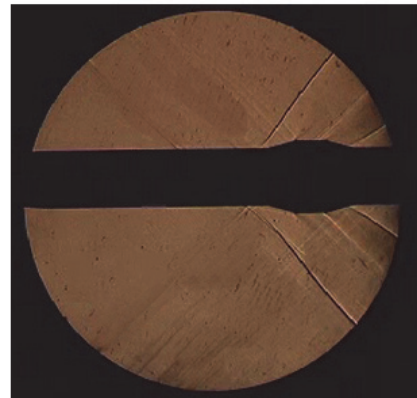
#### 4. Results and discussion

A supersonic turbulent flow over a long axisymmetric body was investigated both experimentally and computationally. The experimental study consisted of a series of wind tunnel tests for the flow over an ogive-cylinder body at Mach number of 1.6 and at angles of attack between  $-2$  and  $6$  degrees. To study the effects of the cross section variations on the pressure distribution and on the boundary layer profiles, several belts with various leading edge angles were installed at different locations along the cylindrical portion of the model. The wind tunnel tests included the surface static pressure and the boundary layer profile measurements. Further, the flow around the model was visualized using Schlieren technique. All tests were conducted in the QRC's trisonic wind tunnel. On the other hand, for the above body, a 1.6 Mach number and a  $8 \times 10^6$  Reynolds number flow at zero angle of attack was computationally investigated, using a multi-block grid (with patched method around the block interfaces) to solve the TLNS equations. The numerical scheme used was implicit Beam and Warming central differencing, while Baldwin-Lomax turbulence model was used to close the RANS equations.

First, at various angles of attack, the Schlieren visualization technique was used to study the shape of the shocks formed around the model nose and places where the area changed (and their variations with angle of attack). Figure 2 shows the shock waves, as well as the expansion waves, on the large strip at zero angle of attack. The related numerical results are also shown there for comparison purposes. From this figure, it is seen by inspection that, there exists relatively close correlations between the numerical and the experimental results for both cases.



a) Numerical

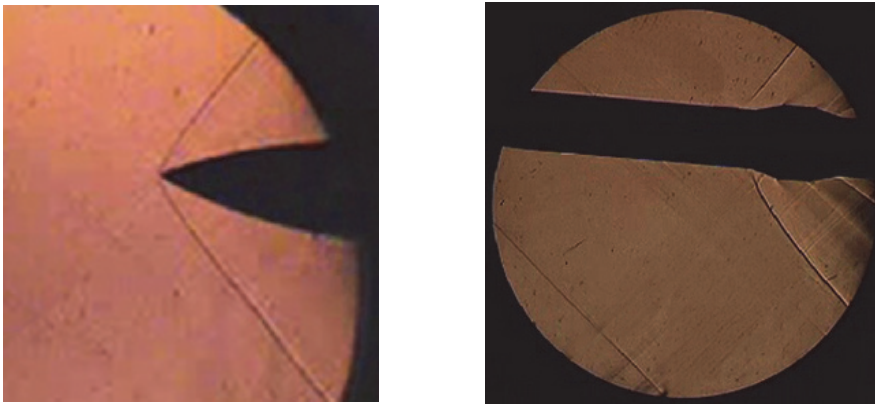


b) Experimental

Fig. 2. Experimental and numerical flow field over the model with large belt ( $15^\circ$ ) at  $\alpha = 0$ .

Figure 3 shows the shock wave formed in front of the model and ahead and behind the belt used for varying the model cross section at 6 degrees angle of attack. It is seen from this figure that, the shock wave is not symmetric resulting in a lower strength on the leeward side of the model causing higher pressure on the windward portion of the nose and lower pressure on its leeward side (thus, a normal force is generated). Figure 3.b clearly shows the oblique shock, as well as the expansion waves, formed in the front and on the surface of the belt installed at  $x/d=7.5$ . Furthermore, the oblique shock formed behind the belt to reduce the flow velocity and to turn it parallel to the model surface is clearly visible in this figure. Again, the strengths and the shapes of upper and lower shock formed ahead of the belt are not the same.

Figure 4 shows the longitudinal static pressure distribution over the model surface. Figure 4a compares our experimental and CFD results for zero angle of attack, while Fig. 4b compares our experimental results with theoretical ones (SOSE; Second Order Shock Expansion) for 4 and 6 degrees angle of attack (Moore, 2000). Note, the measurement errors are calculated and shown in Fig. 5b. From these figures, it is clearly seen that all three methods predict the surface pressure very closely for  $0 < L/d < 12$  at  $\alpha = 0$  degree. From Fig. 4.b the experimental and the theoretical data compare well up to about  $x/d=12$ . The differences are probably due to the base flow affecting the boundary layer on the model surface near its end. Note that, by increasing the angle of attack, the pressure taps located at zero circumferential angle ( $\theta = 0$ ) will be located at the leeward side of the model. Therefore, their static pressure should decrease. These pressure losses are however considerable only along the nose section of the body. This confirms that, for axisymmetric bodies, the contribution of the nose in generating the lift force is greater than that of its after body portion (Soltani et al., 2004, 2005; Heidari et al., 2005). Increasing  $\alpha$  from 4 to 6 degrees has small effects along the nose section.



a) Oblique shock in the nose region of the model      b) Compression and expansion waves around the large belt ( $15^\circ$ )

Fig. 3. Schlieren photograph illustrating the shock formation at  $\alpha = 6^\circ$ .

The experimental and the theoretical circumferential pressure data at  $x/d=3$  and  $11.5$  for 4 and 6 degrees angles of attack are shown in Fig. 5. For the first station, by increasing the

angle of attack,  $C_p$  increases slightly at the windward side, as expected. As  $\alpha$  increases, the vortices separate from the nose and extend to the end of the body. These vortices in Fig. 5b are in general asymmetric and cause asymmetry of the circumferential pressure distribution on the leeward side of the body (Moore, 2000). In addition, the sensitivity of the model installation is high due to its large fineness ratio; hence a small error can cause a considerable sideslip angle. Note, the flow field study showed that, the flow has a small yaw angle too (Masdari, 2003).

Figure 6 shows the grid, the velocity vector field, and the pressure and density contours for flow over the small belt model at zero angle of attack, Mach number of 1.6, and Reynolds

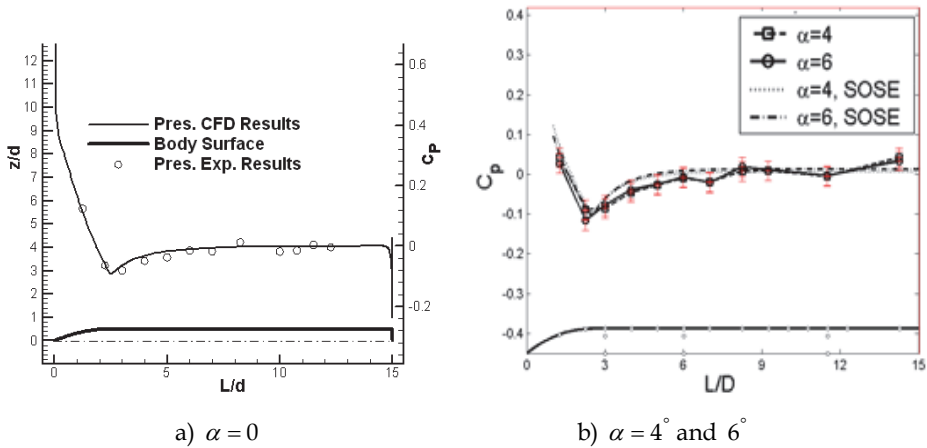


Fig. 4. Comparison of experimental, theoretical, and numerical longitudinal pressure distribution.

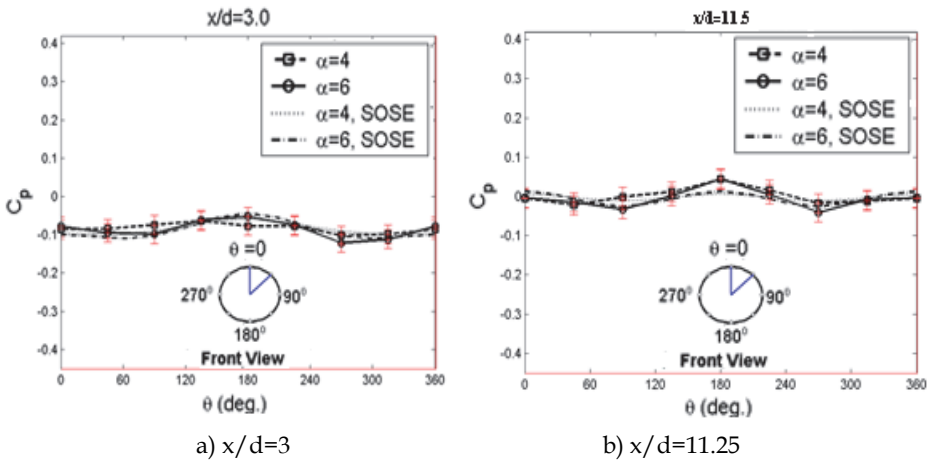


Fig. 5. Comparison of experimental and theoretical circumferential pressure distribution at  $\alpha = 4^\circ$  and  $6^\circ$ .

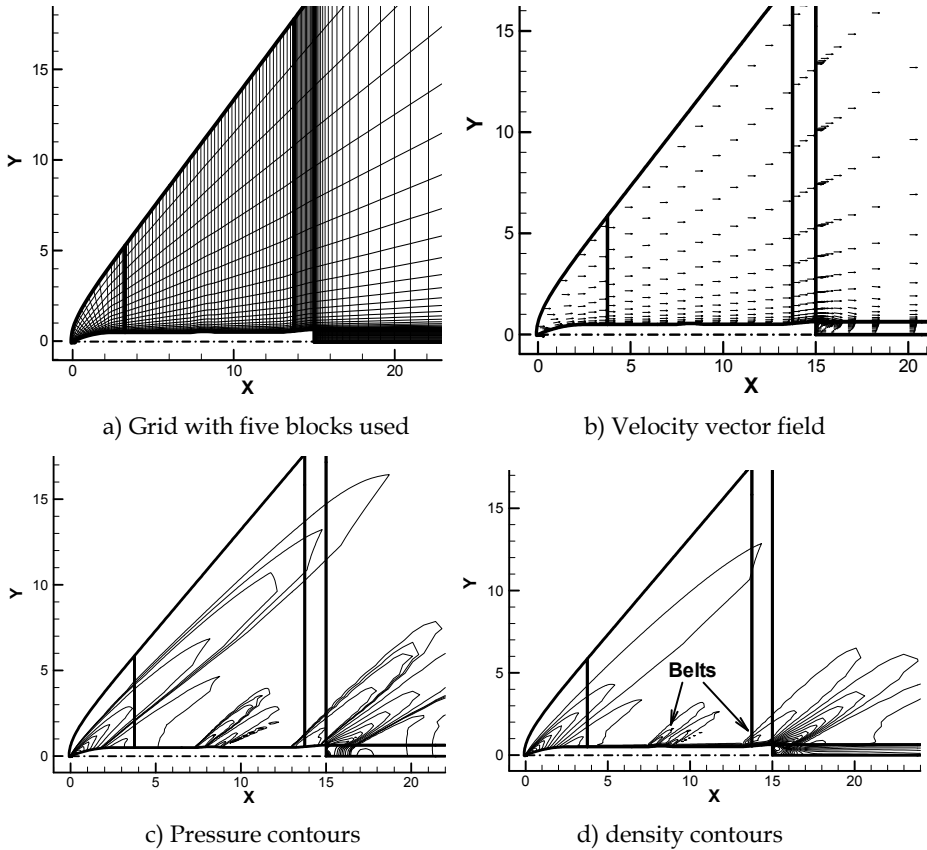
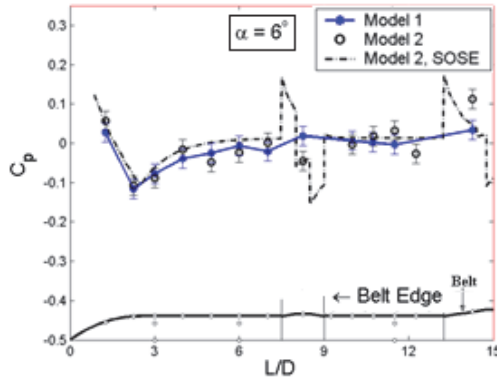


Fig. 6. Experimental Flow around the model with small  $5^\circ$  belt.

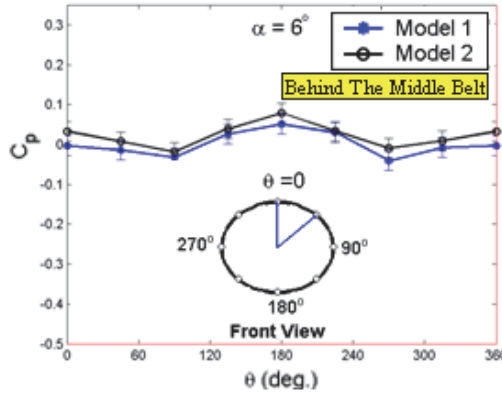
number of  $8 \times 10^6$  (described before). Note, the flow domain has been broken into five blocks. Also, note from the pressure and the density contours that, the solution is very smooth and continuous at the block interfaces. In all these solutions, the optimal grid has been determined and used. Also note that, the bow shock near the body nose has been captured with suitable accuracy and other flow shock and expansion waves along with the flow vortices have been shown near the belts.

The effect of varying the model cross section (by adding belts with different leading edge angles) and the circumferential pressure distribution at 6 degrees angle of attack are shown in Fig. 7. The computational drag coefficient is obtained from the viscosity and pressure gradient effects on the body surface. Here, the longitudinal pressure distribution for both the numerical and the theoretical predictions compared well with the experimental data up to the location where the model frontal area was changed via the belt. Behind the belt however, all results are almost identical. The presence of the belt increases the longitudinal surface pressure by formation of an oblique shock as seen in Fig. 3.b over the inclined part of the belt. However, around the surface of the belt and behind it, the pressure decreases due to the formation of the expansion waves (also seen in Fig. 3.b). The results of the circumferential pressure

distributions show that, sudden changes in cross sectional area have small effects on the pressure distribution around the perimeter of the model behind the belt (Fig. 7.b).



a) Experimental, theoretical, and numerical longitudinal pressure distribution.



b) Circumferential pressure distributions behind the middle belt ( $x/d=11.25$ ).

Fig. 7. Effect of cross section variations on the model pressure distribution (model 2).

The drag coefficient is obtained from shear viscosity and pressure gradient effects on the body surface. In this work, for the small belt model, a wave drag of 0.223, a friction drag of 0.071, and a base drag of 0.369 have been computed (thus, the total drag was 0.663). The drag coefficients for all models are shown in Table 1.

Model	Middle Belt Angle (Deg.)	End Belt Angle (Deg.)	Wave Drag	Friction Drag
Body Alone	-	-	0.146	0.077
Body with Small Belts	5	5	0.223	0.071
Body with Big belts	15	12	0.776	0.068

Table 1. The drag coefficients for the three cases studied.

The computational and the experimental boundary layer profiles for the simple model (uniform cross section) were compared at three different longitudinal stations and at zero angle of attack in Fig. 8. From this figure, the agreements of data are relatively close, particularly for  $z < 7$  mm.

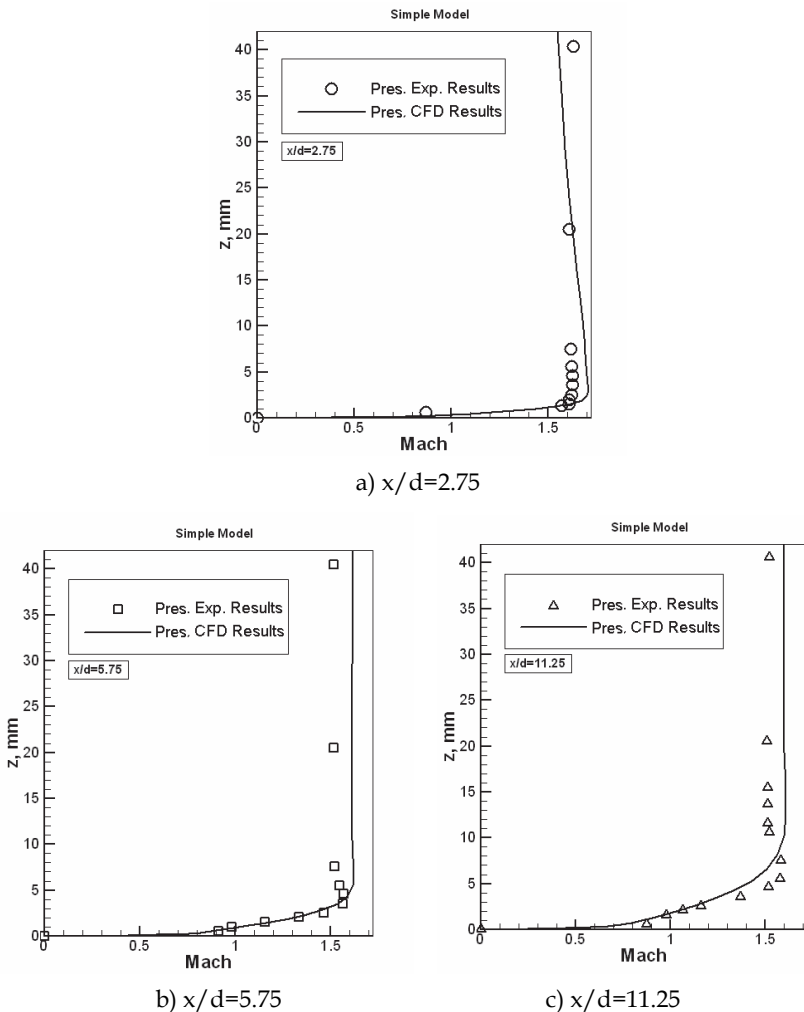


Fig. 8. Experimental and numerical boundary layer profiles for simple model at  $\alpha = 0$ .

Figure 9 shows the boundary layer profiles above the model at three different stations:  $x/d = 2.75$ ,  $5.75$ , and  $11.25$  for two different angles of attack ( $0$  and  $6$  degrees). From this figure, it is clearly seen that the boundary layer thickness increases, with  $x/d$ . Further, this figure shows that for  $x/d = 2.75$  and at  $\alpha = 6^\circ$ , the velocity at the edge of the boundary layer ( $z \cong 5$  mm) is slightly higher than that outside of it ( $z \cong 18$  mm). While, for other locations



( $x/d=5.75$  and  $11.25$ ) the velocity outside the boundary layer never reaches that of  $V_\infty$  at  $M_\infty=1.6$ . The increased velocity at the boundary layer edge is related to the increase in the mass flow rate at the outer portion of the boundary layer due to the velocity reduction in the inner layers (entrainment). Since the decrease in the velocity inside the boundary layer causes lower mass flow rate there, it must be compensated by an increase in the velocity at the edge of the boundary layer.

At  $\alpha=6^\circ$  and at  $x/d=11.25$ , the value of  $\partial M/\partial z$  is different in comparison with the other data shown in Fig. 9.b. This change is probably due to the separation of the body vortices (Jorgensen & Perkins, 1955). Moreover, the growth of the boundary layer at  $x/d=11.25$  is greater than that of the other stations (e.g.,  $x/d=2.75$  and  $5.75$ ). Note, for all three stations, as the  $x$  increases, the boundary layer thickness increases considerably. However, the increase in the velocity at the boundary layer edge decreases marginally. This increase is due to the growth of the momentum layer thickness,  $\delta^*$ , which permits the required mass flow rate through the boundary layer (Heidari et al., 2005).

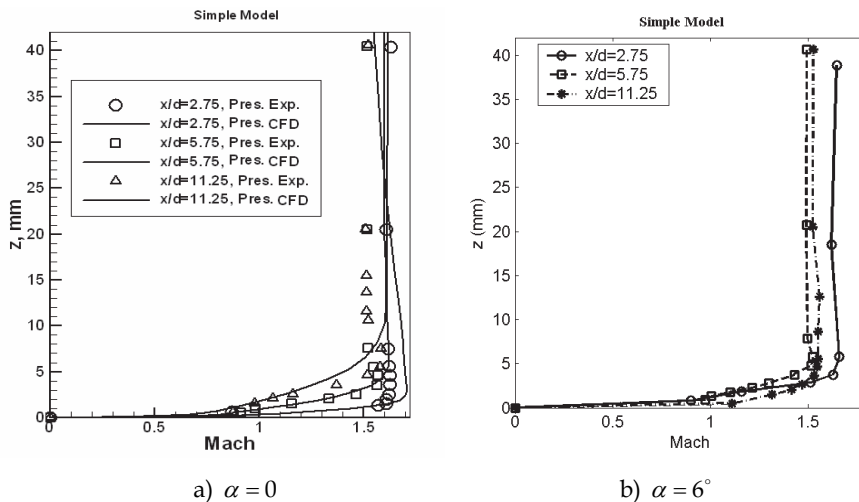


Fig. 9. Comparison of the boundary layer profiles around the body.

The variations of the experimental boundary layer Mach numbers for the simple model at  $x/d=5.75$  and  $11.25$  (at various angles of attack) are shown in Fig. 10. At  $x/d=5.75$ . With increasing the angle of attack, the boundary layer thickness grows. However, a slight increase in the boundary layer thickness is noted for small angles of attack. At higher angles of attack, the boundary layer thickness decreases appreciably for  $x/d=11.25$ . It is presumed that, the boundary layer fluid is shifted to form a pair of vortices along the sides of the model at large  $\alpha$ , hence reducing the boundary layer thickness.

The comparison of the numerical and the experimental boundary layer profiles over model 2 ahead and behind the middle belt at zero angle of attack is shown in Fig. 11. This data compares relatively well, especially for  $x/d=5.75$ . Note, the differences between the CFD and experimental results obtained are at most 15%. However, it is noted that such difference is much less (less than 7%) in other figures.

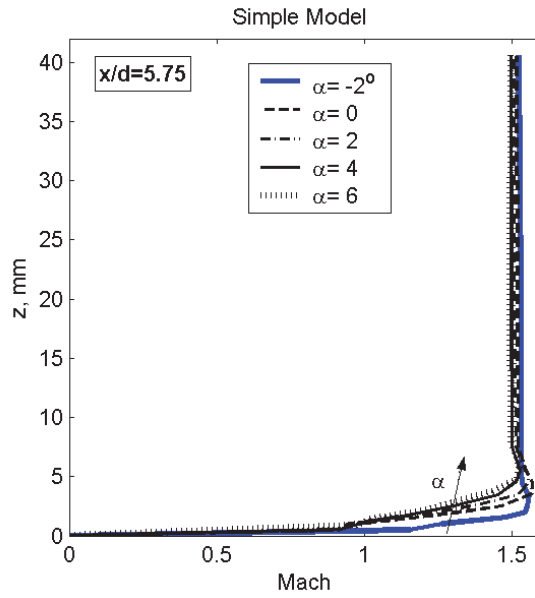
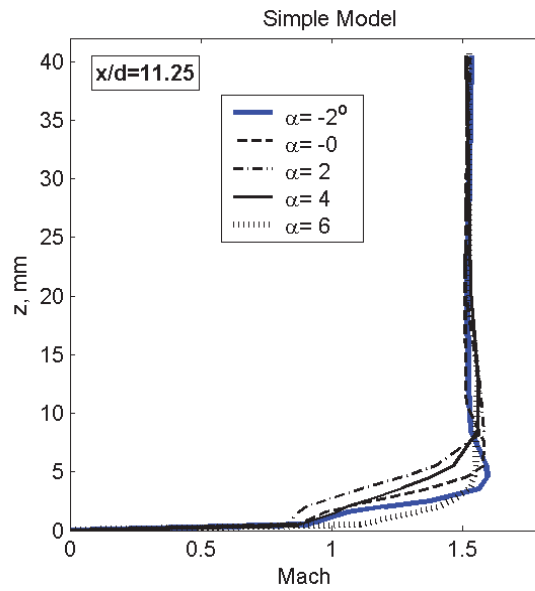
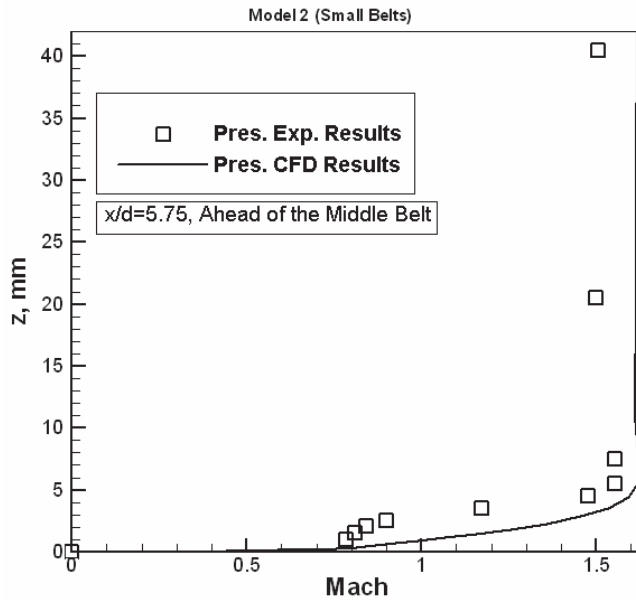
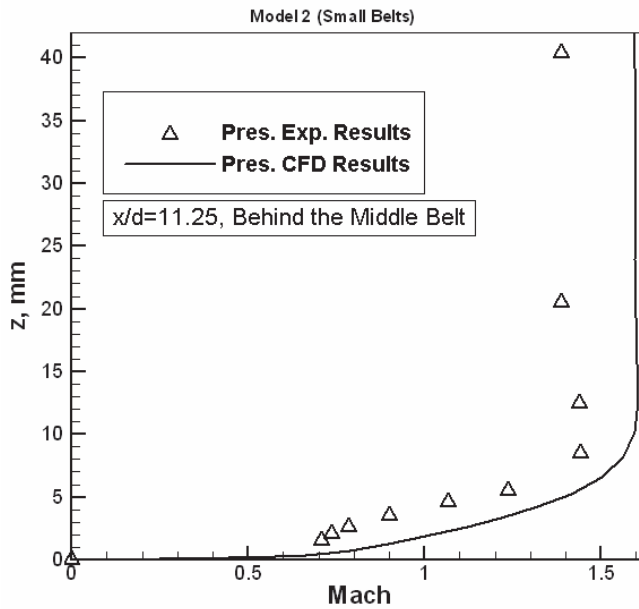
a)  $x/d=5.75$ b)  $x/d=11.25$ 

Fig. 10. Effects of angle of attack on boundary layer profiles.



a)  $x/d=5.75$



b)  $x/d=11.25$

Fig. 11. Experimental and numerical boundary layer profiles for model 2 at  $\alpha = 0$ .

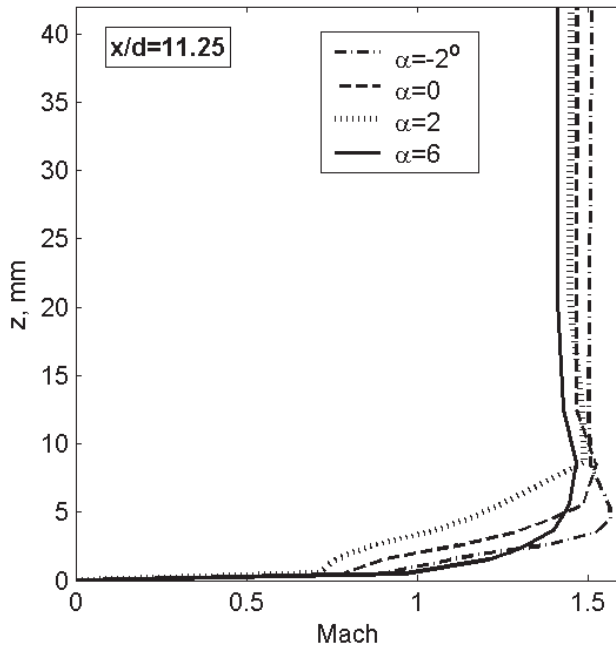


Fig. 12. The effects of angle of attack on boundary layer profiles for model 3.

The variations of the experimental Mach number in the boundary layer for model 3 at  $x/d=11.25$  at various angles of attack are presented in Fig. 12. The trend of the boundary layer profiles for this model is the same as the simple model (Fig. 10.b). With increasing the angle of attack up to  $2^\circ$ , a slight increase in the boundary layer thickness is noted, while at higher angles of attack, the boundary layer thickness decreases appreciably. Note, the presence of the belts has almost no effect on the variations of the boundary layer profiles with angle of attack.

## 5. Conclusion

An extensive experimental study on a long axisymmetric tapered body in a turbulent supersonic flow was performed to mainly investigate the pressure distributions and the boundary layer profiles at various angles of attack. In order to study the effects of the model cross section variations, several belts with various leading edge angles were installed at different locations along the cylindrical portion of the model. In addition, the same flow at zero angle of attack, using structured multi-block grid (with patched method at the block interfaces) and Baldwin-Lomax turbulence model, solving the TLNS equations, was computationally simulated.

The experimental static surface pressure results show that, the circumferential pressure at different nose sections vary significantly with angle of attack (in contrast to the circumferential pressure signatures along the cylindrical part of the body). On the other hand, the total pressure measurements in the boundary layer vary significantly both radially and longitudinally.

Also, the experimental results obtained indicate that, the installation of the belts with various leading edge angles has little effects on the pressure distributions along the forebody, while it has considerable effects on the after body pressure signatures. Also, the belts affect the boundary layer profiles, increasing their thicknesses and changing their shapes. Note, for the models with belts, the value of  $\partial M / \partial z$  at  $z=0$  is considerably different.

The computational results obtained were compared to some of our related experimental data showing relatively close agreements. Note, at the block interfaces, there are not shown to be any noticeable discontinuities. Also, the flow shock and expansion waves are clearly shown in our numerical results and the computational shock angles compare well with the Schlieren results. These indicate suitable accuracy of our numerical methodology. The Mach number contours at  $6^\circ$  angle of attack showed vortices at the end of the body. It seems that, the addition of the belts increases the strength of these vortices and makes them more symmetric. It was also demonstrated that, for the same number of grid points, the single block case requires much more memory than the multi-block cases. The MBTLNS computer code obtained during this research is considerably robust, fast, and applied; it can be used for many other axisymmetric complex geometries.

According to table 1, the drag coefficient, as an important performance quantity, is reduced with decrease in the belt angle. Also, for high belt angles, not only drag, but the lift coefficient is reduced due to flow separation downstream of the belt. Note, as far as design is concerned, it is hard to make major conclusions, since we have only studied this problem from a certain points of view.

## 6. Nomenclature

$a$	Speed of Sound
$D$	Body Diameter
$L$	Body Length
$M$	Mach Number
$x$	Longitudinal Distance from the Nose
$z$	Perpendicular Distance from the Body Surface
$C_p$	Pressure Coefficient
$L/d$	Fineness Ratio
$\alpha$	Angle of Attack
$\theta$	Circumferential Angle

## 7. References

- Amdahl, D.J. (1988). Interactive Multi-Block Grid Generation, Numerical Grid Generation in Computational Fluid Mechanics, *Eds.* S. Sengupta, J. Hauser, P. R. Eiseman and J. F. Thompson, Pineridge Press, pp. 579-588
- Beam, R.M. & Warming, R.F. (1978). An Implicit Factored Scheme for the Compressible Navier-Stokes Equation, *AIAA Journal*, Vol. 16, No. 4, pp. 393-402
- Boerstoel, J.W.; Jacobs, A.; J.M. & Kassies. (1989). Design and Testing, Norway
- Bohbot, J.; Bertin, D. & Darracq, D. (2000). A Conservative Patched Grid Algorithm for Turbulent Flow Computations of 3-D Complex Configurations, *European Congress*

- on Computational Methods in Applied Sciences & Engineering*, ECCOMAS 2000, Barcelona, 11-14 September 2000
- Cebeci, T. (1986). Three Dimensional Boundary Layer on Missiles, *Tactical Missile Aerodynamics*, Vol. 104, pp. 723-777
- Chin, S.S. (1965). *Missile Configurations Design*, McGraw-Hill
- Fleeman, E.L. (2001). *Tactical Missile Design*, *AIAA Education Series*, AIAA, New York
- Heidari, M.R.; Soltani, M.R.; Farahani, M. & Taeibi-Rahni, M. (2005). Experimental Investigations of Supersonic Flow around a Long Axisymmetric Body, *Esteghlal Journal of Engineering*, ISSN 1025-2851, Vol. 24, No. 2, pp. 171-192
- Jorgensen, L.H. & Perkins, E.W. (1955). Investigation of Some Wake Vortex Characteristics of an Inclined Ogive-Cylinder Body at Mach Number 2, NACA-RM A55E31
- Masdari, M. (2003). The Flow Study in the Test Section of the Trisonic Wind Tunnel of Qadr Research Center, *M.Sc. Thesis, Aerospace Engineering Dept., Sharif Univ. of Technology*, Tehran, Iran
- Moore, F.G. (2000). Approximation Methods for Weapon Aerodynamics, *Progress in Astronautics and Aeronautics, AIAA Journal*, ISSN 1-56347-399-2, Vol. 186, Reston, VA 20191-4344 USA
- Perkins, E.W. & Jorgensen, L.H. (1975). Comparison of Experimental and Theoretical Normal-Force Distributions (Including Reynolds Number Effects) on Ogive-Cylinder Body at Mach number 1.98, NACA-TN 3716
- Soltani, M.R.; Fazeli, H. & Farhanie, B. (2002). Experimental Investigations of Aerodynamic Behaviors of Two Wrap Around Fins, *Esteghlal Journal of Engineering*, ISSN 1025-2851, Vol. 21, No. 1, pp 141-152
- Soltani, M.R.; Taeibi-Rahni, M.; Farahani, M. & Heidari, M.R. (2004). Experimental Investigations of Surface Pressure Distributions and Boundary Layer Profiles around a Long Axisymmetric Body with Varying Cross Section, *IMECE2004*, Kuwait
- Soltani, M.R.; Taeibi-Rahni, M.; Farahani, M. & Heidari, M.R. (2005). Flow Measurements around a Long Axisymmetric Body with Varying Cross Section, *43rd AIAA Aerospace Sciences Meeting and Exhibit*, 10-13 January 2005, Reno, Nevada
- Sorenson, R.L. & McCann, K.M. (1990). A Method for Interactive Specification of Multiple-Block Topologies, *AIAA-91-0147*

# SCIROCCO Plasma Wind Tunnel: Synergy between Numerical and Experimental Activities for Tests on Aerospace Structures

Rosario Borrelli and Adolfo Martucci  
*Italian Aerospace Research Center – CIRA  
Italy*

## 1. Introduction

Spacecraft structures are subjected to aerodynamic heating during launch and re-entry phases of their operations. The design of these structures poses several challenges to structural designer since the aerodynamic heating, which is the predominant load (Kelly et al., 1983; Shih et al., 1988), induces elevated temperatures that can affect the structural behaviour in several harmful ways: degradation of the elastic material properties, reduction of allowable stresses and generation of high thermal stress due to restrained local thermal expansion/contractions.

The success of a re-entry spatial mission in the Earth atmosphere, as well known, is strongly related to the performances of the Thermal Protection Systems (TPSs), which play the most important role (Thornton, 1996). The TPS is the most critical component of a spacecraft since if they are somehow damaged during the mission, a chain reaction can be triggered, leading to a quick propagation of the damage on the whole structure, inestimable economic losses and, above all, losses of human lives. The task of a TPS is to protect the substructure of the vehicle against local and global overheating. In order to ensure the feasibility of interplanetary missions, and in general for the qualification of the critical parts of reentry vehicles, TPS concepts have to be first qualified on-ground and then tested and validated in flight conditions. Thus, Plasma Wind Tunnel facilities have a key role during this qualification process. They should be able to simulate hypersonic air flows encountered during re-entry into Earth atmosphere and to test TPS concepts on full scale demonstrator.

Nevertheless, reproducing hypersonic conditions in the wind tunnels is harder, if not impossible, with respect to other motion conditions. As matter of fact, it is very complicated to reproduce simultaneously the enthalpy, the hypersonic speed, the chemical composition of gases and the dimensions of the model, which are the main factors which characterize the motion.

As a consequence, a choose is needed between wind tunnels designed for the aerodynamic simulation and those ones designed for the thermal simulation.

## 2. Plasma wind tunnels in the world

Thus, wind tunnels can be classified in two categories:

- Aerodynamic, for the simulation of the Mach number;

- Aero-thermodynamic, for the simulation of heat fluxes.

The main feature of the “blow down” aerodynamic wind tunnels is that to reach high Mach numbers it is needed to pre-heat the air before the expansion through a nozzle. In this kind of wind tunnels, the flux is characterized by a very high stagnation pressure which is indispensable to obtain elevated Mach numbers. The duration of the tests is rather limited because it is related to the emptying time of the tank. Typically, they last some dozens of seconds. The aerodynamic wind tunnels work in an intermitting fashion since it is needed to wait for a certain time to recompress the fluid, in such a time the wind tunnel is inactive.

On the other hands, the aerothermo-dynamic wind tunnels are mainly fed by an electric arc and they work in a continuous fashion. The gas heated by the arc reaches very high temperature. Such kind of wind tunnels are mainly used to reproduce heat fluxes in order to test the performances of ablative materials or TPSs, as well as to investigate aerothermo-chemical problems. In the aero-thermodynamic wind tunnels, it is very complicated to determine the thermo-fluid dynamic parameters such as Mach, Reynolds, Knudsen numbers and so on.

One of the most crucial difficulty is that after the gas has been heated by the arc-heater and has passed through the nozzle, its composition is unknown and sophisticated diagnostics techniques are needed to evaluate it. Numerical models are also conveniently used to predict the gas thermo-chemical evolution and to characterize the fluid in the test chamber.

### **2.1 SCIROCCO plasma wind tunnel**

In the mid eighties the European Space Agency (ESA) feels the need of an appropriate facility to carry out experimental ground tests. The intention was to realize a wind tunnel with high enthalpy and very large dimensions so that full scale component of spacecrafts could be tested. Indeed, in hypersonic conditions, the heat fluxes distribution is affected by the sizes of the model.

Since Italy was very interested to the project, the conceptual design, the feasibility study and the preliminary design activities were assigned to the Italian Aerospace Research Centre (CIRA) and were performed between the 1988 and 1989.

In that period was noticed the need to have stagnation temperatures close to 10000 K. Hence, such a value was used to define the technical specifications of the arc-heater.

The air flux in the wind tunnel should be characterized by very high temperature and for this reason, the name “Scirocco”, which is the warm wind coming from the Sahara Desert and acting on the Mediterranean coasts, was given to the facility.

The final design started in observance to a grant agreement between ESA and the Italian Ministry of University and Scientific and Technologic Research (MURST).

The facility started to be built in December 1994 and the work finished in 2001.

As shown in Figure 1, Scirocco is the largest arc jet test facility in the world in terms of arc heater power (about 70 MW).

Moreover, a nozzle with a 2 metre diameter exit allows full-scale models of space-vehicle thermal protection systems to be tested for up to 30 minutes, a period which corresponds to the duration of re-entry. The facility, providing thermal energy to the gas, is able to generate an elevated massive flow and very high temperature, allowing hypersonic conditions to be easily reproduced. The peculiar characteristics of the hypersonic regime, extensively described above, make the requirements of the test to be very constrained.



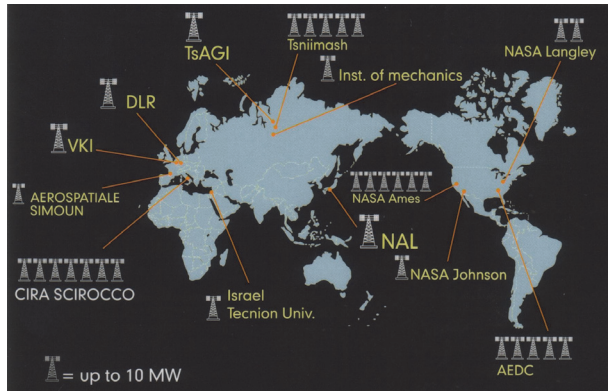


Fig. 1. Plasma wind tunnels in the world

The Scirocco PWT is used in the field of aerospace technology development and its main applications can be summarized as follows:

- Investigate aerothermodynamic phenomena related to the re-entry of both space vehicles and capsules: this is the primary use, indeed Scirocco is able to simulate the re-entry trajectory of several space vehicles, e.g. the Space Shuttle.
- Investigate the aerothermodynamic of launch vehicles during the ascending phase: problems related to the aerodynamic heating raise also in the launch phase and they are caused by the high acceleration values; such problems are similar to those ones induced by the re-entry with the difference that in this case the heating occurs in a lower atmosphere characterized by a higher value of the air density.
- Investigation on exhaust nozzles for launch vehicles and missiles.
- Investigation on the aerothermochemical of internal fluxes: such an analysis is aimed at developing of aerospace propulsion systems (ramjet, scramjet)
- Study on the interaction between the plasma and the electromagnetic fields: in particular, the communications black-out between the ground and the vehicles occurring during the re-entry phase is investigated.
- Study on industrial processes which induce a variation of the chemical composition of the used gas.

A typical test performed in the SCIROCCO wind tunnel can be sketched as shown in Figure 2 where the different phases are outlined.

An air mass flow rate varying between 0.1 and 3.5 Kg/s and with a pressure of 87 bar is supplied by a compression system and then is introduced in the arc heater together with a little argon mass flow rate which is used to help the arc heater ignition and to reduce the oxidation of the electrodes.

Once the arc heater reaches the steady state conditions, it converts the electric energy in the thermal one, thus increasing the air temperature.

The electrodes receive the electric energy which is provided by a Power Supply System. Such system converts the alternate current, coming from the external power supply, in direct current. Inside the arc heater, the air reaches pressures varying between 1 and 17 bar and temperatures varying between 2000 and 10000K. Successively, the air is expanded through a conical nozzle and crosses the test chamber at the thermodynamic conditions required by the test.

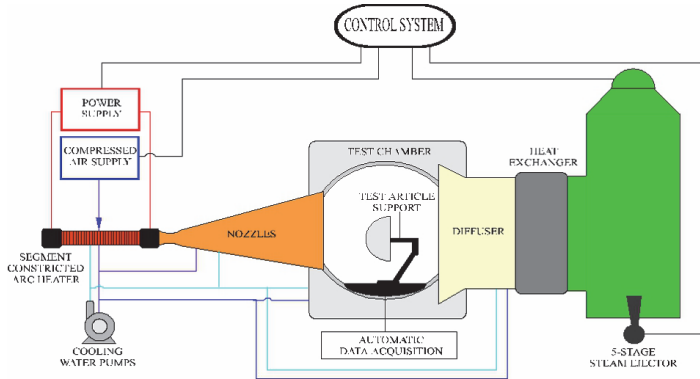


Fig. 2. Sketch of a typical test performed at the SCIROCCO Plasma wind tunnel

After that, the test article is inserted in the plasma flow by means of an automatic robot which is named Model Support System (MSS) fixed to the base of the test chamber. The main physical parameters are monitored by means of a Data Acquisition System (DAS). Advanced instrumentations are installed both inside and outside the test chamber.

The plasma flow is then collected in the diffuser whose main task is to reduce the plasma speed from supersonic values to subsonic ones. The diffuser is made by a convergent-divergent horizontal nozzle with a long central part at uniform section and it is cooled by an external cooling system.

At the end of diffuser, the air flow encounters the heat exchanger which reduces the temperature of the air consistently with the thermal strength of the materials used for the vacuum system which is located afterwards. The vacuum system generates and keeps the vacuum conditions required by the test. All the components located between the arc heater and the heat exchanger identify the SCIROCCO Test Leg.

A system, named "DeNOx" system, follows the vacuum system and its aim is to reduce the amount of nitrogen oxide produced in the Test Leg during the test.

In order to reduce the thermal energy produced in the various components of the Test Leg a water cooling system is used. Two water cooling circuits are used with two different values of the water pressure. In both the water is demineralised for two reasons, first, to avoid the salt deposition along the exchange surfaces which may reduce the heat exchange coefficients, and second, to avoid problems related to the electric conductivity of non demineralised water. The high pressure circuit is used to cool critical component of the Test Leg where very high heat exchange coefficients are needed, the other components are cooled by the low pressure circuit. Moreover, cooling water is used both to cool some components of the facilities and to decrease the temperature of the demineralised water.

The SCIROCCO PWT has an advanced control and automation system, able to reproduce with a good accuracy the re-entry trajectory of space vehicles. Every subcomponent has a dedicated Local Central Unit (LCU) which monitors the process from an operative and safety point of view. The LCUs are connected each other and are also connected to a Central Computer System (CCS) which acts as supervisor of the whole facility. The connection between all the components is made through an high velocity transmission system.

The operating envelope of the SCIROCCO PWT, in terms of plasma total pressure and enthalpy which can be obtained in the test chamber, is shown in Figure 3.

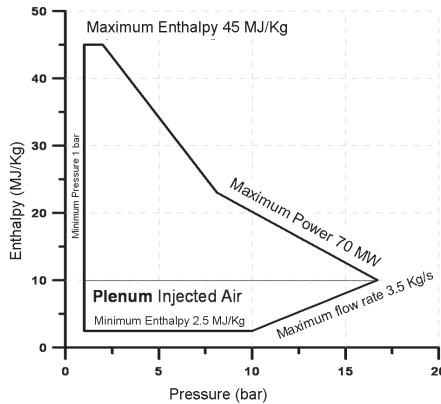


Fig. 3. Operating envelope of the SCIROCCO PWT

It was obtained by taking into account the operating and technological limits of the facilities which can be summarized as follows:

- Minimum allowable power provided by the Power Supply System equal to 1 MW;
- Minimum air pressure able to make steady the arc heater equal to 1 bar;
- Maximum allowable total enthalpy of the gas equal to 45 MJ/Kg
- Maximum direct current value equal to 9000 A;
- Maximum allowable heat flux at the nozzle groove equal to 5 KW/cm<sup>2</sup>;
- Maximum allowable power provided by the Power Supply System equal to 70 MW;
- Maximum air massive flow equal to 3.5 kg/s;
- Minimum allowable total enthalpy of the gas equal to 2.5 MJ/Kg

In the next paragraph, the main components of the whole facility is described in detail.

### 2.1.1 The arc heater

The arc heater installed at the SCIROCCO PWT is the largest of its kind in the world. It is located between the air compressor system and the nozzle and its main task is to heat the air by converting electric energy in thermal one. Such conversion is activated by a spark which is generated between an anode and a cathode having different electric potentials.

The arc heater shown in Figure 4, is made of a column 5500mm long, with an internal diameter of 110 mm. The anode and the cathode, each one made of 9 electrodes, are located at the two ends of the columns. The electric current is provided by a power cabin and the ballast resistors, which uniformly canalize the current, are installed before the electrodes.

In Table 1, the arc heater design technical specifications are reported.

The arc heater structure is divided into several blocks (in order to optimize the phase of maintenance and the cooling) and each single block consists of several discs inside which there is the passage of demineralised water at high pressure for the cooling (used because, as said, the absence of minerals makes it not electrically conductive), and compressed air coming from the external line. The air and water ducts that enter the individual blocks have different colours, and both the inlet pressure demineralised water, and the compressed air pressure vary along the length of the arc depending on the areas that need more cooling.

The anode is made of a copper alloy that resists to high thermo-mechanical stresses and it is connected with the power lines coming from the power unit.

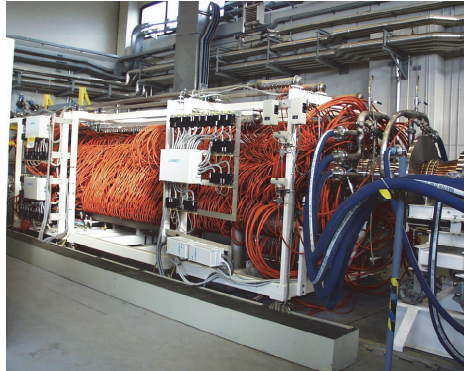


Fig. 4. Arc heater

	Min	Max
Air pressure (bar)	1	16.7
Air mass flow rate (kg/s)	0.1	3.5
Enthalpy (MJ/kg)	2.5	45
Electrical power (MW)	1	70
Electrical current (A)	1000	9000
Voltage (V)	1000	30000

Table 1. Arc heater design technical specifications

In the anode high pressure argon is introduced whose primary purpose is to avoid a direct contact between the electrodes and the flow of electrons, thereby avoiding a localized corrosion of the inside of the electrodes which obviously would cause serious problems. The second purpose related to the use of argon is to help the ignition of the arc, since it increases the conductivity of the air flow. The cathode has a configuration similar to the anode and it is at the other end of the arc.

The column is inserted between the anode and the cathode. As mentioned, it has a maximum length of 5500 mm and a variable configuration (it consists of 28 members each in turn composed of 20 rings) depends on the enthalpy level required.

The column is designed to confine the plasma as possible along the axial direction and to avoid problems of corrosion and melting of materials. Between the rings there is a layer of insulator (spacer) and both demineralised water and air, which is fed into the column with a velocity component tangential to the duct, enter. Following this tangential velocity is going to settle with the axial velocity component coming from the vacuum created by the vacuum system, generating a spiral motion.

It should be noted that a part of the flow remains attached to the inner walls of the column, creating a sort of gap that prevents the fusion of this.

Inside the column there is the motion of electrons from anode (high potential) to cathode (low potential) submitted to the Lorentz force. In this phase the conversion of electrical energy into heat energy takes place, because the electrons collide with the moving particles of air and argon, heating for viscous friction and energizing the flow.

As the temperature increases to levels high enough to trigger such vibration and dissociation of molecules and ionization of atoms the gas becomes "plasma". Immediately downstream of the cathode there is the plenum, which has a constant cross section of 172 mm and is essentially intended to lower the total enthalpy of the air below the limit imposed by the minimum value of electric current. This is done by injecting air into this section at room temperature, which generates a resulting reduction in temperature of the plasma which, of course, will change its chemical composition.

**2.1.2 Conical nozzle**

The nozzle is composed of a convergent-divergent duct that has the function to expand the flow by increasing the speed and reducing the static pressure, in order to obtain the required thermo-fluid dynamic test conditions. Table 2 shows the nozzle design specifications:

	Min	Max
Inlet pressure (bar)	1	16.7
Outlet pressure (mbar)	0.01	2.9
Inlet velocity (m/s)	120	350
Outlet velocity (m/s)	2000	7000

Table 2. Design requirements for the nozzle

The first part of this component is a convergent trait in which the motion is subsonic. In the throat (i.e., the minimum diameter section, which in this case is 75 mm), the Mach reaches the unit value, and in the divergent part a further expansion occurs up to supersonic Mach numbers in the output section. The mach depends on the configuration of the nozzle used. In fact it is divided into seven parts with different diameters of the output section, which allow to configure the nozzle so as to achieve different test conditions. As noted in Table 3, the maximum diameter of the outlet section is equal to 1950 mm, which corresponds to a ratio of the areas (outlet area divided by the area of the throat) equal to 676.

	Length (mm)	Inlet diameter (mm)	Outlet diameter (mm)
Throat section	560	170	188
Expansion section A	692	188	432
Expansion section B	692	433	677
Expansion section C	638	678	900
Expansion section D	1347	678	1150
Expansion section E	1914	678	1350
Expansion section F	1701	1350	1950

Table 3. Nozzle configurations

The critical part in terms of thermo-mechanical stress is the throat where very high temperature can be reached. In fact, while the entire nozzle is cooled with demineralised water at low pressure (which runs in conduits placed lengthwise along the outer surface),

the throat is cooled by demineralised water pipes dedicated at high pressure through a mechanism that guarantees a higher forced convection heat transfer coefficient. At the nozzle exit, then, there are four sensors that follow the evolution of static pressure.

### 2.1.3 Test chamber

The Test Chamber (TC) has a cylindrical shape (Figure 5) and it is the place where the flow field to be simulated is realized (Figure 6). In fact, inside it the plasma coming from the nozzle impacts the model and the experimental measurements of pressure and temperature are carried out. Such measurements, properly treated, represent the ultimate goal of the entire system.



Fig. 5. Test chamber

The test chamber is 9217 mm high and has an inner diameter of 5170 mm, it has three openings necessary to allow the entrance to the maintenance staff and to allow to do the assembly on the support of the model, it also has a number of side windows to allow monitoring and diagnostics of the plasma flow. This component has a sliding floor to the entrance of the model and is not cooled.



Fig. 6. Plasma flow inside the Test Chamber.

During a test performed under special conditions, such as a low flow, it is possible to inject inside the test chamber a small amount of air called "bleed air" in order to increase the value of chamber pressure and limiting the recirculation of plasma.

In the test chamber, static pressure meters and temperature meters are located at various points, moreover, two tools called "probes" are introduced within the plasma flow before the entry of the support model.

The purpose of this process is monitoring the status of thermo-fluid dynamic conditions of plasma in terms of pressure and temperature at various locations of the jet, they are adequately cooled by a circuit of demineralised water and make an arc of a circle driven by electric motors.

#### **2.1.4 Model Support System**

The "Model Support System" (MSS), is essentially an automated arm cooled by internal circuits of demineralised water and its function is related to the proper positioning of the model within the plasma jet.

The MSS allows a maximum vertical displacement equal to 1650 mm, and can also move in the longitudinal direction, helping to compensate for positioning errors with respect to the direction of flow of plasma. The support also allows a rotational movement and thus makes it possible to make tests in a dynamic manner.

#### **2.1.5 Diffuser**

The diffuser is designed to collect the flow of plasma out of the test chamber and slow down to subsonic speed values. It consists of a short convergent, followed by a long stretch of constant section and final section of duct diverts slightly upstream of the heat exchanger (Figure 7). Part of the converging section is located inside the test chamber.



Fig. 7. Diffuser

The geometry of the diffuser is summarized in Table.4:

Shape		Conical
Total length		49800 mm
Diameter	Converging	2650 mm
	Throat	2120 mm
	Diverging	2120 mm (min) - 3000 mm (max)
Parts	Converging	1
	Throat	4
	Diverging	2

Table 4. Diffuser geometrical data.

### 2.1.6 Heat exchanger

The heat exchanger is used to cool the flow of plasma from diffuser up to temperatures compatible with the operation of the vacuum system which is located just downstream.

This component consists of an input section cooled by an external circuit water tower, followed by tubes that run longitudinally in the conduit and exposed to direct current. They form the part that removes heat from the plasma.

Downstream of these tubes two circular sections of different diameters are placed that allow the connection to the vacuum system. There is also an expansion joint that allows to control the thermal deformation of the various components between the test chamber and heat exchanger.

### 2.1.7 Vacuum system

The function of the vacuum system is to maintain low pressure in the test chamber and it is located directly downstream of the heat exchanger (Figure 8).

The design specifications of the vacuum system are described in Table 5.

	Min	Max
Operating temperature (°C)	50	270
Operating inlet pressure (mbar)	0.35	15
Operating outlet pressure (mbar)	1013	1073

Table 5. Design specifications of the vacuum system

The vacuum system basically consists of three lines (plus an additional line called "by-pass line, which serves to maintain the vacuum in case of pressure fluctuations).

These three lines, which can provide different operating configurations depending on the level of vacuum that is required, are as follows:

- Line A: consists of 5 ejector in series (they are converging-diverging duct with circulating high temperature steam) and has a maximum capacity of 0.5 kg/s, it can work in conjunction with the other two lines;
- Line B: consists of four ejectors in series and has a maximum capacity of 1 kg/s;
- Line C: consists of three ejectors in series and has a maximum capacity of 2 kg/s.



The opening lines are controlled by corresponding on/off valves automatically controlled by the control system once set the conditions for conducting the test.



Fig. 8. Vacuum System

### 2.1.8 The DeNOx system

The DeNOx system serves to substantially reduce the percentage of nitrogen oxide (NO or NOx) inevitably present in the flow of plasma.

The DeNOx is essentially composed of two large reservoirs, "scrubber", which reduce the concentration of NO, a complex system of pumps, and three tanks. The first one is the largest and contains the washing solution, the second one contains sodium hypochlorite, NaOCl, and the third one contains caustic soda NaOH.

The DeNOx is able to maintain the concentration of nitric oxide (NO) below the limits fixed by the Italian law, and this is possible by means of a series of chemical reactions that occur within it.

### 2.1.9 Electrical system and power supply system

The system receives electricity from two external lines and it is equipped with an internal circuit for distribution. The power supply lines, through a complex system of processors, are reduced in a single line of industrial output voltage related to two different boxes: the first one is an electrical line of medium voltage (20 KV electrical system) which is connected to different users; a second cabin is the one of very high loads (32.5 kV, main load).

The cabin of the electrical system is designed to reduce the voltage and distribute electric power to the various units. It is equipped with four resin transformers powered with a medium voltage. The first two transformers make a conversion 20-0.4 KV providing power to the laboratories, while the remaining two transformers operating a conversion KV 20-6 feeding the engine and pump system. Inside the cabin, the power systems of the control system are installed, moreover an emergency instrumentation is present which ensures the supply of electricity in case of black-out. The Power Supply System is an independent unit and receives macro-command from the central system.

This unit provides electric power to the arc, up to a maximum of 70 MW. The subsystem is also equipped with appropriate filters suppressor of particular harmonics of the network. The Power Supply System uses oil transformers which, depending on the required load current and voltage, may give rise to two different configurations: the first one guarantees 6000 at 20,250 V and the second one 9000 at 13500 V, the change of Configuration is done with remote-controlled pneumatic arms, which open or close certain circuits. Downstream of the processors there are the current converters (AC / DC converter) that basically consist of thyristors cooled by demineralised water. Finally, the reactors have the task of eliminating the oscillations of the current (so-called "ripple"). The final closure of the circuit is done manually and, in cases of emergency, to disconnect the arch, a "Grow bar" that dissipates current through a coil is used. Finally, the "ballast resistors" are connected to the electrodes of the arc and are of the order of micro-ohm resistors, used to distribute the current.

### **2.1.10 Data Acquisition System and control system**

The Data Acquisition System (DAS) is used to acquire data from sensors of various typologies. The instrumentation system is divided broadly into two classes: the first is called field instrumentation and is the set of sensors used for the acquisition of measurements relative to the facility, the second is named test instrumentation and refers to measurement on the models or inside the test chamber (for scientific targets).

In the electric arc there is a static pressure sensor appropriately certified, while there are no temperature gauges because any intrusive sensor that would measure temperatures of 10000 K would have problems immediately.

The basic functions of the acquisition system are both the measurement of thermodynamic parameters on the model (for example, to study the behaviour of materials during the return from a space mission) and the measurement of parameters related to plasma and aerothermodynamics and, in Test Leg for that purpose, the instrumentation is divided in "virtual instruments", that means installed outside the test chamber and therefore not intrusive, and "conventional instruments", i.e. inside the test chamber instrumentation (intrusive).

At the nozzle exit section there are four static pressure gauges, they are essentially four small holes in the order of half a millimetre in diameter spaced 90 degrees from each other, used to measure static pressure fluctuations in various positions. This situation is in fact indicative of a lack of uniformity of plasma.

Inside the test chamber there are four more pressure sensors, in addition to the two probes. The latter are basically two ways that are intended to measure the thermo-fluid dynamics characteristics of the flow in terms of stagnation pressure and heat flux on the surface of the probe exposed to the plasma.

The pressure sensors are small diameter holes using a suitable transducer that guarantees operation even in environments at low pressures.

In the next paragraph the heat flow meter in the stagnation point of the probe is described.

### **2.2 Heat flux measurement at the stagnation point**

The heat flux is measured at the probe stagnation point by means of a Gardon gauge (Gardon, 1953) which is a heat flux sensor primarily intended for the measurement of high intensity radiation. It consists in a constantan foil hanging in a copper heat sink (see Figure

9). The foil is thermally and electrically connected to the copper cylinder through specific metallurgic techniques and it acts as first thermoelectrical material while the copper acts as the second thermoelectrical material. Thus, the foil and heat sink are respectively the hot and the cold joint of a thermocouple. A thin wire is then connected at the centre of the foil in order to generate a differential thermocouple which measures the temperature jump between the centre and the side of the foil.

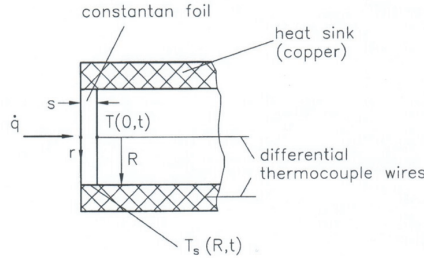


Fig. 9. Gardon gauge

In a polar coordinate system, the heat conduction equation can be written as:

$$\frac{\rho \cdot C_p}{K} \cdot \frac{\partial T}{\partial t} = \frac{1}{r} \cdot \frac{\partial T}{\partial r} + \frac{\partial^2 T}{\partial r^2} + \frac{\dot{q}}{s \cdot K} \tag{1}$$

where  $\rho$ ,  $C_p$ ,  $K$  and  $s$  are the density, the specific heat, the thermal conductivity and the thickness of the constantan foil, respectively, while  $\dot{q}$  is the heat flux acting at the centre of the foil.

Let us consider the following initial and boundary conditions:

$$\begin{aligned} T(r,0) &= T_s && \text{per } 0 < r < R \\ T(r,t) &= T_s && \text{per } 0 < t < \infty \end{aligned} \tag{2}$$

In the steady state regime and taking into account Eq.(2), the solution of Eq.(1) is:

$$\dot{q} = \frac{4sK}{(R^2 - r^2)} \cdot (T - T_s) \tag{3}$$

Thus, the heat flux at the centre of the foil ( $r=0$ ) is:

$$\dot{q} = \frac{4sK}{R^2} \cdot (T - T_s) \tag{4}$$

Equations (3) and (4) show that the temperature jump between the centre and the side of the foil is proportional to the heat flux which then can be evaluated by measuring such temperature jump.

**2.3 Specific total enthalpy measurement**

The specific total enthalpy  $H_0$  is computed through an energy balance in the arc heater and by using the following measurements: voltage, electrical current, gas mass flow rate, cooling

water flow rate and temperature jump of the cooling water. Once these quantities are measured, the specific total enthalpy is computed as follows:

$$H_0 = \frac{V \cdot I \cdot K - m_{H_2O} \cdot C_p \cdot \Delta T}{m_{gas}} \quad (5)$$

Where  $V$  is the potential difference between the ends of the arc heater,  $I$  is the electrical current,  $K$  is a conversion coefficient needed to keep consistent the units of measure,  $m_{H_2O}$  is the mass flow rate of the cooling water,  $C_p$  is the water specific heat and  $m_{gas}$  is the mass flow rate of the gas.

By using this approach and because of the uncertainty of the various measure instruments, the specific total enthalpy is estimated with an error which sometimes results notable. Such error can be computed by using Eq.(6).

$$\frac{dH_0}{H_0} = \frac{dV}{V} + \frac{dI}{I} + \frac{dm_{H_2O}}{m_{H_2O}} + \frac{d(\Delta T)}{\Delta T} - \frac{dm_{gas}}{m_{gas}} \quad (6)$$

### 3. SCIROCCO test procedure

The design of a test in a Plasma Wind Tunnel is complicated by the circumstance that many differences exist between flight and test chamber conditions (model size, dissociated flow conditions in test chamber, density level, etc.). All these aspects play an important role on the real gas non-equilibrium phenomena and make difficult the duplication of real flight conditions in wind tunnel. The main problem is to find the correct similitude parameters: to this effect, it is firstly needed to define the goal of the simulation, i.e. the phenomenon we are interested in reproducing; this is often a flight condition to be simulated on the test article in wind tunnel, but it can be a particular customer's request as well (Marini et al. 2007). Hence, the design of ground-based experiments, as well the interpretation of experimental data, needs an appropriate support of numerical simulations. As matter of fact, in order to meet the specific test requirements (Stagnation heat flux, stagnation pressure, test time and test article size), Computational Fluid Dynamics (CFD) calculations are needed to accurately design the configuration of the facility. Successively, a structural safety analysis is carried out with the aim of verifying the structural integrity of the test article. After the test is performed and experimental data are acquired, numerical activities are again needed to rebuild the test and to support in the interpretation of the test results. Moreover, the ability of the developed finite element model in predicting the temperature field in the test article is verified by comparing numerical data with experimental one.

The present paragraph deals with the description of the procedure for the execution of a test in the facility SCIROCCO. An overview of the test procedure is given in the flow chart of Figure 10.

Each steps of such procedure will be described in detail hereafter:

**Requirements:** The first aspect that is taken into account when a test in SCIROCCO is designed is the definition of the requirements.

Requirements can be formulated in terms of heat flux (more often), or in terms of pressure, temperature or they can also be formulated in terms of scientific phenomena reproduction such as shock wave -boundary layer interaction and so on.

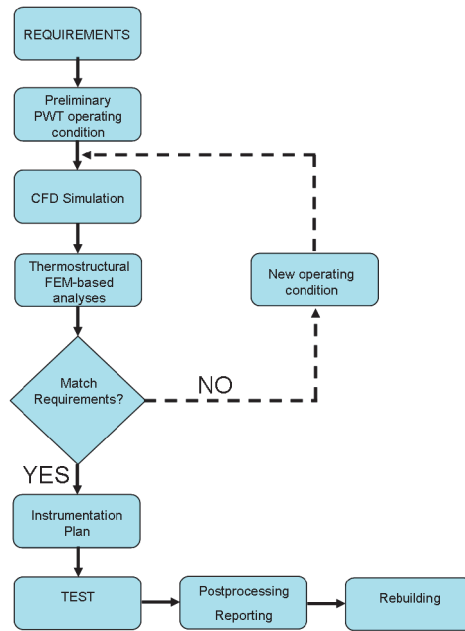


Fig. 10. SCIROCCO Test Procedure

The requirements are given by the customer and a process of trade-off begins. Indeed a feasibility study verifies the compatibility of both test requirements with the PWT theoretical envelope and test article dimensions with test chamber capability, in order to avoid blockage phenomenon. Then, a first operating condition is defined by means of both engineering tools, to derive the stagnation point heat flux and pressure from requirements on the test article, and the curve-fit calibration law for fast PWT Test Setting (De Filippis et al. 2003).

**Preliminary PWT operating condition:** Once the first operating condition has been defined, the driving parameters of the facility (current and air mass flow) and the PWT performances in terms of reservoir pressure ( $P_0$ ) and reservoir enthalpy ( $H_0$ ) are obtained, and consequently the stagnation pressure ( $P_s$ ) and stagnation heat flux ( $Q_s$ ) on the PWT calibration probe are evaluated.

**CFD Simulations:** Starting from the preliminary condition, the final PWT settings able to match the test requirements are defined by means of an iterative procedure, which involves both CFD computations and evaluations with simplified engineering correlations.

Free stream conditions to be used for the simulation of the flow around the model in the test chamber are obtained from the numerical computation of the nozzle flow. If the CFD simulation of the flow past the model shows that test requirements over the model are not still achieved, a new reservoir condition ( $P_0, H_0$ ) is deduced by using simplified engineering correlations and the procedure restarts from the CFD simulation of the nozzle flow. As an alternative, test requirement fulfilment could be reached with the same reservoir conditions, properly modifying the model position inside the test chamber and/or the model attitude. In this last hypothesis only model computation has to be iterated.

Once the final PWT operating condition has been defined, simulation of the flow past the PWT calibration probe provides pressure ( $P_s$ ) and heat flux ( $Q_s$ ) at the probe stagnation point. These values, measured during the test, ensure the achievement of the desired operating condition in terms of ( $P_0, H_0$ ) in test chamber.

**Thermostructural FEM-based analysis:** once the PWT operating condition ensuring the achievement of test requirements has been identified, the structural integrity of the model under that conditions has to be verified. At this stage a FEM transient thermal analysis is carried out by applying on the model the heat flux distribution (usually multiplied by a safety coefficient equal to 1.2) computed by CFD simulations. The thermal analyses are highly nonlinear since radiation to the environment must be taken into account. The temperatures predicted by the FE model are checked against the temperature limits of the materials under investigation. Critical instants are then identified as those ones at which high gradients of temperature (and thus high thermal stresses) are expected. Nonlinear static structural analyses are then carried out by applying the temperature field predicted at the critical instants as a structural load. FE codes able to perform non linear contact analyses are used at this stage. Thermal and structural simulations are very useful also to identify critical parts which have to be properly monitored during the tests. In other words, expected temperatures predicted by numerical simulations are the input data for the test instrumentation plan whose objective is accurately choose the kind of instruments, their location and range, that are used to monitor the test and to reach its scientific aim.

**Instrumentation plan:** When the trade-off phase for the definition of the test conditions is concluded, the instrumentation setup to be used for the test is designed. Indeed, the particular environment typical of hypersonic regime and the scientific aims of the tests require a number of parameter measurements. Hence, different kind of instruments, both intrusive (thermocouples) and not intrusive (pyrometers and thermocameras), measuring at different locations have to be properly chosen.

Similarly to the test conditions definition phase, a trade-off phase for the definition of the instrumentation is performed, at the end of which the instrumentation plan is made, that is a design report containing all the information about the test instrumentation.

**Test execution and post processing reporting:** Once the test conditions (including test duration and all the other parameters) and the test instrumentation are fixed, the test is executed. After the test a period of time is necessary for the post processing (data treatment) and the reporting, at the end of which a complete report, the "Test Report", is carried out.

In this document all the information about the test and all the instrumentation measured and treated data are reported.

**Rebuilding:** The numerical rebuilding is another important phase, that, differently from all the other phases, follows the test itself. It is performed starting from the measured values of stagnation heat flux and pressure rather than the values of reservoir pressure and enthalpy, and its aim is to provide a meaningful heat flux distribution on the model during the test as input for the thermo-structural rebuilding analysis, whose results (wall temperature distribution) can be compared with the IR thermo-graphic acquisition generally performed in PWT tests.

From a numerical point of view it determines the condition ( $P_0, H_0$ ) that provides the better agreement with the probe measurements and then, with the same condition, the heat flux over the model is recomputed.

#### 4. Rebuilding of a nose cap demonstrator

In order to show the importance of “rebuilding” a PWT test, this step will be presented in detail referring to a specific application.

Within the context of the research project Sharp Hot Structures (SHS), focused on the assessment of the applicability of Ultra High Temperature Ceramics (UHTCs) to the fabrication of high performance and sharp hot structures for reusable launch vehicles, the nose cap demonstrator named Nose\_2 was tested in the SCIROCCO Plasma Wind Tunnel. The architecture of the nose is shown in Figure 11. The basic idea of the Nose\_2 design was to couple conventional C/SiC materials to novel Ultra-High Temperature ZrB<sub>2</sub>-SiC Ceramics (UHTC) in order to create a multi-material structure able to withstand the severe condition associated with slender-shaped hot structures and non-conventional reentry mission profiles. The nose is made of two main components: the tip and the dome.

The conical tip, which was intended to sustain the greatest thermal load in the whole nose cap structure, was made of ultra-high temperature ZrB<sub>2</sub>-SiC ceramic. The tip was produced by hot pressing sintering and then finished by EDM (Electrical Discharge Machining). The outer dome was made of C/SiC and has the shape of a hollow frustum of cone. It was manufactured by Polymer Infiltration and Pyrolysis (PIP) process. A ZrB<sub>2</sub>-SiC coating, about 500 μm thick, was applied by Plasma Spray Deposition technique on the external surface of the outer dome to protect the fibres from oxidation.

The inner dome was made of graphite and its main function was to increase the thermal capacity of the system. A mechanical interface in AISI304 allowed the connection between the nose cap demonstrator and the Model Support System.

Finally, the coupling between tip and dome of the nose cap was guaranteed by a coupling pin in titanium alloy which was preloaded by a spring. One end of the pin was not axial-symmetric and it was introduced into the hole and then rotated by 90 degrees in order to ensure the contact. The coupling hole dimensions are the results of a sensitivity analysis (Ferraiuolo et al., 2008) performed with the aim to reduce stress concentration next to the coupling hole of the tip component and, at the same time, to reduce the massive volume taken away by spark erosion. The bend radius, the entire length and the diameter of the hole were chosen as parameters of the sensitivity analysis.

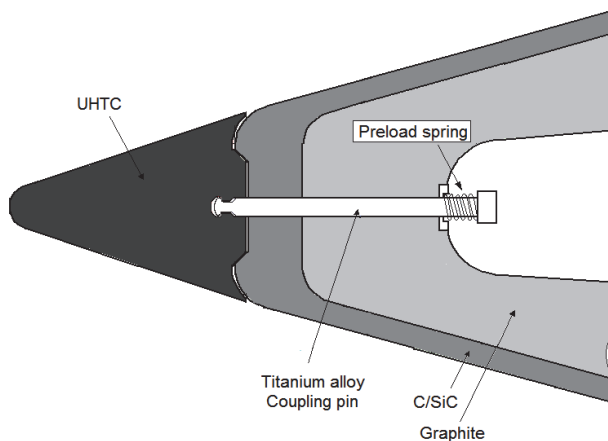


Fig. 11. Schematization of tip-dome coupling

In Figure 12, the experimental data, in terms of temperature curves measured by an IR thermocamera along the nose profile and at several time steps, are shown. Experimental data were not available within the range  $[x=0, x=0.025\text{m})$  since this area was characterized by a low view factor with respect to the IR thermocamera.

The enthalpy ( $H_0$ ) and the pressure ( $P_0$ ) at the stagnation point measured during the experimental test were  $13.5\text{ MJ/Kg}$  and  $1.9\text{ bar}$ , respectively. These data were used by CFD simulation to compute the heat flux distribution acting on the nose cap during the test.

The change in manufacturing process passing from coupon level to sub-component level makes it very difficult to determine some experimental parameters which are needed in numerical computations. One of these experimental parameters is the catalysis of the UHTC. Hence, in order to verify the influence of catalysis on the thermal behaviour of the nose cap, both the Non-Catalytic Wall (NCW) model and the Finite Rate Catalysis (FRC) one were used to compute heat fluxes acting on its external surface.

The heat flux distributions computed by using the two different catalysis models are shown in Figure 13 where the profile of the nose (red curve) is also represented. The stagnation heat flux, that is the heat flux computed for  $x=0$  and  $y=0$ , for the NCW and FRC catalysis models were found respectively to be  $1310\text{ kW/m}^2$  and  $1490\text{ kW/m}^2$ . However, because of the uncertainty in the measurements of both the probe stagnation heat flux and the probe stagnation pressure (measurements that affects the CFD calculations), the heat flux distributions plotted in Figure 13 were estimated with an uncertainty equal to  $\pm 8.9\%$ .

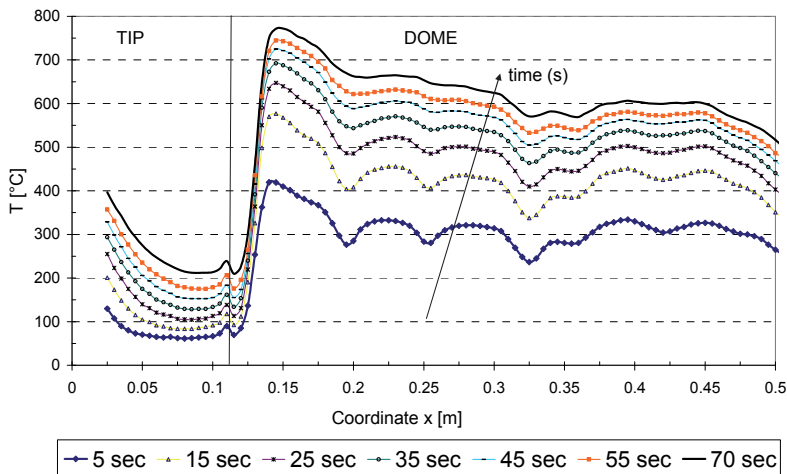


Fig. 12. Experimental temperature curves at several time steps

A 3D FE model (Figure 14) was built by using the FE commercial code ANSYS which was found able to deal with these thermo-mechanical problems. The heat flux distribution computed via CFD simulation was applied on the exposed external surfaces and, in order to reproduce the same conditions occurred in the PWT during the experimental test, heat fluxes were applied constantly for 72s, then they were set to zero to simulate the cooling. The duration and the heat fluxes magnitude are representative of a re-entry trajectory which was one of the requirements of the nose design. The radiation to the environment was taken into account in the FE model.



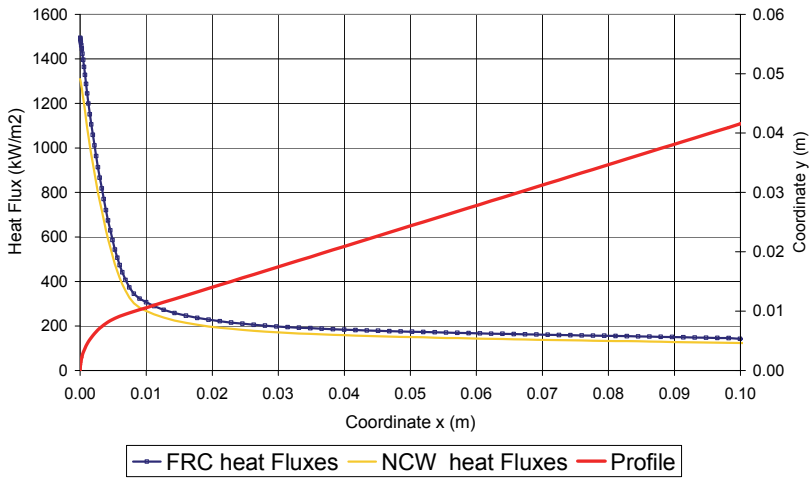


Fig. 13. Heat flux distribution on the profile of the nose

In Figure 15 the numerical temperature curve, predicted on the tip profile and obtained by applying NCW heat fluxes, is compared to that one obtained by applying FRC heat fluxes. The plotted curves are predicted at time 50s of the simulation and they are compared to the experimental data registered at same time instant. The NCW model was found to provide better agreement with experimental data with respect to the FRC model and was adopted for the rest of this research work.

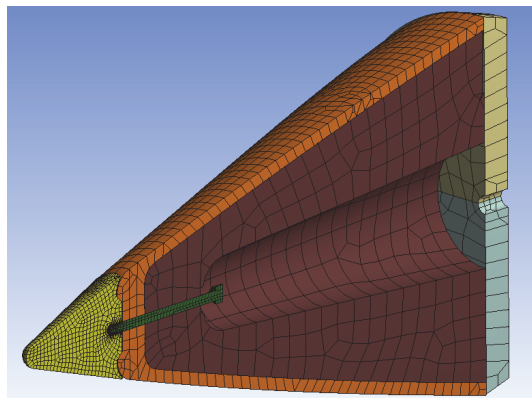


Fig. 14. Section of the 3D FE model

After the test, in the post-processing phase, it was found that the dome surface temperature was higher than the tip surface temperature, though the heat flux acting on the tip was considerably higher as shown in Figure 13. In order to interpret so high temperatures measured on the dome surface, a numerical study was performed. Such study was just qualitative and was focused to the improvement of knowledge on the physical phenomenon under investigation. In particular, two different simulations, with two different assumptions

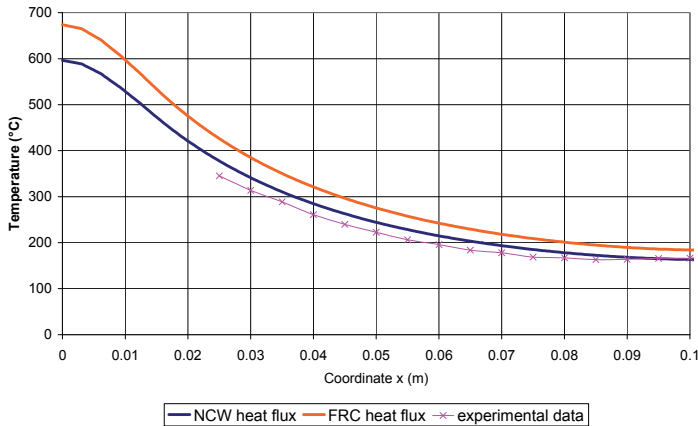


Fig. 15. Comparison between numerical and experimental tip surface temperature at 50s.

on the modelling of the C/SiC-coating interface, were carried out. Comparison between temperatures predicted by the two simulations at time 70s and those measured during the test at the same time instant are shown in Figure 16. In the first simulation, the coating layer was assumed perfectly bounded to the C/SiC, hence it was not modelled because its thermal resistance was assumed negligible. The strong discrepancy between experimental temperatures measured at the outside of the dome and those predicted by this simulation justified further investigations to better understand how to model the C/SiC - coating interface. Therefore, in the second simulation the coating layer was assumed completely detached from the C/SiC, hence it was modelled by a thin surface completely not in contact with the C/SiC, in such a manner the coating was not able to transfer heat to the C/SiC by conduction but only by internal radiation.

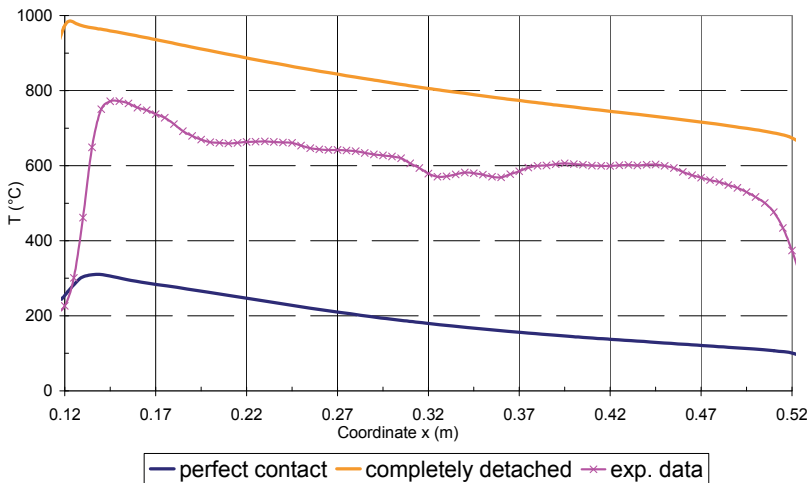


Fig. 16. Comparison between numerical and experimental dome surface temperature at 70s.

Temperatures predicted in the case of coating completely detached are closer to the experimental data with respect to those predicted in the case of perfect contact suggesting that most likely the contact between the coating and C/SiC during the PWT test was neither perfect nor completely separated but local detachments occurred in unknown regions of the interface. The wavy trend of the experimental temperatures confirms this hypothesis. Indeed, where the detachment occurred, the coating was not able to transfer heat to the C/SiC and a peak in temperature was measured by the IR thermocamera. On the other hand, where the contact was perfect, the heat was drained towards the inner dome and a lower temperature value was registered. Destructive inspections confirmed later that the coating was locally detached by the outer dome in several zones.

Further investigations were made during the rebuilding phase of a second PWT test performed on the same nose cap demonstrator (Borrelli et al., 2010). Experimental data were compared with numerical results in order to help in interpreting the experimental test itself. The knowledge on the physical phenomenon under investigation was greatly improved thanks to the synergy between numerical and experimental activities. In particular, a qualitative study of the modeling of the tip-dome interface was performed in order to estimate the thermal contact resistance that heat flux encounters in passing through the demonstrator. Modeling this interface as imperfect greatly improved the accuracy of the numerical predictions.

## 5. Conclusion

A brief introduction on the characteristics of a plasma wind tunnel facilities, as well as their performances and applications, was provided. Particular attention was given to the SCIROCCO PWT facility, that is the plasma wind tunnel developed by CIRA, which is the World's most powerful ground test facility. Successively, each step performed for the success of a plasma wind tunnel test was examined in detail. In particular, the synergy between the experimental team and the numerical one in each step of the test procedure was stressed by providing explanatory examples.

## 6. Acknowledgment

The authors would like to thank the entire CIRA PWT staff for providing useful information needed to write this work.

## 7. References

- Borrelli, R.; Riccio, A.; Tescione, D.; Gardi, R. & Marino, G. (2010). Numerical/Experimental Correlation of a Plasma Wind Tunnel Test on a UHTC-made Nose Cap of a Reentry Vehicle, *Journal of Aerospace Engineering*, Vol.23, No.4, pp. 309-316, ISSN 0893-1321
- De Filippis, F.; Caristia, S.; Del Vecchio, A. & Purpura C. (2003). The Scirocco PWT Facility Calibration Activities, *3rd International Symposium Atmospheric Reentry Vehicle and Systems*, Arcachon, France.
- Ferraiuolo, M.; Riccio, A.; Tescione, D.; Gardi, R. & Marino, G. (2008). Contact Sensitivity Analysis of a Coupling Pin for the Nose Cap of a Launch of a Re-entry Vehicle, *Journal of the Interplanetary Society*, Vol.61, pp. 14-19, ISSN 0007-084X

- Gardon, R. (1953). An Instrument for the Direct Measurement of Intense Thermal Radiation. *Review of Scientific Instruments*, Vol.24, pp. 366-370.
- Kelly, H. N.; Rummeler, D. R. & Jackson, R. (1983). Research in Structures and Materials for Future Space Transportation Systems - An Overview. *Journal of Spacecraft and Rockets*, Vol.20, No.1, pp. 89-96, ISSN 0022-4650
- Marini, M.; Di Benedetto, S.; Ruffolo, G. C.; Di Clemente, M. & Borrelli, S. (2007). Test Design Methodologies for Flight Relevant Plasma Wind Tunnel Experiments, *Proceedings of West-East High Speed Flow Field Conference*, Moscow, Russia
- Shih, P. K.; Prunty, J. & Mueller, R. N. (1988). Thermostructural Concepts for Hypervelocity Vehicles. *AIAA paper*, No. 88-2295
- Thornton E. A. (1996). *Thermal Structures for Aerospace Applications*, AIAA, ISBN 1-56347-190-6, Reston, Virginia.

# Study of Turbulent Supersonic Flow Based on the Optical and Acoustic Measurements

Viktor Banakh<sup>1</sup>, Dmitri Marakasov<sup>1</sup>,  
Ruvim Tsvyk<sup>1</sup> and Valeri Zapryagaev<sup>2</sup>

<sup>1</sup>*V.E. Zuev Institute of Atmospheric Optics SB RAS*

<sup>2</sup>*Khristianovich Institute of Theoretical and Applied Mechanics SB RAS  
Russia*

## 1. Introduction

Aircraft and missiles moving in the atmosphere with supersonic velocities form air flows of a complicated spatial structure, in which compression shocks of different configurations and intensities arise. Since an air flow is strongly spatially inhomogeneous, the air density in the flow experiences random pulsations much exceeding turbulent pulsations of the air density in the atmosphere. Mean characteristics of supersonic flows are investigated rather well both theoretically and experimentally, but characteristic properties of turbulence in a supersonic flow are studied insufficiently.

To study turbulence in supersonic flows, the real-time measurements of the value and spectral composition of pulsations are required. Currently used sensors distort the flow structure and often have the low response rate. The dynamics of fluid or gas flows can also be studied and the turbulent velocity field in fluid and gas flows can be visualized with the use of noncontact optical methods. Among these are speckle photography and speckle interferometry methods (Fomin, 1998), in which the source of information is represented by intensity fluctuations of the laser radiation passed through the flow and a diffuse plate, as well as Doppler methods (laser Doppler anemometers (LDA)) (Abbrecht et al, 2003) and Particle Image Velocimetry (PIV) methods (Raffel et al, 2007) based on the measurement of velocities of microparticles suspended in a flow. LDA and PIV devices are very expensive and difficult in use. They are successfully used mostly for the investigation of fluid flows and subsonic gas flows. In the supersonic gas dynamics, their application is limited owing to such factors as increased requirements to the instrumentation (laser pulse energy, operation rate and sensitivity of recording instruments) and still open problems of velocity relaxation of tracing particles. In the seeding process, the tracing particle sizes are not identical and their concentration is not always uniform in a flow and this inevitably leads to the loss in accuracy of measurements.

The widely used methods of shadow visualization (Schlieren photography) do not allow the spatial spectrum of refractive index fluctuations to be determined from the obtained images. Shadow images are integral characteristics of the refractive index in the entire radiation propagation path, and the spatial distribution of the refractive index in different flow layers cannot be reconstructed from them. In this connection, it is interesting to study possibilities

of the remote diagnostics of gas flow turbulence from the intensity fluctuations of the optical radiation crossing a flow. This method does not require the presence of scattering particles and diffusors and allows the spatial structure of pulsations in a flow to be studied at dimensions of the probing beam much smaller than the flow transverse size.

In this research field, intensity fluctuations of the laser beam passed through a model plane layer of a turbulent flow and the beam propagating through a jet of a jet engine have been studied experimentally (Joia et al, 1997, 1995) and (Dmitriev et al, 2004, Sirazetdinov et al, 2001), respectively). However, these results (Joia et al, 1997, 1995, Dmitriev et al, 2004, Sirazetdinov et al, 2001) correspond to subsonic velocities of studied flows, and for their interpretation it is sufficient to use the results of the theory of incompressible fluid mechanics (Monin & Yaglom, 1971, 1975) and optical radiation propagation in such turbulent media (Gurvich et al, 1976, Zuev et al, 1988). In case of supersonic flows, for the interpretation of measured results, it is necessary to take into account not only temperature fluctuations, but also pressure fluctuations, as well as the strong spatial inhomogeneity of the flow. In recent years, the theoretical papers were published, in which the authors undertook attempts to construct an electrooptical model of parameter fluctuations in compressible gas flows (Offer Pade, 2001, 2003, 2004, 2005). However, the results obtained can be considered only as an initial stage of the study of radiation propagation in supersonic flows. In (Offer Pade, 2001, 2003, 2004, 2005), only the variance of phase fluctuations of an optical wave passed through a supersonic flow was calculated and the variance of gas density fluctuations in a flow was estimated. The calculations were based on the Fluent Dynamic 6 turbulence model.

The existing theoretical models of turbulence of compressible flows can be found, in particular, in (Yoshizawa, 1995, Smits & Dussauge, 1996, Canuto, 1997). However, in this field there is no versatile model similar to the case of developed turbulence of incompressible flows (Monin & Yaglom, 1971, 1975).

This chapter presents the results of both experimental and theoretical studies of optical turbulence in supersonic flows. The experiments on laser beam propagation through supersonic flows were conducted in T-326 and T-313 wind tunnels of the Institute of Theoretical and Applied Mechanics of the Siberian Branch of the Russian Academy of Sciences (ITAM SB RAS). The theory of laser beam propagation through a supersonic flow was based on dynamical models of the Fluent 6.0 software. The transport equations for calculation of turbulent parameters were selected according to the  $k$ - $\epsilon$  ring model.

## **2. T-313 and T-326 wind tunnels**

The batch-operated T-313 and T-326 wind tunnels use compressed air for their operation. Air is compressed by high- and medium-pressure compressors at a turbocompressor station. After pre-drying, air enters high- (up to 200 bar, volume of 96 m<sup>3</sup>) and medium-pressure (up to 18 bar, volume of 5600 m<sup>3</sup>) cylinders. The modern automated control system provides the trouble-proof operation of the station, gathering of information about the equipment functioning and volumes of generated compressed air and circulated water (Garkucha et al., 2009).

### **2.1 T-313 supersonic wind tunnel**

The batch-operated T-313 supersonic wind tunnel is operated since 1965 and has the closed working part with the rectangular  $0.6 \times 0.6 \times 2$  m cross section (Fig. 1). The range of Mach

numbers, which can be obtained in this tunnel, is 1.75 - 7. The discrete variation of the Mach number  $M = 1.75, 2, 2.25, 2.5, 2.75, 3, 3.5, 4, 5, 6,$  and 7 is provided by replacement of hard nozzle profiled inserts.

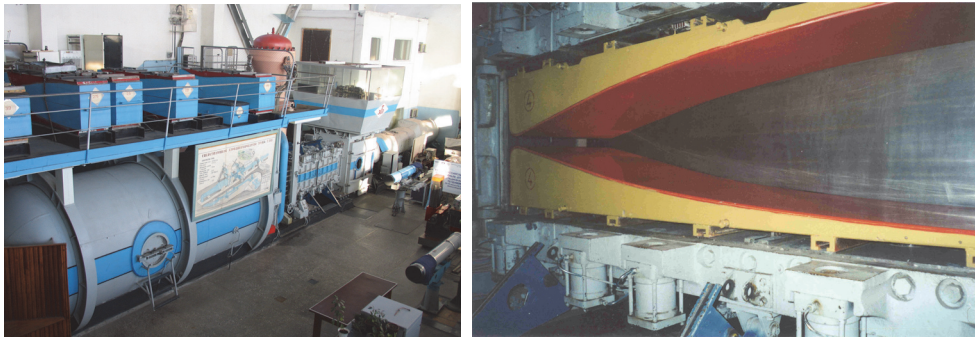


Fig. 1. T-313 supersonic wind tunnel and the nozzle unit with changeable profiled inserts for the Mach number  $M = 4.0$ .

A gas-cylinder station with the maximal air pressure up to 18 bar allows the working conditions to be maintained for about 10 min with the extreme Reynolds number  $Re \approx 8 \cdot 10^7 m^{-1}$  at the direct-flow operation and the Mach number of the flow  $M = 4$ . There are two air paths, namely, the cold one (direct-flow path without air heating) for the range  $M = 1.75-4$  and the hot one for  $M = 5, 6, 7$ . A hot channel houses a 6-MW ohmic heater, which heats the air up to  $500^\circ C$ , thus preventing the nitrogen and oxygen condensation at a temperature decrease accompanying the adiabatic dilatation in the nozzles. A supersonic diffuser and then a two-stage ejector system are set downstream from the working part. The two-stage ejector system provides the continuous supersonic flow in the working part of the setup, decreases the load on the model during the start-up time, and allows the Reynolds number to be varied during experiments. Depending on the preset working conditions, the supersonic flow can be obtained in the working part of the setup at the operation of one or two ejectors or without ejector (direct-flow conditions).

The setup is equipped with two pressure regulation systems to maintain the preset pressure in the settling chamber at the operation in the cold or hot channel. The regulation systems are based on the application of specialized chokes moved by hydraulic actuators, which are controlled by a pneumatic hydraulic control. The air exits the gas-dynamic channel of the setup through the silencing chamber installed beyond the aerodynamic hall. Each of the two ejectors has individual regulation systems.

The setup is equipped with 4-component aerodynamic mechanic external-type weighting scales, which allow the measurement of aerodynamic characteristics of models such as resistance force, lift, pitching moment, and rolling moment. The angle of attack of the model during the test can be changed manually or automatically by a preset program in a range from  $-5^\circ$  to  $+22^\circ$ . The application of intramodel strain-gage weighter is possible.

To visualize the flow field near the model, the working part of the tunnel is equipped with optical windows and the coaxial IAB-451 Maksutov-system optical shadow device with the observation field 230 mm in diameter. The methods of colored oil visualization of limiting flow lines on the surface and the laser knife method are also used.

The experiments have determined that the degree of nonuniformity of the Mach number distribution in the zone of models was ~1% in the supersonic velocity range and 1.5% at hypersonic velocities. The level of mass-flow pulsations varied depending on Mach numbers from 0.27% to 0.86%.

The automation system ensures the real-time acquisition of experimental data simultaneously from a large number of channels, the graphic presentation of measured results, and the primary data processing. The multiprocessor automation system for supersonic and hypersonic periodic wind tunnels is developed in accordance with the following principles: unification of the automatic data acquisition at the level of hardware and software interfaces and the possibility of fast setting for particular experimental conditions.

The T-313 supersonic wind tunnel allows the following experimental investigations of the gas-dynamic structure of complex turbulent supersonic flows:

- Study of stationary aerodynamic characteristics of aircraft models;
- Study of the structure of detached supersonic flows with the measurement of the distribution of the average pressure and pressure pulsations on the model surface;
- Measurement of the pressure distribution in the boundary layer of the model;
- Study of the structure of supersonic flows with the use of optical visualization methods (shlieren visualization of optical inhomogeneities of the flow, laser knife method, colored oil visualization of limiting flow streamlines as a model surface is approached);
- Study of the problem of sonic boom level decrease at the flow of an aircraft flying with supersonic velocity;
- Study of interference of shock waves;
- Study of the mechanism of interaction of an intense tip vortex with a shock wave;
- Study of the interaction of supersonic jets with a supersonic wake flow;
- Study of flows in internal channels of super- and hypersonic aerojet engines, as well as study of problems of the integration of a planer and an engine of promising aircraft.

## 2.2 T-326 hypersonic wind tunnel

The batch-operated T-326 hypersonic wind tunnel (Fig. 2) is in work since 1971. Its working part is made as an Eiffel's test chamber.

The setup is equipped with profiled axisymmetric nozzles with a section diameter of 200 mm. The range of feasible Mach numbers is  $M = 6-14$ . The range of Reynolds numbers is  $Re = (0.6-70) \cdot 10^6 \text{ m}^{-1}$ . The pressure in the settling chamber is  $p_0 \leq 100 \text{ atm}$ , the temperature in the settling chamber is  $T_0 \leq 1500 \text{ K}$ . The wind tunnel is equipped with two air heaters. The first ohmic-type heater with power of 2.2 MW provides the Pitot temperature in the settling chamber  $T_0 \leq 600 \text{ }^\circ\text{C}$  and is intended to generate a flow with the Mach number  $M = 6-10$ . The second arc plasma heater with power of 1.6 MW allows the temperature  $T_0 \leq 1500 \text{ K}$  to be achieved and is intended for investigations with  $M \leq 14$ . The design maximal pressure in the settling chamber is 150 bar. The measured inhomogeneity of the Mach numbers at the nozzle section in the zone of the model does not exceed 1.5%.

The tunnel is equipped with a slit ejector with the high degree of compression, which ensures the setup operation at rather small Reynolds numbers. The ejector is connected to a medium-pressure system, and the main flow comes from a high-pressure gasgolder chamber through the heater. In this setup, the hypersonic flow with the Mach number  $M = 6$  at the nozzle section can be obtained at a pressure of 10 bar in the settling chamber. Under



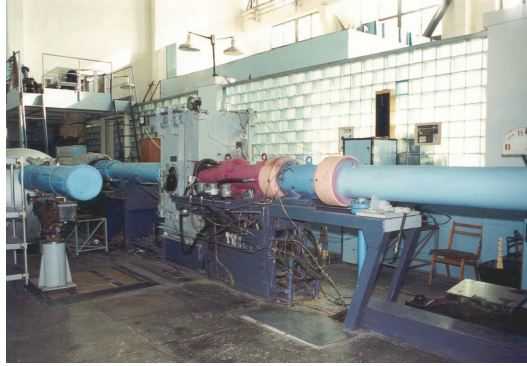


Fig. 2. T-326 hypersonic wind tunnel.

these conditions, to prevent the nitrogen and oxygen condensation in the flow, the air should be heated to the Pitot temperature no less than 400 K according to Daum recommendations.

The working part of the wind tunnel is equipped with optical windows. In addition, the wind tunnel is equipped with the IAB-451 Maksutov-system optical shadow device. The automatic data acquisition system allows one to record gas-dynamic flow parameters and readouts of pressure and temperature sensors set on the model surface.

The setup design allows one to study the shock-wave structure of supersonic anisobaric jets with the use of a specialized jet unit installed in place of the supersonic nozzle. The settling chamber of the jet unit is a tube with an inner diameter of 113 mm and has a mounting seat for changeable nozzles. The jet flows into the working chamber. The nozzle section falls within the field of view of optical windows with a diameter of 200 mm. The pointing device allows the total-pressure sensor (or other probe) to be moved in the jet flow field with the high positioning accuracy. The supersonic jet flows into the pressure chamber and is emitted into the silencing shaft through the supersonic diffusor of the exhaust line of the wind tunnel.

The T-326 hypersonic wind tunnel of the ITAM SB RAS allows the following types of experiments to be conducted: study of the laminar-turbulent transition at the hypersonic flow speed; study of heat exchange characteristics, study of flow pulsations in the anterior detachment zone; study of the structure of detached flows at the high supersonic flow speed with the measurement of the distribution of the average pressure and pressure pulsations on the model surface, as well as study of the shock-wave structure of the flow at the initial part of supersonic anisobaric jets.

### 3. Experimental setup for laser beam transmission through supersonic flow and acoustic measurements

#### 3.1 Experimental setup based on T-326

Experimental investigations on the T-326 wind tunnel were conducted with the use of the jet unit with the convergent nozzle, whose section diameter was  $d = 30$  mm. The Mach number at the nozzle section was  $M = 1$ . The pressure in the settling chamber of the jet unit was maintained so that the ratio  $npr = p_0/p_c$  varied from 1.7 to 9. Here,  $p_0$  is the pressure in the settling chamber of the wind tunnel,  $p_c$  is the pressure in the Eiffel's test chamber ( $0.8 \times 0.8$  m

working part of the wind tunnel). Some experiments were conducted on the jet unit with the vertical exit of the supersonic jet in a large room. Intensity fluctuations of the laser radiation (wavelength  $\lambda = 0.63 \mu\text{m}$ ) crossing the jet and the acoustic waves generated by the jet were measured in the experiments.

In the experiments, the laser radiation passed through the jet in the transverse direction at different distances  $x$  from the nozzle section along jet axis. In every cross section, the laser beam intersected the jet at different distances  $r$  from the jet axis down along the vertical. The measured results were used to calculate the relative variance and spectral functions of intensity fluctuations of the laser radiation.

The acoustic measurements were conducted in the frequency range 20 Hz-100 kHz with the use of 5 microphones 6 mm in diameter for three different configurations of microphone arrangement with respect to the jet (Fig. 3):

1. in parallel to the jet at a distance  $r = -135 \text{ mm}$  from the jet axis down in the vertical direction. The measurements were conducted simultaneously by 4 microphones displaced synchronously with a step  $\Delta x = 20 \text{ mm}$  from  $x = 25$  to  $x = 245 \text{ mm}$ ;
2. around the circle 140 mm in radius (with an interval of  $45^\circ$ ) at a distance  $x = 135 \text{ mm}$  from the nozzle;
3. horizontally across the jet along the axis  $y$  in the cross sections  $x = 25$  and  $135 \text{ mm}$  at  $r = -135 \text{ mm}$ . The measurements were conducted with a step  $\Delta y = 20 \text{ mm}$  at distances  $y = -30$  to  $110 \text{ mm}$  from the jet axis.

The measured results were used to calculate the value and spectral density of the sonic pressure, as well as mutual correlation functions of the sonic wave between the fixed microphone and each of 4 movable microphones.

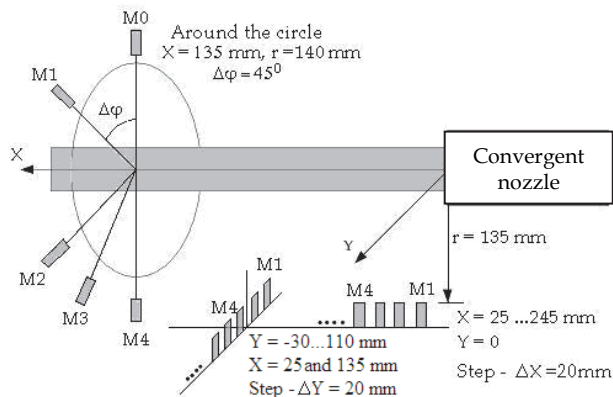


Fig. 3. Arrangement of microphones in the Eiffel's test chamber.

In some experiments, the convergent nozzle with chevrons, which changed the flow structure and, consequently, the turbulence strength and the acoustic field, were used.

### 3.2 Experimental setup based on T-313

In the experiments with the T-313 wind tunnel, the supersonic flow (SF) above a model of an aircraft element was studied by passing the laser beam through the flow. A plane wing model was used. The angle of attack of the wing  $\alpha^\circ$  (slope with respect to the SF axis)

varied from  $-4.7^\circ$  to  $19.7^\circ$  toward the flow. Three lasers were used. The data recording started once the steady-state regime was established in the flow. The schematic of the optical experiments is shown in Fig.4.

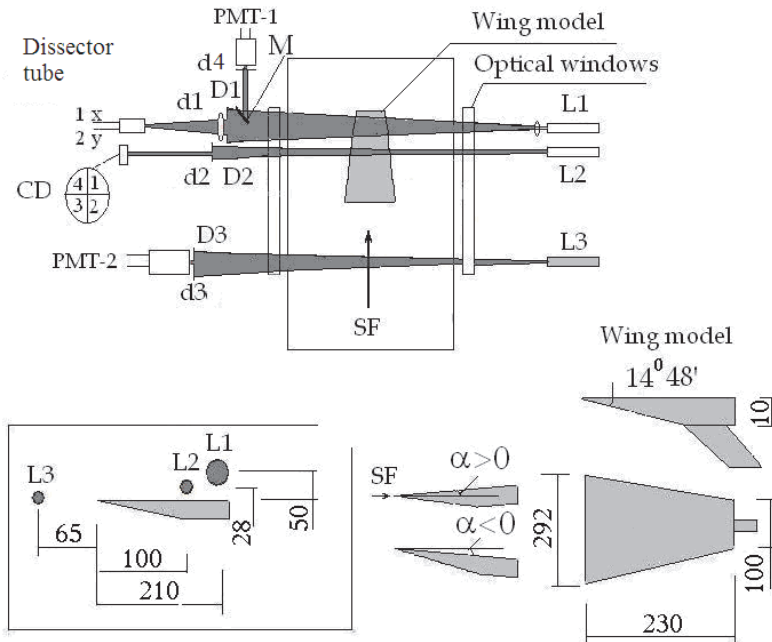


Fig. 4. Schematic of the experiment with the T- 313 wind tunnel.

The following parameters were recorded:

*In front of the wing:* intensity fluctuations of laser radiation in the flow incoming to the wing (photomultiplier (PMT) PMT2 and laser L3 with the beam  $D3 = 40$  mm in diameter). The signal digitization rate was 10 MHz, the band pass of the receiving system was 0-3 MHz, and the diameter of a diaphragm set in front of the PMT was  $d3=0.2$  mm.

*Above the wing:*

1. Intensity fluctuations of the laser radiation in the part of the laser beam separated by the mirror M (PMT 1 with a diaphragm  $d4 = 0.2$  mm and laser L1 with a beam  $D1 = 90$  mm in diameter).
2. Fluctuations of displacements of the laser beam image (system tracing the image centroid based on a dissector tube and laser L1) at the focus of an objective with a focal length of 450 mm and a diaphragm  $d1 = 10$  mm. The signal digitization rate was 100 kHz, and the frequency range of the system was 0-1.5 kHz along every coordinate.
3. Fluctuations of the laser beam direction (four-quadrant coordinate photodiode CD and laser L2 with the beam  $D2 = 40$  mm in diameter). The digitization rate of a signal from each element was 250 kHz. A diaphragm  $d2 = 2$  mm in diameter was set at a distance of 700 mm in front of CD.

The data recorded were used to calculate spectral functions and relative variances of signal fluctuations.

#### 4. Model of optical turbulence of supersonic flow

To develop a model of optical turbulence in a supersonic flow, it is necessary to know the spatial distribution of the gas density and the gas flow velocity. In addition to average values of the density and flow velocity, we also should know the characteristics of turbulent pulsations of these parameters, such as the variance and spectra of the density and the velocity components.

Average values of the flow parameters are usually determined with the system of averaged Navier–Stokes equations. The system is closed through the introduction of additional equations for the variance and the mutual correlation of fluctuations of medium parameters. There are several semiempiric models of turbulence, which allow the parameters  $k$  (turbulent kinetic energy) and  $\varepsilon$  (dissipation rate of the turbulent energy) to be calculated from the system of transport equations (Launder & Spalding, 1972, Yakhot & Orszag, 1986, Shih et al., 1995).

Within the framework of these models, we have derived the transport equation for the variance of fluctuations of the gas density  $\overline{\rho'^2}$  from the equations proposed in (Yoshizawa, 1995). The equation derived looks as

$$\operatorname{div} \left( \mathbf{u} \overline{\rho'^2} - \frac{\nu_T}{\sigma_{\rho\rho}} \operatorname{grad} \overline{\rho'^2} \right) = 2 \frac{\nu_T}{\sigma_\rho} (\operatorname{grad} \rho)^2 - \left( \operatorname{div} \mathbf{u} + C_D \frac{\varepsilon}{k} \right) \overline{\rho'^2} \quad (1)$$

where  $\rho$  is the mean gas density, the convective transfer of the density variance has the velocity equal to the average flow velocity vector  $\mathbf{u}$ , and the turbulent kinematic viscosity  $\nu_T$  serves as the diffusion coefficient. The sources in the right-hand side of Eq. (1) show that density fluctuations are generated by the inhomogeneity of the average density and gas velocity components, and the dissipation processes are determined by the dissipation of the kinetic energy of turbulent vortices ( $\varepsilon/k$ ). In Eq. (1)  $\sigma_\rho = \sigma_{\rho\rho} = 1$  and  $C_D = 5.7$  are constant.

In flows with velocities  $\sim 10$  M and lower, the effects associated with the gas compressibility are significant for the calculation of average jet parameters, but in the turbulent component they manifest themselves only slightly (Smits & Dussauge, 1996). Therefore, the spectral distribution of density fluctuations correspond to the Kolmogorov–Obukhov model. The main parameters of the model, namely, the structure characteristic of the refractive index fluctuations  $C_n^2$  and the inner scale of turbulence  $l_0$  were calculated from the equations

$$l_0 = (\nu^3 / \varepsilon)^{1/4}, C_n^2 = 1.91 G^2 L_0^{-3/2} \overline{\rho'^2} / \rho^2 \quad (2)$$

where  $\nu$  is the air kinematic viscosity,  $G = 0.000207$  is the Gladstone–Dale constant,  $L_0$  is the outer scale of turbulence, which can be estimated from scales of spatial variations of mean values of jet parameters serving as sources of turbulence. Thus, the results of calculation of mean flow parameters based on Computational Fluid Dynamic model Fluent-6 complemented with Eqs. (1, 2) form the optical model of a supersonic jet.

In the jet in the jet module of the T326, we can see elements (barrels) formed by the characteristic configuration of density and velocity stepwise changes (hanging and reflected), the Mach disk, where the flow velocity decreases down to subsonic values, and the outer boundary of the jet. This repeated structure can be seen over several tens of

centimeters from the nozzle (4 to 5 barrels). At longer distances, the jet structure blurs due to the flow turbulization, generation of acoustic noise, and decrease of the mean flow speed down to subsonic values. The internal structure of barrels is shown in Fig. 5a. We can separate the following elements:

- Along the outer surface of the jet, there is a gradually widening mixing zone (zone 5), in which the velocity and the velocity gradient achieve their maximal values. Over the jet cross section, the mean velocity and pressure vary depending on the distance of the cross section plane from the nozzle (zones 1-3).
- Along the jet axis, the barrel-like structures repeat, their number is determined by the initial velocity of the flow. In the mean, the turbulence strength is minimal in the first barrel and grows up in the following barrels.
- The third region is the near-axis area 30–40 mm in diameter with the supersonic velocity of the flow, high pressure and density and their gradients (zones 1, 4).

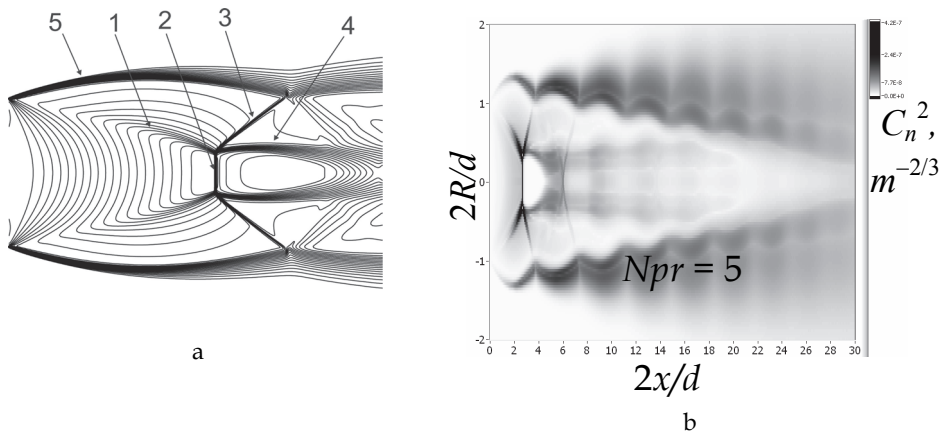


Fig. 5. Structure of the air density and distribution of  $C_n^2$  in the jet in T-326 (optical model).

To estimate perturbations induced by the supersonic flow in the optical wave propagating through it, we have simulated numerically air flows arising in the jet unit of the wind tunnel with the convergent nozzle having a diameter  $d = 30$  mm. The calculation of turbulence parameters have shown that density fluctuations are mostly caused by stepwise changes of averaged values of parameters on the Mach disk and on the outer boundary of the jet (Fig. 5b). Near the jet axis, the turbulence is most strong in the first two barrels, where the gradients of the density and velocity components on the Mach disk and the hanging step are maximal. As the jet structure destructs with the distance from the nozzle, density fluctuations on the jet axis decrease fast. Along the whole jet, the turbulence develops on the jet outer boundary. The turbulized zone of the jet widens with the distance from the nozzle and at a distance of 20–30 cm occupies the large part of the jet cross section. In this zone, according to the results of acoustic measurements in the T-326 jet unit, acoustic noise are mostly generated. Thus, both the results of numerical simulation and the experimental findings indicate that in this zone the jet loses its kinetic energy which is expended on turbulence and acoustic noise generation.

## 5. Methods of computer simulation of laser beam propagation through supersonic flow and retrieval of the parameters of the flow optical turbulence

Laser radiation distortions caused by regular and random inhomogeneities of air density in the supersonic flow can be used as a source of information on optical parameters of the flow. In the general case, the problem of reconstruction of optical model parameters is a complex mathematical problem. However, for certain flow configurations it can be solved rigorously. In particular, it is possible for axially symmetric flows.

Let an axisymmetric supersonic jet propagate in the positive direction of the axis  $x$  of the Cartesian coordinate system. The laser source is at the plane  $z = -l_1$ , where the collimated beam with the Gaussian amplitude distribution is formed. The beam optical axis is shifted with respect to the jet axis toward the vertical axis  $y$  by the impact parameter  $b$ . The laser beam propagates through the jet and distorts at inhomogeneities of the air density in the jet. Large-scale inhomogeneities deflect the beam from the axis  $z$ , while small-scale ones distort the beam structure. A photodetector recording the beam intensity distribution in the plane  $\mathbf{r} = (x, y)$  is in the plane  $z = l_2$ . This allows us to determine the vector of displacement of the beam energy centroid

$$\mathbf{d}(b) = \frac{\int \bar{I}(\mathbf{r}) \mathbf{r} d\mathbf{r}}{\int \bar{I}(\mathbf{r}) d\mathbf{r}} - b \mathbf{e}_y \quad (3)$$

which depends mostly on the distribution of the mean gas density  $\rho(\mathbf{r}, z)$ , and the relative variance of intensity fluctuations on the beam axis

$$\sigma^2(b) = \overline{(I / \bar{I} - 1)^2} \quad (4)$$

Assuming that the beam radius is small compared to characteristic scales of variation of jet parameters, we can consider the dependence of measured parameters (3, 4) on the impact parameter  $b$  as a way to estimate the radial dependence of the mean density and the structure characteristic of the refractive index fluctuations in the jet. In many applied problems, the angles of beam deflection due to optical refraction are small ( $\sim 10^{-3}$  rad), and the displacement of the probing beam energy centroid inside the jet is small as well. This allows us to obtain an approximate equation for the inversion of the refractive index dependence of the  $y$ -component of the beam energy centroid displacement vector and to find the radial distribution of the mean refractive index in the jet cross section

$$n(R, x) = \frac{1}{\pi} \int_R^\infty d_y(b) \left[ (l_2^2 + d_y^2(b))(b^2 - R^2) \right]^{-1/2} db + n(\infty, x) \quad (5)$$

where  $R = \sqrt{y^2 + z^2}$  is the distance to the jet axis. The mean air density in a flow is directly proportional to the mean refractive index.

For the regime of weak intensity fluctuations (Zuev et al., 1988) which realized for the laser beam passed through the jet, we can obtain the equation analogous to Eq. (5) for the structure characteristic of the refractive index fluctuations in the axisymmetric flow

$$C_n^2(R, x) = -\frac{1}{\pi A} \int_R^\infty (b^2 - R^2)^{-1/2} \frac{\partial}{\partial b} \sigma^2(b; x) db, \quad (6)$$

where  $A$  is a constant determined by the position and parameters of the radiation source.

Thus, if a narrow laser beam propagates repeatedly through the jet in some cross section  $x$  and the recorded intensity distributions are then used to determine the dependence of displacements of the energy centroid of the beam and the relative variance of the intensity at the beam axis on the impact parameter, we can reconstruct the radial dependence of parameters of the optical model in this cross section using Eqs. (5, 6).

The algorithms of reconstruction of flow parameters have been tested in a series of closed numerical experiments. The geometry of the experiments corresponded to the T-326 jet unit. We considered the flow of the supersonic air jet into a half-space filled with air at an atmospheric pressure and temperature of 300 K, as well as the airflow of a conic model of an aircraft nose cone. For the simulation of the laser beam propagation, we used the method of splitting by physical factors (Kandidov, 1996). For each given cross section  $x$ , we determined the area occupied by the flow, where the parameters of its optical model differed from their background values by more than 1%. Beyond this area, we neglected atmospheric turbulence, assuming the refractive index to be unit. The flow area was divided into 30 layers of the same thickness. Perturbations introduced by each layer into the laser beam were simulated by phase screens placed at the center of the corresponding layer. At each screen, the phase of the laser beam field was distorted by regular distortions calculated from the mean value of the refractive index at the current screen point and by random additions, which had zero means and were distributed by the normal law with the power-law power spectrum corresponding to the Kolmogorov–Obukhov model of turbulence (Monin & Yaglom, 1971, 1975) for air refractive index fluctuations. The parameters of the turbulent model (structure characteristic and characteristic scales) were determined from the optical model of the flow. As a result, in each random realization the beam propagation through the jet was simulated by a series of propagation steps in vacuum between screens, where the computations were performed in the paraxial approximation, and phase perturbations at the screens. The accumulation of random realizations of the intensity distribution in the receiving plane allowed us to determine the displacement of the beam energy centroid and the variance of intensity fluctuations at the beam axis by Eqs. (3, 4). This procedure was repeated for other values of the impact parameter  $b$ , and this allowed us to find ultimately the radial distributions of the mean air density and the structure characteristic of the refractive index fluctuations in the flow through the calculation of the integrals in Eqs. (5, 6).

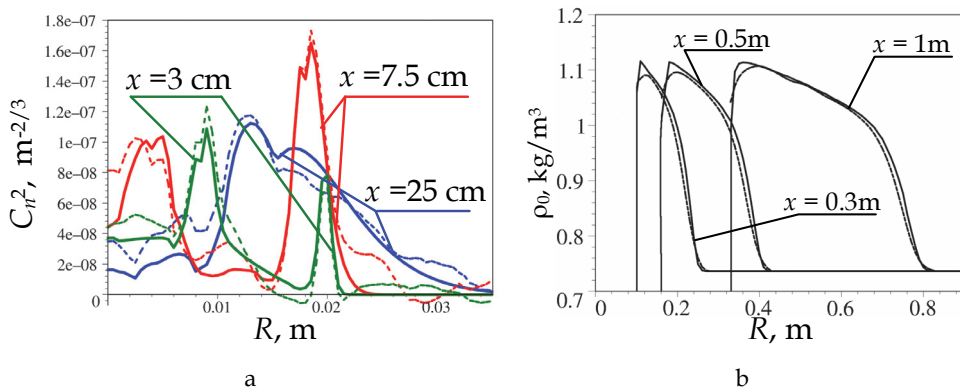


Fig. 6. Initial and reconstructed radial dependences of the structure characteristic in the free jet (a) and mean density in the jet flowing over the model (b).

Figure 6 shows the results of reconstruction of parameters of the optical model for the free jet (a) and the jet flowing over the conic model (b). The good agreement between the reconstructed values and initial data of the optical model of the flow both in the region of the turbulent decomposition of the jet and at the initial part of the jet with pronounced stepwise changes of averaged parameters demonstrate the possibility of the contactless determination of supersonic jet characteristics by optical methods.

## 6. Experimental and theoretical study of optical turbulence in supersonic flow of the T-313 and T-326 wind tunnels

### 6.1 T-326 wind tunnel

The propagation of laser radiation through a supersonic jet differs significantly from the case of atmospheric propagation. In the atmosphere, mean characteristics and turbulence on the path vary quite smoothly. In the jet, to the contrary, we observe strong gradients of the mean pressure and velocity (Fig. 5), and, consequently, the density and the refractive index of air. We should also take into account the propagation of probing beam outside the jet, where the sonic waves generated by the jet can affect significantly the beam.

#### 6.1.1 Laser radiation intensity fluctuations

First experiments on the laser beam propagation through the jet used the scheme with reflection. The laser radiation passed through the Eiffel's test chamber below the jet, reflected from a mirror 300 mm in diameter, and came back to a photodetector through the jet. The FFT method was used to calculate the spectral function  $U(f)=fW(f)$ , where  $f$  is frequency,  $W(f)$  is the spectral density of laser radiation intensity fluctuations.

The spectra of intensity fluctuations measured at  $npr = 5$  have two peaks at frequency  $f_{m1} \approx 1000-1200$  Hz and  $f_{m2} \approx 35-60$  kHz. At  $npr = 9$ , the spectra in the region of the second peak extend toward higher frequency. The analysis has shown that the first peak is caused by the influence of acoustic waves generated by the jet on the beam during its propagation along the path part beyond the jet. The estimates based on obtained spectra have shown that the length of acoustic waves generated by the jet was  $\Lambda \approx 110.7-132.8$  mm. The second peak is caused by inhomogeneities of the air density (air refractive index) in the jet.

In the further experiments, the beam path length beyond the jet was much shorter to minimize the effect of acoustic noise on intensity fluctuations of the probing beam.

Spectral functions of intensity fluctuations of the probing beam without influence of acoustic waves at different  $npr$  are shown in Fig.7. Figure 7b shows the spectra normalized to their values of  $U(f_{m2})$  at the peak. The frequency normalized to  $f_{m2}$  is shown as abscissa. One can see from the figure that an increase in  $npr$  leads to a significant increase in power and to a shift of the spectrum toward higher frequencies.

At a distance  $x = 15$  mm from the nozzle, the spectral peaks lie in a range  $f_{m2} \sim 50-55$  kHz, and the high-frequency part of the spectrum ( $f > f_{m2}$ ) in the frequency range below 2 MHz drops as  $\sim f^{-3.5}$ . At  $x > 100$  mm, the peak frequencies increase up to  $f_{m2} \sim 70-77$  kHz, and the high-frequency part of the spectrum ( $f > f_m$ ) drops as  $\sim f^{-4}$ . In the low-frequency range, the spectral density increases as  $\sim f^{0.8}$ . The scales of inhomogeneities of intensity fluctuations of the probing beam corresponding to the frequencies  $f_{m2} \sim 70-75$  kHz are close to  $l = 2.4-2.5$  mm.

For the nozzle with chevrons, the behavior of the intensity spectrum of the probing beam remains the same as for the nozzle without chevrons.



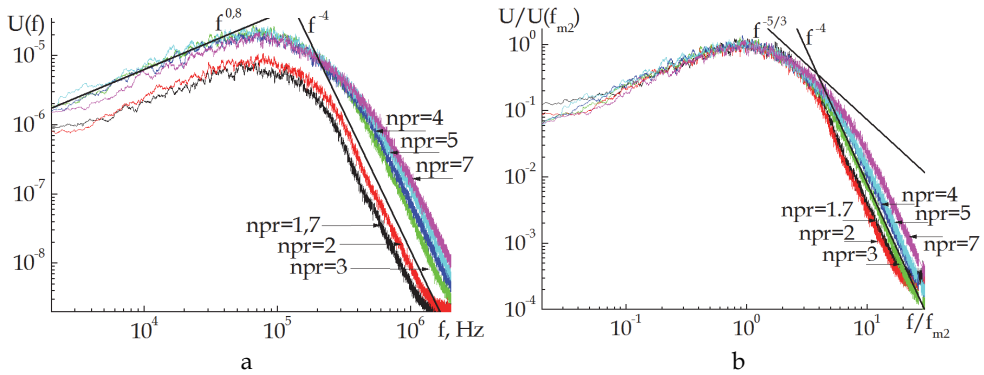


Fig. 7. Spectra of intensity fluctuations at different  $npr$ .

Figure 8a shows the dependence of the relative variance of intensity fluctuations of the probing beam  $\sigma^2$  on the distance  $x$  along the jet axis at different distances from the jet axis  $r$ . The measurements were conducted with the use of the convergent nozzle with and without chevrons. It follows from the depicted data that without chevrons as  $x$  increases, intensity fluctuations first increase at the first two barrel-like structures up to  $x \sim 100$  mm, remain at a constant level up to  $x \sim 270$  mm, and then increase fast. An increase in  $npr$  from 1.7 to 7 leads to intensification of intensity fluctuations. The installation of chevrons increases the intensity fluctuations of the beam 6 to 8 times compared to that without chevrons in the jet part near the nozzle. As  $x$  increases, intensity fluctuations decrease.

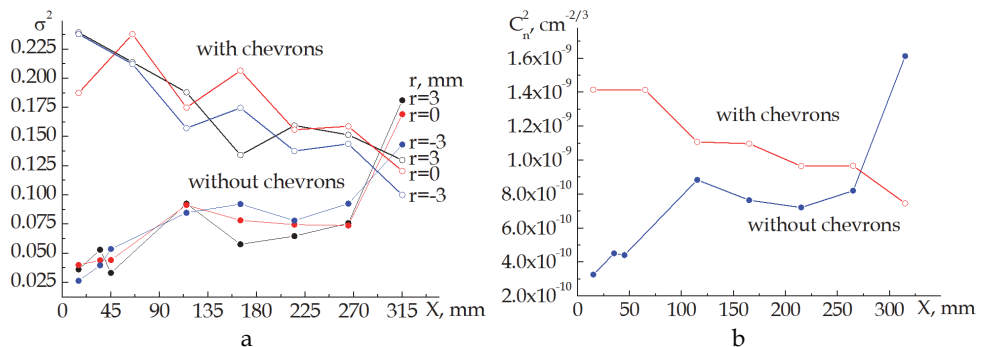


Fig. 8. Variance of intensity fluctuations along the jet axis (a), calculated values of the structure characteristic of fluctuations of the refractive index (b).

Assuming that turbulent intensity fluctuations of the probing laser beam can be described based on the Kolmogorov model of turbulence and using for the intensity relative variance  $\sigma^2$  the equation  $\sigma^2 = 0.46 C_n^2 k^7 / 6 L^{11/6}$  obtained in the first approximation of the Rytov method (Tatarskii, 1967, 1971) we can estimate the structure characteristic of fluctuations of the refractive index  $C_n^2$  in the jet from measured values of  $\sigma^2$ . Here  $k = 2\pi/\lambda$  is the wave number,  $L$  is the path length in the jet. The estimates of the average values of  $C_n^2$  along the axis (Fig. 8b) exceed the maximal atmospheric values by 4 to 5 orders of magnitude. With

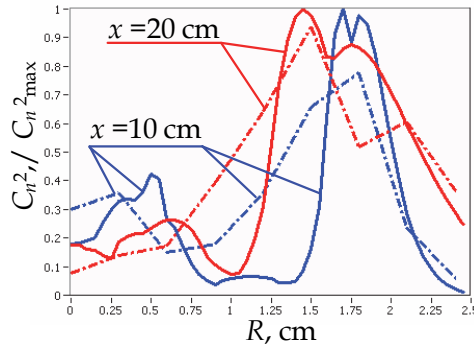


Fig. 9. Radial dependence of the structure characteristic in the jet in different cross sections calculated by the optical model (solid curves) and reconstructed from the results of laser probing (dashed curves).

the increase of  $x$ , the values of  $C_n^2$  in the jet without chevrons increase from  $3 \cdot 10^{-10}$  to  $1.6 \cdot 10^{-9} \text{ cm}^{-2/3}$ , while with chevrons they decrease from  $1.4 \cdot 10^{-9}$  to  $8 \cdot 10^{-10} \text{ cm}^{-2/3}$ . The dependence of the variance of the beam intensity measured at different distances from the jet axis was then used to reconstruct the radial dependence of the structure characteristic of the refractive index in the jet without chevrons with the use of the reconstruction algorithm (6) modified for a quickly divergent beam. The results of the reconstruction shown in Fig. 9 are in a good agreement with the dependences drawn based on the optical model of the jet.

**6.1.2 Acoustic measurements**

The acoustic measurements on the jet unit of the T-326 wind tunnel with the use of microphones (Fig. 3) have shown that at  $npr = 5$  the sound generated by the jet had one pronounced harmonic component at the frequency  $f_m \approx 3030 \text{ Hz}$  (Fig.10a). The Strouhal number for this frequency can be estimated as  $St = fd/V_c = 0.265$ , where  $V_c$  is the sound speed,  $d$  is the nozzle diameter. This estimation is close to the literature data (Kuznetsov, 2008). At  $npr = 9$  there is no pronounced main harmonic, and the sound is generated in several spectral intervals.

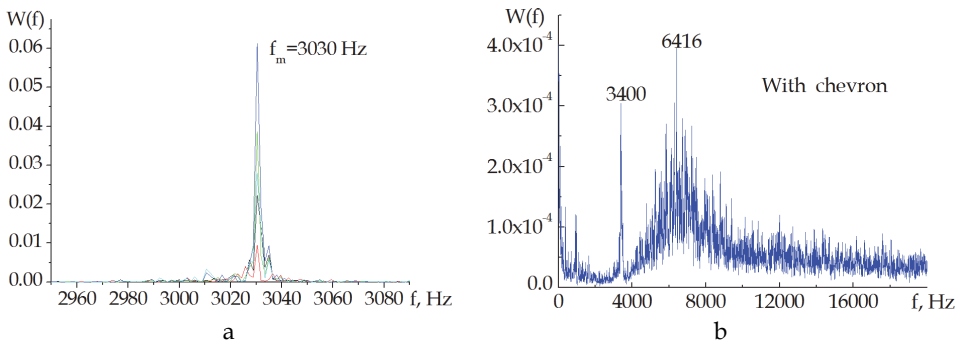


Fig. 10. Spectral power density of the sound generated by the jet at  $npr = 5$  with the use of a nozzle without chevrons (a) and with chevrons (b).

If a nozzle with chevrons is used in the jet unit (Fig.10b), then the separate harmonic at the frequency  $f = 3400$  Hz (close to the frequency of the main harmonic in the case without chevrons) remains and spectral components in a band of 4-20 kHz peaking near  $f = 6.4$  kHz appear. The wavelength of the main harmonic at  $npr = 5$  is roughly equal to 113 mm, and at  $npr = 9$  it is 146 mm. For comparison, the acoustic wavelength determined from the frequency  $f_{m1}$  of the maximum of the spectral function of intensity fluctuations of the probing laser beam (Section 6.1.1.) is 110.7-132.8 mm.

To determine the form of the acoustic wave, we calculated the mutual correlation of acoustic signals measured by microphones M0, ..., M4. As an example, Fig. 11 shows the coefficients of mutual temporal correlation of acoustic signals between the microphones in configuration 1 (Section 3.1, Fig. 3).

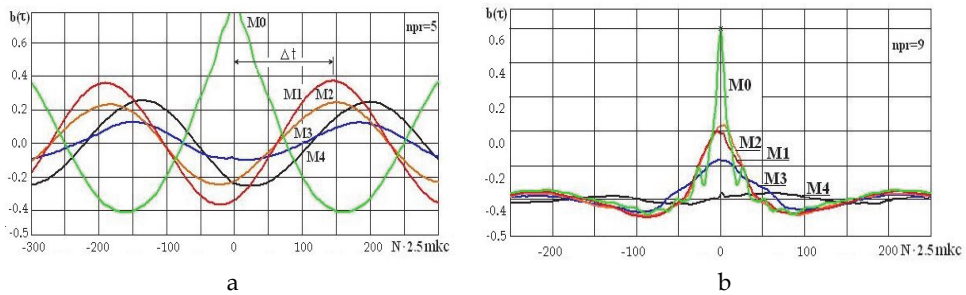


Fig. 11. Time correlation coefficients of the acoustic wave: M0 is the autocorrelation coefficient of the first microphone, M1, ..., M4 are the coefficients of mutual correlation between microphone M0 and microphones M1, M2, M3, M4,  $\varphi$  is the phase shift,  $N$  is the readout number.

It can be seen from Fig. 11 that the mutual correlation coefficients at  $npr = 5$  vary by the harmonic law in the range 0.15–0.40 and keep their amplitude in time. This corresponds to the presence of the pronounced main harmonic in the spectrum. At  $npr = 9$ , the correlation decreases quickly with time in accordance with the noise form of the spectrum in this case.

### Phase shift of the acoustic wave

The phase shift of the acoustic wave was determined from the position of the maxima of the correlation functions of M0, M1, M2, M3, M4 on the time scale, as shown in Fig. 11. The results of the determination of the phase shift at different configurations of the microphones (Fig. 3) are shown in Fig. 12.

For configuration 1, the phase shifts were determined with respect to the microphone installed at a distance of 135 mm from the nozzle. It follows from the data presented that the phase shift increases linearly as the distance to the nozzle shortens and has a minimum at a distance of 225 mm. To interpret experimental data, we have estimated the phase shift  $\varphi$  between the microphones on the assumption that the generated acoustic wave is spherical. The phase shift was calculated from the difference in distances  $\Delta L$  between the microphone set at a distance  $x_0 = 225$  mm from the nozzle and all other microphones (Fig. 12 d) by the equation

$$\varphi(x) = \pi \Delta L / \lambda,$$

where

$$\Delta L = [(x - x_0)^2 + h^2]^{1/2} - h.$$

It can be seen from Fig. 12 *a* that the calculated data are close to the experimental dependence. This suggests that the sound source is at a distance of about 225 mm from the nozzle, and at a distance of 135 mm from the jet axis the acoustic wave is close to a spherical one. The phase shift between the microphones set at distances of 225 and 25 mm from the nozzle is  $\approx 2.75\pi$  or  $1.4\lambda$ .

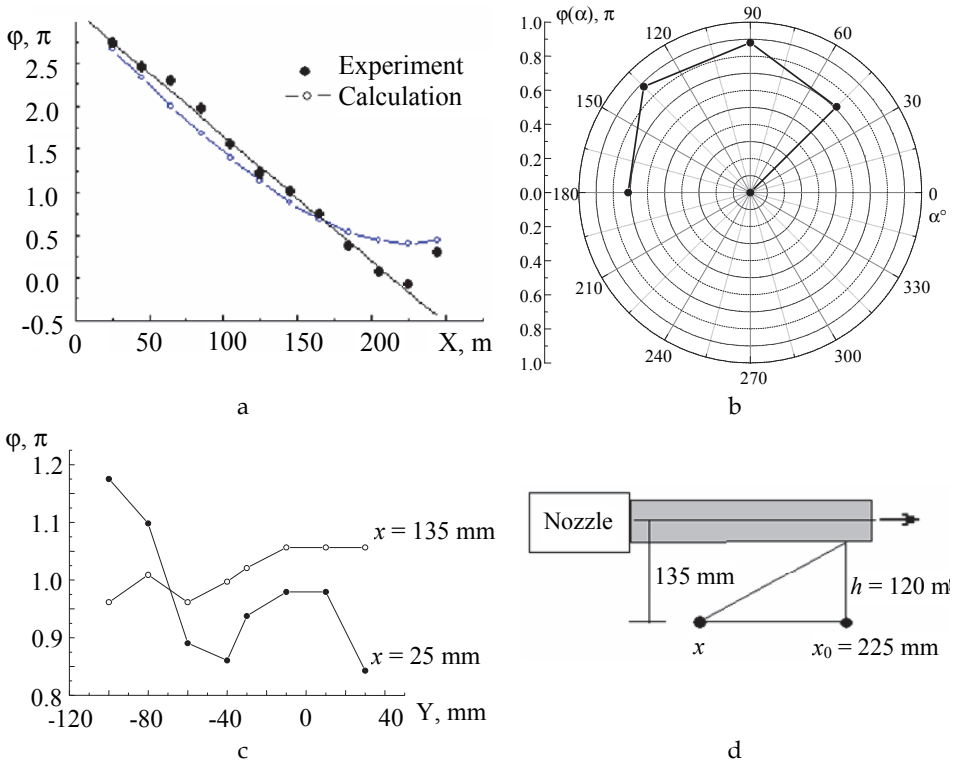


Fig. 12. Phase shift of acoustic waves at measurements with microphone configurations (Sec. 3.1) 1 (a), 2 (b), 3 (c) and illustration to the calculation of the phase shift (d).

The measurements with configuration 2 show that the phase shifts between microphone M0 and the others are close and range within  $0.7-0.9\pi$ . The conclusion about the close phase shifts between the microphones is also valid for configuration 3 at measurements at a distance  $x = 135 mm$  from the nozzle. In this case, the phase shifts range within  $0.95-1.05\pi$  (Fig. 12c).

Figure 13 shows the results of numerical simulation of the acoustic field generated by the supersonic jet (Bodony, 2005). It can be seen that the source of the acoustic wave is near the area of the transition from supersonic flow velocities to subsonic ones. At some distance from the source, the acoustic wave becomes close to a spherical one and the phase shift is

observed in the wave front above and below the jet. This is in a qualitative agreement with the experimental data in Fig. 12.

For the more detailed comparison, Fig. 13 shows the approximate (with respect to the simulated acoustic field) arrangement of the microphones along the jet in accordance with configuration 1 (Section 3.1) and the estimated phase of the simulated acoustic field at different distances along the jet. One can see that the phase of the acoustic wave near the beginning of the jet  $\varphi = 2.7\pi$  is close to the experimental value  $\varphi = 2.75\pi$  at a distance of 25 mm from the nozzle. The arrangement of the microphones was determined with respect to the nozzle diameter  $d$  (see Fig. 13) so that  $r/d$  and  $x/d$  to be equal to the experimental data  $x/d = 85/30$  ( $\varphi = 2\pi$ ),  $x/d = 225/30$  ( $\varphi = 0$ ),  $x/d = 25/30$  ( $\varphi = 2.7\pi$ ).

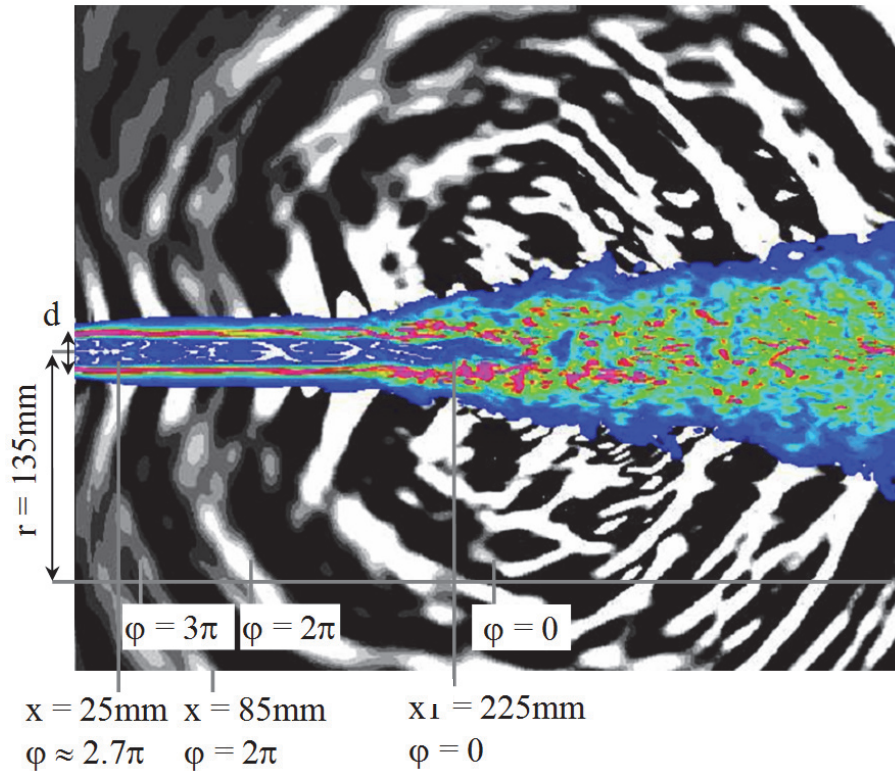


Fig. 13. Results of numerical simulation of the acoustic field (Bodony, 2005) in comparison with experimental data on the phase shift in configuration 1.

## 6.2 T-313 wind tunnel

### 6.2.1 Laser radiation intensity fluctuations

Figure 14 shows the spectra of intensity fluctuations  $U(f)$  of the laser radiation propagating in the supersonic flow in T-313 over the model wing as shown in Fig. 4. It can be seen from Fig. 14 that in the region of high frequencies  $f \geq f_2$  the spectra is qualitatively close to the spectra of intensity fluctuations obtained in T-326 (Fig. 7). As the angle of attack increases,

fluctuations become much stronger in the region of low frequencies and more slightly intensify in the region of the high-frequency maximum  $f_2$ . Figure 14b depicts the spectra normalized to their values at the frequency of the maximum  $f_2$  as functions of the frequency normalized to  $f_2$ .

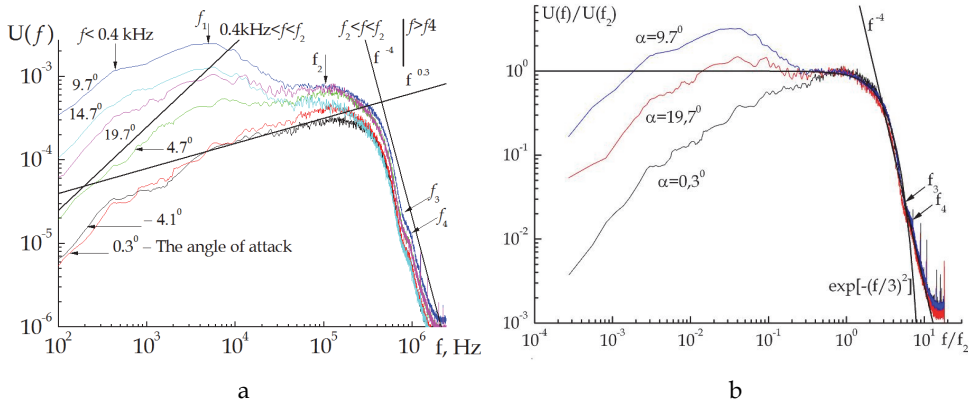


Fig. 14. Spectra of intensity fluctuations at different angles of attack (a) and normalized spectra (b).

Low-frequency fluctuations are caused by the effect of acoustic noise generated by the supersonic flow above the model. The wavelength of the generated sound can be estimated as  $\Lambda \approx V_c/f_1$ , where  $V_c \approx 20.1 \cdot T^{1/2} = 200 - 250$  m/s is the sound speed at the flow temperature. In this case  $\Lambda \approx 3-6$  cm.

The dependence of the relative variance of intensity fluctuations in the probing laser beam on the angle of attack is shown in Fig. 15. In this figure, the vertical axis is divided into two sections having different scales for the presentation of significantly different values. It can be seen from the figure that incoming flow is actually laminar, and the relative variance of intensity fluctuations is only  $\sigma^2 \sim 3 \cdot 10^{-5}$  in this case. Above the wing, the relative variance is four orders of magnitude higher, thus indicating the significant turbulization of the flow above the model.

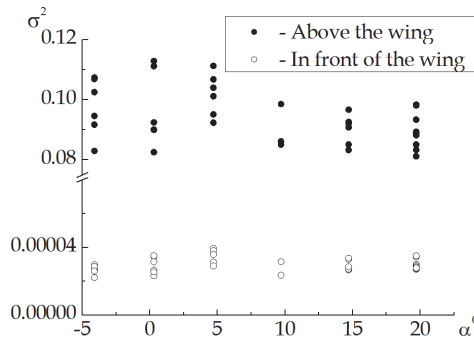


Fig. 15. Relative variance of intensity fluctuations at different angles of attack.

### 6.2.2 Fluctuations of the laser beam propagation direction

The spectra of fluctuations of the laser beam propagation direction in the supersonic flow in T-313 above the model were measured by a quadrant detector (QD) by the scheme shown in Fig. 4.

It follows from the analysis of the measurement results that the spectra of beam propagation direction fluctuations along the  $x$  axis have a peak near 19-24 kHz, while those along the  $y$  axis have a peak near 16-26 kHz. The frequency of the spectral maximum depends on the angle of attack. It is minimal at the negative angle of attack, maximal at  $\alpha = 0.3^\circ$ , and decreases slightly with an increase in the angle of attack (Fig. 16a). Vertical bars in the figure show the spread in values.

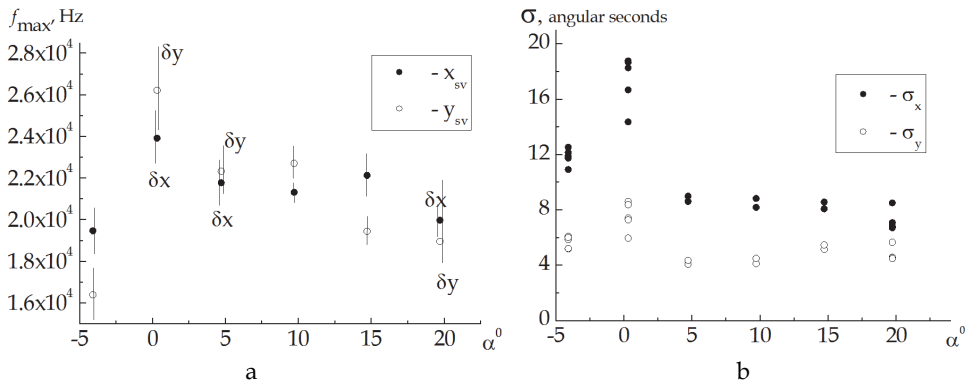


Fig. 16. Dependence of the frequency of the spectral maximum (a) and the standard deviation (b) of fluctuations of the laser beam propagation direction on the angle of attack  $\alpha^\circ$ .

In the high-frequency region  $f > f_{\max}$ , the spectra of random beam displacements decrease as  $\sim f^{-4/3}$  in the horizontal direction ( $x$  axis) and as  $\sim f^{-(0.6-0.8)}$  in the vertical direction ( $y$  axis). The difference of the slopes is indicative of the nonisotropic fluctuations of the probing beam propagation direction in the horizontal and vertical directions. Fluctuations in the vertical direction are roughly halved compared to those in the horizontal direction and weakly depend on the angle of attack (Fig. 16b). The variance of random displacements of the beam is maximal at the angle of attack  $\alpha = 0.3^\circ$ , that is, at the maximal flow speed above the wing.

The frequency of the maximum in the spectrum of laser beam image jitter recorded by the dissector tube (Fig. 4) is 250-300 Hz along the horizontal axis and 200-270 Hz along the vertical axis at angles of attack  $\leq 15^\circ$  and increases sharply up to 500 Hz at an angle of attack of  $19.7^\circ$ . These fluctuations are possibly caused by the vibration of the wing under the effect of the incoming flow. The standard deviation of the image jitter is 12-17 arc sec. and is maximal at an angle of attack of  $\sim 15^\circ$ .

## 7. Conclusions

Thus, the experimental results obtained show that the spectra of intensity fluctuations of the probing laser beam has roughly the same form both in the case of the supersonic jet

generated by the T-326 jet unit and in the case of a model wing blown by a supersonic flow in T-313. The maximum of turbulent intensity fluctuations in the both cases falls on frequencies in the region of 50 kHz and higher. The estimates based on the Kolmogorov–Obukhov model of developed turbulence show that the structure characteristic of the refractive index in the studied supersonic flows is several orders of magnitude higher than  $C_n^2$  in the atmosphere.

The optical model of turbulence developed on the basis of Fluent-6 allows one to simulate the propagation of a probing laser beam in supersonic flows with arbitrary geometric and thermodynamic parameters. The results of simulation and reconstruction of optical model parameters from simulated data on the probing of a supersonic jet in T-326 are close to the experimental findings.

From the results of acoustic measurements as well as from the probing laser beam intensity fluctuations, it follows that the supersonic jet generates sound. The source of sound lies in the region of the transition from the supersonic flow speed to the subsonic one. For the jet unit of the T-326 wind tunnel, the sound source is on the jet axis at a distance of 225 mm from the nozzle. With the distance from the source, the generated acoustic wave becomes close to a spherical one.

The work was financially supported in part by the Russian Foundation for Basic Research, grant 11-08-01059.

## 8. References

- Abbrecht, H.-E., Damaschke, N., Borys, M. & Tropea, C. (2003). *Laser Doppler and Phase Doppler Measurement Techniques. Series: Experimental fluid Mechanics*. Springer-Verlag, ISBN: 978-3-540-67838-0, Berlin.
- Bodony, D.J. (2005). *The prediction and understanding of jet noise*. Center for Turbulence Research Annual Research Briefs, pp.367-377.
- Canuto, V.M. (1997). Compressible Turbulence. *The Astrophysical J.*, V.482, No.2, pp. 827-851, ISSN: 0004-6256.
- Dmitriev, D.I., Ivanov, I.V., Sirazetdinov, V.S. & Titterton, D.H. (2004). Statistics of structural state fluctuations of a laser beam disturbed by a jet of aircraft engine. *Atmospheric and Oceanic Optics*, Vol. 17, No.01, pp.39-45, ISSN 0235-6880.
- Fomin, N.A. (1998). *Speckle Photography for Fluid Mechanics Measurements. Series: Experimental Fluid Mechanics*. Springer-Verlag, ISBN: 978-3-540-63767-7, Berlin.
- Garkusha, V.V., Sobstel, G.M., Surodinn, S.P., Yakovlev, V.V., Gilev, V.M, Zapryagaev, V.I. & Pishchik, B.M. (2009) Automatic Control System for Technological Processes of a Turboblower Station. *Problems of Informatics*. No.3(4), pp. 85-93, ISSN 2073-0667.
- Gurvich, A.S., Kon, A.I., Mironov, V.L. & Khmelevtsov, S.S. (1976). *Laser Radiation in the Turbulent Atmosphere*. Nauks. Moscow.
- Joia, I.A., Perkins, R.J., Uscinski, B.J., Balmer, G., Jordan, D. & Jakeman, E. (1995). Optical properties of a planar turbulent jet. *Appl. Opt.*, Vol.34, No. 30, pp.7039-7053, ISSN: 1559-128X.



- Joa, I.A., Uscinski, B.J., Perkins, R.J., Balmer, G., Jordan, D., & Jakeman, E. (1997). Intensity fluctuations in a laser beam due to propagation through a plane turbulent jet. *Waves in Random Media*, Vol.7, No. 2, pp.169-181, ISSN: 1745-5030.
- Kandidov, V.P. (1996) Monte Carlo Technique in Nonlinear Statistical Optics *Physica-Uspekhii* V.166, No.12, pp. 1309-1338, ISSN: 1063-7869.
- Kuznetsov, V.M. (2008) *Principles of Theory of Noise of Turbulent Jets*. Fizmatlit, ISBN: 9785922109703, Moscow.
- Launder, B.E. & Spalding D.B. (1972) *Lectures in Mathematical Models of Turbulence*. Academic Press, London, England.
- Monin, A. S. & Yaglom, A.M. (1971) Statistical fluid mechanics, vol.1. Ed. J. Lumley. MIT Press, Cambridge, MA.
- Monin, A. S. & Yaglom, A.M. (1975) Statistical fluid mechanics, vol.2. Ed. J. Lumley. MIT Press, Cambridge, MA.
- Pade, O. (2001). Models of turbulence for aero-optics application. *Proceedings SPIE*. Vol.4419, pp.494-498, ISBN: 9780819441263.
- Pade, O., Frumker E. & Rojt P.I. (2004). Optical distortions caused by propagation through turbulent shear layers. *Proceedings SPIE*. Vol.5237, pp.31-38, ISBN: 9780819451200.
- Pade, O. (2004). Optical propagation through turbulent jets. *Proceedings SPIE*. Vol.5572, pp. 24-33, ISBN: 9780819455192.
- Pade, O. (2006). Optical propagation through Shear Layers. *Proceedings SPIE*. Vol.6364, p.63640E, ISBN: 9780819464590.
- Raffel, M., Willert, C., Wereley, S.T. & Kompenhans, J. (2007). Particle image velocimetry: A practical guide. Springer-Verlag, ISBN: 978-3-540-72307-3, Berlin.
- Shih, T.-H., Liou, W. W., Shabbir, A. & Zhu, J. (1995) A New k- $\epsilon$  Eddy-Viscosity Model for High Reynolds Number Turbulent Flows - Model Development and Validation. *Computers Fluids*, Vol.24, No.3, pp.227-238, ISSN: 0045-7930.
- Sirazetdinov, V.S., Dmitriev, D.I., Ivanov, I.V. & Titterton, D.H. (2001) Effect of turbo-engine jet on laser radiation. Part 2. Random wandering of disturbed beam. *Atmospheric and Oceanic Optics*, V. 14, No.10, pp.830-834, ISSN: 0235-6880.
- Smits, A.J. & Dussauge, J.-P. (1996). *Turbulent shear Layers in supersonic flow*. American Institute of Physics Press. USA.
- Tatarskii, V.I. (1961) *Wave propagation in a turbulent medium*. Translated from the Russian by R.A. Silverman. McGraw-Hill, New York, Toronto, London,. Second edition: Dover Publications, New York, 1967.
- Tatarskii, V.I. (1971) The effects of the turbulent atmosphere on wave propagation. Translated from the Russian by the Israel Program for Scientific Translations, Jerusalem,. Available from the U.S. Dept. of Comm., Nat. Tech. Inf. Serv., Springfield, VA, 22151.
- Yakhot, V. & Orszag, S.A. (1986) Renormalization Group Analysis of Turbulence: I. Basic Theory. *Journal of Scientific Computing*, Vol.1, No.1, pp.1-51, ISSN: 0885-7474.
- Yoshizawa, A. (1995). Simplified statistical approach to complex turbulent flows and ensemble-mean compressible turbulence modeling *Phys. Fluids*. V.7, No.12, pp.3105-3117, ISSN: 1070-6631.

Zuev, V.E., Banakh, V.A. & Pokasov, V.V. (1988). *Optics of the Turbulent Atmosphere*.  
Gidrometeoizdat. ISBN: 5286000533, Leningrad.

# Guidance of a Supersonic Projectile by Plasma-Actuation Concept

Patrick Gnemmi and Christian Rey  
*French-German Research Institute of Saint-Louis (ISL)*  
France

## 1. Introduction

The change in the trajectory of a flying vehicle is made possible by unbalancing the pressures exerted on the body surface. This pressure imbalance can be produced by the deployment of control surfaces (Berner & Dupuis, 2001; Dupuis & Berner, 2001; Berner & Dupuis, 2002; Berner et al., 2002; Dupuis et al., 2004; Srulijes et al., 2004; Patel et al., 2002; Siltan, 2004; Massey et al., 2004) or by the use of one or more pyrotechnical mechanisms judiciously distributed along the vehicle (Gnemmi & Seiler, 2000; Schäfer et al., 2001; Seiler et al., 2003; Gnemmi & Schäfer, 2005; Havermann et al., 2005; Yamanaka & Tanaka, 1996). In the case of supersonic projectiles, the major drawback to using the surface spreading technique is that large forces are involved in the deployment of surfaces in order to overcome the very high pressures encountered at high velocities. Thus, the use of pyrotechnical mechanisms is more appropriate for high-speed vehicles, but the fact that the pyrotechnical mechanism works only once and produces all or nothing is a main drawback when a controlled angle of attack must be given.

The application concerns guided anti-aerial projectiles launched by a 40-mm gun and designed to increase their precision when faced with increasingly agile aerial vehicles flying up to a few kilometers of altitude. The underlying idea consists of giving the projectiles a maneuvering capacity, allowing them to compensate for the trajectory prediction error. In the case of a high-speed vehicle, a shock wave occurs at its nose tip or ahead of it, depending on the nose geometry. When the vehicle flies without any angle of attack, the pressures distributed on its surface balance one another out and the shock wave has symmetries dependent on the vehicle geometry. For example, for a supersonic projectile forebody having a conical nose, the shock wave is attached to the cone tip and also has a conical shape. The plasma-actuator steering concept consists of obtaining the asymmetry of the flow variables around the projectile nose by generating one or several plasma discharges at the nose tip in order to give the projectile an angle of attack (Wey et al., 2005; Gnemmi et al., 2008). The objective consists of generating one long or several short plasma discharges so that the asymmetry is large and long enough to cause the deviation of the projectile with respect to its initial trajectory.

A patent describing the concept and a first high-voltage system was registered in February 2002 and was issued in France in January 2005 and in the USA in February 2006 (Gnemmi et al., 2002). A new low-voltage device was designed to avoid the high-voltage apparatus

drawbacks and a patent was also registered in September 2005 and was issued in France in December 2007 and in the USA in January 2010 (Gnemmi & Rey, 2005).

The flow control around aerial vehicles by using plasma has been one of the concerns of the fluid dynamics flow control community for over a decade. The most recent state of the art concerning a type of plasma actuator is given by Corke et al., 2009. This plasma actuator, now widely in use, is based on a dielectric barrier discharge (DBD) mechanism that has desirable features for use in the air at atmospheric pressures. It has been employed in a wide range of applications that include: drag reduction at supersonic speeds (Kuo, 2007; Elias et al., 2007a; Shneider et al., 2008); steering vehicles at supersonic speeds (Girgis et al., 2006); exciting boundary-layer instabilities at supersonic speeds (Kosinov et al., 1990; Corke et al., 2001; Matlis, 2004; Elias et al., 2007b); lift increase on a wing section (Corke et al., 2006; Nelson et al., 2006; Patel et al., 2006; Goeksel et al., 2006); low-pressure turbine-blade separation control (Huang, 2005; Huang et al., 2006a; Huang et al., 2006b; Suzen et al., 2007; Ravir, 2007; Risetta & Visbal, 2007); turbine tip clearance flow control (Douville et al., 2006; Van Ness et al., 2006); bluff-body flow control (Thomas et al., 2006; Asghar et al., 2006; Do et al., 2007); turbulent boundary-layer control (Balcer et al., 2006; Porter et al., 2007); unsteady vortex generation and control (Visbal & Gaitonde, 2006; Nelson et al., 2007); and airfoil-leading-edge separation control (Post, 2004; Post & Corke, 2004a; Post & Corke, 2004b; Corke et al., 2004).

The analysis of the above-mentioned publications shows that few studies are being conducted on supersonic projectile steering by using a plasma discharge. Therefore, the work described in this paper is original; indeed, a plasma-discharge production on the surface of a supersonic projectile flying in the low atmosphere has not been applied up to now to the control of projectiles in terms of change of trajectory.

Section 2 of the present chapter deals with the principle of the concept of controlling a supersonic projectile by a plasma discharge. Section 3 describes the experimental setups and details the plasma-discharge actuator and the instrumentation used for the experiments. Section 4 presents the experimental results of the surface-pressure and temperature measurements made in order to investigate the complex physical phenomenon involved in the process and the results of the tests on the angular deviation of a fin-stabilized projectile model carried out in the wind-tunnel facility at a Mach number of 3. This Section also presents the experimental results of the free-flight of a simple projectile model deviated by a plasma discharge performed in the shock-tunnel facility at Mach 4.5. Section 5 concludes the chapter and proposes future investigations.

## 2. Principle of the concept

In the case of a high-speed vehicle, a shock wave occurs at its nose tip or ahead of it, depending on the nose geometry. When the vehicle flies without any angle of attack, the pressures distributed on its surface balance one another out and the shock wave has symmetries dependent on the vehicle geometry. For example, for a supersonic projectile forebody having a conical nose, the shock wave is attached to the conical tip and also has a conical shape. The proposed concept consists of producing the asymmetry of the flow variables around the projectile nose by generating one or several plasma discharges at the nose tip in order to give the projectile an angle of attack.

Some theoretical investigations illustrate the feasibility of such a system. Figure 1 presents the qualitative result of a numerical computation of a projectile forebody, flying from right

to left near the ground level at a Mach number of 3.2. A plasma discharge modelled as a transverse hot jet is applied near the nose tip for a certain length of time. The figure shows the forebody in blue and the halves of two surfaces in red. The red surfaces represent a constant pressure in the flow field which is chosen to highlight the main structure of the latter. The attached shock wave is perfectly visible at the tip of the conical nose as well as the Prandtl-Meyer expansion wave at the junction of the conical nose with the cylindrical part of the forebody. On the side of the conical nose where the plasma discharge is activated, the geometry of the shock wave is clearly distorted due to the generation of the plasma discharge. On the contrary, on the opposite side, the geometry of the shock wave remains unperturbed.

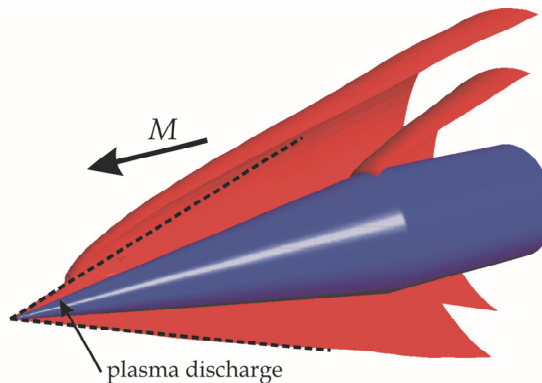


Fig. 1. Surfaces of constant pressure in the flow field of a supersonic projectile forebody having modelled plasma-discharge action

The final objective consists of the production of one or several plasma discharges so that the asymmetry is large and long enough to cause the deviation of the projectile facing its initial trajectory. The absence of mobile parts and the repetitive action of discharges are the main advantages of this technique. In fact, the control of the vehicle can be realized by repetitive discharges activated on demand, depending on the required trajectory.

### 3. Experimental setup and instrumentation

#### 3.1 Wind-tunnel facility

The “Aerodynamics and Wind-Tunnel Laboratory” has two facilities for supersonic flow investigations. The experiments involving pressure and temperature measurements are conducted in the supersonic blow-down wind tunnel S20 (Schäfer et al., 2001; Gnemmi et al., 2006). The test chamber has a square section of  $0.2 \text{ m} \times 0.2 \text{ m}$  and has interchangeable Laval nozzles adjusted for Mach numbers ( $M$ ) of 1.4, 1.7, 2, 2.44, 3, 4 and 4.36. The present experiments are carried out at  $M = 3$  for a static free-stream pressure of  $P_\infty = 0.19 \cdot 10^5 \text{ Pa}$  and a static free-stream temperature of 108 K. This facility operates in blow-down mode with a blow duration of typically 50 s. For these experimental conditions, the free-stream velocity is 611 m/s and the density is  $0.643 \text{ kg/m}^3$ .

Section 3.4 describes the projectile forebody fixed in the test chamber and equipped with surface-pressure transducers, which is also used for the temperature measurement in the plasma plume. The model-related Reynolds number based on the body diameter is  $2.6 \cdot 10^6$ . The fin-stabilized projectile model used for investigations of the angular deviation is described in Section 3.5. The model-related Reynolds number based on the body diameter is  $9.1 \cdot 10^5$ .

### 3.2 Shock-tunnel facility

The “Aerothermodynamics and Shock-Tube Laboratory” has two high-energy shock tubes (STA and STB) able to supply up to 8 MJ/kg to carry out high-speed flow experiments (Patz, 1970, 1971; Oertel, 1966). The inner shock-tube diameter is of 100 mm and each facility is about 22 m long.

Nowadays, the ISL shock tubes are mainly used as supersonic/hypersonic shock tunnels. A shock tunnel is a very-short-duration test wind tunnel consisting of a shock tube connected to a supersonic/hypersonic nozzle, a measurement chamber and a dump tank. The shock tube itself is divided into a high-pressure driver tube and a low-pressure driven tube, as depicted in Figure 2. The STA driver tube is 3.6 m long, the STB one is 4.0 m long and the driven tube is 18.4 m long for both facilities. Behind the driven tube are situated the nozzle, the measurement section and the dump tank.

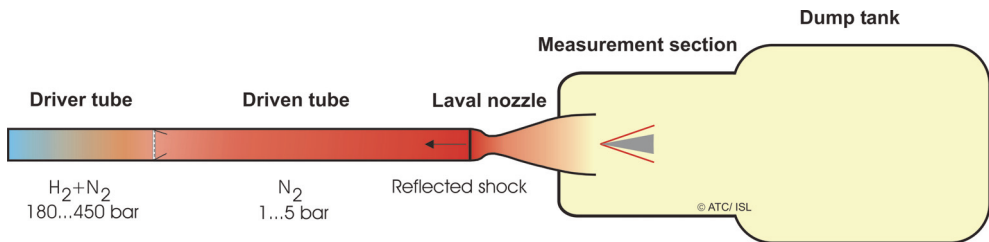


Fig. 2. Schematic of the ISL shock tunnels

A preferably light driver gas is compressed in the driver tube up to 450 bar. The steel membrane separating the high-pressure from the low-pressure parts is designed to burst at a determined pressure dependent on the required experimental conditions. At this moment a shock wave propagates through the driven tube where the test gas (usually nitrogen) is contained at a pressure of up to 5 bar. Simultaneously, an expansion wave runs in the opposite direction and is reflected off the driver-tube end. The shock wave propels the gas into the driven tube in front of the entrance to the nozzle where it is compressed and heated and where it remains almost stationary for a very short time. Then, the driven gas expands through the nozzle, resulting in a quasi-stationary supersonic/hypersonic flow inside the measurement section. The resulting measurement time ranges from 1 to 4 ms for quasi-stationary flow conditions. Additionally, because the Mach number only depends on the nozzle geometry, it remains constant over a time period of 15 more milliseconds, until the driver gas arrives. During this extended measurement time, it is necessary to know how the history of the flow conditions (e.g. velocity and density) changes at the nozzle exit. Therefore, the transient velocity change is measured with the Laser-Doppler Velocimeter (LDV) (Smeets and George, 1978) by using seeded titanium dioxide particles. The density is obtained from both the static pressure measured at the nozzle wall close to the nozzle exit

and the LDV-measured velocity at a constant Mach number. The measurement section contains the model to be studied and catches the shock-tube gases after the experiment. The gases are then stored inside the dump tank attached to the measurement section. The dump tanks have a volume of about 10 m<sup>3</sup> and 20 m<sup>3</sup> for STA and STB, respectively.

After each shot, the free-stream flow conditions are recalculated by using a one-dimensional shock-tube code, which requires the measured shock-wave speed in the driven tube to be input into the code (Smeets et al., 1980-2009). By varying the tube pressure, the free-stream flow can be adjusted in order to reproduce the flow conditions present in the atmosphere. Real atmospheric flight conditions can be produced in these facilities from ground level up to a flight altitude of 70 km, depending on the Mach number, as shown in Figure 3.

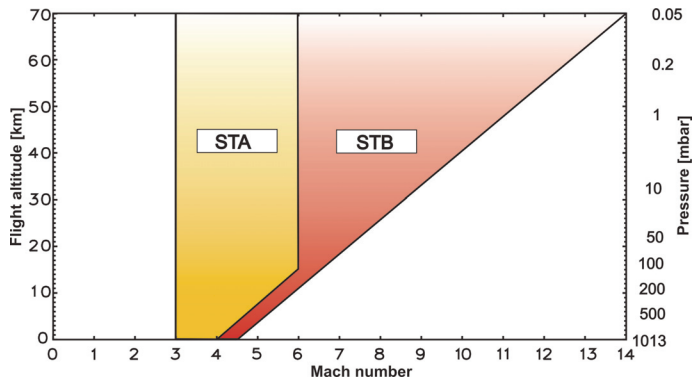


Fig. 3. Red and overlapped yellow areas representing the working range of the ISL STB and STA shock tunnels, respectively

The experimental flow conditions, i.e. the ambient pressure and temperature, are based on the US Standard Atmosphere (1976) model. Experiments can be conducted either in the STA shock tunnel or in the STB one at various Mach numbers and simulated altitudes. Nozzles having a Laval contour are available for experiments at Mach numbers of 3, 4.5, 6 and 8. Divergent nozzles are used for Mach numbers of 3.5, 4, 10, 12 and 14. The nozzle-exit diameters range from 200 mm to 400 mm. Experiments reported in this chapter were carried out in the STA shock tunnel at a Mach number of 4.5 and at a simulated altitude of 2.5 km.

### 3.3 Plasma-discharge actuator

In the present application, the projectile has to be steered at an altitude lower than a few kilometers, where the pressure ranges from 10<sup>5</sup> to about 10<sup>4</sup> Pa. As an example and taking into account the Paschen curve, for an electrode distance of 5 mm and for a pressure of 10<sup>4</sup> Pa, it is necessary to apply a voltage higher than 3 000 V to break the electric barrier. For a supersonic flight the pressure on a projectile forebody, where the electrodes are flush with the surface, is higher than the atmospheric pressure (depending on the projectile velocity) and consequently, the breakdown voltage also has to be higher. The plasma-discharge actuator is composed of a high-voltage low-energy activating system and of a low-voltage high-energy plasma generator capable of producing a plasma discharge between two electrodes (Fig. 4).

Let us consider a projectile flying from right to left and composed of a conical forebody equipped with two pairs of electrodes, as represented in Figure 5, step 1. The role of the high-voltage activating system only consists of breaking the electric barrier between two

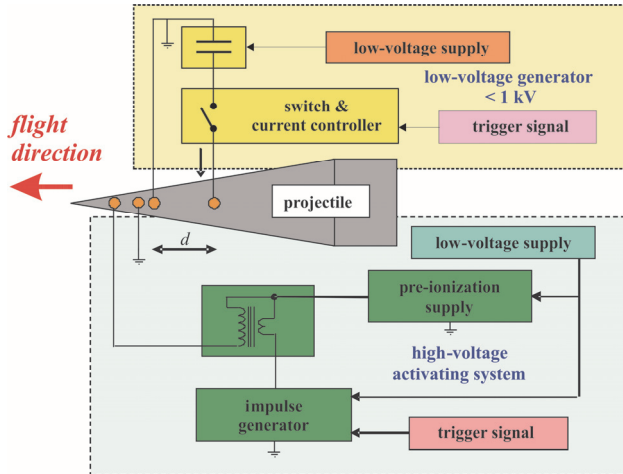


Fig. 4. Principle of the plasma-discharge actuator

electrodes, then of ionizing a small gas volume (step 2). As the projectile flies, the ionized gas volume moves along its surface (steps 3 and 4). The ionized gas volume, which has a low impedance, activates a plasma discharge when it encounters two other electrodes supplied with a low voltage (step 5). The role of that low-voltage plasma generator consists of feeding the energy to the pair of electrodes and then producing the plasma discharge. It is obvious that the high-voltage activating-system electrodes have to be ahead of the electrodes of the low-voltage plasma generator.

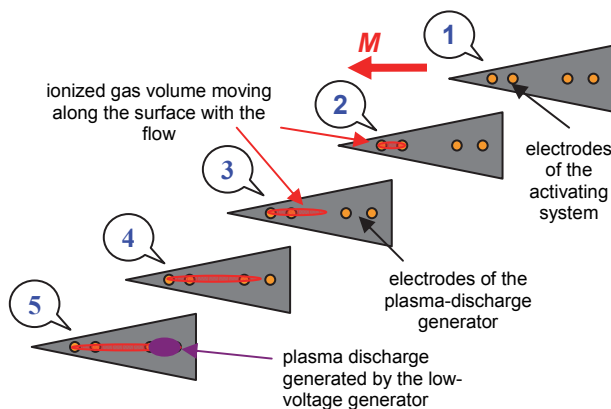


Fig. 5. Principle of the activation of a low-voltage plasma-discharge actuator

The high-voltage activating system is composed of a low-voltage power supply providing little energy to the ionizing power supply and to the impulse generator. The ionizing supply and the impulse generator are connected to a step-up transformer generating the high voltage. The transformer is itself connected to the pair of electrodes. An external signal allows the triggering of the activating system. The transformer is the main part of the latter.



In the experiments presented in the current studies, a 320 V / 5 000 V transformer is used; however, the plasma-actuator design could be adapted to any projectile flight conditions.

The low-voltage plasma-discharge generator is composed of a capacitor connected to the electrode pair through a current controller and a switch activating the actuator. The current controller allows the plasma power and therefore, the plasma duration to be controlled for a given energy. The capacitor is charged by a low-voltage supply. Aluminum electrolytic capacitors meet the requirements for the present application; indeed, they have a large capacity/volume ratio and a low equivalent series resistance (ESR), allowing the use of a large discharge current. As an example, a capacitor of a 35-mm diameter and a 50-mm length supplied with 550 V has a stored energy of 50 J.

Figure 6 shows the plasma-discharge actuator embedded in a 50-mm-diameter test model. The low-voltage supply used for charging the capacitor before the test is carried out, is not embedded in the test model; an autonomous low-voltage supply based on a 7.2 V battery and a step-up transformer is being studied so that it can be embedded in the same test model.

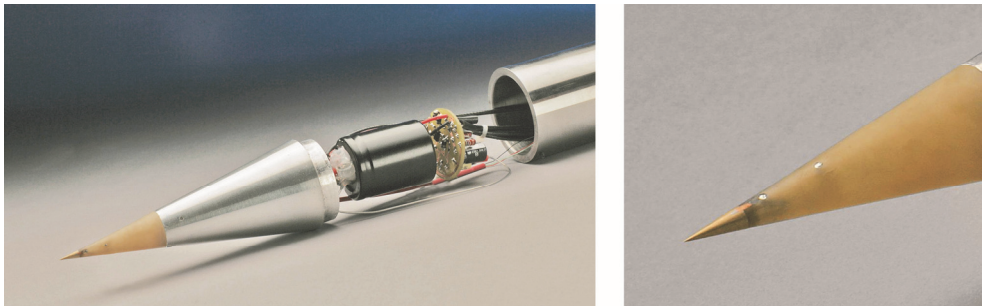


Fig. 6. Embedded low-voltage plasma-discharge actuator in a 50-mm-diameter test model and zoom on the electrodes

### 3.4 Fixed projectile forebody for surface-pressure and temperature measurements in the wind tunnel

A series of experiments is performed with a projectile forebody mounted in the wind tunnel in order to analyze the flow field disturbed by the plasma discharge by means of pressure and temperature measurements and visualizations. The experimental study is conducted for the 50-mm test model of Figure 7, which is mounted without any angle of attack on a shaft assembly along the wind-tunnel centerline. The model is composed of two electrically insulating parts mounted on a steel support ensuring the mechanical connection between the model and the wind-tunnel shaft assembly.

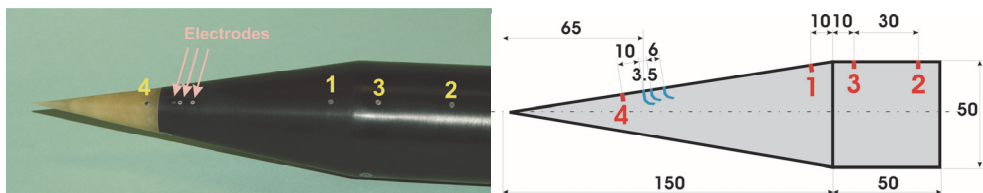


Fig. 7. Projectile forebody for surface-pressure measurements

The copper electrodes flush with the conical surface are embedded in the PVC part and are arranged along the longitudinal axis of the model, allowing the production of a geometrically quasi-linear discharge. The cathode of the activating system and that of the low-voltage plasma generator are put together, limiting the number of electrodes to three. The common cathode is located between the anodes of the activating system and of the low-voltage plasma generator. The anode of the activating system is located at a distance of 65 mm from the projectile tip. The distance between the electrodes of the activating system is 3.5 mm and the distance between the electrodes of the low-voltage generator is 6 mm. The plasma discharge is produced by using the low-voltage actuator embedded in the projectile. Four pressure transducers also flush with the surface are embedded in the model according to Figure 7. Transducer No. 1 is located 10 mm ahead of the cone-cylinder junction. Transducers Nos. 2 and 3 are 40 and 10 mm downstream from the cone-cylinder junction, respectively. Transducer No. 4 is located 10 mm upstream from the anode of the activating system. The model CCQ-093-1.7BARA from the Kulite-Semiconductor company is used: the rated absolute pressure is 1.7 bar, the maximum absolute pressure is 3.4 bar and it is compensated in temperature within a 78 K-235 K range. The accuracy of the measurement is 0.1% of the rated absolute pressure. That model is particularly designed to be protected against electromagnetic perturbations. The data acquisition is carried out by using 16-bits National Instrument RACAL boards cadenced at 100 kHz. The complete projectile forebody equipped with pressure transducers and their acquisition chains have been calibrated at rest in the shock-tunnel test chamber; indeed, the shock tunnel is airtight when the installation is closed and a defined pressure can be set from 5 to  $10^5$  Pa to calibrate the measurement chains.

### 3.5 Free-pitching projectile motion device

Another series of experiments is conducted with a projectile model mounted on a sting ending with an axis in such a way that the model can rotate around this pitching axis located right at the center of gravity of the model. The aim of the experimental study consists of recording the free-pitching motion of the projectile model by using a high-speed camera. The analysis of the recorded images allows the determination of the pitching response of the projectile model as far as the evolution of the measured angle of attack is concerned.

The main difficulty encountered in that study concerns the projectile model stability. Figure 8 shows the free-pitching projectile motion device supporting the model (part 1) which can have an angle of attack. Before the experiment starts, the model is horizontal and locked by a pneumatic jack (parts 2 and 3) and remains locked until the steadiness of the supersonic flow is reached (about 10 s). Then the pneumatic jack fixed to the wind-tunnel

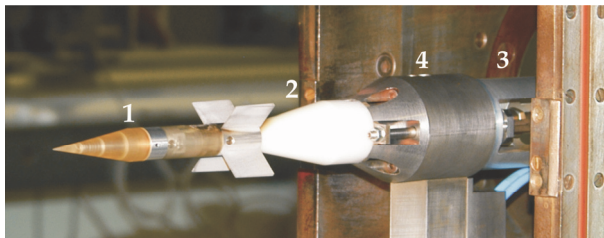


Fig. 8. Projectile model mounted on the free-pitching motion device in the wind tunnel

support (part 4) releases the model; it is now able to rotate freely around its center of gravity. If the projectile model remains horizontal, it is stable in the flow; otherwise, it rotates until the angular stop is reached. The maximum amplitude of the projectile model deviation is  $\pm 3.4^\circ$ . Three projectile models have been tested; they have the same geometry, except for the fin height  $L$ , which is  $0.5D$ ,  $D$  and  $1.5D$ , respectively (Fig. 9). The diameter  $D$  of the cylindrical part is 20 mm and is the reference dimension. The models are composed of many parts so that the center of gravity is located right at the pitching axis, as mentioned before. The electrodes flush with the conical surface are situated just in front of the fins. The plasma discharge is produced by using the low-voltage actuator located outside the wind tunnel, due to the dimensions of the actuator and projectile models.

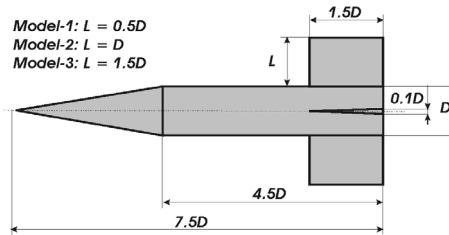


Fig. 9. Projectile model geometries for the free-pitching motion study

### 3.6 Projectile model for free-flight experiments in the shock tunnel

Another series of experiments is conducted in the shock tunnel by using a very light model of an Explosively Formed Projectile (EFP) for free-flight investigations. This projectile is chosen because it has been studied at ISL in terms of flight stability and it has been found that it is very stable without any spin (Rondot & Berner, 1998). Another advantage is that it is very easy to manufacture the projectile model as its geometry is axisymmetric. It is composed of an ogive, a cylindrical part, a flare having a conical angle of  $17^\circ$  and a second one with a conical angle of  $40.8^\circ$  (Fig. 10). The model is made of AU4G, except for the support of the electrodes which is made out of PVC. The model mass is 20.5 g, and the center of gravity is located at 47.9 mm from the projectile tip. The electrodes are embedded near the junction between the ogive and the cylindrical part.

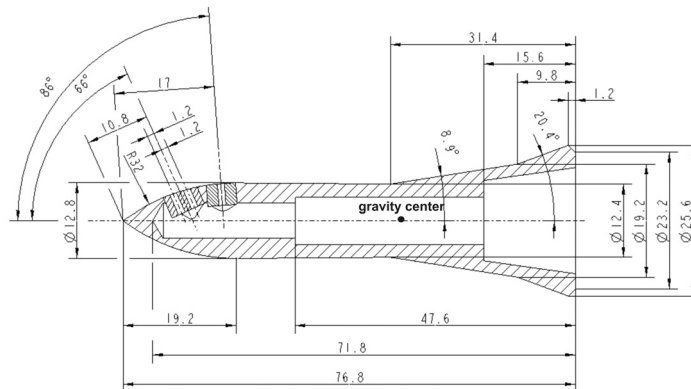


Fig. 10. EFP model for free-flight tests

Figure 11 shows model No. 1 hung up in the test chamber of the shock tunnel by means of two very thin and small disks of paper (No. 2) linked to Nylon threads that are fixed on the test-chamber wall.

The plasma discharge is produced by using the low-voltage actuator located outside the shock tunnel, due to the dimensions of the actuator and of the projectile model. The electric wires (No. 3) connected to the plasma-discharge actuator are very flexible and they slide through a small tube (No. 4) fixed in the test chamber. The displacement of the model is of the order of the model length. The Pitot-pressure probe (No. 5) allows the determination of the flow conditions.

The aim of the experimental study consists of recording the free-flight motion of the projectile by using a high-speed camera. The analysis of the recorded images allows the determination of the free motion of the projectile model subjected to a plasma discharge.

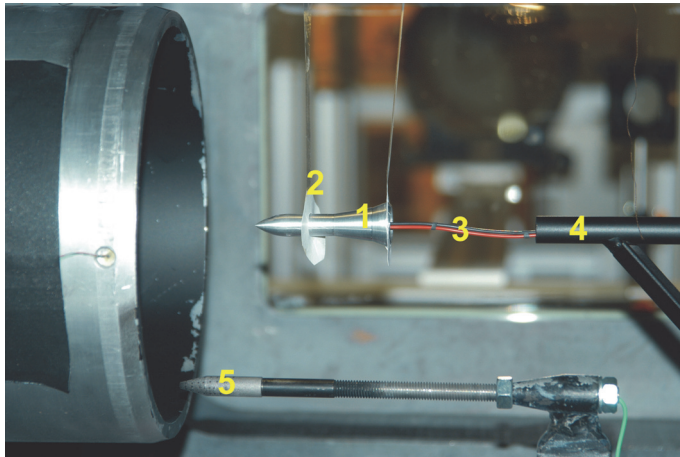


Fig. 11. EFP model hung up in the test chamber

### 3.7 Spectroscopic temperature estimation in the plasma plume

Spectra of the plasma emission have been recorded at different positions by means of two spectrometers: a miniature spectrometer covering the visible region from 400 nm to 800 nm (Ocean Optics HR2000) and a grating spectrograph (SPEX,  $f = 500$  mm, grating: 2400 lines/mm) for measuring spectra at certain wavelengths with a higher resolution (Eichhorn et al., 1998). A gateable ICCD camera (PRINCETON INSTRUMENTS ICCD-MAX 1024 ELD), which is connected to the grating spectrograph, is used for taking one spectrum per discharge at a precise chosen moment (delay with respect to the trigger signal) with an exposure time of 10  $\mu$ s. The schematic of the optical setup is shown in Figure 12.

The plasma temperature can be calculated by means of the copper spectrum at 510 nm. Copper is the electrode material and therefore the Cu lines are clearly visible in the measured spectrum (Sect. 4.2). If the local thermal equilibrium can be assumed, the intensity of a spectral line can be expressed as:

$$S_n = \gamma \cdot \frac{(gf)_n}{\lambda_n^3} \cdot \exp\left(-\frac{E_n}{kT}\right) \quad (1)$$

with:

- $S_n$  : intensity of line No.  $n$ ,
- $\gamma$  : factor, containing all constants,
- $(gf)_n$  : weighted oscillator strength of line No.  $n$ ,
- $\lambda_n$  : wavelength of line No.  $n$ ,
- $E_n$  : energy of the upper level of line No.  $n$ ,
- $k$  : Boltzmann constant ( $0.69503 \text{ cm}^{-1}/\text{K}$ ),
- $T$  : temperature.

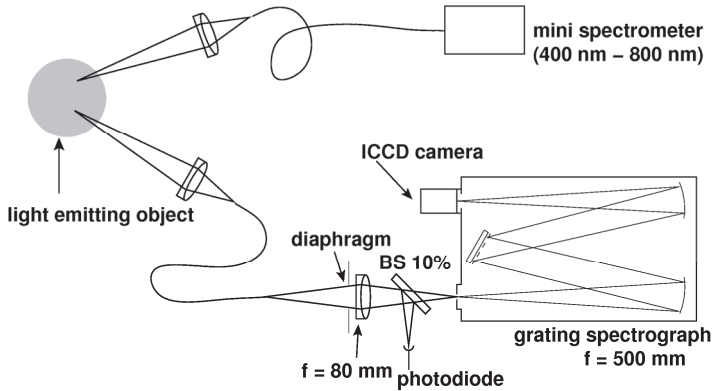


Fig. 12. Optical setup for the recording of spectra

The spectrum of Section 4.2 shows one Cu II line and several Cu I lines; two of them, numbered 1 and 2, are used for calculating the temperature. From Eq. (1) we can deduce:

$$\frac{S_1}{S_2} = \frac{\lambda_2^3 \cdot (gf)_1}{\lambda_1^3 \cdot (gf)_2} \cdot \exp\left(\frac{E_2 - E_1}{kT}\right)$$

$$\Rightarrow T = \frac{E_2 - E_1}{k} \cdot \frac{1}{\ln\left(\frac{S_1 \cdot \lambda_1^3 \cdot (gf)_2}{S_2 \cdot \lambda_2^3 \cdot (gf)_1}\right)} \quad (2)$$

The uncertainty depends on the relative uncertainties of the line intensities:

$$\Delta T = \frac{\partial T}{\partial S_1} \cdot \Delta S_1 + \frac{\partial T}{\partial S_2} \cdot \Delta S_2 = T \cdot \frac{\frac{\Delta S_1}{S_1} + \frac{\Delta S_2}{S_2}}{\ln\left(\frac{S_1 \cdot \lambda_1^3 \cdot (gf)_2}{S_2 \cdot \lambda_2^3 \cdot (gf)_1}\right)} \quad (3)$$

### 3.8 Voltage and current measurements

The measurements of the voltage and current during the plasma discharge are recorded. The voltage measurement performed at the electrode bounds indicates the lifetime of the

plasma discharge. The current measurement gives a representation of the impulsiveness of the plasma discharge.

### 3.9 Flow-field visualizations

The plasma discharge is produced on the projectile surface when the flow is quasi-steady around the model. A differential interferometer (DI), a classical schlieren picture or a simple photograph is used for visualizing the flow-field structure by means of a CCD camera. DI works as a flow visualization technique (Smeets, 1990) based on the density gradient field, thus allowing the gathering of information on an interferogram showing the flow pattern around the model. The differential interferometer is set for a gas at rest so as to obtain fringe patterns or an infinite fringe width showing a homogeneous light intensity distribution. In the current experiments the DI is used by following the second adjustment and the pictures look like schlieren pictures. In this way, the density gradient field in the gas flow is visualized by the light intensity distribution shown on interferogram pictures. The DI is adjusted in such a way that the density gradient direction is vertical.

## 4. Experimental results

### 4.1 Wind-tunnel experiments, $M = 3$ , fixed model device, flow-field visualization

Many experiments have been carried out with the low-voltage actuator embedded in the 50-mm-diameter model for different electrode distances, capacitors and supply voltages. The current study only focuses on the first 60 millimeters of the conical nose in order to highlight the evolution of the plasma discharge in detail.

The DI pictures (interferograms) are recorded by a 12-bit PCO SENSICAM camera with a spatial resolution of 1280 pixels by 1024 pixels and an exposure time of  $0.2 \mu\text{s}$ . The plasma discharge is produced under wind-tunnel conditions at  $M = 3$  without any angle of attack. The electrode distance is 3.5 mm.

A first series of interferograms is taken for a configuration in which the energy ( $E$ ) stored in the capacitor amounts to 12 J. Figure 13 shows shots taken at 3 instants after the beginning of the plasma discharge, allowing the analysis of the evolution of the flow field modified by the plasma. The flow direction is from left to right. The formation and growth of the disturbance and its propagation along the conical model surface are clearly highlighted. At  $t = 17 \mu\text{s}$ , the plasma causes an expansion of the air leading to the distortion of the attached

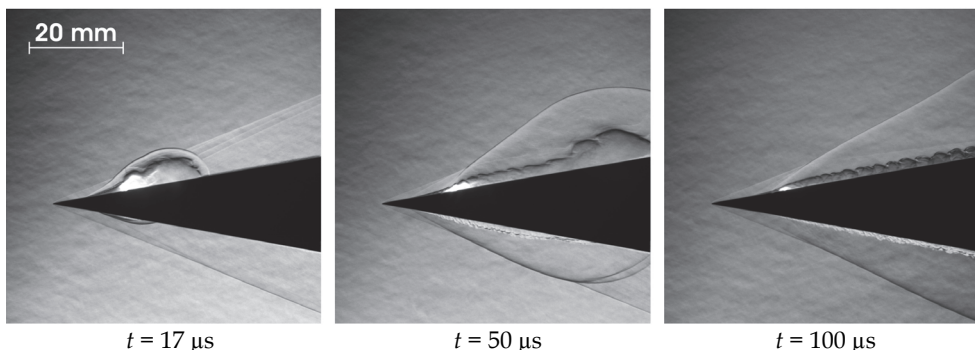


Fig. 13. Plasma-discharge visualizations at  $M = 3$ ,  $E = 12 \text{ J}$ , time evolution

shock wave present at the conical tip. The boundary layer is also perturbed by the plasma, but the flow-field modification is larger on the plasma side than on the opposite side. At  $t = 50 \mu\text{s}$ , the plasma power decreases, the bubble due to the sudden expansion is convected along the model surface and the attached shock wave remains distorted. At  $t = 100 \mu\text{s}$ , the plasma power slightly decreases as long as the capacitor is able to provide sufficient energy to maintain it. Its extinction occurs after nearly  $250 \mu\text{s}$ .

A second series of interferograms is taken for an energy  $E = 50 \text{ J}$ . Figure 14 shows pictures taken at the same instants, so that the influence of the energy delivered to the plasma discharge can be analyzed; a saturation of some CCD pixels is visible for the first instant, due to the very high light intensity. The effects of the plasma are much greater when the energy is increased and the plasma-discharge duration is longer. Indeed, its extinction takes place after nearly  $400 \mu\text{s}$ .

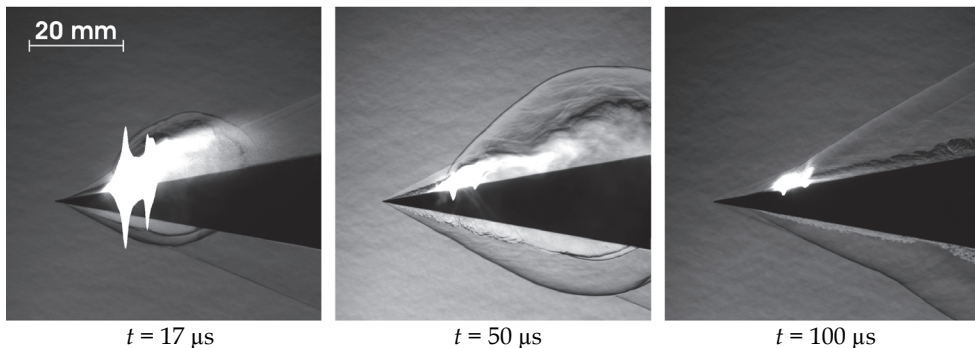


Fig. 14. Plasma-discharge visualizations at  $M = 3$ ,  $E = 50 \text{ J}$ , time evolution

The visualizations show that the generation of a plasma discharge causes a perturbation between the projectile surface and the shock wave attached to the conical projectile tip. The perturbation is much greater than the one obtained with the high-voltage generator (Gnemmi et al., 2008). It is maintained for a certain length of time and is strong enough to distort the attached shock wave: the higher the energy, the stronger the perturbation and the longer the plasma-discharge duration. The perturbation is more important on the plasma-discharge side than on the opposite side of the projectile tip, leading to an imbalance in the flow field.

The influence of the energy is clearly examined by using capacitors capable of supplying 7, 12 and 50 J. Figure 15 shows interferograms taken  $50 \mu\text{s}$  after the beginning of the plasma discharge for an electrode distance of 9.5 mm: the higher the supplied energy, the larger the perturbation. The analysis of these flow-field structures must be considered very carefully: the fact that the perturbation is greater when the highest energy is used does not mean that the pressure imbalance on the projectile surface is stronger.

The influence of the electrode distance is examined by performing other series of interferograms taken for four electrode distances ( $l$ ) and an energy of 50 J. Figure 16 shows interferograms taken  $50 \mu\text{s}$  after the beginning of the plasma discharge.

The sparks indicating the electrode pairs of the low-voltage plasma generator are visible on each interferogram. There are small differences in the flow structure just after the beginning of the process, which means that the delivered power is nearly the same. However, the plasma duration depends on the electrode distances, as can be seen in Figure 17.

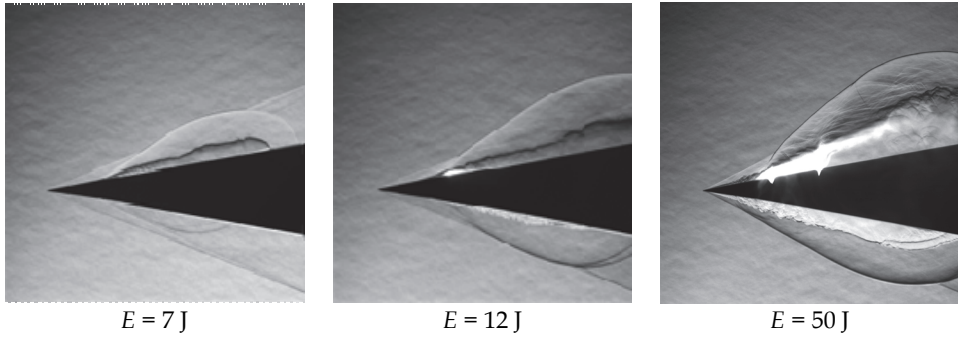


Fig. 15. Plasma-discharge visualizations at  $M = 3$ ,  $t = 50 \mu\text{s}$ , energy influence

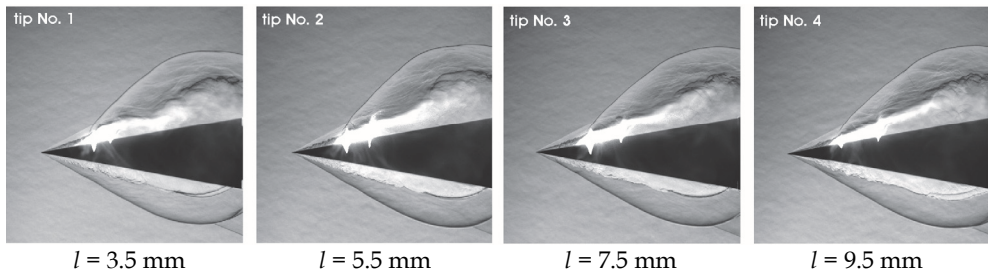


Fig. 16. Plasma-discharge visualizations at  $M = 3$ ,  $t = 50 \mu\text{s}$ ,  $E = 50 \text{ J}$ , electrode-distance influence

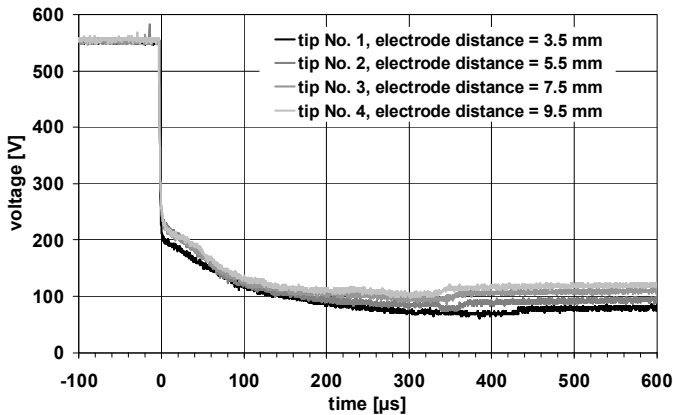


Fig. 17. Voltage measurement during the plasma discharge with 4 electrode distances

Figure 17 represents the voltage evolution measured between the electrodes of the low-voltage plasma generator during the previous experiments. Before the plasma discharge occurs at  $t = 0$ , the voltage between the electrodes is 558 V, corresponding to the capacitor voltage. The start of the plasma discharge causes a voltage drop down to about 220 V,



depending on the electrode distance, as the same capacitor is used. The voltage slightly decreases and the plasma extinction takes place when a slight voltage increase occurs up to a residual value. The plasma duration increases from 0.34 ms for tip No. 4 to 0.42 ms for tip No. 1 as the electrode distance decreases: indeed, the longer the electrode distance, the higher the voltage necessary to keep the discharge active.

#### 4.2 Wind-tunnel experiments, $M = 3$ , fixed model device, pressure and temperature measurements, flow-field visualization

The experiments presented previously and many others reported in Gnemmi & Rey, 2008 and Gnemmi & Rey, 2009 were carried out with the low-voltage actuator embedded in the 50-mm-diameter model for different electrode distances, capacitors and supply voltages in order to analyze the flow-field modification due to a plasma discharge by using interferograms pictures. The plasma discharge is produced under wind-tunnel conditions at  $M = 3$  without any angle of attack. The current study focuses on time-resolved pressure and temperature measurements recorded synchronously with the flow-field visualizations.

The plasma discharge is produced by an electric arc between the electrodes, which causes electromagnetic perturbations. It is therefore necessary to verify that the pressure measurements are not disturbed by these perturbations. The first test consists of masking the pressure transducers by means of adhesive tape covering each of them, of realizing the experiment with the plasma discharge and of analyzing the pressure evolution.

The energy stored in the plasma discharge actuator amounts to 83 J: it is distributed to the electrodes without any current regulation, but limited by the use of a coil. Figure 18 presents the absolute pressure recorded on transducers  $P1$  to  $P4$  covered with adhesive tape and the current  $I$  measured at the same time. The pressure data acquisition is performed at 100 kHz and filtered at 10 kHz. The plasma duration is 1.05 ms. The dielectric barrier disruption produces perturbations on the pressure signal during about 80  $\mu$ s and then the pressure remains constant. It is noticeable that the perturbation amplitude varies with the transducer-plasma distance: the shorter the distance, the larger the perturbation amplitude. The absolute pressure has a certain value (near 0.23 bar) because the projectile model is not airtight.

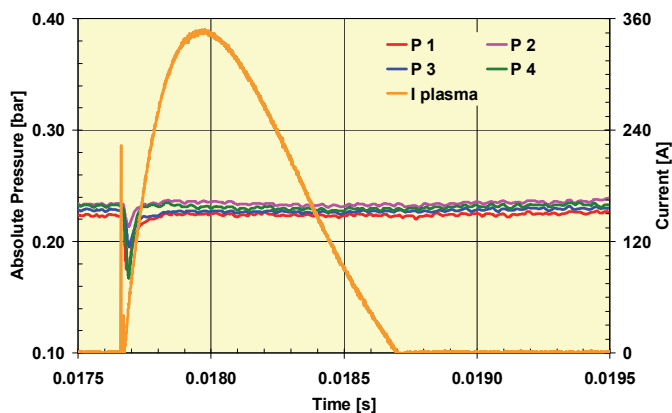


Fig. 18. Pressure and current measurements during a plasma discharge,  $M = 3$ ,  $E = 83$  J (test 12-08-11-26-02): transducers protected by adhesive tape

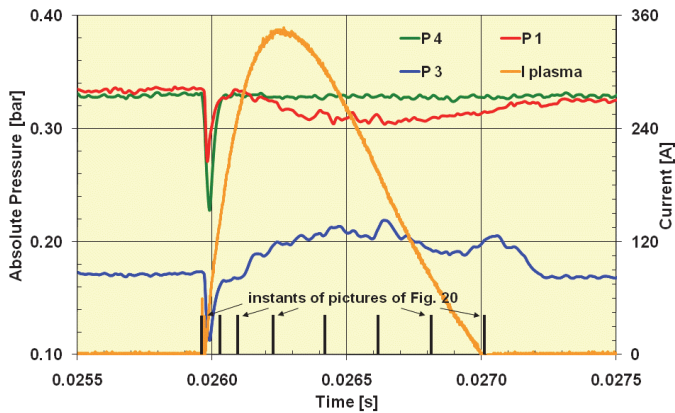


Fig. 19. Pressure and current measurements during a plasma discharge,  $M = 3$ ,  $E = 83 \text{ J}$  (test 13-08-11-27-01)

The second test consists of reproducing the same experiment by removing the adhesive tape from the transducers. Figure 19 also shows the absolute pressure recorded on transducers  $P1$ ,  $P2$  and  $P4$  during the plasma discharge and the current  $I$  measured at the same time. The black bars correspond to the instants whose visualizations are presented in Figure 20. This allows the correlation between the pressure and the visualized flow-field structure. The dielectric barrier disruption is also visible on the pressure signals and the amplitude also depends on the transducer-plasma distance. The plasma discharge does not influence the pressure 10 mm ahead of it ( $P4$ ). The measurement indicates that it produces an underpressure on the conical part just ahead of the cone-cylinder junction ( $P1$ ), whereas it causes a reinforcement of the pressure in the expansion region just behind the cone-cylinder junction ( $P3$ ); this is not understandable because it is antinomic.

The DI technique is used to visualize the flow-field structure around the model. Interferogram pictures are recorded by using a Photron-Fastcam camera at 15 000 frames per second with a spatial resolution of 896 pixels by 206 pixels and an exposure time of  $2 \mu\text{s}$ . Figure 20 depicts 8 pictures showing the evolution of the plasma discharge. The flow direction is from left to right. The location of the plasma-discharge generator anode is indicated on each picture as well as the location of transducers  $P1$  and  $P3$ .

The first picture ( $t = 25.960 \text{ ms}$ ) corresponds to the ignition of the plasma discharge producing the disruption of the electric barrier and leading to the perturbation on the pressure signals: the shock wave attached to the conical nose is visible in the upper left corner, the boundary layer and the expansion region at the cone-cylinder junction can also be observed. The second picture ( $t = 26.027 \text{ ms}$ ) clearly highlights the plasma-discharge glow and the changes in the density gradient in the flow field which interacts with the boundary layer of the model. A slightly visible bow shock forms ahead of the plasma discharge. This instant nearly corresponds to the one at which the pressure levels are recovered after the perturbation due to the plasma-discharge ignition. The third picture ( $t = 26.093 \text{ ms}$ ) shows the growth of the plasma discharge, the modification of the boundary layer and the reinforcement of the bow shock in front of the plasma. At this instant, transducer  $P1$  is affected by the structure change, which is not the case of  $P3$ , as can be seen in Figure 19. The fourth picture ( $t = 26.227 \text{ ms}$ ) is taken when the current is at its maximum:

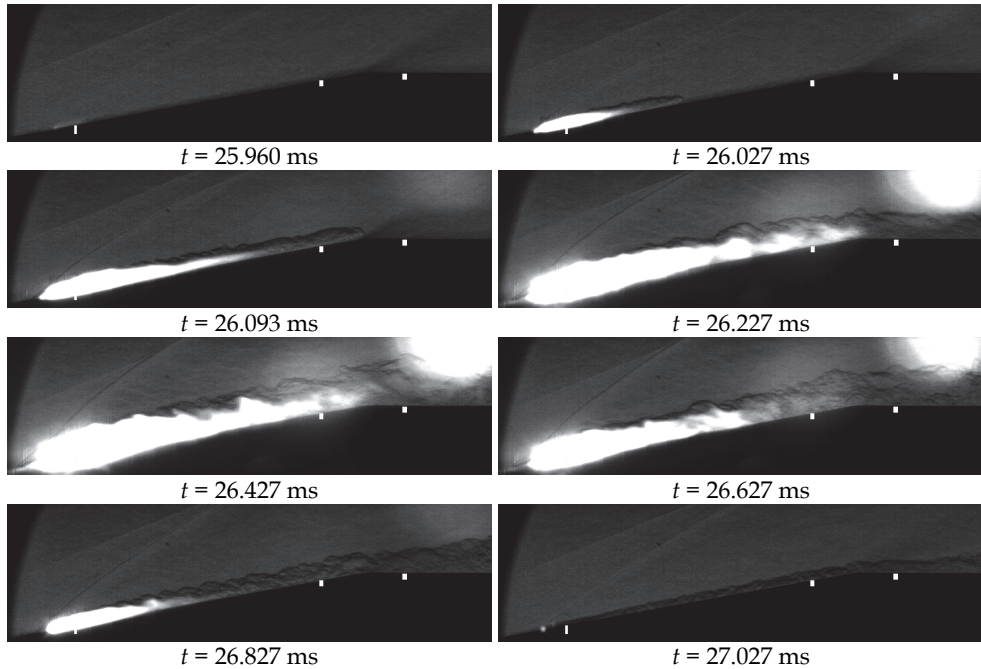


Fig. 20. Visualization of the evolution of a plasma discharge,  $M = 3$ ,  $E = 83$  J (test 11-08-11-26-01)

the bow shock reinforces itself and its angle with respect to the cross-flow increases, the perturbation expands and the glow extends to the cone-cylinder junction, covering the  $P1$  transducer. An optical reflection is produced by the discharge glow in the upper right corner of the picture. The next 3 pictures ( $t = 26.427$ ,  $26.627$  and  $26.827$  ms) display the evolution of the flow structure. The last one ( $t = 27.027$  ms) shows the extinction of the plasma discharge and the decrease in the structure modification until the steady-state structure of the flow field is recovered. On the fourth and fifth interferograms the discharge glow covers the  $P1$  transducer, whereas  $P3$  is unaffected; it tends to demonstrate that the  $P1$  pressure measurement is distorted by the discharge glow, which leads to a probably wrong pressure measurement. This proves the difficulty in measuring the surface pressure under plasma-discharge conditions and it should be clarified by other measurements.

Other experiments making use of the energy of 50 J stored in the plasma-discharge actuator are carried out in order to measure the temperature in the plasma plume: the energy is also distributed to the electrodes without any current regulation or coil. As an example, Figure 21 presents copper spectra recorded 12 mm behind the anode of the plasma-discharge generator and very near the conical surface by using the spectrograph.

Spectra are shown at 3 instants after the ignition of the plasma discharge. It must be kept in mind that electrodes are made of copper so as to make the copper lines stand out within the measured spectrum. The method shortly described in Section 3.7 and detailed in Eichhorn et al., 1998 allows the determination of the temperature by using the copper spectrum as the reference spectrum. For the two lines taken into account the atomic parameters are:

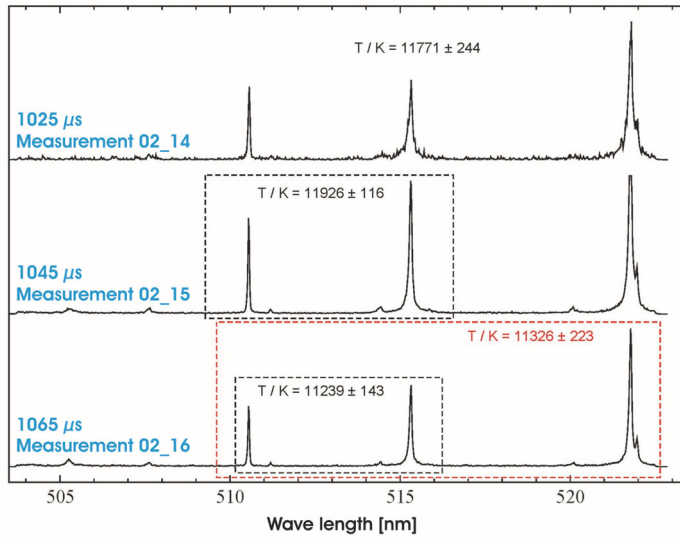


Fig. 21. Cu lines in the measured spectrum during a plasma discharge,  $M = 3$ ,  $E = 50$  J

$$\lambda_1 = 510.554 \text{ nm}, \quad E_1 = 30\,784 \text{ cm}^{-1}, \quad (gf)_1 = 0.0309;$$

$$\lambda_2 = 515.324 \text{ nm}, \quad E_2 = 49\,935 \text{ cm}^{-1}, \quad (gf)_2 = 0.9772.$$

The temperature and its uncertainty are calculated by using Equations 1 and 2, respectively, for three different delay times  $t$ :

$$t = 1.025 \text{ ms: } T = 11\,771 \text{ K} \pm 244 \text{ K}$$

$$t = 1.045 \text{ ms: } T = 11\,926 \text{ K} \pm 116 \text{ K}$$

$$t = 1.065 \text{ ms: } T = 11\,239 \text{ K} \pm 143 \text{ K}.$$

The maximum temperature reaches about 12 000 K at the location of the measurement point with an uncertainty of  $\pm 240$  K.

### 4.3 Wind-tunnel experiments, $M = 3$ , free-pitching projectile motion

The free-pitching projectile motion device defined in Section 3.5 is fixed in the measurement chamber of the wind tunnel (Figure 22). The projectile-model behavior is tested without any plasma discharge in a first step. As mentioned in Section 3.5, at the beginning of the experiment the projectile model is horizontal and remains locked until the steadiness of the supersonic flow is reached. The model is then unlocked and is able to rotate freely around its pitching axis, which is also its center of gravity. The model is stable, which means that the projectile model remains horizontal. About 20 series of experiments are conducted in order to examine the behavior of the projectile model subjected to a plasma discharge.

Two series of tests with plasma discharges are analyzed in this section; they are examples, in terms of flow-field visualization, of the projectile-tip displacement corresponding to the angle of attack deviation and of the voltage-current evolution. The plasma discharge is

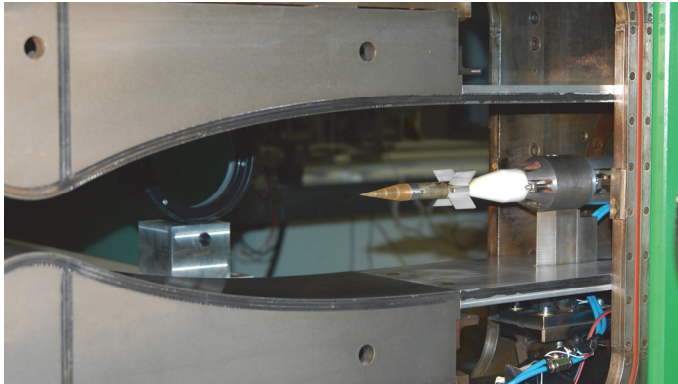


Fig. 22. Fin-stabilized projectile model of the finned model located in the S20 wind tunnel

generated in front of the fins (electrode distance of 5 mm) of the projectile model having a fin height of  $L = D$ . The low-voltage actuator is located outside the wind tunnel, due to the dimensions of the model (diameter of 20 mm) compared to those of the actuator (diameter of 45 mm). One value of the capacitor is considered in such a way that the stored energy corresponds to 243 J; the total capacity is 2400  $\mu\text{F}$  and the charge voltage is 450 V. Two current thresholds are taken into account in order to examine the influence of the plasma-discharge power (or duration) on the projectile-model angular deviation.

The flow-field perturbation during the plasma discharge is visualized by means of the differential interferometry technique. The images are recorded by using the Photron-Fastcam camera at 12 000 frames per second with a spatial resolution of 896 pixels by 288 pixels and an exposure time of 1  $\mu\text{s}$ .

#### 4.3.1 Current threshold regulated at 100 A (test 07-08-12-08-01)

The test 07-08-12-08-01 analyzed hereafter is carried out with the current regulation in such a way that its threshold is set to 100 A. Figure 23 presents 8 interferograms of the interaction between the plasma discharge and the cross-flow of the projectile model.

The instant  $t = 0$  corresponds to the state at which the cross-flow is stationary and the projectile model has a free-pitching motion; it can be observed that the projectile model remains horizontal, thus proving its stability, and the plasma discharge is triggered at this moment. The instant  $t = 85.33 \mu\text{s}$  corresponds to the first recorded frame after the plasma-discharge activation; the plasma discharge is clearly visible. Up to  $t = 3.75 \text{ ms}$ , the interferograms allow the follow-up of the growth of the plasma discharge and of its interaction with the cross-flow of the projectile model; in particular, the bow shock formed by the interaction can be clearly seen. From  $t = 3.75 \text{ ms}$  to  $t = 9.75 \text{ ms}$ , the plasma discharge is maintained and acts on the cross-flow in a quasi-stationary manner. It is also clearly highlighted that the projectile model takes a positive angle of attack (nose up). The instant  $t = 11 \text{ ms}$  corresponds approximately to the time when the angle of attack is at its maximum and when the extinction begins. At  $t = 11.25 \text{ ms}$  the plasma is almost extinguished.

The displacement of the tip of the projectile model during the plasma discharge is extracted from each interferogram by using an adaption of the Particle-Image Velocimetry software (PIV) used at ISL (Gnemmi et al., 2011). A sub-pixel method with an accuracy of 0.1 pixel allows the detection of the intercorrelation peaks on the images. Taking into account the

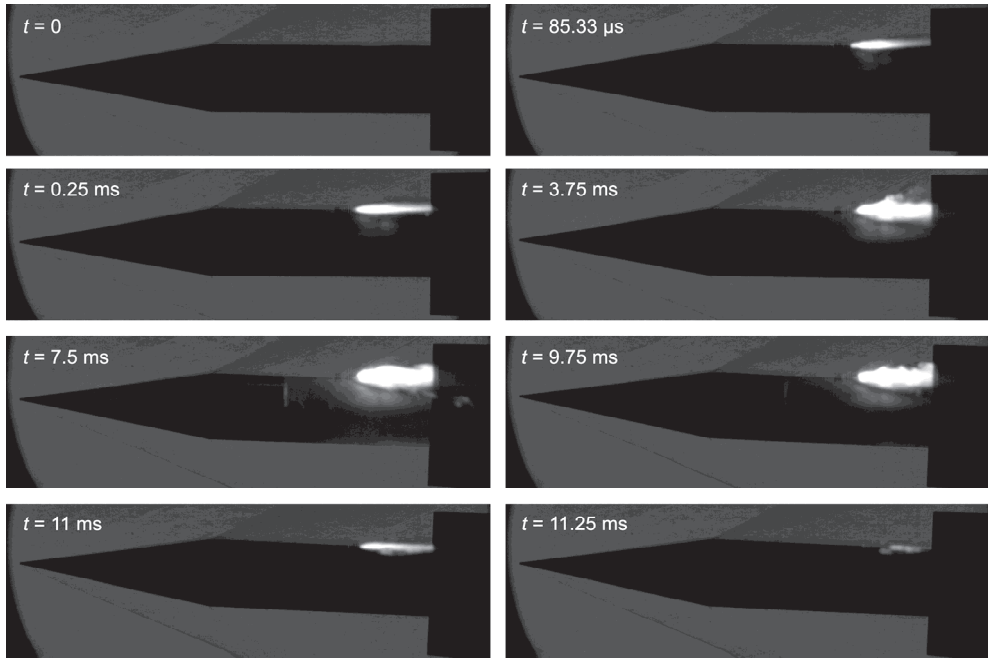


Fig. 23. Free-pitching projectile evolution during the plasma discharge,  $M = 3$ ,  $E = 243$  J (test 07-08-12-08-01)

optical calibration system, the accuracy of the displacement measurement is  $34 \mu\text{m}$  per pixel, leading to a measured angle uncertainty of  $10^{-5}$  degree. The angle of attack of the projectile model is then determined by the knowledge of its rotation axis location. Figure 24 depicts the evolution of that angle of attack and of the current circulating in the circuit. The instant  $t = 0$  corresponds to the one shown in Figure 23.

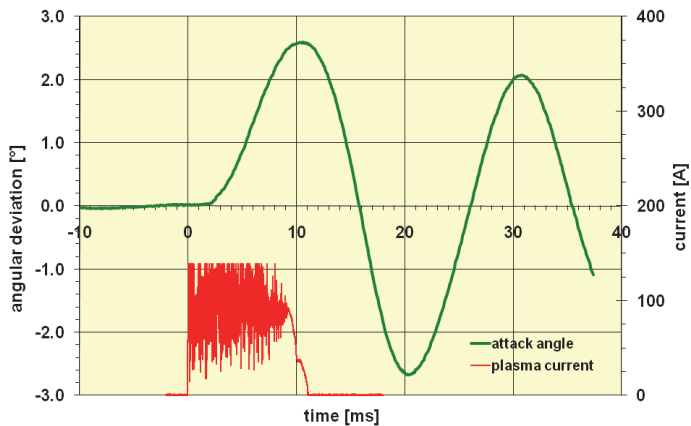


Fig. 24. Angle of attack of the fin-stabilized projectile model subjected to a 243 J plasma discharge with a 100-A current regulation (test 07-08-12-08-01)

Before the activation of the plasma discharge, the projectile model oscillates freely at its natural pitching frequency of 50.7 Hz. The model starts to move upwards around 2 ms after the plasma-discharge activation and its angle of attack increases up to a maximum of 2.6°, nearly corresponding to the extinction of the plasma. Afterwards, the angle of attack decreases and the projectile oscillates at its pitching frequency in a damped motion. According to the result found in Section 4.2 concerning the pressure measurements, the projectile model takes a positive angle of attack as the overpressure generated by the plasma discharge is located behind the pitching axis, inducing a nose-up moment.

The analysis of the plasma-current profile shows that the plasma-discharge duration is nearly 9.7 ms and the extinction duration is 1.7 ms. The correlation of the two profiles shows a delay of about 2 ms between the generation of the plasma discharge and the response of the projectile model.

Figure 25 presents the evolution of the voltage and of the current measured in the circuit. The signals are probably perturbed by the fact that the electrodes are eroded and a transfer of copper occurs from the cathode to the anode, leading to an irregular path of the electric arc; this irregular electric arc induces voltage fluctuations on the electrodes. The current regulation at 100 A is perfectly achieved, the mean voltage is 100 V, leading to a mean power of 10 kW and an energy of 97 J; considering the stored energy of 243 J, the efficiency is of about 40%.

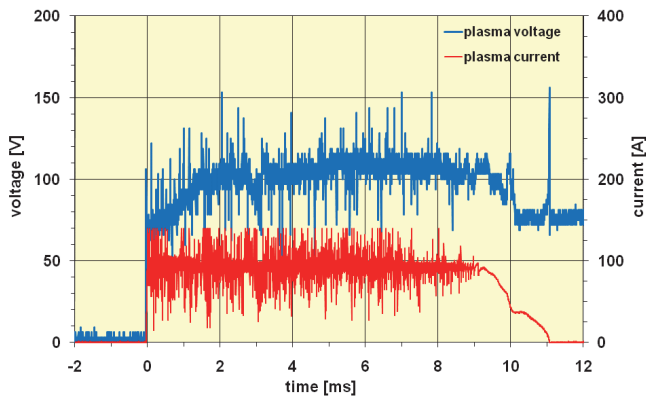


Fig. 25. Voltage and current in the discharge circuit (test 07-08-12-08-01)

#### 4.3.2 Current threshold regulated at 50 A (test 09-08-12-08-03)

The other test 09-08-12-08-03 is carried out with the same energy stored in the actuator, but it is distributed with a current threshold regulated at 50 A. Figure 26 presents the evolution of the angle of attack and of the current circulating in the circuit.

The duration of the plasma discharge is of about 25.4 ms, which is higher than the natural pitching period, the latter being lower than 20 ms. The projectile model moves upwards roughly 1 ms after the plasma-discharge activation and reaches its maximum angle of attack of 1.3° nearly after 10 ms; this corresponds to half the natural pitching period. Afterwards, in spite of the plasma being maintained, the angle of attack decreases down to 0.6° near 20 ms. Then, while the plasma is still maintained, the angle of attack increases again up to 1.2° near

28 ms. At 28 ms the plasma is completely extinguished and the angle of attack decreases again and it resumes its natural pitching motion. During the test, it is demonstrated that the projectile model has a mean angle of attack of about  $0.9^\circ$  for a duration nearly equivalent to that of the plasma discharge.

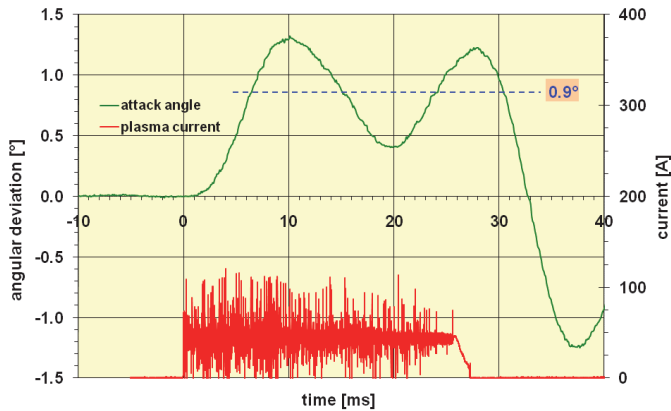


Fig. 26. Angle of attack of the fin-stabilized projectile model subjected to a 243 J plasma discharge with a 50-A current regulation (test 09-08-12-08-03)

Figure 27 presents the evolution of the voltage and the current measured in the circuit. The signals are also perturbed. The current regulation at 50 A is also perfectly reached, the mean voltage is 90 V, yielding a mean power of 4.5 kW and an energy of 114 J; considering the stored energy of 243 J, the efficiency is close to 47%.

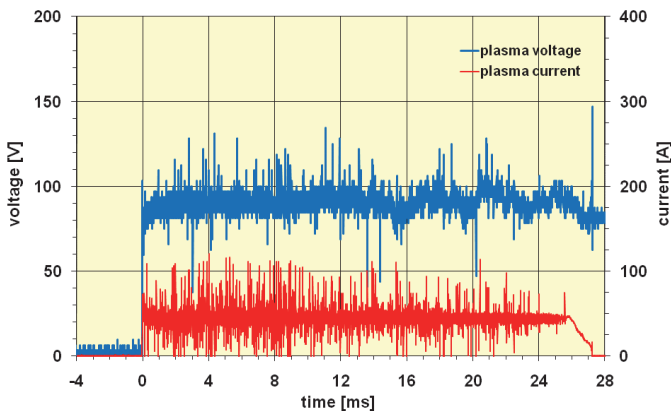


Fig. 27. Voltage and current in the discharge circuit (test 09-08-12-08-03)

The results show a significant change in the angle of attack of the projectile about 2 ms after the plasma-discharge generation of 243 J. However, the experiments cannot demonstrate that such a plasma discharge induces a significant change in the trajectory of the projectile, because it is fixed at its gravity center. The remaining questions are: “Does this disturbance



last long enough to cause the trajectory of the projectile to change?" and "Is the power large enough for a change in the projectile trajectory to take place?" The trajectory change will be computed in the future by running a 3-DoF program which will use data extracted from these experimental results.

#### 4.4 Shock-tunnel experiments: Free-flight projectile behavior at the altitude of 2.5 km, $M = 4.5$

More experiments are carried out in the shock-tunnel facility to show the free-flight motion of a projectile under realistic conditions, for the purpose of answering the previous remaining questions. Therefore, the very light EFP model described in Section 3.6 is hung up inside the test chamber of the shock tunnel in front of the nozzle. When the membranes of the shock tube burst, the airflow is accelerated up to the desired pressure, temperature and flight velocity, leading to  $M = 4.5$  for the altitude of 2.5 km. The Nylon threads and paper disks break and the projectile can fly freely in the test chamber. Because our main interest lies in the projectile-model behavior, it is important to focus on the projectile model so that its trajectory can be determined. Therefore, simple photographs are taken by the Photron-Fastcam CCD camera, allowing the projectile motion to be recorded and analyzed at a rate of 10 000 frames per second with an exposure time of  $2 \mu\text{s}$ . Two sets of pictures are taken during each experiment: one picture of the motion in the horizontal plane and one in the vertical plane.

##### 4.4.1 Without any plasma discharge (test 02-09-03-11-01)

A first test consists of verifying the free-flight stability of the projectile model. Therefore, Figure 28 presents 6 pictures taken at different instants in the vertical and horizontal planes.

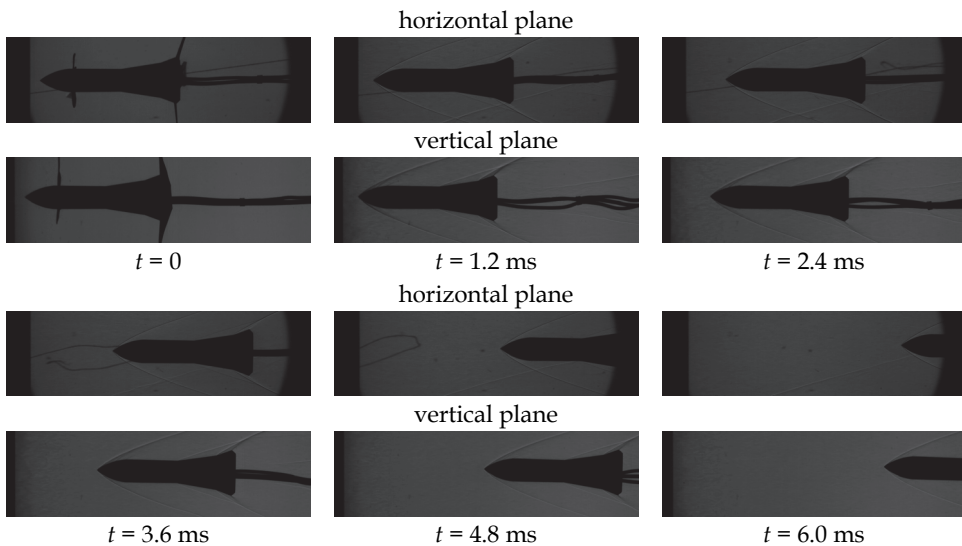


Fig. 28. Visualization of the displacement of the free-flight EFP model,  $M = 4.5$  (test 02-09-03-11-01)

The pictures show the vertical and horizontal displacements of the model without any plasma discharge.  $t = 0$  corresponds to the burst of the diaphragm and the model is still hung up in the test chamber. At  $t = 1.2$  ms, the model moves to the right because the flow comes from the left and the shock-wave patterns are visible. During the complete flight, the model moves along its longitudinal axis, thus proving its flight stability. It is important to notice that the electric wires used later for the plasma discharge do not disturb the behavior of the model during its flight.

The next experiments consist of generating a plasma discharge when the flow field is constant and then analyzing the trajectory of the model. Two test results are presented for 2 plasma discharges generated by different amounts of stored energy in the actuator for the same current threshold of 100 A. The plasma discharge is produced in the horizontal plane in order to avoid the influence of the gravity on the model trajectory.

#### 4.4.2 With a plasma discharge, stored energy of 65 J (test 07-09-03-25-01)

The result in Figure 29 is obtained for an energy of 65 J, inducing a plasma duration of 2.5 ms. The latter is deduced from the current measurement depicted on the left-hand side of Figure 31.

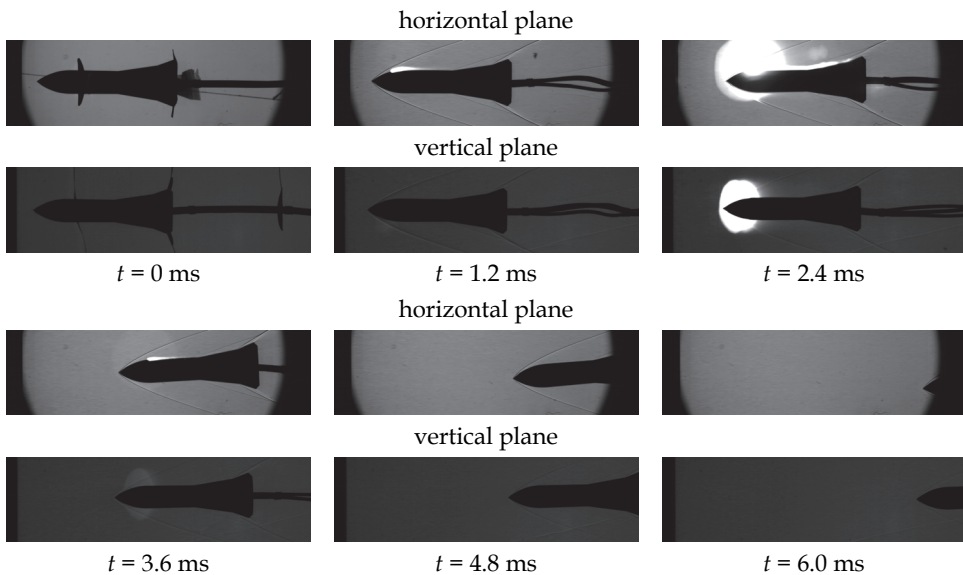


Fig. 29. Visualization of the displacement of the free-flight EFP model subjected to a plasma discharge,  $M = 4.5$ ,  $E = 65$  J (test 07-09-03-25-01)

In Figure 29,  $t = 0$  corresponds to the burst of the diaphragm and the model is hung up in the test chamber. At  $t = 1.2$  ms, the model slightly moves to the right and the plasma discharge is activated on the ogive of the model at the beginning of the free-flight motion. At  $t = 2.4$  ms, i.e. about 1.2 ms after the plasma-discharge activation, the plasma is shown by the glow on the pictures: in the horizontal plane, the plasma is produced on one side of the model and in the vertical plane, the plasma acts symmetrically on the model. Shock-wave

patterns can also be seen, but the detailed structure of the flow field does not appear as it is a simple photograph. At  $t = 3.6$  ms, the plasma extinguishes itself and the model moves in the opposite direction to the plasma. From  $t = 4.8$  ms, the plasma is extinguished and the model continues to move in the opposite direction to the plasma, whereas it keeps its rectilinear trajectory in the vertical plane.

#### 4.4.3 With a plasma discharge, stored energy of 120 J (test 08-09-03-26-01)

The result in Figure 30 is obtained for an energy of 120 J, which is about twice the energy of the previous test, leading to a plasma duration of 4.5 ms.

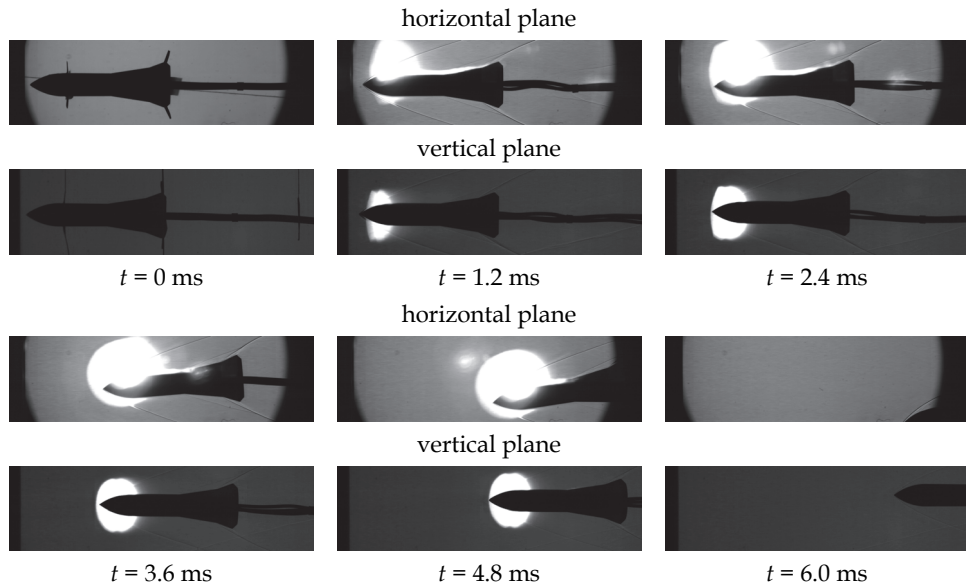


Fig. 30. Visualization of the displacement of the free-flight EFP model subjected to a plasma discharge,  $M = 4.5$ ,  $E = 120$  J (test 08-09-03-26-01)

At  $t = 0$  the model is hung up in the test chamber. At  $t = 1.2$  ms, the model slightly moves to the right and the plasma discharge is activated on the ogive. At  $t = 2.4$  ms, the model begins to deviate from its trajectory in the horizontal plane. From  $t = 2.4$  ms to 4.8 ms, the plasma is delivered to the electrodes with a constant power. In the end ( $t = 6.0$  ms), the plasma is extinguished, the model continues to move in the opposite direction to the plasma, reaching an angle of attack of about  $11^\circ$  and a slight translation is observed in the vertical plane.

#### 4.4.4 Comparison of the results with a plasma discharge

Figure 31 shows the voltage and current measurements recorded during the previous tests demonstrating the correct control of the current delivered to the plasma discharge. The plasma duration is deduced from the current measurement.

Each picture recorded during the tests is analyzed in order to reproduce the displacement of the model tip. A displacement of 45 mm represents 270 pixels in the vertical plane and

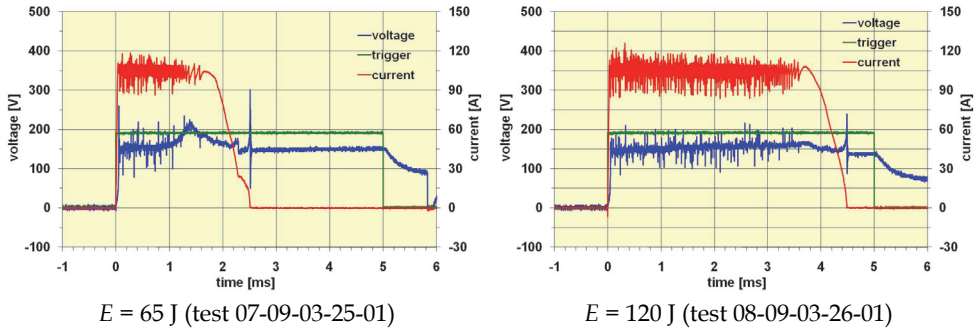


Fig. 31. Voltage and current measurements during the free-flight EFP model subjected to a plasma discharge,  $M = 4.5$

41 mm corresponds to 251 pixels in the horizontal one. An error of less than  $\pm 2$  pixels is estimated for the analysis, leading to a displacement error lower than  $\pm 0.3$  mm. Figure 32 shows the analysis of the displacement in the horizontal and vertical planes for the tests 07 and 08. In the case of the test 08, the lateral displacement is 21 mm for a longitudinal displacement of 86 mm.

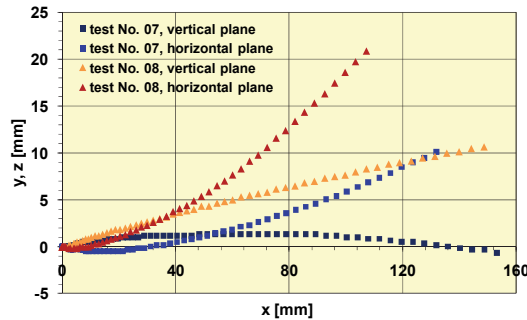


Fig. 32. Displacement measurement during a plasma discharge,  $M = 4.5$  (tests 07-09-03-25-01 and 08-09-03-26-01)

According to results found in the previous Sections concerning the pressure measurements and the pitching-motion analysis, the plasma discharge producing an overpressure on the projectile model leads to a negative angle of attack. Indeed, this overpressure generated by the plasma discharge is mainly located in front of the gravity center of the model, creating a nose-down moment and a lateral displacement opposite to the plasma discharge.

## 5. Conclusion

The ISL wind-tunnel and shock-tube facilities have been used for studying in detail the interaction of a plasma discharge generated on the projectile surface with its supersonic cross-flow by using a low-voltage plasma actuator. A current controller has been developed

in order to generate a power-controlled plasma discharge anywhere on the surface of any aerial vehicle.

Pressure and temperature measurements as well as flow-field visualizations were carried out in the wind tunnel at a Mach number of 3. The plasma discharge was produced on the conical part of a projectile model of a 50 mm diameter in which the plasma actuator was embedded. Flow fields were visualized by means of a CCD camera located behind a differential interferometer or a schlieren method set-up. These measurements and visualizations allowed the analysis of the perturbation evolution along the projectile surface due to the plasma discharge. Some difficulties occurred during the pressure-measurement experiments probably due to the radiation of the plasma; however, the plasma was expected to produce an overpressure. The spectrography technique was used for obtaining the copper spectrum which allowed the determination of the temperature in the plasma plume. The main result was that a maximum temperature of about 12,000 K was obtained 12 mm behind the plasma-discharge generator anode and very near the conical surface.

The wind tunnel was also used for demonstrating that the plasma discharge generated the angular deviation of a 20-mm-caliber fin-stabilized projectile, but the low-voltage plasma actuator was outside the model. For a 243 J stored energy, an angle of attack of  $2.6^\circ$  was reached by means of a power-controlled plasma discharge of 10 kW delivered in 9.7 ms in front of the projectile-model fins. For the same stored energy, a constant angle of attack of  $0.9^\circ$  was reached by means of another power-controlled plasma discharge of 4.5 kW delivered in 25.4 ms at the same location. The efficiency of the actuation system was nearly of 40% to 50%. However, the experiments could not demonstrate that such a plasma discharge induced a significant change in the trajectory of the projectile, because it was fixed at its gravity center. The remaining questions are: "Does this disturbance last long enough to cause the trajectory of the projectile to change?" and "Is the power large enough for a change in the projectile trajectory to take place?" The trajectory change will be computed in the future by running a 3-DoF program which will use data extracted from these experimental results.

The shock tunnel proved to be a facility well adapted to the experimental study of the steering of a supersonic projectile flying under low-atmosphere conditions. Flow-field visualizations showed that a plasma discharge produced on the ogive of a projectile flying at an altitude of 2.5 km and at a Mach number of 4.5 could deviate a projectile from its trajectory. The angular deviation of  $11^\circ$  was demonstrated with a very light flare-stabilized Explosively-Formed-Projectile with the low-voltage plasma actuator mounted outside the shock tunnel.

The studies will continue in wind-tunnel and shock-tube facilities with new surface-pressure measurements with the purpose of confirming the results obtained up to now. Other experiments will be conducted with the aim of increasing the angular deviation of the projectile and of evaluating the trajectory deviation. Some experiments will go on in order to increase the plasma-discharge lifetime, maintaining the angle of attack for a longer duration. New experiments will be carried out, simulating the application of the concept to a spin-stabilized projectile.

The electrodes of such a type of plasma actuator can be mounted anywhere on the projectile surface or embedded in other parts of it, especially in fins, canards, etc. This concept can also be applied to other subsonic, supersonic or hypersonic flying vehicles such as missiles,

UAVs, MAVs, waveriders, etc. However, an optimization phase will be necessary for each application and this is long-term work. This is due to the fact that the resulting aerodynamic forces and moments depend on the Mach number, angle of attack, number of actuators, delivered energy and voltage, actuator location, electrode distance, etc.

## 6. Acknowledgements

The authors thank the Aerodynamics and Wind-Tunnel and the Aerothermodynamics and Shock-Tube Department staff members for their efficiency. In particular, they want to highlight the professionalism of Denis Bidino, Michel Meister and Dominique Willme who allowed the wind-tunnel tests to take place. Myriam Bastide, in charge of the optical visualization, Berthold Sauerwein and Jean-Luc Striby, in charge of the shock tunnel and Remy Kempf as technician, are warmly thanked for the very good quality of the shock-tunnel experiments. Alfred Eichhorn, responsible for the difficult temperature measurements is also associated in our success.

## 7. References

- Asghar, A., Jumper, E.J. & Corke, T.C. (2006). On the Use of Reynolds Number as the Scaling Parameter for the Performance of Plasma Actuator in a Weakly Compressible Flow, AIAA Paper 2006-21
- Balcer, B.E., Franke, M.E. & Rivir, R.B. (2006). Effects of Plasma Induced Velocity on Boundary Layer Flow, AIAA Paper 2006-875
- Berner, C. & Dupuis, A. (2001). Wind Tunnel Tests of a Grid Finned Projectile Configuration, 39<sup>th</sup> Aerospace Sciences Meeting & Exhibit, Reno/NV, USA, January 08-11, AIAA Paper 2001-0105
- Berner, C. & Dupuis, A. (2002). Wind Tunnel Tests of a Long-Range Artillery Shell Concept, AIAA Atmospheric Flight Mechanics Conference and Exhibit, Monterey/CA, USA, August 5-8, AIAA Paper 2002-4416
- Berner, C., Fleck, V. & Dupuis, A. (2002). Experimental and Computational Analysis for a Long-Range Spinning Artillery Shell with Lifting Surfaces, 20<sup>th</sup> International Symposium on Ballistics, Orlando/FL, USA, September 23-27
- Corke, T.C., Cavalieri, D. & Matlis, E.H. (2001). Boundary Layer Instability on a Sharp Cone at Mach 3.5 with Controlled Input, AIAA Journal, Vol. 40, No. 55, pp. 1015-1018
- Corke, T.C., He C. & Patel, M. (2004). Plasma Flaps and Slats: an Application of Weakly-Ionized Plasma Actuators, AIAA Paper 2004-2127
- Corke, T.C., Mertz, B. & Patel, M.P. (2006). Plasma Flow Control Optimized Airfoil, AIAA Paper 2006-1208
- Corke, T.C., Post, M.L. & Orlov, D.M. (2009). Single Dielectric Barrier Discharge Plasma Enhanced Aerodynamics: Physics, Modelling and Applications, *Experiments in Fluids*, Vol. 49, pp. 1-26
- Do, H., Kim, W., Mungal, M. & Capelli, M. (2007). Bluff Body Flow Control Using Surface Dielectric Barrier Discharges, AIAA Paper 2007-0939
- Douville, T., Stephens, J., Corke, T.C. & Morris, S.C. (2006). Turbine Blade Tip Leakage Flow Control by Partial Squealer Tip and Plasma Actuators, AIAA Paper 2006-20

- Dupuis, A. & Berner, C. (2001). Aerodynamic Aspects of a Grid Finned Projectile at Subsonic and Supersonic Velocities, *19<sup>th</sup> International Symposium on Ballistics*, Interlaken, Switzerland, May 7-11
- Dupuis, A., Berner, C. & Fleck, V. (2004). Aerodynamic Characteristics of a Long-Range Spinning Artillery Shell. Part 1: From Aeroballistic Range Free-Flight Tests, *21<sup>st</sup> International Symposium on Ballistics*, Adelaide, Australia, April 19-23
- Eichhorn, A., Mach, H. & Rösch, D. (1998). Optische und spektroskopische Untersuchungen an einem Plasmabrenner mit evakuierbarer Messkammer und Ermittlung der Plasmatemperatur mit Hilfe von Kupferlinien, *ISL Report R 124/98*
- Elias, P.Q., Chanetz, B., Larigaldie, S. & Packan, D. (2007a). Study of the Effect of Glow Discharges Near a  $M = 3$  Bow Shock, *AIAA Journal*, Vol. 45, No. 9, pp. 2237-2245, Sept. 2007
- Elias, P.Q., Chanetz, B., Larigaldie, S., Packan, D. & Laux, C.O. (2007b). Mach 3 Shock Wave Unsteadiness Allevation Using a Negative Corona Discharge, *AIAA Journal*, Vol. 46, No. 8, pp. 2042-2049, Sept. 2007
- Girgis, I.G., Shneider, M.N., Macheret, S.O., Brown, R.B. & Miles, R.B. (2006). Steering Moments Creation in Supersonic Flow by Off-Axis Plasma Heat Addition, *Journal of Spacecraft and Rockets*, Vol. 43, No. 3, pp. 607-613, May-June 2006
- Gnemmi, P. & Seiler, F. (2000). Interaction of a Lateral Jet with the Projectile External Flow, *Atmospheric Flight Mechanics Conference & Exhibit*, Denver/CO, USA, August 14-17, AIAA Paper 2000-4196
- Gnemmi, P., Samirant, M. & Charon, R. (2002). ISL, Saint-Louis, France, French Patent for "Piloteage d'un projectile par décharge plasma," No. 02 12906 filed 17 Oct. 2002, issued 7 Jan. 2005. US Patent for "Projectile Steering by Plasma Discharge," No. US 7,002,126 B2 filed 17 Oct. 2003, issued 21 Feb. 2006
- Gnemmi, P. & Rey, C (2005). ISL, Saint-Louis, France, French Patent for "Nouveau dispositif embarqué de génération de décharge(s) plasma pour le pilotage d'un engin supersonique ou hypersonique," No. 05 09831 filed 27 Sept. 2005, issued 14 Dec. 2007. US Patent for "Low Voltage Device for the Generation of Plasma Discharge to Operate a Supersonic or Hypersonic Apparatus," No. US 11/525,169 filed on 22 Sept. 2006, issued 12 Jan. 2010
- Gnemmi, P. & Schäfer, H.J. (2005). Experimental and Numerical Investigations of a Transverse Jet Interaction on a Missile Body, *43<sup>rd</sup> AIAA Aerospace Sciences Meeting and Exhibit*, Reno/NV, USA, January 10-13, , AIAA Paper 2005-0052
- Gnemmi, P., Eichhorn, A., Leopold, F., Schäfer, H.J., Emunds, H., Esch, H., & Gülhan, A. (2006). Experimental and Computational Study of the Interaction between a Lateral Jet and the Supersonic External Flow on a Generic Missile Body, *NATO-RTO Symposium on Innovative Missile Systems, AVT-135/RSY*, Amsterdam, The Netherlands, May 15-18, ISL report PU 622/2006
- Gnemmi, P., Charon, R., Dupéroux J.P. & George A. (2008) Feasibility Study for Steering a Supersonic Projectile by a Plasma Actuator, *AIAA Journal*, Vol. 46, No. 6, pp. 1308-1317

- Gnemmi, P. & Rey C. (2008). Plasma Actuation for the Control of a Supersonic Projectile, *Atmospheric Flight Mechanics Conference & Exhibit*, August 18-21, 2008, Honolulu, Hawaii, AIAA Paper 2008-6885
- Gnemmi, P. & Rey C. (2009). Plasma Actuation for the Control of a Supersonic Projectile, *AIAA Journal of Spacecraft and Rockets*, Vol. 46, No. 5, pp. 989-998, Sep.-Oct. 2009
- Gnemmi, P., Srulijes, J. & Seiler, F. (2011). Overview of Activities at the ISL Hypersonic Shock Tunnels, *Int. J. Engineering Systems Modelling and Simulation*, Vol. 3, Nos. 1/2
- Goeksel, B., Rechenberg, I., Greenblatt, D. & Paschereit, C. (2006). Steady and Unsteady Plasma Wall Jets for Separation and Circulation Control, AIAA Paper 2006-3686
- Havermann, M., Seiler, F., Ende, H. & George, A. (2004). Untersuchungen im Stossrohr-Windkanal zur Steuerung eines Hochgeschwindigkeits-Flugkörpers mit Seitenstrahlen, ISL report RV 232/2004
- Huang, J. (2005). Documentation and Control of Flow Separation on a Linear Cascade of Pak-B Blades Using Plasma Actuators, *Dissertation*, University of Notre Dame
- Huang, J., Corke, T.C. & Thomas, F.O. (2006a). Plasma Actuators for Separation Control of Low Pressure Turbine Blades, *AIAA Journal*, Vol. 44, No. 1, pp. 51-57, January 2006
- Huang, J., Corke, T.C. & Thomas, F.O. (2006b). Unsteady Plasma Actuators for Separation Control of Low-Pressure Turbine Blades, *AIAA Journal*, Vol. 44, No. 7, pp. 1477-1483, July 2006
- Kosinov, A, Maslov, A & Shevelkov, S (1990). Experiments on the Stability of Supersonic Laminar Boundary Layers, *Journal of Fluid Mechanics*, pp. 219: 621
- Kuo, S.P. (2007). Plasma Mitigation of Shock Wave: Experiments and Theory, *Shock Waves*, Vol. 17, pp. 225-239
- Massey, K.C., McMichael, J., Warnock, T. & Hay, F. (2004). Design and Wind Tunnel Testing of Guidance Pins for Supersonic Projectiles, Georgia Inst. of Technology / GTRI / ATAS Report, Atlanta/GA, USA, Dec. 2004
- Matlis, E.H. (2004). Controlled Experiments on Instabilities and Transition to Turbulence on a Sharp Cone at Mach 3.5. *Dissertation*, University of Notre Dame
- Nelson, C., Cain, A., Patel, M. & Corke, T.C. (2006). Simulation of Plasma Actuators Using the Wind-US Code, AIAA Paper 2006-634
- Nelson, R., Corke, T.C., Patel M. & Ng, T. (2007). Modification of the Flow Structure over a UAV Wing for Roll Control, AIAA Paper 2007-0884
- Oertel, H. (1966). *Stossrohre*, Springer Verlag, Wien-New York, Austria
- Patel, M.P., Prince, T.S., Carver, R., DiCocco, J.M., Lisy, F.J. & Ng, T.T. (2002). Deployable Flow Effectors for Phantom Yaw Control of Missiles at High Alpha, *1<sup>st</sup> Flow Control Conference*, St.-Louis/MO, USA, June 24-26, AIAA Paper 2002-2827
- Patel, M.P., Sowle, Z.H., Corke, T.C. & He, C. (2006). Autonomous Sensing and Control of Wing Stall Using a Smart Plasma Slat, AIAA Paper 2006-1207
- Patz, G. (1970). Das Hyperschallstossrohrlabor des ISL, 3. Teil: Stossrohr B, *ISL Report N 30/70*
- Patz, G. (1971). Das Hyperschallstossrohrlabor des ISL, 2. Teil: Stossrohr A, *ISL Report N 27/71*
- Porter, C., McLaughlin, T., Enloe, L. & Font, G. (2007). Boundary Layer Control Using DBD Plasma Actuator, AIAA Paper 2007-0786



- Post, M.L. (2004). Plasma Actuators for Separation Control on Stationary and Unstationary Airfoils, *Dissertation*, University of Notre Dame
- Post, M.L. & Corke, T.C. (2004a). Separation Control Using Plasma Actuators - Stationary and Oscillatory Airfoils, AIAA Paper 2004-0841
- Post, M.L. & Corke, T.C. (2004b). Separation Control on High Angle of Attack Airfoil Using Plasma Actuators, *AIAA Journal*, Vol. 42, No. 11, pp. 2177-2187, November 2004
- Rivir, R. (2007). Effects of Pulsed dc Discharge Plasma Actuators in a Separated LPT Boundary Layer, AIAA Paper 2007-0942
- Rizzetta, D. & Visbal, M. (2007). Numerical Investigation of Plasma-Based Flow Control for a Transitional Highly-Loaded Low-Pressure Turbine, AIAA Paper 2007-0938
- Rondot, F & Berner, C. (1998). Performance of Aerodynamically Optimized EFP Simulants, *17<sup>th</sup> International Symposium on Ballistics*, Midrand, South Africa, March 23-27
- Schäfer, H.J., Augenstein, E., Esch, H. & Emunds, H. (2001). Experimental Investigation of Transverse Jet Interaction on a Missile Body Using Laser Velocimetry and Flow Visualization," *IEEE Xplore Digital Library, 19<sup>th</sup> International Congress on Instrumentation in Aerospace Simulation Facilities*, Cleveland/OH, USA, August 27-30
- Seiler, F., Gnemmi, P., Ende, H., Schwenger, M. & Meuer R. (2003). Jet Interaction at Supersonic Cross-Flow Conditions," *Shock Waves*, Vol. 13, No. 1, pp. 13-23, July 2003
- Shneider, M.N., Macheret, S.O., Zaidi, S.H., Girgis, I.G. & Miles, R.B. (2008). Virtual Shapes in Supersonic Flow Control with Energy Addition, *Journal of Propulsion and Power*, Vol. 24, No. 5, pp. 900-915, Sept.-Oct. 2008
- Silton, S.I. (2004). Comparison of Predicted Actuator Performance for Guidance of Supersonic Projectiles to Measured Range Data, *22<sup>nd</sup> Applied Aerodynamics Conference and Exhibit*, Providence/Rhode Island, USA, August 16-19, AIAA Paper 2004-5195
- Smeets, G. & George, A. (1978). Instantaneous Laser Doppler Velocimeter Using a Fast Wavelength Tracking Michelson Interferometer, *Rev. Sci. Instrumentation*, Vol. 49, No. 11, pp. 1589-1596
- Smeets, G., Patz, G., Srulijes, J., Seiler, F. & Havermann, M. (1980-2009). Software Codes Developed in the Shock-Tube Laboratory of ISL
- Smeets, G. (1990). Interferometry, ISL Report CO 214/90, May 1990
- Srulijes, J., Seiler, F., Hennig, P. & Gleich, P. (2004). Visualisierung der Umströmung von Lenkflügeln im Stoßrohr-Windkanal bei realen atmosphärischen Strömungsbedingungen, ISL report RV 229/2004
- Suzen, Y., Huang, G. & Ashpis, D. (2007). Numerical Simulations of Flow Separation Control in Low-Pressure Turbines Using Plasma Actuators, AIAA Paper 2007-0937
- Thomas, F.O., Kozlov, A. & Corke, T.C. (2006). Plasma Actuators for Bluff Body Flow Control, AIAA paper 2006-2845
- Van Ness, D.K., Corke, T.C. & Morris, S.C. (2006). Turbine Tip Clearance Flow Control Using Plasma Actuators, AIAA Paper 2006-21
- Visbal, M.R. & Gaitonde, D.V. (2006). Control of Vortical Flows Using Simulated Plasma Actuators, AIAA Paper 2006-505

- Wey, P., Berner, C., Sommer, E., Fleck, V., & Moulard, H. (2005). Theoretical Design for a Guided Supersonic Projectile, *22<sup>nd</sup> International Symposium on Ballistics*, Vancouver, BC, Canada
- Yamanaka, T. & Tanaka, H. (1996). "Effects of Impulsive Thruster on Exterior Ballistics Accuracy Improvement for a Hypervelocity Rocket, *16<sup>th</sup> International Symposium on Ballistics*, San Francisco/CA, September 23-27

# Wind Tunnel Experiments for Supersonic Optical-electrical Seeker's Dome Design

Qun Wei, Hongguang Jia, Ming Xuan and Zhenhai Jiang  
*Changchun Institute of Optics, Fine Mechanics and Physics  
China*

## 1. Introduction

Missiles play a more and more important role in the modern wars. The seeker is the most important sub-system of a guided missile. As long as the development of optics, most missiles use optical-electrical seekers. This kind of seeker has plenty of benefits such as high resolving power, anti-camouflage and low cost. Optical guided missile has a optical dome which plays a very important role on the seeker system. The seeker's dome has two jobs: first, it is the first element of the imaging system, so the dome should have good optical performance; second, it protects the sensitive optical, detector, and processor components of the missile seeker from hostile environments such as rain, sand, or large temperature gradients. When missile flies at supersonic, the aero load has serious impacts on seeker's dome. These loads mainly include aerodynamic, aero-thermodynamic, turbulence around the dome and aero vibration. The aerodynamic and aero-thermodynamic make the dome's shape change. The aero-thermodynamic causes heat barrier. And the turbulences and aero vibration make the image dithering and blur. Because all of the above effects are important for dome design, the study of this chapter is necessary. The study of domes has begun for many years, scientists got a lot of achievement in this field. The research is mainly divided into three parts: materials and fabrication[1,2], test and measurement[3,4], aerodynamic and aerothermal[5,6]. For recent years, there is a new branch of optics : conformal optics[7]. Conformal optical systems are characterized as having external optical surfaces that are optimized for non-optical system requirements. This typically implies blending smoothly with a host platform to achieve an optimum shape. Although the open literature provides extensive discussions on current developments in conformal system design, little information is available to study the conformal seeker's dome wind tunnel experiments. This chapter describes a method for researching the supersonic dome's aero-optical phenomena and their influences on optical image by wind tunnel experiments. Combined with thrice wind tunnel experiments and CFD (computational fluid dynamics) numerical simulation, this chapter studies the aerodynamic, aero-thermodynamic and the turbulent of the dome's out surface when it flies at supersonic speed. Then, by using the wind tunnel experiments results, the seeker's image which is affected by missile flies at supersonic speed is studied. After analyzing the results, the conclusion will be the fundamentals to design future domes. The straight matter describes the methods of wind tunnel experiments, and it is divided into three parts.

Part one: simulated spherical dome wind tunnel experiment study. Most traditional seeker's dome's shape is spherical, so we study its aero-optical effects by wind tunnel experiment first. A model with spherical dome is designed for CFD simulation. After the CFD simulation, all kinds of parameters such as the dome's surface pressure and temperature field are got. Using these results, we analyze their influents on seeker's imaging. Then, the wind tunnel model is made with the same shape of the CFD simulation model. The wind tunnel experiment is done with this model at different kinds of speed and attack angles. After the experiment, actual pressure field of the dome's surface and schieren photography around the dome are got. Comparing the wind tunnel results and the simulation results, the veracity of the simulation is 90% at average. These two kinds of results are all used to analyze seeker's image influenced by aero-optical phenomena.

Part two: simulated conformal dome wind tunnel experiments study. Along with the development of optical design, optical fabrication and optical test technologies, the new conformal dome will be instead of the traditional spherical dome. This part will study the conformal dome's aero-optical effects caused by missile flies at supersonic speed, and its influences on seeker's image. A model for both CFD simulation and wind tunnel experiments used is designed. The CFD simulation is as same as what have done in part one. The simulation results are prepared for further use. The wind tunnel experiments are done at another wind tunnel. This wind tunnel has bigger experiment part then the one used in part one. Besides that, the wind tunnel models are different too. One model is designed for dome's surface pressure field along with time test experiments, and the other one is designed for dome's surface temperature field along with time test experiments. Wind tunnel experiments are done with different speed and attack angles for both models. The results together with the simulation results got before are used for coupling simulation FEA software. After analyzing and computing, the conformal dome's aero-optical effects are studied, and based on that the MgF<sub>2</sub> dome and the seeker shell are designed.

The last part of this chapter is conclusion, and some discussion about future dome design.

## 2. Simulated spherical dome wind tunnel experiments study

Most optical guided missiles use spherical domes, so the first wind tunnel experiment is about spherical dome. The purpose of this wind tunnel experiment is to value the veracity of CFD simulation compared with wind tunnel experiments and to find a way to analysis how the shock wave affect the seeker's dome and optical system.

### 2.1 Model definition

The model of CFD and wind tunnel should be the same, and for this study dome is the only one who will be studied. So the model is designed like below. The model is composed by

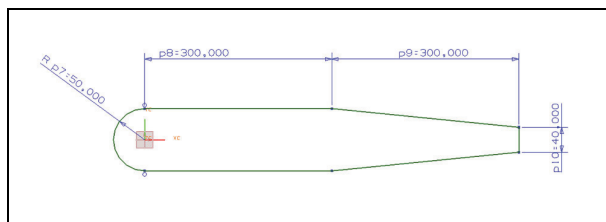


Fig. 1. CFD simulation model

three parts. The first part is half of a spherical, and the diameter of the spherical is 100mm. The second part is a column, and its diameter is 100mm with a length of 300mm. The last part is a round platform. The model is shown in figure 1. The first part is the simulated dome, and the last two parts represent body. The wind tunnel model is made by 30CrMnSiA as in figure 2.



Fig. 2. Wind tunnel model

## 2.2 Grid generation

The first step to build the grid is to define the outflow area of the model. The outflow figure is shown in figure 3.

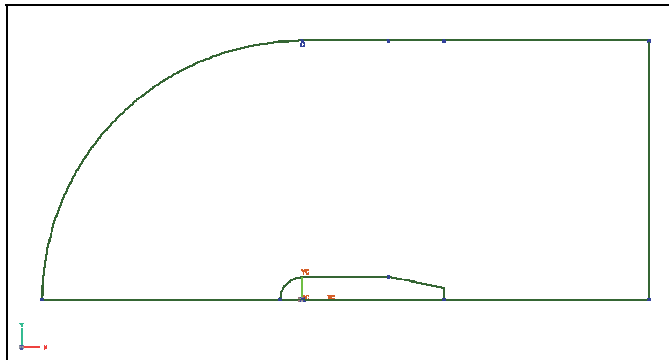


Fig. 3. The outflow of the dome

For compare, there are four kinds of grid used in this simulation. First, the structure grid is used for the dome's grid as in figure 4. The black part is the dome and the body. The yellow grid is symmetry boundary, and the red grid is outflow. And the un-structure grid, mix grid and polyhedra grid are shown in figure 5 figure 6 and figure 7.

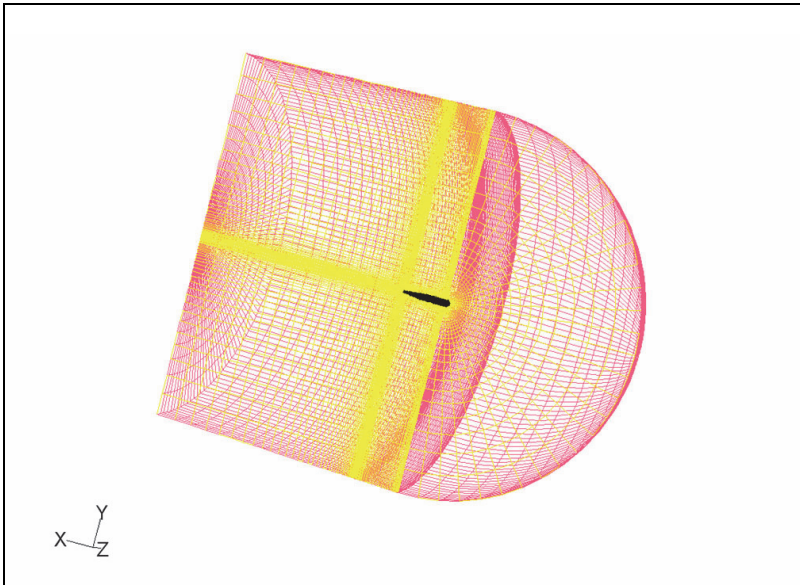


Fig. 4. Grid of the simulation dome outflow

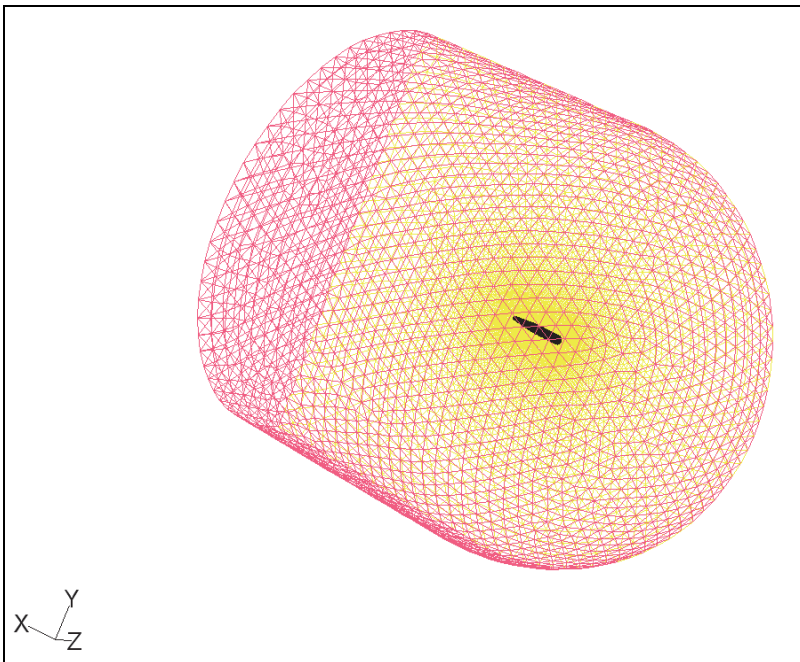


Fig. 5. Un-structure grid

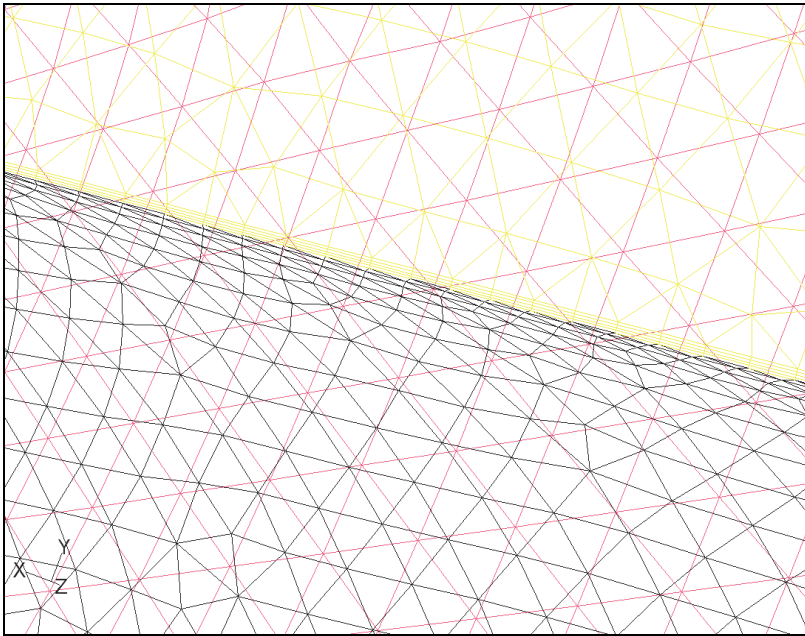


Fig. 6. Mix grid

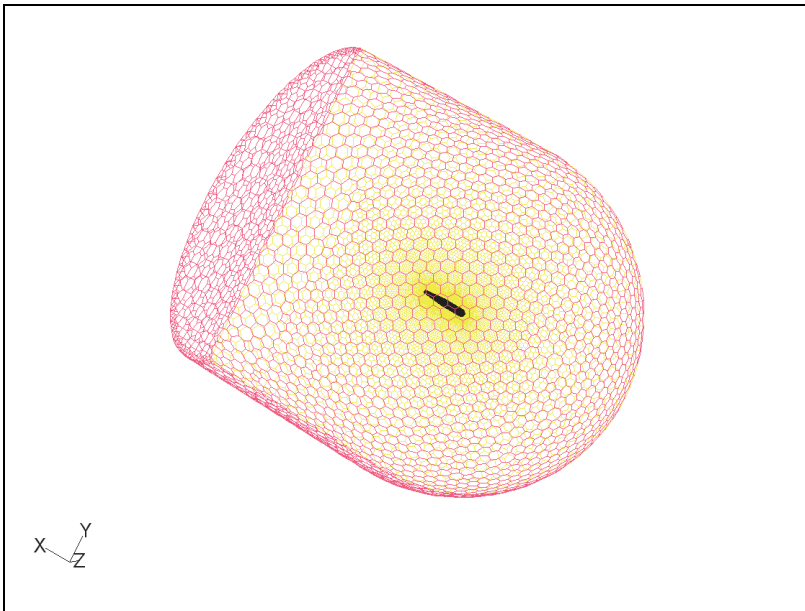


Fig. 7. Polyhedra grid

### 2.3 CFD setup

The flow solver uses a finite-volume technique with multi-zone method to solve multi-dimensional flow in a body-fitted grid system[8]. The blending of density- and pressure-based numerical methodology in the code allows efficient computation of compressible flow regimes. For turbulent flow computations, the Partially-Average Navier-Stokes (PANS) technique was implemented in the  $k-\epsilon$  model[9,10].

### 2.4 Wind tunnel experiment

The wind tunnel experiment is done in trisonic wind tunnel of China Academy of Aerospace and Aerodynamics (CAAA). This wind tunnel is an intermittent semireturn type with Mach number ranging from 0.4 to 4.5. The cross area of the test section is  $0.6\text{m}\times 0.6\text{m}$  and the length is 1.575m. The flow quality in the wind tunnel is satisfactory and completely up to the national standards of high speed wind tunnel. This tunnel has steady performance characters[11]. The experiment is shown in figure 8. The model is fixed on the "force-balance" and can be seen through the view window.



Fig. 8. Spherical dome wind tunnel experiment

## 2.5 Results

### 2.5.1 wind tunnel experiment data processing and precision

On the assumption that the air flow from front area to experiment area is isentropic process. So the total pressure and total temperature of experiment area are equal to front area. The effects of the wind tunnel model and balance's self weigh has been modified. The RMS random error is shown in table 1.

### 2.5.2 Wind tunnel results and analysis

As the data of the wind tunnel experiments are a great many, the data is shown in figures. Normal force coefficient with attack angle is shown in figure 9.



$\epsilon_{\alpha}$	$\epsilon_{cn}$	$\epsilon_{caf}$	$\epsilon_{cab}$
$\pm 0.02^{\circ}$	$\pm 0.0010$	$\pm 0.0050$	$\pm 0.0060$
$\epsilon_{Cz}$	$\epsilon_{mz0}$	$\epsilon_{my0}$	$\epsilon_{mx}$
$\pm 0.0020$	$\pm 0.0005$	$\pm 0.0005$	$\pm 0.0004$

Table 1. RMS random error

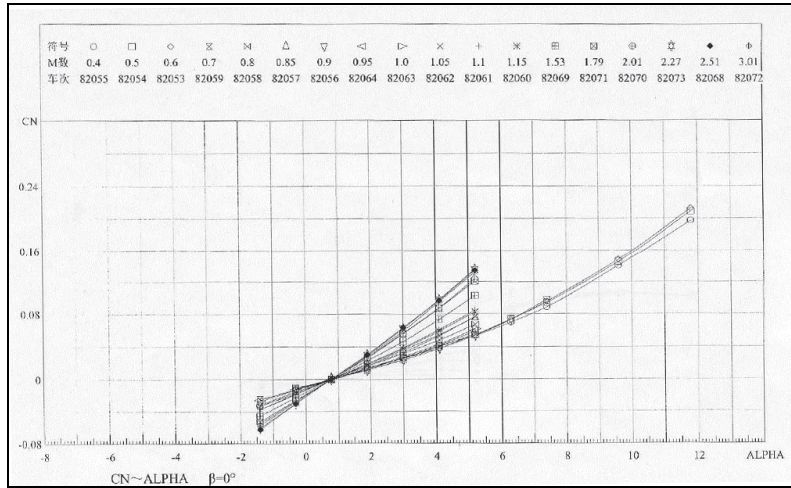


Fig. 9. Normal force coefficient with attack angle

Normal force coefficient with Mach number is shown in figure 10.

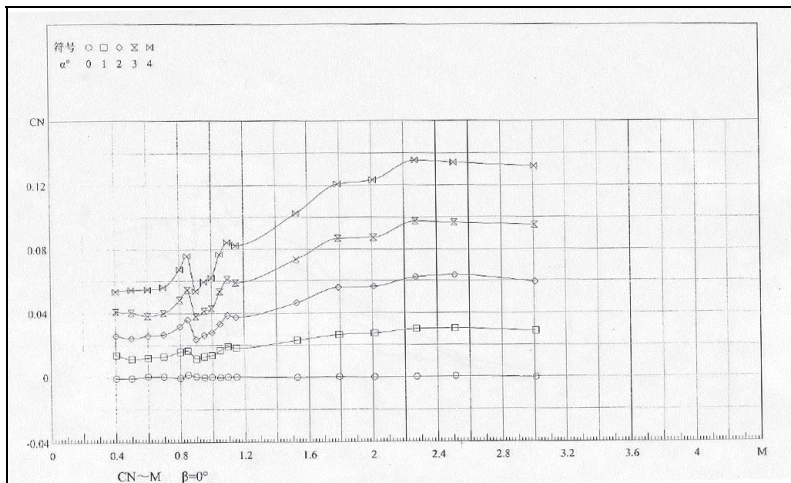


Fig. 10. Normal force coefficient with Mach number

Lengthwise pressure centre coefficient is shown in figure 11.

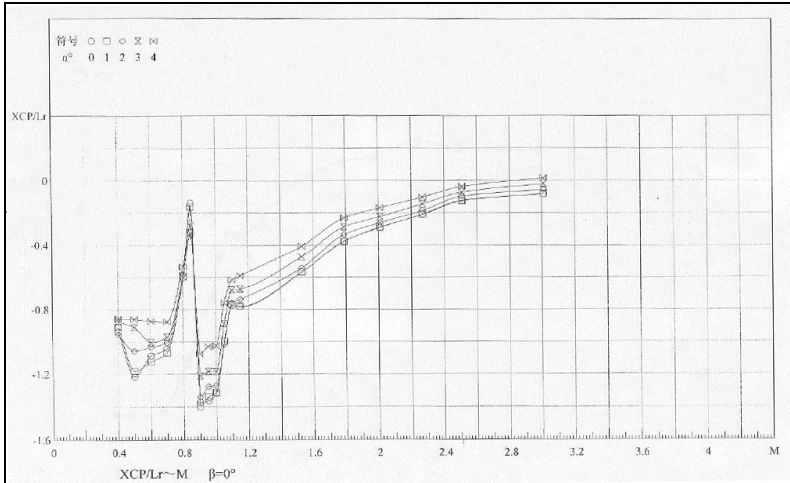


Fig. 11. Lengthwise pressure centre coefficient

Front axial force coefficient is shown in figure 12.

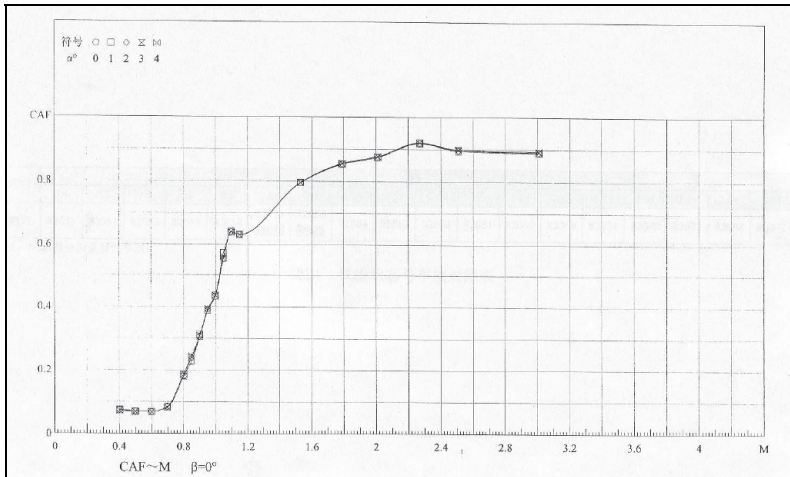


Fig. 12. Front axial force coefficient

**2.5.3 CFD results**

There are four kinds of grid. The first step is to value which kind of grid is more suitable for this dome CFD simulation. The drag comparison table is shown in table 2.

Compared with the wind tunnel experiments' result, the structure grid is more suitable for this kind of simulation. Then using the structure grid, more CFD simulations have been done. And we can get the precision of CFD simulation. The comparison table is shown in table 3.

Speed (Ma)	0.6	0.95	1.5	2	2.6
Structure grid	12.915	109.535	486.925	950.299	1625.430
Un-structure grid	26.973	138.798	509.046	969.552	1704.025
Mix grid	30.069	158.682	508.339	978.657	1708.466
Polyhedra grid	17.373	111.899	501.365	970.484	1672.004

Table 2. Drag comparison table

		CFD	Wind tunnel	error
0.4Ma 4°	Drag	74.6	70.5	5%
	Lift	289.9	272.3	6%
	Pressure centre	1306	1418	7.8%
0.6Ma 6°	Drag	169.3	149.4	13%
	Lift	1016.6	982.9	3.5%
	Pressure centre	1362	1448	6%
0.8Ma 8°	Drag	308.1	272.7	13.2%
	Lift	2643.2	2569.1	2.9%
	Pressure centre	1526	1457	4.5%
1.1Ma 4°	Drag	1367.9	1164.5	17%
	Lift	2815.4	2640.7	6%
	Pressure centre	1561	1408	10%
1.5Ma 0°	Drag	2619.4	2289.3	14%
	Lift	-43	0	-
	Pressure centre	1182	1294	9%
2Ma 2°	Drag	4349.9	4154.2	3.8%
	Lift	2198.3	2594.6	15%
	Pressure centre	1528	1434	6.5%
2.5Ma 5°	Drag	6374.3	6260.2	0.98%
	Lift	8220.2	8462.9	2.9%
	Pressure centre	1497	1462	2.4%
3Ma 10°	Drag	8372.5	8591.5	2.5%
	Lift	23255.2	23469.4	0.9%
	Pressure centre	1529	1471	3.9%

Table 3. CFD and wind tunnel experiments comparison table

The biggest error is the drag value at Mach 1.1 attack angle 4°, and the best CFD simulation is the lift value at Mach 3 attack angle 10°. The average drag error is 8.685%, the average lift value is 5.314%, and the average pressure centre value is 6.263%. According to these results, the CFD simulation is good enough for dome design.

#### 2.5.4 CFD contours

In this experiment, the outline of shock wave can be seen clearly, and accurate aerodynamic force of all kinds of flight conditions are obtained. The comparison of the shock wave, which is shown in Figure 13, can prove the simulation is accurate. After this experiment, the density field of the outflow can be obtained.

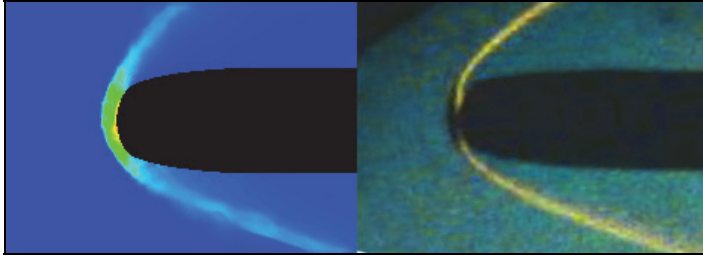


Fig. 13. Shock wave comparison figure

## 2.6 Equivalent lens design

The Lorentz-Lorentz formula provides a bridge linking Maxwell's electromagnetic theory with the micro substances[11]. The relationship between the flow-field density  $\rho$  and the refractive index  $n$  is modeled by[12]:

$$\left( \frac{n^2 - 1}{n^2 + 2} \right) \frac{1}{\rho} = \frac{2}{3} K_{GD} \quad (1)$$

Here  $K_{GD}$  is the G-D constant. Generally, the refractive index of air relies on the density in normal temperature. If the temperature is very high, the index of refraction will be dependent mainly on the temperature and components of fluids. This paper neglects the influences of aerodynamic heating and ionization on the index and considers only the effects of varying flow densities on the refractive index. Because the index of normal airflow is approximately equal to 1, the G-D relationship can be gained by the following:

$$n = 1 + K_{GD}\rho \quad (2)$$

Where  $\rho$  is the local density of outflow, and for visible light  $K_{GD}$  is 0.22355[13]. Using the formula above, the refractive index of the outflow can be obtained accurately. The density field calculated by CFD is discrete, so the refractive index of outflow is discrete too. In that case, the refractive index is divided into three zones, and each of them has an equal refractive index. The figure 14 shows the refractive index zones by different colors.

Through the key points' coordinates, the formulas of the two boundaries can be calculated. Together with the refractive index, the two equivalent lenses are gotten. The inside lens (the red zone in the above figure) has a refractive index of 1.004, 52.535702mm for radius and its thickness is 2.535702mm. The outside lens (the yellow zone)'s refractive index is 1.010 with the radius is 57.804844mm and the thickness is 5.269142mm.

## 2.7 Conclusions

In this section, the spherical dome wind tunnel experiments have been done. By comparing the result of CFD simulation and wind tunnel experiments, we can get that the average drag error is 8.685%, the average lift error is 5.314%, and the average pressure centre error is 6.263%. The shock wave figures which are got from wind tunnel experiments and CFD simulation are nearly the same. By using these results, the equivalent lens is designed for missile's dome design.

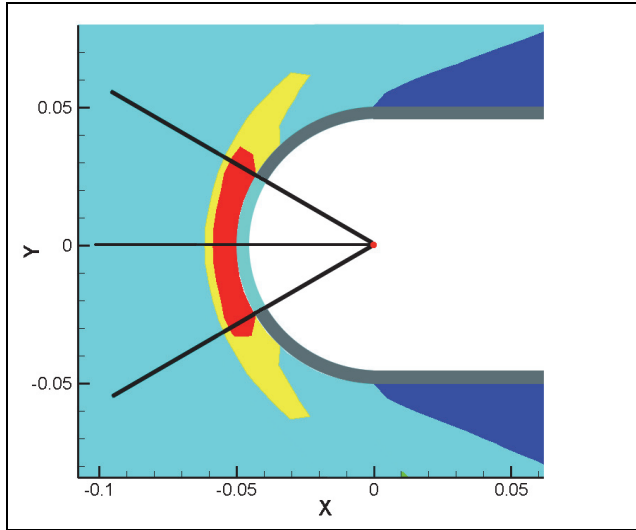


Fig. 14. The refractive index zones. The black lines are line of sight.

### 3. Simulated conformal dome wind tunnel experiments study

#### 3.1 Background

Conformal optics systems contain optical components such as windows or domes that a shape which reduces the effect of the atmosphere on system aerodynamic, mechanical, electrical or thermal performance. The most obvious application concept is that of a missile nose cone. Traditional missiles use a flat or spherical window covering an optical tracker or seeker. Neither of these shapes interacts well with the high-speed airflow across the front end of the missile. An optimum shape would be given by a vonkaiman tangent ogive, which provides a minimum drag front end to the airflow. Between the blunt spherical shape and the pointed ogival shape there is a continuum of shapes that permit reduced drag but do produce a range of optical aberration effects that must be compensated by elements following the missile front end window.

The conformal dome has so many benefits, but there are some problem which should be considered first. When the missile flies at supersonic speed, the aerodynamic will make the dome's shape change. Not only must the dome withstand high pressure and forces of hundreds of pounds during the high speed flight of the missile, it must also withstand severe thermal gradients from the increases in temperature at these speeds. The elevated temperatures heat the dome surface while the interior of the dome remains at a lower temperature, which causes thermal stress across the dome interior. The capability of the dome to withstand thermal stress is very important for dome design. So the conformal dome wind tunnel experiments are done to value how the aerodynamic and thermal affect the conformal dome.

#### 3.2 Wind tunnel experiment model

The aim of this wind tunnel experiment is not the same as the spherical dome wind tunnel experiments. Differently, the aim of this wind tunnel experiment is to get the pressure and

temperature of the conformal dome surface. Because the way to measure the pressure and temperature is different, this wind tunnel experiment is divided into two parts. So the first model is design for pressure measurement. The figure of pressure measurement model is shown in figure 15.

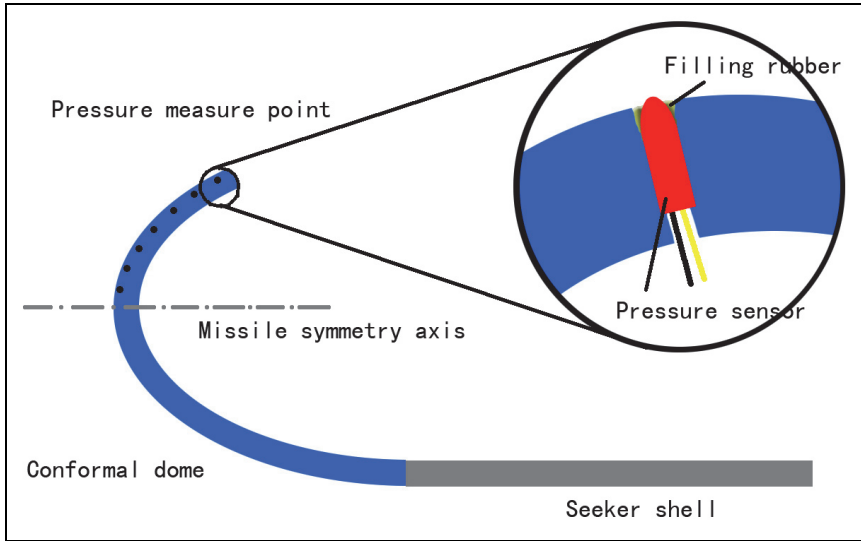


Fig. 15. Pressure measure model figure

The position of the pressure measure point is shown in figure 16.

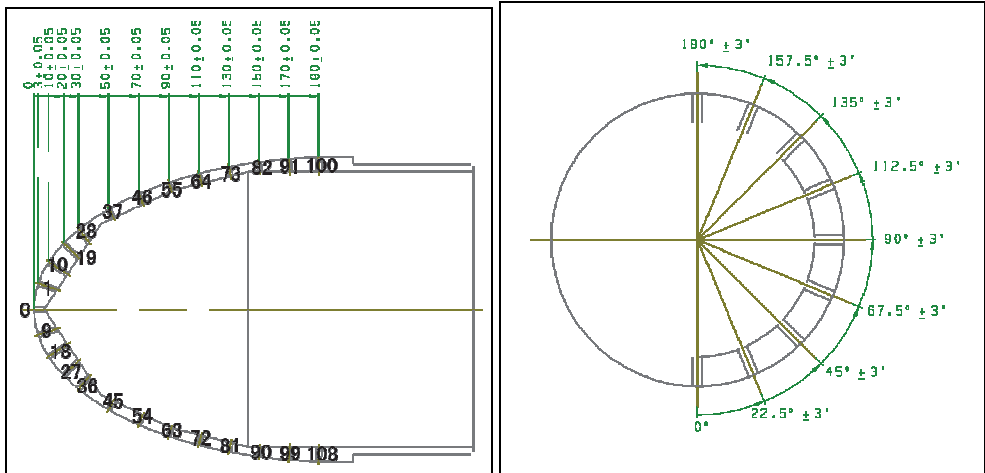


Fig. 16. The position of pressure measure points

The model is designed as above figure, and made by 30CrMnSiA. The wind tunnel model is shown in figure 17.

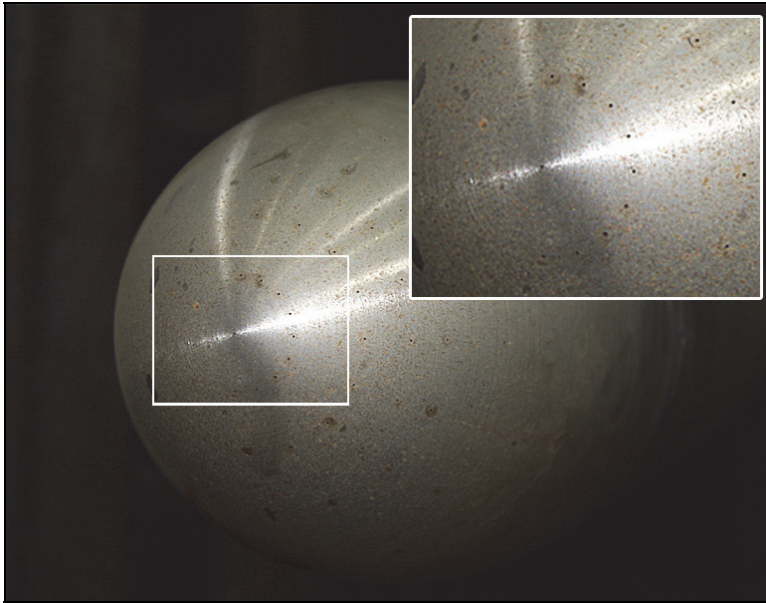


Fig. 17. Pressure measure wind tunnel experiment model

The same as pressure measure model, the temperature measure model is designed as in figure 18.

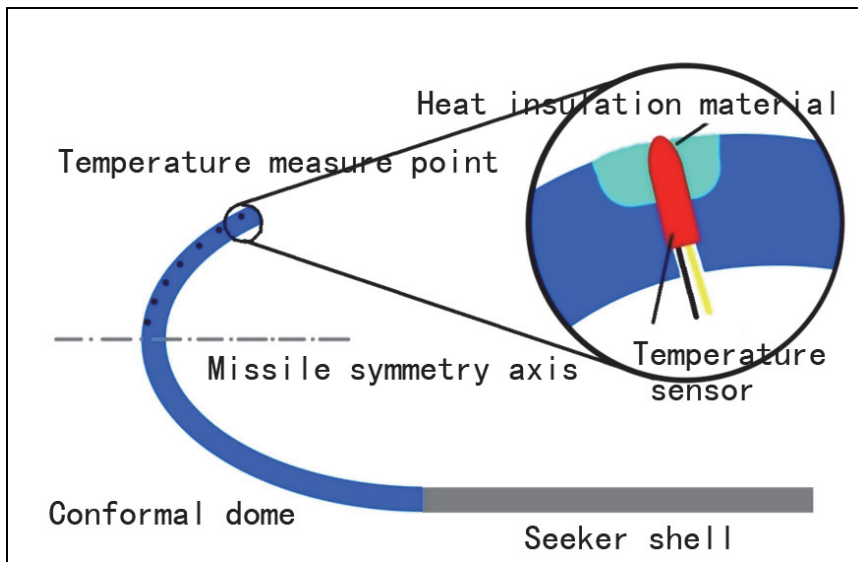


Fig. 18. Temperature measure wind tunnel model

The position of temperature measure point is shown in figure 19.

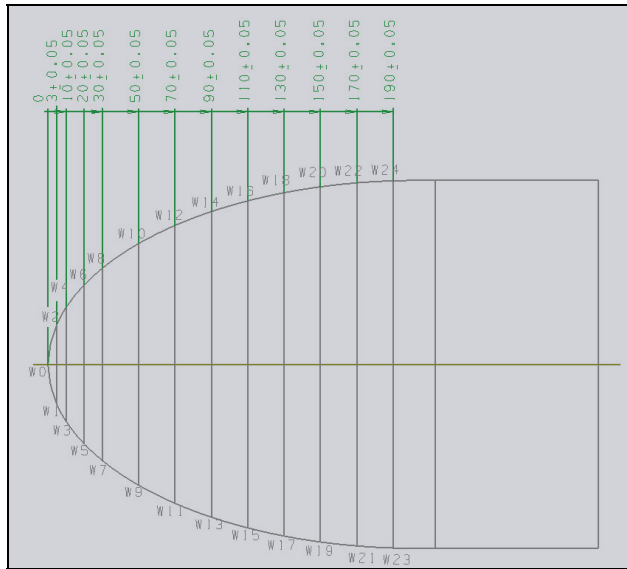


Fig. 19. The position of temperature measure point

The temperature measure wind tunnel experiment model is made by 30CrMnSiA, and shown in figure 20.



Fig. 20. Temperature measure wind tunnel model

### 3.3 CFD model and grid generation

According to the wind tunnel model above, the CFD model for simulation is designed and shown in figure 21.



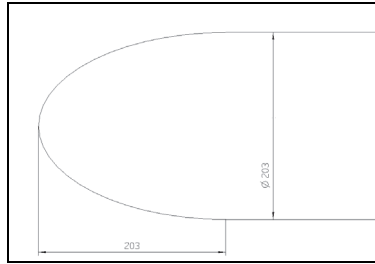


Fig. 21. CFD simulation model

The structure grid generation of the conformal dome surface is shown in figure 22.

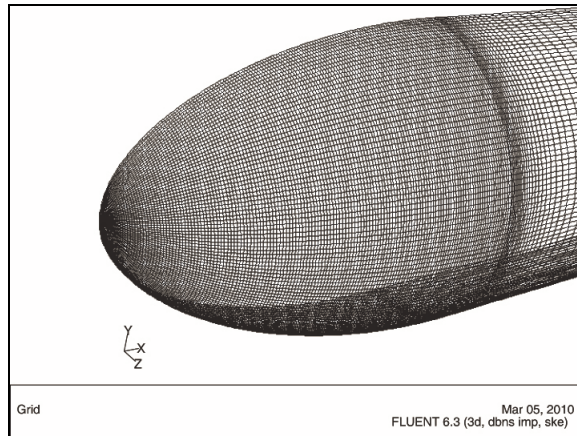


Fig. 22. Conformal dome surface grid

The outflow grid is shown in figure 23.

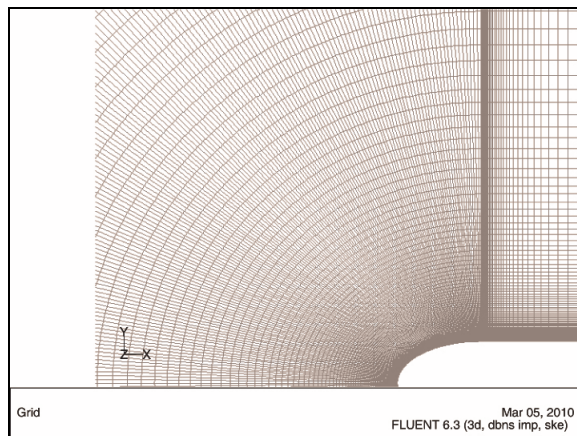


Fig. 23. The outflow grid

### 3.4 Wind tunnel experiments

#### 3.4.1 Pressure measure wind tunnel experiment

This wind tunnel experiment is get the pressure distributing of the conformal dome's surface. The flight condition is according the missile's attacking mission. So the wind tunnel experiments are taken at Mach number 2, 2.5 and 3. The attack angles are  $0^\circ$ ,  $10^\circ$ ,  $20^\circ$  and  $25^\circ$ . The wind tunnel experiment photo is shown in figure 24.

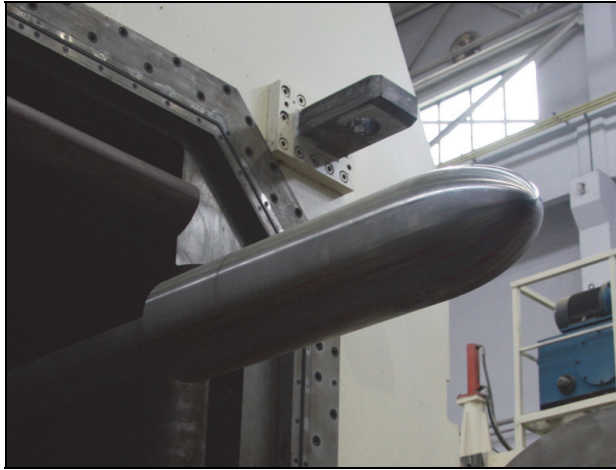


Fig. 24. Pressure measure wind tunnel experiment

#### 3.4.2 Temperature measure wind tunnel experiment

Temperature measure wind tunnel experiment is taken as the same condition as the pressure measure wind tunnel experiment. The wind tunnel experiment photo is shown in figure 25.



Fig. 25. Temperature measure wind tunnel experiment

### 3.5 Results

#### 3.5.1 CFD simulation results

The pressure data of conformal dome surface will be discussed later together with the real wind tunnel data. The figure of static pressure is shown in figure 26. The attack angle are 10°, 20°, 30° and 40°.

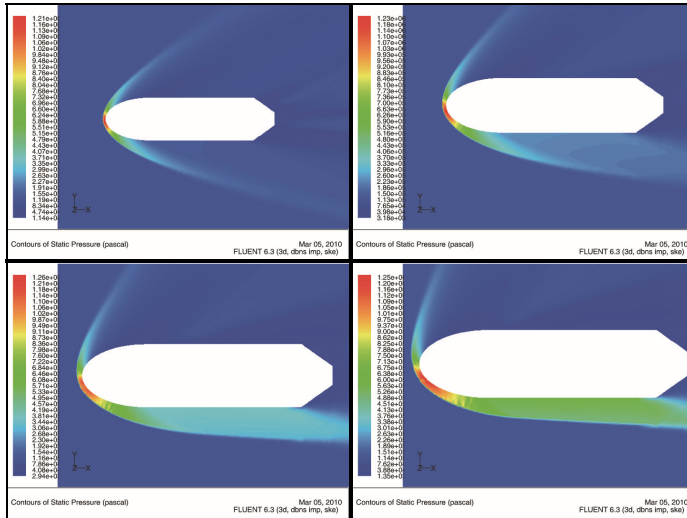


Fig. 26. Static pressure contour

Studying the figure above, it is clearly seen that when missile flies at one speed such as 3Ma the angle between shock wave and the missile body is becoming smaller when the attack angle goes higher. The high pressure zone(the red and orange aera) gets larger. The windward surface and the leeward surface are under different pressure load, so it is very important to consider this uneven force in conformal dome design section. The static temperature figure is shown in figure 27. The attack angle is 20°, and the mach number is 2, 2.5, and 3.

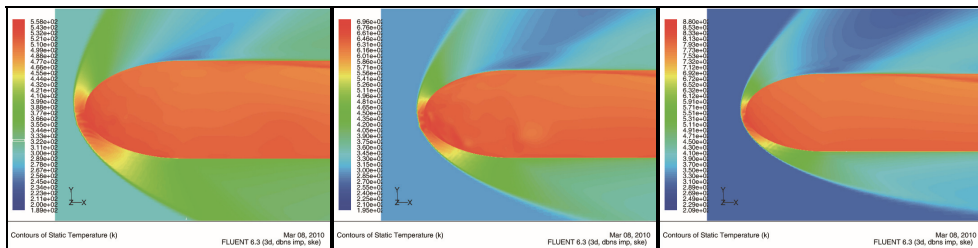


Fig. 27. Static temperature contour

#### 3.5.2 Wind tunnel results

The conformal dome surface pressure data of 2Ma is shown in figure 28. The attack angles are 0°, 10°, 20° and 25°.

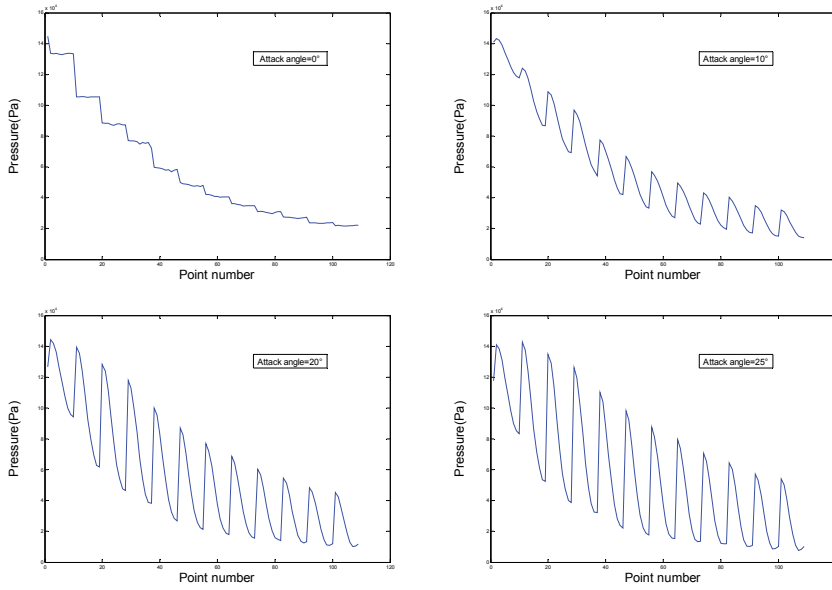


Fig. 28. Conformal dome surface pressure data of 2Ma

The data of 2.5Ma is shown in figure 29. The attack angle is the same as 2Ma.

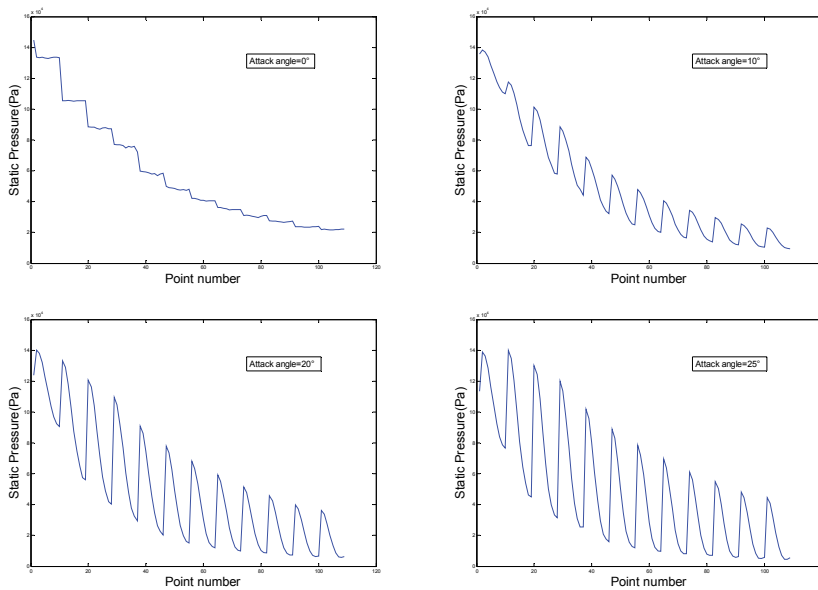


Fig. 29. Conformal dome surface pressure data of 2.5Ma

The data of 3Ma is shown in figure 30.

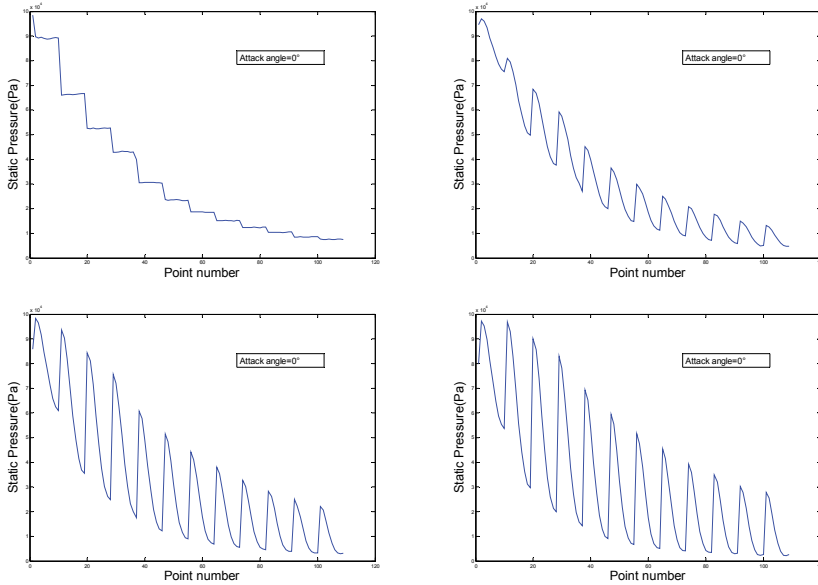


Fig. 30. Conformal dome surface pressure data of 3Ma

The wind tunnel data is used for conformal dome design. The surface pressure is the input parameter of FEA. The surface pressure data is used to calculate the distortion of the conformal dome when it is under great load of outflow. But wind tunnel data can not provide all point value of pressure on the dome's surface. So CFD simulation data is used when the wind tunnel data is not enough. In this situation, the accuracy of CFD simulation becomes significant in this study. In the above part, the accuracy of force is discussed. The pressure of

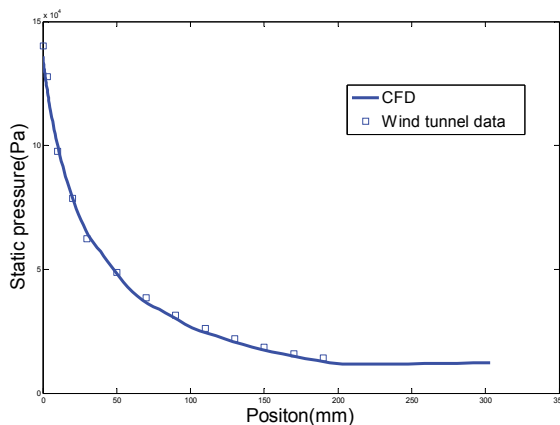


Fig. 31. CFD and wind tunnel data comparison of 2.5Ma attack angle 0°

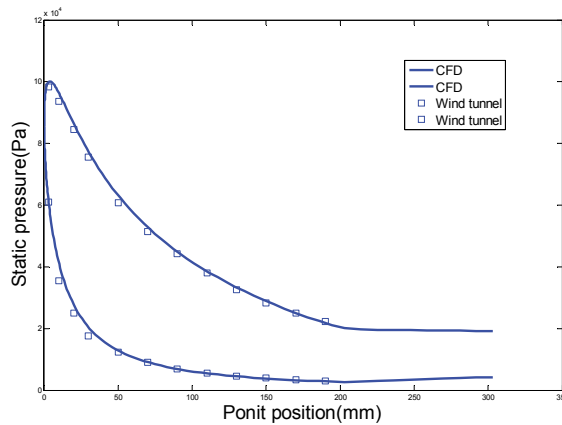


Fig. 32. CFD and wind tunnel data comparison of 3Ma attack angle  $20^\circ$

conformal dome's generatrix will be compared to value whether the pressure data of CFD simulation is correct. Figure 31 shows the data of CFD and wind tunnel at 2.5Ma with the attack angle is equal to  $0^\circ$ , and figure 32 shows the comparison of condition 3Ma  $20^\circ$ .

From the figures above, it is clearly seen that the wind tunnel data and the CFD simulation data match perfectly. This means that the CFD simulation data can be used for further design. The temperature data of the surface will not be shown here, because the data is processed in the way.

### 3.6 Conformal dome analysis

In the above study, we can get the exact pressure and temperature data of conformal dome's surface from wind tunnel experiments and CFD simulation. This data is used for conformal dome's FEA simulation. The purpose to progressing the FEA simulation is to value how the aerodynamic load and aerothermal affect the conformal dome's performance. The shape of the dome will change when missile flies at different speed and attack angle. The conformal dome's grid is shown in figure 33.

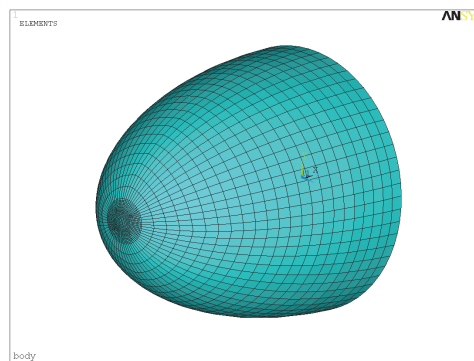


Fig. 33. Conformal dome grid

The temperature data of the dome's surface is the input file of FEA simulation. The result of conformal dome's temperature distribution is shown in figure 34. In this figure, we can get that along with the speed gets higher, the red area which means high temperature becomes larger.

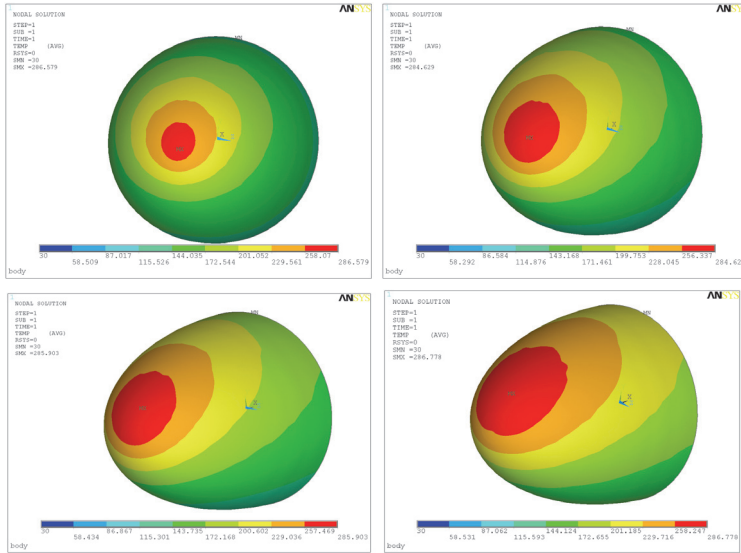


Fig. 34. Conformal dome temperature

Through the equilateral stress simulation, the conformal dome's SEQV figure is got as shown in figure 35.

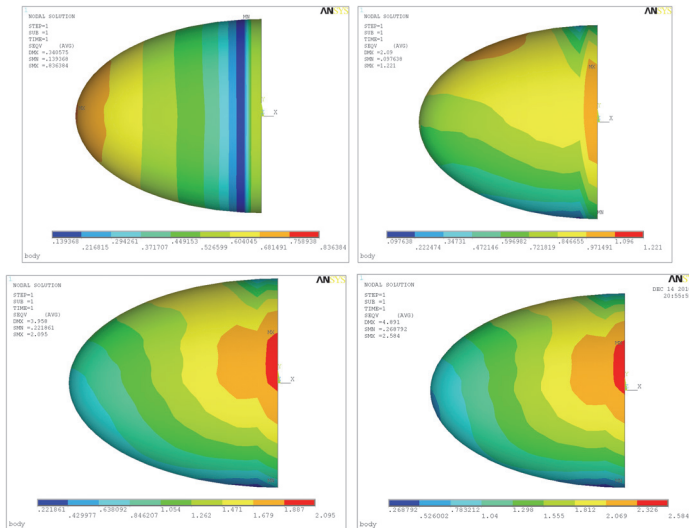


Fig. 35. Conformal dome equivalent stress simulation

These stresses caused by aerodynamic load make the dome's shape change, and the some shape's change will bring the seeker's optical system additional aberrations. For example, the change of conformal dome's shape at 2.5Ma speed 0° attack angle is put in optical design software ZEMAX. The MTF change is shown in figure 36. The left figure is original MTF of conformal optical system, and the right one is the MTF after dome's shape change. The spot diagram comparison is shown in figure 37.

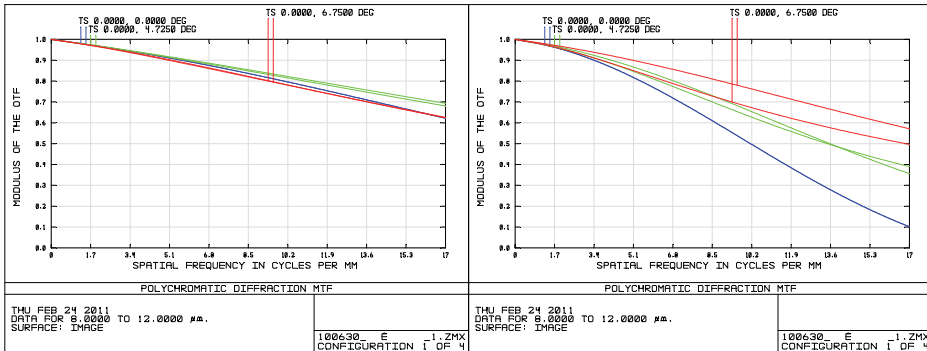


Fig. 36. Conformal optical system MTF comparison

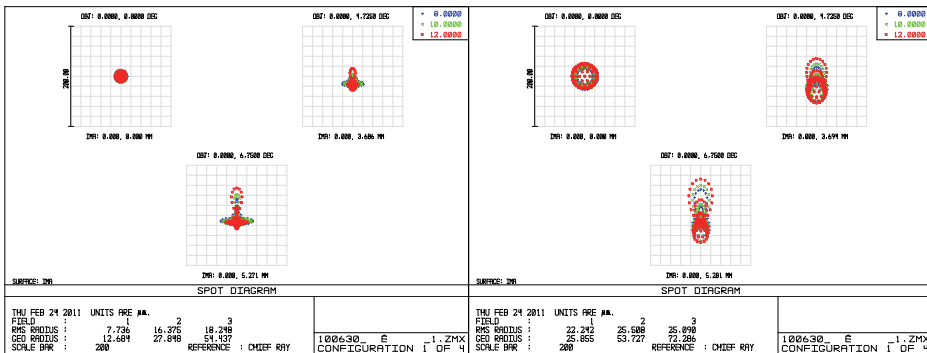


Fig. 37. Conformal optical system spot diagram comparison

### 4. Conclusion

In this chapter, two different kind of wind tunnel has been done. The first wind tunnel experiment is about spherical dome. The experiment is done from 0.4Ma to 3Ma with the attack angle from 0° to 10°. The comparison of force and shock wave figure ensure the reliability of spherical dome wind tunnel experiment. The data of wind tunnel experiment is used to study how aerodynamic affects the dome. The conclusion is the shock wave and the outflow can be considered as one or several air lenses which loacts before the dome. So when the missile flies, the outflow of the dome will add aberration to the optical system. The second wind tunnel experiment is about conformal dome which is focus topic now. This wind tunnel experiment is divided into two parts: pressure measurement wind tunnel



experiment and temperature measurement wind tunnel experiment. Besides, CFD simulation is used when wind tunnel data is not enough. The comparison of the pressure of conformal dome's surface shows that the CFD simulation has a very high accuracy. The pressure and temperature data is the input file of conformal dome FEA simulation which is used to value how the shape and temperature change. After simulation, the shape change data is put in optical design software, and the MTF and spot diagram of optical system goes down.

## 5. References

- K. V. Ravi. Diamond Technology for Endo-KEW Seeker Windows. AIAA, 92-2801.
- Scott B., Mike B., & Scott D.. Recent Development in Finishing of Deep Concave, Aspheric, and Plano Surfaces Utilizing the UltraForm 5-axes Computer Controlled. SPIE, 2009, Vol.7302, 73020U.
- Paul E. M., Jon F., & Greg F.. High precision metrology of domes and aspheric optics. SPIE, 2005, Vol.5786, 112-121.
- William P. K., Matthew B. D., & Robert S. L.. Measurement results for time-delayed source interferometers for windows, hemispherical domes, and tangent ogives. SPIE, 2009, Vol.7302, 73020R.
- Thomas J. H., W. Lance R., & Leslie G.. A technique for transient thermal testing of thick structures. SPIE, 1997, Vol.3151, 73-91.
- Claude A. K.. How Missile Windows Degrade the Noise-Equivalent Irradiance of Infrared Seeker Systems. SPIE, 1994, Vol.2286, 458-470.
- Zhao N., Chang J., & Sun Z.. Summarize of Conformal Optics. SPIE, 2007, Vol.6624, 66241N.
- Juan M. Ceniceros, David A. Nahrstedt, & Y-C Hsia, et al.. Wind Tunnel Validation of a CFD-Based Aero-Optics Model. AIAA, 2007-4011.
- Girimaji S. S., Abdol-Hamid K. S.. Partially-averaged Navier-Stokes Model for Turbulence: Implementation and Validation. AIAA, 2005-502.
- Tosh A., Frendi A., & Girimaji S.. Partially Averaged Navier Stokes: A New Turbulence Model for Unsteady Flows with Application to Acoustics. 11# AIAA/CEAS Aeroacoustics Conf, Monterey, CA, May 23-25, 2005.  
<http://www.bia701.co/html/e17fd0602.htm>
- M Born & E. Wolf. Principles of Optics. Cambridge U. Press, 1999, 92-93.
- G. Havener. Optical Wavefront Variance: a Study on Analytic Modes in Use Today. AIAA, 92-0654.
- G. C. Li. Aero-optics. National Defense Industry Press, 2006.
- Xingqiao Ai, Xin Zhang, & Zhenhai Jiang, et al.. Modulation transfer function in seeker camera limits resulting from missile flutter caused by aerodynamic force. ICIMA, 2010, 146-151.
- Huhai Jiang, Qun Wei, Hongguang Jia. Analysis of impact of gyroscope synthetical error on an electric-optical stabilized control system. BMEI, 2010, 2623-2625.
- Qun Wei, Hongguang Jia, Ming Xuan. Equivalent lenses of supersonic seeker's outflow refractive index field obtained by simulation and experiment. SPIE, 2009, Vol.7156, 71561Q.
- Wei Qun, Bai Yang, & Liu Hui. Optimized design of the inside surface of supersonic missile's elliptical dome. SPIE, 2009, Vol.7384, 73840E.

- Ai Xingqiao, Wei qun, Jia Hongguang. Dome design and coupled thermal-mechanical analysis of supersonic missile. SPIE, 2009, Vol.7506, 75061Q.
- Wei Qun, Zhang Xin, & Jia Hongguang. The design of missile's dome that fits both optical and aerodynamic needs. SPTE, 2010, Vol.7659, 76590F.
- Jiang Zhenhai, Zhang Xin, & Ai Xingqiao. Gimbal displacement errors analysis on an electro-optical seeker. SPIE, 2010, Vol.7849, 784924.
- Wei Qun, Ai Xingqiao, & Jiang Huhai. The optimize design of supersonic seeker's dome. Optics and Precision Engineering, Vol.18, No.2, 384-389.

# Design, Execution and Rebuilding of a Plasma Wind Tunnel Test Compared with an Advanced Infrared Measurement Technique

Marco Di Clemente, Giuseppe Rufolo,  
 Francesco Battista and Adolfo Martucci  
*Italian Aerospace Research Centre  
 Italy*

## 1. Introduction

### Nomenclature

<i>AC</i>	= Actively Cooled
<i>AoA</i>	= Angle of Attack
<i>ASA</i>	= Advanced Structural Assembly
<i>ASI</i>	= Italian Space Agency
<i>CFD</i>	= Computational Fluid Dynamics
<i>CIRA</i>	= Italian Aerospace Research Centre
<i>ESA</i>	= European Space Agency
<i>EXPERT</i>	= EXPERimental Re-entry Test bed
<i>FCW</i>	= Fully Catalytic Wall
<i>FRC</i>	= Finite Rate Catalysis
<i>FLPP</i>	= Future Launcher Preparatory Program
<i>FTB-X</i>	= Flying Test Bed X
<i>IR</i>	= Infrared
<i>MSS</i>	= Model Support System
<i>NE</i>	= Non Equilibrium
<i>NS</i>	= Navier-Stokes
$\dot{q}$	= Heat Flux
<i>PG</i>	= Perfect Gas
<i>PWT</i>	= Plasma Wind Tunnel
<i>TAS-I</i>	= Thales Alenia Space - Italia
<i>TPS</i>	= Thermal Protection System
<i>UHTC</i>	= Ultra High Temperature Ceramics

The extreme difficulties of testing, in a flight environment, technologies developed for the thermal protection of a re-entry vehicle put emphasis on the validation of numerical prediction tools. The ground testing in a Plasma Wind Tunnel facility entails a series of limitations in terms of cost and representativeness of the flight environment; therefore to find the way of improving CFD tools, both with flight and ground experimental data, is the key for a more reliable and robust Thermal Protection System (TPS) design. Existing in-flight measurements database are extremely poor and the need for improving them is testified by actual European program as EXPERT (Ratti et al., 2008) or FLPP-IXV (Tumino,

2006). On a parallel way it is also fundamental to improve the reliability of the experimental data acquired from ground tests. The validation of numerical methodology with ground measurements necessarily asks for a correct rebuilding of the test. To this aim, in the frame of the ASA program, a technological program carried out in Italy in the past years, funded by the Italian Space Agency, different TPS technologies have been developed and then tested under representative conditions not only to validate the design tools but also to gather data to be used for code validation. ASA program faced the aerothermal heating on a wing leading edge of a re-entry vehicle by developing, four TPS technologies for the different parts of the wing, namely two interchangeable systems for the leading edge (an UHTC-based and an actively cooled leading edge) and two for the panels (an Hybrid C/C and a Metal Matrix Composite panel); the experimental vehicle FTB-X, whose preliminary analysis was carrying out in the framework of the USV program (Pezzella et al., 2007), was considered as reference target in terms of thermal loads to be handled by the thermal protection system. The project team, led by TAS-I and with the cooperation of different Italian research centres and institutions, encompassed the development of these technologies and their qualification during different tests performed in the Plasma Wind Tunnel Scirocco. In the present analysis, the definition of the requirements, derived from the analysis of the FTB-X trajectory, the design and rebuilding of one of the performed tests, will be presented in order to validate an aerothermal coupling procedure developed. Traditionally, an aerodynamicist assumes a rigid isothermal or adiabatic body, with or without radiative equilibrium assumption, in order to predict surface pressure and heating rate. The aerodynamic heating is used to compute the temperature distribution inside the structure by means of a heat transfer analysis. Such an uncoupled approach may result to be quite inaccurate especially in a case, as the present one, in which the test procedure foresees a variation of flow condition and model attitude and the material to be tested has a relatively high thermal conductivity. Therefore, an integrated procedure to couple the external aerodynamic field to the internal thermal state of the structure has been adopted for the numerical rebuilding. The results of such aerothermal rebuilding have been compared with the experimental data provided by an Advanced Infrared Thermo-camera technique.

## **2. Model description: geometry and materials**

The main purpose of the Advanced Structural Assembly project was to qualify, in a high enthalpy ground facility, a certain number of new technologies potentially applicable as wing thermal protection system to new generation of re-entry vehicles; to this aim it was proposed to realize an adequate test article to be tested in Scirocco, the CIRA Plasma Wind Tunnel (PWT) facility (De Filippis et al., 2003), that should be representative of the wing of FTB-X vehicle. The test article has been conceived to be compatible with the facility itself in terms of dimensions, sustainable weights, auxiliary requested equipments, available measurement systems, etc., by guaranteeing the most valuable scientific feedback and, at the same time, an adequate safety level. As a matter of fact, it cannot be possible to test a real full-scale delta wing complete of the fuselage in the existing plasma facilities. The presence of chemical effects does not allow to simply scale the geometry to wind tunnels allowable dimensions; moreover, in the present case, the need to have a full scale test article is due to the necessity to test TPS technologies developed for flight. Moreover, it makes no sense to test only a portion of the delta wing because of the non-reproducibility of the real three-dimensional effects. For this reason it was decided to realize the test article by extruding a longitudinal section directly derived from FTB-X wing as described in Fig. 1.

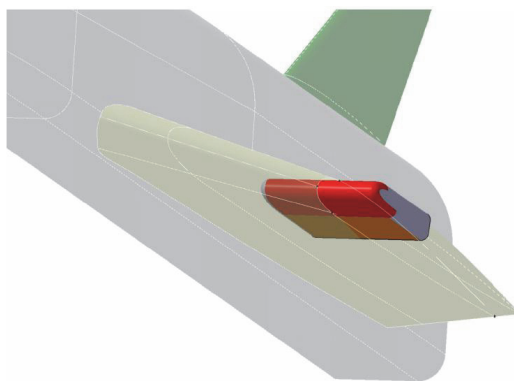


Fig. 1. FTB-X wing and test article derivation

Two lateral rounded fairings have been also defined in order to reduce as much as possible the overheating due to the finite span effects of the test article. Additionally some small modifications to the original wing section profile were necessary in order both to simplify the assembly and to allow the compatibility of the test article with the PWT. The conceived test article has been used to test in the PWT facility the innovative thermal protection system technologies and materials suitable for re-entry vehicles and thermo-structural applications, developed in the frame of the same project. In detail, four different technologies were developed and tested within the ASA project, applicable to the different parts of a wing (two for the leading edge and two, respectively, for the windward and leeward side) but, for what concerns the aims of the present work, only the so-called FTB-2 configuration will be taken under consideration. In this case, the test article is equipped with an actively cooled leading edge, a Metal Matrix panel on the windward (which is the object of the present analysis) and an Hybrid C/C panel on the leeward side. As a matter of fact from the test design activity, that will be described hereinafter, it comes out that in order to reproduce as much as possible the in-flight heat flux distribution of the FTB-X delta wing over the designed test article with no-sweep angle it is necessary to perform the test at an angle of attack of at least 35 deg while the angle of attack along the flight trajectory was 25deg at its maximum. To this aim it was decided to have a mechanical incidence of 25 deg provided by the model holder and to manage the remaining deflection angle by means of the moveble facility Model Support System (MSS). In Fig.2 the test article mounted on the MSS and ready to be tested is shown.

### 3. Numerical aspects

In the following sections the numerical results obtained for the rebuilding of the test will be presented; hereinafter, some details regarding the numerical codes used for the computations and the grids for the spatial discretization are presented.

#### 3.1 Numerical codes

##### CFD code

CIRA code H3NS has been used to perform the external flowfield computations. It is a structured multiblock finite volume solver that allow the treatment of a wide range of compressible fluid dynamics problems. The fluid can be treated or as a perfect gas or as a mixture of perfect gases in the case of thermo-chemical non equilibrium flows. In the latter case the chemical model for air is due to Park and it is characterized by 17 reactions between

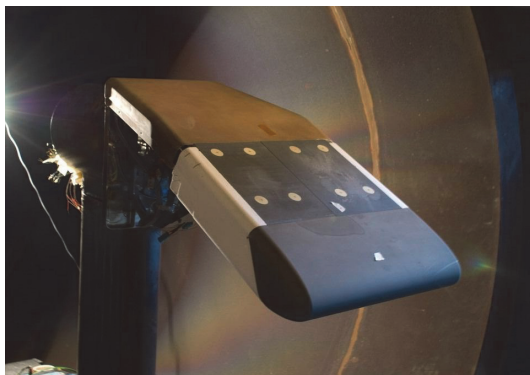


Fig. 2. Test Article with the model holder and the PWT Model Support System

the five species ( $O, N, NO, O_2, N_2$ ), neglecting the presence of noble gas in the air (e.g. Ar). The energy exchange between vibrational and translational modes (TV) is modelled with the classical Landau-Teller non-equilibrium equation, with average relaxation times taken from the Millikan-White theory modified by Park. For what concerns transport coefficient, the viscosity of the single species is evaluated by a fit of collision integrals calculated by Yun and Mason, the thermal conductivity is calculated by means of the Eucken law; the viscosity and thermal conductivity of the gas mixture are then calculated by using the semi-empirical Wilke formulas. The diffusion of the multi-component gas is computed through a sum rule of the binary diffusivities of each couple of species (from the tabulated collision integrals of Yun and Mason). Transport coefficient, in the hypothesis of an ideal gas, are derived from Sutherland law, suitably modified to take into account low temperature conditions. With respect to the numerical formulation, conservation equations, in integral form, are discretized with a finite volume, cell centred, technique. Eulerian flux are computed with a Flux Difference Splitting method (Borrelli & Pandolfi, 1990). Second order formulation is obtained by means of an Essentially Non Oscillatory reconstruction of interface value. Viscous flux are computed with a classical centred scheme. Integration in time is performed by employing an explicit multistage Runge-Kutta algorithm coupled with an implicit evaluation of the source terms.

#### Thermal code

The numerical solution of the thermal field inside the solid is carried out by means of an unsteady explicit two-dimensional multiblock in house developed code (Di Clemente et al., 2008). The code is capable of solving the heat conduction equation over a generic 2D or axi-symmetric geometry provided a structured quadrilateral multiblock grid. A finite volume approach is used for the spatial discretization, i.e. for each cell the laplacian term of the heat equation is treated as the divergence of the temperature gradient and the Gauss theorem is applied to transform the divergence into a surface integral over the cell border of the flux of the temperature derivative. A nine points centered stencil is adopted for the flux discretization, thus allowing an higher accuracy with respect to the classical five points stencil especially for irregular grids (high aspect ratio and/or skeweness of the cells). The time integration is based on a first-order explicit Euler integration. The code allow the use of temperature dependent material properties: thermal conductivity, heat capacity, emissivity. Different types of boundary conditions have been implemented in order to allow different kind of coupling with the external flow field:

- fixed temperature;

- fixed heat flux;
- adiabatic wall;
- heat flux variable in time (trajectory simulation) and variable along the geometry;
- as the previous with radiation of the wall;
- heat flux varying also with temperature by using a time and space distribution of the convective coefficient.
- as the previous with radiation of the wall;

In case of aerothermal coupled simulation the transferring of information with the external flow is allowed also if the fluid and solid grid are not coincident. To this aim a suitable interpolation procedure has been developed to transfer the heat flux deriving from the flow field computation to the solid wall and viceversa to transfer the wall temperature deriving from the thermal computation to the boundary condition of the external flow solver. Concerning the accuracy in time of the results it has to be said that despite the first order of the adopted scheme, the explicit character of the solver impose very small  $\delta t$  thus preserving the final accuracy of the results.

### 3.2 Grids for computations of the vehicle

In this section, some details about the computational grids used for the simulation of the flow field around the vehicle, are given. As it will be clarified hereinafter, the simulation along the trajectory has been done according to a simplified methodology to reduce CPU time; for this reason, a combination of two dimensional and three dimensional computations has been adopted therefore different grids have been considered. In particular, Fig.3(a) shows the grids used for the 2D wing section calculations, the number of grid points is 80x72; the grids are stretched to the wall with  $\Delta y_{wall}$  of  $10^{-6}$  m in order to perform viscous calculations; Fig.3(b) shows the grid used to perform 3D wing-alone computations characterised by 350000 points and a  $\Delta y_{wall}$  of  $10^{-6}$  m; in Fig.3(c) it is reported the 3D Eulerian grid and topology used for the fuselage whose points are 365000.

### 3.3 Grids for computations of the test article

Different computational grids have been generated with the commercial grid generator IcemCFD either for the three-dimensional mesh around the entire model either for the two-dimensional simulations carried out to design the test. The topology of the mesh is characterized by 38 structured blocks with a double C-type grid around the wing model, in the longitudinal and lateral direction; moreover an O-type local topology has been used to describe the lateral extremity of the model. The block decomposition is shown in Fig. 4. Of course, due to the symmetry of both the flow and the model, only an half of the model has been simulated in order to reduce the needed CPU time. In order to verify the spatial convergency of the results, three different grid levels have been considered: each level is obtained by the previous one by doubling the number of cells in each directions. The total number of the cells for the finest level, which assures spatially converged results, is about 1.7 millions.

In Fig. 5(a) the grid on the symmetry plane, used also for the two-dimensional simulations, is shown; a local grid refinement in the region of the bow shock in front of the model has been done in order to better describe the steep gradient of flow variables and to reduce the numerical instabilities which can arise in this area. In Fig. 5(b) it is shown the detail of the wing tip.

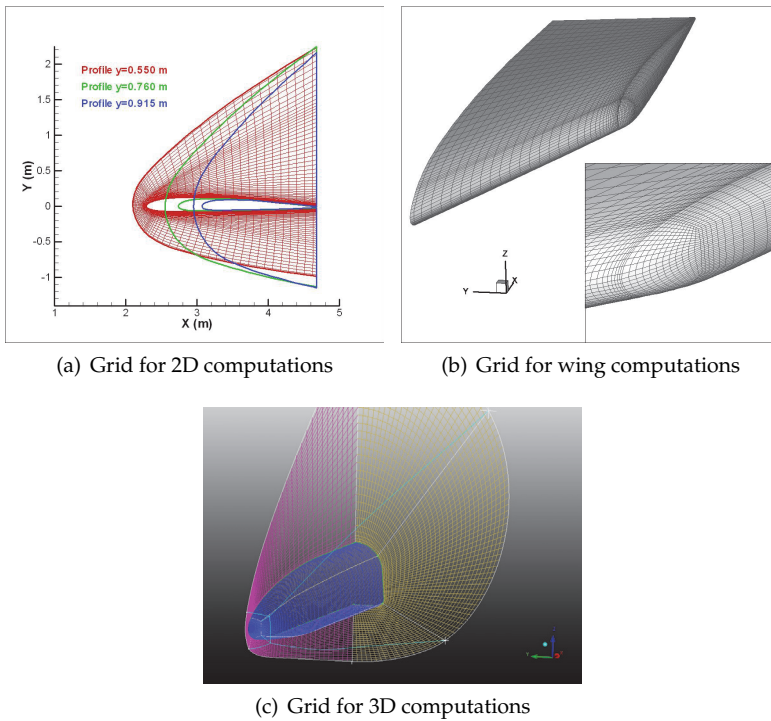


Fig. 3. Computational grids

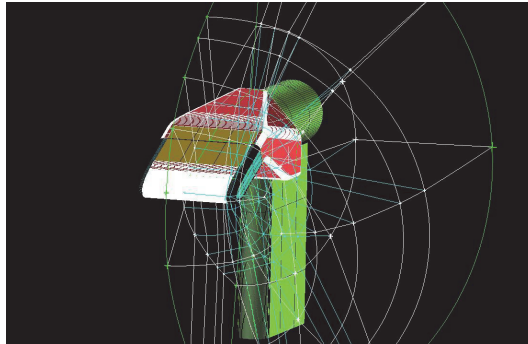


Fig. 4. Block decomposition around the test article

### 3.4 Grid for internal field

As it will be clarified hereinafter, the numerical rebuilding of the PWT test has been done through an aero-thermal coupled methodology which foresees the computation of either the external flowfield surrounding the model either the internal thermal field inside the model. In particular, the attention of the rebuilding has been focused on the MMC panel in the upper part of the model. Thermal computations inside the panel have been carried out considering



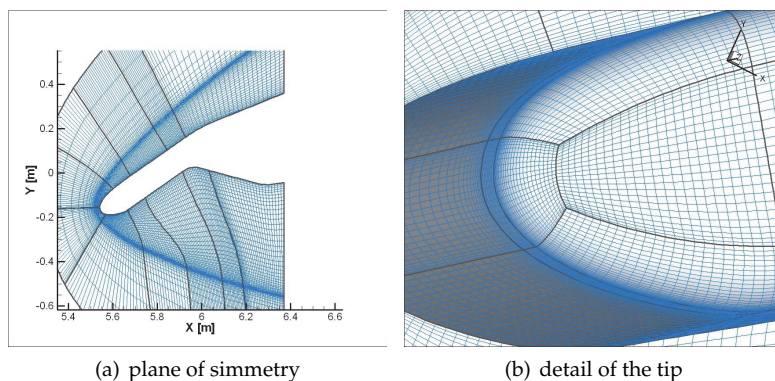


Fig. 5. Computational mesh

a two-dimensional section neglecting the heat conduction in the lateral direction. The grid used for these computations is shown in Fig. 6; points distribution along the wall is the same of the distribution used for the CFD computations, in order to simplify the exchange of informations (heat flux and temperature) between the external and the internal fields. In the direction normal to the wall it has been suitably tuned to describe in detail the region of stronger thermal gradients. The panel is formed by a metal matrix of 2 mm thickness and an insulator in the lower part of 2.5 cm thickness which have been discretized with two different blocks (see the green and blue mesh in Fig.6(b)).

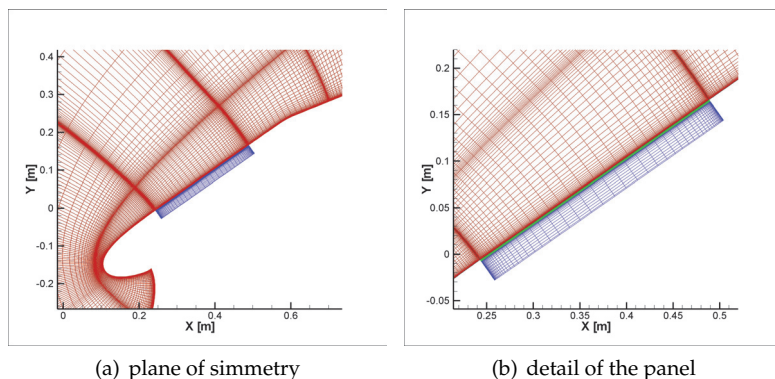


Fig. 6. Computational mesh for thermal computation

#### 4. Definition of requirements

The development of the wing leading edge thermal protection system for a re-entry vehicle requires a deep understanding of the aero-thermal environment surrounding the vehicle; among the others the two key parameters that influence the selection and the design of a TPS suitable for a certain vehicle and trajectory are the peak-heating rate and the integrated heating over the time along the flight. The former determines the maximum temperature environment, and thus the materials selection, whereas the latter determines the thermal

budget that the structure has to manage either with a passive insulation material and/or with an active cooling system. Due to the lack of experimental data concerning the thermal database of the FTB-X vehicle, and the impossibility to carry out an accurate numerical investigation of the aero-heating phenomenology, which would involve an high number of full three dimensional thermo-chemical non equilibrium Navier-Stokes simulations of the vehicle configuration along the flight path, a scaling simplified methodology to evaluate the time history of the aerothermal environment over the wing, capable of giving results as much reliable as possible in a reasonable time available, have been developed and applied (for major details, see Battista et al. (2007)); the level of approximation of this approach has been considered suitable for the purposes of the overall project whose main aim was to develop technologies for a re-entry vehicle under representative loads and not to design the real TPS system of the FTB-X vehicle. In the simplified methodology a series of two dimensional planar computations along the trajectory has been performed on different profiles of the wing, shown in Fig. 7, to describe the time evolution of the aerothermal environment and, in order to take into account the realistic three dimensional features of the investigated flow, over the finite span length and swept wing, the two dimensional results have been suitably scaled by means of 3D computations carried out over a reduced number of trajectory points.

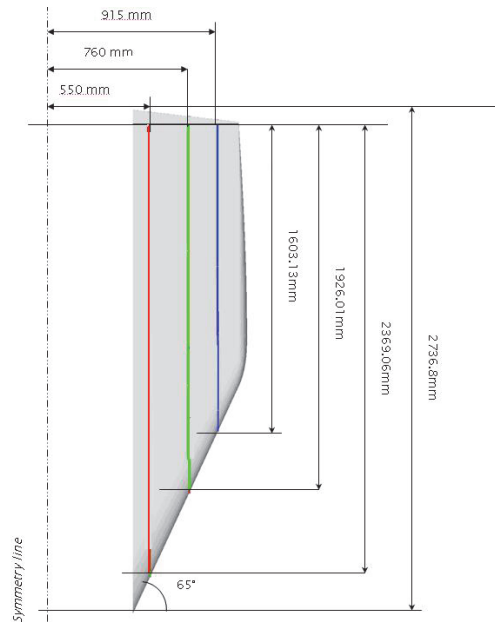


Fig. 7. Wing planform

A preliminary assessment analysis has been done to find out the most reliable conditions to perform the two dimensional non equilibrium calculations. In particular, it has been analyzed the boundary layer state (laminar/turbulent) and the wall boundary conditions in terms of catalysis and wall temperature. In this simplified methodology for the heat flux estimation over the wing no attempt has been made to describe regions of interaction of the fuselage bow shock with the leading edge bow shock. Even though this choice allowed for a relatively easy and reliable (except for the profiles interested by the shock-shock interaction) evaluation of the

heat flux over the wing along the flight trajectory, the problem of the shock-shock interaction has been analyzed during a refinement of the present analysis since this type of interaction can cause highly localized peaks in the heat flux distribution (Edney, 1968).

Referring to the flowchart shown in Fig. 8, the scaling methodology consists mainly of two different steps:

- determining the most reliable flow conditions ahead each wing profile: as matter of fact along the trajectory, a part of the wing is positioned inside the bow shock coming from the nose; therefore the wing sections that falls inside the fuse bow shock are exposed to a flow field with different characteristics with respect to the freestream conditions and this is accounted for considering three-dimensional computations around the fuselage and by evaluating from these computations the freestream conditions to be used for the computations around the selected wing profiles;
- two dimensional computations are performed, in non-equilibrium conditions, on the selected wing profiles along the trajectory considering the freestream conditions determined at the previous point;
- scaling of two-dimensional results to take into account the sweep angle and three dimensional effects, mainly induced by the finite length of the wing; this is done by comparing the two-dimensional and three-dimensional wing alone computations performed in some points of the flight trajectory.

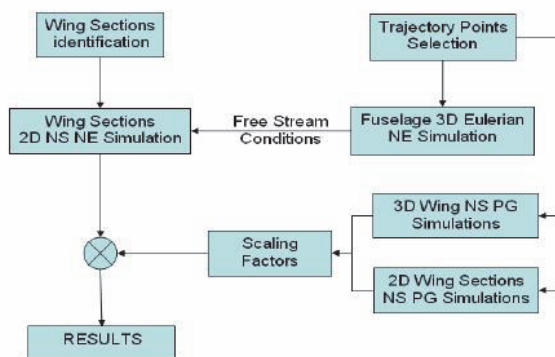


Fig. 8. Flow chart of scaling methodology

The scaling strategy can be summarized as follows: the ratio of the heat flux values of the 2D computation over the 3D ones, for a certain point along the trajectory, is assumed as scaling factor:

$$\chi_s(x, \bar{y}, t) = \frac{\dot{q}_{3D}}{\dot{q}_{2D}} \quad (1)$$

where  $\bar{y}$  indicates a function of the  $x$  variable, describing the wing section profile. The scaling factors determined for a subset of selected points along the trajectory have been applied without loss of generality to all the other selected cases, following the equation:

$$\dot{q}(x, \bar{y}, \bar{t})_{NE}^{3D} = \chi_s(x, \bar{y}, t)_{PG} \cdot \dot{q}(x, \bar{y}, \bar{t})_{NE}^{2D} \quad (2)$$

In eq. 2 the scaling factor  $\chi_s$  has been evaluated by applying perfect gas hypothesis both to 3D wing-alone and to 2D computations. Moreover it has to be pointed out that the scaling factor has obviously not been determined for each point of the trajectory so suitable interpolation with time has been used. In this way, it has been possible to have an estimation of heat flux distribution over the wing along the trajectory by reducing the needed CPU time and, anyhow, with a good level of approximation.

An orbital re-entry trajectory obtained with preliminary aerodynamic and inertial databases is available for the FTB-X vehicle. In order to be able to respect a thermal barrier of  $1100 \text{ kW/m}^2$  at the nose stagnation point a guidance strategy with a modulation of AoA has been adopted. Due to the relatively high efficiency of the vehicle a very long re-entry time is obtained. In Fig. 9 the profiles of Altitude, Mach number and AoA are reported versus Time elapsed, starting from an altitude of 120 km. The descending phase is performed with an angle of attack exceeding  $20^\circ$  in order to reach a sufficiently low energetic level and low speeds. More in detail, ten different points along the re-entry trajectory have been considered for the CFD analysis according to the described methodology.

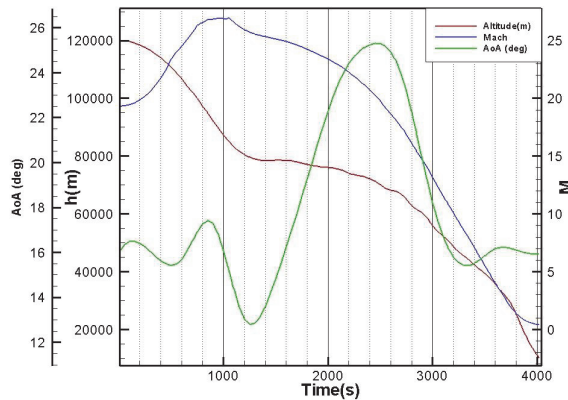


Fig. 9. Reference trajectory

The effects of the bow shock generated by the nose some Eulerian, thermo-chemical non equilibrium computations have been performed over the fuselage geometry. In order to understand the level of approximation related to this assumption a comparison with a full vehicle Navier-Stokes non equilibrium computation has been carried out and the results are reported in Fig. 10 for one point of the trajectory. It is evident that the error in the position of the bow shock is not very significant.

Once determined the freestream conditions for each profile, two-dimensional planar steady state<sup>1</sup> non equilibrium computations have been performed for the selected points along the flight trajectory in order to obtain a time history of heat flux spatial distribution. From the 3D Eulerian computations, it comes out that the section 1 ( $y=0.550 \text{ m}$  from the symmetry plane of the vehicle) and section 2 ( $y=0.760 \text{ m}$ ) are positioned in a part of the wing that is inside the bow shock for all the selected points along the flight trajectory, whereas section 3 ( $y=0.915 \text{ m}$ ) is outside the bow shock at higher altitudes therefore it feels an undisturbed flow field, and

<sup>1</sup> Characteristic flow time are of order of milliseconds for this regimes therefore the assumption of steady state with respect to the variation of freestream conditions along the flight trajectory is fully adequate.

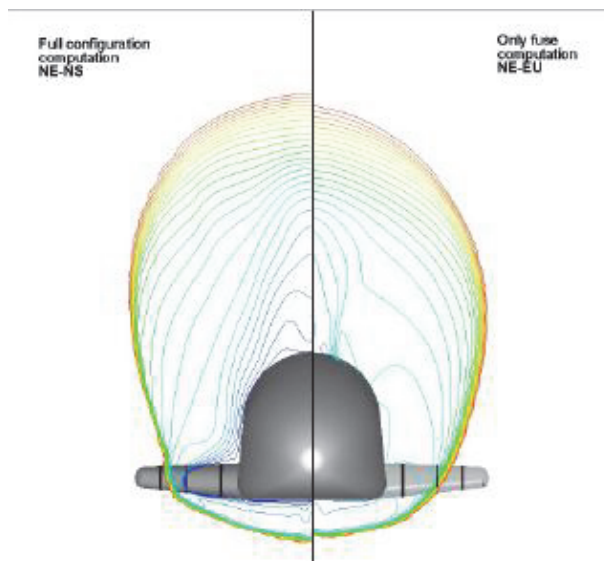


Fig. 10.  $M_\infty=20.29$   $AoA=25.30$  deg: Mach Contours

it is inside the bow shock for the lower altitudes points because the shock angle increases as Mach number decreases.

In Fig. 11 the stagnation point heat flux over the selected profiles is reported versus the flight time. All the computations have been performed in laminar conditions with radiative equilibrium assumption at the wall; clearly, according to the 2D computations, the profile 2 ( $y=0.760$  m) experiences the highest heat flux along the trajectory, with a maximum equal to about  $2.1 \text{ MW}/\text{m}^2$  reached at point 5 of the trajectory ( $h=75$  km,  $M_\infty=22.79$ ). Of course it has to be kept in mind that these results refer to the 2D computations and that they do not take into account the effect due to the finite span length of the wing therefore in order to predict realistic value of heat flux over the wing, it is necessary to scale these results to take into account the three-dimensionality of the flow, as sweep angle effect and finiteness of the wing. Three-dimensional computations have been performed assuming a perfect gas environment, for some of the selected points along the trajectory to suitably describe the plateau of heat flux during the re-entry trajectory, considering the undisturbed freestream variables as inlet conditions. For each of the selected points, additional two-dimensional computations, respect to those already presented, have been performed assuming a perfect gas environment and undisturbed freestream conditions for all the sections; these additional computations are necessary to find out the scaling factors are reported in Eq. 1. In Fig. 12 pressure coefficient and heat flux distribution over the wing is shown for one of the the trajectory points mentioned above.

In order to provide the heat flux distribution over the wing along the trajectory, two-dimensional non equilibrium computations have been then scaled according to the scaling factors obtained through three-dimensional computations around the wing (see Eq. 2). The results of the scaling methodology are reported in Fig. 13: in particular, in Fig. 13(a) it is reported the variation along the trajectory of the stagnation point heat flux over the three selected profiles whereas in Fig. 13(b) it is reported the heat flux distribution over the three selected profiles for one point of the trajectory. Maximum heat flux is almost constant in

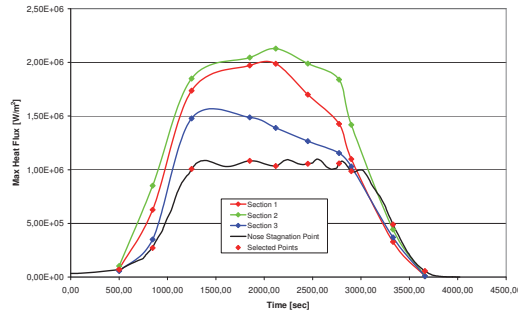


Fig. 11. Two-dimensional stagnation point heat flux over the selected profiles

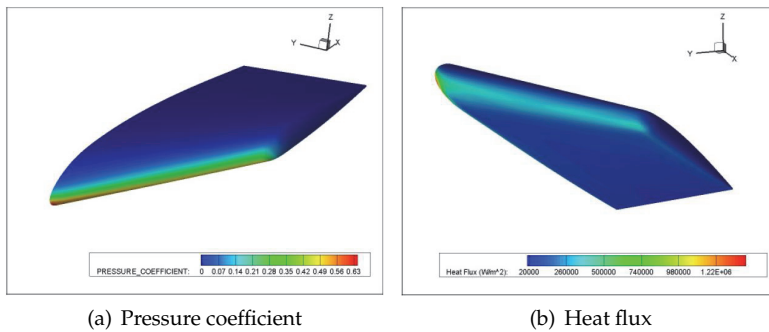


Fig. 12. Results over the wing

the middle part of the trajectory for the section 1 and 3 and equal, respectively, to about  $400 \text{ kW/m}^2$  and  $300 \text{ kW/m}^2$ , whereas it increases for the section 2 up to a value slightly above  $400 \text{ kW/m}^2$  reached after 2000 s. The stagnation point is located immediately downstream of the leading edge (due to the effect of the angle of attack), then, after the rapid expansion, it assumes an almost constant value along the entire geometry. The difference on the heat flux value between leeside and windside is lower than  $100 \text{ kW/m}^2$ .

## 5. PWT test design

Hereinafter a brief description of the activities carried out to numerically design the PWT test are reported. The starting point for the design of a test to be performed in the Plasma Wind Tunnel Scirocco, is the definition of the requirements, generally in terms of heat flux and pressure to be realized on the model, that is necessary to achieve during the test itself. For the considered test, the requirements were determined through the simplified procedure already described; loads foreseen during the re-entry trajectory of FTB-X vehicle are summarized, for the different part of the model, in Table 1 in terms of heat flux. These loads have been used to design the TPS therefore they have to be reproduced in the wind tunnel in order to validate the design procedure. For each part of the model in the same table it

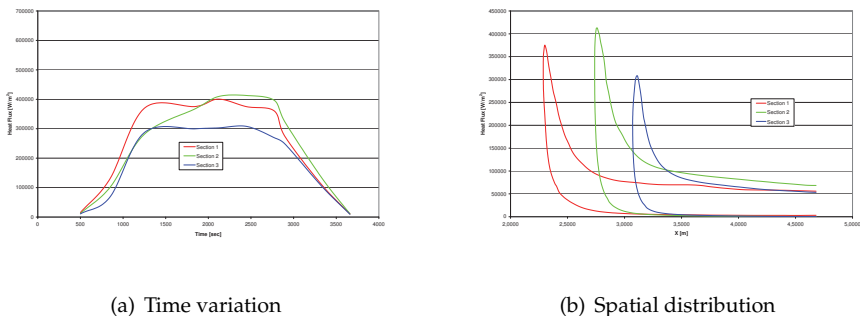


Fig. 13. Heat flux over the selected profiles

ID req.	Test Article Part	Wall Conditions	Catalysis	Temp	q[kW/m <sup>2</sup> ]	Position
A	LE UHTC	FRC	Rad.Eq.		410	Stagnation Point
B	WINDSIDE PANEL	FRC	Rad.Eq.		170	Panel Apex - x=0.2m
C	LE AC	FCW	Tfix		410	Stagnation Point
D	LEESIDE PANEL	FCW	Rad.Eq.		90	Panel Apex - x=0.1m

Table 1. Requirements for PWT test design

is shown also the wall boundary conditions, in terms of catalysis and temperature, to be considered. The test has been numerically designed, in terms of values of reservoir enthalpy and pressure and model positioning/attitude within the test chamber to be considered, through an extrapolation-from-flight methodology already used for previous test campaigns as reported in Marini et al. (2007).

For what concerns the present test, the requirement was to achieve a value of heat flux over the MMC panel equal to 90 kW/m<sup>2</sup> and the following operating conditions and model attitude have been determined:

- Reservoir Enthalpy = 13.5 MJ/kg.
- Reservoir Pressure = 3.6 bar.
- Final Model attitude = 35 deg (25 deg mechanical angle + 10 deg of MSS tilting).
- Distance from nozzle exit: 950 mm.

In order to guarantee the safety of the test both in terms of flow blockage occurrence and test article integrity it was decided to consider some intermediate steps for the test procedure. These steps can be summarized as follow:

- insertion of the model with a mechanical angle of attack of 25 deg at a distance from the nozzle exit section equal to 200 mm;
- backward movement of the test article up to a distance from the nozzle exit section equal to 950 mm;
- 10 deg tilting to reach the final attitude of 35 deg that assures the achievement of the requirements over the model.

The achievements of the right operating conditions within the test chamber during the test is assured by the presence of a copper water-cooled hemi-spherical calibration probe which is inserted in the plasma flow before the insertion of the model to measure the stagnation point heat flux and pressure. Facility regulation parameters (air mass flow and current in the arc) are tuned in order to match on this probe a certain couple ( $P_s, q_s$ ) which corresponds to the desired operating condition in terms of the couple ( $H_0, P_0$ ) evaluated through the extrapolation-from-flight methodology generally used. For the present test, the requirement was to achieve on the calibration probe a stagnation heat flux equal to  $870 \text{ kW/m}^2$  and a stagnation pressure equal to 10 mbar. The application of such procedure requires to carry out a lot of CFD computations of the flowfield around the model. Therefore, in order to reduce the CPU time, the flow has been simulated considering a two-dimensional approach. The validity of this hypothesis has been verified through a comparison between two and three-dimensional results. In Fig. 14 heat flux distribution over the surface of the test article is shown; the represented configuration refers to the model equipped with the actively cooled leading edge. Heat flux distribution on the leading edge is strongly bi-dimensional for a great portion of the span. In Fig. 15 the comparison between two and three-dimensional flowfield on the symmetry plane is shown; close to the leading edge the position and the shape of the bow shock are practically the same whereas a certain difference has been found downstream where the stronger expansion due to the three dimensional side effects leads a deviation of the shock toward the wall.

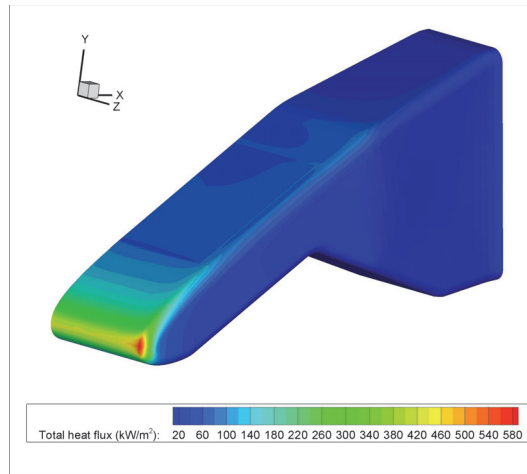


Fig. 14. Heat flux distribution over the test article

### 5.1 Model flowfield simulation

As already said, in order to guarantee the safety of the test, either in terms of flow blockage either in terms of structural integrity of the model, the adopted test procedure foreseen some intermediate steps before the final test condition. For each of the selected conditions, in terms of model positioning and angle of attack a numerical computation has been performed as summarized in Table 2. The four computations have been performed assuming a steady state of the flow by neglecting possible non-stationary effects due to the movement of the model within the test chamber. Wall temperature has been considered equal to 300K for all the parts of the model in the first phases of the test in order to provide conservative results for heat flux



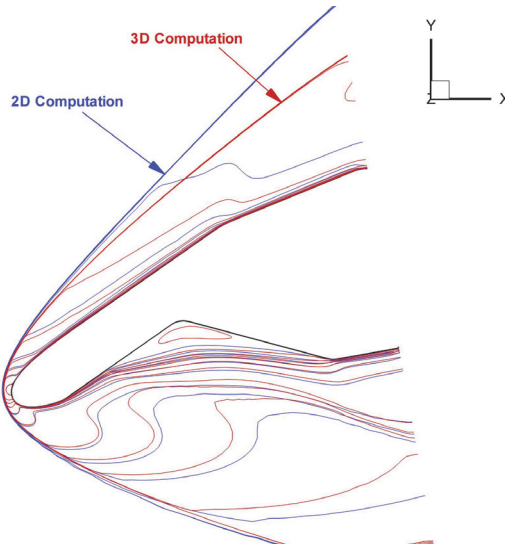


Fig. 15. Comparison between 2D and 3D flowfield on the symmetry plane

Run ID	Description	Position	AoA	Wall Temperature		
				LE	WS	LS
1	Insertion of the model	x=200mm	25	300	300	300
2	Backward movement	x=950mm	25	300	300	300
3	Tilting	x=950mm	35	300	300	300
4	End of the test	x=950mm	35	410	RE	RE

Table 2. CFD Matrix

estimation, whereas it has been assumed equal to the radiative equilibrium temperature (with different emission coefficients) for the 4<sup>th</sup> computation, except than for the AC leading edge which has been considered at a fixed wall temperature equal to 410K. For what concerns the catalytic conditions, the leading edge and MMC panel have been considered as fully catalytic, whereas the C-C/SiC panel has been considered as partially catalytic. Heat flux distribution computed in Run-4 over the model is shown in Fig. 16(a); peaks, clearly visible at the interfaces between the different part of the model, are due to discontinuities in the boundary conditions in terms of catalytic behaviour and emission coefficients. In Fig. 16(b), the detail of the heat flux on the MMC panel for the four computations of Table 2 is shown: at model insertion (Run-1) the maximum heat flux reaches a value slightly above  $100 \text{ kW/m}^2$  either for the effect of wall temperature (equal to 300K) either the reduced distance from nozzle exit section; the backward movement (Run-2) causes a decrease of heat flux over the model because the expansion of the flow continues also in the test chamber outside the conical nozzle; the tilting of the MSS (Run-3) leads an increase of heat flux, then in Run-4 a decrease of heat flux (till the final value at the tip equal to  $90 \text{ kW/m}^2$ , as for the requirement) is found due to the effect of the radiative equilibrium hypothesis.

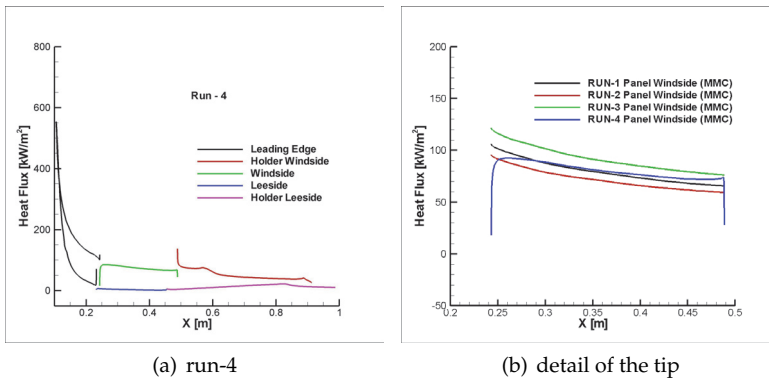


Fig. 16. Heat flux over the model

## 6. Test execution

The test has been executed on October 2008,; in Fig. 17 the model within the test chamber, ready to test, is shown. On the left side it is visible the expansion nozzle exit section with 1950 mm of diameter whereas on the right the diffuser need to slow down the hypersonic flow and for the recovery of pressure is visible. During the test, after the ignition of the arc heater, the qualification of the flow within the test chamber has been done through the hemispherical calibration probe; air mass flow and current have been then tuned to match the requirements. Nominal values of heat flux and pressure measured at the probe stagnation point during the test were slightly different with respect to those determined before the test due to the necessity to maintain stable conditions in the arc heater but, in any case, within the associated measurement uncertainty; in detail, heat flux was equal to  $930 \text{ kW/m}^2$  with a difference with respect to the required value of  $60 \text{ kW/m}^2$ , whereas wall pressure was 11 mbar instead of 10 mbar.

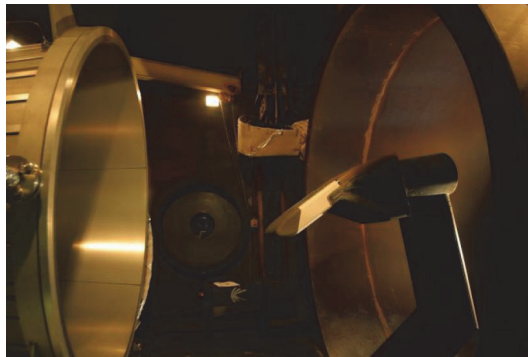


Fig. 17. Model ready to be tested

In Fig. 18 different images during the test execution are shown and they are specified also in the following:

- (a). model enter the plasma flow;
- (b). model arrives at centreline at a distance from nozzle exit section of 200 mm;

- (c). after 570s the backward movement starts;
- (d). model reaches the final position, distance from nozzle exit section 950 mm;
- (e). after 10s in this position the model rotates to achieve the final angle of attack of 35 deg;
- (f). after 300s in this position the test finishes.

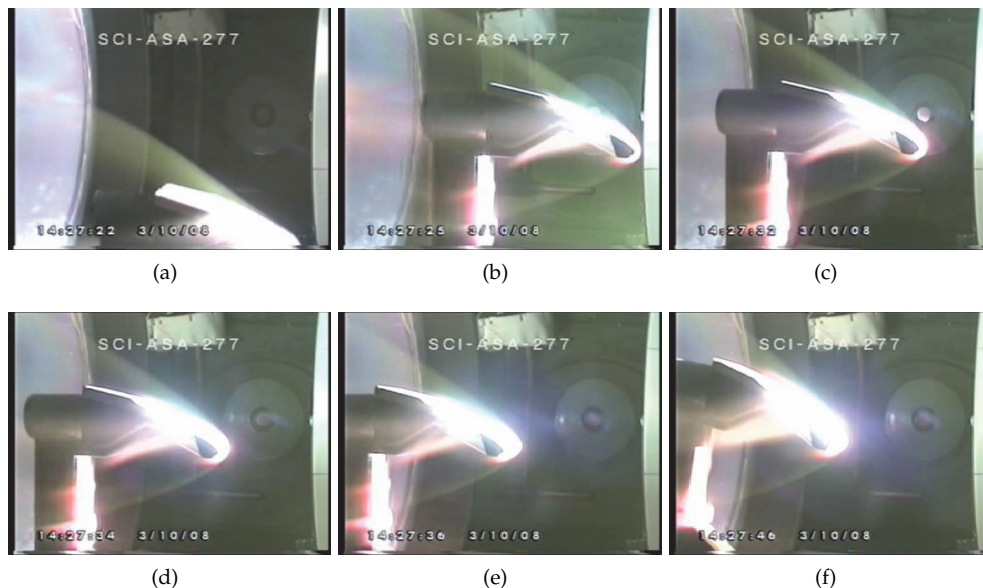


Fig. 18. Test execution

The test total test duration was 916s starting from the insertion of the model in the plasma flow; the numerical rebuilding, whose results will be reported hereinafter, has been done considering the first part before the backward movement and the rotation of the model.

## 7. IR measurements

Not intrusive thermographic techniques for temperature measurement have always played an important role among the diagnostics of the wind tunnel facilities. It has been developed and it is foreseen to become even more important for the future. During the present test, surface temperature measurements have been carried out with IR thermography to collect useful data for post-test analysis and comparison with numerical prediction tools (see also Di Clemente et al. (2008)). A proper calibration, using a blackbody Mikron M300, has been performed on the temperature range expected during the test; this apparatus is a compact portable blackbody calibration source with a built-in digital indicating controller that can be set at any temperature between ambient 5°C and 1150°C. Once set, the source temperature is controlled to within  $\pm 0.2^\circ\text{C}$  by an internal RTD sensor. The unit has an emissivity of 0.966 in the 8-12  $\mu$  wavelength range (the range of acquisition of the thermocamera AGEMA Thermovision 900). The M300 is easy to transport to a calibration location, either in laboratory or in the plant. It has a dedicated PID controller with 0.1°C resolution.

The thermocamera has been positioned on the top of the test chamber to acquire measurements on the upper part of the model; the positioning has been made by optimizing

the view angle in the different phases of the test as injection in the plasma flow, backward movement and tilting. The total time of acquisition has been equal to 45min, starting from the injection in the plasma flow ( $t=0s$ ), considering the first 15 min of the test itself and 30 min of the cooling phase after the shut down of the facility. In Fig. 19 some images of the thermocamera in different time instants are reported.

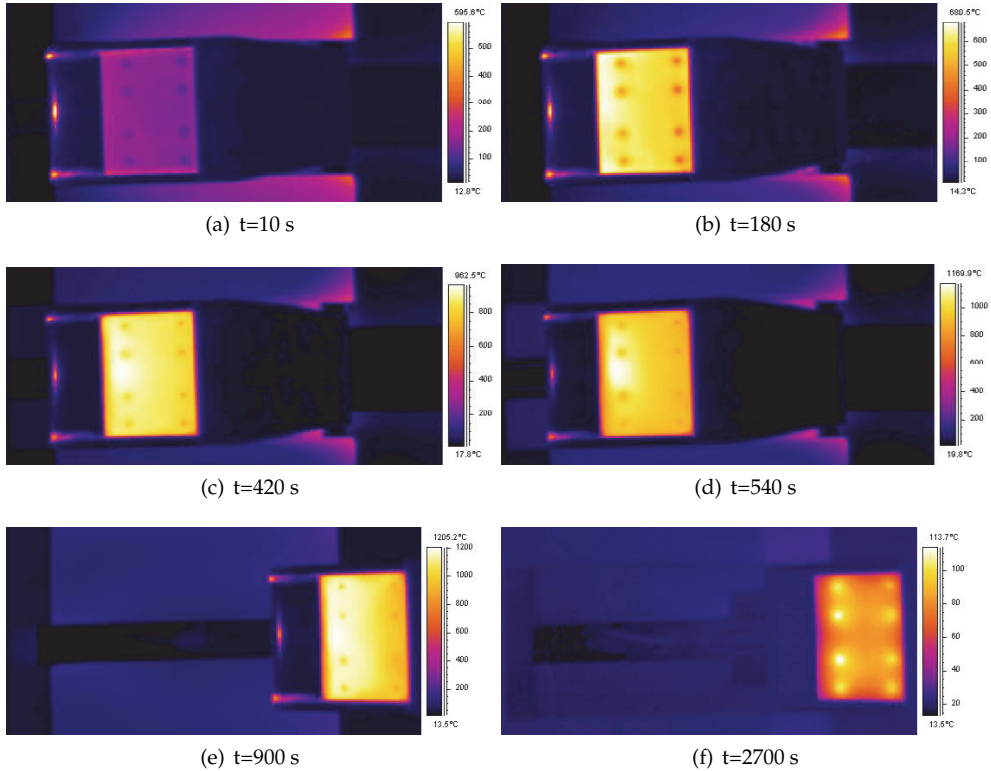


Fig. 19. Thermocamera acquisitions

Once the thermocamera is calibrated it is possible to perform all the operations with its infrared acquisition. In order to evaluate the temperature of an object by means of a single thermocamera acquisition, it is necessary to know the value of emissivity of its surface. In the present case, this determination has been made through the comparison of thermocamera acquisition with the measurements provided by a dual color pyrometer pointed on the panel surface. The comparison is shown in Fig. 20 for a value of emissivity equal to 0.91. The comparison has been made in the second phase of the test, because the pyrometer has been positioned to acquire measurements after the backward movement and for temperatures higher than  $800^{\circ}C$ .

In order to provide quantitative and not only qualitative measurements the results of the thermocamera have been extracted along longitudinal and transversal lines over the model shown in Fig. 21; in particular seven lines have been extracted in the longitudinal direction (named from L01 to L07) and four in the transversal one (named from L08 to L11). As an example, in Fig. 22 the results at  $t=180$  s along the longitudinal and transversal lines: at panel

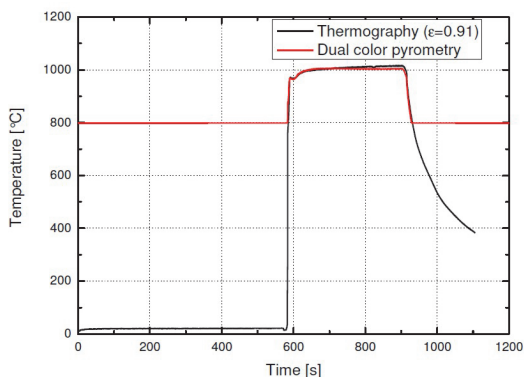


Fig. 20. Comparison between thermocamera and pyrometer acquisition

tip, temperature is low due to the presence of the actively cooled leading edge whose effects extends for 4-5 cm on the panel (see Fig.22(a)); the same is predicted at the trailing edge, due to the model holder that is cooled as well. Transversal lines reported in Fig.22(b) show an almost flat distribution in the central part of the panel and a lateral decreases due to the rounded edges of the model. The presence of the bolts which fix the panel to the underlying structure causes a local decrease of temperature due to the enhanced heat conduction. In Fig.23, time evolution of temperature along the symmetry line and one of the transversal lines is reported: temperature increases quickly in the first 180 s of the test then it seems to reach an almost constant condition even though it continues slowly to increase. In order to better analyze time dependant behaviour of temperature, the evolution versus time in two points of the panel, located on the symmetry line near the tip (P5) and near the trailing edge (P12) is shown in Fig.24:

- the initial heating is almost quick, temperature reaches a value of about 800° C at point P5 and 600° C at point P12 in about 200 s;
- after this time, the slope of the curve decreases and temperature continues to increase slowly reaching an almost constant behaviour;
- at  $t=570$ s the model is moved downstream and then rotated of 10 deg to reach an angle of attack respect to the flow equal to 35 deg (this part of the acquisition is neglected to the high error associated to the measurement);
- after the rotation temperature starts to increase again due to the higher value of heat flux up to the shut down of the facility after 900 s;
- the last phase of the acquisition regards the cooling of the model.

## 8. Numerical rebuilding and comparison with experimental results

Generally, an aerothermodynamic simulation to estimate heat flux is carried out considering the wall as an isothermal surface or adiabatic, with or without the hypothesis of radiative equilibrium; computed heat flux values are then used to simulate the thermal field inside the material. As matter of fact, due to the intrinsic unsteady behaviour of the test under investigation and to the thermal properties of the materials involved this uncoupled approach could be not adequately accurate for the rebuilding of the test itself; therefore, it has been

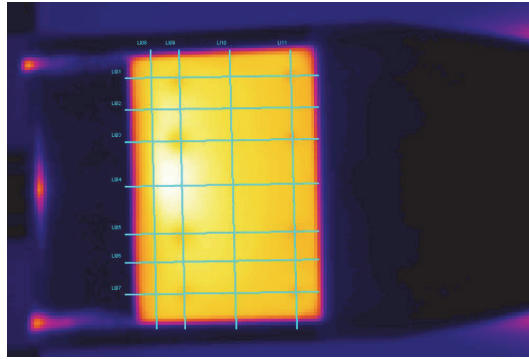


Fig. 21. Extraction lines for thermocamera results

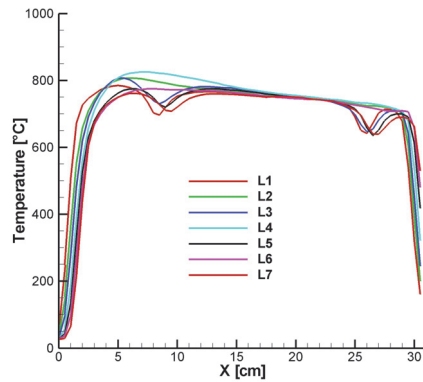
carried out considering a coupled simulation between the aerodynamic and the internal thermal field.

### 8.1 Set point definition

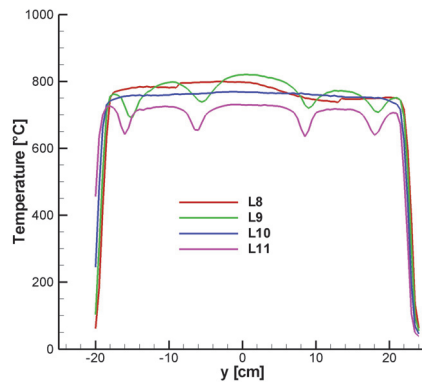
As already specified, the achievement of the desired test conditions within the test chamber is assured by the insertion in the plasma flow of the hemispherical calibration probe. Numerical rebuilding, consequently, has to be carried out considering the actual values of heat flux and pressure measured by the probe. In this case, considering these values, the operating condition in terms of reservoir enthalpy and pressure which allows to obtain these results on the probe have been determined and then used to compute the flow inside the PWT conical nozzle and then around the model for the rebuilding of the test. This procedure assures a good characterization of the flow within the test chamber and then that the selected operating condition is suitable for the rebuilding of the results over the model. The selected condition for the rebuilding is characterized by a reservoir enthalpy of 13.7 MJ/kg and a reservoir pressure equal to 3.9 bar.

### 8.2 Aerothermal coupling

The numerical rebuilding procedure has been applied considering a weak coupling between the external fluiddynamic field and the internal thermal field, considering different freestream conditions ahead the model according to its movement within the test chamber. By analyzing the characteristic times of the phenomenon, it has been deduced that it was possible to consider different steady state computations of the fluiddynamic field whose dynamic behaviour is much faster than heat propagation inside the material, on the other side, through unsteady thermal simulations. In synthesis, the internal thermal field in the panel has been evaluated through a series of successive unsteady computations considering the heat flux due to the external flow as a fixed input for each step; at the end of each thermal computation, this input due to the external flow has been updated by repeating the CFD computations considering either different freestream conditions due to the movement of the model within the test chamber either the updated wall temperature distribution derived from the thermal analysis. Due to the symmetry of the flow and to the already shown "almost" two dimensional characteristics of the flowfield around the model, numerical rebuilding has been made considering two-dimensional planar computations therefore the results will be compared with those obtained on the symmetry line through the thermocamera system. Moreover only the upper part of the model has been simulated. The rebuilding has been done starting from the



(a) symmetry line



(b) transversal line (L10)

Fig. 22. Temperature acquisition at t=180 s

entrance of the model in the plasma flow by carrying out 9 computations (CFD + thermal) as shown in Table 3 where for each time also the positioning of the model, in terms of distance from nozzle exit and angle of attack, is indicated. After each CFD computation, the thermal state inside the panel is computed through an instationary simulation of a certain time, and at the end, wall temperature distribution is imposed as boundary condition for the following CFD computation. Moreover, during the instationary thermal simulation, the effect of temperature on heat flux at the wall is accounted for through the following equation:

$$q_{wall}(x, T) = h_c(x, \bar{T}) \cdot (h_{aw} - cp \cdot T_{wall}) \quad (3)$$

being  $h_c(x, \bar{T})$  evaluated at the beginning of each thermal simulation from the results of the previous CFD calculation.

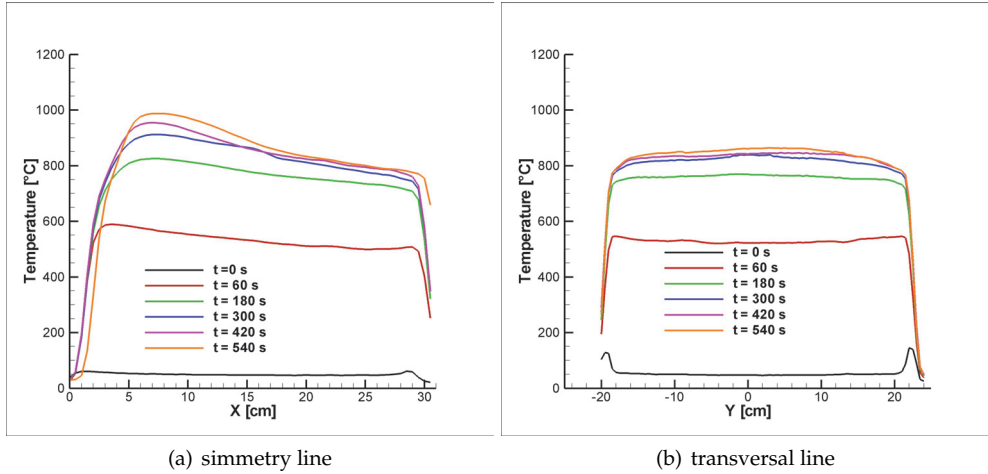


Fig. 23. Temperature time history

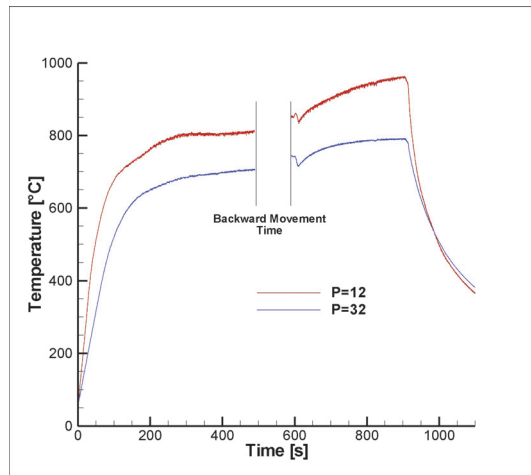


Fig. 24. Temperature time evolution

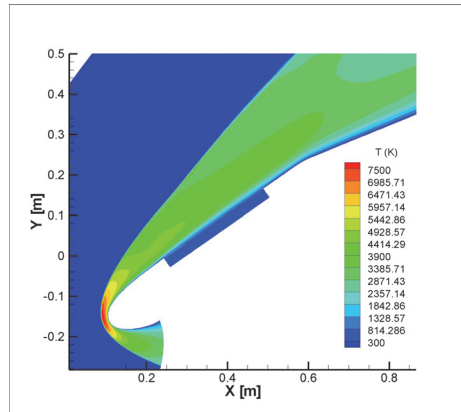
In Fig.25 external and internal temperature field at the end of the first phase (i.e.  $t=570$  s) is shown; heat flux propagation inside the panel, whose temperature reaches values of about 800K, is quite evident whereas the underlying layer, which protect the inner part of the model, remains relatively cold due to its insulating properties.

Temperature evolution over the surface for this first phase is reported in Fig.26 and compared with the experimental results extracted from the thermocamera measurements. The comparison shows a rather good agreement; the experimental results are affected by the cooling of the leading edge and the holder that is not simulated in the numerical rebuilding therefore the comparison at the tip and the trailing edge of the panel is not meaningful. In order to compare the time evolution of temperature on the panel, two points located near the tip and near the trailing edge have been considered. The results are shown in Fig.27. The

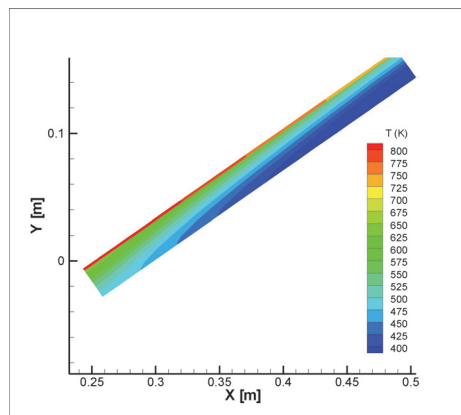


Run ID	Time [s]	Distance from nozzle exit [mm]	AoA [deg]
1	0	200	25
2	570	200	25
3	575	450	25
4	580	750	25
5	589	950	25
6	597	950	25
7	603	950	30
8	612	950	35
9	916	950	35

Table 3. Conditions for the numerical rebuilding



(a) entire field



(b) panel

Fig. 25. External and internal temperature field at t=570 s

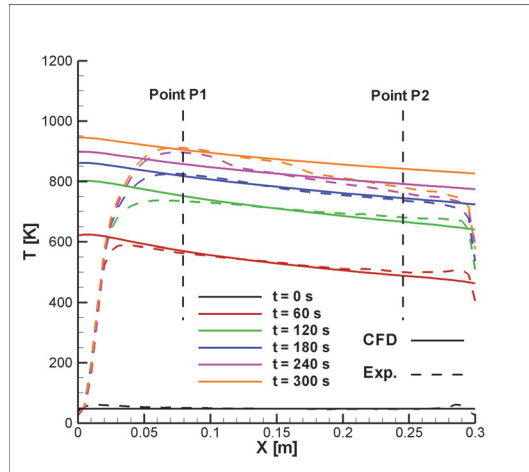


Fig. 26. Temperature evolution for different time instants

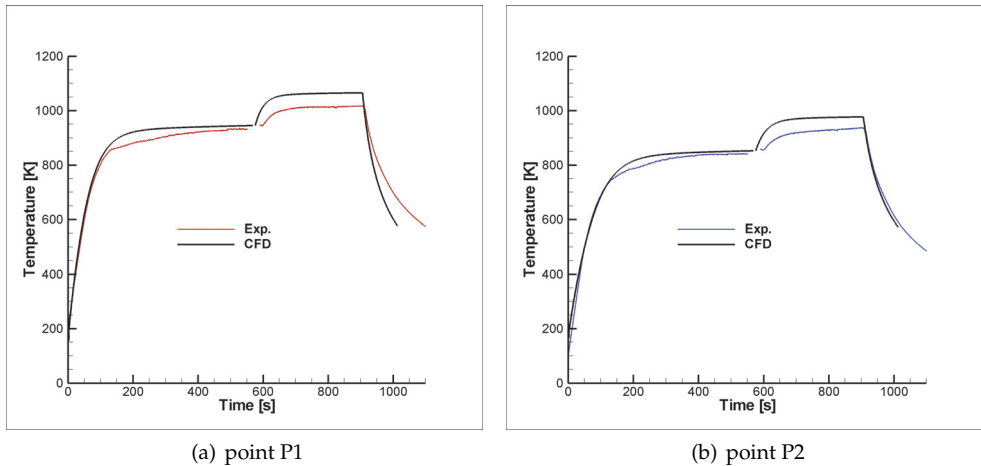


Fig. 27. Time evolution of temperature on the panel

comparison between numerical and experimental results is quite good for the first phase of the test, both during the initial heating (from  $t=0$  s to  $t=200$  s) and the following phase up to the steady state (from  $t=200$  s to  $t=570$  s). On the other side, after the backward movement, the comparison shows some discrepancies. In this case, in addition to the error associated to the numerical simulation there is also the increased uncertainty associated to the experimental measurement induced by a non optimized angle of view between the thermocamera and the model since this factor was optimized for the first position of the model. The behaviour of the curve is represented quite well by the numerical results, being differences found in the absolute value of temperature of about 50K. The same consideration apply also for the analysis of the cooling phase.

## 9. Conclusions

The experimental and numerical activities carried out for the analysis of the PWT test on the wing leading edge model have been presented. The IR thermo-graphic images have been processed through an ad-hoc developed mapping procedure to be directly compared with the results of the numerical analysis carried out through a non standard approach based on the unsteady simulation of the test and a coupling between the external aerodynamic field and the internal thermal field. Differences of about 100K have been found between the experimental and numerical results at the end of the test. It has been found that these differences increased during the second phase of the test when the angle of view between the thermocamera and the panel was not optimized. It has to be remarked that some uncertainties can be also associated to this type of numerical rebuilding especially for what concerns the surface characteristics of the material, in terms of emissivity (for thermocamera measurement) and catalytic behaviour (for CFD numerical rebuilding). In order to use experimental data to validate the numerical models, the main sources of these uncertainties should be reduced. In detail:

- It should be preferable to have direct measurements of the heat flux which can be directly compared with the numerical results.
- The real test conditions should be determined more in detail; a variation of the energetic level in the plasma flow during the test can cause a different dissociation of air mixture ahead the model and therefore different catalytic recombination processes at the wall. The measurement of the heat flux carried out in the test chamber through the calorimetric copper probe (fully catalytic), beyond the instrumental uncertainties, is not able to completely describe the different energetic contributes of the flow exiting from the expansion nozzle. As matter of fact, the measured heat flux is the sum of the convective and diffusive term whereas the correct repartition of these two terms is important especially dealing with partially catalytic materials.
- The uncertainties related to the knowledge of the material should be reduced: not only in terms of emissivity or catalysis but also thermal conductivity, capacity and density to accurately rebuild also the thermal field inside the model.

In any case, the possibility to apply the developed numerical/experimental procedure to rebuild a so articulated test, due to the adopted procedure and the dimensions of the model itself, has been demonstrated even though the main sources of errors, both from an experimental and numerical point of view, need to be further reduced.

## 10. Acknowledgments

Authors would like to thank the Italian Space Agency, that funded the current project, in particular dr. Emanuela D'Aversa, and Thales Alenia Space as Prime contractor and test article assembly responsible, in particular the Program Manager dr. Roberto Viotto and Project Manager, dr. Franco Fossati. They are also grateful to the CIRA project manager dr. Giuliano Marino and to the PWT facility team, in particular to Eduardo Trifoni for his work during the entire project.

## 11. References

- Battista, F., Rufolo, G. & Di Clemente, M. (2007). Aerothermal environment definition for a reusable experimental re-entry vehicle wing, *Proceedings of 39<sup>th</sup> AIAA Thermophysics Conference*. Miami, USA.

- Borrelli, S. & Pandolfi, M. (1990). An upwind formulation for the numerical prediction of non equilibrium hypersonic flows, *12<sup>th</sup> International Conference on Numerical Methods in Fluid Dynamics*. Oxford, United Kingdom.
- De Filippis, F., Caristia, S., Del Vecchio, A. & Purpura, C. (2003). The scirocco pwt facility calibration activities, *Proceedings of 3<sup>d</sup> International Symposium Atmospheric Reentry Vehicle and Systems*. Arcachon, France.
- Di Clemente, M., Rufolo, G., Cardone, G. & Ianiro, A. (2008). Aerothermal coupling methodology for the rebuilding of a plasma wind tunnel test and comparison with an advanced infrared measurement technique, *Proceedings of 6<sup>th</sup> European Symposium on Aerothermodynamics for Space Vehicles*. Versailles, France.
- Edney, B. (1968). Anomalous heat transfer and pressure distribution on blunt bodies at hypersonic speeds in the presence of an impinging shock wave, *Technical report*, FFA. Rep.115.
- Marini, M., Di Benedetto, S., Rufolo, G., Di Clemente, M. & Borrelli, S. (2007). Test design methodologies for flight relevant plasma wind tunnel experiments, *Proceedings of West-East High Speed Flow Field Conference*, Moscow, Russia.
- Pezzella, G., Battista, F., Schettino, A., Marini, M. & De Matteis, P. (2007). Hypersonic aerothermal environment preliminary definition of the cira ftb-x reentry vehicle, *Proceedings of West-East High Speed Flow Field Conference*. Moscow, Russia.
- Ratti, F., Muylaert, J., Gavira, J. & Walpot, L. (2008). European experimental re-entry testbed expert: Qualification of payloads for flight, *Proceedings of 6<sup>th</sup> European Symposium on Aerothermodynamics for Space Vehicles*. Versailles, France.
- Tumino, G. (2006). Hypersonic systems and technologies developments at esa, *14<sup>th</sup> AIAA/AHI International Space Planes and Hypersonic Systems and Technologies Conference*. Canberra, Australia.